Jianzhong Xu
Yulin Wu
Yangjun Zhang
Junyue Zhang

Fluid Machinery and Fluid Mechanics
4th International Symposium (4th ISFMFE)

Jianzhong Xu
Yulin Wu
Yangjun Zhang
Junyue Zhang

Fluid Machinery and Fluid Mechanics

4th International Symposium (4th ISFMFE)

With 626 figures

TSINGHUA UNIVERSITY PRESS

Springer

EDITORS:

Prof.Jianzhong XU
CSET Chinese Academy of Sciences
No.11 Bei Si Huan Xi Lu
100190, Beijing, China

Prof.Yangjun ZHANG
Department of Automotive Engineering
Tsinghua University
100084, Beijing, China

Prof.Yulin WU
Department of Thermal Engineering
Tsinghua University
100084, Beijing, China

Prof.Junyue ZHANG
National Key Laboratory of Diesel Engine
Turbocharging Technology P.O.Box 22
030706, Datong, Shanxi, China

ISBN 978-7-302-18728-8 **Tsinghua University Press, Beijing**
ISBN 978-3-540-89748-4 **Springer Berlin Heidelberg New York**
e ISBN 978-3-540-89749-1 **Springer Berlin Heidelberg New York**

Library of Congress Control Number: 2008940137
This work is subject to copyright. All rights are reserved, whether the whole or part of the material is concerned, specifically the rights of translation, reprinting, reuse of illustrations, recitation, broadcasting, reproduction on microfilm or in any other way, and storage in data banks. Duplication of this publication or parts thereof is permitted only under the provisions of the German Copyright Law of September 9, 1965, in its current version, and permission for use must always be obtained from Springer-Verlag. Violations are liable to prosecution under the German Copyright Law.

© 2009 Tsinghua University Press, Beijing and Springer-Verlag GmbH Berlin Heidelberg
Co-published by Tsinghua University Press, Beijing and Springer-Verlag GmbH Berlin Heidelberg

Springer is a part of Springer Science+Business Media
springer.com

The use of general descriptive names, registered names, trademarks, etc. in this publication does not imply, even in the absence of a specific statement, that such names are exempt from the relevant protective laws and regulations and therefore free for general use.

Cover design: Frido Steinen-Broo, EStudio Calamar, Spain
Printed on acid-free paper

ORGANIZING COMMITTEE

Chairman	Jianzhong XU (Chinese Academy of Sciences)
Vice Chairmen	Kangmin CHEN, Chuanggang GU, Leqin WANG, Zengquan Wang, Zhongqi WANG, Yulin WU, Guang XI, Shuyong ZHANG, Yangjun ZHANG, Xiaolu ZHAO
General Secretary	Xingqi LUO
Secretary	Hongying KE

INTERNATIONAL TECHNICAL COMMITTEE

AVELLAN Francois	BOHN Dieter E.	DICK Erik	EGUSQUIZA Eduard
GAJIC Aleksandar	GOTO Akira	GOULAS Apostolos	HAYAMI Hiroshi
HELLMANN D. H.	IKOHAGI Toshiaki,	KATO Chisachi	KIM Kwang Ho
KIM Kwang Yong	LEE Young Ho	SUN Zixiang	TSUJIMOTO Yoshi
TSUKAMOTO Hiroshi	WALKER G. J.	WINOTO S. H.	

INTERNATIONAL ADVISORY COMMITTEE

AHMED Rafiuddin M.	BÖHLE Martin	CHUNG Jin Taek	FRISCHKORN Petra
FURUKAWA Akinori	KIM Man Eung	KIM Youn Jea	KOUIDRI Smaine
LEE Dae Sung	LEE Tea Seak	MARTINEZ-BOTAS R.	MATSUMOTO Y.
MIYAGAWA K.	NISHI Michihiro	OH Min Hwan	SERRANO J. R.
SHIN Byeong Rog	SHYY Wei	SUSAN-RESIGA Romeo	WU Jingchun
YOON Joon Yong			

FOREWORD

Following the experience gained in organizing the International Symposium on Fluid Machinery and Fluid Engineering in 1996, 2000 and 2004, it was decided to hold the Fourth International Symposium on Fluid Machinery and Fluid Engineering. This fourth symposium is now to convene on November 25-27 in Beijing.

The Chinese Society of Engineering Thermophysics (CSET) is a well-established engineering society devoted to theoretical and applied research in the thermal and fluid sciences. It was first founded by the late Dr. C.H. Wu, well-known leader in the field of turbomachinery. The Chinese Society of Engineering Thermophysics (CSET) organized the First, the Second and the Third International Symposium on Fluid Machinery and Fluid Engineering, in 1996, in 2000, and in 2004 successfully. Fluid machinery is a kind of widely used machines and has a great action to all fields of the national economy. The purpose of the Fourth Symposium is the same as before, to provide a common forum for exchange of scientific and technical information worldwide on fluid machinery and fluid engineering for scientists and engineers. The main subject of this symposium is "Fluid Machinery for Energy saving". There is the "Mei lecture" in the symposium to make reports on the development and the new research area of fluid machinery in order to commemorate the late professor Mei Zuyan in the field of fluid machinery in China.

This volume of proceedings contains 69 highly informative technical papers that have been selected by peer review and are to be presented at the Mei lecture session and the technical sessions of the symposium. They cover very well the latest practice and findings in the fields of fluid machinary and fluid engineering.

Jianzhong XU, Professor

Chairman of the Organizing Committee

September 2008

CONTENTS

Invited Mei Lecture Session

1. Heat Transfer in an Automotive Turbocharger Under Constant Load Points: an Experimental and Computational Investigation
   A. Romagnoli, R.M.F. Botas 1-7
2. Multi-Scale Thermal Measurement and Design of Cooling Systems in Gas Turbine
   Hyung Hee Cho, Kyung Min Kim, Sangwoo Shin, Beom Seok Kim and Dong Hyun Lee 8-13
3. Reduced Size Bi-Flow Centrifugal Pump as Ventricular Assist Device for End-Stage Patients
   Andy C C Tan 14-19
4. Experimental Investigation of Wall Pressure Fluctuations in Axial Flow Fans with Different Swept
   J. Hurault, S. Kouidri, F. Bakir and R. Rey 20-26
5. Meso and Macro-Scales Fluid Flow Simulations with Lattice Boltzmann Method
   A.A. Mohamad 27-32
6. Engineering Flow Performance by Local Dynamics: Theories and Applications
   Jiezhi Wu, Feng Mao, Weidong Su, Hong Wu and Qiushi Li 33-43
7. One-Dimensional Analysis of Full Load Draft Tube Surge
   Yoshinobu Tsujimoto, Koichi Yonezawa, Changkun Chen 44-56
8. Future Aspects and Developments for Advanced CO_2-Free Power Station Technologies
   D. Bohn 57-65
9. Numerical Analysis of Impeller-Volute Tongue Interaction and Unsteady Fluid Flow in a Centrifugal Pump
   K.W Cheah, T.S. Lee, S.H Winoto and Z.M Zhao 66-71
10. A Procedure for the Unsteady Characterization of Turbochargers in Reciprocating Internal Combustion Engines
    A. Torregrosa, J. Galindo, J.R. Serrano and A. Tiseira 72-79
11. Cavitation and Turbopump Hydrodynamics Research at Alta S.P.A. and Pisa University
    Angelo Cervone, Lucio Torre, Angelo Pasini and Luca d'Agostino 80-88
12. Decelerated Swirling Flow Control in the Discharge Cone of Francis Turbines
    Romeo Susan-Resiga and Sebastian Muntean 89-96
13. Hydraulic Oscillations Caused by the Earthquake
    Aleksandar Gajic 97-106

Fundament and Analysis

14. A Numerical Investigation of the Effect of End-Wall Boundary Layer Skew on the Aerodynamic Performance of a Low Aspect Ratio, High Turning Compressor Cascade
    Martin Böhle, Udo Stark 107-114
15. Design and Analysis of a Radial Turbine with Back Swept Blading
    Liam Barr, Stephen Spence and Paul Eynon 115-121
16. Swirl Flow and Heat Transfer Through Square Duct with Twisted Tape Insert
    Ho-Keun Kang, Soo-Whan Ahn, Bachtiar-Krishna-Putra Ary and Jong-Woong Choi 122-129
17. Multi-Objective Automated Optimization of Centrifugal Impeller Using Genetic Algorithm
    Wenbin Zhang, Xiaomin Liu 130-136
18. Axisymmetric Weakly Compressible Transient Pipe Flow and Water Hammer Control
    Lijun Xuan, Feng Mao and Jiezhi Wu 137-144
19. Research on the Optimization Method of Impeller Meridional Contour and 3-D Blade
    Jinling Lu, Guang Xi and Xingqi Luo 145-152

Experimental Study

20. LDV and PIV Techniques Applied to Turbomachinery Geometry Constrains
G. Bois, P. Dupont, A. Dazin and G. Caignaert 153-160
21. Limiting Streamlines Measurement in Contra-Rotating Axial Flow Pump
Akinori Furukawa, Satoshi Usami, Yusuke Tsunenari, Satoshi Watanabe and Kusuo Okuma 161-166
22. Experimental Modeling of Polluted Air Dispersion in Street Canyons of Metropolitan.
Hyoung-June Kim, Joon-Yong Yoon and Nak-Won Sung 167-172
23. PIV Study of Tip Leakage Flow in Linear Compressor Cascade
Ren Dai, Zhonghua Huang, Ze Chen and Kangmin Chen 173-178
24. Study on Cavitating Turbulent Flow around a Hydrofoil
Mindi Zhang, Guoyu Wang and Xiangbin Li 179-184

Numerical Simulation

25. Microchannel Heat Sinking: Analysis and Optimization
Afzal Husain, Kwang-Yong Kim 185-190
26. A Numerical Simulation of a Flow in Pem Fuel Cell Stack Using Lattice Boltzmann Method
Jae-Hoon Lee, Seok-Yun Jeon, Joon-Yong Yoon, Sung-Joon Byun and Myung-Seob Shin 191-194
27. Simulation of Gas Flow in a Microchannel by Lattice Boltzmann Method
In-Won Park, Myung-Seob Shin, Sung-Joon Byun, Joon-Yong Yoon 195-200
28. Numerical Solution of Navier-Stokes Equations for Separating and Reattaching Flow over a Double Steps Expansion and Contraction
Khaled Alhussan 201-205
29. Computation of Several Turbulent Flows with the Des-Sa Model
Yang Guo, Chisachi Kato, Yoshinobu Yamade and Hong Wang 206-214
30. Comparative Study of Turbulence Models in Separated-Attached Diffuser Flow
Liu Chen, Ailing Yang, Ren Dai and Kangmin Chen 215-220
31. Simulating the Blood Flow for the Aorta with a Stenosis
Ying Li, Xianwu Luo, Mingkui Zhang, Yao Zhang, Shuhong Liu and Hongyuan Xu 221-226

Turbocharger

32. Through Flow Models for Engine Turbocharging and Exhaust Heat Recovery
Yangjun Zhang, Weilin Zhuge, Shuyong Zhang and Jianzhong Xu 227-233
33. Study on the Seal Leakage of Turbocharger
Hong He, Siyou Xu, Ruiqian Yan and Jianbo Ji 234-237
34. Study on the Pre-Tightening Force About the Nut of the Turbocharger Shaft
Li Long, Hong He and Wei Pei 238-241
35. Vibration Property Analysis of Turbocharger Turbine Blade Under Different Loads
Wei Pei, Dongmei Zhang and Jizhong Zhang 242-245
36. A Method to Solve the Problem of the Application of Ti-Al Turbine
Xiujuan Wang 246-248

Compressor and Fan

37. A Study on Rotor Blades for a Two-Stage Jet Fan
Michihiro Nishi, Kouichi Yoshida, Minoru Okamoto and Hiroyasu Nakayama 249-254

38. Flow Characteristics in a Cross-Flow Fan with Various Design Parameters
Youn J. Kim 255-261
39. Determination of an Optimum Orbiting Radius for an Oil-Less Scroll Air Compressor
Yong Ho Lee, Tae Hun Kwon and Hyun Jin Kim 262-267
40. Studies on Moving Coil Linear Compressor Used for Refrigerator
Zhihai Li, Shuiying Zheng and Rongren Wu 268-272
41. Two-Zone Modeling Prediction Method of Centrifugal Compressor Performance
Shuqi Li, Junyue Zhang and Weidong Xing 273-278
42. Effect of Swept Blade on Performance of a Small Size Axial Fan
Ailing Yang, Tao Tang, Hui Zhang and Kangmin Chen 279-284

Pump

43. Multi-Objective Optimization of Blood-Pump with Conical Spiral Groove Bearings
Masahiro Kaneko, Yoichi Nakamura, Koji Miyazaki and Hiroshi Tsukamoto 285-290
44. Analysis of Unsteady Flow in a Radial Diffuser Pump
Jianjun Feng, Friedrich-Kar Benra, Hans Josef Dohmen 291-296
45. Design and Research of Vertical Multistage Barrel Condensate Pump
Jiegang Mu, Shuihua Zheng, Hongying Deng and Shengchang Zhang 297-300
46. Influence of Support Shapes on the Efficiency of Bulb Tubular Pumps
Yan Jin, Chao Liu, Fangping Tang 301-305
47. Computing Critical Speeds for Multiple-stage Centrifugal Pumps with Dependent Support Properties
Chunxin Chen, Dazhuan Wu, Shanguang Tan and Leqin Wang 306-309
48. Numerical Investigation on Impeller-Volute Interaction in a Low Specific Speed Centrifugal Pump with Tongue Profile Variation
Pengcheng Guo, Xingqi Luo, Jinglin Lu and Xiaobo Zheng 310-315

Turbine

49. Experimental Study on a Direct Drive Turbine for Wave Power Converter System
Young-Ho Lee, Young-Do Choi, Chang-Goo Kim, Young-Jin Cho, Sang-Hyun Nam and You-Taek Kim 316-321
50. Determination of Optimum Nozzle Shape of a Direct Drive Turbine by CFD Analysis
Young-Do Choi, Chang-Goo Kim, You-Taek Kim and Young-Ho Lee 322-327
51. Comparison of Several Subgrid-Scale Models for Large-Eddy Simulation of Turbulent Flows in Water Turbine Jiamei Ma, Fujun Wang and Xuelin Tang 328-334
52. Flow Simulation and Performance Prediction of a Kaplan Turbine
Shuhong Liu, Shangfeng Wu, Michihiro Nishi and Yulin Wu 335-340
53. Analysis of Pressure Fluctuation in Draft Tube of Kaplan Turbine
Xiaobo Zheng, Xingqi Luo and Pengcheng Guo 341-344
54. Numerical Simulation of Hydraulic Turbine Based on Fluid-Structure Coupling
Demin Liu, Shuhong Liu, Yulin Wu and Xiao-bing Liu 345-351

System of Fluid Machinery

55. Numerical Simulation of Drawdown in Pump Sumps
S.N. Shukla and J.T. Kshirsagar 352-356
56. Recent Development of Lagrangian Vortex Method and Its Application into Fluid Machinery and Fluid Engineering Kyoji Kamemoto and Akira Ojima 357-362

57. Computer Stimulation of Air-Flowed Smashing Process
Yan Cui, Xiaoling Ge 363-365
58. Analysis on Modeling Rotor System with Sidling Bearing and Ring Seal by Using FEM
Shiliang Ping, Shanguang Tan, Dazhuan Wu and Leqin Wang 366-370
59. Cavitating Flow Analysis in a Closed Pump Sump
Yu Xu, Shuhong Liu, Yong Li and Yulin Wu 371-376

Jet and Seal

60. Aerodynamic Performance of Double-Sided Labyrinth Seals
Tong Seop Kim, Yungmo Kang and Hee Koo Moon 377-382
61. Study on the Leakage Flow Field in the Shaft Brush Seal of Steam Turbines
Jun Li, Xin Yan, Zhenping Feng, Shinnosuke Obi 383-388
62. Transverse Jets Analysis on High Speed Rotating Body of Revolution
Khaled Alhussan 389-393
63. Numerical Investigation of High-Power Synthetic Jet Actuator Flowfield and Its Influence on Vectoring Control Yanming Liu, Baoguo Wang, Shuyan Liu, Naiming Wu 394-398

Other Fluid Machinery

64. Use of CFD for Thermal Coupling in Aeroengine Internal Air Systems Applications
Zixiang Sun, John W. Chew and Nicholas J. Hills 399-404
65. Optimization of Patterned Grooves Micromixer Using the Design of Experiments
Chul-Kyu Kim, Joon-Yong Yoon, Hyun-Jong Lee, Myung-Seob Shin and Sung-Joon Byun 405-410
66. Numerical Study on Mechanical Characteristics of Aerostatic Bearing
Zhaoqin Yin, Dongsheng Li 411-414
67. Valve Dynamic Characteristic and Stress Analysis of Reciprocating Compressor Under Stepless Capacity Regulation
Jiangming Jin, Weirong Hong, Rongren Wu 415-420
68. Influence of the Floating-Ring Bearing Parameters on Stability of Turbocharge Rotor-Bearing System
Xinjun Zhao, Hong He and Siyou Xu 421-425
69. Investigation of the Meter Factor of Turbine Meter with Unsteady Numerical Simulation
Gang Chen, Yulin Wu, Suhong Fu, Mingjie Li, Guangjun Cao 426-433

Author Index 434-435

The 4th International Symposium on Fluid Machinery and Fluid Engineering
November 24-27, 2008, Beijing, China
NO. 4ISFMFE-IL09

Heat Transfer in an Automotive Turbocharger Under Constant Load Points: an Experimental and Computational Investigation

A. Romagnoli[1], R.M.F. Botas[*2]

[1] Dept. of Mechanical Engineering, Imperial College of Science and Technology
[*2] Dept. of Mechanical Engineering, Imperial College of Science and Technology
Exhibition Road, South Kensington SW7 2AZ, London, United Kingdom
Tel: +44 – 2075947241
E-mail: r.botas@imperial.ac.uk

Abstract Nowadays the turbocharger is one of the most commonly used devices to supercharge an engine. Heat fluxes in the turbocharger are not negligible and affect the performance prediction of the turbine. From different experimental investigations it has become clear that heat fluxes from the turbine to the compressor have a great influence on the compressor performance and therefore on the overall turbocharger performance. For this reason understanding the heat transfer within the turbocharger components and from the turbocharger to the ambient environment is essential important to determine the critical heat paths to be considered in the design tools.

In order to investigate the behavior of the heat fluxes occurring in the turbocharger an experimental and computational study has been carried out at Imperial College on a Ford 2.0 liter diesel engine. Beyond the standard measurements necessary to determine the operating points of the compressor and turbine, a novel set of seventeen thermocouples was installed on the turbocharger measuring the inner and outer wall temperature of the turbine and compressor casing, the bearing housing and exhaust manifold temperatures. In addition to these, the air and oil flow rate, temperature and pressure were also measured.

A one-dimensional model was also developed. The developed algorithms are merged using a MATLAB programme that calculates the compressor non-adiabatic efficiencies and exit temperatures based on the turbocharger geometry, the turbine inlet temperature and the maps of the turbine and the compressor in adiabatic conditions. The simplification of the turbocharger was kept as low as possible and, unlike the other models, no heat transfer coefficients were used.

The test results provided profound insight into the temperature distributions occurring within the turbochargers and in particular the role played by the exhaust manifold. Furthermore, the data generated with the test enabled us to quantify the heat fluxes and to validate the one-dimensional model. The model prediction of the temperature and non-adiabatic efficiencies is a significant improvement on previous models. The main outcomes of the research carried out at Imperial are reported in this paper.

Keywords heat transfer, turbocharger, turbine, compressor, engine, model, experimental, performance

Nomenclature

Eng	*Engine side*
Top	*Top side*
Ext	*External side*
I/O	*Ratio between Inner and Outer wall*
O/I	*Ratio between Outer and Inner wall*
η	*Efficiency*
h	*Enthalpy* [W/mK]
T	*Temperature* [K]

Subscripts

adi	*Adiabatic*
dia	*Non-adiabatic*
C	*Compressor*
is	*Isentropic*
1	*Inlet to the compressor*
2	*Exit to the compressor*

1 Introduction

In general, most processes occurring in turbo machinery applications are treated as adiabatic since the influence of heat transfer on the calculation is often negligible. However in some cases, heat transfer can have an influence on performance thus making a non-adiabatic treatment more appropriate. Since the hot turbine of the turbocharger is located in close proximity to the relatively cold compressor, it is obvious that there will be heat exchange between turbine and compressor. In general, the non-adiabatic process can be separated into three stages of heat transfer. The first stage involves heat that is transferred before the compression or expansion process starts. In the second stage, a fraction of heat is introduced during the process and the third stage accounts for the heat that is added after the process is completed.

Heat transfer analysis usually involves quantifying the heat transfer rate for some known temperature difference. It is recognised that heat can be transferred by one or a combination of three separate modes known as conduction, convection and radiation. Conduction occurs in a stationary medium; convection requires a moving fluid while radiation occurs in the absence of any medium distinguishing it as a part of the electromagnetic spectrum. Although it is useful to look at each one of these processes in a distinct way, they often occur together. In particular, on a turbocharger all of these three processes occur at the same time and are closely interrelated. The complexity of turbocharger geometry introduces many possible heat transfer mechanisms inside the turbocharger as well as from the turbocharger to the environment, as illustrated in Fig. 1.

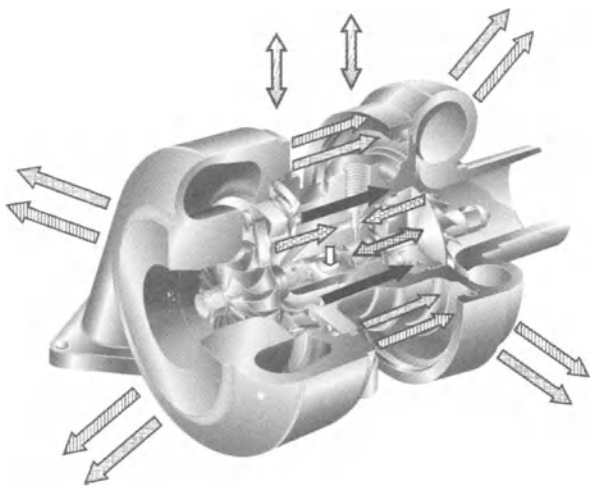

Fig. 1 Heat fluxes in a turbocharger (Shaaban 2006)

Heat transfer from the turbine to the compressor through the bearing housing must be considered even though the cooling oil reduces the amount of heat transfer that is transferred by conduction from the turbine to the compressor; in addition heat transfer from the turbine to the environment takes place by means of radiation and free convection and heat transfer from the compressor to the environment takes place likewise by means of radiation and free convection, even though radiation heat transfer from the compressor is very small because of the low emissivity.

Such a complex pattern of heat fluxes makes experimental investigation of the heat transfer very difficult. As a consequence of this, not many experiments on heat transfer have been carried out in the past. Rautenberg et al. (1983 and 1984) first analysed the influence of heat transfer from the hot turbine to the compressor by testing two different turbochargers with different axial distance. The results showed that the axial length plays an important role in the deterioration of the mechanical power. Beyond the standard measurements necessary to determine the operating point of a compressor and turbine, Bohn et al. (2003) also measured the surface temperature of the turbine casing, showing that the temperature of the turbine casing varies linearly with the inlet temperature.

All of the experiments carried out so far were performed in a purpose-built test facility that enabled a wide range of test conditions to be covered. However the facility did not permit the analysis of the real conditions occurring when the turbocharger is installed on the engine. These are extremely important since the close proximity to the engine and in particular to the exhaust manifolds make the effects of heat transfer on the turbocharger performance even more relevant. Therefore the aim of the current research is to estimate the role played by the engine in the overall heat transfer occurring within the turbocharger from both a qualitative and quantitative point of view. A commercial turbocharger was installed on a 2.0 litre diesel engine and an experimental and computational investigation was carried out and is reported here.

2 Experimental Investigation

A schematic diagram of the engine test rig at Imperial College is shown in Fig. 2. A 25kW DC electric motor/ generator supplies air to the inlet manifold via the intercooler either by the compressor of the turbocharger or by a roots blower supercharger externally driven through a multiplication gearbox. An eddy current dynamometer was used to keep the engine load constant at a desired

value. The engine was operated via an instrumentation rack consisting of controls to operate the dynamometer, to crank and run the engine and to stop operation in case of an emergency.

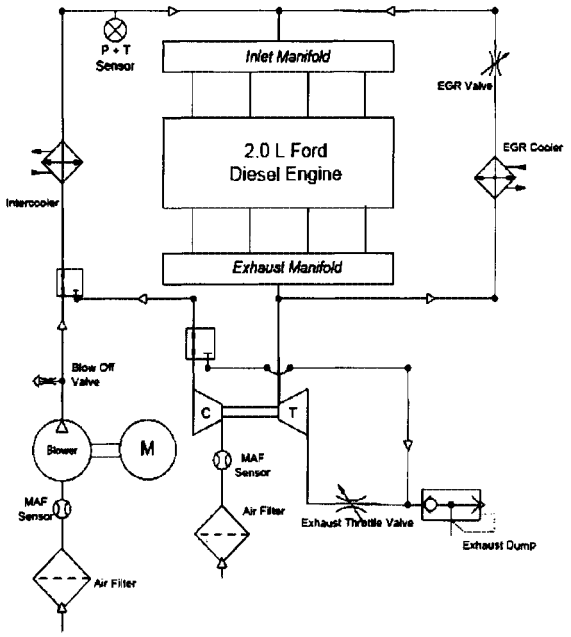

Fig. 2 Test rig layout (Kyartos 2006)

Beyond the standard measurements necessary to determine the operating points of the compressor and turbine, the turbocharger was set up in order to enable the monitoring of the temperatures at seventeen stations, as shown in Fig. 3.

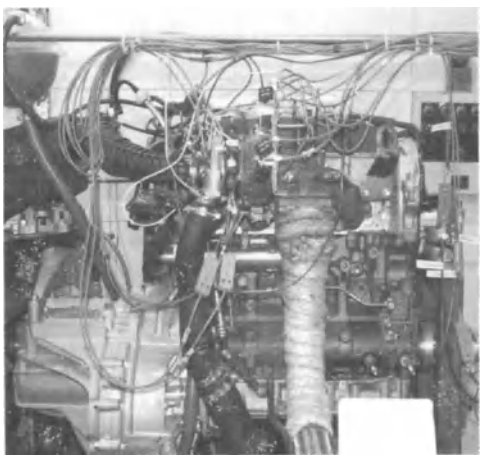

Fig. 3 Test rig

In detail the following measurements have been carried out:

- Inlet and exit air temperature to the compressor
- Total pressure at the inlet and exit to the compressor
- Inlet and exit air temperature to the turbine
- Total pressure at the inlet and exit to the turbine
- Inner and outer temperatures along the compressor casing in three different locations
- Inner and outer temperatures along the turbine volute in three different locations
- Surface temperature of the intake manifolds
- Surface temperature of the bearing housing
- Inlet and exit temperature of the oil flow
- Air and oil flow rate
- Shaft speed

3 Test Results

The turbocharger under study was tested under constant load points for a range of engine speeds. Measurements were obtained for engine speeds of between 1000 and 3000 rpm at steps of 500 rpm. For each engine speed the load applied was varied from 16 to 250 Nm, as reported in Table 1.

Table 1 Test conditions

Speed [RPM] / Torque [Nm]	16	50	100	125	150	200	250
1000	√	√	√				
1500	√	√	√	√	√	√	√
2000	√	√	√		√	√	√
2500	√	√	√		√	√	
3000	√	√	√		√	√	

(1) Performance comparison

In order to evaluate the effects of heat transfer on the deterioration of the mechanical power, the non-adiabatic efficiency was used as dimensionless parameter. The non-adiabatic efficiency represents the apparent compressor efficiency measured under non-adiabatic operating conditions and it is defined as the ratio between the isentropic and the actual enthalpy rise.

$$\eta_{dia,c} = \frac{\Delta h_{adi,is}}{\Delta h_{dia}} = \frac{T_{2,adi,is} - T_1}{T_2 - T_1} \tag{1}$$

$\eta_{dia,c}$ differs from the adiabatic efficiency (below) in which the adiabatic enthalpy rise is taken into account:

$$\eta_{adi,c} = \frac{\Delta h_{adi,is}}{\Delta h_{adi}} = \frac{T_{2,adi,is} - T_1}{T_{2,adi} - T_1} \tag{2}$$

A comparison between the non-adiabatic efficiencies and the correspondent adiabatic efficiencies extrapolated by the cold maps provided by the turbocharger manufacturer is reported in Fig. 4 in terms of *relative efficiency*. This

parameter has been introduced for reasons of confidentiality and is defined as the ratio between the compressor peak efficiency and the measured efficiencies. It can be seen that the difference existing between the adiabatic and the non-adiabatic efficiencies tends to increase as the turbine inlet temperature increases. The deviation of the non-adiabatic efficiency from the adiabatic efficiency goes from a maximum of 30% (at low speeds) to a minimum of 15% (at high speeds). This can be explained if we consider that at high rotational speeds, the turbocharger works in conditions similar to those at design point. At this point all of the losses occurring within the turbocharger are assumed to be at a minimum and the efficiency drop is less significant.

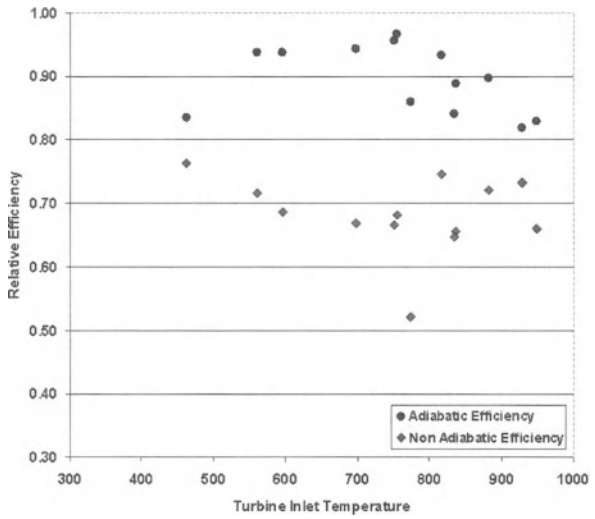

Fig. 4 Comparison between adiabatic and non-adiabatic compressor performance

(2) Temperatures on the Turbine and Compressor casing

For a fixed engine speed, the inner and outer wall temperature of the turbine and compressor casings was measured in three different locations (*Engine, Top, and External*), as shown in Fig. 5.

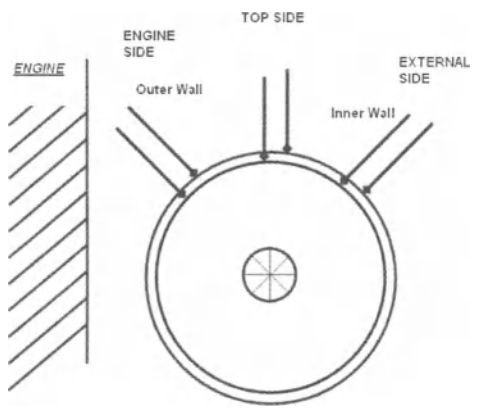

Fig. 5 Thermocouple positions

The heat transfer mechanism occurring in the turbine can be described as follows: the hot gases flowing into the turbine heat up the inner surface of the casing by forced convection. A temperature gradient between the inner and the outer surface of the casing is therefore created, leading to the generation of a heat flux towards the external wall where, by means of radiation and natural convection to the environment, the turbine is cooled down. In contrast to the turbine, the inner wall temperature of the compressor casing is lower than the outer one. This can be attributed to the air flowing in the compressor which tends to cool down the casing subjected to radiation and conduction due to the turbine, the bearing housing and the exhaust manifold.

Table 2 reports the temperature difference between the inner and the outer wall for both the turbine and the compressor casings. The maximum temperature observed on the compressor casing at maximum engine speed and load is almost five times lower than the maximum temperature of the turbine. Furthermore, a gradient of up to 4.23% has been measured between the outer and inner wall of the compressor casing at 3000 rpm on the external side. This is more than 50% less than the temperature gradient seen in the turbine and demonstrates that, although the effects of heat transfer on the compressor side is less significant than those occurring in the turbine; they are nevertheless not negligible since they significantly affect the compressor performance.

Table 2 Temperature difference between the inner and the outer wall for both the turbine and the compressor

	Turbine			Compressor		
	Eng	Top	Ext	Eng	Top	Ext
1050 rpm	I/O	I/O	I/O	O/I	O/I	O/I
8 Nm	2.99%	2.63%	7.34%	0.16%	0.54%	0.32%
50Nm	3.22%	3.53%	10.63%	0.38%	0.93%	1.16%
1500 rpm						
8 Nm	3.12%	2.73%	9.91%	0.03%	0.45%	1.47%
250 Nm	3.40%	5.51%	11.01%	7.22%	4.12%	2.15%
2000 rpm						
8 Nm	3.42%	4.33%	10.13%	2.35%	1.70%	1.91%
250 Nm	4.98%	5.56%	10.64%	12.2%	3.57%	2.31%
2500 rpm						
8 Nm	2.95%	2.57%	10.38%	6.16%	2.35%	2.40%
200 Nm	5.52%	4.90%	10.61%	8.46%	3.84%	4.09%
3000 rpm						
16 Nm	3.81%	3.64%	9.04%	1.36%	1.96%	2.79%
200 Nm	4.54%	5.52%	11.09%	2.38%	4.23%	4.17%

(3) Bearing housing and Exhaust manifold surface temperature

The surface temperatures of the bearing housing and of the exhaust manifold were also measured. The results are reported in Table 3.

Table 3 Surface temperature of the exhaust manifold and bearing housing

	Exhaust Compressor side	Bearing Housing	Exhaust Turbine side
1050 rpm			
8 Nm	333.5 °K	330.3 °K	343.2 °K
50 Nm	366.6 °K	335.1 °K	385.4 °K
1500 rpm			
8 Nm	336.9 °K	326.5 °K	348.0 °K
250 Nm	593.4 °K	418.8 °K	659.6 °K
2000 rpm			
8 Nm	341.6 °K	345.0 °K	361.6 °K
250 Nm	613.6 °K	422.0 °K	683.4 °K
2500 rpm			
8 Nm	370.9 °K	350.9 °K	382.8 °K
200 Nm	615.0 °K	411.3 °K	654.6 °K
3000 rpm			
16 Nm	414.2 °K	366.9 °K	437.8 °K
200 Nm	614.9 °K	406.1 °K	698.6 °K

The surface temperature of the bearing housing can be considered as the sum of the cooling effects of the oil and of the convective, radiative and conductive heat fluxes due to the proximity of the turbine. However, the test results demonstrate that the surface temperature of the bearing housing is of the same order of magnitude as the oil. This means that the role played by the oil on the overall temperature of the bearing housing is greater than that played by the turbine and, since most of the heat transferred from the turbine to the compressor occurs through the bearing housing, this implies that the heat flux through the bearing housing will have to be predicted very accurately in the model.

In addition to the surface temperature of the bearing housing, the surface temperatures of two pipes of the exhaust manifold were also measured. As can be seen in Table 3 a significant temperature difference exists between the pipes on the compressor and turbine sides. Such a difference ranged from a minimum of 10 °K at 1000 rpm to a maximum of 80 °K at 3000 rpm. Since the temperatures on the turbine casing are of the same order of magnitude as those measured on the exhaust manifold, the close proximity of the exhaust manifold to the turbine casing is unlikely to affect the turbine heat transfer. However, since the surface temperatures measured on the compressor casing are much lower than those on the turbine casing, the close proximity of the exhaust manifold to the compressor will tend to transfer heat by radiation and convection to the compressor casing and this will tend to heat up the air flowing inside. As a consequence, a temperature rise in the air flowing through the compressor is expected to occur, leading to a further decrease in the compressor efficiency. The exhaust manifold has not been considered in the model but there are good reasons however for including it in a future model development.

4 One-Dimensional Model

In this section a description of the one-dimensional model implemented in MATLAB is provided. The model was developed considering the main heat transfer mechanisms: conduction, radiation and convection. The estimation of the heat fluxes made it possible to calculate the following parameters:

- exit temperatures for both the turbine and the compressor
- non-adiabatic efficiency of the compressor

A good prediction of the compressor exit temperature is crucial to the model validation; this is because these temperatures form the boundary conditions for any engine model and they are significantly affected by the heat transfer processes.

In Fig. 5 the physical model of the turbocharger is illustrated. The compressor, the turbine and the bearing housing were modelled as three cylinders and for each of these three bodies the heat fluxes were calculated. Such a simplification was necessary for several reasons: first of all, a full description of the turbocharger geometry would require geometrical data that were not available, as the design of the turbine could not be disclosed for reasons of confidentiality. Secondly an over-detailed geometrical analysis of the turbocharger would make the model too complex and would also constrain the outcomes to the particular case under study.

The heat fluxes that are of direct interest in the estimation of the non-adiabatic efficiencies are the heat fluxes that enter or leave the turbine and the compressor, as illustrated in Fig. 6. Due to the hot exhaust gases entering the turbine volute, a high surface temperature can be expected on the turbine side while the compressor is comparatively cold and hence only a negligible amount of heat is transferred at the compressor. The surface of the bearing housing lies between the turbine and the compressor and is therefore also taken into account. In the oil channel between the shaft and the bearing housing the oil flow causes forced convection on the shaft and on

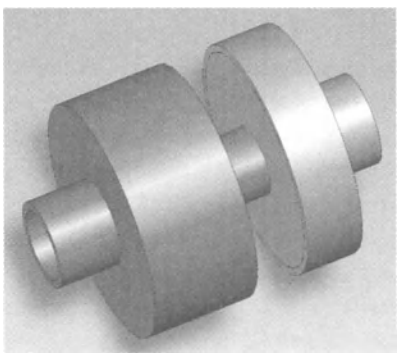

Fig. 6 Turbocharger physical model

the inside of the bearing housing. As the shaft is rotating at high speeds the flow field in the oil channel is very complex and must be carefully treated.

In order to evaluate the amount of heat transferred within the turbocharger, the heat transfer coefficients and the temperature distributions occurring on the surfaces constituting the model have been calculated. Since only the steady state is treated in the developed model, no change in internal energy has been taken into account, allowing to simplify the energy balance.

5 Model Results And Validation

(1) Compressor exit temperature

As already shown in the Test Results section, the compressor non-adiabatic efficiency is lower than the compressor adiabatic efficiency and this means that the exit temperature of the compressor in non-adiabatic conditions is higher than in the adiabatic conditions. This is not irrelevant because it leads to a significant inaccuracy in the estimation of the compressor power requirement. The compressor outlet temperature forms one of the boundary conditions used in the engine simulation models and, since the combustion process and the formation of pollutants in the combustion chamber of the engine are very sensitive to the combustion temperature, the boundary conditions have a great influence on the results. Hence the compressor outlet temperature has to be calculated as accurately as possible.

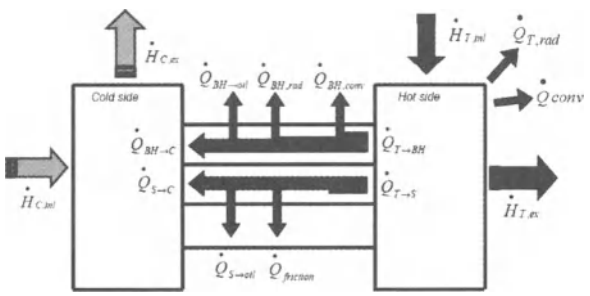

Fig. 7 Heat fluxes

The one-dimensional model here developed enables to calculate the compressor exit temperature under non-adiabatic conditions. A comparison between the predicted and the measured temperatures is given in Fig. 7 against the compressor pressure ratio. The model seems to provide an accurate prediction over a wide range of turbine inlet temperatures. The deviation of the calculated temperatures from the measured temperatures is not greater that 5.8% at 774 °K and drops to 1.9% at 755 °K. On average the deviation is not greater than 4% for both low and high engine speeds and torques and this seems to confirm the effectiveness of the choices made on the heat fluxes occurring within the turbocharger.

Table 4 Compressor exit temperature

Pressure Ratio	1.27	1.57	1.73	1.85	2.08
Turbine Inlet Temperature [°K]	774	755	836	949	928
Deviation: Model – Test [%]	5.8	1.9	2.4	3.8	4.3

(2) Compressor non-adiabatic efficiency

The non-adiabatic efficiencies are calculated as the ratio between the isentropic and the actual enthalpy rise occurring in the compressor (Equation 2). The predicted and the experimental relative compressor non-adiabatic and adiabatic efficiencies are provided in Fig. 8 as a function of the pressure ratio. The model provides a good prediction of the non adiabatic performance over a wide range of pressure ratios from 1.2 to 2.1.

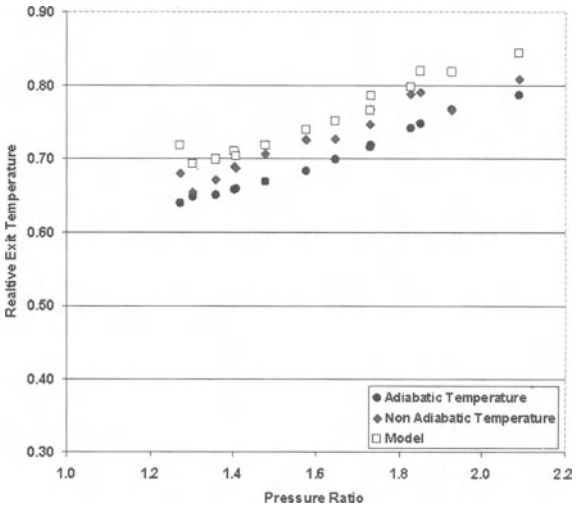

Fig. 8 Relative exit temperature vs. pressure ratio

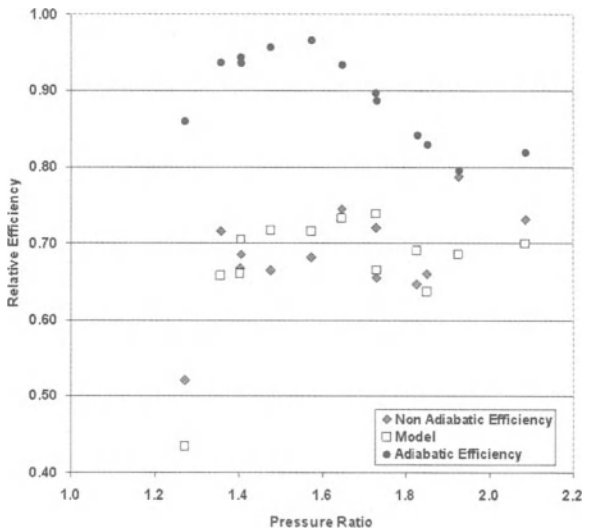

Fig. 9 Compressor relative efficiency vs. pressure ratio

In Table 5 a comparison between the efficiencies is reported. The deviation of the computed data from the test data is not significant for most of the measured points even though a significant scatter can be observed at low pressure ratio. This is because at low rotational speeds (corresponding to a low pressure ratio), the effects of heat transfer on the compressor performance are greater since the compressor works in conditions far removed from the design point. This can lead to instability effects within the flow that are difficult to match in the model as no assumption was made regards the aerodynamic conditions of the flow.

Table 5 Efficiency comparison

Pressure Ratio	1.27	1.57	1.73	1.85	2.08
Turbine Inlet Temperature [°K]	774	755	836	949	928
Deviation Model-Test [%]	17.28	4.73	1.36	3.63	4.30

6 Conclusion

This study has investigated the influence of heat fluxes from the turbine to the compressor in a turbocharger. Firstly a set of tests was carried out on a 2.0 litre diesel engine, monitoring the surface and flow temperatures for both the compressor and the turbine. Secondly, a one-dimensional model was implemented to predict the compressor exit temperature and non-adiabatic efficiencies and the model was validated against experimental data.

The tests were carried out at Imperial College in cooperation with Prof. Alex Taylor and Dr. Yanis Hardalupas. The engine speed was varied from 1000 rpm to 3000 rpm and, for each of these speeds the load was varied from 8 Nm to 250 Nm. The data obtained showed that the non-adiabatic conditions strongly affect the compressor performance. At lower engine speeds and torques, the overall non-adiabatic compressor efficiency deviates by about 30% from the adiabatic efficiencies whilst, at higher engine speeds and loads, the deviation drops to 3%. The test also showed that the bearing housing temperature is strongly affected by the coolant oil and that the close proximity of the exhaust manifold to the compressor casing is an additional source of efficiency loss.

The data generated from the tests were then used to validate a simplified one-dimensional model developed in MATLAB. The turbocharger geometry was simplified and considered as being constituted of an assembly of flat plates with known thermal properties. Heat transfer correlations were used to quantify the heat coefficients for convective heat transfer and were based on the inlet conditions and the geometrical properties. The compressor exit temperature and the compressor non adiabatic efficiencies were calculated.

Comparison between the experimental and computed data showed that the predicted compressor exit temperatures were found to be in very good agreement. An average deviation of 4% was found to occur for the compressor. This result is remarkable since the exit temperatures form the boundary conditions for any engine model available on the market. In addition to the compressor temperatures, the compressor non-adiabatic efficiencies were also computed. An overall averaged deviation from the test values was found to be not greater than 4% at lower engine speeds and around 10% at higher engine speeds. Although these deviations are not negligible, the results obtained here provide a significant improvement over other methods, in which deviation of up to 30% was seen.

In conclusion it can be said that the accuracy of the model can be increased by decreasing the level of simplification on the turbine side. This includes the development of more appropriate heat transfer correlations for the turbine volute and the turbine wheel. Furthermore the level of simplification of the turbine geometry can be reduced to obtain more accurate values for the overall heat loss of the turbine. Besides these basic improvements further experimental work is needed to gain a better insight in the temperature distributions on the surfaces of the turbine and the bearing housing in order to estimate the occurring heat fluxes more accurately.

Acknowledgements

The authors would like to acknowledge Ricardo plc, Ford UK and University of Brighton. This consortium along with Imperial College are part of funded program (DTI UK) named VERTIGO (Virtual Emission Research Tools and Integration). Furthermore the authors would also like to acknowledge Prof. Alex Taylor and Dr. Yanis Hardalupas who made their test facility available, Mr. K. Spyridon whose support was essential throughout the tests and the technicians E. Benbow, H. Flora and J. Laker.

References

M. Rautenberg, A. Mobarak, M. Malobabic, "Influence of heat transfer between turbine and compressor on the performance of small turbochargers", *International Gas Turbine Congress, Tokyo, Japan, 1983*

M. Rautenberg, N. Kammer, "On the thermodynamics of non-adiabatic compression and expansion processes in turbo-machines", *Fifth International Conference for Mechanical Power Engineering, Cairo, Egypt, 1984*

D. Bohn, T. Heuer, K. Kusterer, "Conjugate flow and heat transfer investigation of a turbocharger: Part i—numerical results" *Proceedings of ASME Turbo Expo, Atlanta, Georgia, USA, 2003*

D. Bohn, N. Moritz, M.Wolff, "Conjugate flow and heat transfer investigation of a turbo charger: Part ii—experimental results" *Proceedings of ASME Turbo Expo, Atlanta, Georgia, USA, 2003*

The 4th International Symposium on Fluid Machinery and Fluid Engineering
November 24-27, 2008, Beijing, China
NO. 4ISFMFE-IL17

Multi-Scale Thermal Measurement and Design of Cooling Systems in Gas Turbine

Hyung Hee Cho*[1], Kyung Min Kim[1], Sangwoo Shin[1], Beom Seok Kim[1] and Dong Hyun Lee[1]

*[1] Department of Mechanical Engineering, Yonsei University, 134 Sinchon-dong, Seodaemoon-gu, Seoul 120-749, Korea
Tel: +82-2-2123-2828 / Fax: +82-2-312-2159
E-mail: hhcho@yonsei.ac.kr

Abstract The present gas turbine technology increases the turbine inlet temperature to a limitation which is very high gas temperature accomplished by recently developed material and cooling technology. In order to overcome the limitation and enhance higher thermal efficiency, the multi-scale thermal design technique must be considered in development of modern gas turbines. This study investigates to present a direction of research to overcome the limitation in a course of macro-scale cooling technology, multi-scale thermal measurement/application for precise thermal design, multi-scale thermal analysis/design with aid of micro/nano-scale technology, and thermal reliability and optimal thermal/cooling design technology. This multi-scale thermal design technique will be widely used for vane, blade, and combustor cooling design to develop higher thermal efficiency of modern gas turbines.

Keywords gas turbine cooling, thermal barrier coating, multi-scale, thermal conductivity, thermal design

1 Introduction

For brisk development and performance maximization of gas turbine, macro-to-micro combined multi-scale device development as well as optimum thermal design technology is required. That is, these methods have overcome the performance limit with aid of micro/nano-scale technology. For example, in present gas turbine technology, conventional cooling methods (macro-scale) and thermal barrier coatings (micro-scale) are simultaneously used. They protect a material surface which is exposed to high temperature environment. However, by increasing the turbine inlet temperature, the thermal expansion mismatch between TBC and substrate increases, which generates high thermal stresses and thereby TBC delamination. In addition, TBC delamination causes thermal cracks on the hot gas sides. Such damages and failures can be resolved with understandings of multi-scale technologies.

Macro-scale heat transfer can be controlled by understanding micro/nano-scale thermal transport and optimal thermal design using multi-scale characteristics. Also, this advanced technology is applicable to cooling technologies for macro-scale high/precise temperature devices: gas turbine, ramjet/rocket, fuel cell, electronics, semiconductor equipments, etc.

For accomplishment of optimum multi-scale thermal analysis and design, thermal reliability for high temperature multi-scale devices is required. Also, accurate thermal sensor is needed for better understanding of multi-scale heat transfer. Furthermore, array-type thermal sensors for detailed local measurements are useful in gas turbine design.

The present study investigates multi-scale thermal measurement and multi-scale thermal design technologies to protect hot components such as combustors, vanes, and blades and to predict their lifetime and safety.

2 Multi-scale Thermal Design

The multi-scale thermal design for advanced development in gas turbines needs the research on multi-scale thermal characteristics from macro to micro/nano-scale, the integration research of macro heat transfer and micro/nano-technology, the research on fabrication and reliability improvement of precise thermal measurement sensors, and accomplishment of optimum thermal design technology for wide industry fields as shown in Fig. 2.

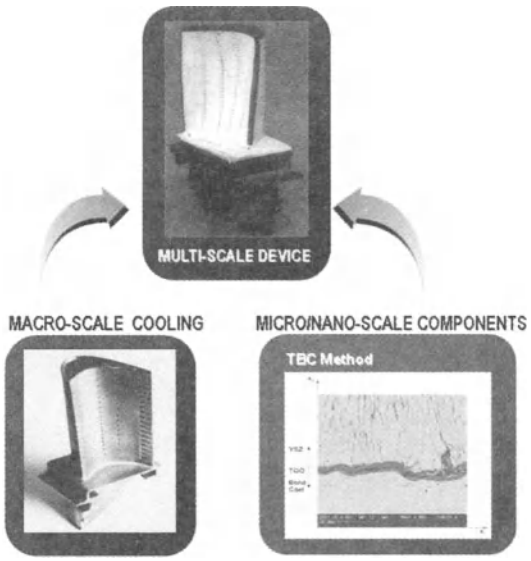

Fig. 1 Multi-scale thermal design

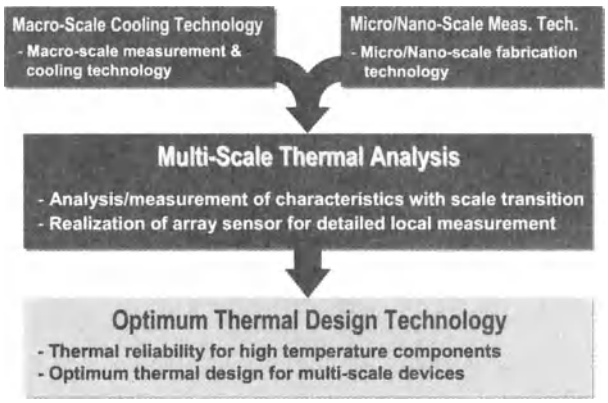

Fig. 2 Multi-scale thermal design

The detailed research methodology is as follows:

(a) Macro-scale cooling technology for high temperature devices: (1) Accumulation of macro-scale heat transfer technology through many previous studies; (2) thermal characteristics measurements via thermocouple, TLC (thermochromic liquid crystal), infrared camera, naphthalene sublimation method, etc.; (3) design of cooling technology through film cooling, impinging jet cooling, internal passage design, thermal analysis of electronic devices, etc.

(b) Multi-scale thermal measurement and application for precise thermal design: (1) Mechanisms of thermal sensors such as thermocouple, thermopile, RTD, diode, transistor, etc.; (2) fabrication of array-type micro-sensor for multi-point sensing using MEMS technique; (3) application of fabricated micro-sensors for accurate thermal analysis/ design.

(c) Multi-scale thermal analysis and design with aid of micro/nano-scale technology: (1) Crossover between mscro heat transfer technology and micro/nano-scale fabrication technology; (2) analysis of thermal characteristics change with scale transition: macro-scale heat transfer technology and micro/nano-scale thermal characteristics research; (3) thermal design considering micro/nano-scale regime to overcome conventional performance limitation; (4) heat transfer control using micro/nano-scale technology to improve thermal design.

(d) Thermal reliability and optimal thermal/cooling design technology: (1) Performance improvement for macro-scale device through multi-scale design and measurement; (2) reliability improvement for multi-scale regime through analysis and measurement process; (3) optimum cooling technique design through thermal analysis/ measurement for various applications.

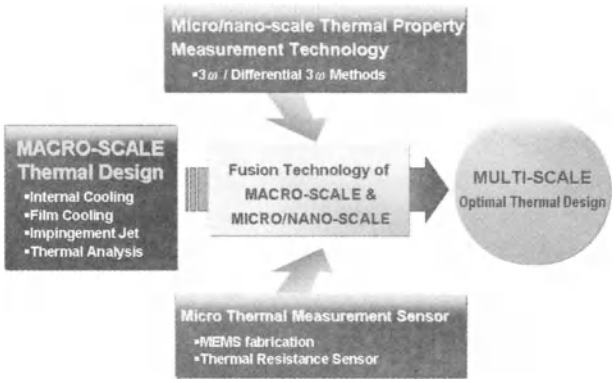

Fig. 3 The detailed research methodology

3 Macro-Scale Cooling Technology

To develop the hot components of gas turbine with high performance, a thermal design must be investigated as shown in Fig. 4. The thermal design affects directly the thermal damage and load. Moreover, to predict engine life and damage of the hot components, the metal temperature of the blade is estimated by the given thermal environment. Therefore, it is necessary to conduct the thermal design in order to enhance system performance.

In the most of previous studies, thermal analyses were performed using only numerical analysis processes. The local heat transfer coefficient and film cooling effectiveness are not exactly obtained in complicate cooling systems although the numerical scheme is developed a lot recently. Therefore, in the present works, temperature, thermal stresses, and thermal damages are predicted using the measured local heat transfer coefficient and film cooling effectiveness data. Also, an optimization for preventing thermal damage is conducted using a response surface method with functional design variables in the film cooling system with normal injection flow.

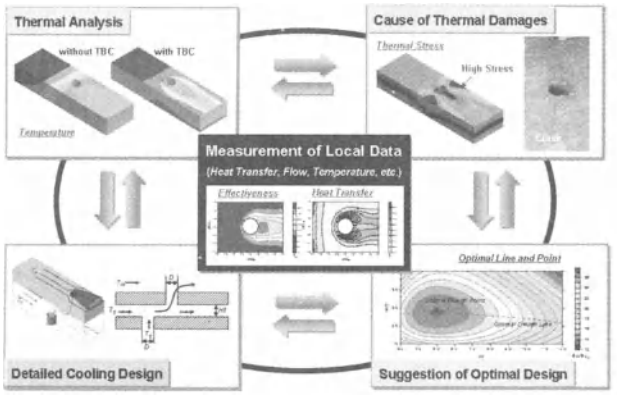

Fig. 4 Development procedures of thermal design

For measurements of the detailed local heat transfer distributions and film cooling effectiveness, our laboratory is using a thermal liquid crystal method, an IR-camera measurement and a naphthalene sublimation method as well as array of thermo-couples. To measure fluid flow, pressure drop, heat transfer, and film cooling effectiveness, the experimental apparatuses have been used as shown in Fig. 5. They are the test rigs for experiments of film cooling, turbine blade, heat exchanger, impinging jet/effusion cooling, rotating internal passage cooling, leading edge array jet cooling, and film cooling/impinging jet cooling in gas turbine.

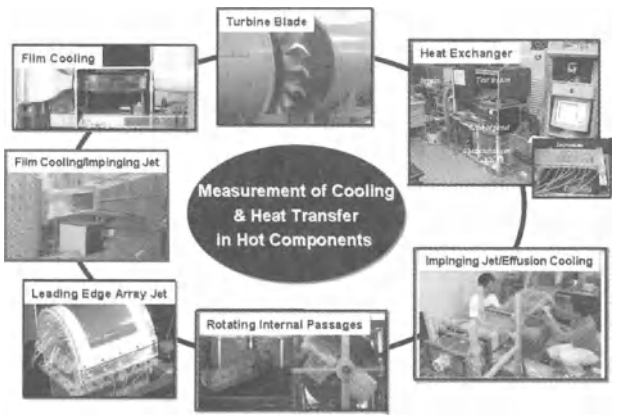

Fig. 5 Experimental apparatuses

Figure 6 shows the results such as measured heat transfer coefficients (HTC) and film cooling effectiveness distributions. We have investigated the thermal analysis (temperature and thermal stress) using these experimental data. We have predicted the thermal damage. To reduce the thermal stress, we have considered the optimal cooling design using an advanced response surface method. The detailed explanation of optimal cooling design is described by Cho et al. (2008).

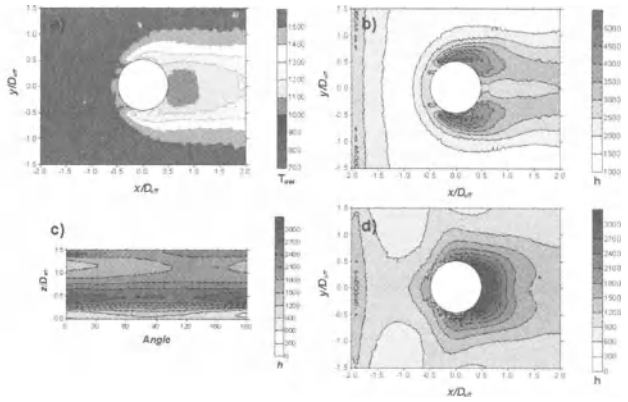

Fig. 6 Converted data for thermal analysis; (a) adiabatic wall temperature on exposed surface, (b) HTC on exposed surface, (c) HTC on hole surface, (d) HTC on back surface

4 Micro/Nano-SCAle MeAsurement Schemes

In usual, heat transfer characteristics of thermal barrier coatings (TBC) with thin thickness are different behavior from those of thick thickness. The measurement of thermal conductivity of dielectric thin films is important to exactly predict the temperature and thermal stress. Therefore, we have investigated 3ω method to measure thermal conductivity. The detailed methods and results are depicted by Shin et al. (2006). The 3 omega method has been suggested for the measurement technique. Figure 7 shows a schematic diagram of fabricated metal (Au) heater deposited on the target sample. The heater line simultaneously operates as not only a heater but also a temperature sensor. By sending an input current of ω frequency into the heater line, surface of the sample is heated with frequency of 2ω via Joule heating. As long as the target film is thermally thin and the thermal conductivity of the film is much smaller than that of the substrate, the temperature drop across the target film is postulated as the temperature difference between the heater and the substrate. The temperature oscillation of the heater line is determined by obtaining the 3ω frequency voltage signal, which is occurred due to variation of electrical resistance with temperature. Furthermore, if the thermal penetration depth in the substrate is shorter compared to the thickness of the substrate, temperature oscillation of the substrate could be determined analytically. The solution for 2-dimensional diffusion equation of the sample within the mentioned approximation is expressed. Therefore, the temperature oscillation of the target film is obtained. Finally, thermal conductivity of the target film can be calculated from 1-dimentional heat conduction.

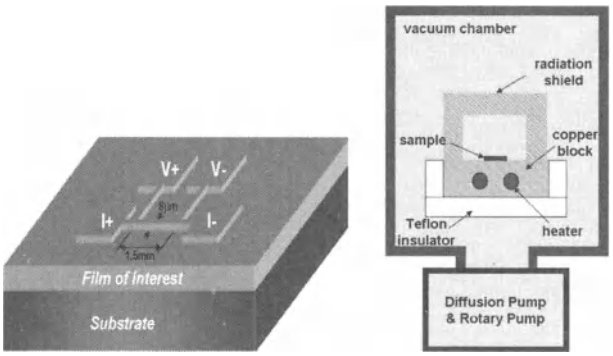

Fig. 7 Schematic diagram of the fabricated metal heater with sample

Via this method, thermal conductivities of silicon nitride thin films were measured with various thicknesses such as 30nm, 50nm, 70nm, and 100nm thick. Figure 8 shows a distribution of measured thermal conductivities of thin films respect to temperature. It is shown that the measured values rise gradually with temperature. Thermal conductivity of bulk silicon nitride is about 14.5W/m-K at room temperature. Compared to this value, the thin films have lower thermal conductivity. Also, 10nm of Cr layer was deposited by thermal evaporation for adhesion layer. The measuring temperature was in a range of 50℃ to 150℃. These experimental results show that the measured thermal conductivities of the thin films show smaller value than that of bulk material. Also, the results tend to increase with temperature as well as thickness.

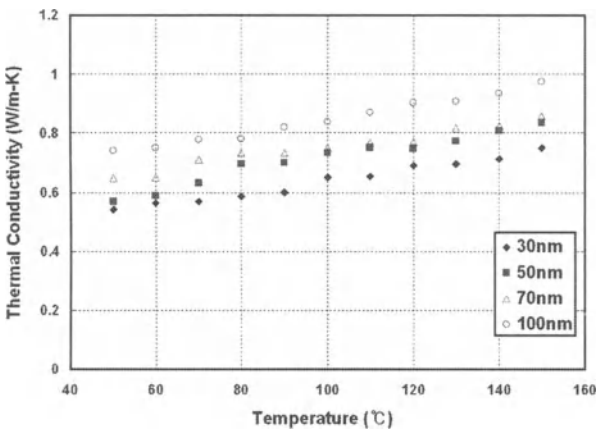

Fig. 8 Measured thermal conductivity of various thicknesses of silicon nitride thin films on temperature range of 50℃ to 150℃

In addition, we carry out measurement of heat flux using the micro-machined layered type heat flux sensors, which are fabricated by means of MEMS technique as shown in Fig. 9. The detailed fabrication and calibration are explained in Kim et al. (2005a, 2005b). The thermopile, 21 pairs of Cu-Ni thermocouples, is used in the heat flux sensor for EMF measurement generated by the temperature difference between hot and cold junctions. The calibration of the machined heat flux sensors is performed in heat flux range of 0.3~5.5 kW/m^2. As a result, we identify the linear correlation between the heat flux and EMF and present that the sensitivities of this sensor is 343.0 μV/(W/cm^2) as presented in Fig. 10. This sensor is also applied to measure the thermal contact resistance by thermal growth oxidation (TGO) and bonding.

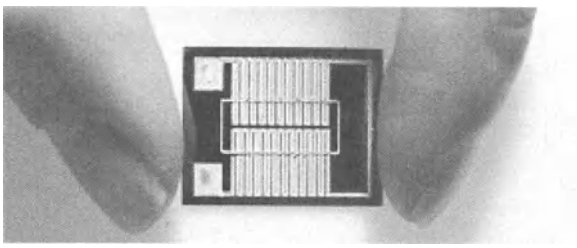

Fig. 9 Photograph of the micro heat flux sensor

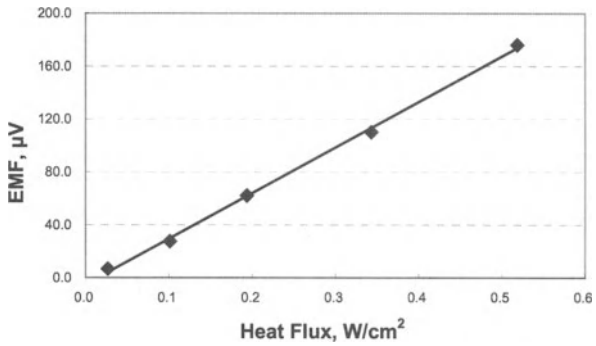

Fig. 10 Correlation between applied heat flux and EMF from heat flux sensor

5 Multi-SCAle Thermal analysis

We have investigated TBC delamination using the measured thermal properties and the detailed local data of heat transfer and film cooling effectiveness distributions. The operating and material conditions were considered as follows: coolant flow temperature (T_2) of 700K; main hot flow temperature (T_m) from 1600K; TBC thickness of 0.5 mm while substrate thickness of 5.5 mm. After imposing boundary conditions, stress analysis was conducted to determine the thermal damage in the film cooling system. Analysis was performed using a commercial code, ANSYS Workbench-11, to calculate the thermal stresses. To calculate the thermal stresses, uniform deformation in the x-axis direction due to the existence of additional materials and symmetric conditions were imposed as shown in Fig. 11.

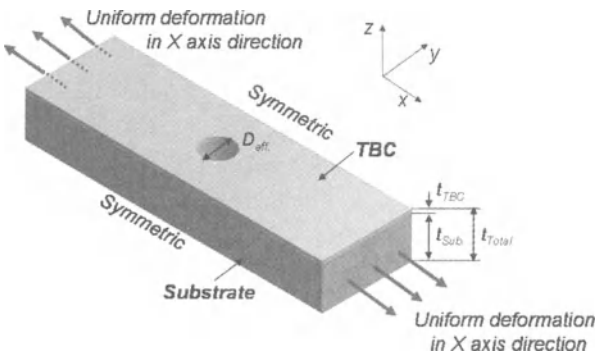

Fig. 11 Geometry and boundary conditions of the film cooling system

Figure 12 shows the temperature and thermal stress distributions in the film cooling system at t_{TBC}=0.5 mm and T_m=1600K. The temperature distributions on the exposed surface are similar to film cooling effectiveness. The temperature gradients in the x- and y-axis directions are generated by conduction between the hot gas section and cold section as shown in Fig. 12(a). Moreover, the temperature gradient in the side regions of the cooling hole becomes steeper than other regions due to high heat transfer rate. Maximum temperatures of TBC and substrate are 1147.0℃ and 909.4℃ in the upstream region on external surface, respectively. Minimum temperatures of TBC and substrate are 627.9℃ and 614.9℃ in the rear of

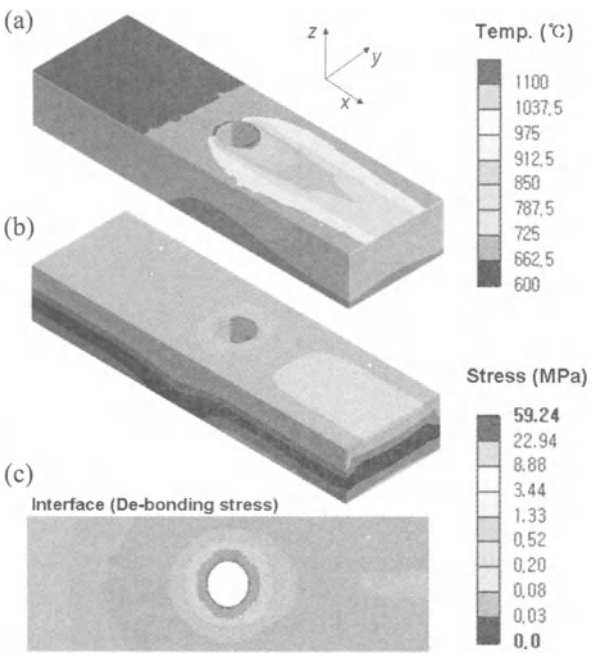

Fig. 12 Results of thermal analysis in the film cooling system; (a) temperature distributions, (b) thermal stress distributions, (c) de-bonding stress at the interface

injection hole on inner hole surface, respectively. In this case, the performance (temperature difference) of TBC is approximately 240 K in the upstream hot region; furthermore, the gradient magnitudes of substrate in x- and y-axis directions are about 100~120 K and 120~200 K, respectively, because of the low thermal conductivity of TBC.

The thermal stresses resulting from these temperature distributions are presented in Fig. 12(b). High thermal stress distributions appear in the interface between TBC and substrate. That is, the maximum vertical (or debonding) stress with magnitude of 59.24 MPa occurs at the edge of the cooling holes due to the highest momentum induced by thermal expansion mismatch (Fig. 12(c)). Such stress decreases exponentially as being more distant from the cooling hole. These stresses are enough to yield TBC delamination after numerous thermal cycles with such stress.

6 Multi-scale Optimal Thermal Design

To reduce the thermal debonding stress as shown in Fig. 12, we optimized TBC thickness and main hot gas flow temperature, and presented maximum stresses at the edge of cooling holes as a function of thickness of TBC and main temperature of main flow for design of actual TBC systems.

In present works, the advanced response surface method (RSM) with functional variables is selected among various optimization methods. This method is derived in efforts of solving disadvantages (bad application to complex function, low physical response, and etc.) of general RSM.

As a result, the maximum temperature of both TBC and substrate increases with increment of the main flow temperature. However, as TBC thickness increases, the maximum temperature of substrate decreases while that of TBC increases. Using a response surface method and calculating the maximum temperature difference between TBC and substrate, the TBC performance (reduction of material temperature by TBC) is deduced as shown in Fig. 13(a) and following equation.

$$\Delta T = -126.863x_2^2 + 0.279677x_1x_2 + 0.127346x_1 + 103.23x_2 - 142.311 \quad (1)$$

(x_1: main flow temperature; x_2: TBC thickness)

Figure 13(b) shows the maximum debonding stresses calculated from these temperature distributions which are expressed as follows.

$$\sigma_{max}\,[MPa] = 251.32[\exp(-1/x_2)]^2 - 0.097x_1 \exp(-1/x_2) + 0.0569x_1 - 117.56[\exp(-1/x_2)]^2 + 12.909 \quad (2)$$

(x_1: main flow temperature; x_2: TBC thickness)

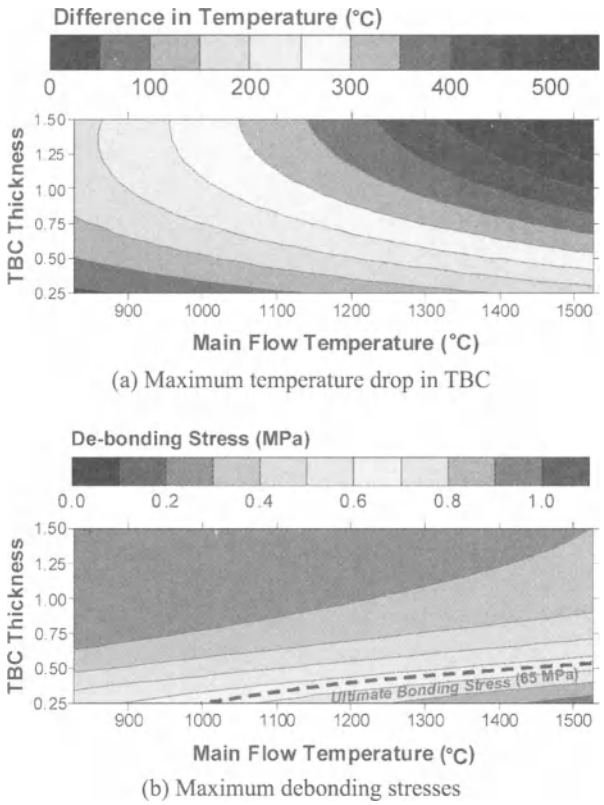

Fig. 13 Contour plots of results by TBC thickness and main flow temperature

The maximum debonding stress increases as main flow temperature increases; while the stress decreases as TBC thickness increases. The reason is that difference in deformation by thermal expansion between TBC and substrate is reduced as TBC thickness increases. That is, the thick TBC increases TBC temperature, but decreases substrate temperature; thus, the deformations of two materials are similar to each other because the discrepancy in thermal expansion coefficients between two materials becomes smaller. In addition, the dashed line in Fig. 13(b) indicates the location of the tensile ultimate strength of 65 MPa That is, TBC will be fractured or cracked when exposed to higher stress than such value. The detailed methods and explanation in optimal design is described by Kim (2008).

7 Summary

The multi-scale thermal design will be widely used for vane, blade, and combustor cooling for development in a gas turbine. The following researches are important: (a) Macro-scale cooling technology for high temperature devices; (b) multi-scale thermal measurement and application for precise thermal design; (c) multi-scale thermal analysis and design with aid of micro/nano-scale technology; (d) thermal reliability and optimal thermal/ cooling design technology.

The multi-scale thermal design can expect following contributions: (a) Employing micro/nano-technology to conventional macro-scale devices could overcome the performance limit, which leads to cost reduction. (b) precise sensors for local thermal measurement could contribute to performance enhancement of macro-to-micro combined multi-scale devices by providing required precise thermal characteristics data for accurate thermal analysis; (c) optimum thermal design technology can be utilized to wide industry fields such as gas turbine, energy, ramjet/ rocket, semiconductors and electronics, resulting technology improvement; (d) advanced technology for multi-scale heat transfer could be accomplished, which leads to establishment of foundation for specialized human resource development; (e) precise measurement technology for micro/nano fields is high value-added, and competitive to forefront nations which can contribute to economic growth and technology development.

References

Cho, H.H., Kim, K.M., and Lee, D.H., 2008, "Thermal Design of Cooling Systems in Gas Turbine and Ramjet (Invited Paper)", *Proceeding of UKC 2008*, USA, Paper No. MRM-4.1

Kim, B.S., Kim, J.-H., Kim, Y.-J., and Cho, H.H., 2005a, "Fabrication and Calibration of a Micro Heat Flux Sensor for Heat Flux Measurement", *Proceeding of KSME 2005 Fall Annual Meeting*, Korea, pp. 1251 – 1255

Kim, J.-H., Kim, B.S., Cho, H.H., and Kim, Y.-J., 2005b, "Fabrication and Evaluation of a Micro Heat Flux Sensor using Thermopile", *Proceeding of KSPE 2005 Spring Annual Meeting*, Korea, pp. 1210 – 1213

Kim, K.M., 2008, "Optimal Design of Heat Transfer Systems for Enhancing Thermal Performance and Preventing Thermal Damage", Ph.D. Thesis, Yonsei University, Korea

Shin, S.W., Cho, H.N., and Cho, H.H., 2006, "Measurement of Thermal Conductivity of Silicon Nitride Thin Films", *13th International Heat Transfer Conference*, Australia, Paper No. THP-05

The 4th International Symposium on Fluid Machinery and Fluid Engineering
November 24-27, 2008, Beijing, China
NO. 4ISFMFE-IL12

Reduced Size Bi-Flow Centrifugal Pump as Ventricular Assist Device for End-Stage Patients

Andy C C Tan

School of Engineering Systems
Queensland University of Technology
Brisbane, QLD 4001, Australia
Tel: +81-7-3138-1982 / Fax: +81-7-3138-1469
E-mail: a.tan@qut.edu.au

Abstract The shortage of donor hearts for patients with end stage heart failure has accelerated the development of ventricular assist devices (VAD) to support the left (LVAD) and right (RVAD) ventricles of a failing heart. Current BVAD technology is either too bulky or necessitates having to implant two pumps working independently. This paper illustrates the combination of the LVAD and RVAD as one complete device to augment the function of both the left and right cardiac chambers with double impellers. The device has two impellers rotating in counter directions. Our work to date has clearly shown the benefit of using a double sided impeller through studies of axial force imbalance and flow visualisation to assess possible sites of flow stagnation. The results illustrate that with proper impeller configurations and volute design of the output chambers, differential flow dynamics can be achieved to deliver an output of 4-6 lit/min and delivery pressure of 20-100 mmHg. With the outputs from the pump flowing in counter directions, there is significant benefit in eliminating the necessity of the body muscles and tubing/heart connection to restrain the pump.

Keywords left ventricular assist device, biventricular assist device, right ventricular assist device, centrifugal heart pump-artificial organs, counter flow pump

1 Introduction

Approximately 23 million people worldwide suffer from heart failure with 800,000 new cases of congestive heart failure each year. In the US, 500,000 new cases of heart failure are diagnosed annually. According to the American Heart Association, 4000 end-stage heart patients are on waiting list for heart transplantation with only 2100 donor hearts become available to these patients. As of June 2000, the waiting list for heart transplantation exceeded 4100, with only 2198 transplants performed in 1999, according to American Heart Association (2002). In Australia, 44 percent (50,797) of all deaths each year are related to heart disease and accounted for 12% (A$3.9Billion) of total recurrent health expenditure in 1993-94 (AIHW, 2001). The shortage of donor hearts for patients with end stage heart failure has accelerated the development of ventricular assist devices (VAD) that act as a replacement heart.

Application of a VAD as a "bridge" to heart transplantation was first attempted in 1978 but the patient died of infection soon after implantation (Norman, et. al., 1978). VAD's now come in several configurations pulsatile type pumps are similar in operation to the human heart. They require valves and moving actuators, which can cause destruction of red blood cells, and are relatively large in size (Sun, et. al., 2003). Axial flow pumps are relatively simple in their design and construction, but required high rotating speed (Okada, et. al., 2003). Centrifugal flow pumps have high efficiency and most of the current designs make use of magnetic bearing technology to overcome the problem of bearings and seals which are the main cause of blood destruction (Hoshi et. al., 2005; Yamana, 2000). A recent centrifugal pump developed in Australia (VentrAssist) utilizes a completely passive hydrodynamically suspended impeller (Watterson, et. al.,

2000). The main problem with hydrodynamic technique used in this device, is the suspension capacity of the impeller which is dependent on high rotational speed with low rotational speed resulting in impeller instability.

Clinical developments (Orime, et. al., 2000; Sezai, 1997) indicate that such centrifugal devices are not only beneficial for bridge to transplantation applications, but may also aid myocardial recovery. Patients who received a permanent left ventricular assist device (LVAD) reduced their risk of dying within one year by 47%. Unfortunately 25% of these patients develop right heart failure syndrome, sepsis and multi-organ failure (Nose, 1997). Santamore and Gray, 1996 reported 17% of patients initially receiving an LVAD later required a right ventricular assist device (RVAD). Hence, current research focus is in the development of a bi-ventricular assist device (BVAD).

Farrar, et. al, 1996, recognised the need for a RVAD and in their study where 48% of the patients received BVAD support as a bridge to cardiac transplantation. Yoshikawa et.al, 2000, developed a small and yet efficient RVAD that could be used in conjunction with a conventional LVAD to provide BVAD support. In order to have the function of a total biventricular assist device, Nose et. al., 1997, installed two identical VADs implanted in the abdominal wall as a left and a right ventricular bypass device. Each pump has its own independent control and actuation system. The study lasted for 72 days and was terminated due to functional inflow obstruction. Current development of a combined BVAD for total artificial heart (TAH) centered around extracorporeal and paracorporeal pulsatile systems, such as the moving actuator mechanism proposed by Park, et.al., 2003. Their device is relatively large, $106 \times 87 \times 67$mm and weighs 0.8kg, and has a moving actuator which is prone to wear.

Current BVAD technology is either too bulky or necessitates having to implant two pumps working independently (Magliato et.al., 2003). The latter requires two different controllers for each pump leading to the potential complication of uneven flow dynamics and the requirements for a large amount of body space.

This paper describes a preliminary design concept of a BVAD centrifugal pump which combined the LVAD and RVAD as one complete device with dual outputs flowing in counter directions. Our work to date has clearly shown the benefit of using a double sided impeller through studies of axial force imbalance (Timm, et. al., 2003, 2004) and flow visualization to assess possible sites of flow stagnation (Tan, et. al. 2004). The proposed device has two impellers rotating in counter directions for both the left and right ventricles and will have similar impeller blade design but with different output volutes to cater to differential output pressures. The device can simulate two separate pumps in parallel with separate outputs using a single controller to monitor and maintain the rotational speeds of the left and right impellers. The rotation in counter directions is achieved using two sets of magnetic drives running in series to provide levitation/control and rotation in opposite directions. The left and right chambers will be independent to avoid blood contamination between the oxygenated and deoxygenated blood. To reduce the potential for thrombosis events and thus reducing the requirement for excessive anticoagulant administration, the impeller design will incorporate bleed holes to provide blood circulation in the impeller/housing gaps.

2 Centrifugal Pump Design

The centrifugal pump needs to be designed to deliver the required pressure and blood flow around the body. Matching the flows and pressures required by this BVAD pump will require theoretical calculations and experimentations to accomplish the optimum working condition. In a centrifugal pump, the radial and axial gaps, blade profile, and inlet / outlet volute designs must be carefully considered and designed to minimize damage to the red blood cells. CAD (Solidworks) is used in the design of volutes, the blade profiles and the inlet and outlet ports. Our initial design involved a set of epicyclic gears to provide motion in counter directions. The drawback of this design is the friction caused by the meshing gears and required seals to separate the left and the right chambers. A single controller will be used to control and monitor the left and right impellers. For use as a BVAD, this requires different pressure characteristics for each chamber and hence different geometry of the volutes and blade profiles.

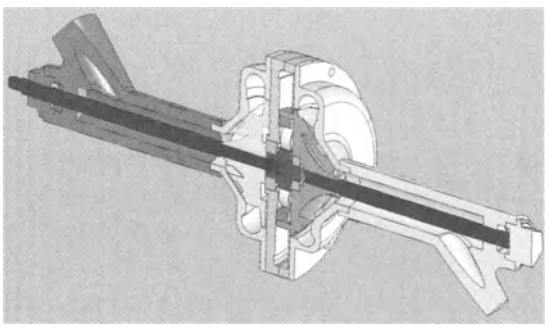

Fig. 1 A conceptual BVAD centrifugal pump with counter flow output

The pump was designed in a modular form to allow for a range of tests involving radial and axial gaps, volute design and input/output ports. An assembly of a conceptual pump is shown in Fig 1. The pump has two impellers of 41mm diameter attached to the central motoring body, an

upper and lower housing casings. The overall dimension of the pump is 50 by 70mm (the extended tubes are included for experimental tests).

3 Results And Discussion

The conceptual counter-flow BVAD pump will be designed based on theoretical calculations to determine the pump characteristics relating to the pressure head, efficiency and pumping power to the flow through the pump over a range of different pumping speeds. The pump theory was sourced from Zaher (2001) to determine the geometric parameters of the pump to obtain the resulting pump characteristic curves.

One of the main issues with implantation of a mechanical device within the body is trauma arises as a result of the tissues in restraining the pump due to differential reaction forces and the cannulas connecting the pump entry and exit to the human heart. The output torque is determined by the output pressure (P) of the pump and the radius to the centre of pressure (r_{cp}) of the throat cross sectional area (A). The resultant torque for a BVAD will depend on the direction of the LVAD output with respect to the RVAD outlet and is given by,

$$T_{BVAD,tot} = ((\mathrm{PA} \times \mathrm{r_{cp}})_{throat})_{LVAD} + ((0.2\mathrm{PA} \times \mathrm{r_{cp}})_{throat})_{RVAD} \quad (1)$$

where the pressure of RVAD is 0.2 times of the LVAD.

If direction of rotation of the left and the right impellers are the same direction with respect to the LVAD the resultant torque is given by,

$$T_{BVAD,tot} = 1.2(\mathrm{PA} \times \mathrm{r_{cp}})_{throat} \quad (2)$$

If the outlets are directed in the opposite direction, the inherent torque of the counter flow heart pump with respect to the LVD, is given by,

$$T_{BVAD,cf} = 0.8(\mathrm{PA} \times \mathrm{r_{cp}})_{throat} \quad (3)$$

In theoretical calculations, the counter flow configuration decreases the inherent torque by 33% which can effectively reduce the reaction torque and provides less strain on the tissue holding the device in position.

The pump characteristics calculations are determined based on a number of assumptions as well as experimental dimensionless coefficients to accommodate pump inefficiencies. The calculations determine the magnitude and direction of the fluid velocity as the fluid enters and leaves the pump. It does this by considering the impeller and casing geometry and the inlet conditions of the pump whist the pump is running at a particular speed. It is assumed that the flow at the outer impeller edge comprises of radial and tangential components only. This does not take into account the axial flow phenomenon such as fluid swirl and secondary flow within the pump cavity. The calculations also consider experimentally determined geometry dependant, non-dimensional coefficients to account for losses within the pump such as turbulence, leakage at the cut water and other inefficiencies. The equations basically assume that the radial velocity at the impeller edge is proportional to the flow rate through the pump whilst the radial velocity at the impeller tip contributes to the induced pressure head obtained across the length of the impeller blade.

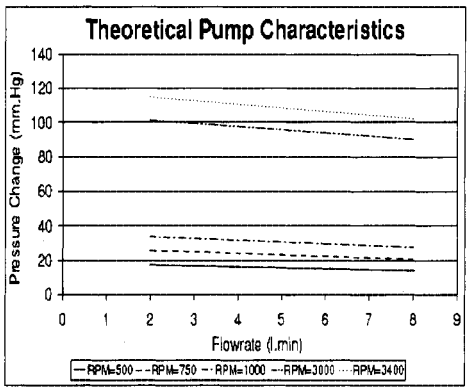

(a)

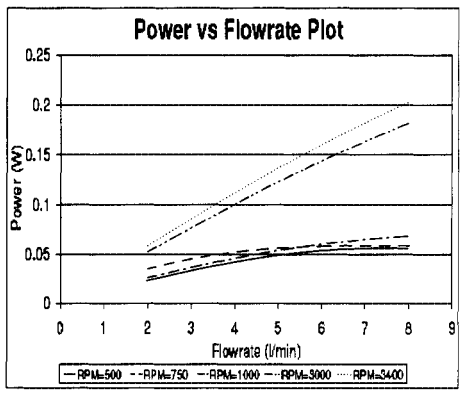

(b)

Fig. 2 Pump curves showing (a) the pressure head and (b) power against flow rate over a range of pump speeds (impeller diameter 41mm)

The resulting pump characteristics curves for the counter flow pump are shown in Fig. 2. To maintain a flow of 5 lit/min at a pressure head of 100 mmHg and 20 mmHg for the left and right ventricles, the respective impeller speeds are approximately 3200 rpm and 600 rpm. The corresponding power gain by the fluid for the left and right impellers based on an efficiency of 10% for the left ventricle, and 20% for the right ventricle are 0.15 W and 0.05 W, respectively. However, the idea shaft power based on the above given flow rate, pump head and for blood as the fluid is 1.16 W for the LVAD and 0.23 W

for the RVAD. The reaction torques from the LVAD and RVAD are 0.0175 Nm and 0.0035 Nm respectively, when running as separate units. These are a result of the inherent reaction torque from the fluid's momentum changing 90 degrees from the inlet to the outlet. If these VADs were connected and running in the counter flow configuration then the resulting reaction torque for the BVAD will be 0.016 Nm. The ratio of the reaction torques of the BVAD counter flow configuration to the combined reaction torques of the LVAD and RVAD is surprising close to our theoretical calculations and represents an effective reduction of 33%. This confirms the benefit of the counter flow configuration.

Table 1 Impeller speeds and power for the left and right pumps at a flow rate of 5 lit/min and pressure heads of 100 (left) and 20 (right) mmHg

	30mm		41mm		50mm	
	Left	Right	Left	Right	Left	Right
Speed (rpm)	n/a	1,000	3,200	600	2,000	400
Power (W)	n/a	0.025	0.15	0.05	0.2	0.1

Following the determination of the theoretical model, the impeller diameter was altered to see the change in the pump characteristics. Impeller diameters of 30mm and 50mm were simulated using all the other existing impeller dimensions. The impeller design was then changed to analyse the effect of a changing impeller diameter. All dimensions from the current ϕ41mm impeller were kept and the impeller diameters were changed to ϕ30mm and ϕ50mm. Table 1 shows the impeller rotating speeds for the left and right pumps at a flow rate of 5 lit/min and delivery pressure of 100 mmHg and 20 mmHg, respectively. It can be seen that as the impeller diameter increases, the rotating speed decreases. The power gain by the fluid for the left and right pumps also increases with the impeller diameter.

4 Cfd Analysis

Computational fluid dynamics and flow visualisation were conducted to understand the flow process within the individual pumps (LVAD and RVAD) separately. The understanding gained from this individual study will be incorporated in the design of double-sided counter flow pump as a single device. Hence, this section illustrates the dynamics and flow characteristics to identify regions of stagnation and turbulent for a single centrifugal pump.

To analyse the dynamics within the pump cavity for either the left or the right pump, both CFD model and experimental scaled-up (4:1) model were constructed to model the fluid flow in the chamber. The CFD 3-D model using finite volume CFD code FLUENT 6 is shown in Fig. 3. The CFD model is based on the experimental scaled-up model, which include an inlet flow region, the flow region of the entire pump, the impeller configurations and the pump exit region. The fluid enters the pump through the straight inlet pipe perpendicular to the impeller and exits in the radial direction. The fluid passes through the volute and two gap regions, namely, between the upper impeller shroud and the upper pump housing; and underneath the base of the impeller shroud and the lower pump housing. These regions play a crucial role in determining the thrombolytic and hemolysis of the blood cells. A small gap can increase the efficiency of the pump, but have detrimental effect on the blood cells.

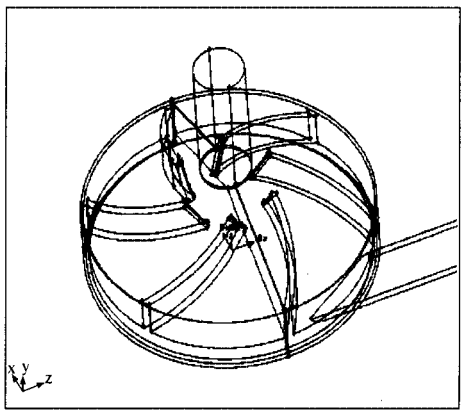

Fig. 3 3-D CFD Model

In this study, the CFD model is constructed based on the assumption that the fluid flowing in the pump was Newtonian with a viscosity of 1.003e-3 *Pa* and a density of 1000 kg/m^3. The boundary conditions of the pump were set based on the operating conditions of the pump which are, the inlet flow rate was set at 0.0239 kg/s and the outlet pressure was 1500 *Pa* at 125 rev/min. The flow was modelled as steady with a standard k-ε model for turbulence.

The results from CFD model includes fluid streamlines and velocity profiles and allows any computational fluid field to be examined to identify the regions of recirculation, stagnation and large gradients resulting in fluid stresses. Fig. 4 shows the fluid recirculating patterns between the impeller blades and with increasing intensity as it reaches the exit volute. Included in the figure are regions of stagnation which lead to blood thrombosis. The highlighted box in the figure shows the flow pattern at the volute tongue and the exit of the diffuser. It indicates regions of turbulent which causes destruction to blood cells. Recirculation is normally caused by stagnation and large energy losses. In the design of blood pump this need

to be eliminated so as to reduce the possibility of blood damage and improve the fluid dynamic efficiency.

Fig. 4 CFD Flow Pattern

In order to physically observe the flow pattern, a scaled-up experimental model was constructed based on Reynolds similarity law. This enabled the rotational speed to be reduced, hence allowing the flow pattern to be captured in a high speed camera. The pump material was Perspex to allow a light source to penetrate the casing and illuminate the seeding particles. The set up is to mimic the operating conditions of the smaller prototype whilst increasing the accuracy of the high speed camera images.

The flow images recorded at 25 film/sec. are shown in Fig. 5. At normal operating speed, there is minimal turbulent in the cutwater region (Fig. 6(a)). As the speed decreases, increased turbulent and recirculation can be seen in Fig. 6(b). Increased turbulence was found at the

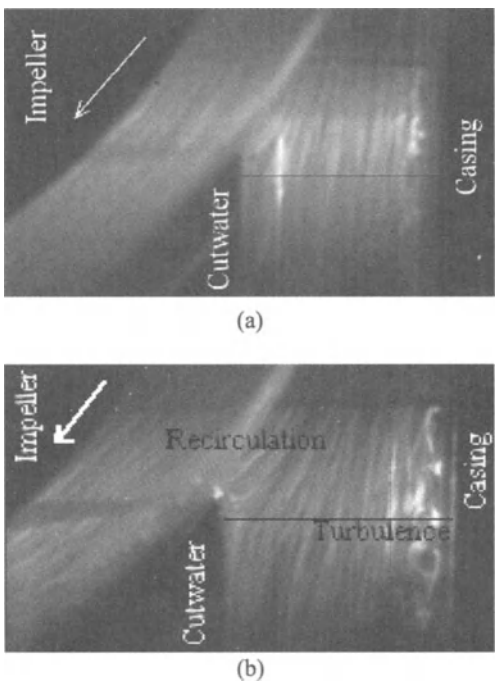

Fig. 5 Flow Patterns at cut-water region (a) normal speed and (b) low speed (Tan et.al 2004)

cutwater section under low capacity conditions, with eddy's forming at the outer section of the outlet pipe. This can also be seen in the velocity profile as there is a degree of reverse flow. Not only would this turbulence give rise to hemolysis, but the continual recirculation allows for blood to stagnate in this region, leading to a potential site of thrombus formation (Tan et al. 2004). Operating the pump at design capacity reduced the level of turbulence, but gave rise to a smaller boundary layer thickness, that is the distance from the casing to the maximum velocity. This gives rise to a higher shear rate, as shear is determined by the rate of velocity change multiplied by the fluid viscosity. Further calculations are required to determine the value of shear stress and relate this to the hemolysis threshold.

5 Conclusion

It is demonstrated by theoretical analysis that a self-balanced BVAD is achievable by arranging the pump outputs flowing in counter directions to augment the functions of the left and right ventricles. To have the function of two outputs in a single unit, this requires the left and the right chambers to be totally segregated to prevent the mixing of the oxygenated and deoxygenated blood with the set of impellers rotating in counter directions. The differential heads at the outputs are achievable by rotating the impellers at different speeds. The theoretical calculations show that for a flow rate of 5 lit/m, this is achieved by rotating the left impeller at 3200 rpm and the right impeller at 600 rpm for pressure heads of 100 mmHg and 20mmHg, respectively. Furthermore, with the impellers rotating at counter directions, the pump power is significantly reduced, hence leading to self-balance. Work is in progress to conduct an experimental valuation using a mock circulation loop and CFD to optimise the design and the results will be reported in due course.

Acknowledgements

The author wishes to acknowledge the financial support for this work provided by the Australian Research Council (DP0666078) and the Prince Charles Hospital Foundation (FRC0204-26), and Mr Nick Gaddum and Mr Daniel Sin for supplying the results.

References

Abe Y, Chinzei T, Isoyama T, Saito I, Ono T, Mochizuki S, Kouno A, Imachi K., 2003, "Basic study to develop an electromagnetic drive mehtos for the rotary undulation pump", *Artificial Organs*, 27(10): 870 – 874

AIHW, Heart, Stroke and Vascular Diseases—Australian Facts, 2001. Cat. no. CVD13, AIHW, NHF of Australia, National Stroke Foundation of Australia (Cardiovascular Disease Ser No. 14), Canberra

American Heart Association, 2002, "Heart and Stroke Statistical Update", American Heart Association: Dallas, Texas. p. 35

Farrar DJ, Hill JD, 1997, "Pennington DC. Preoperative and post-operative comparison of patients with univentricular and biventricular support with the Thoratec ventricular assist device as a bridge to cardiac transplantation". *J. Thorac Cardiovasc Surg*; 113: 202 – 209

Hoshi H, Asama J, Shinshi T, Ohuchi K, Nakamura M, Mizuno T, Arai H, Shimokhobe A, Takatani S, 2005, "Disposable Magnetically levitated Centrifugal blood Pump: Design and In Vitro Performance", *Artificial Organs*; 29:7: 520 – 526

Magliato KE, Kleisli T, Soukiasian H, Tabrizi T, Coleman B, Hickey A, Czer LS, Blanche C, Cheng W, Fontana G, Kass RM, Raissi SS, Trento A, 2003, "Biventricular support in patients with profound cardiogenic shock: A single centre experience". *ASAIO Journal* 2003; 49: 465 – 479

United Network for Organ Sharing (UNOS): U.S., Facts about Transplant. 2000

National Institute of Heart (NHLBI-NIH), Fact Sheet. National Heart, Lung and Blood Institute. 1996

Norman JC, Cooley DA, Kahan BD, Keats AS, Masin EK, Solis RT, Luper WE, Brook MI, Klima T, Frazier OH, Hacker J, Duncan JM, Dasco CC, Winston DS, Reul GL, 1978, "Total support of the circulation of a patient with postcardiotomy stone-heart syndrome by a partial artificial heart (ALVAD) for five days followed by heart and kidney transplantation", *Lancet*; 1: 1125 – 7

Nose Y, Ohtsubo S, Tayama E., 1997, "Therapeutic and physiological artificail heart: future prospects". *Artificial Organs*; 2: 592 – 6

Nose Y., 1997, "Development of a totally implantable biventricular bypass centrifugal blood pump system". *Annals of Thoracic Surgery*; 68:2: 775 – 9

Okada Y, Masuzawa T, Matsuda KI, Ohmori K, Yamane T, Konishi Y, Fukahori S, Ueno S, Kim S, 2003, "Axial type self-bearing motor for axial flow blood pump". *Artificial Organs*, 27(10): 887 – 891

Orime Y, Shiono M, Yagi S, Yamamoto T, Okumura H, Kimura S, Hata M, Sezai A, Kashiwazki S, Choh S, Negishi N, Sezai Y, Matsui T, Suzuki M., 2000, "Clinical evaluation of the Gyro pump C1E3 as a cardiopulmonary bypass pump". *ASAIO J*; 46: 128 – 133

Park CY, Park JW, Lee JJ, Kim WE, Hwang CM, Om KS, Choi JS, Kim JW, Shim EB, Jo YH, Min BG, 2003, "Development of totally implantable pulsatile biventricular assist device". *Artificial Organs* 27: 1: 119 – 123

Santamore WP., 1996, "Left ventricular contributions to the right ventricular sysstolic function during LVAD support". *Ann Thorac Surg*; 61: 350 – 356

Seza Y., 2001, "Progress and Future Perspectives in Mechanical Circulatory Support". *Artificial Organs*; 25:5: 318 – 322

Song XW, Throckmorton AL, Untaroiu A, Patel S, Allaire PE, Wood HG, Oslen DB., 2003, "Axial flow blood pumps". *ASIO Journal*; 49: 355

Sun Y, Son HS, Jung JS, Cheong BK, Shin JS, Kim KT, Lee HW, Ahn SS, Park SY, Oh KJ, Lee HS, Shim EB, Rho YR, Lee HS, Min BG, Kim HM., 2003, "Korean Artificial Heart (AnyHeart): An experimental study and the first human application". *Artificial Organs*, 27(1): 8 – 13

Tan AC, Timms D, Pearcy MJ, McNeil K, Galbraith A., 2004, "Experimental Flow Visualisation of an Artificial Heart Pump". *J of the Korean Society of Marine Eng*; 28:2: 210 – 216

Timms D, Tan AC, Pearcy M, McNeil K, Galbraigth A., 2004, "Hydraulic Force and Impeller Evalluation of a Centrifugal Heart Pump". *J of the Korean Society of Marine Eng*; 28:2: 376 – 381

Timms D, Tan AC, Pearcy M, McNeil K, Galbraigth A., 2003, "Force Characteristics of Centrifugal Blood Pump Impellers". Proc of the World Congress on Medical Physics and Biomedical Engineering. Sydney

Watterson, PA, et al., 2000, "VentrAssist Hydrodynamically Suspended, Open, Centrif Blood Pump". *Artificial Organs*; 24:6: 475 – 477

Yamane T., 2000, Artificial Heart Pump. US Patent No. 6015434, Jan

Yoshikawa M., 2000, "Development of an implantable small right ventricular assist device". *ASAIO Journal*; 46:3: 338 – 43

Zaher M., 2001, Design of mixed flow pumps and fans. Magenta Publ

The 4th International Symposium on Fluid Machinery and Fluid Engineering
November 24-27, 2008, Beijing, China
NO. 4ISFMFE-IL04

Experimental Investigation of Wall Pressure Fluctuations in Axial Flow Fans with Different Swept

J. Hurault[*1], S. Kouidri[2], F. Bakir[1] and R. Rey[1]

[*1] Laboratoire d'Energétique et de Mécanique des Fluides Internes, Arts et Métiers ParisTech,
151 Bd de l'hôpital, 75013 Paris, France
Tel: +33-1-44246412 / Fax: +33-1-44246411
E-mail: jeremy.hurault@paris.ensam.fr

[2] Laboratoire d'Informatique pour la Mécanique et les Sciences de l'Ingénieur, CNRS,
BP 133, 91403 Orsay CEDEX, France

Abstract Nowadays, car manufacturer work hardly on reducing energy consumption and the CO_2 emission responsible of the global warming. The goal of this work is to increase the efficiency of the fan cooling systems in order to reduce fuel consumption. To achieve this purpose, it is necessary to have a better understanding of the internal flow and particularly the different losses location.

The sweep is an effective tool to modify the efficiency, and we want to quantify its influence on the unsteady pressure field on fan blades. Both numerical simulation and experimental techniques are used in order to reach this purpose. However neither has given yet entire satisfaction. The CFD tools using the resolution of the averaged Navier Stokes equations do not really give the unsteady aerodynamic characteristics of the flow needed for an accurate noise prediction. In addition, tools using large eddy simulation are still expensive for industrial users in the case of a complex geometry such as turbomachinery.

Unsteady surface pressure measurements were carried out on one fan blade with an array of pressure transducers with high sensitivity. The fan studied is a low pressure and low Mach number axial flow fan. Investigations of unsteady surface pressure are carried out in different configuration, spanwise, chordwise, pressure side and suction side. Data are gathered through a slip ring by an analyzer. Moreover overall features are measured to validate design and fan simulation. These results are presented and analyzed.

A 3D URANS numerical simulation with Reynolds stress model (RSM) is carried out in accordance with an experimental setup. The simulation taking into account the tip clearance is confine to an inter-blade channel in order to minimize computing time. This numerical simulation allowed obtaining Reynolds stress tensor components that is a characteristic feature of the turbulent flow. First, we want to validate this RSM simulation on a radial sweep fan.

We want to determine the sweep effect on the distribution of mean pressure and unsteady pressure on the blade of the fans. A simulation for fans with different sweep is carried out and results are compared between numerical and experimental. The understanding of the influence of the sweep of the fan on the flow behavior is the goal of the present work. Moreover, it is known that the forward sweep is an effective tool to reduce noise emission and the wall pressure fluctuations are important for the broadband noise source.

Keywords axial flow fans, wall pressure fluctuations, broadband noise, reynolds stress model

1 Introduction

The unsteady pressure is an important investigation topic. Numerical simulation with different turbulence models are used in order to achieve this purpose. However neither has yet given entire satisfaction. The CFD tools using the resolution of the averaged Navier Stokes equations do not really give the unsteady aerodynamic characteristics of the flow needed for an accurate noise prediction. In addition, tools using Direct Numerical Simulation or Large Eddy

Simulation are still expensive for industrial users in the case of a complex geometry such as turbomachinery. The validation and development of these high level simulation tools require data and understanding from experiments.

The aeroacoustic noise of low Mach number axial fans results from the encounter of blades with space-varying and time-varying disturbances (interaction noise) or the flow over the blades themselves (self-noise). Axial-flow fans, used in automotive cooling systems in our case, are often subjected to poor inflow conditions. This inflow conditions may be steady state but spatially asymmetric velocity profiles (due to imperfect intake geometry) or timevarying ingested vortices, turbulence or secondary inflow distortions. The resulting periodic and random forces cause tonal and broad-band interaction noise. On the other hand, if the inflow is homogeneous in time and space, the force fluctuations due to the turbulent boundary layer on the blade surfaces and their interaction with the trailing edge cause the inevitable self-noise of the fan which in most cases is broad-band. Moreover the vortex shedding from the blunt trailing edge generate broad-band noise too.

The focus of this work is to examine blade sweep as a mean for alleviating the dominant source of noise, while providing a method of estimating the influence on fan performance, especially the efficiency. The use of blade sweep for noise reduction appears to have been effective. Hanson [1] studied the problem dealing primarily in terms of reduction of blade tonal noise through phase-shift cancellation of noise generated at different radial stations on a blade and by blade-to-blade interference. While his work shows that very large angles of blade sweep may be required, particularly for low-speed rotors, the works of Fukano [2], Brown [3], Cummings [4], and Fujita [5], have shown experimentally that reasonable amounts of sweep may be very beneficial in reducing noise.

In particular, the works of Kerschen [6] and Envia and Kerschen [7] seem to provide a theoretical basis for selecting a distribution of sweep angles along a blade, which provide sharp reductions in the noise associated with turbulence ingestion.

Applied to low-speed axial fans, the backward and forward sweeps alter the spatial distribution of the elementary noise sources so that they are not generated simultaneously on one blade radius (which is the case of the radial swept fan). The phase shift thus produced results in destructive or constructive interferences of the spanwise components (pressure and velocity) and consequently in a modification of the radiated noise. A complete literature on aerodynamic and acoustic properties of axial fans with swept blades is presented in reference [8].

Kouidri et al. [9] investigated the response of swept blades to a gust. Their numerical simulation yields steady and unsteady loading on the blades; the Ffowcs Williams & Hawkings formulation was used to derive the tonal part of the acoustic spectra of the unducted impeller. However, for the spatially uniform but temporal unsteady inflow, the URANS-method fails. The prediction of broad-band noise sources requires a high level numerical method.

In [10], Amiet investigated the noise and unsteady surface pressure characteristics of an isolated airfoil in a uniform mean velocity with unknown turbulence statistics. Brooks and Hodgson [11] report a study of the noise and pressure field beneath the turbulent boundary layer on a isolated NACA 0012 airfoil in a low turbulence jet.

However, even if one restricts oneself to the individual blade response rather than on the correlated thrust response of the rotor to large scale inflow distortions, the situation in a fan rotor is by far more complicated. Secondary flows in the hub and tip region of the blade occur; the tip clearance causes locally highly unsteady flow patterns and thus unsteady forces [9]; the inflow distortions are spacially distributed, parts of the blade intersect the duct wall turbulent boundary layer; the incident turbulence may not be isotropic [12].

Carolus et al. [13] used hot wire anemometry to obtain a database for detailed verification, the turbulence statistics for a variety of different inflow configurations. He found that the LES predicted effects of the ingested turbulence on the fluctuating blade forces and the fan noise compare favourably with experiments.

Several models which have been designed to predict the radiated broadband noise of a fan need information on the surface pressure fluctuations and their correlation area. This data are not readily available for turbomachinary contrary to airfoil.

2 Experimental Set Up

The goal of this research work is to investigate the unsteady wall pressure field in axial flow fans with low Mach number. Ultra-light pressure transducers are flush mounted in order to measure unsteady phenomenon governing the acoustics of turbomachinery.

The fans used in this study are prototypes developed for an automotive engine cooling system application (Fig.1). They are of the axial flow type and have the same geometrical characteristics except the sweep. The first fan

has a radial sweep perform on the leading edge and the second is swept in the rotational direction (forward sweep). Each of these fans has 8 blades. The design characteristics of the two axial fans are as follows: an external radius $R2 = 187.5$ mm, an internal radius $R1 = 85$ mm (hub-to-tip radius ratio $R1/R2 = 0{,}453$) and a stagger angle 75° at mid-span. The shroud has a thickness of 2,5 mm.

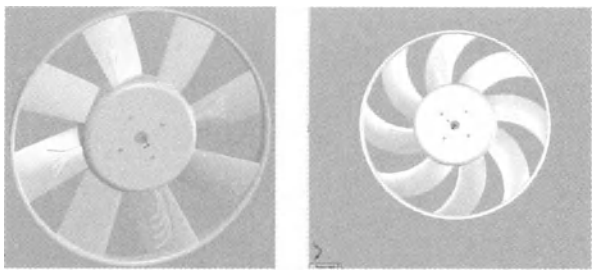

Fig. 1 Axial flow fan with radial sweep (left) and forward sweep (right). Pressure transducer location in green

All the measurements are performed at the nominal flow rate (Qn) and 130% of the nominal flow rate (1.3Qn) for the two fans.

According to the radial equilibrium hypothesis, an axial fan should present a flow field with 2D-structure: the radial component of the absolute velocity should be negligible. This situation is rarely observed since an energy transfer occurs between the concentric air tubes, so that a 3D-description of the axial fan flow field is needed. The axial component Ca, tangential component Ct and also the radial component Cr of the velocity vector must be measured.

Figures 2 and 3 show the experimental facility. The air test bench, designed and built at LEMFI-Arts et Métiers ParisTech according to the ISO 5801 standard [14], enables a controlled air flow rate to operate at the design point, choosing the adequate orifice plate diameter.

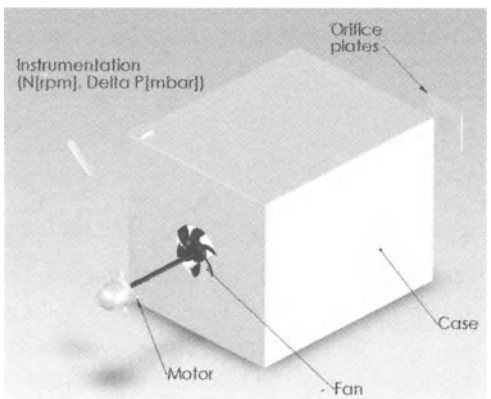

Fig. 2 ISO 5801 test bench

A test bench was designed and made in order to carry out wall pressure fluctuation (Fig. 3). Very small high accuracy piezoresistive transducers were chosen in order to get the mean and the unsteady pressure (Fig. 4). Their size allow a non intrusive measurement on the small blade of a engine cooling fan prototype design to be manufacture.

All the test bench is design in order to reach a rotation speed of 3000 rpm, especially the slip ring. An effective work had been performed to balance and reduce the mass in rotation. Measurement is performed on a ISO 5801 test bench in order to control the flow rate.

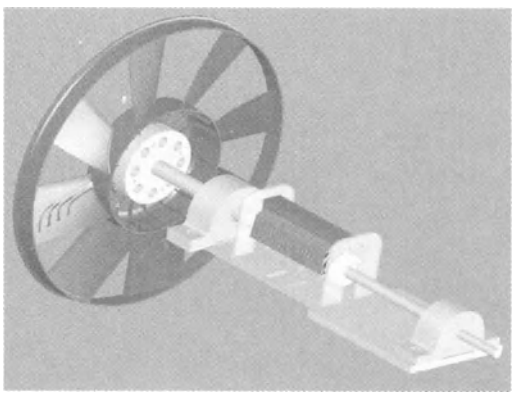

Fig. 3 Test bench with slip ring (red and yellow), special hub and shaft (grey) design to work à 3000rpm

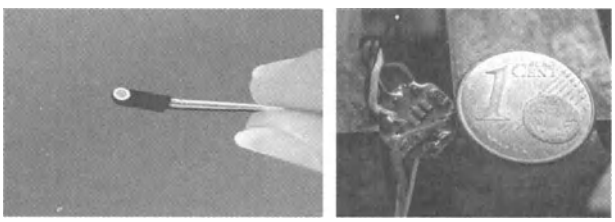

Fig. 4 Ultra compact pressure transducer (left) and amplifier (right)

Eight sensors are simultaneously flush mounted. Four by four on opposite blade in order to balance the mass. Four on the suction side and four on the pressure side chordwise, then four by four spanwise (Fig.1). The sensor are located as close as possible to the trailing edge in order to carry out the pressure fluctuations source of the trailing edge noise. The fan is fast prototype in polymeric material in order to keep the behavior compare to the mass-product industrial fans.

Each sensor are calibrate with a test bench specially developed for this application. A controlled leak flow allow a very good stability of the pressure in the calibration chamber. A voltmeter with 10-5 V and a manometer with 10-1 Pa accuracy are used.

3 Numerical Simulations

The 3D simulations were performed with the commercial CFD code Fluent 6.3. In this study, principally unstructured tetrahedral meshes are used because the geometry near the blade is complex. A fully implicit solution strategy is employed.

The rotor is built up from blades of NACA0065, with a thin profile of maximum thickness 5. 5 mm along the camber lines, rounded at the leading and trailing edges. The blades, however, are radially swept in two different ways as shown in figure 1. The first fan presents a radial sweep (G2radial) and the second one is swept in the direction of rotation (G2forward).

The Reynolds Stress Model involves calculation of the individual Reynolds stresses, $\overline{u'_i u'_j}$, using differential transport equations. The RSM model is a RANS second-moment closure which solves six equations for the Reynolds Stress Tensor. It represents the influence of turbulence on the mean flow. The individual Reynolds stresses are then used to obtain closure of the Reynolds-averaged momentum equation.

The exact form of the Reynolds stress transport equations may be derived by taking moments of the exact momentum equation. This is a process wherein the exact momentum equations are multiplied by a fluctuating property, the product then being Reynolds-averaged. Unfortunately, several of the terms in the exact equation are unknown and modelling assumptions are required in order to close the equations.

The convergence criteria are 10^{-5} for the residuals of 12 equations (continuity, the three components of the velocity, the k and the ε, and the 6 Reynolds stress tensor components).

Geometry and meshing

In order to well compare the predicted results to the experiments, a numerical test rig was created to reproduce the experiments performed in the real test rig shown in figure 2. This numerical test rig was created using SolidWorks and meshing with Gambit 2.2. Figure 2 shows an over view of the modelled test rig following the ISO5801 including the fan location. The simulation is made on an inter-blade channel in order to minimize computing time. One eighth of the domain is modelled with periodic boundary condition because we have an eight blades fan. A tip clearance of 4mm is modelled according to the experimental set up. Two different geometries were created, one for the radial sweep blade and another one for the forward sweep fan (Fig. 5).

Fig. 5 Geometry and boundary condition for the radial fan (right) and the forward fan (left) in the ISO 5801 test bench

In figure 5, the blue, grey, yellow and red colours correspond to the inlet, the walls, the fan interfaces with the box and the outlet, and the outlet respectively. The box has the same dimension as the experimental box but is rounded to respect the periodicity in rotation. Velocity inlet boundary condition is used because of the very low Mach number. Pressure outlet is atmospheric condition. The mesh was created using the unstructured Gambit 2.2 mesh generator. The total number of cells is 4 millions. It equals to 32 millions of cells for the entire box/fan/outlet domain. The mesh size is very small near the fan about 1mm, and becomes progressively bigger far from the fan. Figure 6 illustrates the mesh over view for a given fan.

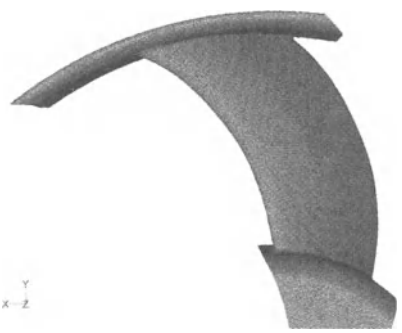

Fig. 6 Mesh of the forward swept fan

The fans are rotating at 2700 rpm (45Hz). Static pressures are measured on the box wall. In the experimentation, orifice plates with different diaphragm's diameter are used to fit the flow rate. In the simulation, the velocity inlet boundary condition fitted the flow rate.

The general problem was made up of three domains. The fan sucks the airflow from inside the box to the atmospheric conditions. Therefore, the boundary conditions imposed are mass flow at the inlet and static pressure at the outlet. Modelling is focus on details which are very important on measurement and simulation results like the tip clearance and the inlet diaphragm's chamfer.

4 Results and Discussion

Acoustics results

Figure 7 compare the sound pressure level between the G2radial and the G2forward fans. Measurement are performed with a ½" GRAS free-field microphone type 40AE at 1 meter downstream of fans with a height equal this of the fan axis. The angle between the rotational axis of the fan and the axis of the microphone is 45°. This measurement is performed at 1.3Qn. This graphics confirm the decrease of the broadband and tonal noise with the G2forward. The tonal component at 4k Hz, 8k Hz and 12k Hz are electromagnetic perturbation due to the variable speed drive of the electric engine. Figure 8 show the decrease of the level of the blade passage frequency tonal noise (BPF = 8*45 = 360Hz) and its harmonics for the G2forward. This results validate the fact that the forward swept reduce the noise emission. We must be careful because in the next section we can see that the forward sweep reduces the aerodynamic power produce by the fan.

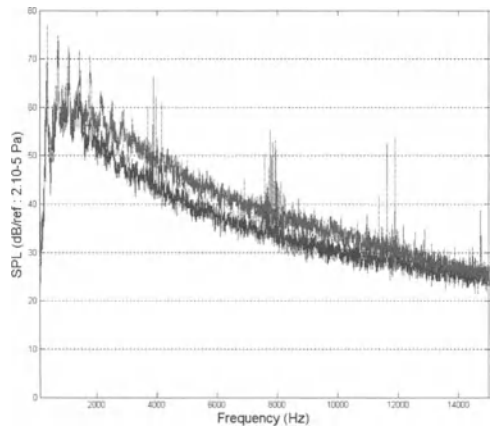

Fig. 7 Sound pressure level between the G2radial (Red) and the G2forward (Blue) at 1.3*Nominal flow rate

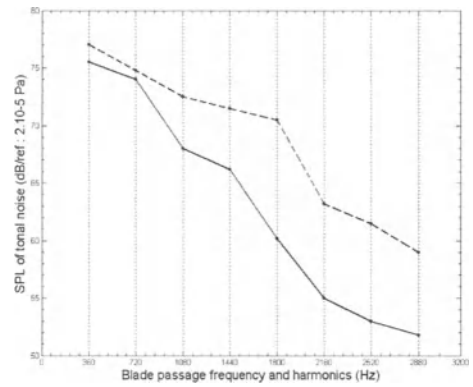

Fig. 8 Level of the tonal noise at BPF and its harmonics between the G2radial (Red) and the G2forward (Blue)

Overall characteristics

The pressure rise versus the flow rate is represented in Fig. 9. We can see that the numerical RSM results with the two fans are close to the experiment, more especially around the nominal flow rate. There are some discrepancies at the very high flow rate due to the non adjustment of the flow which yield to difficult convergence in the simulation. Five flow rates are calculated around the radial swept fan nominal flow rate. The blue curve is the result of calculation with the RSM turbulence model for the G2forward. Its pressure rise is below the G2radial.

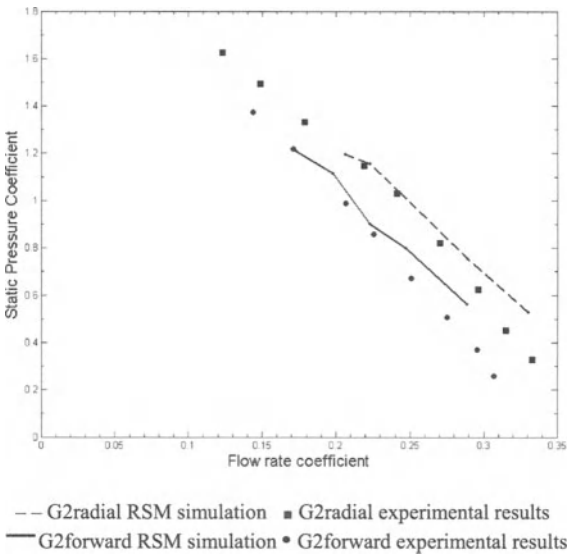

Fig. 9 Static pressure coefficient VS Flow rate coefficient for the two fans

The efficiency calculation is based on the following relation:

$$\eta = \frac{\Delta P_{Stat} \times Q_v}{\omega \times C} \quad (1)$$

Where Q_v is the flow rate in [m³/s], ω is the rotation speed [rad/s], C the torque on the fan [N·m] and ΔP is the predicted static pressure difference between the casing and the atmospheric conditions [Pa].

The static efficiency is shown Fig. 10. A maximum of 6% of error is observed between the experimental and the simulation. The G2forward has a nominal flow rate lower than the G2radial (0.23 vs 0.25). The maximum efficiency of the G2forward is lower than the G2radial one. This depends on the geometrical behavior of the fan because on different fan with get the opposite results for the efficiency evolution.

The sweep of the fan is known to improve the acoustic behavior, but aerodynamic ones are quite different. The maximum static efficiency of the G2radial is better and at a higher flow rate than the G2forward, and the pressure rise is higher. Looking the overall behavior, the RSM simulation is validated on the fans.

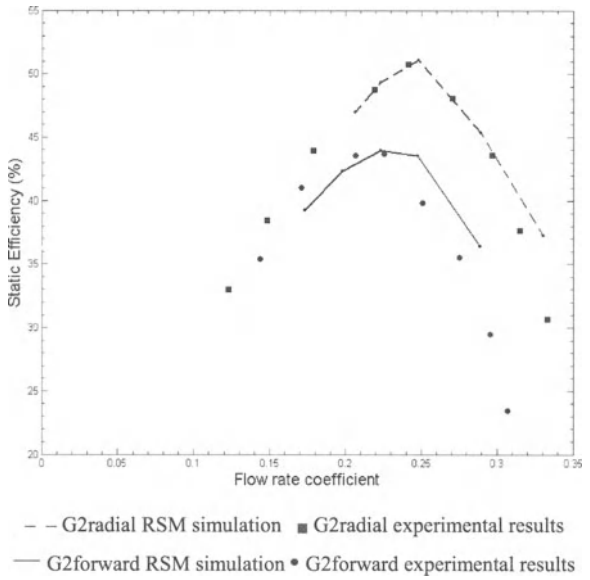

Fig. 10 Static efficiency VS Flow rate coefficient for the two fans

5 Wall Pressure Measurement

The pressure measurement with flush mounted transducer is very difficult. The unsteady pressure is very low above all compare with mean pressure. Precision of this sensor are the lowest possible nowadays. This is the first results (Fig. 11) but we need more work to carried out more precise Power Spectrum Density. For example, the peak at 8k Hz shouldn't appear, in fact it is due to electromagnetic perturbation of the speed velocity controller. We see that the higher level of the PSD of the pressure fluctuation is for the suction side, in accordance to previous measurement [13].

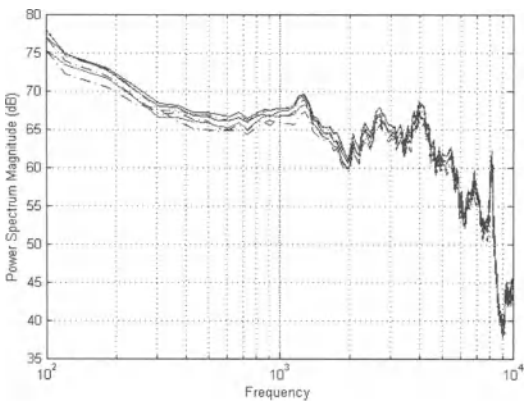

Fig. 11 Power spectral density of the raw data for 3 sensor on the suction side (straight line) and 3 sensor on the pressure side (dash line) at the design flow rate. This sensor is in the spanwise configuration

6 Conclusion

This is an overview of the work in progression at LEMFI concerning the understanding of unsteady flow. The goal is to be capable of predicting with good accuracy and in a fast way the behavior of the fan for efficiency or noise emission. The measurement of wall pressure fluctuations is a very difficult topic and we need more work to achieve reference measurement, even if good first result are already carried out.

The forward sweep can reduce noise emission but decrease aerodynamic power of the fan. In our case the efficiency is reduce but on other fan it can increase the maximum efficiency compare to radial sweep fan.

The second perspective is to validate analytical model for trailing edge noise prevision. The model developed at LEMFI by FEDALA for the leading edge interaction noise for fan using the Amiet model for thin airfoil will be adapt to the fan trailing edge noise. The far field noise spectrum obtain will be compare to the experimental one.

References

Hanson, D.B., *Near-field frequency-domain theory for propeller noise*. AIAA Journal, Vol.23, No.4, pp 499 - 504, 1984

Fukano, T., Kodama, Y. and Takamatsu, Y., —*Noise generated by low-pressure axial flow fans*, Journal of Sound and Vibration, vol. 56, 1978

Brown, N.A., —*The use of the skewed blades for ship propeller and truck fans*. Bolt, Beranek and Newman, 1973

Cummings, R.A., Morgan W.B., and Boswell, R.J., —*Highly skewed propeller*. Transaction of the SNAME, Vol.80, 1972

Fujita, H., —*Noise characteristics and outlet flow field of axial flow fans*. Noise-Con Proccedings, Purdue University, 1979

Kerschen, E.J., —*Noise generation by a finite span swept airfoil*. AIAA paper No. 83, 1983

Envia, A., Kerschen, E.J., —*Noise generated by convected gusts interacting with swept airfoil cascades*. AIAA paper No.86, 1986

Wright,T., and Simmons, W.E., —*Blade sweep for low-speed axial fans*. Journal of turbomachinery, pp. 151-158, 1990

Kouidri, S., Fedala, D., Belamri, T., Rey, R. —*Comparative study of the aeroacoustic behavior of three axial flow fans with different sweeps*. FEDSM, 2005

R. K. Amiet. Acoustic radiation from an airfoil in a turbulent stream. J. Sound Vib, 41, 1975

T.F. Brooks, T.H. Hodgson, —*Trailing edge noise prediction from measured surface pressure*—Journal of sound and vibration, vol. 78, 1981

D.B. Hanson—*Spectrum of rotor noise caused by atmospheric turbulence*. Journal of acoustic Soc. Am., vol. 56, 1974

Carolus, T., Schneider, M., Reese, H. —*Axial Flow fan broad-band noise and prediction*. Journal of sound and vibration, vol. 300, 2006

AFNOR, *ISO 5801: Industrial fans, performance testing using standardized airways*, 1999

The 4th International Symposium on Fluid Machinery and Fluid Engineering
November 24-27, 2008, Beijing, China
NO. 4ISFMFE-IL03

Meso and Macro-Scales Fluid Flow Simulations with Lattice Boltzmann Method

A.A. Mohamad

Dept. of Mechanical and Manufacturing Engineering
Schulich School of Engineering,
University of Calgary, Calgary, AB, T2N 1N4, CANADA
E-mail: mohamad@ucalgary.ca

Abstract An overview is given on application of Lattice Boltzmann method (LBM) for simulations of wide range of isothermal and non-isothermal fluid flows. Flows in meso systems, Knudsen number order of 0.1, to macro systems, Knudsen number of order of 0.0, are discussed and illustrated. It seems that LBM is powerful technique for simulations fluid flow and may replace conventional CFD (computational fluid dynamics) techniques, such as finite volume, finite element, etc. Despite the power of LBM for simulations of complex and multiphase flows, yet there are few issues needed to be addressed. Multi-scale and Entropy versions of LBM are promising in enhancing the stability of LBM.

Keywords Lattice Boltzmann method, lid driven cavity, natural convection

1 Introduction

Computational Fluid Dynamics (CFD) is based on solving Navier Stokes equations reached maturity level within last 50 years. It became design tool and helped to understand physics of many complex fluid flow problems. Now a days there are attempts to automate CFD for design process and reduce human interface with the design process. CFD engineering applications is very wide, from aerodynamics of planes and automobile to nano-scale fluid flows and transport processes. Historically, finite element is used to solve fluid flow problems in early 1960's and finite volume (control volume) method took the momentum in late 1970 [1, 2]. Despite all progress, still some of the modelling process is state of art, such as complex flow modeling, multi-phase and multi-component flows, combustion process and turbulent flows. For instance, turbulent modelling still needs more research, especially near boundary modelling and buoyancy driven flows. Complex boundary condition is no more an issue. However, complex physics and multi-scale problems need further works. On small scale level, i.e., micro scale (Knudsen number order of less than 0.001), the physics is the same, except that the surface area per unit volume increases, for example for flow in conduit the ratio of surface area per unit volume (RSV) is proportional with inverse of hydraulic diameter. To be more specific, for a tube of diameter one micro meter, the RSV is order of $10^6 m^{-1}$. Hence, the contact surface conditions (such as roughness, adsorption, catalytic effects, etc) on the flow characteristic become important. For scales of order of Knudsen number of 10 larger above (nanoscale), continuum mechanics fails to predict the correct physics of the problems, i.e, Navier Stokes equations predictions break down. Molecular Dynamics simulation (MD) or Monte Carlo (MC) is usually used for simulation nano-scale phenomena. For, scale of Knudsen number of order of less than unity, which called meso-scale, usually Navier Stokes equation can been used with modified boundary conditions, slip condition. In the previous paragraphs, the history of the development and application of CFD based on Navier Stokes equation is glanced.

In late 1980, another method of fluid flow simulation is started merging. The method is based on Boltzmann equation, which is called Lattice Boltzmann method (LBM) [3]. The method gained high momentum in applications, where scientists and engineers applied the method for many problems, such as flow in complex

geometries, flow in porous media, multi-phase flows. Within last two decades, the number of papers published on the topic is about 900,000. Just last year and in one journal (PR) the number of papers with title LBM was about 50.

The main reason for the popularity of LBM is its simplicity in coding. LB equation is linear, where the non-linearity is embedded implicitly in the collision operator. Also, handling complex geometry is not challenging. Furthermore, LBM is based on collision and streaming processes, both processes are local in nature and easily can be adopted on parallel processor machines. Moreover, multiphase and multi-physics can be injected into the method as an external force. Hence, combing thermodynamics with transport phenomena can be done naturally. All these advantages gives upper hand for LBM compared with conventional CFD methods. However, there are many issues that need to be resolved. Grid refining somehow is not straightforward. Stability issue of LBM is not clear, etc.

In the following section, the LBM will be introduced, boundary condition will be discussed and incorporating other physics with LBM will be elaborate. Finally, few simulations will be illustrated.

2 Lattice Boltzmann Method

Single relaxation time collision Boltzmann equation, BGK model (Bhatnager-Gross-Krook [4]) without force can be written as,

$$\frac{\partial f}{\partial t}+e\cdot\nabla f=-\frac{f-f^{eq}}{\tau} \tag{1}$$

Where f is the particle distribution function, e is the particle velocity, τ is the relaxation time due to particle collision, and f is the equilibrium Boltzmann-Maxwell distribution function. In Lattice Boltzmann Method (LBM), the particle velocity can be discretized along the lattice links, as,

$$f_k(x+e_k\,\delta t,t+\delta t)=f_k(x,t)-\frac{\delta t}{\tau}\left[f_k(x,t)-f_k^{eq}(x,t)\right] \tag{2}$$

Where f_k is the distribution density function along k-direction moving with velocity of, e_k. For D2Q9 the equilibrium distribution function can be expressed as,

$$f_k^{eq}=w_k\,\rho(x,t)\left[1+\frac{c_k\cdot\mathbf{u}}{c_s^2}+\frac{1}{2}\frac{(c_k\cdot\mathbf{u})^2}{c_s^4}-\frac{1}{2}\frac{\mathbf{u}^2}{c_s^2}\right] \tag{3}$$

where $c_s=\frac{c_k}{\sqrt{3}}$, $c_k=\frac{\Delta x}{\Delta t}i+\frac{\Delta y}{\Delta t}j$. In selecting number o lattice linkage and direction of particle velocity, th conservation of isotropy and Galilean invariance need t be insured.

Analysis shows that LBM resembles Navier-Stoke equations for incompressible flow for low Mach numbe (Ma=flow speed/sound speed=U/c). The error in LBM i order of Ma^2.

The fluid viscosity is related as,

$$\nu=\frac{\Delta x^2}{3\Delta t}(\omega-0.5)=\frac{c_s\,\Delta x}{3}(\omega-0.5) \tag{4}$$

Where w is equal to dt/t.

Reynolds number, $\mathrm{Re}=U\,L/\nu$, where U and L ar characteristic velocity and characteristic length, respectively

Using above equations, it can be shown that Ma relate to Re as,

$$Ma=\frac{\Delta x}{3L}(\omega-0.5)\,\mathrm{Re} \tag{5}$$

The value of $L/\Delta x$ is the number of lattices in th direction of the chrematistic length, say N. For Δx o unity as a normal practice in LBM, $L=N$, hence $\mathrm{Re}=U$ N/ν. For accurate solution, Ma should be kept small therefore, ω or N should be chosen to insure low Ma value. In general, U order of 0.1 is very practical.

Also, Knudsen number can be related to dimensionles relaxation time (t/dt) and number of lattice (N) as [4],

$$Kn=\sqrt{\frac{8}{2\pi}}\,\frac{\frac{\tau}{\delta t}-0.5}{N} \tag{6}$$

The summation of distribution function at each lattic site represents the macroscopic fluid density,

$$\rho=\sum_{k=0}^{8}f_k \tag{7}$$

The momentum can be represented as an average of th lattice (microscopic) velocities c_k, weighted by th distribution function,

$$\rho\mathbf{u}=\sum_{k=0}^{8}f_k\,c_k \tag{8}$$

The pressure is given by $p=\rho/3$, which postulates a constant sound speed of $c_s=\frac{c_k}{\sqrt{3}}$.

3 Boundary Conditions

One of the important and crucial issues in LB simulation of flow is accurate modeling of the boundary conditions. Adapting boundary condition for Navier Stokes equations is somehow straightforward. This is not the case for LBM, where the inward distribution functions to the integration domain need to be determined at the boundaries. Therefore, we need to determine appropriate equations for calculating those distribution functions at the boundaries for given boundary conditions. In the literature different approaches are suggested and tested. In the following paragraphs two types of boundary conditions are explained. The mean idea is not to review different attempts, but to discuss, in our point of view, the simple and more robust methods.

3.1 Bounce Back

Bounce back is used to model solid stationary boundary condition, non-slip condition, or flow over obstacles. The method is quite simple and mainly implies that an incoming particle towards the solid boundary is bounced back into fluid. In the literature few version of bounce back scheme have been suggested. One of the schemes is to locate the wall at the half distance from the lattice sites, as shown in Fig. 1. The distribution functions, f_4, f_7 and f_8 are known from streaming process. It is assumed that, when these known distribution functions hit the wall they bounce back. Therefore,

$f_5 = f_7, f_2 = f_4$ and $f_6 = f_8$

The bounce back insures conservation of mass and momentum at the boundary. Other authors used different strategies, yet the wall at the mid way between two lattice sites. However, the domain is extended inside the solid wall. The bounce back is taking place inside the wall. Another scheme, yet the simple one is to locate the lattice directly at the solid surface and not at middle plane. Some authors claim that this scheme is first order accurate. This scheme is quite simple compared with the pervious schemes and our experience with this scheme showed that for all tested problems we carried the scheme works quite well and results are comparable with other schemes. As a summary, for practical applications the simple scheme is recommended.

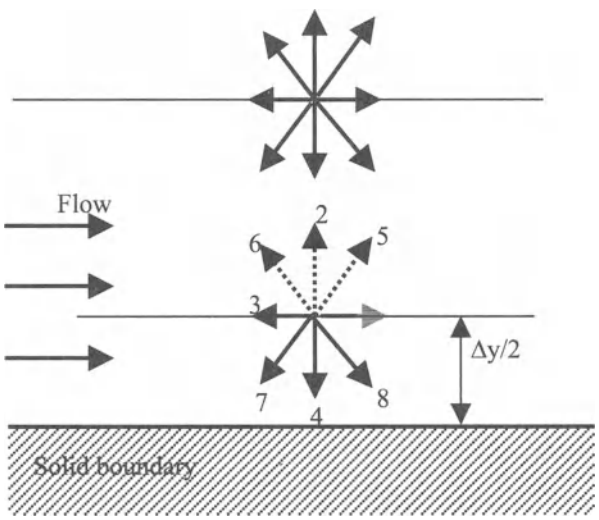

Fig. 1 Bounce back scheme

Bounce back can be applied to all lattices on the solid surfaces in modeling flow over an obstacle. For instance flow in porous medium, Fig. 2, can be simulated by discrete solids embedded in a fluid flow. Bounce back used for nodes on the solid surfaces.

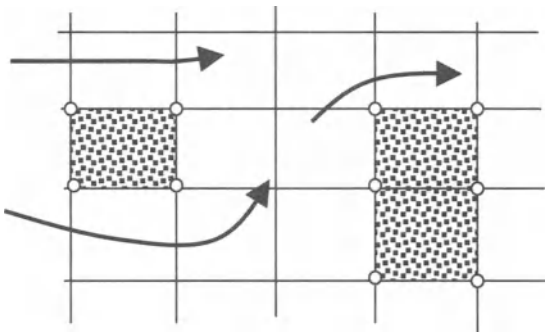

Fig. 2 Flow through porous medium

3.2 Boundary Condition With Known Velocity

It is very common in practical applications that we know velocity component at the boundary, for example inlet velocity for a channel flow. In LBM method we need to specify inward distribution functions at the boundaries. For instance, if the flow velocity is given at the left hand boundary, the distribution function streaming from the boundary toward the fluid need to be calculated (in Fig. 1, f_5, f_2 and f_6 are unknowns).

Zhu and He [5] described a method to calculate these three unknown distribution functions based on definitions of velocity and density with equilibrium conditions assumption normal to the boundary.

The density is defined as,

$$\rho = f_0 + f_1 + f_2 + f_3 + f_4 + f_5 + f_6 + f_7 + f_8 \tag{9}$$

The x-component of momentum can be expressed as,

$$\rho u = f_1 + f_5 + f_8 - f_6 - f_3 - f_7 \tag{10}$$

And for y-component as,

$$\rho v = f_5 + f_2 + f_6 - f_7 - f_4 - f_8 \quad (11)$$

The above three equations with extra unknown, ρ, at the boundary, hence, we need another condition to solve for four unknowns (three distribution function and ρ). The condition comes from assumption equilibrium condition normal to the surface.

3.3 Open Boundary Condition

In some problems, the outlet velocity is unknown. In this case it is normal practice to use extrapolation for distribution functions. For instance, if the east boundary condition on Fig. 1, represents the outlet condition. Then f_3, f_6 and f_7 need to be calculated at the east boundary, $i = n$. Second order polynomial can be used, as:

$$f_{3,n} = 2 \times f_{3,n-1} - f_{3,n-2}$$

$$f_{6,n} = 2 \times f_{6,n-1} - f_{6,n-2} \quad (12)$$

and

$$f_{7,n} = 2 \times f_{7,n-1} - f_{7,n-2}$$

Second order extrapolation may lead to unstable solution for some problems. In such case, first order extrapolation may work. Applying this kind of boundary condition does not always give accurate results. This is due to wave propagation toward the domain due to compressibility nature of LBM.

4 Force Term and other Physics

Force term is key issue of adding extra physics to the LBM method, such as buoyancy term, multi-phase, surface tension, nano particles, etc. Hence, the LBM method is the same as explained before and only an extra term needs to be added to simulate complex flow problems.

Martys, Shan and Chen [6] and Luo [7,8] adding source term to the distribution function.

Guo, et al [9] showed that the mentioned method can work properly if the force has zero gradient. Otherwise, the LBM does not properly recover from the Navier Stokes equation. Their analysis showed that the extra terms in mass and momentum conservation equations (non-hydrodynamic) are a function of the gradient of the force. Ladd and Verberg [10] shifted mass-velocity field by Δt F/2, hence the mass conservation is insured. However, the momentum equation is not accurately recovered as the analysis of Guo et al revealed [9]. Buick and Greated [11] reviewed and introduced a modification for the pervious methods of treatment external force. Guo et al argued that the method introduced by Buick and Greated is incorrect. In the literature, the most popular methods are either adding extra force term to the collision term or by modifying the velocity field with force term using Newton 2nd law.

In the following section few simulation results will be shown to illustrate the application of LBM for few fluid flow problems.

5 Simulation Results

Lid driven cavity is a typical benchmark solution used to validate CFD codes. By using LBM, flow in a lid driven cavity is simulate up to Re = 15,000, Figure 3 shows time series for x and y-component velocities at the center of the cavity for Re = 15,000. The oscillatory flow with high amplitude asymptotically approached low amplitude aperiodic solution. Figure 4 shows streamlines for the same problem. Multi-vortices are evident at the corner of the cavity. Results of flow in a channel with moving upper wall are shown in Fig. 5. The channel's bottom has many intruded obstacles. Figure 6 shows the x-component velocity profiles at different sections of the channel. The velocity profile on the top of the obstacle is almost linear and reverse flow is evident at the lee of the obstacles. Figure 7 shows dimensionless pressure distribution along the channel at mid height and at the moving lid. The figure reflects the physics of flow. Figure 8 shows flow over an obstacle. Furthermore, natural convection in an open cavity is shown in Fig. 9. This problem is interesting, because the flow at the opening is not known prior to solution. The results obtained by LBM matches results obtained by finite volume method. Due to space limitation other simulation results will be presented in the meeting.

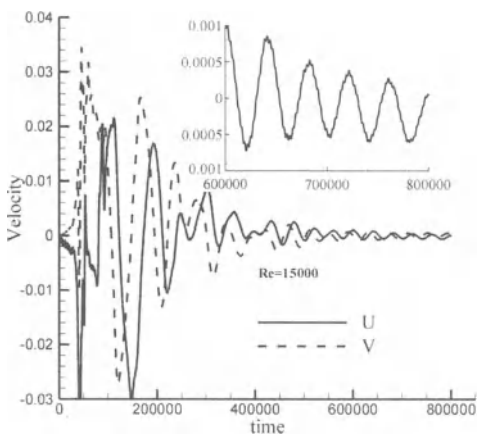

Fig. 3 Time series for U and V velocity at the centre of the cavity for Re = 15,000

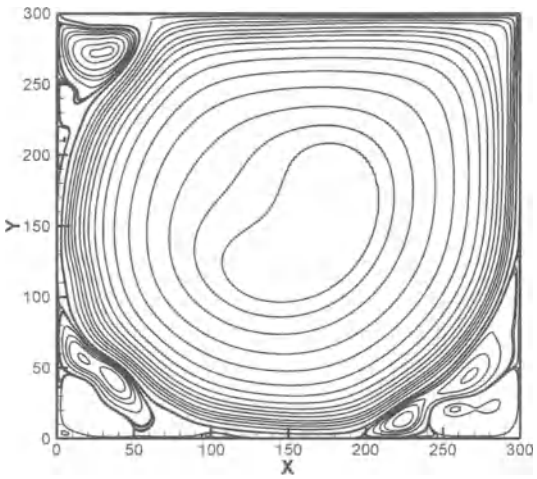

Fig. 4 Streamlines, Lid driven cavity, Re = 15,000

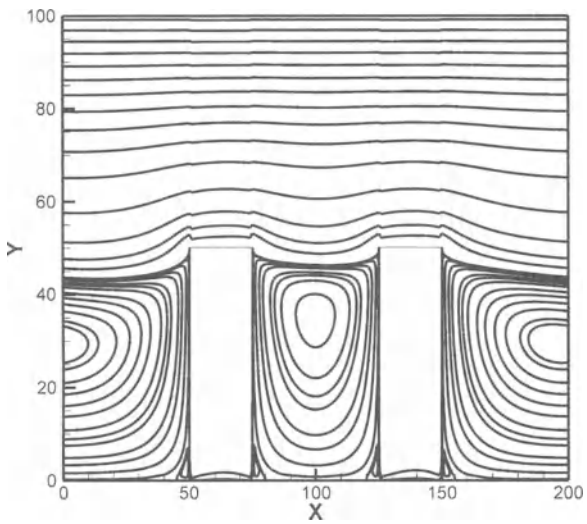

Fig. 5 Streamlines for flow in a channel with moving lid

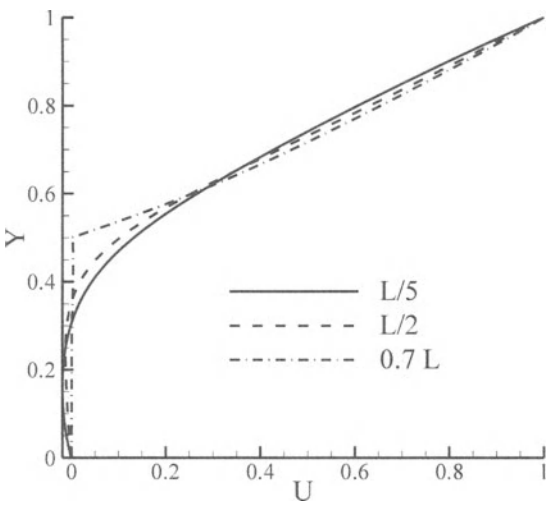

Fig. 6 U-velocity profiles at different sections of the channel

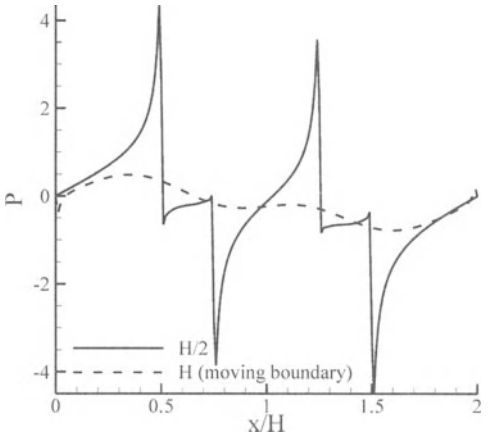

Fig. 7 Dimensionless pressure variation along the channel

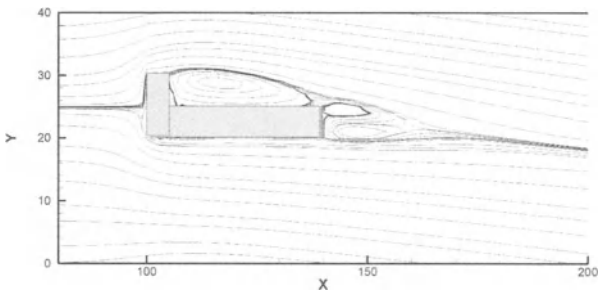

Fig. 8 Streamlines over an obstacle

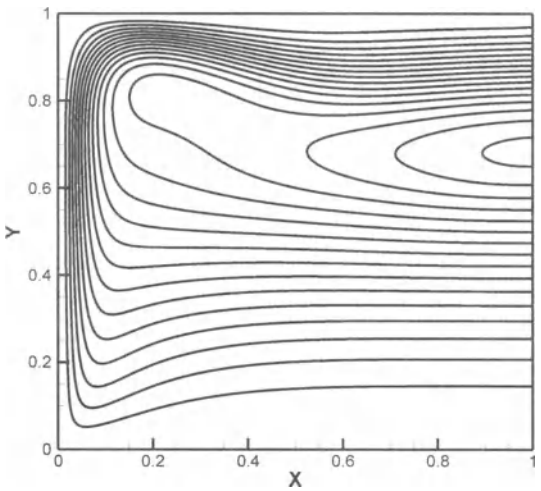

Fig. 9 Streamlines in an open cavity, the flow is buoyancy driven, $Ra = 10^5$

6 Conculuding Remarks

Lattice Boltzmann method applied for many fluid dynamics problems and compared with predictions of conventional method. Namely flow in lid driven cavity at high Reynolds number, Re = 15000, flow in a channel with

moving lid and with many obstacles, flow over an obstacle, finally buoyancy driven flow in an open cavity, Rayleigh number of 10^5. The method is easy to apply to complex flow and other physics can be injected into the model as an external force.

References

A. A. Mohamad, 2007, Applied Lattice Boltzmann Method, for Transport Phenomena, Momentum, Heat and Mass Transfer, *Sure Print, Dalbrent, Calgary*, Canada

S. V. Patankar, 1980, Numerical Heat Transfer and Fluid Flow, *Hemisphere, New York*

G. R.McNamara and G. Zanetti, 1988, Use of the Boltzmann equation to simulate lattice gas automata, *Phyical Review Letters*, 61, pp. 2332 – 2335

Y. H. Zhang, R. S. Qin, Y. H. Sun, R. W. Barber and D. R. Emerson, 2005, Gas Flow in Micro Channels- A Lattice Boltzmann Method Approach, *J. Statistical Physics*, 121, 257 – 267

Q. Zou and X. He, 1997, On Pressure and Velocity Boundary Conditions for the Lattice Boltzmann BGK Model, *Physics of Fluids*, 9, 6, 1591 – 1690

N.S. Martys, X. Shan and H. Chen, 1998, Evaluation of the external force term in the discrete Boltzmann equation, *Phys. Rev.* E 58, 6855

L.S., Luo, 1998, Unified theory of lattice Boltzmann Methods for nonideal gases, *Phys. Rev. Letter*, 81, 1618

L.S., Luo, 2000, Theory of the lattice Boltzmann method: Lattice Boltzmann models for nonideal gases, *Phys. Rev.* E 62, 4982 – 4996

Z. Guo, C. Zheng and B. Shi, 2002, Disceter lattice effects on the forcing term in the lattice Boltzmann method, *phys. Rev.* E, 65, 046308

R. Verberg and A.J.C. Ladd, 2001, *Phys. Rev.* E 65, 016701

J. M. Buick and C. A. Greated, 2000, Gravity in a lattice Boltzmann model, *Phys. Rev.* E 61, 5307 – 5320

The 4th International Symposium on Fluid Machinery and Fluid Engineering
November 24-27, 2008, Beijing, China
NO. 4ISFMFE-IL24

Engineering Flow Performance by Local Dynamics: Theories and Applications

Jiezhi Wu[*1,2], Feng Mao[1], Weidong Su[1], Hong Wu[3] and Qiushi Li[3]

[*1] State Key Laboratory for Turbulence and Complex Systems
College of Engineering, Peking University
Beijing, 100871, China

[2] University of Tennessee Space Institute, Tullahoma, TN 37388, USA

[3] National Key Laboratory on Aero-engines School of Jet Propulsion
Beijing University of Aeronautics and Astronautics
Beijing, 100083, China

Abstract The performances of various flows in engineering applications are conventionally defined and assessed in terms of primary variables. But these performances are dominated by local dynamic processes and structures measured not by these variables themselves but their spatial-temporal derivatives. To fully understand what key local processes/ structures in a flow dominate its performance, and to rationally optimize flow management, theories are needed to re-express the performances by local dynamics. The more complex the flow is, the more urgently is such theories needed. In this article we present a critical review of the relevant theories, applicable to both external and internal flows with large Reynolds numbers and wide range of Mach numbers. Examples are given to demonstrate the combined theoretical-numerical local-dynamics approach to complex flow management, showing how it leads to unique physical insight and significant performance improvement.

Keywords flow diagnosis, optimal design, vorticity dynamics, applied aerodynamics

1 Introduction

Any practical external or internal engineering flow has a set of performances as its design objectives. These performances are defined globally by integrated quantities, e.g. the lift and drag of a wing, the pressure ratio and efficiency of a compressor, or the operation stability of a fluid machine. Ever since Helmholtz (1858), it has now been well recognized that all global performances are dominated and organized by various local dynamic structures, such as boundary layers, free shear layers, vortices, turbulent coherent structures, shock waves and other nonlinear acoustic waves, as well as entropy waves. Even a single local process or structure, say the early separation of a boundary layer or a shock, may have strong impact on the global flow performance. In a viscous compressible flow, these structures are the product of three fundamental processes and their coupling: shearing process, compressing process, and thermal process (Chu et al. 1957, Kovasnay 1953). It is the richness of flow structures, along with their nonlinear evolution and interaction, which makes a big variety of complex flows. Modern flow engineering needs more urgently than ever deep insight into the underlying physics of these complex flows, which is the very basis of *optimal flow management* including configuration designs and flow controls.

As a general rule, flow structures are measured not by primary variables themselves (e.g., velocity $\boldsymbol{u}$, pressure p, and entropy s) but their spatial-temporal derivatives, e.g. vorticity, dilatation, pressure gradient, and entropy gradient. The standard definitions of the performance of engineering flows, however, are mostly in terms of primary variables that do not exhibit local structures. Consequently, even if all local structures of a complex flow can be identified by an accurate numerical Navier-Stokes (NS) solver, one still does not know quantitatively

which of these structures have dominant effect on the performances, favorable or unfavorable, how much, and *why*. These issues have to be addressed by proper physical theories that can express flow performances by local dynamic structures explicitly. Because generically no analytical solution is available for practical complex flows, the theories have to be used in close interaction with numerical simulations. In this article we make a critical review of relevant theories. For the simplicity of presentation, throughout the article we consider viscous incompressible flow at large Re only, in which all structures are vortical and measured by the vorticity.[1]

Various vortical structures, their evolution, and stability have been familiar in fluid engineering community and studied extensively. What is relatively less known is the *local dynamics on a boundary*, which serves as both the signatures and root of the vortical structures in the interior of the flow, and is most relevant to the on-wall flow management. Therefore, we address this issue first in Section 2, where the central concept is the boundary vorticity flux (BVF). In Section 3 we derive two major existing theories on the total force and moment in terms of vorticity dynamics from a general formulation, showing that these two theories are precisely mutually complementary. Section 4 illustrates the applications of the theories to the flow diagnoses and optimal configuration designs in terms of local dynamics, for both external and internal flows, showing how the approach leads to unique physical insight and significant performance improvement.

2 Local Dynamics on Boundary at LargE Reynolds number

2.1 On-Wall Local Dynamics at Large Re

We start from the incompressible NS equation

$$\rho \boldsymbol{a} = -\nabla p - \mu \nabla \times \boldsymbol{\omega} \tag{1}$$

in which the acceleration $\boldsymbol{a} = D\boldsymbol{u}/Dt$ can be written

$$\boldsymbol{a} = \boldsymbol{u}_{,t} + \boldsymbol{\omega} \times \boldsymbol{u} + \nabla\left(\frac{1}{2}q^2\right), \quad q \equiv |\boldsymbol{u}|. \tag{2}$$

The shearing and compressing processes are not only coupled in the interior of the flow via inviscid and nonlinear mechanisms such as the *Lamb vector* $\boldsymbol{\omega} \times \boldsymbol{u}$ and kinetic energy, but also on boundaries through the viscosity and adherent condition, of which the effect reaches the interior of the flow field. The basis of the on-wall local dynamics is nothing but the application of (1) to a solid wall ∂B of normal $\boldsymbol{n}$ (pointing out of the fluid) and the use of the acceleration adherence, $\boldsymbol{a} = \boldsymbol{a}_B$, where $\boldsymbol{a}_B$ is the known acceleration of the wall. Corresponding to the compressing-shearing process decomposition inside the flow, this on-wall equation can be split into a pair of *normal-tangent* $(\boldsymbol{\omega}, p)$ *couplings*:

$$-\frac{1}{\rho}\frac{\partial p}{\partial n} = \boldsymbol{n} \cdot \boldsymbol{a}_B + \nu(\boldsymbol{n} \times \nabla) \cdot \boldsymbol{\omega}, \tag{3}$$

$$\nu \frac{\partial \boldsymbol{\omega}}{\partial n} = \boldsymbol{n} \times \boldsymbol{a}_B + \frac{1}{\rho}\boldsymbol{n} \times \nabla p + \nu(\boldsymbol{n} \times \nabla) \times \boldsymbol{\omega} \tag{4}$$

where $\nu = \mu/\rho$ and on the right-hand side $\boldsymbol{a}, p, \boldsymbol{\omega}$ all take their on-wall values.

The relative importance of (3) and (4) varies as the Reynolds number. Here we are interested only in the case with $Re \gg 1$. Viewing (3) and (4) as having been nondimensionalized, generically there is $|\boldsymbol{\omega}| = O(Re^{1/2})$. Along with the fact that $\boldsymbol{n} \times \nabla$ is an $O(1)$ operator, the explicit viscous terms on the right-hand side of (3) and (4) are both of $O(Re^{-1/2}) \ll 1$. Thus, in (3) the normal gradient of p is dominated by the normal wall acceleration, and in (4) the *boundary vorticity flux* (BVF) $\nu\partial\boldsymbol{\omega}/\partial n \equiv \boldsymbol{\sigma}$ is of $O(1)$ at any $Re \gg 1$. Therefore, (4) is far more important than (3). The BVF is in turn dominated by the tangent pressure gradient and acceleration. Note that on a fluid surface element inside the flow $\boldsymbol{\sigma}$ merely measures how much vorticity is diffused from one side of the surface to the other, but on a solid boundary it measures how much vorticity is *newly created* per unit area in unit time (Lighthill 1963).

2.2 Boundary Vorticity Flux

By (4) we may write $\boldsymbol{\sigma} = \boldsymbol{\sigma}_a + \boldsymbol{\sigma}_p + \boldsymbol{\sigma}_{\text{vis}}$, with

$$\boldsymbol{\sigma}_a = \boldsymbol{n} \times \boldsymbol{a}_B, \tag{5}$$

$$\boldsymbol{\sigma}_p = \frac{1}{\rho}\boldsymbol{n} \times \nabla p, \tag{6}$$

$$\boldsymbol{\sigma}_{\text{vis}} = -\nu(\boldsymbol{n} \times \nabla) \times \boldsymbol{\omega}. \tag{7}$$

Here, $\boldsymbol{\sigma}_a$ is important mainly for flows with flexible boundaries, such as in nonlinear aeroelasticity, animal flight and fish swimming, as well as flow controls by flexible walls.[2] $\boldsymbol{\sigma}_p$ is also important when there is a

1 For extension to compressible flow see Wu et al. (2006,2007).

2 Of this kind of flow controls see, e.g. the turbulent friction reduction by flexible wall which makes spanwise oscillation that forms tangent traveling waves in $\boldsymbol{n} \times \boldsymbol{a}_s$ to control the BVF (Zhao et al. 2004), and vortical-wake elimination by flexible wall which makes up-down oscillation that forms a traveling wave in $\boldsymbol{n} \cdot \boldsymbol{a}_s$ to control the normal pressure gradient (C.J. Wu et al. 2007).

nonuniform fluid injection from a porous wall, say flow control by injection (Gad-el-Hak 2000) or in a combustor with fuel injection from the wall. In that case $\boldsymbol{a}_B$ is prescribed as the local acceleration of the injected fluid at the boundary. Here we confine our discussion to flow over a non-porous rigid surface, so that $\boldsymbol{a}_B$ can be eliminated by working in the frame of reference fixed to the body. Then $\partial p/\partial n$ as well as σ_{vis} are of only $O(Re^{-1/2}) \ll 1$, the latter existing only in three-dimensional flow. In contrast, σ_p must be of $O(1)$ and is the major and most common constituent of the BVF. To focus on the key physics, we will often neglect the $o(1)$ viscous terms. Consequently, the on-wall dynamics is hightlighted by

$$\sigma \equiv \nu \frac{\partial \omega}{\partial n} \simeq \sigma_p \equiv \frac{1}{\rho} \boldsymbol{n} \times \nabla p \tag{8}$$

Equation (8) clearly indicates that the BVF plays a dual role. On the one hand, the tangent pressure gradient is a result or on-wall signature of the entire fluid motion, which measures the local compressing process. On the other hand, once that tangent pressure gradient is formed on the wall, it becomes an on-wall root of new vorticity, which measures the shearing process. Therefore, *in a generic viscous flow the local balance between the vorticity creation rate and tangent pressure gradient stands at the center of the entire on-wall dynamics.* It is of crucial importance to notice that *the estimate* $\sigma_p = O(1)$ *is independent of* Re *and remains true as* $Re \to \infty$ *or* $\nu \to 0$.

2.3 Boundary Layer Separation and BVF Peaks

The most important on-wall local process at large Re is boundary-layer separation that often considerably alters the global flow performance. Figure 1(a) shows an example of a primary three-dimensional boundary-layer separation from a prolate spheroid at an angle of attack, and its induced secondary separation. The separation process is well explained by the *triple-deck theory*, from which a few on-wall criteria have been deduced to signify where a boundary layer is separating. For a systematic introduction of the triple-deck theory and separation criteria in both two- and three-dimensional flows see Wu et al. (2006, Sect. 5.3). Of these criteria the most convenient and effective one is based on BVF. The triple-deck theory asserts that an *interactive pressure* $\Delta p = O(Re^{-1/4})$ must appear in the narrow separation zone of width of only $O(Re^{-3/8})$, which should be added to the pressure at the outer edge of the attached boundary layer. Thus, although Δp is small and can hardly be detected from numerical data, its tangent gradient or associated BVF peak must be strong and easily identified:

$$\sigma_p = O(Re^{1/8}) \gg 1 \text{ in separation zone.} \tag{9}$$

This fact makes strong local BVF peaks a very effective marker to signify separation. Moreover, (8) implies that this σ_p-peak must be in the direction perpendicular to the interactive pressure gradient. In a three-dimensional flow, since the boundary-layer separation line is a skin-friction line (a τ_w-line[3]), it can be shown that the interactive $\sigma_p = O(Re^{1/8})$ must be basically aligned to the τ_w-line direction (Wu et al. 2000). This feature occurs only in the narrow separation zone. Figure 1(b) exemplifies this situation on a prolate spheroid, which shows the vector lines of both the τ_w-field and σ-field. The convergence of the former was the separation criterion proposed by Lighthill (1963), which is insufficient to identify whether the boundary-layer separation indeed occurs; but (8) and the (σ_p, τ_w) alignment criterion do.

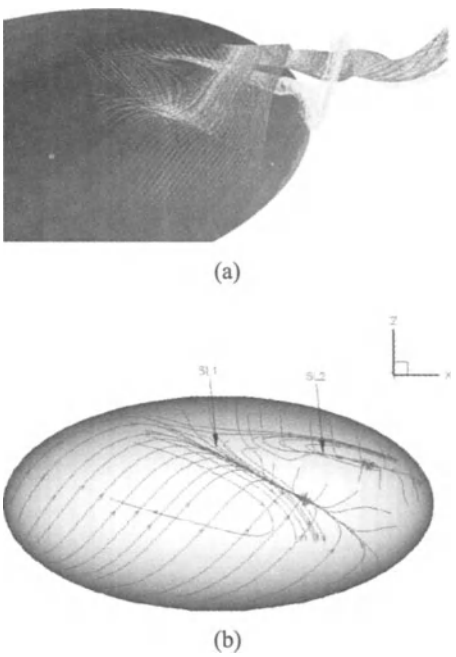

Fig. 1 Three-dimensional boundary layer separation and separated flow from a prolate spheroid at incidence. From Wu et al.(2000). (a) Flow pattern. (b) The skin-friction lines (red) and BVF-lines on the spheroid surface. SL1 and SL2 are the primary and secondary separation lines

Note that the triple-deck structure also occurs at places where the wall condition has certain discontinuities, even if the flow remains attached (Stewartson 1970, Goldstein & Hultgren 1987). This causes BVF of $O(Re^{1/8})$ peaks as well that are often unfavorable, and should be taken into

3 $\tau_w = \mu \omega \times \hat{n}$ is the skin-friction, with $\hat{n} = -n$ being the unit normal out of the wall.

the consideration of flow diagnosis as exemplified in Sect. 4.

3 Aerodynamic Forces by Vortical Structures

We now turn to the integrated flow performance, focusing on the *aerodynamic force and moment* acting on a closed or open body surface by the surrounding fluid. It suffices to consider the force, as the treatment for the moment is the same. Referring to Fig. 2, let B be any solid body bounded by closed surface ∂B on which the total force $\boldsymbol{F}$ is to be found, V_f be the volume occupied by the fluid bounded by $\partial V_f = \partial B + \Sigma$ with Σ being a fixed control surface, $\boldsymbol{n}$ be the unit normal pointing *out of* the fluid, and $\boldsymbol{\tau} = \mu\boldsymbol{\omega}\times\boldsymbol{n}$ be the shear stress. Then on ∂B the standard force formulas read[4].

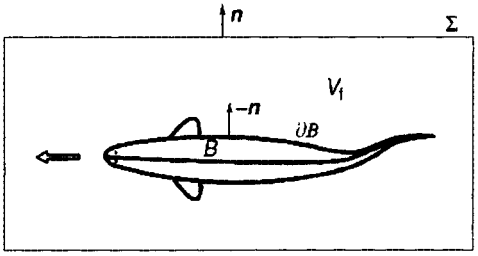

Fig. 2 An arbitrary unsteady flow caused by the arbitrary motion and deformation of a body

$$\boldsymbol{F} = -\int_{\partial B}(-p\boldsymbol{n}+\boldsymbol{\tau})dS \tag{10}$$

$$= -\rho\int_{V_f}\boldsymbol{a}dV + \int_{\Sigma}(-p\boldsymbol{n}+\boldsymbol{\tau})dS \tag{11}$$

$$= -\rho\frac{d}{dt}\int_{V_f}\boldsymbol{u}dV + \int_{\Sigma}(-p\boldsymbol{n}+\boldsymbol{\tau}-\rho\boldsymbol{u}u_n)dS. \tag{12}$$

Extension to the force on open surface will be mentioned later. None of these performance formulas, formulated in terms of primary variables $\boldsymbol{u}$ and p, can reveal the local physical structures and processes that are responsible for the force. Our task is to cast them to innovative but non-standard forms.

3.1 General Theory

The shearing process is governed by the curl of (1), the Helmholtz equation:

$$\nabla\times\boldsymbol{a} = \boldsymbol{\omega}_{,t} + \nabla\times(\boldsymbol{\omega}\times\boldsymbol{u}) = \nu\nabla^2\boldsymbol{\omega}, \tag{13}$$

of which different terms express respective processes and vortical structures inside the flow domain. Compare (13) and (11), we see that the force will be expressed in terms of vorticity if the integral of $\boldsymbol{a}$ can be replaced by that of $\nabla\times\boldsymbol{a}$. This can be easily done by the help of certain integral transformations, which are the extension of the elementary one-dimensional formula

$$\int_a^b d[xf(x)] = [xf(x)]_a^b = \int_a^b xf'(x)dx + \int_a^b f(x)dx$$

to multiple-dimensional space using the Gauss and Stokes theorems. This method permits expressing the integral of a vector by that of the moment of its proper derivatives. In n dimensions with n =2,3, a most frequently used DMT identity is

$$\int_V f dV = \frac{1}{k}\int_V \boldsymbol{x}\times(\nabla\times\boldsymbol{f})dV - \frac{1}{k}\int_{\partial V}\boldsymbol{x}\times(\boldsymbol{n}\times\boldsymbol{f})dS \tag{14}$$

where and below $k = n-1$. We name this kind of transformations the *derivative moment transformation* (DMT). Some more DMT identities can be deduced; for example, on an *open* surface S bounded by closed loop C, there is

$$\int_S \phi\boldsymbol{n}dS = -\frac{1}{k}\int_S \boldsymbol{x}\times(\boldsymbol{n}\times\nabla\phi)dS + \frac{1}{k}\oint_C \phi\boldsymbol{x}\times d\boldsymbol{x} \tag{15}$$

if the original integral is already a moment, the DMT may cast it to an integral of second-order moment. This is evidently useful in transforming the total moment on the body as will be seen later.

We now set $\boldsymbol{f} = \boldsymbol{a} = D\boldsymbol{u}/Dt$ in (14). This casts at once the volume integral of $\boldsymbol{a}$ to that of $\boldsymbol{x}\times(\nabla\times\boldsymbol{a})$, plus boundary integrals of $\boldsymbol{a}$ over ∂B and Σ. Of the two boundary integrals, the former is considered prescribed due to the adherence condition $\boldsymbol{a} = \boldsymbol{a}_B$; while the latter can be transformed by using (1) and (15). Then, as we substitute these into (11), the pressure integral over Σ is cancelled, and by using (13) we obtain the general force formulas (Wu et al 2006, Sect. 11.5; Wu et al 2007)

$$\boldsymbol{F} = -\frac{\mu}{k}\int_{V_f}\boldsymbol{x}\times\nabla^2\boldsymbol{\omega}dV + \boldsymbol{F}_B + \boldsymbol{F}_\Sigma \tag{16}$$

$$= -\rho\int_{V_f}\boldsymbol{x}\times(\boldsymbol{\omega}_{,t}+\nabla\times\boldsymbol{l})dV + \boldsymbol{F}_B + \boldsymbol{F}_\Sigma, \tag{17}$$

in which $\boldsymbol{l} \equiv \boldsymbol{\omega}\times\boldsymbol{u}$ is the Lamb vector, and the volume integrals in (16) and (17) express alternatively the same force by vorticity diffusion and advection. $\boldsymbol{F}_B$ and $\boldsymbol{F}_\Sigma$ are boundary integrals over body surface and control surface,

4 Equation (10) comes directly from Newton's third law and expressed as the negative of the fluid-stress integral over the body surface. Equation (11) comes from the integral of (1) over V_f and the use of (10). Equation (12) comes from the rate of change of the total fluid momentum in V_f with fixed outer boundary Σ and the use of (10).

respectively:

$$\boldsymbol{F}_B = \frac{\rho}{k}\int_{\partial B}\boldsymbol{x}\times(\boldsymbol{n}\times\boldsymbol{a}_B)dS = \frac{\rho}{k}\int_{\partial B}\boldsymbol{x}\times\boldsymbol{\sigma}_a dS \tag{18}$$

$$\boldsymbol{F}_\Sigma = -\frac{\mu}{k}\int_\Sigma \boldsymbol{x}\times[\boldsymbol{n}\times(\nabla\times\boldsymbol{\omega})]dS + \mu\int_\Sigma \boldsymbol{\omega}\times\boldsymbol{n}dS \tag{19}$$

The second expression of (18) indicates that this integral comes from the vorticity creation at ∂B due to body-surface acceleration. In (19), the second term is directly the shear stress, but the first term is a moment of the viscous force per unit volume. These two viscous terms represent the influence on $\boldsymbol{F}$ of those vortical structures outside Σ. It should be stressed that at ∂B the effect of viscosity is very strong and can never be neglected, but on Σ it decays quickly as the control surface is shifted away from the body. At large Re, as long as Σ does not cut through boundary layers and initial wake shear layers, $\boldsymbol{F}_\Sigma$ is usually negligible and hence the flow on Σ can be considered inviscid and governed by the Euler equation.

It is sometime convenient to continue the fluid into the body as "the fluid displaced by the body", so that the domain $V = V_f + B$ has only an external boundary Σ. This continuation is effective owing to the velocity continuation across ∂B. Then applying (14) to B casts (17) to an alternative form

$$\begin{aligned}\boldsymbol{F} = &-\frac{\rho}{k}\int_V \boldsymbol{x}\times\boldsymbol{\omega}_{,t}\,dV + \rho\int_B \boldsymbol{a}_B dV \\ &-\rho\int_V \boldsymbol{l}dV - \frac{\rho}{k}\int_\Sigma \boldsymbol{x}\times(\boldsymbol{n}\times\boldsymbol{l})dS\end{aligned} \tag{20}$$

where $\boldsymbol{F}_\Sigma$ has been dropped. We can then immediately identify two exclusive special cases of (20). The first case holds if the body is stationary and in V the flow is steady, such that the first line of the right-hand side of (20) vanishes. This case serves as the basis of entire steady aerodynamics. On the contrary, when the body and its generated vortex system contained in V is surrounded by potential flow, and moreover the Lamb-vector integral vanishes, the second line on the right-hand side of (20) vanishes. Generically, the flow in this case is unsteady, which may serve as the basis of unsteady aerodynamics. We will discuss these two special DMT-based theories in Sects. 3.2 and 3.3, respectively.

There is yet the third special case: in (20) the control surface Σ shrinks to coincide with the body surface ∂B and V_f shrinks to zero. This leads to force and moment formulas in terms of the BVF moments to be discussed in Sect. 3.4.

It is worth mentioning that DMT can also transform the global performances other than total force and moment to new expressions in terms of local dynamics. Yang et al. (2008) have exemplified its application to internal flow by casting the standard formulas of mass flux and total-pressure ratio of a compressor flow to vortical forms that permit making innovative diagnosis and introducing local-dynamics constraint in optimal design.

3.2 Steady Aerodynamics: Vortex-Force Theory

This section considers the first special case of (20), for which we have (Wu et al.(2006), Yang et al. (2007)):

$$\boldsymbol{F} = -\rho\int_V \boldsymbol{l}dV - \frac{\rho}{k}\int_\Sigma \boldsymbol{x}\times(\boldsymbol{n}\times\boldsymbol{l})dS \tag{21}$$

which can be equally expressed as

$$\boldsymbol{F} = -\rho\int_V \boldsymbol{l}dV + \int_\Sigma P\boldsymbol{n}dS \tag{22}$$

Equation (22) is nothing but the direct consequence of substituting (1) into (11) and neglecting the viscous force on Σ. This theory remains crucially important for engineering flows, of which the performances at design condition are mostly defined by assuming flow steadiness.

As $Re\to\infty$, as long as all streamlines on Σ come from far upstream, their total pressure P recovers the constant value P_∞. Then we have the *vortex-force* formula

$$F = -\rho\int_{V_f} \boldsymbol{\omega}\times\boldsymbol{u}dV \tag{23}$$

as Prandtl(1918) named it, which is exact for steady incompressible flow at $Re\to\infty$. We may write $\boldsymbol{u} = \boldsymbol{U} + \boldsymbol{v}$ where

$$\boldsymbol{v} = (u,v,w) = \frac{1}{2k\pi}\int_{V_f}\frac{\boldsymbol{\omega}\times\boldsymbol{r}}{r^n}dV' \tag{24}$$

is the disturbance velocity due to the vorticity, $\boldsymbol{r} = \boldsymbol{x} - \boldsymbol{x}'$, and the primed quantity takes the value at the integration point $\boldsymbol{x}'$. Kármán and Burgers (1935) have shown that the combination of (23) and (24) contains the entire classic aerodynamic theory, including the famous *Kutta-Joukowski theorem*

$$\boldsymbol{F} = \rho U\Gamma\boldsymbol{e}_z \tag{25}$$

as an exact result for 2-D inviscid flow over an airfoil, and Prandtl's *lifting-line theory* as a linearized approximation for 3-D flow over a finite-span wing.

For viscous steady flow with finite $Re \gg 1$, we return to (21) and (22), which indicate that *the aerodynamic force in viscous steady flow is entirely from the Lamb vector field generated by the body.* In this case, as a streamline enters a finite-thickness boundary layer, fluid particles will loss some kinetic energy and hence total pressure P. This streamline will carry smaller P to enter the wake so that ∇P no longer vanishes. Then even if the viscous stress is negligible there, a vortical wake with nonzero Lamb vector $\boldsymbol{\omega} \times \boldsymbol{u}$ occurs. This physics explains the Σ-integrals in (21) and (22), which are nonzero only on the downstream part of Σ, say a wake plane W with $\boldsymbol{n} = \boldsymbol{e}_x$. Then by (21)

$$\boldsymbol{F} = -\rho \int_{V_f} \boldsymbol{l} dV - \rho \boldsymbol{e}_x \int_W (y l_y + z l_z)\, dS \tag{26}$$

Thus, the wake integral represents the *profile drag* of viscous source, which is a finite-Re effect. Yang et al. (2007) have examined the formation of the Lamb vector inside the boundary layer and applied (26) to the diagnosis of a slender delta-wing flow with detached leading-edge vortices. It is well known that the leading-edge vortices bring in additional *vortex lift*, for which various qualitative or approximate explanations were proposed on the underlying physics but none is exact. The interpretation of Yang et al. based on (26) is the first exact one and differs quite substantially from previous ones.

3.3 Unsteady Aerodynamics: Vorticity Moment Theory

We now consider the second special case of (20). The vortex force on any domain D can be kinematically cast to a boundary integral over ∂D (c.f. Wu et al. 2006):

$$\int_D \boldsymbol{\omega} \times \boldsymbol{u} dV = \int_{\partial D} \left(\boldsymbol{n} \cdot \boldsymbol{u}\boldsymbol{u} - \frac{1}{2} q^2 \boldsymbol{n} \right) dS \tag{27}$$

Assume that (a) the vortex system generated by the motion of body B is surrounded by potential flow, and (b) the potential flow on Σ can be continued analytically to infinity where the fluid is at rest.[5] Then the asymptotic behavior of $\boldsymbol{u}$ ensures the surface integral in (27) vanishes. We call such vortex system a *vortex-force free system*, for which terms in the second line of (20) all disappear. Then, since B is a material body, for a vortex-force free system, (20) yields the major result of the *vorticity moment theory*,[6] first obtained by Burgers (1920) in an unnoticed paper discovered by Biesheuvel & Hagmeijer (2006), and then formulated by Wu (1978, 1981, 2005) systematically and independently:

$$\boldsymbol{F} = -\frac{\rho}{k} \frac{d}{dt} \int_V \boldsymbol{x} \times \boldsymbol{\omega} dV + \rho \frac{d}{dt} \int_B \boldsymbol{u}_B dV \tag{28}$$

$$= -\frac{\rho}{k} \frac{d}{dt} \int_{V_f} \boldsymbol{x} \times \boldsymbol{\omega} dV - \frac{\rho}{k} \frac{d}{dt} \int_{\partial B} \boldsymbol{x} \times (\boldsymbol{n} \times \boldsymbol{u}_B) dS \tag{29}$$

These formulas were originally derived by applying (12) to an isolated system with Σ retreating to infinity.

Conventionally, the incompressible unsteady force is split into two parts: a *cyclic* (with circulation) part associated with the vortex system generated from the body surface, and the other, the *acyclic* (circulation-free) part as a *direct* product of $\boldsymbol{a}_B$ known as the *virtual mass effect*, expressible by an acyclic velocity potential ϕ_{ac}. The latter exists even if the flow is nominally irrotational in V_f. But as long as the fluid has viscosity (no matter how small), $\boldsymbol{a}_B$ must generate a shear layer. *The accelerating body is never "naked" but always dressed in an attached acyclic vortex layer.* Therefore, the virtual mass effect should have been included in the above viscous vortical theories. Indeed, imagine the vorticity field in V_f consists of two parts: a body-acceleration caused acyclic vortex sheet of strength $\gamma_{ac} = \hat{\boldsymbol{n}} \times (\nabla \phi_{ac} - \boldsymbol{u}_B)$, where $\hat{\boldsymbol{n}} = -\boldsymbol{n}$, and the rest of $\boldsymbol{\omega}$ or the *additional vorticity* $\boldsymbol{\omega}_a$, then it can be shown (Wu et al. 2006) that (29) becomes the formula of Lighthill (1986a, 1986b)[7]:

$$\boldsymbol{F} = -\frac{\rho}{k} \frac{d}{dt} \int_{V_f} \boldsymbol{x} \times \boldsymbol{\omega}_a dV + \rho \frac{d}{dt} \int_{\partial B} \phi_{ac} \boldsymbol{n} dS. \tag{30}$$

Wu et al. (2006) have also shown that as $Re \to \infty$ so that the vorticity field can be approximated by vortex sheets, (30) is reduced to the force formula in the general *unsteady lifting-surface theory*, of which the two-dimensional linearized version for flow over an oscillating airfoil is precisely the classic Theodorson theory developed in the study of wing flutter (e.g. Bisplinghoff et al. 1955). An interesting application and confirmation of the full vorticity moment theory was made by Sun and Wu (2004) in a numerical study of insect flight.

Since by nature the flow steadiness is an approximate concept that holds in near field, the classic steady aerodynamic theory can also be derived from the vorticity

5 In practice, outside Σ there can be other vortices or motion of bodies, but they have to be sufficiently far from body B so that their induced potential flows are negligible in the study of the force and moment on B, as if they do not exist.

6 Or the *hydrodynamic impulse theory* as Burgers (1920) and Lighthill (1986a, 1986b) named it.

7 The concept behind (30) has appeared in Lighthill (1979) without giving explicit formulation.

moment theory, provided that the entire vortex system generated by a wing including the starting vortex is included in V_f and vortex-force free, where the continuously downstream motion of the latter causes the flow unsteadiness. Then this unsteady theory can be applied to give a very neat derivation of (25) and its 3-D counterpart as addressed by Kármán & Burgers (1935) and Wu (1981), see also Wu et al. (2006).

3.4 Force and Moment by Boundary Vorticity Flux

In their respective applicable ranges, the above theories can identify various vortical structures responsible for the aerodynamic force and moment, but from different angles of view. These physical pictures are necessary for a rational understanding on how a complex flow reacts to a body that generates it. The understanding will be complete only if the ultimate root of these structures at the body surface can be pinpointed. This task is accomplished by returning to the BVF. Wu et al. (2006, 2007) have shown that, when V_f in (17) reduces to zero the force and moment formulas become the integrals of the first and second moments of the boundary vorticity flux σ over ∂B. This BVF-based force and moment theory was first obtained by Wu(1987) and systematically developed and reviewed by Wu and Wu(1993, 1996) and Wu et al.(2006). For example, for two-dimensional flow over an airfoil contour C, the lift and drag due to pressure force reads

$$L = \rho \oint_C x\sigma_p ds, \quad D = -\rho \oint_C y\sigma_p ds \tag{31}$$

where

$$\oint_C \sigma_p ds = 0 \tag{32}$$

A unique property of BVF-based formulas is that, like (10), they can be extended to open boundary. This situation is frequently encountered in practical applications. To make the extension, one cannot start from (17) but rather to use DMT identities directly to cast (10) and corresponding moment formula to BVF-based expressions. For the neatness of the resulting force and moment formulas, in what follows we consider the pressure force only and ignore the shear stress on body surface. Then, with the help of (15) and (17), for a piece of open surface S of ∂B in a three-dimensional flow, we obtain

$$\boldsymbol{F} = \frac{\rho}{2}\int_S \boldsymbol{x}\boldsymbol{\sigma}_p dS - \frac{1}{2}\int_{\partial S} \boldsymbol{x}\, p d\boldsymbol{x} \tag{33}$$

$$\boldsymbol{M} = \frac{\rho}{2}\int_S x^2\boldsymbol{\sigma}_p dS - \frac{1}{2}\int_{\partial S} x^2 p d\boldsymbol{x} \tag{34}$$

4 Applications

This section exemplifies the application of the complex flow diagnosis and optimal design using local-dynamic theory. Due to the page limitation, our presentation has to be solely focused on the BVF-based on-wall approach; but as a necessary procedure the flow fields of all cases have been diagnosed by the preceding theories. The BVF diagnosis alone can by no means lead to a full physical understanding of the key local structures and processes in the interior of the flow (Wu et al. 2007). In practice the BVF theory has to be used in combination with (16)-(22) or their special versions (if applicable), such as (21)-(26) or (28)-(30).

4.1 BVF as Marker of Strong On-Wall Local Events

A remarkable example of using BVF peaks as the marker of strong on-wall local dynamic event is the diagnosis of experimentally found radial cracks at certain fixed azimuthal locations of the inducer of a high-speed centrifugal pump. The root of the trouble can not at all be captured by the numerically obtained pressure distribution over the inducer surface, see Fig. 3(a), but it is easily done by the BVF distribution, see Fig. 3(b): its peaks did precisely pinpoint the locations where the cracks had happened, strongly

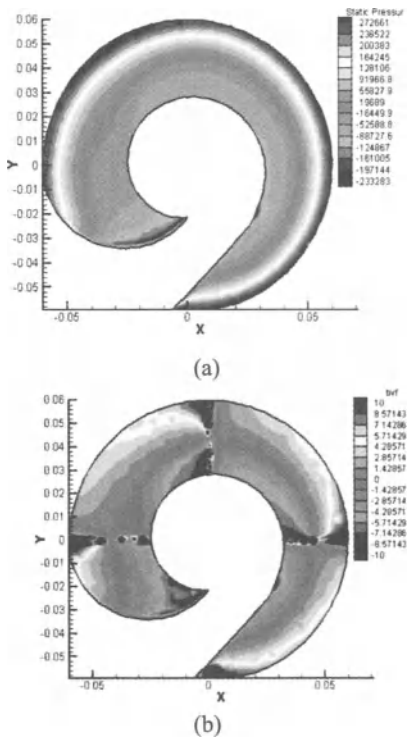

Fig. 3 Axial view of the distributions of pressure (a) and boundary vorticity flux (b) over the inducer surface of a high-speed centrifugal pump. Only the latter can reveal the physical root of the cracks. Courtesy of Dr. Z. H. Xu (2003)

suggesting that the problem was caused by the curvature discontinuities in the inducer design. Once the curvature was made continuous the cracks disappeared. Further examples of using BVF as very effective markers of on-wall local dynamic events will be given below.

4.2 Airfoil Flow Diagnosis and Optimal Design

The distributions of pressure and BVF over a helicopter rotor airfoil VR-12 at $\alpha = 6^\circ$ are compared in Fig. 4. The lift can be measured by either the area enclosed by the pressure curve or the highly localized x-moment of BVF peaks. It is convenient to locate the origin of the x-coordinate at the mid-chord point; then whether a BVF peak has favorable or unfavorable effect on L is simply determined by the sign of $x\sigma$. An optimal design would be to enhance positive $x\sigma$ and suppress negative $x\sigma$ as much as possible, under the constraint (32) and other conventional ones. For example, the positive peak at front part of VR-12 airfoil (Fig. 4b) should be suppressed, which by (32) will likely lead to a favorable positive BVF on the rear part. This is in full consistency with keeping the boundary layer attached in as wide range of angles of attack as possible, but implies a new optimal design rule:

Add a local-dynamic constraint to the conventional objective function of integral type in optimal design.

Figure 5 shows the result of a simple and quick optimal design aiming at improving the stall performance of VR-12 airfoil, using such a local-integral combined objective function (Zhu 2000). The re-designed airfoil fully retains the excellent performance of VR-12 till stall, but delays the stall by about 1.5°.

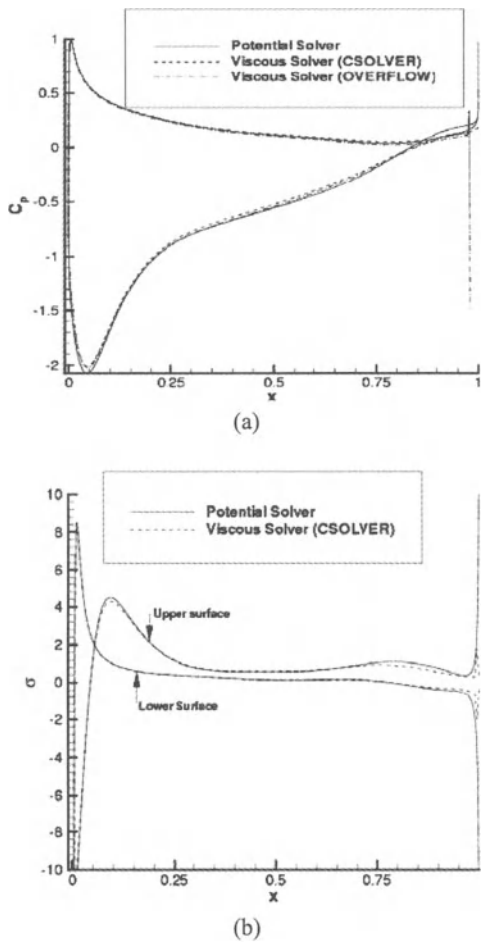

Fig. 4 Distributions of p (a) and BVF (b) over airfoil VR12 at $\alpha = 6^\circ$, computed by both potential flow theory and NS solvers. From Zhu (2000)

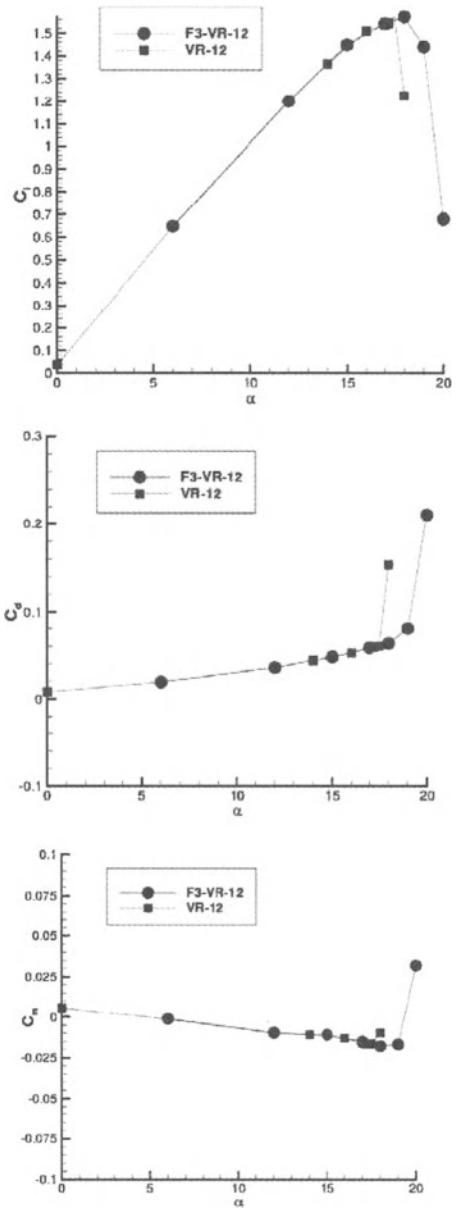

Fig. 5 The lift, drag, and moment of the VR-12 airfoil (blue) and its redesigned version (red) by a simple optimization program. From Zhu (2000)

4.3 BVF-Based Compressor Rotor Blade Design

The local-dynamic flow diagnosis and optimal design method has recently been applied to the internal flow of a transonic axial compressor, which extends the study of Yang et al. (2008), who used the inviscid axisymmetric and compressible flow model (as in the preliminary through-flow design) to perform the fully 3-D DMT-based diagnosis and rotor blade optimization of that compressor. While the focus of Yang et al. (2008) was the core flow away from the boundary layers of the rotor blades, hub, and shroud, now the attention is concentrated to the near-wall flow behavior, for which the BVF naturally plays a central role.

In this problem, the goal is to enhance the work done to the compressor flow by the rotor blades, which is proportional to the axial moment *acted to the fluid by the blade*. By (34), in cylindrical coordinates this moment reads (viscous stresses are neglected)

$$M_z = -\frac{1}{2}\int_S \rho r^2 \sigma_{pz} dS + \frac{1}{2}\oint_{\partial S} p r^2 dz \tag{35}$$

The rotor blade surface S is treated open at both its root and tip, where the line integral in (35) is dominant. The integral of $\rho r^2 \sigma_p$ alone in (35) over the middle part of S *does not* equal the common pressure moment integral but is the net contribution of localized σ_{pz} to M_z in that region.

Figure 6(a) is the BVF diagnosis on the suction side of the rotor blade. A strong positive σ_{pz} peak in the middle of the blade, which is due to the *boundary-layer separation caused by a shock* and results in a reduction of M_z according to (35). This observation is confirmed by the approximate alignment of the τ_w-lines and σ_{pz}-lines in that region (Figure not shown). Then a BVF-based optimal blade design scheme was constructed to enhance M_z, where the surface integral in (35) was simplified by sectional line integrals at different r. At the root and tip the sum of both terms was maximized. 3D RANS simulation then showed that the optimization increased M_z by 6%. The distribution of σ_{pz} on the optimized blade surface (Fig.6b) indicates that the original unfavorable σ_{pz} peak is weakened and shrunk, and shifted toward downstream. This implies that the shock and its induced separation is significantly suppressed.

In addition to the blade design, it was also found that the sudden changes of curvature distribution along the hub of the original compressor is strongly correlated to the BVF peaks there, some of which caused a local separation zone. A curvature smoothing was therefore performed. This reshaping eliminated that separation zone (Figure not shown).

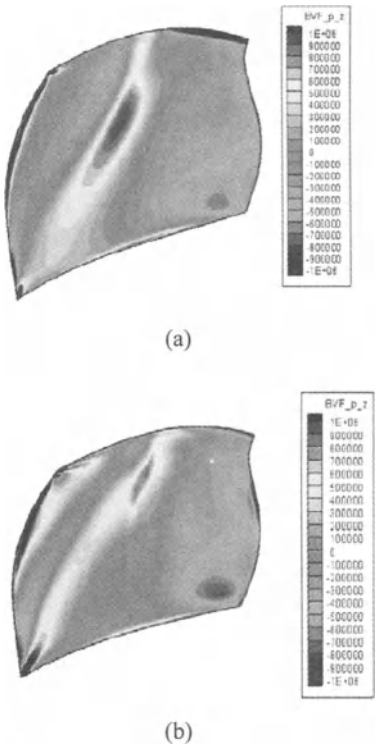

Fig. 6 Contour of the axial component of BVF σ_p on the suction side of the rotor blade in a transonic compressor. (a) Original blade. (b) Optimized blade

Figure 7 compares the total-pressure ratios and adiabatic efficiencies before and after BVF-based optimization. At the peak-efficiency point, the total-pressure ratio and adiabatic efficiency were increased by 5.73% and 1.11%, respectively. Figure 8 compares the profiles of these performances at the exit section, indicating that the main improvement occurs at the mid portion of the blade.

5 Concluding Remarks

(1) The global performance of engineering flows is dominated by local dynamic processes and structures that cannot be identified from the primary-variable fields. Special theories are necessary to re-express the commonly defined global performances by local dynamics. These theories enhance our physical understanding of complex aerodynamic flows and lead to innovative optimal configuration design and flow control.

(2) A widely effective method of re-expressing commonly defined integrated performances by local dynamics is the derivative-moment transformations, which transform integrals of primary variables to those of the moments of

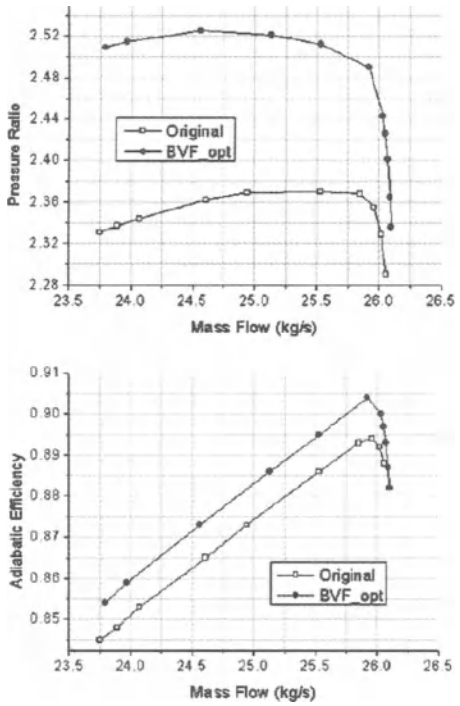

Fig. 7 The performance comparison vs. mass flux of original and optimized rotor blade

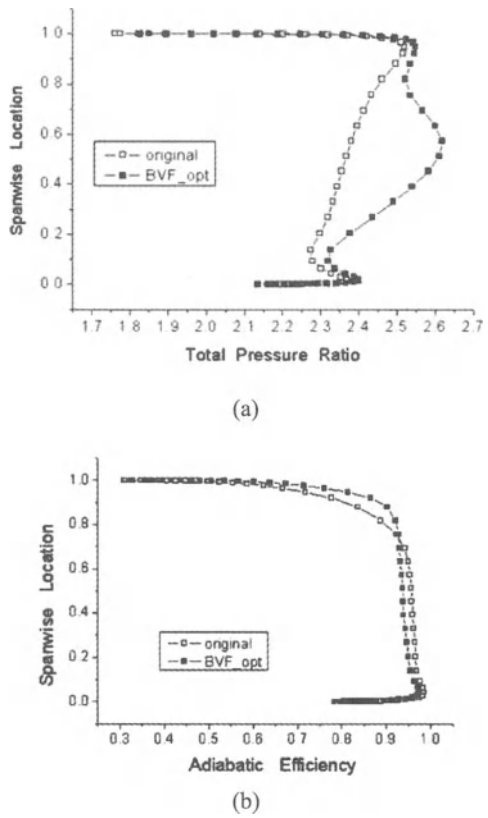

Fig. 8 The top performance comparison of original and optimized rotor blade at the rotor exit

their space-time derivatives as seen in local dynamic equations. Since generically no analytical solution is available for complex flows, to be practically useful these theories have to be closely combined with numerical simulations of the Navier-Stokes equations.

(3) A single complex flow may exhibit a variety of local structures at their different evolution stages. Similarly, a given integrated performance can have different local-dynamic expressions, each capturing one aspect of the flow but yielding exactly the same integral performance. Only a combined use of these expressions can lead to a complete physical understanding.

(4) The on-wall local-dynamic processes bear direct relevance to the configuration optimization and on-wall flow control, for which the boundary vorticity flux theory is of critical importance.

(5) As the Mach number increases, the global performance is gradually dominated by longitudinal compressing process. Thermal process also enters. The three processes are closely coupled. While all local-dynamics theories for global performances are either directly applicable or able to be extended to compressible flow, how to accurately identify the three fundamental processes and their couplings remain to be further studied.

References

Biesheuvel, A. and Hagmeijer, R. 2006, "On the force on a body moving in a fluid". *Fluid Dyn. Res.* **38**, 716 – 742

Biesplinghoff, R.L., Ashley, H. and Halfman, R.L. 1955, *Aeroelasticity*, Addison-Wesly

Burgers, J.M. 1920, "On the resistance of fluid and vortex motion". *Proc. K. Akad. Wet.* **23**, 774 – 782

Chu, B.-T. and Kovasnay, L. S. G. 1957, "Non-linear interactions in a viscous heat-conducting compressible gas". *J. Fluid Mech.* **3**, 494 – 514

Flandro, G.A., Fischbach, S.R., Majdalani, J. and French, J.C. 2006, "Nonlinear rocket motor stability prediction: limit amplitude, triggering, and mean pressure shift". *AIAA Paper* 2004 – 4054

Gad-el-Hak, M. 2000, *"Flow Control"*. Cambridge University Press.

Goldstein, M.E. and Hultgren, L.S. 1987, "A note on the generation of Tollmien-Schlichting waves by sudden surface-curvature change". *J. Fluid Mech.* **181**, 519 – 525

Föppl, A. 1897, *Die Geometric der Wirbelfelder.* Leipzig

Kármán, Th. von and Burgers, J.M. 1935, "Gerneral aerodynamic theory—perfect fluids". In: Duran, W.F.(ed.) *Aerodynamic Theory,* II, Dover

Helmholtz, H. 1858. "Über Integrale der hydrodynamischen Gleichungen, welche den Wirbelbewegungen ensprechen". *J. Reine Angew. Math.* **55**, 25 – 55

Kovasnay, L. S. G. 1953, "Turbulence in supersonic flow". *J. Aero. Sci.* **20**, 657 – 674, 682

Lighthill, M. J. 1962, "Physical interpretation of the mathematic theory of wave generation by wind". *J. Fluid Mech.* **14**, 385 – 398

Lighthill, M. J. 1963, "Introduction of boundary layer theory". In: Rosenhead L. (ed.) *Laminar Boundary Layers*, Oxford University Press, 46 – 113

Lighthill, J. 1979, "Waves and hydrodynamic loading". In: *Proc. 2nd Int. Conf. Berhavior of Off-Shore Structures*, BHRA Cranfield, vol. **1**, 1 – 40

Lighthill, J. 1986a, *An Informal Introduction to Theoretical Fluid Dynamics*. Oxford University Press

Lighthill, J. 1986b, "Fundamentals concerning wave loading on offshore structures". *J. Fluid Mech.* **173**, 667 – 681

Prandtl, L. "Tragflügel theorie I. Mitteilungen", *Nachrichten Ges. Wiss. Göttingen, Math-Phys. Kl.* 151 – 77. (Also: Gesammelte Abhandlungen, vol. **1**, pp. 322 – 345.) 1918

Saffman, P. G. 1992, *Vortex Dynamics*. Cambridge University Press

Stewartson, K. 1970, "On laminar boundary layers near corners", *Quart. J. Mech. Appl. Math.* **23**, 137 – 152 (and corrections, 1970, **24**, 387 – 389)

Sun, M. and Wu, J.H. 2004, "Large aerodynamic force generation by a sweeping wing at low Reynolds number". *Acta Mech.* Sinica **20**, 24 – 31

Thomson, J. J. 1883, *A treatise on the Motion of Vortex Rings*. Macmillan, London

Wu, C.J., Wang, L. and Wu, J.Z. 2007, "Suppression of the von Karman vortex street behind a circular cylinder by a traveling wave generated by a flexible surface". *J. Fluid Mech.* **574**, 365 – 391

Wu, J. C. 1978, "A theory for aerodynamic forces and moments". Georgia Institute of Technology Interim Technical Report. ONR Contract N00014-75-C-249

Wu, J. C. 1981, "Theory of aerodynamic force and moment in viscous flows". *AIAA J.* **19**, 432 – 441

Wu, J. C. 2005, *Elements of Vorticity Aerodynamics*. Tsinghua University Press, Beijing

Wu J.Z. 1987, "The force on moving bodies by vorticity field". *Acta. Aerodyn.* **5**: 22 – 30(in Chinese)

Wu, J. Z., Lu, X. Y. and Zhuang, L. X., 2007, "Integral force acting on a body due to local flow structures". *J. Fluid Mech.* **576**, 265 – 286

Wu, J.Z., Ma, H.Y. and Zhou, M.D. *Vorticity and Vortex Dynamics*, Springer-Verlag, 2006

Wu, J.Z., Roach, R.L., Lo, C.F., Zhu, F.L., Dowgwillo, R.M., Jiang, L.B., and Tramel R. W. (1999) "Aerodynamic Diagnostics Based on Boundary Vorticity Dynamics". *AIAA Paper* 99 – 3103

Wu, J. Z., Tramel, R. W., Zhu, F. L., and Yin, X. Y. 2000, "A vorticity dynamic theory of three-dimensional flow separation". *Phys. Fluids*, **12**, 1932 – 1954

Wu, J.Z. and Wu, J.M. 1993, "Interaction between a solid surface and a viscous compressible flow field". *J. Fluid Mech.***254**, 183 – 211

Wu, J.Z. and Wu, J.M. 1996, "Vorticity Dynamics on boundaries". *Adv. Appl. Mech.* **32**, 19 – 275

Xu, Z.H. 2003, "The analysis of impact of three-dimensional unsteady flow in high-speed pump". Ph. D. Thesis, Tshinghua University, Beijing. (in Chinese)

Yang, Y.T., Zhang, R.K., An, Y.R. and Wu, J.Z. 2007, "Steady vortex force and slender wing flow diagnosis". *Acta Mech.* Sinica. **23**, 609 – 619

Yang, Y.T., Wu, H., Li, Q.S., Zhou, S. and Wu, J.Z. 2008, "Vorticity dynamics in axial compressor flow diagnosis and design". *J. Fluid Enging.* **130**, 041102

Zhang, R.K., Cai, Q.D., Wu, J.Z., Wu, Y.L., Liu, S.H. and Zhang, L. 2005, "The physical origin of severe low-frequency pressure fluctuations in giant Francis turbines". *Mod. Phys. Lett. B***28 – 29**, 1527 – 1530

Zhang, R.K., Mao, F. Wu, J.Z., Chen, S.Y., Wu, Y.L. and Liu, S.H. 2008, "Characteristics and control of the draft-tube flow in part-load Francis Turbine". *J. Fluid Enging*. Accepted

Zhao, H., Wu, J.Z. and Luo, J.S. 2004, "Turbulent drag reduction by traveling wave of flexible wall". *Fluid Dyn. Res.* **34**, 175 – 198

Zhu, F.L. 2000, "Applications of boundary vorticity dynamics to flow simulation, airfoil design, and flow control". Ph.D. Dissertation, University of Tennessee, Knoxville

The 4th International Symposium on Fluid Machinery and Fluid Engineering
November 24-27, 2008, Beijing, China
NO. 4ISFMFE-IL14

One-Dimensional Analysis of Full Load Draft Tube Surge

Yoshinobu Tsujimoto[*1], Koichi Yonezawa[1], Changkun Chen[1]

[*1] Dept. of Mechanical Science and Bioengineering, Graduate School of Engineering Science, Osaka University,
1-3 Machikeneyama, Toyonaka, Osaka 560-8531, Japan
Tel / Fax: +81-6-6850
E-mail: tujimoto@me.es.osaka-u.ac.jp

Abstract One-dimensional stability analysis of a hydraulic system composed of a penstock, a runner and a draft tube was carried out to determine the cause of the full load draft tube surge. It is assumed that the cavity volume at the runner exit is a function of the pressure at the vortex core evaluated from the instantaneous local pressure at the runner exit and an additional pressure decrease due to the centrifugal force on the swirling flow. It was found that the diffuser effect of the draft tube has a destabilizing effect over all flow rates while the swirl effects stabilize/destabilize the system at larger/smaller flow rates than the swirl free flow rate. Explanations of the destabilizing mechanism are given for the diffuser and swirl flow effects. The effect of finiteness of sound velocity in the penstock is also discussed

Keywords hydraulic turbine, draft tube, surge, cavitation, instability

Nomenclature

		Standard values	
a	=	500 [m/s]	Sound velocity in the penstock
A_c	=	0.125 [m^2]	Draft tube inlet area
A_i	=	0.22 [m^2]	Inlet pipe area
A_e	=	0.67 [m^2]	Draft tube exit area
C	=	97.2×10^{-7} [m^4s^2/kg]	Cavitation compliance
c_2			Runner exit absolute velocity
c_{m2}			Runner exit meridional velocity
$c_{\theta 2}$			Runner exit tangential velocity
D	=	$(A_e/A_c)^2$-1=27.7	Diffusion factor of draft tube
d	=	0.4 [m]	Runner exit diameter
f_n	=	12.5 [Hz]	Rotational speed
H	=	14.8 [m]	Head
j			Imaginary unit
L_e	=	4.36 [m]	Effective length of draft tube
L_i	=	50 [m]	Inlet pipe length
p			Pressure
Q	=	0.51 [m^3/s]	Flow rate
Q_{sf}	=	0.618 [m^3/s]	Swirl free flow rate
$\bar{Q}$			Steady part of flow rate
$\tilde{Q}$			Unsteady part of flow rate
S	=	0.125[m^2]	Runner exit area
u			Flow velocity
U_2	=	15.7[m/s]	Runner exit circumferential velocity
V_c			Volume of cavity
α	=	10 [-]	Pressure coefficient of swirl
β_2	=	17.5[deg]	Runner exit blade angle
ρ	=	1000[kg/m^3]	Fluid density
ω	=	$\omega_R+j\omega_I$	Complex frequency
ω_e	=	12.56[rad/s]	Draft tube resonance frequency
ζ_2	=	0.207	Loss coefficient of draft tube
ζ_T	=	54.2	Runner resistance

1 Introduction

Securing stable operation is one of the most important issues in hydraulic power generation systems. At part load, a draft tube surge occurs when the frequency of the vortex rope whirl agrees with the resonant frequency of the hydraulic system [1] – [4]. It is also known that a surge can occur even at full load [5] but the cause is still not clear. Koutnik et al. [6] simulated the full load surge by

representing the effect of the cavitation in the draft tube by using cavitation compliance $C = -\partial V_c / \partial p_D$ and mass flow gain factor $\chi = -\partial V_c / \partial Q_D$, where V_C is the volume of the cavity, p_D and Q_D are pressure and flow rate downstream of the cavity. It was shown that the instability occurs when the absolute value of negative mass flow gain factor is larger than a certain value which depends on the value of cavitation compliance and system head losses. This model was combined with the numerical analysis software SIMSEN to analyze the full load surge observed in a real plant [7].

Although [6] and [7] show that full load surge can be successfully simulated by using an appropriate value of mass flow gain factor, the flow mechanism determining the value of mass flow gain factor is not clear yet. The present study is intended to clarify the diffuser effect of the draft tube and the effects of swirl in the downstream of the runner on the hydraulic instabilities in power generation plants [8]. The effect of finiteness of sound velocity in the penstock is also discussed [9].

2 Analytical model

As shown in Fig. 1, we consider a system composed of an inlet pipe of length L_i and area A_i, a turbine runner, and a draft tube with the inlet and exit areas A_c and A_e, respectively. A cavity of volume V_c is assumed downstream of the turbine and upstream of the draft tube. Then, the continuity equation between upstream and downstream flow rates Q_1 and Q_2 is:

$$Q_2 - Q_1 = dV_c / dt \tag{1}$$

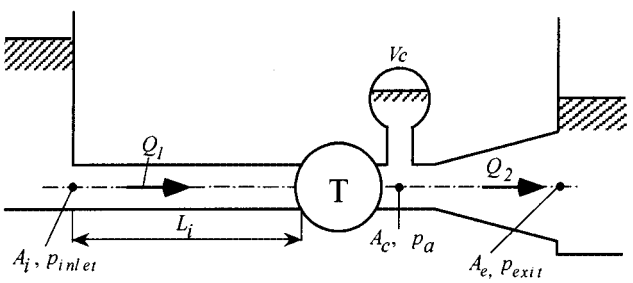

Fig. 1 Hydraulic system for the analysis

By applying Bernoulli's equation to the draft tube, we obtain,

$$p_a = p_{exit} + \rho \frac{L_e}{A_e} \frac{dQ_2}{dt} + \rho \frac{\zeta_2 - D}{2A_e^2} Q_2^2 \tag{2}$$

where $L_e = \int (A_e / A(s)) ds$ is the effective length of the draft tube, $D = (A_e / A_c)^2 - 1$ the diffuser factor, ζ_2 the loss coefficient of the draft tube. For simplicity, ζ_2 is assumed to be constant although it may depend on the swirl of the discharge flow [10]. Equation (2) ignores the flow compressibility in the draft tube.

At off-design operating point, the discharge flow from the runner swirls and a vortex is formed. If the pressure p_c at the vortex center is lower than the vapor pressure, a cavity will appear. The volume of cavity can be considered to be a function of the core pressure p_c,

$$V_c = V_c(p_c) \tag{3}$$

Due to the centrifugal force on the swirling flow, the core pressure p_c is lower than the ambient pressure p_a and can be expressed

$$p_c = p_a - \rho \alpha c_{\theta 2}^2 \tag{4}$$

Here, $c_{\theta 2}$ is a representative swirl velocity and α is a pressure coefficient for the swirl effects. If we assume a Rankine's combined vortex with the core radius r and the outer radius R, α is determined to be $\alpha = (R/r)^2 - 1/2$, with $c_{\theta 2}$ evaluated at the outer radius R, although the real flow from the runner is much more complicated [10].

From the velocity triangle at the runner discharge as shown in Fig. 2, we obtain

$$c_{\theta 2} = c_{m2} \cot \beta_2 - U_2 = \frac{Q_1}{S} \cot \beta_2 - U_2 \tag{5}$$

where β_2 is the runner exit vane angle, S the runner exit area and U_2 the runner exit peripheral speed.

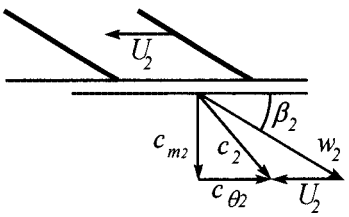

Fig. 2 Velocity triangle at the runner exit

By putting Eqs. (2) and (5) in Eq. (4), we obtain

$$p_c = p_{exit} + \rho \frac{L_e}{A_e} \frac{dQ_2}{dt} + \rho \frac{\zeta_2 - D}{2A_e^2} Q_2^2 - \rho \alpha \left(\frac{\cot \beta_2}{S} Q_1 - U_2 \right)^2 \tag{6}$$

The cavitation compliance C is defined by

$$C = -dV_c / dp_c \tag{7}$$

Then, the continuity equation (1) can be expressed as

$$Q_2 - Q_1 = dV_c / dt = (dV_c / dp_c)(dp_c / dt) = -C(dp_c / dt)$$

$$= -\rho C \frac{L_e}{A_e} \frac{d^2 Q_2}{dt^2} + \rho C \frac{D - \zeta_2}{A_e^2} Q_2 \frac{dQ_2}{dt}$$

$$+2\rho C\alpha \frac{\cot\beta_2}{S}\left(\frac{\cot\beta_2}{S} Q_1 - U_2\right)\frac{dQ_1}{dt} \tag{8}$$

The second term with dQ_2/dt represents the diffuser effect corresponding to the mass flow gain factor. If the discharge flow Q_2 is increased, the ambient pressure p_a is decreased if the diffuser effect D is larger than the loss ζ_2, resulting in an increase in cavity volume, which would promote further increase of Q_2. The third term with dQ_1/dt represents the effect of swirl. This term may also be called "mass flow gain factor" but this term is associated with the upstream flow Q_1. At flow rates lower than design ($Q_1 < Q_{sf} = U_2 S \tan\beta_2$), the tangential velocity $c_{\theta 2}$ and the cavity volume decrease as the upstream flow rate Q_1 is increased. This would promote further increas in Q_1.

Considering the compressibility of the fluid and the elasticity of pipe wall, the momentum and continuity equations applied to the flow in upstream penstock are

$$\frac{\partial u}{\partial t} + \frac{1}{\rho}\frac{\partial p}{\partial x} = 0 \tag{9}$$

$$\frac{\partial p}{\partial t} + \rho a^2 \frac{\partial u}{\partial x} = 0 \tag{10}$$

where a is the wave speed and can be evaluated from the speed of sound and the geometry of penstock section. The convective term has been ignored as being small with respect to other terms.

By taking the partial derivative of Eq. (10) with respect to t and Eq. (9) with respect to x, one may eliminate u, which yields

$$\frac{\partial^2 p}{\partial t^2} - a^2 \frac{\partial^2 p}{\partial x^2} = 0 \tag{11}$$

In a similar manner, p may be eliminated, giving

$$\frac{\partial^2 u}{\partial t^2} - a^2 \frac{\partial^2 u}{\partial x^2} = 0 \tag{12}$$

The general solutions of Eqs.(9)-(12) can be expressed as

$$p = R\left(t - \frac{x}{a}\right) + L\left(t + \frac{x}{a}\right)$$

$$\rho a u = R\left(t - \frac{x}{a}\right) - L\left(t + \frac{x}{a}\right)$$

The function $R(t-x/a)$ expresses a wave propagating towards positive x and $L(t+x/a)$ is another wave towards negative x. For the stability analysis, we separate each quantity into steady and unsteady components: $Q = \bar{Q} + \tilde{Q}(t)$, $p = \bar{p} + \tilde{p}(t)$ and $u = \bar{u} + \tilde{u}(t)$. The absolute value of steady part is assumed to be much larger than unsteady part. Assuming sinusoidal fluctuation, we can express the unsteady part as follows, using an imaginary unit j:

$$\tilde{p} = p_R \cdot e^{j\omega\left(t - \frac{x}{a}\right)} + p_L \cdot e^{j\omega\left(t + \frac{x}{a}\right)} \tag{13}$$

$$\rho a \tilde{u} = p_R \cdot e^{j\omega\left(t - \frac{x}{a}\right)} - p_L \cdot e^{j\omega\left(t + \frac{x}{a}\right)} \tag{14}$$

Solutions (13) and (14) satisfy Eqs. (11) and (12) generally even with a complex value of ω. Assuming no pressure fluctuation ($\tilde{p} = 0$) at the entrance of the inlet pipe ($x = 0$), we can obtain $p_R + p_L = 0$ from Eq. (13). By putting this result back into Eqs. (13) and (14), we obtain the pressure and velocity fluctuations along the inlet pipe

$$\tilde{p} = p_R e^{j\omega t}\left(e^{-j\omega\frac{x}{a}} - e^{j\omega\frac{x}{a}}\right) = -2j \cdot p_R e^{j\omega t} \sin\left(\omega\frac{x}{a}\right) \tag{15}$$

$$\rho a \tilde{u} = p_R e^{j\omega t}\left(e^{-j\omega\frac{x}{a}} + e^{j\omega\frac{x}{a}}\right) = 2 \cdot p_R e^{j\omega t} \cos\left(\omega\frac{x}{a}\right) \tag{16}$$

By combining Eqs.(15) and (16), the pressure fluctuation can be correlated with the velocity fluctuation. The pressure fluctuation $\tilde{p}_{inlet}$ at the inlet of the runner $x = L_i$ can be correlated with the velocity fluctuation $\tilde{u}_{inlet}$ there:

$$\tilde{p}_{inlet} = -j \cdot \rho a \tan\left(\omega\frac{L_i}{a}\right) \cdot \tilde{u}_{inlet} \tag{17}$$

We assume that the pressure difference between the inlet and exit of runner can be present by

$$p_{inlet} - p_a = \frac{\rho}{2}\zeta_T u_{inlet}^2 = \frac{\rho}{2}\zeta_T\left(\bar{u}_{inlet}^2 + 2\bar{u}_{inlet}\tilde{u}_{inlet} + \tilde{u}_{inlet}^2\right)$$

where p_a is the pressure at the runner discharge and ζ_T is a coefficient which represents the effect of runner. The unsteady part is

$$\tilde{p}_{inlet} - \tilde{p}_a = \rho\zeta_T \bar{u}_{inlet}\tilde{u}_{inlet} = \frac{\rho\zeta_T}{A_i^2}\bar{Q}_1\tilde{Q}_1 \tag{18}$$

The unsteady part of Bernoulli's equation (2) applied to the draft tube is

$$\tilde{p}_a = \tilde{p}_{exit} + \frac{\rho L_e}{A_e} j\omega\tilde{Q}_2 + \frac{\rho(\zeta_2 - D)}{A_e^2}\bar{Q}_2\tilde{Q}_2 \tag{19}$$

By applying Eqs. (18) and (19) into (17), we obtain

$$-j\cdot\rho a\tan\left(\omega\frac{L_i}{a}\right)\cdot\frac{\tilde{Q}_1}{A_i}-\left(\frac{\rho L_e}{A_e}j\omega\tilde{Q}_2+\frac{\rho(\zeta_2-D)}{A_e^2}\bar{Q}_2\tilde{Q}_2\right)=\frac{\rho\zeta_T}{A_i^2}\bar{Q}_1\tilde{Q}_1$$

which can be reduced to

$$\tilde{Q}_1=-\frac{\frac{\rho L_e}{A_e}j\omega+\frac{\rho(\zeta_2-D)}{A_e^2}\bar{Q}_2}{\frac{\rho\zeta_T}{A_i^2}\bar{Q}_1+j\cdot\frac{\rho a}{A_i}\tan\left(\omega\frac{L_i}{a}\right)}\tilde{Q}_2 \tag{20}$$

The unsteady part of continuity equation (8) between upstream and downstream flow rates Q_1 and Q_2 is

$$\tilde{Q}_2-\tilde{Q}_1=-\frac{\rho L_e C}{A_e}\frac{d^2\tilde{Q}_2}{dt^2}+\frac{\rho C}{A_e^2}(D-\zeta_2)\bar{Q}_2\frac{d\tilde{Q}_2}{dt}+\frac{2\rho C\alpha\cot\beta_2}{S}\left(\frac{\cot\beta_2}{S}\bar{Q}_1-u_2\right)\cdot\frac{d\tilde{Q}_1}{dt} \tag{21}$$

By applying Eq. (20) into (21) and using $\tilde{Q}_1=A_i\tilde{u}_1$, the system characteristic equation assuming the finiteness of sound velocity in the penstock is obtained:

$$\begin{aligned}&\left(\frac{\rho a}{A_i}\frac{\rho L_e}{A_e}jC\right)\omega^2\tan\left(\omega\frac{L_i}{a}\right)\\&+\left[\frac{\rho\zeta_T}{A_i^2}\bar{Q}_1\cdot\frac{\rho L_e C}{A_e}+\frac{2\rho C\alpha\cot\beta_2}{S}\left(\frac{\cot\beta_2}{S}\bar{Q}_1-u_2\right)\cdot\frac{\rho L_e}{A_e}\right]\omega^2\\&-\left[\frac{\rho a}{A_i}\frac{\rho C}{A_e^2}(D-\zeta_2)\bar{Q}_2\right]\omega\tan\left(\omega\frac{L_i}{a}\right)\\&+\left[-\frac{\rho L_e}{A_e}j+\frac{\rho\zeta_T}{A_i^2}\bar{Q}_1\cdot\frac{\rho C}{A_e^2}(D-\zeta_2)\bar{Q}_2 j\right.\\&\left.-\frac{2\rho C\alpha\cot\beta_2}{S}\left(\frac{\cot\beta_2}{S}\bar{Q}_1-u_2\right)\cdot\frac{\rho(\zeta_2-D)}{A_e^2}\bar{Q}_2\right]j\omega\\&-j\cdot\frac{\rho a}{A_i}\tan\left(\omega\frac{L_i}{a}\right)+\left[-\frac{\rho(\zeta_2-D)}{A_e^2}\bar{Q}_2-\frac{\rho\zeta_T}{A_i^2}\bar{Q}_1\right]=0\end{aligned} \tag{22}$$

Eq. (22) is a transcendential equation in terms of ω. From the characteristic equation (22), we can determine the complex frequency $\omega=\omega_R+j\omega_I$. The expression $e^{j\omega t}=e^{j\omega_R t}\cdot e^{-\omega_I t}$ shows that the real part ω_R gives the frequency and the imaginary part ω_I the damping rate.

3 Discussions on instabilities with a large sound velocity

When the sound velocity a is large, we can approximate $\tan\left(\omega\frac{L_i}{a}\right)\approx\omega\frac{L_i}{a}$ and $j\cdot\frac{\rho a}{A_i}\tan\left(\omega\frac{L_i}{a}\right)\approx\frac{\rho L_i}{A_i}j\omega$. For this case, the characteristic equation is reduced to a third order equation, which has been obtained for the case of incompressible flow in the penstock [8].

$$\begin{aligned}&-\left(\frac{\rho L_i}{A_i}\frac{\rho L_e}{A_e}C\right)(j\omega)^3\\&-\left[\frac{\rho\zeta_T}{A_i^2}\bar{Q}\frac{\rho L_e C}{A_e}-\frac{\rho L_i}{A_i}\frac{\rho C}{A_e^2}(D-\zeta_2)\bar{Q}\right.\\&\left.+2\rho C\alpha\frac{\cot\beta_2}{S}\left(\frac{\cot\beta_2}{S}\bar{Q}-U_2\right)\frac{\rho L_e}{A_e}\right](j\omega)^2\\&+\left[-\frac{\rho L_e}{A_e}-\frac{\rho L_i}{A_i}+\frac{\rho\zeta_T}{A_i^2}\frac{\rho C}{A_e^2}(D-\zeta_2)\bar{Q}^2\right.\\&\left.-2\rho C\alpha\frac{\cot\beta_2}{S}\left(\frac{\cot\beta_2}{S}\bar{Q}-U_2\right)\frac{\rho(\zeta_2-D)}{A_e^2}\bar{Q}\right](j\omega)\\&+\left[-\frac{\rho(\zeta_2-D)}{A_e^2}\bar{Q}-\frac{\rho\zeta_T}{A_i^2}\bar{Q}\right]=0\end{aligned} \tag{23}$$

By taking the complex conjugate of Eq. (23), we can show that, if $\omega_1=\omega_{1R}+j\omega_{1I}$ is a solution of Eq. (23), $\omega_2=-\omega_{1R}+j\omega_{1I}$ is another solution. The solutions ω_1 and ω_2 are practically the same solution with the same frequency ω_{1R} and the common damping ω_{1I}. This also requires that the real part of the third solution be zero ($\omega_{3R}=0$). So, the solutions can be expressed as $\omega_1=\omega_{1R}+j\omega_{1I}$, $\omega_2=-\omega_{1R}+j\omega_{1I}$, and $\omega_3=j\omega_{3I}$

Since Eq. (23) is a 3rd order equation in terms of $j\omega$ with real coefficients, Hurwitz' criterion can be applied to obtain the stability condition:

$$\begin{aligned}&\left[\frac{\zeta_T}{A_i^2}\bar{Q}\frac{L_e}{A_e}-\frac{L_i}{A_i}\frac{D-\zeta_2}{A_e^2}\bar{Q}+2\alpha\frac{\cot\beta_2}{S}\left(\frac{\cot\beta_2}{S}\bar{Q}-U_2\right)\frac{L_e}{A_e}\right]\\&\times\left[\frac{L_e}{A_e}+\frac{L_i}{A_i}-\frac{\zeta_T}{A_i^2}\frac{\rho C}{A_e^2}(D-\zeta_2)\bar{Q}^2\right.\\&\left.-2\rho C\alpha\frac{\cot\beta_2}{S}\left(\frac{\cot\beta_2}{S}\bar{Q}-U_2\right)\frac{(D-\zeta_2)}{A_e^2}\bar{Q}\right]\\&>\frac{L_i}{A_i}\frac{L_e}{A_e}\left[\frac{\zeta_2-D}{A_e^2}+\frac{\zeta_T}{A_i^2}\right]\bar{Q}\end{aligned} \tag{24}$$

Equation (24) can be used to determine the stable/ unstable flow rate regions. However, the equation is rather complicated and we will discuss about the stability mainly based on the direct solution of the characteristic equation (23).

3.1 Diffuser Effect of the Draft Tube

Equation (21) can be written as

$$\rho C\frac{L_e}{A_e}\frac{d^2\tilde{Q}_2}{dt^2}+\rho C\frac{\zeta_2-D}{A_e^2}\bar{Q}\frac{d\tilde{Q}_2}{dt}+\tilde{Q}_2$$

$$= \tilde{Q}_1 + 2\rho C\alpha \frac{\cot\beta_2}{S}\left(\frac{\cot\beta_2}{S}\bar{Q} - U_2\right)\frac{d\tilde{Q}_1}{dt} \tag{25}$$

If we consider the case of $\tilde{Q}_1 = 0$, negative damping occurs when

$$D > \zeta_2 \tag{26}$$

This is caused by the diffuser effect of the draft tube. The frequency is given by

$$\omega_e = \sqrt{\frac{A_e}{\rho L_e C}} \tag{27}$$

This mechanism can be explained as follows. We consider the case when Q_2 is increased. From Eq. (2), p_a will decrease if $D>\zeta_2$, due to the diffuser effect and the cavity volume V_c is increased. Then Eq.(1) shows that Q_2 is increased further, if Q_1 is kept constant. This positive feedback is the cause of the instability due to the diffuser effect.

3.2 Swirl effect

From Eq. (8), we obtain the following equation.

$$\rho C\frac{L_i}{A_i}\frac{d^2\tilde{Q}_1}{dt^2} + [\rho C\frac{\zeta_T}{A_i^2}\bar{Q}$$
$$+2\rho C\alpha\frac{\cot\beta_2}{S}\left(\frac{\cot\beta_2}{S}\bar{Q} - U_2\right)]\frac{d\tilde{Q}_1}{dt} + \tilde{Q}_1 = \tilde{Q}_2 \tag{28}$$

Here, we consider the case with $\tilde{Q}_2$=0. The first term of the multiplier on $d\tilde{Q}_1/dt$ shows the damping caused by the resistance of the runner. The second term representing the effect of swirl becomes negative or positive depending on the value of tangential velocity $c_{\theta 2} = c_{m2}\cot\beta_2 - U_2 = (\bar{Q}/S)\cot\beta_2 - U_2$. The tangential velocity becomes zero at the flow rate Q_{sf}=$SU_2\tan\beta_2$ and this is called swirl free flow rate. At a flow rate smaller than the swirl free flow rate Q_{sf}, the swirl has an effect to cause instability by reducing the damping coefficient. At a larger flow rate than the swirl free flow rate, the swirl has an effect to enhance damping. These effects can be explained as follows.

The velocity triangle at the runner exit is shown in Fig. 3, for three flow rates Q_a, Q_{sf}, and Q_b. At smaller flow rate Q_a, the absolute value of the tangential velocity will decrease if the flow rate Q_a is increased. Then, the pressure in the vortex core will increase and the cavity volume is decreased. The continuity equation (1) shows that the inlet flow rate Q_a is increased further. This positive feedback is the cause of the instability. At larger flow rate Q_b, the tangential velocity increases if the flow rate is increased. Then the core pressure is decreased and the cavity volume is increased. This results in the decrease of the upstream flow rate Q_b. This negative feedback is the cause of the stabilizing effect at higher flow rate.

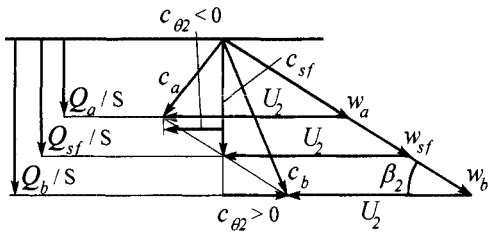

Fig.3 Velocity triangle at the runner exit for three flow rates

3.3 Energy Balance

We consider the displacement work of the cavitation region

$$E = \int p_a(Q_2 - Q_1)dt = \int p_a Q_2 dt - \int p_a Q_1 dt = E_2 - E_1 \tag{29}$$

under a steady oscillation condition. The pressure p_a near the cavitation region can be evaluated from Eq.(2). Here we separate each quantity p_a into steady $\bar{p}_a$ and unsteady $\tilde{p}_{a0}e^{j\omega t}$ components and assume $\tilde{p}_{a0} \ll \bar{p}_a$. From Eqs.(17) and (18) we obtain

$$\bar{p}_a = p_{inlet} - \rho\frac{\zeta_T}{2A_i^2}\bar{Q}^2 \tag{30}$$

$$\tilde{p}_a = -\rho\frac{L_i}{A_i}j\omega\tilde{Q}_1 - \rho\frac{\zeta_T}{A_i^2}\bar{Q}_1\tilde{Q}_1 \tag{31}$$

And Eq. (2) leads to

$$\bar{p}_a = p_{exit} + \rho\frac{\zeta_2 - D}{2A_e^2}\bar{Q}_2^2 \tag{32}$$

$$\tilde{p}_a = \rho\frac{L_e}{A_e}j\omega\tilde{Q}_2 + \rho\frac{\zeta_2 - D}{A_e^2}\bar{Q}_2\tilde{Q}_2 \tag{33}$$

First, we consider the upstream energy transfer within a period T

$$E_1 = \int_0^T p_a Q_1 dt = \int_0^T (\bar{p}_a + \tilde{p}_a)(\bar{Q}_1 + \tilde{Q}_1)dt$$
$$= \bar{p}_a\bar{Q}_1 T + \int_0^T \tilde{p}_a\tilde{Q}_1 dt = \bar{E}_1 + \tilde{E}_1 \tag{34}$$

In the same way,

$$E_2 = \int_0^T p_a Q_2 dt = \bar{p}_a\bar{Q}_2 T + \int_0^T \tilde{p}_a\tilde{Q}_2 dt = \bar{E}_2 + \tilde{E}_2 \tag{35}$$

We consider the unsteady displacement work $\tilde{E}_1$ and $\tilde{E}_2$.

Using the expression (31), we obtain the upstream work $\tilde{E}_1$ as follows

$$\tilde{E}_1 = \int_0^T \tilde{p}_a \tilde{Q}_1 dt = -\rho \frac{L_i}{A_i} \int_0^T \left(j\omega \tilde{Q}_1 \right) \tilde{Q}_1 dt - \rho \frac{\zeta_T}{A_i^2} \bar{Q}_1 \int_0^T \tilde{Q}_1 \tilde{Q}_1 dt$$
$$= -\rho \frac{\zeta_T}{A_i^2} \bar{Q}_1 \left| \tilde{Q}_{10} \right|^2 \frac{\pi}{\omega} \tag{36}$$

By using Eq. (33), we obtain

$$\tilde{E}_2 = \rho \frac{\zeta_2 - D}{A_e^2} \bar{Q}_2 \left| \tilde{Q}_{20} \right|^2 \frac{\pi}{\omega} \tag{37}$$

So,

$$\tilde{E} = \tilde{E}_2 - \tilde{E}_1 = \rho \bar{Q} \frac{\pi}{\omega} \left(\frac{\zeta_2 - D}{A_e^2} \left| \tilde{Q}_{20} \right|^2 + \frac{\zeta_T}{A_i^2} \left| \tilde{Q}_{10} \right|^2 \right) \tag{38}$$

This simply shows that the displacement work is dissipated by the upstream and downstream resistances.

The above discussions based on the dynamics of the upstream and downstream flow channel, Eqs. (31) and (33) do not include the dynamics of cavitation. To clarify the contribution of cavitation, we use the continuity equation under cavitation Eq. (21).

$$\tilde{Q}_2 - \tilde{Q}_1 = -\rho C \frac{L_e}{A_e} \frac{d^2 \tilde{Q}_2}{dt^2} + \rho C \frac{D - \zeta_2}{A_e^2} \bar{Q} \frac{d\tilde{Q}_2}{dt}$$
$$+ 2\rho C \alpha \frac{\cot \beta_2}{S} \left(\frac{\cot \beta_2}{S} \bar{Q} - U_2 \right) \frac{d\tilde{Q}_1}{dt} \tag{39}$$

By appropriately using Eqs. (31) and (33), we obtain

$$\tilde{E} = \int_0^T \tilde{p}_a \left(\tilde{Q}_2 - \tilde{Q}_1 \right) dt$$
$$= -\rho \frac{L_i}{A_i} \cdot 2\rho C \alpha \frac{\cot \beta_2}{S} \left(\frac{\cot \beta_2}{S} \bar{Q}_1 - U_2 \right) \cdot \omega^2 \frac{\pi}{\omega} \left| \tilde{Q}_{10} \right|^2 \tag{40}$$

By equating (38) and (40), we obtain

$$\rho \bar{Q} \frac{\pi}{\omega} \left(\frac{\zeta_2 - D}{A_e^2} \left| \tilde{Q}_{20} \right|^2 + \frac{\zeta_T}{A_i^2} \left| \tilde{Q}_{10} \right|^2 \right) =$$
$$-\rho \frac{L_i}{A_i} \cdot 2\rho C \alpha \frac{\cot \beta_2}{S} \left(\frac{\cot \beta_2}{S} \bar{Q} - U_2 \right) \cdot \omega^2 \frac{\pi}{\omega} \left| \tilde{Q}_{10} \right|^2 \tag{41}$$

Equation (41) shows the followings.

(1) The displacement work by the cavity due to swirl shown by the right hand side should be dissipated by the resistance in the upstream and downstream.

(2) With $D = \zeta_2$, steady oscillation is possible only for $\bar{Q}_1 < SU_2 \tan \beta_2$.

(3) With $\alpha = 0$, steady oscillation is possible only for $D = \zeta_2 + \left(A_e / A_i \right)^2 \cdot \left| \tilde{Q}_{10} / \tilde{Q}_{20} \right|^2 \zeta_T$.

(4) The cavity provides energy only through the swirl flow effects. With the diffuser effects, the energy is provided by the diffuser and the cavity does not contribute to the energy supply. The cavity is needed only for constituting a vibration system.

4 Numerical Results

The values of parameters used for sample calculations are given in the nomenclature. These values are determined by considering a test facility at EPFL and used for sample calculations as standard values except for the parameters specified for each case. The value of the loss coefficient ζ_T representing the effect of the runner was determined by assuming that the applied head H equals to the head $(\zeta_T / 2g)(\bar{Q} / A_i)^2$ across the runner. The value of the cavitation compliance C was determined so that the frequency given by Eq. (27) becomes 0.16 times the rotational frequency of the impeller f_n.

The swirl free flow rate Q_{sf} which gives no swirl at the runner exit is calculated to be

$Q_{sf} = SU_2 \tan\beta_2 = 0.618 \mathrm{m}^3/\mathrm{s}$

Due to the term of $j \cdot \frac{\rho a}{A_i} \tan\left(\omega \frac{L_i}{a} \right)$, the characteristic equation (22) is a transcendental equation, having higher order solutions. An iterative method is used to solve Eq.(22).

4.1 The Case with Infinite Sound Velocity in Penstock

4.1.1 Mode of oscillation. The ratio of the amplitudes of flow rate fluctuation in the upstream and downstream can be determined from Eq. (20) to be

$$\frac{\tilde{Q}_{1,0}}{\tilde{Q}_{2,0}} = -\left[\frac{\rho(\zeta_2 - D)}{A_e^2} \bar{Q} + \frac{\rho L_e}{A_e} j\omega \right] / \left[\frac{\rho \zeta_T}{A_i^2} \bar{Q} + \frac{\rho L_i}{A_i} j\omega \right] \tag{42}$$

Since $(\zeta_2 - D)/A_e^2 << \zeta_T / A_i^2$ and $L_e << L_i$, inlet flow rate fluctuation $\tilde{Q}_1$ is much smaller than the outlet flow rate fluctuation $\tilde{Q}_2$. In this case Eq. (25) with $\tilde{Q}_1 = 0$ is expected to give a good approximation.

Table 1 shows the result for the standard case. "3rd order equation" shows the results from Eq. (23) and "2nd order equation" shows the results from Eq. (25) with $\tilde{Q}_1 = 0$. The 3rd order equation has solutions ω_1 and ω_2 with the same imaginary part, and positive and negative real parts with the same absolute value. The real part of ω_3 is zero and the imaginary part is positive, suggesting an exponentially decaying mode. This shows that the 3rd order characteristic equation (23) gives substantially only one oscillatory mode. As expected, $\left| \tilde{Q}_{1,0} / \tilde{Q}_{2,0} \right|$ is much

smaller than 1 for ω_1 and ω_2. The 2nd order equation (25) also gives the solutions ω_1 and ω_2 with positive and negative real parts with the same absolute value. We discuss about the absolute value of the real part of ω_1 and ω_2 as the frequency and the common imaginary part of the ω_1 and ω_2 as the damping rate. The difference of the values of ω_1 and ω_2 from the 2nd and 3rd equations is not as small as expected from the small value of $\left|\tilde{Q}_{1,0}/\tilde{Q}_{2,0}\right|$. This shows that the swirl has a significant effect even if the upstream flow rate fluctuation is small, perhaps caused by larger values of cot $\beta_2 = 3.17$ and $\alpha = 10$.

Table 1 Solutions of characteristic equations for standard case

3rd order equation, Eq. (23)	
$\omega_{1,2} = \pm 13.14 - 5.17j$	$\tilde{Q}_{1,0}/\tilde{Q}_{2,0} = -0.0217 \mp 0.018j$
$\omega_3 = 0 + 1.88j$	$\tilde{Q}_{1,0}/\tilde{Q}_{2,0} = -0.303 \mp 0j$
2nd order equation, Eq. (25)	
$\omega_{1,2} = \pm 12.33 - 2.34j$	$\tilde{Q}_{1,0}/\tilde{Q}_{2,0} = -0.0228 \mp 0.015j$

4.1.2 Effects of mean flow rate and contributions of diffuser and swirl effects. A large effect of mean flow rate $\bar{Q}$ on the instability is expected from the discussion in the last section. So, the effect of flow rate is examined from the numerical results from Eq. (23). Here, the head is assumed to be constant and the mean flow rate $\bar{Q}$ is changed by changing the value of ζ_T. Figure 4 shows the results with three values of the pressure coefficient of swirl α. With the standard value $\alpha = 10$, the instability occurs for $\bar{Q} < 0.760\,\mathrm{m^3/s}$ or $\bar{Q} > 0.889\,\mathrm{m^3/s}$, which includes the standard flow rate $Q_s = 0.51\,\mathrm{m^3/s}$ and the swirl free flow rate $Q_{sf} = 0.618\,\mathrm{m^3/s}$. For $\bar{Q} < 0.76\,\mathrm{m^3/s}$, the value of $\left|\tilde{Q}_{1,0}/\tilde{Q}_{2,0}\right|$ is smaller but it increases significantly for $\bar{Q} > 0.889\,\mathrm{m^3/s}$. With smaller values of $\alpha = 5$ and $\alpha = 1$, ω_I is negative for all flow rate $\tilde{Q}$ shown. To understand this result, diffuser effects and the swirl effects are examined independently.

First, calculations were made with $\alpha = 0$ to examine the diffuser effects and the results are shown in Fig.5 with

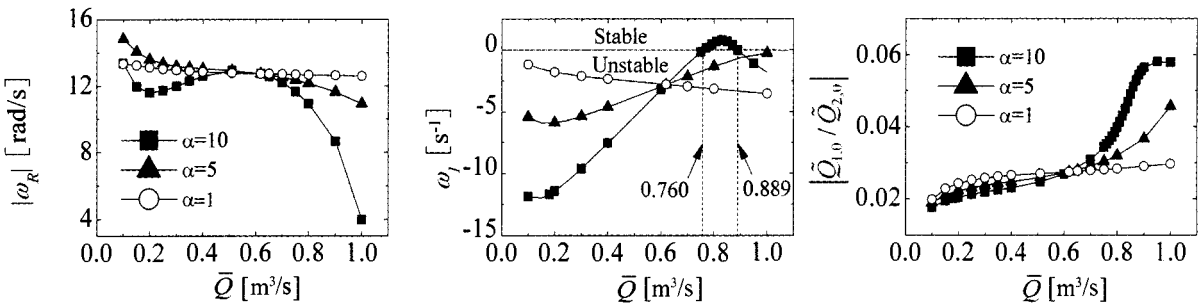

Fig. 4 Effects of mean flow rate $\bar{Q}$ under standard conditions

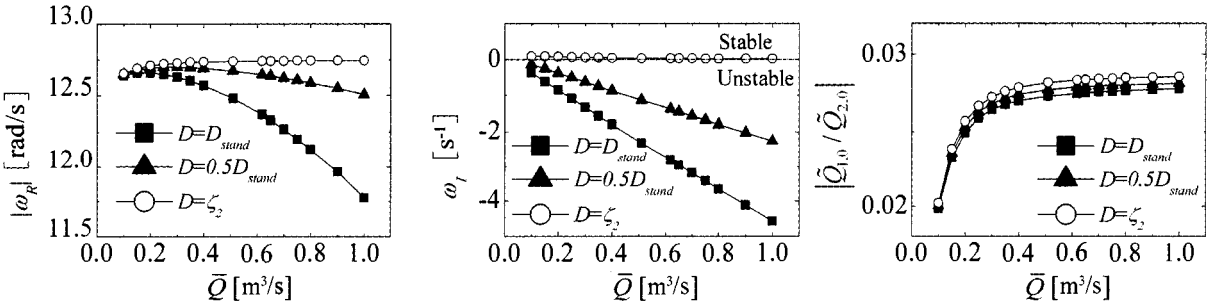

Fig. 5 Effects of diffusion factor D under α=0

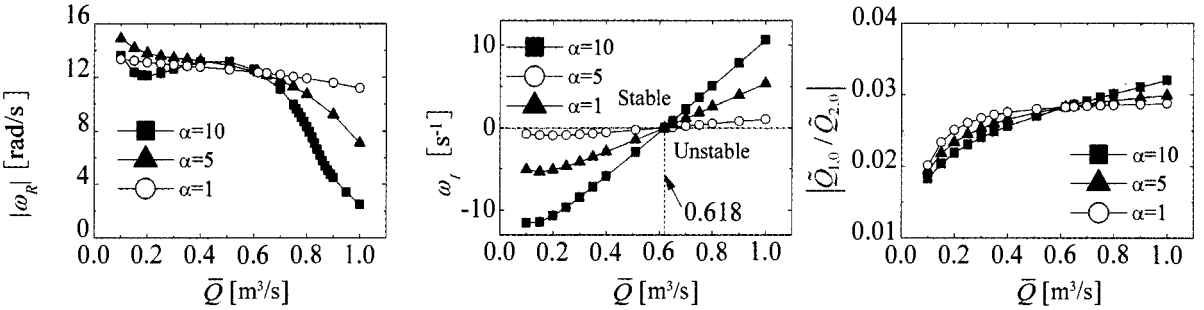

Fig. 6 Effects of pressure coefficient of swirl α under D - $\zeta_2 = 0$

various values of the diffusion factor D. D_{stand} = 27.7 is the standard value of the diffusion factor. We should note that small but positive damping $\omega_I > 0$ is obtained for the case of D-$\zeta_2 = 0$. This shows that the diffuser effect represented by D is the cause of the instability. For $D = D_{stand}$ and $D = 0.5D_{stand}$, the instability occurs for all flow rates and the amplifying rate $-\omega_I$ increases with the flow rate and the value of the diffusion factor D. This is expected from the damping term in Eq. (25).

Second, the effect of swirl is examined by putting D-ζ_2 =0 and the results with several values of swirl pressure coefficient α are shown in Fig.6. Equation (28) with $\tilde{Q}_2 = 0$ suggests the upstream resonant frequency $\omega_i = \sqrt{A_i / \rho L_i C}$ = 2.13 rad/s. However, the frequency is closer to the downstream resonant frequency $\omega_e = \sqrt{A_e / \rho L_e C}$ =12.56 rad/s of Eq. (27).

The critical flow rate at which the damping coefficient on $d\tilde{Q}_1 / dt$ in Eq. (28) becomes zero is obtained to be $\bar{Q} = 0.569\text{m}^3/\text{s}$. However, the critical flow rate with ω_I =0 shown in Fig.6 is closer to the swirl free flow rate Q_{sf} = $0.618\text{m}^3/\text{s}$ irrespective of the value of α. The damping rate ω_I is nearly proportional to the value of α. For the case of D-ζ_2=0, Hurwitz' criterion (24) reduces to

$$\bar{Q} > \frac{2\alpha U_2 \cot\beta_2 / S}{\frac{\zeta_T}{A_i^2} + 2\alpha\left(\frac{\cot\beta_2}{S}\right)^2 - \left(\frac{\zeta_T}{A_i^2}\frac{L_i}{A_i}\right) \Big/ \left(\frac{L_e}{A_e} + \frac{L_i}{A_i}\right)} \tag{43}$$

For the present case with $L_i / A_i >> L_e / A_e$, the third term in the denominator on the right hand side almost cancels the first term and (43) can be approximated by

$$\bar{Q} > \frac{2\alpha U_2 \cot\beta_2 / S}{2\alpha(\cot\beta_2 / S)^2} = S \cdot U_2 \tan\beta_2 = Q_{sf} \tag{44}$$

These results show that in real cases with $L_i/A_i >> L_e/A_e$, the swirl effect causes the instability at smaller flow rates than the swirl free flow rate irrespective of the larger loss coefficient ζ_T of the runner. This result is in good agreement with Dorfler's study [11], which indicates that the self-excited surge can also occur at low flow rate. The amplitude of the upstream flow rate fluctuation is much smaller and the frequency is closer to the downstream resonant frequency ω_e.

If we consider the case with D-ζ_2=0 and ζ_T =0, the characteristic equation (23) is reduced to

$$-\left(\frac{\rho L_i}{A_i}\frac{\rho L_e}{A_e}C\right)\omega^2 + j\left[\frac{2\rho C\alpha\cot\beta_2}{S}\left(\frac{\cot\beta_2}{S}\bar{Q} - U_2\right)\frac{\rho L_e}{A_e}\right]\omega + \left[\frac{\rho L_e}{A_e} + \frac{\rho L_i}{A_i}\right] = 0 \tag{45}$$

This equation shows that the damping is caused by the swirl effects and the resonant frequency is given by

$$\omega_r = \sqrt{\frac{L_e / A_e + L_i / A_i}{\rho C (L_i / A_i)(L_e / A_e)}} \tag{46}$$

We obtain the downstream resonance with $\omega_r = \omega_e = \sqrt{A_e / \rho C L_e}$ for $L_i/A_i >> L_e/A_e$ and the upstream resonance with $\omega_r = \omega_e = \sqrt{A_i / \rho C L_i}$ for $L_i / A_i << L_e / A_e$. This shows that the swirl effect can cause both upstream and downstream flow oscillations although the upstream flow rate fluctuation is essential in the positive feedback loop of the instability through the swirl.

In order to discuss about the combined effects of the diffusion and the swirl, we compare the results shown in Figs.4-6. The similarity of the plots of ω_R in Figs.4 and 6 shows that, the swirl has the most significant effects on ω_R under standard conditions. The comparison of the plots of ω_I shows that ω_I for the standard case in Fig.4 approximately equals to the sum of those in Fig.5 with $D = D_{stand}$ and in Fig.6 except for the case of α = 10 with larger value of $\bar{Q}$. Examination of $\left|\tilde{Q}_{1,0} / \tilde{Q}_{2,0}\right|$ in each figure shows that the value is generally small but relatively larger values are obtained at larger values of $\bar{Q}$ with α = 10 for the general case shown in Fig.4. This and the behavior of ω_I in Fig.4 for the case of α = 10 with larger value of $\bar{Q}$ are considered to be a result of combined effects of diffusion and swirl.

4.2 The Case with Finite Sound Velocity in Penstock

4.2.1 Effect of inlet pipe length L_i. Fig. 7 shows the solutions when the wave speed is a = 500 m/s for the standard condition shown in the nomenclature. The mean flow rate $\bar{Q}$=0.51 m^3/s is smaller than the swirl free flow rate Q_{sf} =0.618 m^3/s. The full line curves represent different order modes. The draft tube resonant frequency $\omega_e = \sqrt{A_e / (\rho L_e C)} = 12.56$ rad/s is also shown in Fig. 7. The multiple quarter wavelength resonance frequencies $\omega_n = 2\pi na/4L_i$ of the penstock are also plotted as dashed lines. We observe the followings in the figure:

1) At frequencies higher than about twice the draft tube frequency $2\omega_e$, the frequency obtained agrees with ω_n with even number of n. It will be shown later that these correspond to open to open resonant frequencies of the penstock.

2) As the frequencies approach the draft tube resonant frequency ω_e, the obtained frequencies deviates from ω_n in the direction away from ω_n. This is opposite to the

"lock in" phenomena observed for Karman vortex from flexibly supported cylinders.

3) When $\bar{Q} < Q_{sf}$, most of the modes have negative damping ($\omega_I < 0$).

Table 2 First 3 order frequencies at L_i =50m, 150m and 300m

order	Frequency ω		
	L_i =50 m	L_i =150 m	L_i =300 m
1	13.683-3.158j	15.335-2.561j	9.381+0.504j
2	31.909-5.126j	21.256-2.787j	13.763-0.597j
3	62.937-4.140j	31.465-1.753j	17.274-2.606j

At L_i = 50m, 150m and 300m the lowest 3 mode frequencies are listed in Table 2 and the velocity and pressure fluctuation modes in Fig. 8 to 10. The corresponding frequencies are also shown in Fig. 7. At L_i = 50m, the fluctuations of 1st mode has about 1/4 wavelength, and 2nd and 3rd order are about 1/2 and 1 wavelength respectively, as expected from the comparison with the multiple quarter wavelength frequencies shown in Fig.7. At L_i = 50m and 150m, for the 1st order mode with the frequency closer to ω_e, the runner inlet is a node of velocity fluctuation. However, the runner inlet is a loop for higher order modes. At L_i = 300 m, the runner inlet is a node of velocity fluctuation for the 2nd order mode, whose frequency is closer to ω_e than other order frequencies. The 1st order mode with the frequency less than ω_e is a damping mode as shown in Fig. 7 and Table 2

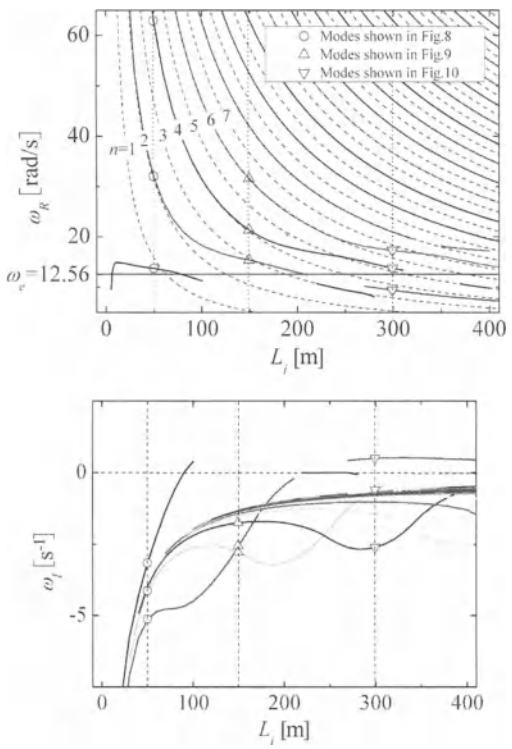

Fig. 7 Higher order frequencies under a = 500 m/s

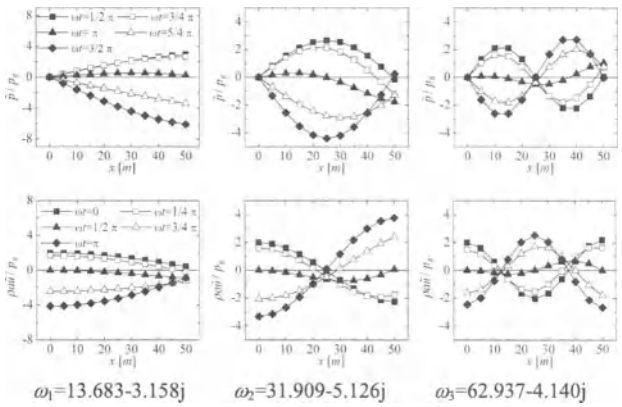

Fig. 8 Velocity and pressure distributions along the inlet pipe of L_i = 50m

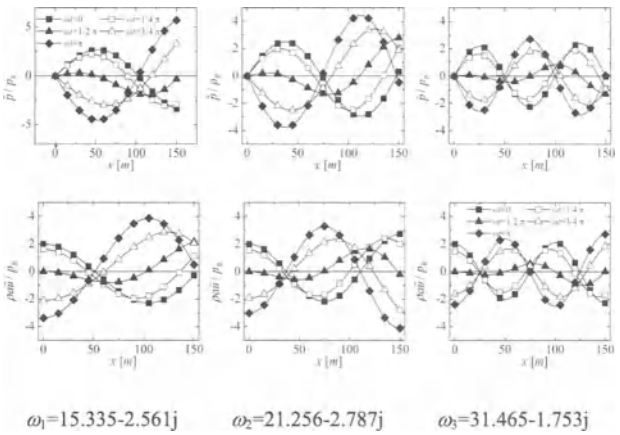

Fig. 9 Velocity and pressure distributions along the inlet pipe of L_i = 150m

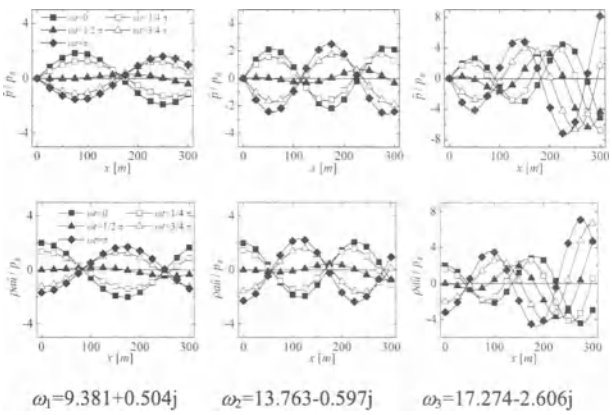

Fig. 10 Velocity and pressure distributions along the inlet pipe of L_i = 300m

Figure 12 shows the effects of mean flow rate on the lowest 3 frequencies under a = 500 m/s. The real parts of 2nd order frequency ω_2 and 3rd order frequency ω_3 increase as the flow rate departs from the swirl free flow rate Q_{sf}. While ω_1 shows negative damping in a wider region of mean flow rate, ω_2 and ω_3 have negative damping in the region of $\bar{Q} < Q_{sf}$.

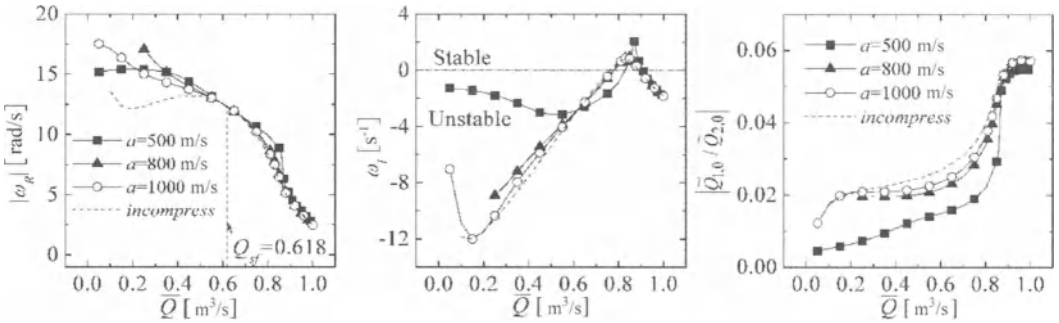

Fig.11 Effect of mean flow rate $\bar{Q}$ on the lowest mode under standard condition (L_i = 50 m)

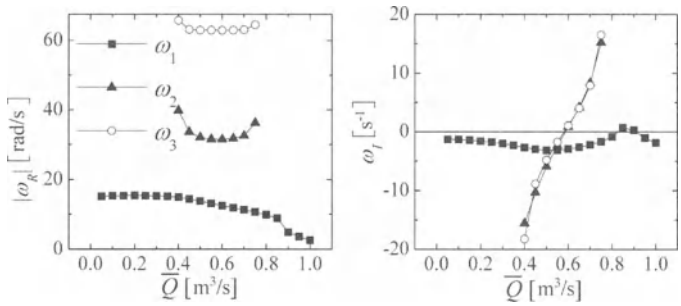

Fig. 12 Effect of $\bar{Q}$ to first 3 order frequencies L_i = 50m, under a = 500 m/s

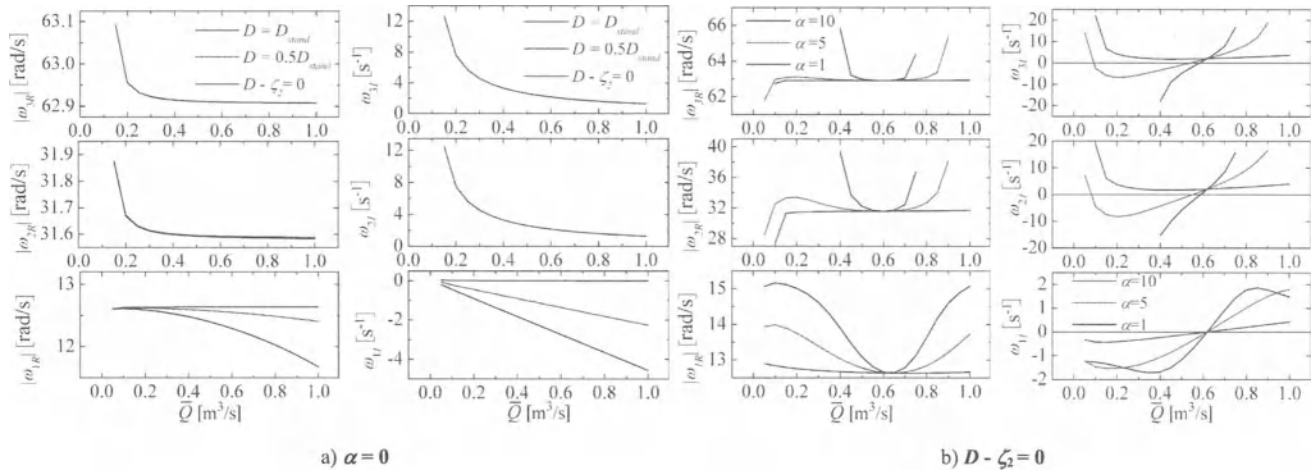

Fig. 13 Diffuser and swirl effects to lowest 3 frequencies at L_i = 50 m, a = 500 m/s

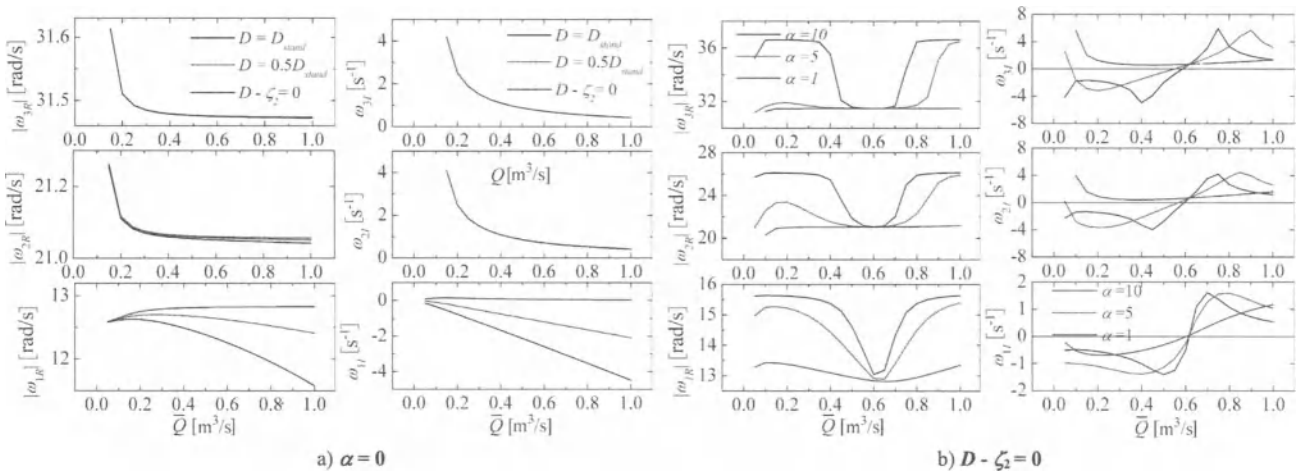

Fig. 14 Diffuser and swirl effects to lowest 3 frequencies at L_i = 150 m, a = 500 m/s

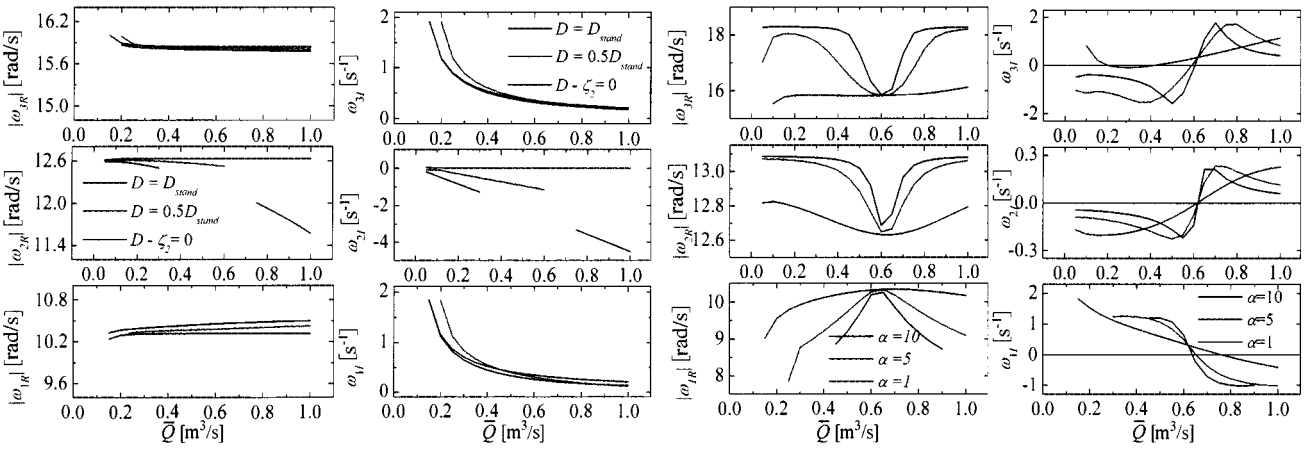

a) $\alpha = 0$ b) $D - \zeta_2 = 0$

Fig. 15 Diffuser and swirl effects to lowest 3 frequencies at L_i = 300 m, a = 500 m/s

We examine the diffuser and swirl effects separately by putting $\alpha = 0$ or D-ζ_2=0. Fig.13 shows the results for L_i = 50 m and a = 500 m/s. With $\alpha = 0$, ω_2 and ω_3 are always damping without the effect of value of D. This shows that the diffuser effect does not cause higher order modes in the penstock. With D-ζ_2 =0 and larger values of α, all modes have negative / positive damping for $\bar{Q}$ </>Q_{sf}. This shows that the swirl effect affects all modes and causes instabilities when $\bar{Q} < Q_{sf}$.

Table 3 First 3 order frequencies and modes under α = 0, $D = 0.5D_{stand}$

order	ω	$\tilde{Q}_{1,0} / \tilde{Q}_{2,0}$
	L_i=50 m	
1	12.574 -1.151j	-0.010 -0.006j
2	31.594+2.544j	-5.242 -1.495j
3	62.912+2.563j	-23.983 -2.991j
	L_i=150 m	
1	12.657 -1.004j	-0.0232-0.0299j
2	21.059+0.838j	-1.7912-0.5412j
3	31.476+0.852j	-5.2567-0.8144j
	L_i=300 m	
1	10.375+0.324j	0.3239-0.1991j
2	12.536 -1.065j	-0.0041-0.0199j
3	15.824+0.386j	-0.5789-0.3161j

The effects of swirl and diffusion at L_i = 150 m are shown in Fig. 14. Figure 7 shows that the lowest order frequency ω_1 at L_i = 150 m corresponds to the second order frequency ω_2 at L_i = 50m. However, comparing Figs. 13 and 14, the results of L_i = 150 m for ω_1 are similar to the results for ω_1 of L_i = 50 m, with the values of ω_1 close to ω_e for both cases. The diffuser still has a significant effect on ω_1 but little on ω_2 and ω_3. This shows that the diffuser effect affects the modes with the resonant frequency close to ω_e, independently on the mode shape in the penstock. On the other hand, swirl has larger effect on all of the lowest 3 frequency modes.

The smaller diffuser effect on higher order frequencies may be explained by the draft tube resonance frequency ω_e =12.56 Hz. Table 3 shows $\tilde{Q}_{1,0} / \tilde{Q}_{2,0}$ for each case with the values of ω. $\tilde{Q}_{1,0}$ and $\tilde{Q}_{2,0}$ are flow rate fluctuations at the runner inlet and outlet. For the cases with ω_1 for L_i =50m and 150m and ω_2 for L_i=300m, the frequencies are closer to ω_e. For these cases $\left|\tilde{Q}_{1,0} / \tilde{Q}_{2,0}\right|$ has smaller values suggesting that oscillations in the draft tube is much larger. For these cases the effects of D is significant. For other cases, $\tilde{Q}_{1,0} / \tilde{Q}_{2,0}$ has larger values suggesting larger amplitude of oscillations in the penstock.

We also check the diffuser and swirl effect at L_i = 300 m in Fig. 15. The diffuser has larger effect on ω_2 but little on ω_1 and ω_3. This is because ω_2 has the nearest value to the draft tube resonance frequency ω_e at L_i = 300 m, as listed in Table 2. The swirl effect on the 1st order mode with the frequency less than ω_e is totally different from other cases. This will be discussed later.

Comparing Figs. 13 to 15, for the diffuser effects (α=0), only the modes with the frequency closest to the draft tube resonant frequency ω_e are affected and the instability is caused. Other modes with the frequencies far from ω_e are not affected nor destabilized by the diffuser effect.

On the other hand, the swirl effects (D-ζ_2 = 0) affects all modes except for the first order mode of L_i = 300m, which has a resonant frequency lower than ω_e, and destabilizes them at $\bar{Q} < Q_{sf}$. The destabilizing swirl effect for the general case has been explained in Section 3.3 as follows. Consider the case when the upstream flow

rate Q_1 increases under the mean flow rate $\bar{Q} < / > Q_{sf}$. Then the swirl velocity decreases / increases and the pressure in the vortex core is increased / decreased. This results in decreased / increased cavity volume V_C. From the continuity equation $dV_C/dt = Q_2 - Q_1$, Q_2 will be decreased / increased and Q_1 will be increased / decreased for the general cases. This means that the cavity volume fluctuation provides positive / negative feed back at the mean flow rate $\bar{Q}$ smaller / larger than the swirl free flow rate Q_{sf}.

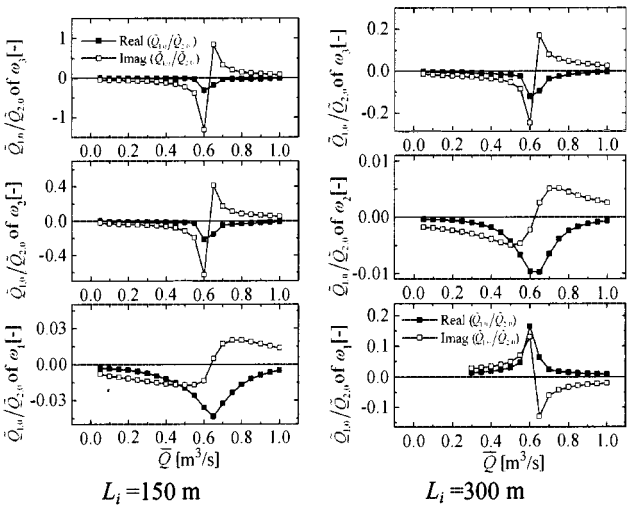

Fig. 16 Modes of first 3 order frequencies at D -$\zeta_2 = 0$ and $\alpha = 5$

Figure 16 shows the plot of $\tilde{Q}_{1,0}/\tilde{Q}_{2,0}$ for the cases of D-ζ_2=0, α=5, L_i =150m and 300m. Almost for all cases, $\left|\tilde{Q}_{1,0}/\tilde{Q}_{2,0}\right| \ll 1$. For these cases, the cavity volume fluctuation is delayed behind the $\tilde{Q}_2$ fluctuation by about 90°, from the continuity relation $\tilde{Q}_2 = dV_c/dt$. Except for the case of $\omega_1 < \omega_e$ with L_i=300m, $\mathrm{Real}\left(\tilde{Q}_{1,0}/\tilde{Q}_{2,0}\right) < 0$ and the phase difference between $\tilde{Q}_{1,0}$ and $\tilde{Q}_{2,0}$ is larger than ±90°. For this case upstream flow rate is decreased ($\tilde{Q}_{1,0} < 0$) when the cavity volume is increasing ($dV_c/dt > 0$), as assumed in the discussion above. For the case of $\omega_1 < \omega_e$ with L_i =300m, $\mathrm{Real}\left(\tilde{Q}_{1,0}/\tilde{Q}_{2,0}\right) > 0$ and the phase difference between $\tilde{Q}_{1,0}$ and $\tilde{Q}_{2,0}$ is smaller than ±90°. In this case, both upstream and downstream flow rates becomes positive when $dV_c/dt > 0$. This is opposite to the assumption in the above discussion. The positive feedback and the instability occur for the flow rates larger than the swirl free flow rate. The relationship between the cavity volume and flow rate fluctuation is shown in Fig.17 for the typical cases with phase difference equals to 180° (general cases) or 0° (for ω_1 with L_i = 300m).

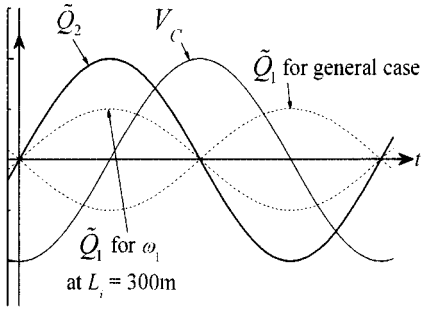

Fig. 17 Relationship among flow rate fluctuations and cavity volume

5 Conclusion

It was found that the diffuser effect of the draft tube destabilizes the hydraulic system over the entire flow range. The swirl flow from the runner stabilizes/ destabilizes the system above/below the swirl-free flow rates. In both cases, the frequency of oscillation is determined from the compliance of the cavitation and the inertial length of draft tube. For general cases with larger penstock length and runner resistance, the amplitude of flow rate fluctuation is much larger in the downstream of the runner as compared with the upstream.

For the application to real system, we need to take account of the flow compressibility effects in the penstock. It was shown that various acoustic modes in the penstock can be destabilized by diffuser and swirl effects. At higher frequency than the draft tube resonant frequency ω_e, open-to-open acoustic modes occur in the penstock, when the flow rate is smaller than swirl free flow rate Q_{sf}. When the frequency of acoustic modes gets closer to ω_e, the oscillation frequency has a tendency to depart from ω_e. The diffuser effect of draft tube affects only the modes with the frequency closest to ω_e and causes the instability at all flow rates. For these modes, the flow rate fluctuation in the upstream of the runner is much smaller than the downstream and the velocity node occurs at the runner inlet. The swirl effect affects all modes and cause instability at smaller flow rates than Q_{sf}, except for the mode with the frequency less than ω_e. Thus, the higher order modes are caused by swirl effect. For the modes with the frequency less than ω_e, the phase difference between upstream and downstream flow rate fluctuation becomes less than 90° and the instability occurs at higher flow rate than Q_{sf}.

The present analysis can be applied not only to the full

load surge but also to the part load surge which has been considered to be a forced oscillation due to the vortex rope whirl. However, further research is needed to correlate these findings with experimental observations in real hydropower systems. Various simplifying assumptions have been made in present study. For lower frequency oscillations, we may need to take account of the changes in the runner speed and guide vane opening. Swirl in the draft tube may have an effect to mitigate the flow separation and thus reduce the value of draft tube resistance ζ_2 [10]. At higher mean flow rate than design, this effect might destabilize the system, and the stability would be enhanced at lower flow than design. These effects should be clarified in future study.

Acknowledgements

The present manuscript is prepared by combining the papers of [8] and [9]. The present authors would like to thank Dr. C.Nicolet, Dr. M.Farhat and Prof. F.Avellan for their contributions in preparing the original papers.

References

Jacob, T., Prenat, J-E., 1996, "Francis Turbine Surge: Discussion and Data Base," Proc. 18th IAHR Symposium, Valencia, Spain

Nishi, M., 1984, "Surging Characteristics of Conical and Elbow Type Draft Tubes," Pro. 12th IAHR Symposium on Hydraulic Machinery and System, Stirling, pp. 272 – 283

Nishi, M., Matsunaga, S., Kubota, T., Senoo, Y., 1982, "Flow Regimes in an Elbow-Type Draft Tube," Proc. 11th IAHR Symposium on Hydraulic Machinery and System, Amsterdam, pp. 1 – 13, paper 38

Nishi, M., Wang, X., Okamoto, M., Matsunaga, S., 1994, "Further Investigation on the Pressure Fluctuations Caused by Cavitated Vortex Rope in an Elbow Draft Tube," Cavitation and Gas Fluid Flow Machinery and Devices, ASME, pp. 63 – 70

Prenat, J-E., Jacob, T., 1986, "Investigating the Behavior at High Load of a Francis Turbine Model," Proc. 13th IAHR Symposium, Montreal

Koutnik, J., Pulpitel, L., 1996, "Modeling of the Francis Turbine Full-Load Surge," Modeling, Testing and Monitoring for Hydro Power Plants, Lausanne

Koutnik, J., Nicolet, C., A.Schoul, G., Avellan, F., 2006, "Overload Surge Event in a Pumped Storage Power Plant," Proc. 23rd IAHR Symposium, Yokohama, paper 135

Chen, C., Nicolet, C., Yonezawa, K., Farhat, M., Avellan, F., Tsujimoto, Y., 2008, "One-Dimensional Analysis of Full Load Draft Tube Surge", ASME Trans. J. Fluids Eng., 130, 041106 (2008)

Chen, C., Nicolet, C., Yonezawa, K., Farhat, M., Avellan, F., Tsujimoto, Y., 2008, "One-Dimensional Analysis of Full Load Draft Tube Surge Considering the Finite Sound Velocity in the Penstock", Proc. 24th IAHR Symposium, Foz do Iguassu, Brazil

Susan-Resiga, R., Ciocan, G.D., Anton, I., Avellan, F., 2006, "Analysis of the Swirling Flow Downstream a Francis Turbine Runner," J. Fluid Eng., 128, pp. 177 – 189

Dorfler, P.K., 1985, "Francis Turbine Surge Prediction and Prevention," Proc. Waterpower' 85, pp. 952 – 961

The 4th International Symposium on Fluid Machinery and Fluid Engineering
November 24-27, 2008, Beijing, China
NO. 4ISFMFE-IL08

Future Aspects and Developments for Advanced CO_2-Free Power Station Technologies

D. Bohn

Institute of Steam and Gas Turbines
Templergraben 55, D-52056, Aachen, Germany
Tel: +49-241-80-25450/1 / Fax: +49-241-80-22307
E-mail: post-bohn@rwth-aachen.de

Abstract The reduction of CO_2-emissions is the pre-eminent goal of most current developments in modern power plant engineering. The developments in CO_2-capture and storage focus on three different solutions: gasification, oxyfuel-processes and (chemical) washes. Although the technological basis for these three methods differs, their common disadvantage is the reduction in efficiency they inevitably cause. This does not only reduce the economical viability of the power plant but also the life-span of the natural resources at the basis of the processes.

In order to mitigate these side-effects a considerable increase in power plant efficiency has to be achieved. Only then can these technologies be introduced on a commercial base. In the short-term the research efforts will concentrate on the improvement of existing technologies.

Keywords CO_2-reduction, CO_2-capture, combined cycle power plant, cooling technology, effusion cooling, gas turbine

1 Introduction

Global warming is one of today's most hotly debated issues, but a general consensus exists that the CO_2-emissions of industrialised and industrialising countries make a significant contribution to the increase in the temperature of the earth's atmosphere. Two of the most obvious solutions to the problem, the use of nuclear energy and a reduction of the energy consumption, are in most countries neither politically nor socially acceptable. Since the number of possible solutions is reduced, the preservation of natural (fuel) resources and the reduction of gases that are harmful to the environment are presently the driving forces behind many of the power industry's technological innovations.

The challenge for the power plant industry in the near future will be to cope with the demand for higher efficiencies and to fulfil the increasingly severe environmental laws while simultaneously guaranteeing the availability of the plant at reduced operating costs.

Within the technological developments a distinction should be made between short-, mid- and long-term developments. Whereas the short-term developments focus on the improvement of existing technologies, the mid-term developments will see new power plant processes, including innovative hybrid power plants incorporating renewables. Only in the long-term completely CO_2-free technologies are to be expected (Fig. 1).

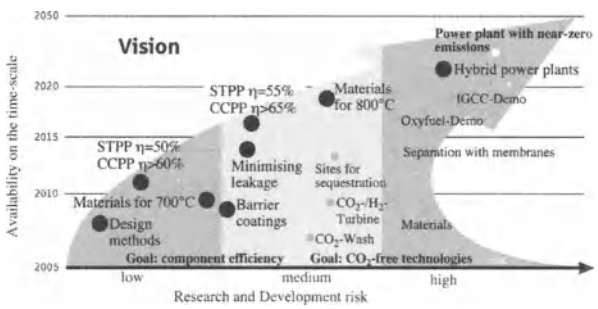

Fig. 1 Projected

2 Importance of CO_2-Emissions

World-wide carbon dioxide emissions are expected to increase by 1.9 percent annually between 2001 and 2025;

www.eia.doe.gov (2008). Much of the increase in these emissions is expected to occur in the developing world where emerging economies, such as China and India, fuel their economic development with fossil energy. This increase is accelerated further by the rapid population growth in most developing countries. The developing countrie's emissions are expected to grow above the world average at 2.7 percent annually between 2001 and 2025 and surpass emissions of industrialized countries around 2018. Already, China is nearing surpassing the U.S.A. as the world largest emitter of greenhouse gases.

Apart from the fear that the world fossil fuel supplies risk depletion if the current rate of consumption continues, concern has grown over the years on the effect of increase in fossil fuel consumption on CO_2-emissions and the effect this is having on the environment, especially global warming.

Concentrations of carbon dioxide in the atmosphere are naturally regulated by numerous processes, collectively known as the "carbon cycle". While these natural processes can absorb some of the net 6.1 billion metric tons of anthropogenic carbon dioxide emissions produced each year (measured in carbon equivalent terms), an estimated 3.2 billion metric tons is added to the atmosphere annually. The principal cause of this increase in emissions has been fossil fuel consumption and deforestation. This increase in greenhouse gases is directly correlated to the annual temperature increase in the earth's atmosphere.

The Kyoto protocol on climate change has played a major role in the efforts to reduce global carbon emissions. Although not all countries in the developed world are signatory to the treaty (e.g. the U.S.A.), those that are signatories to it are required to cut carbon emissions by a certain amount. Although the introduction of the clean development mechanism (CDM) at this summit gave developing countries the opportunity to trade their carbon credits to more developed countries that are unable to cut their CO_2-emissions to the required level industrialised countries should take active measures against CO_2-emissions.

In recent years the sequestration technology has been discussed as a way of combining this continued use of fossil fuels with the increasingly severe emission restrictions. Given this trend, CO_2 capture and storage (CCS: Carbon Capture and Storage) will become a viable option for reducing CO_2 emissions and global warming in the long-term. These measures are called secondary, as they do not directly reduce the emissions, but merely capture the emissions that are caused. They mainly consist of different techniques for separating the CO_2 in the exhaust gases and storing it. At the moment three different separation technologies are being investigated:

- gasification (efficiency: 42%)
- washes (estimated efficiency: ca. 37%)
- oxy-fuel (estimated efficiency: ca. 35%)

Gasification plants or IGCC (Internal Gasification Combined Cycle) do not burn coal but gasify it by exposing powdered coal to oxygen in a high-pressure heated chamber. The system yields several gases which are processed into hydrogen, which is burned in a gas turbine combustion chamber, and carbon-dioxide. Proponents say that gasification is easier than capturing CO_2 from a regular power plant because it produces a smaller volume of exhaust gases. Gasification has, apart from its relatively high efficiency, several other important advantages: all process steps are already commercially available (a IGCC plant exists, for example, at Buggenum, The Netherlands), which means that the technological and economical statements about the technology are well-founded. Furthermore the plants are flexible with regard to their fuel and can be operated without CO_2-capture as well. The capture itself can take place at different stages of the process. In steam power plants capture after combustion, in CCPP capture before combustion is more popular; Ewers (2007). The most important disadvantages are that the process is relatively complex, which may lead to availability issues and relatively low degree of carbon capture (ca. 85%).

CO_2-washes are based on the absorption of CO_2 and are purely chemical or physical processes. At twice the costs of normal plants, the investment costs are fairly high and, again, the process is complex and yields only a fairly low degree of carbon capture. First experiences with washes are gathered at the Danish Esbjerg power plant in the framework of the European CASTOR-project; Ewers (2007).

The oxy-fuel processes, which burn fuel with pure oxygen, are considered to be very promising, especially as up to 90% of the carbon in the exhaust gas can be captured. Although the process is based on known technologies, the development of the membrane that separates the oxygen from the other ambient gases is problematic. Above all, the operating costs of these plants will be considerably higher than those of the other two technologies; Ewers (2007).

In CO_2 capture, carbon dioxide is collected from anthropogenic gaseous emissions arising from fossil-fuelled power plants. In CO_2 storage, the captured gases are injected into geologic formations like sandstone or limestone saline aquifers or old oil and gas fields where they should remain indefinitely. Questions about the suitability and availability of the different storage options

is still under investigation, as is the question as to what happens to the gas once it is underground (Fig. 2).

Several projects are currently looking at ways of making carbon storage economically competitive and safe. Among these are the International Weyburn CO_2 Monitoring Project, a collaboration among the United States, Canada, the European Commission and Japan; www.usinfo.state.gov (2008), the Frio Brine Sequestration Pilot, a joint project between the United States and Australia; www.usinfo.state.gov (2008). In Europe, the CO_2SINK (www.co2sink.org (2008)) demonstration project at Ketzin in Germany, which is coordinated by GeoForschungsZentrum (GFZ) in Potsdam, is also a good example of CO_2-sequestration. A total of 60,000 tonnes of CO_2 is expected to be injected into a saline aquifer at a rate of about 100 tonnes a day.

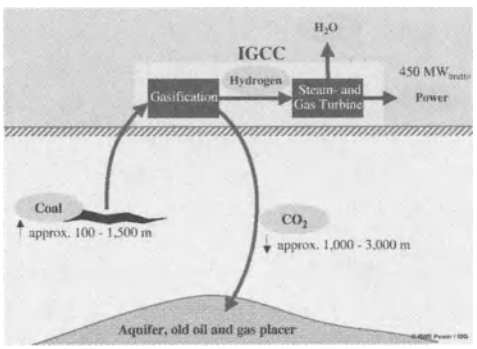

Fig. 2 CO_2 storage in aquifers and depleted oil- and gas-fields

The efficiencies of all of these processes are well below those of the current state-of-the-art in normal power plants. This implies that more fuel resources have to be used to attain the same power output and costs will increase. Therefore commercial operation of these plants, even when CO_2-emissions become increasingly more expensive, will only be possible if the efficiency of these plants can be ameliorated.

3 CO_2-Reducing Measures

Primary CO_2-reducing measures are those that reduce or avoid the formation of CO_2 in the process for a given power output rather than capturing and storing it. In all probability, the short-and mid-term developments within the industry will be dominated by the improvement of existing technologies and the development of innovative new ones, both of which aim at increasing the efficiency of the power plant. Another option is the use of renewables, which avoid the production of CO_2 altogether.

The world power plant market is, at present, dominated by an increasing demand for combined cycle power plants and, in countries with large coal reserves like China and the U.S.A., by a demand for modern steam turbine plants with highest efficiencies. In Europe there will be a significant demand for additional power plants with increased power output as well. This is putting pressure on the industry, as the power plants that are currently build will dominate power generation for the next decades.

The development of the efficiency of both single and combined cycle power plants over the last 15-20 years has shown a continuous increase based on the improvement of existing technologies (Fig. 3). The last 5-10 years have seen the introduction of new turbines by almost every manufacturer. These turbines show a tendency not only towards increased efficiency but also an ever-increasing power output. The latest development in the field of heavy-duty gas turbines, the Siemens SGT8000-H, is a prime example. It is designed for a power output of 340 MW_{el} at an efficiency of 39% and is largely based on existing technologies within the Siemens and former Westinghouse companies.

The development of new technologies in power plant engineering focuses on new high-temperature materials and advanced cooling technologies. An interesting approach, which for now remains limited to prototypes of small gas turbines, is the application of fully ceramic components. A Japanese development, the Kawasaki CGT-302, could deliver 300 kW_{el} at an efficiency of over 42% (Fig. 4). Even at this small size, the connection between the ceramic and metallic parts remains an issue due to the different

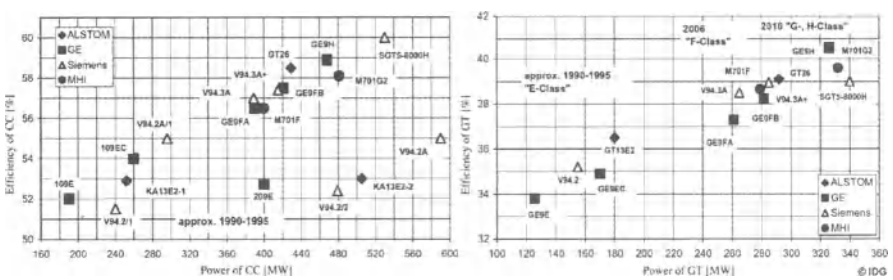

Fig. 3 Efficiency and power output of today's gas turbines and combined cycles

thermal expansion coefficients of the materials. Although cooling is not an option for these small turbines, the combination of material and cooling technology developments has the highest potential of increasing the efficiency of modern gas turbines.

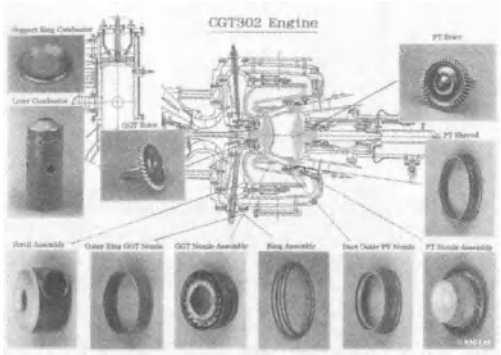

Fig. 4 Small gas turbine with ceramic components (KHI-CGT-302)

The challenges arising from the formulation of the fundamentals for the innovative design of the thermally and mechanically highly loaded components in combination with an optimal process configuration can only be mastered by the joint efforts of fluid flow experts, structural engineers, materials' scientists and production engineers. Therefore, the Collaborative Research Centre (SFB) 561 "Thermally Highly Loaded, Open-Porous and Cooled Multi-Layer Systems for Combined Cycle Power Plants" was founded at RWTH Aachen University in 1998 (Fig. 5).

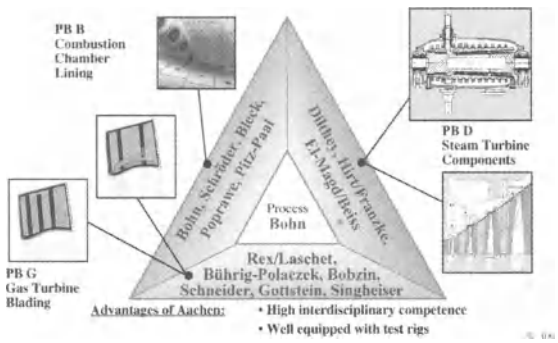

Fig. 5 Project partners within SFB 561

The envisaged innovative cooling- and water subtraction technologies have to be realised by the subsequent development of open-porous structures, that are made from:

- drilled open-porous multi-layer systems (gas turbine)
- grid-sheets (high- and intermediate-pressure steam turbines)
- open-porous metallic foams (mechanically low-loaded gas turbine components as well as low-pressure steam turbines)

The basis for these developments are materials that are currently state-of-the-art in both gas and steam turbine design, e.g. single-crystal Ni-base alloys for gas and P92 for steam-turbines. The open-porous components are constructed in a way that comprises of a load-bearing structural material combined with a coated outer material and cooling films. This ensures that the temperature of the component remains below its maximum.

Gas Turbine Technology

With the gas turbine in particular, it shows that the amelioration of the structural materials by itself will not suffice to handle the high temperatures prevailing in the working fluid (Fig. 7).

Only by intensively cooling the thermally highly loaded components, like the vanes and blades in the first stage of the gas turbine, temperatures close to or even above the melting point of super alloys become possible. Over the last decades cooling has evolved from convection over impingement to film cooling. The next step in this chain is a cooling system that brings the advantages of an open cooling system while minimising its main disadvantage, i.e. the "loss" of compressor air to the cooling system.

With open cooling systems, like current state-of-the-art film cooling, the interaction between coolant and hot gas can lead to an increased level of turbulence and locally overheated surfaces, significantly reducing the life-span of turbine blades. Moreover, the discrete nature of the cooling holes in current applications leads to an excessive amount of coolant being introduced into the system in order to guarantee a closed cooling film. Therefore, effusion cooling (also know as full-coverage cooling) in the gas turbine, as the first step in the realisation of transpiration cooling using open porous structures, is one of the main foci of the SFB. Effusion cooling can provide full-coverage cooling using much lower amounts of coolant than film cooling, due to the much smaller holes that are being used here. The effectiveness of this cooling can be raised by distributing the cooling holes on the surface according to the local demand. It can be increased even further by contouring the holes (Fig. 6).

The coolant is fed through the structural material to a cavity underneath a porous interlayer. This layer is protected against a direct contact with the hot gas by a permeable TBC, through which the coolant leaves the component as full-coverage cooling. Two different concepts for realising this cooling concept are pursued within the SFB: both laser-drilled multi-layer systems and coated open-porous metallic foams can be applied, depending on the prevailing boundary conditions (Fig. 7).

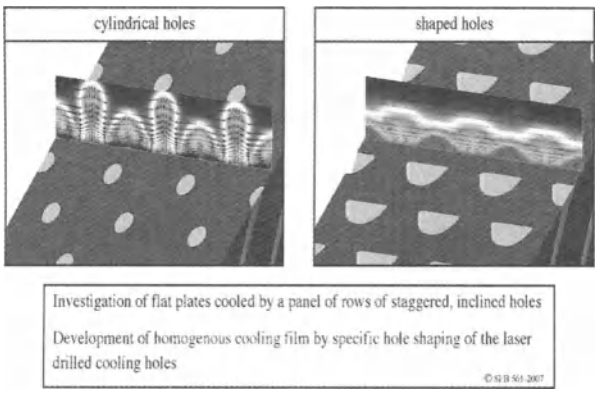

Fig. 6 Homogeneous cooling film due to hole contouring

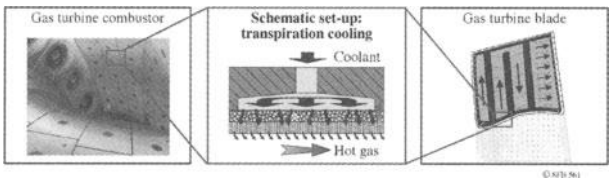

Fig. 7 Application of porous cooling structures

A further rise of the gas turbine inlet temperature with almost 150°C would be possible by applying thermal barrier coatings on the basis of ZrO_2, but this potential can currently not be unlocked completely, because the life-span of these coatings cannot be predicted with certainty. This means that the coolant has to compensate for a possible failing of the TBC. Within the SFB a novel approach to this problem, whereby a graded layer of bondcoat and TBC is applied to the blade surface, is being tested. This approach promises to reduce the spalling of the TBC and to improve its life-span considerably; Bobzin et al. (2006).

Laser drilling is used for manufacturing the cooling holes in the coated multi-layer system. By using trepanning for drilling the inclined cooling holes, precise contours can be achieved in the TBC while keeping a cylindrical inlet geometry in the substrate. To avoid under-cutting the TBC while drilling the inclined cooling holes, a process for applying a TBC to already drilled structures has been developed. The holes are kept open by emitting Argon through them during the application of the TBC, but the contour of the holes cannot be controlled as precisely as when drilling directly through the three-layer system. This means that a processing step has to be added, in which the hole contour is improved using ps-radiation; Poprawe et al. (2008).

The calculation of hundreds or even thousands of cooling holes will not be feasible in the foreseeable future. Therefore the SFB tries to develop a methodology for determining the equivalent material properties of porous materials using the homogenisation technique, Laschet et al. (2007). These equivalent properties are implemented in a conjugate flow solver that simulates large arrays of effusion cooling holes.

When using only open porous materials the creep resistance of the gas turbine blade cannot be guaranteed. Therefore, a new concept is pursued in which a load-bearing core made of NiAl with inlaid ceramic fibres supports a thin outer contour. This contour will be shielded from the hot gas by a thermal barrier coating and arrays of cooling holes. The temperatures within the blade can be raised considerable while at the same time reducing the cooling fluid by using this concept; Zhong et al. (2007).

The core of this blade with Al_2O_3-fibres is manufactured with diffusion-welding. The connection between the fibres and the NiAl-matrix is problematic due to the different thermal expansion coefficient of the materials. Because of the brittle fraction behaviour of NiAl at ambient temperature, a weak connection is required in this temperature range. At high temperatures a strong connection is required because the matrix material softens and the load has to be borne by the fibre-reinforced core. To master this problem, the fibres receive a coating of hexagonal Boron-Nitrite (MAX-Phase) and NiAl-FG75 prior to welding in order to maximise the adhesion between the fibres and the matrix; Zhong et al. (2007). In order to achieve a pore-free composite, the cores are welded at 1300-1350°C and pressures of up to 30-40 MPa for over 2 hours; Hajas et al. (2006), Echsler et al. (2006). MAX phases are compositions of metal, a intermediate material and carbon. This lends the composite strength and ductility, but also the temperature stability normally associated with ceramics. The chemical composition of the MAX-phase interlayer is of crucial importance for the mechanical connection of the fibres and the NiAl-matrix. An optimisation of the composition of the chemical systems is at present still necessary, although significant improvements have been made in the first three project phases; Hu et al. (2005), Zhong et al. (2007).

The outer contour will be provided with laser-drilled fields of cooling holes and a TBC. The cooling hole distribution will vary over the blade surface depending on the temperature and pressure level as well as the flow field over the blade. With this concept, the temperatures inside the blade can be increased substantially, and the required cooling fluid decreased proportionally, compared to current materials.

All of the developments mentioned above serve to realise the vision of the SFB as depicted in Fig. 8.

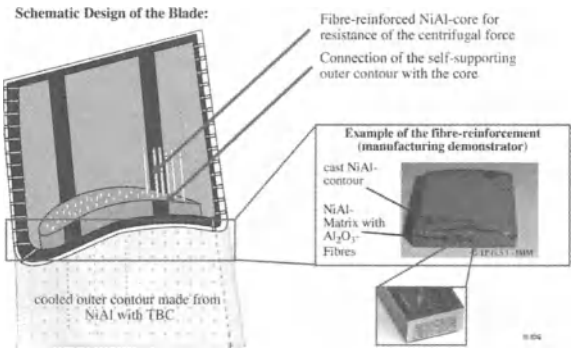

Fig. 8 Vision of a future gas turbine blade

The ReactionSlipFoamSintering(RSFS)-Process has been developed for the manufacturing of open porous structures for combustion chamber linings. By systematically investigating the variations in dispersant, solvents and expanding agent proportions as well as the sintering temperature, parameter combinations leading to a certain, well-defined porosity can be found. The RSFS-process leads to foams with large primary pores that are connected by smaller, secondary, pores. Computertomographic images show that cell walls form a coherent, interconnected structure, providing strength to the foam. The relatively continuous distribution of the primary pores can be seen clearly from Fig. 9. Providing both a numerical and experimental characterization of the manufactured foams is actively pursued within the SFB. Numerical models describing the permeability and pore distribution have been developed. These models can provide detailed information on the foam properties, including their heat conductivity and the pressure loss over the foam (Fig. 9), Laschet et al. (2008). Several test specimens for experiments on the heat transfer properties have been manufactured.

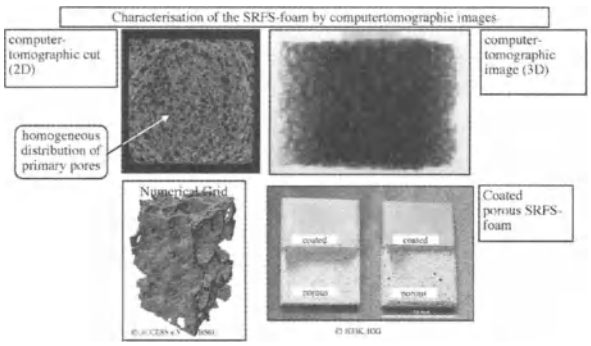

Fig. 9 Open-porous metallic foams developed by SFB 561

Laser welding the foams onto the structural material remains a challenge for the current phase of the project (Fig. 10).

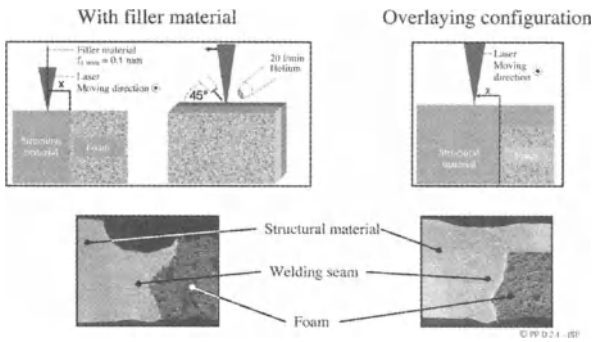

Fig. 10 Application of open porous structures in gas and steam turbines

The difficulties with manufacturing a weld that can withstand a continuous thermal load of 1000°C over a period of 10,000 operating hours are mainly due to the porous structure of the foam. This leads, depending on the pore distribution, to a locally different heat flux into the material; Bleck et al. (2007). Due to the thermal load, the walls of the caverns can melt, which can lead to extremely large cavities in the material. The minimal density of the foam that facilitates reasonable welds currently lies at 2.8 g/cm³.

It has been proven that the application of a TBC on the metallic foams is possible. The ZrO_2-TBC is deposited on an MCrAlY-bondcoat with Atmospheric Plasma Spraying (APS). The porous sublayer will provide a homogeneous distribution of the coolant before it is emitted through the opened TBC into the hot gas flow. The permeability of the closed thermal barrier coating will be ensured by drilling cooling holes with a diameter of 0.2 mm through the covering layers into the porous foam; Bobzin et al. (2006), Lugscheider et al. (2005), Walther et al. (2006). This will ultimately lead to full-coverage cooling of the part.

Steam Turbine Technology

The development of new 9-12% Cr steels pushed the maximum temperature of these steels to 620°C over the last decade, but a further increase in the maximum bearable temperature for these steels is not to be expected. For the steam turbine constructive solutions for mastering the live steam temperature of about 700°C and highest pressures have therefore to be found. This entails developing cooling techniques for the casing and the live steam pipes of the thermally highly loaded high and intermediate pressure turbines. This avoids the application of NiAl-alloys and enables a further use of ferritic steels. Cooling thermally highly loaded steam turbine components using grid-sheets structures with a through-flow is another focus of the SFB (Fig. 11). These cooling structures consist

of two sheets and one woven-wire mesh interlayer and facilitate using live steam at 300 bar and 690°C without the need to manufacture the casing from Nickel-base alloys. The woven-wire mesh boosts the turbulence in the coolant and therewith the heat transfer from the structure into the flow in the grid-sheets.

The grid-sheet structures are manufactured using capacitor impulse-welding. First, segments consisting of sheets and woven-wire meshes are joined. The connection between the wire-meshes and the sheets has to be of excellent quality, because this structure has to withstand the forces resulting from the prevailing pressure difference between cooling and live steam under an operating temperature of ca. 700°C as well as the different loads resulting from start-up, shut-down and load changes (Low-Cycle-Fatigue). In order to influence the heat transfer and the pressure losses in a controlled manner, graded structures are being manufactured during the final project phase (see Fig. 11); Dilthey (2005), Echsler et al. (2006).

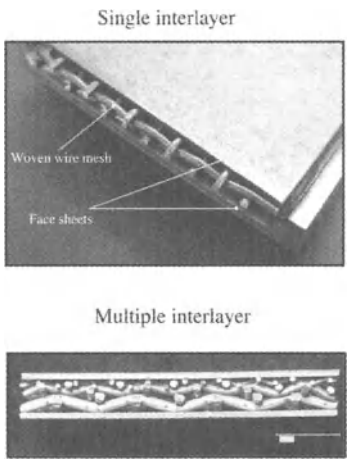

Fig. 11 Grid-sheets with single and multiple interlayer

Because of the extremely short welding time of the capacitor-discharge welding, the thermal load on the base material outside of the direct welding zone is relatively low. The mechanical and metallurgical characteristics of the material are therefore only minimally changed. A further advantage of this method is that a large number of welds can be made simultaneously. The size and the geometric complexity of the grid-sheets structures manufactured by capacitor impulse-welding is limited due to causes arising from production technology and practical considerations, though. The segments are joined by laser welding to ensure that sufficiently large grid sheets can be provided. The high intensity of the laser beam ensures high welding speeds, which means that only very small zones along the weld are influenced thermally. Therefore, the mechanical and corrosive characteristics of the materials are only slightly changed. Also, the thermal stresses remain low and the distortion due to welding is minimal. The complex three-dimensional geometry of the parts that are to be inserted into the turbine means that the weld can often only be made from one side of the grid-sheet. A welding procedure that enables welding the lower sheet through an increased gap in the upper sheet has been developed; Dilthey et al. (2004). Critical is a possible spot weld failure in the grid-sheets, which is therefore investigated with thermographic vigorously within the SFB (Fig. 12).

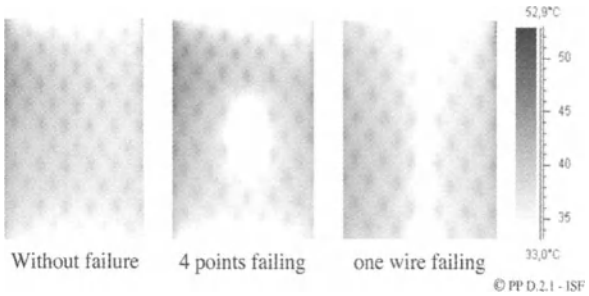

Fig. 12 Thermographic investigation of grid-sheets

The welded structures are then adjusted to the contour of the structure using rolling and deep-drawing. The spring-back of the grid-sheets has to be taken into account here, Kopp et al. (2005).

A further contribution to the goal of 65% efficiency of power plants lays with an improved water extraction with less losses in the low pressure steam turbines (Fig. 13). With the currently applied water extraction, using slots, a considerable amount of steam is extracted with the water from the turbine. By applying the water extraction method proposed by the SFB, which entails porous materials covering larges areas of the steam turbine casing, the water extraction can be controlled more precisely, e.g. by grading the materials. Above all, the aerodynamic losses will be reduced due to the smoother surface of the porous materials. These measures will not only increase the efficiency of the turbines but also their operating time.

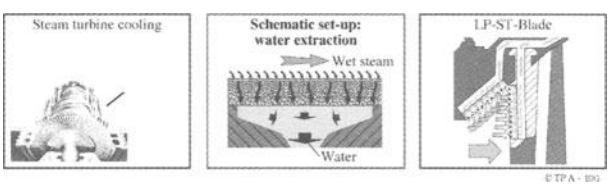

Fig. 13 Water extraction with open porous foams in steam turbines

The foams for the water extraction in steam turbines are manufactured using the same ReactionSlipFoamSintering

(RSFS)-Process as those applied for gas turbine cooling. The challenges for joining these foams to the structural material are therefore the same. Because the thermal load on these foams is negligible, no thermal barrier coating is applied, but this increases the requirements on the surface quality of the weld.

Project Coordination

The phases in the development of the technologies in a joint research project of this size have to be projected in advance (Fig. 14). In the first phase, the theoretical possibility of manufacturing open-porous structures for power plant applications could be proven. In the second phase, the manufacturing of these structures was started, with an emphasis on real component geometries. The third phase focused on the next step towards application, i.e. more complex models for a more detailed depiction of the porous structures in numerical simulations, capable of making more precise predictions on the cooling effectiveness of the structures. The experimental investigation of first test specimens for the novel cooling techniques was started and demonstrator parts were manufactured. The current fourth phase will see the manufacturing and testing of graded structures. This testing will happen under or close to real engine conditions.

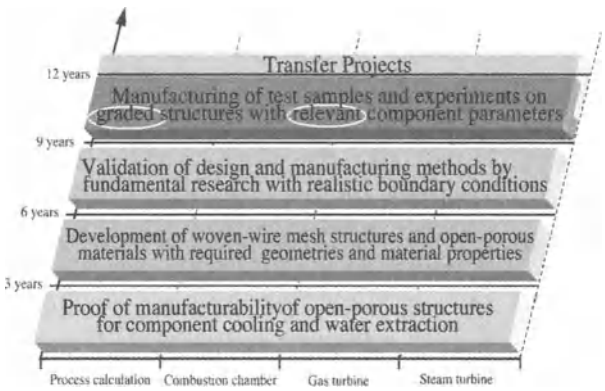

Fig. 14 The "Road Map" of SFB 561

The developments on both the gas and steam turbine processes within the power plant have to be tuned optimally onto each other. In order to achieve this, the coordinating project also performs stationary and transient process calculations, Bohn et al. (2008), which give direct feedback to all project partners about the goals that have to be achieved. These goals are also discussed with several experienced counsellors from industry and the emphasis for further work can be specified on the basis of these analyses and discussions.

It is planned to start several transfer projects in which the results from the SFB will be shared with industrial partners during this phase as well.

The abovementioned developments concentrate on fossil-fuel fired power plants, as these will remain the backbone of the power supply in the foreseeable future. At the same time, the recent surge in oil prices is adding to the urgent need for developing alternative sources of energy. These high price levels increase the likelihood of a reduced dependency on oil by investments in new energy technologies from renewable sources.

The currently available renewable technologies range from solar power, wind power and hydroelectricity to biomass and biofuels for transportation. A promising option is the use of hybrid power plants, in which conventional technologies are combined with renewables like solar or wind energy. This would increase the overall efficiency of the plant (e.g. by using solar energy in the gas/steam-turbine cycle) and make the power output of the renewables more reliable; Bohn (2007).

4 Summary and Conclusion

The pressing issue of anthropogenic CO_2-emissions has induced governments all over the world to impose legislation regarding emission targets. New technologies have to be developed to meet the future demands, especuially since all of the three existing CO_2-capturing technologies share the problem that their costs will be high. They will also deplete the resources much earlier than technologies without sequestration because of their relatively low efficiency. Therefore an efficiency increase will be necessary before sequestration becomes economically viable.

By the founding of Collaborative Research Centre 561 "Thermally Highly Loaded, Porous and Cooled Multi-Layer Systems for Combined-Cycle Power Plants" at RWTH Aachen University, the basis was lead for the development of new technologies with which a total efficiency of 65% in combined cycle power plants can be reached in the year 2025. An efficiency potential of 12% and a CO_2-reduction potential of 15% are possible by the application of the results from the SFB.

All technologies, including renewables, have to be incorporated in future power generation to ensure long-term economical and efficient power production.

Acknowledgements

The author gratefully acknowledge the financial support of the Deutsche Forschungsgemeinschaft (DFG) within Collaborative Research Centre 561 "Thermally Highly Loaded, Porous and Cooled Multi-Layer Systems for Combined-Cycle Power Plants".

References

www.co2sink.org viewed at 01/06/08

http://www.eia.doe.gov/oiaf/1605/ggccebro/chapter1.html viewed at 01/06/08

http://usinfo.state.gov/gi/Archive/2004/Dec/15-595073.html viewed at 01/06/08

Bleck, W.; Dilthey, U.; Angel, S.; Piontek, D.; Longerich, S.; Harms, A., 2007, "Joining Strategies for Open Porous Metallic Foams on Base of Iron and Nickel Materials", *Advanced Engineering Materials*, Vol. **9**, No. **8**

Bobzin, K.; Lugscheider, E.; Bagcivan, N.: "Thermal cycling behaviour of lanthanum zirconate as EB-PVD thermal barrier coating", *Advanced Engineering Materials* (2006), Vol. **7**, No. **3**, pp. 142 – 152

Bohn, D., 2007, "Anforderungen an die Kraftwerkstechnik bei Hybridkraftwerken", E-World 2007, Essen, February 06-08

Bohn, D.; Krewinkel, R.; Rakut, C., 2008, "Proposing a Novel Approach in Power Plant Design: the Combined Calculation of Power Plant Processes and Component Stress", Paper No. 2008-20008, *ISROMAC-12,* Honolulu, Hawaii, U.S.A., February 17 – 22

Dilthey, U.; Ohse, P.; Piontek, D., 2004, "Welding of hollow structures made of high-temperature materials", *Schweißen und Schneiden*, Vol. **56**, No. **1**, pp. 11 – 15

Dilthey U.; El-Magd E.; Brandenburg A.; Piontek D.; Gebhard J., 2005, "Lasergeschweißte Hohlraumstrukturen aus dem martensitischen Werkstoff P92 als neuartiges Kühlkonzept für hochbelastete Teile der Dampfturbine", *Proceedings of the 28th Vortragsveranstaltung der Forschungsvereinigung Warmfeste Stähle (FVW)*, Düsseldorf

Echsler, H.; Shemet, V.; Quadakkers, W.J.; Schütze, M.; Singheiser, L., 2006, "Cracking in and Around the Thermally Grown Oxide in Thermal Barrier Coatings: A Comparison of Isothermal and Cyclic Oxidation", *Journal of Materials Science*, Vol. **41**, No. **4**, pp. 1047 – 1058

Ewers, J., 2007, "Die Clean Coal Power Strategie von RWE Power und die Projekte zum CO2-freien Kraftwerk", presentation in the framework of the lecture series *Wege in eine CO2-reduzierte Kraftwerkstechnologie für das 21. Jahrhundert*, RWTH Aachen, January 10

Hajas, D.E.; Krysta, S.; Schneider, J.M., 2006 "Effects of a BN Interlayer on the Tensile Strength of NiAl Coated Sapphire Fibers", *Scripta Materialia*, Vol. **55**, No. **3**, pp. 219 – 222

Hu, W.; Chen, H.; Zhong, Y.; Gottstein, G., 2005, "Interface Structure, Chemistry and Mechanical Properties of NiAl Composites Reinforced by Continuous Al_2O_3 Fibres", EUROMAT 2005, Prague, Czech Republic, September 5 – 8

Kopp, R.; Franzke, M.; Hohmeier, P.; van Santen, J., 2005, "Bending of Sandwich Structures with Usable Cavities for Active Cooling Applications in Steam Turbines", *Annals of the German Academic Society for Production Engineering*, Vol. **12**, No. **1**, pp. 71 – 76

Laschet, G.; Rex, S.; Bohn, D.; Krewinkel, R., 2007, „3-D Analysis of curved transpiration cooled plates and homogenization of their aerothermal properties", *ASME Journal of Turbomachinery*, October 2007, Vol. **129**, Issue **4**, pp. 791 – 799 (Revised version of GT2006-90377)

Laschet, G.; Kashko, T.; Angel, S.; Scheele, J.; Nickel, R.; Bobzin, K.; Bleck, W., 2008, "Microstructure based model for permeability predictions of open-cell metallic foams via homogenization", *Materials Science & Engineering A*, Vol. **472**, Issues **1 – 2**, pp. 214 – 226

Lugscheider, E.; Bobzin, K.; Maes, M.; Lackner, K.; Poprawe, R.; Kreutz, E.W.; Willach, J., 2005, "Laser Drilled Microholes in Zirconia Coated Surfaces Using Two Variants to Implement the Effusion Cooling of First Stage Turbine Blades", *Advanced Engineering Materials*, Vol. **7**, No. **3**, pp. 145 – 152

Poprawe, R; Kelbassa, I.; Walther, K.; Witty, M.; Bohn, D.; Krewinkel, R., 2008, "Optimising and manufacturing a laser-drilled cooling hole geometry for effusion-cooled multi-layer plates", Paper No. 2008-20091, *ISROMAC-12*, Honolulu, Hawaii, U.S.A., February 17 – 22

Walther, K.; Brajdic, M.; Kreutz, E.W., 2006, "Enhanced Processing Speed of Laser Drilling of Stainless Steel by Spatially and Temporally Superposed Pulsed Nd:YAG Laser Radiation", *Int. Journal of Adv. Man. Tech.*, DOI 10.1007/s00170-006-0768-z

Zhong, Y.; Hajas, D.; Hu, W.; Chen, H.; Gottstein, G., 2007, "Microstructure and mechanical properties of continuous Al_2O_3 fiber reinforced $Ni_{45}Al_{45}Cr_{7,5}Ta_{2,5}$ alloy (IP75) matrix composites", *Philosphical Magazine*, Vol. **87**, Issue **7**, pp. 1019 – 1032

The 4th International Symposium on Fluid Machinery and Fluid Engineering
November 24-27, 2008, Beijing, China
NO. 4ISFMFE-IL10

Numerical Analysis of Impeller-Volute Tongue Interaction and Unsteady Fluid Flow in a Centrifugal Pump

K.W Cheah[*1], T.S. Lee[1], S.H Winoto[1] and Z.M Zhao[2]

[*1] Department of Mechanical Engineering, Block EA, 07-08
National University of Singapore,
9 Engineering Drive 1, Singapore 117576
Tel: +65-6516-2212/ Fax: +65-6779-1459
E-mail: g0500401@nus.edu.sg (*Corresponding Author)

[2] 48A, Changi South Street 1, Singapore 486114
Tel:+65-6545-7735/ Fax:+65-6545-3411

Abstract Unsteady flow analysis has been carried out within a centrifugal pump with six twisted blade impeller to study the impeller/volute tongue interaction. The numerical analysis is done by solving the three-dimensional RANS codes with standard k-ε two-equations turbulence model. The wall regions are modeled with a scalable log-law wall function. The numerical simulation is carried out with multiple frames of reference (MFR). Dissimilar tetrahedral mesh for the impeller/volute casing has been used and is connected via Transient Rotor Stator interface. Current investigation will study the unsteady fluid flow interaction between impeller/volute tongue and the casing at various operating point. The results of the numerical analysis are used to predict and visualize the unsteady flow interaction between the impeller and volute casing. From the numerical analysis, it shows that a recirculation zone near to suction-front shroud side just after the leading edge even at design point due to non-tangential inflow condition. The flow within the impeller passage is very smooth and congruent with the curvature of the blade in stream-wise direction. When the flow is discharged into volute casing circumferentially from the impeller exit, the high velocity flow is severely distorted and formed a spiral flow pattern within the volute casing. The axisymmetrical, dual core vortex flow developed inside the volute near the tongue will slowly evolved into non-axisymmetrical, non-equal dual core vortex flow near volute exit in angular flow direction. Near volute tongue region, the impeller/volute tongue strong interaction is observed based on the periodically fluctuating pressure at outlet. The uneven pressure distribution is observed at impeller outlet circumferential position. The existing analysis results showed that the pressure fluctuation periodically is due to the position of impeller blade relative to tongue and the flow field within the volute casing is always unsteady and turbulent.

Keywords unsteady flow, impeller, volute tongue, pressure fluctuation

Nomenclature

d	impeller diameter, m
g	gravity constant, 9.81 m/s^2
H	head, m
N	pump speed, rad/s
P.S	pressure side
Q	volume flow rate, m^3/s
R	impeller radius, m
S.S	suction side
V_r	radial velocity, m/s
V_c	circumferential velocity, m/s
U_2	blade tip velocity, m/s
θ	Theta, degree
ψ	Head coefficient, gH/N^{2}d^2
ϕ	Flow Coefficient, Q/Nd^3

1 Introduction

The flow field inside a centrifugal pump is strongly three dimensional with recirculation flows at inlet and exit, flow separation, cavitations, and so on. In addition, the geometry of the impeller is complex and rotating with respect to the volute casing. Strong interactions between the impeller and volute tongue also contributed to the unsteadiness of the flow field within the volute casing. The distorted flow structures from impeller into volute casing could further developed as swirling flow and dissipating much of the kinetic energy. Pump research for the past are mainly focus on the steady flow, either by experimental or numerical approaches, due to the inherent difficulties of setting up the test rig or numerical model. Much effort has been spent on study the time averaged or phased average steady flow. These quantities are useful to understand the pump performance. The effect and understanding of the unsteadiness flow field due to strong impeller and volute tongue interaction, are of great interest for designing high efficiency pumps.

Dong et al (1992) and Chu et al (1995) used PIV measuring the velocity within the volute casing of a centrifugal pump at different impeller blade orientations, on and off-design conditions to study effect of impeller/ volute tongue interaction. They found that jet-wake structures and pulsating flow near impeller exit. The orientation of the blades could affect the leakage and the pressure distribution. A vortex train generated as a result of non-uniform outfluxes from the impeller. Kaupert (1999) made an experimental investigation within a high specific speed centrifugal pump impeller and found that pressure fluctuations from the impeller volute interaction grew as the volume flux became further removed from the best efficiency point and as the trailing edge of the impeller approached. These fluctuations reached 35% of the pump head in deep part load. The upstream influence of the volute steady pressure field dominates the unsteady pressure field within the impeller at all off design load points.

Parrondo-Gayo et al (2002) investigated the pressure fluctuations at the blade passage frequency in the volute of a centrifugal pump and found that the pressure fluctuations registered around the volute is strongly dependent on both angular position and flow-rate; maximum values corresponded to the tongue region for off-design condition. Wang & Tsukamoto (2003) has made the experiment and numerical investigation of unsteady flow in a diffuser pump and off-design point and showed that the impeller blade passing frequency and its higher harmonics are always dominant in the pressure downstream of the impeller for the whole range because of the rotor-stator interaction. They further classified the unsteady flow range based on the volume flow rate. The pump will be stable or unstable depends on the separating flow and stall occurs at both impeller and diffuser.

However, it seems difficult to fully understand the unsteady flow phenomenon generated by impeller and volute tongue interactions, not to mention at off-design point. In recent years, with the advancement of computational power coupled with robust and accurate computational fluid dynamics (CFD) codes, CFD now is feasible and widely used to investigate the unsteady impeller/volute casing interaction. Gonzalez et al (2002) validated the capability of CFD in capturing the dynamics and unsteady flow effects inside a centrifugal pump. The amplitude of the fluctuating pressure field at blade passing frequency is successfully captured for a wide range of flow rates. Similarly, Majidi (2005) and Asuaje et al (2006), simulated the unsteady flow in centrifugal pump and obtained a satisfactory agreement with well established theoretical and experimental data.

The centrifugal pump impeller considered in this study is shrouded and has six backswept blades. The leading edge of blade is twisted and straight at trailing edge. The flow from impeller is discharged into a vaneless volute casing. Table 1 shows the main dimensions and characteristic of the investigated pump configuration.

Table 1 Basic pump dimensions

Impeller:		
Z	= 6	blade number
α_{shroud}	= 40^0	blade inlet angle at shroud
α_{hub}	= 35^0	blade inlet angle at hub
α_2	= 23^0	blade outlet angle
d_1	= 202 mm	impeller inlet diameter
d_2	= 356 mm	impeller outlet diameter
b_2	= 46.8 mm	impeller outlet width
Volute Casing:		
d_3	= 374 mm	mean circle diameter
R_t	= 183.2 mm	radial position of tongue
Design point:		
ω	= 1450 rpm	Design speed
Q	= 600 m^3/hr	Design volume flow rate
H	= 30 m	Design pump head

1.1 Numerical techniques

With the advancement of computational power coupled with robust and accurate computational fluid dynamics (CFD) codes, CFD is widely used to investigate the unsteady impeller/volute casing interaction. For present study, a commercially available CFX 11.0 is used to model and simulate the 3D and unsteady turbulent flow through the centrifugal pump. The standard k-ε two-

equation turbulence model is used and the walls are modeled using a scalable wall function. Validation of this code can be found from the work done by Asujae et al (2006) and Feng et al (2007) that have used it in pump applications.

Figure 1 shows the pump and impeller meshes. The computation domains at the inlet of intake section and at the outlet of volute section are extended to allow recirculation. The extension length is equal to two times of intake inlet and volute outlet diameter, which is same as the actual pressure measurement location.

Current numerical computation is carried out in two parts, quasi-steady and unsteady. For quasi-steady simulation, it is carried out with a multiple frames of reference (MFR) approach in which the impeller flow field is with reference to a rotating frame whereby the volute casing and intake section refer to a stationary frame. The tetrahedral elements of intake section, impeller and volute are generated separately, so the dissimilar meshes are connected by means of a Frozen-Rotor interface. The quasi steady numerical computation is carried out with the following boundary conditions imposed: At the inlet of the intake section the total pressure, the turbulence intensity and a reference pressure are specified. The absolute velocity vector at the inlet is defined in such a way that is perpendicular to the inlet mesh surface. Turbulent intensity was specified to be 5%. Mass flow rate is prescribed at volute outlet. Wide range of mass flow rate is specified in order to numerically predict the pump characteristics. All the other variables are free to float. Solid walls of the impeller blades, hub and shroud in rotating frame and the walls of the volute casing and intake are in stationary frames and modeled using a no-slip boundary condition. The numerical computation is considered converged when the maximum residual 10E-4 is reached.

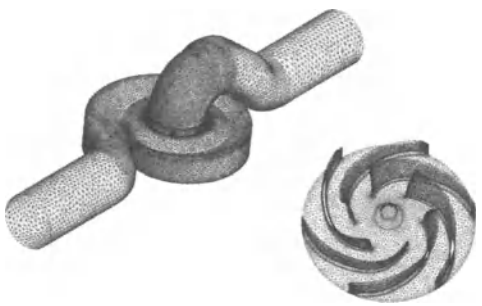

Fig. 1 Impeller and pump meshes

The quasi-steady result is used to initialize the unsteady calculation. The boundary conditions are the same as the quasi steady state calculation. The time step of the unsteady calculation has been set to 3.4483E-04 seconds. This time step size is corresponding to 3 degree per time step for the rotational speed of the impeller of 1450 rpm. One complete impeller revolution is performed after 120 time steps. The total number of time step 1320, which is equal to 11 revolutions of the impeller and the total time is 0.45517s. The maximum number of iterations in each time step has been set to 10. This number of iterations is enough to reduce the maximum residuals by three orders of magnitude. For the unsteady calculation, the dissimilar mesh at the intake, impeller and volute interface are connected by means of Transient Rotor/Stator interface.

Figure 2 shows the plan-view of the pump and the mid-plane is located at z/b = 0.5. Eight cross-sectional planes are cut in according to the various angular locations in volute casing for later discussion. With Plane I at 0° is closest to volute tongue and the following Plane II to Plane VIII with an increment of 45° in anti-clockwise angular direction up to 315°. Plane IX is 350 mm away from Plane III-VII. The impeller passages are labeled from 1 to 6 in anti-clockwise direction with Passage 1 closest to the volute tongue. Similarly, the impeller blades are labeled as Blade 1 to 6 in anti-clockwise direction with Blade 1 is between Passage 1 and 6; Blade 2 is between Passage 1 and 2, and so on.

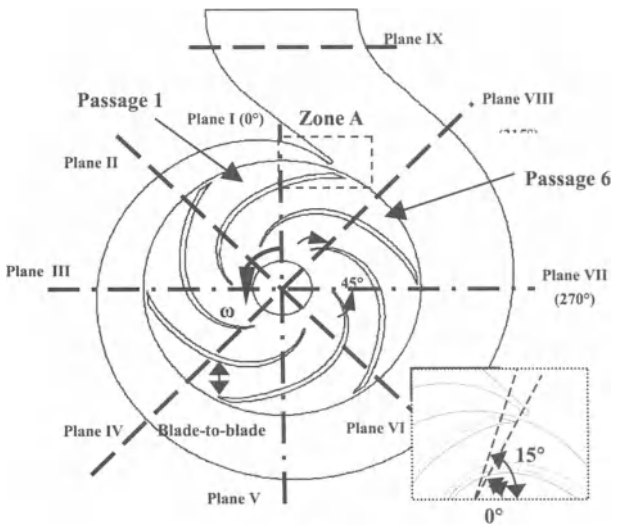

Fig. 2 Plan view of the centrifugal pump

1.2 Results and discussions

Prior to any discussion of the unsteady numerical results, a comparison of the quasi-steady numerical and experimental characteristics curve is presented. The numerical global characteristics curve obtained is based on the quasi-steady computation. The numerical predicted head coefficient is compared well and in good agreement with the experimental result as shown in Fig. 3. At the design volume flow rate, Q_{design} of 600 m^3/hr, or equal to flow coefficient ϕ of 0.024, the computed head coefficient

is only 3.8% less than the experimental result. The computation of numerical result stopped at 60% of the Q_{design} is due to convergence difficulty that caused by large recirculation within the impeller passage and volute casing. At lower flow rate, the difference between the numerical result and experimental result is slightly larger and it is believed that the numerical computation is over predicting losses incurred by the highly turbulent and recirculation flow inside the volute.

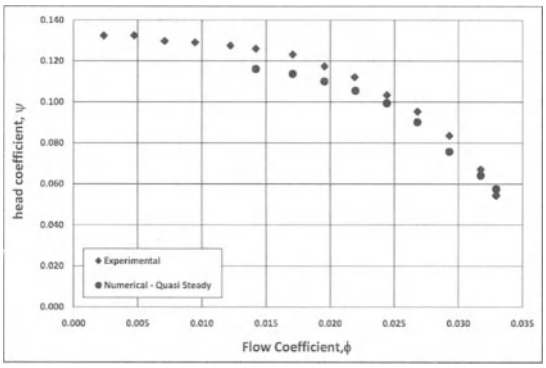

Fig. 3 Numerical predicted and experimental H-Q curve

Author investigated the number of revolutions required in order for the unsteady computation to reach a stable result. The quasi-steady result is used to initialize the unsteady computation and the global pump head is used to judge convergence of result. From Fig. 4, it can be seen that the head coefficient fluctuate as the unsteady computation continued from the quasi-steady solution. As the number of impeller revolutions increases, the global head coefficient reached a steady value. It can be said that at least 8 revolutions is needed to achieve a steady-state solution. For present study, the unsteady solution is obtained after 11 impeller revolutions.

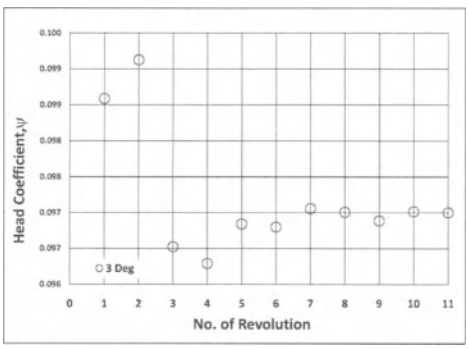

Fig. 4 Unsteady head coefficient initiated by steady state result

1.3 Velocity Vector

The impeller passage flow at design point is very smooth and well guided except at the leading edge. Fig. 5 is a cross-sectional plane cut at b/z=0.5. As the flow entering the impeller eye, it is diverted into the blade-to-blade passage. Due to the unsteady effect developed upstream, the flow entering the passage is no longer tangential to the leading edge of impeller blade. Those so called shockless velocity to impeller passage is no longer guaranteed. Flow separation can be observed at leading edges. Fig. 5 shows the leading edge velocity vector field with separation and inflow incident angle that is non-tangent to the blade leading edge. In actual case, pre-swirl should have developed at the impeller inlet and depends on the volume flow rate, the difference between the entry angle of the fluid and blade inlet angle can reduce the shock losses at the inlet. This leading edge separation could lead to energy loss in the pump and could further influence the flow field in impeller passage in stream wise direction.

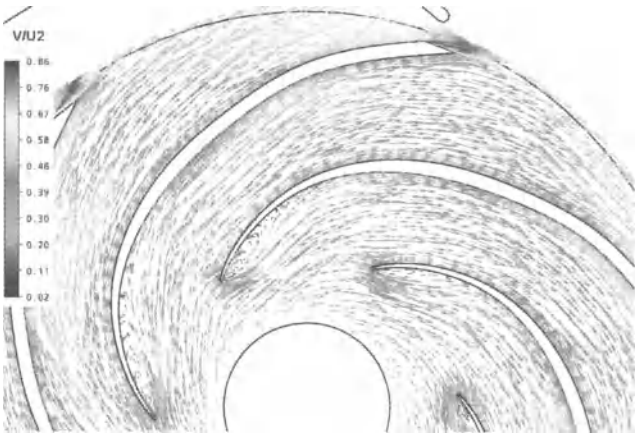

Fig. 5 Velocity vector at impeller mid plane

1.4 Impeller / volute tongue interaction

Figure 6 shows the periodic fluctuating pump delivery head plot against the relative angular position of an impeller blade to the volute tongue. For time step size 3 degree

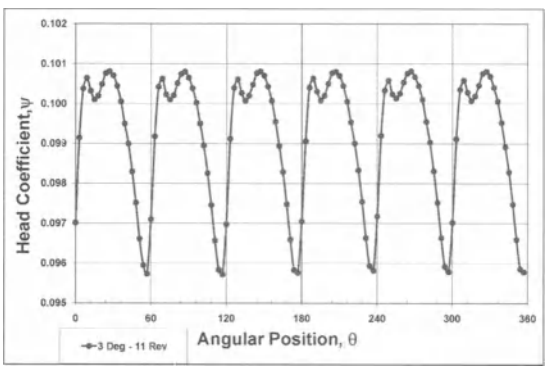

Fig. 6 Pressure fluctuation due to impeller and volute tongue interaction

blade rotation per time step, the global head fluctuation that rises from lowest point actually is not smooth and shows a dip and hump before reaching the peak value. Based on this finding, it suggests that there is strong impeller and volute tongue interaction. The peak of the delivery head represents half a pitch of blade-to-blade rotation. The lowest point of the pump delivery head represents full pitch blade-to-blade rotation where the blade is aligned with volute tongue at 0°. The higher head coefficient obtained by unsteady computation method is because the quasi-steady method only considered the average flux at the rotating and stationary components interfaces, unlike the unsteady computation method update the flow fields for very times step between the rotating and stationary components interfaces.

The flow discharged from the impeller can resolved into radial and circumferential components. In order to understand the strong impeller and volute tongue interactions, the radial velocity, V_r is plot against the impeller blade relative position towards the tongue. The radial velocity V_r is extracted at 4 different locations, $1.00R_2$, $1.02R_2$, $1.04R_2$ and $1.06R_2$.

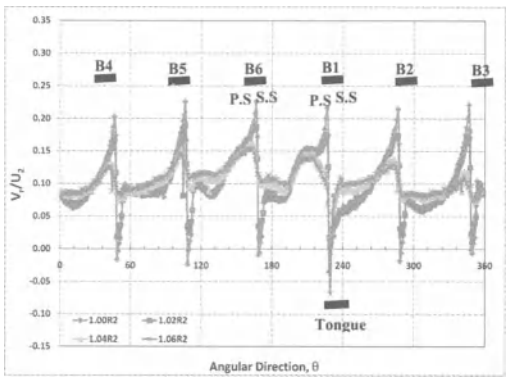

Fig. 7 Radial Velocity of relative position of blade trailing edge towards volute tongue, 0°

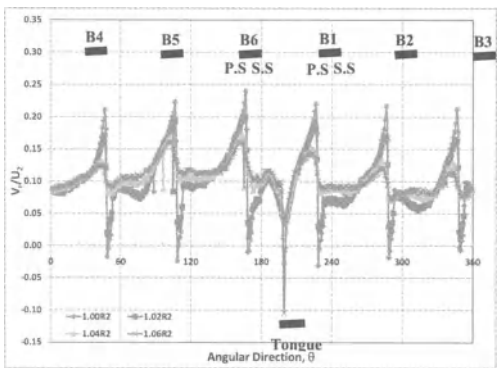

Fig. 8 Radial Velocity of relative position of blade trailing edge towards volute tongue, 30°

From Figs. 7 and 8, it can be seen clearly that how the radial velocity changes according to the relative position of blade trailing edge against the volute tongue. When the blade trailing edge is matching the volute tongue, the out fluxes from impeller can be considered very uniformly distributed. The radial velocity, V_r increases from suction side towards pressure side. When impeller rotated 30^0, where the tongue is located between Blade 1 and Blade 6, there is a reversal of radial velocity. This is because the radial velocity is discharged from impeller exit, approaching the volute and reversed because of the confined space near volute tongue. The reversal of the radial velocity is matching the two bumps in Fig. 5. This is in strong agreement that radial velocity reversal is coupled with the pressure fluctuation.

As for the instantaneous static pressure, it is fluctuating circumferentially. Fig. 9 shows the temporal and spatial static pressure distribution near volute tongue. When the tongue is at 0^0 relative to the volute tongue, it can be seen that the isobar contours within the blade-to-blade overlap region are parallel and perpendicular to the blade pressure and suction sides. However, after the blade-to-blade overlap region, or so called the "throat" area, the isobar lines no longer smooth and wavy. The volute tongue has a localized high pressure envelop is due to the stagnation pressure point. As the impeller rotating in anti-clockwise direction, the wavy isobar lines wiggle around the impeller periphery line and these localized pressure fluctuation is affecting the global pump delivery head as well.

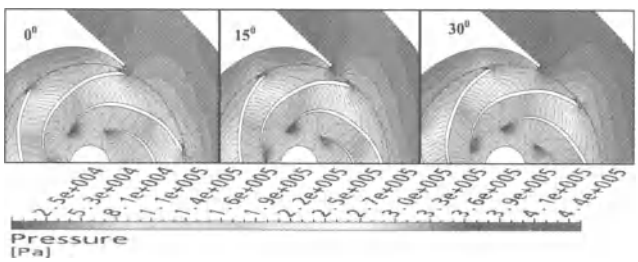

Fig. 9 Static pressure distribution near volute tongue

When the flow within the impeller discharges into the volute casing, Fig. 10, a strong recirculation flow developed. Near volute tongue (Plane I), dual small vortex cores observed at the upper and lower corners. The small gap between the impeller exit and the volute wall causes the flow discharging from impeller exit acting as a high speed impinging jet on the volute wall and lower and upper round corners of the volute wall are inducing the vortex flow at the corner. Axisymmetric vortex flow advancing in angular direction at Plane II, III, IV and V formed a spiraling flow even when distance from the impeller exit to volute wall is increasing. However, the axisymmetric

vortex flow becomes asymmetric when the spiraling flow approaches volute outlet. The formation of the asymmetric vortex flow at the lower corner of volute and impeller exit/shroud edge can be explained by the jet/wake flow pattern developed inside the impeller passage. The wake has a low velocity region near shroud/suction corner and the jet flow pattern is a high speed region near huh/ pressure side. Hence the flow exiting from impeller is experiencing a shearing effect due to the distorted velocity profile and a counter rotating vortex formed. The single and double vortical flow structure inside the volute casing has been reported by many researchers. Based on the vortices pattern formed inside the volute, the secondary flow inside the volute is sensitive to the volute geometry and the jet wake structure from the impeller passage. The relative gaps between the shroud and volute casing, hub and volute casing will have influence on the secondary flow formation as well in stream wise direction. This is because there will be always a back flow (leakage) from the gaps between hub, shroud and volute casing.

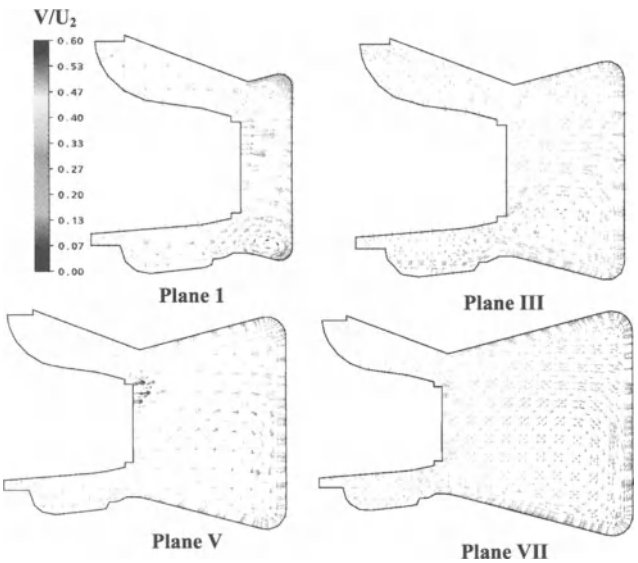

Fig. 10 Unsteady spiraling flow in volute

2 Conclusions

Current numerical computation has studied the complex and unsteady internal flow field of a centrifugal pump. At design point, the internal flow or velocity vector is very smooth along the curvature along the blades. However, flow separation developed at the leading edge due to non-tangential inflow conditions. The recirculation flow at the shroud/suction corner is considered as a pre-mature wake flow development.

The out flow from impeller shows a strong impeller and volute tongue interaction. When the blade trailing edge is aligned with the volute tongue, the radial velocity is very uniform and increases from suction of pressure side. However, when the blade trailing edge and volute tongue is mismatched, then the radial velocity reversal occurs.

The results of existing analysis showed that the periodically pressure fluctuation is due to the position of impeller blade relative to tongue. The pressure rises to maximum when the volute tongue is located at between blade-to-blade and falls to minimum when the blade trailing edge is aligned with the volute tongue.

References

Asuaje, M., Bakir, F., Kergourlay, G., Noguera, and Rey, R., 2006, "Three-dimensional quasi-unsteady flow simulation in a centrifugal pump: comparison with experimental results", *Proc. IMechE Vol. 200, Part A: J. Power and Energy*, pp. 230 – 256

Chu S., Dong R., Katz J., 1995, "Relationship Between Unsteady Flow, Pressure Fluctuations, and Noise in a Centrifugal Pump; Part B: Effects of Blade-Tongue Interactions", *ASME J. of Fluids Engineering*, Vol. 177, pp. 30 – 35

Dong R., Chu S., Katz J., 1992, "Quantitative Visualization of the Flow Within the Volute of a Centrifugal Pump. Part B: Results and Analysis", *ASME J. of Fluids Engineering*, Vol. 114, pp. 396 – 403

Feng, J.J., Benra, F.K. and Dohmen, H.J., 2007, "Numerical investigation on pressure fluctuations for different configurations of vaned diffuser pumps", *International J. of Rotating Machinery*, Vol. 2007, Article ID 34572

González, J., Fernádez, J, Blanco, E. and Santolaria, C., 2002, "Numerical simulation of the dynamic effects due to impeller volute interaction in a centrifugal pump", *ASME J. of Fluids Engineering*, Vol 124, pp 348 – 355

Parrondo-Gayo, J.L., González-Pérez, J., and Fernández-Francos, J., 2002, "The effect of the operating point on the pressure fluctuations at the blade passage frequency in the volute of a centrifugal pump", *ASME J. of Fluids Engineering*, Vol. 124, pp. 784 – 790

Kaupert, K.A. and Staubli, T., 1999, "The unsteady pressure field in a high specific speed centrifugal pump impeller part i: influence of the volute", *ASME J. of Fluids Engineering*, Vol. 121, pp. 621 – 626

Majidi, K., 2005, "Numerical study of unsteady flow in a centrifugal pump", *ASME J. of Turbomachinery*, Vol. 127, pp. 363 – 371

Wang, H. and Tsukamoto, H., 2003, "Experimental and numerical study of unsteady flow in a diffuser pump at off-design conditions", *ASME J. of Fluids Engineering*, Vol. 125, pp. 767 – 778

The 4th International Symposium on Fluid Machinery and Fluid Engineering
November 24-27, 2008, Beijing, China
NO. 4ISFMFE-IL13

A Procedure for the Unsteady Characterization of Turbochargers in Reciprocating Internal Combustion Engines

A. Torregrosa[1], J. Galindo[1], J.R. Serrano*[1] and A. Tiseira[1]

*[1] CMT-Motores Térmicos, Universidad Politécnica de Valencia
Camino de Vera s/n, Valencia, 46010, Spain
Tel: +34-96-387-9675 / Fax: +34-96-387-7659
E-mail: jrserrano@mot.upv.es

Abstract In actual scenario of turbocharged automotive engines a precise knowledge of unsteady effects on turbocharger performance, such as pulsating flow influence, is needed. The paper exposes several methodologies to characterize unsteady phenomena in both compressor and turbine of the turbocharger. The experimental work goes along with compressor and turbine models that account for the unsteady effects. These models, implemented in a 1D gas-dynamic code, become a powerful tool in turbocharging system development. A methodology mixing calculation and experiments is presented that allows for measuring and modeling the pulsating effects in turbocharger performance at close to engines conditions and calculating the average turbine isentropic efficiency, under pulsating flow.

The combination of experimental and modeling work gives a good description of all the relevant unsteady processes involved in current diesel engine turbochargers. Some selected results are presented and discussed in the paper.

Keywords reciprocating internal combustion engine, turbocharging, pulsating flow, radial compressor, radial turbine

Nomenclature

AFT	Angle fixed turbine of variable geometry
A_i	Incident Pulse Amplitude
A_r	Reflected Pulse Amplitude
A_t	Transmitted Pulse Amplitude
C_d	Discharge coefficient
fa	Factor of Amplitude
FGT	Fixed Geometry Turbine
K	Pressure loss coefficient
$k_$	Power Ratio coefficient
MFT	Mixed Flow Turbine
n	Polytrophic exponent
p	Pressure
PF	Pulses Frequency
T	Temperature
TCS	Turbocharger Speed (rpm)
u	Flow speed
VGT	Variable Geometry Turbine
ρ	Density

1 Introduction

Diesel engines in automotive application have undergone an important evolution in the two last decades. In this period, direct injection and variable geometry turbocharger technologies have spread to all engine displacements and all segments of the market. Simultaneously a huge reduction of exhaust emissions has been achieved.

In the nineties the introduction of flexible high pressure direct injection systems has been the key-factor for the improvement of diesel engines. In the last years engine developers are carrying out further optimization that includes split injection and improvement of intake and exhaust lines.

Downsizing is a trend in engine development that allows for better efficiency and lower emissions based on the increase of power output in reduced displacement engines. In order to achieve this high output it is necessary to increase boosting pressure. In the last times there is the feeling that the improvement of the diesel engine is attaining a phase where no further improvement is expected unless

a breakthrough in the engine air management becomes possible. Nowadays, new turbocharging technologies are been evaluated by engine developers such as variable geometry compressors, sequentially turbocharged engines or two-stage compressed engines 0. This downsizing trend also applies to gasoline engines where turbocharging is becoming necessary to reach high efficiency targets.

In the authors' research institution, CMT-Motores Térmicos at the Universidad Politécnica de Valencia, modeling and experimental methodologies have been developed for the analysis of the flow phenomena in turbochargers. In this paper these methodologies are depicted focusing in the interesting unsteady phenomena that are becoming more and more relevant.

2 Experimental and Modelling Tools

The experience shows that the best strategy to do research and development in internal combustion engine is to combine experimental tests with accurate modeling work. Other research strategy in the engine is the use of facilities where parts of the engine are tested separately in a more controlled situation. This is why the authors foster the use of facilities such as the turbochargers test bench 0. However, it is important to reproduce in these rigs the relevant phenomena that are present in engine operation. Two examples, it is known that steady turbine efficiency is far from the actual pulsating flow turbine. Also, it is known that the surge limit measured in gas-stands can be very different to that measured on engine. Therefore, it is important to account for these unsteady effects when the turbocharger is characterized in a turbo test bench.

2.1 Engine Test Bench

The engine test bench is the experimental tool to assess all the engine development improvements carried out in the design of the different parts of the engine. However, engine test bench is not always the best environment to analyse certain phenomena. Talking about turbochargers, it is not easy to measure accurately compressor and turbine variables. Besides, engine test facilities are expensive, e.g. dynamic brakes are needed to measure transient response of the engine.

On the positive side, engine tests include all the involved phenomena and the bench can be modified to ease the task of measuring. The paper shows an example of the use of a modified engine test bench. More examples can be found in 0. In order to measure actual pressure wave transmission and reflection in compressors and turbines, a method that decomposes incident and reflected pressure waves is applied 0.

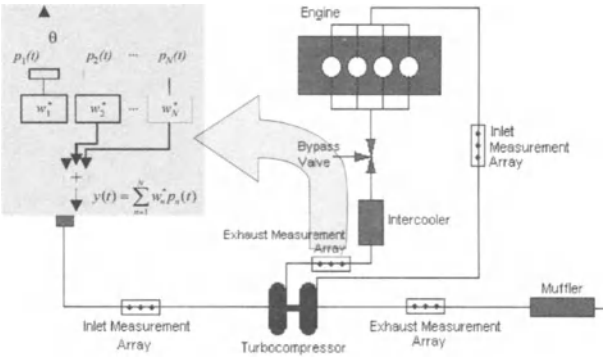

Fig. 1 Measurement configuration

The turbocharger testing in unsteady flow was performed in a four-cylinder Diesel engine with 1.6 L. of displacement, mounted on an asynchronous brake regulated test bench. The main difference between this rig and others reported in the literature 00 is that it is a device capable of closely reproducing, with real exhaust gas mass flow, the flow conditions found at the turbine and compressor inlet in real engine conditions. Figure 1 shows a schematic of the test rig and pressure transducer array positions.

Four turbochargers of different sizes and with different turbine technologies were tested: Fixed Geometry Turbine (FGT), Variable Geometry Turbine (VGT), Mixed Flow Turbine (MFT) and Angle Fixed Turbine (AFT). Details about the turbochargers can be found in 0.

An example of the turbocharger charts is shown in Fig. 2 and Fig. 3 for the VGT case. Turbine and compressor charts have been measured with steady flow conditions in a different facility 0. Obviously, the testing range with the unsteady flow bench of Fig. 1 is much more limited than ad hoc benches, due to the only way of decoupling engine and turbocharger mass flow is the bypass valve.

The bold points in Fig. 2 charts are those tested with unsteady flow conditions in the rig shown in Fig. 1. The turbocharger operating points were tested at constant turbocharger speed. For each compressor corrected speed line, it was tried to keep the engine speed also constant, while the engine load was modified in order to obtain each tested point. Beam-forming techniques were used for wave decomposition 0. Figure 1 shows also a scheme of how the information recorded by the pressure transducer arrays is used for feeding the beam-former software. Other variables measured during the tests were: average gas pressure, flow temperature, mass flow rate, turbo-compressor rotation speed and the usual engine performance test parameters. Details about the instrumentation and measurement procedure can be found in 0.

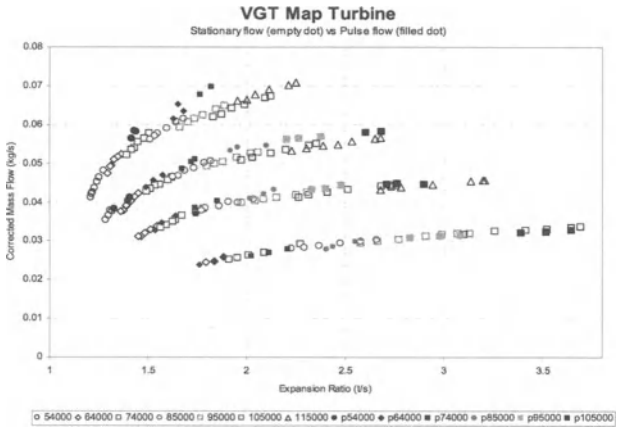

Fig. 2 VGT charts

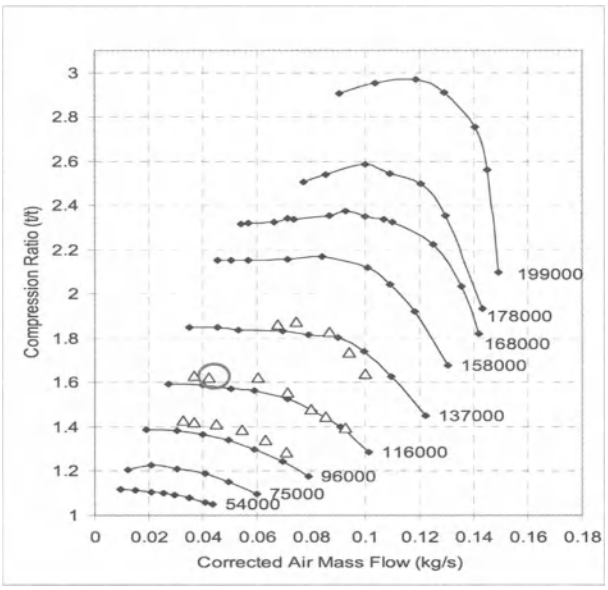

Fig. 3 Compressor characteristic lines (from a turbocharger with VGT)

An example for a tested point on the compressor side is shown in Fig. 4 for the point marked with a red circle in F. In Fig. 4 the mean value has been eliminated and only the fluctuation is depicted. At the top of Fig. 4 the excitations to the compressor unit can be observed: here, the incident pulse coming from the engine is identified as A_i. At the bottom of Fig. 4 the response of the compressor to the excitations can be observed: here, A_t and A_r refer to the transmitted and reflected pulses, as shown by the schematic included between the two plots.

2.2 1D-Wave Action Model

1D-Models are the day-to-day tool used by engine developers for the design of intake and exhaust systems including the turbocharging and EGR issues. Most 1D codes calculate turbines and compressor in a purely quasi-steady manner using the information of their steady maps.

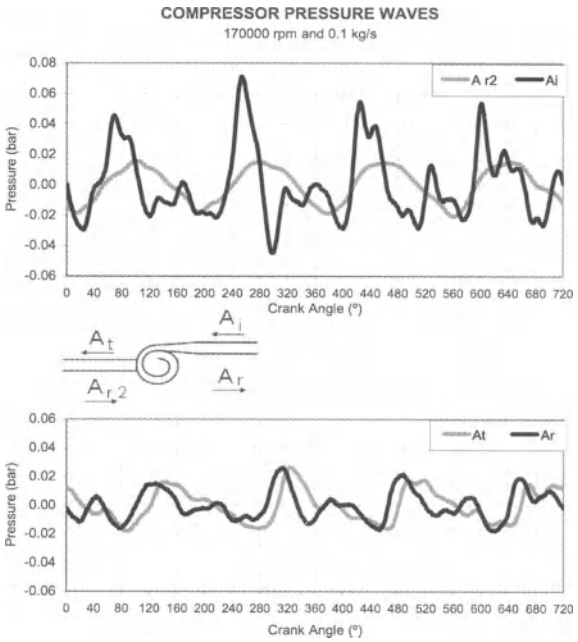

Fig. 4 Example of pressure wave decomposition

The authors developed a 1D code where the flow in the intake and exhaust ducts is calculated by finite differences [7]. The calculation at the duct boundaries and in elements where the flow is not one-dimensional is based in conservative equations [8].

The compressor model used for years had a purely quasi-steady behavior and the compression ratio in the operative point was obtained from the steady flow map. This model was not able to predict surge on engine operative conditions or negative flows and has been updated to deal with these problems [9]. Turbine model is based in the representation of a turbine as two non-dimensional nozzles separated by an intermediate reservoir [10]. The nozzle effective section is obtained to fit the steady maps. However, once the nozzles size is selected the model is itself unsteady. This allows for a pretty good representation of pressure pulses reflection and transmission for single entry, two entry and variable geometry turbines [10]. The efficiency is considered to be function of the blade speed ratio and is also fitted by steady efficiency maps. This assumption permits the calculation of unsteady efficiency as a function of the gas instantaneous velocity.

3 Research on Compressor Unsteadiness

The 1D-model used for the compressor combines the purely quasi-steady approach (interpolations in the compressor chart) with unsteady elements that represent compressor geometry. This is achieved by a proper combination of

equivalent volumes, ducts and orifices available in standard 1D gas-dynamic code. Different configurations were studied before a definitive solution was chosen. The proposed model is shown in Fig. 5, where the dimension of volumes and ducts (length and diameter) are related with geometrical parameters of the compressor unit to be modeled.

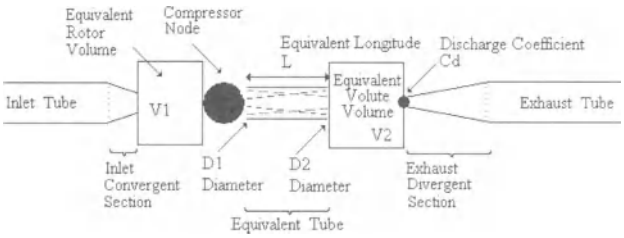

Fig. 5 Geometrical scheme of the unsteady flow compressor model

Due to the relation of compressor model with geometrical aspects of the compressor is looked for, the values of those inputs that are not evident to obtain (*D*1, *D*2, *L* and *Cd* in Fig. 5) has to be defined accordingly to geometrical characteristics. These relations have been obtained by running the model with different values in these inputs and the results of the model have been processed with a multifactor variance analysis (ANOVA). The different levels (different values) used for the unknown model inputs are following detailed:

1. Discharge coefficient (***Cd***), 3 levels: 0.7, 0.8 and 0.9.
2. Diameter ***D1***, 2 levels (Fig. 6). Low level: Diameter of a circular section equivalent to the **available cross section at the rotor inlet**. High level: Diameter of a circular section equivalent to the **rotor outlet cross section**.
3. Diameter ***D2***, 3 levels (Fig. 7). Low level: Diameter of a circular section equivalent to the **volute exhaust section at the compressor tongue.** Medium level: Diameter of a circular section equivalent to the ***cross* section in the compressor outlet** (at the very end of the outlet tapered duct). High level: Diameter of a circular section equivalent to the **volute inlet cross section**.
4. Length ***L***, 3 levels (Fig. 8). Low level: **1/3** of the largest run of a particle from rotor outlet to volute outlet (tongue). Medium Level: **1/2** of the largest run of a particle from rotor outlet to volute outlet. High Level: **2/3** of the largest run of a particle from rotor outlet to volute outlet.

The optimum results from this analysis correspond with the lowest level of each parameter. Table 1 illustrates these values for the studied compressors.

Table 1 Exact values of the optimum model inputs

	PARAMETERS					
COMPRESSOR	V1	V2	Cd	D1	D2	L
1 (FGT)	20 cm^3	80 cm^3	0.7	28	28	100
2 (VGT)	20 cm^3	80 cm^3	0.7	28	28	100
3 (MFT)	20 cm^3	130 cm^3	0.7	28	28	110
4 (AFT)	20 cm^3	50 cm^3	0.7	20	20	90

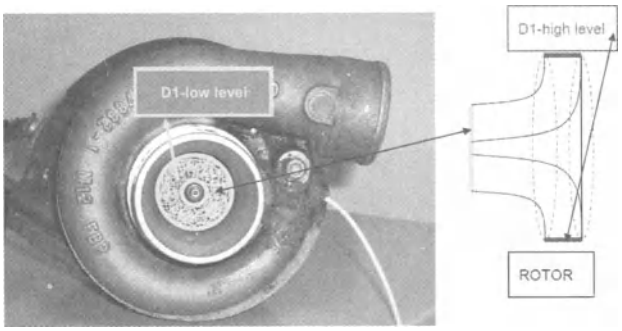

Fig. 6 D1 levels scheme

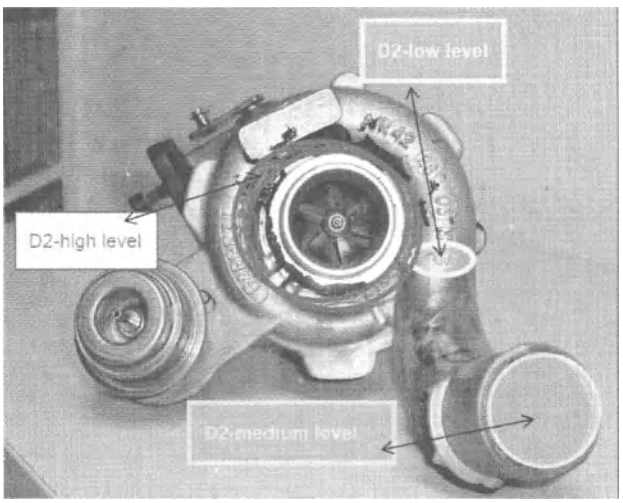

Fig. 7 D2 levels scheme

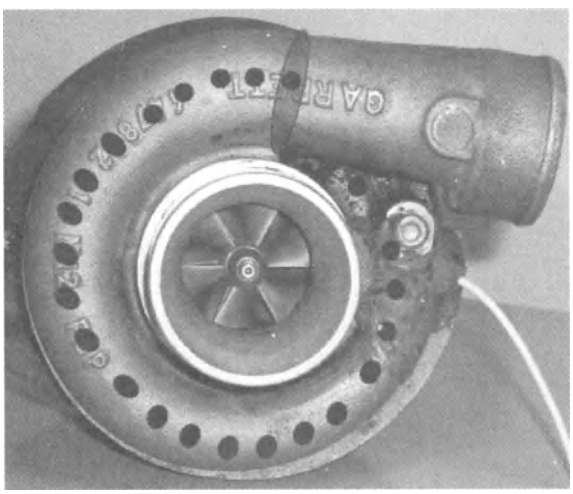

Fig. 8 Largest run of a particle from rotor outlet to volute outlet (tongue)

As can be observed $D1$ and $D2$ are always equal, therefore the definition of the parameters can be simplified to only one diameter corresponding to a circular section equivalent to the exhaust section at the compressor tongue (or what is equivalent the rotor inlet available section).

Figure 9 shows an example of the results obtained in the case of the compressor coupled to the AFT. It can be observed that the proposed 1D compressor model reproduces quite accurately the unsteady behavior of reflected and transmitted pressure pulses, both in the time and the frequency domains.

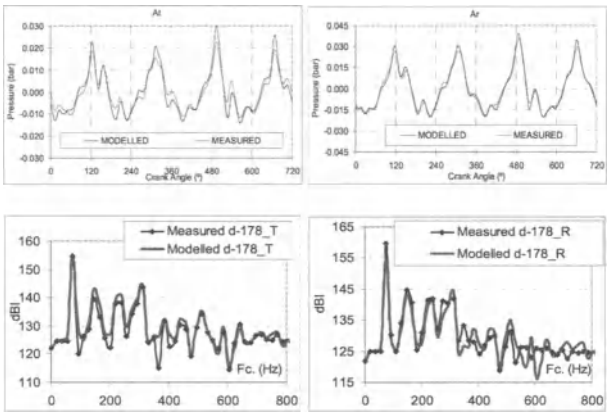

Fig. 9 1D unsteady compressor model, Compressor coupled to an AFT. Operation point at 178000 rpm.(left: transmitted pressure, right: reflected pressure)

The average turbocharger speed and the average temperature measured upstream of the compressor were imposed as model inputs. In addition, the incident pressure pulse (A_i in Fig. 4) measured upstream of the compressor and the reflected pressure pulse (A_{r2} in Fig. 4) measured downstream of the compressor are also input variables of the model. Similar results to those shown in Fig. 9 were obtained in the approximately 150 points tested for the four centrifugal compressors considered.

In order to highlight the advantages of 1D unsteady compressor modeling, the calculated results have been compared with a purely quasi-steady model that uses the boundary condition of the compressor chart just between two ducts, instead of using the configuration shown in Fig. 5. The differences are especially evident in the frequency domain predictions. Figure 10 shows the more accurate predictions obtained when calculating with the unsteady model the pressure pulses that travels through the ducts upstream the compressor (noise source radiated upstream the compressor).

Obviously, the compressor chart introduced in the boundary condition (Compressor Node) has to be previously modified in order to well predict the pressure ratio for a given mass flow. This is done by substracting the pressure losses that, for a given mass flow, are generated by the elements used in the 1D code (volumes and ducts in Fig. 5) to represent the internal geometry of the compressor, due to those losses have been already included in the compressor characteristic chart.

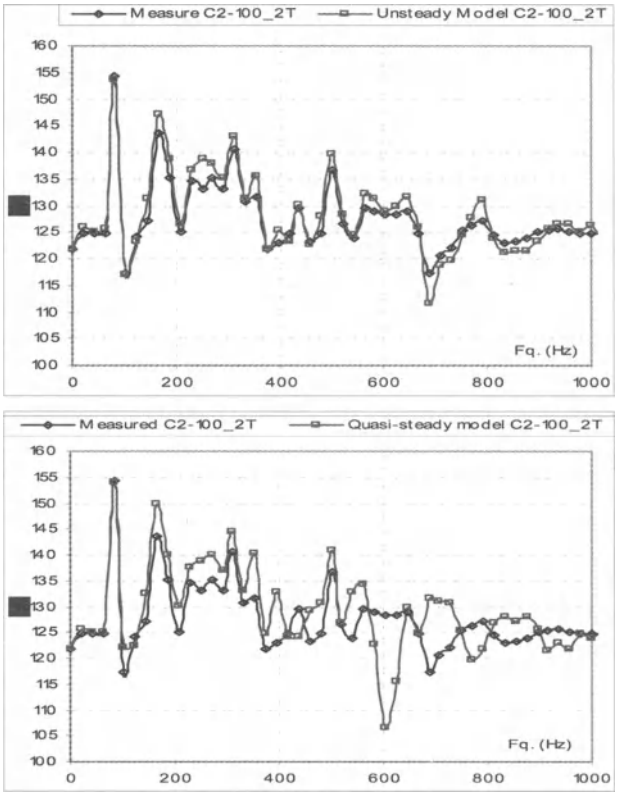

Fig. 10 1D unsteady model (top) vs. Quasi-steady model (bottom), Transmitted pressure pulses in frequency domain at 100000 rpm

The following methodology is proposed. First, to calculate with the gas-dynamics code the pressure losses introduced upstream and downstream the 'compressor node' (i.e. the boundary condition that contains the compressor map) by the model elements showed in Fig. 5. Second, to discount these pressure losses from the characteristic compressor map.

If a coefficient of turbulent pressure loss (K) is defined according to equation [1]. The evolution of K versus Reynolds is shown in Fig. 11. Figure 11 shows that the higher pressure losses are produced in the elements downstream the 'compressor node'.

$$\Delta p_{00} = K \cdot \frac{1}{2} \rho_0 u_0^2 \qquad (1)$$

It is worth noting that all the calculated values comes from a correction a priory that is made once the model geometry is decided, therefore the proposed model continues being feasible to extrapolate to other codes and keeping its simplicity.

In Fig. 12 is depicted the map taking into account the pressure losses and the original measured map, which is the same already shown in Fig. 3. This modification does not affect the results shown in Fig. 9 and Fig. 10, just correct the average values results.

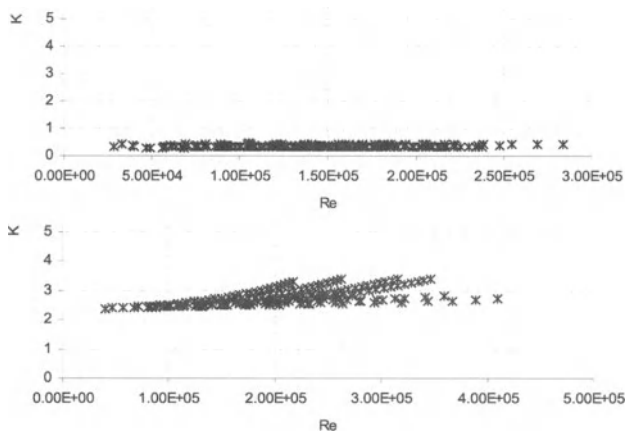

Fig. 11 Evolution of K vs. Reynolds for upstream compressor node elements (top) and for downstream compressor node elements (bottom)

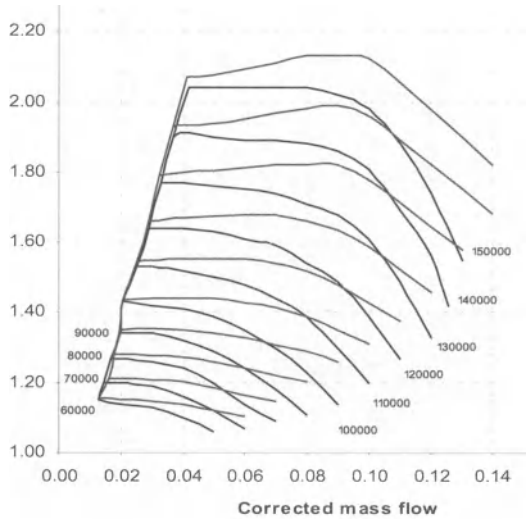

Fig. 12 Compressor map. Steady flow (blue) and steady flow with pressure losses of 1D model discounted (red)

4 Research on Turbine Unsteadiness

To model the turbine isentropic efficiency the information from manufacturer maps is used. The turbine isentropic efficiency is introduced in the 1D gas-dynamic model as a function of the ratio between blade speed and gas velocity (blade speed ratio) due to centripetal turbines generally show the maximum efficiency at a value of this ratio around 0.7 and iso-speed lines trends to collapse in a unique curve.

Nevertheless, the efficiency provided by the manufacturer with steady flow tests is not the same that the turbines have on engine operation when they work with highly unsteady flow. Moreover, the turbines are assumed as adiabatic machines, but when the gas temperatures are very high (as in this case) the power radiated from the turbine case or transmitted to the compressor side can be not negligible. Therefore, the efficiency of the turbine obtained from unsteady tests and calculated as adiabatic should be reduced to take into account these phenomena.

This is done by modeling the engine operative points imposing constant turbocharger speed and calculating the ratio between compressors consumed power and turbine provided power. When all the engine thermodynamic variables (pressures, mass flow and temperatures) are correctly modeled (in average and instantaneous values) and the turbocharger is considered as an adiabatic machine working at steady operation (average constant turbocharger speed) the ratio between compressor and turbine power must be equal to one. Modeling experience in turbocharged reciprocating engines shows that this is not possible if the efficiency form manufacturer's map is used.

Going deeper in the explanation how turbine efficiency is corrected on engine operation following example is presented corresponding to the VGT.

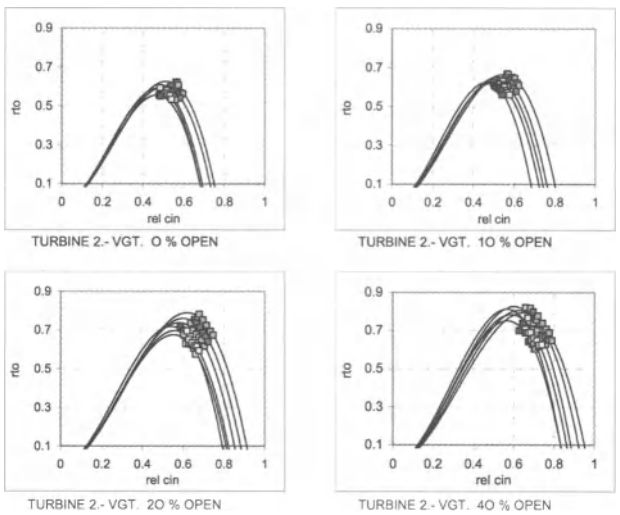

Fig. 13 Turbine efficiency vs. blade to speed ratio measured at steady flow conditions (FGT and VGT)

Turbine efficiency is introduced in the gas dynamic code versus blade to speed ratio and the model interpolates every time instant (assuming quasy-steady behavior) among the data measured with steady flow. Due to the measured range is very narrow the efficiency data measured are previously fitted to a third degree polynomial curve as shown in Fig. 13, where the different curves correspond to the different speed lines.

The third degree polynomial allows generating non-symmetric curves. In addition the curves have to full fill two other requirements that efficiency is cero for cero blade to speed ratio and that the maximum efficiency is contained within the measured data.

As previously stated, if all the thermodynamic variables and associated efficiencies are not well modeled upstream and downstream the turbocharger there should be a discrepancy between the turbine power and the compressor power when the turbocharger speed is imposed in the gas-dynamic model.

Figure 14 shows the interface of the gas dynamic model that reproduces this situation. In this case the turbocharger speed and the boundary conditions upstream and downstream the turbine and the compressor are inputs for the model. While upstream and downstream the turbine the boundaries are instantaneous and incident pressure pulses [2][4], in the compressor case the boundaries are average pressure and temperature measured on engine operation.

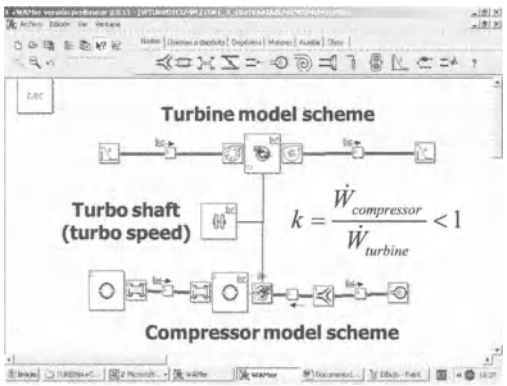

Fig. 14 Interface of the gas dynamic model with turbocharger power balance

In spite of there are not instantaneous values imposed in the compressor side the calculation of the pulsating behavior in the turbine is not severely affected, since the turbine is the main responsible of the pulsation in the turbocharger and the pulses upstream and downstream the compressor are low compared with those in the turbine. Other authors [11][12] also use this simplification to calculate instantaneous variables in the turbine when it is excited by unsteady flow.

If the ratio between modeled compressor power and turbine power is computed the "*k*" coefficient of Fig. 14 is obtained, which has always a value lower than 1.

If by the one hand we assume that the average compressor power is well calculated, due to it is working with flow almost steady and the comparison with measured outputs is accurate enough; and by the other hand we consider the fact that "*k*" is always lower than unity. It can be clearly stated that the turbine working on engine operation has lower efficiency (and therefore provides lower power) than working with steady flow conditions for the same operative point in the turbine map.

The main causes are the un-steady effects on turbine efficiency and the higher heat transfer losses when the turbine is working on engine conditions. Correlations of this factor with engine operative variables can be found in the literature for FGT turbines [13] and have been also obtained for the VGT studied turbine as it is shown in Fig. 15. These types of correlations take into account the two causes of the lower efficiency and therefore they are not physically explicit enough. It would be necessary to separate heat transfer from unsteady flow phenomena for better modeling turbine efficiency.

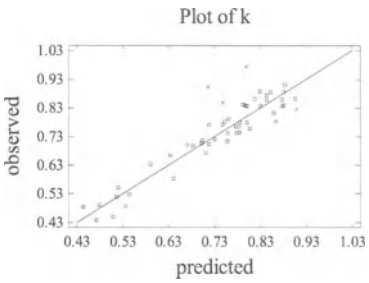

Fig. 15 Correlation of "*k*" coefficient as a function of turbine and flow parameters (VGT)

Figure 15 correlation corresponds to Equation 2 and the details can be found in Table 2. Equation 2 shows that for a VGT it is possible to find a high level of correlation between "*k*" and parameters like engine pulses amplitude (A_i) and engine pulses frequency (*PF*), turbocharger speed (*TCS*), opening of the VGT ($VGT_{opening}$) and factor of amplitude (*fa*).

$$k=k1+k2\cdot VGT_{opening}+k3\cdot TCS_{krps}+k4\cdot fa+k5\cdot A_i+k6\cdot PF_{kHz} \quad (2)$$

Table 2 Details of "*k*" coefficient correlation

Estimation Results

Parameter	Estimate	Asymptotic Standard Error	Asymptotic 95.0% Confidence Interval Lower	Upper
k1	0.457928	0.0573739	0.342059	0.573797
k2	-0.474861	0.118546	-0.714271	-0.235452
k3	0.454308	0.0653446	0.322341	0.586274
k4	0.276832	0.061614	0.1524	0.401264
k5	-0.525091	0.122512	-0.772509	-0.277673
k6	-2.0277	0.880402	-3.80571	-0.24969

Analysis of Variance

Source	Sum of Squares	Df	Mean Square
Model	25.8868	6	4.31446
Residual	0.054383	41	0.00132642
Total	25.9411	47	
Total (Corr.)	0.789323	46	

R-Squared = 93.1102 percent

Equation 3 shows the factor of amplitude (*fa*) definition and Fig. 16 shows that is possible to correlate *fa* with

engine and turbine operative parameters. In addition, Fig. 17 shows that also A_i highly correlates with easy to measure engine operative variables, like the engine torque or the turbine opening.

$$fa = \frac{Max_peak_{pressure} - Min_peak_{pressure}}{Average_{pressure} - Ambient_{pressure}} \quad (3)$$

$$fa = k_1 + k_2 \cdot e^{(k3 \cdot TCS_{krps})} \cdot e^{(k_3 \cdot Torque_{kNm})} + (k_4^{VGT_{opening}}) \cdot e^{(PF_{kHz})}$$

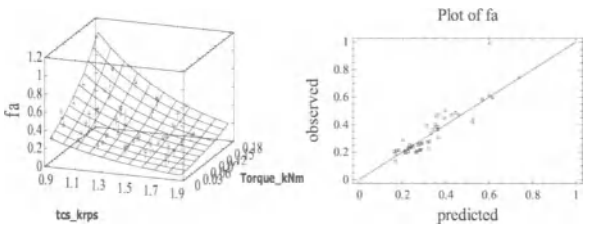

Fig. 16 Correlation of amplitude factor as a function of turbine and engine parameters (VGT)

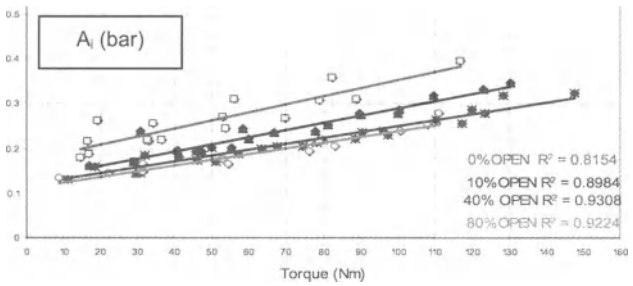

Fig. 17 Incident wave amplitude (A_i) vs. engine torque for different openings of the AFT

5 Summary and conclusions

In this paper a holistic procedure to analyze the complex unsteady phenomena in turbochargers of reciprocating internal combustion engines is presented. This includes combining accurate testing in close to real engine operative conditions and advanced modeling.

The 1D unsteady modeling of centrifugal compressors is described using a procedure able to be implemented in whatever 1D code. The obtained results show clear advantages in comparison with standard quasi-steady modeling, especially in the frequency domain predictions (noise prediction).

A procedure to characterize centripetal turbines efficiency using a 1D code and experimental data is also proposed. The procedure is based in the calculation of a factor that corrects isentropic turbine efficiency provided in turbine maps. Such turbine correction factor is not only a function of pulses amplitude and frequency but also on VGT opening and speed. In addition, it has been concluded that it is possible to correlate the needed pulsating information with other feasible to measure turbocharger and engine parameters.

Acknowledgements

The authors thank Renault SA for the material and financial support of this study.

References

J. Portalier, N. Schorn, J. Galindo et al., "Twin Turbo Boosting system design for the new generation of PSA 2,2 liter HDI Diesel engines", Proc. of Thiesel Conference, Valencia, 2006

J. Galindo, J.R. Serrano, C. Guardiola, et al., "Surge limits definition in a specific test bench for the characterization of automotive turbochargers". Experimental Thermal and Fluid Science. Vol 30/5, pp. 449, 462. 2006

A.J. Torregrosa, J.R. Serrano, S. Soltani et al. "Experiments on Wave Transmission and Reflection by Turbochargers in Engine Operating Conditions". SAE Paper 2006-01-0022. 2006 SAE Transactions-Journal of Engines. V115-3 pp 1 – 12. 2007

G. Piñero, L. Vergara, L., J.M. Desantes, et al. "Estimation of velocity fluctuation in internal combustion engine exhaust systems through beam forming techniques". Meas. Sci. Technol. 11, pp. 1585 – 1595. 2000

H. Chen, I. Hakeem, and R.F. Martínez-Botas, "Modelling of a turbocharger turbine under pulsating inlet conditions". Proc. IMechE, Part A, A04695, vol. 210, pp. 397 – 408. 1996

M. Capobianco and S. Marelli "Unsteady flow behaviour of the turbocharging circuit in downsized SI automotive engines" FISITA 2006 World Automotive Congress. F2006P119. 2006

F. Payri, J. Galindo, J.R. Serrano, et al. "Analysis of numerical methods to solve one-dimensional fluid-dynamic governing equations under impulsive flow in tapered ducts". International Journal of Mechanical Sciences, 46 (7), pp. 981 – 1004. 2004

J. Galindo, J.R. Serrano, F.J. Arnau, et al., "Description and analysis of a one-dimensional gas-dynamic model with independent time discretization". Proceedings of the ASME Internal Combustion Engine Division 2008 Spring Technical Conference ICES2008-1610. Chicago. 2008

J. Galindo, J.R. Serrano, H. Climent, et al. "Experiments and modeling of surge in small centrifugal compressor for automotive engines". Experimental Thermal and Fluid Science, 32, pp. 818 – 826. 2008

J.R. Serrano, F. Arnau, V. Dolz, et al. "A model of turbocharger radial turbines appropriate to be used in zero- and one-dimensional gas dynamics codes for internal combustion engines modeling", Energy Conversion and Management. doi: 10.1016/j.enconman.2008.06.031. 2008

H-E. Angstrom and F. Westin. "A method of investigating the on-engine turbine efficiency combining experiments and modeling" c602/029/2002. Proceedings of the seventh international conference on Turbochargers and Turbocharging. pp 199 – 211. 2002

H-E. Angstrom and F. Westin. "Calculation Accuracy of Pulsating Flow through the Turbine of SI-Engine Turbochargers—Part 1 Calculation for Choice of Turbines with Different Flow Characteristics" SAE paper 2005-01-0222. 2005

JM. Luján, J. Galindo, J.R. Serrano."Efficiency characterization of centripetal turbines under pulsating flow conditions". SAE paper 2001-01-0272. 2001 SAE Transactions-Journal of Engines. V110 pp 233 – 239. 2002

The 4th International Symposium on Fluid Machinery and Fluid Engineering
November 24-27, 2008, Beijing, China
NO. 4ISFMFE-IL16

Cavitation and Turbopump Hydrodynamics Research at Alta S.P.A. and Pisa University

Angelo Cervone[1], Lucio Torre[2], Angelo Pasini[3] and Luca d'Agostino[4]

[1] Senior Engineer, Alta S.p.A., Via Gherardesca, 5, 56121, Ospedaletto - Pisa, Italy, a.cervone@alta-space.com

[2] Project Manager, Alta S.p.A., l.torre@alta-space.com

[3] Ph. D. Student, Alta S.p.A., a.pasini@alta-space.com

[4] Professor, Aerospace Engineering Department — University of Pisa, Via G. Caruso, 56126, Pisa, Italy.
luca.dagostino@ing.unipi.it

Abstract The paper introduces and briefly outlines the research activities on cavitation and turbopump hydrodynamics conducted in the last 20 years at the Department of Aerospace Engineering of Pisa University, at Centrospazio, a nonprofit space propulsion laboratory established in 1989, and at Alta S.p.A., a private spin-off company founded in 2000 and active in the aerospace sector. Both the experimental activities conducted in a dedicated facility called Cavitating Pump Rotordynamic Test Facility (CPRTF) and the analytical/numerical work is described. A valuable experience has been gained by the research group throughout the years, and important results have been obtained in the definition of experimental techniques for the detection of flow instabilities, the understanding of thermal cavitation effects on pump performance and instabilities, and the development of reduced order analytical tools for the preliminary design and performance prediction of axial inducers.

Keywords cavitation, turbopump, rocket engine, flow instabilities, axial inducer

Nomenclature

Latin symbols

b_2	Impeller outlet width [m]
e	Whirl eccentricity [m]
f_R	Normalized rotordynamic radial force [-]
M	Main motor torque [N*m]
P	Main motor power [W]
p_{t1}	Total pressure at pump inlet [Pa]
p_{t2}	Total pressure at pump outlet [Pa]
$\dot{Q}$	Volumetric flow rate [m^3/sec]
r_{T1}	Tip radius at pump inlet [m]
r_{T2}	Tip radius at pump outlet [m]
T	Flow temperature [°C]

Greek symbols

α	Incidence angle [deg]
ϕ	Flow coefficient [-]
σ	Cavitation number [-]
ψ	Head coefficient [-]
Ω	Pump rotational speed [rad/sec]
ω	Whirl rotational speed [rad/sec]

Acronyms

ASI	Agenzia Spaziale Italiana (Italian Space Agency)
CFD	Computational Fluid Dynamics
CIRA	Centro Italiano Ricerche Aerospaziali
CPRTF	Cavitating Pump Rotordynamic Test Facility
ESA	European Space Agency
ODE	Ordinary Differential Equation
STS	Space Transportation System
TCT	Thermal Cavitation Tunnel

1 Introduction

Chemical rocket propulsion and its derivative concepts play a central role in the design of current space vehicles, as well as future STSs (Space Transportation Systems),

being the only viable technology capable of generating the relatively high levels of thrusts necessary for launch and most primary propulsion purposes in a large number of space missions. Currently, the main specifications for STSs are concerned with reusability, operational life, rapid maintenance, higher launch frequencies and more efficient scale economies. Propulsion systems have therefore a crucial impact on their design and total cost, and attention is progressively shifting from solid propellant rockets, which have comparatively lower specific impulse and generate fixed thrust schedules, to liquid propellant rockets and their derivatives, in view of their utilization both for primary and upper-stage propulsion.

Propellant feed turbopumps are an essential component of all primary propulsion concepts powered by liquid propellant rocket engines. The quest for weight reduction typically leads to the design of faster and lighter turbopumps, often operated at supercritical conditions, where the combined effects of rotordynamic instabilities and cavitation represent the dominant fluid mechanical phenomena that adversely affect the pumping performance and dynamic stability of the machine (Brennen, 1994). In particular, cavitation is the major source of degradation of the suction performance, reliability, useful life and power density, also causing other undesirable effects such as the reduction of the overall efficiency and the drastic increase of noise generation (Stripling and Acosta, 1962). Even more importantly for space applications, cavitation can provide the necessary flow excitation and compliance for triggering dangerous rotordynamic and/or fluid mechanic instabilities of the turbopump (Brennen and Acosta, 1973, 1976; Braisted and Brennen, 1980), or even, through the coupling with thrust generation, of the entire propulsion system (POGO auto-oscillations of liquid propellant rockets, Rubin, 1966). The occurrence of flow instabilities like rotating cavitation has been extensively reported in the development of most high performance liquid propellant rocket fuel feed systems, including the Space Shuttle Main Engine (Ryan et al. 1994), the European Ariane 5 engine (Goirand et al. 1992) and the LE-7 engine of the H-II and H-II-A Japanese rockets (Kamijo et al., 1993). Recently, Japanese researchers have postulated that the resonance of higher-order surge instabilities with the first bending mode of the inducer blades was responsible for the November 1999 fatigue failure of the H-II rocket liquid hydrogen pump inducer (Tsujimoto and Semenov, 2002).

Research on cavitation and turbopump hydrodynamics has been developed in the last 20 years at the Department of Aerospace Engineering of Pisa University, at Centrospazio, a nonprofit space propulsion laboratory established in 1989, and at Alta S.p.A., a private spin-off company founded in 2000 and active in the aerospace sector. Analytical and numerical investigations have been supported by an extensive experimental activity since 1999, after the completion of the Cavitating Pump Rotordynamic Test Facility (CPRTF), jointly funded by the Italian Space Agency (ASI) and the European Space Agency (ESA).

The most significant experimental activities carried out in the CPRTF will be described in the paper, including: the characterization of cavitating/noncavitating performance and cavitation-induced flow instabilities of several prototypes of axial inducers used in the rocket engines of the Ariane launcher, the analysis of the pressure profile, cavitation instabilities and thermal effects on a NACA 0015 two-dimensional hydrofoil, and the visual characterization of cavitating flow and instabilities on inducers by means of high-speed movies. Current and future activities, mainly devoted to the detailed study of thermal cavitation effects, flow instabilities and rotordynamic forces on tapered helical inducers with designs representative of those of modern space rocket turbopumps, will be briefly outlined.

In addition, previous and present theoretical activities carried out by the research group will be presented, including: the development of a homogeneous-flow isenthalpic cavitation model with thermal cavitation effects, easily implementable in CFD cavitating codes, a rotordynamic analytical model of cavitating inducers which provided the first deductive explanation of the observed coupled subsynchronous and supersynchronous free whirl motions of cavitating turbopumps, and a reduced order model for the preliminary design and noncavitating performance prediction of tapered axial inducers.

2 Experimental Activities

※ Test facility

The CPRTF (Figure 1) is a low-cost, versatile and instrumentable cavitation test facility, operating in water at temperatures up to 90°C (Rapposelli et al., 2002). The facility is intended as a flexible apparatus that can readily be adapted to conduct experimental investigations on virtually any kind of fluid dynamic phenomena relevant to high performance turbopumps in a wide variety of alternative configurations (axial, radial or mixed flow, with or without an inducer). The CPRTF has been especially designed for the analysis of unsteady flow phenomena and rotordynamic impeller forces in scaled cavitation tests under fluid dynamic and thermal cavitation similarity conditions. It can also be configured as a small water tunnel to be used for thermal cavitation tests for experimental validation of numerical tools and simulations.

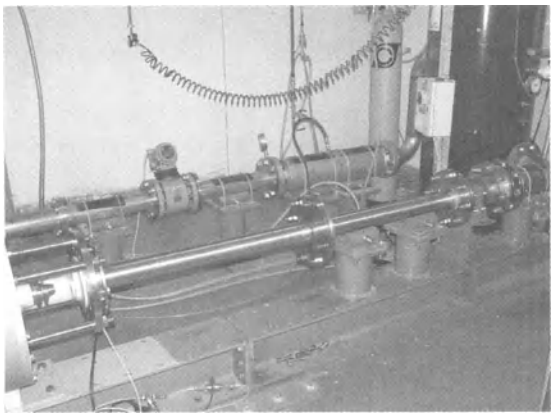

Fig. 1 The cavitating pump rotordynamic test facility

The test section (Fig. 2) is equipped with a rotating dynamometer, for the measurement of the instantaneous forces and moments acting on the impeller, and with a mechanism capable of adjusting and rotating the eccentricity of the impeller axis in the range 0÷2 mm and ±3000 rpm, for rotordynamic experiments. The inlet section, made in plexiglas, is transparent in order to allow for the optical visualization of cavitation in the inducer. It can be instrumented with several flush-mounted piezoelectric pressure transducers, located at three axial stations: the flow inlet and outlet sections and the inducer blade channels (Fig. 3). At each station up to eight transducers can be mounted with a given angular spacing, in order to cross-correlate their signals for coherence and phase analysis. As a result, waterfall plots of the power spectral density of the pressure fluctuations can be obtained as functions of the cavitation number, in order to identify the presence of flow instabilities in the flow conditions under consideration. Cross-correlation of two pressure signals from different locations allows determining the axial or azimuthal nature of each instability and, in the second case, the number of rotating cells involved.

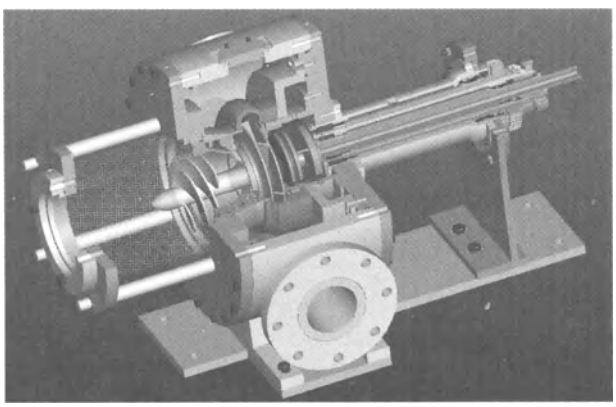

Fig. 2 Cut-out drawing of the CPRTF test section

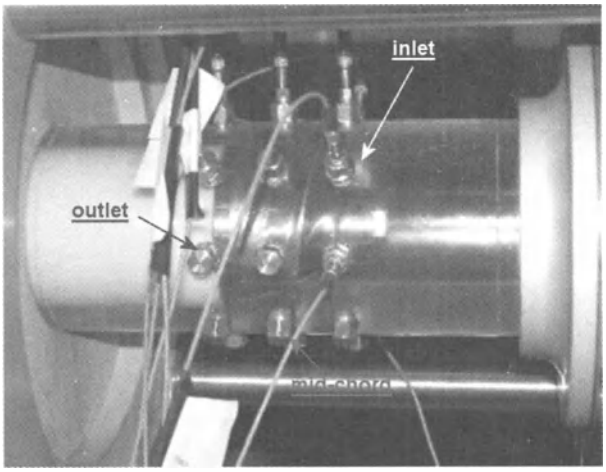

Fig. 3 The transparent inlet section of the facility instrumented with piezoelectric pressure transducers

The water pressure at the inlet of the test section can be adjusted by means of an air bag, while the temperature regulation is obtained by a 5 kW electrical heater. A Silent Throttle Valve is used for the variation of the pump load. Two electromagnetic flowmeters, mounted on the suction and discharge lines of the water loop, provide the measurement of the inlet and outlet flow rates. The inlet pressure is monitored by an absolute transducer mounted immediately upstream of the test section, while a differential transducer measures the pump pressure rise. Photo cameras and high-speed video cameras are used to allow for the optical visualization of the cavitating flow on the test article.

The main specifications and operational parameters of the CPRTF are summarized in Table 1.

Table 1 Main specifications and operational parameters of the facility

Pump rotational speed	$\Omega = 0 \div 6000$ rpm
Main motor power	$P \leq 30$ kW
Main motor torque	$M \leq 100$ Nm
Suction pressure	$p_{t1} = 0.01 \div 6$ bar
Discharge pressure	$p_{t2} \leq 11$ bar
Volumetric flow rate	$\dot{Q} \leq 0.1 \mathrm{m}^3/\mathrm{s}$
Flow temperature	$T = 10 \div 90$ °C
Whirl eccentricity	$e = 0 \div 2$ mm
Whirl rotational speed	$\omega = -3000 \div 3000$ rpm
Impeller eye radius	$r_{T1} \leq 90$ mm
Impeller outlet radius	$r_{T2} \leq 112$ mm
Impeller outlet width	$b_2 \leq 30$ mm

※ *Characterization of space rocket inducers*

Several space rocket inducers have been tested and characterized in the CPRTF, with particular emphasis on cavitating/noncavitating performance, flow instabilities and their dependence on thermal effects. In particular, two inducers used in the European Ariane 5 rocket turbopumps have been extensively studied (Cervone et al., 2005, 2006b). The first is a prototype of the liquid oxygen inducer of the Vulcain MK1 engine (first stage engine). It is a four-bladed axial inducer made in Monel alloy, with a tip radius $r_T = 84$ mm, a profiled, variable-radius hub (36 mm inlet radius, 58 mm outlet radius) and backswept blades with sharp leading edges, variable thickness and nonuniform blade angle. The inlet tip blade angle is 7.7° and the tip solidity is 2.1. The second one, called FAST2, is a prototype of the liquid oxygen inducer of the VINCI engine (second stage engine). It is a two-bladed stainless steel axial inducer with a tip radius $r_T = 41.1$ mm, an inlet hub radius of 15 mm and outlet hub radius of 28 mm. The inlet tip blade angle is 7.38°, the outlet tip blade angle is 21.24° and the tip solidity is 1.59. Both inducers, a picture of which is shown in Figure 4, have been manufactured by Avio S.p.A. in Italy.

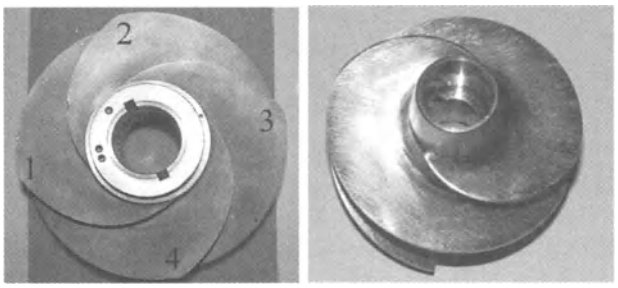

Fig. 4 Pictures of the MK1 (left) and FAST2 (right) inducers

With regard to flow instabilities, very few oscillating phenomena were found on the MK1 inducer, including an auto-oscillation and smooth surge mode instability at low frequency (about 1 Hz). In particular, no significant flow oscillations were detected near the design point, thus confirming the effectiveness of its design. On the other hand, several interesting instability phenomena were detected on the FAST2 inducer, including a rotating stall cavitation at a frequency of 0.31 times the inducer rotating speed and some higher-order longitudinal phenomena (at 4.4 Ω and 6.6 Ω), showing very similar characteristics to those of the high-order cavitation surge instability observed by Tsujimoto and Semenov (2002) on the Japanese LE-7 inducers. These higher order instabilities are evident in the waterfall plot shown in Figure 5, where they are denoted by f_2 and f_3.

Furthermore, several experiments were conducted on the test inducers at higher values of the water temperature (up to 70 °C), in order to investigate the influence of thermal effects on the characteristics and range of occurrence of the detected instabilities. It was observed that the rotating stall cavitation was not affected by the flow temperature, showing the same field of existence, intensity and frequency of oscillations as in "cold" water experiments. On the other hand, longitudinal instabilities seemed to be significantly mitigated at higher temperatures, or even disappeared in the case of the surge mode at 1 Hz. Their range of occurrence was also affected, being evidently shifted towards higher values of the cavitation number at higher flow temperatures.

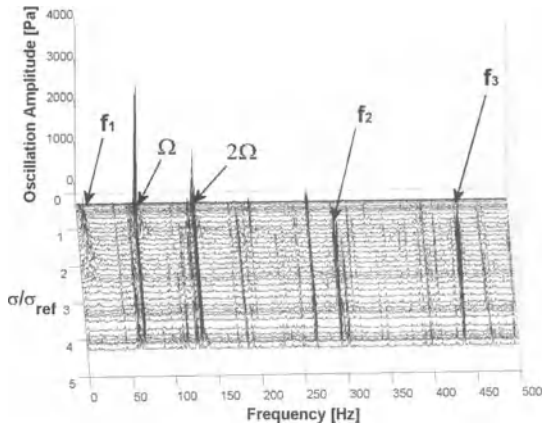

Fig. 5 Waterfall plot of the power spectrum of the inlet pressure fluctuations in the FAST2 inducer at $\phi/\phi_{ref} = 0.9$, 4000 rpm and room water temperature

※ *Cavitation and thermal effects on hydrofoils*

An extensive test campaign has been conducted in the Thermal Cavitation Tunnel (TCT) configuration of the facility on a NACA 0015 two-dimensional hydrofoil (Cervone et al., 2006a). The main objectives of the tests consisted in the characterization of the pressure profile on the test body surface under different operational conditions and the study of the "cloud cavitation" instability, whose characteristics represent the basis for understanding many of the oscillating flow phenomena observed in rotating machines. Also in this case particular attention has been paid to the influence of thermal effects, investigated by means of tests conducted at elevated flow temperatures.

With reference to the flow pressure, Figure 6 compares the profiles on the suction side of the hydrofoil under cavitating conditions for three different freestream water temperatures, at the same cavitation number and incidence angle. At higher temperatures the absorption of the latent heat at the cavity interfaces increases, reducing the vapor pressure below the unperturbed saturation value. This trend is well reflected in the figure: at 70 °C, due to pressure decrement below the saturation value, the pressure recovery occurs further upstream than at room temperature.

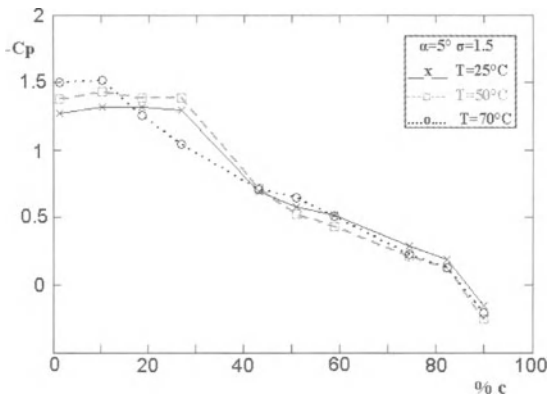

Fig. 6 Influence of thermal cavitation effects on the suction side pressure distribution of a NACA 0015 hydrofoil at constant angle of attack α and cavitation number σ for several water temperatures T

By analyzing the cavity length and oscillations it was shown that three different regimes of cavitation can be recognized on the hydrofoil, corresponding to different ranges of the cavitation number:

- Supercavitation (at lower cavitation numbers): the cavity extends completely downstream of the hydrofoil, and little cavity oscillations are observed.
- Bubble+Cloud cavitation (at intermediate cavitation numbers): an initial zone of bubbly cavitation is present on the hydrofoil, followed by a second zone where the bubbles coalesce and strong cloud cavitation oscillations are detected. The typical cavitation appearance in this case is shown in Fig. 7.
- Bubble cavitation (at higher cavitation numbers): after a short transition zone, cloud cavitation disappears, and only the traveling bubble cavitation zone remains, with drastically reduced pressure oscillations.

At higher freestream temperatures the "Bubble+Cloud cavitation" zone was observed to spread over a wider range of cavitation numbers and to initiate at higher values of σ, even if the frequency of the oscillations remained the same. Similarly, supercavitation also began at higher cavitation numbers.

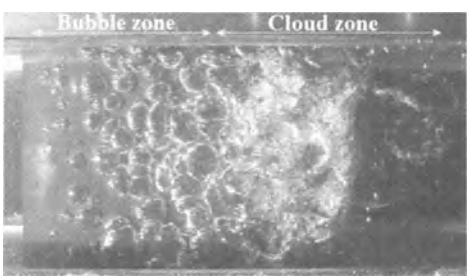

Fig. 7 Cavitation on the NACA 0015 hydrofoil in the "Bubble+Cloud" case ($\alpha=4°, \sigma=1.25, T=25°C$)

※ Visual characterization of cavitating flows

The capabilities of the CPRTF have been recently improved after the installation of an integrated system for the optical analysis of cavitating flows (Cervone et al., 2007). The core of the system is represented by a high-speed video camera with a recording rate up to 16000 fps. The required illumination level is provided by three halogen lamps with a power of 1250 W. Alternatively, the camera can be synchronized with a stroboscopic light having a maximum flash frequency of 1000 lamps/second.

This optical instrumentation can be used for analyzing the cavitating region on the test body and, in particular, for studying in detail the oscillating behavior of the cavity under flow instability conditions, in order to confirm and better understand the results obtained from pressure measurements. To this purpose a dedicated image processing algorithm has been implemented, capable of converting the movie frames into "black & white" images, where white pixels correspond to the cavitation region and black pixels to the noncavitating flow. More in detail, a "threshold" segmentation technique has been used for separating the cavitating regions from the remainder of the image. The pixels whose intensity in the original image exceedes a certain threshold value (selected by an appropriate threshold identification method) are set as white, while all other pixels are set as black. The resulting images can then be easily analyzed by computational tools in order to determine the extension and characteristics of the cavitating region as functions of the time. Figure 8 shows an example of a frame before and after the application of the algorithm.

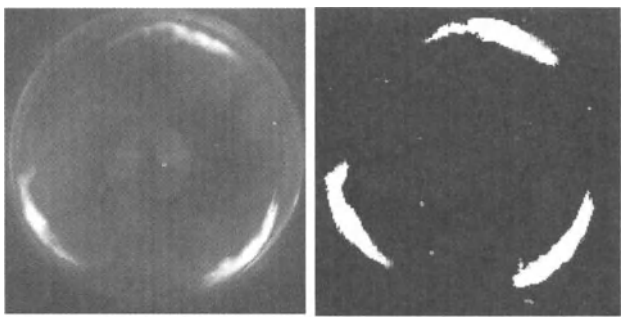

Fig. 8 Sample case of comparison between the original frame and the processed binary image obtained by the algorithm developed at Alta S.p.A

The image processing algorithm was validated by applying it to a 3-bladed, aluminum-made commercial inducer of extremely simple helical geometry, with a tip radius of 81 mm, a hub radius of 22.5 mm, a tip blade angle of 9°, a tip solidity of 3.05 and 2 mm thick back-swept

blades with blunt leading and trailing edges. Experiments based on pressure oscillations measurements showed the occurrence of rotating stall cavitation at a frequency of about 0.34 times the rotational speed. Movies of the cavitating inducer were taken under the same flow conditions for which this instability was detected and analyzed by means of the above image processing algorithm. The cavity lengths obtained by the algorithm were studied by Fourier analysis and cross-correlation between the different blades. The results showed the presence of a rotating phenomenon at the same frequency and phase of the previously detected rotating stall cavitation, thus confirming the effectiveness of the optical analysis procedure.

※ Current and future work

The present experimental work carried out in the CPRTF is mainly devoted to the extensive characterization of cavitation instabilities, rotordynamic forces and thermal cavitation effects on prototype inducers with geometries representative of those of typical space rocket inducers. The activity, sponsored by European Space Agency under a Technology Research Program contract, is based on the design, realization and testing of two different inducers, a 3-bladed and a 4-bladed one. Tests will be conducted at different water temperatures (up to 75°C), at design flow coefficient as well as slightly off-design conditions, and several values of the whirl eccentricity and whirl/rotating speed ratio for the characterization of the rotordynamic instabilities.

On the other hand, the main activities foreseen for the next future include: the characterization of the dynamic transfer matrix of axial inducers by means of tests conducted under externally imposed flow oscillations; the extension of the operational capabilities of the CPRTF in order to carry out performance tests on axial inducers at higher, full-scale rotating speeds (up to 20000 rpm).

3 Analytical and Numerical Activities

The development of reduced order analytical models is an important support tool for the experimental work, capable of providing fast and sufficiently accurate information about the cavitating/noncavitating behavior of the test items and their design (as well as the design of experimental facility upgrades and modifications). On the other hand, numerical investigations are an useful support tool for validating the results of both analytical models and experimental activities.

An overview of the main theoretical activities conducted at Alta S.p.A. in recent years is provided in this section of the paper.

※ Development of cavitation models for CFD codes

Cavitating flows, with the presence of free surfaces whose shape, location and evolution are not known "a priori" and rate-controlled evaporation/condensation at the interface, pose formidable obstacles in terms of both physical and numerical modeling. Therefore, the development of a simplified cavitation model which includes only the essential physical phenomena represents a useful tool to be integrated in today's CFD codes.

The analytical model developed at Alta S.p.A. (Rapposelli and d'Agostino, 2003) consists in a modified bubbly isenthalpic flow model that naturally accounts, in an approximate but physical-based way, for the effects of thermal cavitation and the concentration of active nuclei. The model, able to take into account the presence of both nearly incompressible zones (pure liquid) and regions where the flow becomes highly supersonic (liquid-vapor mixtures), has been successfully validated using experimental data for the measured choked mass flow rate in convergent/divergent nozzles operating in water. The model has also been tested for calculating the flow around a modified NACA 66-109 hydrofoil at 20°C and 100°C, in a pressure-based code that uses a 2D shock-capturing semi implicit algorithm for the solution of the viscous/inviscid equations for cavitating flows on body-fitted grids (d'Agostino et al., 2001). In all cases under consideration the simulations were in satisfactory agreement with the measured data both in terms of the characteristics of the cavitation region and the shape of the surface pressure profile.

※ Rotordynamic analytical models of cavitating inducers

Because of their greater complexity, rotordynamic fluid forces in whirling and cavitating turbopump impellers have not received yet sufficient attention in the open literature and a satisfactory understanding of their behavior is still lacking. However, it is widely recognized that turbopump cavitation in axial inducers can promote the onset of dangerous self-sustained whirl instabilities, and the available experimental evidence indicates that inducer cavitation reduces the magnitude of the rotordynamic fluid forces, significantly affecting the added mass of the rotor. A second major effect of inducer cavitation is the introduction of a complex oscillatory dependence of the rotordynamic fluid forces on the whirl frequency, due to the occurrence of resonance phenomena in the compressible cavitating flow inside the blade channels under the excitation imposed by the eccentric motion of the rotor. On the other hand, no significant resonant phenomena seem to occur in whirling radial impellers, where the

limited available evidence indicates that cavitation only has a marginal effect on rotordynamic whirl forces.

For better understanding the physical phenomena at the basis of these findings, an effort was started at Alta S.p.A. for developing a simplified model of the cavitating flow on whirling machines. The model is based on rather stringent assumptions: the cavitation is considered as a thin layer attached to the pump blades; the sound speed in the two-phase mixture is calculated by applying the equations for homogeneous liquid/vapor mixture with thermal effects; the unperturbed flow is inviscid, incompressible and fully-guided, with zero radial velocity and uniform axial velocity. The resulting ODEs are obtained by writing the first-order linearized Laplace equation in the rotating coordinate system, and solved by separation of variables.

The model has been applied to both the cases of multi-bladed axial helical inducers (d'Agostino and Venturini-Autieri, 2002) and radial impellers with logarithmic-spiral blades (d'Agostino and Venturini-Autieri, 2003). In particular, for the case of axial inducers, the simplified equations were able to successfully predict the occurrence of resonance peaks for definite values of the whirl ratio, and their dependence on the extent of cavitation. Figure 9 shows a sample case for the rotordynamic radial force on a 3-bladed inducer having a tip blade angle of 9°, a tip radius of 50.5 mm and a constant hub radius of 20.2 mm.

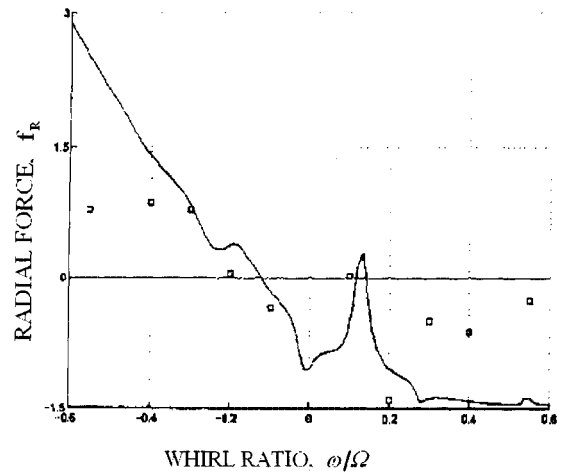

Fig. 9 Comparison of the normalized rotordynamic radial force obtained by experiments (circles) and by the simplified model (solid line) for a 9° helical inducer ($\phi = 0.049, \sigma = 0.106, e = 0.254$mm)

※ Reduced order model of inducer flow and performance

A reduced order model for the preliminary design and noncavitating performance prediction of tapered axial inducers has been recently developed (d'Agostino et al., 2008a). In the incompressible, inviscid, irrotational flow approximation, the model expresses the 3D flow field in the blade channels by superposing a 2D cross-sectional vorticity correction to a fully-guided axisymmetric flow with radially uniform axial velocity. Suitable redefinition of the diffusion factor for bladings with non-negligible radial flow allows for the control of the blade loading and the estimate of the boundary layer blockage at the specified design flow coefficient, providing a simple criterion for matching the hub profile to the axial variation of the blade pitch angle. Carter's rule is employed to account for flow deviation at the inducer trailing edge. Mass continuity, angular momentum conservation and Euler's equation are used to derive a simple 2nd order boundary value problem which can be solved numerically for the far field axisymmetric flow at the inducer discharge. Alternatively, a closed form approximate solution is possible by suitable simplification of the equations, which proved to yield equivalently accurate results in the prediction of the inducer performance. Starting from the results obtained for the inducer flow, the noncavitating pumping performance of the inducer is obtained by introducing suitably adapted correlations of pressure losses and flow deviation effects.

The model has been successfully validated by comparing its performance prediction to the experimental results obtained in the CPRTF for the MK1 and FAST2 inducers, as well as those related to several inducers tested in Japanese facilities and documented in the open literature. As an example, Figure 10 shows the results of this comparison in the case of the MK1 inducer.

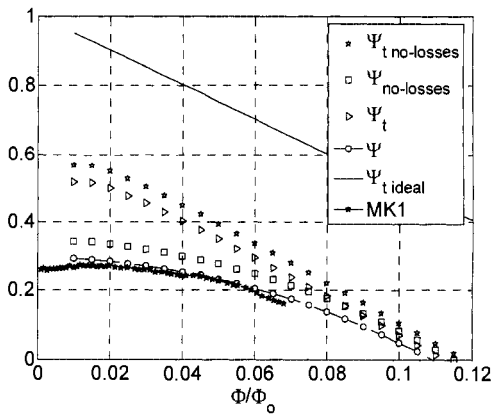

Fig. 10 Comparison between the experimental noncavitating performance of the MK1 inducer (red stars) and the predictions of the analytical model (cyan circles)

Another important characteristic of the model is the possibility of using it as a tool for the preliminary geometric definition and operational design of new tapered inducers for space rocket turbopumps (d'Agostino et al., 2008b). In this case, the starting point of the design

process is represented by the required values for the main inducer geometrical and operational parameters: number of blades, tip radius, inlet tip blade angle, inlet and outlet hub radii, axial length and design flow coefficient. The final result is the detailed inducer geometry in terms of hub shape, blade angle (or pitch) axial schedule, and tip solidity. As an example, Figure 11 shows the rendering of a 3-bladed inducer designed by means of the above model. The inducer has a tip radius of 81 mm, a hub radius of 44.5 mm at the inlet and 58.5 mm at the outlet, a tip blade angle of 6.9° at the inlet and 25.42° at the outlet and a tip solidity of 2.03.

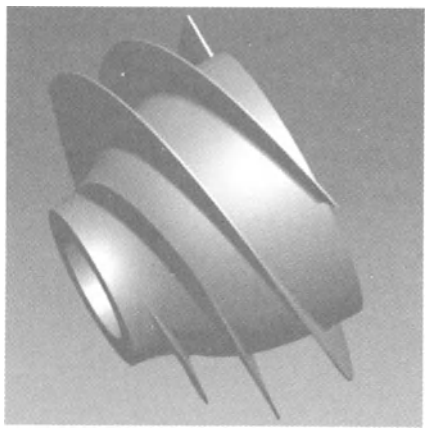

Fig. 11 Computer rendering of a 3-bladed inducer designed by means of the reduced order analytical model

4 Conclusions

In the last two decades a significant experience has been gained by the Chemical Propulsion research group at University of Pisa, Centrospazio and Alta S.p.A. in the field of cavitation, flow instabilities and rotordynamic phenomena on space rocket turbopumps. The combined use of experimental activities and reduced order analytical models, capable of capturing the most significant features of the physical phenomena and their dependence on the relevant geometrical and operational parameters, have provided the possibility of characterizing the behavior of different axial inducers and test bodies, developing advanced test procedures, and better understanding some of the fundamental principles on which the rational and effective design of space rocket turbomachines components can be based. Consequently, the main effort for the future consists in the improvement of the design of the most challenging among these components, in particular axial inducers, both in terms of pumping performance and reduction of the cavitation extent and its undesired negative effects, including flow instabilities.

Acknowledgements

The research activities presented in this paper have been supported and funded by European Space Agency and Italian Space Agency contracts, as well as collaborations with Centro Italiano Ricerche Aerospaziali (CIRA) and Avio S.p.A. The authors would like to express their gratitude to Profs. Mariano Andrenucci, Renzo Lazzeretti and Fabrizio Paganucci of the Dipartimento di Ingegneria Aerospaziale, Università di Pisa, Italy, for their constant and friendly encouragement. A special acknowledgement goes to all the students and colleagues who have joined the research group throughout the years, giving their precious support and invaluable contributions.

References

Braisted D.M., Brennen C.E., 1980, "Auto-oscillation of Cavitating Inducers", *Polyphase Flow and Transport Technology*, ed. R.A. Bajura, ASME Publ., New York, pp. 157 – 166

Brennen C.E.,Acosta A.J., 1973, "Theoretical, Quasi-Static Analysis of Cavitation Compliance in Turbopumps", *J. Spacecrafts & Rockets*, Vol. 10, No. 3, pp. 175 – 180

Brennen C.E., Acosta A.J., 1976, "The Dynamic Transfer Function for a Cavitating Inducer", *ASME J. Fluids Eng.*, Vol. 98, pp. 182 – 191

Brennen C.E., 1994, "Hydrodynamics of Pumps", *Concepts ETI, Inc. and Oxford University Press*

Cervone A., Testa R., Bramanti C., Rapposelli E., d'Agostino L., 2005, "Thermal Effects on Cavitation Instabilities in Helical Inducers", *AIAA Journal of Propulsion and Power*, Vol. 21, No. 5, pp. 893 – 899

Cervone A., Bramanti C., Rapposelli E., d'Agostino L., 2006a, "Thermal Cavitation Experiments on a NACA 0015 Hydrofoil", *ASME Journal of Fluids Engineering*, Vol. 128, Is. 2, pp. 326 – 331

Cervone A., Torre L., Bramanti C., Rapposelli E., d'Agostino L., 2006b, "Experimental Characterization of Cavitation Instabilities in a Two-Bladed Axial Inducer", *AIAA Journal of Propulsion and Power*, Vol. 22, No. 6, pp. 1389 – 1395

Cervone A., Bramanti C., Torre L., Fotino D., d'Agostino L., 2007, "Setup of a High-Speed Optical System for the Characterization of Flow Instabilities Generated by Cavitation", *ASME Journal of Fluids Engineering*, Vol. 129, Is. 7, pp. 877 – 885

d'Agostino L., Rapposelli E., Pascarella C., Ciucci A., 2001, "A Modified Bubbly Isenthalpic Model for Numerical Simulation of Cavitating Flows", AIAA Paper 2001 – 3402, *37th AIAA/ ASME/SAE/ASEE Joint Propulsion Conference*, Salt Lake City, USA

d'Agostino L., Venturini-Autieri M.R., 2002, "Three-Dimensional Analysis of Rotordynamic Fluid Forces on Whirling and Cavitating Finite-Length Inducers", *9th Int. Symp. on Transport Phenomena and Dynamics of Rotating Machinery (ISROMAC-9)*, Honolulu, USA

d'Agostino L., Venturini-Autieri M.R., 2003, "Rotordynamic Fluid Forces on Whirling and Cavitating Radial Impellers", *CAV 2003-5th International Symposium on Cavitation*, Osaka, Japan

d'Agostino L., Torre L., Pasini A., Cervone A., 2008a, "A Reduced Order Model for Preliminary Design and Performance Prediction of Tapered Inducers", *The 12th International Symposium on Transport Phenomena and Dynamics of Rotating Machinery*, Honolulu, USA

d'Agostino L., Torre L., Pasini A., Baccarella D., Cervone A., Milani A., 2008b, "A Reduced Order Model for Preliminary Design and Performance Prediction of Tapered Inducers: Comparison with Numerical Simulations", *44th AIAA/ASME/SAE/ASEE Joint Propulsion Conference*, Hartford, USA

Goirand B., Mertz A.L., Jousselin F., Rebattet C., 1992, "Experimental Investigations of Radial Loads Induced by Partial Cavitation with Liquid Hydrogen Inducer", *IMechE*, C453/056, pp. 263 – 269

Kamijo K., Yoshida M., Tsujimoto Y., 1993, "Hydraulic and Mechanical Performance of LE-7 LOX Pump Inducer", *AIAA J. Propulsion & Power*, Vol. 9, No. 6, pp. 819 – 826

Rapposelli E., Cervone A., d'Agostino L., 2002, "A New Cavitating Pump Rotordynamic Test Facility", AIAA Paper 2002 – 4285, *38th AIAA/ASME/SAE/ASEE Joint Propulsion Conference*, Indianapolis, USA

Rapposelli E., d'Agostino L., 2003, "A Barotropic Cavitation Model with Thermal Effects", *CAV 2003–5th International Symposium on Cavitation*, Osaka, Japan

Rubin S., 1966, "Longitudinal Instability of Liquid Rockets due to Propulsion Feedback (POGO)", *J. of Spacecraft and Rockets*, Vol.3, No. 8, pp.1188 – 1195

Ryan R.S., Gross L.A., Mills D., Michell P., 1994, "The Space Shuttle Main Engine Liquid Oxygen Pump High-Synchronous Vibration Issue, the Problem, the Resolution Approach, the Solution", *AIAA Paper 94-3153, 30th AIAA/ASME/SAE/ASEE Joint Propulsion Conference*, Indianapolis, USA

Stripling L.B., Acosta A.J., 1962, "Cavitation in Turbopumps—Part 1", *ASME J. Basic Eng.*, Vol. 84, pp. 326 – 338

Tsujimoto Y., Semenov Y. A., 2002, "New Types of Cavitation Instabilities in Inducers", *4th Int. Conf. on Launcher Technology*, Liege, Belgium

The 4th International Symposium on Fluid Machinery and Fluid Engineering
November 24-27, 2008, Beijing, China
NO. 4ISFMFE-IL18

Decelerated Swirling Flow Control in the Discharge Cone of Francis Turbines

Romeo Susan-Resiga[*1] and Sebastian Muntean[2]

[*1] Dept. of Hydraulic Machinery and National Center for Engineering of Systems with Complex Fluids
"Politehnica" University of Timisoara
Bvd. Mihai Viteazu, No. 1, Timisoara, 300222, Romania
Tel: +40-256-403692 / Fax: +40-256-403692
E-mail: resiga@mh.mec.upt.ro (Corresponding Author)

[2] Hydrodynamics and Cavitation Laboratory, Center for Advanced Research in Engineering Science
Romanian Academy — Timisoara Branch
Bvd. Mihai Viteazu, No. 24, Timisoara, 300223, Romania
Tel: +40-256-491816 / Fax: +40-256-491816
E-mail: seby@acad-tim.tm.edu.ro

Abstract The decelerated swirling flow in the draft tube cone of Francis turbines is a complex hydrodynamic phenomenon, particularly when the turbine is operated at partial discharge. In this case, the self-induced instability of an incoming steady axisymmetric swirling flow evolves into a three-dimensional unsteady flow field, with precessing helical vortex (also called vortex rope) and associated severe pressure fluctuations. The paper presents the development of a swirling flow apparatus designed to generate the same flow conditions as in a Francis turbine at partial discharge, with corresponding helical vortex breakdown in a conical diffuser. This experimental setup allows the investigation of a novel flow control method aimed at mitigating the precessing vortex rope by injecting a water jet along the cone axis. Earlier investigations considered a high speed jet, with relatively small discharge, for stabilizing the flow. However, further parametric studies revealed that a jet with a discharge of up to 10% the turbine discharge and velocity close to the average value at the turbine throat is more effective for mitigating the quasi-stagnant central region associated with the vortex rope. It is shown in this paper that such a control jet can be produced by using a flow feedback method, where a fraction of the discharge is collected from downstream the cone wall and injected upstream along the axis without any additional energy input.

Keywords francis turbine, vortex rope, swirling flow control, axial control jet, flow feedback

Nomenclature

p	static pressure
p_0	total pressure
Q	volumetric flow rate
r	radial coordinate
V_z, V_θ	axial and circumferential velocity components
z	axial coordinate

Greek symbols

α	absolute flow angle
β	relative flow angle
ρ	density
ψ	Stoke's streamfunction
ω	runner angular velocity

Superscripts

(1)	survey section downstream guide vanes
(2)	survey section downstream free runner

1 Introduction

Modern Francis turbines tend to be operated over an extended range of regimes quite far from the best efficiency point because of the variable demand on the energy market which require a great flexibility in operating hydraulic turbines. Therefore, such turbines with fixed pitch runner have a high level of residual swirl at the draft

tube inlet as a result of the mismatch between the swirl generated by the guide vanes and the angular momentum extracted by the runner. When decelerating this swirling flow in the draft tube cone the flow becomes unstable, leading to a helical vortex breakdown, also called precessing vortex rope in the engineering literature. This hydrodynamic phenomenon leads to severe pressure fluctuations that hinder the turbine operation.

It was only recently shown by Zhang et al. (2005) that the vortex rope is formed as a result of the absolute instability of the swirling flow in the turbine's draft tube cone. By performing a stability study on the swirling flow downstream a Francis runner, Susan-Resiga et al. (2006 a) found that the flow becomes unstable as the turbine discharge decreases, and the eigenmodes develop mostly near the symmetry axis. This prompted the idea of injecting a water jet, from the runner crown downstream along the machine axis in order the remove the main cause of the flow instability associated with the severe flow deceleration in the axis. The water jet injection has been proved successful in mitigating the vortex rope and the corresponding pressure fluctuation, Susan-Resiga et al. (2006b), Zhang et al. (2007). As a practical implementation, Susan-Resiga et al. (2006 b) proposed that the jet be supplied with a fraction of the turbine discharge taken from upstream the spiral case. This approach has the benefit of producing a high speed water jet, corresponding to the turbine head, but the jet discharge bypasses the runner and therefore introduces additional volumetric losses. Further parametric studies revealed that a more effective swirling flow control should use a jet with lower velocity and larger discharge, around 10% from the overall turbine discharge. Obviously it is not acceptable to bypass the runner with such a large fraction of the turbine discharge. However, Susan-Resiga et al. (2007) have identified a flow feedback approach for the draft tube cone which allows the control jet to be supplied without any additional losses in the turbine. Moreover, as shown in this paper as well, the hydraulic losses in the draft tube cone are significantly reduced while increasing the pressure recovery.

In this paper, we first present the development of a swirling flow apparatus designed to reproduce the flow conditions encountered in Francis turbine's draft tube cone when operated at partial discharge, as well as to test various flow control approaches using water jet injection. The overall test rig and a previous version of the apparatus are detailed in Susan-Resiga et al. (2007). Here we present a different setup, with swirling flow generated by guide vanes followed by a free runner. The resulting swirling flow further downstream in the conical diffuser is compared against measurements on a Francis turbine model operated at partial discharge. Finally, we present our flow feedback method and show numerically that it can remove the quasi-stagnant region associated with the vortex rope without any additional energy input in the system.

2 Swirling Flow Apparatus

The swirling flow apparatus developed at the Politehnica University of Timisoara—National Center for Engineering of Systems with Complex Fluids is shown in Fig. 1.

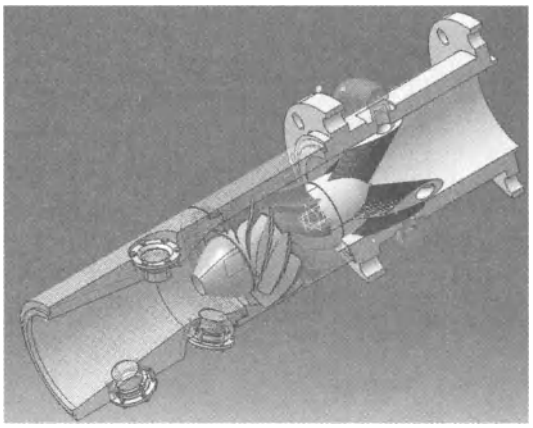

Fig. 1 Three-dimensional cross-section of the swirling flow apparatus, with swirl generator and test section

The swirl generator ensemble has an upstream ogive with four forward leaned strouts, followed by a set of guide vanes and a free runner, and ending with a nozzle. The control water jet issued from the nozzle is supplied through the hollow strouts. The test section has a convergent-divergent shape, and three optical windows have been installed for Laser Doppler Velocimetry investigations of the velocity profiles. This particular setup is aimed at producing a swirling flow at the throat section similar to the one encountered in Francis turbines operated at partial discharge.

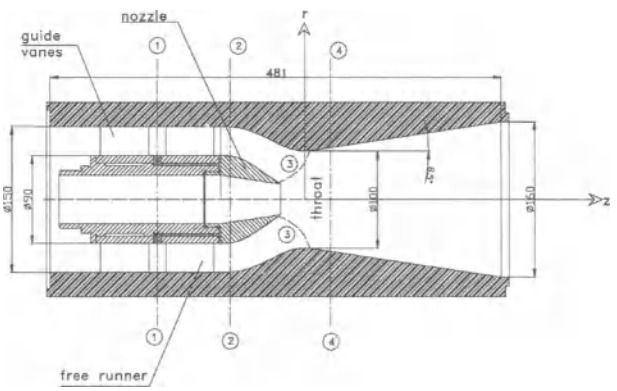

Fig. 2 Cross-section of the swirling flow apparatus, and the four survey sections: S1 – downstream guide vanes, S2 – downstream free runner, S3 – circular section, S4 – upstream conical diffuser

A cross section of the swirling flow apparatus is shown in Fig. 2, with the main dimensions. The throat diameter is 100 mm, with a nominal discharge of 30 liter/sec. The conical diffuser has a 8.5° half-angle and 200 mm in length. The design of the convergent-divergent test section is presented in Bosioc et al. (2008), and it has been manufactured from plexiglass in order to allow flow visualization. The closed loop test rig allows the overall pressure setup such that we can visualize the cavitating vortex rope.

3 Swirling Flow Design and Analysis

The first version of the swirl generator, Susan-Resiga et al. (2007) used only fixed guide vanes. However, this setup produces a flow with practically constant total pressure, which is not the case downstream the Francis runners when operated at partial discharge. The analysis of the swirling flow computed by Stein et al. (2006) and measured by Ciocan et al. (2007), for the Francis turbine investigated in the FLINDT project, Avellan (2000), shows that there is a total pressure excess near the band at runner outlet and a corresponding deficit near the crown. As a result, we found that at the inlet of the convergent part of our test section both axial and circumferential velocity profiles must increase monotonically from hub to shroud. This swirling flow configuration cannot be achieved by a single stationary row of blades, thus we have developed the configuration shown in Figs. 1 and 2.

In order to compute the velocity profiles for the swirl downstream guide vanes, we assume an inviscid flow and use the constant total pressure condition,

$$\frac{p_0^{(1)}}{\rho} \equiv \frac{p^{(1)}}{\rho} + \frac{\left(V_z^{(1)}\right)^2}{2} + \frac{\left(V_\theta^{(1)}\right)^2}{2} = \text{const.}, \tag{1}$$

together with the radial equilibrium equation,

$$\frac{dp}{dr} = \frac{\rho V_\theta^2}{r}. \tag{2}$$

By introducing the absolute flow angle as design parameter,

$$\frac{V_z^{(1)}(r)}{V_\theta^{(1)}(r)} = \tan\alpha^{(1)}(r), \tag{3}$$

we obtain a differential equation for the axial velocity profile,

$$\frac{dV_z^{(1)}}{dr} = \left(\frac{1}{\tan\alpha^{(1)}}\frac{d\alpha^{(1)}}{dr} - \frac{\cos^2\alpha^{(1)}}{r}\right)V_z^{(1)}. \tag{4}$$

This equation can be integrated analytically for simple $\alpha^{(1)}(r)$ variation, and the integration constant (axial velocity at the hub) is found from the overall discharge condition,

$$Q = 2\pi \int_{R_{hub}}^{R_{tip}} V_z^{(1)}(r)\, r\, dr. \tag{5}$$

The free runner downstream the guide vanes has the main purpose of re-distributing the total pressure by inducing an excess near the shroud and a corresponding deficit near the hub. The runner blade acts like a turbine near the shroud and like a pump near the hub, with a vanishing total torque. As a result, the runner of our swirl generator spins freely on the hub.

In order to compute the flow downstream the runner we use the Bernoulli equation in relative flow,

$$\begin{aligned} &p + \frac{\rho W^2}{2} - \frac{\rho U^2}{2} = p + \frac{\rho V_z^2}{2} + \frac{\rho V_\theta^2}{2} - \rho U V_\theta, \\ &= p_0 - \rho U V_\theta = f(\psi) \end{aligned} \tag{6}$$

where the Stoke's streamfunction is defined as

$$\frac{1}{r}\frac{\partial\psi}{\partial r} = V_z(r). \tag{7}$$

Within the quasi-three-dimensional approximation the relative total pressure remains constant on a streamtube,

$$\left[\frac{p_0}{\rho} - UV_\theta\right]^{(2)}(\psi) = \left[\frac{p_0}{\rho} - UV_\theta\right]^{(1)}(\psi). \tag{8}$$

After introducing the relative flow angle,

$$V_\theta^{(2)} = \omega r - \frac{V_z^{(2)}}{\tan\beta^{(2)}}, \tag{9}$$

and using the radial equilibrium condition (2), we obtain the differential equation for the axial velocity profile downstream the free runner,

$$\begin{aligned} &\frac{dV_z^{(2)}}{dr} + \left(\frac{\cos^2\beta^{(2)}}{r} - \frac{1}{\tan\beta^{(2)}}\frac{d\beta^{(2)}}{dr}\right)V_z^{(2)} \\ &= \omega\left[\sin 2\beta^{(2)} - \sin^2\beta^{(2)}\left(\frac{\sin 2\alpha^{(1)}}{2} - r\frac{d\alpha^{(1)}}{dr}\right)\right]. \end{aligned} \tag{10}$$

There are two parameters to be found, namely the axial velocity at the hub and the runner angular speed, using the overall discharge condition and the conservation of the angular momentum flux,

$$\int_{R_{hub}}^{R_{tip}} V_z^{(2)}(r)\, r\, dr = \frac{Q}{2\pi}, \tag{11a}$$

$$\int_{R_{hub}}^{R_{tip}} \left(\omega r V_\theta^{(2)}\right) V_z^{(2)} 2\pi r \, dr = \int_{R_{hub}}^{R_{tip}} \left(\omega r V_\theta^{(1)}\right) V_z^{(1)} 2\pi r \, dr. \qquad (11b)$$

The system of equations (11a) and (11b) is solved numerically using the NEQNF subroutine (solve a system of nonlinear equations using a modified Powell algorithm and a finite-difference approximation of the Jacobian) from the IMSL library to obtain the $V_{z\,hub}^{(2)}$ and ω values, with $V_z^{(2)}$ obtained by integrating Eq.(10) with specified $\alpha^{(1)}(r)$ and $\beta^{(2)}(r)$, while $V_\theta^{(2)}$ is given by (9).

We have assumed a linear variation from hub to shroud for both relative and absolute flow angles, and have performed a parametric study by varying the flow angle values at hub and shroud, respectively. The final values chosen for further guide blade design are $\alpha_{hub}^{(1)} = 45^\circ$ and $\alpha_{tip}^{(1)} = 60^\circ$, while for the runner blade we have chosen $\beta_{hub}^{(2)} = 25^\circ$ and $\beta_{tip}^{(2)} = 55^\circ$. The actual blade design details are presented in Susan-Resiga et al. (2008 b).

Figure 3 shows the axial and circumferential velocity profiles designed for the swirling flow downstream the guide vanes (dashed lines) and the corresponding velocity profiles obtained after a turbulent 3D flow analysis of the guide vanes. One can see that the swirl has a free-vortex configuration, with quasi-constant axial velocity.

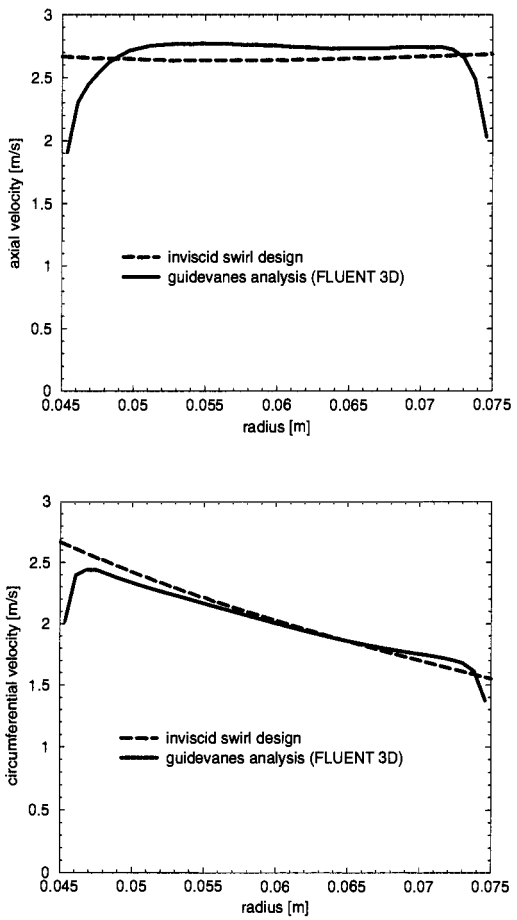

Fig. 3 Axial and circumferential velocity profiles at survey section S1 downstream the guide vanes

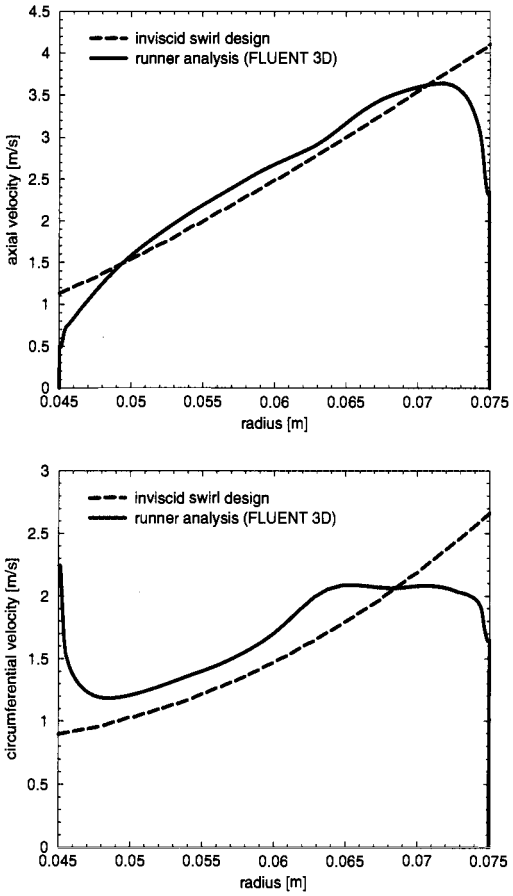

Fig. 4 Axial and circumferential velocity profiles at survey section S2 downstream the free runner

The design of the runner blades is more difficult because of the turbine behaviour near the hub and pump near the shroud. Figure 4 shows the inviscid design of the swirl (dashed lines) and the actual velocity profiles from the turbulent 3D analysis of the runner blades. Although the axial velocity closely follows the intended profile, the circumferential velocity cannot reach the intended value near the shroud. However, this swirling flow is further used to assess the flow field in the test section, using a 2D axisymmetric turbulent swirling flow model developed and validated in Susan-Resiga et al. (2008 b).

Once the flow is computed within the domain shown in Fig. 5, we examine the velocity profiles in two survey sections, S3 and S4, shown in Fig. 2.

The survey section S3 corresponds to the similar one downstream the runner blades of the FLINDT turbine, and the numerical results for the meridian and circumferential velocity components, calculated by Stein at al. (2006), are

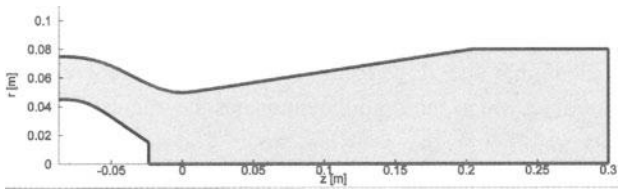

Fig. 5 Computational domain in a meridian half-plane for the swirl apparatus test section

showed with dashed lines in Fig. 6. The solid lines are the velocity profiles obtained with the upstream swirl from Fig. 5. It is clear that the swirl in our apparatus has similar characteristics to the one in a Francis model turbine operated at part load.

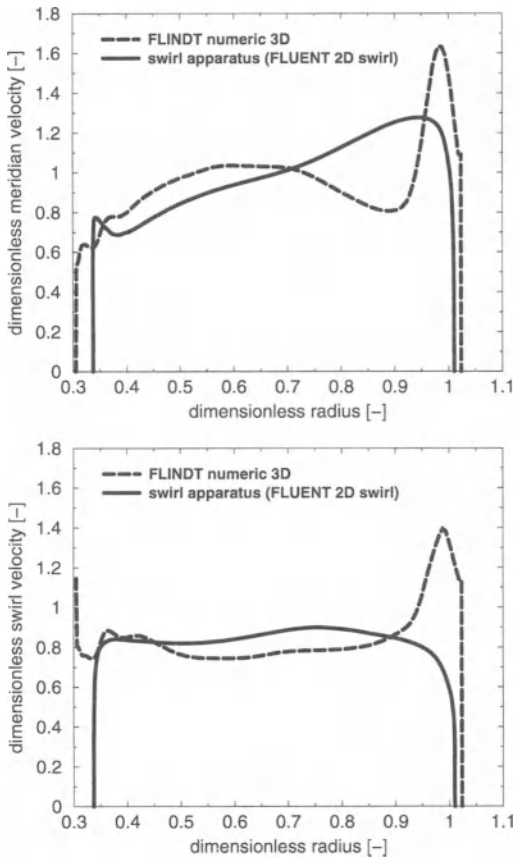

Fig. 6 Axial and circumferential velocity profiles at survey section S3

The survey section S4 is located immediately downstream the throat section, where LDV measurements for the axial and circumferential velocity profiles have been performed by Ciocan et al. (2007). The velocity profiles computed for our swirl generator are in close agreement with the measured one, insuring that the flow further downstream into the conical diffuser will have the same characteristics as the one in the Francis turbine model.

The data in Figs. 6 and 7 are made dimensionless, with respect to the throat radius and throat average discharge velocity, in order to allow the comparison of the flow field in our swirl generator with the Francis turbine model. Further details on the flow field are discussed in the next section.

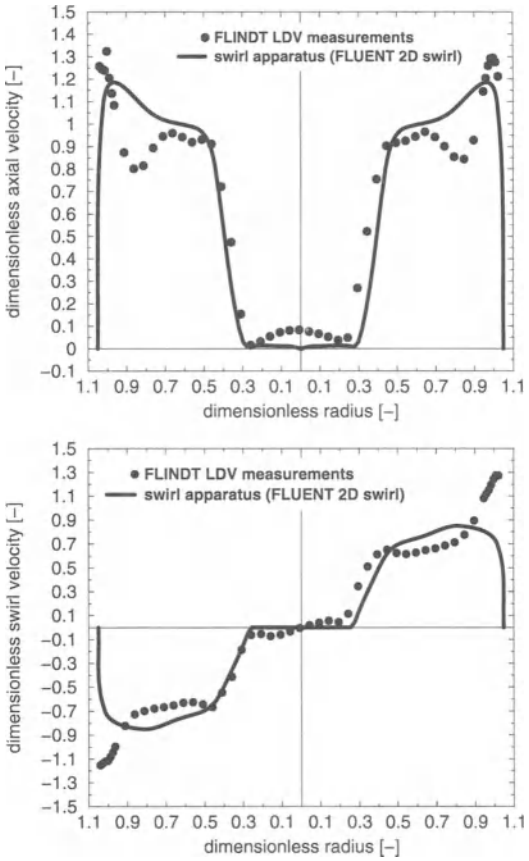

Fig. 7 Axial and circumferential velocity profiles at survey section S4 in the conical diffuser

4 Vortex Breakdown Mitigation

As shown in Fig. 7, downstream into the conical diffuser the swirling flow develops a central quasi-stagnant region. The vortex rope is exactly wrapped around this region, as shown in Susan-Resiga et al. (2008 a). One can see the extent of this quasi-stagnant region in the streamline pattern shown in Fig. 9, upper half plane. In order to mitigate the vortex rope, this region must be significantly reduced in size or eliminated. One possibility is to energize the stagnant region near the axis by injecting a water jet along the axis, from a location upstream the throat (e.g. Francis runner crown). However, it was found that for large stagnant regions the jet must have a large discharge and a velocity comparable to the discharge velocity at the throat section. As a result, the question on

how to supply such a control jet without reducing the overall turbine efficiency must be addressed separately.

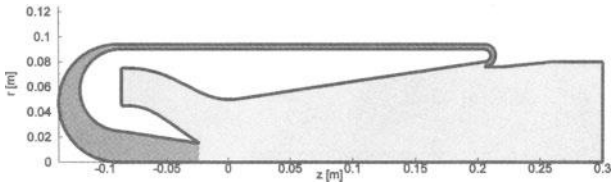

Fig. 8 Computational domain in a meridian half-plane for the swirl apparatus test section with flow feedback control system

By examining the swirling flow in the draft tube cone of Francis turbines operated at partial discharge, one can see that there is a significant excess of both static and total pressure near the cone wall, with respect to the central region near the axis. This observation led Susan-Resiga et al. (2007) to introduce a flow feedback, as shown in Fig. 8, where a fraction of the discharge is collected near the wall at the downstream end of the cone, and re-directed toward the nozzle that issues the control jet. Note that this approach does not require any additional water supply, and removes the drawback of bypassing a fraction of the turbine discharge from upstream the runner. However, it is not obvious if the jet produced through flow feedback is strong enough to remove the central stagnant region.

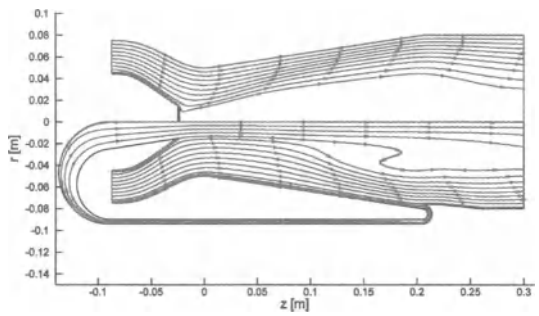

Fig. 9 Streamlines for the axisymmetric swirling flow without flow control (upper half-plane) and with flow feedback control (lower half-plane)

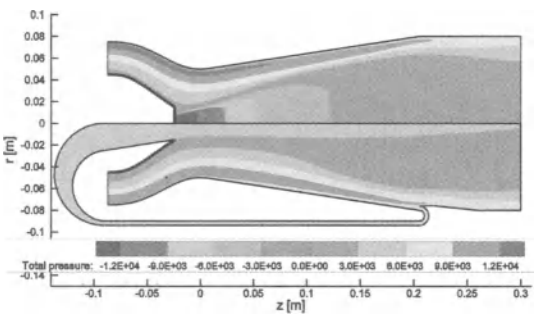

Fig. 10 Total pressure for the axisymmetric swirling flow without flow control (upper half-plane) and with flow feedback control (lower half-plane)

Figures 9 and 10 show a comparison between the swirling flow in the conical diffuser without and with jet control. It is clear that the flow feedback mechanism generates a control jet which successfully eliminates the stagnant region, thus stabilizing the swirling flow. The total pressure distribution shown in Fig. 10 emphasizes the excess of total pressure near the cone wall with respect to the central region (upper half-plane), and shows the increase in total pressure near the axis when the flow feedback is implemented.

From an engineering point of view, the diffuser must convert the dynamic pressure into static pressure with minimum loss of total pressure. In practice, one measures the wall static pressure and uses it to evaluate the wall pressure recovery coefficient. However, a more rigorous hydrodynamic analysis should employ the flow weighted averaged pressure,

$$\bar{p}(z) = \frac{\int_0^{R_{wall}} p(z,r) V_z(z,r) 2\pi r \, dr}{\int_0^{R_{wall}} V_z(z,r) 2\pi r \, dr}. \qquad (12)$$

Obviously, the same definition holds for the dynamic and total pressure, respectively. The averaged pressure values shown in Fig. 11 are made dimensionless with respect to the specific kinetic energy corresponding to the throat discharge velocity (without jet control) and the axial coordinate is made dimensionless with respect to the throat radius.

Figure 11 shows with solid lines the distribution along the conical diffuser of the flow weighted averaged static, dynamic and total pressure when no flow control is employed. The average static pressure increases almost at a constant rate over the whole diffuser length, with a

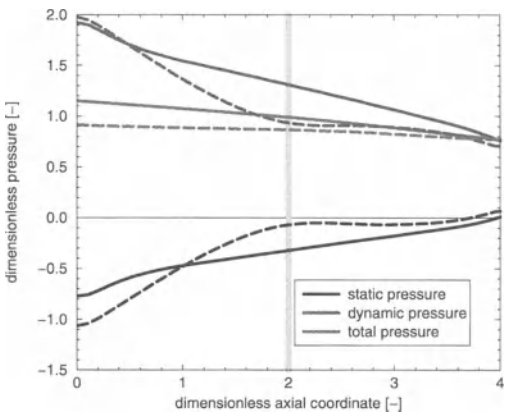

Fig. 11 Static, dynamic and total pressure evolution in the conical diffuser. Solid lines without flow control, dashed lines with flow feedback

corresponding decrease in dynamic pressure. The total pressure monotonically decreases corresponding to the viscous losses. On the other hand, as shown with dashed lines in Fig. 11, the static pressure recovery is significantly improved while reducing the loss of total pressure when the jet control with flow feedback is employed. Moreover, with flow control the conversion of dynamic pressure into static pressure takes place practically on the upstream half of the diffuser, over a length equal to the throat diameter. As a result, such flow control approaches allow the use of more compact turbine discharge cones.

Table 1 presents quantitatively the benefits of employing the above flow control approach. One can see that for the first half of the conical diffuser the losses are reduced by 70% while increasing the pressure recovery by 120%. For the whole diffuser length we still have a 63% reduction in the overall hydraulic loss, while increasing the pressure recovery by 43%. One can conclude that using the jet flow control approach allows the use of shorter, more compact, conical diffusers in hydraulic turbines while retaining good performances over an extended operating range.

Table 1 Total pressure loss and static pressure recovery

	$\Delta\overline{p}_{tot} = \overline{p}_{tot}^{throat} - \overline{p}_{tot}(z)$		$\Delta\overline{p} = \overline{p}(z) - \overline{p}^{throat}$	
$z =$	$2R_{throat}$	$4R_{throat}$	$2R_{throat}$	$4R_{throat}$
No flow control	1194 Pa	2802 Pa	3305 Pa	5811 Pa
With flow feedback	360 Pa (-70%)	1038 Pa (-63%)	7278 Pa (+ 120%)	8286 Pa (+43%)

The jet discharge for the flow feedback is 3.26 liter/sec., representing 10.86 % from the inlet discharge. This value of the jet discharge is self-adjusting with the operating regime. When approaching the best efficiency operating point, the swirl intensity decreases, and the difference in pressure between the cone wall and the axis decreases, thus reducing the jet discharge.

5 Conclusions

We present in this paper the design and analysis of a swirling flow generator that produces a swirling flow with helical vortex breakdown in a conical diffuser, quite similar to the flow encountered in Francis turbines draft tube cone when operating at partial discharge. A novel solution is proposed and analyzed for supplying the control jet that stabilizes the swirling flow, thus mitigating the vortex rope and its associated pressure fluctuations.

The flow feedback approach we propose takes a fraction of the discharge near the cone wall and re-directs it toward the jet nozzle. It is shown that the jet discharge adjusts itself to more than 10% of the overall swirling flow discharge, thus successfully removing the central stagnant region. As a result, the overall performances of the conical diffuser with swirl are significantly improved by reducing the hydraulic losses while increasing the pressure recovery. Moreover, the present flow control approach allows the use of shorter, more compact, conical diffusers in hydraulic turbines with improved hydraulic performances over an extended operating range.

The axisymmetric turbulent flow analysis used in this paper does not allow the evaluation of pressure fluctuations associated with the vortex rope. However, the mitigation of the central stagnant region associated with the precessing vortex rope allows us to infer the significant reduction or elimination of the pressure fluctuations.

Acknowledgements

The present research was supported by the Romanian National Authority for Scientific Research through the CEEX-C2-M1-1185 "iSMART-Flow" and by the Swiss National Science Foundation through the SCOPES Joint Research Project IB7320-110942/1. The authors take this opportunity to thank the partners in the FLINDT Project Eureka No. 1625, Alstom Hydro, Electricité de France, GE Hydro, VA Tech Hydro, Voith-Siemens Hydro, PSEL (Funds for Projects and Studies of the Swiss Electric Utilities), and the CTI (Commission for Technology and Innovation) for the experimental data used in the present paper.

References

Avellan, F., 2000, "Flow Investigation in a Francis Draft Tube: the FLINDT Project", Proc. 20th IAHR Symposium on Hydraulic Machinery and Systems, Charlotte, U.S.A., Paper DES-11

Bosioc, A., Susan-Resiga, R., and Muntean, S., 2008, "Design and Manufacturing of a Convergent-Divergent Section for Swirling Flow Apparatus", Proc. 4th German-Romanian Workshop on Turbomachinery Hydrodynamics, GROWTH-4, Stuttgart, Germany

Ciocan, G. D., Iliescu, M.S., Vu, T. C., Nennemann, B., and Avellan, F., 2007,"Experimental Study and Numerical Simulation of the FLINDT Draft Tube Rotating Vortex", Journal of Fluids Engineering, Vol. 129, pp. 146 – 158

Stein, P., Sick, M., Doerfler, P., White, P., and Braune, A., 2006, "Numerical Simulation of the Cavitating Draft Tube Vortex in a Francis Turbine", Proc. 23rd IAHR Symposium on Hydraulic Machinery and Systems, Yokohama, Japan, paper F228

Susan-Resiga, R., Ciocan, G. D., Anton, I., and Avellan, F., 2006 a, "Analysis of the Swirling Flow Downstream a Francis Turbine Runner", Journal of Fluids Engineering, Vol. 128, pp. 177 – 189

Susan-Resiga, R., Vu, T. C., Muntean, S., Ciocan, G. D., and Nennemann, B., 2006 b, "Jet Control of the Draft Tube Vortex Rope in Francis Turbines at Partial Discharge", Proc. 23rd IAHR Symposium on Hydraulic Machinery and Systems, Yokohama, Japan, paper F192

Susan-Resiga, R., Muntean, S., Bosioc, A., Stuparu, A., Milos, T., Baya, A., Bernad, S., and Anton, L. E., 2007, "Swirling Flow Apparatus and Test Rig for Flow Control in Hydraulic Turbines", Proc. 2nd IAHR Int. Meeting of the Workgroup on Cavitation and Dynamic Problems in Hydraulic Machinery and Systems, Timisoara, Romania, Scientific Bulletin of the Politehnica University of Timisoara, Transactions on Mechanics, Tom 52(66), Fasc. 6, pp. 203 – 216

Susan-Resiga, R., Muntean, S., Stein, P., and Avellan, F., 2008 a, "Axisymmetric Swirling Flow Simulation of the Draft Tube Vortex in Francis Turbines at Partial Discharge", Proc. 24th IAHR Symposium on Hydraulic Machinery and Systems, Foz do Iguassu, Brasil

Susan-Resiga, R., Muntean, S., and Bosioc, A., 2008 b, "Blade Design for Swirling Flow Generator", Proc. 4th German-Romanian Workshop on Turbomachinery Hydrodynamics, GROWTH-4, Stuttgart, Germany

Zhang, R.-K., Cai, Q.-D., Wu, J.-W., Wu, Y.-L., Liu, S.-H., and Zhang, J., 2005, "The Physical Origin of Severe Low-Frequency Pressure Fluctuations in Giant Francis Turbines", Modern Physics Letter B, Vol. 19, No. 28-29, pp. 99 – 102

Zhang, R.-K., Mao, F., Wu, J.-Z., Chen, S.-Y., Wu, Y.-L., and Liu, S.-H., 2007, "Analysis and Control of Part-Load Unsteady Flow in Francis Turbine's Draft Tube", Proc. ASME Turbo Expo 2007, Montreal, Canada, Paper GT2007-27440

The 4th International Symposium on Fluid Machinery and Fluid Engineering
November 24-27, 2008, Beijing, China
NO. 4ISFMFE-IL25

Hydraulic Oscillations Caused by the Earthquake

Aleksandar Gajic

Faculty of Mechanical Engineering, University of Belgrade
11120 Belgrade 35, Kraljice Marije 16, Serbia
Tel / Fax: ++381-11-3370-342
E-mail: agajic@mas.bg.ac.yu

Abstract Hydraulic ooscillations caused by hydraulic, electrical or mechanical excitations may provoke very strong pressure pulsations, power fluctuations and mechanical vibrations, especially if the resonance appears. Some of the cases are described in the paper. Extremely strong and massive hydrodynamic loads in a hydraulic system may also be provoked by an earthquake, which sets in motion water masses enclosed in the system. The designer of the system should always aware in mind this fact and take appropriate measures to prevent any possible accident.

Two methods for computation of possible hydrodynamic loads in a system: the method of characteristics (MOC) and the transfer matrix method (TMM), in case of a typical earthquake (selected by the seismologists) are presented in this paper.

The theory of transient flow was applied to two cases:

- Bottom outlet of an existing dam,
- Penstock and the bottom outlet of a low-head power plant.

Keywords earthquake, oscillations, hydraulic system, loads, pressure

Nomenclature

A [m²]	flow area
a [m/s]	wave
$C = gA/a^2$	hydraulic capacitance
$\{C\}$	excitation vector
D [m]	pipe diameter
g [m/s ²]	ravity acceleration
H [m]	pressure amplitude oscillation
H [m]	piezometric head
L= 1/ ga	hydraulic inertance
[P]	transfer matrix of the branch
p [bar]	pressure
Δp [bar]	pressure oscillation
Q= v * A [m³/s]	discharge
Q [m³/s]	flow amplitude oscillations
$R = Q/gDA^2$	hydraulic resistance
$s = \sigma + i\omega$	complex frequency
t [s]	time
$[u]$	transver matrix of pipe
$\{V\}$	state vector
v [m/s]	flow velocity
x [m]	distance along the pipe
$Z = \gamma / C * s$	characteristics impedance
α [°]	pipe inclination
$\gamma = Cs\,(Ls + K)$	propagation constant
σ	coefficient of attenuation
ω	angular frequency
λ [-]	friction coefficient

Subscripts

E	end
D	downstream
U	upstream

1 Introduction

Oscillations in the hydraulic systems caused by hydraulic, electrical or mechanical excitations may provoke strong pressure pulsations, power fluctuations and mechanical vibrations, especially if the resonance appears. Maximum pressures surges during transient may influence dangerous stresses followed incidents and even accidents: destroy pipelines, valves or other hydro mechanical components and cause considerable damage and sometimes loss of human lives.

Earthquakes can be highly dangerous and destructive for manmade structures, especially in the case of hydro power plants and dams. Great damage may be caused by an earthquake, since it sets in motion huge masses of water in the tunnels and penstocks. The worst that can happen is when frequency of forced oscillations fits one of the natural frequencies of the system - and accordingly, the oscillations near to the resonant oscillations can destroy it. We should try to prevent such conditions and find the solution to such dangerous cases and its problems.

At the first glance this task looks quite futile — no one can foresee the time and place of an earthquake and whether it would hit the plant. Nor can we foresee its characteristics — frequencies, direction, duration and intensity. But our hopes are not completely destroyed — the designer can make a sensitivity analysis of possible earthquake effects upon the hydropower plant (Zienkiewicz 1964. and Jaeger 1977.) raised this issue earlier. This kind of analyses is described here, but with the use of a different approach, Gajic 1983., 1993., Obradovic at all, 1986., Gajic at all, 1984., 1986., 1986.a., Swingen at all, 1998.

2 Case studies

Hydraulic ooscillations caused by hydraulic, electrical or mechanical excitations may provoke very strong loads, followed by the accidents and incidents. Serious problems with that have occurred in more than 50 hydroelectric and thermoelectric plans, according to the author's database.

Self-excited oscillations are very dangerous, because they are always resonant. They are happened in many plans and hydraulic systems. They may be caused by the wheel gates, ball valves, guide vanes and other hydro mechanical equipment.

In the pump storage power plant, shown schematically in Fig. 1, (turbine operation: output 2×250MW, head 213 to 227m; pump operation: input 2×217 MW, head 210 to 239m) self-excited oscillations of the ball valve had occurred.

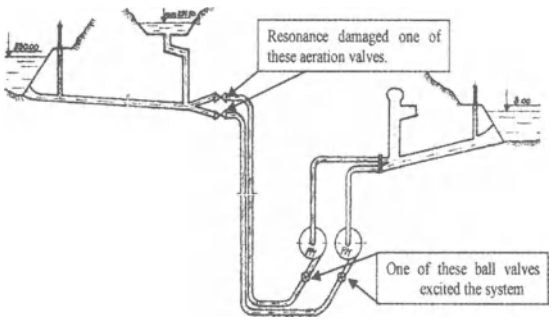

Fig. 1 Pump Storage Powerplant

Autooscillations had happened when one of the units was out of operation, with the closed its ball valve, while the other unit was running in turbine mode (; Pejovic S et all, 1986, 1986.a, 1989, 1992, Karney et all, 2003.) The damaged aeration valve is shown in Fig. 2.

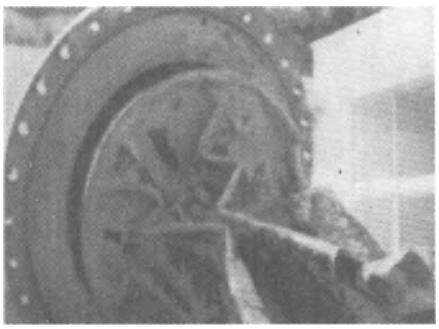

Fig. 2 Damaged aeration valve

Horizontal bulb unit, shown in Fig. 3 has had some problems with hydraulic oscillations and vibrations (see Gajic at all, 1993.a, 2003, Pejovic at all, 1992.b, 1994, Karney at all, 2003.).

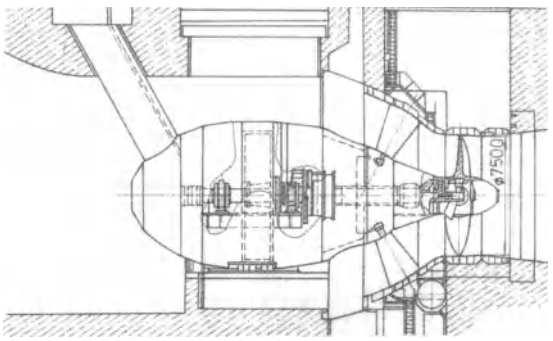

Fig. 3 Bulb unit in low head plant

The twenty bulb turbines installed, each rated at 28 MW, but have large vibrations at higher heads starting at the rated head. After app. 20 years of operation, shaft failure occurred; see Fig. 4 (Maricic at al, 2007, Pejovic at al, 2007.).

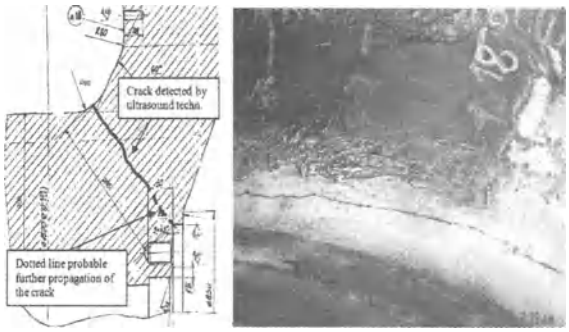

Fig. 4 Horizontal shaft crack, damaged protective coating and shaft material crack along the perimeter

Cracks on stay vanes of a large Kaplan turbine (194 MW) were caused by flow induced vibrations, see Fig. 5 (Gajic et all, 1990., 1994., 1996.)

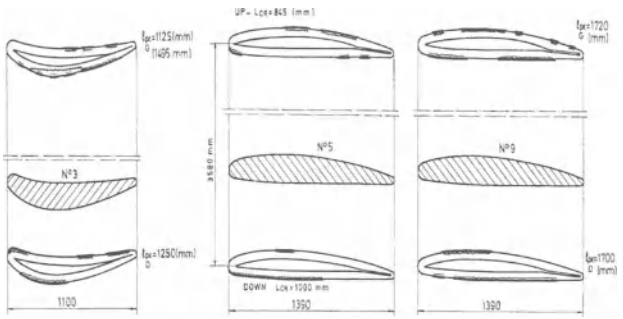

Fig. 5 Cracks on stay vanes

In many other plants resonant oscillations excited by the wheel gate leakage (Pejovic at all, 1982), draft tube surging (Pejovic at all, 1985, 1989, 1992, 1992.a, 1992.b, 1994) and other excitations had occurred. Great damage may be caused by the earthquake, since it sets in motion huge masses of water in the tunnels and penstocks, with similar and even worse consequences.

3 The Approach

These are the main steps in the analysis:

- select typical earthquakes,
- estimate the natural frequencies of the power plant (i.e., natural frequencies of hydraulic oscillations, not of mechanical vibrations),
- simulate the most dangerous situations on a mathematical model,
- rate the extent of danger in these cases and design the appropriate system of protection,
- a structural engineer must design the protection of the system.

In order to reach the useful results, there has to exist a good cooperation among these specialists. This paper presents the task of the hydraulic engineers only.

4 The Tools for Hydraulic Analysis

Two methods have been used:

- the method of characteristics (MOC),
- the transfer matrix method (TMM).

Both of the methods begin with the familiar equations on transient flow in closed conduit systems which read:

- equation of motion

$$g\frac{\partial h}{\partial x}+v\frac{\partial v}{\partial x}+\frac{\partial v}{\partial t}+\frac{\lambda|v|v}{2D}=0 \tag{1}$$

- equation of continuity

$$\frac{\partial h}{\partial t}+v\frac{\partial h}{\partial x}+\frac{a^2}{g}\frac{\partial v}{\partial x}-v\sin\alpha=0 \tag{2}$$

where: h [m] = piezometric head, v [m/s] = velocity, x [m] = distance measured along the pipe axis, t [s] = time, λ [-] = friction coefficient, D [m] = pipe diameter, g [m/s²] = gravity acceleration, a [m/s] = wavespeed, α [deg] = pipe inclination. Discharge Q is equal $Q= v * A$, while A [m²] being the flow area.

The transfer matrix method (TMM) is based upon the assumption that oscillations of pressure h' and of flow q' around there mean value are quite small. If hydraulic inertance $L = 1/g\,a$, hydraulic resistance $R = Q/gDA^2$, and hydraulic capacitance $C = gA/a^2$, and complex frequency $s = \sigma + i\omega$ (σ = coefficient of attenuation, ω = angular frequency), are introduced, one can relate the amplitudes of pressure (H) and flow (Q) oscillations at the end of a single pipe as

$$\begin{Bmatrix} H \\ Q \end{Bmatrix}_D = \begin{vmatrix} \cosh(\gamma l) & -Z_C \sinh(\gamma l) \\ \dfrac{-\sinh(\gamma l)}{Z_C} & \cosh(\gamma l) \\ & 1 \end{vmatrix} \begin{Bmatrix} H \\ Q \end{Bmatrix}_U \tag{3}$$

Here the characteristics impedance of the pipe is $Z= \gamma / C*s$, with $\gamma = Cs\,(Ls+K)$ = the propagation constant (s= complex number). Subscript "D" denotes the downstream and "U" the upstream end.

In matrix notation, this reads:

$$\{V\}_D = |U|\,\{V\}_U \tag{4}$$

The matrix U is called the transfer matrix of the pipe.

The other systems consisting of several pipes and nodes can be presented in a similar way, by

$$\{V\}_D = |U|_S\,\{V\}_U + \{C\} \tag{5}$$

The matrix **U** is the transfer matrix for the whole system, specified by multiplying matrices of unit elements in the proper way. The vector {**C**} is the excitation of the system. Further details are given in Gajic at all, 1984, 1986, 1986.a, 1996, Pejovic at all, 1986, Swingwn 1998, Wylie and Streeter, 1978.

All the necessary computations are made easy by using the digital program, regardless of the complexity or size of the given system.

The method of characteristics (MOC) deals with full equations of transient flow. These are partial differential equations of hyperbolic type, meaning that there are two sets of characteristic lines (hence the name of the method) In the plane *x, t* determined by

$$\frac{dx}{dt} = v + a \tag{6}$$

and

$$\frac{dx}{dt} = v - a \tag{7}$$

Along these lines the partial differential eqs. become ordinary ones:

$$\pm\frac{g}{a}\frac{dh}{dt} + \frac{dv}{dt} - \frac{g}{a}v\sin\alpha + \frac{\lambda|v|v}{D} = 0 \tag{8}$$

Such equations are more suitable for numerical integration. A digital computer redoes the necessary computations. The method is much more time- consuming than the previous one.

The proper choice of boundary conditions affects the solution, in both cases.

A art from the usual conditions, a new condition is introduced: the condition for a closed end. An earthquake dictates the manner of the close-end moves, with a velocity $ve = f(t)$, where the function f is taken from the time history of the typical earthquake. It can be described as movements of a piston in the same pipeline (see Gajic at all 1986, 1986.a, Obradovic at all, 1986).

The flow generated at the close-end of pipe is ΔQ (m^3/s) equal to

$$\Delta Q = \left(\vec{v}_e, \vec{A}\right) = v_e A\cos\alpha \tag{9}$$

where α is the angle between the pipe axis and the direction of earthquake movements; A [m^2] is the net flow area. Subsequently, the flow (disturbance of the system) is the greatest when $\alpha = 0$.

5 CASE I: The Bottom Outlet Of An Existing Dam

The bottom outlet of an existing dam is schematically shown in Fig. 6. A set of nodes, with adequate boundary conditions, and links represent the system, see Fig. 7. The total length is approximately 240m, with max diameter of 11,30m. The system is closed at the downstream end (node 11), where are situated two segment—type valves (total area equal to $120m^2$.)

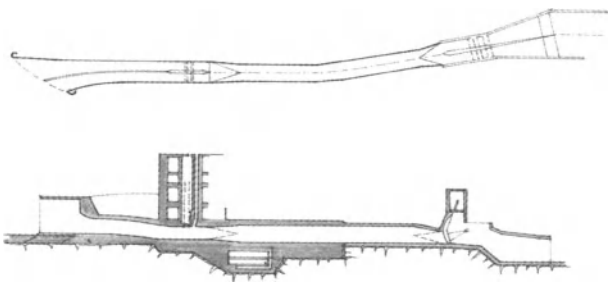

Fig. 6 Cross section of the bottom outlet

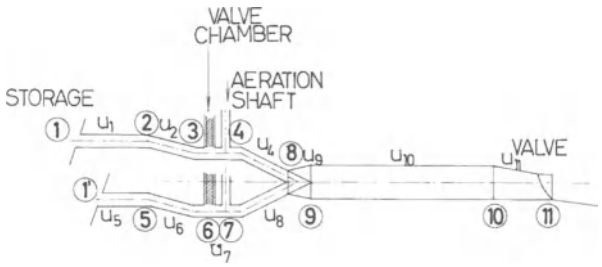

Fig. 7 Mathematical model of the bottom outlet
(Nodes: 1-storage; 2,3,5,6,9,10-conections; 11-valve; 12,13-aeration)

According to the several cases with different initial and boundary condition analyzed, hydrodynamic loads are the greatest when there is no flow (not even leakage!), i.e., the average flow is equal to zero, Q = 0.

The transfer matrix of the system is equal to

$$|u| = |u_1||u_2||u_3||P_4||u_4||P_8||u_9||u_{10}||u_{11}| \tag{10}$$

with

$$|P_8| = \begin{vmatrix} 1 & 0 \\ -f_{11}/f_{12} & 1 \end{vmatrix} \tag{11}$$

Where f_{11} and f_{12} are taken from the transfer matrix of the other branch (line 1 to 8) which reads:

$$|F| = |u_5||u_6||u_7||P_7||u_8| = \begin{vmatrix} f_{11} & f_{12} \\ f_{12} & f_{22} \end{vmatrix} \tag{12}$$

Then the matrix equation for the whole system is

$$\begin{Bmatrix} H \\ Q \end{Bmatrix}_1 = |U| \begin{Bmatrix} H \\ Q \end{Bmatrix}_{11} \tag{13}$$

with the boundary conditions:

- at the storage basin (node 1)

$$H_1 = 0 \tag{14}$$

- at the closed – end (node 11)

$$Q_{11} = \Delta Q \exp(i\phi_q) \tag{15}$$

The disturbance, ΔQ, is determined by Eq. (9), and the phase angle φq may be zero, ($\varphi q = 0$) if there is only one excitation within the system.

The impedance in the node is infinitely great, $Z_{11} = \infty$.

The angular frequency ω, could be replaced by frequency $f = \omega / (2\pi)$. The response of the system was computed, by means of varying the frequency in a rather wide range, see Fig. 8.

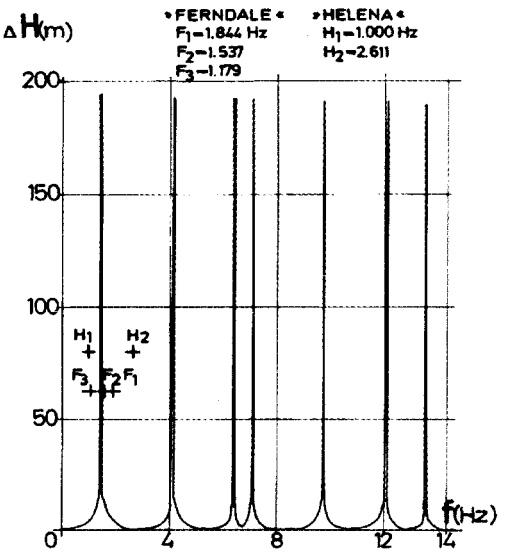

Fig. 8 Frequency response of the system (computed by TMM and compared with main frequencies of model earthquakes)

It is shown that the system has several natural frequencies within the range considered here, and the response of the system in the case of resonance should be violent.

In the meantime, the seismologist had completed the study of possible earthquakes in the region. It is concluded that the future earthquakes in this region may be similar to" FERNDALE" AND "HELENA" earthquakes.

Time histories of both earthquakes adapted from CIT, 1951 represented in Figs. 9a. and 9.b. Note that the maximum velocity was $V_{max} = 6{,}2$ cm/s for "FERNDALE" earthquake, and $V_{max} = 12,3$ cm/s for "HELENA" earthquake (which is nearly twice stronger).

The first few harmonics of both "model" earthquakes were put in the system response diagram, see Fig. 8. Note that the second harmonic of "FERNDALE" is quite close to the first natural frequency of the system (1,487Hz).The conclusion was that the "FERNDALE" might be more dangerous for the system, in spite of the fact that it's intensity is smaller!

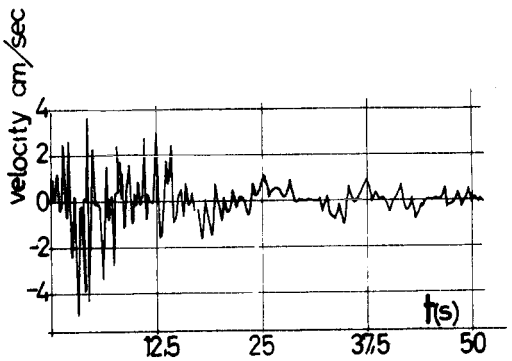

Fig. 9a Time history of Ferndale earthquake (component S44W horizontal)

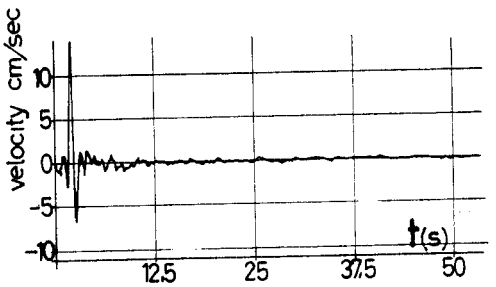

Fig. 9b Time history of Ferndale earthquake (component West horizontal)

The simulation of the same event is represented, by full equations of the transient flow (Eq. 8). The boundary condition in node 11 was $\Delta Q = AVe(t)$ (Eq. 9), i.e. the time-histories of the earthquake velocities was used.

Computed pressure oscillations (MOC) at closed valve are shown in Figs. 10a and 10b.

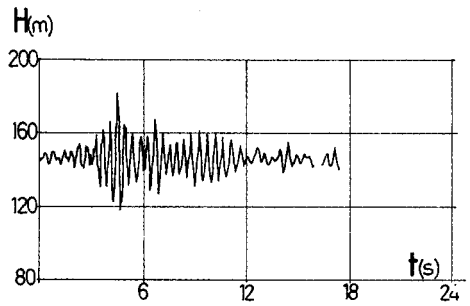

Fig. 10a Pressure oscillations at closed valve for "FERNDALE"

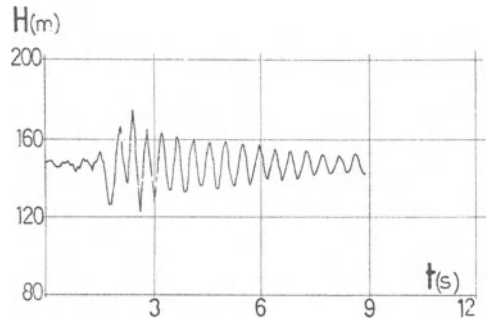

Fig. 10b Pressure oscillations at closed valve for "HELENA"

The range is acceptable app. $\Delta p = +3{,}3 / -3{,}0$ bars for "FERNDALE" and a little less $\Delta = +2{,}7/-2{,}5$ bars for "HELENA" earthquake.

The response of the system on earthquake is given in Figs. 11a and 11b.

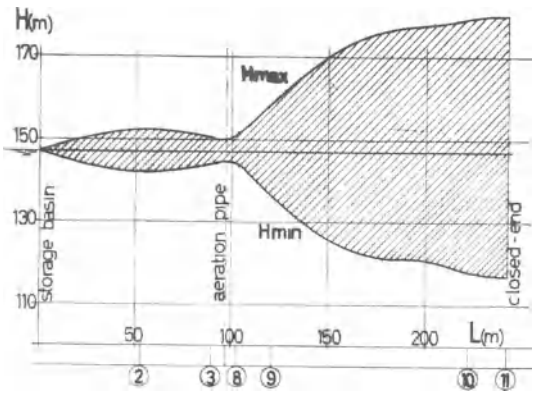

Fig. 11a Pressure oscillations at closed valve for "RNDALE"

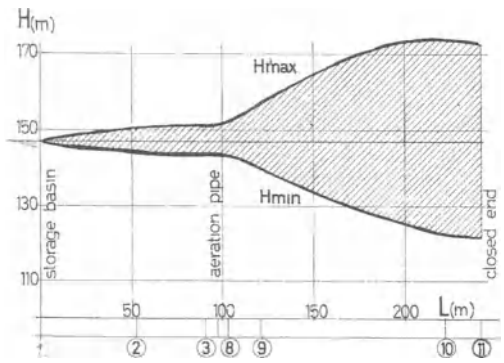

Fig. 11b Pressure oscillations at closed valve for "HELENA"

Compare Figs. 11a and 11b one can see that the shapes of pressure envelopes are quite similar, the extreme values of over and under pressures are also of the same order of magnitude. Since the designer bore in mind that these two earthquakes are rather different, he accepted these results as inputs for his part of the job, as dynamic loads on the walls of the outlets- and designed the system accordingly to withstand the strains of this order.

6 CASE II: Low-Head Hydropower Plant

The hydro power plant located in the area where a dangerous earthquake happened some 20 years before the construction of the plant. All the constructions made since that time can withstand earthquakes up to 8 degrees of Mercali scale. (i.e. acceleration up to 200cm/s²). And the design of the dam can maintain max acceleration up to 300 cm/s².

An analysis of hydrodynamic loads in the penstock and in the bottom outlet, provoked by an earthquake, is presented here.

Plant is schematically shown in Fig. 12. The basic data are: rated output 50 MW, operating head from 35 to 55 m. The penstock is around 65m long, with average diameter equal to 5,5m.

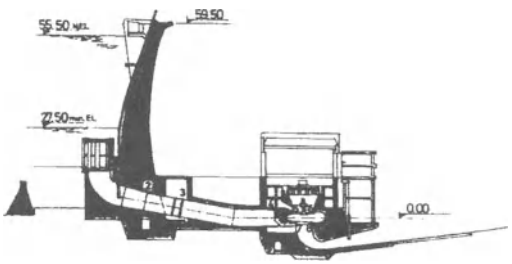

Fig. 12 Cross section through the plant

According to the procedure described before the analysis was carried out. The strong—motion records, taken during the catastrophic earthquake in Montenegro in Petrovac town 1979. Were adopted—see Fig. 13. Max velocity recorded was 40,4cm/s², max acceleration 440cm/s² and max displacement of soil 11cm. Also, several other recorded earthquakes in Bar, Budva, Ulcinj were investigated Both of the methods were applied, as in Case I. Water level in the storage basin was close to its maximum. The envelopes of pressure surges in the penstock are shown in the Fig. 8. The surges are in the range of +2,2/-2,1 bar, near the closed wicket gates. Surges caused by rapid closing down of the plant are of the same order of magnitude as these changes.

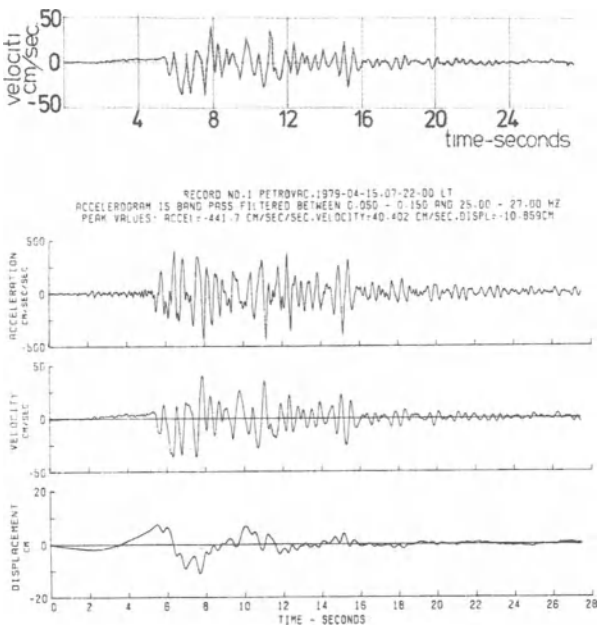

Fig. 13 Strip chart of the earthquake in Petrovac

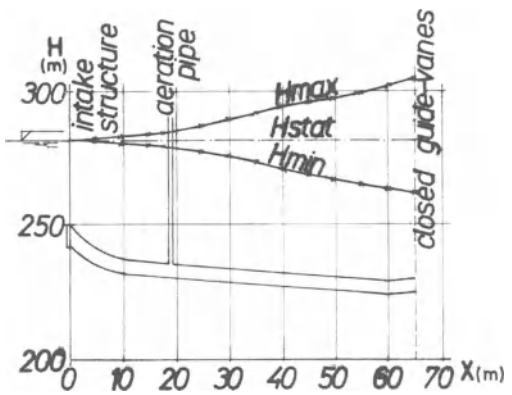

Fig. 14 Pressure envelopes in the penstock (earthquake Petrovac)

The similar analysis for the bottom outlet is presented. The outlet is 10m longer than the penstock and has the average diameter of 3,4m, see Fig. 15.

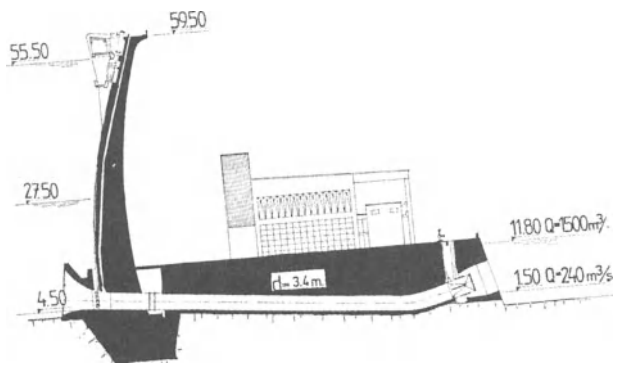

Fig. 15 Cross section through the bottom outlet

Pressure envelopes—for the same initial conditions as before- are represented in Fig. 16. The amplitudes are the strongest at the closed gate (this is a dead-end) where they attain -5,3 bar/ -5,7 bar. At the section about 10m long the cavitation appears, starting from the closed gate, see Fig. 16a.

Vacuum will appear in a much larger portion of the outlet- some 50m, and the cavity could be 40m long, if the water level in the storage basin is at the lowest mark, see Fig. 16b. Nevertheless, it can be presupposed that this vacuum will not damage the pipe because it is very short-lived; the frequency of pressure oscillations is rather high.

By varying the frequency over rather a wide range the pressure oscillations in the system was computed and it can be seen that several natural frequencies are within the range of earthquake excitations. Therefore the response of the system in the case of resonance could be violent (Fig. 17a and 17b). Finally, the discharge through the system has very strong influence on pressure oscillations. Max amplitudes in the bottom outlet decrease rapidly with the raise of the discharge thought it, see Fig. 18.

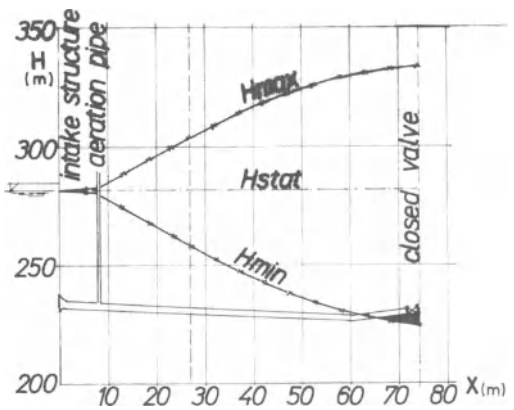

Fig. 16a Pressure envelopes in the bottom outlet for maximum water level in the storage (earthquake Petrovac)

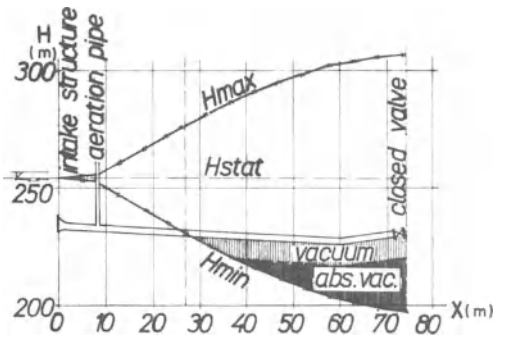

Fig. 16b Pressure envelopes in the bottom outlet for min. water level in the storage (earthquake Petrovac)

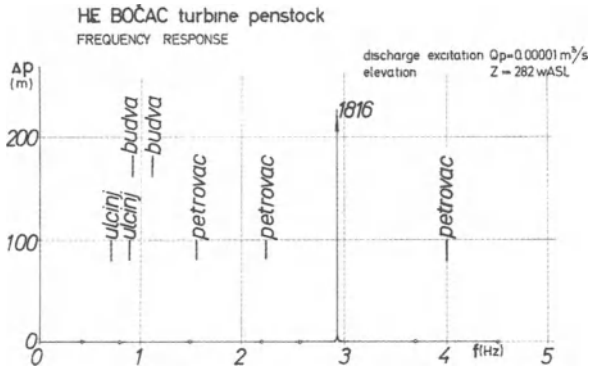

Fig. 17a Frequency Response of the Turbine Penstock

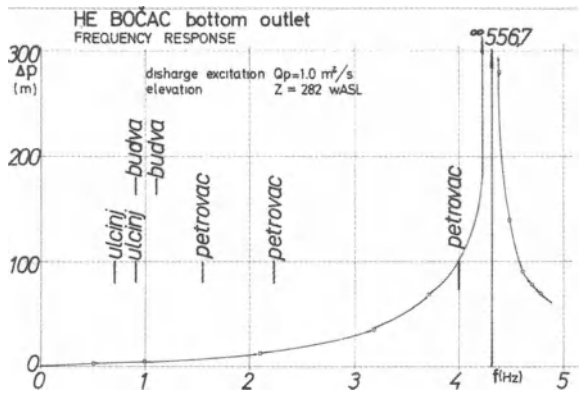

Fig. 17b Frequency Response of the Bottom Outlet

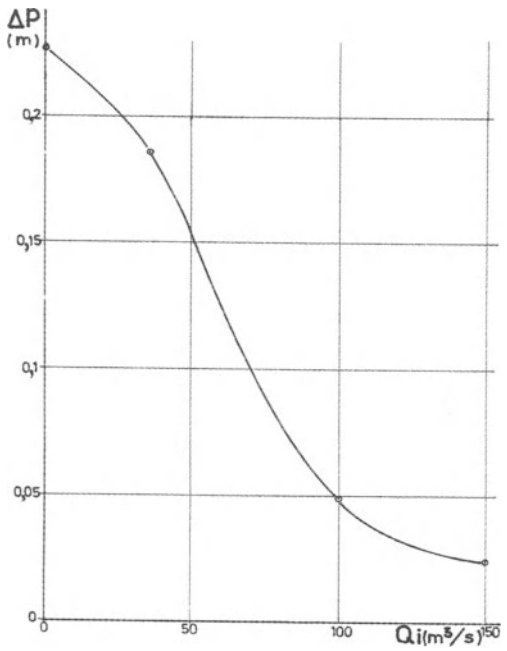

Fig. 18 Influence of the flow through the bottom outlet on pressure amplitudes

7 Conclusions

Earthquakes can cause serious hydraulic forces within the system, especially in the case of the closed pipe or penstock. An earthquake's characteristics (intensity, duration, first few harmonics) and the characteristics of the system investigated (its position, length, velocity, and configuration) influence on the magnitude of these forces. Since this problem is quite multiphase, it calls for collaboration among specialists in seismology, hydraulics and structural analysis. The greater problem is the mere set of possible earthquakes, which might occur in any given region.

This paper offers a relatively simple procedure to get reliable results. It is based on the assumption that transversal movements of the system and its inertia may be disregarded, i.e., pressure waves travel along the pipes as if the system were immobilized. The transfer matrix method and the method of characteristics were used for the computation of the effects of the earthquakes. Further investigation in order to take into account other effects is recommended.

The results of the preliminary analyses discover that drawing conclusions on the basis of few parameters, without analysis, might be very dangerous and misleading. Take into account the results of the velocity of the earthquake "HELENA"(V_{max} = 12,3 cm/s), which is twice stronger than the earthquake "FERNDALE"(V_{max} = 6,2 cm/s), and yet the latter causes greater pressure surges (Δp= +2,7 / –2,5bar for "Helena" and Δp = +3,3/–3,0 bar for "Ferndale"). This phenomenon is due to the fact that "FERNDALE" consists of several shocks, and "HELENA" is one stronger stroke.

In the second case analyzed, the same earthquake was applied to two hydraulic systems, not so dissimilar, but with very different results: pressure surges in the penstock were Δp = +2,2/–2.1 bar, but in the bottom outlet, the corresponding figures were much higher- Δp = +5,3/–5,7 bar. Before the results of computation have appeared, this difference could not be predicated. The computations for this case show one of the ways haw it is possible to strongly amplify pressure oscillations in the penstock.

Finally, what is necessary in this area is to do further investigations in order to develop a more sophisticated

model along the lines proposed in literature, which can take into account interactions between fluid and the structure more precisely. Further investigation should also take into account effects of 3-D flow and two-phase flow. In addition to this, closer collaboration with seismologists in selecting and describing "model" earthquakes is essential.

Acknowledgements

The author wants to acknowledge all the colleagues and the investors who supported this research. Particularly gratitude is expressed to retired prof. Stanislav Pejovic and late prof. Dusan Obradovic whom this paper is dedicated to.

References

California Institute of Technology (CIT) Earthquake Engineering research Laboratory, 1951., Digitized accelerograms of the earthquakes "Ferndale", California, October 8, 1951 (*IA2, 51.1T, o21/CIT*), and "Helena" Montana, October 31, 1951 (*IB25, 35.1, 251/CIT*)

Gajic A., 1983., A contribution to the Study of Nonstationary Phenomena in Hydroelectric Power Plant, (in Serbian), *Ph. D. Dissertation, Faculty of Mechanical Engineering, University of Belgrade*

Gajić A., Pejović S., 1984., Computations of the Hydraulic Oscillations, (in Serbian), *XVI Yugoslav Congress of Rational and Applied Mechanic*, Becici, Vol. C., pp. 211 – 219

Gajic A., Pejovic S, 1986, Hydraulic Loads in Hydraulic Systems During an Earthquake (in Serbian), *XVII Yugoslav Congress of Rational and Applied Mechanic*, Zadar, Vol. C1, pp. 281 – 288

Gajic A., Pejovic S, Obradovic D., 1986.a, Hydraulic Loads in Hydropower Plants During the Earthquake (in Serbo-Croatian), *Elektroprivreda,* Zagreb, No. 9-10, pp. 362 – 365

Gajić A., Predić Z., Muskatirović J., Pejović S., Manzalović P., 1990., Investigations of Cracks on the Kaplan Turbine Stay Vanes, *15 IAHR Symposium,* Belgrade, p. A4, pp. A4.1 – A4.12

Gajic A., 1993.,Hydraulic Oscillations and Earthquake Effects upon Hydraulic Systems, *Seminar at the Faculty of Mechanical Engineering, Nagoya University,* December 17-th

Gajić A., Pejović S., Stojanović Z., 1993.a, Hydraulic Oscillations Stability of low-Head HPP, *6-th IAHR WG1 Meeting*, Lausanne, p 6.3, pp.6.3.1 – 6.3.14

Gajić A., Oba R., Ikohagi T., Ignjatović B., Muškatirović J., 1994., Flow Induced Vibrations and Cracks on Stay Vanes of a Large Hydraulic Turbine, *17-th IAHR Symposium*, Int. Res. Centre of Hydr. Mach., Beijing, p. J12., pp.1283 – 1293

Gajic A., Pejovic S., Stojanovic Z., 1995., Fluid-Structure Interaction Analysis in Frequency Domain, *7-th IAHR WG1 Meeting,* Ljubljana, p.F.5., pp. F.5.1 – F.5.13

Gajić A., Pejović S., Stojanović Z., 1996., Hydraulic Oscillation Analysis using the Fluid-Structure Interaction Model, *18-th IAHR Symposium*, Valencia, (Cabrera E. et al, Hydraulic Machinery and Cavitation, ISBN 7923-4210-0, *Kluwer Academic Publishers*), pp. 845 – 854

Gajic A., 2003., Case Studies in Hydraulic Systems- CSHS'03 (editor), *Faculty of Mechanical Engineering*, ISBN 86-7083-469-3, Belgrade

Institute for Seismic Engineering and Seismology, 1979., Preliminary Analysis of Strong Motion, Records obtained at Budva, Ulcinj, Bar and Petrovac from April 15, 1979, Motenegro, Yugoslavia Earthquake, *University "Kiril & Metodij", Publ. ISES No.64/79*, Skopje

Jaeger C., 1977, Fluid Transients in Hydro-Electric Engineering Practice, *Blackie*, New York

Karney B., Gajic A., Pejovic S., 2003., Case Studies—Our Experience in Hydraulic Transients and Vibrations, (invited paper), *Int. Conference on Case Studies in Hydraulic System s-CSHS'03*, Belgrade, ISBN 86-7083-469-3., pp. 131 – 154

Maricic T., Haber D., S. Pejovic, B. W. Karney, Standardization as Prevention of Fatigue Cracking of Hydraulic Turbine-Generator Shaft, *IEEE Electrical Power Conference "Renewable and Alternative Energy Resources"*, Montreal, pp 1 – 8

Obradovic D, Pejovic S., Gajic A., 1986, Analysis of Earthquake Effects upon Hydraulic Structures, *5th International Conference on Pressure Surges*, BHRA, Hannover, pp. 35 – 41

Pejović S., Krsmanović Lj., Gajić A., Obradović D., 1982., Resonance in the Piping System of a Power Plant During Filling-in, *11-th IAHR Symposium*, Amsterdam, pp. 43.1 – 43.10

Pejović S., Gajić A., Obradović D., 1984., The Effects of Air Supply to the Draft Tube upon Hydraulic Oscillations in a Hydropower Plant,*12-th IAHR Symposium,* Stirling, pp. 242 – 253

Pejović S., Obradović D., Gajić A., 1985., Resonance in Hydropower Plants—Experiences in Yugoslavia, *IAHR Work Group on the Behaviour of Hydraulic Machinery under Steady Oscillatory Conditions*, Mexico City, pp. 1.1 – 1.13

Pejović S., Gajić A., 1986., Auto—Oscillations of a Ball Valve and Mode Shapes in the Tunnel, *UNIPEDE Attelier*, Dubrovnik, pp. 7.1 – 7.17

Pejović S., Gajić A., Obradović D., 1986.a, Auto—Oscillations of the Ball Valves—Mode Shapes in the Penstock PSPP (in Russian), *Int. Conf. Hydroturbo,* Varna, pp. 6.1 – 6.12

Pejović S., Gajić A., Obradović D., 1988., Auto—Oscillations of the Intake Wheel Gate, *14 IAHR Symposium*, Trondheim, p. G5. pp. 443 – 450

Pejovic S, 1989, Pressure Surges and Vibrations in Hydropower Plants—Experiences in Yugoslavia, The Current State of Technology in Hydraulic Machinery, International Editorial

Committee Book Series on Hydraulic Machinery, *Glower Technical,* pp. 177 – 204

Pejović S., Gajić A., 1992.a, Sensitivity and Stability Analysis of Pumping Systems and Air Chamber Influence on Hydraulic Vibrations, *Int. Conference Unsteady Flow and Fluid Transients*, Durham, *Balkema*, Roterdam, pp.229 – 239

Pejovic S., Gajic A., 1992.b, Cases and Incidents Due to Hydraulic Transients—Yugoslav Experiences, *Int. Congress on Cases and Accidents in Fluid Systems*, Sao Paulo, pp181 – 223

Pejovic S., Gajic A., Savic Z., Stojanonic Z., 1994., Hydraulic Stability of Bulb Turbines, *17-th IAHR Symposium,* Int. Res. Centre of Hyd. Mach., Beijing, p. J2, pp. 1195 – 1206

Swingen S., Stojanovvic Z., Brekke H.,Gajic A., 1998., Two Numerical Methods of Hydraulic Oscillation Analysis in Piping Systems including Fluid-Structure Interaction, *JSME CENTENNIAL GRAND CONGRESS, International Conference on Fluid Engineering ICFE 97,* Tokyo, Vol. III, pp. 1601 – 1606

Pejovic S., Karney B. W., Q., Zhang, and G. Kumar, 2007., Smaller Hydro, Higher Risk, *IEEE Electrical Power Conference "Renewable and Alternative Energy Resources"*, Montreal, pp 1 – 6

Zienkiewitcz O.S., 1964., Hydrodynamic Pressures due to Earthquakes, *Water Power*, Vol. 8., pp.382 – 388

Wylie B.E., Streeter V. L., Fluid Transients, *Mc Graw-Hill*, 1978

The 4th International Symposium on Fluid Machinery and Fluid Engineering
November 24-27, 2008, Beijing, China
NO. 4ISFMFE-IL02

A Numerical Investigation of the Effect of End-Wall Boundary Layer Skew on the Aerodynamic Performance of a Low Aspect Ratio, High Turning Compressor Cascade

Martin Böhle[*1], Udo Stark[2]

[*1] Bergische University of Wuppertal
FB D, Gaußstrasse 20, 42097 Wuppertal, Germany
Tel: +49-202-439-2020 / Fax: +49-202-439-3756
E-mail: mboehle@uni-wuppertal.de (Corresponding Author)

[2] Technical University Braunschweig
Institute of Fluid Mechanics, Bienroeder Weg 3, 38106 Braunschweig, Germany

Abstract The paper reports on a numerical investigation into the effects of inlet boundary layer skew on the aerodynamic performance of a high turning (50°), 2D compressor cascade. The cascade geometry is representative of stator hub sections in highly loaded single-stage axial-flow low-speed compressors. 2D blades with NACA~65 thickness distribution on circular arc camber lines were used. The blade aspect ratio was 1.0, the space/chord ratio 0.5 and the stagger angle 25°. The simulations were done with a commercially available, steady three-dimensional RANS solver with the Spalart-Allmaras turbulence model. The incoming end-wall boundary layers were assumed to be collateral or skewed. In both cases the profile boundary layers were fully turbulent. The Reynolds-number was fixed at 600000 and the thickness of the incoming end-wall boundary layer was 0.1. Results are shown for an inlet-air angle of 50°, representing the impact free inlet-air angle of a hypothetical cascade with zero-thickness blades. Contrary to what has been expected, the results do not show (hub) corner stall, neither with nor without end-wall boundary layer skew. Flow reversal happens to occur almost exclusively on the suction surface of the blades, not on the end-walls. The end-wall flow is highly overturned, when the incoming boundary layer is collateral and is much less curved when the incoming boundary layer is skewed and (re)energized. This in turn leads to an interaction between the end-wall and blade suction surface flow which is much stronger in the first than in the second case with corresponding higher and lower losses, respectively.

Keywords secondary flow, skewness of boundary layer flow

Nomenclature

b	skewed boundary layer parameter
i	incidence
c	absolute boundary layer velocity
l	blade chord
C	absolute freestream velocity
n	skewed boundary layer parameter
C'	relative freestream velocity
p	static pressure
d	maximal profile thickness
p_t	total pressure
D	diffusion parameter
q	dynamic pressure
DF	diffusion factor
R	hub radius
H	blade height
Re	Reynolds number
t	blade pitch
ε_W	maximal skew angle at the wall
u, v, w	axial, tang. and spanw. vel. comp.
ζ_{V1}	loss coefficient = $(p_{t1} - p_{t2})/(p_{t1} - p_1)$
x, y, z	axial, tan. a. spanw. coordinates
β	absolute flow angle

λ stagger angle
δ boundary layer thickness
ϕ camber angle
ε skew angle

Subscripts / Superscripts

1, 2 upstream/downstream
- pitchwise average
n, s normal and streamwise comp.&
= pitch- and spanwise average

1 Introduction

Turbomachinery investigations are often performed in stationary, linear cascades, in which, however, a number of important turbomachinery effects are usually missing. In fact, the flow along the end-wall of a stationary cascade is different in many important respects from that over a rotor tip or a stator hub in a compressor, where the relative motion between adjacent blade rows causes the end-wall boundary layers to be skewed and reenergized. This is illustrated in Fig. 1 for the particular case of the compressor hub flow at rotor exit and stator inlet. A boundary layer leaving a rotor hub with large velocity deficiency is reenergized and has a new start as it enters the stator hub. Machine effects of this type are almost always missing in experimental cascade work, but may have been included after some suitable modifications to the cascade tunnel (R.W. Moore et al, 1956; J.A. Walsh, 1989). But this has rarely been done with the consequence that there is very little published work on the effects of inlet boundary layer skew. For this reason an experimental

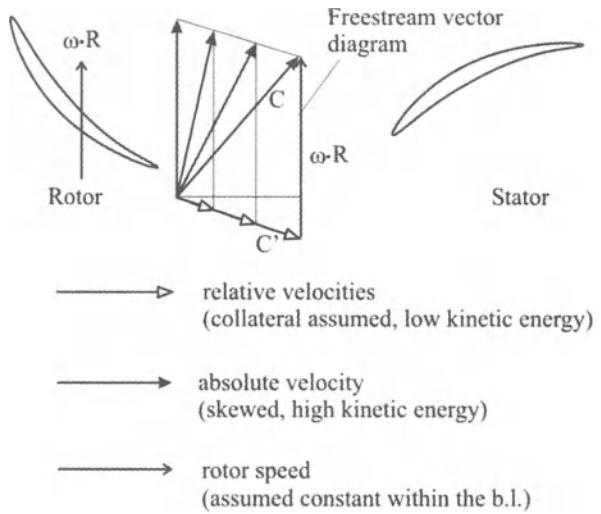

Fig. 1 Stator hub, velocity vector diagram

and numerical research project was initiated with the main objective to advance our understanding of the effects of end-wall boundary layer skew on the aerodynamic performance of linear compressor cascades. The current paper reports on first numerical results for a low aspect ratio, high turning compressor cascade at impact-free-entry inlet angle for zero thickness blades. Calculations were performed with and without skew of the inlet boundary layer and by comparison of the results the effects of skew, especially on losses, were elucidated.

2 Compressor cascade

The cascade geometry used in the present investigation corresponds to the hub section geometry of a low aspect ratio stator of a highly loaded single-stage axial-flow low-speed compressor. 2D blades with NACA~65 thickness distribution ($d/l = 0.08$) on circular arc camber lines ($\phi = 64.5°$) were utilized. The blade aspect ratio was h/l=1.0, the space/chord ratio t/l=0.5 and the stagger angle $\lambda = 25°$. The design inlet and outlet angle were β_1= 50° and β_2 = 0°, respectively. The Reynolds number was fixed at Re_1 = 600000 and the thickness of the incoming end-wall boundary layer was $\delta/l = 0.1$. A summary of the main geometric and aerodynamic parameters is shown in Fig. 2. with a diffusion factor

$$DF = 1 - \frac{\cos\beta_1}{\cos\beta_2} - \frac{\cos\beta_1}{2}\cdot\frac{t}{t}\cdot(\tan\beta_1 - \tan\beta_2) \qquad (1)$$

of $DF = 0.55$ (S. Lieblein et al., 1953) and a diffusion parameter

$$D = \frac{t}{t}\cdot\left[1 - \left(\frac{\cos(i+\lambda+\varphi/2)}{\cos(\lambda-\varphi/2)}\right)^2\right]\cdot(i+\varphi) \qquad (2)$$

for zero skew of $D = 0.29$ (V-M. Lei et al., 2006) the numerical results were expected to show beginning blade stall but not a corner stall (flow reversal on both the blade suction surface and the end-wall.

3 Inlet boundary layer profiles

Two inlet boundary layer profiles were selected for the present study. The first one is a collateral (2D) power law velocity profile

$$\frac{c}{C_1} = \left(\frac{z}{\delta}\right)^{1/7} \qquad (3)$$

which has often been used to model the upstream end-wall flow in compressor cascade work (see Fig. 3).

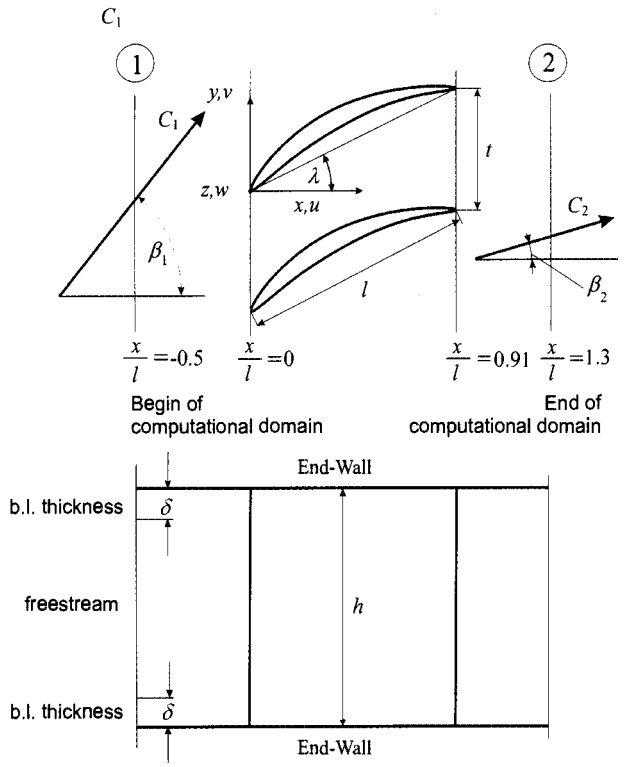

Fig. 2 Low aspect ratio, high turning compressor cascade with computational domain

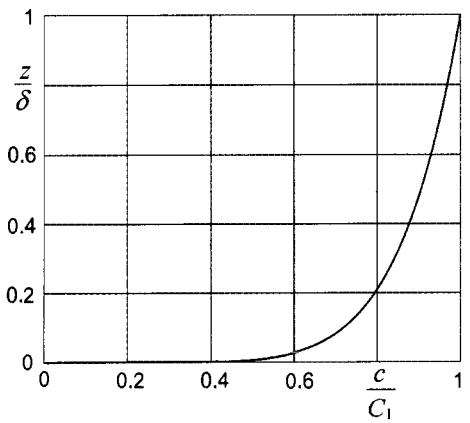

Fig. 3 2D Inlet boundary layer profile

The second one is a highly skewed (3D) velocity profile with components

$$\frac{c_s}{C_1} = 1 - b \cdot \left(1 - \frac{z}{\delta}\right)^n \tag{4}$$

and

$$\frac{c_n}{C_1} = (1-b) \cdot \tan \varepsilon_W \cdot \left(1 - \frac{z}{\delta}\right)^n \tag{5}$$

in streamwise and crosswise direction, respectively. The profile represents a typical start profile of the stator hub flow with non-zero velocity components at the wall (see Fig. 4). In (4) and (5) the velocity C_1 is the freestream velocity at station 1 and station 1 is

- the stator hub leading edge in compressor stage investigations or
- the beginning of the computational domain in the present compressor cascade investigation (see Fig. 2)

ε_W is the wall skewing angle and with $\beta_1 = 50°$ the value of

$\varepsilon_W = 40°$ in the present study. b has been determined graphically to about 0.3 while n was set at 3.

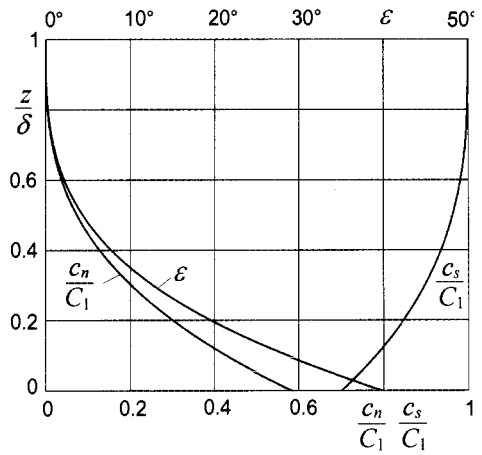

Fig. 4 Velocity vectors of the skewed inlet boundary layer, $x/l = -0$

A plot of c_s/C_1 and c_n/C_1 together with ε is shown in Fig. 5. The length of the resulting velocity vectors may be seen to be nearly constant, including the length of the velocity vector at the wall, which does not go to zero. It should however be mentioned that these velocity profiles,

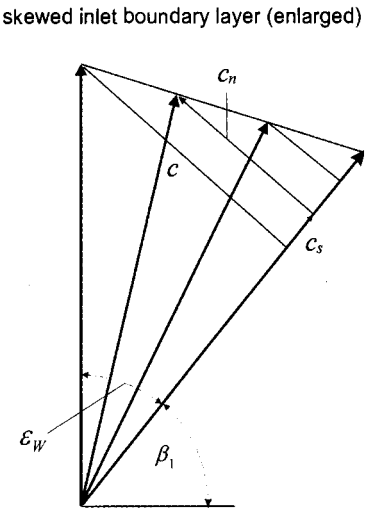

Fig. 5 Velocity vectors of the skewed inlet boundary layer

in particular the non-zero velocity at the wall, will soon be attenuated as the flow develops along the stator hub or cascade end-wall.

The component expressions (4) and (5) were taken from J. De Ruyck, et al. 1978 where they were used to approximate end-wall boundary layer profiles in velocity defect form neglecting the viscous sublayer.

4 Numerical method

CFD simulations were performed with the software package FLUENT 6.2.16 (s. References). The code solves the full Reynolds-Averaged Navier{}-Stokes equations (RANS) on unstructured grids. A second-order finite-volume-discretisation was applied on a collocated grid. This was refined along the blade/end-wall corner (see Fig. 6) in such a way that at least one grid point lies inside the laminar sublayer. The computations were continued until the residuum was reduced down to six order of magnitudes. For turbulence modeling the Spalart-Allmaras turbulence model was used (P. Spalart, S. Allmaras, 1992). This model is a one-equation, low Reynolds number model which has been used first in aerospace applications and is now quite common in turbomachinery applications. At the inlet and exit of the computational domain an inflow and outflow boundary condition was set, respectively. For each computation, only one blade passage was modeled with periodic boundary conditions as depicted in Fig. 6. The inlet velocity and air angle distribution were prescribed inside and outside the end-wall boundary layers. The corresponding static pressure distribution was calculated. All calculations were two- or three-dimensional, incompressible and fully turbulent. The turbulence level of the inlet flow was $Tu = 2\%$.

5 Results and discussion

The stator hub inlet flow in an axial-flow compressor differs from the upstream end-wall flow in a stationary linear cascade in that the velocity vectors do not only vary in magnitude but also in direction in going from the freestream towards the wall. Such end-wall flows are referred to as being skewed. A collateral and a skewed boundary layer were already introduced to represent the initial end-wall conditions in a numerical investigation into the effects of the inlet skew on the flow field of a low aspect ratio, high turning compressor cascade.

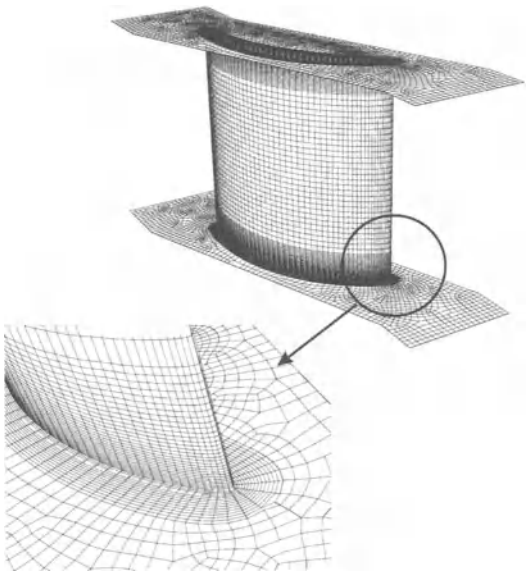

Fig. 6 Numerical grid

5.1 Limiting Streamlines on End-Walls and Blades

The computed limiting streamlines on the end-wall and blade suction surface are shown in Fig. 7 and 8 for case one and two with the collateral and the skewed inlet boundary layer, respectively. For well known reasons the end{}-wall flow is overturned in Fig. 7 as well as in Figure 8. However, the introduction of skew results in a decreased level of overturning when compared to that produced in the collateral case. Therefore, the following interaction between the overturned end-wall flow and the blade suction surface flow is much less in Fig. 8 than in Fig. 7. In both cases the interaction starts at the blade ends at special points (multiple node-saddle singularities) in the end-wall/suction side corner and then spreads out along and downstream a symmetric 3D separation line representing the characteristic feature of the suction surface flow.

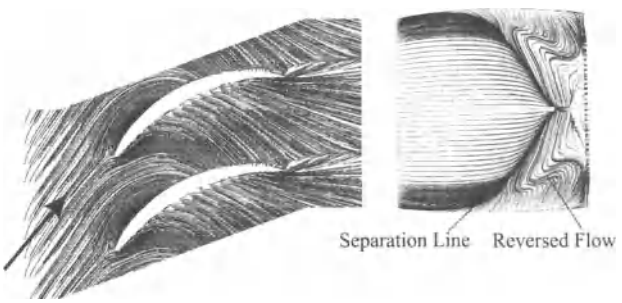

Fig. 7 Limiting streamlines on end wall and blade suction surface, case one without skew

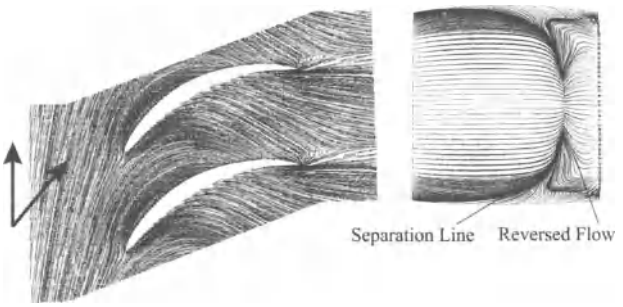

Fig. 8 Limiting streamlines on end wall and blade suction surface, case two with skew

So-called corner stall is a three-dimensional phenomenon with flow reversal on both the end-wall and the blade suction surface. In Fig. 7 and 8 the end-wall flow is not reversed, but there is flow reversal on the blade suction surface, which is, however, not corner stall. This result is in agreement with the predictions of a new criterion for corner stall described by V-M. Lei et al., 2006. Following V-M. Lei the formation of corner stall is to be expected, when the diffusion parameter D (defined by V-M. Lei) exceeds its critical value $D_{crit.} = 0.4+/-0.05$. The corresponding D-values of case one and two of the present investigation are ~0.3 and ~0.2, respectively.

5.2 Local Results

Numerical data were acquired for a series of successive y/z-planes along the $x\{\}$-axis. The last $y/z\{\}$-plane coincides with the exit plane of the computational domain at x/l = 1.3. For this plane Figure 9 and 10 show contour plots of the total pressure loss coefficient ζ_{V1}, depending on y and z, for case one and two, respectively. The total pressure loss was determined relative to the inlet total pressure p_{t1} at midspan and subsequently normalized with the corresponding dynamic head $q_1 = p_{t1} - p_1$. In Fig. 9 as well as in Figure 10 the highest losses appear on the suction surface of the blades, where they concentrate in loss cores of different size and loss magnitude. At a loss coefficient of 0.5 the size of the loss cores in Fig. 9 (case one without skew) is about five times as large as the corresponding loss cores in Fig. 10 (case two with skew) at a loss coefficient of 0.4. This result confirms the above mentioned conclusion that the interaction of the end-wall cross flow with the blade suction surface boundary layer is much stronger in case one than in case two.

The corresponding vector plots of the secondary flow in the exit plane x/l = 1.3 are shown in Fig. 11 and 12 for case one and two, respectively. These plots were obtained by calculating a set of local flow velocities projected onto a plane which is normal to the mean yaw direction at midspan. For the presentation in Fig. 11 and 12 each secondary flow vector is turned around the z-axis until it lies in the exit plane (s. P. Marchal eta, 1977). The resulting vector plots show classical secondary flow (s. L.H. Smith, 1955) of similar structure but different extention, that is one pitch in circumferential direction, both cases, and approximately 20% and 10% blade height in spanwise direction for case one and two, respectively.

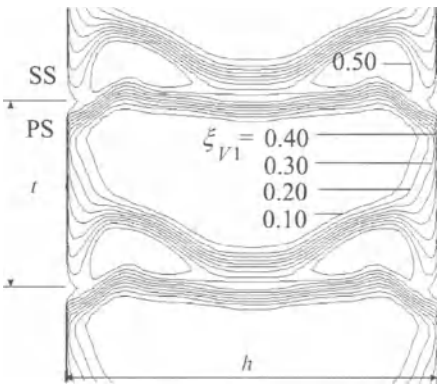

Fig. 9 Total pressure loss contours, case one without skew, x/l = 1.3

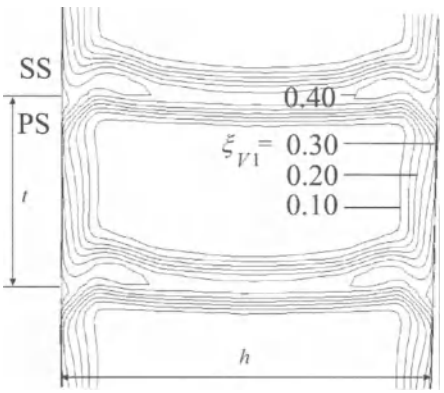

Fig. 10 Total pressure loss contours, case two with skew, x/l = 1.3

5.3 Pitchwise Averaged Results

For the exit plane, the pitch averaged results include the outlet-air angle β_2 (Fig. 13) and the total pressurecoefficient ζ_{V1} (Fig. 14). A comparison of the case one and two results in Fig. 13 and 14 clearly reveals that the introduction of inlet skew has a significant effect on the exit flow. In Fig. 13, for the case of zero skew, a well defined over-/underturning of the exit flow is shown associated with a strong passage vortex. By contrast the introduction of inlet skew results in a nearly uniform exit

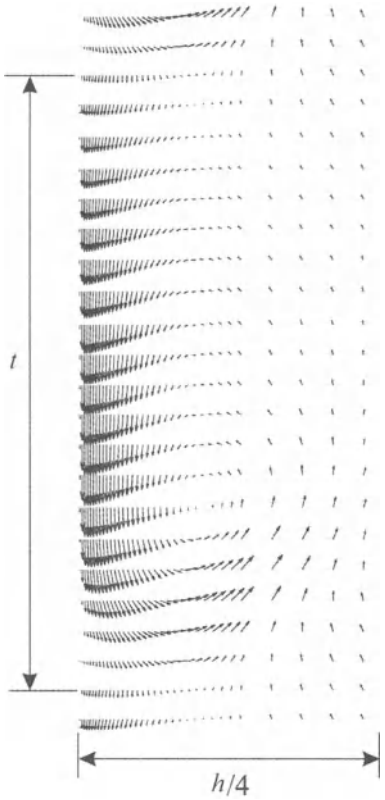

Fig. 11 Secondary flow chart, case one without skew, $x/l = 1.3$

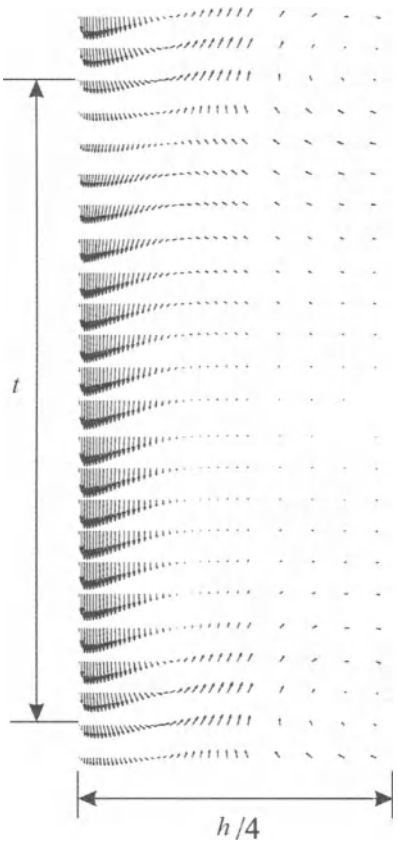

Fig. 12 Secondary flow chart, case two with skew, $x/l = 1.3$

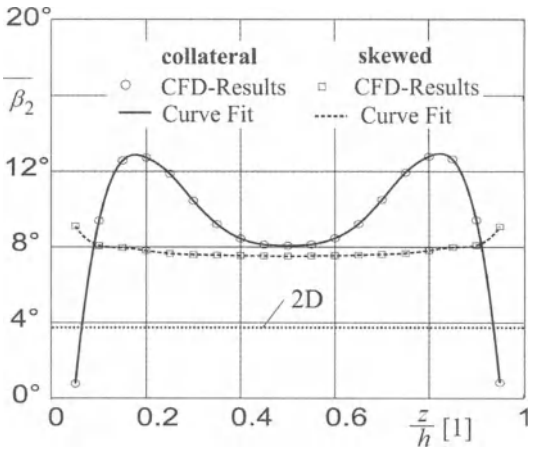

Fig. 13 Pitchwise averaged outlet angle, case one and two, $x/l = 1.3$

angle distribution with indication of a small and weak passage vortex only. For comparative purposes the 2D exit angle $\beta_{2,2D}$ is also shown in Fig. 13. In Fig. 14, the case one loss distribution exhibits two characteristic bumps which are due to the extended high loss cores in Fig. 9. The case two distribution is free of bumps, as has been expected, and shows overall similar trends, however, with significantly lower losses. Again, for comparative purposes the 2D loss coefficient $\zeta_{V1,2D}$ is also shown in Fig. 14.

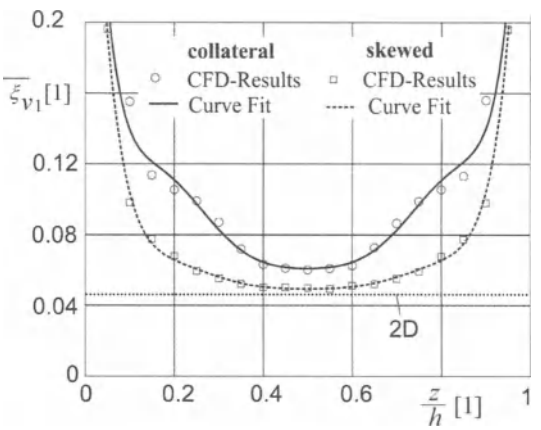

Fig. 14 Pitchwise averaged pressure losses, case one and two, $x/l = 1.3$

5.4 Pitch-and Spanwise Averaged Results

Pitch-and spanwise averaged loss coefficients for case one and two are shown in Fig. 15 as a function of the normalised axial coordinate x/l between $x/l = -0.5$ and $x/l = +1.3$. The two upper curves represent the overall losses and the two lower curves the net losses, including and excluding the inlet boundary losses, respectively.

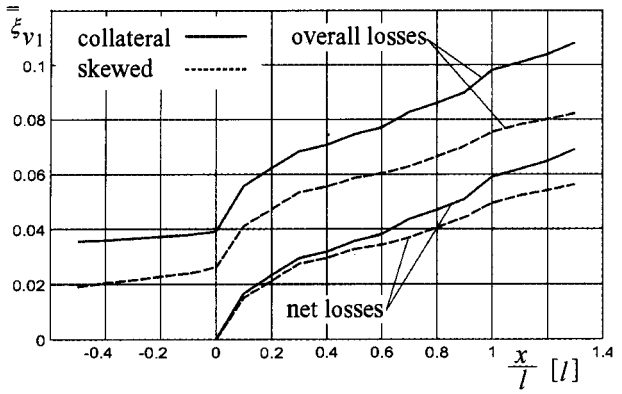

Fig. 15 Pitch- and spanwise averaged total pressure losses, case one and two

The solid curve of the overall loss curves is for case one and shows, starting with the inlet boundary layer losses at $x/l = -0.5$, the growth of the total pressure losses in a conventional cascade experiment with collateral boundary layers on the upstream end-walls. The dashed curve of the overall loss curves is for case two and shows, again starting with the inlet boundary layer losses at $x/l = -0.5$, the growth of the total pressure losses in a more advanced cascade experiment with skewed, i.e. engine like boundary layers on the upstream end-walls. The skewed inlet boundary layer is modeled on the stator hub inlet flow of a highly loaded axial fan and appears to be reenergized, resulting in significantly lower losses when compared to the corresponding losses of the zero skewed inlet boundary layer. Downstream of the leading edge plane at x/l = 0 the overall losses increase rapidly and continue to increase downstream of the trailing edge plane up to the exit plane at $x/l = +1.3$.

The two lower curves in Fig. 15 represent the cascade net losses for case one and two. These curves were derived from the overall loss curves by subtracting the inlet boundary layer loss for case one and two at $x/l = 0$ from the corresponding overall loss curve. The resulting loss curves show an increasing difference with the case two losses always below the case one losses. At $x/l = 1.0$ the difference has increased to remarkable 18.5% of the case one losses at the same position.

Table 1 shows the key performance parameters at $\beta_1 = 50°$. They were numerically determined and additionally estimated according to I.A. Johnsen et al, 1965. Although there are some differences between the estimated and 2D calculated results, there is a great deal of similarity between the two data sets and this adds some confidence to both, the estimated and the numerical results. A comparison between the 3D calculated data sets for case one and two leads to the conclusion that the presence of (positive) inlet skew results in higher pressure differences and lower total pressure losses, locally as well as spanwise integrated.

6 Comparision with Previous Work

The probably first paper on skewed inlet boundary layers in compressor cascades is from R.W. Moore, 1956. Without having made wake measurements the authors were unable to report on exit angle and loss distributions. They did, however, find that the spanwise distribution of the blade forces is much more uniform, when the inlet boundary layer is skewed. Similar results were obtained in the present investigation, where case-two exit angle and loss distributions are shown to be much more uniform than the corresponding case-one distributions (Figs. 13 and 14). A more recent investigation is described by J.A. Walsh et al., 1989. Measurements outside and inside a high turning turbine cascade were performed and analysed for three different cases of inlet skew, that is negative skew, collatoral and positive skew. As reported by J.A. Walsh et al., 1989, the introduction of positive skew, corresponding to the inlet skew of the present investigation, was found to have a profound effect on the magnitude of the generated losses, which is completely analogous to the findings of the present investigation (Figs. 9, 10, 13 and 14).

The passage vortex in the work of J.A. Walsh et al., 1989 was found to be much reduced in strength compared to the other cases (zero and negative skew), which is also confirmed by the present results.

Table 1 Comparison of Results

	β_2	$\Delta p/q_1$	ζ_{v1}	β_2	$\Delta p/q_1$	ζ_{v1}
NASA SP 36	4.35	0.544	0.040			
2D RANS	3.90	0.522	0.046			
	collateral inlet b.l.			skewed inlet b.l.		
3D RANS (mid span)	8.08	0.414	0.060	7.52	0.512	0.050
3D RANS (full span)	8.76	0.412	0.108	7.72	0.510	0.082

References

FLUENT-Software Package: "Aircraft Engines and Gas Turbines", Centerra Resource Park, 10 Cavendish Court, Lebanon, NH 03766

I.A. Johnsen and R.O. Bullock (Editors), 1965: "Aerodynamic design of axial-flow compressors", NASA SP 36

V-M. Lei, Z.S. Spakovszky, E.M. Greizer, 2006: "A criterion for axial compressor hub-corner stall", ASME Paper No. 2006-GT-91332

S. Lieblein, F.C. Schwenk and R.L. Broderick, 1953: "Diffusion factor for estimating losses and limiting blade loadings in axial-flow compressor blade elements", NACA RM E53DO1, 1953

P. Marchal and C.H. Sieverding, 1977: "Secondary flows within turbomachinery bladings", AGARD-CP-214

R.W. Moore, Jr. and D.L. Richardson, 1956: "Skewed boundary-layer flow near the end walls of a compressor cascade", ASME Paper No. 56-A-131

De Ruyck, C. Hirsch, P. Kool, 1978: "An axial compressor end-wall boundary layer calculation method", ASME Paper No. 78-GT-81

L.H. Smith, 1955: "Secondary flow in axial-flow turbomachinery", Trans. ASME, Vol. 77

P. Spalart, S. Allmaras, 1992: "A one-equation turbulence model for aerodynamic flows", Technical Report AIAA-92-0439, American Institute of Aeronautics and Astronautics

J.A. Walsh, D.G. Gregory-Smith, 1989: "Inlet skew and the growth of secondary losses and vorticity in a turbine cascade", ASME Paper No. 89-GT-65

The 4th International Symposium on Fluid Machinery and Fluid Engineering
November 24-27, 2008, Beijing, China
NO. 4ISFMFE-Ab01

Design and Analysis of a Radial Turbine with Back Swept Blading

Liam Barr*[1], Stephen Spence[2] and Paul Eynon[3]

*[1] School of Mechanical & Aerospace Engineering, Queen's University Belfast,
Ashby Building, Stranmillis Road, Belfast BT9 5AH, Northern Ireland.
Tel: +44-028-9097-4569 / Fax: +44-028-9066-1729
E-mail: lbarr01@qub.ac.uk

[2] School of Mechanical & Aerospace Engineering, Queen's University Belfast,
Ashby Building, Stranmillis Road, Belfast BT9 5AH, Northern Ireland.
Tel: +44-028-9097-4677 / Fax: +44-028-9066-1729
E-mail: s.w.spence@qub.ac.uk

[3] Cummins Turbo Technologies Ltd,
St. Andrews Road, Huddersfield HD1 6RA, United Kingdom.
Tel: +44-014-8483-2339
E-mail: paul.a.eynon@cummins.com

Abstract This report documents the detailed design and numerical analysis of an 86 mm radial turbine with a 25° back swept inlet blade angle. The original blade geometry, which was from an 86 mm radial turbine for a turbocharger, contained purely radial blades, as conventional design dictates. The original blade design was subsequently modified to include back swept blading at inlet to increase performance at lower than optimum velocity ratios. Results from the numerical analysis are presented and compared. It is shown that the 25° back swept blade offers significant increases in efficiency while operating at lower than optimum velocity ratios (*U/C*). Improvements in efficiency at off-design conditions would notably improve turbocharger performance where the turbine typically experiences lower than optimum velocity ratios while accelerating during engine transients. Automotive turbochargers, particularly those of city bound vehicles, would tend to spend a significant portion of their time operating at lower than optimum velocity ratios. Thus, an increase in turbine efficiency within this operating range would result in more torque available for turbocharger acceleration, increasing boost air pressure during engine transients, benefiting engine response and emissions. A CFD study of the 86 mm baseline radial rotor and the 86 mm 25° back swept rotor was conducted. Numerical predictions show off-design performance gains of 2% can be achieved, while maintaining design point efficiency. A finite element analysis has been carried out to assess the changes in blade stress levels as a result of introducing a non-radial angle at turbine rotor inlet. A modal analysis was also performed in order to identify the natural frequencies of the turbine geometry, thus calculating the critical speeds corresponding to the induction of excitational frequencies from the stator vanes. While the new blade design experiences increased stress levels within some regions, the numerical study has shown that it is feasible from both an aerodynamic and structural point of view to increase the performance of a radial turbine through the addition of back swept blading. Several rotors have been manufactured at Queen's University of Belfast and are currently being tested to obtain experimental performance measurements for radial turbines with a range of inlet blade angles in order to verify the numerical predictions detailed herein.

Keywords radial, turbine, blade, back-swept, non-radial, off-design

Nomenclature

1D	One dimensional
3D	Three dimensional
C	Isentropic jet velocity (m/s)
CFD	Computational Fluid Dynamics
U	Blade tip speed (m/s)
U/C	Isentropic velocity ratio

α Flow angle (degrees)
β Blade angle (degrees)

1 Introduction

Radial turbines manufactured for turbocharging are designed to withstand the harsh environment of high stresses and high temperatures. Blade vibration as a result of thermal cycling and unsteady flow is also a problem, as is the increased root stresses brought about through the thickening of blades to avoid excessive vibration. Conventionally, a radial turbine is designed with radial fibred blades to avoid any additional bending stresses that may be incurred from non-radial blading. This design limitation severely restricts the radial turbine aerodynamicist when defining blade shape, particularly at inlet. However, a small number of published studies have shown that improvements at off-design conditions can be achieved by changing the blade angle at inlet. A preliminary one-dimensional investigation into the effects of incorporating back sweep at rotor inlet was carried out by Meitner and Glassman (1983). This study demonstrated that a back swept inlet blade angle improved efficiency when operating in regions where most modern radial turbines are likely to perform, i.e. low *U/C* values. This shows that the peak efficiency point may be shifted to a different velocity ratio as a result of changing the inlet blade angle. This suggestion is confirmed by Hakeem (1995). Derived from a 1D treatment of inlet and exit velocity triangles, Hakeem presented equation 1 which highlights how the optimum velocity ratio *U/C* varies as a function of the inlet blade and flow angle.

$$\left(\frac{U}{C}\right)_{optimum} = 0.707\sqrt{1-\frac{\tan\beta_{inlet}}{\alpha_{inlet}}} \qquad (1)$$

The derivation of Equation 1 assumes zero incidences between the inlet flow angle α_{inlet} and the inlet blade angle β_{inlet}. For a conventional radial turbine with a purely radial inlet blade angle, tan $\beta_{inlet} = 0$ and the optimum velocity ratio *U/C* is 0.7, but for a back swept inlet blade angle the optimum velocity ratio *U/C* is less than 0.7. For example, an inlet blade angle of $\beta_{inlet} = 30°$ and an inlet flow angle of $\alpha_{inlet} = 60°$ corresponds to a velocity ratio of $U/C = 0.58$.

Mulloy and Weber (1982) highlighted the rationale of having a turbine wheel that could tolerate greater variations in wheel inlet angle. They contended that a wheel of this capability would increase turbine efficiency by reducing the magnitude of exit swirl. Exit swirl would decrease as a result of the reduction in flow separation and/or recirculation brought about by the variation of inlet blade angle. Their tests concluded that at low rotor speeds a backward curved blade, i.e. one with a portion of the inlet region curved against the direction of rotation, appeared to align better with the flow, thus yielding an increase in turbine efficiency.

Fredmonski et al (1991) detailed their findings following a research program in which they designed and tested two compact radial turbines with equal or better efficiencies relative to conventionally proportioned radial turbines. Of the two rotors tested one was designed with purely radial blading while the other incorporated a slightly back swept leading edge with the intention of minimising losses associated with positive incidence. While it was not the focal point of their investigation, Fredmonski et al concluded that the back swept rotor achieved an efficiency of 88.1% at its design velocity ratio of $U/C = 0.65$, which equated to an increase in efficiency of approximately half a percentage point over the purely radial rotor. The authors did not specify the back sweep angle used, but were of the opinion that the improved efficiency may have resulted from the non-radial inlet blading.

The aims of this paper are; firstly to present how the overall performance of a radial inflow turbine can be improved through the implementation of back swept blading at rotor inlet; and secondly, to show that the increases in stress that arise from back swept blading at rotor inlet are not necessarily detrimental to rotor functionality. For this study, a commercially available radial turbine, from a turbocharger application, was selected and used as the baseline model. The radial blades were modified to include a 25° inlet blade angle, creating a second turbine to be compared against the baseline model.

2 One-Dimensional Performance

One-dimensional performance predictions for both the baseline radial rotor and the 25° back swept rotor where obtained in order to asses the potential gain in efficiency offered by back swept blading. The 1D modelling procedures was based on the method described by Connor and Flaxington (1994). To maintain consistency the same loss coefficients were used for each of the rotor geometries analysed. With the exception of the inlet blade angle, all other data input into the 1D modeller was identical. The sign convention used was the same as that

adopted by Meitner and Glassman (1983) and Barr et al (2006), denoting a back swept inlet blade angle as the angle measured from the radial direction opposite to the direction of blade rotation, as depicted in Fig. 1, which is positive since it aligns with what is conventionally considered to be positive incidence at inlet to a radial turbine.

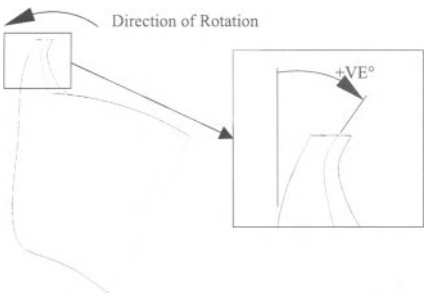

Fig. 1 Blade angle sign convention

Figure 2 details the 1D predicted efficiencies and mass flow rates plotted against velocity ratio *U/C* for the baseline radial rotor and the 25° back swept rotor respectively. The values have been non-dimensionalised by dividing by the design point values. The predictions are plotted at a constant pressure ratio of 3.68 and hence, the scale of increasing velocity ratio is directly proportional to increasing rotor speed. It is clear from Fig. 2 that the 25° back swept rotor offers significant increases in efficiency at lower than optimum velocity ratios. At approximately 50% of the design speed ($U/C = 0.30$), the 25° back swept rotor offers an increase in efficiency of 2.44% over the baseline radial rotor. As expected, the reduction in losses offered from the 25° back swept rotor correspond to an increase in mass flow through the rotor. This is a result of better blade alignment with the more tangential relative flow at inlet experienced at low speeds, as suggested by Mulloy and Weber (1982). This improvement in performance is evident up until a velocity ratio of approximately 0.47 after which the efficiency level of the 25° back swept rotor is seen to drop slightly below that of the baseline radial rotor. At the design speed ($U/C = 0.58$ for the baseline turbine rotor) the efficiency of the 25° back swept rotor drops 1.78% below the predicted efficiency of the baseline radial rotor. While offering generous advantages at lower than optimum velocity ratios, the 1D analysis predicts that the 25° back swept rotor suffers a penalty of approximately 2.2% in peak efficiency relative to its radial counterpart.

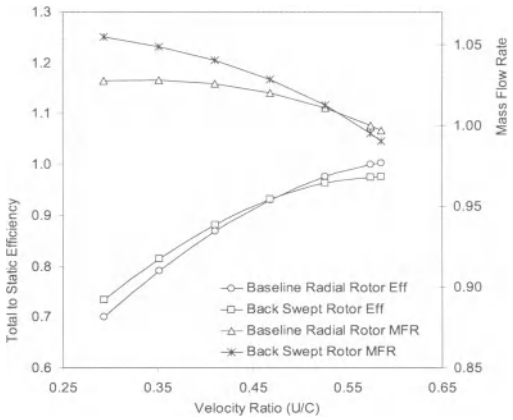

Fig. 2 1D predictions of radial and back swept rotors

3 Numerical Model Validation

Since the initial 1D analysis could not account for the real flow structures existing within the rotor blade passage, a 3D numerical investigation was undertaken using the CFX-10 Computational Fluid Dynamics (CFD) software. Calibration and benchmarking of the numerical modelling strategy was undertaken using results from an extensive experimental performance investigation of a 99 mm radial turbine with a vaned stator published by Doran (1999). The construction of the turbine test rig in question, along with the measurements taken, provided confidence that the turbine inlet flow was axisymmetric in nature. Consequently only a single blade passage was modelled. The stator and rotor meshes each comprised 400,000 cells, i.e. 800,000 cells in total per blade passage. The cell density of the grids was similar to that used by Dunham and Meauzé (1998). Both stator and rotor grids were constructed using H-grid cells, with particular attention being directed towards avoiding extreme skew angle values; the minimum skew angle was 25.86°. The rotor domain included a blade tip clearance of 0.5 mm, which was modelled using 10 equispaced cells in the spanwise direction. A mixing plane model was employed at the interface between the stationary and rotating domains, which takes the circumferentially averaged fluid properties at exit from the stator domain and applies them to the inlet of the rotor domain. The k-ε turbulence model was used with a blend factor of 1.0 chosen as the advection scheme setting. Setting the blend factor to 1.0 is equivalent to using second order differencing to calculate the advection terms within the discrete finite volume equations. The numerical procedure adopted close to the wall was the standard Log Law of the Wall with scalable

wall functions. The average value of the non dimensional wall distance y+ lay within the range of 36 to 51. The solution was considered to have reached convergence when the maximum values of all of the residuals and global imbalances fell below 5.0×10^{-4}. Experimental values for total pressure and total temperature at inlet and static pressure at outlet were used as boundary conditions. The flow upstream of the stator was assumed to approach in a radial direction, which was representative of the test rig used. Figure 3 compares the numerically predicted and the experimentally measured turbine performance at a range of pressure ratios across a constant speed line corresponding to 55 000 revs/min corrected to 288K inlet temperature. The experimental total-to-static efficiency was calculated from the measured temperature drop across the turbine stage, and therefore did not include bearing or windage losses. The predicted efficiencies lie within a band of 0% to 4% below the measured values, while the predicted mass flow rates are between 1.7% and 3.5% above the measured values.

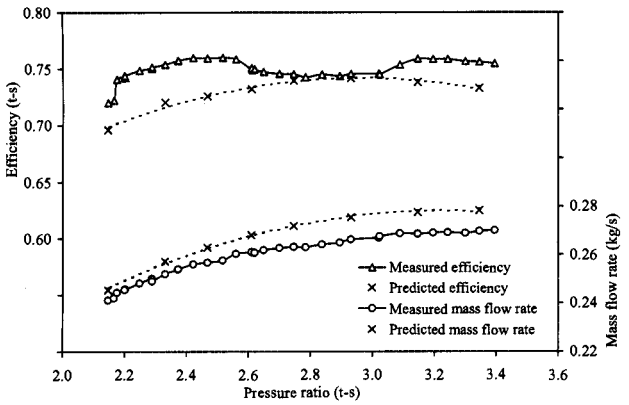

Fig. 3 Validation of modelling strategy with experimental results from a previous turbine investigation

A CFD study was conducted with the aim of determining the percentage of meridional length over which the inlet blade angle should be swept in order to gain the largest improvement in efficiency across the operating range. It was decided that 0-50% of the meridional blade length would sensibly define the inlet region. CFD predictions were then obtained for the performance of the backswept rotor over 10-50% of the meridional blade length in increments of 10%. The percentage of swept meridional length that was seen to give the largest gain in performance over the operating range was 20%.

The FEA investigation of each model involved a centrifugal analysis to determine the stress levels associated with the maximum rotational speed and a modal analysis from which the natural frequencies and mode shapes were extracted. Material properties of aluminium alloy 7075 T6 at room temperature were used. High temperature materials such as Inconel are normally chosen for the manufacture of radial turbines. However, as the experimental tests were to be conducted at temperatures much lower than those typically experienced during turbocharging, the material selected for the manufacture of the experimental test turbines was the aerospace aluminium alloy 7075 T6. A rotor backface treatment study was conducted with the aim of determining which treatment would yield the lowest maximum principal stresses, and thus, be best suited for a rotor with non-radial inlet blading. Further details of this study are published in Barr et al (2008). It was found that a complete disc backface would be best suited to counteract the additional bending stresses at inlet.

4 Results and Discussions

4.1 CFD Results

Numerical models were set up for the baseline radial rotor and the 25° back swept rotors in accordance with the CFD modelling strategy detailed in the previous section. Fig. 4 details the CFD performance predictions of efficiency and mass flow rate plotted against velocity ratio *U/C* for the baseline radial rotor and the 25° back swept rotor. Like the 1D results, the CFD predictions are plotted at a constant pressure ratio and, therefore the velocity ratio is proportional to rotor speed.

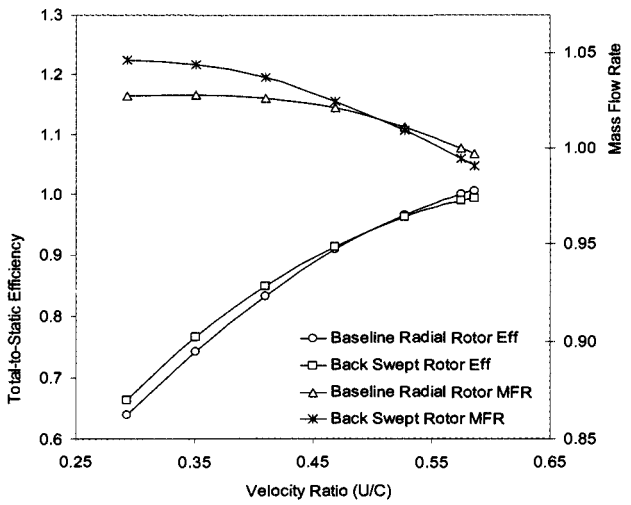

Fig. 4 CFD predictions of radial and back swept rotors

It is evident from Fig. 4 that the 25° back swept rotor delivers an increase in efficiency while operating at lower than optimum velocity ratios when compared to the baseline radial rotor. A slight loss in efficiency is seen to occur at speeds equal to and above the design speed. However, the small losses in efficiency displayed at high velocity ratios are outweighed by the significantly larger gains in efficiency offered at lower velocity ratios. At approximately 50% of the design speed ($U/C = 0.30$), the 25° back swept rotor offers an increase in efficiency of 1.76% over the baseline radial rotor. The reduction in losses offered by the 25° back swept rotor at low values of velocity ratio are seen to correspond to an increase in mass flow through the rotor. This improvement in performance is evident up until a velocity ratio of approximately 0.5 after which the efficiency level of the 25° back swept rotor is seen to drop slightly below that of the baseline radial rotor. At the design speed ($U/C = 0.58$) the efficiency of the 25° back swept rotor is seen to drop 0.78% below the predicted efficiency of the baseline radial rotor. The predicted mass flow of the 25° back swept rotor at the design speed lies within 0.55% of the baseline radial rotor.

5 FEA Results

Table 1 lists the maximum principal stresses at regions of most interest on the baseline radial rotor and the 25° back swept rotor. Note that the stress values shown in table 1 have been normalised.

Table 1 Stresses within the baseline and back swept rotors

Region	Maximum Principal Stress		Percentage Change in Max Principal Stress
	86mm Baseline Rotor	86mm 25° Back Swept Rotor	
Blade-Suction Side	0.5831	0.4967	-14.81
Blade-Pressure Side	0.5815	0.7108	22.24
Blade Fillet-Suction Side	0.9538	0.9071	-4.89
Blade Fillet-Pressure Side	0.8349	0.8492	1.71
Hub	0.7727	0.7593	-1.73
TE Fillet	0.7441	0.8138	9.37
Backface	0.7765	0.8079	4.04
Machined Radius	0.8074	0.8231	1.94
Overall Max	1.0000	0.9975	-0.25
Max Deformation	1.00	1.75	75.00

The centrifugal stress analysis was performed at the maximum rotational speed proposed for the experimental rotor tests. Also shown is the percentage change in maximum principal stress relative to the baseline radial rotor. As shown in Table 1, the difference in the overall maximum principal stresses experienced by the baseline radial rotor and the 25° back swept rotor is only 0.25%. This marginal decrease in maximum principal stress represents an almost insignificant change. The area of interest which saw the largest increase in stress was the pressure side of the blade; rising by 22.24%. It must be noted that this is not a highly stressed region to begin with. The rise of stress in this region as a result of the increased tensile and bending stresses brought about by back sweeping the inlet blade angle is to be expected. Figs. 5 and 6 depict contours showing the stress distribution on the pressure side of the blades on the baseline radial rotor and the 25° back swept rotor respectively.

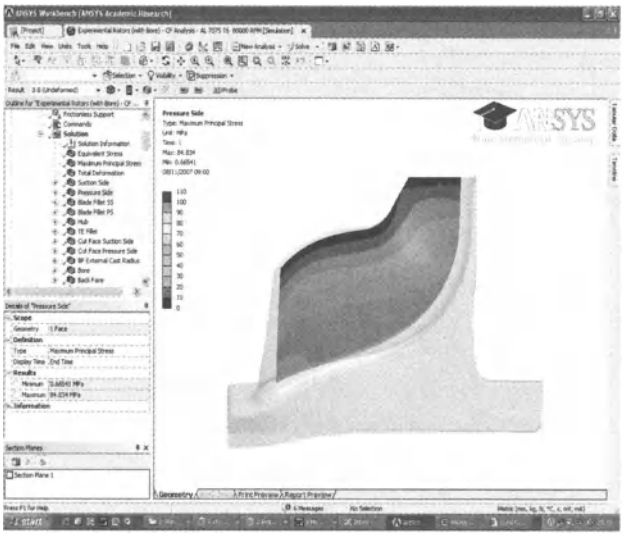

Fig. 5 Baseline rotor

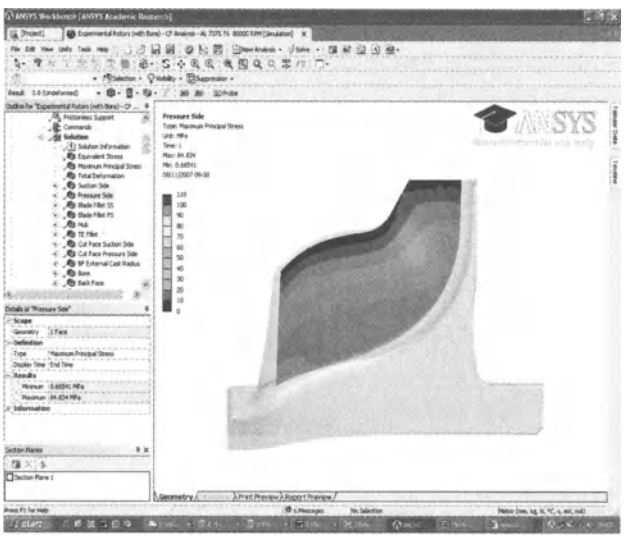

Fig. 6 25° back swept rotor

An associated decrease in stress on the suction side of the blade was observed. This, also to be expected, is a result of the back swept blade at inlet deforming towards the radial direction thus inducing a compressive stress on the suction side. The maximum principal stresses at all other regions were seen to change by less than ±10%.

Changes in material properties at elevated temperatures and thermal transients experienced by the rotor during experimental testing may contribute to stresses that are higher than the equivalent steady state values. Moustapha et al (2003) suggested that in spite of the advances in finite element methods, rotor life estimation remains an inexact science because it depends on factors that are wholly or partially outside the control of the designer.

Modal results were also obtained from the analysis of the baseline radial rotor and the 25° back swept rotor. Having extracted the natural frequencies for both rotors and calculated the excitational frequencies induced by the surrounding stator vanes, interference diagrams were produced. The interference diagrams have been plotted on a speed scale corrected to experimental test rig conditions. Figs. 7 and 8 show interference diagrams for the baseline radial rotor and the 25° back swept rotors respectively. The critical speeds, i.e. the points at which the excitational frequency matches a natural frequency, are circled.

As shown in Figs. 7 and 8 the interference diagrams for both the baseline radial rotor and the 25° back swept rotors are almost identical. Only the first seven natural frequencies were seen to lie within the test speed range. Each of the first seven natural frequencies, and hence critical speeds, predicted for the 25° back swept rotor were seen to lie within ±3.7% of those predicted for the baseline radial rotor. These results demonstrate that back sweeping a small portion of the inlet blade region by 25° results in a relatively small change in natural frequency and critical speed.

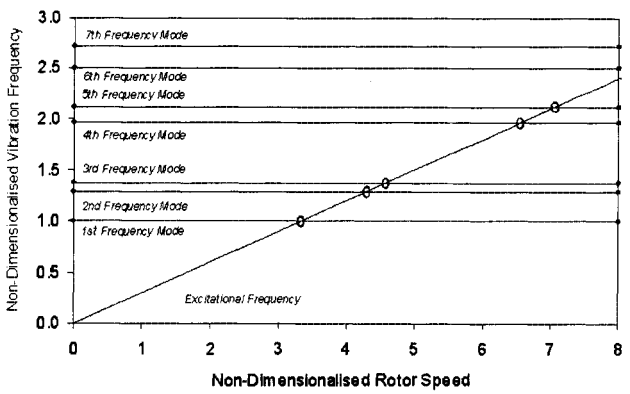

Fig. 7 Interference diagram for the baseline radial rotor

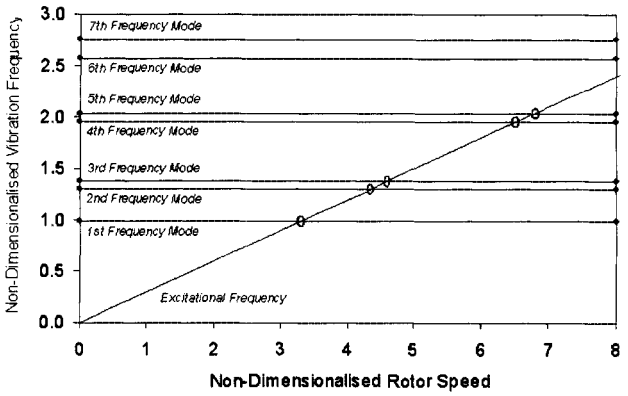

Fig. 8 Interference diagram for the 25° back swept rotor

6 Conclusions

An increase in turbine efficiency, particularly at lower than optimum values of *U/C*, would result in more torque available for turbocharger acceleration, increasing boost air pressure during engine transients, benefiting engine response and emissions.

A review of existing literature demonstrated the potential for enhancing turbine efficiency at low *U/C* through the implementation of a non-radial inlet blade angle.

A radial turbine rotor, used for commercial turbo-charging, was used as the baseline rotor. A second rotor geometry was produced by modifying the inlet blade region to incorporate a 25° back swept blade angle. A 1D analysis revealed that the 25° back swept rotor delivered increased efficiency levels at low velocity ratios when compared to the baseline radial rotor.

A thorough validation of the CFD numerical modelling strategy was conducted. Subsequent numerical modelling showed that the 25° back swept rotor delivered a considerable increase in efficiency while operating at lower than optimum velocity ratios, mirroring the trends predicted from the 1D analysis. The numerical modelling showed that at approximately 50% of the design speed (U/C = 0.30), the 25° back swept rotor offered an increase in efficiency of 1.76% over the baseline radial rotor. The reduction in losses offered from the 25° back swept rotor at low values of velocity ratio were seen to correspond to an increase in mass flow through the rotor. The CFD analysis predicted that the 25° back swept rotor would offer enhanced performance up until a velocity ratio of approximately 0.5, after which the efficiency level of the 25° back swept rotor would drop slightly below that of the baseline radial rotor. At the design speed (U/C = 0.58) the efficiency of the 25° back swept rotor is seen to drop 0.78% below the predicted efficiency of the baseline radial

rotor, however, the small losses in efficiency displayed at high velocity ratios are outweighed by the larger gains in efficiency offered at lower velocity ratios.

A centrifugal stress analysis revealed that the maximum principal stress experienced by the baseline radial rotor and the 25° back swept rotor differed by only 0.25%. Natural frequencies and thus critical speeds were calculated from a modal analysis of the baseline radial and back swept rotors. Each of the first seven natural frequencies, and hence critical speeds, predicted for the 25° back swept rotor were seen to lie within ±3.7% of those predicted for the baseline radial rotor. Although this modal analysis is based purely on the values of the Eigenfrequency, it does however, indicate that only small changes in natural frequency occur. It was concluded that back sweeping the inlet region of the blade by 25° significantly improves turbine efficiency at low velocity ratio without having a detrimental effect on the stress levels or changing the critical speeds of the rotor.

Acknowledgements

The authors would like to thank Cummins Turbo Technologies for ongoing technical and hardware support, and their enthusiasm and generous time. The technical support of staff at ANSYS Europe in the use of the CFX software was appreciated. Thanks are also due to John Doran for providing experimental turbine performance measurements.

References

Barr, L., Spence, S. W. T. and McNally, T., 2006, "A Numerical Study of the Performance Characteristics of a Radial Turbine with Varying Inlet Blade Angle", Instn. Mech. Engrs. 8th International Conference on Turbochargers and Turbocharging, pp. 169 – 181

Barr, L., Spence, S. W. T. and Eynon, P., 2008, "Improved Performance of a Radial Turbine Through the Implementation of Back Swept Blading", ASME Paper No. GT2008-50064. ASME Turbo Expo 2008

Connor, W. A., and Flaxington, D., 1994, "A One-Dimensional Performance Prediction Method for Radial Turbines," Proc. Inst. Mech. Eng., Part C: Mech. Eng. Sci., Proceedings of IMechE C484/041

Doran, W.J., 1999, An Experimental Assessment of the Effects of Shroud Profile on the Performance of a Radial Inflow Turbine, PhD Thesis, School of Mechanical Engineering, Queen's University of Belfast

Dunham, J., and Meauze, G., 1998, "An AGARD Working Group Study of 3D Navier-Stokes Codes Applied to Single Turbomachinery Blade Rows," ASME Paper No. 98-GT-50

Fredmonski, A. J., Huber, F. W., Roelke, R.J., & Simonyi, S., 1991, "Design and Experimental Evaluation of Compact Radial Inflow Turbines", NASA Lewis Research Centre, Report AIAA-91-2127

Hakeem, I., 1995, "Steady and unsteady performance of mixed flow turbines for automotive turbochargers", Imperial College of Science, Technology and Medicine, London, England

Meitner, P.L. & Glassman, A.J., 1983, "Computer Code for Off-Design Performance Analysis of Radial-Inflow Turbines with Rotor Blade Sweep", NASA Technical paper 2199, pp. 24

Moustapha, H., Zelesky, M. F., Baines, N. C., Japikse, D., "Axial and Radial Turbines", Concepts NREC, Wilder, VT. 2003

Mulloy, J.M. & Weber, H.G., 1982, "Radial Inflow Turbine Impeller for Improved Off-Design Performance", 27th International Gas Turbine Conference and Exhibit. ASME, New York, NY, USA, London, England, pp. 10

The 4th International Symposium on Fluid Machinery and Fluid Engineering
November 24-27, 2008, Beijing, China
NO. 4ISFMFE-Ab16

Swirl Flow and Heat Transfer Through Square Duct with Twisted Tape Insert

Ho-Keun Kang[*1], Soo-Whan Ahn[2], Bachtiar-Krishna-Putra Ary[3] and Jong-Woong Choi[4]

[*1] Research and Development Center, Korean Register of Shipping
60 Sinseongno, 23-7 Jang-dong Yuseong-gu Daejeon, Korea
Tel: +82-42-869-9215 / Fax: +82-42-862-6096
E-mail: hkkang@krs.co.kr (Corresponding Author)
[2] Soo-Whan Ahn, School of Mechanical and Aerospace Engineering, Gyeongsang National University, Korea
[3] Bachtiar-Krishna-Putra Ary, Department of Mechanical System Engineering, Graduate School, Gyeongsang National University, Korea
[4] Jong-Woong Choi, Advanced Numerical Simulation Technology, Korea

Abstract In this paper, numerical predictions and experiment of characteristics of a hydrodynamic and thermally developed turbulent flow through a square duct (30 × 30 mm) with twisted tape inserts and with twisted tape inserts plus axial interrupted ribs are conducted to investigated regionally averaged heat transfer and friction factors. Turbulent swirl flows having Reynolds numbers ranging from 8,900 to 29,000, a rib height-to-channel hydraulic diameter (e/D_h) of 0.067, and a length-to hydraulic diameter (L/D_h) of 30, are considered. The square ribs are arranged to follow the trace of the twisted tape and along the flow direction defined as axial interrupted ribs. The twisted tape is 1.0 mm thick carbon steel sheet with diameter of 28mm, length of 900mm, and 2.5 turns. Each wall of the square channel is composed of isolated aluminum sections. Two heating conditions are investigated for test channels with twisted tape inserts and rib turbulators: (i) electric heat uniformly applied to four side walls of the square duct, and (ii) electric heat uniformly applied to two opposite ribbed walls of the square channel. The correlation for friction factor and Nusselt number are derived from the predicted date. The results show that uneven surface heating enhances the heat transfer coefficient over uniform heating conditions, and significant improvements can be achieved with twisted tape inserts plus axial interrupted ribs compare to the case of twisted tape inserts.

Keywords heat transfer, twisted tape, swirl flow, rough square duct, number of heating wall, friction factor

1 Introduction

Heat transfer augmentation techniques find application mainly in the design of more compact heat exchangers. Among the various augmentation techniques, the use of twisted tape inserts is an effective method to improve the thermo-hydraulic performance of turbulent flow heat exchangers, since it offers significant increase in heat transfer as compared to the pressure drops.

Twisted tapes inserts and rib turbulators in square or circular duct provide a simple passive technique for enhancing the convective heat transfer coefficient on the tube side of a heat exchanger. Twisted tape inserts are used to achieve compact heat exchangers as well as to prevent hot spots in high heat flux transfer situations encountered with gas flows. The heat transfer enhancement with twisted tape inserts is influenced by tape-induced highly complex vertical flow, and higher flow velocity due to the tube blockage. On the other hand, rib turbulators break up the laminar sublayer and create local wall turbulence due to flow separation from the ribs and reattachment between the ribs; thus, the heat transfer rate is enhanced. Significant investigations (Manglic and Bergles, 1993; Eiamsa-ard et al., 2006; Chang, 2007) on

pressure drop and heat transfer characteristics of the fully developed flow in circular tubes containing twisted tape inserts can be found in the literature. These studies show that twisted tape inserts achieve sizeable heat transfer enhancement with a significant pressure loss penalty. Heat transfer coefficients and pressure losses in a tube with twisted-tape inserts depend upon the twisted tape pitch-to-tube diameter ratio and the flow Reynolds number. Since the twisted tape in the tube divides the flows into two parts, each part of the flow goes through a semi-circular tube that spirals along the tube length. The spiral-rotated semi-circular tube generates a swirling motion. Thus, the pressure drop increases and the heat transfer enhancement from the generating swirling flow. It is well known that rib turbulators also enhance the convective heat transfer rate in internal flow passages. Webb (1981) showed that heat augmentation and pressure drop in a tube with rib turbulators depend on configurations and the flow Reynolds number. Han (1988) and Ahn et al. (2008) investigated heat transfer and friction characteristics in rectangular channels with rib turbulators. They concluded that heat transfer enhancement and pressure drop depend on rib height, spacing, and angle of attack, and heating condition.

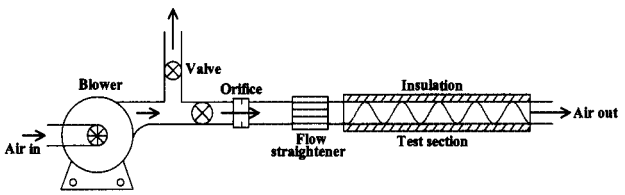

Fig. 1 Schematic diagram

Considering the increasing effects of both twisted tape and rib turbulators on heat transfer, Zhang et al. (2000) used a compound technique (twisted tape inserts plus rib turbulators) to enhance heat transfer in tube flows. Their results show that heat transfer is enhanced by combining twisted tape and interrupted ribs rather than twisted-tape or interrupted ribs only.

Several questions still remain unsolved that must be analyzed systematically since previous results are for flow in circular tubes. In reality, square channels are more common than circular tubes in most applications (e. g. turbine blade internal cooling passage). It is questionable whether the twisted tape can provide the same heat transfer performance in a square channel as in a circular tube. The question arises because the secondary flow generated by the swirling motion due to the twisted tape is different in square channels than in circular tubes. Heat transfer performance from the combined use of a twisted tape and interrupted ribs in a square must also be investigated.

There are very few numbers of research works conducted numerically to capture more detail of the fluid flow pattern and heat transfer phenomena in twisted square ducts or in the duct with twisted tape insert. Wang et al. (2001) examined the experimental and numerical study of three mildly twisted square ducts (twisted uniform cross section square duct, twisted divergent square duct and twisted convergent square duct). They showed that the twisted divergent duct can always enhance heat transfer, the twisted convergent duct always deteriorates heat transfer, and the twisted constant cross section duct is somewhat in between. Moreover, Ray and Date (2003) presented numerical prediction of characteristics of laminar ($40 \leqslant Re \leqslant 1100$), as well as, turbulent flow ($4000 \leqslant Re \leqslant 60{,}000$) and heat transfer in a square duct inserted with a twisted tape, whose width equals the length of the duct side. They clearly showed the presence of strong secondary circulation in the duct, where the maximum change in the axial velocities occurs neat the solid surfaces.

The objective of the present study is therefore to investigate experimentally as well as numerically the effect of the twisted tape and the combined effect of the twisted tape and interrupted ribs on heat transfer distribution and friction in square channels. The surface heating effect on the heat transfer coefficient is also investigated. The regionally averaged and channel averaged heat transfer distributions are plotted and compared with previous correlations and experimental data for circular ducts with twisted tape inserts.

2 Experimental apparatus

The experimental apparatus is shown in Fig. 1. The main components of the facility consist of a blower, an orifice flow meter, an entrance channel, and a test section. A 0.86 kW blower forces air into the pipe and the orifice meter and then through the straightener, entrance channel, and test section. The air is exhausted into the atmosphere from the end of the test channel. The square duct test section used with only twisted tape inserts and twisted tape plus interrupted ribs have a cross section of 3.0 cm by 3.0 cm. The twisted tape inserts and axial interrupted ribs are placed inside the test section square channels with length

L = 90cm as shown in Fig. 2. The twisted tape is 0.1mm thick carbon steel with a diameter (D) of 2.8cm and length (L) of 90cm. It has 2.5 turns throughout the entire duct length. The twisted tape is thermally insulated from the four side walls of the square duct to reduce heat conduction between tape rims and the aluminum duct.

The dimension of an axial interrupted rib is 2mm × 2mm × 23mm as shown in Fig. 3. The gaps between the ribs are 23mm in the axial direction and 15mm in the traverse direction. Test channels with the twisted tape plus interrupted ribs have aluminum ribs glued periodically on the inner bottom wall of the test section. The thin wood strips (0.2mm thick) are placed between the aluminum plates in the axial direction. The thin stainless foil heater (0.1mm thick) is installed at the backside of the aluminum plates. Two heating conditions are investigated for test channels with twisted tape inserts and rib turbulators: (i) electric heat uniformly applied to the four side walls of the square duct, and (ii) electric heat uniformly applied to two opposite ribbed walls of the square channel.

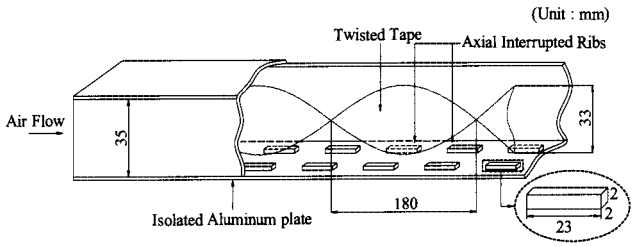

Fig. 2 Square test duct with twisted tape insert rib turbulators

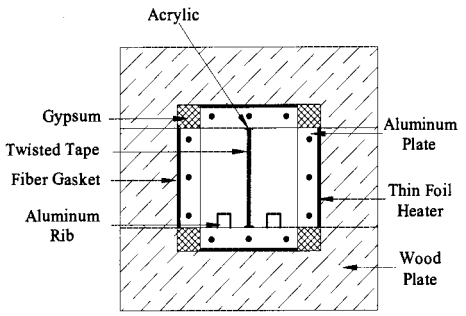

Fig. 3 Details of cross test section

The local surface temperatures of the test section are measured by copper-constantan thermocouples distributed along the length and placed at each aluminum plate of each wall. These thermocouples are embedded into the pre-drilled holes on the outer surface of each aluminum plate. Thermocouples inserted and suspended in the center of duct measure the bulk mean air temperature entering and leaving the test section. The bulk temperature is calculated by averaging the local temperatures in vertical direction from bottom to top of the channel. A 48-channel Hybrid Data Logger and a computer are used for data acquisition and data reduction.

3 Mathematical model

The numerical simulations of the fluid flow and heat transfer in the analyzed square duct geometries are conducted with the CFX 11.0 commercial code. For the working fluid, material properties of air are taken. Since the description of the basic conservation equations (mass, momentum and thermal energy) used in the code can be found in any classical fluid dynamics textbook or CFX manual, it is not repeated, here, but just explained the shear stress transport (SST) model.

The turbulence stresses and the turbulence viscosity μ_t were calculated with the transient shear stress transport model, which was developed and improved by Menter (1993). It is a combination of the $\kappa-\varepsilon$ and the $\kappa-\omega$ model of Wilcox (1986), where the turbulence eddy frequency is used as

$$\omega = \rho\kappa / \mu_t. \tag{1}$$

At the wall, the turbulence frequency ω is much more precisely defined than the turbulence dissipation rate ε. Therefore, the SST model activates the Wilcox model in the near-wall region by setting the blending function F_1 to 1.0. Far away from the wall, F_1 is 0.0, thus activating the $\kappa-\varepsilon$ model for the rest of the flow fields:

$$\text{SST model} = F_1 \cdot (\kappa-\omega \text{ model}) + (1-F_1)\cdot(\kappa-\omega \text{ model}) \tag{2}$$

where $F_1 = \tanh(\arg_1^4)$. Using Eq. (2), the transport equation for turbulence kinetic energy κ has been formulated as

$$\partial_t(\rho\kappa) + \partial_j(\rho\bar{v}_j\kappa) = P + \partial_j\left(\left(\mu + \frac{\mu}{\sigma_{\kappa^3}}\right)\partial_j\kappa\right) - \beta^*\rho\omega\kappa \tag{3}$$

and for turbulence eddy frequency ω as

$$\partial_t(\rho\omega) + \partial_j(\rho\bar{v}_j\omega) = \alpha_3\frac{\omega}{\kappa}P + \partial_j\left(\left(\mu + \frac{\mu}{\sigma_{\omega^3}}\right)\partial_j\omega\right) + (1-F_1)\frac{2\rho}{\sigma_{\omega 2}}\partial_j\kappa\partial_j\omega - \beta_3\rho\omega^2 \tag{4}$$

Based on turbulence kinetic energy κ and turbulence eddy frequency ω, eddy viscosity μ_t has been defined as follows.

$$\mu_t = \rho \frac{a_1 \kappa}{\max(a_1 \omega; SF_2)} \tag{5}$$

The SST model requires the distance of a node to the nearest wall for performing the blending between $\kappa - \varepsilon$ and $\kappa - \omega$. The wall scale equation is the equation solved to get the wall distance, simply:

$$\nabla^2 \phi = -1 \tag{6}$$

where ϕ is the value of the wall scale. The wall distance can be calculated from the wall scale through:

$$\text{Wall Distance} = -|\nabla \phi| + \sqrt{|\nabla \phi|^2 + 2\phi} \tag{7}$$

Since ϕ is always positive, the wall distance is also always positive.

4 Data reduction

The regional heat transfer coefficient is calculated from the regional heat transfer rate per unit surface area from the inner wall to the cooling air, the local wall temperature (T_w) on each aluminum plate, and the local bulk mean air temperature (T_b) as:

$$h = (q - q_{loss})/[A(T_w - T_b)] \tag{8}$$

The regional total heat transfer rate (q) generated from the stainless thin heaters is determined from the measured resistance and current ($q = I^2 R$) on each side of the test channel. The heat loss (q_{loss}) is determined experimentally by supplying electrical power to the test section until a steady condition is achieved for a no flow condition. The heat loss is 5% of the power inputs for a Reynolds number of 10,000.

It is found that the foil provides nearly uniformly heat flux on the entire test channel. The local bulk mean air temperature in Eq. (8) is also calculated by energy conservation as:

$$T_{b,i} = T_{in} + \Sigma(q - q_{loss})/\dot{m}c_p \tag{9}$$

with the measured inlet air temperature (T_{in}) and the accumulated net heat input from the test duct inlet to the *i th* position. Eq. (9) is calculated from the local bulk mean air temperature (T_b) at the *i th* position. The calculated outlet bulk mean air temperature agrees with the measured values within 5%. The inlet bulk mean temperature is about 21-28℃ and the wall temperature is around 50-60℃, depending on the test conditions. The local Nusselt number is normalized by the Nusselt number for a fully developed turbulent flow in smooth circular tubes correlated by Dittus- Boelter (1930) as:

$$Nu_r / Nu_s = (hD_h / k)/(0.023 \mathrm{Re}^{0.8} \mathrm{Pr}^{0.4}) \tag{10}$$

A manometer measures the pressure drop across the square channel. The average friction factor in fully developed flow is calculated from the measured pressure drop across the test channel and the mass flow rate of the air as:

$$f = \Delta p/[4(L/D_h)(\rho u_b^2/2)] \tag{11}$$

The uncertainty associated with the length scale used in the data reduction was ±1.0mm. The thermophysical properties of the air were assigned an uncertainty of ±3.0%, based on the observed variations in the reported values in the literature. The standard deviation in the air bulk velocities was found to be within ±4%, and the maximum uncertainty in the heat transfer rate ($\dot{Q}$) was estimated to be ±6.2%. These uncertainties would result in the maximum uncertainty of the convective heat transfer coefficient of about ±8.9% at Re = 19,100.

5 Results and discussion

Figure 4(a) represents the local Nusselt numbers in the smooth channel with twisted tape inserts in the two-sided heating and four-sided heating conditions, respectively. The results show that the local Nusselt numbers in the two-sided heated case are slightly higher than the four-sided heated case. This occurs because the colder fluid moves from the two unheated walls toward the two heated walls, which results in a higher heat transfer coefficient. Values of the fully developed Nusselt numbers with heating applied to two opposite walls were 1.08 to 1.19 times greater than those obtained with heating applied to all four walls at the same Reynolds number. Thus, the effect of the Reynolds number was more prominent in the two-sided heating condition than in the four-sided heating condition. The local Nusselt number decreases as the x/D_h increases, and maintains a nearly constant value from $x/D_h = 7$.

Fig. 4(b) shows the streamwise Nusselt number distributions based on the top wall temperature, left or right wall temperatures, and bottom wall temperature for the test section with the addition of ribs with twisted tape, respectively. The Nusselt numbers based on the bottom wall were 16 and 27 % greater than those on the adjacent smooth sides and opposite smooth side at a *Re* = 29,000.

The higher Nusselt numbers on the ribbed bottom wall were due to the increased level of turbulence generated by the ribs, which broke up the growth of the thermal boundary layer.

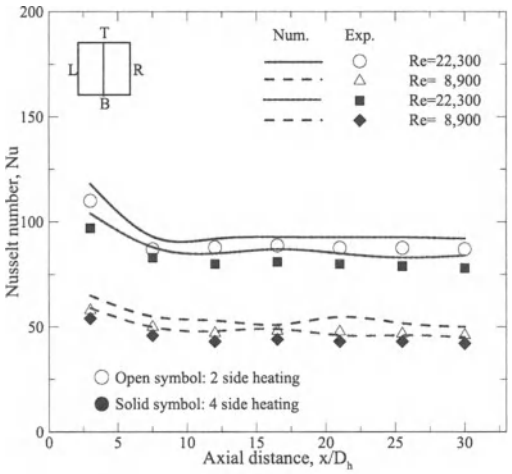

(a)

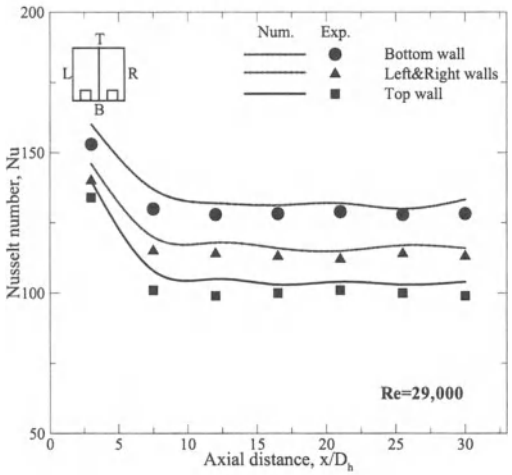

(b)

Fig. 4 Local Nu numbers (twisted tape inserts) (a), and Nu numbers (twisted tape inserts + rib turbulators) (b)

The twisted tape creates a swirling motion in the square channel as shown in Figs. 5(a),(b). Thus, a centrifugal force is superimposed over the main longitudinal flow that produces a secondary motion in the channel. The net effect of this change in the flow field increased the pressure drop and heat transfer enhancement. Interrupted ribs also act as turbulence promoters in the main flow field (Figs. 5(c),(d)). Thus, the addition of ribs with twisted tape increases local turbulence and secondary motion. Figure 6 shows the temperature distributions for each case.

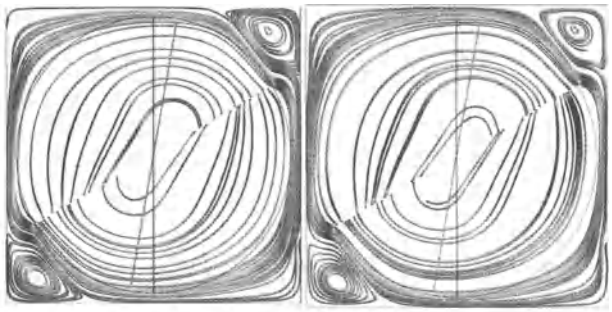

(a) 2 sided heating (b) 4 sided heating

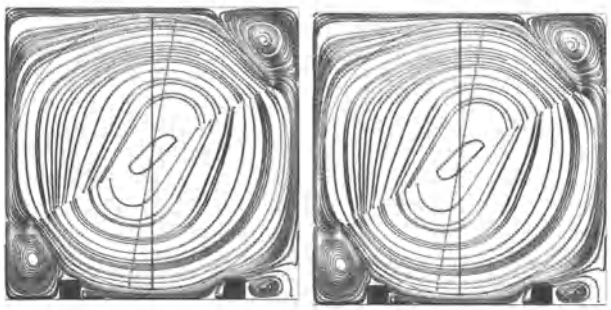

(c) 2 sided heating (d) 4 sided heating

Fig. 5 Streamlines for each case

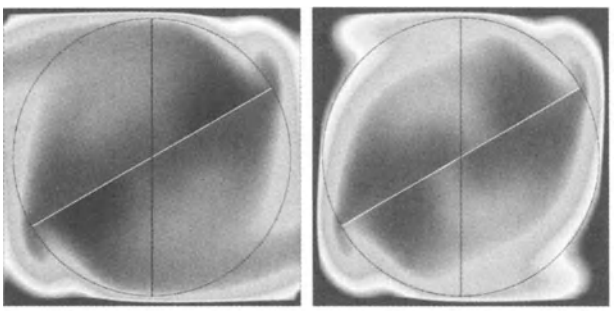

(a) 2 sided heating (b) 4 sided heating

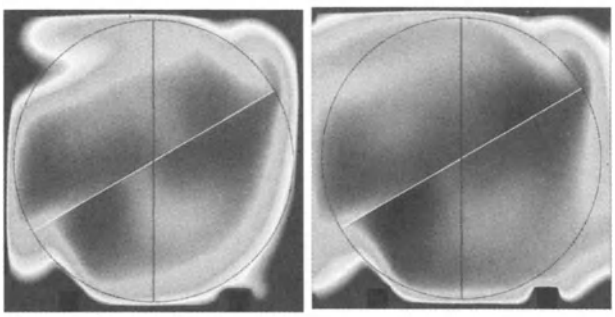

(c) 2 sided heating (d) 4 sided heating

Fig. 6 Temperature distributions for each case

Figure 7(a) shows the average Nusselt numbers for the fully developed flow in the smooth channel only, in the

smooth channel with the twisted tape, and in the bottom ribbed channel with the twisted tape, respectively. The test section with the twisted tape plus the ribbed wall has the greatest Nusselt number. The empirical correlation by Dittus and Boelter (1930) for a smooth channel is also plotted for a comparison. It is evident from Fig. 6 that there is an excellent agreement between the existing correlation and our results on the condition that the entire channel walls are heated.

Figure 7(b) shows the average channel friction factors by obtaining from experimental and numerical data for the smooth channel, the channel with the twisted tape, and the channel with the twisted tape and ribs on the bottom wall, respectively. The empirical equation by Blasius for a smooth circular tube is included for a comparison. The present results for a smooth channel agreed well with the Blasius correlation within 2.5%. The result also showed that the friction factor decreased with increasing Reynolds

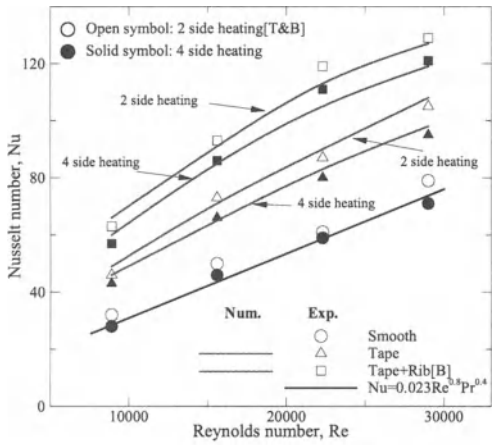

Fig. 7 Average Nusselt numbers (a) and friction factors (b)

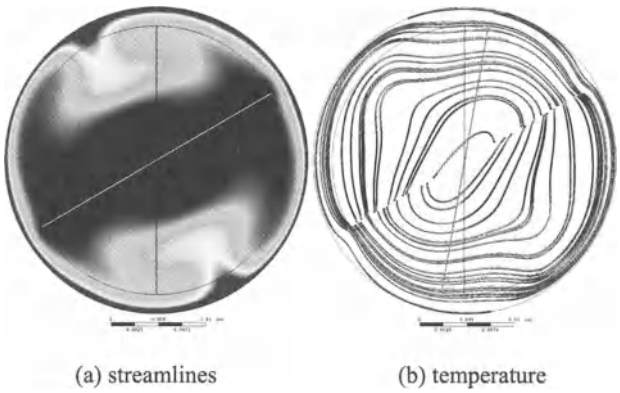

Fig. 8 Flowfields in a circular tube

number since the relative increase in the magnitude of the fluid velocity squared was greater than the increase in the wall shear stress with increasing Reynolds number. The channel with the twisted tape and ribs on the bottom wall has the maximum friction factor in the present work. This was due to the greater flow resistance experienced with additional turbulators, leading to higher friction factor values.

The experimental data by Zhang et al. (2000) for the smooth tube with the twisted tape is included for a comparison. The friction factor by Zhang et al was nearly 3.6 times greater than our present work at a Reynolds number of 29,000. The results may occur from the edge or corner effect in square channels. The flow field inside a square channel with twisted tape is more complicated than that in a circular tube (Fig. 8) because the secondary flow entrains in the four corners and creates corner vortices. This reduces a greater pressure drop in the square channels compared to the circular tubes. Interrupted ribs produce a higher heat transfer coefficient and friction factor. The interrupted ribs induce flow separation and reattachment, resulting in a secondary flow relative to the swirl flow generated by the twisted tape. This combined effect of swirl flow and turbulence secondary flow produces a higher pressure drop penalty.

Figure 9 shows the performance curve, $(Nu_r/Nu_s)/(f_r/f_s)^{1/3}$ as a function of the Reynolds number. This curve reflects the overall heat transfer performance of a channel taking the friction factor effect into account. Results show for the smooth channel only, the smooth channel with the twisted tape, and the ribbed channel with the twisted tape, respectively. Wall heating conditions are incorporated into the results. The results show that the two-sided heating

condition provides better overall heat transfer performance than the four-sided heating condition. In addition, the twisted tape with interrupted ribs provides a higher overall heat transfer performance over the twisted tape with no ribs.

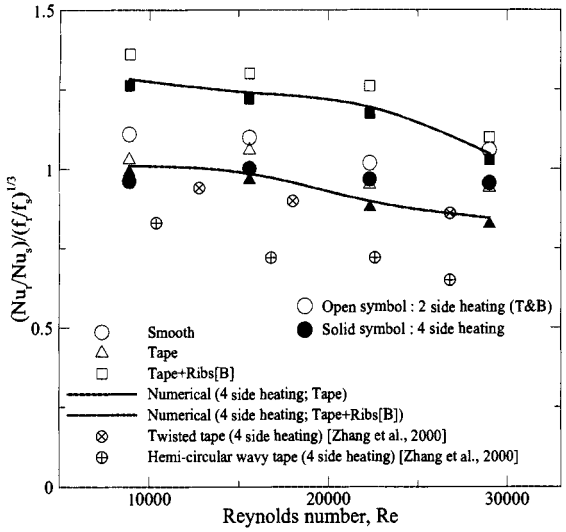

Fig. 9 Heat transfer performance under a constant pumping power

It is because the ribs give a better increment in heat transfer than in friction factor. For a comparison, the results obtained by Zhang et al. (2000) in a 4-side heated square channel with the twisted tape only were included. The present data agrees well with the data produced by Zhang et al.

A duct of square cross-section provides higher surface to volume ratio than a circular tube. Further, if a square duct is inserted with a twisted tape, whose width equals the side of the duct, the flow and heat transfer become periodically fully developed with the distance of periodicity equals to 90° rotation of the tape. Thus, both the flow and heat transfer are under continuous state of periodic development. Therefore, compared to a circular tube with a twisted tape insert, a higher thermal hydraulic performance can be expected from a square duct with a twisted tape insert. However, the twisted tape insert in a channel produces a higher pressure drop. Due to this high pressure drop, the use of tape insert may be limited and worse than some existing technology for turbine blade cooling. In this paper, we presented the results and it will be available in the literature. The turbine cooling system designer can decide whether or not they can use the results for any specific needs.

6 Conclusions

(1) In the smooth channel with twisted tape inserts, values of the fully developed Nusselt numbers with heating applied to two opposite walls were 1.08 to 1.19 times greater than those obtained with heating applied to all four walls at the same Reynolds number.

(2) For the test section with the addition of ribs with twisted tape, the Nusselt numbers based on the bottom wall were 16 and 27 % greater than those on the adjacent smooth sides and opposite smooth side at a Reynolds number of 29,000.

(3) The friction factor in the smooth circular tube with twisted tape was nearly 3.6 times greater than in the smooth square channel with twisted tape at a Reynolds number of 29,000. The results may occur from the edge or corner effect in square channels.

(4) The twisted tape with interrupted ribs provides a higher overall heat transfer performance over the twisted tape with no ribs. It is because that the ribs give a better increment in heat transfer than in friction factor.

References

Ahn, S.W., Kang, H.K., Bae, S.T. and Lee, D.H., 2008, "Heat Transfer and Friction Factor in a Square Channel with One, Two, or Four Inclined Ribbed Walls", *ASME. J. Turbomachinery*, Vol. 130, 034501-1

Chang, S.W., Jan, Y.J. and Liou, J.S., 2007, "Turbulent Heat Transfer and Pressure Drop in Tube Fitted with Serrated Twisted Tape", *Int. J. Thermal Sciences*, Vol. 28, pp. 97 – 115

Dittus, F.W. and Boelter, L.M.K., 1930, University of California, Berkeley, CA, Publications in Engineering, Vol. 2, pp. 443 – 452

Eiamsa-ard, S., Thianpong, C. and Promvonge, P., 2006, "Experimental Investigation of Heat Transfer and Flow Friction in a Circular Tube Fitted with Regularly Spaced Twisted Tape Elements", *Int. Commun. Heat Mass Transfer*, Vol. 33, pp. 1225 – 1233

Han, J.C., 1988, "Heat Transfer and Friction Characteristics in Rectangular Channels with Rib Turbulators", *ASME, J. Heat Transfer*, Vol. 110, pp. 321 – 328

Manglik, R.M. and Bergles, A.E., 1993, "Heat Transfer and Pressure Drop Correlations for Twisted-tape Inserts in Isothermal Tubes: Part II-Transition and Turbulent Flows", *ASME J. Heat Transfer*, Vol. 115, pp. 890 – 896

Menter, F.R., 1993, "Zonal Two Equation $\kappa-\omega$ Turbulence Models for Aerodynamic Flows", *AIAA Paper*, 98-0522

Ray, S. and Date, A.W., 2003, "Friction and Heat Transfer Characteristics of Flow through Square Duct with Twisted Tape Insert", *Int. J. Heat Mass Transfer*, Vol. 46, pp. 889 – 902

Wang, L.B., Tao, W.Q., Wang, Q.W. and He, Y.L., 2001, "Experimental and Numerical Study of Turbulent Heat Transfer in Twisted Square Ducts", *ASME. J. Heat Transfer*, Vol. 123, pp. 868 – 877

Webb, R.L., 1981, "Performance Evaluation Criteria for Use of Enhanced Heat Transfer Surface in Heat Exchanger Design", *Int. J. Heat Transfer*, Vol. 24, pp. 715 – 726

Wilcox, D., 1986, Turbulence Modeling for CFD, DCW Industries, Inc., La Canada, CA

Zhang, Y.M., Azad, G.M., Han, J.C. and Lee, C.P., 2000, "Turbulent Heat Transfer Enhancement and Surface Heating Effect in Square Channels with Wavy, and Twisted Tape Inserts with Interrupted Ribs," *J. of Enhanced Heat Transfer*, Vol. 7, pp. 35 – 49

The 4th International Symposium on Fluid Machinery and Fluid Engineering
November 24-27, 2008, Beijing, China
NO. 4ISFMFE-Ch08

Multi-Objective Automated Optimization of Centrifugal Impeller Using Genetic Algorithm

Wenbin Zhang, Xiaomin Liu

School of Energy & Power Engineering, Xi'an Jiaotong University
Xi'an Jiaotong University, Xi'an, 710049, China
Tel: +86-29-8266-3777/ Fax: +86-29-8266-4686
E-mail: liuxm@mail.xjtu.edu.cn

Abstract A development and application of an automated optimization method for aerodynamic design of centrifugal impeller blades has been presented in this paper. A Non-uniform mutation and Pareto tournament and Fitness-sharing techniques based Multi-Objective Genetic Algorithm (MOGA) has been developed. The fast speed to convergence and well ability to search the Pareto front of the MOGA has been demonstrated through single-objective and multi-objective function tests. By introducing the MOGA, a three-dimensional reconstruction system for centrifugal impeller blades using non-uniform rational B-spline (NURBS) and a commercial software NUMECA, an aerodynamic automated optimization design system has been established. To a centrifugal impeller, the maximization of the absolute total pressure ratio and the isentropic efficiency has been taken as the design targets. The Pareto solutions have been obtained by using the present optimization technique. Through analysis and comparison the optimized design and the initial design, the validity and feasibility of the developed optimization design system is confirmed. The optimized results showed the performance of the optimized impeller has been improved.

Keywords centrifugal impeller, genetic algorithms, NURBS, automated optimization

Nomenclature

θ	A parameter of the impeller in cylindrical coordinates
π	Absolute total temperature ratio
η_i	Isentropic efficiency
η_p	Polytropic efficiency

1 Introduction

The optimization of centrifugal impeller is very complex for the objective of optimization design can be a multimodal function of many design parameters. Some mutual restrictive objects are involved, such as efficiency and pressure ratio, et al. It is almost impossible to finish the optimization if only dependence on experience and reduplicative modification. Nowadays, with high development of computer technology, advanced CFD solvers are capable of analyzing there- dimensional (3-D), viscous, transonic and turbulent flows. The aerodynamic performance of complex shape can be obtained by CFD [Lakshminarayna B. 1991], and the experiment research can be reduced even be avoided in some conditions.

Genetic algorithm (GA) is a globe evolutionary algorithm based on natural selection and biological evolutionary mechanism. It has recently received considerable attention because of its potential of being a very effective optimization technique. When it is used in multi-objective problem, fitness and individuals and gene respectively corresponding to function value, candidate solution and design variable. GA starts from a population of individuals and each individual is evaluated to give some measure of its fitness. Because of these characteristics, GA is robust and it can easily be combined with aerodynamic performance calculation program to make optimization design [FENG Zhen-ping et al. 2003]. There always exist several conflicting objectives in an optimization problem and multi-objective genetic algorithm (MOGA) is

developed to handle these multiple objective optimization problem. MOGA is used popular among global optimization problems, including multi-objective optimization of wings [Obayashi S et al. 1996, WANG Xiao-peng. 2001, K. Chiba et al. 2006], cascade design [Tong Tong et al. 1999, Giuseppe Briasco. 2008], turbine blade optimization design [Özhan ÖKSÜZ et al. 2008]. Although MOGA is popular applied in the fields of turbomachine, there are few reports about the optimization design of centrifugal impeller.

By introducing a MOGA and a three-dimensional reconstruction system for turbomachine blades using non-uniform rational B-spline and a commercial software NUMECA, an aerodynamic automated optimization design system for centrifugal impeller blade optimization design has been established in this paper. An existing centrifugal impeller is used as a starting point for the optimization, and the results of the optimized design are compared with the performance of this existing design. The presentation shows that the method presented provides a new design that outperforms the original impeller with respect to the particular objective.

2 Aerodynamic Optimization Design System

2.1 MOGA

Many papers and books [David E et al. 1989, Mitsuo Gen et al. 2000] have introduced the basic knowledge and engineering application of MOGA. How to encode a solution of the problem into a chromosome is a key issue when using genetic algorithms. There are many encoding methods, but binary encoding and real-number encoding are more popular. Since the topological structure of the genotype space for real-number encoding is identical to that of the phenotype space, it is easy to form effective genetic operators by borrowing useful techniques from conventional methods. It has been widely confirmed that real-number encoding performs better than others for function optimizations and engineering optimizations [Davis L. 1991]. So real number encoding has been selected in this paper. And tournament selection and blend crossover [Eshelman L. 1993] are taken in the MOGA.

The traditional mutation always takes a random number which uniform distribute in a certain range to mutate the individual and the individual can move freely in whole searching space. This method does not convenient for local search in mainly regional search. So, nonuniform mutation is introduced in the MOGA. For a give parent x, if the element $x(k)$ of it is selected for mutation, the resultant offspring is $x'(k)$, where $x'(k)$ is selected from the following choice:

$$x'(k) = x(k) + f(t,r,b) \tag{1}$$

Where r is a random number from [0, 1], t local generation number and b a parameter determining the degree of nonuniformity. When generation number t is increased, the value of $f(t,r,b)$ will approaches 0. This property makes the operator to search space uniformly initially and very locally at later stages. So, fine-tuning capabilities aimed at achieving high precision are obtained in this technique.

The Pareto ranking method in this paper is based on the definition of nondominated solutions. Firstly, the non-dominated individuals are identified and assigned a large dummy fitness value. Then, to maintain diversity in the population, these individuals are shared with their dummy fitness values. After sharing, these nondominated individuals are ignored temporarily and the second nondominated front in the rest of the population is identified and assigned a dummy fitness value that is kept smaller than the minimum shared dummy fitness of the previous several fronts. The flowchart of this algorithm is shown in Fig. 1.

Fitness sharing method introduced by Goldberg [1989] and Richardson is adopted after Pareto ranking in this paper. Fitness sharing is a technique used to maintain population diversity. A sharing function is a way of determining the degradation of an individual's fitness due to crowding by its neighbor and it derates fitness according to the number and closeness of neighboring points. It is operated based on following function:

$$S_i = \sum_{i=1}^{n} S(d_i) \tag{2}$$

$$f_s(i) = f(i)/S_i \tag{3}$$

Where d_i is the distance of an individual from others, $S(d_i)$ the sharing function, $f_s(i)$ the new fitness.

Table 1 Single-objective function

Objective functions	n	Variable bounds	Max (min)
$F_1 = \sum_{i=1}^{3} x_i^2$	3	[-5.12,5.12]	0.0
$F_2 = 100(x_1^2 - x_2)^2 + (1 - x_1)^2$	2	[-2.048,2.048]	0.0
$F_3 = \sum_{i=1}^{5} \text{int}(x_i)$	5	[-5.12,5.12]	-25
$F_4 = \sum_{i=1}^{30} i x_i^4 + Gauss(0,1)$	30	[-1.28,1.28]	1248.4

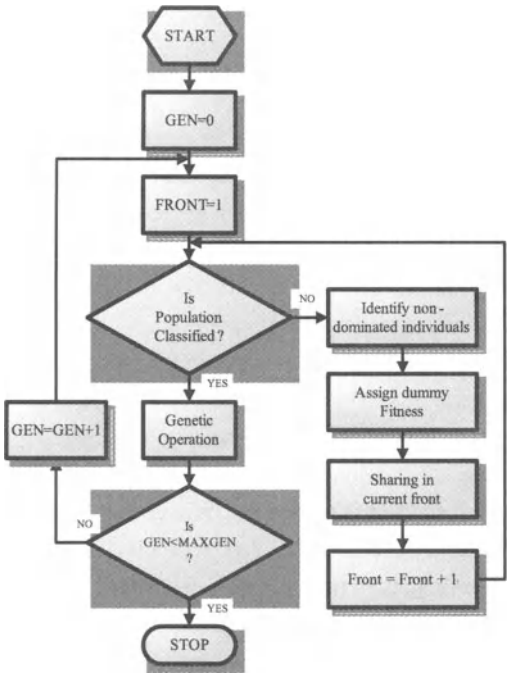

Fig. 1 Flowchart of non-dominated sorting method

If there are too many other individuals near an individual, the fitness value for the individual will be degraded to reduce their reproduction abilities. Fitness sharing can effectively ensure the fairness of tournament and prevent premature convergence. Using this technique the searching efficiency of MOGA is also improved and the Pareto solutions we obtained are uniformly spaced at the Pareto front.

How to maintain set of Pareto solution during the evolutionary process is a special issue for multi-objective optimization [Mitsuo Gen et al. 2000]. Pareto solution preserving mechanisms are obtained in the MOGA. A special pool for preserving Pareto solution is added to the basic structure of MOGA. In each generation, the set of Pareto solution is updated by getting off all dominated solutions and adding all newly generated Pareto solutions. To research the advancement of the MOGA, single-objective and multi-objective function tests for MOGA have been taken in this paper. Four classical test functions introduced by De Jong [1975] have been used to single-objective function test. The functions are given in Table 1.

The evolution history of optimization research is shown in Fig. 2. In Fig. 2, the max fitness and average fitness of each generation are shown and each problem has been found the best solution. From the test results, we can see that the global optimum solution has been obtained quickly and the GA developed in this paper has good convergence performance.

Functions for multi-objective test selected from reference [Kalyanmoy Deb et al. 2002] are taken for testing the MOGA's ability of multi-objective optimization. The functions are shown in Table 2.

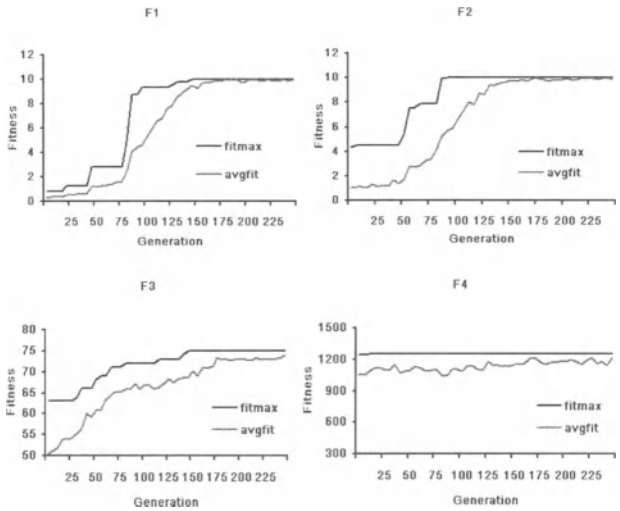

Fig. 2 GA evolution history of single-objective function test

Table 2 Function for multi-objective test

Problem	n	Variable bounds	Objective functions
SCH	1	[-1000, 1000]	$f_1(x) = x^2$ $f_2(x) = (x-2)^2$
KUR	3	[-5,5]	$f_1(x) = \sum_{i=1}^{n-1}(-10\exp(-0.2\sqrt{x_i^2 + x_{i+1}^2}))$ $f_2(x) = \sum_{i=1}^{n}(\lvert x_i \rvert^{0.8} + 5\sin x_{i+1}^3)$
ZDT2	30	[0,1]	$f_1(x) = x_1$ $f_2(x) = g(x)[1-(x_1/g(x))^2]$ $g(x) = 1 + 9(\sum_{i=2}^{n} x_i)/(n-1)$

The number of population is 60 and max generation is 200. The Pareto solution is calculated for each problem and they are shown in Fig. 3. Comparing with the Pareto-optimal front from reference, the Pareto front we maintained has a better spread of solutions and converges bettering the non-dominated front.

Through single-objective and multi-objective function tests, the fast speed to convergence and well ability to search the Pareto solutions of the MOGA has been demonstrated. The MOGA developed in the paper is suitable to turbomachine optimization.

2.2 NURBS blades profile parameterization and Objective function evaluation

Blade profile reshaping is an important part of automatic optimization design. Especially genetic algorithm has strong

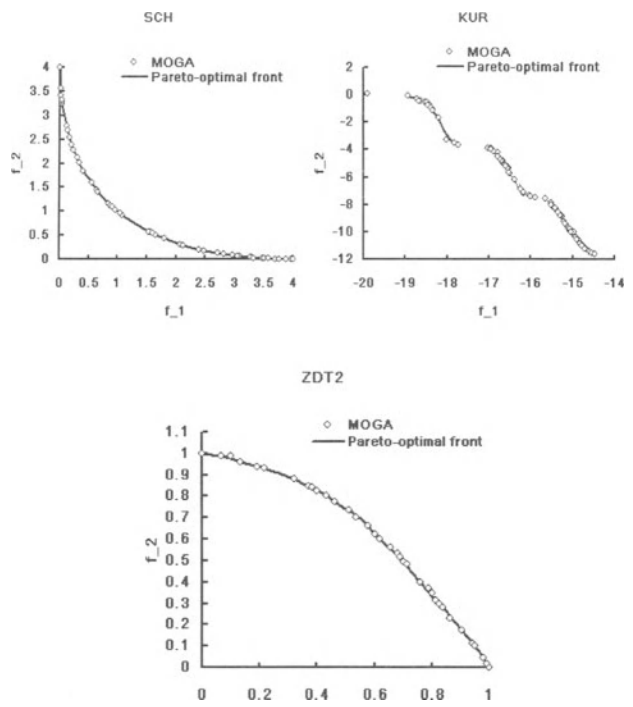

Fig. 3 Optimization search result

dependence on parameterization method, for evolution calculation is beginning with producing design individual randomly in design space. If the parameterization method easily to produce void individuals, the optimization design will be difficult. Because those void individuals must be disposed in particular, the time and degree of difficulty of the optimization design are also increased. In the other hand, the number of the design variables is influenced directly on the population size. GA can handle wholesale population problem, but if proper blade profile reshaping method is used, the performance of GA will be improved efficiently. The design cycle will be shortened and the optimization design result could be improved. Therefore designer must not only guarantee the precision of Blade profile reshaping, but also reduce the number of variables.

Non-Uniform Rational B-Spline (NURBS) has been taken for blade profile reshaping in this paper. It is efficient in an automated design process for the definition of new geometries. The pressure and suction sides on hub or on shroud are both defined with just two curves which are represented by 3rd degree B-Spline curves. The 3-D blade model is rebuilt through there steps: Firstly, the blade curves are handled with approximate arc-length parameterization. So the relationship between arc-length and θ can be established. Then the relationship curve will be rebuilt by NURBS. Finally, the curves are imported to NUMECA/IGG and the 3-D blade profile is reshaped based on Skinning Surface.

In this paper each curve has been reshaped and controlled by 7 control point. There is an example, the intersection between suction surface and the hub surface is reshaped by this method, see Fig. 4. In order to investigate the influence of blade head position, six control point of each curve have been taken as variables and the control point at outlet is fixed. The changes of the curves at shroud are set the same to the curves at hub. There are 12 variables at all.

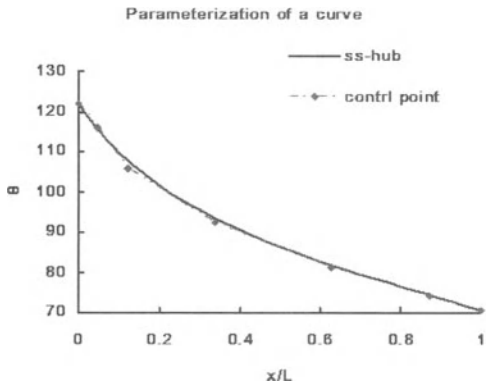

Fig. 4 An example of parameterization

The object function value is obtained by 3-D flow analysis of FINE/Turbine. 3-D Reynolds time-averaged N-S equation is taken as the governing equation and Spalart-Allmaras algebraic model is used for turbulence simulation. The governing equation is discrete by central difference method and using fourth order Runge-Kutta integration in time to get steady solution. Local time step and implicit residual smooth and multi-grid technique is used to accelerate the convergence procedure. After 3-D flow analysis the objective function values will be return to the MOGA.

2.3 Optimization flow chart

The MOGA combine with a 3-D reconstruction system for turbomachine blades using NURBS and a commercial software NUMECA for 3-D flow analysis, the aerodynamic automated optimization design system has been established. The optimization flow chart can be seen Fig. 5.

3 Optimization design application

To demonstrate the reliability of the complete optimization procedure, a test centrifugal impeller [Krain H. 1989] is used. For the data of blade at impeller exit region is not given, the data of blade in this paper is got from other reference [XI Guang. 2000]. The calculation parameters are shown in table 3. The tip between blade and shroud is 0.5mm at leading and 0.3mm at trailing.

Table 3 The calculation parameters of the impeller

Blade Number		24
inlet radius(mm)	(shroud)	112.74
	(hub)	44.93
Outlet radius (mm)		200
Backswept degree (°)		30
Shaft speed (rpm)		22363
Design (kg/s)		4
Total Pressure Ratio		4.7:1

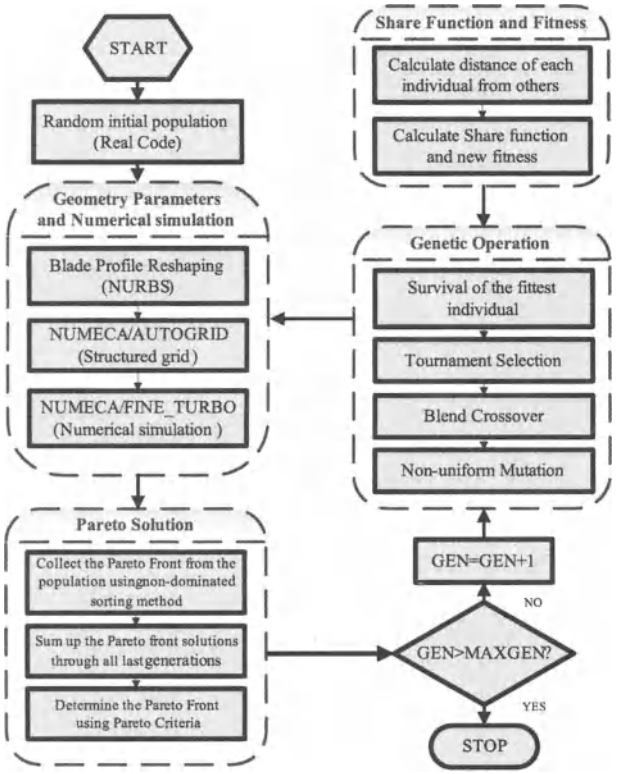

Fig. 5 Optimization flow chart

Figure 6 shows the geometrical shape of the centrifugal impeller. The test impeller is called the reference impeller for further use. Because only stationary calculations are done, it is sufficient to generate a flow channel for one segment of 15° within the impeller. The flow channel is arranged between two adjacent blades. The impeller exit is precisely connected to a vaneless constant area diffuser and the influence of the tip clearance is considered in this optimization.

To compare the experiment results and the calculated results of the reference impeller, numerical simulations in different conditions are calculated. Multi-block structured grid is used in the computation region. The grid of impeller can be seen in Fig. 7. The inlet boundary conditions are ambient conditions of total pressure and total temperature. The outlet is given discharge and static pressure.

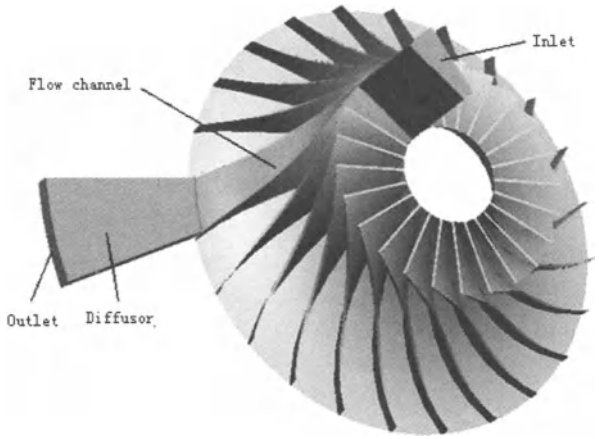

Fig. 6 Impeller model and the computational region

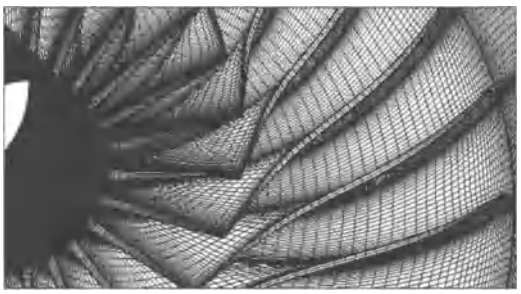

Fig. 7 Grid of impeller

The total pressure ratio and polytropic efficiency curve of experiment and computation results of impeller at design shaft speed is displayed respectively in Fig. 8. In Fig. 8, good agreement is shown by comparison of performance curve between computation and experiment results. At the design condition, the computation result of 4.63 is close to the total pressure ratio 4.7 and the relative error is 1.49%. The simulation results are basically reasonable and FINE/Turbine for 3-D flow analysis is accurate.

Figure 9 shows the static pressure distribution along the dimensionless arc length in the meridional cut at the shroud. Here the pressure is averaged along the circumferential direction of the impeller and the measurement and the calculation results show good agreement.

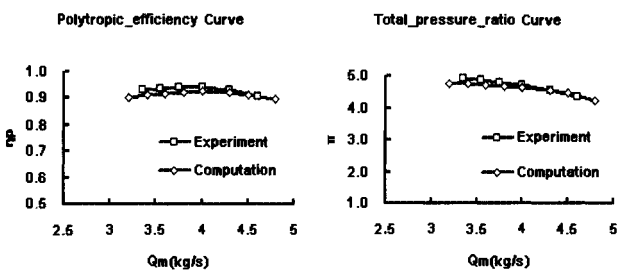

Fig. 8 Comparison of total pressure ratio and polytropic efficiency curve between computation and experiment

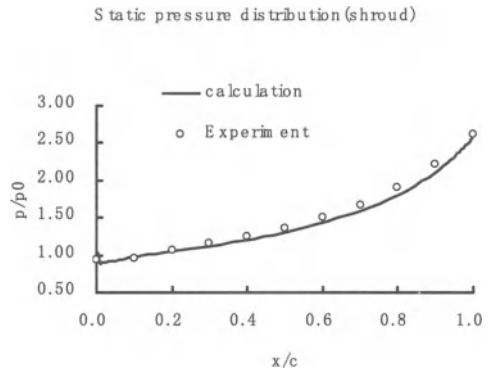

Fig. 9 Static pressure distribution at the shroud

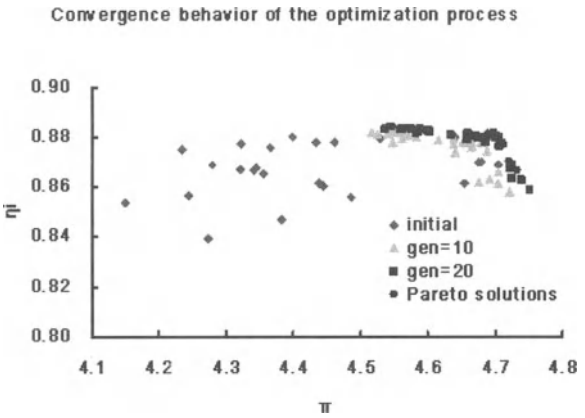

Fig. 10 The convergence history of optimization design

In Fig. 10, the convergence history of the evolution strategy is displayed. The number of population is set as 30 and the 3-D viscous flow analysis for each individual is carried out. Finally 16 Pareto solutions are obtained after 25 generations.

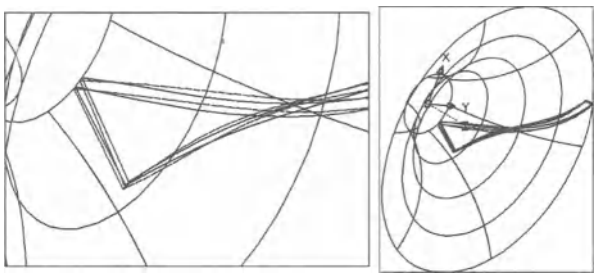

Fig. 11 The optimized and initial blade

A point from the Pareto solutions is taken for further analysis. The optimized blade and the initial blade have been shown in Fig. 11. The red blade is the optimized blade and the gray one is the initial. Comparing with the initial blade, the optimized blade has great change at the head of blade. The isentropic efficiency and total pressure ratio at design condition have been calculated and they are listed in table 4 with the initial results. The isentropic efficiency is promoted almost 1% and the total pressure ratio is improved 0.56.

Table 4 Impeller performance at design condition

	Initial	Optimized
η_i	0.8713	0.8808
π	4.636	4.692

The performance of the optimized impeller was compared with the initial and the efficiency and pressure ratio curve are shown in Fig.12. Obviously, the performance of the optimized blade improves not only at design point but also at off-design points and the performance at the low flow rate conditions is improved more than large flow rate conditions.

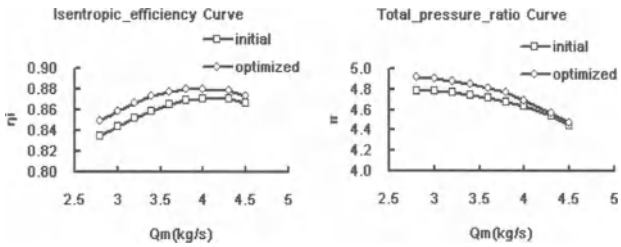

Fig. 12 Pressure ratio and isentropic efficiency curve of optimized and initial impeller

Figure 13 is the distribution of relative Mach number at inlet of blade. The distribution trend of optimized impeller is similar to the initial impeller. But the Value of Mach number near the suction-side is lower than initial. So the velocity at inlet of blade is decreased and impact loss is reduced.

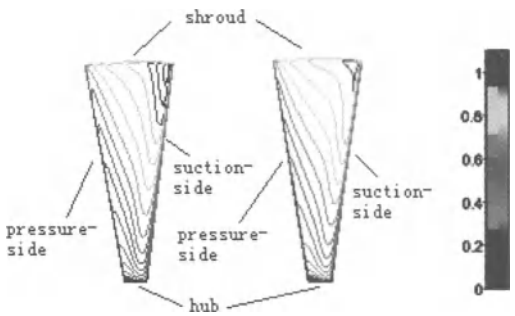

Fig. 13 Relative Mach number at inlet of blade

Absolute Mach number distribution at 90% blade height has been shown in Fig. 14. Obviously, the high Mach number region near the end of suction side is reduced and the Mach number distribution of optimized impeller at inlet is more uniform than initial design.

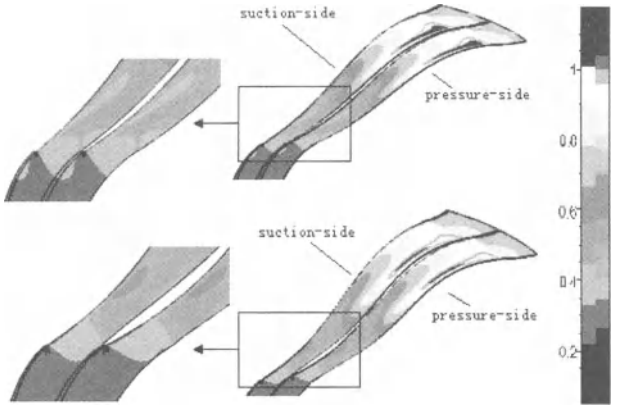

Fig. 14 Absolute Mach number at 90% blade height

4 Conclusions

(1) A MOGA based on tournament selection, blend crossover and non-uniform mutation has been developed. The Function sharing, non-dominated sorting approach and Pareto solution preserving mechanism are used in the MOGA. The tested results of some single-objective and multi-objective test problems show that the proposed MOGA has a good global convergence and a uniform spread of Pareto solution.

(2) By introducing the MOGA, the 3-D reconstruction system for turbomachine blades using NURBS and the commercial software NUMECA, the aerodynamic automated optimization design system has been presented and discussed. The applications have shown its capabilities to improve the performance of centrifugal impeller.

(3) Through numerical simulations, the performance of the reference impeller and the optimized impeller is compared. As we know, the flow state influenced by the impeller blade is mainly embodied at the head of the blade. In this paper, better flow distribution at the impeller inlet is obtained by using automated optimization technique.

(4) A set of Pareto solutions provided can be selected according to the practical application. Through comparison results of the optimized design and the initial design, the validity and feasibility of the optimization design system is also confirmed.

References

David E, Goldberg, 1989, "Genetic algorithms in search, optimization, and machine learning", *Addison-Wesley Pub. Co.*, Mass

Davis L,1991, "Handbook of Genetic Algorithms", *Van Nostrand Reinhold*, New York

De Jong, 1975, "An Analysis of the Behavior of a Class of Genetic Adaptive Systems", *University of Michigan*

Eshelman L, J Schaffer, 1993, "Real-coded genetic algorithms and intervalschemata", *Foundations for Genetic Algorithms*, vol.2, pp.187 – 202

FENG Zhen-ping, LI J un, REN Bin, SONG Li-ming, 2003, "Evolutionary Computation in Aerodynamic Optimization Design", *THERMAL TURBINE*, pp. 6 – 16

Giuseppe Briasco, Dario Bruna, Carlo Cravero, 2008, "A Nurbs-based Optimization Tool for Axial Compressor Cascade at Design and Off Design Conditions", *Proceedings of ASME Turbo Expo 2008*, GT2008-50622

K Chiba, S Obayashi, K Nakahashi, 2006, "Design Exploration of Aerodynamic Wing Shape for Reusable Launch Vehicle Flyback Booster", *Journal of Aircraft*, Vol.43, No. 3, pp. 832 – 836

Kalyanmoy Deb, Amrit Pratap, Sameer Agarwal, and T Meyarivan, 2002, "A Fast and Elitist Multiobjective Genetic Algorithm: NSGA-II", *IEEE Transactions on Evolutionary Computation*, Vol. 6, No. 2

Krain H, and Hoffman W, 1989, "Verification of an Impeller Design by Laser Measurements and 3D-Viscous Flow Calculations", ASME Paper ,89-GT-159

Lakshminarayna B, 1991, "An Assessment of Computational Fluid Dynamic Techniques in the Analysis and Design of Turbo-machinery", Journal of Fluid Engineering, *Transaction of the ASME*, Vol.113

Mitsuo Gen, Runwei Cheng, 2000, "Genetic algorithms and engineering optimization", *Wiley-Interscience*, New York

Obayashi S, Takanshi S, 1996, "Genetic optimization of target pressure distributions for inverse design method", *AIAA Journal*, pp:881 – 886

Özhan ÖKSÜZ—brahim Sinan AKMANDOR, "Mnuti-objective Aerodynamic Optimization of Axial Turbine Blades using Novel multi-level Genetic Algorithm", *Proceedings of ASME Turbo Expo 2008*, GT2008-50521

Tong Tong, Feng Zhen-ping, Li Jun, 1999, "Application of gentic algorithm to multiobjective optimization design for turbine cascades", *Proceedings of the CSEE*, Vol 19, No.6, pp. 74 – 77

WANG Xiao-peng, 2001, "Hybrid genetic algorithm and its application in multi-objective aerodynamic optimization design of airfoil", *ACTA Aerody Namica Sinica*, Vol.19, No.3, pp. 256 – 261

XI Guang, 2000, "Discussion on the geometry and the secondary flow vortex structure of krain's experimental compressor impeller", *Journal of engineering thermophysics*, Vol.21, No.4, pp. 440 – 442

The 4th International Symposium on Fluid Machinery and Fluid Engineering
November 24-27, 2008, Beijing, China
NO. 4ISFMFE-Ch33

Axisymmetric Weakly Compressible Transient Pipe Flow and Water Hammer Control

Lijun Xuan*[1], Feng Mao[1] and Jiezhi Wu[1,2]

[1] State Key Laboratory for Turbulence and Complex System, College of Engineering, Peking University, Beijing, 100871, China
Tel: +86-10-6275-6145
E-mail: ljxuanstar@gmail.com

[2] University of Tennessee Space Institute, Tullahoma, TN 37388, USA

Abstract The transient flow in a long cylindrical pipe caused by the motion of a valve is a subject of significant interest in wide engineering applications. Despite the partial success of existing theoretical models in explaining certain transient flow phenomena, they can hardly predict the evolution of strong water hammer, in particular the one downstream the valve caused by its closing (reversed water hammer). We attack this important problem by a new theory based on the unsteady axisymmetric and compressible Navier-Stokes equations, so that the viscous effect and inevitable coupling between the pressure wave and vortical wave can be fully taken into account. The weak compressibility of water naturally permits applying perturbation approach, of which the leading-order transient solution is found to be in excellent agreement with the result of direction simulation of the original N-S equation. We establish a simple connection between the valve motion and adjacent pressure in reversed water hammer, which enables the optimization of the valve motion to minimize the strength of the water hammer. Extension of the present laminar theory to turbulent flow with cavitation is being investigated and will be reported elsewhere.

Keywords unsteady pipe flow, perturbation analysis, H-p relation, water hammer control

Nomenclature

(All variables with ~, as well as axial velocity U, radial velocity V, pressure P, pipe length L and radius R, are dimensional; otherwise are dimensionless)

(z,r,t) axial, radial coordinates and time

a	Speed of sound at normal state of water in elastic pipe
a_0	Speed of sound at normal state of water
C	Initial dimensionless pressure gradient
C_n	Bessel-expansion coefficients of the initial velocity
e	Thickness of the pipe wall
E	Modulus of elasticity of the pipe wall
$F_\varepsilon(t)$, $G_\varepsilon(t)$, and $H_\varepsilon(t)$	Functions of t depending on ε
$h(r,t)$	Boundary condition of velocity at z=0
L_0	Pipe length
L_α	Scale of variable α, which represents z,r,t,u,v,p,ρ.
M	Mach number
p	Pressure
p_0	0th order expansion of pressure
P_0	Pressure at open side of the pipe
$\bar{p}(0,t)$	Pressure at z=0 with zero pressure gradient
$Q_v(t)$	Volume flux at $z = 0$
r_0	Pipe radius
R	Local pipe radius
R_0	Initial pipe radius
Re	Reynolds number
s	Laplace transform variable
T_n	Function in separation of variables
u	Axial velocity
u_0	0th order expansion of axial velocity
u_{00}	Initial velocity
v	Radial velocity
v_0	0th order expansion of radial velocity

$w_n (n \in \mathbb{N})$ The root of $J_0(w_n) = 0$

y Radial variable scaled by R

Y_n Function in separation of variables

Superscripts

$\wedge$ Laplace transform

β Ratio of elasticity coefficient of water and pipe wall

δ Ratio of radius and length of the pipe

ε $\varepsilon = 1/(\delta \mathrm{Re})$

μ Viscosity coefficient

ν Kinematic viscosity coefficient

θ Dilatation

ρ Density

σ_{ij} Components of Stress tensor

1 Introduction

Unsteady flow in a long pipe has long been of common interest at both fundamental and applied levels. This subject is related to a wide range of engineering flow problems, with most flows being highly turbulent. Pressures triggered by flow unsteadiness are known to cause rupture of pipelines, damage to other hydraulic devices and fire-related damage in the case of natural gas pipelines (Wylie & Streeter 1993). The pressure in unsteady flow can be low enough to cause cavitation with associated unfavorable effects (Brunone *et al.* 2000). On the other hand, the instability and transition of unsteady pipe flows has been an interesting issue as well (e.g. Ghidaouui & Kolyshin 2001, Zhao *et al* 2007).

Due to the intrinsic unsteadiness and compressibility, as well as the inevitable turbulent state of the flow, a satisfactory and practically applicable theoretical prediction of the long-pipe flow behavior is still beyond our reach. Various simplified theoretical models have been proposed, such as the classical one-dimensional (1-D) theory (Wylie & Streeter 1993, Yu 2004, Chang 2005, Brunone & Bolia 2008), and the axisymmetric unidirectional-flow theory (Hall & Parker 1976, Ghidaouui & Kolyshin 2001, 2002). But despite the partial success of these models in explaining certain transient flow phenomena, they can not always predict the evolution of strong water hammer in all major cases. One of the major reasons for this situation is the oversimplified treatment of the viscous friction effect on the pressure-wave propagation in these models.

As sketched in Fig. 1, a valve motion may cause two types of water hammer phenomena. As the valve is closing, its upstream flow will be stagnated and the pressure will immediately increase. The whole transient process happens only in a short time, during which the accurate frictional effect does not matter. Thus, the theoretical prediction of this type of water hammer is relatively easy.

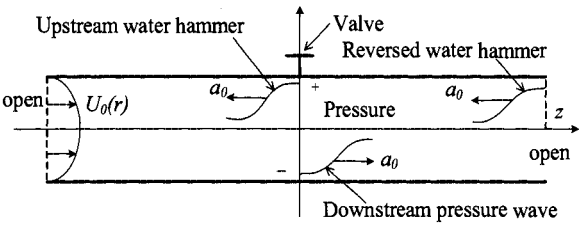

Fig. 1 A sketch of the water hammers upstream and downstream the valve

In contrast, as also sketched in Fig. 1, the flow right downstream the valve will first gain a low pressure due to its inertia. This pressure drop will propagate to and reflected back at the far-downstream open end of the pipe, to become a high-pressure "*reversed water hammer*" that propagates upstream toward the valve. Therefore, when the reversed water hammer hits the valve the pressure wave, it has traveled over the full pipe length twice in a relatively much longer time, during which the friction must have significant accumulated effect on the wave evolution. The 1-D model cannot capture this effect at all since there the friction has to be mimicked by an empirical formula. Nor can the unidirectional-flow model (where the velocity has to be axially uniform) be good enough, because the pressure wave must trigger a vortical Stokes layer near the wall and associated shear stress that varies in both space and time.

It is this difficulty that motivated the present study. In this paper we initiate a new theory based on the unsteady, axisymmetric and compressible Navier-Stokes (N-S) equations, so that the inherent coupling of the pressure wave and vortical wave (and so the unsteady friction) can be fully taken into account. The weak compressibility of the water naturally permits perturbation approach, of which the leading-order transient solution is found to be in excellent agreement with the direction simulation of the original N-S equations. Moreover, a simple connection between the valve's closing motion and the nearby pressure evolution is established, which enables the optimization of the closing rule to minimize the strength of the reversed water hammer.

As is well known, a rational treatment of the viscous effect alone still cannot overcome all the difficulties in predicting the reversed water hammer. For example, as the valve is quickly closed, the adjacent downstream pressure could be very low such that the commonly used linearized state equation for the water becomes questionable and sometimes cavitation appears. Then one has to consider two-phase flow. Extension of the present laminar

theory of single-fluid model to multiphase and turbulent flow is being investigated and will be reported elsewhere.

We formulate the problem in Sect. 2. Sect. 3 presents our perturbation approach which, after the discussion of the leading-order solution, will be focused on the relation between the valve motion and its adjacent pressure, the key information for the optimal design of the valve closing motion. In Sect. 4 we verify the perturbation theory by numerical calculation. A strategy to control the reversed water hammer is given is Sect. 5, followed by concluding remarks.

2 General Formulations

2.1 Model Flow and Governing Equations

Consider an unsteady and axisymmetric swirl-free compressible flow in a circular pipe of finite length L_0 and radius R in cylindrical coordinates $(\tilde{r},\ \tilde{z})$, see Fig. 2.

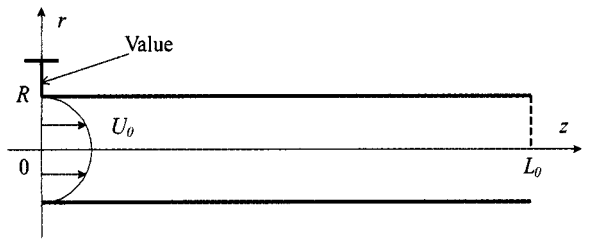

Fig. 2 The configuration of the model

The dimensional velocity along axial, radial direction, dimensional pressure and dimensional density are denoted by

$$U(\tilde{z},\tilde{r},\tilde{t}),\ V(\tilde{z},\tilde{r},\tilde{t}),\ P(\tilde{z},\tilde{r},\tilde{t}),\ \tilde{\rho}(\tilde{z},\tilde{r},\tilde{t}). \tag{1}$$

where $\tilde{t}$ is dimensional time. Let the valve be located at $\tilde{z}=0$ and the downstream end of the pipe be open. At $\tilde{t}=0$, the flow is assumed to be unidirectional, driven by a constant pressure gradient $\partial P/\partial\tilde{z}=const.$ Then the valve is gradually closed according to a prescribed rule. Our task is to determine the flow field for $\tilde{t}>0$. This model flow is governed by compressible Navior-Stokes equations

$$\begin{cases} \tilde{\rho}_{\tilde{t}}+\partial_{\tilde{r}}(\tilde{r}\tilde{\rho}V)/\tilde{r}+\partial_{\tilde{z}}(\tilde{\rho}U)=0 \\ \tilde{\rho}D_{\tilde{t}}V=\left[\partial_{\tilde{r}}(\tilde{r}\sigma_{rr})+\partial_{\tilde{z}}(\tilde{r}\sigma_{zr})\right]/\tilde{r}-\sigma_{\theta\theta}/\tilde{r} \\ \tilde{\rho}D_{\tilde{t}}U=\left[\partial_{\tilde{r}}(\tilde{r}\sigma_{zr})+\partial_{\tilde{z}}(\tilde{r}\sigma_{zz})\right]/\tilde{r} \\ P-P_0=a_0^2(\tilde{\rho}-\rho_0) \end{cases} \tag{2}$$

where

$$\begin{aligned} &\partial_{\tilde{x}}\equiv\frac{\partial}{\partial\tilde{x}}\ (x=\tilde{z},\tilde{r},\tilde{t}),\ D_{\tilde{t}}\equiv\partial_{\tilde{t}}+V\partial_{\tilde{r}}+U\partial_{\tilde{z}}, \\ &\sigma_{rr}=-P+2\mu(V_{\tilde{r}}-\tilde{\theta}/3), \\ &\sigma_{zz}=-P+2\mu(U_{\tilde{z}}-\tilde{\theta}/3), \\ &\sigma_{\theta\theta}=-P+2\mu(V/\tilde{r}-\tilde{\theta}/3), \\ &\sigma_{zr}=\mu(V_{\tilde{z}}+U_{\tilde{r}}),\ \tilde{\theta}=\partial_{\tilde{r}}(\tilde{r}V)/\tilde{r}+U_{\tilde{z}}; \end{aligned} \tag{3}$$

and P_0, ρ_0 and a_0 are the pressure, density and speed of sound in water at the normal state. As in previous theories we use the linearized state equation.

2.2 Assumptions and Nondimensionalization

One of the key issues in analysis is the choice of scales in nondimensionalization. We introduce the following non-dimensional variables:

$$\begin{aligned} &z=\tilde{z}/L_z,\ r=\tilde{r}/L_r,\ t=\tilde{t}/L_t,\ u=U/L_u, \\ &v=V/L_v,\ p=(P-P_0)/L_p,\ \rho=(\tilde{\rho}-\rho_0)/L_\rho, \end{aligned} \tag{4}$$

where L_α is the scale of any variable α to be determined. Substituting (4) and (3) into (2) yields

$$\frac{L_z}{L_uL_t}\frac{L_\rho}{\rho_0}\rho_t+\partial_z\left[\left(1+\frac{L_\rho}{\rho_0}\rho\right)u\right]+\frac{L_vL_z}{L_uL_r}\frac{1}{r}\partial_r\left[\left(1+\frac{L_\rho}{\rho_0}\rho\right)rv\right]=0 \tag{5}$$

$$\frac{\rho_0L_u}{L_t}\left(1+\frac{L_\rho}{\rho_0}\rho\right)\left[\partial_t+\frac{L_vL_t}{L_r}v\partial_r+\frac{L_uL_t}{L_z}u\partial_z\right]u=-\frac{L_p}{L_z}p_z+\frac{2\mu L_u}{L_z^2}\partial_z(u_z-\theta/3)+\mu\frac{L_u}{L_r^2}\frac{1}{r}\left[r\left(u_r+\frac{L_vL_r}{L_uL_z}v_z\right)\right] \tag{6}$$

$$\frac{\rho_0L_v}{L_t}\left(1+\frac{L_\rho}{\rho_0}\rho\right)\left[\partial_t+\frac{L_vL_t}{L_r}v\partial_r+\frac{L_uL_t}{L_z}u\partial_z\right]v=-\frac{L_p}{L_r}p_r+\frac{2\mu L_u}{L_rL_z}\left\{\frac{1}{2}\partial_z\left(u_r+\frac{L_vL_r}{L_uL_z}v_z\right)+\frac{L_vL_z}{L_uL_r}\left[\frac{\partial_r(rv_r)}{r}-\frac{v}{r^2}\right]-\frac{\theta_r}{3}\right\} \tag{7}$$

$$p=(a_0^2L_\rho/L_p)\rho, \tag{8}$$

where $\theta=u_z+\frac{L_vL_z}{L_uL_r}\partial_r(rv)/r$. Here and below variables with suffix α denotes derivative on α.

The assumption of the linearized state equation of water implies $L_\rho/\rho_0\ll1$. Moreover, we further assume:

1. The unsteady term in continuum equation cannot be neglected *a priori*;

2. The term containing radial velocity v in continuum equation cannot be neglected *a priori*.

Assumption 1 makes the formulation suitable for dealing with transient flow, while assumption 2 distinguishes our theory from the unidirectional-flow model.

With these assumptions, (5) yields

$$\frac{L_z}{L_t L_u}\frac{L_\rho}{\rho_0}=1,\quad \frac{L_v L_z}{L_u L_r}=1. \tag{9}$$

Then the balance in (6) and (8) leads to

$$\rho_0 L_u / L_t = L_p / L_z,\quad a_0^2 L_\rho / L_p = 1. \tag{10}$$

Combining (9) and (10) yields

$$L_\rho = \rho_0 M,\ L_p = \rho_0 a_0^2 M,\ \frac{L_u L_t}{L_z}=\frac{L_v L_t}{L_r}=M, \tag{11}$$

where $M = L_u / a_0$ is Mach number. This set of scaling casts (5)~(8) to dimensionless equations:

$$\rho_t + \partial_z\left[(1+M\rho)u\right]+\partial_r\left[(1+M\rho)rv\right]/r=0 \tag{12}$$

$$(1+M\rho)\left[\partial_t + Mv\partial_r + Mu\partial_z\right]u = -p_z + \frac{1}{\delta\,\mathrm{Re}}\frac{1}{r}\partial_r(ru_r)+\frac{\delta}{3\,\mathrm{Re}}\left[4u_{zz}+\partial_r(rv_z)/r\right] \tag{13}$$

$$\delta^2(1+M\rho)\left[\partial_t + Mv\partial_r + Mu\partial_z\right]v = -p_r + \frac{\delta}{3\,\mathrm{Re}}\left[u_{rz}+3\delta^2 v_{zz}+4(v_{rr}+v_r/r-v/r^2)\right] \tag{14}$$

$$p=\rho \tag{15}$$

where

$$\mathrm{Re}=\rho_0 a_0 L_r/\mu \gg 1,\quad \delta = L_r/L_z \ll 1. \tag{16}$$

Meanwhile, the initial condition assumed before now reads

$$u(z,r,0)=u_{00}(r),\ \ v(z,r,0)=0,\qquad p_z(z,r,0)=const.,\ \ p_r(z,r,0)=0. \tag{17}$$

The boundary conditions including the no-slip condition at the pipe wall are

$$u(0,r,t)=h(r,t),\ p(L=1,r,t)=0;\qquad u_r(z,0,t)=p_r(z,0,t)=0;\qquad u(z,r_0,t)=v(z,r_0,t)=0,\ \ r_0=R/L_r. \tag{18}$$

Note that $h(r,t)$ defines the *valve motion* to be prescribed. We will make an indepth discussion on its optimization later. We choose $L_z = L_0$ so $L = L_0 / L_z = 1$.

2.3 On the Elasticity of Pipe Wall

For elastic pipe, its radius R will be a variable. It can be modeled in the same way as in the classic one-dimensional theory, by which the local cross-sectional area is directly related to the local pressure as (Wylie & Streeter 1993)

$$\frac{dA}{A}=\frac{2R}{Ee}dP, \tag{19}$$

where A is the cross-sectional area, E and e are the modulus of elasticity and thickness of the pipe wall, respectively. Integrating (19) and nondimensionalizing it by (4) give

$$r_0(z,t)=\frac{R}{R_0}=\exp\left(\frac{\beta Mp}{2}\right),\ \ \beta=\frac{2R_0\rho_0 a_0^2}{Ee}, \tag{20}$$

where R_0 is the initial radius of the pipe.

The length scale L_r is naturally chosen to be R_0. But due to the variation of R, we may choose

$$y = r/r_0(z,t) \tag{21}$$

as the new radial variable. Alternatively, we may modify the sound speed a_0 with the classical sound speed formula

$$a = a_0(1+\beta)^{-1/2}, \tag{22}$$

See, e.g., Wylie & Streeter (1993). While it is not difficult to account for the pipe elasticity, for neatness we only consider rigid pipe in what follows. Then the boundary condition on the pipe wall is reduced to

$$u(z,1,t)=v(z,1,t)=0. \tag{23}$$

3 Perturbation Analysis

3.1 Perturbation Expansion

In common practice of long-pipe water flow, the Mach number M is of order 0.01, permitting the Rayleigh-Janzen expansion

$$(u,v,p)(z,r,t)=\sum_{n=0}^{\infty}(u_n,v_n,p_n)(z,r,t)M^n. \tag{24}$$

The substitution of (24) into (12)~(15) and the initial-boundary condition yields, to the leading order, the perturbation equations:

$$p_{0t}+u_{0z}+(rv_0)_r/r=0 \tag{25}$$

$$u_{0t}+p_{0z}=\frac{1}{\delta\,\mathrm{Re}}\left(r\partial_r u_0\right)_r/r+\frac{\delta}{3\,\mathrm{Re}}\left[4u_{0zz}+\left(r\partial_z v_0\right)_r/r\right], \tag{26}$$

$$\delta^2 v_{0t}+p_{0r}=\frac{\delta}{2\,\mathrm{Re}}\left\{u_{0rz}+3\delta^2 v_{0zz}+4\times\left[(r\partial_r v_0)_r/r-v_0/r^2\right]\right\}, \tag{27}$$

along with the boundary and initial conditions:

$$\begin{aligned} &z=0\,\&\,1:\ u_0(0,r,t)=h(r,t),\ p_0(1,r,t)=0;\\ &r=0:\ u_{0r}(z,0,t)=p_{0r}(z,0,t)=v_0(z,0,t)=0;\\ &r=1:\ u_0(z,1,t)=v_0(z,1,t)=0, \end{aligned} \tag{28}$$

$$\begin{aligned} &t=0:\ u_0(z,r,0)=u_{00}(r),\ v_0(z,r,0)=0,\\ &\quad p_0(z,r,0)=C(1-z); \end{aligned} \tag{29}$$

where C is a constant determined by the initial velocity profile $u_{00}(r)$. We only reserve the largest viscosity term ($1/(\delta\,\mathrm{Re})$) and omit the δ^2 term, which is far smaller. Because only the 0^{th}-order equations will be discussed, the suffix '0' in equation (25)~(29) will be omitted. Then the following neat perturbation equations follow:

$$r(p_t+u_z)+(rv)_r=0, \tag{30}$$

$$u_t+p_z-\varepsilon(ru_r)_r/r=0, \tag{31}$$

$$p=p(z,t). \tag{32}$$

where $\varepsilon=1/(\delta\,\mathrm{Re})$, of which the order should not be larger than 1. We stress that although M dose not enter these equations explicitly, the compressibility has been implied by the state equation $\rho=p$.

As an immediate simplification, we eliminate $v(z,r,t)$ from (30) by integrating it over r=0~1 and use $v(z,1,t)$=0. This gives

$$p_t+2\int_0^1 ru_z\,dr=0 \tag{33}$$

Equations (31) and (33) are the basis of our analysis, to be discussed analytically and numerically.

3.2 Leading-Order Solutions

We apply the method of separation of variables and set

$$u(z,r,t)=\sum_{n=1}^{\infty}T_n(z,t)Y_n(r). \tag{34}$$

Substituting this into the momentum equation (31) and using boundary conditions at $r=0$ and 1, the eigenfunction $Y_n(r)$ is found to be Bessel function of the first kind of order 0. Thus, (31) and (33) can be reformed to

$$\partial_t T_n(t,z)+cw_n^2T_n(t,z)+\frac{2}{w_nJ_1(w_n)}p_z(t,z)=0, \tag{35}$$

$$p_t(z,t)+2\sum_{n=1}^{\infty}\partial_z T_n(z,t)J_1(w_n)/w_n=0, \tag{36}$$

where $J_m(r)$ is a Bessel function of the first kind of order m and $w_n(n\in\mathbb{N})$ is the roots of the equation $J_0(w_n)=0$.

Equation (35) gives

$$\begin{aligned} &T_n(z,t)=\left[C_n-2\int_0^t\frac{p_z(z,\tau)}{w_nJ_1(w_n)}e^{\varepsilon w_n^2\tau}d\tau\right]e^{-\varepsilon w_n^2t},\\ &C_n=\frac{2}{\left[J_1(w_n)\right]^2}\int_0^1 ru_{00}(r)J_0(w_nr)dr, \end{aligned} \tag{37}$$

and so the analytical relation between u and p_z is:

$$\begin{aligned} u(z,r,t)&=\sum_{n=1}^{\infty}T_n(z,t)J_0(w_nr)\\ &=\sum_{n=1}^{\infty}\left[C_n-2\int_0^t\frac{p_z(z,\tau)}{w_nJ_1(w_n)}e^{\varepsilon w_n^2\tau}d\tau\right]e^{-\varepsilon w_n^2t}J_0(w_nr). \end{aligned} \tag{38}$$

Substituting (37) into (36) leads to

$$\begin{aligned} &p_t-\int_0^t p_{zz}(z,\tau)F(t-\tau)d\tau=0,\\ &F_\varepsilon(t)=4\sum_{n=1}^{\infty}\exp(-\varepsilon w_n^2t)/w_n^2, \end{aligned} \tag{39}$$

which controls the evolution of pressure. If we set $\varepsilon=0$ in (39) and take derivative with respect to t, we will have the classical wave equation in inviscid flow:

$$p_{tt}-p_{zz}=0. \tag{40}$$

If ε is nonzero but very small, we may truncate $F_\varepsilon(t)$ to only one term and obtain a wave equation

$$p_{tt}-4p_{zz}/w_1^2+\varepsilon w_1^2p_t=0 \tag{41}$$

with wave speed close to $2/w_1\approx0.832$, slightly smaller than 1 as predicted by the classical 1-D theory with the present nondimensionalization. This observation identifies (39) as a wave-type equation with a memorable dispersion.

The Laplace transform of (39) with respect to t can be solved analytically. The solution is

$$\begin{aligned} \hat{p}(z,s)&=-\left[\hat{p}_z(0,s)+C/s\right]\frac{\sinh\left[G_\varepsilon(s)(1-z)\right]}{G_\varepsilon(s)\cosh\left[G_\varepsilon(s)\right]}\\ &\quad+C(1-z)/s,\\ \hat{F}_\varepsilon(s)&=4\sum_{n=1}^{\infty}\frac{1}{w_n^2(s+\varepsilon w_n^2)},\quad G_\varepsilon(s)=\sqrt{s/\hat{F}_\varepsilon(s)}, \end{aligned} \tag{42}$$

where $\hat{p}_z(z=0,s)=\hat{p}_z(0,s)$. The inverse transform of (42) will give the relation between the pressure $p(z,t)$ and the pressure gradient at the valve, $p_z(0,t)$. Along with the u-p_z relation (38), the transient flow evolution in the entire pipe could be attained. Unfortunately, the inverse transform of (42) is not analytical obtainable.

Our main concern in practice is the velocity-pressure relation right at the valve location $z=0$, which is the critical information for optimizing the valve motion.

Therefore, in what follow we leave the complete perturbation solution and focus on that relation.

3.3 The Pressure Evolution at the Valve

We first notice that in the present theoretical model (38) imposes a relation at $z = 0$ that the valve motion $h(r,t) = u(0,r,t)$ has to satisfy:

$$h(r,t) = \sum_{n=1}^{\infty}\left[C_n - 2\int_0^t \frac{p_z(0,\tau)}{w_n J_1(w_n)} e^{\varepsilon w_n^2 \tau} d\tau\right] e^{-\varepsilon w_n^2 t} J_0(w_n r). \quad (43)$$

Or, set $h(r,t) = \sum_{n=1}^{\infty} h_n(t) J_0(w_n r)$, there is

$$\begin{aligned} h_n(t) &= C_n e^{-\varepsilon w_n^2 t} - \frac{2}{w_n J_1(w_n)} p_z(0,t) * e^{-\varepsilon w_n^2 t}, \text{ or} \\ p_z(0,t) &= -\left[c w_n^2 h_n(t) + h_n'(t)\right] w_n J_1(w_n)/2, \end{aligned} \quad (44)$$

where $*$ denotes the convolution with respect to t and prime denotes the time derivative. Because $p_z(0,t)$ does not depend on n but its right-hand side does, (44) imposes a nontrivial constraint on the possible valve motion $h(r,t)$, of which the full implication is yet to be explored. Nevertheless, (44) is inconvenient for engineering use, and a much simpler relation can be derived from the following approach.

Integrating (31) times $2\pi r$ over $r = 0 \sim 1$ yields

$$\partial_t Q_v + \pi p_z - 2\pi\varepsilon u_r\big|_{r=1} = 0, \; Q_v = \int_0^1 2\pi r u dr, \quad (45)$$

where Q_v is the volume flux at the valve. Here, $-2\pi\varepsilon u_r\big|_{r=1}$ is the friction drag per unit pipe length that for long distance and time causes an attenuation of the amplitude of water hammer. It can not be always neglected. However, right at the valve, relative to other terms in (45), this term is very small ($\varepsilon \ll 1$) in laminar flow and can be neglected (even in turbulent flow this neglect may still be feasible). Thus, in the neighborhood of the valve (45) can be simplified to

$$\partial_t Q_v + \pi p_z = 0. \quad (46)$$

On the other hand, at the valve (z=0), (42) gives

$$\hat{p}(0,s) = -\left[\hat{p}_z(0,s) + \frac{C}{s}\right]\frac{\tanh\left[G_\varepsilon(s)\right]}{G_\varepsilon(s)} + \frac{C}{s}, \quad (47)$$

of which the inverse Laplace transform yields the *H-p* relation (referred to as HPR):

$$p(0,t) = -\int_0^t \left[p_z(0,t-\tau) + C\right] H_\varepsilon(\tau) d\tau + C, \quad (48)$$

where $H_\varepsilon(t)$ is the inverse Laplace transform of $\tanh\left[G_\varepsilon(s)\right]/G_\varepsilon(s)$, which is still hard to determine. But we can choose a special valve motion to make $p_z(0,t) = 0$ and obtain the corresponding $\bar{p}(0,t)$ numerically, which suffices for determining $H_\varepsilon(t)$:

$$H_\varepsilon(t) = -\bar{p}_t(0,t)/C. \quad (49)$$

Note that for a given ε the function $H_\varepsilon(t)$ is fixed and can be obtained once for all. The combination of (46) and HPR can then be used to study the pressure evolution for various valve motions (see Sect. 5).

4 Numerical Validations

To confirm the preceding perturbation theory, we have made numerical tests for two cases. One was used to verify the leading-order perturbation equations (31) and (33), and the other to test the correctness of the HPR given by (47).

Case 1: We solved (31) and (33) numerically (marked by PES, perturbation-equation simulation) and compared the result with the direct numerical simulation (DNS) of the full compressible NS equations (2). The boundary conditions for both calculations are (28) and (29). For computational convenience, we chose

$$\begin{aligned} &L_u = 10\text{m/s}, \; L_0 = 800.0\text{m}, R = 1\text{m}, \\ &\nu = 0.2\text{m}^2/\text{s}, \; a_0 = 1450\text{m/s}, \\ &\rho_0 = 1000\text{kg/m}^3, \; L_t = L_0/a_0 \approx 0.552\text{s}, \end{aligned} \quad (50)$$

Where L_u is the maximum initial velocity. To simplify the valve motion, $p_z(0,t)$ was assigned to be 0 such that

$$h(r,t) = \sum_{n=1}^{\infty} C_n e^{-\varepsilon w_n^2 t} J_0(w_n r). \quad (51)$$

The DNS was performed on two grids by an implicit scheme of FLUENT, in which the scales are chosen differently. Thus, in the comparison we will use two sets of scales. Grid 1 was 40×6400 ($r \times z$) with time step 0.016s, and Grid 2 was 40×800 with time step 0.002 s. The PES was based on (35) and (36), in which we used 15 Bessel modes, 150 nodes on z direction, and an explicit scheme with *CFL*=0.05. The independence of the simulation from the number of modes and the grid was carefully tested.

The comparison of PES and DNS of the pressure at the valve, $p(0,t)$, is shown in Fig. 3. The agreement is excellent.

Note that in Fig. 3 as well as Fig. 5 below there appears meaningless negative pressure since the cavitation is not considered in both our theoretical model and DNS with linearized equation of state. While these figures still have merit in verifying the theory, as we approach water hammer control strategy in Section 5 we have to modify the flow parameters to avoid the negative pressure.

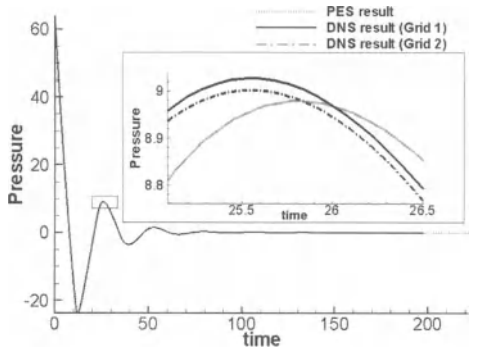

Fig. 3 Comparison of $p(0,t)$ attained by PES and DNS. Pressure scale: $\rho_0 L_u^2 = 10^5$, time scale: $L_r / L_u = 0.1s$. The difference between PES and DNS with two grids can be seen only in the zoom-in block

Case 2: To verify HPR, we used $p(0,t)$ attained in the Case 1 as $p(0,t)$ and set the valve motion as a step function shown in Fig. 4 (a little smoothing at the beginning is added to remove the oscillation).

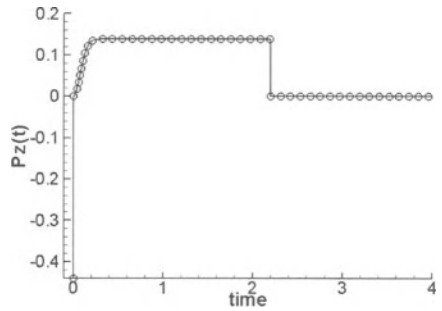

Fig. 4 The evolution of $p_z(0,t)$ by theoretical scales

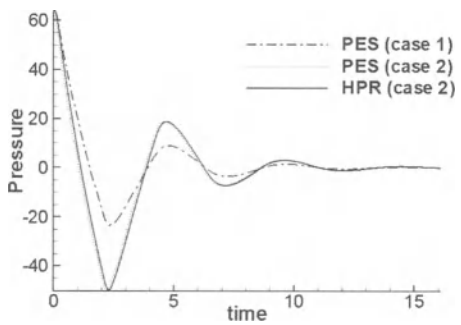

Fig. 5 Comparison of $p(0,t)$ attained by PES and HPR. The $p(0,t)$ for the valve motion (51) in Case 1 is also shown as reference. Pressure scale: $\rho_0 L_u^2$, time scale: L_t

By (46), in this case, Q_v decreases linearly to zero. We then compare $p(0, t)$ obtained by PES and HPR at the same time, using the same grid as in PES for Case 1. Fig. 5 shows the comparison. The result is again excellent except at beginning, where the jump of pressure gradient deteriorates the accuracy and stability of PES. But HPR as a convolution is free from this kind of problem; it has better performance. In addition, HPR is so simple with almost no computational cost. It is very convenient for engineering application. Therefore, we will use HPR and (49) exclusively in our discussion on the control of reversed water hammer.

5 Water hammer control Strategies

The water hammer control amounts to minimize the pressure peak as it reaches the valve, denoted by p^m_{RWH}. As mentioned in the Sect. 4, to be realistic we reassign the flow parameters as follows:

$$L_u = 0.1\mathrm{m/s},\ L_0 = 100.0\mathrm{m},\ R = 0.05\mathrm{m},$$
$$\nu = 3.625\times10^{-4}\mathrm{m^2/s},\ a_0 = 1450\mathrm{m/s}, \quad (52)$$
$$\rho_0 = 1000\mathrm{kg/m^3},\ L_t = L_0 / a_0 \approx 0.069\mathrm{s}.$$

We then obtain $\varepsilon = 0.01$ and $L_p = \rho_0 a_0 L_u = 1.45\times10^5\, Pa$. The pressure at the open end of the pipe is assumed to be $P_0 = 10^5\,\mathrm{Pa}$. Because the pipe the initial velocity is small enough, negative pressure is avoided. The procedure of the optimization contains two steps.

Step 1: With $\varepsilon = 0.01$, assume $p_z(0,t) = 0$ and compute $H_\varepsilon(t)$ by PES and (49). The result is shown in Fig. 6.

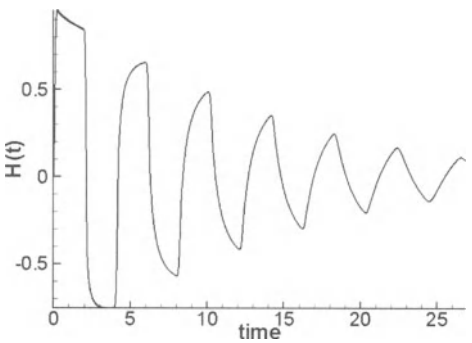

Fig. 6 The $H(t)$ curve for $\varepsilon = 0.01$

Step 2: Use the obtained $H_\varepsilon(t)$ to optimize p^m_{RWH} by HPR.

This can be done by many methods and we only consider the simplest one. Assume a linear decrease of volume flux Q_v, we adjust the total closing time T_0 to see if larger T_0 always leads to weaker reversed water hammer. For the upstream water hammer, the 1-D theory predicts that for a linearly decreasing Q_v the water hammer strength decreases simply as T_0 increases. But this is not the case for reversed water hammer; the situation is shown in Fig. 7. The horizontal lines in Fig. 7 marks the initial pressure at the valve, which depends only on the initial condition.

From Fig. 7 we see that, as T_0 increases, the overall level of p^m_{RWH} is decreasing, but *the instantaneous* p^m_{RWH} *varies non-monotonically*. It reaches a very low pressure (close to the open side 10^5Pa) at certain discrete T_0s. On the other hand, as T_0 is shortened to 0, the p^m_{RWH} appro-aches

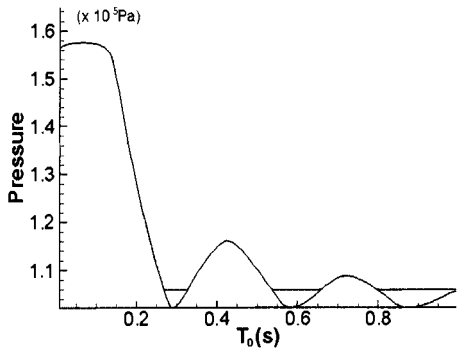

Fig. 7 The variation of the p^m_{RWH} as T_0

a constant, which can be predicted theoretically (the slight curve near 0 in Fig. 7 is caused by the beginning-smoothness in computing $H(t)$). Evidently, *the optimal closing time T_0 should only be chosen as one of those discrete values with p^m_{RWH} minima.*

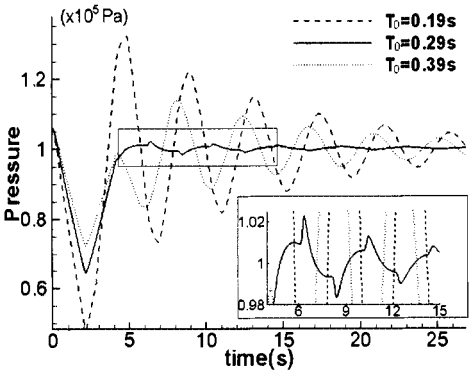

Fig. 8 $p(0,t)$ for different closing time T_0

To further examine the effect of this choice of T_0, Fig. 8 gives the time evolution of $p(0,t)$ at the valve for different T_0, where $T_0 = 0.29$s is the first low-p point in Fig. 7, while the other two T_0 are arbitrarily chosen. Remarkably, if the valve is linearly closed during $T_0 = 0.29$s, the reversed water hammer will be almost totally eliminated.

Note that unlike the oscillating p^m_{RWH}, the first valley of $p(0,t)$ decreases monotonically as T_0 increases. In fact, since the perturbation equations are linearized, a reflection of the $p(0,t)$ curves in Fig.8 with respect to p=1 is precisely the pressure evolution for upstream water hammer, where the first $p(0,t)$ peak is nothing but the maximum pressure upstream the valve.

6 Conclusions

To overcome the intrinsic disadvantages of the previous theories on the transient flow in cylindrical pipe, where the unsteady friction has to be modeled empirically, we have constructed an axisymmetric swirl-free theoretical model with the friction effect fully included. By using perturbation technique, we have analyzed the leading-order equations and found a simple relation between the pressure gradient at the valve and the adjacent pressure (*H-p* relation). With this relation, we have designed a procedure to optimize the valve motion and demonstrated its significant effect in reducing or even eliminating the reversed water hammer. The easier prediction of upstream water hammer is automatically included as a corollary. The numerical tests show that both the leading-order equations and the *H-p* relation give excellent approximation to the problem. The present theory is sufficiently accurate for axisymmetric swirl-free and laminar flow.

The theory in this paper represents the physically natural and self-consistent approach to the water hammer problem for the first time, and yet the control strategy is very simple. It provides a platform for developing a complete prediction of the whole transient pipe flow problem in engineering applications. Adding the effects of cavitation, turbulence, and pipe-wall elasticity to the theory should have no principal difficulty and is being investigated.

Acknowledgements

The authors wish to thank L. Zeng, R.-K. Zhang, Y.-T. Yang and M. Han for valuable discussions. We are also grateful to Prof. J. Majdalani for his useful comments.

References

Brunone B., Karney B., Mecarelli, M. & Ferrante M. (2000), Velocity profiles and unsteady pipe friction in transient flow. *J. Water Resource Planning and Management*, ASCE **126**, 236 – 244

Brunone B. & Golia UM (2008) systematic evaluation of one-dimensional unsteady friction models in simple pipelines-Discussion. *J. Hydraulic Engineering*. ASCE **134**, 282 – 284

Chang J. S. (2005) *Transients of Hydraulic Machine Installations*. Higher Education Press Beijing, China (in Chinese)

Ghidaoui M. S. & Kolyshkin A. A. (2001), Stability analysis of velocity profiles in water-hammer flows. *J. Hydraul. Engng* ASCE **127**, 499 – 512

Ghidaoui M. S. & Kolyshkin A. A. (2002) A quasi-steady approach to the instability of time-dependent flows in pipes. *J. Fluid Mech.* **465**, 301 – 330

Hall P. & Parker K. H. (1976) The stability of the decaying flow in a suddenly blocked channel flow. *J. Fluid Mech.* **75**, 305 – 314

Wu J. Z., Ma H. Y., Zhou M. D. (2006) *Vorticity and Vortex Dynamics*. Springer-Verlag Berlin Heidelberg

Wylie E. B. & Streeter V. L. (1993), *Fluid Transient in Systems*, Prentice-Hall

Yu G. D. (2004) Handling Method of Unsteady Friction in Water Hammer Evaluation. *Design of Hydroelectric Power Station.* **20(2)**, 3 – 6

Zhao M., Ghidaoui M. S. & Kolyshkin A. A. (2007), Perturbation dynamics in unsteady pipe flows. *J. Fluid Mech.* **570**, 129 – 15

The 4th International Symposium on Fluid Machinery and Fluid Engineering
November 24-27, 2008, Beijing, China
NO. 4ISFMFE-Ch37

Research on the Optimization Method of Impeller Meridional Contour and 3-D Blade

Jinling Lu [1], Guang Xi [2] and Xingqi Luo [1]

[1] Dept. of Hydropower Engineering, Xi'an University of Technology Xi'an 710048, China
[2] School of Energy And Power Engineering, Xi'an Jiaotong University, Xi'an 710049, China

Abstract An optimization method for centrifugal or mixed-flow pump impeller was proposed. The blade was indirectly parameterized using the angular momentum distribution and calculated by inverse design method. The design variables were separated into two categories: the meridional contour design variables and the blade design variables. Firstly, the blade shape was optimized using genetic algorithm and the meridional contour remained constant. The ANN techniques with the training sample data schemed according to design of experiment theory were adopted to build the response relation between the blade design variables and the impeller performance. Then, based on ANN approximated relation between the meridional contour design variables and the impeller performance, the meridional contour was optimized. This approach could be used to optimize the impeller, including the 3-D blade and the meridional contour, and fewer variables and less time were required. An optimized impeller in a mixed-flow pump, with the head and the efficiency were treated as objective functions, confirms the validity of this newly proposed method.

Keywords optimization, meridional contour, blade, genetic algorithm, artificial neural network

Nomenclature

D	diameter
P	controlling point of the shroud contour
B	outlet blade width
Δx	blade axial length
α	blade inlet leaning angle
R_c	radius of the arc
R	radial coordinate
θ	angular coordinate
H	Head
η	efficiency
X	bbreviation of the meridional contour design variables
Y	abbreviation of the blade design variables
y	ptimum of the blade design variables
BPNN	back-propagation neural networks
RBF	radial basis function neural networks

Subscripts

1	inlet edge of the blade
2	outlet edge of the blade
r	radial coordinate
z	axial coordinate

1 Introduction

Numerical optimization technique seems to be a promising tool for the aerodynamic design of turbomachinery and has received attention of a lot of researchers. The optimization method can usually be categorized into two groups: gradient based optimization and exploratory techniques. Both techniques have been successfully applied to the optimization of the axial flow machine blade profiles, and a literature review and some research publications can be found in the reference (Newman in 1999, Xu in 2002). In the last few years, the techniques have also been used to the design of centrifugal or mixed-flow machines. Ashihara and Goto (2002) used inverse design method coupled with both gradient based techniques and exploratory techniques to optimize a mixed-flow pump impeller, and showed that only the latter are able to find the optimum value of a multi-peak problem. Bonaiuti and Arnone (2002) conducted an optimization of three

centrifugal impellers using the technique of Design of Experiments together with a 3-D CFD solver. Van den Braembussche (2001) combined genetic algorithm with neural network to improve the efficiency of a centrifugal impeller. Pazzi and Marteli (2002) conducted an optimization of blade return channel for industrial centrifugal compressors using artificial neural networks. However, in the centrifugal or mixed-flow machines field, fewer application of optimization method for both the 3-D blade shape and meridional contour of an impeller have been reported. Generally speaking, such a problem as optimization of a 3-D blade and meridional contour may have the following difficulties: Firstly, how to parameterize the complex 3-D blade shape and the meridional contour with fewer design variables? If we define the geometry parameter directly to represent complex 3-D blade shapes, the number of design variables tends to be very large and many cases that do not satisfy the design specification may be explored in optimization. Secondly, the optimization of 3-D blade was a multi-peak one and only the exploratory techniques were able to find the optimum value (ASHIHARA, 2001), but the objective function evaluation in exploratory techniques, such as fitness evaluation in GA, is much time-consuming if all the candidate impellers in the optimization process were analyzed using 3-D viscous CFD codes. How to balance the optimization time and the 3-D viscous CFD codes? Finally, the meridional contour and the 3-D blade shape are interactional. If the blade and the meridional contour were optimized synchronously, it is very difficult to construct the response relation between impeller performance and the design variables.

In this paper, an indirect parameterization method is proposed to solve the first problem, and Artificial Neural Networks (ANN) were adopted to construct the response relations between the impeller performance and the design variables. All the design parameters were separated into two categories, the blade design parameters treated as subsystem and the meridional contour design parameters treated as main system. The 3-D blade was firstly optimized in the subsystem, and the meridional contour was then optimized in the main system. A mixed-flow pump impeller was used as an example to demonstrate and discuss the capabilities of these approaches mentioned above.

2 Impeller Parameterization method

The meridional contour and 3-D blade shape of a centrifugal or mixed-flow impeller can be parameterized in various ways, each of which employs different mathematical models and introduces different design variables. In this paper, an indirect parameterization method was proposed for the 3-D blade, where the angular momentum $V_\theta r$ was treated as design variables and the blade was calculated by S_2 stream surface based inverse design method. The detailed inverse design method can be referred to reference[3] and was not repeated here.

The input data for this design method are: (i) meridional contour, (ii) angular momentum ($V_\theta r$) distribution, (iii) blade thickness distribution, (iv) flow rate and rotational speed, (v) blade number. By controlling the angular momentum distribution and the meridional contour, it is possible to design an impeller having different characteristics such as high efficiency or head.

To demonstrate the optimization method, a mixed-flow pump impeller was used as an example, and the corresponding design specification was as list in Table 1.

Table 1 Design specification

Design flow rate	784 m^3/h
Design pump head	7.73 m
Rotational speed	980 rpm
Blade number	5

The distribution of $V_\theta r$ in the meridional channel is a complex spatial surface and unknown in advance. In order to reduce the number of design variables, only the distributions of $V_\theta r$ at hub and shroud of the impeller were taken as design variables in this paper. The $V_\theta r$ values at other relative meridional streamlines between hub and shroud were linearly interpolated and the blade with a constant blade thickness can then be calculated according to the S_2 stream surface based inverse design method. The $V_\theta r$ distribution at hub and shroud of the impeller were supposed to be a quartic polynomial:

$$(V_\theta R)_m = am^4 + bm^3 + cm^2 + dm + e \tag{1}$$

Where m is the relative length of the meridional streamline ($m \in [0,1]$). a,b,c,d,e are coefficients which can be determined according to 5 specified constraints. The value of $V_\theta r$ at the inlet (m=0) of the blade was zero, and that at the outlet (m=1) can be calculated according to the theoretic head of the impeller. Three other constraints, namely the value of $d(V_\theta R)/dm$ at inlet and outlet of the blade and $V_\theta r$ at the middle of meridional streamline ($m = 0.5$) were regarded as design variables and were specified manually. Then the 5 coefficients in equation (1)

can be worked out and the distributions of $V_\theta r$ at hub and shroud of the impeller were revealed.

The initial meridional contour of this impeller was shown in Fig. 1. D_{1H} , D_{1S} , D_{2H} , D_{2S} B are blade inlet and outlet radius at hub and shroud of the impeller and blade width at the impeller outlet, respectively, which can be specified according to the design parameters. The hub contour is composed of a line with the slope equal to $\tan\alpha_H$ and an arc with the radius equal to R_c , and the shroud contour is a forth-order Bezier curve with P_1 , P_2 , P_3 , P_4 being the control points. The meridional projection of the blade inlet is supposed to be linear and was specified according to the value of Δx and α . According to our experience, the contour shape of the hub has a relatively weaker effect on the fluid flow than that of the shroud, in order to lessen design variables the hub contour was supposed to be constant. P_1 and P_4 are already specified in advance and P_{2R} and P_{3Z} are assigned to some fixed value in this article, and only P_{2Z} and P_{3R} are taken as variables. As a result, only four parameters, namely P_{2Z} P_{3R} Δx and α were taken as design variables of the meridional contour.

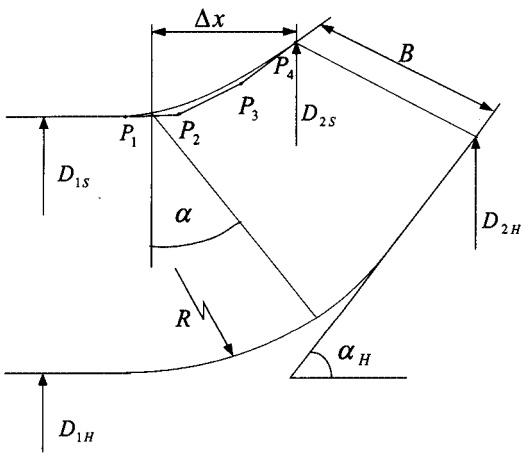

Fig. 1 Parameterization of meridional contour

The design variables was separated into two categories, one was related to meridional contour namely P_{2Z} P_{3R} Δx and α , and was substituted for X for convenience, the other was related to 3-D blade shape, namely k_{0S} k_{1S} y_H y_S k_{0H} k_{1H} , and was substituted for Y . Disturbing each variable around its original value to the negative and positive directions, respectively, constituted the design space, as listed in Tab 2.

Table 2 Design space specification

	Var	Min	Max	Description of the Var
X	P_{2Z}	22	30	Axial coordinate of P_2
	P_{3R}	154	161	Radial coordinate of P_1
	Δx	53	62	blade axial length
	α	33°	43°	Blade inlet leaning angle
Y	k_{0S}	0	1	$d(V_\theta R)/dm$ at shroud inlet
	k_{1S}	0	1	$d(V_\theta R)/dm$ at shroud outlet
	y_H	0.3	0.6	$V_\theta R$ at $m = 0.5$ neat hub
	y_S	0.4	0.7	$V_\theta R$ at $m = 0.5$ neat shroud
	k_{0H}	0	1.2	$d(V_\theta R)/dm$ at hub inlet
	k_{1H}	0	1.2	$d(V_\theta R)/dm$ at hub outlet

3 Objective Function

The objective of our optimization is to maximize the efficiency and head simultaneously. This is a Multi-objective optimization problem and conflicts between the two objective functions arise because of the different relationships they have with the independent parameters. To simplify the question, a new utility function was defined as follow[15]:

$$Y = 1 - \sqrt{\left(\frac{\eta - \eta^*}{\eta^*}\right)^2 + \left(\frac{H - H^*}{H^*}\right)^2} \tag{2}$$

Where H^* and η^* are the optimal Head and efficiency obtained by the corresponding single objective function optimization. This approach requires three outer iterations, two single and one global optimization, and the optimal design variables can be obtained after the last iteration.

4 Artificial Neural Networks

ANN is powerful interpolators for that can reproduce relationships existing between input and output variables in highly non-linear system. In this case, radial-basis neural network (RBNN) and BP neural networks are studied to predict the performance of candidate impellers for its excellent performance in function approaching.

Two phases, namely training and generalization phases, are required to make ANN operative. In the training phase, the selecting of training sample data in design space is critical[17]. In order to maximize the amount of information generated within the least number of data,

design of experiment technique ensuring a balanced comparison of any design variable is applied to scheme the training sample data of ANN.

5 Impeller Optimization

The optimization of the 3-D blade was a multi-peak problem and only the exploratory techniques were able to find the optimum value. Genetic algorithm, which is a kind of exploratory techniques, is a very robust optimization algorithm in that it does not depend on an initial condition and can explore the whole design space. Therefore, the genetic algorithm was adopted in this paper.

The meridional contour and the 3-D blade shape are interactional. If both of them were optimized synchronously, large numbers of training sample data were required and the training process of ANN would be very time-consuming and complicated. Therefore, it is very difficult, or even impossible, to construct the response relation between impeller performance and the design variables. To solve this problem, the idea of bi-level programming method was adopted. That is to say, the blade design variables, Y, were treated as subsystem and the meridional contour design variables, X, were treated as main system. The blades corresponding to the given meridian contours were firstly optimized in the subsystem. Then, the meridional contour was optimized in the main system and impeller with best performance can be achieved. This process can be expressed as follows:

$$\begin{cases} \max\limits_{X} F_1(X, y) & 2.a \\ y = \max\limits_{Y} F_2(X, Y) & 2.b \end{cases} \tag{3}$$

Where y is the optimal value of Y corresponding to the specific X value.

5.1 3-D blade

In this section, only the 3-D blade was optimized and the meridional contour remained to be the original one. There are totally 6 design variables, as list in Table 1. Four levels of data were selected for each variable and the orthogonal DOE method was used to scheme the training sample data of ANN. Generally speaking, the more training sample data were adopted, the more accurate of the ANN was. But on the other hand, the more complex the training process was and the longer the training time was, too. Therefore, a moderate number of training sample data should be selected. According to the reference, 28 training sample data were adopted. The 4 testing sample data of ANN were selected arbitrarily, but different from the training sample data. Since the training process of one ANN with 2 nodes in the output layer for both head and efficiency is more difficult, two ANNs with only one node in the output layer for head and efficiency, respectively, were designed and trained.

Table 3 Comparison of *CFD* result and ANN prediction

a. (Efficiency, %)

No.	*CFD*	*BP*	Error	*RBF*	Error
1	87.106	86.905	0.231%	87.012	0.108%
2	86.701	86.206	0.571%	86.929	0.336%
3	87.466	87.240	0.258%	87.028	0.501%
4	87.222	87.656	0.497%	87.068	0.211%

b. (Head, m)

No.	*CFD*	*BP*	Error	*RBF*	Error
1	7.9721	7.9817	0.120%	7.9743	0.027%
2	7.8976	7.9091	0.146%	7.9164	0.238%
3	7.9654	7.9327	0.411%	7.9927	0.343%
4	8.2212	8.2189	0.028%	8.1898	0.382%

The prediction values of trained RBNN and BPNN and the CFD result were listed in Table 2. Compared with the CFD result, both the RBNN and RBNN were acceptable, with maximum relative errors of 0.571%, 0.501% (for efficiency) and 0.411%, 0.382% (for head), respectively. The RBNN was adopted in the following process for the relative less training time and higher predict precision compared with BPNN.

In the optimization program using genetic algorithm (Cravero), each generation was comprised of 50 individuals encoded with the floating point numbers. Different initialization was adopted and the same best individual was obtained after 100 evolutions.

The angular momentum along the relative streamline was shown in Fig. 6, and there is a big difference between the original and the optimized angular momentum distribution. Figure 2 shows the radial coordinate R and angular coordinate θ of the blade. Compared with the original one, the θ of the optimized blade was smaller at the same R position. The decrement at the hub is relatively larger than that at the shroud. The static pressure distribution of the original and the optimized blade ative to the same operating pressure was shown in Fig. 3 and 4, respectively. On the pressure surface, the static pressure of the optimized blade is higher than that

of the original one. But on the suction surface, compared with the original one, the pressure of the optimized blade is higher near the outlet and lower near the inlet. The low-pressure zone at the suction surface may depress the suction performance which was not taken as the objective function.

The performance of the original and the optimzed impeller was shown in Fig. 9. The head and efficiency of the original impeller at design point was 7.94m and 86.64%, and that of the optimized was 8.49m and 88.25%, with an enhancement of 6.92% and 1.61%, respectively.

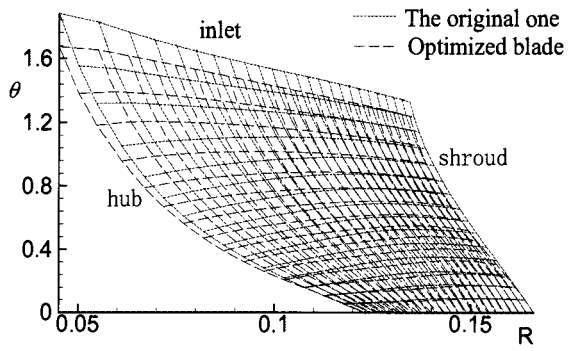

Fig. 2 Comparison of the original and optimized blade

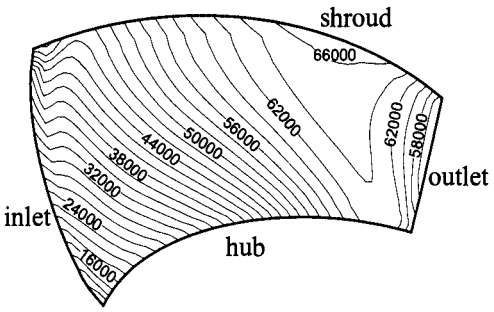

(a) pressure surface

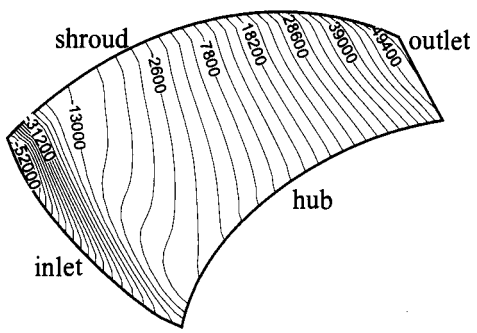

(b) suction surface

Fig. 3 Static pressure distribution of the original blade

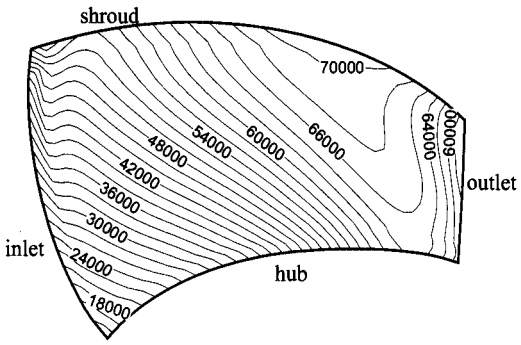

(a) pressure surface

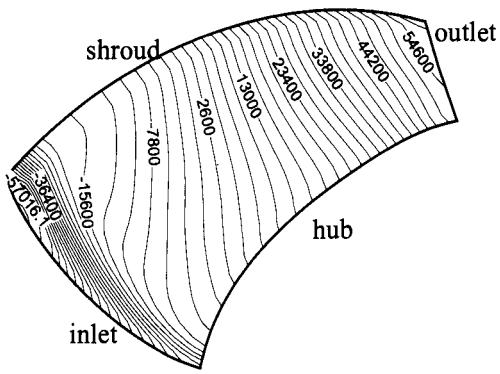

(b) suction surface

Fig. 4 Static pressure distribution of the optimized blade

5.2 Meridional Contour

Since the meridional contour and the blade shape are interactional, the optimal value of the blade variables for a certain meridional contour may be different if another meridional contour was given. Therefore, the meridional contour could not be optimized independently with the blade variables remaining to be the value obtained from above segment.

In main system, as shown in equation 2, the input variables include the meridional contour design variables (X) and the corresponding optimal value of blade variables (y). That is to say the impeller performance is a function of X and y. But for the ANN techniques, if all the variables of equation 2.a were treated as the ANN input, the training process would be very time-consuming and complex and the precision would be decreased. Actually, the optimal value of blade variables y is a function of X and can be uniquely determined with the specified X value. Therefore, we can conclude that the impeller performance is a complicated function of X. Since the ANN technique is capable of approaching any nonlinear functional relations, it can substitute the relation between impeller performance and X.

As listed in Tab.1, there are 4 meridional variables in the design space. Three levels of data were selected for each variable and 6 training sample data were schemed according to the uniform DOE theory (Fang). Two testing data were selected arbitrarily. As a result, there were total 8 different meridional contours. Repeating the process mentioned above in 5.1, we obtained the optimal 3-D blade shape corresponding to each meridional contour. Two RBNNs, with head and efficiency in output layer, respectively, were trained and then used to predict the impeller performances corresponding to the two test meridional contours. Compared with the CFD result, the maximum errors of the prediction value of RBNN for head and efficiency were 0.0768% and 0.554%, respectively. The meridional contour was optimized using the genetic algorithm, too. Each generation was comprised of 30 individuals, different initialization was adopted and the same best individual was obtained after 100 generations.

Figure 5 showed the meridional contour of the optimized and the original impeller. Compared with the original one, the shroud contour has relatively small difference, but the projection of blade inlet edge extends to the impeller inlet near the shroud and shrinks largely to the outlet near the hub.

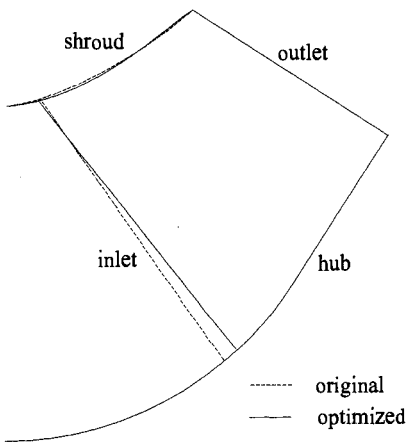

Fig. 5 Meridional contour of the impeller

The blade of best performance was achieved by rerunning the blade optimization procedure in 4.1 based on the optimal meridional contour. Figure 6 shows the angular momentum distribution along the relative meridional streamline and Fig. 7 shows the radial and angular coordinate of the optimization blade. Compared with the optimization result in 4.1, the angular momentum of this blade is small near the inlet and large near the outlet. The result confirms that the optimum angular momentum distribution of the blade is subjected to the meridional contour as mentioned in section 1.

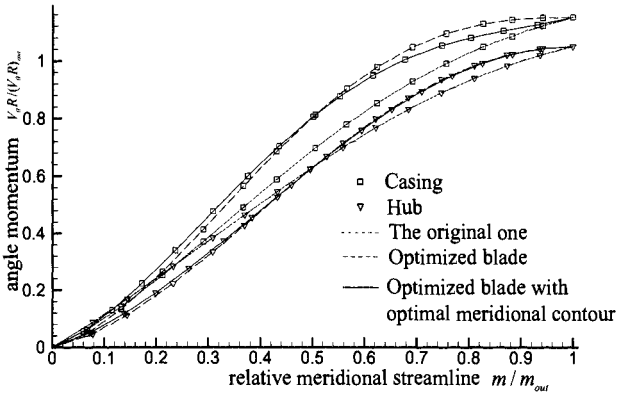

Fig. 6 Angular momentum distribution

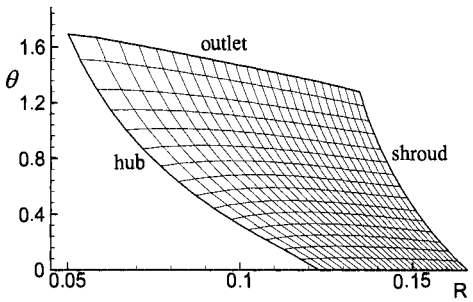

Fig. 7 The radial and angular coordinate of the optimized blade

Figure 8 shows the static pressure distribution. The static pressure on both pressure surface and suction surface of the blade with the optimal meridional contour is higher than that in Fig. 3 and 4, and the low-pressure zone near the shroud inlet in Fig. 7 disappears in Fig. 8.

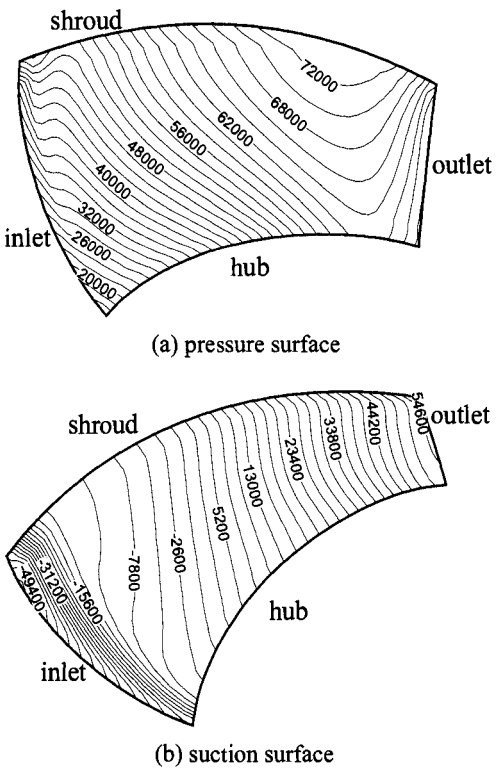

Fig. 8 Static pressure distribution of the optimized blade

Figure 9 shows the performance curve of this impeller obtained with the CFD tools. As can be seen, the head of the optimized impeller at the design point was 8.53m, with an increment of 0.58m or 7.43% relative to the original impeller, and of 0.04m or 0.47% relative to the impeller with the optimal blade shape. The efficiency at the design point is 90.01%, the increment is 3.37% relatively to the original impeller, and 1.76% relative to the impeller with the optimal blade shape and the original meridional contour, respectively. Highly performance is also achieved at the off-design point.

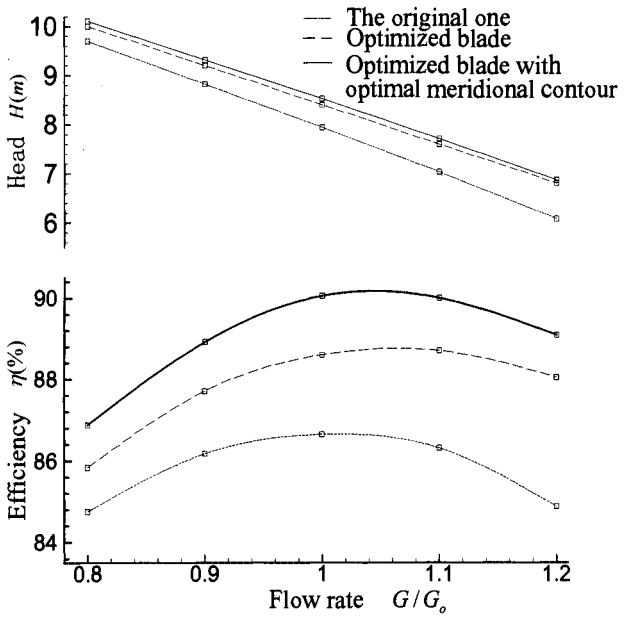

Fig. 9 Performance curve of the impeller

6 Discussion

This paper is intended to present an innovative procedure for optimization of mixed-flow or centrifugal impeller, including the 3-D blade and meridional contour. The accuracy and reliability of this method can be obviously improved by increase the training and testing sample data. Due to the errors between the ANN prediction and CFD result, our result may just be the approximation of the best performance impeller. In order to obtain the more exact one, further optimization in a smaller design space centered on the result above is necessary. Generally speaking, one or two of the optimization repetition is ok. The impeller performance of the result is highly enhanced and the optimization goal was achieved, therefore, no optimization was repeated here.

7 Conclusion

A new optimization approach for both 3-D blade shape and meridional contour of centrifugal or mixed-flow impeller was presented, and an example of application was shown. Since the blade was indirectly parameterized with the angular momentum, fewer variables were required. ANN technology was adopted to construct the response relation between the design variables and the objective function, and the blade was optimized according to the genetic algorithm. In order to maximize the amount of information generated with the minimum number of data, the design of experiment method was adopt to reasonably scheme the training sample data of ANN in the design space. The design variables were separated into two categories: the blade design variables and the meridional contour design variables, and were optimized in sequence. The optimized impeller in a mixed-flow pump, where the head and efficiency at the design point, relative to the original impeller, was increased by 0.58m (or 7.43%) and 3.37%, respectively, confirmed the validity of this newly proposed method.

Acknowledgements

This work is part of a project supported by the National Natural Science Foundation of China (90410019), Specialized Research Fund for the Doctoral Program of Higher Education of China (20040700009) and Specialized Research Plan in The Education Department of Shaanxi Province of China (05JK264). The supports are gratefully acknowledged.

References

Newman, J.C., Taylor, A.C., Barnwell, R.W., Newman, P.A., Hou, G.J., 1999,Overview of Sensitivity Analysisi and Shape Optimization For Complex Aerodynamic Configurations, Journal of Aircraft, Vol.36,No.1,1999: 87 – 96

C.Xu, R.S.Amano, 2002, A Turbmanchinery Blade Design and Optimization Procedure, ASME paper, GT-2002-30541

ASHIHARA, K., Goto, A., 2001, Turbomachinery Blade Design Using 3-D Inverse Design Method CFD and Optimization Algorithm, ASME paper 2001-GT-0358

Bonaiuti, D., Arnone, A., Ermini, M., Baldassarre, L., 2002, Analysis and optimization of transonic centrifugal compressor impeller using the design of experiment technique, ASME paper GT-2002-30619

Cosentino, R., Alsalihi,Z.,Van den Braembussche, R. A., 2001, export system for radial impeller optimization. Proceedings of Euroturbo4, ATI-CST-039/01

Pazzi, S., Marteli, F., Michelassi, V., Giachi,M., 2002, The Use of Artificial Neural Networks for Performance Prediction of Return Channels for Industrial Centrifugal Compressors, ASME papers, GT-2002-30392

Cravero, C., Satta, A., 2001, A Navier-Stokes Based Strategy for The Aerodynamic Optimization of A Turbine Cascade Using A Genetic Algorithm. ASME paper 2001-GT-0508

Goto, A., Zangeneh, M., 2002, Hydrodynamic Design of Pump Diffuser Using Inverse Design Method and CFD, Journal of Fluids Engineering, Transaction of The ASME, 124(2): 319 – 328

Fang, K.T., Uniform Design of Experiment and Uniform Design of Experiment Form, Beijing, Scientific publishing company, 35 – 49

The 4th International Symposium on Fluid Machinery and Fluid Engineering
November 24-27, 2008, Beijing, China
NO. 4ISFMFE-IL15

LDV and PIV Techniques Applied to Turbomachinery Geometry Constrains

G. Bois[*1], P. Dupont[2], A. Dazin[3] and G. Caignaert[3]

[*1] Dept. FISE, Fluid Mech and Energetics, LML(UMR CNRS 8107) Arts et Métiers Paris Tech.
8, Bd Louis XIV- 59000 Lille- France
Tel: +33320622223 / Fax: +33320622240
E-mail: gerard.bois@lille.ensam.fr

[2] LML (UMR CNRS 8107)- Ecole Centrale de Lille, Bd. P. Langevin, BP48, 59651 Villeneuve d'Asq- France

[3] LML (UMR CNRS 8107)- Arts et Métiers Paris Tech. 8, Bd Louis XIV- 59000 Lille- France

Abstract Laser experimental results performed in a centrifugal pump are analyzed taking into account constrains due to experimental set up and data reduction techniques. Two different configurations of the pump are selected: a vaneless diffuser one for with PIV and LDV techniques are compared in terms of velocity distributions inside the impeller, a second one with vane diffuser usind PIV only but with different light sheet arrangement. The paper mainly focuses on experimental investigations and data reduction problems uncounted in such configurations of the pump.

Keywords pump, optical techniques, PIV, data reduction

Nomenclature

K	$(\overline{C_u}^2 + \overline{C_r}^2)/2$	
R	radius	[m]
Re	Reynolds number $Re = R_2 * U_2/\nu$	
R_1	inlet tip radius of the impeller	[m]
R_2	outlet radius of the impeller	[m]
Z	number of blades of the impeller	[rpm]
N	speed of rotation	
Ω	impeller angular velocity	[s^{-1}]
Q	flow rate	[m^3/s]
Q_n	design flow rate	[m^3/s]
B_3	constant width of the diffuser	[m]
B	distance between the laser sheet and the hub	[m]
$\overline{C_u}$	peripheral component of phase averaged absolute velocity	[m/s]
$\overline{C_r}$	radial component of phase averaged absolute velocity	[m/s]
U_2	$U_2 = \Omega R_2$	[m/s]
W	phase averaged relative velocity	[m/s]
Tu	$K^{0.5}/U_2$ Turbulent kinetic energy	m^2/s^2

1 Introduction

LDV and PIV technique have already been recognized to give accurate measurements of temporal representation of velocity distribution in a spatial location of a turbomachine allowing interaction analysis between the impeller and its surrounding. For LDV, a number of authors have treated this kind of problem like Miner and Beaudoin (1989) for the case of volute. Liu and Vafidis (1994), Inoue and Cumsty (1984), Sideris , Van Den Breambusche (1987), Arndt and Acosta (1989) and (1990) have been concerned with the influence of vane diffuser. Because of the need of more detailed experimental data in order to calibrate new design techniques including the unsteady character of the flow, Particle Image Velocimetry (PIV) appears to be a very useful non intrusive technique for a better understanding of phenomena associated with rotor-stator interactions at design and off design conditions. Up to now, this technique is not so widely used as LDV one to perform investigations of internal flow pattern of turbomachinery especially in air test rig. A few results are given for the case of vaneless diffuser by Hayashi and

Koyama (2000); more detailed measurements in water have been performed since 1988 by Paone (1989), Eisele (1997), Ciocan (1998) among several other contributions.

Results presented in this paper refer to investigations performed in the so called SHF impeller, shown in Fig. 1. An experimental program has been elaborated on air and water test rigs. Among the several results obtained for different operating conditions starting from Wuibaut's work (2000) up to now, the paper focuses on experimental investigations and data reduction problems uncounted in such configuration of the pump.

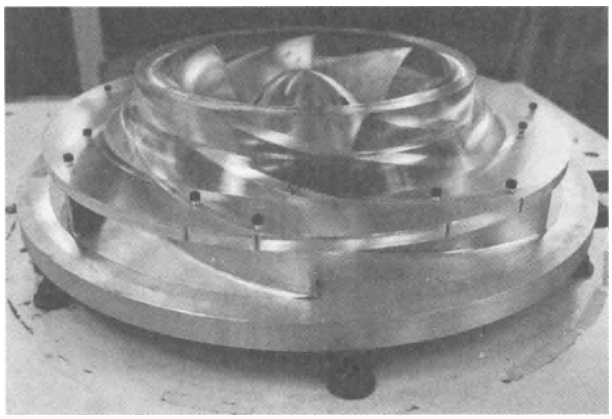

Fig. 1 SHF impeller with transparent shroud

2 LDV and PIV Measurement Comparisons

Table 1 give all kind of tests that have been performed on the SHF pump with the PIV method. Only some particular results will be shown in this paper. First experimental works have been done with PIV system inside the rotor with a vaneless configuration of the whole pump. The objective was to compare LDV and PIV measurements inside the rotor near optimum operating flow conditions both for mean velovities and fluctuating terms as reported by Wuibant (2006). For such a configuration (named as Test A in Table 1), two different camera positions were chosen (see Fig. 2) in order to cover the maximum blade to blade passage in the outlet part of the impeller. Due to the data acquisition capability at that time, the image capture was done each 2 rotor revolutions for the same blade to blade passage. This automatically supposed an axisymetric flow assumption that must be valid. The LDV measurements were performed in water with an existing vane diffuser and a volute. In order to make comparisons with PIV measurements, a specific data reduction was conducted in order to class all information with respect to the tangential position of the vane diffuser blade with the rotor passage. A tangential zone was then defined to be sure that the blade diffuser has no impact inside the impeller blade passage.

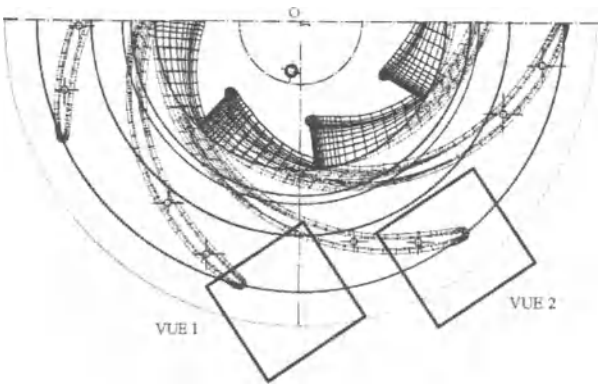

Fig. 2 PIV measurement positions in the impeller with short vaneless diffuser (Table 1, case A)

The main characteristics of the so called "SHF" impeller are:

- Outlet radius: R_2=256.6 mm
- Tip inlet diameter: 282.2 mm
- Number of blades: $Z = 7$
- Outlet width: 38.5 mm
- Outlet blade angle measured from the peripheral direction: 22.5°
- Mean blade thickness: 9 mm
- Nominal speed of rotation: $N = 2500$ rpm
- Design flow rate: $Q_n = 0.492$ m^3/s (at 2500 rpm)

In order to compare the results obtained by these two experimental techniques, PIV data have been selected for three radial positions imposed by the LDV measuring plane. More information about LDV set up can be found in El Hajem's work (2001).

Measurements are compared on five specific planes located between hub and shroud for three radii located in the outer part of the impeller.

From each PIV and LDV measurements, one can obtained the two components of the absolute velocity components C_r and C_u. One can also compute phased averaged velocity components $\overline{C_r}$ and $\overline{C_u}$ as described by Wuibaut (2000).

The deduced non dimensional, blade to blade mean relative velocities are presented only for one radius in Figures 3. Each figure represents the W/U_2 evolutions from pressure to suction side for different location B/B_3 between hub and shroud from PIV technique (a) and LDV technique (b).

Table 1 Experimental conditions

		2001	2005
Diffuseur	Lisse court		
	Lisse long		
	Type A	[redacted]	[redacted]
	Type B	[redacted]	
Laser	marque	BMI	QUANTEL
	Type	YAG	ND :YAG
	Laser wave length: λ (nm)	532	532
	Laser impulse frequency (Hz)	10 à 15	12
	Energy impulse (mJ)	750 à 532	200
	Impulsion time	10 ns	
Cameras	Type	Kodak	Kodak Flow master 300
	Resolution	1008*	1280*
	Pixel*pixel	1018	1024
	Acquisition frequency level (Hz)	30	20
	Cameras number	2	2
	Flow rate number	6	6
	B number	3	3
	Vane diffuseur position number		7 (see Fig. 8)
		Wuibaut (2000)	Dupont (2005)
		Wuibaut (2001-a)	Caignaert (2004)
		Wuibaut (2001-b)	Wuibaut 2002-a
		Wuibaut (2001-c)	Wuibaut 2002-b

Table 2 Experimental conditions (cont)

2006	2007	Test #
		A
[redacted]	[redacted]	B
		C
		D
QUANTEL	DARWIN PIV	
ND :YAG	ND :YLF	
532	532	
12	980	
200	20	
	110/130 µs	
Kodak Flow master 300	Phantom V9	
1280* 1024	1488* 664	
	1500	
2	2	
6	5	
1	3	
7 (see Fig. 8)		
Llevar 2006-a	Dazin 2007	
Llevar 2006-b		

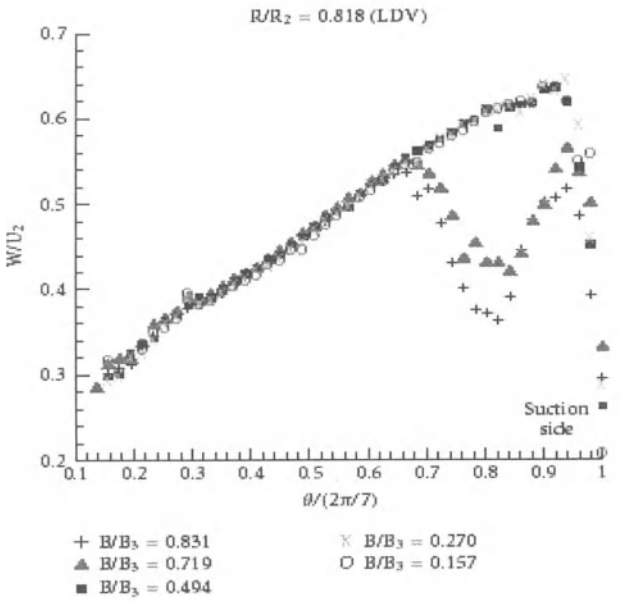

Fig. 3(a) Blade to blade relative velocity distribution for a particular radial position inside the impeller

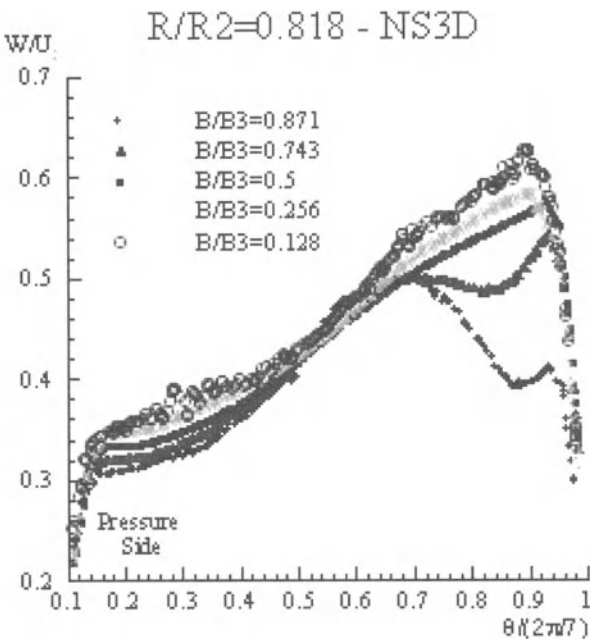

Fig. 4(a) Calculated blade to blade relative velocity distributions for different hub to shroud positions

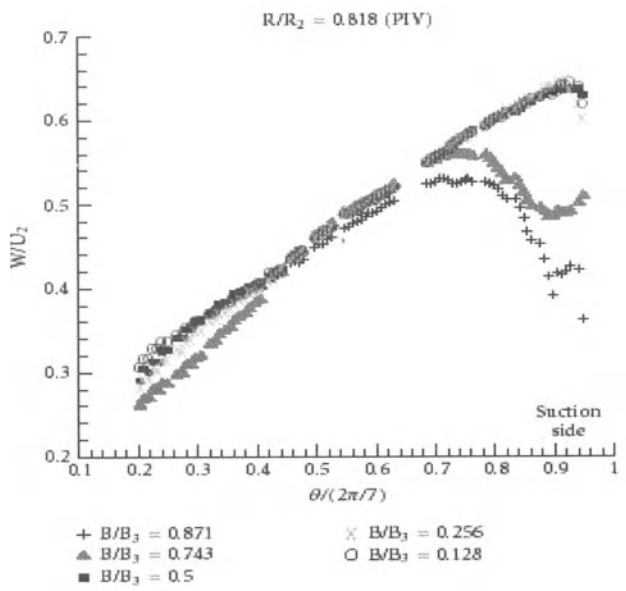

Fig. 3(b) Blade to blade relative velocity distribution for a particular radial position inside the impeller

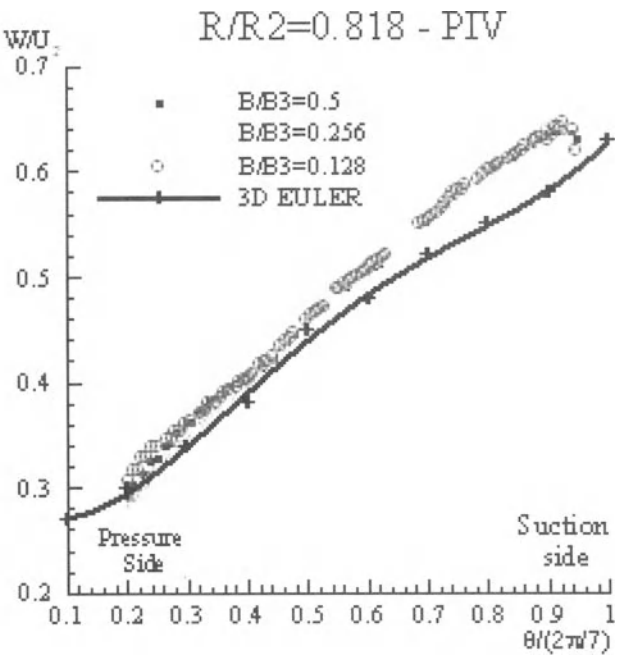

Fig. 4(b) Comparison between EULER calculation results with PIV results in the core region of the jet inside the impeller

Concerning the comparisons between experiments and calculations, flow computations within the SHF impeller were performed using a finite element technique. It allows the computation of a wide variety of 2D or 3D unsteady incompressible flows, by solving the Reynolds-averaged Navier-Stokes equations together with a k-ε turbulence model. The flow domain consists in $1/7^{th}$ of the impeller, including the inlet pipe and the vaneless diffuser. The corresponding finite element mesh consists in 78950 elements and 122012 nodes.

For a better comparison with experimental results, the blade to blade relative velocity distributions are plotted for the same hub to shroud locations and the same radius inside the impeller passage in Figures 4(a) an 4(b).

The wake location and extension inside the blade passage is correctly predicted by the calculation. Low energy fluid region near the pressure side seems to be over estimated. As a consequence, the local blockage seems to modify the jet zone gradient for R/R_2=0.818.

Experimental results indicates small boundary layer thickness in the pressure side blade vicinity, this may indicate that Coriolis forces are strong enough to have a destabilizing effect on the turbulent boundary layer as shown by Johnston (1976).

It is also interesting to show results of a 3D EULER calculation in order to emphasize isentropic flow region. The results are plotted on Figure 4(b). Some of the experimental gradient observed in Figures 3, corresponding to the so called "jet flow" region are reported on these last figures for a better comparison. They are very close to the EULER calculation which also show the two dimensional character of the flow from hub to shroud direction. Wake development is equivalent to a blockage effect; and do not modify the equilibrium of the jet region. Results for higher radii inside the impeller also show good agreements between PIV experimental results and calculations.

A last point concerns the velocity fluctuation rates obtained with the PIV and LDV measurements. An example of results is given in Figure 5 at impeller outlet section. One can see that levels are quite similar. Levels increase (in red) only for one particular vane diffuser position corresponding to a relative position face to the impeller pressure side.

3 Diffuser Flow Studies with Rotor Stator Interactions

In order to perform these measurements, special arrangements such as transparent diffuser blades with two light sheets as shown in Figure 6 from Wuibaut (2002), then

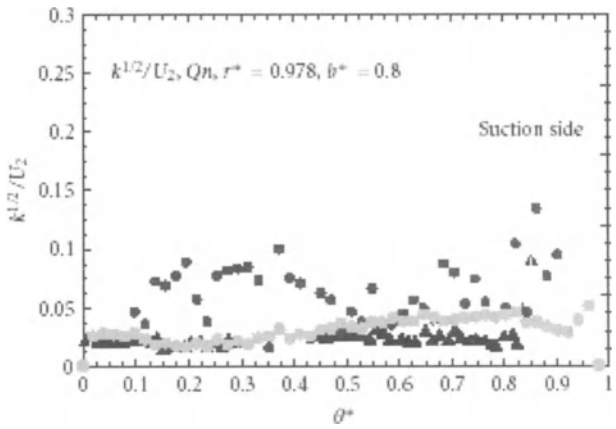

Fig. 5 Blade to blade *Tu* distributions: LDV in red and green; PIV in blue

one light sheet with another twin camera arrangement as shown in the next Figure 10, were performed.

a) In the first case, one has to superpose the two images in order to reconstruct the whole flow. It can be seen first in Figure 7, that a strong flare appears in the leading edge zone of the diffuser blade. Secondly, Figures 9 show results of the relative velocity fluctuation contours for different mass flow rates are presented. for one specific vane diffuser position relative to the impeller. The border corresponding to the image superpositions, can easily be seen for the highest mass flow rate corresponding to high negative incidence on the vane diffuser leading edge. This is also the case for the lower mass flow rate but with smaller discrepancies. This show that there is no more continuity in the velocity fields in these cases and that the vane diffuser has an influence inside the impeller and also inside the vaneless diffuser part of the pump.

It has been shown by Caignaert (2004) that the velocity evolution on pressure side was mainly affected by the presence of the leading edge blade diffuser.

b) For the second case, only one vane diffuser channel was chosen (see Table 1, Test Case B) but with a modify data acquisition and data reduction techniques allowing more detailed flow analysis based on statistical rules done by Pavesi (2007). Flare problems still remains, but the image continuity become quite good in this case because it was the same blade channel that was illuminated.

Experimental comparisons between case a) and case b) with unsteady calculations performed by Pavesi (2007) show that a very strong velocity gradient exist near the diffuser pressure side (see Figure 10). This gradient is slightly captured by the fist set of measurements (Table 1, case A) and not by the new set as shown in Figure 11 which represents the velocity distribution at diffuser inlet

throat at mid height. This means that quite local flow structure may be completely hidden by light sheet configurations.

4 Conclusions

Main conclusions concerning A and B cases are the following:

(1) Concerning the mean relative blade to blade velocity distributions at nominal conditions

- Both PIV and LDV techniques capture the jet and wake structure and relative velocity gradients:

a) Velocity gradients and levels are comparable in the jet region.

b) They are slightly different in some wake locations inside the blade passage.

- These differences may be explained as follow:

a) PIV plane location error in regions with large velocity gradients.

b) Different inlet boundary layer characteristics between air and water tests.

c) Different inlet recirculation configuration due to leakage.

d) Different diffuser configuration.

(2) Concerning the velocity fluctuation rate distributions

a) Fluctuation rates are more important near the pressure side for small radii.

b) Fluctuation rates seem to be lower inside the wake region but quite strong in the jet and wake border.

c) PIV and LDV technique results are comparable taking into account some particular conditions.

d) Blade to blade PIV distributions show more continuous distributions than LDV ones.

e) On the contrary, LDV ones are better for hub to shroud distributions.

(3) CFD results show

- Same relative blade to blade velocity levels and gradients in the core region.

- Strong relative velocity gradients at the jet and wake border.

(4) For vaneless diffuser at off design conditions and for vaned diffusor for all mass flows, more details measurements are requided with high speed cameras using PIV 2D 3C techniques. This work is now in progress in our lab.

Acknowledgements

These works have been performed with the support of SHF (Société Hydrotechnique de France), partner of AFM (Association Française de Mécanique).

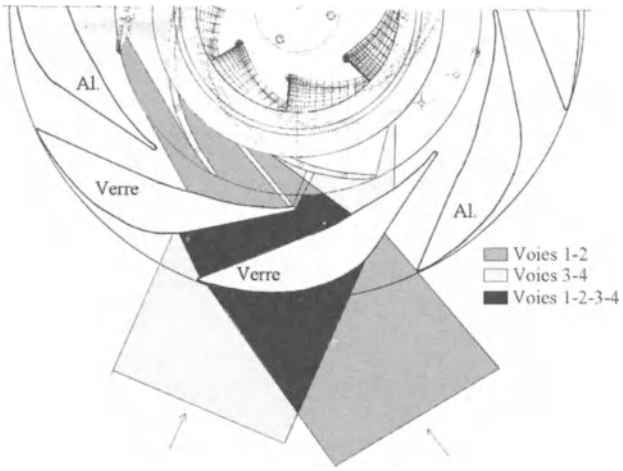

Fig. 6 Light sheet configurations with transparent diffuser blades

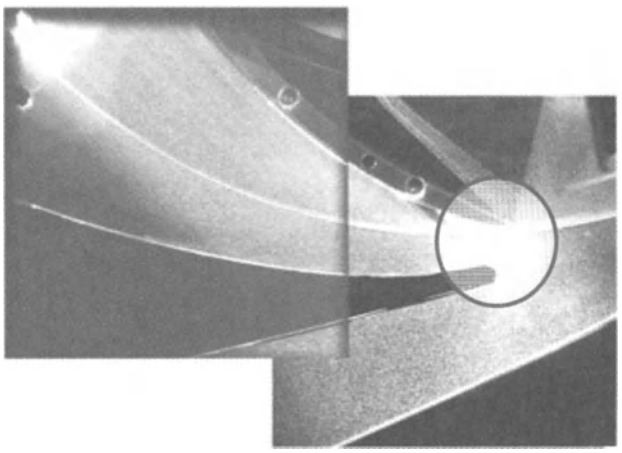

Fig. 7 An example of flare problem in configuration shown in Figure 6 (Fist laser sheet arrangement)

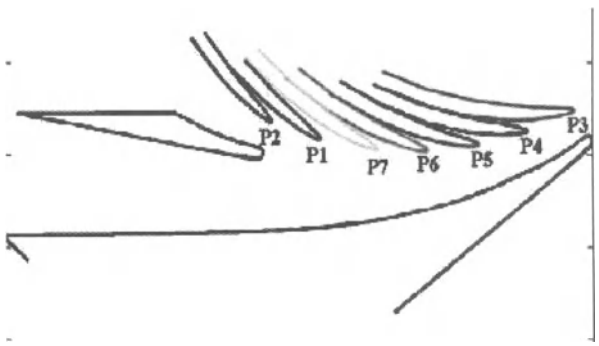

Fig. 8 Different vane diffuser position chosen for rotor stator studies

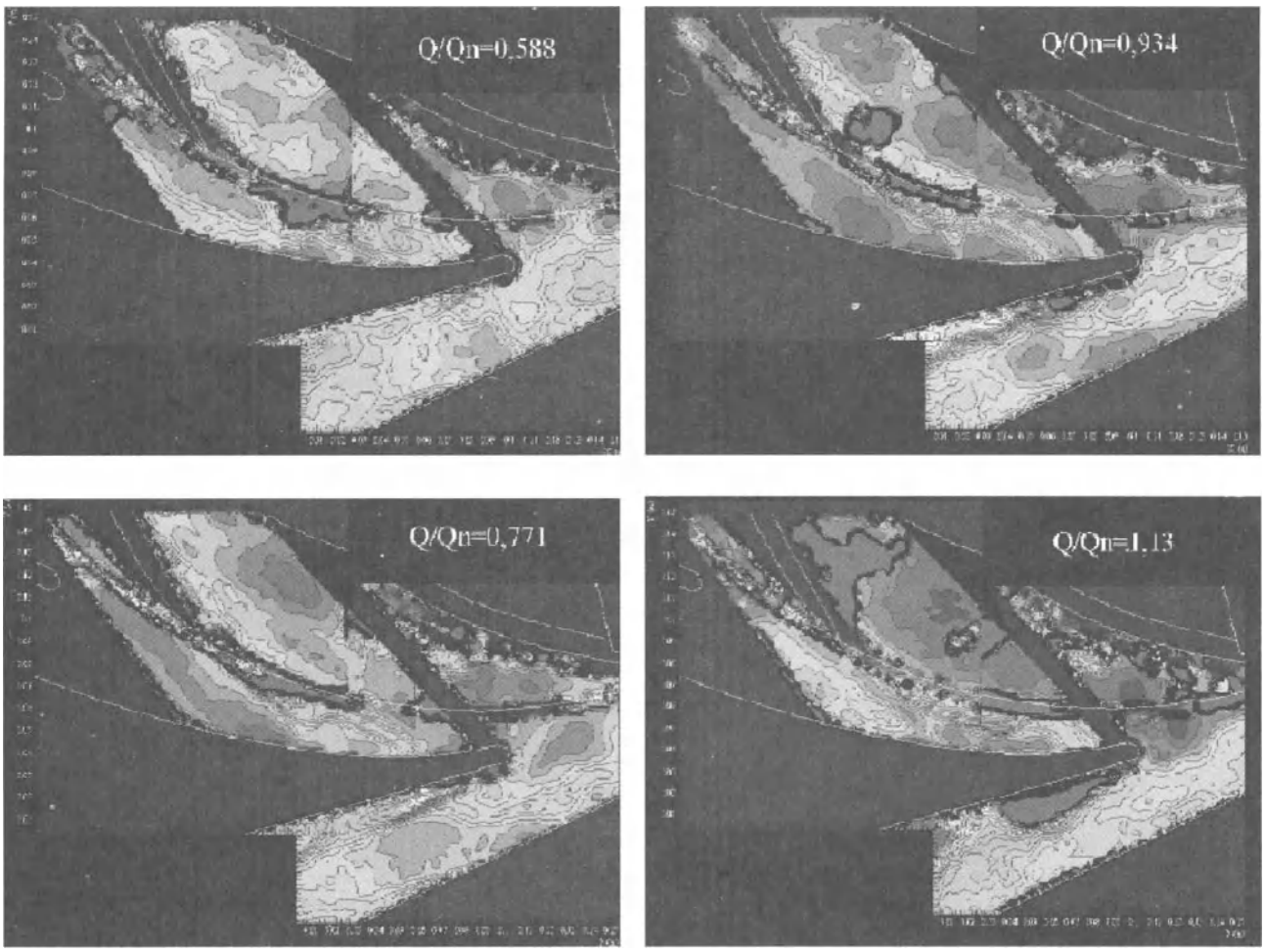

Fig. 9 Velocity fluctuations for different mass flow rates at mid height of hub to shroud passage

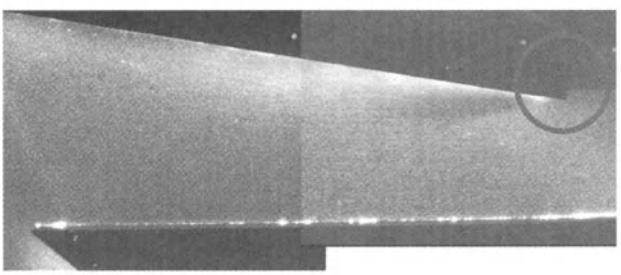

Fig. 10 An example of flare problem for the second laser sheet arrangement

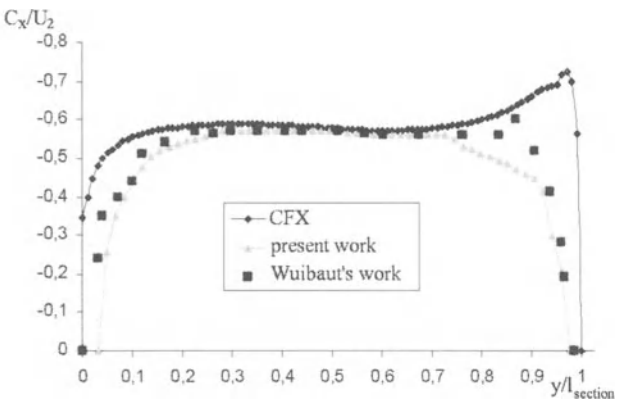

Fig. 11 Comparisons of velocity distribution at first throat inlet section

References

Miner S.M., Beaudoin R. J., Flack R.D., 1989, "Laser Velocimetry measurements in a centrifugal flow pump", Journal of Turbomachinery, Vol. 111, N°3, p 205 – 212

Liu C.H. , Vafidis C., Whitelaw J.H., 1994, "Flow Characteristics of a Centrifugal Pump", Journal of Fluids Engineering, Vol. 116, N°2, p303 – 309

Inoue M., Cumspsty N. A. Experimental Study of Centrifugal Impeller Discharge Flow n Vaneless and Vaned Diffusers, Journal of Engineering for Gas Turbines and Power, 1984, Vol. 106, N°2, p. 455 – 467

Sideris M. Th., Van Den Breambusche R.A., 1987, "Influence of centrifugal exit pressure distortion on the flow in a impeller and diffuser.", Journal of Turbomachinery, 1987, Vol. 109, N°1, p. 48 – 54

Arndt N., Acosta A.J., Brennen C.E., Caughey J.K., 1989, "Rotor-Stator interaction in a diffuser pump.", Journal of Turbomachinery, Vol. 111, N°3, p. 213 – 221

Arndt N., Acosta A.J., Brennen C.E., Caughey J.K., 1990, "Experimental investigation of the Rotor-Stator interaction in a centrifugal pump with several diffusers.", Journal of Turbomachinery, Vol. 112, N°1, p. 98 – 108

Hayashi N., Koyama M., Ariga, 2000, "Study of Flow Patterns in Vaneless Diffusers of Centrifugal Compressors using PIV.", 10th International Symposium on Applications of Laser Techniques to Fluid Mechanics, Lisboa, Portugal

Paone N., Riethmullerm L., Vandenbrambussche R., 1989, " Experimental investigation of the flow in vaneless diffuser of a centrifugal pump by Particle Image Displacement Velocimetry, Experiments in fluids 7, p. 371 – 378

Eisele K., Zhang Z., Casey M. V., Gülich J., Schachenmann A., 1997, "Flow analysis in a Pump Diffuser Part 1: LDA and PTV Measurements of the Unsteady Flow." Transactions of ASME, Journal of Fluids Engineering, Vol. 119

CiocanI G.D., Desvignes V., Combes J.F., Parkinson E., Kueny J.L., 1998, "Experimental and numerical analysis of rotor-stator interaction in a pump turbine.", the XIX International Symposium on Hydraulic Machinery and cavitation, Singapore.

Johnson J.P., Eide SA, 1976, "Turbulent Boundary Layers on Centrifugal Compressors Impeller", Journal of Fluids Engineering, p. 374 – 381

Wuibaut G., Dupont P., Caignaert G., Stanislas M., 2000, "Experimental analysis of velocities in the outlet part of a radial flow pump impeller and the vaneless diffuser using particle image velocimetry", XX IAHR Symposium, Charlotte (USA)

El Hajem M., Akhras A., Morel R., Champagne J.Y., 2001, "The Rotor stator interaction in a centrifugal pump equipped with a vaned diffuser", 4th European Conference On Turbomachinery Fluid Dynamics and Thermodynamics, March 20-23, 2001 Firenze, Italy

Caignaert G., Wuibaut G., P.Dupont, G. Bois, 2004 "Rotor-stator Interactions in a Vaned Diffuser Radial Flow Pump XXIInd IAHR symposium hydraulic machinery and systems", Stockholm (Sweden), in "proceedings of the XXII IAHR symposium hydraulic machinery and systems", p B5 – 2

Dupont P., Schneider T., Caignaert G., Bois G., 2005, "Rotor-stator interactions in a vaned diffuser radial flow pump." 5th International Symposium on pumping machinery (ASME), Houston (USA), FEDSM2005-69038, June 2005

Llevar 2006-a: Llevar S., H. C de Lange, A.A. van Steenhoven., 2006a, "Two dimensional Rotating stall analysis in a wide vaneless diffuser". International Journal of rotating machinery. DOI 10.1155/IRJM/2006/56420

Llevar 2006-b: Llevar S., H.C. de Lange., A.A van Steenhoven, P Dupont., G. Caignaert, G. Bois, 2006b "Core flow instability in wide vaneless diffusers on behalf of rotating stall investigation. The 13th international Conference on Fluid Flow technologies. Budapest, Hungary, September 2006

Wuibaut G., Dupont P., Bois G., Caignaert G., Stanislas M., 2001a, "PIV Measurements in the impeller and the vaneless diffuser of a radial flow pump in design and off design operating conditions", ASME Journal of Fluids Engineering, september 2002, vol 124, p.791 – 797

Wuibaut G., Bois G., Dupont P., Caignaert G., 2002a, "Rotor stator interactions in a vaned diffuser of a radial flow pump for different flow rates using PIV measurement technique", 9th International Symposium on Transport Phenomena and Dynamics of Rotating Machinery, ISROMAC 9, Hawaii, USA, paper FD-ABS-018, 10 – 14 Février 2002

Wuibaut G., Dupont P., Bois G., Caignaert G., Stanislas M., 2001b, "Application de la vélocimétrie par images de particules à la mesure simultanée de champs d'écoulements dans la roue et le diffuseur d'une pompe centrifuge.", La Houille Blanche, revue internationale de l'eau, N° 2/2001, p. 75 – 80

Wuibaut G., Dupont P., Bois G., Caignaert G., Stanislas M., 2001c, "Analysis of flow velocities within the impeller and the vaneless diffuser of a radial flow pump", ImechE Journal of Power and Energy, part A, 215, p.801 – 808

Wuibaut. G., Bois G., Dupont. P., Caignaert G., 2002a, "Rotor stator interactions in a vaned diffuser of a radial flow pump for different flow rates using PIV measurement technique", 9th International Symposiumon Transport Phenomena and Dynamics of Rotating Machinery, ISROMAC 9, 10 -14 Février 2002, Hawaii, USA, paper FD-ABS-018

Wuibaut G., Bois G., Dupont P., Caignaert G., Stanislas M., 2002b, "Experimental analysis of interactions between the impeller and the vaned diffuser of a radial flow pump", International Association on Hydraulic Research 2002 Symposium, paper GU03, Ecole Polytechnique Fédérale de Lausanne, Switzerland, September 9 – 12th, 2002

Wuibaut G., Bois G., El Hajem M., Akhras, J.Y. Champagne J.Y., 2006, 'Optical PIV and LDV comparisons of internal flow investigations in SHF Impeller 'International Journal of Rotating Machinery' IJRM. 50507, Volume

Dazin A., Coudert S., Dupont P., Caignaert G., Bois G., 2007, "Combined high speed stereoscopic P.I.V. measurement and unsteady pressure measurements in the vaneless diffuser of a centrifugal pump", XIX Biannual Symposium on Measuring Techniques in Turbomachinery Transonic and Supersonic Flow in Cascades and Turbomachines, 1 Rhode-St-Genèse, Belgium

G. Pavesi, G. Cavazzini, G. Ardizzon, P. Dupont, S. Coudert, G. Caignaert, G. Bois, "Analysis of Rotor-Stator Interactions Effects within the Vaned Diffuser of a Radial Flow Pump" IAHR Symposium 2006, October 2006, YOKOHAMA, Japan

The 4th International Symposium on Fluid Machinery and Fluid Engineering
November 24-27, 2008, Beijing, China
NO. 4ISFMFE-IL20

Limiting Streamlines Measurement in Contra-Rotating Axial Flow Pump

Akinori Furukawa[*1], Satoshi Usami[2], Yusuke Tsunenari[2], Satoshi Watanabe[3] and Kusuo Okuma[4]

[*1] Professor, Dept. of Mechanical Engineering, Kyushu University,
744 Motooka Nishi-ku, Fukuoka 819-0395, Japan
Tel: +81-92-802-3107 / Fax: +81-92-802-0001
E-mail: fmfuru@mech.kyushu-u.ac.jp

[2] Graduate student, Dept. of Mechanical Engineering Science, Kyushu University, Japan

[3] Associate Professor, Dept. of Mechanical Engineering, Kyushu University, Japan

[4] Technical Assistant, Dept. of Mechanical Engineering, Kyushu University, Japan

Abstract An application of contra-rotating rotors, in which a rear rotor is in tandem with a front one and these rotors rotate in the opposite direction each other, has been proposed against a demand for developing higher specific speed axial flow pump. It is necessary to understand the internal flow behavior for higher performance design. In the present study, limiting streamlines on the blade passage walls were observed by multi-colored oil-film method at design and partial flow rates. The flow behaviors are discussed by observed results of limiting streamlines with measured results of blade-to-blade velocity distribution by Laser Doppler velocimetry and static head distributions on casing wall by pressure sensors.

Keywords axial flow pump, contra-rotating blade row, limiting stream lines, internal flow behavior

1 Introduction

Recently, there is a strong demand for developing higher specific speed axial flow pump in reduction of pump installation space and costs [1, 2]. However, higher specific speed pump suffers from deterioration of the efficiency and cavitation performance. Then, authors have proposed an application of contra-rotating rotors and investigated usefulness of them [3]. The most important feature of contra-rotating axial flow pump is that the rear rotor, installed instead of the stator of conventional type, plays a role not only to recover the static head but also to give the energy to the fluid directly. Although contra-rotating axial flow pump has complex biaxial shafts structure, the rotational speed or the pump size enables to be reduced under the same specification of conventional axial flow pump [4]. Additionally, according to performance compared to conventional axial flow pump, an application of contra-rotating rotors results in better cavitation performance because of lower rotational speed design, improvement of the efficiency at design point, and higher performance at partial flow rate because of reduction of remaining swirl flow at downstream section of rear rotor by rotational speed control [5, 6].

The understanding of the internal flow in contra-rotating axial flow pump is necessary to establish the design guideline of higher efficiency at the design flow rate and negative sloped head-characteristics in partial flow rate region. After the internal flow measurement [7, 8] with Laser Doppler velocimetry (LDV) and casing wall pressure measurement related on blade row interaction [9], limiting streamlines observation on the blade passage was performed with multi-colored oil-film method. In the present paper, the difference of flow behaviors between front and rear rotors is cleared and the flow mechanism is discussed though it will not be solved completely due to the complexity.

2 Experimental Apparatus

Pump head $H_d = 4.0$ m and flow rate $Q = 70$ *l*/s were specified in pump design. When specific speed of each rotor was determined as 1500[min^{-1}, m^3/min, m], the

rotational speed was determined as $N_f = N_r = 1225\text{min}^{-1}$ for contra-rotating rotors combination (called RR type). The blade rows were designed by using conventional empirical method [4]. RR type has 4 front rotor blades and rear ones.

Figure 1 shows designed cascades developed at $r =$ 92.5mm and the corresponding comparisons of velocity triangles at design and off-design points $Q = 70$ and 42 *l*/s, by which the principle of rotor works is explained. In contra-rotating type, the inlet flow with no pre-swirl receives a rotational torque by front rotor, and gets swirling at the outlet (V_{2f}). Its swirling flow ($V_{1r} = V_{2f}$) subsequently obtains the counter-rotational torque from rear rotor while flowing through the rear rotor. Therefore the rear rotor not only recovers the swirling energy $V_{\theta 2f}$ but also theoretically imparts the flow turning ($\Delta V_{\theta r}$) and the work to the through-flow. At the design point, while the rotational speed of rear rotor is kept the same as that of front rotor, the same flow turning ($\Delta V_{\theta f} = \Delta V_{\theta r}$) is respectively given by front and rear rotors and water flows out in the axial direction. However, just since rear rotor makes use of $V_{\theta 2f}$ to do the above same work at the design point, relative velocities W and stagger angles γ are taken as $W_{1r} > W_{1f}$, $\gamma_r > \gamma_f$, as we can see from Fig.1. And as V_{2r} varies a great deal at off-design point, the rear rotor undergoes considerable variation on flow turning $\Delta V_{\theta r}$. Its flow turning $\Delta V_{\theta r}$ meaning the blade loading clearly gets larger than that of front rotor in the range of partial flow rate, that is, $(dH/dQ)_f < (dH/dQ)_r$ when $N_f = N_r$.

Figure 2 shows the sectional view of the test pump. The hub diameter is 100mm, the casing one is 200mm and a blade tip clearance is 1.0mm. A set of two shafts, which are inner and outer ones, is required for each front and rear rotor and each shaft is connected via a torque-meter to a respective motor. For the pressure performance evaluation, the static head differences on the casing wall are measured between the up- and downstream sections of rotors, Pos.0, III and V in Fig.2. Then, the head rises of front and rear rotors, H_f, H_r and the total pump head $H_{RR} = H_f + H_r$ are evaluated by adding the dynamic head difference of the sectional averaged axial velocity into the corresponding measured static head difference. The flow rate Q is obtained from an orifice meter installed far upstream of the pump. Then, the hydraulic efficiency of pump η is calculated as the ratio of the water power to the shaft power after eliminating the mechanical losses obtained in advance.

The pump casing is made of acrylic transparent resin. Therefore, the internal flow measurement with LDV is possible. The measurement basically can be done at arbitrary axial and radial positions based on phase- locked sampling method of the rotation [7], whereas the velocity near the casing and hub walls and blade surfaces cannot be measured because of the dispersion of the laser beam. Moreover, the instantaneous static head was also measured at sixteen axial positions on the casing wall and pressure distribution between front and rear rotors is obtained from our measuring method [9].

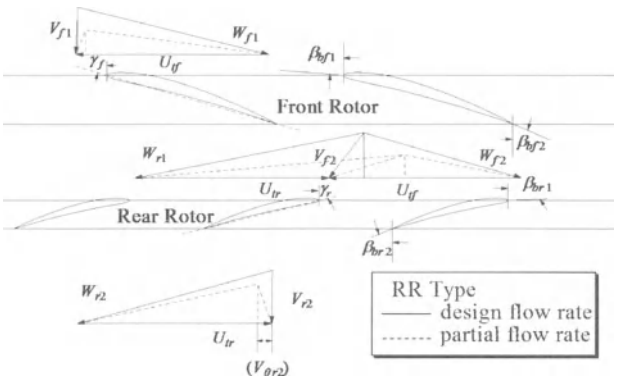

Fig. 1 Linear cascades and velocity triangles of *RR* type

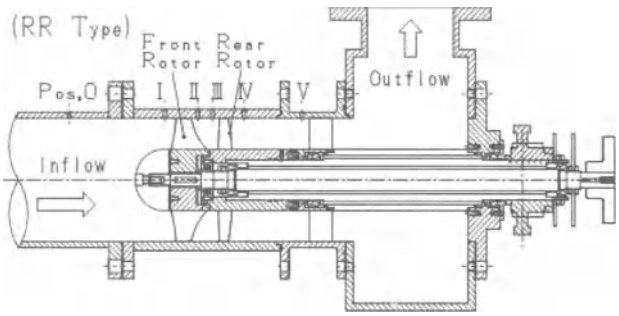

Fig. 2 Pump test section

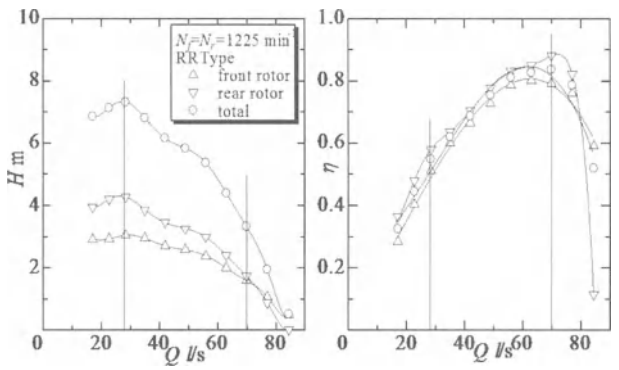

Fig. 3 Pump characteristics on head and efficiency

In the present study, in addition of above mentioned measurement, limiting streamlines on the rotating walls of flow passages are visualized by multi-colored oil-film method [10].

3 Experimental Results and Discussion

Figure 3 shows the pump characteristics of contra-rotating RR type. The pump of RR type yields pump head H_{RR} = 3.6m, which does not satisfy the designed head of H = 4m, and the maximum efficiency η_{RR} = 83% at the design point of Q = 70 *l*/s. As the feature of contra-rotating type, rear rotor head of H_r becomes higher than front rotor one H_f at partial flow rates as seen in Fig.3, which means more stable head characteristic curve with negative slope of $dH/dQ<0$. However the positive slope appears in the flow rate range of $Q<$ 28 *l*/s. The efficiency of rear rotor η_r is higher than that of front rotor η_f at partial and design flow rates.

In the present paper, we focus on the flow behaviors at design flow rate of Q = 70 *l*/s to improve the efficiency and at partial flow rate of Q=28 *l*/s to avoid the appearance of positive slope of head curve $dH/dQ>0$.

Figure 4 shows the radial distributions of axial and tangential components of absolute velocity, V_z and V_θ at the positions of I, III and V, which are evaluated as time-averaged from instantaneous velocities. At flow rate of Q = 70 *l*/s, V_z components are uniform in radial direction at all measuring positions and V_θ components takes values of zero at positions up- and downstream sections of contra-rotating rotors in accordance with the working principle of $\Delta V_{\theta f} = \Delta V_{\theta r}$. At the mid-position between the front and rear rotors V_θ components (symbol of ▲) takes finite values.

On the other hand, at Q = 28 *l*/s backflow regions appear near the blade tip region of front rotor inlet (pos. I) and near the blade hub region of front rotor outlet (pos. III). At the position V downstream of rear rotor, there is no appearance of backflow region. V_θ components at Q=28 *l*/s are changed in response to the appearance of backflow. The positive direction of V_θ components in Fig. 4 corresponds to the rotational direction of front rotor. Thus, V_θ components of $V_{\theta 2f}$ at pos. III takes positive and that of $V_{\theta 2r}$ at pos. V takes negative. The value of ($V_{\theta 2f}$ - $V_{\theta 2r}$) contributes to pump head increasing at partial flow rate. Meridional streamlines at Q = 28 *l*/s is shown in Fig. 5, obtained from time-averaged V_z components by LDV measurement. Broken lines mean axial velocity components are zero. The backflow regions are found near both blade tip side inlet and hub side outlet of front rotor in Fig. 5, in the same manner to conventional pump. Although front rotor has outlet backflow region near hub side, the negative slope of front rotor H_f-Q characteristics becomes only gradual (Fig.3). According to that, it is considered that head drop due to the blockage effect with inlet backflow at blade tip side is stronger than head rise due to centrifugal force to fluid with outlet backflow. On the other hand, rear rotor doesn't have outlet backflow region at hub side, though it has inlet backflow region at blade tip.

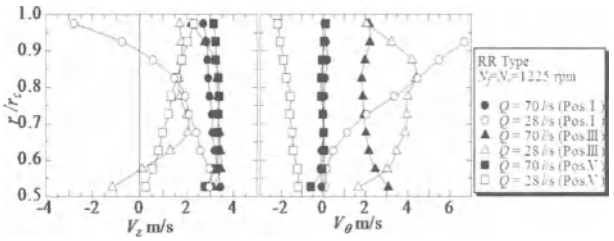

Fig. 4 Radial distributions of velocity at I, III, V sections

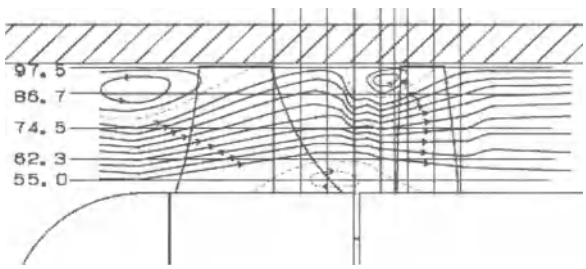

Fig. 5 Meridional streamlines at Q = 28*l*/s

It is considered that static head drops between front and rear rotors due to blockage effect with inlet backflow region at blade tip side of rear rotor.

3.1 Flow behavior at design flow rate of Q=70 *l*/s

Figure 6 shows the relative velocity distribution at radial position of r = 97.5mm measured by LDV synchronized with front/rear rotor rotation and the corresponding static head-rise distribution from the front rotor inlet, measured on casing wall. As synchronization is conducted only on one rotor in this experiment, there is no effect of another rotor on velocity and static head distributions. The low static head region stretching to the blade-to-blade region is observed as broken line. This low pressure region is considered as the leakage vortex from blade tip and backflow appears due to the leakage vortex. The relative velocity on suction surface near the trailing edge of front rotor is increased by the flow from radial inner section in Fig. 6. On the other hand the leakage flow from the rear rotor blade tip becomes weakened in comparison with front rotor because rear rotor blade loading is small. It is recognized that the suppression of leakage flow is important for the improvement of efficiency. The outlet flow from the front rotor becomes uniform in downstream direction although the wake is observed near the trailing edge of the blade in the case of synchronized field with front rotor rotation and is decayed. The flow becomes uniform by the

mid-position between front and rear rotors. On the other hand, when the same region is focused from the synchronized field with rear rotor rotation the rear rotor blade blockage influence appears near the front rotor outlet due to the high stagger angle of rear rotor blade. Figure 7 shows the axial distribution of the maximum and minimum static heads and time averaged one on casing wall. Head rise of front rotor is kept constant near the inlet of the rear rotor. Therefore, it is considered that the influence of the wake and blockage effect on the pump performance are small. Though it is found that the head difference between the maximum and minimum values near the front rotor inlet is lower than that near the rear rotor inlet, the leakage flow in rear rotor is not clearly observed.

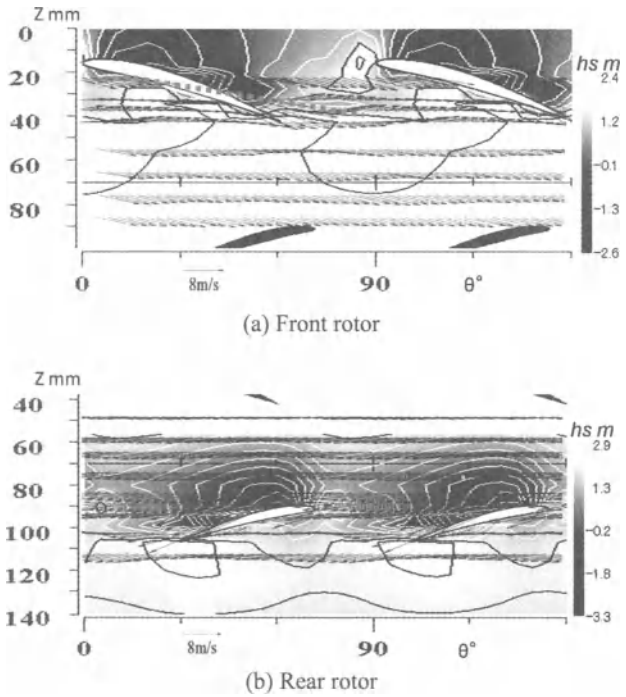

Fig. 6 Casing wall static head distribution and velocity vectors at r = 97.5mm (r/r_t = 0.98) at Q = 70*l*/s

Figures 8 and 9 show visualized limiting streamlines on the blade passage of front and rear rotors. In comparison between Figs. 8 and 9, the secondary flow of low energy fluid on the hub to the suction surface as shown in Fig. 8(a) and limiting streamlines appear in radial direction on both pressure and suction surfaces in front rotor. Especially the radial streamlines in the tip region of the pressure surface is observed due to the tip leakage flow. On the other hand, in the rear rotor these secondary flow cannot be observed as can be seen in Fig.9. In this case, the swirl entry of $V_{\theta 2f} = V_{\theta 1r} > 0$ (Fig. 4) becomes weakened the secondary flow in radial direction.

3.2 Flow behavior at partial flow rate of Q = 28 *l*/s

Figure 10 shows the relative velocity distribution at corresponding static head-rise distribution from the front rotor inlet, measured on casing wall as the same synchronization method as Fig. 6. In Fig. 10 red-colored velocity vectors are normal (downstream) flow and blue-colored ones are backflow. The low static head appears in blade tip region of front rotor, different from the behavior at Q = 70 *l*/*s*, due to the backflow region as shown in Fig. 5. Therefore, the obvious tip leakage flow is not found at this flow rate. In Fig. 10(a), it has low velocity region at the suction surface of front rotor outlet and axial velocity increases at downstream section. At further downstream section, backflow region due to rear rotor is observed. Looking at the same position in Fig. 10(b), the backflow region appears not only at leading edge but also at every inlet region, where velocity widely varies in circumferential direction because of flow turning at leading edge of rear rotor though flow from front rotor becomes uniform. In spite of rising static head due to

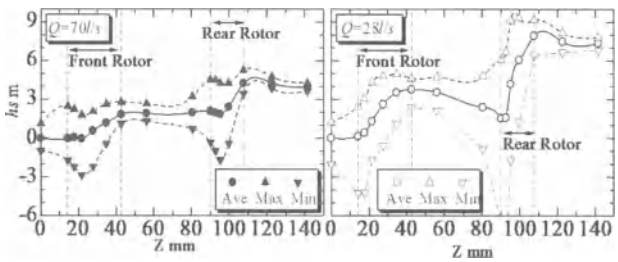

Fig. 7 Axial distributions of time averaged casing wall static heads and circumferentially maximum and minimum heads

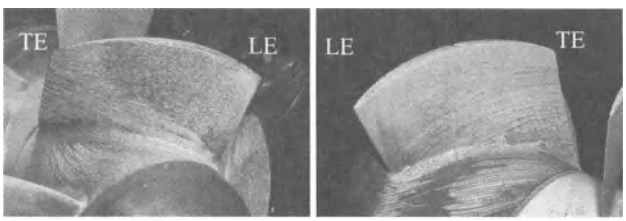

Fig. 8 Limiting streamlines on front rotor blade at Q = 70*l*/s

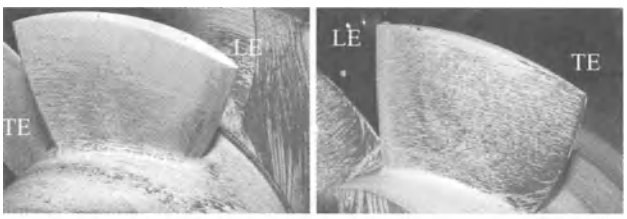

Fig. 9 Limiting streamlines on rear rotor blade at Q = 70*l*/s

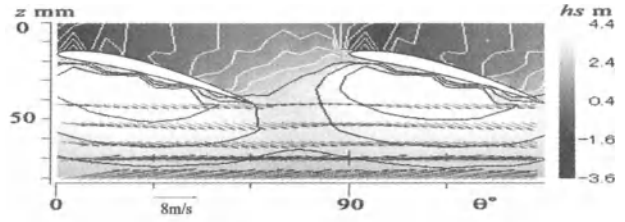

(a) Front rotor

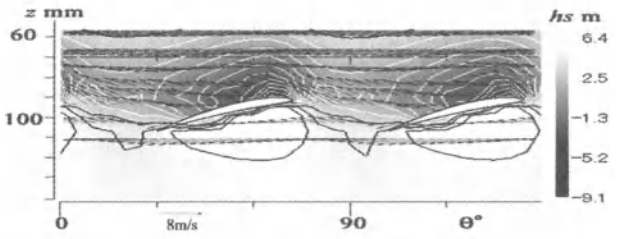

(b) Rear rotor

Fig. 10 Casing wall static head distribution and velocity vectors at r = 97.5mm (r/r_t = 0.98) at Q = 28 *l*/s

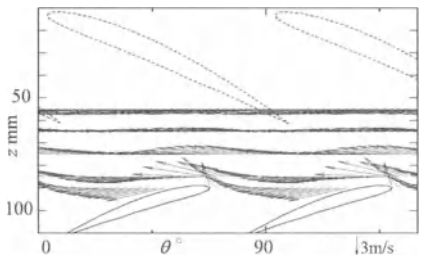

Fig. 11 Velocity vectors at r = 55.0mm (r/r_t = 0.56) at Q = 28*l*/s

front rotor, low static head region is widely observed in circumferential direction on suction surface as seen in Figs. 5 and 10(b). Then a backflow or low velocity region, spreading to outlet of rotor, is observed in mid-passage, while there is no backflow region with stall on suction surface. On the other hand, except for r = 97.5 and 55.0mm (Fig. 11), blade-to-blade distribution of relative velocity vectors seems normal distribution which shows high velocity on suction surface and low velocity on pressure surface as shown in Fig. 12.

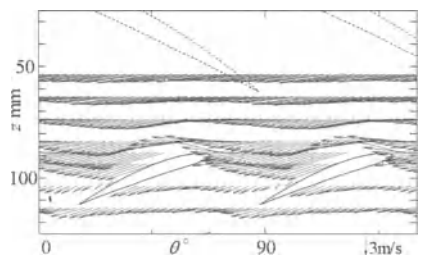

Fig. 12 Velocity vectors at r = 62.5mm (r/r_t = 0.63) ar Q = 28*l*/s

Figures 13 and 14 show visualized limiting streamlines on the blade passage of front and rear rotors and Fig. 15 also shows visualized one on hub surface in the left figure and near the trailing edge of suction surface in more details. Looking at the behavior in front rotor of Fig. 13, due to the backflow in tip region of leading edge the limiting streamlines appears from radial toward the upstream directions on both pressure and suction surfaces. Then low energy fluid in normal (downstream) flow region on the hub flows from the pressure to the suction surfaces and discharges from the trailing edge of suction surface. On the other hand, low energy fluid in backflow region, appearing in hub side of outlet, impinge to normal flow and a part of fluid flows to the suction surface with normal flow and the other fluids flow to the pressure surface and discharges from the trailing edge of the pressure surface as seen in Fig. 13(b). The secondary flow on the pressure and suction surfaces becomes stronger in comparison with that at Q=70 *l*/s. Focusing the behavior in rear rotor of Fig.14, the secondary flow on the blade surfaces is not so strong relatively due to the flow entry with $V_{\theta 2f}$ >0 (or $V_{\theta 1r}$<0) as shown in Fig. 4. The well-known behavior of secondary flow is found near the trailing edge of suction surface in hub side. There is a passing around of flow from the trailing edge of pressure surface to the suction one. Though the main reason for head drop of H_r at this flow rate is the appearance of backflow in the tip region of rear rotor outlet as Fig.10(b), this passing around may be also one reason of the head drop. From Figs. 4, 11 and 12 the main flow near hub side

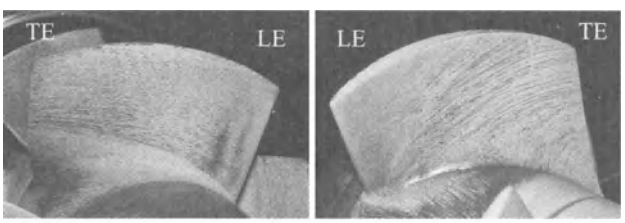

(a) Suction surface (b) Pressure surface

Fig. 13 Limiting streamlines near front near rotor blade outlet at Q = 28*l*/s

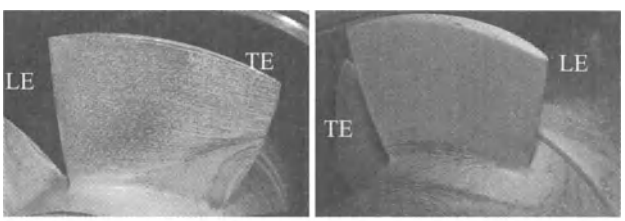

(a) Pressure surface (b) Suction surface

Fig. 14 Limiting streamlines near rear rotor blade outlet at Q = 28 *l*/s

of rear rotor seems to be normal except for the inlet region, where the flow is influenced by the backflow due to outlet flow from front rotor as Fig. 11.

However, the limiting streamlines on the hub surface of rear rotor forces us reconsideration on the flow as the left figure of Fig. 15. Two saddle points appear there. For one saddle point, low energy fluids flow near the pressure surface is divided to two directions of up- and downstream after impinging the flow from the trailing edge of suction side to the upstream of rear rotor inlet. For the other saddle point, the flow from the trailing edge of suction side is divided to two directions of rear rotor inlet and the suction surface impinging the flow along the suction surface from the leading edge. Then, a part of low energy fluids on the hub side flow to downstream only through the suction surface. A remaining of low energy fluids flows from the trailing edge of suction side to the leading edge of pressure side of adjacent blade. And low energy fluids from the trailing edge of suction side after passing around from the pressure surface impinge and change the flow direction to the suction surface. Due to this behavior, there is no flow from the hub side appears as downstream red-zone in the right figure of Fig. 15. That is extremely complex to consider the flow mechanism, which will be clarified by further experiment and CFD simulation in future.

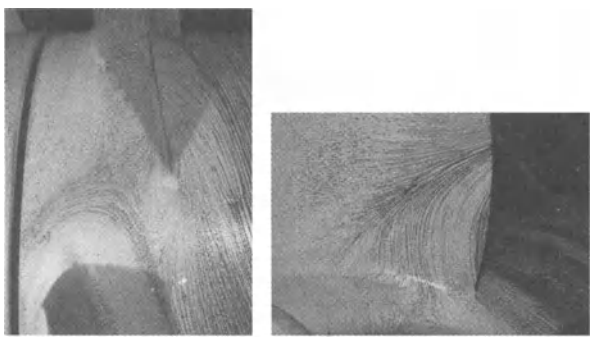

Fig. 15 Limiting streamlines on hub surface and suction surface near trailing edge of rear rotor at $Q = 28$ *l*/s

4 Concluding Remarks

In order to understand an internal flow in contra-rotating axial flow pump, experiments on LDV, casing wall pressure and limiting streamline measurement has been done. The conclusions are as follows.

(1) At design flow rate, the internal flow in rear rotor is more straightforward in comparison with the flow in front rotor. The secondary flow on the rear rotor blade is weakened because of $V_{\theta 1r}>0$. The leakage flow between the rear rotor blade tip and casing wall does not appear clearly in contrary with the front rotor. Therefore the hydraulic efficiency of rear rotor is superior in that of front rotor.

(2) At partial flow rate, the backflows in hub side of front rotor outlet and in tip side of rear rotor inlet yield large head loss. Though the backflow never appears at hub side of rear rotor outlet, the inlet backflow at the blade tip is elongated with flow rate decreasing and head rize is deteriorated with $dH/dQ>0$.

(3) At partial flow rate, the complex limiting streamline behavior on the hub surface is observed with two saddle points. The cause of this behavior will be investigated with further experiment and CFD simulation.

References

[1] Wada, A. and Uchida, S., 1999, "Improvement of Performance for Higher Specific Speed Axial-Flow Pump", *Torishima Review*, (in Japanese) 13, pp.32 – 35

[2] White, J. W., Purnell, J. G. and Stricker, J. G., 1993, "In-Line Submersible Pump", *Proc. ASME, FED Summer Meeting*, Pa. No. 246, pp.1 – 8

[3] Furukawa, A., Cao, Y., Okuma, K. and Watanabe, S., 2000, "Experimental Study of Pump Characteristics of Contra-Rotating Axial Flow Pump", *Proc. 2nd Int. Symp. on Fluid Machinery and Fluid Eng.*, Beijing, 67-657, pp. 245 – 252

[4] Furukawa, A., Shigemitsu, T. and Watanabe, S., 2007, "Performance Test and Flow Measurement on Contra-Rotating Axial Flow Pump", *J. Thermal and Science*, 16-1, pp.7 – 13

[5] Shigemitsu, T. et al., 2002, "Experimental Study on Rear Rotor Design in Contra-Rotating Axial Flow Pump", *Proc. 5th JSME/KSME Fluids Eng. Conf.*, Nagoya, pp.1453 – 1548

[6] Shigemitsu, T. Furukawa, A., Watanabe, S. and Okuma, K., 2005, "Air/water Two-phase Flow Performance of Contra-Rotating Axial Flow Pump and Rotational Speed Control of Rear Rotor", *Proc. FEDSM2005 ASME*, Pa. No.77002, pp.1 – 6

[7] Shigemitsu, T. Fukuyama, T., Furukawa, A., Okuma, k. and Watanabe, S., 2007, "Flow Measurement with LDV in Contra-Rotating Axial Flow Pump", *Proc. 23rd IAHR Symposium*, Yokohama, No.045, pp.1 – 10

[8] Yamashita, S. Watanabe, S., Okuma, K., Shirasawa, K. and Furukawa, A., 2005, "Flow Measurement at Partial Flow Rate with LDV around Rear Rotor of Contra-Rotating Axial Flow Pump", *Proc. 5th ASME/JSME Fluids Eng. Conf.*, Pa. No.3727, pp.1 – 6

[9] Furukawa, A., Takano, T., Shigemitsu, T., Okuma, K. and Watanabe, S., 2006, "Blade Rows Interaction of Contra-Rotating Axial Flow Pump in Pressure Field on Casing Wall", *JSME Int. J.*, Ser.B, 49-3, pp. 670 – 677

[10] Goto, A., Zangeneh, M. and Takemura, T., 1996, "Suppression of Secondary Flows in a Mixed Flow Pump Impeller by Application of 3-D Inverse Design Method; Part2—Experimental Validation", ASME J. Turbomachinery, Vol.118, pp. 544 – 551

The 4th International Symposium on Fluid Machinery and Fluid Engineering
November 24-27, 2008, Beijing, China
NO. 4ISFMFE-Ab13

Experimental Modeling of Polluted Air Dispersion in Street Canyons of Metropolitan

Hyoung-June Kim[1], Joon-Yong Yoon[*2] and Nak-Won Sung[1]

[1] Department of Mechanical Engineering, Hanyang University, Seoul, Republic of Korea
[*2] Division of Mechanical and Management Engineering, Hanyang University,
1271 Sa-3-dong, Sangnok-gu, Ansan City, Gyeonggi-do 426-791, Republic of Korea
Tel: +82-31-400-5282 / Fax: +82-31-400-4707
E-mail: joyoon@hanyang.ac.kr (Corresponding Author)

Abstract This paper investigates the two-dimensional polluted air dispersion in metropolitan street canyons using visualization. Recently, many papers have been written likely this. But, those treated old cities. The building of old cities has lower layers than the big city. This paper paid attention to the point studied different modeling that has large ratio between perpendicular and horizontal likely skyscrapers in Seoul, Tokyo, Shanghai, N.Y.C., etc. Experiments had been carried out in the wind tunnel. The field was investigated with an ultra high speed CCD camera and digital imaging processing. The lightening source was used the halogen lamp. The photo image was captured by ImCam commercial program at IMI Technology Co.

Keywords pollutant, urban street canyon, dispersion, visualization

1 Introduction

Many metropolitans have problems from their shape. Above all, they have many skyscrapers and transport vehicles. These structures and air pollution sources have been interrupting air flow, and dispersion of polluted gas in huge cities. Pollutant dispersion in metropolitans is a vital question for the health of the citizens. Many of citizens are troubled with respiratory ailments. Then, this paper will verify air flow around skyscrapers, find the pertinent positioning of lofty buildings. Especially, this paper aim to air flow around the skyscrapers, it is different from another paper that investigated dispersion in old town.

A limitation of direct field measurements of atmospheric phenomena is that all possible governing parameters are simultaneously operative and it is not simple to determine which are important, which are secondary and insignificant (Meroney, 1997).

In this study, parameters are building geometry (height, width, positioning), test point (center of street, behind of building etc.). The air flow was substituted wind tunnel. The measure of visualization used high speed CCD camera. The source was dry fog for broadcasting's special effects. The steaming data was captured with IM-Image Process. And, the velocity profile was measured with TSI 8389 anemometer.

2 Measurement Set-Up

2.1 Wind-tunnel for atmospheric condition

The experiments have been conducted in the open type wind-tunnel (the whales, Co.) of the Fluid Engineering Lab. of Hanyang University. The wind tunnel can blow amount of 161 m^3/min. and consisted of an inlet nozzle (9:1 contraction ratio), flow straighteners (honeycombs), Turbulence screen (4 EA), and a squirrel-cage centrifugal fan. A DC motor (Fan Diameter: 500 mm, Max. rpm: 1800 rpm, 2.2kW) maintains test-section wind speeds ranging from 0 to 30 m/s. The effective working section is 1315mm high, 6260mm length. The turbulence intensity is calibrated about 10 (at 100mm from the bottom of test section).

Generally, it is impossible that the static pressure and the total pressure are measured directly on the experiment because of measurement error in the measuring section. The velocity in measuring section is measured by static pressure tap (P_s, P_t) in nozzle of inlet, and calculated with the wind speed calibration constants (k_p, k_q) .

$$k_p = \frac{p_s}{p_{c1}} \tag{1}$$

$$k_q = \frac{p_t}{p_{c1}} \tag{2}$$

The wind speed calibration constants are defined on pretest of wind-tunnel. Where, P_{c1}, P_{c2}, P_s, and Pt are measured with A Pitot—static Tube on the same time.

The density of air is calculated with temperature and humidity using FCO-510-1. The following equation is the algorithm of velocity calibration.

$$U = \sqrt{\frac{2q}{\rho_s}} \tag{3}$$

In incompressible flow, the dynamic pressure is defined the following.

$$q = P_t \tag{4}$$

The more important the flow rate is raise, the larger the compressible effect cause incorrect result. The equation of dynamic pressure (q), which allow for the compressible effect,

$$q = \rho \tag{5}$$

Where,

$$P_s = \rho_s \tag{6}$$

$$q = \rho_s \frac{U^2}{2} \tag{7}$$

$$a = \sqrt{k} \tag{8}$$

$$\frac{p_t}{p_s} = \left(1 + \frac{k-1}{2} M^2\right)^{k/\rho} \tag{9}$$

All of parameter was calculated and controlled with LabView 7.1 in real-time.

2.2 Physical modeling

The experiments were performed in the L-3B wind-tunnel. This facility is a open circuit of suction type. The test section is a square of 300mm side and a length of 900mm.

The skyscraper is defined various ways. It means that its aspects ratio, *H/B*, is more than 5 in the early days. It is defined what have a lateral dimension resistances system (in technical standard), stories above 30 – 40 (normally standard), more than 50 stories and 220m height (the standard of the Council on Tall Buildings and Urban Habitat, CTBUH). This paper selects the definition of early days. The building dummy up with LEGO™ elements (Fig. 1).

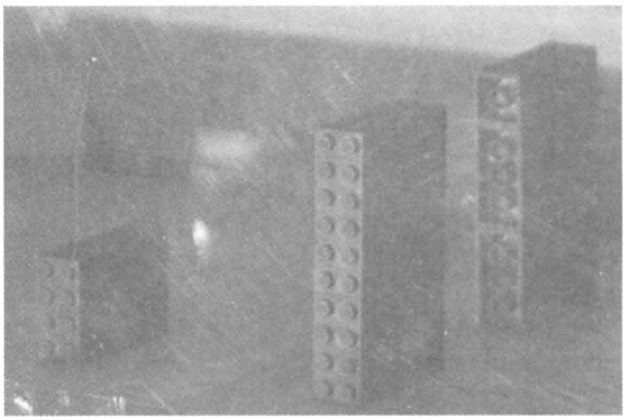

Fig. 1 The buildings made of LEGO™ elements

3 The Technic of Measurement

3.1 The source of smoke

The followings are standards of smoke source:

- The lower viscosity
- The specific gravity is the same or less than the air
- Easily visualization
- Harmless

This paper uses a dry fog generator which is used on special effects of broadcasting or cinema. It is not sticky, not harm human being. And smoke's life span is so long, that it can be detected for CCD camera very clearly.

3.2 Velocity

The measure of velocity is using a hot-wire anemometer, TSI 8389. It has a thermometer and a hydrometer, which displays a calibrated velocity. It can log to the personal computer with a direct cable, logging data are storage by Microsoft Excel sheet.

The probe of anemometer locates 20mm and 100mm from the bottom of test section. This sensor is fixed on the traverse: it can measure the same point repeatedly with step-motor.

3.3 The detail modeling

There are three buildings in the test section. The first structures (H_1) are fixed their positions. Figure 2 is the detail.

The B means a width of building. The probe is located the middle point between H_1 and H_2. The height of H_1 is the same as 5 times of B. Cases of H_2 are 5 types, 1B, 2B, 3B, 4B, and 5B. The velocity of air is 2.2m/s in non-structures.

H_2 has variable locations. Figure 3 is shown what are located each measuring point. It means of the character of street from zigzag to perpendicularity (T1-T4).

Table 1 Free flow in test section(m/s)

	20mm	80mm
None Block	1.93	1.96
P1 Free Flow	0.38	1.94
P2 Free Flow	1.85	2.07
P3 Free Flow	0.5	2.15

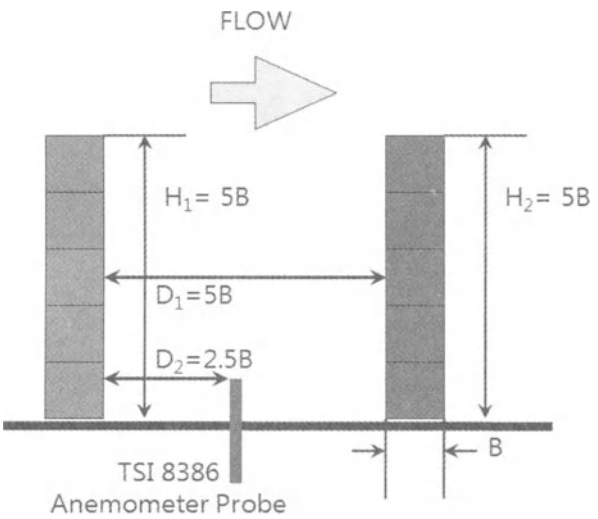

Fig. 2 The modelling of skyscraper

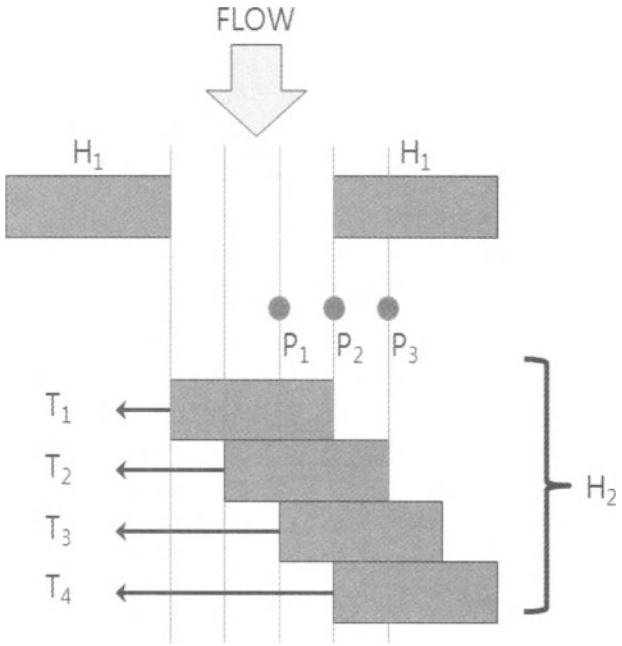

Fig. 3 The cases for building's locations

4 The Result of the Urban Canyon

4.1 H_2 = 1B

This table shows the velocity profile at H_2=1B. The name of label (e.g. T1_20, etc.) shows block position (T1) and the height of probe is 20mm from the bottom.

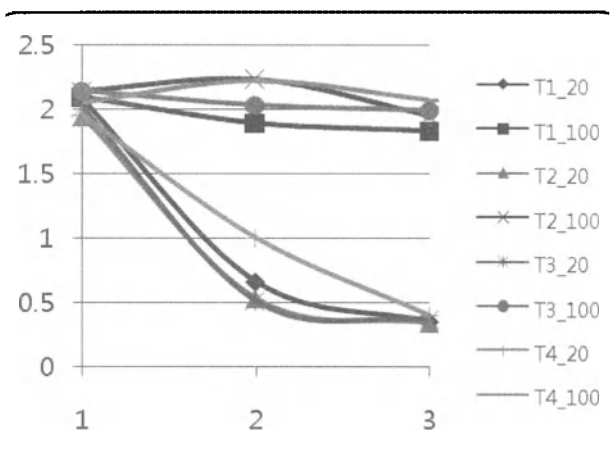

Fig. 4 The velocity profile (H_2 = 1B)

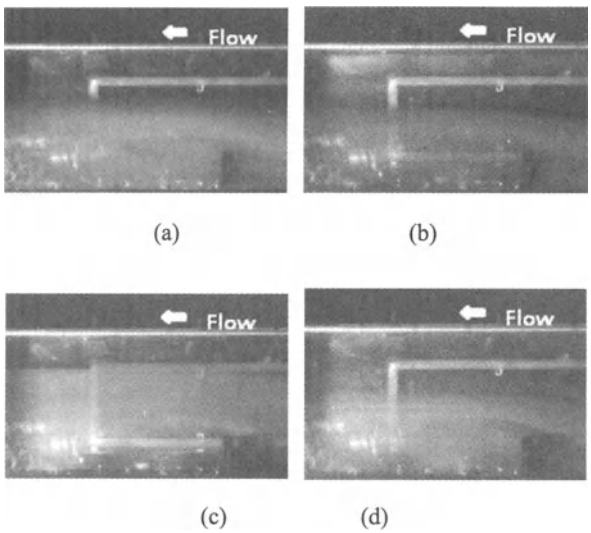

Fig. 5 The visualization of street canyon ($H_2 = 1B$)
(a) T_1, (b) T_2, (c) T_3, and (d) T_4

4.2 $H_2 = 2B$

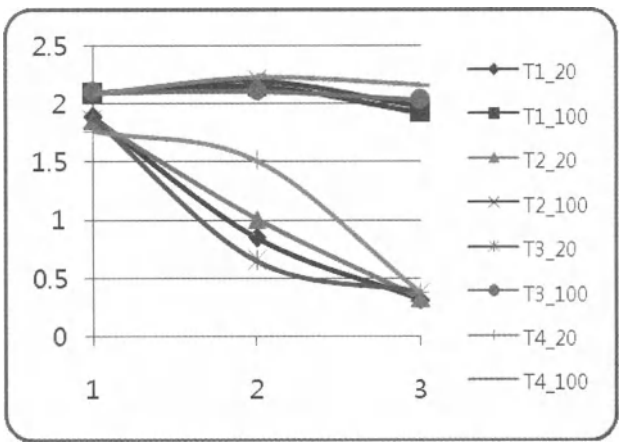

Fig. 6 The velocity profile (H_2=2B)

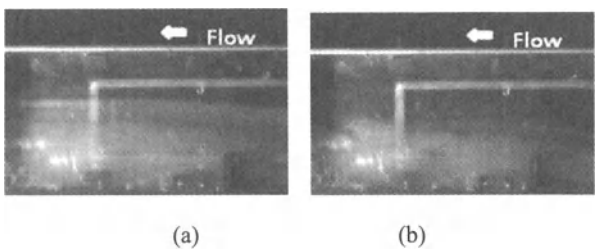

Fig. 7 The visualization of street canyon ($H_2 = 2B$)
(a) T_1, (b) T_2, (c) T_3, and (d) T_4

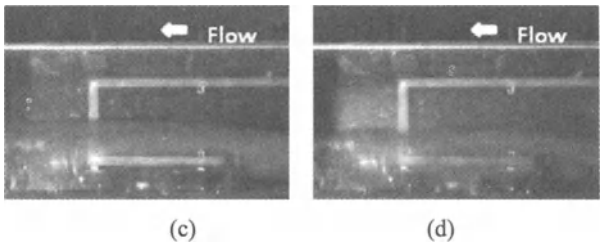

Fig. 7 (Continued)

4.3 $H_2 = 3B$

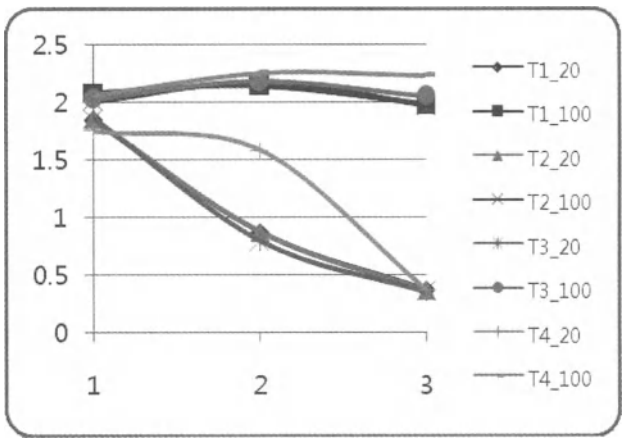

Fig. 8 The velocity profile ($H_2 = 3B$)

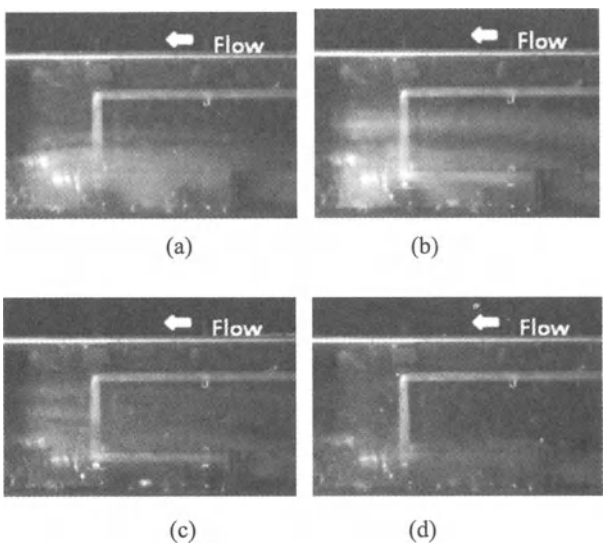

Fig. 9 The visualization of street canyon (H_2=3B)
(a) T_1, (b) T_2, (c) T_3, and (d) T_4

4.4 $H_2 = 4B$

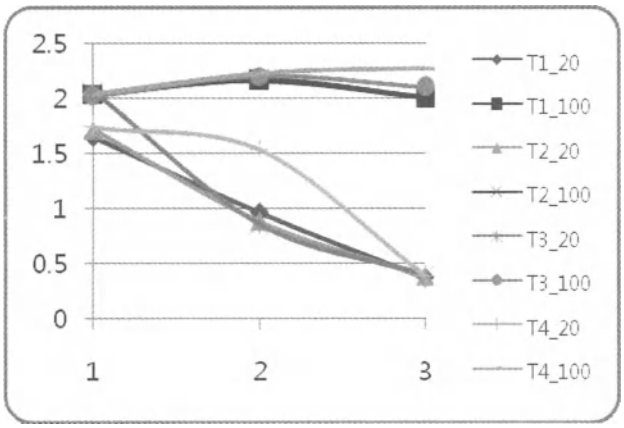

Fig. 10 The velocity profile (H_2=4B)

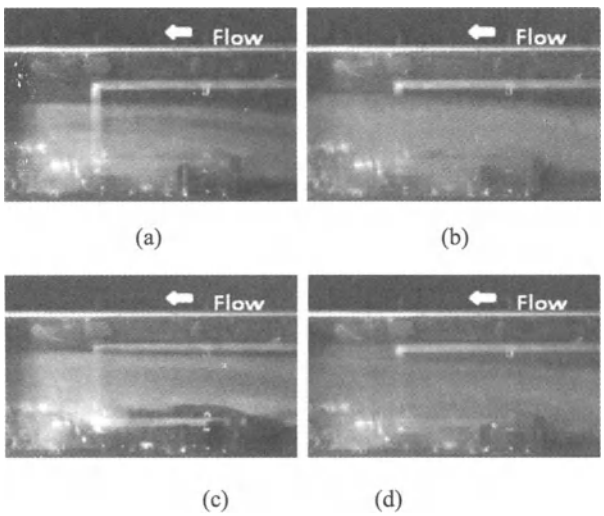

Fig. 11 The visualization of street canyon (H_2=4B)
(a) T_1, (b) T_2, (c) T_3, and (d) T_4

4.5 $H_2 = 5B$

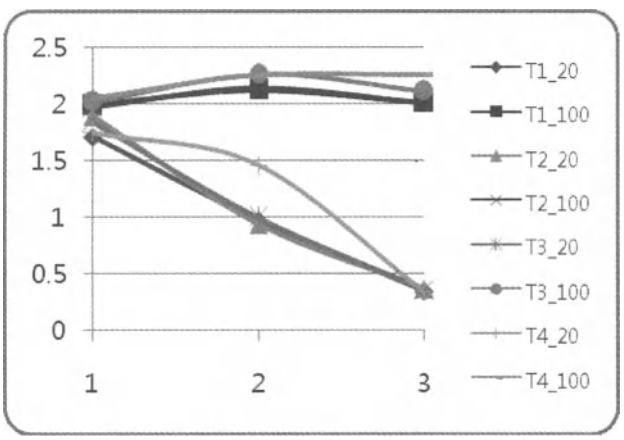

Fig. 12 The velocity profile (H_2 = 5B)

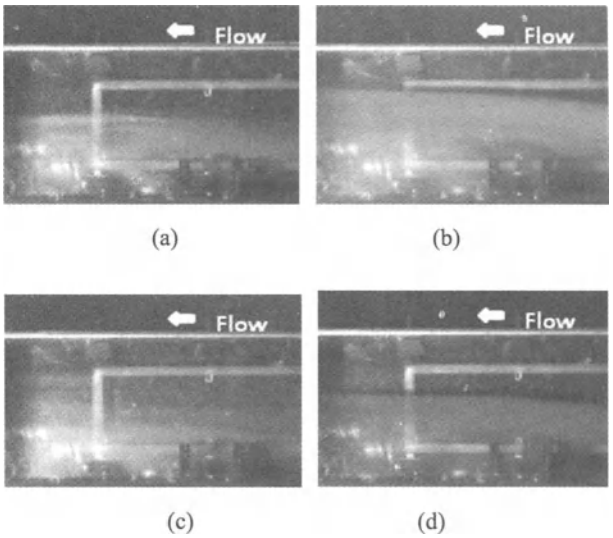

Fig. 13 The visualization of street canyon (H_2 = 5B)
(a) T_1, (b) T_2, (c) T_3, and (d) T_4

4.6 Occurrence of vortex side by building

In Figs. 14, 15, there is occurred the vortex around the H_1. This flow was not mentioned why almost experiments have been 2-D modeling, lower and long width dummy.

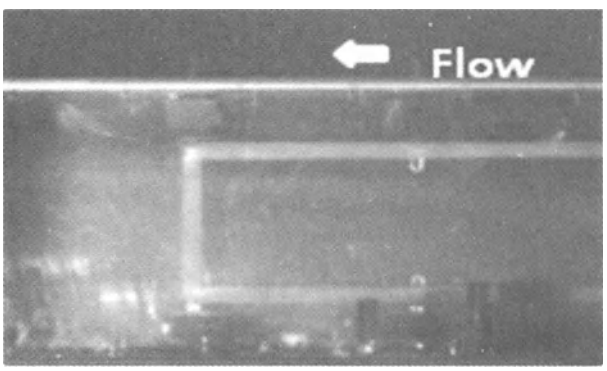

Fig. 14 The occurrence of vortex (1)

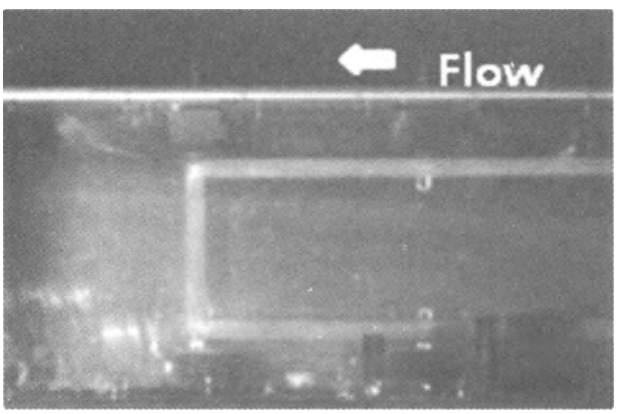

Fig. 15 The occurrence of vortex (2)

The occurrence is detected a flow stream line that was turning around the structure instead of circulating down behind H_1. This flow influences to velocity profile. For example, there is different velocity at "T4_20" when it compares its velocity with another. It must be the effect of vortex. But, It would be clearly defined with 3-D visualization.

5 Future Work

This paper was poor at information for 3-D flow data. And it also needs the more various case of building position, wind speed. The object of this paper was searching the method of visualization and velocity profile. So, the next paper would have much more data than this paper.

Acknowledgements

This work was supported by the second stage of the Brain Korea 21 Project in 2008. The authors are thankful to Mr. Inwon, Park for his assistance of the experimental set up and measuring.

References

Robert N. Meroney, Michel Pavageau, Stilianos Rafailidis, Micheal Schatzmann, 1996, "Study of line source characteristics for 2-D physical modeling of pollutant dispersion in street canyons", Journal of wind Engineering and Industrial Aerodynamics 62, pp. 37 – 56

F. Gerdes, D. Olivari, 1999, "Analysis of pollutant dispersion in ana urban street canyon", Journal of wind Engineering and Industrial Aerodynamics 82, pp. 105 – 124

Xiaomin Xie, Chun-Ho Liu, Dennis Y.C. Leung, 2007, "Impact of building facades and ground heating on wind flow and pollutant transport on street canyons", Atmospheric Environment 41, pp. 9030 – 9049

Ana Pilar Garcia Sagrado, Jeroen van Beeck, Patrick Rambaud, Dominico Olivani, 2002, "Numerical and experimental modeling of pollutant dispersion in a street canyon", Journal of wind Engineering and Industrial Aerodynamics 90, pp. 321 – 339

Bernd M. Leitl, Robert N. Meroney, 1997, "Car exhaust dispersion in a street canyon. Numerical critique of a wind tunnel experiment", Journal of wind Engineering and Industrial Aerodynamics 67&68, pp. 293 – 304

Cheng-Hsin Chang, Robert N. Meroney, 2003, "Concentration and flow dispersions in urban street canyons: wind tunnel and computational data", Journal of wind Engineering and Industrial Aerodynamics 91, pp. 1141 – 1154

Drew Landman, James Simpson, 2007, "A Wind Tunnel External Balance Calibration using Design of Experiments", U.S. Air Force T&E Days, AIAA 2007 – 1604

The 4th International Symposium on Fluid Machinery and Fluid Engineering
November 24-27, 2008, Beijing, China
NO. 4ISFMFE-Ch03

PIV Study of Tip Leakage Flow in Linear Compressor Cascade

Ren Dai*, Zhonghua Huang, Ze Chen and Kangmin Chen

* College of Power Engineering, University of Shanghai for Science and Technology
JunGong Road 516, Shanghai 200093, China
Tel: +86-021-5527-0508 / Fax: +86-021-5527-2376
E-mail: dairen@usst.edu.cn

Abstract Tip leakage flow between axial fan rotor and casing plays an important role in the aerodynamic performance of the fan. One of the new techniques to control tip leakage is developed as tip winglet which is also named as partial shroud in turbine cascade. Based upon NACA65-010 airfoil, it is proposed in this paper a linear cascade model to investigate the tip leakage flow patterns with and without blade winglets. Uniform width winglet is chosen for comparing the effect of different winglet orientations under alternative tip clearance conditions. Flow structures obtained from PIV measurements showed that tip winglet can not change the fundamental leakage flow structure. Its main effort is to provide extra flow resistance to the leakage flow which i alleviates leakage flow to limited extent.

Keywords tip leakage flow, tip winglet, linear cascade

Nomenclature

C	blade chord
$\bar{s} = t/c$	solidity
t	cascade pitch
v	flow velocity
X	x-coordinate along blade chord or cascade pitch
Y	y-coordinate along blade height

Abbreviation

AOA	angle of attack
NW	no tip winglet
PW	tip winglet on pressure side
SW	tip winglet on suction side

1 Introduction

Tip leakage flow between turbo-rotor and casing exerts important influence upon aerodynamic characteristics of turbomachinery. Yang, etc. (2001) concluded that its intensity may be controlled by four factors as: (1) static pressure difference between blade pressure and suction sides; (2) the status of boundary layer on casing; (3) the relative movement between rotor and casing; (4) geometric size and profile of tip clearance. In low speed axial compressor, no shock exists in tip region and no interaction with boundary layer. Main features of tip leakage flow come from endwall secondary flow as well as its interaction with leakage vortex.

Different methods were proposed to control tip leakage flow such as: endwall treatment, profiled tip clearance, isolation of boundary layer, bowed-swept blade and shrouded rotor. Tip winglet was firstly proposed by Whitecomb (1976) which was designed for air-vehicle and now popular in Boeing 737. As one new idea to control tip vortex flow, it attracted attention in turbomachinery. Bindon (1992) studied winglets in turbine cascade in which suction side winglet provided little positive gains while pressure sided winglet reduce 10% leakage vortex. Kota (2003) experimented with fix-ringed rotor like winglet and showed prospective results of reduced leakage flow together with tip turbulence losses. However friction loss might be increased over loss reduction from leakage controlling.

YI, etc. (1990) experimented with axial fans of singular arc blades. Results showed that well defined fan blade

with adequate tip winglets could provide positive effects on performance as well as sound emission. Lu (1995) studied fans with winglets and found winglet on blade pressure side improved fan's efficiency, sound and off-design performance.

Jia etc. (2001) found that the influence of tip leakage flow on the 3-D viscous flow field is investigated for different blade tip gap shapes under the condition of rotating hub or stationary hub. The analysis of the results shows, at least for these test cases, on the same working conditions and within a certain range of gap scale, the blade row with smaller tip gap height can attain higher efficiency.

Zheng etc. (2006) studied one axial fan with winglet and found its effects on endwall secondary flow and tip leakage flow. Winglet influenced the static pressure difference of tip leakage flow rather than the pressure load along blade camber line.

Due to flow's complexity, various results and explanation can be found in literature. It can be suggested that different research models should be responsible for the disputes. Only with detailed insight into the active flow in tip clearance, could it be possible to explain the real flow mechanism in fan's winglet efforts. For this purpose, one linear compressor cascade with popular NACA65-010 airfoil for axial fans was proposed to study winglet effects. Particle Image Velocimetry (PIV) was used to capture flow field inside the narrow blade tip clearance.

2 Cascade Model

Based upon NACA65-010 airfoil, one linear cascade was built for flow measurement as indicated in Table 1. Airfoil maximum thickness was 10% of blade chord. Blade camber was chosen as singular arc for simplicity and accurate distribution of blade thickness along camber line, which is also a popular way to design cascade upon NACA airfoils.

Table 1 Cascade parameters

Camber Radius	400mm
Camber center angle	24°
Blade stagger angle	45°
Blade chord	166mm
Solidity (t/b)	1.0
Aspect ratio (h/b)	1.2

Blades with and without tip winglet are illustrated in Fig. 1 which are named as NW for no winglet, PW for pressure side, NW for suction side. Tip clearance was set alternatively for 2% and 3% of blade chord, namely 3.2mm and 5mm respectively. Particle Image Velocimetry (PIV) was used to measure the flow pattern inside tip clearance. Winglets of uniform width from blade leading to trailing edges were positioned next to blade pressure and suction side respectively. Winglet width was chosen 16mm, the same as the maximum thickness along blade camber. Local rounding was taken to reduce possible flow separation, as shown in Fig. 1.

Cascade tested is composed of 5 blades, as shown in Fig. 2 with blade pitch of 100mm. To adapt for different incidences, 5 special positions were chosen to fix each blade, which can be tuned around its centroid for incidences of ±10°, ±20° and 0° inlet flow conditions respectively.

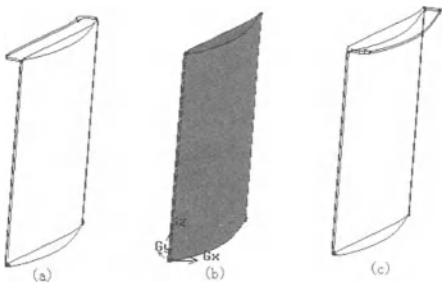

Fig. 1 Blade model with winglet

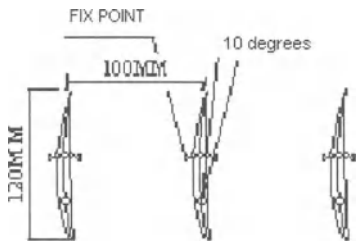

Fig. 2 Cascade geometry

3 Experiment Techniques

Experiment setup was composed of PIV system, low speed two dimensional open wind tunnel, cascade model, particle generator, compressed air resource, PC data reduction as well as necessary volume flow rate nozzle. The cross area of test section was rectangular with width of 125mm and height of 460mm. Volume flow rate was controlled via adapting rotational speed of air blower and measured by a normal inlet nozzle. Inlet flow velocity before cascade could then be assigned with 5m/s, 8m/s, 12m/s, 15m/s respectively. Reynolds number was defined upon blade chord and inlet flow speed to achieve the order 10^5.

PIV system was provided by TSI company including Nd: Yag Laser beam (Model Solo120, CCD camera (Model: 630049) and synchronizer (Model: 610034). Laser beam could work at 15Hz while camera had pixels of 786×1024.

Positions of PIV measurements are shown in Fig. 3 for inside tip clearance and Fig. 4 for downstream ones which were located from blade trailing edge respectively at $t/c = 1.05, 1.3, 1.5$. Laser sheet was kept parallel to the exit plane of cascade.

Fig. 3 Laser sheet position in tip clearance

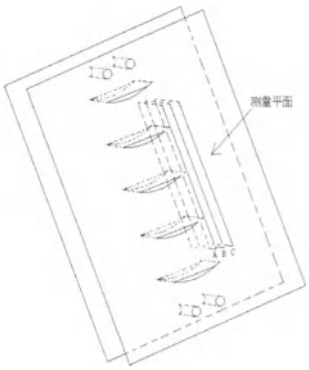

Fig. 4 Laser sheet position downstream of cascade

4 Data Analysis

To achieve full illustration effects of tip clearance flow field, each measurement result was taken as an averaged one from 15 independently obtained PIV pictures at the same position. However, due to limited tip space, light reflection from surrounding solid boundaries was hard to eliminate when laser sheet was positioned inside tip clearance. Therefore certain local "bugs" exited from light signal contamination. They were removed manually as shown in Fig. 5 and then local blankness left on the picture shown in Fig. 5 as one example. Flow pictures were then refined with the SMOOTH tool provided in TSI-Insight 6 software by the method of matrix interpolation. Figure 6 shows the final picture after smooth treatment from which it can be seen that blankness was removed and original flow characteristics maintained to form a continuous flow pattern. It has to be addressed here that carefulness should be necessary when relative large area of bug regions occurred in original PIV pictures, smoothed and then averaged results may deviate from original ones.

PIV is a technique to acquire instant flow field information. PIV pictures taken at different time sequence were difficult to coincide with each other absolutely. In experiment, it was also noticed tip vortex center varied from picture to picture with slight floating indicating certain unsteady flow features. Average treatment is necessary to get relative steady flow field. Alternative number of pictures was tried to for steady flow and 15 pictures showed satisfactory results in present experiment conditions. Representative averaged vortex center is shown in Fig. 7 within an rectangular area of 6mm times 10mm.

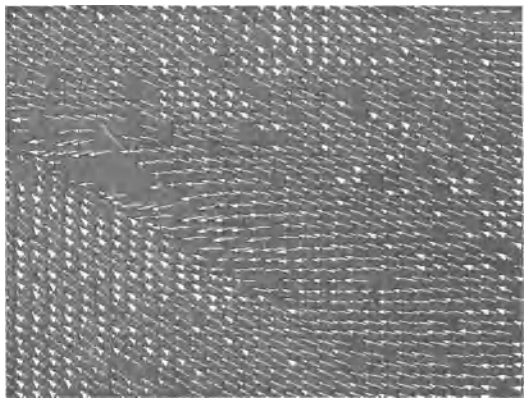

Fig. 5 Original PIV picture

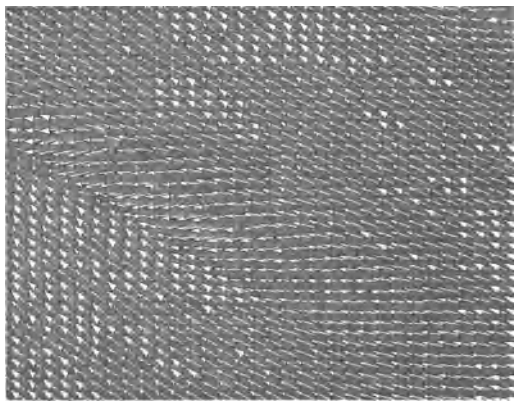

Fig. 6 Smoothed PIV picture

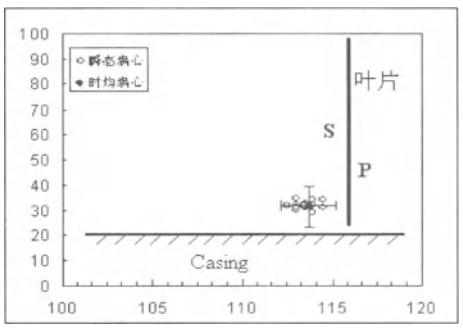

Fig. 7 Averaged vortex center of 15 pictures

5 Results and Discussion

Tip leakage flow may be influence by alternative factors such as inlet flow velocity, incidence situation, relative size of tip clearance, as well as geometry profile. In this study, three factors were taken to investigate tip leakage flow: inlet flow velocity, clearance size, and winglet direction.

5.1 Inlet flow velocity

As mentioned before, inlet flow velocity may be changed

via fan's motor frequency adaptation from 5m/s to 15m/s. Higher velocity were possible, but not used. What important was not the absolute inlet velocity value but its corresponding Reynolds number Re was able to control within 3 times range. Five cases of inlet velocity were done among which two ones were chosen for presentation here respectively 5m/s and 15m/s. Their Reynolds number were 3.1×10^5 and 9.3×10^5 based upon blade chord.

Figure 8 compares the tip gap flow pattern under 5 and 15m/s inlet flow conditions. Similar ones were observed as indicated by velocity vector lines. When inlet flow velocity was increased, the separation line of tip leakage flow runs relatively further into main flow region. It can then be deduced that intensity of tip leakage is related with the blade static load which is proportional to inlet flow velocity. From Fig.8 it can be also concluded that the flow patterns inside tip gaps resemble for alternative gap sizes.

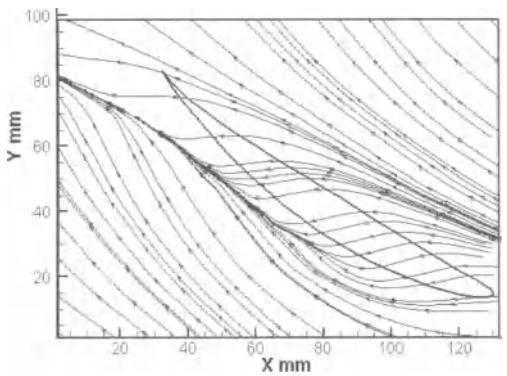

Fig. 8(a) Inlet flow of 5m/s

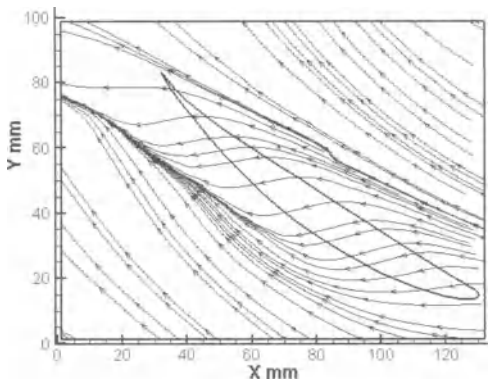

Fig. 8(b) Inlet flow of 15m/s

5.2 Tip clearance size

In Fig. 9 compared are flows in tip clearance of 3 and 5 mm respectively. Inlet flow velocity was taken as 5m/s and zero incidences. Similar flow patterns can be observed for both clearance sizes except the position of "separation line" away from the blade suction surface. Tip leakage started from the leading edge crossing blade camber and then mixed with main flow near suction side near the mid point of blade chord. For 3mm tip clearance, the mixing point occurred before blade chord while for 5mm clearance, it was later. Therefore, the separation line due to mixing developed slight different path which was further far away into main flow region.

From Fig. 9, it can then be speculated that the intensity and influence of tip leakage flow may be connected with clearance height. As to larger clearance height, flow velocity is analogue to planar tube flow while smaller clearance height ejection effects from blade load may be more obvious and stronger leakage vortex flow.

Another point to be addressed is the progress of tip leakage flow deviated from main flow after leading edge. It could be explained as the fluid near tip casing did not flow in the same path as main flow since blade force in clearance region was not available to make flow deviate.

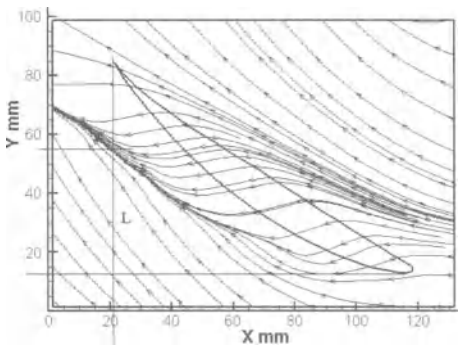

Fig. 9(a) Flow in Tip clearance of 3mm

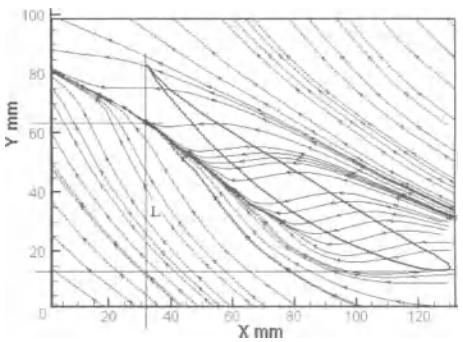

Fig. 9(b) Flow in Tip clearance of 5mm

5.3 Inlet flow directions

Figure 10 illustrated tip leakage flow for 3mm tip gap for flow at 5 different inlet flow AOA. With large negative incidence, local flow near tip casing tended to cross tip gap directly even with certain cross over flow suction side to pressure side at the blade mid-chord. With larger positive incidence, local flow in tip gap tended to reinforce the leakage flow and push the separation line

further into passage main flow region. Since positive incidence inlet flow would provide extra flow momentum normal to the blade chord, tip leakage flow gained higher power to enter tip gap and flowed rigorously for larger extent. As concluded from those figures, flow incidences influenced more evidently on the tip leakage flow pattern than other factors. The driven momentum available to tip leakage flow either from blade static load or azimuth component of inlet flow momentum determined the tip leakage pattern. Only those measures which could control such driven momentum will be prosperous in the reduction of negative effects of tip leakage flow.

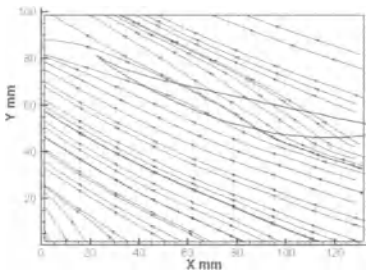

Fig. 10(a) Incidence of −20°

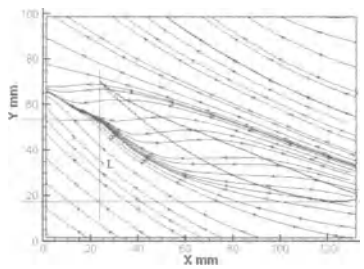

Fig. 10(b) Incidence of −10°

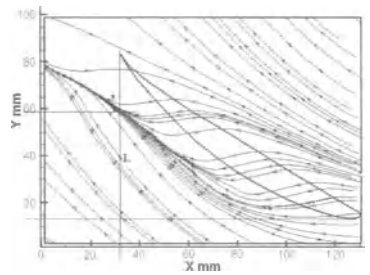

Fig. 10(c) Incidence of 0°

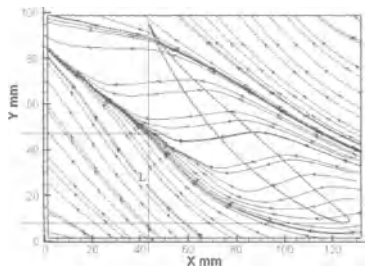

Fig. 10(d) Incidence of +10°

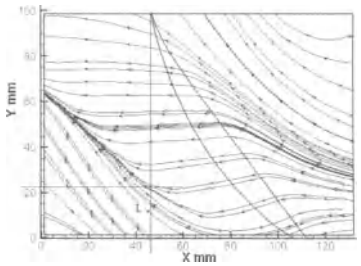

Fig. 10(e) Incidence of +20°

5.4 Winglets in two directions

Tip winglet, which is also named as partial shroud in turbine cascade, has two fold effects on flow. One is to increase flow resistance through tip clearance, the other is increase the disk friction due to enlarged tip surface area. In rotating fan rotor, the later effect is so important that it may reduce fan's efficiency evidently. However, in non-rotating linear cascade it can not be observed here.

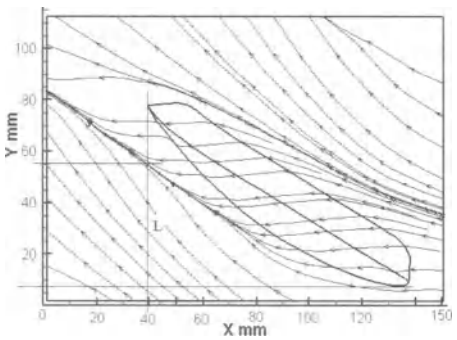

Fig. 11(a) Flow in PW Tip clearance (3mm)

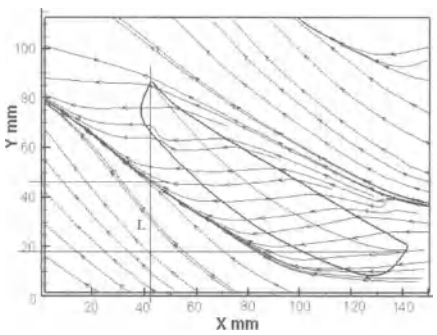

Fig. 11(b) Flow in SW Tip clearance (3mm)

Figure 11 compares the effect of two tip winglet installed along blade pressure side and suction side separately. The tip clearance height was 3 mm and no incidence. It is really not possible to identify any distinguished difference between them. Compared with Fig. 9(a), flow pattern was so similar that attached winglet failed to control any leakage flow. Separation line relative to blade trailing edge point reflects leakage flow intensity. Through flow mass or volume flow rate might be reduced due to

increase flow resistance in tip region. However it could not be detected in present testing conditions of limited flow rate measuring accuracy.

5.5 Downstream leakage vortex

To illustrate leakage vortex, Fig. 12 compared three flow vector fields down stream at $x/c=1.3$ axial positions with and without tip winglets. Clearance height was 3mm and inlet velocity of 5m/s. Evident leakage vortex can be showed at the blade suction and casing corners. In comparison to NW case, vortex centers varied in PW and SW cases. Leakage vortex in PW one appeared closer to blade trailing line while SW one was farther away from trailing line which was in certain conflict to results in Fig. 11.

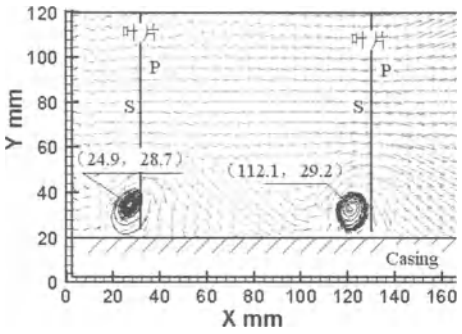

Fig. 12(a) Downstream Flow in NW Tip clearance ($x/c=1.3$)

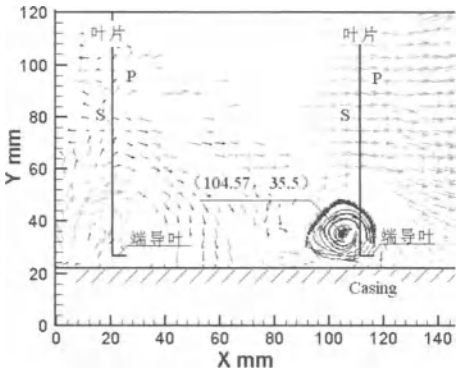

Fig. 12(b) Downstream Flow in PW Tip clearance ($x/c=1.3$)

6 Conclusion

Tip clearance flow in a linear compressor cascade was studied with PIV measuring techniques at the mid-height position of the tip gap. It can be concluded from those results that:

(1) Tip leakage flow pattern resembles in local flow direction for possible inlet velocity.

(2) Cascade incidences will influence tip leakage flow in the way of inlet momentum component normal to blade chord.

(3) For larger gap height, tip leakage flow may be reduced because of reduced local blade loading.

(4) Tip winglet does not alter the tip clearance flow in nature. Possible effect comes from its evident flow resistance to the flow cross tip gaps. In annual rotating cascade, it can be of two-folded effects. Possible winglet configuration may be installed on blade pressure side with optimized width profile.

Acknowledgements

This research is supported by Leading Academic Discipline Project of Shanghai Municipal Education Commission under Project Number: J50501. Discussion from Dr. Wang H.G. and Mr. Bai Z.X who prepared testing model available are both acknowledged in sincerity.

References

Bindon J.P.and Morphis.G., 1992, Development of an Axial Turbine leakage loss for two profiled tip geometries using linear cascade data. *ASME Journal of Turbomachinery*, Vol. 114(1): 198 – 203

Kota Shimada, Kazuhide Kimura, 2003, A study of radiator cooling fan with labyrinth seal, *JSME Review*, 24: 431 – 439

Yi F.M. 1990. Expriment study of axial flow fan with tip winglet (in Chinese), *Fluid Engineering*, Vol.19 (7): 2 – 4

Lu Wencan, 1995, An Investigation on the aerodynmics noise in the axial flow fan with additional guide vanes (in Chinese), *Journal of Huazhong University of Science and Technology*, Vol. 23, supplement (I), 156 – 159

Jia X.Ch, Wang Zh.M., Cai R.X., 2001, Numerical investigation of the effects of tip gas shapes on aerodynamic performance in turbomachinery, (in Chinese), *Journal of Engineering Thermodynamics*, Vol., 22(4): 431 – 434

Whitecomb R.T., 1976, A design approach and selected wind-tunnel results at high subsonic speeds for wing-tip mounted winglets, NASA TN D-8260, 1976

Yang C., Ma Ch., Wang Y. Lao D., 2000, A review of studies on turbomachinery tip gas clearance flow (in Chinese), *Advances of Mechanics*, Vol. 31(1): 70 – 83

Zheng G.S, Dai R. 2006: An investigation of Tip winglet of axial flow fan, (in Chinese), *Journal of Engineering Thermodynamics*, vol. 27, Suppl. 1, 176 – 181

The 4th International Symposium on Fluid Machinery and Fluid Engineering
November 24-27, 2008, Beijing, China
NO. 4ISFMFE-Ch15

Study on Cavitating Turbulent Flow around a Hydrofoil

Mindi Zhang[*1], Guoyu Wang[1] and Xiangbin Li[2]

[*1] School of Mechanical Vehicular Engineering, Beijing Institute of Technology, Beijing 100081, China
Tel: +86-6891-2395-801
E-mail:zmd1971@bit.edu.cn

[2] North China Electric Power University, Beijing 102206, China

Abstract In this paper, the development, flow structures and characteristics of the cavitation regimes around a hydronautics foil are studied experimentally by employing high speed visualization and particle image velocimetry(PIV). The results show that four cavitating flow regimes are observed: inception cavitation, sheet cavitation, cloud cavitation and supercavitation as the cavitation number is progressively lowered. Some individual cavitation traveling bubbles are observed at incipient cavitation, and attached structure in the leading edge and an oscillatory, wave structure in the trailing edge with sheet cavitation are assessed. Phenomena with large-scale vortex structure and rear re-entrant jet associated with cloud cavitation, and subsequent development in supercavitation are described. The velocity in the cavitation regions in the different cavitation conditions is low compared to that of the free stream, resulting in a shear layer flow with large vorticity between the cavity and the free stream. Large velocity gradient is also observed in the inner layer near the foil surface and near the interface between the main flow and the cavitation flows.

Keywords cavitation, hydrofoil, particle image velocimetry (PIV), high speed visualization

Nomenclature

ρ	water density
σ	cavitation number
v	kinematic viscosity of the water
c	chord length of the foil
P_∞	reference static pressure
Re	Reynolds numbe
P_v	vapor pressure
U_∞	reference velocity
α	incidence angle

1 Introduction

Hydrofoil sections are the basic elements of lifting surfaces such as hydrofoil wings and propeller blades, which are widely used in marine applications and hydrodynamic machinery. Cavitation can occur and cause acoustic and vibration problems. Cavitation also damages the lifting surface devices in severe conditions. Avoiding cavitation is one of the most important issues in designing lifting surfaces at high speed, as discussed by Yamaguchi (1999). By decreasing the cavitation number, four regimes can be identified, including inception cavitation, sheet cavitation, cloud cavitation, and supercavitation (Wang, 2001). While the cavitating zone increases from discreet bubbles to contiguous domains, the cavitation generation mechanism varies from localized, instantaneous pressure drop found in inception cavitation (Rood, 1991), to sustained, time dependent cavities observed in sheet and cloud cavitations (Kawanami, 1997. Leger, 1998. Delange, 1998. Kjeldsen, 2000). Compared with the other types of cavitation, supercavitation exists a distinct interface between the main flow and the supercavitation region. In recent years, the studies on supercavitation have attracted growing interests due to its potential for vehicle maneuvering and drag reduction (Hrubes, 2001. Kuklinski, 2001). The potential flow analysis method does not account for the viscous and turbulent effects, and is insufficient as a predictive framework. Various of experimental techniques have been developed to study the flow structures to help guide the refinement of the cavitation models (Wang, 2001. Tassin, 1995. Claudia, 2002. Gopalan, 2000). In particular, the particle image

velocimetry (PIV) technique is frequently used (Tassin, 1995. Claudia, 2002). Based on the PIV and high-speed photography measurements, Gopalan and Katz (Gopalan, 2000) have studied the flow structure in a closure region of an attached cavity. Recently, Foeth et al.(Foeth, 2006) have applied the time-resolved PIV to study fully developed sheet cavitation around a hydrofoil with a varying angle of attack along the spanwise direction. PIV with both the vapor and air bubbles as "the tracer particles" improved insight into the flow structure (Wosnik, 2005).

In this paper, the development, flow structures and characteristics of cavitation regimes around a hydronautics foil are discussed based on high-speed visualization and PIV techniques. A high speed vedio camera is used to observe the cavitation development and fluid structure in the cavitating region. The PIV technique is used to map the instantaneous and average velocity and vorticity of cavitation flow.

2 Experimental Setup

2.1 Water tunnel

The experiments are carried out in a closed-loop cavitation tunnel. A schematic description of the tunnel is provided in Fig. 1. The water is driven by an axial flow pump located about 5 m below the test section.The rectangular test section is 700mm in length, 70mm in width and 190mm in height. There are three windows, one on the top, one on the bottom and the other one on the side, which are made of perspex for optical access. The experimental conditions are maintained within 1% uncertainty on the hydrofoil angle of incidence, and 2% uncertainty on both the flow velocity and the upstream pressure.

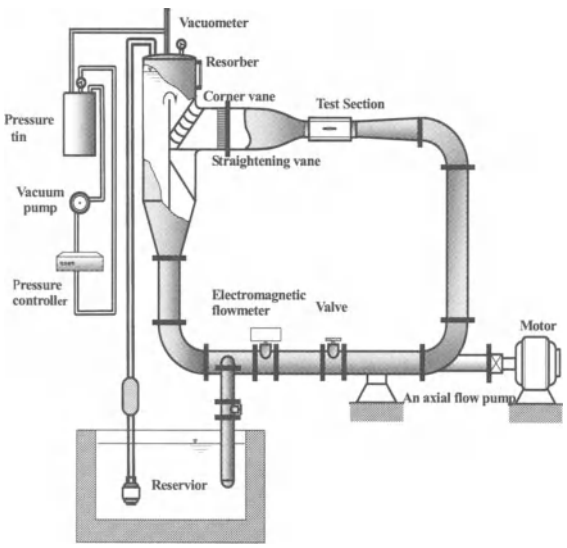

Fig. 1 Schematic of the cavitation tunnel

2.2 Hydrofoil

As shown in Fig. 2, a special hydrofoil investigated by Tulin(2001) named hydronautics foil which is different from a Clark-Y hydrofoil, is adopted in the present study. The hydrofoil with 70 mm in both chordwise and spanwise directions is made of stainless steel and its surface is highly polished. The hydrofoil is set in the horizontal test section with a prescribed incidence angle α (seen in the Fig. 2). The suction side of the foil is mounted toward the bottom for the convenience of viewing the flowing field.

2.3 High-speed visualization

The cavitation phenomena are documented by a high-speed digital camera (HG-LE, by Redlake), up to a rate of 10^5 frames per second (fps). In order to maintain desirable spatial resolutions, much lower recording speed is adopted. The experimental setup is shown in Fig. 3(a).

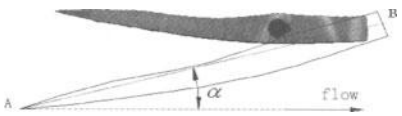

Fig. 2 Schematic of hydronautics foil

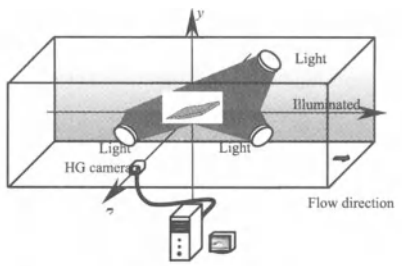

(a) High-speed visualization for entire flowing field

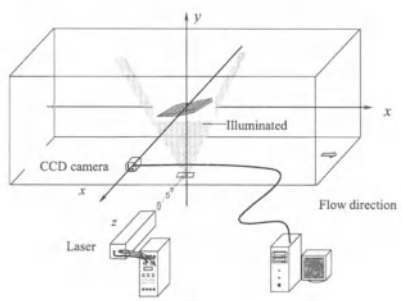

(b) The setup of the DPIV system

Fig. 3 Schematic of the layout of the experimental setup

2.4 PIV setup

In the present study, a 2D-PIV system, manufactured by TSI, is employed. A CCD camera with a resolution of 12

bits, 1024×1024 pixels collecting the instantaneous images, and one type of synchronizer providing the timing and sequencing of events are used. The precision of the whole system is within 0.5%~2%. As shown in Fig.3 (b), the flow field at the mid-span of the foil is illuminated by the laser sheet from the bottom wall.

The cavitation parameter and the Reynolds number are typically defined as follows:

$$\sigma = 2(P_\infty - P_v)/\rho U_\infty^2 \quad (1)$$

$$\mathrm{Re} = U_\infty c/\nu \quad (2)$$

where, P_∞, U_∞, P_v, ρ, c, and ν are, respectively, the reference static pressure, and the reference velocity measured at 210 mm upstream from the hydrofoil mid-chord, the vapor pressure, the water density, the chord length of the foil, and the kinematic viscosity of the water.

3 Results and Discussion

By comparing of images, the characteristics of the flow field associated with various cavitation regimes and their influences on the subsequent development of the cavitation dynamics are discussed. Velocity profiles are documented in a number of cases to offer a quantitative basis to further our understanding of the cavitating flow structures. In the following study, the Reynolds number and the incidence angle are respectively fixed at a value of 5.95×10^5 and $\alpha=5^0$ while systematically varying the cavitation number to explore the structure of the unsteady cavitating flow by changing the pressure upstream the test section. The salient features of the various cavitating flow regimes are reviewed. The results are based on the study of the hydronautics hydrofoil, and are meant to convey a sense of dynamic evolution of the flow characteristics. With the decreasing of the cavitation number, there are four regimes which are expressed as the following parts.

3.1 Incipient cavitation (σ=1.86)

Figure 4 shows time evolution of the cavitating flow patterns in the incipient cavitation stage with the cavitation number of 1.86. The sequence begins with the formation of a pair of clustered micro-sized bubbles at about 15% chord length from the leading edge of the hydrofoil. In the photographs, the cavitating flow appears in white, indicating that it contains a number of micro-sized vapor bubbles. In the subsequent frames, from t = 0 to 1.32 ms, the cavitating flow grows, forming a collection of bubbles. At t = 0.99ms, the bubbles structure grows to the maximum size. Then, the bubbles collapse, as shown in frame t = 1.32ms. From the top and side view, the bubbles concentrate on the foreside of foil. The onset-growth-collapse process is repetitive and also consistent. The average velocity and vorticity distributions are given in Fig. 5. The velocity distributions in the cavitating regions are different from those in the main flow. When the velocity decreasing extends along the whole downstream field with the vortex shedding, the low velocity area becomes smaller, and the lowest one appears at the rear region of hydrofoil.

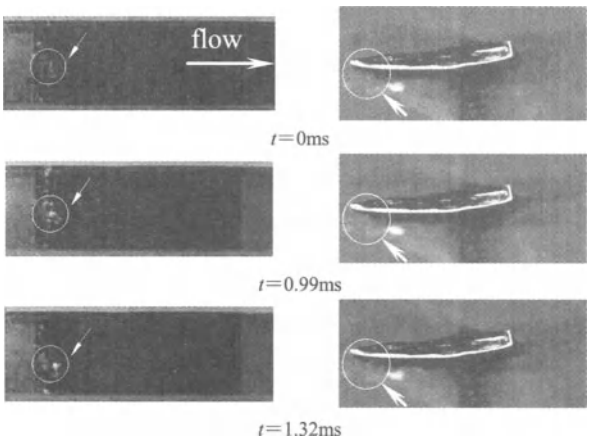

Fig. 4 Time evolution of the inception cavitation. (Top and side view, σ=1.86)

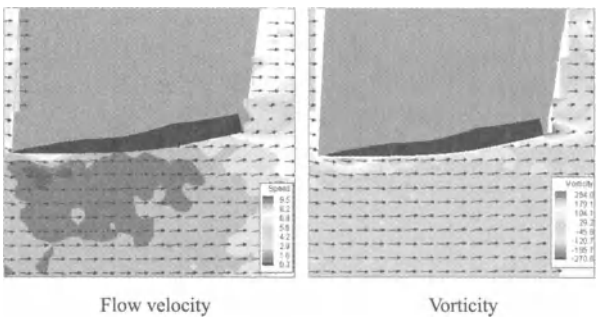

Fig. 5 The average flow velocity and vorticity distributions of the inception cavitation. (The side view, σ=1.86)

3.2 Sheet cavitation (σ = 1.4)

When the cavitation number is 1.40, the cavitation changes from the incipient cavitation to a sheetlike cavity. Fig.6 shows the time evolution of a sheet cavitation process. The leading edge of a sheet cavity exhibits a sheet-like structure as shown in Fig. 6. The cavity is attached, the rear region of the sheet is unsteady, 3-D, and rolls up into a series of bubbly eddy that are shed intermittently.The average velocity and vorticity distributions with the cavitation number of 1.4 are given in Fig. 7. The low velocity area becomes more extensive than incipient cavitation and sweeps from the front region to the end of hydrofoil. The cavitating vortices are attached to the

surface, and at the rear region of hydrofoil the shedding pair of vortex are stronger.

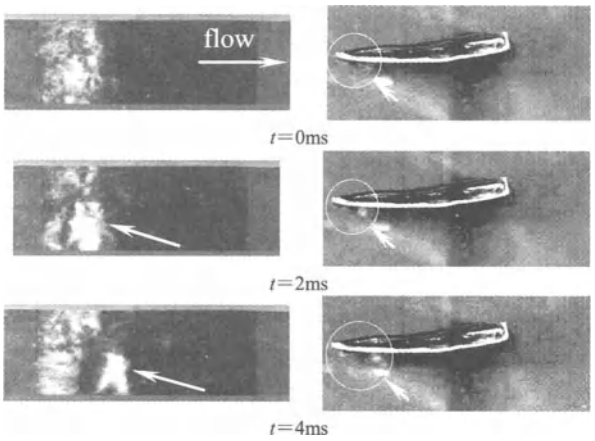

Fig. 6 Time evolution of the sheet cavitation (Top and side view, σ =1.4)

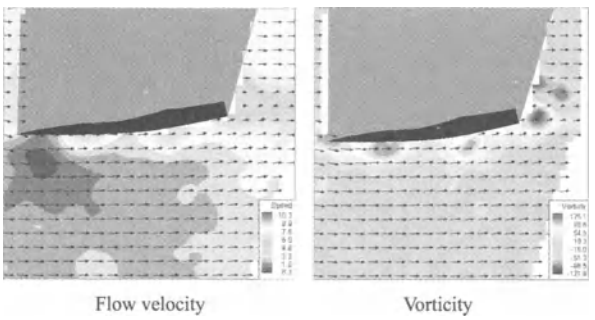

Fig. 7 The average flow velocity and vorticity distributions of the sheet cavitation (Side view, σ =1.4)

3.3 Cloud cavitation (σ = 1.02)

Further decreasing the cavitation number, bubbles are shedded massively in the rear portion of the cavity and the cloud cavitation is formed. It is observed that cloud cavitation has a distinctly quasi-periodic pattern. Fig. 8 shows the results of visualization from the side view within a single cycle of the events. Figure 9 indicates the average velocity and vorticity distributions.

As shown in Fig.8, the development of the cavity is an attached front portion and an unsteady rear region. The cavity grows at t = 0ms. While traveling downstream, the cavity expands with packets of bubbles moving with a clockwise rotation from t=12.9ms to 25.8ms. It shows that the massive vortex shedding appears seen the image at t=51.6ms. In the near wall region, due to the reduced fluid velocity (as shown in the Fig.9), caused by the large-scale vortex dynamics, the cavitating flow is pushed away from the wall. Associated with the departing vortical flow (as shown in the Fig.9), one observes substantial growth of the cavity thickness in the rear region of the cavity. Accompanying the large-scale vortex dynamics, shown at t = 51.6 ms, a re-entrant flow in the wall region is induced toward the upstream. The propagation velocity of the re-entrant flow is estimated to be 0.8 m/s, based on the data of Fig. 9, which is about 10% of the free stream velocity. The relationship between the area of cloud cavitation and time has been illuminated in the Fig. 10, and the data is obtained by using self-developed software. Figs. 8 and 10 indicate that the shedding of cavitating vortices is mainly responsible for the quasi-periodic characteristics of cloud cavitation. This is the reason that the cloud cavitation induces stronger structural vibration and noise. Estimated from the images of ten cycles, the period of the cloud cavitation under the given parameters is shown in Table 1. And average period and frequency of the cloud cavitation are respectively about 74.05ms and 13.5 Hz, respectively.

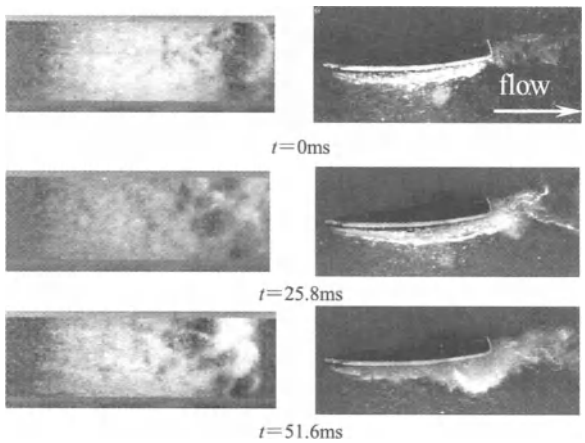

Fig. 8 Time evolution of the cloud cavitation (Side view, σ = 1.02)

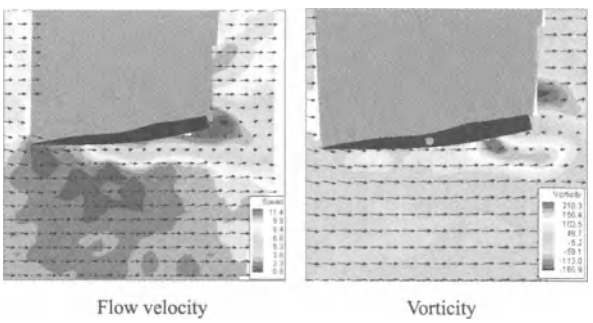

Fig. 9 The average flow velocity and vorticity distributions of the cloud cavitation (Side view, σ =1.02)

Table 1 Period of cloud cavitation around foil (σ = 1.02)

Events	1	2	3	4	5
Period (ms)	73.1	74	72	73	76
Events	6	7	8	9	10
Period (ms)	74	78	75	73.4	72

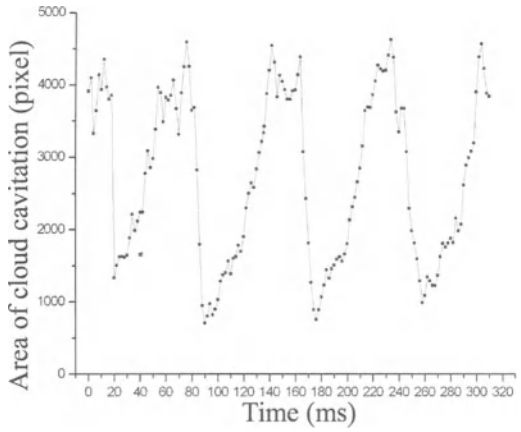

Fig. 10 The area curve of cloud cavitation

3.4 Supercavitation (σ = 0.7 and 0.4)

Supercavitation is the final state of cavitation, which is caused by further decreasing the cavitation number from the cloud cavitation regime.

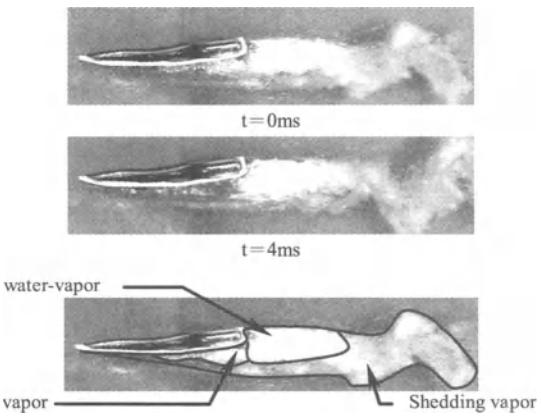

Fig. 11 Time evolution of the mix supercavitation (Side view, σ =0.7)

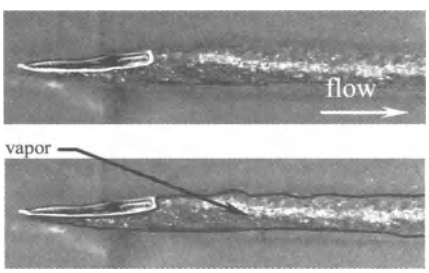

Fig. 12 Time evolution of the full supercavitation (Side view, σ =0.4)

Figure 11 and Fig. 12 show images of the flow structure corresponding to the supercavitation regime with the cavitation number of 0.7 and 0.4. The average flow velocity and vorticity distributions under these conditions have been figured out in Fig. 13. While the supercavitation appears, the cavitating area covers the entire hydrofoil, extending to the downstream region of the solid object and there is a distinct interface between the main flow and the supercavitating region. When the cavitation number is 0.7, the cavity comprise water-vapor, vapor and shedding vapor areas as seen in the Fig. 11. The velocity distributions in the cavitating regions are different from those in the bulk flows. Inside the two-phase mixture region of the cavity, the fluid velocity is low compared to that of the free stream. Especially, the lowest velocity appears at the rear of hydrofoil. When the cavitation number is 0.4, a vapor cavity is shaped around the surface and back of the hydrofoil, and the area only occupies a narrow region, as shown in Fig. 12. Otherwise, as seen in the Fig. 13, the velocity distribution is almost same as σ = 0.7, but the cavitatin regions become narrow. There is a stipe of the vortex(the upper runs clockwise and the lower unti-clockwise) which moves back form the rear part of the hydrofoil. With decreasing the cavitation number, the vorticity dirtribution become steadier.

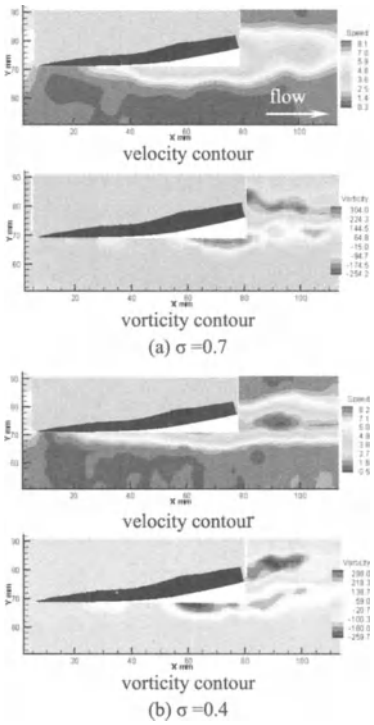

Fig. 13 The average flow velocity and vorticity distributions of the supercavitation (Side view)

4 Conclusions

Cavitations around a hydrofoil are studied experimentally by using the high-speed visualization and PIV with bubbles

particles. Decreasing of the cavitation number, four cavitating flow regimes are observed: inception cavitation, sheet cavitation, cloud cavitation and supercavitation. Several conclusions are drawn from the observations: In the incipient cavitation stage, the onset-growth-collapse process is repetitive and also consistent. The velocity of the cavitating regions extend along the whole downstream field with the vortex shedding and become smaller. In sheeting cavitating, the cavitating vortices are attached to the surface of the hydrofoil, and the shedding pair of vortex at the rear region of hydrofoil are stronger. The cloud cavitation has a distinctly quasi-periodic pattern with a period of 13.5Hz. A re-entrant flow in the wall region is induced toward the upstream which results into the shedding of cavitating vortices and stronger structural vibration and noise. Two kinds of typical supercavitation appeared: the mix supercavitation and the full supercavitation. A distinct interface exists between the main flow and the supercavitating region of two supercavitation. A stipe of the vortex (the upper runs clockwise and the lower unti-clockwise) moves back from the rear part of the hydrofoil.

Acknowledgements

The authors gratefully acknowledge support by Excellent young scholars Research Fund of Beijing Institute of Technology (2006Y0308), Foundation Research Fund of Beijing Institute of Technolog(BIT-UBF-200503E4206) and the National Natural Science Foundation of China (NSFC, Grant No.: 50276004 and No.: 50679001).

References

Claudia, O., and Ceccio, S., 2002, "The Influence of Developed Cavitation on the Flow of a Turbulent Shear Layer", Phys. of Fluids, 14, pp. 3414 – 3431

Delange, D.F., and Debruin, G.J., 1998, "Sheet Cavitation and Cloud Cavitation, Re-entrant Jet and Three-dimensionality", Appl. Sci. Res., 58, pp. 91 – 114

Foeth, E.J., van Doorne, C.W.H, van Tersiega T., and Wieneke B., 2006, "Time Resolved PIV and Flow Visualization of 3D Sheet Cavitation", Exp. in Fluids, 40, pp. 503 – 513

Gopalan, S., and Katz J., 2000, "Flow Structure and Modeling Issues in the Closure Region of Attached Cavitation", Phys. of Fluids, 12, pp. 895 – 911

Hrubes, J.D., 2001, "High-speed Imaging of Supercavitating Underwater Projectiles" HExp. in FluidsH, 30, pp. 57 – 64

Kawanami, Y., Kato, H., Yamauchi, H., Tanimura, M., and Tagaya Y., 1997, "Mechanism and Control of Cloud Cavitation", J. Fluids Eng., 119, pp. 788 – 794

Kjeldsen M., Arndt R. E. A., and Effertz M., 2000, "Spectral Characteristics of Sheet/Cloud Cavitation," Transactions of the ASME, J. Fluids Eng., 122, pp. 481 – 487

Kuklinski, R., Henoch C. and Castano J, 2001, "Experimental Study of Ventilated Cavities on Dynamic Test Model", Cav2001, Session B3.004

Leger, A.T. and Ceccio, S.L., 1998, "Examination of the Flow near the Leading Edge of Attached Cavitation. Part 1. Detachment of Two-dimensional and Axisymmetric Cavities", J. Fluid Mech., 376, pp. 61 – 90

Rood, E. P., 1991, "Review-Mechanisms of Cavitation Inception," J. Fluids Eng., 113, pp. 163 – 175

Tassin, A.L., Li, C.Y., Ceccio, S.L. and Bernal, L.P., 1995, "Velocity Field Measurements of Cavitating Flows" Exp. in Fluids, 20, pp. 125 – 130

Tulin M.P., 2001, "The History and Principles of Operation of Supercavitating Propellers," RTO AVT/VKI Special Course: Supercavitating Flows, Von Karman Institute for Fluid Dynamics, Rhode-Saint-Genese, Belgium

Wang, G.Y., Senocak, I., Shyy, W., Ikohagi, T., and Cao, S.L., 2001, "Dynamics of Attached Turbulent Cavitating Flows", Prog. Aerosp. Sci., 37, pp. 551 – 581

Wosnik, M., and Milosevic, I., 2005, "Time-resolved Particle Image Velometry (TR-PIV) in Ventilated and Naturally Cavitating Flows", the Sixth International Symposium on Particle Image Velocimetry, Pasadena,California, USA

Yamaguchi, H., Maeda, M., Kato, H., and Toyoda, M., 1999, "High performance foil sections with delayed cavitation inception", Proceedings of the 3rd ASME/JSME Joint Fluids Engineering Conference

The 4th International Symposium on Fluid Machinery and Fluid Engineering
November 24-27, 2008, Beijing, China
NO. 4ISFMFE-IL01

Microchannel Heat Sinking: Analysis and Optimization

Afzal Husain[1], Kwang-Yong Kim[*2]

[1] Dept. of Mechanical Engineering, Inha University, Incheon, Korea
[*2] Dept. of Mechanical Engineering, Inha University,
253 Yonghyun-Dong, Nam-Gu, Incheon, Korea
Tel: +82-32-872-3096 / Fax: +82-32-868-1716
E-mail: kykim@inha.ac.kr

Abstract The present study reviews numerical optimizations of microchannel heat sink with the help of surrogate analysis. The design variables are decided from geometric and shape parameters that influence the performance of the microchannel heat sink. The basic surrogate models are explored with three-dimensional numerical analysis. The single objective optimization is performed taking thermal resistance as objective function and pumping power as constraint while multiobjective optimization is performed taking both thermal resistance and pumping power as objective functions. The sensitivity of the objective function is explored near the optimum point and distribution of the design variables are checked over the Pareto optimal front to analysis the contribution of the design variables to the objective functions. This analysis provides the designer a wide view to economically compromise with design variables considering fabrication methods and available pumping power sources.

Keywords microchannel heat sink, numerical analysis, surrogate methods, multiobjective optimization, pareto optimal front, sensitivity analysis

Nomenclature

A_c	cross-section area of microchannel
A_s	surface area of substrate base
C_p	specific heat
h	height of rib
H_c	microchannel depth
k	thermal conductivity
L_x,	length of heat sink
L_y	width of heat sink
L_z	height of heat sink
n	number of microchannels
P	pumping power
p	pressure
p_r	pitch of the ribs
q	heat flux
R_{th}	thermal resistance
T	temperature
u	liquid velocity in microchannel
$\mathbf{V}$	velocity vector
w	width of rib
W_c	width of microchannel
W_w	fin width
x, y, z	orthogonal coordinate system

Greek symbols

α	ratio of rib height-to-width of channel
β	ratio of rib width-to-height
ϕ	ratio of fin width-to-depth of channel
γ	ratio of channel width-to-pitch of rib
μ	dynamic viscosity
θ	ratio of channel width-to-depth
ρ	density

Subscripts

avg	average value
f	fluid
max	maximum value
s	substrate

1 Introduction

The growing demand for removing higher heat flux from the high performance microdevices and stacking of high performance microprocessors have challenged researchers to design and optimize the cooling system to fulfill the requirement of the current ultra large scale integration (ULSI) technology. The liquid cooled microchannel heat sink has been researched as a feasible option to enhance the heat transfer capability of these devices. The sophisticated fabrication processes have yielded economically competitive microchannels having a high surface area to volume ratio and opened the way to implement new designs in silicon based micro cooling systems. However, the limitations of space in microdevices and cost involve to fabricate these devices had opened the doors for the optimization of microcooling devices.

The microchannel heat sink was first studied by Tuckerman and Pease (1981) for the application of cooling microdevices. Later on Weisberg et al. (1992) presented a design algorithm for the selection of a rectangular micro-channel heat exchanger using a two-dimensional conjugate heat transfer model. Some analytical studies (e.g., Knight et al. 1992, Fisher and Torrance 2001, Wei and Joshi 2003) have focused on modeling of the heat transfer and optimization of the micro-channel geometry. A state-of-the-art of single-phase forced convection has been reviewed by Yener et al. (2005). They found that liquid flow in microchannels is in continuum regimes, but classical correlations used for conventional size channels indicate significant departure from the experimental investigations. Morini (2004) reviewed experimental studies on fluid flow and heat transfer in microchannels and concluded that the understanding of heat transfer mechanism and pressure drop is an open question at the moment. Herwig and Hausner (2003) suggested that certain scaling effects can be of different importance for micro systems. Xu et al. (2003) investigated liquid flows in microchannels and found that viscous dissipation effects tend to be significant due to higher velocity gradients existed in channel with small hydraulic diameters. They proposed a criterion for the significance of the viscous dissipation effects in microchannel flows. The three-dimensional numerical analysis for fluid flow and heat transfer was performed for a rectangular microchannel heat sink assuming constant and temperature dependent fluid properties. Herwig and Mahulikar (2006) investigated that the importance of temperature dependent properties increased when heat transfer is due to scaling effect with respect to different orders of magnitude of the Reynolds number and the axial temperature gradient. When characteristic lengths are changed from macro to micro size constant property results are always only approximations. Li et al. (2007) carried out three-dimensional numerical analysis for laminar water flow and heat transfer in a rectangular microchannel using the inlet, average and variable thermal properties. They proposed that variable property method is superior in engineering applications since it more accurately characterizes the actual phenomena. In the light of the above literature review, it can be concluded that fluid flows and heat transfer in microchannels can be predicted much accurately by considering the viscous dissipation effects and temperature dependent thermophysical properties. However, the ever growing demand for higher heat flux dissipation has compelled the researchers to investigate alternative heat transfer enhancement techniques for these applications.

In the recent years microchannel has been investigated for passive surface microstructures such as dimples, pin fins and ribs for surface heat transfer augmentation. Wei et al. (2007) investigated heat transfer augmentation inside a microchannel with dimpled surface for steady, laminar flow in a rectangular microchannel. They found out secondary and recirculatory flow structures and discussed heat transfer enhancement mechanism. Cheng (2007) simulated two-layer stacked microchannel heat sink with enhanced mixing passive microstructures. These structures led to higher heat transfer and lower thermal resistance. Wang et al. (2005) investigated friction characteristics in a microchannel with various roughness elements for two-dimensional single-phase flow. Ligrani et al. (2003) carried out exhaustive review of heat transfer augmentation techniques and observed that recirculation and shear layer reattachment are significant phenomena in heat transfer enhancement around the rib.

Traditional micropumps posed limitations in terms of efficiency and reliability which opened the door for alternative methods to drive the fluid through microchannels. Joshi and Wei (2005) identified the need of further research in the area of micropumps which appears to be insufficient to provide potential pumping power for electronic cooling. Electroosmotic flow (EOF) is the bulk motion of the fluid under the influence of externally applied electric field. Arulanandam and Li (2000) investigated EOF with the help of two-dimensional Poisson-Boltzmann and two-dimensional momentum equations. Morini et al. (2006) investigated numerically the EOF in a rectangular and trapezoidal microchannel heat sink. They studied the effect of electroosmotic diameter kDh and geometry aspect ratio on the cross sectional Nusselt number and suggested the application of electroosmotically driven microchannel heat sink for low heat flux removal rate.

Optimization methods with numerical analyses (e.g., Vanderplaats 1984) are regarded as general design tools and offer a number of advantages, including automated

design capability, varieties of constraints, and multi-objective applications (e.g., Deb 2000). The past studies (e.g., Liu and Garimella 2003, Kim 2004, Li and Peterson 2007) reveal that pressure and/or pumping power constrained optimization limits the applicability of pumping source used at the micro level. On the other hand, multi-objective optimization eliminates these constraints and provides a group of optimal solutions at various levels of objective functions and constraints. These advantages associated with the multi-objective optimization provide impetus to the application of multi-objective evolutionary algorithm (Deb 2000) to investigate ribbed microchannel heat sink. Evolutionary algorithm has been used as an effective tool for generating global Pareto optimal solutions in various engineering designs.

The current paper summarizes the optimization methods for microchannel heat sink based on contemporary accurate numerical models and surrogate analysis. This study explores both single and multiobjective optimization which involves the usage of hybrid multi-objective evolutionary approach (MOEA) (e.g., Deb 2001) in combination with three-dimensional Navier-Stokes analysis and surrogate model. As a surrogate model, response surface approximation (e.g., Myers and Montgomery 1995), Kriging model (e.g., Lophaven et al. 2002) and Radial Basis Neural Network (e.g., Orr 1996) are used to evaluate objective function values required by search algorithm to find optimal solutions. A hybrid multi-objective evolutionary approach is implemented using NSGA-II (e.g., Deb 2001) and local search strategy. The global Pareto optimal front is explored to get inside of the trade-off analysis between the two competing objectives.

2 Microchannel Model

A schematic of the rectangular micro-channel heat sink optimized in the current study is shown in Fig. 1. The dimensions of the heat sink under consideration are 10mm×10mm×0.5mm. The thickness of the base of the micro-channel is 100μm while the depth of the micro-channel is kept constant at H_c = 400μm. Simulations are performed for varying fin width and channel width. A uniform heat flux (q=100 W/cm^2) is applied at the bottom of the heat sink to elucidate the effect of micro-channel geometry on the thermal resistance and pressure drop. The laminar and fully developed and is maintained by low flow rates and low Reynolds numbers. Application of the micro-rib in microchannels should not be impractical from manufacturing and design points of view. Therefore, rectangular ribs are chosen as a passive heat transfer augmentation structures. Staggered micro-ribs are placed at both side walls of the microchannel which comprise large part of the channel surface area subjected to wall heat transfer as shown in Fig. 2. Simulations are performed by varying design variables of the heat sink introduced in the later part. A uniform heat flux is applied at the bottom of the heat sink to elucidate the effect of microchannel geometry on the thermal resistance and pumping power.

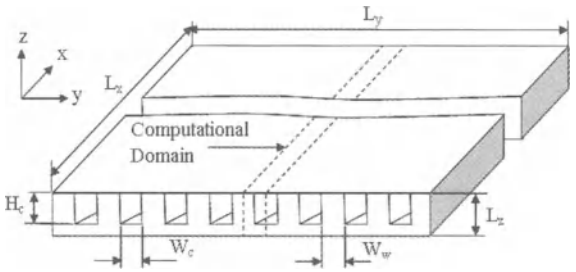

Fig. 1 Schematic diagram of microchannel heat sink

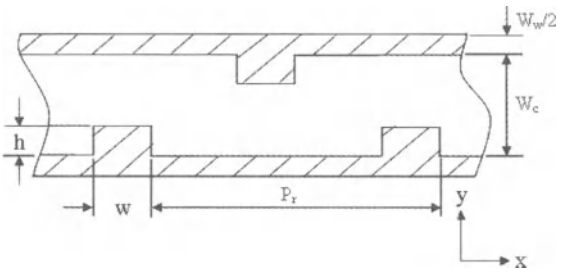

Fig. 2 Schematic of rib structures

3 Numerical Methods

Governing equations for conservation of mass, momentum, and energy for the conjugate heat transfer in the microchannel can be written in vector form as:

Mass: $$\nabla \cdot (\rho_f \mathbf{V}) = 0 \quad (1)$$

Momentum: $$\mathbf{V} \cdot \nabla(\rho_f \mathbf{V}) = -\nabla p + \nabla \cdot (\mu_f \nabla \mathbf{V}) \quad (2)$$

Energy: $$\mathbf{V} \cdot \nabla(\rho_f C_{p,f} T_f) = \nabla \cdot (k_f \nabla T_f) \text{ (for the fluid)} \quad (3)$$

$$\nabla \cdot (k_s \nabla T_s) = 0 \text{ (for the substrate)} \quad (4)$$

The flow is assumed to be steady, incompressible and laminar and radiation effects are neglected. The governing equations were solved using commercial code ANSYS CFX 11.0 (ANSYS 2006). The code used finite volume discretization of governing differential equations and the solution was based on the SIMPLE algorithm (Patankar 1980). Due to symmetry of the microchannels, single microchannel was selected as computational domain, as shown in Fig. 1. To implement the practical conditions of rate of heat transfer at the fluid and solid interface of the ribbed channel, full length of the microchannel was taken to consideration comprising ribs on both of the side walls

of the microchannel. A hexahedral mesh was generated in the specified computational domain.

Water flows into the microchannel at the inlet of the heat sink and leaves at the outlet; the remainder of the heat sink is occupied by the silicon substrate. The silicon part of the heat sink at the inlet and outlet of the channel is maintained as an adiabatic boundary. No-slip condition is applied at the interior walls of the channel, i.e. $V = 0$. For the conservative analysis of the heat transfer enhancement and optimization the thermal conditions in the z-direction are:

$$-k_s \frac{\partial T_s}{\partial z} = q \qquad \text{at} \qquad z = 0$$

and

$$k_s \frac{\partial T_s}{\partial z} = 0 \quad \text{at} \quad z = L_z$$

The left and right surfaces of the computational domain shown in Fig. 1 are assigned as symmetric boundary conditions.

4 Optimization Techniques

4.1 Design variables and objective functions

For smooth microchannel heat sink two design variables $W_c/H_c (=\theta)$, and $W_w/H_c (=\phi)$ and for ribbed microchannel three design variables, $h/W_c (=\alpha)$, $w/h (=\beta)$, and $W_c/p_r (=\gamma)$ are chosen for the optimization (e.g., Husain and Kim 2008a, 2008b). For smooth microchannel four level full factorial whereas for ribbed microchannel three-level fractional factorial design is used. Table 1 shows these design variables with their ranges. Two different objective functions are employed to optimize the microchannel heat sink; one is thermal resistance related to the heat transfer performance, and the other is pumping power to drive the coolant through the microchannel. In single objective optimization pumping power is considered as constraint whereas in multiobjective optimization both thermal resistance and pumping power is considered as objective functions. Thermal resistance is defined by:

$$R_{th} = \frac{\Delta T_{\max}}{qA_s} \tag{5}$$

The pumping power required to drive the fluid through microchannel heat sink can be evaluated as:

$$P = n \cdot u_{avg} \cdot A_c \cdot \Delta p \tag{6}$$

Theses objective functions are calculated by solving Navier-Stokes and heat conduction equations at specified design points.

4.2 Surrogate construction

Three surrogate models, Response Surface Approximation (RSA), Kriging (KRG), and Radial Basis Neural Network (RBNN), are constructed and trained on the numerically obtained solutions to predict the optimal design point.

Table 1 Design variables and their ranges

Design variables	*Lower limit*	*Upper limit*
θ	0.1	0.25
ϕ	0.04	0.1
α	0.3	0.5
β	0.5	2.0
γ	0.056	0.112

4.3 Multi-objective (MOEA)

The present problem is associated with two competing objectives in which improvement of one objective leads to deterioration of other objective. Husain and Kim (2008c) described the methodology used to generate global Pareto optimal front for microchannel heat sink.

5 Results and Discussion

For smooth microchannel a grid of 401×16×61 is used for half of the microchannel taken as computational domain microchannel while for ribbed microchannel a 501×41×61 grid is used after carrying out a grid independence test for a geometry of design variables $\alpha = 0.3$, $\beta = 1.25$, and $\gamma = 0.084$ and one full length microchannel has been taken to study (e.g., Husain and Kim 2008a and 2008b). The numerical scheme is validated for both smooth and ribbed microchannels. The numerical predictions are found close to the analytical solutions and within the experimental uncertainties for both smooth and ribbed microchannels.

The single objective optimization was performed by Husain and Kim (Husain and Kim 2008a) using basic surrogate models i.e., RSA, KRG and RBNN. All the surrogate models predict almost same thermal resistance. The CFD calculations at these surrogate predicted optimum design points are also very close to surrogate predictions as shown in Table 2. A sensitivity analysis of the objective function is performed by varying the design variables around the optimum design as shown in Fig. 3. Each design variable is varied from the optimum point in both directions while keeping the other variables fixed. The objective function (thermal resistance) increases sharply with a change in θ while keeping ϕ fixed. On the other hand, change of ϕ has a smaller effect on the objective function for a fixed θ, as shown in Fig. 3. It can

be seen that the optimal design is highly sensitive to θ as compared to ϕ in the specified range. Therefore, the design variable ϕ can be suitably adjusted for the optimum number of channels in order to obtain minimum thermal resistance for the specified channel depth of the heat sink.

A multiobjective optimization of the smooth microchannel was performed considering temperature dependent thermophysical properties of the coolant taking both thermal resistance and pumping power as objective functions (e.g., Husain and Kim 2008c). The Pareto optimal solutions obtained by Hybrid MOEA are shown in Fig. 4. The Pareto optimal solutions provide functional relationship between thermal resistance and pumping power.

The ribbed microchannel was studied and optimized for its capability to enhance heat transfer at micro scale. Table 3 shows the distribution of the design variables at three different locations on the Pareto optimal front. The Pareto optimal front and distribution of the design variable along the Pareto optimal front was analyzed in view of the sensitivity and contribution of the design variables to objective functions. The ratio of rib height-to-width of the channel is found to be more sensitive than the other two design variables.

6 Conclusion

A rectangular microchannel heat sink can be efficiently optimized with three-dimensional numerical analysis and basic surrogate models to reduce computational or experimental expenses and time. The ratio of microchannel width-to-depth was found to be more sensitive to objective function as compared to fin width-to-depth of channel for smooth microchannel. in multiobjective optimization design and fabrication constraints can be handled in a better way by compromising the least influencing design variable and available pumping source. The temperature dependent properties solutions of the microchannel heat sink provide more realistic optimum solutions taking into account micro scale effects. The ribbed microchannel heat sink though requires higher pumping power to remove the heat flux but suitable for carrying away higher heat flux at higher pumping power, therefore the application of the ribbed microchannel heat sink is highly dependent upon the design conditions.

Acknowledgements

This research was supported by the Korea Science & Engineering Foundation (KOSEF) grant funded by the Korea government (MOST) (No. R01-2006-000-10039-0).

Table 2 Optimum points (normalized) predicted by different surrogates and corresponding CFD calculated values (Husain and Kim 2008a)

Model	RBNN	KRG	RSA
θ	0.490	0.492	0.671
ϕ	0.306	0.226	0.430
R_{th} (Surrogate Prediction)	0.164	0.165	0.166
R_{th} (CFD Calculation)	0.171	0.171	0.170

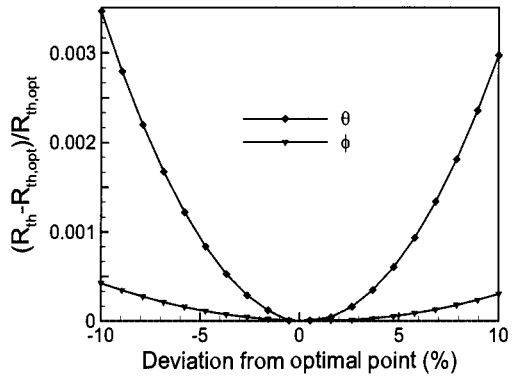

Fig. 3 Sensitivity analysis of thermal resistance near the optimum point (Husain and Kim 2008a)

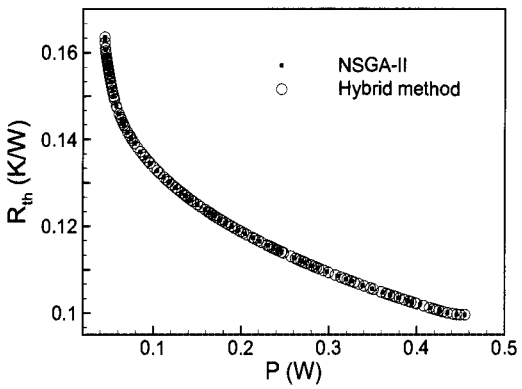

Fig. 4 Pareto optimal solutions using NSGA-II and hybrid multiobjective evolutionary approach (Husain and Kim 2008c)

Table 3 Objective functions and design variables for three clusters from global Pareto optimal solutions (Husain and Kim 2008b)

S. No.	1	3	5
α	0.010	0.120	0.831
β	0.528	0.995	1.000
γ	0.000	0.972	1.000
R_{th} (K/W)	0.1865	0.1820	0.1745
P (W)	0.0423	0.0585	0.1082

References

Arulanandam S., and Li D., 2000, "Liquid transport in rectangular microchannels by electroosmotic pumping," Coll Surf-A: Physicochemical Engineering Aspects, Vol. 161, pp. 89 – 102

CFX-11.0, 2006, Solver Theory

Cheng, Y. J., 2007, "Numerical Simulation of stacked microchannel heat sink with mixing-enhanced passive structure," *Int. Comm. in Heat Mass Trans.*, Vol. 34, pp. 295 – 303

Deb, K., Agrawal, S., Pratap, A., and Meyarivan, T., 2000, "A Fast and Elitist Multi-Objective Genetic Algorithm for Multi-Objective Optimization: NSGA-II," *Proceedings of the Parallel Problem Solving From Nature VI Conference*, Paris, pp. 849 – 858

Deb, K., and Goel, T., 2001"A Hybrid Multi-Objective Evolutionary Approach to Engineering Shape Design," *Proceedings of evolutionary multi-criterion optimization conference*, Zurich, pp. 385 – 399

Fisher, T. S., and Torrance, K. E., 2001, "Optimal Shapes of Fully Embedded Channels for Conjugate Cooling," *IEEE Trans. Adv. Packag.*, Vol. 24(4), pp. 555 – 562

Herwig, H., Hausner, O., 2003, "Critical View on "New Results in Micro-fluid Mechanics": an Example", *Int. J. Heat Mass Transf.* Vol. 46, pp. 935 – 937

Herwig, H., and Mahulikar, S. P., 2006, "Variable property effects in single-phase incompressible flows through microchannels", *International Journal of Thermal Sciences* Vol. 45(10), pp. 977 – 981

Husain, A., and Kim, K.-Y., 2008a, "Shape Optimization of Micro-channel Heat Sink for Micro-Electronic Cooling," *IEEE Trans. Compon. Packag. Technol.*, Vol. 31(2), pp. 322 – 330

Husain, A., and Kim, K.-Y., 2008b, "Microchannel heat sink designed roughness: Analysis and optimization", J. Therm. Heat Transf., Vol. 22, No.3, pp. 342 – 351

Husain, A., and Kim, K.-Y., 2008c, "Optimization of microchannel heat sink with temperature dependent fluid properties", Appl. Therm. Eng. Vol. 28. pp. 1101 – 1107

Joshi Y., and Wei X., 2005, "Micro and meso scale compact heat exchangers in electronics thermal management-A review," In: Shah R. K., Ishizuka M., Rudy T. M., and Wadekar V. V. (ed), *Proceedings of fifth international conference on Enhanced, Compact and Ultra-Compact Heat Exchangers: Science, Engineering and Technology*, Engineering Conferences International, Hoboken, NJ, USA

Kim, S. J., 2004, "Methods for Thermal Optimization of Microchannel Heat Sinks," *Heat Transf. Engg.*, Vol. 25(1), pp. 37 – 49

Knight, R. W., Hall, D. J., Goodling, J. S., and Jaeger, R. C., 1992, "Heat Sink Optimization with Application to Microchannels," *IEEE Trans. Compon., Hybrids, Manufact. Technol.*, Vol. 15(5), pp. 832 – 842

Li, J., and Peterson, G. P. "Bud", 2006, "Geometric Optimization of a Micro Heat Sink with Liquid Flow," *IEEE Trans. Compon. Packag. Technol.*, Vol. 29(1), pp. 145 – 154

Li, Z., Huai, X., Tao, Y. and Chen, H., 2007, "Effects of Thermal Property Variations on the Liquid Flow and Heat Transfer in Microchannel Heat Sinks", *Appl. Thermal Eng.*, Vol. 27, 2803 – 2814

Ligrani, P. M., Oliveira, M. M., and Blaskovich, T., 2003, "Comparison of Heat Transfer Augmentation Techniques," *AIAA Journal*, Vo. 41(3), pp. 337 – 362

Liu, D., and Garimella, S. V., 2005, "Analysis and Optimization of the Thermal Performance of Microchannel Heat Sinks," *International Journal for numerical methods in Heat and Fluid flow*, Vol. 15(1), pp. 7 – 26

Lophaven, S. N.; Nielsen, H. B. and Sondergaard, J., 2002, "A MATLAB Kriging Toolbox", *Technical Report IMM-TR2002-12*

Morini, G. L., 2004, "Single-Phase Convective Heat Transfer in Microchannels: A Review of Experimental Results, Int. J. Thermal. Sci., Vol. 43, 631 – 651

Morini G. L., Lorenzini M., Salvigni S., and Spiga M., 2006, "Thermal performance of silicon micro heat-sinks with electrokinetically-driven flows," International Journal of Thermal Science, Vol. 45, pp. 955 – 961

Myers, R. H., and Montgomery, D. C., 1995, "Response Surface Methodology: Process and Product Optimization using Designed Experiments", *John Wiley & Sons, Inc.*, New York

Orr, M. J. L., 1996, "Introduction to radial basis neural networks, *Center for cognitive science, Edinburgh University*, Scotland, UK. http://anc.ed.ac.uk/RBNN/

Patankar, S. V., 1980, "Numerical Heat Transfer and Fluid Flow", *McGraw-Hill*, New York

Tuckerman, D. B., and Pease, R. F. W., 1981, "High-performance Heat Sinking for VLSI," *IEEE Electron device Lett.*, EDL-2, pp. 126 – 129

Vanderplaats, G. N., 1984, "Numerical Optimization Techniques for Engineering Design: with Applications, *McGraw-Hill,* New York

Wang, X.-Q., Yap, C., and Mujumdar, A. S., 2005, "Effects of Two-Dimensional Roughness in Flow in Microchannels," *Journal of Electronic Packaging*, Vol. 127, pp. 357 – 361

Wei, X., and Joshi, Y., 2003, "Optimization Study of Stacked Micro-channel Heat Sinks for Micro-electronic Cooling," *IEEE Trans. Compon. Packag. Technol.*, Vol. 26(1), pp. 55 – 61

Wei, X. J., Joshi, Y. K., and Ligrani, P. M., 2007, "Numerical Simulation of Laminar Flow and Heat Transfer Inside a Microchannel With One Dimpled Surface," *Journal of Electronic Packaging*, Vol. 129, pp. 63 – 70

Weisberg, A., Bau, H. H., and Zemel, J. N., 1992, "Analysis of Microchannels for Integrated Cooling," *Int. J. Heat Mass Transf.*, Vol. 35(10), pp. 2465 – 2474

Xu, B., Ooi, K. T., Mavriplis, C. and Zaghloul, M. E., 2003, "Evaluation of Viscous Dissipation in Liquid Flow in Microchannels", *J. Micromech. Microeng.* Vol. 13, 53 – 57

Yener, Y., Kakac, S., Avelino, M., Okutucu, T., 2005, "Single-phase forced convection in microchannels: A State-of-the-Art Review", in Microscale Heat Transfer: Fundamentals and Applications, Ed. by Kakac, S., Vasiliev, L. L., Bayazitoglu, Y. and Yener, Y., *Springer*, Neatherlands, 1 – 24

The 4th International Symposium on Fluid Machinery and Fluid Engineering
November 24-27, 2008, Beijing, China
NO. 4ISFMFE-IL21

A Numerical Simulation of a Flow in Pem Fuel Cell Stack Using Lattice Boltzmann Method

Jae-Hoon Lee[1], Seok-Yun Jeon[1], Joon-Yong Yoon[*2], Sung-Joon Byun[1] and Myung-Seob Shin[1]

[1] Department of Mechanical Engineering, Hanyang University, Seoul, Republic of Korea
[*2] Division of Mechanical and Management Engineering, Hanyang University,
1271 Sa-3-dong, Sangnok-gu, Ansan City, Gyeonggi-do 426-791, Republic of Korea
Tel: +82-31-400-5282 / Fax: +82-31-400-4707
E-mail: joyoon@hanyang.ac.kr

Abstract The objective of the present work using one of the methods of numerical simulation on Computation Fluid Dynamics (CFD), is to identify the diffusion of reactant (hydrogen, oxygen, etc) arising in the proton exchange membrane fuel cell (PEMFC), and the flow characteristics of the product (H_2O). The field of this analysis is a two-dimensional channel form and is consisted of Gas channel, Gas Diffusion Layer (GDL), and membrane. This study is analyzed by applying the Lattice Boltzmann BGK D2Q9 model. The actual GDL and membrane have different porosities and thus this research includes solid obstacles with varied forms and sizes according to each area ratio in order to scrutinize this difference.

Keywords computation fluid dynamics, Lattice Boltzmann method, PEM fuel cell, porous medium

1 Introduction

According to an increase of environmental concern and the demand for energy, all its forms have been rising recently. However, continued use of fossil fuels are limited in amount and sooner or later will be depleted, so fuel cells and hydrogen technology have been at the center of active research among the renewable energy alternative. Fuel cells are electrochemical reactors generating electricity directly from oxidation reactions of fuels. Due to their high efficiency (typically twice of the energy conversion efficiency of internal combustion engines), near-zero emissions, low noise, and portability, fuel cells are being considered as a viable energy-conversion devise. Research of fuel cells has been conducted and is currently being conducted into several types of fuel cells, such as alkaline fuel cells, proton exchange membrane (PEM) fuel cells, phosphoric acid fuel cells, molten carbonate fuel cells, solid oxide fuel cells, and so forth. Among types of fuel cells above, the proton exchange membrane fuel cell (PEMFC) is a preferred type for automotive applications due to its low operation temperature.

A PEM cell consists of a membrane electrolyte assembly (MEA) sandwiched between two bipolar plates. The gas diffusion layer (GDL), catalyst layer and polymer electrolyte membrane are referred to as MEA where current is produced. Fuel and oxidant are supplied to both sides of MEA through the flow channels on the bipolar plates producing electron in the anode catalyst layer and water in the cathode catalyst layer. The GDL is a porous medium generally made of carbon cloth or paper and plays an essential role in fuel cells of permitting gas to be transported from the flow channel to the catalyst layer. The GDL must permit liquid water to be transported from the catalyst layer into the flow channels to remove the liquid water from the cell. When the liquid water is accumulated in the GDL the gas transport from the gas flow channel to the catalyst layer is hindered limiting the performance of a PEM fuel cell. Thus, more complex computational models are currently being developed to better understand issues related to the performance of PEM fuel cell, such as pressure loss and temperature distribution in the flow channels, species transport through porous gas diffusion layers, and water management on the cathode side.

A porous medium such as the GDL having generally very complex structures and shapes makes it difficult to simulate fluid flow in PEM fuel cell by the traditional CFD. Here we explore the use of lattice-Boltzmann (LB) approach as a modeling tool for predicting fluid flows relevant to PEM fuel cell. The LB method is based on a kinetic formulation and could have certain advantages over the traditional CFD. LB models of addressing thermal flows, flows through porous media, multiphase flows, electro-osmotic flows, and contact line, etc., have been proposed in recent years.

2 Lattice Boltzmann Method

LB method solves the microscopic kinetic equation for particle distribution $f(x, v, t)$, where x and v is the particle position and velocity vector, respectively, in phase space (x, v) and time t, where the macroscopic quantities (such as velocity and density) are obtained through moment integration of $f(x, v, t)$. The most widely used collision operator in LB equation is the single relaxation time (SRT) or BGK model, and listed as follows:

$$f_i(\mathbf{x}+\mathbf{c}_i\Delta t, t+\Delta t) - f_i(\mathbf{x},t) = \Omega_i(\mathbf{x},t) \tag{1}$$

$$\Omega_i(\mathbf{x},t) = -\frac{1}{\tau}\left[f_i(\mathbf{x},t) - f_i^{eq}(\mathbf{x},t)\right] \tag{2}$$

where $\mathbf{c}_i$'s are the discrete velocities, Δt the time step and τ is the relaxation time. $\Omega_i(x,t)$ is the discrete collision operator. f_i^{eq} represents the equilibrium distribution of f_i given as

$$f_i^{eq} = \omega_i \rho\left[1 + \frac{\mathbf{c}_i\cdot\mathbf{u}}{RT} + \frac{(\mathbf{c}_i\cdot\mathbf{u})^2}{2(RT)^2} - \frac{\mathbf{u}\cdot\mathbf{u}}{2RT}\right]$$

$$\omega_i = \begin{cases} 4/9 & i=0 \\ 1/9 & i=1,2,3,4 \\ 1/36 & i=5,6,7,8 \end{cases} \tag{3}$$

where ω_i's are the associated weight coefficients, R the universal gas constant and T is the absolute temperature. The velocity vectors shown in Fig. 1, $\mathbf{c}_i$ for the two-dimensional 9-speed model (D2Q9) are given to be

$$\mathbf{c}_i = \begin{bmatrix} (0,0) & for \quad i=0 \\ c\left(\cos\frac{i-1}{2}\pi, \sin\frac{i-1}{2}\pi\right), & for \quad i=1,2,3,4 \\ \sqrt{2}c\left(\cos\frac{i-4-1/2}{2}\pi, \sin\frac{i-4-1/2}{2}\pi\right), & for \quad i=5,6,7,8 \end{bmatrix} \tag{4}$$

where $c = \Delta x/\Delta t$, and Δx is the distance between lattice point. The speed of the sound is $c/\sqrt{3}$ in the phase space and accordingly we have $RT = c^2/3$. The macroscopic number density, $\rho(\mathbf{x},t)$, and the velocity, $\mathbf{u}(\mathbf{x},t)$, of the fluid are obtained as

$$\rho = \sum_i m f_i \tag{5}$$

$$\rho\mathbf{u} = \sum_i m f_i \mathbf{c}_i \tag{6}$$

where m is the molecular weight. The kinematic viscosity is relates to the relaxation time as

$$\nu = \frac{2\tau - 1}{6}\frac{\Delta x^2}{\Delta t} \tag{7}$$

In this work, Δx and Δt are set to be unity for convergence, and thus, the fluid pressure is given as $p = \rho/3$.

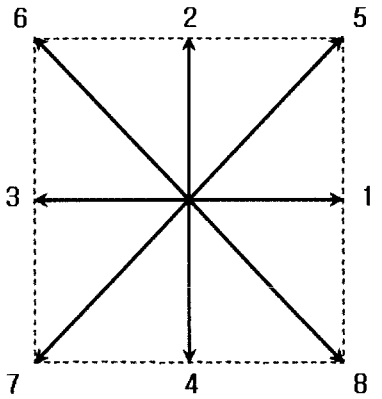

Fig. 1 A schematic of lattice Boltzmann D2Q9 model

3 Lattice Boltzmann Equation for Reacting Flow

We simulate simple one step reaction in PEM fuel cell stack and bring fluid flow into focus. The simplifying assumptions used in this work are listed:

- There are no external forces in the field
- The chemical reaction does not affect the flow field; temperature and concentration fields are solved separately.
- Nitrogen is inert.
- Only simple one step reaction is considered

$$2H_2 + O_2 \rightarrow 2H_2O \tag{8}$$

For temperature and concentration (mass ratio R^s, $s \in \{H_2, O_2, H_2O\}$) fields, there is an extra computational

sub-step, reaction, besides conventional computational sub-steps of collision and advection. A reaction term is added to Eq. (1).

$$f_i(\mathbf{x}+\mathbf{c}_i\Delta t, t+\Delta t) - f_i(\mathbf{x},t) = \Omega_i(\mathbf{x},t) + \omega_i Q_{R^s} \tag{9}$$

and the over over-all reaction rate is given by

$$\omega_{OV} = \kappa_{OV} C_{H_2} C_{O_2} e^{-E/RT} \tag{10}$$

concentrations

$$C_s = \rho R^s / M_s, \; R^s = \sum_i R_i^s \tag{11}$$

reaction term

$$Q_{R^s} = \lambda_s \frac{M_s}{\rho} \omega_{OV} \tag{12}$$

where λ_s are the stoichiometric coefficients for the various species.

4 Modeling and Assumptions

A schematic of the analyzed domain is shown in Fig. 2. The half-cell model in this work is quasi two-dimensional and consists of four different regions extending from the air gas channel to the membrane. The actual GDL and membrane have different porosities and thus we include solid obstacles with varied forms and sizes. The following assumptions are made in the present model: (i) axial convection is considered only in the gas channel and the gas velocity is assumed constant; (ii) diffusion in the y direction is the only mode of transport in the GDL and the catalyst layer; (iii) the system considered is steady and isothermal; (iv) oxygen is transported to the catalyst sites as a gaseous component only, and liquid water does not constitute a barrier to oxygen transport; (v) fuel (hydrogen) is diffused from the boundary of the domain into porous medium uniformly along x direction.

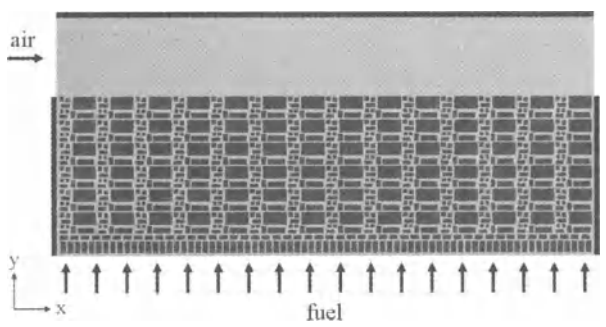

Fig. 2 The domain

5 Numerical Result and Discussion

The velocity profile in the analyzed domain is shown in Fig. 3. The interface between porous region and the open channel region is set to be $y = 0$. To validate the numerical simulation of a flow in PEM fuel cell stack using Lattice Boltzmann Method, the velocity profile is compared in Fig. 4. with the analysis of Wang and Afshapoya.

The discrepancy in two results may be caused by the fact that the domains are slightly different in structure and assumptions. Thus further investigations such as the modification of the domain and the correction of the assumptions are underway to understand the origin of this discrepancy.

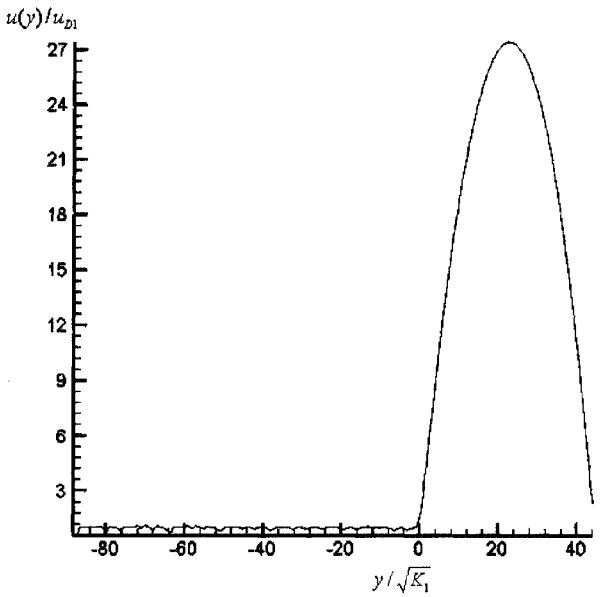

Fig. 3 Velocity profile in the domain

6 Conclusions

The porous media such as the GDL having generally very complex structures and shapes makes it difficult to simulate fluid flow in PEM fuel cell by the traditional CFD. Thus we applied Lattice-Boltzmann (LB) approach as a modeling tool for simulating fluid flows relevant to PEM fuel cell. For the modeling porous medium in this work, solid obstacles are included with varied forms and sizes according to each area ratio in LBM code. However, numerical results are not satisfactory against expectation. In conclusion, this work is in an early stage, thus there are several related facts to improve the points at issue.

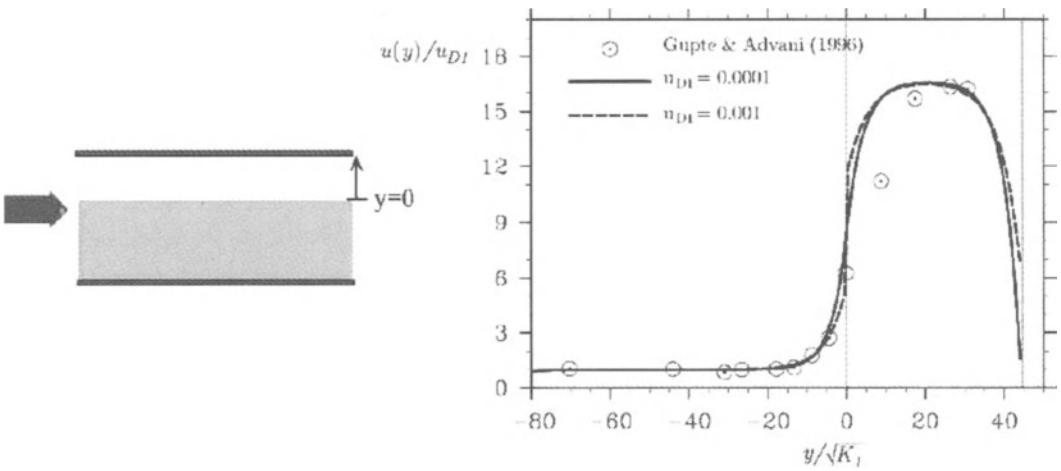

Fig.4 Velocity profile in a 2D channel partially filled with porous medium (L.-P. Wang, B. Afsharpoya, 2006, pp. 247, Fig. 7)

Acknowledgements

This work was supported by the second stage of the Brain Korea 21 Project in 2008.

References

Frano Barbir, 2005, "PEM fuel cells :theory and practice", *Elsevier Academic Press*

H. Yu, LS. Luo, and S.S. Girimaji, 2002, "Scalar Mixing and Chemical Reaction Simulations Using Lattice Boltzma-nn Method", *International Journal of Computational Engineering Sciences*, Vol. 3, No.1, pp. 73 – 87

J. Park, M. Matsubara and X. Li, 2007, "Application of lattice Boltzmann method to a micro-scale flow simulation in the porous electrode of a PEM fuel cell", *Journal of Power Sources*, Vol 173, Issue 1, pp. 404 – 414

L.-P. Wang, B. Afsharpoya, 2006, "Modeling fluid flow in fuel cells using the lattice-Boltzmann approach", *Mathematics and Computers in Simulation*, Vol 72, Issue 2-6, pp. 242 – 248

M. Spaid, F. R. Phelan Jr, 1997, "Lattice Boltzmann methods for modeling microscale flow in fibrous porous media", *Physics of Fluids*, Vol. 9, Issue 9

N. Sammes (Editor), 2006, "Fuel cell technology : reaching towards commercialization", *Springer*, London

Q. Kang, D. Zhang, S. Chen, and X. He, 2002, "Lattice Boltzmann simulation of chemical dissolution in porous media", *Physical Review E*, Vol. 65, Issue 3

R. O'Hayre, S. Cha, W. Colella, and F. Prinz, 2006, "Fuel cell technology :reaching towards commercialization", *John Wiley & Sons*

YT. Lin, CT. Lin, YC. Chen, KM. Yin, and CT. Yang, 2007, "An analytical study of the PEM fuel cell with axial convection in the gas channel", *International Journal of Hydrogen Energy*, Vol. 32, Issue 17, pp. 4477 – 4488

Z. Guo, TS. Zhao, 2002, "Lattice Boltzmann model for incompressible flows through porous media", *Physical Review E*, Vol. 66, Issue 3

The 4th International Symposium on Fluid Machinery and Fluid Engineering
November 24-27, 2008, Beijing, China
NO. 4ISFMFE-Ab15

Simulation of Gas Flow in a Microchannel by Lattice Boltzmann Method

In-Won Park[1], Myung-Seob Shin[1], Sung-Joon Byun[1], Joon-Yong Yoon[*2]

[1] Department of Mechanical Engineering, Hanyang University, Seoul, Korea
[*2] Division of Mechanical and Management Engineering, Hanyang University,
1271 Sa-3-dong, Sangnok-gu, Ansan City, Gyeonggi-do 426-791, Korea
Tel: +82-31-400-5282 / Fax: +82-31-400-4707
E-mail: joyoon@hanyang.ac.kr

Abstract In recent years, microflow has become a popular field of interest due to the appearance of microelectromechanical systems (mems). Generally, the navier-stokes equations cannot adequately describe gas flows in the transition and free-molecular regimes. In these regimes, the boltzmann equation of kinetic theory is applied to govern the flows. However, this equation cannot be solved easily, either by analytical techniques or by numerical methods. In this work, the lattice boltzmann method is applied to simulate the two-dimensional isothermal pressure driven microchannel flow. This method is regarded as a numerical approach for solving the boltzmann equation in discrete velocity. We have been applied for rarefied shear-driven and pressure driven flows between parallel plates at knudsen numbers between 0.01 and 1.0. Our numerical results correspond well with those obtained analytically and experimentally. From this study, we may conclude that the lattice boltzmann method is an efficient approach for simulation of microflows.

Keywords Lattice Boltzmann method, knudsen number, knudsen layer

1 Introduction

In recent years, gas flows in microscale has become a popular field of interest due to the appearance of microelectromechanical systems (MEMS). In order to optimize the design of MEMS, an understanding of the behaviors of fluid flows at microscales is critical. However, since microscopic gaseous flow phenomena are quite different from those at macro scale, their study poses a unique challenge for research. Generally, Microscopic gas flows are usually distinguished by relatively small Mach numbers ($Ma=U/Cs\leqslant 0.3$, where U is the characteristic velocity of the flow and Cs is the sound speed) and large Knudsen numbers ($Kn=\lambda/L$, where λ is the molecular mean free path of fluid and L is the characteristic length of the flow domain.). The gas flows are typically classified as one of three regimes according to its Knudsen number : "slip-flow" ($0.001\leqslant Kn<0.1$) and "transition" ($0.1\leqslant Kn<10$) regimes and finally the "free-molecular" ($Kn\geqslant 10$) regime. As Kn increases, the continuum assumption may break down. Consequently, the Navier-Stokes equations based on the continuum assumption will fail to work for such flows.

Since Cercignani (1975) and Chapman (1970) has studied that processes in these kinds of flows are described by the Boltzmann equation(BE) of the kinetic theory. Actually, some methods based on the Boltzmann equation have been proposed by Loyalka (1975) and Cercignani (2004). Currently, most of the LBM applications are limited to the macro flow. The reason may be due to the ways in which the relaxation time for collision is determined and the boundary condition at the wall is implemented. Through the Chapman-Enskog expansion, the relaxation time in conventional LBM can be computed from the viscosity in such a way that the N-S equation is recovered. However, for the micro flow, the Navier-Stokes equations cannot adequately describe gas flows in the transition and free-molecular regimes. So, the above process cannot be used to compute the relaxation time. To solve this problem, Nie et al. (2002) modified the expression of relaxation time by including the effect of density. Lim et al. (2002) assumed that the

particles relax to their equilibrium state over the time period required to travel a distance of mean free path of molecules. With this assumption, the relaxation time can be linked to the Knudsen number. Niu et al. (2004) can establish the relationship between the relaxation time and the Knudsen number from the kinetic theory.

The objective of the present work is to study the influence of kinetic boundary condition and Knudsen number on the flow pattern in transition regimes. We has been applied for rarefied shear-driven and pressure driven flows between parallel plates at Knudsen numbers between 0.01 and 1.0. Simulation of Couette flow and Poiseuille flow will then be presented and the results are compared with both the previous numerical results DSMC data and linearized BE data.

2 Lattice Boltzmann Equation with Multiple Relaxation Times

LBM method solves the microscopic kinetic equation for particle distribution $f(x, v, t)$, where x and v is the particle position and velocity vector, respectively, in phase space (x, v) and time t, where the macroscopic quantities (velocity and density) are obtained through moment integration of $f(x, v, t)$. The most widely used collision operator in LBE is the single relaxation time (SRT) or BGK model, and listed as follows:

$$f_i(x+c_i\Delta t, t+\Delta t)-f_i(x,t)=\Omega_i(x,t) \tag{1}$$

$$\Omega_i(x,t)=-\frac{1}{\tau}\left[f_i(x,t)-f_i^{eq}(x,t)\right] \tag{2}$$

where $f_i(x,t)$ and f_i^{eq} are the particle distribution function and the equilibrium particle distribution function of the ith discrete particle velocity v_i, respectively, c_i is a discrete velocity, and τ is the relaxation time, and $\Omega_i(x,t)$ is the discrete collision operator. Models with multiple relaxation times (MRT) were also proposed Lallemand and Luo (2000). Where the discrete collision operator is given by

$$\Omega_i=-\sum_j (M^{-1}SM)_{ij}[f_i-f_i^{(eq)}] \tag{3}$$

where M is a $b\times b$ transform matrix projecting the discrete distribution functions fi onto the moment space m=Mf where $f=(f_0,f_1,\cdots,f_{b-1})^{\mathrm{T}}$, and $S=diag(\tau_0,\tau_1,\cdots,\tau_{b-1})^{\mathrm{T}}$ is a non-negative diagonal matrix with i being the relaxation time for the ith moment. As $\tau_i=\tau$, the MRT model reduces to the BGK model. The equilibrium distribution function in either Eqs. (2) or (3) can be expressed as

$$f_i^{(eq)}=w_i\rho\left[1+\frac{\vec{c}_i\cdot\vec{u}}{c_s^{\,2}}+\frac{(\vec{c}_i\cdot\vec{u})^2}{2c_s^{\,4}}+\frac{\vec{u}\cdot\vec{u}}{2c_s^{\,2}}\right] \tag{4}$$

where w_0=4/9, $w_{1\text{-}4}$=1/9, and $w_{5\text{-}8}$=1/36, and $c_s=c/\sqrt{3}$ is the sound speed. In addition, the discrete velocities for the two-dimensional nine-velocity (D2Q9) model are

$$\vec{c}_i=\begin{cases}(0,0)\,c, & i=0\\ (\pm1,0)c,(0\pm1)c, & i=1\sim4\\ (\pm1,\pm1)c, & i=5\sim8\end{cases} \tag{5}$$

For an isothermal system, the temperature appears only as a free parameter, and the density ρ and momentum $\rho\vec{u}$ are defined as

$$\rho=\sum_i f_i,\quad \rho\vec{u}=\sum_i \vec{c}_i f_i \tag{6}$$

Based on the discrete velocity vectors given by Eq. (5), we can define nine discrete velocity moments of the distribution function,

$$m=Mf=(\rho,e,\varepsilon,j_x,q_x,j_y,q_y,p_{xx},p_{xy})^{\mathrm{T}} \tag{7}$$

where $f=(f_0,f_1,\cdots,f_8)^{\mathrm{T}}$. In column ρ is the fluid density, ε is related to the square of the energy e, j_x and j_y are the mass flux in two directions, q_x and q_y correspond to the energy flux in two directions, and p_{xx} and p_{xy} correspond to the diagonal and off-diagonal component of the viscous stress tensor. One immediate advantage of the LBE-MRT model is that macroscopic variables of interest can be obtained readily by simply performing the matrix multiplication Mf if f is known. In addition, due to the conservation of mass and momentum before and after particle collision, the total mass and momentum should not relax at all. However, Eq. (2) in standard LBGK method requires all f_i's are relaxed at the same rate and, hence, all macroscopic quantities of interest. Physically speaking, different physical modes should have different relaxation rates. With the ordering of moments specified by Eq. (7), the relaxation times in the diagonal matrix S are given by

$$S=diag(\tau_\rho,\tau_e,\tau_\varepsilon,\tau_j,\tau_q,\tau_j,\tau_q,\tau_s,\tau_s)^{-1} \tag{8}$$

and the corresponding transform matrix M for the D2Q9 model is given by

$$M=\begin{pmatrix}1&1&1&1&1&1&1&1&1\\ -4&-1&-1&-1&-1&2&2&2&2\\ 4&-2&-2&-2&-2&1&1&1&1\\ 0&1&0&-1&0&1&-1&-1&1\\ 0&-2&0&2&0&1&-1&-1&1\\ 0&0&1&0&-1&1&1&-1&-1\\ 0&0&-2&0&2&1&1&-1&-1\\ 0&1&-1&1&-1&0&0&0&0\\ 0&0&0&0&0&1&-1&1&-1\end{pmatrix} \tag{9}$$

Lallemand and Luo (2000) have shown that the LBE-MRT model can reproduce the same viscosity as that by SRT model if we set $s_8 = s_9 = 1/\tau$. Once this is decided, the rest of the relaxation parameters (s_2; s_3; s_5 and s_7) for different physical modes can then be chosen more flexibly.

3 Kinetic Boundary Condition for the Lattice Boltzmann Equation

3.1 The combined bounce-back and specular-reflection boundary condition

In practical applications, suitable boundary conditions must be supplied for the LBE. Some schemes have been proposed for the LBE-BGK (or SRT) in the literature, such as the discrete Maxwell's diffuse-reflection schemes by Tang (2005) and the combined bounce-back and specular-reflection (CBBSR) schemes by Zhang (2006). Recently, the two schemes were analyzed for both the LBE-BGK and LBE-MRT with constant relaxation times by Zhang (2006) and Guo (2006), and it was found that they are identical in a parametric range and both contain some discrete effects. In this work, we used to CBBSR model for the LBE-MRT proposed by Guo (2008). For simplicity, we consider a surface on wall boundary as sketched in Fig. 1.

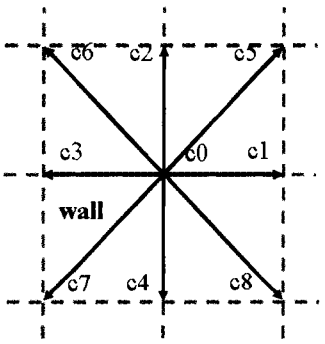

Fig. 1 Schematic of lattice arrangement at the wall boundary

For the nodes at wall boundary, only the distribution functions f_0^1, f_1^1, f_3^1, f_7^1, and f_8^1 can be determined after the streaming, the remaining distribution functions, f_2^1, f_5^1, and f_6^1, cannot be provided by the streaming step and must be specified according to the kinetic boundary condition at the wall. For the CBBSR boundary condition, they are given by

$$\begin{aligned} f_2^1 &= \tilde{f}_4^1 + 2rp\vec{c}_2 \cdot \vec{u}_w / c_s^2 \\ f_5^1 &= r\tilde{f}_7^1 + (1-r)\tilde{f}_8^1 + 2rp\vec{c}_5 \cdot \vec{u}_w / c_s^2 \\ f_6^1 &= r\tilde{f}_8^1 + (1-r)\tilde{f}_8^1 + 2rp\vec{c}_6 \cdot \vec{u}_w / c_s^2 \end{aligned} \tag{10}$$

where $0 \leqslant r < 1.0$ is the portion of the bounce-back part in the combination. In the CBBSR scheme, the parameter r plays an important role in simulations.

3.2 Relaxation time in LBE

In kinetic theory, the relaxation time τ can be defined in terms of viscosity μ as

$$\tau = \frac{\mu}{p} \tag{11}$$

and the viscosity is proportional to a qualitatively defined molecular mean free path λ, and for hard sphere gases it is expressed as

$$\lambda = \frac{\mu}{p}\sqrt{\frac{\pi}{2RT}} \tag{12}$$

Consequently, the relaxation time can be further written as

$$\tau = \sqrt{\frac{2}{\pi}}\lambda c_s = \sqrt{\frac{2}{\pi}} Kn\, c_s\, H \tag{13}$$

where the definition of the sound speed $c_s = \sqrt{RT}$ is used.

Here we use an effective mean free path λ^* to denote the property of gas flows in the bounded system, and it can be formally expressed as

$$\lambda^* = \lambda\psi(Kn) \tag{14}$$

Here Kn is still the conventional Knudsen number without boundary effects. According to previous investigations by Karniadakis (2001) and Guo (2006), the function Ψ can be best expressed as

$$\psi(Kn) = \frac{2}{\pi} Tan^{-1}(\sqrt{2}Kn^{-3/4}) \tag{15}$$

Accordingly, Eq. (15) gives the effective viscosity and relaxation time as

$$\mu^* = \mu\psi(Kn) \tag{16}$$

and

$$\tau^* = \sqrt{\frac{2}{\pi}} Knc_s H\psi(Kn) \tag{17}$$

respectively.

4 Numerical Results

4.1 Planar couette flow

The present LBE-MRT is also applied to the Couette flow between two parallel to the x axis at $y = H$. The upper plate located at y = H moves with a constant velocity $U_0 = 0.1$ and the lower plate remains stationary. Initially, a linear velocity distribution is set in the flow field. In our simulations, the channel height is set to be H = 1.0, and the mean free path is determined from the Knudsen number (Kn), which ranges from 0.01 to 1.0. The Combined bounce-back and specular-reflection (CBBSR) boundary conditions of Eq.(16) are used to describe the gas-surface interactions on the plates, and periodic boundary conditions are again applied to the inlet and outlet of the channel. All simulations are performed on a Ny × Nx = 65 × 65 lattice.

In Fig. 2, the normalized velocity($U = u/U_0$) profiles of Kn = 0.01, 0.1, and 1.0. are shown and compared with the results of the direct simulation Monte Carlo (DSMC) data McNenly (2003) and the standard LBE-MRT.

As shown in this figure, the velocity profiles demonstrate the Knudsen layers near the plates and a linear property inside the domain. With Kn increasing, the Knudsen layers increase. Slip velocities on the plates are also clearly observed for these Knudsen numbers and their magnitudes increase as Kn becomes larger. Clearly, with this small Knudsen number the standard LBE-MRT and the present LBE-MRT all predict a linear velocity profile that agrees well with the DSMC data, and no obvious slip is observed. As shown in Fig. 2 (b) and (c), apparent slip appears at both walls with the increasing Kn. The present LBE-MRT and the DSMC both give nonlinear velocity profiles, although some discrepancies are observed for

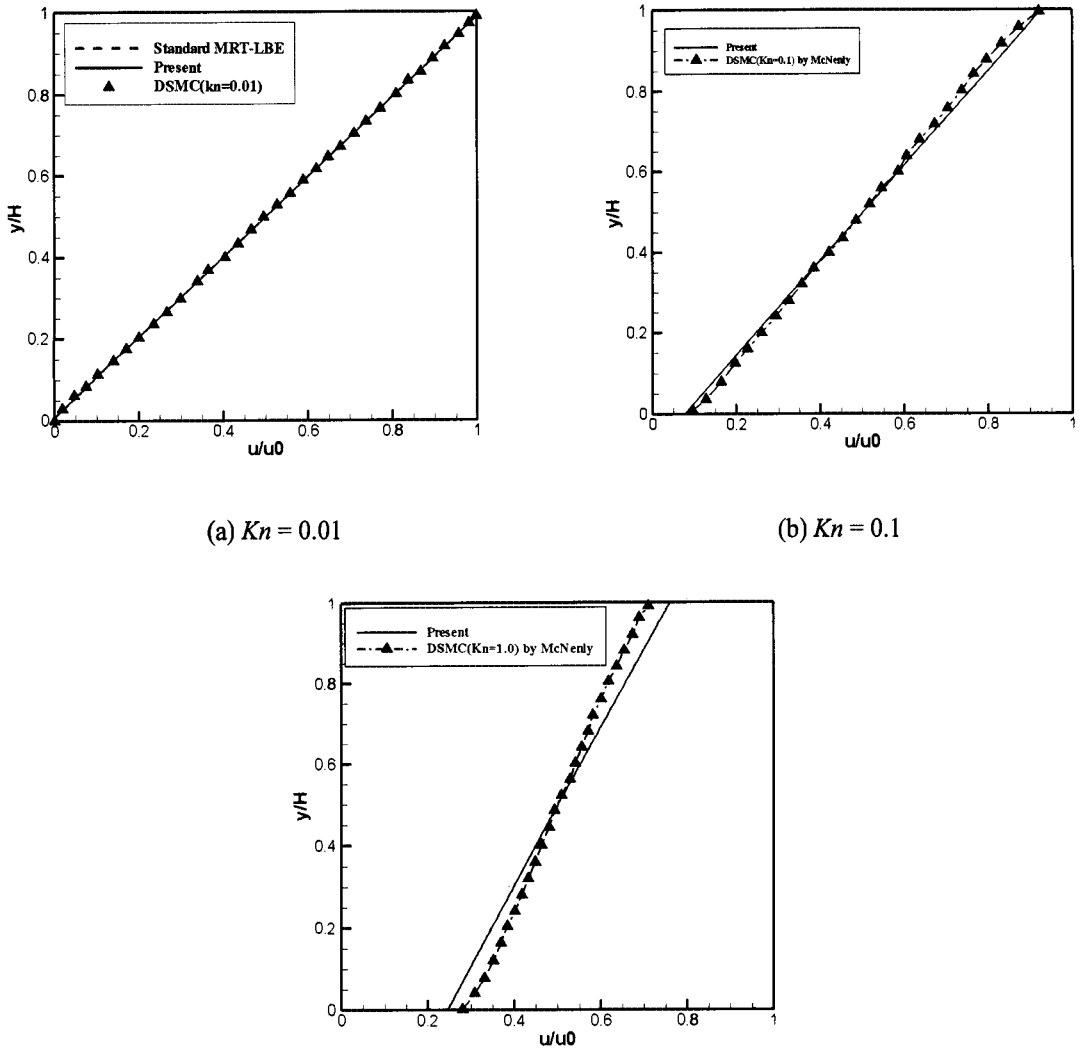

(a) Kn = 0.01

(b) Kn = 0.1

(c) Kn = 1.0

Fig. 2 Velocity profile of the Couette flow at different Kn

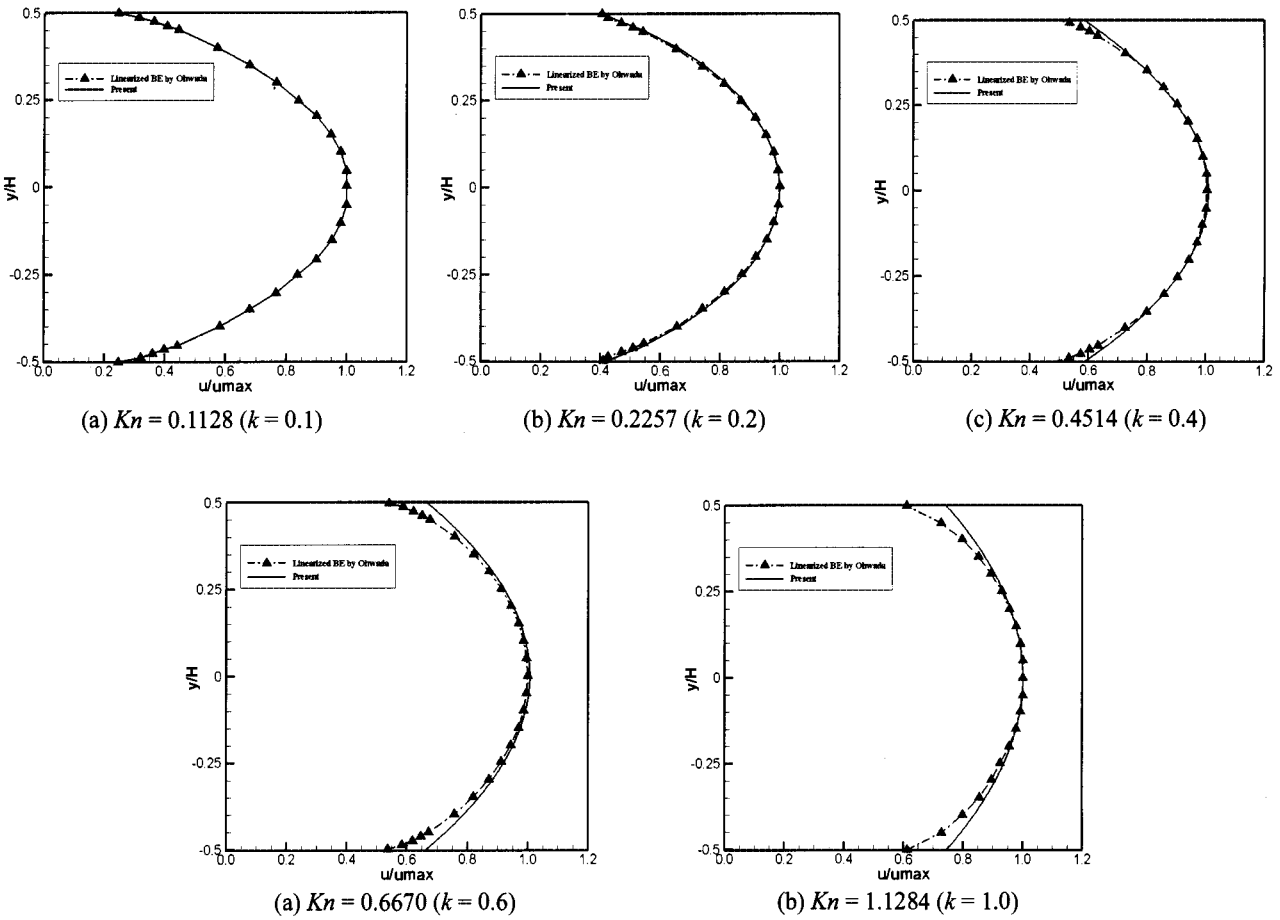

(a) $Kn = 0.1128$ ($k = 0.1$) (b) $Kn = 0.2257$ ($k = 0.2$) (c) $Kn = 0.4514$ ($k = 0.4$)

(a) $Kn = 0.6670$ ($k = 0.6$) (b) $Kn = 1.1284$ ($k = 1.0$)

Fig. 3 Velocity profile of the Couette flow at different Kn

higher Kn. Specifically, at Kn=0.1 and 1.0, the predictions of the present LBE show some slight differences, but both are still in good agreement with the DSMC result. However, it is observed that at over Kn=1.0, the present LBE underpredicts the slip velocity obviously. For the Couette flow between two parallel plates, the two KL will overlap for larger Kn and thus the boundary condition will be inaccurate. More elegant boundary conditions that can treat overlapping KLs are still desirable.

4.2 Force-driven poiseuille flow

The second numerical illustration is the force-driven Poiseuille flows in a 2D channel with height H. This problem has wide engineering application. In numerical simulations, the flow is assumed to be static initially, and a constant force a=0.01 is applied in the streamwise direction while periodic boundary conditions are used at the inlet and outlet. In all of the following simulations, we use the same parameters and boundary conditions as those used in the Couette flow.

In Fig. 1, the normalized velocity ($U = u/U_{max}$, where U_{max} is the maximum velocity value in the channel) profiles at $kn = 2k/\sqrt{\pi}$ with k ranging from 0.1 to 1.0 are shown and compared with the results of the linearized Boltzmann equation (BE) data by Ohwada (1989). To show the accuracy of the present method, the linearized BE data are also included. As observed from this figure, the results obtained by the present LBE-MRT are in good agreement with the linearized BE predictions. With the increase of the Knudsen numbers, the slip velocities at the channel walls increase. Clearly, with this small Knudsen number the present LBE-MRT predict a velocity profile that agrees well with the linearized BE data, and no obvious slip is observed. As shown in Fig. 2, apparent slip appears at both walls with the increasing Kn. The present LBE-MRT and the linearized BE both give parabolic velocity profiles, although some discrepancies are observed for higher Kn. As shown in Fig. 2(a) and (b), the present LBE, interestingly, provides a satisfied result in the whole region, especially within the two KLs. As k increases from 0.1 to 1.0, the present LBE-MRT gives a

good prediction in the central region, but the Knudsen layers near the two walls.

5 Conclusions

In conclusion, a systematic description of the issues of the kinetic lattice Boltzmann method for simulating the microscale gas flows is presented in this paper. By using the lattice Boltzmann equation with multiple relaxation times, the combined bounce-back and specular-reflection (CBBSR) boundary conditions is directly obtained by projecting the Maxwell kinetic boundary condition on the gas-surface interactions. The relaxation time is linked to the Knudsen number, and a concept of the effective mean free path is introduced in determining the relaxation time by taking into account the boundary effects. With a link to the numerical simulations of the Couette and Poiseuille flows, it is argued that by introducing the effective molecular mean free path with boundary effects of the LBM, the microscale gas flows at a range of the Knudsen numbers can be modeled.

Acknowledgements

This work was supported by the second stage of the Brain Korea 21 Project in 2008.

References

Cercignani, C., 1975, "Theory and Application of the Boltzmann Equation," *Scottish Academic Press*, Edinburgh

Cercignani, C., Lampis, M. and Lorenzani, S., 2004, "Variational approach to gas flows in microchannels,", *Physics of Fluids*, Vol. 16, pp.3426 – 3437

Chapman, S. and Cowling, T. G., 1970, "The Mathematical Theory of Non-Uniform Gases," *Cambridge University Press*, Cambridge, England

Guo, Z., Zhao, T. S., and Shi, Y., 2006, "Physical symmetry, spatial accuracy, and relaxation time of the lattice Boltzmann equation for microgas flows," *Journal of Applied physics*, Vol.99, 074903

Guo, Z., Zheng, C., and Shi, B., 2008, "Lattice Boltzmann equation with multiple effective relaxation times for gaseous microscale flow," *Physics Review E* , Vol. 77, 036707

Huo, C. M. and Tai, Y. C., 1998, "MICRO-ELECTRO-MECHANICAL-SYSTEMS (MEMS) AND FLUID FLOWS," *Annual Review of Fluid Mechanics*. Vol. 30, pp. 579 – 612

Karniadakis, G.K. and Beskok, A., 2001, "Microflows: Fundamentals and Simulation", *Springer*, New York

Lallemand, P., and Luo, L-S., 2000, "Theory of the lattice Boltzmann method: dispersion, dissipation, isotropy, Galilean invariance, and stability," *Physics Review E* , Vol. 61, pp.6546 – 6562

Lim, C. Y., Shu, C., Niu, X. D., and Chew, Y. T., 2002, "Application of lattice Boltzmann method to simulate microchannel flows," *Physics of Fluids*, Vol. 14, pp. 2299 – 2308

Loyalka, S. K., Petrellis, N. and Strovick, T. S.,1975, "Some numerical results for the BGK model: Thermal creep and viscous slip problems with arbitrary accomodation at the surface," *Physics of Fluids*, Vol. 18, pp. 1094 – 1099

McNenly, M. J., Gallis, M. A., and Boyd, I. D., 2003, "Slip model performance for microscale gas flows," AIAA-03-4050, *The 36th AIAA Thermophysics Conference*, Orlando, Florida

Nie. X., Doolen, G. D. and Chen, S., 2002," Lattice-Boltzmann Simulations of Fluid Flows in MEMS," *journal of statistical physics*, Vol. 107, pp. 279 – 289

Niu, X. D., Shu, C., and Chew, Y. T.,2004, "A lattice Boltzmann BGK model for simulation of micro flows," *Europhysics Letters*, Vol. 67, pp. 600 – 606

Ohwada, T., Sone, Y. and Aoki, K., 1989, " Numerical analysis of the Poiseuille and thermal transpiration flows between two parallel plates on the basis of the Boltzmann equation for hard-sphere molecules," *Physics of Fluids A*, Vol. 1, pp. 2042 – 2049

Tang, G. H., Tao, W. Q., and He, Y. L., 2005, "Lattice Boltzmann method for gaseous microflows using kinetic theory boundary conditions," *Physics of Fluids* , Vol. 17, 058101

Zhang, Y-H., Gu, X-J., Barber, R. W., and Emerson, D. R., 2006, "Capturing Knudsen layer phenomena using a lattice Boltzmann model," *Physical Review E*, Vol.74, 046704

The 4th International Symposium on Fluid Machinery and Fluid Engineering
November 24-27, 2008, Beijing, China
NO. 4ISFMFE-Ab18

Numerical Solution of Navier-Stokes Equations for Separating and Reattaching Flow over a Double Steps Expansion and Contraction

Khaled Alhussan

Associate Research Professor, Deputy Director of Space Research Institute
King Abdulaziz City for Science and Technology, Riyadh, Kingdom of Saudi Arabia
Tel: +966-1-4814508/ Fax: +966-1-4813845
E-mail: alhussan@kacst.edu.sa

Abstract This paper shows a numerical solution for Navier-Stokes equations for well known flow phenomenon; the flow separation and the boundary layer reattaching of a double steps expansion and contraction channel. This paper discusses research variables that directly impact the ability to obtain non-circulating flow and techniques to reduce flow separation. This study shows that the separation and the circulation of the flow can be minimized and that is by injecting cross flow (90-degrees) with a magnitude of 0.2 of the inlet velocity.

Keywords numerical analysis, navier-stokes equations, fluid mechanics, flow separations

1 Introduction

Flow separation from the surface of a solid boundaries, and the determination of global changes in the flow field that develop as a result of the flow separation, are the most difficult and fundamental problems of fluid dynamics. Gases and water have extremely small viscosity and, therefore, most practical flows are characterized by very large values of the Reynolds number; both theory and experiment show that increasing Reynolds number almost invariably results in flow separation.

The difference between a separated flow and its theoretical unseparated flow concerns not only the form of trajectories of fluid particles, but also the value of aerodynamic forces acting on the body. Separation imposes a considerable limitation and lead to a significant degradation of total performance. For example, separation is usually accompanied by a loss of the lift force and sharp increase of the drag at the reattachment region. The boundary layer separates from the surface forms a free shear layer and is highly unstable. This shear layer will eventually roll into a discrete vortex and detach from the surface.

The work to be presented herein is a theoretical and numerical analysis of the complex fluid mechanism that occur inside double steps expansion and contraction channel, specifically with regard to the recirculation and flow separation. A number of important conclusions follow from the current research. First, study of the actual flow configuration offers some insight into the complex flow phenomena. Second, the characteristics of the recirculation and flow separation change considerably with the velocity vectors. This research showed the numerical solution for flow inside double steps expansion and contraction duct.

2 Theoritical and Numerical Disscusion

The main problem here is to determine velocity field and the states of the fluid: its pressure and density at all time and all space. There are four unknowns u, v, w, and p. with three independent variables x, y, and z. Hence four independent equations for these four unknowns are needed. The equations for the conservation of mass and momentum are written in terms of the dependent variables velocity, and pressure. In steady laminar flow,

the instantaneous value of a variable at any given position and time in space is equal to its mean value.

Equation of continuity expresses the conservation of mass of the medium. Conservation of mass requires that mass can neither be destroyed nor created. In many engineering applications sometime it is preferable to write the natural equation, by using the index notation, especially when dealing with numerical analysis Alhussan (2005). The continuity equation in index notation is therefore:

$$\frac{\partial \rho}{\partial t}+\frac{\partial}{\partial x_j}\left(\rho \vec{V_j}\right)=0 \tag{1}$$

In this equation, $\vec{V_j}$ represents the three-dimensional velocity vector components of the flow.

There are three equations of motion which express the conservation of momentum.

$$\vec{F}=m\vec{a}=\frac{d}{dt}\left(m\vec{V}\right) \tag{2}$$

The differential form of the momentum equation is:

$$\rho\frac{D\overline{V}}{Dt}=\rho\overline{F}+\overline{\nabla}\cdot\overline{\overline{T}} \tag{3}$$

where $\overline{\overline{T}}$ is the stress tensor, and the constitutive model is:

$$\overline{\overline{T}}=\left(-P+\lambda\overline{\nabla}\cdot\overline{V}\right)\overline{\overline{I}}+2\mu\overline{\overline{e}} \tag{4}$$

where, p is thermodynamic pressure, λ is the bulk viscosity where ($\lambda=\frac{2}{3}\mu$), $\overline{\overline{I}}$ is the identity tensor and $\overline{\overline{e}}$, is the deformation tensor. The momentum equation is therefore:

$$\rho\frac{D\overline{V}}{Dt}=\rho\overline{F}+\overline{\nabla}\cdot\left[\left(-p+\lambda\left(\overline{\nabla}\cdot\overline{V}\right)\overline{\overline{I}}\right)+2\mu\overline{\overline{e}}\right] \tag{5}$$

One may write the shear stresses (viscous forces) as:

$$\tau_{xx}=\lambda\nabla.\vec{V}+2\mu\frac{\partial u}{\partial x} \tag{6}$$

$$\tau_{yy}=\lambda\nabla.\vec{V}+2\mu\frac{\partial v}{\partial y} \tag{7}$$

$$\tau_{zz}=\lambda\nabla.\vec{V}+2\mu\frac{\partial w}{\partial z} \tag{8}$$

$$\tau_{xy}=\tau_{yx}=\mu\left(\frac{\partial v}{\partial x}+\frac{\partial u}{\partial y}\right) \tag{9}$$

$$\tau_{xy}=\tau_{yx}=\mu\left(\frac{\partial v}{\partial x}+\frac{\partial u}{\partial y}\right) \tag{10}$$

$$\tau_{yz}=\tau_{zy}=\mu\left(\frac{\partial w}{\partial y}+\frac{\partial v}{\partial z}\right) \tag{11}$$

The x-momentum therefore is:

$$\frac{\partial(\rho u)}{\partial t}+\nabla.(\rho u\vec{V})=-\frac{\partial p}{\partial x}+\frac{\partial \tau_{xx}}{\partial x}+\frac{\partial \tau_{yx}}{\partial y}+\frac{\partial \tau_{zx}}{\partial z}+\rho f_x \tag{12}$$

The y-momentum therefore is:

$$\frac{\partial(\rho v)}{\partial t}+\nabla.(\rho v\vec{V})=-\frac{\partial p}{\partial y}+\frac{\partial \tau_{xy}}{\partial x}+\frac{\partial \tau_{yy}}{\partial y}+\frac{\partial \tau_{zy}}{\partial z}+\rho f_y \tag{13}$$

The z-momentum therefore is:

$$\frac{\partial(\rho w)}{\partial t}+\nabla.(pw\vec{V})=-\frac{\partial p}{\partial z}+\frac{\partial \tau_{xz}}{\partial x}+\frac{\partial \tau_{yz}}{\partial y}+\frac{\partial \tau_{zz}}{\partial z}+\rho f_z \tag{14}$$

The momentum equation can be written in tensor form where the shear stress tensor is used. The shear stress (viscous) tensor for Newtonian (linear fluid) therefore is:

$$\tau_{ij}=\mu\left(\frac{\partial u_i}{\partial x_j}+\frac{\partial u_j}{\partial x_i}\right)+\delta_{ij}\lambda\overline{\nabla}\cdot\overline{V} \tag{15}$$

Where δ_{ij} is the kronecker delta and δ_{ij} =1 for i=j and δ_{ij} =0 for i≠j, the momentum equation in tensor form is:

$$\frac{\partial}{\partial t}\left(\rho\overline{u_i}\right)+\frac{\partial}{\partial x_j}\left(\rho\overline{u}_i\overline{u}_j\right)=-\frac{\partial p}{\partial x_i}-\frac{\partial \tau_{ij}}{\partial x_j}+\rho\overline{f}_i \tag{16}$$

The three terms on the right-hand side of Eq. 16 represent the x-components of all forces due to the pressure, p, the viscous stress tensor,τ_{ij}, and the body force, f_i.

Now, after stating all the flow equations, mass, momentum, and the constitutive laws that govern the transport relations, it is time to formulate a solution. But, since, these equations are coupled nonlinear, partial differential equations, it is impossible to have a closed form of solution. In order to formulate or approximate a valid solution for these equations they must be solved using computational fluid dynamics technique. In order to solve these equations numerically with a computer, they must be discretized. That is, the continuous control volume equations must be applied to each discrete control volume that is formed by the computational grid. The integral equations are substituted with a set of linear algebraic equations solved at a discrete set of points.

In a finite element discretization the grid breaks up the domain into elements over which the changes of the fluid variables are evaluated. Adding all the variations for each element then gives an overall visualization of how the variables vary over the entire domain. The primary advantage of the finite element method is the geometric flexibility allowed by a finite element grid. In a finite volume discretization the grid breaks up the domain into nodes, each associated with a discrete control volume. The fluxes of mass and momentum for each control volume are then calculated at each node. An advantage of the finite volume method is that the principles of mass, momentum, and energy conservation are applied directly to each control volume, so that the integral conservation of quantities is exactly satisfied for any set of control volumes in the domain. Thus, even for a coarse grid, there is an exact integral flux balance, Alhussan (2005), Bourdon et al. (2003), Vuik (1993), Young et al. (1989), Stern et al. (1988), Stone (1968) and Kan (1986).

A numerical analysis must start with breaking the computational domain into discrete sub-domains, which is the grid generation process. A grid must be provided in terms of the spatial coordinates (x, y and z location) of grid nodes distributed throughout the computational domain. At each node in the domain, the numerical analysis will determine values for all dependent variables including pressure and velocity components. The nodes must be distributed throughout the volume enclosed by the exterior boundary surface of the domain such that they form a complete three-dimensional matrix of nodes. Each node in the matrix will be referred to by the index triplet (i, j, k).

Discretization is the process whereby the governing equations are converted by their discrete form. Discretization identifies the node locations and flux elements to model the flow problem. The differential equations are transformed to algebraic equations, which should correctly approximate the transport properties of the physical processes. Next, the fluxes are evaluated at integration points, which are shared by adjacent control volumes. The same flux that leaves one control volume enters the next one. Thus, even with a low accuracy advection scheme numerical conservation is guaranteed. This is the fundamental advantage of a finite volume method. The discretization is evaluated in an elemental basis, Alhussan (2005).

3 Theoritical Disscusion

Flow separation from the surface of a solid boundaries, and the determination of global changes in the flow field that develop as a result of the flow separation, are the most difficult and fundamental problems of fluid dynamics. Gases and water have extremely small viscosity and, therefore, most practical flows are characterized by very large values of the Reynolds number; both theory and experiment show that increasing Reynolds number almost invariably results in flow separation, Nesteruk (2000) and Nesteruk (2003).

The difference between a separated flow and its theoretical unseparated flow concerns not only the form of trajectories of fluid particles, but also the value of aerodynamic forces acting on the body. For example, for blunt bodies in an incompressible flow, it is known from experimental studies that the drag force is not equal to zero. It does not approach zero as the Reynolds number becomes large. One of the most famous results of the inviscid flow theory is d'Alembert's paradox which says that solid bodies experience zero drag in incompressible flow. It is well known that this contradiction is associated with the assumption of a fully attached form of the flow; this case never happens in reality.

Separation imposes a considerable limitation and lead to a significant degradation of total performance. For example, separation is usually accompanied by a loss of the lift force and sharp increase of the drag at the reattachment region. The first attempts to describe flow separation past blunt bodies are due to Helmholtz (1868) and Kirchhoff (1869) in the analysis of the classical theory of inviscid fluid flows, but there was no adequate explanation as to why separation occurs. Prandtl (1904) was the first to recognize the physical cause of separation at high Reynolds numbers as being associated with the separation of boundary layers that must form on all solid surfaces, Bourdon et al. (2003), Nesteruk (2000) and Nesteruk (2003).

In accordance with the Prandtl's theory, a high Reynolds number flow past a rigid body has to be subdivided into two characteristic regions. The main part of the flow field may be treated as inviscid. However, for all Reynolds numbers, no matter how large, there always exists a thin region near the wall where the flow is predominantly viscous. Prandtl termed this region the boundary layer, and suggested that it is because of the specific behaviour of this layer that flow separation takes place. Flow development in the boundary layer depends on the pressure distribution along the wall. If the pressure gradient is favourable then the boundary layer remains well attached to the wall. However with adverse pressure gradient the boundary layer tends to separate from the body surface. The reason for separation was explained by Prandtl in the following way. Since the velocity in the

boundary layer drops towards the wall, the kinetic energy of fluid particles inside the boundary layer appears to be less than that at the outer edge of the boundary layer, in fact the closer a fluid particle is to the wall the smaller appears to be its kinetic energy. This means that while the pressure rise in the outer flow may be quite significant, the fluid particles inside the boundary layer may not be able to get over it. Even a small increase of pressure may cause the fluid particles near the wall to stop and then turn back to form a recirculating flow region characteristic of separated flows, Bourdon et al. (2003), Nesteruk (2000), Nesteruk (2003), Wesseling et al. (1992), Thangam et al. (1991), and Xu et al. (1993).

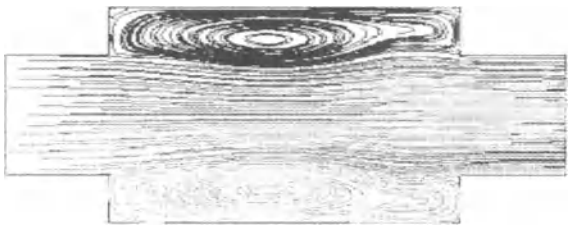

Fig. 1 Path lines of stream function showing flow for double step duct

Figure 1 shows the path lines for stream function of flow inside a double-step expansion and contraction duct. One can see the circulation in the top and bottom regions. However with adverse pressure gradient the boundary layer tends to separate from the body surface. Since the velocity in the boundary layer drops towards the wall, the kinetic energy of fluid particles inside the boundary layer appears to be less than that at the outer edge of the boundary layer, in fact the closer a fluid particle is to the wall the smaller appears to be its kinetic energy. This means that while the pressure rise in the outer flow may be quite significant, the fluid particles inside the boundary layer may not be able to get over it. Even a small increase of pressure may cause the fluid particles near the wall to stop and then turn back to form a recirculating flow region characteristic of separated flows.

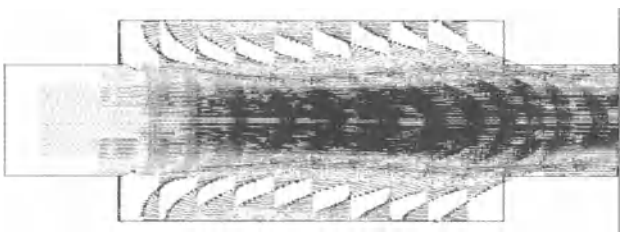

Fig. 2 Velocity vectors showing flow for double-step duct

Figure 2 shows the velocity vectors for the flow inside a double steps expansion and contraction channel. One can notice that the flow is uniform in the center and the recirculation is evident in the top and bottom surfaces. Figure 3 shows path lines of stream function for double-step expansion and contraction channel. This figure shows the injected velocity at the bottom surface of magnitude of 0.2 of the inlet velocity and a direction perpendicular to center line of the duct. Figure 4 shows path lines of stream function of flow inside a double-step expansion and contraction duct. In this figure the flow is injected from the top and the bottom walls as well the main inlet. One can see that the recirculation and the separation is minimized. The injected velocity from the top and bottom walls is perpendicular to the inlet velocity with a magnitude of 0.2 of the main inlet velocity.

Fig. 3 Path lines of stream function showing flow for double step duct with bottom surface injected velocity

4 Conculusion

This paper discusses research variables that directly impact the ability to obtain non-circulating flow and techniques to reduce flow separation. The governing equations are a set of coupled nonlinear, partial differential equations. In order to formulate or approximate a valid solution for these equations they must be solved using computational fluid dynamics techniques. To solve the equations numerically they must be discretized. That is, the continuous control volume equations must be applied to each discrete control volume that is formed by the computational grid. The integral equations are replaced with a set of linear algebraic equations solved at a discrete set of points.

This study shows that the separation and the circulation of the flow can be minimized and that is by injecting cross flow (90-degrees) with a magnitude of 0.2 of the inlet velocity. Figure 4 shows the path lines of the stream function for flow of double-step expansion and contraction duct where the desire characteristics of non-circulation flow were achieved.

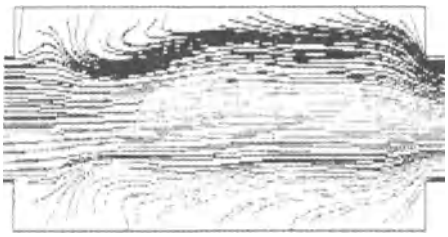

Fig. 4 Path lines of stream function showing flow for double step duct with top-bottom surfaces injected velocity

Acknowledgements

The author gratefully acknowledges sponsorship of this research from the Space Research Institute of the King Abdulaziz City for Science and Technology.

References

Alhussan, K., "Computational Analysis of High Speed Flow over a Double-Wedge for Air as Working Fluid", Proceedings of FEDSM2005 ASME Fluids Engineering Division Summer Meeting and Exhibition FEDSM2005-77441 June 19 – 23, 2005, Houston, TX, USA

Alhussan, K., "Study the Structure of Three Dimensional Oblique Shock Waves over conical rotor-Vane surfaces", Proceedings of FEDSM2005 ASME Fluids Engineering Division Summer Meeting and Exhibition FEDSM2005-77440 June 19 – 23, 2005, Houston, TX, USA

Alhussan, K., "Oblique Shock Waves Interaction in a Non-Steady Three Dimensional Rotating Flow", Proceedings of FEDSM2005 ASME Fluids Engineering Division Summer Meeting and Exhibition FEDSM2005-77442 June 19 – 23, 2005, Houston, TX, USA

Alhussan, K., "Application of Computational Fluid Dynamics in Discontinuous Unsteady Flow with Large Amplitude Changes; The shock Tube Problem" IASME Transaction Issue 1 Volume 2, pp 98 – 104, January 2005

Alhussan, K. "Supersonic Flow over Blunt Body with a Decelerator" IASME Transaction Issue 3 Volume 1, 98 – 104, August 2005

Bourdon, C. & Dutton, J. "Visualization of a Central Bleed Jet in an Axisymmetric Compressible Flow" Physics of Fluids, Vol. 15, No. 2 pp. 499 – 510, 2003

Vuik, C. "Solution of the discretized incompressible Navier-Stokes equations with the GMRES method" *Int. J. Numer. Meth. Fluids*, 16: 507 – 523, 1993

Yung, C-N., Keith, T.G. Jr., and de Witt, K.J. "Numerical simulation of axisymmetric turbulent flow in combustors and diffusers" *Int. J. Numer. Meth. Fluids*, 9: 167 – 183, 1989

Stern, F., Yoo, S.Y, and Patel, V.C. "Interactive and large-domain solutions of higher-order viscous-flow equations" *AIAA J.*, 26: 1052 – 1060, 1988

Stone, H.L. "Iterative solution of implicit approximations of multidimensional partial differential equations" *SIAM J. Numer. Anal.*, 5: 530 – 558, 1968

van Kan J.I.M. "A second-order accurate pressure correction method for viscous incompressible flow" *SIAM J. Sci. Stat. Comput.*, 7: 870 – 891, 1986

Zhu, J. and Leschziner, M.A. "A local oscillation-damping algorithm for higher order convection schemes" *Comput. Meth. Appl. Mech. Engng.*, 67: 355 – 366, 1988

Zhu, J. and Rodi, W. "Computation of axisymmetric confined jets in a diffuser" *Int. J. Numer. Meth. Fluids*, 14: 241 – 251, 1992

Nesteruk I., "Can Shapes with Negative Pressure Gradients Prevent Cavitation", Proceedings of FEDSM'03,4Th ASME_JSME Joint Fluids Engineering Conference, Honolulu, USA, July 6 – 11, 2003, No. FEDSM2003-45323

Nesteruk I., "Experimental Investigation of Axisymmetric Bodies with Negative Pressure Gradients", Aeronautical Journ., v. 104: 439 – 443, 2000

Wesseling, P, Segal, A. van Kan, .J.I.M., Oosterlee, C.W.and Kassels, C.G.M. "Finite volume discretization of the incompressible Navier-Stokes equations in general coordinates on staggered grids" *Comput. Fluid Dyn. J.*, 1: 27 – 33, 1992

Thangam, S. and Speziale, C.G. "Turbulent separated flow past a backward-facing step: a critical evaluation of two-equation turbulence models" ICASE Report 91-23, Institute for Computer Applications in Science and Engineering, NASA Langley Research Center, Hampton, Virginia, 1991

Xu, Z.G., Gotham, D.H.T. and Collins, M.W. "Numerical modelling of three-dimensional turbulent flow in packaged air-conditioning units with inclined heat exchangers" *Proc. Eighth Int. Conf. on Numer. Meth. Laminar and Turbulent Flow*, pages 328 – 337, Pineridge Press, Swansea, U.K., 1993

The 4th International Symposium on Fluid Machinery and Fluid Engineering
November 24-27, 2008, Beijing, China
NO. 4ISFMFE-Ab20

Computation of Several Turbulent Flows with the Des-Sa Model

Yang Guo[*1], Chisachi Kato[1], Yoshinobu Yamade[1] and Hong Wang[2]

[*1] Institute of Industrial Science, The University of Tokyo,
4-6-1 Komaba, Meguro-ku, Tokyo 153-8505, Japan
Tel: +81-3-5452-6686 / Fax: +81-3-5452-6662
E-mail: guoyang@iis.u-tokyo.ac.jp

[2] Institute of Nuclear and New Energy Technology, Tsinghua University,
Tsinghua Garden, Haidian District, Beijing 100084, China

Abstract Due to the high computational cost, well-resolved large-eddy simulation (LES) of wall-bounded turbulent flows at very high Reynolds number is still difficult. To deal with this issue, Detached-eddy simulation (DES) is used in engineering applications. In this study, several turbulent flows are computed with DES based on Spalart-Allmaras (SA) model. The performance of the DES-SA model is validated in fully developed turbulent channel flow, turbulent flow around a NACA0012 airfoil and turbulent flow in a centrifugal pump. In the channel flow, Delayed DES (DDES), which is the update version of DES, is also tested. The advantages and disadvantages of the DES-SA model are summarized. Possible approaches to improve the DES-SA model are discussed.

Keywords detached-eddy simulation, spalart-allmaras model, validation

Nomenclature

ν	molecular kinematic viscosity
$\tilde{\nu}$	working scalar related with turbulent viscosity
ν_t	turbulent viscosity
Δ	size of the grid filter
κ	Karman constant
c	chord length of airfoil
d	wall distance
d_{DES}	length scale of DES
d_{DDES}	length scale of DDES
d^*_{DES}	length scale of modified DES
d^*_{DDES}	length scale of modified DDES
D	diameter of the impeller of a pump
f	frequency
f_d	function to identity the flow state in DDES
H	total head of a pump
r_d	function to identity the flow state in DDES
Re	Reynolds number
St	non-dimensional frequency fc/U_0
u_i	velocity components
U_t	tip speed of the impeller of the pump

1 Introduction

Large-eddy simulation (LES) has become a powerful tool for engineering applications and encouraging computational results can be obtained by using LES. The main challenge of LES of wall-bounded turbulent flow is that the computational cost of a well-resolved LES is very high if the Reynolds number (Re) is very high, because the small vortices in the near-wall region play an active role and should be resolved by the computational mesh. Chapman (1979) estimated that the number of grid points in LES to resolve the wall layer is $N \sim Re^{1.8}$. Spalart et al. (1997) argued that for flow around an airplane wing at $Re=10^7$, the number of grid points that are necessary for a well-solved LES is at least 10^{11}. According to the above

estimations, if the Reynolds number is very high (>10^7), the computational cost of wall-resolved LES is too high to be applied in engineering.

Fröhlich and Rodi (2000) listed several approaches close to solid walls: (a) resolving the near-wall structure; (b) blending with a Reynolds-averaged Navier-Stokes Simulation (RANS) model; (c) application of a wall function and (d) determination of wall stress by boundary layer equation solved along the wall on an imbedded grid. Approach (a) is the most accurate method but with very high cost if Reynolds number is very high; Approach (b) combines an LES model with a RANS model. In the near-wall region, RANS model is used so that the number of mesh points can decrease; Approach (c) uses a wall-stress boundary condition instead of the non-slip condition; however, it is difficult to find a universal wall function for general cases; Approach (d) can be viewed as an improvement of approach (c) and by solving a boundary layer equation along the wall on an imbedded grid, better results than approach (c) can be obtained (see Wang and Moin 2002). However, the implementation of approach (d) is relatively complex and it is not very convenient to be used in complex geometry.

In engineering applications, hybrid RANS/LES methods are popular. Detached-eddy Simulation (DES) (see Spalart et al. 1997) and its updated version Delayed DES (DDES) (see Spalart et al. 2006) are best-known as the representative hybrid RANS/LES methods. The main target of this study is to validate the performance of DES based on Spalart-Allmaras (SA) model (see Spalart and Allmaras 1994) in several turbulent flows. The test cases include fully developed turbulent channel flow, turbulent flow around a NACA0012 airfoil and turbulent flow in a centrifugal pump.

2 DES-SA Model

The SA model (see Spalart and Allmaras 1992, 1994) solves a single transport equation for a working variable $\tilde{\nu}$ that is related to the turbulent viscosity. The DES formulation of the SA model is based on a modification to the length scale of the destruction term. The details of the model formulation can be found in Spalart et al. (1997). The following is the basic formulation of the transport equation,

$$\frac{D\tilde{\nu}}{Dt} = \frac{1}{\sigma}\left\{\nabla\cdot\left[(\nu+\tilde{\nu})\nabla\tilde{\nu}\right]+C_{b2}(\nabla\tilde{\nu})^2\right\} + C_{b1}\tilde{S}\tilde{\nu} - C_{w1}f_w\left[\frac{\tilde{\nu}}{d}\right]^2 \quad (1)$$

In the right-hand side of Eq. (1), the terms from left to right are diffusion term, production term and destruction term, respectively, where,

$$\tilde{S} \equiv S + \frac{\tilde{\nu}}{\kappa^2 d^2} f_{v2},\quad f_{v2} = 1 - \frac{\chi}{1+\chi f_{v1}} \quad (2)$$

$$f_w = g\left[\frac{1+C_{w3}^6}{g^6+C_{w3}^6}\right]^{1/6},\ g = r + C_{w2}\left(r^6 - r\right),\ r \equiv \frac{\tilde{\nu}}{\tilde{S}\kappa^2 d^2} \quad (3)$$

S is the magnitude of the vorticity vector and ν is the molecular viscosity. The turbulent viscosity ν_t is calculated by multiplying a damping function:

$$\nu_t = \tilde{\nu} f_{v1},\ f_{v1} = \frac{\chi^3}{\chi^3 + C_{v1}^3},\ \chi \equiv \frac{\tilde{\nu}}{\nu} \quad (4)$$

The model coefficients are given by,

$$\begin{aligned} &C_{b1} = 0.1355, \sigma = 2/3, C_{b2} = 0.622, \kappa = 0.41, \\ &C_{w1} = C_{b1}/\kappa^2 + (1+C_{b2})/\sigma, C_{w2} = 0.3, C_{w3} = 2, C_{v1} = 7.1 \end{aligned} \quad (5)$$

In the RANS formulation of SA model, d means the distance to the nearest wall. When DES formulation is used, in the region far from the wall, d in the destruction term is replaced by a length scale proportional to the local grid size, thus we obtain a kind of one-equation subgrid-scale (SGS) model. This modified length scale d_{DES} is taken as:

$$\begin{aligned} &d_{DES} \equiv \min(d_{RANS}, d_{LES}) \\ &d_{RANS} = d \\ &d_{LES} = C_{DES}\Delta_{\max},\ \Delta_{\max} = \max\left(\Delta x, \Delta y, \Delta z\right) \end{aligned} \quad (6)$$

C_{DES} is a model constant and a good value for C_{DES} is 0.65 (Shur et al. 1997). $\Delta x, \Delta y, \Delta z$ are the grid spaces in x, y, z direction. In Finite Element Method (FEM), $\Delta_{\max}$ can be calculated as the maximum side length of the grid element. By using DES, the attached eddies in the turbulent boundary layer are modeled by RANS, while the detached eddies outside the boundary layer are resolved with an SGS model. Thus the computational cost of DES can be much less than that of a well-resolved LES if the Reynolds number is very high.

Delayed detached-eddy simulation (DDES, see Spalart et al. 2006) is an update version of DES. In DDES, a function that is related to the flow field is adopted to identify if the grid point is in the boundary layer. The RANS mode is kept if the grid point is in the boundary layer, so that the entire boundary layer is modeled by RANS. DDES can avoid the grid-induced separation on ambiguous grid densities. The formulation of DDES uses the quantity

$$r_d \equiv \frac{\nu_t + \nu}{\sqrt{\frac{\partial u_i}{\partial x_j}\frac{\partial u_i}{\partial x_j}\kappa^2 d^2}} \tag{7}$$

A function f_d is defined as:

$$f_d \equiv 1 - \tanh\left[\left(8r_d\right)^3\right] \tag{8}$$

In DDES, the length scale is redefined as:

$$d_{DDES} \equiv d - f_d \max\left(0, d - C_{DES}\Delta_{\max}\right) \tag{9}$$

In the boundary layers, $f_d = 0$, d_{DDES} is equal to the wall distance, thus RANS mode is kept in the boundary layer. Outside the boundary layer, f_d=1, the new length scale is equal to the length scale of DES-SA.

In DDES, a low-Reynolds-number correction is also introduced to avoid damping of turbulent viscosity in the LES region when the Reynolds number is low (see Spalart et al. 2006).

The governing equations are filtered (in LES region) or Reynolds-averaged (in RANS region) continuity equation and momentum equations. For the numerical methods, Crank-Nicolson implicit scheme is used to integrate the momentum equations in time. For the spatial discretion, FEM is used. The scheme is with second-order accuracy both in time and space. Fractional-Step (FS) method is adopted to solve the pressure equation. Moreover, some special treatments are used in the present study. One is the treatment of source term in Eq. (1). We adopted a method proposed by Spalart and Allmaras (1992), where part of the source term may be treated implicitly to enhance the stability of the computation. The other is about the calculation of distance to the nearest wall. The method of Tucker (2003) is used, where a Poisson equation is solved to get the wall distance, therefore possible problems of the calculation of wall distance in the parallel computation by search method can be avoided.

3 Validation of the DES-SA Model

3.1 Fully developed plane channel flow

As a typical wall-bounded turbulent flow, fully developed plane channel flow at Re_τ=2000 (based on friction velocity U_τ and channel half-width h) was computed in a computational domain of $2\pi h \times 2h \times \pi h$ (streamwise, wall-normal and spanwise respectively) with 64×65×64 grid. The grid spaces in wall units are $\Delta y^+ = 1 \sim 214, \Delta x^+ = 200$, $\Delta z^+ = 100$ (x: streamwise, y: wall-normal, z: spanwise). The mesh is not fine enough to resolve the small eddies in the near-wall region. No-slip and cyclic boundary conditions are prescribed on the walls and the other two directions, respectively. The computational results of DES are compared with the LES results using Dynamic Smagorinsky Model (DSM) (see Germano et al. 1991, Lilly 1992), RANS-SA and the law of wall.

In this case, the DES-SA model acts as a wall model for LES (WMLES). Figure 1 shows the mean velocity profiles in the channel flow. Overall, the mean velocity profiles of DES-SA are better than that of LES with DSM using the same grid. However, mismatch of mean velocity profile can be detected in DES-SA. A solution of this problem can be found in Hamba (2003, 2005, 2006). In this method, an additional filter was added to eliminate the mismatch of the mean velocity profile and it was successfully applied to the channel flow (see Hamba 2003, 2005, 2006). For a general case, further extensions may be necessary.

Another point should be pointed out is that in the LES region of this case, the turbulent eddy viscosity predicted by DES-SA model is larger than that of DSM shown in Fig. 2. One possible reason is using the maximum side length of the element to calculate the local mesh size, which was also found by other researchers (see Breuer 2003).

To understand the effects of high turbulent viscosity near the center of the channel in DES, we (see Guo and Kato 2008) modified the definition of length scale in Eq. (6) by:

$$\begin{aligned} d^*_{DES} \equiv\ & C_{DES}\left(\Delta_{\max} + \Delta_{\min}\right)\tanh\left(\frac{d_{RANS}}{C_{DES}\Delta_{\max}}\right) \\ & - C_{DES}\Delta_{\max}\tanh\left(\frac{d_{RANS}\Delta_{\min}}{C_{DES}\Delta_{\max}^2}\right) \end{aligned} \tag{10}$$

where $\Delta_{\max} = \max\left(\Delta x, \Delta y, \Delta z\right)$, $\Delta_{\min} = \min\left(\Delta x, \Delta y, \Delta z\right)$, $\Delta_{\max}$ is calculated as the maximum side length of the grid element and $\Delta_{\min}$ is calculated as the minimum side length of the grid element. The length scale of Eq. (10) near the interface of RANS region and LES region is smoother than that of (6). In Eq. (10), the length scale will be close to wall distance in the near-wall region. While in the region that is very far from the wall, the new length scale is proportional to the minimum side length of the grid element. The DES-SA model with the modified length scale is denoted by modified DES-SA. In the context of DDES, the modified length scale is rewritten as:

$$d^*_{DDES} \equiv f_d d^*_{DES} + \left(1 - f_d\right) d_{RANS} \tag{11}$$

DDES-SA with the length scale of Eq. (11) is denoted by modified DDES-SA. It should be noted that when the mesh is close to cubic, the new length scale is close to the original length scale of DES-SA or DDES-SA model. However, in the real-world applications, the aspect ratio of the mesh may be high and in the region far from the wall, the new length scale is smaller than the original one, so that the predicted turbulent viscosity can be decreased, as shown in Fig. 2. Figure 1 indicates that the mean velocity profile predicted by modified DES-SA is also closer to the wall-law. However, the mismatch of the velocity profile cannot be solved by only modifying the length scale.

Delayed DES (DDES) based on SA model is also tested in this case. Multiple solutions are possible in this case by using DDES: one is steady RANS, the other is WMLES. Steady RANS using DDES-SA model is not our interest in this case. We use the results of LES-DSM as the initial field of DDES calculation to avoid the steady RANS results, so that DDES is used as a WMLES in this case. By using DDES, switch from RANS to LES is delayed and better prediction of mean velocity can be obtained as shown in Fig. 1. By the combination of DDES and the modification of the length scale, the level of turbulent viscosity can be reduced in the region near the center of the channel thus resolved shear stress in this region increases and further improvement of mean velocity profile can be obtained (see Fig. 1). Since the general problem of DES-SA as a WMLES is that the resolved shear stress is not enough (see Spalart et al. 2006), this modification of the length scale can be expected to improve the result. However, it should be noted that in theoretical sense, there is no guarantee that the mean velocity profile is prefect.

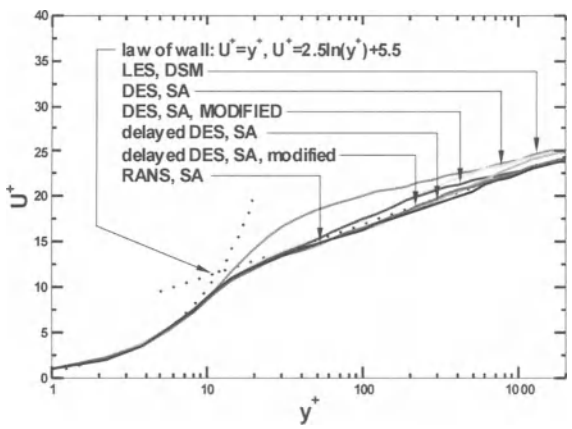

Fig. 1 Mean velocity distribution in channel flow at $Re = 2000$

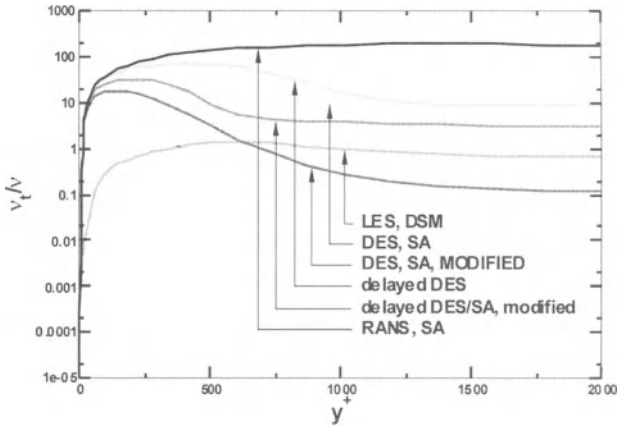

Fig. 2 Distribution of turbulent viscosity in channel flow at $Re = 2000$

3.2 Turbulent flow around a NACA0012 airfoil

This section will present the predictions of the turbulent flow around a two-dimensional NACA0012 airfoil. The flows at two Reynolds number 2×10^5 and 2.5×10^6 (based on the uniform velocity U_0 and the chord length c) with the angle of attack of 9 degrees were computed. The number of mesh elements is about 1.8 million. The turbulent boundary layer as well as the wake region is not resolved by this grid. We hope that we can obtain some reasonable results by using DES on this coarse mesh. A uniform velocity was specified at the inlet. The fluid traction was assumed to zero at the outlet and cyclic boundary condition was used in the spanwise end surfaces. Non-slip condition was used on the wall. The results of DDES-SA are not shown and they will be discussed in the future work.

Table 1 shows the comparison of lift and drag coefficients. The experimental data are from Suzuki (2006). In the result of LES with DSM, the lift coefficient is overpredicted and the drag coefficient is underpredicted. By using DES-SA model or RANS-SA model, the predicted lift coefficient decreases. In the $Re = 2 \times 10^5$ case the effects are not apparent, while in the $Re = 2.5\times 10^6$ case the effects are larger and the lift coefficient in this case is closer to the experimental data of Suzuki (2006). We checked the distribution of predicted turbulent viscosity shown in Fig. 3 and found that RANS-SA model gives a high turbulent viscosity in the wake. The turbulent eddy viscosity of the DES-SA model is slightly lower than that of the RANS-SA model, but still predicts a high turbulent viscosity in the wake, which is not a feature that we require. By modifying the length scale of DES-SA model, a reasonable turbulent viscosity field can be obtained, as shown in Fig. 3(d).

Figure 4 compares the computed power spectrum density (PSD) of streamwise velocity components at three points in the wake region (see Fig. 3(b)): Point A (x/c=1.135, y/c=0.036, z/c=0.1), Point B (x/c=1.283, y/c=0.06, z/c=0.1) and Point C (x/c=2.027, y/c=0.162, z/c=0.1), where the root mean square velocities have the maximum value along the line perpendicular to the free stream velocity. The computational results are compared with the experimental results of Miyazawa (2002). Due to the insufficient mesh resolution in the wake region, none of the computational results are very accurate. Here we make a qualitative comparison for the results. At Point A, the LES-DSM can predict the power spectrum density reasonably in the range of St=2~10, although it is higher than the experimental one. Due to the high turbulent viscosity in the wake region, the power spectrum densities in RANS-SA and DES-SA are much lower than that in LES-DSM. The modified DES-SA gives higher PSD than those of RANS-SA and DES-SA, but still lower than that of LES-DSM. At Point B, things are similar for RANS-SA and DES-SA, while the modified DES-SA can get closer PSD to that of LES-DSM, although is still lower than that of LES-DSM. At Point C, the modified DES-SA can get a little higher PSD than that of LES-DSM in the range of St=2~10. While the RANS-SA and the original DES-SA give much lower PSD than the experimental one. It demonstrates that if the sampling point is far enough from the wall, the modified DES-SA is better than the original DES-SA for predicting the velocity fluctuations.

Table 1 Comparison of lift and drag coefficients (Re=2×10^5 and Re=2.5×10^6, α=9 degrees, 1.8M mesh points)

	Re=2×10^5=9degrees		Re=2.5×10^6=9degrees	
	C_l	C_d	C_l	C_d
Exp. of Suzuki (2006)	0.766	0.0679	0.771	0.0352
LES/DSM	0.883	0.0390	0.918	0.0242
RANS/SA	0.841	0.0364	0.790	0.0471
DES/SA	0.838	0.0345	0.748	0.0449
DES/SA, Modified	0.850	0.0300	0.727	0.0450

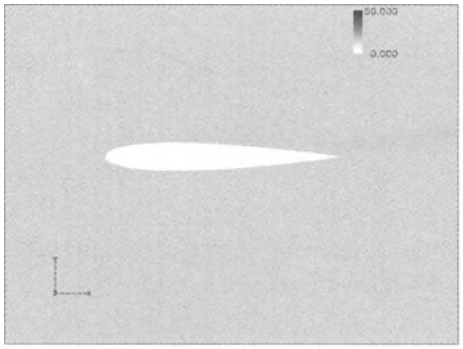

(a) LES-DSM

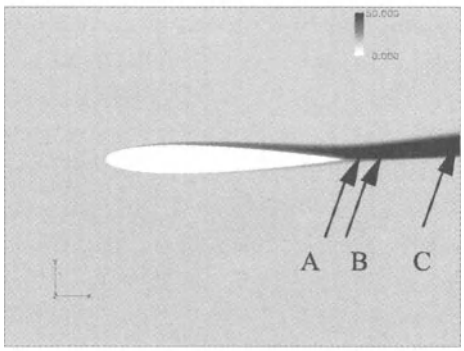

(b) RANS-SA

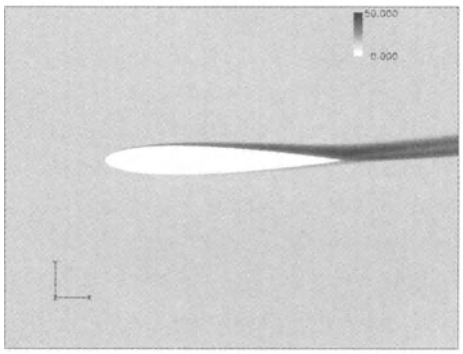

(c) DES-SA

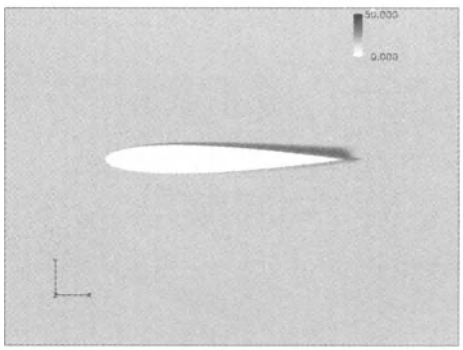

(d) DES-SA, modified

Fig. 3 Distribution of time-averaged normalized turbulent viscosity (ν_t/ν) in mid-span plane for flow around a NACA0012 airfoil at Re=2×10^5 and α=9 degrees

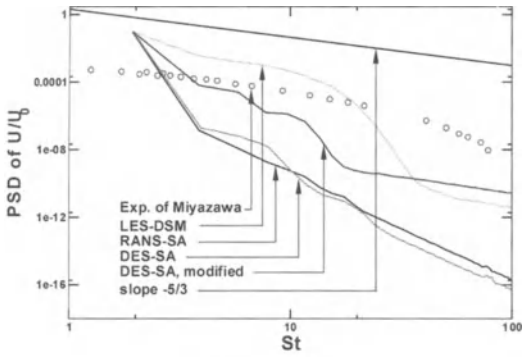

(a) Point A

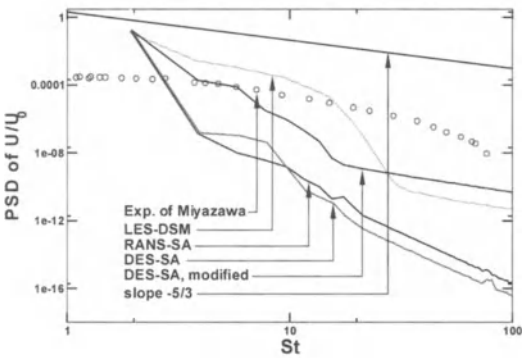

(b) Point B

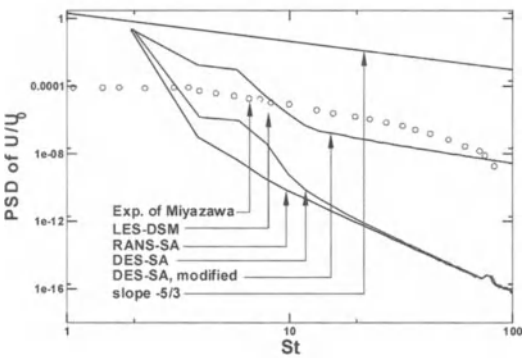

(c) Point C

Fig. 4 Power spectra of U-velocity component (U/U_0) at wake region for flow around a NACA0012 airfoil at Re=2×10^5 and α = 9 degrees

3.3 Turbulent flow in a centrifugal pump

Turbulent flow in a one-stage centrifugal pump was calculated. This case was already calculated by Wang et al. (2004) using LES. Here the purpose of this study is to compare the results of LES-DSM, RANS-SA and DES-SA. The computational domain is composed of an inlet pipe, an impeller, a diffuser and a return channel (see Fig. 5). The impeller is in the rotational frame and the other parts are in the stationary frame. The moving boundary interface is treated with overset method and the details of the method can be seen in Kato (2003). The total mesh points are about 4.7 million. In the impeller part, the number of mesh points per blade is about 0.2 million, which is not enough at all to resolve the turbulent boundary layer (TBL). The flow at the design point was calculated. The Reynolds number based on the tip velocity of the impeller (U_t) and the diameter of the impeller (D), is 9.62x10^6. The computational results are compared with the experimental data in Wang et al. (2004).

The comparison of total head is shown in Table 2. The total head is overpredicted in the DSM result. While in DES or RANS results, the prediction of the total head is improved. To understand the reason, the time-averaged relative velocity at the midspan of the impeller is shown in Fig. 6. The predicted boundary thickness is quite small in DSM result due to insufficient mesh resolution in the TBL. On the contrary, since TBL is modeled in the DES results, the boundary thickness is larger than that in DSM case, especially in the suction side of the blade. As a result, the main flow concentrates to the pressure side of the blade in DES-SA. The time-averaged field of RANS-SA and modified DES-SA are similar to that of DES-SA and they are not shown in Fig. 6. Since the loss due to turbulent mixing in TBL increases in DES-SA result, the total head decreases by using DES-SA, compared with that using LES-DSM and is closer to the experimental one (see Wang et al. 2004). RANS-SA and modified DES-SA give predicted total head similar to that in DES-SA results.

All of the computational results overpredict the Euler head. We assume that the ways by which the Euler head is calculated in the simulation and the experiment (see Wang et al. 2004) may be different. In the simulation, the Euler head is calculated by the change of angular momentum between the inlet and the outlet of the impeller. In the experiment, the Euler head may be estimated in a different way. The details of the experiment are helpful to clarify the problem and this will be done in the future.

The pressure fluctuation at one sampling point on the wall (Point 1, (x, y, z) = (0.57D, 0.053D, 0.61D)) and another point that is not on the wall (Point 2, (x, y, z)=(0, 0.51D, 0.65D)) (see Fig. 6(a)) in the diffuser are plotted in Fig. 7. The pressure fluctuation p^* is defined as: $p^* = 100\sqrt{S_{XX}(p)}/(\rho g H_0)$. $S_{XX}(p)$ is the power spectrum density of the pressure fluctuation and H_0 is the total head at the design point. The pressure fluctuation at Point 1 shows that the broadband fluctuation in LES-DSM agrees well with the experimental data (see Wang

et al. 2004). RANS-SA acts as a low-pass filter and underpredicts the fluctuation too much. The result of DES-SA is a little better than that of RANS-SA. The modified DES-SA give a better result but still underpredicts the pressure fluctuations. Because ensemble-average is used in the near-wall region in DES approach, the damping of resolved pressure fluctuation on the wall in the DES results can not be avoided. We think that it is one limitation of the current DES approach. The pressure fluctuation at Point 2 shows that in the region away from the wall, the predicted pressure fluctuation of modified DES-SA becomes closer to that of LES-DSM, compared with the case of Point 1. Note that the level of pressure fluctuation in the modified DES-SA result is still lower than that in DSM. We assume that the reason is that the point is still not far enough from the wall. In this case, since the flow channel is narrow in the diffuser, none of the sampling points in the diffuser are far enough from the wall, compared with the NACA0012 case. Thus it is reasonable that the pressure fluctuation in DES is still lower than that in LES-DSM even if the sampling point is away from the wall.

4 Discussions and Conclusion

Detached-eddy simulation (DES) is conducted in several turbulent flows including fully developed turbulent channel flow, turbulent flow around a NACA0012 airfoil and flow in a centrifugal pump. The advantages and disadvantages of DES-SA model can be concluded as: SA model solves a single transport equation in a single set of mesh and it is easy to be implemented. In the high-Re cases, the time-averaged result of DES-SA model is better than that of LES-DSM if the mesh resolution is not enough to resolve the turbulent boundary layer. However, since ensemble-average is used in the near-wall region in DES approach, the damping of resolved pressure fluctuation on the wall in the DES results can not be avoided. And for the DES-SA model, the performance in the LES region is not as good as in the RANS region. Especially the turbulent viscosity is overpredicted in LES region in general, which results in the damping of velocity and pressure fluctuations. Mismatch of velocity profile near the interface happens in the DES of channel flow at $Re_\tau = 2000$.

Some approaches to improve DES-SA model will be adopted in the future research. To solve the problem of the overprediction of the turbulent viscosity in LES region, using a more appropriate length scale is one option. By using this modified length scale, the predicted velocity or pressure fluctuations in the LES region are improved, if the sampling point is far enough from the wall. This method was validated in the channel flow at $Re_\tau = 2000$, flow around a NACA0012 airfoil, flow in a centrifugal pump and will be validated in more cases. For the mismatch of the mean velocity profile, the combination of DDES and the modification of length scale improves the result. However, a perfect solution for the mismatch problem is difficult to get. The method in Hamba (2003, 2005, 2006) will be helpful for the problem, but further investigation may be necessary to extend the method to general cases.

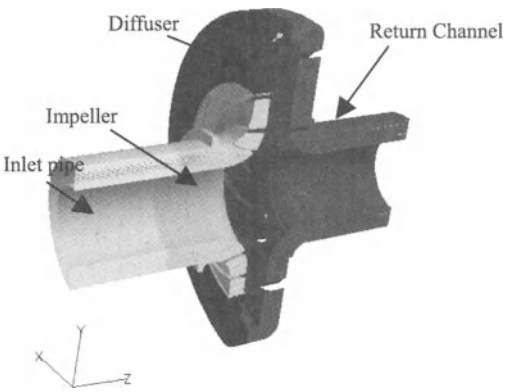

Fig. 5 Computational mesh for a diffuser pump, 4 part meshes of an inlet pipe, an impeller, a diffuser and a return channel

Table 2 Comparison of hydraulic performance at the design point (H: total head, H_{Euler}: Euler head)

Turbulence model	H/H_{exp}	$H_{Euler}/H_{Euler,exp}$
LES/DSM	115.9%	107.9%
RANS/SA	98.0%	109.9%
DES/SA	98.3%	110.3%
Modified DES/SA	101.6%	110.1%

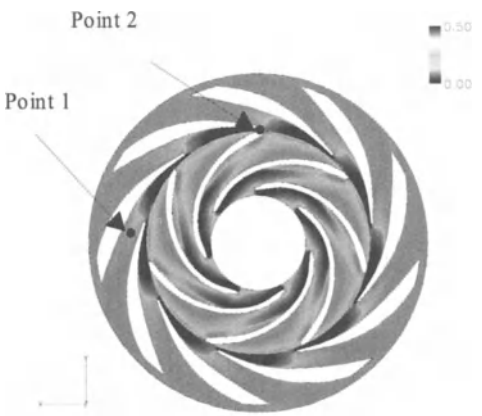

(a) LES-DSM

(b) DES-SA

Fig. 6 Distribution of the magnitude of the time-averaged relative velocity at the mid plane of the impeller

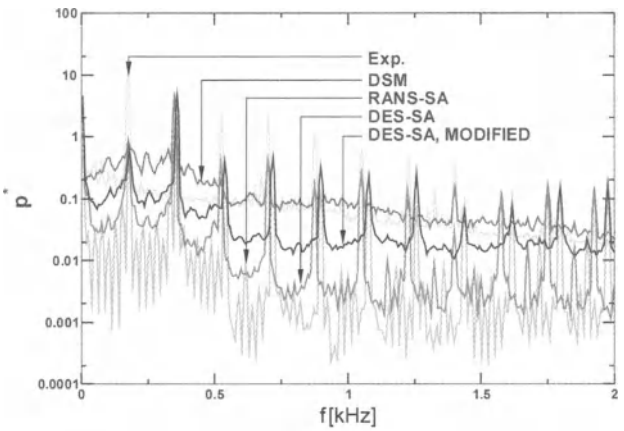

(a) Point 1

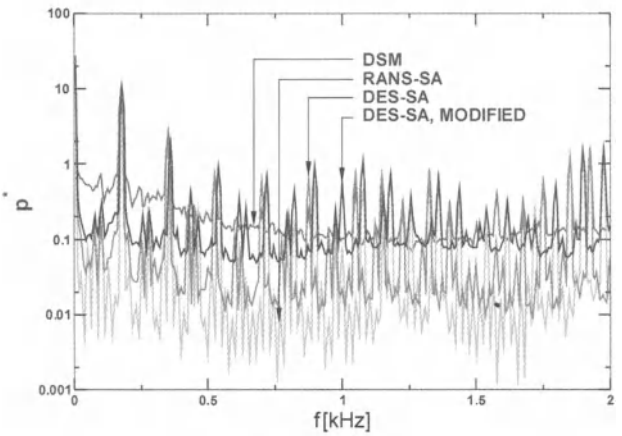

(b) Point 2

Fig. 7 Power spectra of the pressure sampled at the diffuser

Acknowledgements

A part of this research was done in "Revolutionary Simulation Software for the 21st century (RSS21)" project supported by Research and Development for Next-generation Information Technology of Ministry of Education, Culture, Sports, Science and Technology (MEXT), Japan.

References

Breuer, M., Jovicic, N., and Mazaev, K., 2003, "Comparison of DES, RANS and LES for the Separated Flow around a Flat Plate at High Incidence", *Int. J. Numer. Meth. Fluids*, Vol. 41, pp. 357 – 388

Chapman, D. R., 1979, "Computational Aerodynamics: Development and Outlook", *AIAA J.*, Vol. 17, No. 12, pp. 1293 – 1313

Fröhlich, J., and Rodi, W., 2000, "Introduction to Large Eddy Simulation of Turbulent flows", Closure Strategies for Turbulent and Transitional Flows, Launder, B. E. and Sandham N. D., eds., Cambridge University Press, Chap. 8

Germano, M., Piomelli, U., Moin, P., and Cabot, W. H., 1991, "A Dynamic Subgrid-Scale Eddy Viscosity Model", *Phys. Fluids A*, Vol. 3, No. 7, pp. 1760 – 1765

Guo, Y., and Kato, C., 2008, "Investigation of the Performance of DES-SA Model in Several Turbulent Flows", *Seisan Kenkyu*, Vol. 60, No. 1, pp. 75 – 80

Hamba, F., 2003, "A Hybrid RANS/LES Simulation of Turbulent Channel Flow", *Theoret. Comput. Fluid Dynamics*, Vol. 16, pp. 387 – 403

Hamba, F., 2005, "A Finite Difference Approximation to the RANS/LES Hybrid Filter", Proc. of the 19th Symposium on Computational Fluid Dynamics (in Japanese), No. E5-2

Hamba, F., 2006, "A Hybrid RANS/LES Simulation of High-Reynolds-number Channel Flow Using Additional Filtering at the Interface", *Theoret. Comput. Fluid Dynamics*, Vol. 20, No. 2, pp. 89 – 101

Kato, C., Kaiho, M., and Manabe, A., 2003, "An Overset Finite-Element Large-Eddy Simulation Method with Applications to Turbomachinery and Aeroacoustics", *ASME Journal of Applied Mechanics*, Vol. 70, No. 1, pp. 32 – 43

Lilly, D. K., 1992, "A Proposed Modification of the Germano Subgrid-scale Closure Method", *Phys. Fluids A*, Vol. 4, No. 3, pp. 633 – 635

Miyazawa, M., 2002, "Study of Unsteady Separated Flow around a Single Airfoil", Master's Thesis (in Japanese), The University of Tokyo

Shur, M., Spalart, P. R., Strelets, M., and Travin, A., 1999, "Detached-eddy Simulation of an Airfoil at High Angle of Attack", Fourth International Symposium on Engineering Turbulence Modelling and Experiments, Corsica

Spalart, P. R., and Allmaras, S. R., 1992, "A One-Equation Turbulence Model for Aerodynamic Flows", AIAA paper, No. 92-0439

Spalart, P. R., and Allmaras, S. R., 1994, "A One-Equation Turbulence Model for Aerodynamic Flows", *La Recherche Aérospatiale*, Vol. 1, pp. 5 – 21

Spalart, P. R., Jou, W.-H., Strelets, M., and Allmaras, S. R., 1997, "Comments on the Feasibility of LES for Wings, and on a Hybrid RANS/LES Approach", In: Liu, C. and Liu, Z. (eds), Advances in DNS/LES, Proceedings of 1st AFOSR International Conference on DNS/LES, Ruston, Greyden Press, pp. 137 – 147

Spalart, P. R., Deck, S., Shur, M. L., Squires, K. D., Strelets, M. Kh., and Travin, A., 2006, "A New Version of Detached-eddy Simulation, Resistant to Ambiguous Grid Densities", *Theoret. Comput. Fluid Dynamics*, Vol. 20, pp. 181 – 195

Suzuki, Y., Kato, C., Suzuki, T., and Fujita, H., 2007, "Aerodynamic and Aeroacoustical Characteristics of Low Reynolds Number Two-Dimensional Airfoil Flows", *Transactions of the Japan Society of Mechanical Engineers, Series B,* Vol. 73, No. 736, pp. 86 – 96

Tucker, P. G., 2003, "Differential Equation-based Wall Distance Computation for DES and RANS", *J. Comput. Phys.*, Vol. 190, pp. 229 – 248

Wang, H., Kato, C., Yamade, Y., Katsura, H., and Yoshida, T., 2004, "Fluid-Structure Coupled Analysis of a Multi-stage Centrifugal Pump 1st report: Large Eddy Simulation of Unsteady Flow in a Centrifugal Pump", *Seisan Kenkyu*, Vol. 56, No. 1, pp. 28 – 31

Wang, M., and Moin, P., 2002, "Dynamic Wall Modeling for Large-Eddy Simulation of Complex Turbulent Flows", *Phys. Fluids*, Vol. 14, No. 7, pp. 2043 – 2051

The 4th International Symposium on Fluid Machinery and Fluid Engineering
November 24-27, 2008, Beijing, China
NO. 4ISFMFE-Ch04

Comparative Study of Turbulence Models in Separated-Attached Diffuser Flow

Liu Chen*, Ailing Yang, Ren Dai and Kangmin Chen

* University of Shanghai for Science and Technology, College of Power Engineering,
JunGong Road 516#, PO25, Shanghai 200093, China
Tel: +86-021-5527-0508 / Fax: +86-021-5527-2376
E-mail: littleliu6@hotmail.com

Abstract Diffuser flow is characterized by locally attached separation bubble which is also common in compressor cascade flow. To predict the separation region accurately with RANS solvers, turbulence enclosure models are critical to the CFD ability to capture adequately the separation. In general two-equation models are regarded as practical choice and developed for diffusion flow, such as $k-\varepsilon$, $k-\omega$, shear stress transportation (SST), as well as v^2-f .In this paper, five common turbulence models were selected to predict the attached separation flow in an experiment-studied planar diffuser with the software FLUENT. $k-\varepsilon$ model failed to predict the attached separation. S-A model, Wilcox's $k-\omega$ model, SST $k-\omega$ model and v^2-f model predicted the separation bubble near the inclined wall and the S-A model's reattached length is longest while the v^2-f model is smallest. The $k-\omega$ model presented the same capability with SST model in capturing the separation bubble along the inclined wall of the diffuser but smaller gradient of velocity near wall in the outlet part.

Keywords planar diffuser, separated-attached flow, turbulence models

Nomenclature

C_f	Skin friction coefficient
C_p	Pressure coefficient
d	Distance from the closest surface in m
F_2	Blending function
H	Inlet channel height in m/s
v_T	Kinematic eddy viscosity in m^2/s
k	Turbulence kinetic energy in
S_{ij}	The strain-rate tensor
S	Magnitude of the vorticity
t	Time in s
T	Length scale in turbulence
u_0	Inlet velocity in m/s
u_i	Velocity component at i direction in m/s
y^+	Dimensionless, sublayer-scaled, distance
β^*	The closure coefficient
ε	Rate of dissipation
ρ	Mass density in kg/m^3
ω	Specific dissipation rate
Ω	The absolute value of the vorticity
$\tilde{v}$	Eddy viscosity in m^2/s
τ_{ij}	Stress tensor
σ^*	The closure coefficient

1 Introduction

A diffuser is a duct where the flow decreases and the static pressure increases as the fluid moves from inlet to outlet. It's used widely in gas turbine engines, aircraft and

jet engines for variety of purpose, such as supplying uniform flow in the head of combustor, or slowing the air delivered to the inlet face of the compressor or fan (Johnston 1998). Thus, study of the diffuser flow characteristic is important and method to predict the separation and attachment is one of the key challenges in flow simulation. Separation flows are difficult to predict because the separating and reattaching boundary layer are highly out of equilibrium. There are lots of experiments carried out toinvestigate the separation. Two-dimensional flow was investigated by Buice (2000) and Hoefener (2008). The velocity profile was obtained and the relationship with different inlet Reynolds number was presented. Cherry (2006) took the three-dimensional experiment to find out the characterization of the diffuser separation. A lot of numerical studies carried out using Large-Eddy Simulation (LES)were conducted by many researchers. The different kinds of turbulence models were compared. Investigation into the predictive performance of linear and non-linear eddy-viscosity models and differential stress-transport closures for separated flow in a nominally two-dimensional asymmetric diffuser was done by Apsley (1999) and Leschziner (2006). It was demonstrated that advanced turbulence models using strain-dependent coefficients and anisotropy-resolving closure offer tangible advantages in predictive capability, although the quality of their performance can vary significantly, depending on the details of closure approximations adopted. But the second-moment models investigated aren't uniformly better than simpler closure strategies; no model can be said, without qualification and purely on the basis of agreement with experiment, to be clearly superior or inferior to others. Cherry (2006) compared the RANS, LES and LES-fine grid and the results presented that RANS simulation strongly overpredict the strength of separation and the LES computations showed a much better agreement with the data, especially for the fine grid. LES of an incompressible planar, asymmetric diffuser flow was presented by Herbst (2007) with the dynamic smagorinsky model at different Reynolds numbers. It was found that the size of the main separation region is governed by inflow which penetrates further into diffuser at higher Reynolds number and increasing the Reynolds number a larger separated region is evident. Although there so many advanced models have been proposed to predict the separation, due to the limit of the computer resource, the common turbulence models are still widely used now.

Recently, there are many turbulent models developed but none of them is good enough (Wilcox 2001) and different problems required different closure models. In this paper, five common turbulence models are adopted in simulating the planar diffuser flow and the predictive abilities are compared and analyzed systematically in order to supply the foundation to choose turbulence models, modify the present models and develop the method modeling in multi-blocks.

2 Numerical Method

The incompressible Navier-Stokes equations were resolved to simulate the flow in planar diffuser shown as in Fig. 1. The SIMPLE method was adopted with the second order upwind scheme and center difference scheme used to discrete the convection terms and diffusion terms of N-S equations.

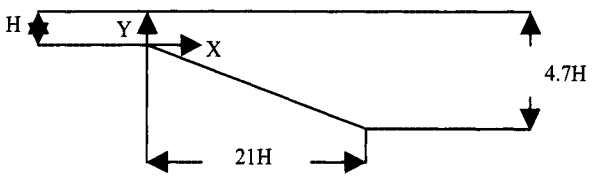

Fig. 1 Schematic of the planar diffuser

As shown above, the diffuser geometry was simple and all of the parameters were defined according to the experimental investigation (Buice & Eaton 2000). The computational domain includes fully developing duct (the length is of 10H which is enough to provide fully developed channel flow) and the outlet region (the length is of 27H). The diffusing section has a length of 21H, where H is the inlet channel height, and overall expansion ratio 4.7. The Reynolds number, based on an upstream average velocity and H, $Re = u_0 H / \nu = 2\times10^4$, H = 0.015m, the inlet velocity was 20 m/s. The grid was clustered at the walls to provide good resolution of the near wall region and the total mesh number is 240×50, shown in Fig. 2. According to the $y^+ < 5$,which is fine enough to make sure in the viscous sublayer, the first mesh layer is set and the real $y^+ < 1$ (minimum cell height $0.001H$).

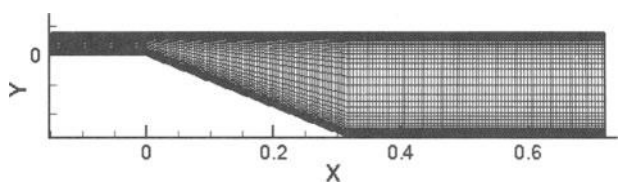

Fig. 2 Mesh for low-Re calculations

Boundary conditions were simple no-slip, adiabatic walls, and velocity inlet and pressure outlet. Five common turbulence models were chosen in this paper, stated as,

S-A model, standard $k-\varepsilon$ model with standard wall function, Wilcox's $k-\omega$ model, SST model and v^2-f model.

3 Turbulence Models

3.1 Spalart-allmaras model (Sparlart et al. 1992)

The transport equation for the turbulent viscosity of S-A model was assembled, using empiricism and arguments of dimensional analysis, Galilean invariance and selective dependence on the molecular viscosity. It's local and compatible with grids of any structure, benign near-wall behavior. Compared with two equation models, it is much easier to use and without wall function in near-wall problems. This model predicts no decay of the eddy viscosity in a uniform stream.

The S-A model is written in terms of the eddy viscosity and includes eight closure coefficients and three closure functions. Its defining equations are as follows.

$$\nu_T = \tilde{\nu} f_{v1} \tag{1}$$

$$\frac{\partial \tilde{\nu}}{\partial t} + u_j \frac{\partial \tilde{\nu}}{\partial x_j} = C_{b1}\tilde{S}\tilde{\nu} + \frac{1}{\sigma}\left[\frac{\partial}{\partial x_j}\left((\nu+\tilde{\nu})\frac{\partial \tilde{\nu}}{\partial x_j}\right) + C_{b2}\frac{\partial \tilde{\nu}}{\partial x_j}\frac{\partial \tilde{\nu}}{\partial x_j}\right]^2 - C_{w1} f_w \left(\frac{\tilde{\nu}}{d}\right)^2 \tag{2}$$

3.2 Standard $k-\varepsilon$ model (Wilcox 2006)

By far, $k-\varepsilon$ model is the most popular two-equation model until the last decades of the twentieth century. The standard $k-\varepsilon$ model is the Lauder-Aharama model. The idea is to derive the extra equation for ε and to find suitable approximation for the exact equation governing its behavior. It's a high Reynolds model and it's need wall function and fine grid in solving the near-wall problem. Its defining equations are as follows.

$$\mu_T = C_\mu k^2 / \varepsilon \tag{3}$$

$$\frac{\partial(\rho k)}{\partial t} + \frac{\partial(\rho k u_i)}{\partial x_i} = \frac{\partial}{\partial x_j}\left[\left(\nu + \frac{\nu_T}{\sigma_k}\right)\frac{\partial k}{\partial x_j}\right] + G_k - \rho\varepsilon \tag{4}$$

$$\frac{\partial(\rho \varepsilon)}{\partial t} + \frac{\partial(\rho \varepsilon u_i)}{\partial x_i} = \frac{\partial}{\partial x_j}\left[\left(\nu + \frac{\nu_T}{\sigma_\varepsilon}\right)\frac{\partial \varepsilon}{\partial x_j}\right] + C_{1\varepsilon}\frac{\varepsilon}{k}G_k - C_{2\varepsilon}\rho\frac{\varepsilon^2}{k} \tag{5}$$

3.3 Wilcox (2006) $k-\omega$ model (Wilcox 2006)

The most difference from the other two equation models is that the wall damping function is not needed in Wilcox (2006) model. It includes two equations about the turbulence kinetic energy k and the specific dissipation rate ω. Its defining equations are as follows.

$$\nu_t = \frac{k}{\tilde{\omega}} \tag{6}$$

$$\tilde{\omega} = \max\left\{\omega, C_{\lim}\sqrt{\frac{2S_{ij}S_{ij}}{\beta^*}}\right\}, C_{\lim} = \frac{7}{8} \tag{7}$$

$$\frac{\partial k}{\partial t} + u_j\frac{\partial k}{\partial x_j} = \tau_{ij}\frac{\partial u_i}{\partial x_j} - \beta^* k\omega + \frac{\partial}{\partial x_j}\left[\left(\nu + \sigma^*\frac{k}{\omega}\right)\frac{\partial k}{\partial x_j}\right] \tag{8}$$

$$\frac{\partial \omega}{\partial t} + u_j\frac{\partial \omega}{\partial x_j} = \alpha\frac{\omega}{k}\tau_{ij}\frac{\partial u_i}{\partial x_j} - \beta\omega^2 + \frac{\sigma_d}{\omega}\frac{\partial k}{\partial x_j}\frac{\partial \omega}{\partial x_j} + \frac{\partial}{\partial x_j}\left[\left(\nu + \sigma\frac{k}{\omega}\right)\frac{\partial \omega}{\partial x_j}\right] \tag{9}$$

3.4 SST $k-\omega$ model (Menter 1994)

The SST $k-\omega$ turbulence model combines two models, the $k-\omega$ and the $k-\varepsilon$. The use of a $k-\omega$ formulation in the inner parts of the boundary layer makes the model directly usable all the way down to the wall through the viscous sub-layer, and be used as a low-Re turbulence model without any extra damping function. The use of a $k-\varepsilon$ formulation in the free-stream can avoid the $k-\omega$ problem that is too sensitive to the inlet turbulence properties. Its defining equations are as follows.

$$\nu_T = \frac{a_1 k}{\max(a_1\omega, \Omega F_2)} \tag{10}$$

$$\frac{\partial \rho k}{\partial t} + \frac{\partial}{\partial x_j}\left[\rho u_j k - (\nu + \sigma_k \nu_T)\frac{\partial k}{\partial x_j}\right] = \tau_{ij}S_{ij} - \beta^*\rho\omega k \tag{11}$$

$$\frac{\partial \rho\omega}{\partial t} + \frac{\partial}{\partial x_j}\left[\rho u_j \omega - (\nu + \sigma_{\omega t}\nu_T)\frac{\partial \omega}{\partial x_j}\right] = P_\omega - \beta\rho\omega^2 + 2(1-F_1)\frac{\rho\sigma_{\omega 2}}{\omega}\frac{\partial k}{\partial x_j}\frac{\partial \omega}{\partial x_j} \tag{12}$$

3.5 v^2-f model (Durbin 1995)

The v^2-f model is similar with the standard $k-\varepsilon$ model but incorporates near-wall turbulence anisotropy and non-local pressure-stain effects. The distinguishing feature of the v^2-f model is its use of the velocity scale v^2 instead of the turbulent kinetic energy k for evaluating the eddy viscosity. Thus, it can provide the right scaling in representing the damping of turbulent transport close to the wall. Its defining equations are as follows.

$$\nu_T = \rho C_\mu v^2 T \tag{13}$$

$$\frac{\partial(\rho\varepsilon)}{\partial t} - \frac{\partial}{\partial x_j}\left[\left(\nu + \frac{\nu_T}{\sigma_\varepsilon}\right)\frac{\partial \varepsilon}{\partial x_j}\right] = \frac{C_{1\varepsilon}G_k - C_{2\varepsilon}\rho\varepsilon}{T} \tag{14}$$

$$\frac{\partial(\rho v^2)}{\partial t} - \frac{\partial}{\partial x_j}\left[\left(\nu + \frac{\nu_T}{\sigma_k}\right)\frac{\partial v^2}{\partial x_j}\right] = \rho k f_{22} - \rho v^2 \frac{\varepsilon}{k} \tag{15}$$

4 Results and Analysis

Important conclusions about turbulence models can only be drawn after all significant source of numerical contamination have been eliminated. Thus, the numerical

Simulation here with different models has same boundary conditions and the same grid mesh, for the $y^+ < 1$ can be accepted for all turbulence models.

Figure 3 shows the streamlines for diffuser flow as computed by the different models. The $k-\varepsilon$ model missed the separation which can be predicted by other four models. However, different models predicted different size of the separation bubbles. Table1. gives the approximate sites of separation and reattachment along the inclined wall. S-A model predicted the largest vortex. The SST and $k-\omega$ give the similar results and the v^2-f model produce the smallest vortex. According to Apsley (1999), profiles of u, v, $\overline{u^2}$, $\overline{v^2}$ were measured by two-component laster-doppler anemometry (LDA) at stations between X/H=3.2 and X/H=25.2. Thus, the most agreement with the data is the v^2-f model, though the separation is a little later.

Figure 4 indicates the wall shear-stress distribution for diffuser flow, shows that S-A model predicts the largest amount of separation, whereas the $k-\varepsilon$ model produce no separation. The SST and $k-\omega$ model produce very similar results. Figure 5 shows the inner turbulence viscous for different models. The $k-\varepsilon$ model provides the largest turbulent viscous in the diffuser passage, where the other four models obtain the similar results. After the reattachment point, the $k-\omega$ model became the worst and the v^2-f model always similar with S-A model.

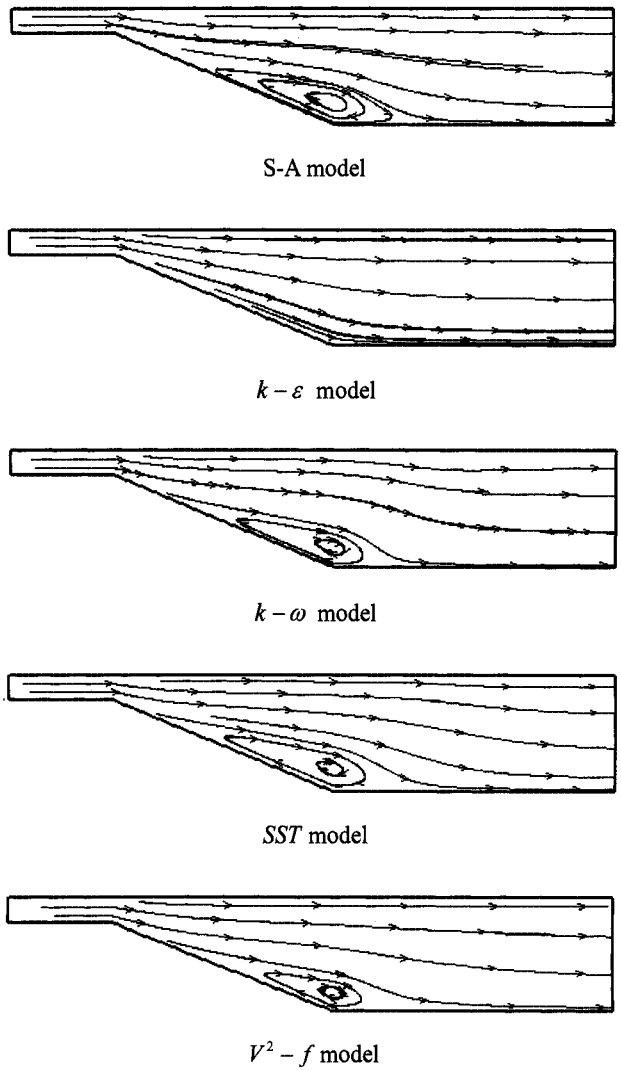

Fig. 3 Streamline for planar diffuser for different models

Table 1 The length of vortex for the planar diffuser

	Separation	reattachment	Length
SA	3.94	31.13	27.19
$k-\varepsilon$	0.00	0.00	0.00
$k-\omega$	0.60	26.40	25.80
SST	2.36	27.41	25.05
v^2-f	6.56	26.74	20.17

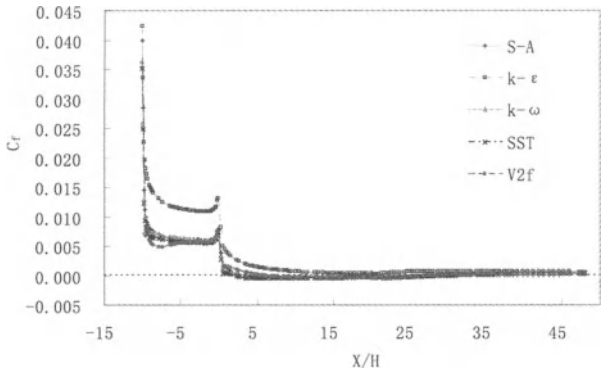

Fig. 4 Wall shear-stress distribution for the planar diffuser

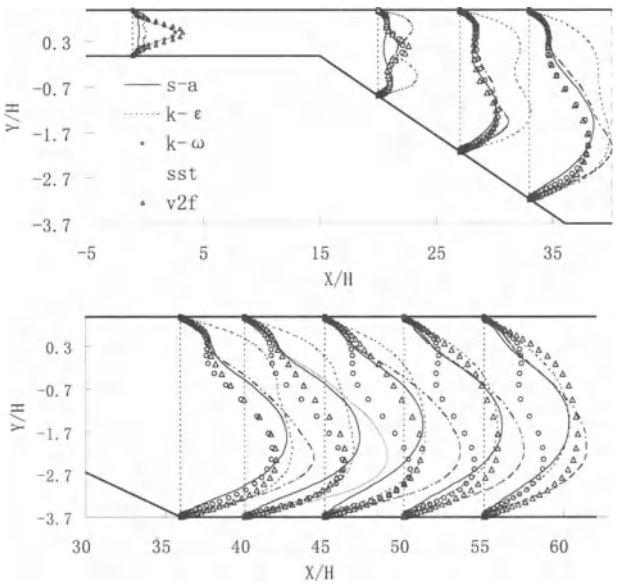

Fig. 5 Turbulent viscous for the planar diffuser

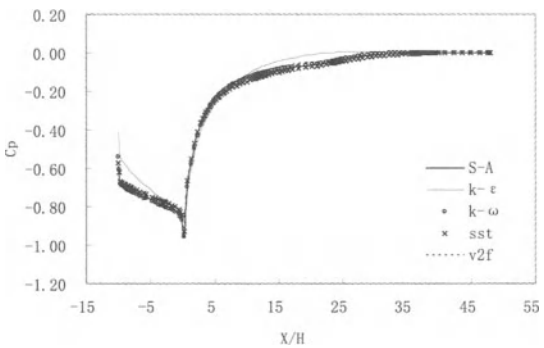

Fig. 6 Wall pressure distribution for the planar diffuser

Figure 6 shows a comparison of the pressure coefficient near the wall. The definition of the pressure coefficient is bellow.

$$c_p = \left(p - p_{ref}\right) / \left(\frac{1}{2}\rho u_\infty^{\ 2}\right) \tag{16}$$

All the distribution is close, except the $k-\varepsilon$ model.

The differences between the models can be seen in Fig.7, which shows the velocity profile. In the diffuser part, except the $k-\varepsilon$ model, the other models provide the similar results. However, after the reattachment, the $k-\omega$ model seems not well and it provides smaller gradient of velocity. The S-A model is consistent with the v^2-f model.

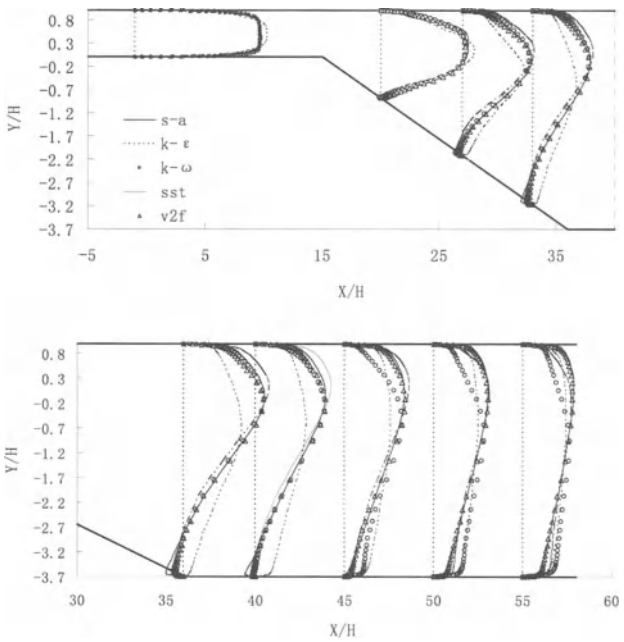

Fig. 7 Velocity profile for the planar diffuser at $X/H = -1,5,12,18,21,25,30,35,40$.

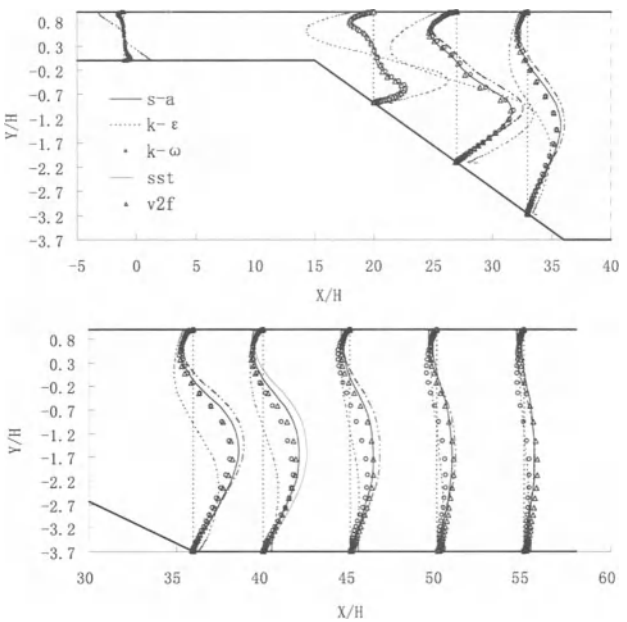

Fig. 8 Turbulent Stress profile for the planar diffuser

Figure 8 compares turbulent shear-stress profiles at different stations. The SST model obviously predicts variable shear-stress level than the other turbulence models and $k-\varepsilon$ model is more unstable in the region where separation is approached. The S-A and v^2-f model are very close to each other in all of the domain. After the reattachment point, $k-\omega$ model becomes lower than S-A, v^2-f SST models and became closer to $k-\varepsilon$ model.

5 Conclusions

The standard $k-\varepsilon$ model performs poorly when faced with non-equilibrium boundary layers. It tends to miss the separation bubble near the wall. Although the S-A model, Wilcox's $k-\omega$ model, SST $k-\omega$ model and v^2-f model can predict the separation bubble, the S-A model produces the longest attachment length and the v^2-f model is shortest. When the flow attaches, the Wilcox's $k-\omega$ model seems not well and produces small gradient of velocity near the wall.

References

Apsley, D.D. and Leschziner, M.A., 1999, "Advanced turbulence modeling of separated flow in a diffuser", Flow", *Turbulence and Combustion*, Vol.63, pp. 81 – 112

Buice, Carl.U. Eaton, John. K., 2000, "Experimental investigation of flow through an asymmetric planar diffuser", *Journal of fluids engineering*, Vol.5, pp. 433 – 435

Cherry, E.M. and G.Iaccarino, 2006, "Separated flow in a three-dimensional diffuser: preliminary validation", Center for Turbulence Research Annual Research Briefs

Durbin, P.A., 1995, "Separated flow computations with the model", *AIAA Journal*, Vol.33, pp. 659 – 664

Herbst A.H and Henningson D.S., 2007, "Simulations of turbulent flow in a planar asymmetric diffuser", *Flow turbulence combustion*, Vol.79, pp. 275 – 306

Hoefener, L. Nitsche, W, 2008, "Experimental investigations of controlled transition in a laminar separation bubble at an axisymmetric diffuser", *New results in numerical and experimental fluid mechanics VI*, Vol.96, pp. 244 – 251

Johnston, J.P., 1998, "Review: Diffuser Design and performance analysis by a unified integral method", Journal *of fluids engineerin*, Vol. 3, pp. 6 – 18

Leschziner, M.A and Wang, C. et al., 2006, "Contribution by ICSTM: modeling generic 2D and 3D separated flow using anisotropy-resoling turbulence closures", *Flomania-an European initiative on flow physics modeling*, Vol.94, pp. 77 – 84

Menter, Florian R., 1994, "Assessment of two-equation turbulence models for transonic flows", *AIAA-2343*

Spalart, P.R. and Allmaras, S.R., 1992, "A one-equation turbulence model for aerodynamic flows", *AIAA-0439*

Wilcox, D.C, 2006, "Turbulence model for CFD", *3rd ed. La Caflada, CA: DCW Industries, Inc*

Wilcox, D.C., 2001, "Turbulence modeling: An overview", *AIAA-0724*

The 4th International Symposium on Fluid Machinery and Fluid Engineering
November 24-27, 2008, Beijing, China
NO. 4ISFMFE-Ch34

Simulating the Blood Flow for the Aorta with a Stenosis

Ying Li[1], Xianwu Luo[*1], Mingkui Zhang[2], Yao Zhang[1], Shuhong Liu[1] and Hongyuan Xu[1]

[*1] State Key Laboratory of Hydroscience and Engineering, Tsinghua University, Beijing 100084, China
Tel: +86-010-6278-9853 / Fax: +86-010-6278-9853
E-mail: luoxw@tsinghua.edu.cn (Corresponding Author)
[2] The First Hospital of Tsinghua University, Chaoyang District, Beijing 100016, China

Abstract This paper treated the blood flow simulation for an aorta with the stenosis based on a clinical example. The physical model of the aorta was established by using the CT pictures. Based on the Reynolds averaged Navier-Stokes equations, three-dimensional turbulent flow were analyzed for the aorta. The numerical results indicated that: (1) the blood flow condition was greatly affected by the stenosis of an aorta. Both the steady and unsteady calculation had shown the same tendency as the clinical measurement; (2) with the existence of the stenosis, the velocity at the aorta greatly increased at the stenotic site. The large pressure-difference between upstream and downstream of the stenotic site, and wall shear stress larger than the critical value occurred; (3) The unsteady calculation depicted that the waves for the section-averaged velocity at the stenosis, the pressure-difference between the upstream and downstream of the stenosis, and the wall shear stress had different components, and their main pulses had different frequency. Those results provide very useful references for clinical treatments.

Keywords stènosis, aorta, wall shear stress, pressure difference, CFD

Nomenclature

d	diameter of vessel section [m]
f	frequency [Hz]
ρ	density of the fluid [g/cm^3]
p	static pressure [Pa]
Q	mass flow rate [g/s]
Re	Reynolds number
t	time [s]
T	period [s]
τ	wall shear stress [Pa]
υ	kinetic viscosity [(g/cm)/s]
v	velocity [m/s]

1 Introduction

The coarctation of aorta i.e. CoA is a kind of congenital deformity of great vessel, which has the percentage of 7%~14% for all congenital heart disease. CoA usually occurs at one's infant period. Since at the infant period of a patient, the constitution, function and immunity are not mature yet, the discovery and diagnosis at the early stage, and operative treatment in time are crucial for saving the life of the infant (Zou (2004)). In recent years, due to the dazzling advances of computing technology, many researchers have treated the flow analysis related to the aorta or stenosis (Yamaguchi (2006)). For examples, Qiu (2004) studied the blood flow at an aortic arch, Meng (2008) investigated the hemodynamics changes caused by arterial stenosis; Beratlis (2005) treated the pulsatile flow in a prototypical stenotic site by DNS and pointed out that before the peak mass flow rate, the strong confined jet that forms just downstream of the stenosis became unstable, forcing a role-up and subsequent breakdown of the shear layer, etc. It is clear that the stenosis greatly affects the blood flow for an aorta. However, many cases applied virtual models (vessels) and quantitative analysis was insufficiency, so that the numerical results could not provide enough practical aids for the cardiovascular surgery. In this paper, an aorta model is built based on the examination materials of a clinical case. The blood flow at the aorta with stenosis has been analyzed by using CFD method. The numerical results revealed the streak lines,

static pressure and pressure vibration, shear stress at vessel wall, etc. at the stenosis condition.

2 Physical Model

The physical model is based on an infant patient, who is 3-month-old and with the weight of 4.3kg. The scanned section is viewed by computed tomography, such as Fig. 1(a) is used to obtain the basic geometry of the aorta. It is noted that the stenotic site is located at the starting part of the descending aorta as shown at Fig. 1(b). Those section views which are two-dimensional pictures can be constructed to be a three-dimensional photography by the aid of software named as "Amira".

(a) CT scanned section view

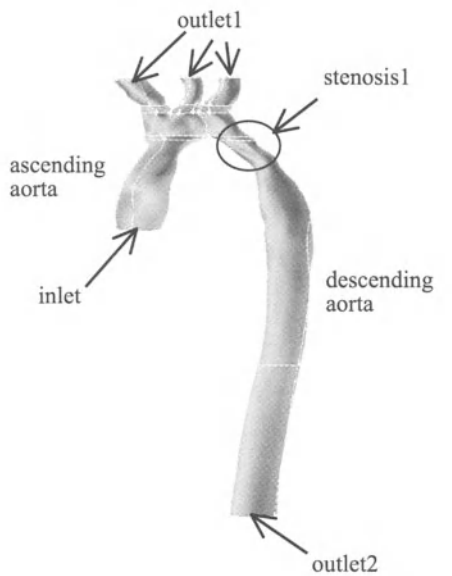

(b) External surface of aorta (calculation domain)

Fig. 1 Physical model of an aorta with stenosis

In order to get the real geometry of the aorta, the scale transformation should be conducted in three direction of x, y and z axis respectively. When every section of the aorta has the definite geometry, the calculation mesh can be generated based on the physical model. Fig. 1(b) shows the external surface of the aorta i.e. calculation domain by using Gambit software.

For numerical simulation, the mesh grid of calculation domain is generated. The total mesh cell number is 197479, which is the suitable mesh density for better calculation accuracy and acceptable convergence time consumption.

3 Simulation Methods

3.1 Basic assumptions

Though the blood flow is nonlinear, and the vessel wall is nonlinear elastic and with limited deformation, it is necessary to simplify the very complicated physical phenomena so as to solve the flow in the vessel. In this paper, the flow is treated as the homogeneous Newtonian flow, the vessel wall is regarded as rigid and its thickness is neglected. The density and kinetic viscosity are set as constants: ρ=1055 kg/m^3, υ=0.0035 (g/cm)/s.

3.2 Basic equations

Based on those assumptions, the conventional Reynolds averaged Navier-Stokes equations as well as continuity equations are applied without the consideration of gravitational force. It is known that the blood flow velocity at the inlet of calculation domain as shown at Fig.1(b) is $v_0 = 0.7 \sim 1.2$ m/s and the diameter of the vessel there is 0.008 m, then the Reynolds number of the flow will be:

$$Re = v \cdot d / \upsilon = 1688 \sim 2894 \quad (1)$$

Since the section dimension of the aorta changes rapid near the stenotic site, the maximum velocity of blood flow will be much larger than the averaged velocity of blood flow near 1.0 m/s, and the boundary layer would be unstable. Nakamura (2007) measured velocity and aorta vessel diameter by Cine Phase-contrast MRI, and reported the results of Reynolds number for three adult subjects: 3660, 3250, and 2670. Thus, the k - ω SST turbulence model would be better for the flow than laminar model.

The flow field is solved by a commercial CFD code named as CFX v11.

3.3 Boundary conditions

The vessel wall is treated as solid wall without velocity slip, so that the wall law is applied near the wall boundary. As shown at Fig. 1(b), the lower left vessel section is set as the inlet of calculation domain, where the blood flow velocity measured by ultrasonic velocimeter is assigned;

the upper sections as well as the bottom section are the outlet of calculation domain, where mass flow-rate is set.

For the unsteady calculation, Fig. 2 shows the distributed points and fitting curve of blood flow velocity. The cardiac cycle is 0.5s. Thus, the time-dependent velocity at the inlet is defined as the following equation:

$$v_0(t) = v_{0,0} + \sum_{i=1}^{6}(a_i \cos(i\omega t) + b_i \sin(i\omega t)) \qquad (2)$$

where $v_{0,0}$, a_i, and b_i are coefficients, m/s. $v_{0,0}$ =0.275, $\{a_i\}$={0.047, -0.317, -0.0044, 0.0317, 0.044, 0.020}^{T}, $\{b_i\}$={0.326, 0.0447, -0.160, -0.036, -0.013, 0.016}^{T}. Because the frequency f equals to 1/T i.e. 2Hz, $\omega = 2\pi f$ = 12.57. The time step is 0.01s, and the start time is 0.0 s.

For the steady-state calculation, the peak velocity of the measured point shown at Fig. 2 is chosen. The mass flow-rate at the inlet Q_0 is 64.978 g/s (corresponding velocity of 1.11 m/s), and that at outlet1 and outlet2 are 33.046 g/s and 31.932 g/s respectively (i.e. mass flow-rate ratio Q_1/Q_2 is 51:49). This mass flow-rate ratio for outlet1 Q_1 and outlet2 Q_2 is determined by clinical measurement. For the usual case of a healthy human being, the ratio Q_1/Q_2 is 26:74 based on the materials of Medonald (1982) and Wang (2005).

For the unsteady calculation, the mass flow-rate ratio is the same as the steady-state case i.e. Q_1/Q_2 = 51:49, though the mass flow-rate is time-dependent.

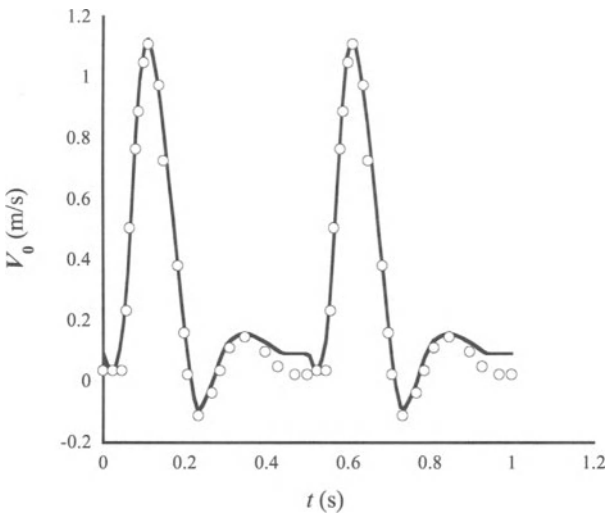

Fig. 2 Velocity at the inlet of the calculation domain

4 Results & Consideration

4.1 Flow pattern analysis for steady-state calculation

Based on the steady-state calculation, the results for the averaged flow are shown at Figs. 3 ~ 6.

Figure 3 shows the streak lines at the aorta. The color at Fig. 3 means the label of velocity with unit of m/s. It is noted that: (1) the velocity at the stenotic site is much larger than the inlet velocity. The calculated section averaged velocity at the stenosis is 3.5 m/s, which is a bit larger than the measured value of 3.4 m/s by ultrasonic velocimeter. This difference would be resulted from the fact that the vessel wall is elastic rather than rigid as assumed; (2) there is a jet flow forming at the stenotic site, and the maximum velocity is large than 4.5 m/s. The streak lines with low velocity are little; (3) the velocity downstream the stenosis becomes small. The streak lines seem to mix together. Those results may indicate that the flow near the stenosis is unstable, the boundary layer would be very thin, and the separation vortex occurs downstream the stenotic section. This phenomenon may be a breakdown of boundary layer as stated by Beratlis (2005).

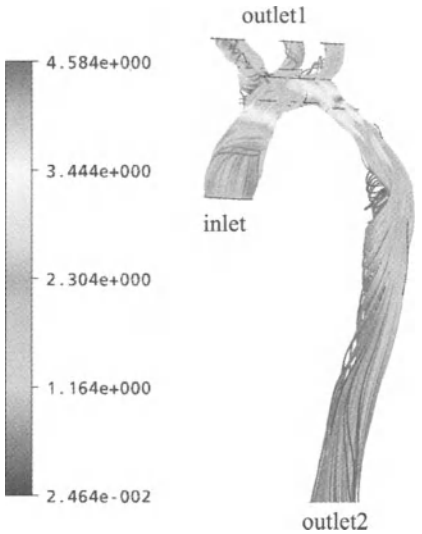

Fig. 3 Streak line at the aorta

Figure 4 shows the static pressure p_s at the aorta. The color means the level of static pressure with unit of Pa. It is noted that: (1) near the stenosis, the static pressure is lowest; (2) at the downstream of the stenotic site, the pressure is much lower than that upstream of the stenosis. This indicates that there is a large pressure drop when the blood flows through the stenotic site, which has been measured as 47 mmHg (i.e. 6.27 kPa). The rapid pressure drop between the upstream and downstream of the aorta is resulted from the flow blockage by the restricted section area at the stenosis. This blockage effect also results in the less flow-rate passing the stenosis to outlet2, and makes more blood flow towards outlet1 compared with the ordinary case.

It is also necessary to note that the too low static pressure at the downstream of the stenosis would induce cavitation

in the vessel. Then, cavitation erosion is dangerous for the blood cells and internal tissue of the vessel wall.

Figure 5 shows the wall shear stress τ at the aorta, and Fig. 6 shows the enlarged view of wall shear stress distribution at the circled area at Fig. 5 near the stenosis. Please note that two figures have the same legend levels for wall shear stress, which is marked by different color. The results indicated that: (1) the distribution of wall shear stress is not homogeneous, and the range is from 0.1 Pa to 393.8 Pa. The wall shear stress near the stenosis is much larger than other sites; (2) the averaged wall shear stress at the area of the stenosis is around 200 Pa, and the maximum value is 393.8 Pa. It is known that the critical wall shear stress which may result in tissue damage for the human vessel is 34.4 Pa. Thus, the maximum wall shear stress at the stenosis would be much larger than the critical value.

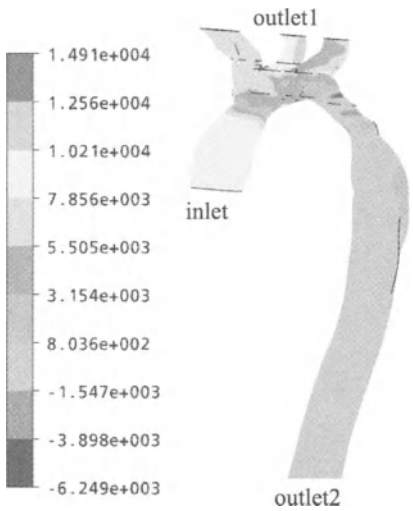

Fig. 4 Static pressure at the aorta

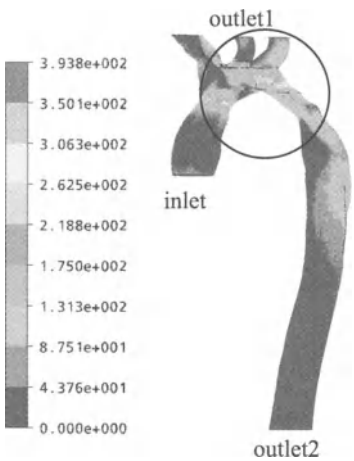

Fig. 5 Wall shear stress at the aorta

Fig. 6 Enlarged view of wall shear stress near the stenosis

Fukui (2007) evaluated the effect of wall motion (including longitudinal and radial direction) on the wall shear stress by applying fluid-solid coupling calculation, and reported that the wall shear stress would reduce 0.5~1.0 Pa for a usual case of a healthy human. Since the wall shear stress near the stenosis is much larger than the usual value for a healthy human such as 20 Pa, the effect of wall is possible to be neglected if only the effect of stenosis is considered.

It is well known that the wall shear stress within the usual value of the healthy human being is helpful for preventing the blood cell gather at the bifurcate and corner of the vessel. But high wall shear stress would tear out the blood cells and induce the damage of endothelial cells. Thus, very large wall shear stress resulted from stenosis is considerably dangerous, and it would result in vessel vulcanization and fracture, and even atherosclerosis.

From the averaged flow analysis, the flow condition inside the aorta can be observed clearly. The effect of stenosis on the blood flow such as large flow velocity at the stenotic site, rapid pressure drop between the upstream and downstream of the stenosis, and large wall shear stress is depicted. So, the direct reference is available for the clinical treatment by a doctor.

4.2 Unsteady flow behaviors

Figures 7~9 is the unsteady calculation results. For each figure of time-dependent curve, the data within 2 cycles i.e. 1.0 s are plotted.

Figure 7 shows time-dependent averaged velocity v_s at the stenotic section of the aorta and its power spectrum. The maximum velocity also occurs at the same time as the maximum inlet velocity. It is noted that there are two outstanding pulses at 2 Hz and 4 Hz (corresponding to 1

time and twice of the frequency of inlet velocity), and a minor pulse at 6Hz. Compared with the case of the setting velocity at the inlet where the outstanding pulse is at 2Hz and two minor pulses at 4Hz and 6Hz, the fraction with higher frequency becomes more intense at the stenosis. It is also observed that the largest value of velocity is around 3.5m/s, which is nearly the same as the steady calculation.

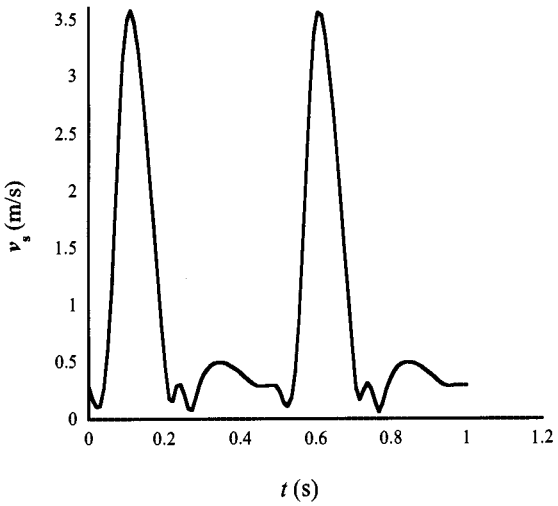

(a) Time-dependent velocity curve

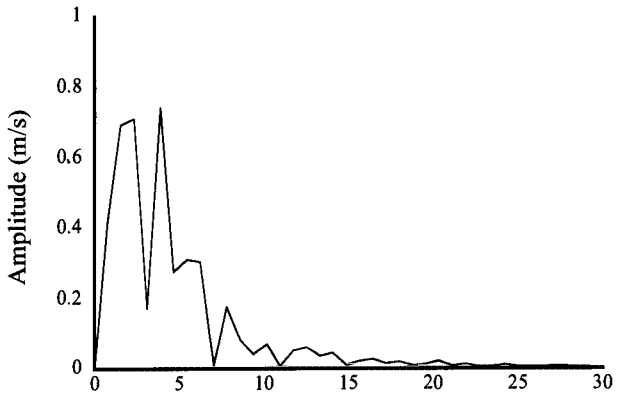

(b) Power spectrum

Fig. 7 Averaged velocity at the stenosis of the aorta

Figure 8 shows the section-averaged pressure-difference between the upstream and downstream of the stenosis of the aorta dp_s. It is noted that the pressure-difference is at the range of -3.15~39 mmHg. Though the maximum value is less than the measured value of 47 mmHg, it is much larger than the ordinary limit of 10 mmHg. The power spectrum indicates that the outstanding pulses are also at 2 Hz and 4 Hz, and the minor pulse occurs at 6 Hz. There are also many small pulses at 8 Hz, 10 Hz, etc. Please note that the maximum pressure difference occurs at 0.1s when the maximum inlet velocity occurs, and minimum pressure difference i.e. -3.15 mmHg occurs at 0.2s. The reverse pressure difference may indicate the drag of blood flowing through the stenotic site became large.

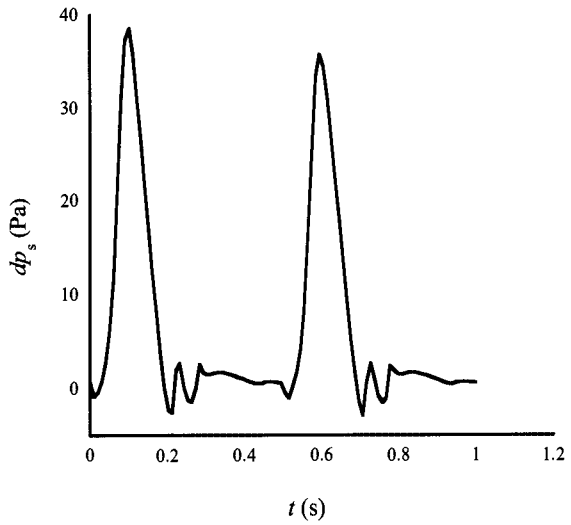

(a) Time-dependent curve

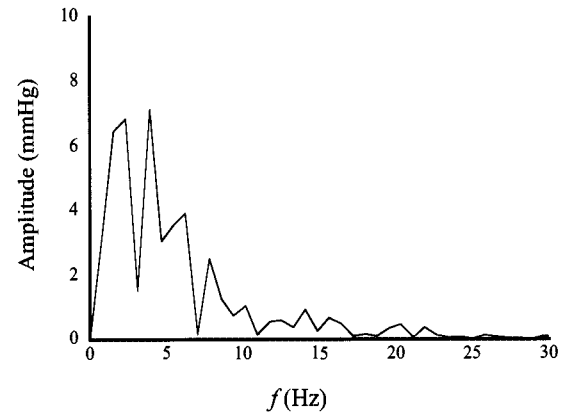

(b) Power spectrum

Fig. 8 Averaged pressure-difference between the upstream and downstream of the stenosis of the aorta

Figure 9 shows the maximum wall shear stress at the stenosis τ_{max}. The maximum value of wall shear stress is 395 Pa, which is very close to the result by the steady calculation, and occurs at 0.11s. It is noted that a main component of the wave with lower frequency than the inlet velocity i.e. 1 Hz is observed. Another outstanding pulse is at 2 Hz, and the minor pulse is at 3 Hz.

Based on both the steady-state calculation and unsteady calculation, the follows can be seen:

(1) The maximum velocity in the present case is larger than the normal standard;

(2) The maximum pressure difference between the upstream and downstream i.e. 47 mmHg is much larger than the standard value of 10 mmHg;

(3) The maximum wall shear stress as larger as 395 Pa is also much larger than the standard value of 34.4 Pa.

Thus, it is very obvious that the stenosis of the aorta is very dangerous and harmful to the patient.

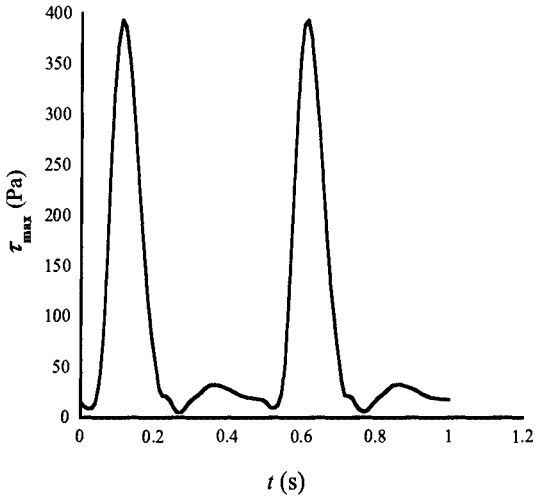

(a) Time-dependent

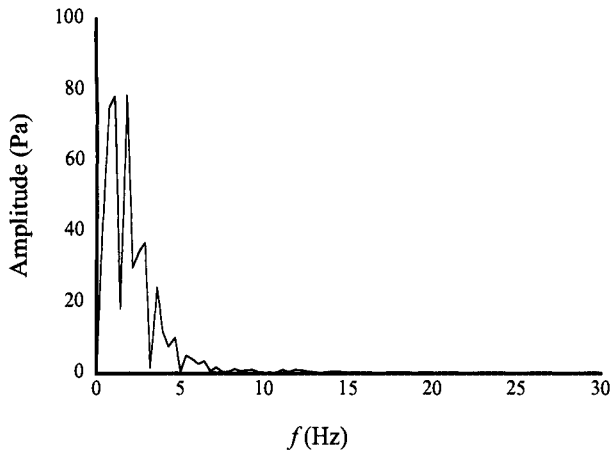

(b) Power spectrum

Fig. 9 Maximum wall shear stress at the stenosis of the aorta

5 Concluding Remarks

Based on those results, the following can be concluded:

(1) The blood flow condition was greatly affected by the stenosis of an aorta. Both the steady and unsteady calculation had shown the same tendency as the clinical measurement;

(2) With the existence of the stenosis, the velocity was much increased at the stenotic site. The large pressure-difference between upstream and downstream of the stenotic site, and wall shear stress much larger than the critical value occurred;

(3) The unsteady calculation depicted that the waves for the section-averaged velocity at the stenosis, the pressure-difference between the upstream and downstream of the stenosis, and the wall shear stress had different components, and their main pulses had different frequency.

Acknowledgements

The research is supported by National Natural Science Fund of China (No: 50676044) and Beijing Natural Science Foundation (No: 3072008). The supports are highly appreciated.

References

Beratlis, N., Balaras, E., Parvinian, B., et al., 2005, "A Numerical and Experimental Investigation of transitional Pulsatile Flow in a Stenosed Channel", *Journal of Biomechanical Engineering, Transactions of the ASME*, Vol. 127, pp. 1147 – 1157

Cheng, C. P., Parker, D., and Taylor, C. A., 2002, Quantification of Wall Shear Stress in Large Blood Vessels Using Lagrangian Interpolation Functions with Cine Phase-Contrast Magnetic Resonance Imaging, *Annals of Biomedical Engineering*, Vol. 30, pp. 1020 – 1032

Fukui, T., Parker, K. H., Imai, Y., et al., 2007, "Effect of Wall Motion on Arterial Wall Shear Stress", *Journal of Biomechanical Science and Engineering*, Vol. 2(2), pp. 58 – 68

Hayashi, S., Hayase, T., Shirai, A., et al., 2006, "Numerical Simulation of Noninvasive Blood Pressure Measurement", *Journal of Biomechanical Engineering, Transactions of the ASME*, Vol.128, pp. 680 – 687

Medonald, D. A., D.A., 1982, "Blood flow in the aorta", *Science Press*, Beijing (in Chinese)

Meng, Q. X., and Yang, B., 2008, "The Hemodynamics Caused by Arterial Stenosis", *Chinese Journal Medical Imaging Technology*, Vol. 24(2), pp. 297 – 300 (in Chinese)

Nakamura, M., Wada, S., Yokosawa, S., et al., 2007, "Measurement of Blood Flow in the Left Ventricle and Aorta Using Clinical 2D Cine Phase-Contrast Magnetic Resonance Imaging", *Journal of Biomechanical Science and Engineering*, Vol. 2(2), pp. 46 – 57

Qiu, L., Fan, Y. F., Dong, B. C., et al., 2004, "The Numerical Simulation of Pulsatile Flow in a Tapered Blood Vessel", *Journal of Biomedical Engineering*, Vol. 21, pp. 558 – 561 (in Chinese)

Wang, Z. W., Liu, W. Y., and Zhang, B. R., 2005, "Cardio Vascular Surgery", *People's Military Medical Press*, Beijing, pp. 251 – 260 (in Chinese)

Yamaguchi, T., Ishikawa, T., Tsubota, K., et al., 2006, "Computational Blood Flow Analysis-New Trends and Methods", *Journal of Biomechanical Science and Technology*, Vol. 1, pp. 29 – 50

Zou, J. Z., Cai, L. L., Wu, S., et al., 2004, "The pathological study of infantile coarctation of aorta-14 cases of pediatric autopsy", *Chinese Journal of Thoracic and Cardiovascular Surgery*, Vol. 20(6), pp. 344 – 347 (in Chinese)

The 4th International Symposium on Fluid Machinery and Fluid Engineering
November 24-27, 2008, Beijing, China
NO. 4ISFMFE-000

Through Flow Models for Engine Turbocharging and Exhaust Heat Recovery

Yangjun Zhang[*1], Weilin Zhuge[1], Shuyong Zhang[2] and Jianzhong Xu[3]

[*1] Engine Thermofluids Group, Dept. of Automotive Engineering, Tsinghua University, Beijing 10084, China
Tel: +86-010-6279-2333 / Fax: +86-010-6279-2333
E-mail: yjzhang@tsinghua.edu.cn (Corresponding Author)

[2] National Key Lab of Diesel Engine Turbocharging Tech., P.O.B 22, Datong, Shanxi 037036, China

[3] Institute of Engineering Thermophysics, Chinese Academy of Science, Beijing 100080, China

Abstract Transportation represents over 30% of energy consumption and 20% to 25% of the carbon dioxide (CO_2) release in the atmosphere, and the shares of which tend to increase. Energy consumption and CO_2 emission of engines are two indissociable factors. Advanced integrated energy system (IES) technology, which combines engine turbocharging system with turbo exhaust heat recovery system by through flow design and integrated cycle optimization, appears to be a promising way to improve engine efficiency and reduce CO_2 emissions. Compressor and turbine through flow models of a turbocharger or a turbogenerator for IES technology has been developed and validated. On the basis of through flow models, turbochargers / turbogenerators, intake and exhaust systems, and engine systems integration can be coordinately designed and optimized.

Keywords internal combustion engine, turbocharging, turbogenerating, integrated energy system, through flow models

1 Introduction

Energy consumption and CO_2 emission of an engine are two indissociable parameters. With over 30% of energy sources spent on transportation systems and 20 to 25% of the CO_2 emission (IEA, 2001), improving the efficiency of vehicle internal combustion engine power systems plays a critical role in the implementation of global energy conservation and environment protection strategies. Governments, industries, and universities around the world are investing significant resources and efforts in exploring a wide range of engine technologies, including variable compression ration, turbocharging, turbo exhaust heat recovery, and alternative propulsion concepts such as fuel cells.

Due to the engine emission control concern, internal combustion engine performance research has been focused on combustion and fueling control in the past. However, advanced combustion technologies do not perform as well on engine fuel economy and CO_2 reduction as they do on the emissions.

Turbocharging and turbo exhaust heat recovery technologies are today considered as promising ways for engine energy saving and CO_2 reduction. The advent of new turbocharging technologies, such as variable geometry turbochargers, two-stage or series turbocharging, sequential turbocharging, electric drive turbocharging, and, recovering the exhaust heat energy by turbogenerating technology, will boost the performance of the internal combustion engines, while adding complexity to turbo components design and system optimization. There are some basic rules of science which describe turbo components design and engine system optimization individually. The science itself has two names, Turbo Fluid Mechanics for turbo design and Engine Thermodynamics for system optimization. The proliferation of turbo design and system optimization requirements has expanded the turbo design and system optimization space, necessitated new strategy development processes, and demanded more efficient design and optimization technologies, thereby leading to an integration approach to thermodynamics and fluid mechanics principles, namely Engine Thermofluids.

The engine overall performance research nature and scope is described in Table 1.

Table 1 Engine performance research nature and scope

Scientific theory	Engine Combustion	Engine Thermofluids
Research focus	Fuel (oil)	Cycling fluid (gas)
Scientific problem	Fuel chemical energy to heat energy	Heat energy to mechanical work
Main objectives	Emission control	Cycle efficiency, CO_2 reduction
Key technologies	Fueling control, Combustion	Turbocharging, Turbo exhaust heat recovery

The engine performance is not simply related to performance of turbocharging and heat turbogenerating processes, but is determined in large part by the processes interaction during operation of the engine. An advanced integrated energy system methodology is proposed in this paper. The IES methodology combines engine turbocharging system with waste heat turbogenerating system, offers the potential for a significant increase in engine overall performance.

2 Engine IES Methodology

2.1 Turbo charging and heat recovery

Turbocharging for engine downsizing. Most of the time, and especially when the vehicle is driven at a constant speed, the engine is run under low load conditions. This leads to an poor engine efficiency especially for conventional existing gasoline engine. Today, much greater emphasis of turbocharging technology is being placed on downsizing the engines to increasing fuel economy and reducing CO2 emissions. Advanced turbocharging technology may reduce the engine displacement volume while keeping the same performance in terms of torque and power than the initial larger engine, and simultaneously to ensure an improvement in engine efficiency.

For example (Leduc P and Dubar B, 2003), typical power required to drive a mid-range car at a constant speed of 70 km/h is only about 7 kW. Considering an engine with a displacement of 2 *l* for example, these 7 kW represent only a very low load of 0.21MPa BMEP if the engine is run at 2000 rpm. Figure 1 shows a representative specific fuel consumption (SFC) map of current conventional gasoline engine. An engine functioning at BMEP = 0.21 MPa/2000 rpm is typically close to a SFC of 400 g/kWh. If the engine downsized by turbocharging to a 1 *l* total displacement, these 7 kW are produced with a load of 0.42 MPa and a SFC of about 300 g/kWh. For the same vehicle at the same 70 km/h constant speed, the use of the turbocharging technology represents a reduction in fuel consumption and CO_2 emissions of 25%, with running conditions closer to the best efficiency area. The turbocharging for engine downsizing could also less the friction losses.

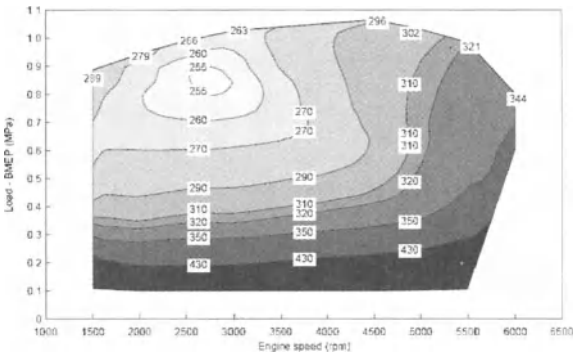

Fig. 1 Typical specific fuel consumption map of a conventional gasoline engine (g/kWh)

Turbogenerating for engine exhaust heat recovery. The energy from the fuel supplied to an internal combustion engine is balanced primarily by the energy converted to mechanical energy, the heat lost to the cooling system, and the energy carried away by the exhaust system. For example, only 25 percents of the fuel energy of one car engine is converted into net power and delivered to the wheels. If one kilogram of fuel burned, the total energy 100% contained in the fuel is distributed approximately in the following proportions: net power to the wheels 25%, cooling water 32%, exhaust gas heat 33%, and mechanical loss 10%. These proportions may vary with each vehicle model or engine type and operating mode (idle, full power or high-speed driving), etc, but they give a good view of where gains can be achieved to improve the overall engine thermal efficiency and reduce CO_2 emissions (Jansen W and Heitmann A M, 2008).

Recovery of heat energy from the engine exhaust represents a potential for at least a 10% improvement in the overall engine thermal efficiency. The efficiency of turbochargers use d to recover part of this energy could be increased from the current 50% to 58% to about 72% to 76% with enhancements such as variable geometry. An electrically driven turbocharger with increased transient response would be another approach.

Turbogenerating technology can recover and convert engine waste heat to useful energy and improve the overall thermal efficiency of diesel engines to greater than 55% while reducing emissions to near-zero levels. Specific goals of the FreedomCAR Partnership and the

21st Century Truck Partnership include the following: By 2010, enable commercially viable turbogenerating units that can produce more than 10 kilowatts (kW) of additional power from light-duty engine waste heat; By 2012, enable commercially viable turbogenerating units that can produce up to 40 kW of additional power from heavy-duty engine waste heat.

2.2 Integrated energy system methodology

Turbo charging and heat recovery technologies are today considered as promising ways for energy saving and CO2 reduction. Engine turbo charging or exhaust waste heat technology is the combination of internal combustion engine and turbomachines. The performance of a turbomachine is very dependent on the gas angles at entry to the impeller, diffuser and turbine rotor. Turbochargers or turbogenerators are designed and developed by turbomachinery experts, on the basis of turbomachinery fluid mechanics, without the consideration of engine system optimization, especially the off-design cycle optimization. Away from the design point, or existing flow field distortion, the gas angle will not match the blade angle and an incidence loss occurs due to separation and subsequent mixing of high and low-velocity fluid. These losses will increase with increasing incidence angle, hence turbo components are not well suited for operation over a wide flow range, and sensitive to the inlet flow fields.

However, an engine that is designed for variable speed operation is well suited to cater for a wide range of mass flow rate, and not sensitive to the inlet flowfield. It is clear that turbochargers or turbogenerators are not ideally suited to operate in conjunction with an engine. Matching of the correct turbochargers or turbogenerators to an internal combustion engine is of great importance and is vital for successful operation of an engine with turbomachines. IC engine cycle based matching is optimized by internal combustion engine experts, on the basis of IC engine thermodynamics, no turbomachines design optimization, and no effects of the inlet flowfield changes due to engine operations on turbomachinery performance have been considered. The methodology is illustrated in Fig. 2.

As mentioned above, the operation of turbomachines is fundamentally different from that of reciprocating engines, so a turbocharged engine or turbocompound engine with exhaust turbogenerating system has many complex characteristics. The turbocharged or turbocompound engine performance is not simply related to performance of turbocharging and turbogenerating processes, but is determined in large part by the processes interaction during operation of the turbocharger, turbogenerator and the engine, especially at off-design operations. It may well be necessary to improve the performance of the combination by turbocharger, turbogenerator and engine design changes at the same time, to encompass new considerations, streamlining component design and system integration, with the consideration of overall operation performance.

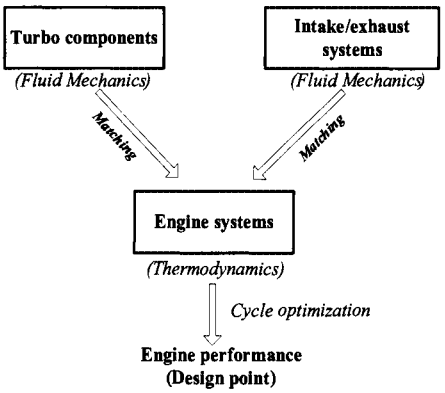

Fig. 2 Traditional methodology of engine turbo charging or heat recovery

Figure 3 illustrates a new technology methodology of engine intake turbocharging and exhaust heat turbogenerating, namely Integrated Energy System, IES technology. The IES technology combines engine intake turbocharging system and exhaust turbogenerating system by integrated cycle optimization. Turbochargers/ turbogenerators, intake and exhaust systems, and engine systems integration are coordinated designed and optimized on the basis of through flow models of turbomachines.

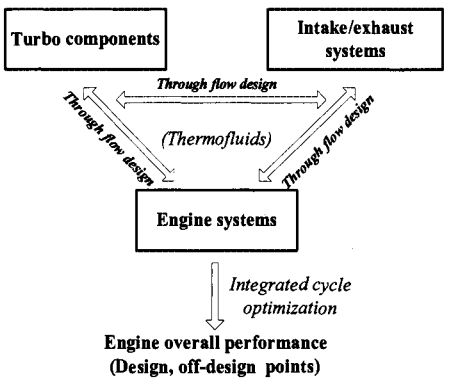

Fig. 3 Methodology of Integrated energy system for engine turbo charging and heat recovery technologies

The turbocharged or turbocompound engine consists of two different kind thermodynamic cycles that are connected

through working fluid (gas) flow. The first is a Diesel or Otto Cycle that the work and heat transfer occurs in a cylinder Closed System in non-flow process. The second is a Brayton or Rankine Cycle that the work and heat transfer occurs in a turbo Open System in flow process. The IES technology for efficient integration of turbomachinery and internal combustion engine systems needs to optimize the combined two kind cycles, i.e. integrated cycle optimization.

For traditional cycle optimization of engine turbo charging or exhaust heat recovery, the turbocharger or turbogenerator is defined as performance maps within the internal combustion engine cycle simulation tools, and it is impossible for IES integrated optimization for the turbomachines, intake/exhaust systems and combined engine cycles. One solution is a computational model of the turbocharger or turbogenerator concerned, namely through flow model, in which the performance of a turbocharger compressor, and a turbocharger or turbo-generator turbine, is determined based on the geometry instead of the performance maps. On the basis of through flow models, turbochargers / turbogenerators, intake and exhaust systems, and engine systems integration can be coordinated designed and optimized.

3 Turbocharger Compressor Through Flow Model

3.1 Mathematical model

The impeller flow is modeled using the two-zone modeling equations established by Japikse (1996). The basic idea of the two-zone model is that the impeller exit flow can be conceptually divided into a primary zone, an isentropic core flow region with high velocities, and a secondary zone, a low momentum non-isentropic region having all the losses occurring in the impeller. The primary zone and secondary zone reach static pressure balance at the impeller exit. The primary zone equations are given by:

$$W_{2p} = W_{1t} DR_2 \tag{1}$$

$$h_{2p} = (h_1 + W_1^2/2 - U_1^2/2) - W_{2p}^2/2 + U_2^2/2 \tag{2}$$

$$\frac{P_{2p}}{T_{2p}^{\frac{k}{k-1}}} = \frac{P_1}{T_1^{\frac{k}{k-1}}} \tag{3}$$

$$\frac{P_{2p}}{T_{2p}\rho_{2p}} = \frac{P_1}{T_1\rho_1} \tag{4}$$

$$\beta_{2p} = \beta_{2b} + \delta_{2p} \tag{5}$$

Where W is the relative velocity, U is the circumferential velocity, DR_2 is the diffusion ratio, h is the gas specific enthalpy, P is the gas pressure, T is the gas temperature, ρ is the gas density, β is the flow angle, β_{2b} is the exit blade angle, δ_{2p} is the exit flow deviation angle, subscript 1 denotes impeller inlet variable, subscript $1t$ denotes inlet tip, subscript $2p$ denotes impeller exit primary flow variable. The follows are the secondary zone equations:

$$W_{2s} = \frac{\chi \dot{m}_{tot}}{\rho_{2s}\varepsilon A_2 \cos(\beta_{2s})} \tag{6}$$

$$h_{2s} = (h_1 + W_1^2/2 - U_1^2) - W_{2s}^2/2 + U_2^2/2 \tag{7}$$

$$P_{2s} = P_{2p} \tag{8}$$

$$\beta_{2s} = \beta_{2b} \tag{9}$$

where χ is the secondary mass fraction, $\dot{m}_{tot}$ is the total mass flowrate, ε is the secondary area fraction, subscript $2s$ denotes impeller exit secondary flow variable. For two zone mixing,

$$\rho_{2m} C_{m2m} A_2 = \rho_{2p} C_{m2p} (1-\varepsilon) A_2 + \rho_{2s} C_{m2s} \varepsilon A_2 \tag{10}$$

$$\begin{aligned}(P_{2p} - P_{2m}) A_2 = {} & \rho_{2m} C_{m2m}^2 A_2 - \rho_{2p} C_{m2p}^2 (1-\varepsilon) A_2 \\ & - \rho_{2s} C_{2s}^2 \varepsilon A_2\end{aligned} \tag{11}$$

$$C_p T_{02a} = \chi C_p T_{02s} + (1-\chi) C_p T_{02p} \tag{12}$$

$$h_{02m} = C_p T_{02a} + (P_{recirc} + P_{leak} + P_{df})/\dot{m}_{tot} \tag{13}$$

where C_m is the absolute meridional velocity, T_0 is the total temperature, h_0 is the total enthalpy, P_{recirc} is the recirculation loss, P_{leak} is the leakage loss, P_{df} is the disk friction loss, subscript $2m$ denotes mixing flow variables. The Daily and Nece (1960) correlation is used as disc friction loss model. Leakage loss is modeled by Aungier (1995).

The recirculation loss is quite important for performance prediction at off-design conditions. Japikse (1996) establishes a parabolic correlation between the recirculation loss and operating mass flowrate.

$$P_{recirc} = K_{recirc} P_{euler} \tag{14}$$

$$K_{recirc} = \alpha(m-1)^2 + K_{recirc-opt} \tag{15}$$

$$\alpha = \begin{cases} \alpha_1, & q \le 1 \\ \alpha_2, & q > 1 \end{cases} \tag{16}$$

$$m = \frac{M}{M_{opt}} \tag{17}$$

where, P_{euler} is the Euler power, K_{recirc} is the recirculation loss coefficient α_1 and α_2. are correlation coefficients, M is the operating mass flowrate, M_{opt} is the optimum mass flowrate, $K_{recirc-opt}$ is the recirculation loss coefficient at the best efficiency point, which is an empirical constant.

The Japikse's model works well at the design rotating speed conditions. At off-design rotating speed conditions, the prediction error becomes larger since the optimum recirculation loss coefficient Krecirc-opt is not constant for different rotating speeds. The Japikse model is modified for better predicting compressor performance at off-design rotating speed conditions, which is important for engine cycle simulations. The modified model assumes a parabolic correlation between Krecirc-opt and rotating speeds.

$$K_{recirc-opt} = an^2 + bn + c \tag{18}$$

$$n = \frac{N}{N_{design}} \tag{19}$$

where: a, b, and c are correlation coefficients, N is the operating rotating speed, N_{design} is the design rotating speed.

3.2 Model validation

Figure 4 and Fig. 5 shows the compressor simulation validation results. The results show that the pressure ratio

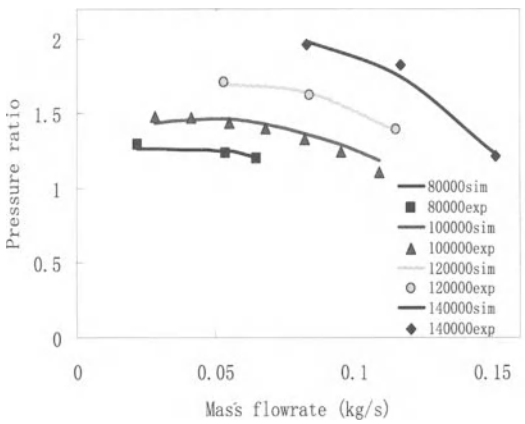

Fig. 4 Comparison of the predicted compressor pressure ratio with validation data

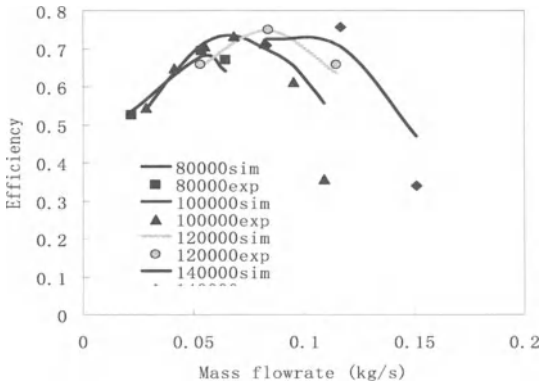

Fig. 5 Comparison of the predicted compressor efficiency with validation data

prediction error is less than 3% and the efficiency prediction error is less than 5% for most points except for high flow (near choking) points. Since the compressor is rarely operated at near choking conditions on real engine, because of the very low efficiency of the compressor operating at these conditions, the prediction inaccuracy at near choking points is not very important. So the developed simulation method is accurate enough for simulating compressor characteristics in engine cycle simulations.

4 Turbine Through Flow Model of a Turbocharger or Turbogenerator

4.1 Mathematical model

The turbine flow is divided into 7 control sections. The computation stations are on the boundary of these sections. Flow variables are solved at these stations, from volute inlet (station 0) to exhaust diffuser exit (station 7). The computation stations are shown in Fig. 6. For the turbocharger without nozzle and diffuser, only the volute

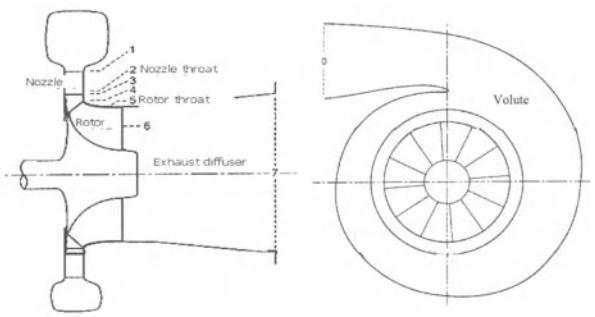

Fig. 6 Turbine flow sections

and rotor sections are solved. The velocities and pressure at volute section may be given by:

$$C_{\theta 1} = S\frac{R_0 C_0}{R_1} \tag{20}$$

$$C_{m1} = \frac{m}{\rho_1 A_1 (1 - B_1)} \tag{21}$$

$$p_{01} = p_{00} - K\left(p_{01} - p_1\right) \tag{22}$$

where, C_θ is the tangential absolute velocity, C_m is the meridional absolute velocity, S is the swirl coefficient, R is the radius, p_0 is the total pressure, m is the mass flowrate, B is the blocking coefficient, K is an empirical loss coefficient, subscript 0 and 1 denotes computation stations. And the rotor section equations are as the follows:

$$\rho_6 W_6 A_6 \cos\beta_6 = \rho_4 W_4 A_4 \cos\beta_4 \tag{23}$$

$$C_p(T_{04} - T_{06}) = U_4 C_{\theta 4} - U_6 C_{\theta 6} \tag{24}$$

$$\frac{T_6}{T_{06}} = 1 - \frac{W_6^2}{W_{6s}^2}\left[1 - \frac{T_{04}}{T_{06}}\left(\frac{p_6}{p_{04}}\right)^{(k-1)/k}\right] \tag{25}$$

$$W_{6s}^2 - W_6^2 = L_i + L_p + L_c \tag{26}$$

where W_{6s} is the isentropic rotor exit relative velocity, L_i is the incidence loss, L_p is the passage loss, L_c is the tip clearance loss.

The incidence and passage loss is modeled using the NASA models.

$$L_i = \frac{1}{2} W_4^2 \sin^2 i \tag{27}$$

where, $i = \beta_4 - \beta_{4,opt}$ is the angle between the incoming flow and that at the best efficiency point, $\beta_{4,opt}$ is not normally equal to the inlet blade angle, but is usually negative.

$$L_p = \frac{1}{2} K_p (W_4^2 \cos^2 i + W_6^2) \tag{28}$$

where K_p is an empirical loss coefficient.

The tip clearance loss is modeled using the Dambach's model.

$$L_c = \frac{U_4^3 Z_R}{8\pi}\left(K_x \varepsilon_x C_x + K_r \varepsilon_r C_r + K_{xr}\sqrt{\varepsilon_x \varepsilon_r C_x C_r}\right) \tag{29}$$

where ε_x is the axial clearance, ε_r is the radial tip clearance, K_x and K_r are discharge coefficients for the axial and radial tip clearance respectively, K_{xr} is the cross-coupling coefficient, Z_R is the blade number.

$$C_x = \frac{1 - (R_{6t}/R_4)}{C_{m4} b_4}, \quad C_r = \frac{R_{6t}}{R_4}\frac{Z - b_4}{C_{m6} R_6 b_6} \tag{30}$$

4.2 Model validation

Figure 7 and Fig. 8 show the validation results. The results show that the pressure ratio prediction error is less than 2% for all the points and the efficiency prediction error is less than 5% for most points except for the lowest speed operating points. The inaccuracy of the turbine efficiency prediction comes mainly from the rough estimation of the bearing loss, since the bearing loss varies largely at low speeds and remains relatively constant at high speeds. Nevertheless, the largest inaccuracy of the efficiency prediction is less than 11.4%, which is acceptable for engine cycle simulations.

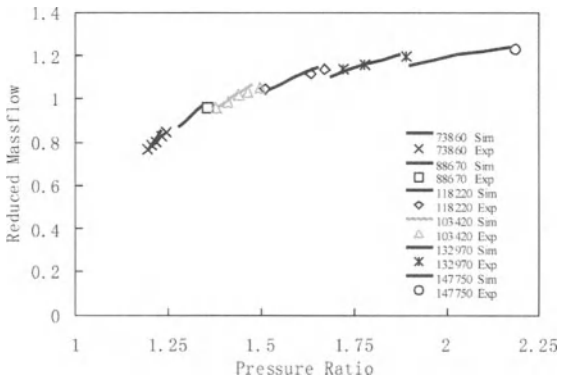

Fig. 7 Comparison of the predicted pressure turbine ratio with validation data

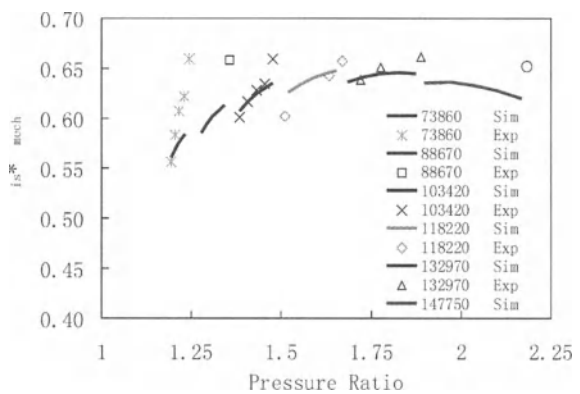

Fig. 8 Comparison of the predicted efficiency with validation data

5 Conclusions

By enabling downsizing the engines and recovering the exhaust waste heat energy, turbocharging and turbo-generating technologies appear to be promising ways to reduce fuel consumption and CO_2 emissions. An advanced integrated energy systems (IES) technology for engine turbocharging has been proposed in the paper. The IES technology combines engine intake turbocharging system and exhaust turbogenerating system by integrated cycle optimization. The through flow models of a compressor of a turbocharger and a turbine of a turbocharger or turbogenerator have been developed and validated, in which the performance is predicted based on the geometry instead of the performance maps. On the basis of through flow models, turbochargers / turbogenerators, intake and exhaust systems, and engine systems integration can be coordinately designed and optimized.

Acknowledgements

The authors would like to acknowledge Dr. Yongsheng He at GM R&D Center for his strong support and helpful discussions to this research work. The National Natural Science Foundation of China is also acknowledged for the financial support (Project 50706020).

References

Aungier R. H., 1995, "Mean Streamline Aerodynamic Performance Analysis of Centrifugal Compressors". *Journal of Turbomachiney*, Vol. 117, pp. 360 – 366

Daily J. W., and Nece R. E.,1960, "Chamber Dimension Effects on Induced Flow and Frictional Resistance of Enclosed Rotating Disks". *ASME Journal of Basic Engineering Series D*, Vol. 82, pp. 217 – 232

International Energy Agency, 2001, "Saving Oil and Reducing CO2 Emissions in Transport: Options and Strategies", *OCED / IEA*

Jansen W. and Heitmann A. M., 2008, "Recovery of Automobile Engine Exhaust Energy", *ASME Paper* No. GT2008-50801

Japikse D., 1996, "Centrifugal Compressor Design and Performance", *Concepts ETI. Wilder*

Leduc P., Dubar B., Ranini A., and Monnier G., 2003, "Downsizing of Gasoline Engine: an Efficient Way to Reduce CO2 Emissions", *Oil & Gas Science and Technology—Rev. IFP,* Vol. 58 (2003), No. 1, pp. 115 – 127

The 4th International Symposium on Fluid Machinery and Fluid Engineering
November 24-27, 2008, Beijing, China
NO. 4ISFMFE-Ch20

Study on the Seal Leakage of Turbocharger

Hong He*, Siyou Xu, Ruiqian Yan and Jianbo Ji

* National Key Lab. of Diesel Engine Turbo-charging Tech.
P.O.B 22, Datong 037036, China
Tel: +86-352-536-2093 / Fax: +86-352-536-2085
E-mail: hehong-sohu@sohu.com

Abstract Piston ring sealing is commonly applied to turbocharger, so there must be some gas leakage due to the non-contact sealing when operating. However, excess leakage will affect the normal operation of turbocharger and engine. In this paper, the computation and the calibration methods of gas flow for the piston ring sealing are described. The numerical simulation which uses the well-orthogonalized hexahedral grid is carried out in the CFD software STAR-CD. It shows that the numerical simulation results fit well with the test results. The computation and test results also show that the side clearance is the determining parameter that affects the leakage rate of double piston ring sealing. Through the study of the position of piston ring in the ring slot on the leakage rate and the measurement of axial displacement of the rotor when operating, the correlation of the computation results and the test results is analyzed. In the seal leakage test, different conditioning ways of turbocharger operating points will greatly affect the measurement of leakage rate.

Keywords turbocharger, piston ring, sealing, gas leakage

The piston ring sealing has a very simple and non-contacting sealing structure. Though there is always some leakage when operating, it can still meet the requirement of the vehicle engine, and is the most popular sealing structure in the turbocharger application.

There are many factors that affect the sealing effect, such as the dimension of clearance, the property of material, the fit tolerance and the operating temperature of the turbine side sealing ring. The increased clearance that caused by the wear of the bearing will also lowers the sealing effect. So the sealing structure is a weak part in the turbocharger, and seal failure is also one of the main failures of turbocharger. The increase of the side clearance that caused by the wear of the bearing will also cut down the sealing performance. So the seal structure is a weak part of the turbocharger, and seal failure is one of the main failures of turbocharger.

Once the seal failure happens, the emission of the engine will become worse, the economical efficiency decreases, even worse it will affect the normal operation of the engine. So how to design the sealing structure and evaluate the sealing performance is always the problems people trying to solve.

1 Sealing Structure

The piston ring sealing structure (see Fig. 1. in order to distinguish from the piston ring used in the piston, we hereafter call it the seal ring) consists of the stationary part, the rotary bearing sleeve and the seal ring. Its main structure parameters are the side clearance between the two sides of the bearing sleeve and the seal ring, the radial clearance between the inner side of the seal ring and the outer side of the bearing sleeve, the seal ring gap and the number of the seal ring.

If more spaces are available, two rings put abreast together are always used, see Fig. 1. The side clearance is less than the axial displacement of the rotor. Tests show that the sealing effect of double rings is better than that of single ring, and double rings structure is more popular in the turbocharger application.

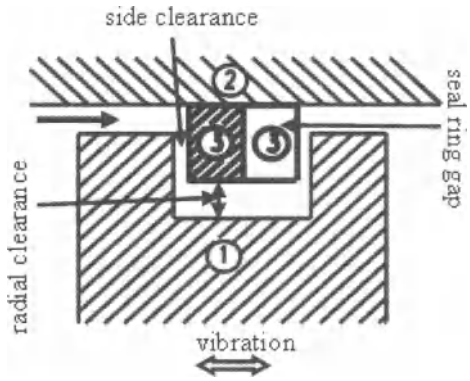

Fig. 1 Piston ring sealing structure in the turbocharger

2 Seal Leakage Rate Computation

The 3D CFD method is used to compute the seal leakage rate of turbocharger. A geometry model is built for the seal structure of turbocharger, and the ICEM-CFD is used to divide the grid for computation. In order to increase the computation accuracy, the well-orthogonalized hexahedral grid is used. Based on the inner leakage flow characteristic of sealing structure of turbocharger, appropriate computation model is built. The numerical simulation is carried out in the STAR-CD. A test is also carried out to verify the computation results. The result shows that the computation results fit well with the test results (see Fig. 2).

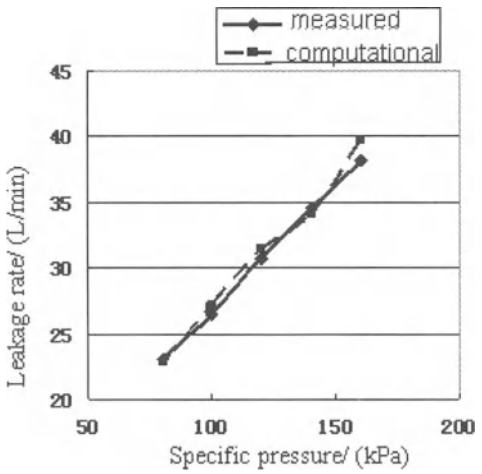

Fig.2 Contrast of the computational and measured results

3 Main Structural Parameters Effects on the Seal Leakage Rate

The side clearance, the radial clearance and the seal ring gap are increased respectively, and then the effects of three different clearances on the leakage rate are computed. Figure 3 shows that the side clearance determines the seal effects. When computing the seal ring is put in the middle of the ring slot, in which position the maximum leakage area appears, so this is useful for the analysis of structural parameters effects on the leakage rate.

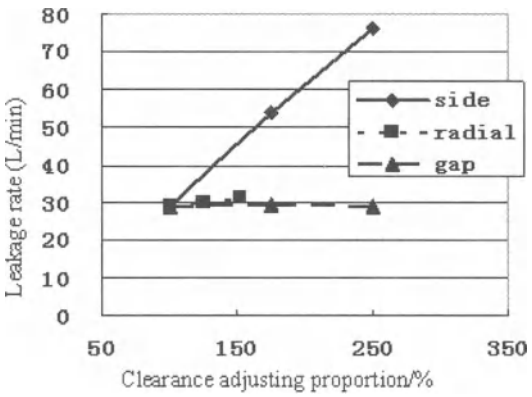

Fig. 3 Results of the main structural parameters effects on the seal leakage rate

4 Analysis of Differences Between Computation and Test

The three clearances used in the tests are the same as those used in the computation. The test results show that the trend of the effects of three clearances on the leakage rate is the same as that of the computation results. But the actual values differ greatly. For example, for the same side clearance, the computation result is about 1.7 to 3.7 times of the test result (see Fig. 4).

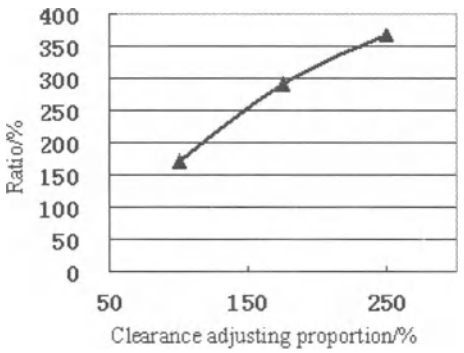

Fig. 4 Ratio of computational and measured leakage rates for an increased side clearance

The reason for the differences is that the side clearance changes in the operation of turbocharger. The position of seal ring in the ring slot depends on the bearing sleeve and the seal ring (see Fig. 1 Sealing structure of turbocharger). The seal ring is embedded in the housing by tension. The bearing sleeve rotaries with the rotor. Its

position is up to the result of mutual effects of the rotor and the thrust bearing. Initially, the seal ring is at one end of the ring slot, and has a certain clearance. When operating, the axial aerodynamic loads are yielded on the compressor and turbine wheels, and then transported to the thrust bearing. Finally the aerodynamic loads are resisted by the oil film that has a given pressure. The test results show that, under the combined action of these aerodynamic loads, the rotor behaves like that shown in Fig. 5. The spectrum of that is shown in Fig. 6. Suppose the rotational frequency of the rotor is X, the spectrum mainly includes the frequencies 0.5X, 1X and 2X.

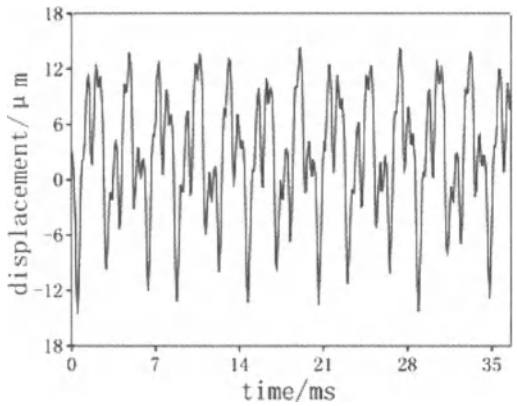

Fig. 5 Time-domain signal of the axial displacement

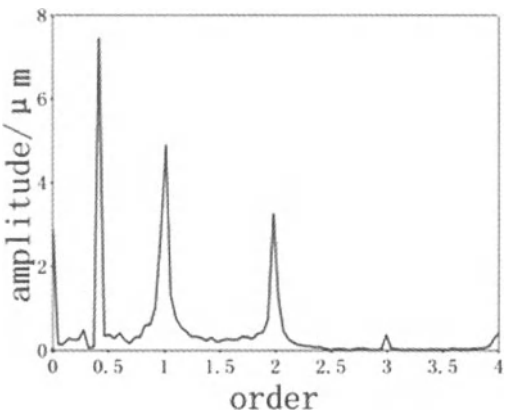

Fig. 6 Spectrum of axial displacement of the rotor

The axial displacement of the rotor corresponds to a certain range of the seal ring in the ring slot. When the seal ring is not in the middle of the ring slot, how the seal leakage changes? Figure 7 shows that for a certain value of the total side clearances, the effect of the positions of seal ring in the ring slot on the seal leakage rate. It can be seen that, the leakage rate reaches to the largest when the seal ring is in the middle of the ring slot, and the changes are not linear. The axial floating range of the rotor corresponds to a certain range of the seal ring in the ring slot, see Fig. 8. The average leakage rate of this range is about 62 percent of the maximum value. Here the computation of average value is reduced by assuming the time that the rotor stays in each place is the same, and the non-steady effect of the leakage flow is also not taken into account. So this average value is close to the value measured in the test.

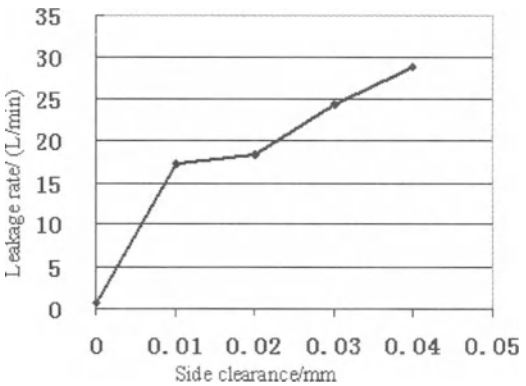

Fig. 7 Leakage rate versus side clearance (total side clearance is 0.08mm)

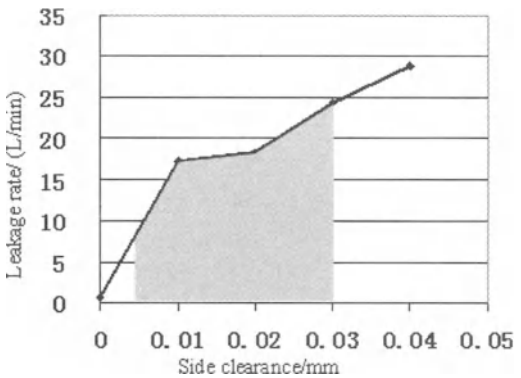

Fig. 8 The range in which the side clearance changes corresponding to the axial float of the rotor (the shadow part, total side clearance is 0.08mm)

It is mentioned above that the computation is executed in the condition of the seal ring in the middle of the ring slot, and the computation result is about 1.7 times the test result (the total side clearances is 0.08mm), i.e. the measured result is 58.8% of the computation results, so this result is very close to the analyzing result (i.e. the average leakage rate is about 62% of the maximum value).

In the case of increased total side clearances, the seal ring still moves in a certain range in the ring slot. However the initial side clearance is increased, i.e. the shadow part moves towards the right side, so the average leakage rate increases, and moreover, the maximum leakage rate increases even larger (see Fig. 9). So the ratio

of the computation result (maximum value) over the test result (average value) increases.

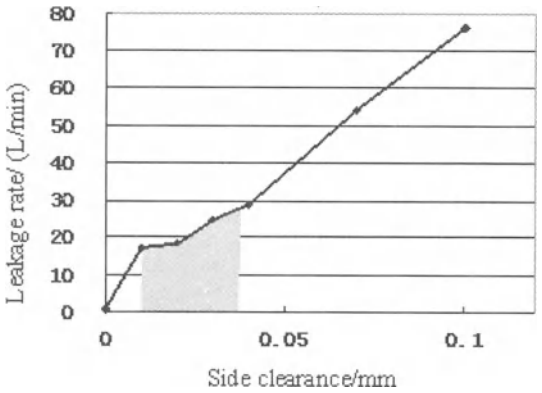

Fig. 9 The range in which the side clearance changes corresponding to the axial float of the rotor (the shadow part, total side clearance is 0.08mm)

For the piston ring sealing in the turbocharger application, it is very difficult to verify the computational and test results mutually. There are many factors that affect the prediction accuracy, such as the seal ring positions of the turbine and compressor end may be different from each other, the initial position of the seal ring in the ring slot may be affected by the assembly, operating state, and the pressure difference between the two sides of the seal ring, and etc. So the computation and test means should both be used. When using the computational means, the affect of rotor vibration can be eliminated, and this is helpful for analyzing the affects of the structural parameters. The test means can be used to verify the sealing performance under the affects of several factors, especially those hardly simulated in the computation.

5 Effects of Operating State Conditioning Ways on the Leakage Rate Measurement

The conditioning ways of operating state will also influence the leakage rate measurement. This also reflects the effect of the relative position of the seal ring and the ring slot on the leakage rate.

Different conditioning ways of turbocharger operating state will influence the magnitude and direction of the axial force on the rotor, so the movements of rotor will differ from each other. So do the relative positions of the seal ring and the ring slot (i.e. the side clearance). The test results shows that in different speed conditioning ways, the changing process of the leakage rate differ greatly by 10% (see Fig. 10).

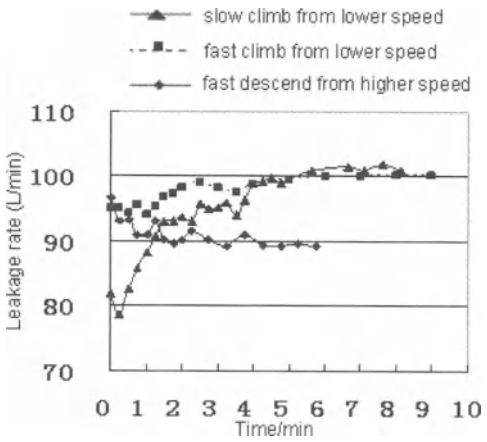

Fig. 10 Effects of three different speed conditioning ways on the leakage rate measurement

6 Conclusions

- The results of the numerical simulation, which is carried out in the CFD software STAR-CD using the well-orthogonalized hexahedral grid, fit well with the test results.
- Computation and test studies all show that the side clearance is the determining parameter of the seal leakage rate for double ring structure.
- Under the combined action of the axial force on the rotor and the thrust bearing, the rotor floats along the axis frequently. The leakage rate measured in the operation of turbocharger is the average leakage rate through these frequently changing side clearances. This can be simulated by computing the leakage rate for each position of the seal ring in the ring slot and by measuring the displacement of the rotor.

The turbocharger operating state conditioning ways greatly influence the leakage rate measurement.

References

Daxin Zhu, "Turbine Charging and Turbocharger", *China Machine Press*, 1996, Beijing

Kazuya Miyashita, "Shaft Seals and Bearings for Automotive Turbo/ Supercharger", *Turbomachinery*, 1998, 26(11), pp. 38 – 46

WEI Ming-shan, "Vehicle Turb0charger Seal Test Methods", *Vehicle Engine*, 2004 (4), pp. 50 – 52

The 4th International Symposium on Fluid Machinery and Fluid Engineering
November 24-27, 2008, Beijing, China
NO. 4ISFMFE-Ch21

Study on the Pre-Tightening Force About the Nut of the Turbocharger Shaft

Li Long*, Hong He and Wei Pei

* National Key Lab. of Diesel Engine Turbo-charging Tech.
P.O.B 22, Datong 030706, China
Tel: +86-352-536-2096 / Fax: +86 -352-536-2085
E-mail:iongrednose@gmail.com

Abstract This paper introduces the domestic actuality about the pre-tightening force about the nut of the turbocharger shaft and some pre-tightening methods, analyzes the effect of the methods on the pre-tightening force. Based on the study on the pre-tightening force of the general bolt, this paper proposes a calculation method which is used to calculate the pre-tightening force about the nut of the turbocharger shaft according to the analysis and experimentation. It proves the feasibility and correctness of the method by reference to the existing specimens.

Keywords pre-tightening force, turbocharger, calculation methods

Nomenclature

d_2	Effective diameter of screw thread
d	External diameter of bolt
λ	Helix angle, here is 2.5°
ρ_v	Equivalent coefficient of friction, here is 9.83°
$d_m=(R+r)/2$	Average diameter of the nut support face
f	Friction coefficient of the nut support face
θ	The rotary angle
P	The pre-tightening force
C_L	The rigidity of the bolt
C_B	The rigidity of the connection part
$P=E*A*$, L/L	The thread pitch
E	Elasticity modulus
A	Cross-sectional area of the bolt
L	Elongation of the bolt
L	Work length of the bolt
W	The power of the turbo
n	The speed of the turbo
f_1, f_2	Friction coefficient of the interface
R_1, R_2	Availability radius of the interface
K_i (i =1,2,3,4,5,6,7)	the elastic modulus of the part
A_i	Cross-sectional area of the part
L_i	Length of the part

There are two methods in the nut-connection: the common nut connection and the pre-tightening force nut connection. The nut of the turbocharger shaft must be sure to keep the steady tightening to the impellers of the compressor, and it should maintain the retention without any self-loosening when it works. This connection is a kind of key nut connections with a pre-tightening force.

1 The Status Quo of the Pre-Tightening About Nut on the Shaft of Turbocharger

As a high-speed rotating turbomachinery, the maximal rotational speed of turbocharger can be 10,000 rpm even to 200,000 rpm. The high speed of the turbocharger shaft and the high working temperature will make the shaft components become deformed. All the deformation will affect the pre-tightening force of the nut on the shaft of turbocharger. The research about this technique is already mature overseas, but at the present time, there isn't anything about the methods which calculate the pre-tightening about nut on the shaft of turbocharger in the documents

published publicly. The domestic people haven't realized the importance of this problem, so there is no research about it. At present, to define the screwing down torque of the turbocharger shaft nut assembly is based on experience or to refer the foreign similar specimen machine.

There are some main methods of pre-tightening nut connection torque method, rotary angle method, mark method, pre- stretching method.

1.1 Torque moment method

The screwing down torque is added by torque-indicating wrench or torque wrench, dynamometer, in order to make the pre-tightening force to fit the design requirement. The calculating formula is as follow:

$$T = \frac{1}{2}[\frac{d_2}{d}\tan(l + r_v) + \frac{d_m}{d} f\ ] * F * d$$

As shown in the formula, in the ideal mode – the friction coefficient f is a constant, the screwing down torque T can be gotten by measuring the pre-tightening force P. But in the actual case, the friction coefficient f is affected by lubricated state, screw thread state, tightening speed, the state of nut on support face, etc. With the same screwing down torque, the pre-tightening force is affected by the friction coefficient a lot.

1.2 Rotary angle method

The rotary angle method is to make the nut close to the connection part, then to rotate the bolt a angle to get a pre-tightening force. The calculating formula is as follow:

$$\theta = 360 * P * (1/C_L + 1/C_B)/S$$

As shown in the formula, the rotary angle is directly proportional to the pre-tightening force. The other parameters are constant. There is an inaccuracy when the clearance is eliminated to define the 0° angle. The nut should be pressed close to the connection part by the Torque moment method firstly, so the 0° angle is affected by the friction, tools, human's. The inaccuracy is a large one.

1.3 Mark method

The mark method is to mark the bolt and nut at the correspondence position after assembly with a certain pre-tightening force, then to aim at the marks the next assembly. This method is only used in assembly after repairs.

1.4 Pre- stretching method

When the high strength blot is in the used in the elastic range, the pre-tightening force follows the Hooke Law:

$$P = E * A * \Delta L / L$$

As shown in the formula, the pre-tightening force is directly proportional to the elongation of the bolt, the other parameters are constant. This method overcomes the deficiency of the other three methods. The bolt only sustains the axial tensile force, no torsional shear or lateral forces. This method improves the blot stress state, increases the bolt fatigue strength. It also can get a reliable pre-tightening force, to improve the accuracy of the pre-tightening. (The inaccuracy is about ±3%～5%)

2 Modeling

2.1 Analysis of the formation mechanism on pre-tightening force

To collect the scewing down torque information of the nut on the shaft of available turbocharger at home and abroad, then to analysis the formation mechanism of the pre-tightening force and the main factors affected pre-tightening force, then the main parameters can be gotten to calculate the pre-tightening force. The preliminary calculating model can be set according to the research plan.

The torque which supercharger should export is calculated according to the supercharger working condition. The torque transmission is achieved by the moment and torque of friction which is caused by the nut on the shaft pressing the compressor impeller and other parts to the turbo shaft shoulder. As the material and the structure are certain, and the friction coefficient and contact area are set, the friction torque depends on the residual pre-tightening force. The pre-tightening force can be calculated according the relation between pre-tightening force and residual pre-tightening force. Thus the calculating formula of the nut on the shaft which fits the actual working condition can be gotten.

The turbocharger actual working condition includes the rotate speed of the turbocharger, the power needed to be transmitted by turbo shaft, the acceleration, the deceleration and so on. The friction coefficient, the contact area, and the residual pre-tightening force are the influencing factors of the friction torque. Here the "residua" means this force is different from the assembly pre-tightening force. It's a little smaller than the assembly

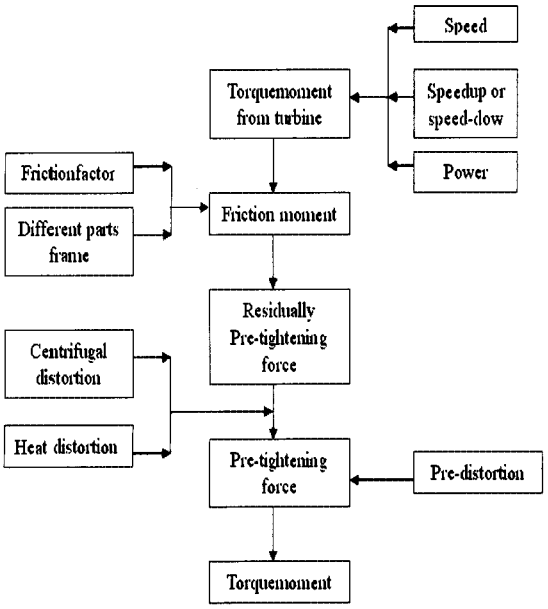

Fig. 1 Study project

pre-tightening force. The friction coefficient is only a scope in the material manual and the mechanical manual. In the scope, it affects the result a lot when different data is chosen. So the specific data should be gotten according the experiments. It's should content many factors such as the roughness concentration of the material surface, the lubricant on the assembly surface and so on.

2.2 Modeling

It is modeling of Pre-tightening force about the nut of the turbocharger shaft in the article as follow:

(1) Research on the effect of the torque moment transmitted by the shaft in the turbocharger actual working condition.

The turbocharger actual working condition includes the rotate speed of the turbocharger, the power needed to be transmitted by turbo shaft, the acceleration, the deceleration and so on. All of these will affect the torque moment transmitted by the shaft. The quantitative relation between the torque and these influential factors can be gotten according to the researches.

As It's difficult to ensure the measuring accuracy and precision of the turbocharger's power and its corresponding speed while increasing speed and decreasing the speed, this paper only considers the invariablenes speed situation. The power is calculated by the experimental measurement of the compressor impeller's rotate speed. The moment needed by impeller shaft can be gotten according the formula:

$$\Gamma=9.55\frac{W}{n} \tag{1}$$

Then, the force needed by impeller shaft can be calculated according the formula:

$$F_R=\frac{\Gamma}{f_1R_1+f_1R_2} \tag{2}$$

(2) Research on the axial deformations of the impeller in high temperature and high speed situation.

There will be some deformation on the impeller in high temperature and high speed. According the finite element methods analysis, this paper only considers the axial deformations. The axial deformations is directly related to the per-tightening force, here means the residual pre-tightening force). According the finite element analysis, within a certain limit turbocharger's rotate speed range, the temperature field affects the axial deformation of the impeller less than 1%. So it can only consider the impact of the speed in the program.

(3) Research on effects of the supercharger axial power transmission parts

Not only to consider the effects of the pre-tightening force in the actual working condition, but also to consider the effects of the supercharger axial power transmission parts. There are 5 to 8 supercharger axial power transmission parts including the nut of the shaft. These parts on the shaft must be considered as they affect the pre-tightening force about the nut on the shaft. The parts on the shaft affect the pre-tightening force about the nut on the shaft. All the parts are not only independent but also interacted. All these are the key points and difficult points in the modeling and calculation. According to the system rigidity theory, it considers all parts as one part to facilitate the modeling and calculation.

The part rigidity calculating formula: K_i (i = 1, 2, 3, 4, 5, 6, 7):

$$K_i = E_i * A_i/L_i$$

The system rigidity calculating formula :

$$\frac{1}{K}=\frac{1}{K_1}+\frac{1}{K_2}+\frac{1}{K_3}+\frac{1}{K_4}+\frac{1}{K_5}+\frac{1}{K_6}+\frac{1}{K_7} \tag{3}$$

2.3 Parameters

These parameters in researches are gotten by the experimentations, including rotate speed of the turbocharger, thermodynamics parameters in calculating the power of the turbo, centrifugal deformation of the working impeller, friction factor of interface and so on.

Thermodynamics parameters are measured in bench test.

In the actual working condition, there will a strong centrifugal force when the supercharger shaft rotates with a high velocity. It will cause the deformation of the impeller, and so does the increase of the temperature. According the calculation by ANASYS program, the max deformation of the impeller in actual working condition is computed.

The friction factor of interface will be measured by the equipment designed as follow. The part material and machining precision are the same as those of turbocharger parts.

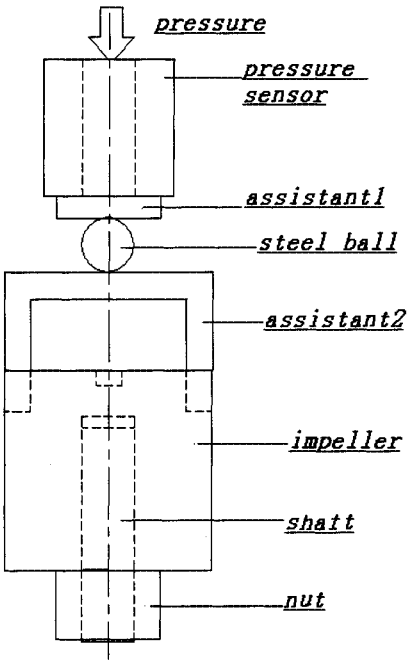

Fig. 2 Measure friction equipment

3 Calculated examples

Based on the calculating model above, calculate the existing turbocharger. The result is 66 N·m. In order to keep the nut on the turbocharger shaft without looseness in the working time, here is a safety factor which is 1.3, then the result becomes 85.8 N·m. The pre-tightening force of the turbocharger is 85N·m. The inaccuracy of this calculation is less than 5%. And the safety factor is ture of the other two model turbochargers. Then, the model is up to the required design standard.

4 Conclusions

(1) The friction coefficient in the actual working condition can affect the precision in calculation result of power factor.

(2) This model is up to the required standard.

Acknowledgements

The authors have immense gratitude to Engineer Wen Shijie for his guidance and help.

References

Zhang fang, 2006, "Discussion of the pretensioning of high strength bolts for diesel engine of locomotive", *Locomotive & Rolling Stock Technology*, Vol.6, pp. 38 – 41

Wu Huixiang, Yang Zhong, Mao Wanhua, 2004, "High-precision test for friction coefficient at high and low temperatures", *Journal of Data Acquisition & Processing*, Vol.19, pp. 111 – 114

"Machine Design Handbook", 2004, *China Machine Press*, Beijing

The 4th International Symposium on Fluid Machinery and Fluid Engineering
November 24-27, 2008, Beijing, China
NO. 4ISFMFE-Ch23

Vibration Property Analysis of Turbocharger Turbine Blade Under Different Loads

Wei Pei*[1], Dongmei Zhang[2] and Jizhong Zhang

*[1] National Key Lab. of Diesel Engine Turbo-charging Tech.
P.O.B 22, Datong 030706, China
Tel: +86-352-536-2083 / Fax: +86-352-536-2085
E-mail: moderatepw@126.com

[2] China North Engine Research Institute
P.O.B 22, Datong 030706, China
Tel: +86-352-536-2381
E-mail: zhangdongmei207@163.com

Abstract The vibration property of turbocharger turbine blade was analyzed with thermal load and centrifugal force of the turbocharger turbine considered. Vibration property was analyzed by FEM and validated by dynamic stress test. Through the analysis of resonance property, the design guideline was put forward.

Keywords turbocharger turbine blade, vibration

Nomenclature

n_T	Turbocharger rotating speed r/min
f_d	Dynamic frequency under thermal load (T_2) and centrifugal force (n_T)
f_c	Static frequency under thermal load (T_1)
B	Dynamic frequency coefficient
E_{T2}	Material Elastic modulus at temperature (T_2) Kg/cm^2
E_{T1}	Material Elastic modulus at temperature (T_1) Kg/cm^2
f_1	Frequency at mode 1
n_C	Turbocharger rated rotating speed
f	Frequency
ε	Microstrain

1 Introduction

Turbocharging is used today more widely than ever in internal combustion engines. Most diesel engines of all types and sizes that are manufactured today are turbocharged, and the naturally aspirated diesel engine is becoming a thing of the past.

As a high speed rotary machine, turbocharger breakdown, especially a moving part breakdown, will cause a whole turbocharger damage in a short time. Owing to the increasing of the compression ratio and rotating speed, more attention is paid to structure intensity and reliability of the rotor component.

Radial flow turbochargers are trend to be easily affected by blade vibration which can then lead to High Cycle Fatigue. High Cycle Fatigue is particularly prevalent on turbine wheels where the aerodynamic forces acting on the wheel induces the blades to resonate at their natural frequencies.

Vibration property of the turbine blade which is affected by thermal load and centrifugal force is analyzed by FEM and validated by dynamic stresses tests. Resonance property is analyzed, and design guideline is putted forward.

2 Prestressed Modal Analysis

This paper described a solid model of a certain turbine, seen in Fig. 1. As a cyclically symmetric structure, the turbine includes 12 identical sectors, and only one sector was analyzed here. Its solid model is shown in Fig. 2.

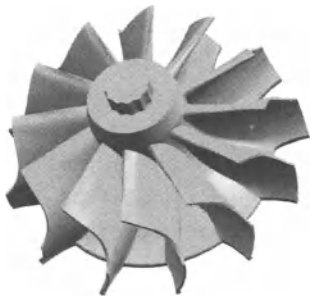

Fig. 1 Solid model of turbine

Fig. 2 One sector of the solid model

The element types of the FEM modal are SOLID as shown in Fig. 3. The elements having three degrees of freedom at each node is defined by eight nodes. The number of elements is 1981, and the number of nodes is 2797.

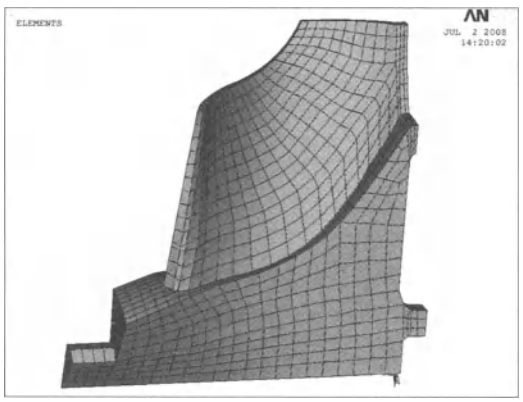

Fig. 3 FEM modal

The inlet temperature of the turbine is 650℃, and outlet temperature is about 540~600℃. Four operation statuses which the turbocharger works in were calculated, they are: 40000r/min, 50000r/min, 60000r/min, 70000r/min.

The frequency was calculated using a prestressed modal analysis. Detail steps are as follow: First obtain temperature distribution by the thermal analysis. The inlet temperature of the turbine is 650 ℃. and the outlet temperature is 600℃, 580℃, 560℃ and 540℃ when the operation statuses of turbine are 40000r/min, 50000r/min, 60000r/min and 70000r/min.

Then read the temperature distribution from the thermal results file, the results derived from the thermal analysis then would be used as loads in the Static Structural Analysis. The frequencies was calculated at the last using a prestress modal analysis. The results are shown in Table 1.

Table 1 Results of prestressed modal analysis

Rotating speed	Modes	Frequency (Hz)
40000r/min	1	6915.2
	2	12002
	3	13495
	4	17108
50000r/min	1	6983.1
	2	12075
	3	13572
	4	17185
60000r/min	1	7058
	2	12149
	3	13653
	4	17264
70000r/min	1	7142
	2	12229
	3	13740
	4	17346

The analyzed result of the static natural frequencies was 7307Hz, in great agreement with the practical measurement result 7200Hz.

Furthermore, as can be seen from table 1 above, the natural frequencies increases as the turbocharger rotating speed increased, but some frequencies were still smaller than the static natural frequencies. The reason is that the equation for calculating natural frequencies when rotating speed and temperature are considered is as follow:

$$f_d^{\,2} = f_c^{\,2} \cdot \frac{E_{T2}}{E_{T1}} + B \cdot n_T^2 \tag{1}$$

Because the value of temperature changes little in different operation statuses, the change of E_{T2} is very small. And f_d increases as rotating speed increased. But because the material elastic modulus at high temperature stutaus is smaller than at lower the influence of temperature is bigger than that of rotating speed. So sometimes the dynamic frequency will be smaller than the static frequency.

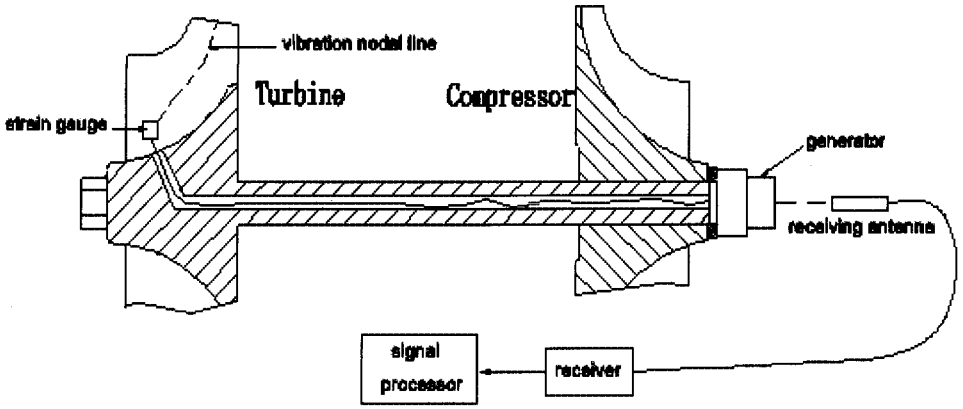

Fig. 4 Schematic diagram of dynamic stress test principle

According to foreign experience, the turbine blade would be safe when $f_c \geqslant 5\ n_C$ (Hz), namely keep a way from the 5 times rotating speed region. In order to verify this conclusion, an verification was carried through a Dynamic Stress Test.

2 Dynamic Stress Test

2.1 Test principle

By measuring the turbine blade natural frequencies, the nodal line of the first order vibration is determined, then attach the strain gauge to the location of the nodal line. The connecting wire of the strain gauge extends from the radial hole on the turbine hub to the axis hole, and then extends to the signal generator at where the nut installed on the compressor end, the signals was received, amplified, and demodulated by the receiver, then the strain signals was sent. Ultimately the graph of speed-strain-frequency was obtained. Shown in Fig. 4.

2.2 Results and analysis

The turbocharger for test is a 360° full admission vaneless scroll . The Campbell map is shown in Fig. 5.

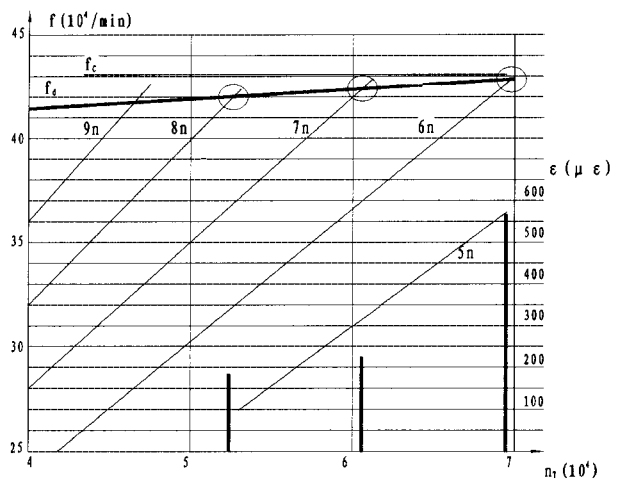

Fig. 5 Dynamic stress test Campbell map (test1)

In Fig. 5, the abscissa indicates turbine speed, ordinate indicates frequency. The radial lines extended from the origin show the changes of excitation frequency along with the rotating speed. Due to the rotating speed continuously changes, in this test, according to the calculate results, the thicker black line will slightly incline upwards.

In addition, duo to the difference of the manufacture precision, the blades natural frequencies has certain dispersion. When shown on the graph, there is a frequency band, so sometimes it is needed to draw a thicker black line to show the dispersion range of the natural frequencies of blades.

The intersections of natural frequencies and radial line on the graph all indicate the resonance conditions, the point like this is not just one, there are certain points spread in an interval.

The abscissa this range corresponding to is the resonant rotating speed region of the turbocharger. As seen from the graph, although there are many resonant points, they are not all harmful, only when be excited by a high strength vibration, it will cause a damage of turbine blade. Therefore the most dangerous mode is the first order vibration mode. In addition, as the exciting force frequency increasing, the amplitude decreased. So as can be see from the graph, the biggest dynamic loading stress is achieved at the sixth order resonance n_T= 70000, it is the most dangerous resonant region.

As could be seen from the graph, the biggest strain value in the region of test speed is the 6 times rotating speed strain at resonance point, namely 500 $\mu\varepsilon$, the 5 times rotating speed resonance was not present, as the turbine blade natural frequencies is essentially high.

We used the same method to do the calculations and tests on another turbine. The natural frequencies of this turbine is a little lower, is 4224Hz. The test results are shown in Fig. 6.

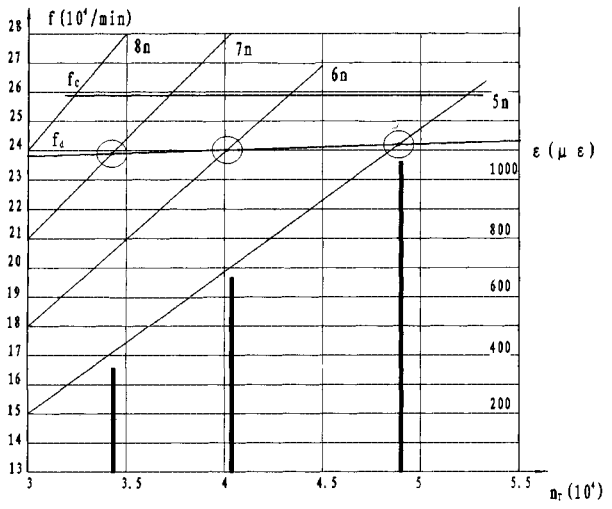

Fig. 6 Dynamic stress test Campbell map (test2)

As see from the graph, the strain value is 695 $\mu\varepsilon$ at 6 times rotating speed resonance point , the strain value at 5 times rotating speed resonance point is bigger than 1000 $\mu\varepsilon$. According to the data from KKK Company, the upper limit of the strain value is 850 $\mu\varepsilon$, at some special cases, it could reach 1100 $\mu\varepsilon$. So the strain value of the tested turbine blade is big, this has some relations with the 180°double channels separation turbine scroll. But if improve the natural frequencies of turbine blade , make it keeping away from the 5 times rotating speed resonance , the strain value will be decreased a lot, and reach the allowable range. So it is an extremely effective method that keeps away from the high. frequency resonance for reducing the blade stress levels.

3 Conclusions

(1) It is an effective method that keeping away from the 5 times rotating speed resonance point at rated turbocharger rotating speed for reducing turbine blades stress levels.

(2) Compared with the 360° full admission turbine scroll, the 180° separation intake turbine scroll has some influence on the increasing of the turbine blade stresses, but this influence is much smaller than that of the 5 times rotating speed resonance.

References

V.RAMAMURTI D.A.SUBRAMANI and K.SRIDHARA, 1995, "Free Vibration Analysis of a Turbocharger Centrifugal Compressor Impeller"

Machine Design Handbook, 2004, *China Machine Press*, Beijing

The 4th International Symposium on Fluid Machinery and Fluid Engineering
November 24-27, 2008, Beijing, China
NO. 4ISFMFE-Ch25

A Method to Solve the Problem of the Application of Ti-Al Turbine

Xiujuan Wang

National Key Lab. of Diesel Engine Turbo-charging Tech.
P.O.B 22, Datong 037006, China
Tel: +86-352-536-2096 / Fax: +86-352-536-2085
E-mail: wxj_2004@163.com

Abstract Ti-Al is a sort of high-temperature resistant material with lightweight, mainly used in medical equipment, chemical equipment, military and sports equipment, and other fields at present. Thereinto, a very important application is on vehicle turbocharger, however owing to the special nature of the material, it has not applied to turbocharger extensively yet. The connection of Ti-Al turbine and steel shaft is a major problem, so a mechanical connecting method was found to solve this problem.

Keywords Ti-Al turbine, mechanical connect, turbocharger

1 Introduction

Ti-Al alloy with low-density, high elevated temperature strength and other merits is considered to be the most potential high-temperature structural material for development and application. One important characteristic of Ti-Al alloy is the characteristic of lightweight, its density ($3.9g/cm^3$) is less than half of the ordinary nickel-based high-temperature resistant alloys ($8.0g/cm^3$), but its specific strength is much higher than ordinary nickel-based high-temperature resistant alloys. At room-temperature, the specific strength of Ti-Al alloy is higher than the K418 nearly 48%, at 800℃, higher than the K418 for 55% [1]. As Ti-Al alloy's poor welding performance, the connection technology of Ti-Al turbine and steel shaft is a major challenge for its application on turbocharger. We adopted a form of mechanical connection to achieve the application of Ti-Al alloy on vehicle turbocharger.

2 Connecting Structure of the Ti-Al Turbine

At present, the most common connecting way of vehicle turbocharger turbine is connecting the high-temperature resistant alloy turbine and steel shaft by friction welding directly or using electron beam welding. The special nature of Ti-Al material decides that the Ti-Al turbine can not adopt this kind of universal way to achieve the connection of Ti-Al turbine and steel shaft. So, is there a connecting structure which can achieve the connection of Ti-Al turbine and steel shaft and do not affect the Ti-Al material performance? Thus, introduce the middle transition, and the middle transition material selects ordinary nickel-based high-temperature resistant alloy.

The connecting structure of Ti-Al turbine and steel shaft adopts three sections connecting structure with the middle transition sleeve, that is Ti-Al turbine and high-temperature resistant alloy sleeve is connected using mechanical connection, and high-temperature resistant alloy sleeve and 42CrMo steel shaft is connected by friction welding.

Such connecting structure has two advantages: firstly, as a result of selecting ordinary nickel-based high-temperature resistant alloy as the middle transition sleeve's material, Ti-Al turbine and middle transition sleeve still can adopt friction welding or electron beam welding directly, the technology is mature and stability, its connecting performance no longer need to be verified; secondly, the middle transition sleeve and Ti-Al turbine using a mechanical connection with interference, this method is simple and easy to implement, and would not make deterioration of Ti-Al material (see the stress simulation analysis of part 3).

3 Stress Simulation of Connecting Part

Because Ti-Al turbine and high-temperature resistant alloy transition sleeve adopts interference fit, the tight contact will produce compressive stress. How the stress distributes, and whether it has adverse effect on the material of contact part. In response to this problem, we use the method of temperature difference and finite element analysis software ABAQUS to study the compressive stress, which produced after the assemblage of Ti-Al turbine and high-temperature resistant alloy transition sleeves. Figure 1 is the overall stress distribution cloud for connecting part, different colors represent different stress; Figures 2 and 3, respectively represent stress intensity and distribution about Ti-Al turbine shaft and nickel-based high-temperature resistant alloy sleeve; Figure 4 is the quantitative description about the two materials stress.

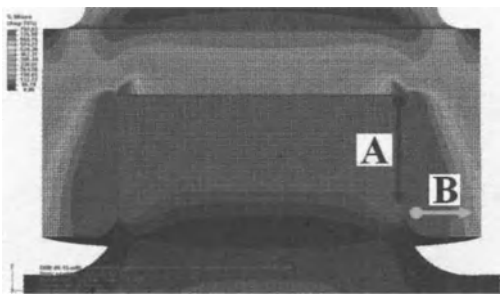

Fig. 1 Stress distribution cloud of connecting part

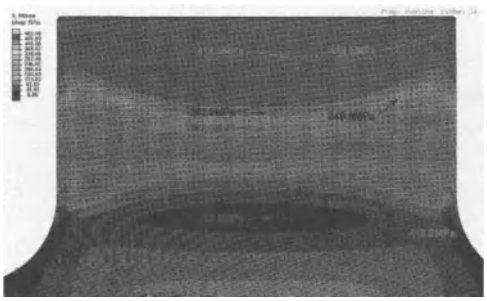

Fig. 2 Internal stress cloud of Ti-Al turbine shaft

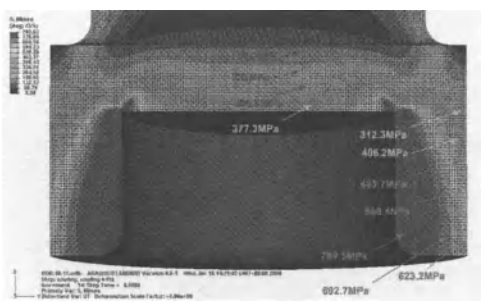

Fig. 3 Internal stress cloud of high-temperature resistant alloy sleeve

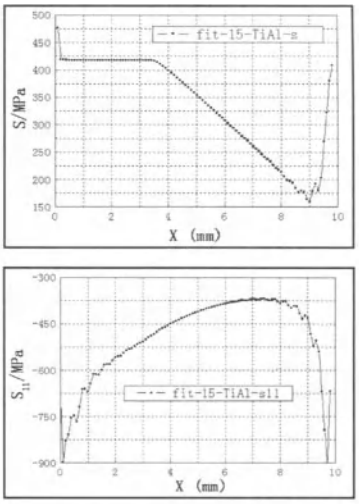

(a) Ti-Al turbine shaft surface stress along the axial and radial

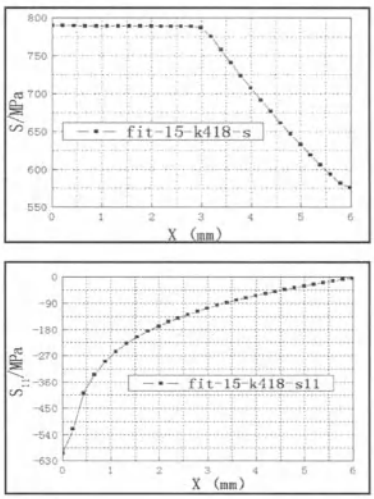

(b) High-temperature resistant alloy sleeve surface stress along the axial and radial

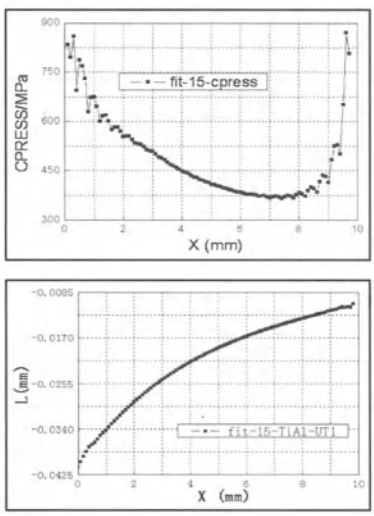

(c) Pressure intensity of connecting surface

Fig. 4 Internal press of two material in connecting section

From the map, it is clear that the maximum stresses of Ti-Al turbine shaft and nickel-based high-temperature resistant alloy sleeve are both in the range of the flexibility of these two materials, and the elastic deformation all occur in these two types of materials.

4 Verify the Reliability

In order to verify the reliability of such connection's structure, we did bench test and whole machine durability test for the Ti-Al turbocharger. Bench test contains 100 hours structure check test, over speed and over heating test, and parameters of the highest circulation experiment test[2], then the turbocharger passed these tests successfully. Figure 5 is the connecting part of Ti-Al turbocharger and Ti-Al turbine which has been tested; we can see the connection is perfect.

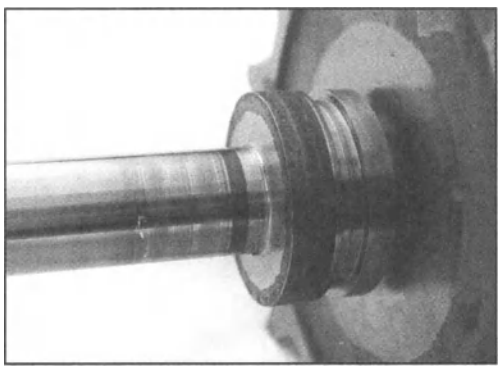

Fig. 5 Ti-Al turbine's connecting section after the examination of 100 hours

5 Conclusions

(1) Ti-Al turbine applied with fit mechanical connecting structure will not make deterioration of Ti-Al alloy or nickel-based high-temperature resistant alloy.

After passing the bench test, the Ti-Al turbocharger went on 500 hours durability check test with the diesel engine and still passed the test perfectly. From Fig. 6, we can see the Ti-Al turbine which has been tested is in good condition.

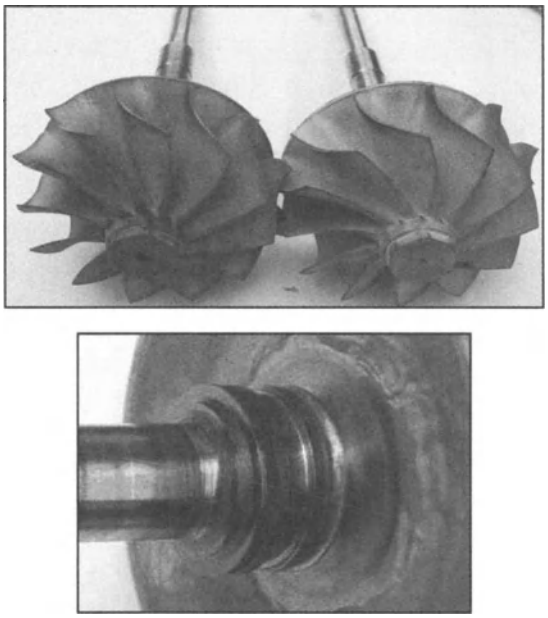

Fig. 6 Ti-Al turbine and its connecting section after the examination of 500 hours

(2) Ti-Al turbine which using machinical connecting structure, its connection reliability has been verified meeting the requirement of application. And it is a simple and workable solution that can solve the application problem of Ti-Al turbines.

Acknowledgements

The author is indebted to Master Li Lei, Lanzhou University of Technology, for supplying the data.

References

[1] He Hong, etc, 2006, "Application of Titanium aluminum Turbocharger", *Journal of Beijing Institute of Technology*, Vol.15, pp. 94 – 98

[2] Zhu Daxin, 1992, Turbo and turbochargers, *Machinery Industry Press*, Beijing

The 4th International Symposium on Fluid Machinery and Fluid Engineering
November 24-27, 2008, Beijing, China
NO. 4ISFMFE-IL19

A Study on Rotor Blades for a Two-Stage Jet Fan

Michihiro Nishi[*1], Kouichi Yoshida[2], Minoru Okamoto[3] and Hiroyasu Nakayama[4]

[*1] Kyushu Institute of Technology, Sensui-cho 1, Tobata, Kitakyushu 804-8550, Japan
Tel: +81-93-881-3167 / Fax: +81-93-871-8591
E-mail: nishi@mech.kyutech.ac.jp

[2] Kyushu Institute of Technology, Sensui-cho 1, Tobata, Kitakyushu 804-8550, Japan

[3] Kyushu Women's University, 1-1 Jiyugaoka, Yahatanishi, Kitakyushu 807-8586, Japan

[4] Kitakyushu National College of Technology, 5-20-1 Shii, Kokuraminami, Kitakyushu 802-0985, Japan

Abstract A jet fan used for road tunnel ventilation is an axial flow fan that has an ability to shift the direction of airflow if necessary. To satisfy the need, the identical performance of jet fan for both flow directions should be fundamental. As shifting the flow direction is made by only switching the rotational direction of an electric motor, a blade having symmetrical section profile has been widely used. In recent years, higher performance of jet fan is expected from the viewpoint of minimum energy consumption. Thus, we have been engaged in R&D of a jet fan using a model of JF600. In this paper, we demonstrate an idea to profile the section of rotor blade suitable for bi-directional flow, which is verified by using the aerodynamic performances of a two-stage jet fan obtained experimentally and numerically.

Keywords jet fan, two-stage, rotor blade, bi-directional flow, aerodynamic performance, turbulent flow analysis

Nomenclature

F	axial thrust (N)
L	shaft power (W)
n	rotational speed (rpm)
P	pressure (Pa)
P_t	total pressure (Pa)
P_T	total pressure rise of fan (Pa)
Q	flow rate (m^3/s or m^3/min)
R	radius of fan casing, = 0.315 m
r	radial distance (m)
SPL	sound pressure level (dB)
U_t	tip speed of rotor blade (m/s)
V_u	circumferential component of velocity (m/s)
V_z	axial component of velocity (m/s)
η	fan total efficiency
θ	setting angle of blade
ρ	density (kg/m^3)

Subscripts

1,2,3,4,5,6	measurement section

1 Introduction

A reversible axial flow fan called jet fan has been widely used for longitudinal ventilation in road tunnels to secure a safe and comfortable environment cost-effectively. Various researches and developments of jet fan have been made, and it is said that the fan has the satisfactory performance for the present needs. However, if the future need is concerned, it is still necessary to develop a jet fan having higher aerodynamic performance, for efficient usage of energy in every engineering system is vital in the low carbon society.

From the aerodynamic aspect, a cambered airfoil is regarded as favorable for the rotor (or impeller) blade like a unidirectional axial fan and the variable pitch mechanism is used to set the blade oppositely if the flow direction should be reversed in case of emergency. But, owing to very heavy duty as a safety measure, a reversible fan without this kind of mechanism has been adopted in actual cases. That is, such a method to drive the rotor in the reverse direction is used for switching the flow direction. As the fan should provide almost the same

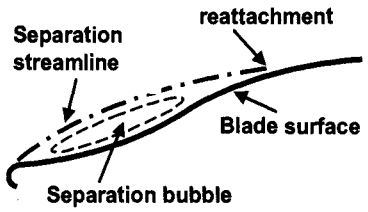

Fig. 1 Reattachment of separating flow to the blade surface

performance in both flow directions, those symmetrical blades without camber are used in the case of single stage fan rotor. The other structure is a 2-stage jet fan where two rotors are assembled to both sides of motor shaft. If higher speed jet from the fan is expected, the latter will be preferable. Though there are vast amounts of studies treating airfoil sections (Abbot and von Doenhoff, 1949), most of them have been done on the assumption of unidirectional flow. Thus, desirable airfoil sections for bi-directional flow are still unresolved.

As one of the typical sections is a symmetrical circular-arc airfoil, this section has been actually used for the rotor blade of a jet fan (Nishioka, et al., 2000). Airflow easily separates from the leading edge at some angle of attack for a blade having the sharp edge. It is known that aerodynamic performance of the blade doesn't deteriorate, once the separating flow reattaches the blade surface downstream. This knowledge indicates that the key to secure the performance is attributed to the stable reattachment of the separating flow on the surface. From this view, the wall surface consisting of concave and convex curves shown in Fig. 1 is taken up for consideration. It will be nice if this profile is usable for the rotor blade of jet fan. To respond the need, we have treated a new profile of rotor blade suitable for a two-stage jet fan in this study.

2 Rotor Blade

For validation of the present idea, the most reliable approach will be the performance test of the jet fan that has the proposed rotor blades. As we have been conducted experimental studies using JF600 models (Tukamoto, et al., 1991, Nishi, et al., 2002), the following two kinds of rotor blades for this class are prepared in this study:

Blade C: conventional symmetrical airfoil
similar to NACA0010
Chord length=150mm, AR=1.0, σ_{tip}=0.61, σ_{root}=1.19

Blade D: new symmetrical airfoil
base on the present idea
Chord length=170mm, AR=0.9, σ_{tip}=0.69, σ_{root}=1.35

Five blade sections (stream surface: root, ¼, ½, ¾, and tip) are stacked for both blades and are shown in Fig. 2, where variation of stagger angle with radial position is determined to satisfy the conditions below:

Inner diameter of cylindrical casing = 630 mm
Tip clearance ratio = 0.64%
Discharge = 9.35 m^3/min
at rotational speed less than 2200 rpm
Constant chord and thickness of 10%
Number of rotor blades = 8
Flow pattern (Vortex type) at the front blade exit:

$$V_u = const. \quad (1)$$

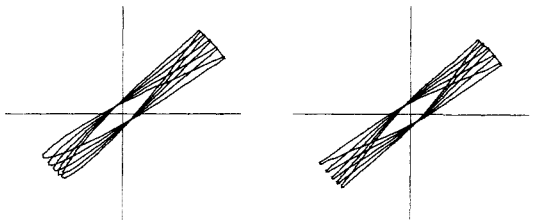

(a) Blade C (b) Blade D

Fig. 2 Cross section of rotor blade

3 Experimental Apparatsus and Method

3.1 Test jet fan and measurement system

Cross sectional view of the test 2-stage jet fan and the measurement system are schematically shown in Fig. 3. It is noted that the axial length of cylindrical casing with silencer is 0.4 m shorter than that of standard jet fan, usually called as JF-600. The test fan is hung on the beam attached to the frame construction. Each of two rotors is mounted on the shaft of an electric motor of 11kW, rotational speed of which is variable between 0 rpm and 2300 rpm by an inverter controller. The motor is supported with three struts of flat plate equally spaced in the cylindrical casing. The setting angle θ of rotor blade is adjustable so as to study its effect on the fan performance.

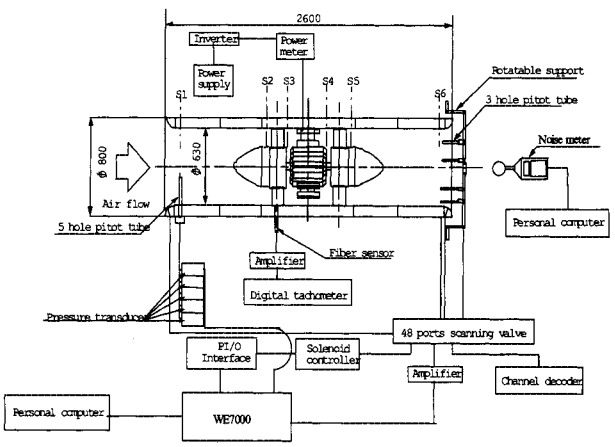

Fig. 3 Jet fan and measurement system (Nishi et al., 2002)

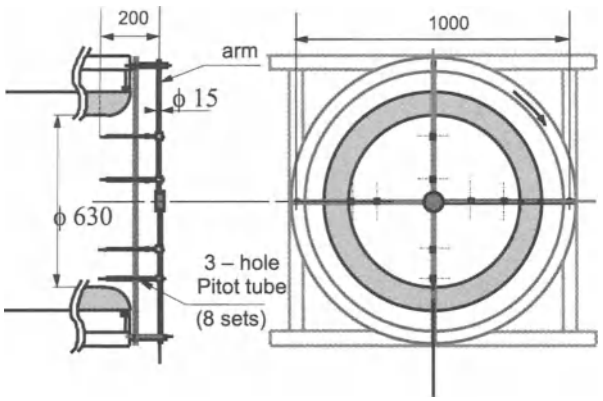

Fig. 4 Flow measurement device at the exit

The flow measurement device is such that eight three-hole Pitot tubes mounted on the rotatable support in the peripheral direction and they are arranged in the radial positions following the Japan Industrial Standard (JIS) for flow-rate measurement, as shown in Fig. 4. This is set at the fan exit to measure pressure P and velocity V near the silencer outlet (represented by S6 section), for variations of them cannot be regarded as negligible.

To investigate the flow field in the casing, a five-hole Pitot tube is traversed in the radial direction at five sections. As S2 and S5 are regarded as the inlet of first stage and the outlet of second stage respectively, the measured data are used to calculate the aerodynamic performance of the fan. Noise measurement was also made at the exit side following the JIS.

3.2 Parameters

As radial component of velocity is disregarded, axial component of velocity V_{z6} at S6 section is calculated from

$$V_{z6} = V_6 \cos\beta_6 \tag{2}$$

where β denotes flow angle from the axial direction.

Flow rate is calculated from equation (3).

$$Q = \int_{A_j} V_{z6}\, dA \tag{3}$$

The number of jet fans installed in a road tunnel is usually decided considering the axial thrust generated by those fans, as the wall friction loss due to the tunnel stream for ventilation is approximately balanced with the longitudinal force provided by the fans. Thus, measurement of the thrust at the performance test should be mandatory. Assuming that a complete jet fan unit tested in the still air condition is regarded as standard, the axial thrust F is measured by using the indirect method (Tukamoto, et al., 1991), which is given by

$$F = \rho \int_{A_j} (V_{z6}^2 - V_{z1}^2)\, dA + \int_{A_j} (P_6 - P_1)\, dA + \int_{A_B} (P_{B6} - P_{B1})\, dA_B \tag{4}$$

where $dA_B = dA\cos\gamma$

A_B: projected area of casing lip normal to z direction

γ: an angle of inclination of casing wall from r direction

P_B: pressure acting on the casing lip

It is noted that the ideal value F_0 given by equation (5) has been used as its index, which is known to overestimate the axial thrust of jet fan.

$$F_0 = \rho Q^2 / A_j \tag{5}$$

Since S2 and S5 represent the inlet and the exit of 2-stage fan respectively, the total pressure rise P_T is specified as an increase in total pressure between S2 and S5 sections, following the standard test codes for fans. Consequently, the fan total efficiency η is expressed as

$$\eta = \frac{QP_T}{L} = \frac{Q(\bar{P}_{t5} - \bar{P}_{t2})}{L} \tag{6}$$

where $\bar{P}_t = \int P_t V_z\, dA / \int V_z\, dA$ and L denotes the shaft power.

To evaluate the fan noise, specific noise level given by the following equation is used.

$$SPL_{SA} = SPL_A - 10\log(QP_T^2) + 2 \tag{7}$$

where SPL_A denotes the sound pressure level (A-characteristic).

4 Results and Discussion

4.1 Experimental performance

As the measurement of axial thrust is inevitable at the performance test, a complete unit should be used for the test. In this case, the aerodynamic performances are obtained at a single operating point only. Thus, the rotational speed n (rpm) and the setting angle of blade θ (θ=0:design stagger angle, and θ>0: decrease in stagger angle) are selected as experimental parameters in this study. Test range of the former was between 1600 rpm and 2200 rpm, and that of the latter was between -5 deg and 5 deg.

Flow rate and axial thrust: Variation of flow rate Q (m^3/min) and that of axial thrust F (N) against the rotational speed n (rpm) are shown in Fig. 5 and Fig. 6 respectively for two jet fans, one of which has Blade C and the other of which has Blade D. Almost the same results are

observed. That is, the difference between Blade C and Blade D is quite slight, but both Q and F for Blade D are a little bit larger than those of Blade C. From the linear relationship between n and Q, the similarity law is valid in the present test range, where the blade load is possible to increase with the increase of setting angle. It is seen that both rotor blades are usable from the Japanese guide line of 480 m^3/min if rotational speed and the setting angle are properly selected. Furthermore, we can realize that the present idea for profiling the blade section of a jet fan rotor is actually usable.

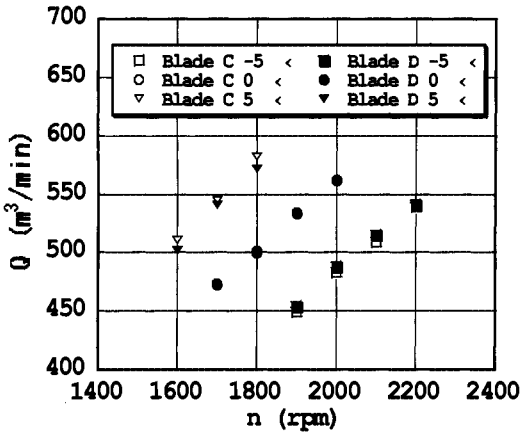

Fig. 5 Variation of flow rate against rotational speed

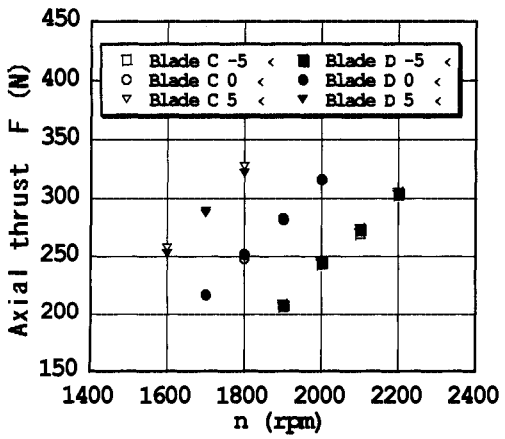

Fig. 6 Variation of axial thrust against rotational speed

Efficiency and noise level: Regarding fan efficiency and specific noise level, they are plotted against the setting angle θ in Fig. 7 and Fig. 8. Similar to flow rate and axial thrust, both results for Blade D are a little bit better than those for Blade C. The maximum efficiency of 65% is obtained at the design condition (θ= 0 deg). The efficiency is nearly constant in the range of positive setting angle up to 5 deg, but it varies with the angle in the negative range.

Regarding the noise level, SPL_{SA} gradually decreases with the increase the setting angle in the present test range. And the minimum value around 32 dB(A) is observed at θ = 5 deg. From the examination that the sound decay with distance is satisfactorily represented by the following equation, SPL_A at the location of 1.5 m is suspected to reach 30 dB(A).

$$\Delta SPL_A = 20 \log \frac{I_0}{I} \tag{8}$$

where I_0: distance from noise source to the standard location I: distance from the source to measurement location.

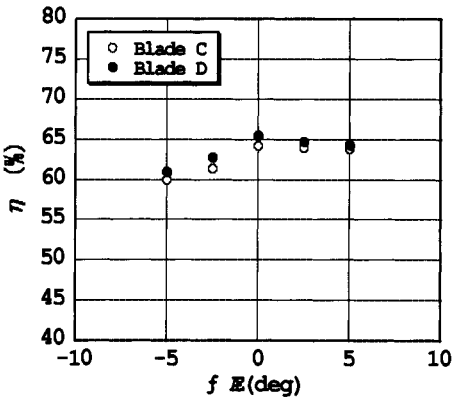

Fig. 7 Fan efficiency vs. blade setting angle

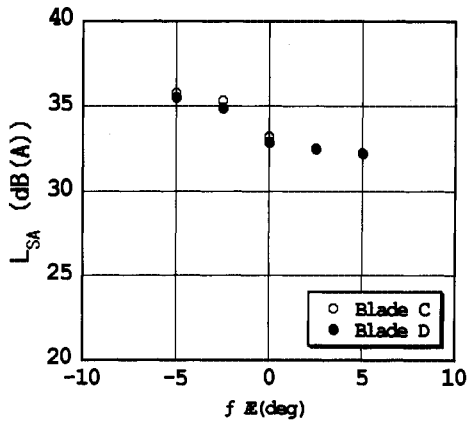

Fig. 8 SPL_{SA} (= L_{SA}) vs. blade setting angle

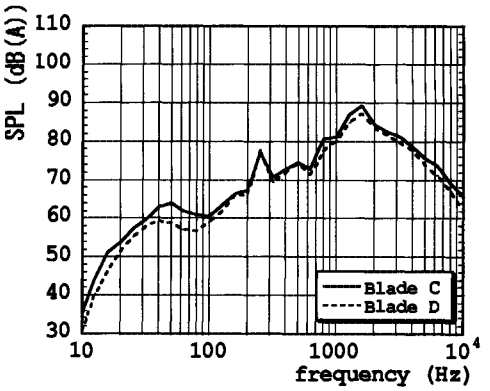

Fig. 9 1/3 octave band analysis of fan noise

As slight decrease is achieved if Blade D is used instead of Blade C, frequencies of the fan noise are investigated by using the one-third octave-band analysis. A typical result is shown in Fig. 9, where the noise component of 1600 Hz and the broad band noise are predominant. Two other dominant components are 267 Hz and 800 Hz. The frequency of 1600 Hz corresponds to $2 Z_r Z_s (n / 60) = 2 \times 8 \times 3 \times (2000/60)$, where Z_r and Z_s are the number of rotor blades and struts respectively.

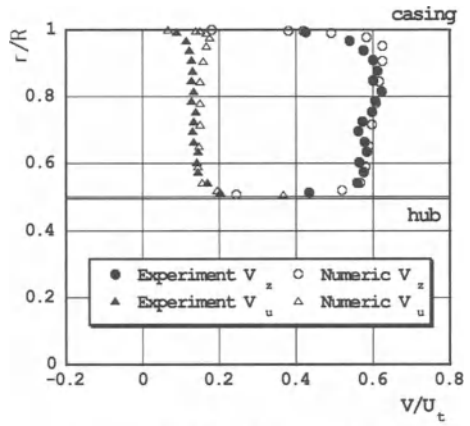

(a) velocity distributions at S3 section

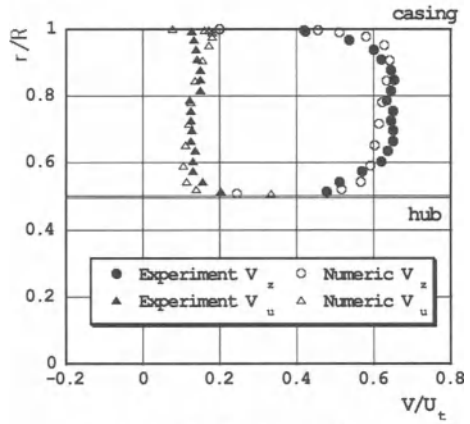

(b) velocity distributions at S5 section

Fig. 10 Radial distributions of velocity (θ= 0 deg, n = 2000rpm)

4.2 Internal flow

Radial distributions of velocities V_z and V_u at two locations, S3 for the front rotor exit and S5 for the rear rotor exit are shown in Fig. 10, were each velocity is normalized by the peripheral velocity at blade tip U_t. They were measured by traversing a five-hole Pitot tube in the radial direction from the casing wall. The following features of flow are observed.

S3 section (front rotor exit):

Axial velocity is nearly uniform in the center region, but its deficit near the casing wall and hub wall cannot be treated negligible.

Circumferential velocity is almost regarded as constant, which reasonably corresponds to the present design vortex type.

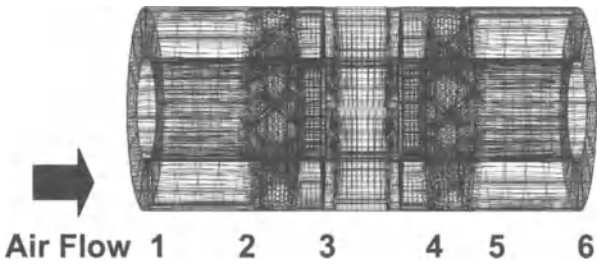

Fig. 11 Computational domain (Grids: 737919)

S5 section (rear rotor exit):

The uniform zone of axial velocity decreased by comparison with that at S3.

As the rear rotor also works, the circumferential velocity is larger than that at S3.

4.3 Numerical simulation for consideration

To deepen our understanding of those test results, the steady turbulent flow analysis based on the continuity equation and RANS equations was conducted by using the commercial CFD software CFX-TASCflow with k-ω turbulence model. As shown in Fig. 11, the computational domain is set between S1 and S6 sections of jet fan so that it is a cylindrical annular pipe where two rotors and the strut between the front rotor and the rear are installed. The axsymmetric uniform velocity is assumed at the inflow plane and a mass flow is set at the outflow plane as the boundary conditions.

Validation: As the simpler domain is treated in the present simulation, computational results of internal flow are at first evaluated by comparison with the experimental data measured by the five-hole tube. One of examples is shown in Fig. 12, where velocity distributions at the exits of two rotors with Blade C are arranged. We can recognize the reasonable correspondence between the experiments and the numerical simulations, though the difference between them is observed in the zone near the casing wall. It is suspected that the assumption of uniform flow at the inflow plane is one of major causes.

Performance prediction: Using the present simulation model, performance prediction is attempted. Table 1 shows the results. The following features are deduced:

(1) Better aerodynamic performance of Blade D than that of Blade C is predicted. It is seen that the steady simulation is qualitatively explained the measurement result.

(2) Total pressure rise ΔP done by the front rotor doesn't differ too much between Blade C and Blade D, but the rise by the rear rotor of Blade C is much smaller than that of Blade D. Same trend is observed in efficiency. This is understandable because the geometry of Blade B is decided based on the unidirectional flow so it doesn't provide a good performance in the case of the counter flow.

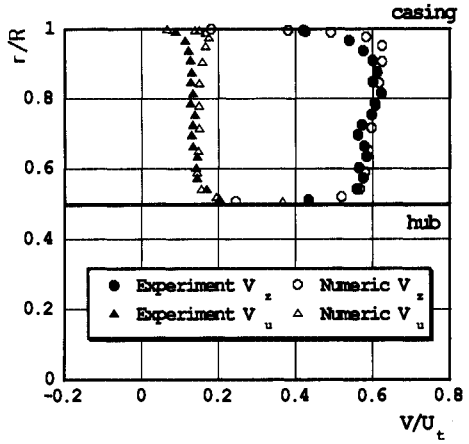

(a) velocity distributions at S3 section

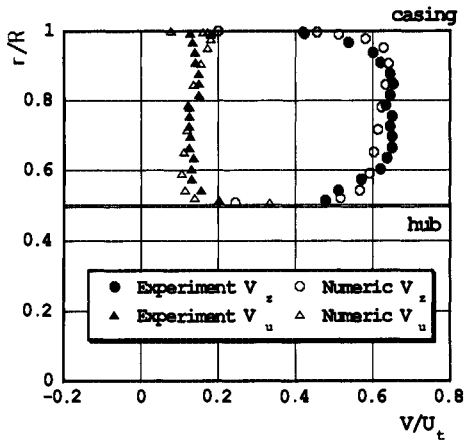

(b) velocity distributions at S5 section

Fig. 12 Comparison of simulation with experiment ($\theta = 0$ deg, $n = 2000$ rpm)

Blade wake: As the broad band noise was one of major causes for the present fan noise from Fig. 9, distributions of axial velocity just downstream of the rear rotor blade are correlated numerically and plotted by using a contour map in Fig. 13(a) and (b). The former is for Blade C and the latter corresponds to Blade D. The wake region of Blade C is greater than that of Blade D so that it is realized that the broad band noise is primarily related to the blade wake.

5 Conclusions

From the present experimental and numerical study on two-stage jet fan by using JF600 models having two kinds of rotor blades, the following conclusions are drawn:

Table 1 Prediction of aerodynamic performance

$n = 2000$ rpm		power (kW)	ΔP (Pa)	η (%)
Blade C	front rotor	5.06	446	80.7
	strut	—	−50	—
	rear rotor	1.6	93	53.2
	2 stage	6.65	489	67.2
Blade D	front rotor	5.25	458	79.7
	strut	—	−55	—
	rear rotor	2.41	194	73.6
	2 stage	7.66	597	71.2

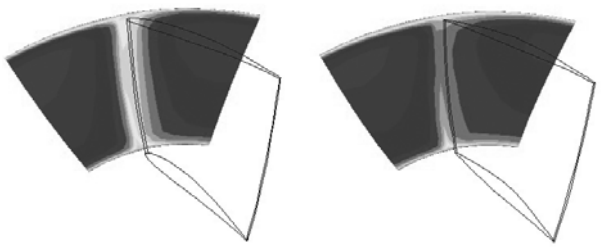

(a) Blade C (b) Blade D

Fig. 13 Contour map of axial velocity at the exit of rear blade ($\theta = 0$ deg, $n = 2000$ rpm)

(1) The symmetrical airfoil section for bi-directional flow, called Blade D in this paper, is sufficiently usable for rotor blades of an advanced jet fan.

(2) The aerodynamic performance is reasonably predicted by a turbulent flow analysis.

Acknowledgements

We would like to thank Fuji Electric Systems Co., Ltd. for their support. We also thank Mr. Hiroki Sunami and Mr. Shingo Shuto for their contributions to this work as their graduate studies.

References

Abbot, I.H., and von Doenhoff, A.E., 1949, "Theory of Wing Sections", *Dover*

Nishioka, T., Terasaka, H., and Kozu, T., 2000, "New Jet Fan for Tunnel Ventilation", *Turbomachinery*, 28-6, pp.357 – 363 (in Japanese)

Nishi, M., Yoshida, K., Matsuda, I., Yamasaki, K., and Kojima, K., 2002, "Aerodynamic Performance of 2-Stage Jet Fan Having Forced-Vortex-Type Rotor", Proceedings of 9th International Symposium on Transport Phenomena and Dynamics of Rotating Machinery, Honolulu

Tukamoto, T., Niikura, Y., and Nishi, M., 1991, "Development of Jet Fans for Tunnel Ventilation", Aerodynamics and Ventilation of Vehicle Tunnels, pp. 847 – 858, *Elsevier*

The 4th International Symposium on Fluid Machinery and Fluid Engineering
November 24-27, 2008, Beijing, China
NO. 4ISFMFE-IL11

Flow Characteristics in a Cross-Flow Fan with Various Design Parameters

Youn J. Kim

School of Mechanical Engineering, Sungkyunkwan University,
300 Cheoncheon-dong, Suwon 440-746, Korea
Tel: +82-31-290-7448/ Fax: +82-31-290-5889
E-mail: yjkim@sku.edu (Corresponding Author)

Abstract The flow behavior and the performance of the cross-flow fan were investigated for various design parameters such as impeller exit angles, rearguider shapes, stabilizer position, setting angle and gap. In order to determine the values of design parameters, equations for design parameters were derived and verified. The design program to solve the parameters was coded using visual basic. Comparisons exiting models and new geometries from the program were carried out by the numerical and experimental methods. Governing equations are descretized by the finite volume method to find the solutions for flow variables. The hybrid scheme was used to handle the convection and diffusion terms in the governing equations. The standard k-ε turbulence model with the wall function was adopted to simulate the behaviors of turbulence. Experimental apparatus, the front suction type fan tester, is arranged to comply with ASHRAE standard 51-75. In order to measure the pressure distribution inside the cross-flow fan, the static pressure and electrical power are measured. In this study, the relation among design parameters is revealed through these analyses and the optimum geometries are found out.

Keywords archimedes spiral, cross-flow fan, rearguider, stabilizer, impeller exit angle

Nomenclature

b	width [mm]
C	absolute flow velocity [m/s]
U	absolute impeller velocity [m/s]
W	relative flow velocity [m/s]
Z_b	number of blade [-]

Greek symbols

α	flow angle [degree]
β	blade angle [degree]
θ_{es}	setting angle of a stabilizer [degree]
θ_{rs}	starting angle of a rearguider [degree]
σ	slip factor [-]

Subscripts

2	exit of impeller
3	basic circle of a rearguider
d	design point
m	direction of radius
θ	tangential direction

1 Introduction

Turbomachinery is classified with blower, fan and compressor in accordance with the pressure difference and operating principle. A cross-flow fan (CFF) with a pressure rise below 10 mAq belongs to fan among them. A cross-flow fan widely used in air conditioning systems and industrial applications is composed of an impeller, a rearguider, a stabilizer and a heat exchanger in case of air conditioning systems (see Fig. 1). Since a working fluid passes through impeller blade twice without distinction between an inlet and exit angles, a cross-flow fan relatively has higher dynamic pressure. Also the forward curved blade produces higher circumferential velocity than other types of blade at the same flow rate.

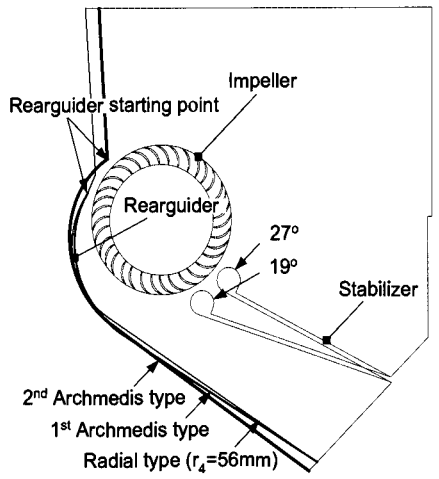

(a) model of a cross-flow fan

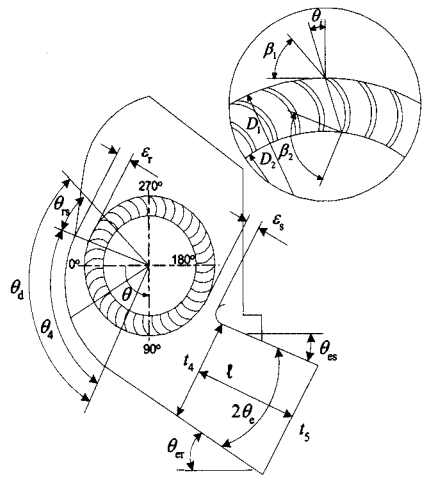

(b) design parameters

Fig. 1 Schematic diagram and design parameters of a cross flow fan

There are two different vortices in the flow fields of the cross-flow fan. One is an eccentric vortex, i.e., forced vortex, and the other is the free vortex in the rearguider. The eccentric vortex makes it difficult to determine the design flow rate in the design process. Therefore, provide that the size and the position of the eccentric vortex are investigated properly, the performance evaluation of the cross-flow fan is expected remarkably.

The majority of the study devoted to the cross-flow fan has been performed by experimental method. But design theory has not been established yet, because design parameters are related to each other and the size and the position of the eccentric vortex have not been examined properly.

Eck (1973) investigated the free vortex along with the forced vortex in cross-flow fan using experimental and analytical methods and studied the flow and noise characteristics with various stabilizer shapes. Tsurusaki *et al.* (1997) found the path line and velocity distribution using a digital camera, calculated the generation and the diffusion of the vorticity induced by the eccentric vortex and measured the velocity of the internal flow in the cross-flow using PTV (particle tracking velocimetry). Murata and Nishihara (1976) found that the gap between the impeller and stabilizer, the setting angle of stabilizer and the rearguider figuration are important design parameters, which affect the performance characteristic of the cross-flow fan. Combes *et al.* (1996) analyzed the turbulence and unsteady flow inside the cross-flow fan using FEM (finite volume method). Gabi and Klemn (2003) verified the results of numerical analysis, comparing the flow characteristics of the cross-flow fan with two-dimensional geometry using STAR-CD with experimental results measured by PIV (particle image voelocimetry).

Table 1 General parameters and operating conditions

Parameter	Dimensions
Impeller diameter, D_2	95 mm
Diameter ratio, D_1/D_2	0.76
Inlet angles	β_2=90°
Exit angles	β_1=16.5°, 24.5°, 32.5°, 40.5°
Number of blade	35
Blade profile	Circular arc
Rotating speed	16.67 sec^{-1}
Re_C (blade chord length)	4,490
Re_D (impeller diameter)	31,458

The purpose of this study is to investigate the performance characteristics of the cross-flow fan with various impeller exit angles, rearguider shapes and stabilizer positions.

2 Theoretical Background

Design parameters and general specifications of the modeled CFF are shown in Fig. 1 and Table 1. In order to investigate the characteristics of the performance, dimensionless parameters, i.e., the pressure coefficient (ψ), the flow coefficient (ϕ) are defined as follows:

$$\psi = 2\Delta p_s / \rho U_2^2, \qquad \phi = q / b_2 D_2 U_2 \tag{1}$$

The relevant formula for the spiral is as follows:

$$r_4(\theta) = r_3 \exp[q_d \theta / (C_{\theta 2} \cdot r_2 \cdot b_2 \cdot \theta_d)] \tag{2}$$

where,

$$r_3 = r_2 + \varepsilon_r,\ C_{\theta 2} = \sigma(C_{m2}/\tan\beta_2)$$

$$\sigma = 1\Big/\left(1+\sin(\pi-\beta_2)\frac{\pi}{Z_b(1-r_1/r_2)^2}\right)$$

Using the above formulas, Archimedes spirals were generated at design point (5 CMM). Two Archimedes spirals are distinguished from the starting angle (θ_{rs}) of the rearguider. As shown in Fig.1, the difference of the starting angle ($\Delta\theta_{rs}$) between the first Archimedes spiral (hereafter 1st Ar) and the second Archimedes spiral (hereafter 2nd Ar) is 13.7°. Each straight part of the rearguiders is a tangential line of the curved part. Also, four different empirical values of impeller exit angles such as 16.5°, 24.5°, 32.5° and 40.5° are used.

Table 2 Stabilizer positions

θ_{es}	Radial (56 mm)		1st Archimedes		2nd Archimedes	
	AR	$2\theta_e$	AR	$2\theta_e$	AR	$2\theta_e$
27°	1.22	6.2°	1.16	4.8°	1.18	5.5°
25°	1.33	8.4°	1.26	7.0°	1.46	12.9°
23°	1.46	10.4°	1.37	9.13°	1.59	14.9°
21°	1.62	12.5°	1.51	11.1°	1.76	17.1°
19°	1.82	14.3°	1.68	12.9°	1.95	19.0°

The stabilizer and the straight part of the rearguider constitute the exit duct performing as a channel diffuser (see Fig. 1). Then, changing the setting angle of the stabilizer (θ_{es}), the area ratio (AR) and the enlargement angle ($2\theta_e$) of the exit duct are varied as shown in Table 2. Especially, the setting angle is varied from 19° to 27° per 2° and the gap between the impeller and the stabilizer is fixed at 3.5 mm.

3 Numerical Analysis

It is helpful to use numerical methods for getting a better understand of the complex flow-phenomena of the cross-flow fan and to reduce the number of experiments in the process of design, development and manufacturing. The conservative equations for two-dimensional, unsteady, turbulence and viscous flows are used as follows:

$$\frac{1}{\sqrt{g}}\frac{\partial}{\partial t}(\sqrt{g}\rho)+\frac{\partial}{\partial x_j}(\rho u_j)=0 \tag{3}$$

$$\frac{1}{\sqrt{g}}\frac{\partial}{\partial t}(\sqrt{g}\rho u_i)+\frac{\partial}{\partial x_j}(\rho\tilde{u}_j u_i-\tau_{ij})=-\frac{\partial P}{\partial x_i}+S_i \tag{4}$$

where t is the time, $\sqrt{g}$ is the matrix equation of a tensor, ρ is the density, u is the velocity and S_i is the source of momentum, respectively.

The above governing equations are discretized by the finite volume method (FVM) to find solutions for flow variables. The hybrid scheme is used to handle the convection and diffusion terms in the governing equations. The standard k-ε turbulence model with the wall function is chosen to simulate the behaviors of turbulence. Because of the distinctive trait of the flow through the impeller, it is necessary to use a transient method in the impeller domain. Analyses are carried out until solutions reached a quasi-steady state, using a commercial code, STAR-CD.

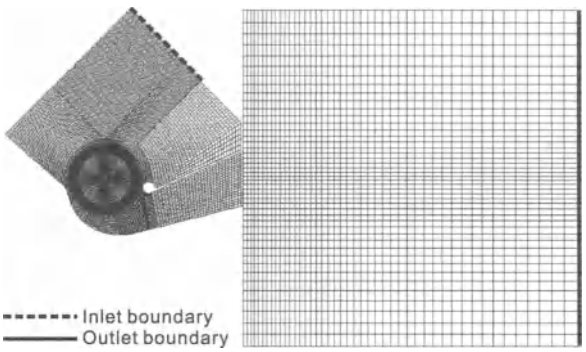

Fig. 2 Grid systems of the modeled cross-flow fan

The multi-block method is used to form the complicated flow domain of a cross-flow fan. The numerical domain consists of the inlet region, the impeller, the rearguider, the stabilizer and the exit duct (see Fig. 2). The links between the rotating and stationary parts are released by a sliding interface. The sliding grid provided with an event module makes a possible to simulate the unsteady and the rotating flow behaviors on the interface. It is assumed that the flow is two-dimensional in the grid systems. The number of cells was fixed at 65,000 to save the calculation time.

In addition, no-slip condition is adopted on walls and it is assumed that there is no mass flux perpendicular to the walls. Wall functions are employed to reduce the number of cells for calculating turbulence variables. Figure 2 shows pressure and outlet boundary conditions applied to the inlet and the outlet boundaries. The attachment boundary condition is used on the interface between the rotating cell near the impeller and the fixed cell at the coordinate system.

4 Experiments

The experimental apparatus, the fan tester, was arranged to comply with ASHRAE standard 51-75. It is a front

suction type as shown in Fig. 3. The static pressure produced by CFF is measured from static pressure taps at the upstream stabilization chamber of the fan tester. The micromanometer (SAMDUK, FCO510, error rate: ±0.25%) was used to record the pressure difference for measuring the flow rate. The volume flow rate is calculated from an empirical equation using the static pressure difference at the upstream and downstream of five nozzles located at the middle of the tester. These are respectively opened or closed to set the operating flow rate. The uncertainty for the volume flow rate is ±2.83%. The power of the working motor connected to CFF is generally obtained by multiplying the torque of the fan shaft and the angular velocity after measuring those respectively using a torque meter and an rpm gauge. However, in this study, it was measured using the digital power meter and corrected using the performance curve of the motor.

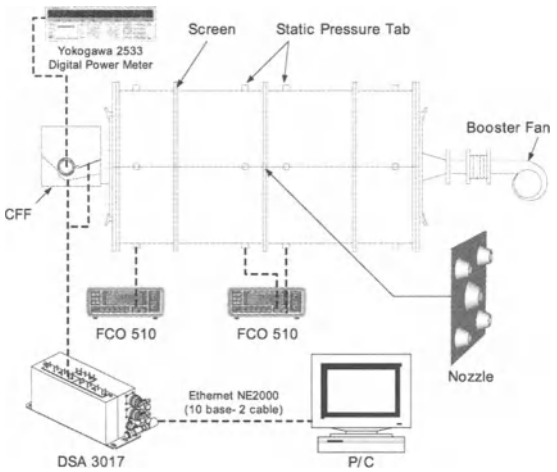

Fig. 3 Schematic diagram of a fan tester

5 Results and Discussion

In order to elucidate the flow field in CFF in detail, the meridional velocity (C_{m2}) around the exit of impeller is presented in Fig. 4. Results are plotted by each rearguider at θ_{es}=21°. The positive value of velocity denotes that the fluid is discharged from the impeller. On the contrary, for a negative value, it denotes that the fluid is sucked. In the aspect of θ, the positions of stabilizer are located at 124.0° (θ_{es}=25°), 129.5° (θ_{es}=23°) and 135.0° (θ_{es}=21°) respectively. Besides, the starting angle of the rearguider is separately 327.6° (for Radial and 1st Ar) and 313.9° (for 2nd Ar). The eccentric vortex occurred at 80°. Periphery flows around the impeller consist of suction, discharge, recirculation and diffusion. First, suction is formed on the right side of the impeller (θ = 120°~240°) and fluid is discharged to the left side (θ = 0°~80° and 330°~360°). Diffusion occurred on the top (θ = 240°~330°) and recirculation region resulted from the eccentric vortex are located at the bottom (θ = 80°~120°).

The meridional velocity in the discharge region increases as θ increases in case of Archimedes spiral, but that is nearly fixed to a regular value. The phenomenon for 1st and 2nd Ar results from the characteristics of the Archimedes spiral. Archimedes spiral is designed to keep the vertical velocity identical for a cross-sectional area at $\theta(x)$. Therefore, the flow rate ($q_{\theta(x)} \propto C_{m2}$) and the cross-sectional area are gradually increased along the spiral. In case of Radial type, the meridional velocity does not increase following with the increasing cross-sectional area, but is uniform. Then, the vertical velocity in the cross-sectional area is varied along the curved part of the rearguider and this may cause the friction loss.

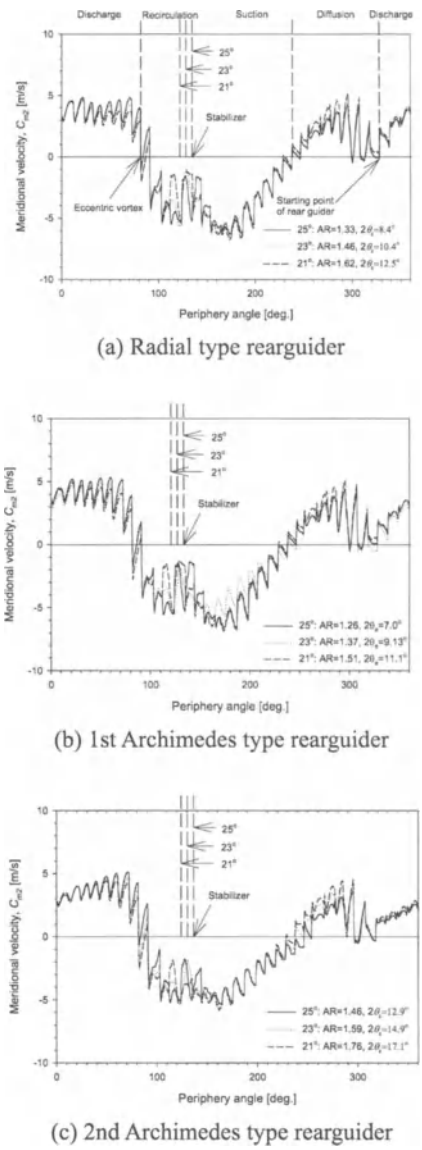

Fig. 4 Meridional velocity profiles around the impeller with different stabilizer positions

Aforementioned, the eccentric vortex is an important parameter on the design of CFF and the recirculation induced by the eccentric vortex makes it difficult to determine the design flow rate in the design process. It is also noted that the distance from the eccentric vortex to the stabilizer is important for improving the performance. If the position of this vortex is located near the stabilizer, the performance becomes higher as generally known. As the setting angle is smaller, the distance becomes smaller because the eccentric vortex hardly moves. This reduces the recirculation quantity. Therefore, in case of the smallest setting angle, the performance is better than the others.

The fluid diffused from the main flow is discharged to the top of the impeller and some of that flows out to the inlet of the CFF. This may result in the increment of the loss and the unsteadiness. In case of 2nd Ar that has the small starting angle of the rearguider as shown in Fig. 1(b), the quantity of the diffusion flow is smaller than the others and suction and diffusion flows increase simultaneously. Therefore, the starting angle of the rearguider should be considered to reduce the diffusion flow.

The operating characteristics with various positions of the stabilizer are shown in Fig. 5. The fluid obtains the momentum from the centrifugal force and the Coriolis force generated by the rotation of the impeller. The working fluid is also discharged into the rearguider within the discharge region (θ_d). However, some of the discharged fluid is recirculated to the impeller, which will result in the eccentric vortex. This vortex occurs necessarily when a cross-flow fan operates. The recirculation is an essential factor to produce the loss of a cross-flow fan. As the setting angle decreases, the inlet area of the diffuser (t_4) is decreased and much less flow is recirculated. The best setting angles (θ_{es}) having the highest ψ are 23° for Radial type, 21° for 1st Ar and 21° for 2nd Ar. The notion about the optimum setting angle is very obscure since there is no relevant design theory. As mentioned above, it is reasonable to define the region between the rearguider straight part and the stabilizer as a simple channel diffuser and find out the optimum area ratio (AR) and the enlargement angle ($2\theta_e$) of the diffuser. Because of the step-shear velocity distribution at the inlet of the diffuser, the best AR is respectively shown as 1.46, 1.51, and 1.55 in order: Radial type, 1st Ar and 2nd Ar. It is also noted that the best $2\theta_e$ is separately 7.4°, 11.1°, and 11.6°.

In order to describe the flow field around the impeller in detail, the meridional velocity (C_{m2}) profiles are prepared in Fig. 6. Circumferential flow patterns around the impeller consist of discharge, recirculation, suction and diffusion. If the value of the velocity is positive, it is

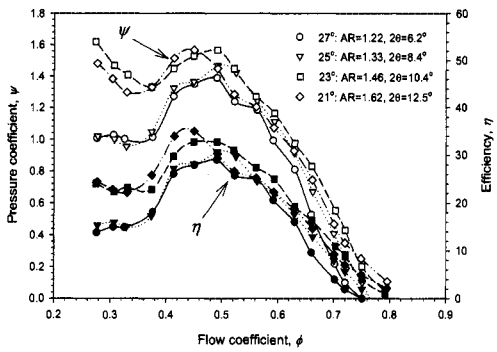

(a) Radial type rearguider

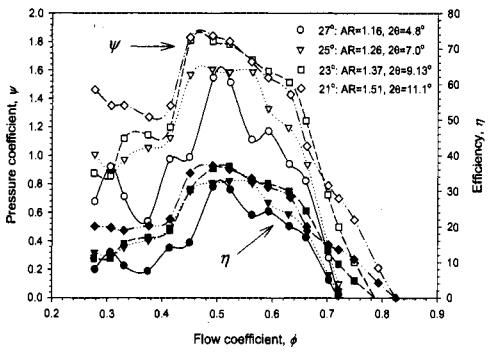

(b) 1st Archimedes type rearguider

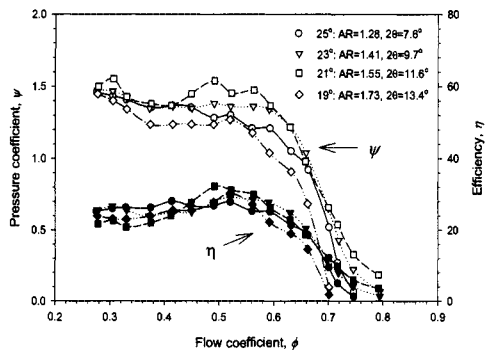

(c) 2nd Archimedes type rearguider

Fig. 5 Pressure coefficient and efficiency with flow coefficient for various stabilizer positions

noted that the flow is discharged from the impeller. On the other hand, for a negative value, it denotes generated by a diffusion of the main flow is discharged from the upper region of the impeller and the recirculation between the stabilizer and impeller is induced by an eccentric vortex. In order to improve the fan performance, one must reduce the recirculation and the discharged working fluid mentioned above. The recirculation zone having negative values of the meridional velocity (denoted as in Fig. 6(a)) represents the size of the eccentric vortex. The smaller this zone is, the better the fan performance is. It is seen that the size of the eccentric vortex of β_2=24.5° and β_2=32.5° for Archimedes spiral types is smaller than those

of β_2=16.5° and β_2=40.5°. Also, results show that the center of the eccentric vortex is located at the same location regardless of rearguider shapes (see Fig. 6).

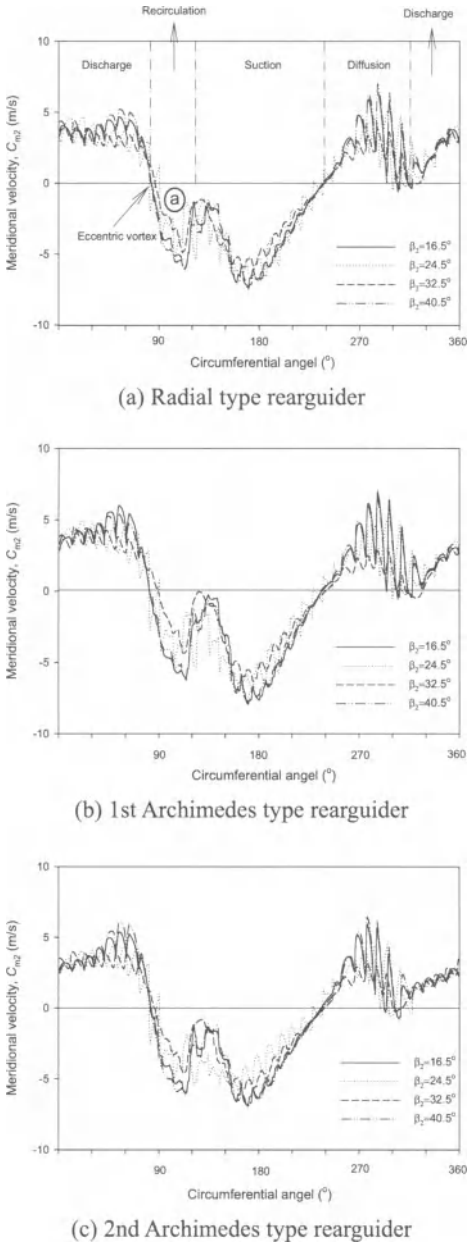

(a) Radial type rearguider

(b) 1st Archimedes type rearguider

(c) 2nd Archimedes type rearguider

Fig. 6 Meridional velocity profiles around the impeller with various exit angles

Figure 7 shows the pressure coefficient and the efficiency against the flow coefficient. As for the pressure coefficient and the efficiency, the results of β_2 = 24.5° and β_2 = 32.5° for R56 show the similar tendency. However, β_2 = 16.5° and β_2 = 40.5° show lower pressure coefficient and efficiency distribution, comparing with β_2 = 24.5° and β_2 = 32.5°. Results also show that the Archimedes spiral types, the 1st Ar5 and the 2nd Ar5 show the same tendency as the Radial one. It is seen that the impeller exit angle having the excellent pressure coefficient and efficiency is around β_2 = 30.0°. In case of Archimedes spiral types, the maximum pressure coefficient occurs at the flow coefficient (ϕ = 0.50) and the pressure coefficient increases after decreasing on the left side of the flow coefficient (ϕ = 0.50). This is a general phenomenon for the multi-blade fan like the sirocco fan and may be resulted from the strong unstable flow fields induced by a stall at the low flow rate (on the left side of ϕ = 0.50). It is noted that the stall causes loss and makes the difference of the pressure coefficient smaller.

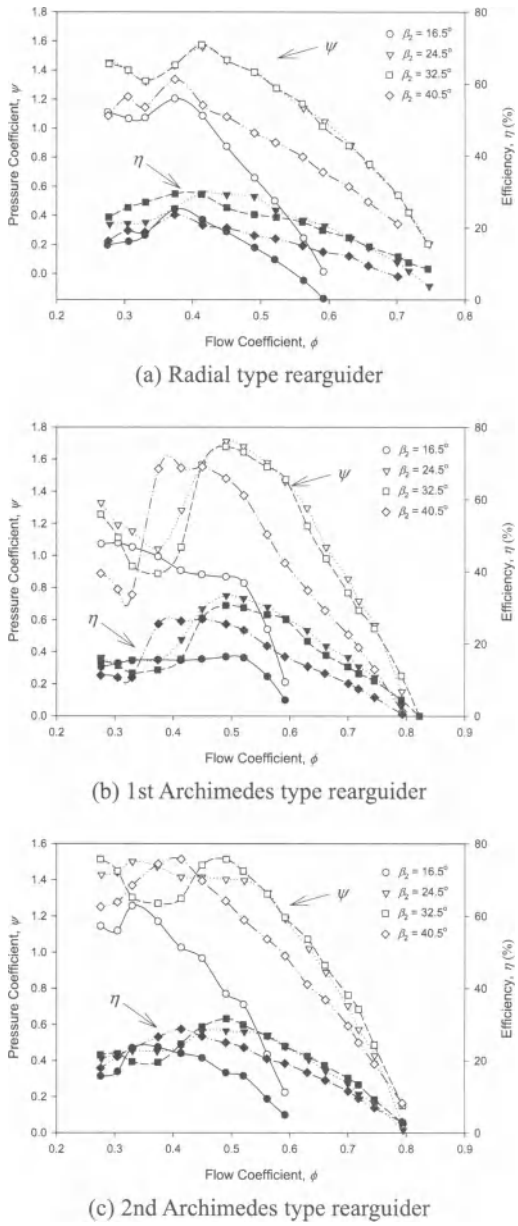

(a) Radial type rearguider

(b) 1st Archimedes type rearguider

(c) 2nd Archimedes type rearguider

Fig. 7 Pressure coefficient and efficiency with flow coefficient for various exit angles

6 Conclusions

(1) The size of the eccentric vortex with $\beta_2 = 24.5^\circ$ and $\beta_2 = 32.5^\circ$ is smaller than that with $\beta_2 = 16.5^\circ$ and $\beta_2 = 40.5^\circ$. Also, the center of the eccentric vortex is located at the almost same location for all rearguider types, such as R56, the 1st Ar5 and the 2nd Ar5.

(2) The rearguider with Archimedes spiral shows a good way to raise the pressure coefficient and efficiency, comparing with the Radial type.

(3) As the setting angle decreases, the inlet area of the diffuser is decreased. In that case, much less flow is recirculated to the impeller. This phenomenon may reduce the loss and lead to increase the velocity in the whole domain.

References

Combes, J. F., Bert, P. F., Pessiani, J. F. and Kueny, J. L., 1996, "Unsteady Flow Calculation in a Cross Flow Fan Using a Finite Element Method", *ASME 96-GT-443*

Eck, B., 1973, "Fans: Design and Operation of Centrifugal, Axis-Fan and Cross-Flow Fan", *Pergamon press*, New York

Gabi, M. and Klemm, T., 2003, "Numerical and Experimental Investigations of Cross Flow Fan", *the 12th International Conference on Modeling Fluid Flow*, pp. 1214 – 1219

Murada, S. and Nishihara, K., 1976, "An Experimental Study of Cross Flow Fan (1st Report, Effects of Housing Geometry on the Fan Perforamnce)", *Bulletin of JSME*, Vol. 19, No. 129, pp. 314 – 321

Murada, S. and Nishihara, K., 1976, "An Experimental Study of Cross Flow Fan (2nd Report, Movement of Eccentric vortex inside Impeller)", *Bulletin of JSME*, Vol. 19, No. 129, pp. 322 – 329

Tsurusaki, H., Tsujimoto, Y., Yoshida, Y. and Kitagawa, K., 1997, "Visualization Measurement and Numerical Analysis of Internal Flow in Cross-Flow Fan", *Journal of Fluids Engineering*, Vol. 119, pp. 633 – 638

The 4th International Symposium on Fluid Machinery and Fluid Engineering
November 24-27, 2008, Beijing, China
NO. 4ISFMFE-Ab17

Determination of an Optimum Orbiting Radius for an Oil-Less Scroll Air Compressor

Yong Ho Lee[*1], Tae Hun Kwon[1] and Hyun Jin Kim[2]

[*1] Graduate school, University of Incheon,
177 Dohwa-dong, Nam-gu, Incheon, 402-749, Korea
Tel: +82-32-770-4372 / Fax: +82-32-770-8423
E-mail: redhuman@incheon.ac.kr

[2] Dept. of Mechanical Engineering, University of Incheon,
177 Dohwa-dong, Nam-gu, Incheon, 402-749, Korea

Abstract Design practice has been made on an oil-less scroll air compressor as an air supply device for a 2 kW fuel cell system where air pressure of 2 bar and flow rate of 120 liter/min are required. Basic structure of the scroll compressor includes double-sided scroll wrap for the orbiting scroll driven by two crankshafts connected to each other by a timing belt. These features can eliminate thrust surface which otherwise would produce frictional heat and jeopardize reliable operation of the orbiting scroll and the scroll element's deformation as well. This study focuses on optimum scroll wrap design; orbiting radius has been chosen as an independent design parameter. As the orbiting radius changes, scroll sizes such as scroll base plate and discharge port diameters change accordingly. Gas compression-related losses and mechanical loss also change with the orbiting radius. With a scroll base plate diameter of 120mm at most and discharge port of at least 10mm, the orbiting radius should be within the range of 2.5 ~ 4.0mm. With this range of the orbiting radius, it was estimated by performance analysis that the compressor efficiency reached to a maximum of $\eta_c = 96\%$ at the orbiting radius of r_s =3.5mm for the scroll wrap height-to-thickness ratio of $h/t = 5$.

Keywords scroll compressor, orbiting radius, wrap design

Nomenclature

F	Force [N]
h	Wrap height [m]
L	Loss [W]
l	Length [m]
l_p	Length from Orbiting scroll center to Crankshaft eccentric center [m]
m_{os}	Mass of Orbiting scroll [kg]
$\dot{m}_s$	Air usage in the stack, mass flow rate [kg/s]
N	Shaft speed [rpm]
P	Pressure [bar]
P_e	Stack power [kW]
Q_s	Flow rate [*lpm*]
r_s	Orbiting radius [m]
t	Wrap thickness [m]
t_s	Suction temperature [°C]
V	Volume [cc]
V_c	Voltage of each cell in the stack [V]
$V.R$	Volume ratio
W_C	Compressor input [W]

Greek symbols

α	Starting angle [°]
ϕ	Involute angle [°]
η	Efficiency [%]
λ	Stoichiometric coefficient
μ	Friction coefficient
θ	Crank angle [°]
ω	Angular velocity [rad/s]

1 Introduction

As the air compressor consumes the most electric power among the peripheral devices of a fuel cell, increasing the efficiency of the air compressor is essential to improve the overall efficiency of the fuel cell system. A turbo-type air compressor is adequate for a large capacity generator since it requires a significant amount of air supply, and a positive displacement air compressor is more suitable for a small or medium capacity system.

The rotary vane type has mainly been used as the positive displacement air compressor for fuel cell applications.

A typical rotary vane air compressor involves a vane rotating by the centrifugal force while it is attached to the cylinder wall, creating substantial friction loss between the vane hem and the cylinder wall, and generating an excessive amount of heat. Several means of resolving these problems have been suggested (Drive, 1999; Kim, 2007), but significant improvements have not yet been reported.

A scroll type compressor has a fundamentally different structure than the rotary vane type. In a scroll compressor, the crankshaft rotates 2-3 times from intake to outlet, which yields smooth compression and little variation of torque to facilitate a less noisy operation. Thanks to the scroll compressor's highly efficient characteristics, low noise and low vibration, oil-less scroll air compressors have been introduced for general industrial purposes, but their compressor ratios are 7 or greater, making them inadequate for fuel cell applications, which require low-pressure air.

Based on the basic structure of the oil-less scroll air compressor for industrial applications, this study proposes an approach for designing a scroll air compressor applicable to the fuel cell system and suggests the estimated size and performance of the scroll air compressor for fuel cell applications under given conditions regarding its capacity and operation.

2 Conceptual Design

2.1 Basic structure of scroll air compressor

Air compressor for fuel cell application should deliver pure air, particularly free of oil containment, and it should also be a highly reliable for long periods of continuous operation. Since oil is essential to compressors in terms of cooling and lubrication, oil-less operations for fuel cell air compressors demand many particular requirements such as special surface treatment on the sliding parts of the compressor and some design techniques such as design of avoiding sliding surfaces as much as possible and of reducing frictional heat generation. Considering these aspects, a schematic of the basic structure of a scroll air compressor is presented in Fig. 1.

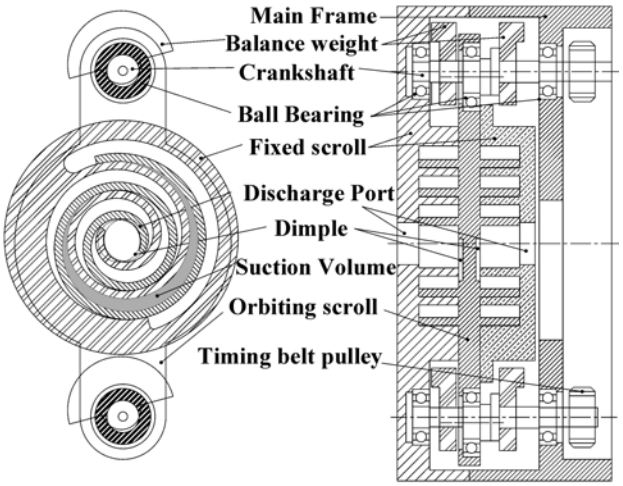

Fig. 1 Basic structure of scroll air compressor

For the double-sided scroll wrap structure, the axial gas forces action on both sides of the orbiting scroll plate to balance each other so that no thrust surface is required and generation of frictional heat is completely eliminated. In refrigerating scroll compressors, Oldham coupling is used to make the orbiting scroll orbit instead of self-rotate. In such a device, Oldham ring keys are inserted into key slots provided on the rear of the orbiting scroll base plate and lubricating oil needs to be applied to the sliding surfaces between the keys and the key slots. For fuel cell application, air free of oil should be applied to the cathode of the fuel cell, such lubricating oil cannot be applied. Instead of using an Oldham coupling device for the present configuration, two crankshafts are inserted into the two hubs located on either of the orbiting scroll base plate, and these two crankshafts are connected to each other by a timing belt so that the crankshafts can function as anti-rotation devices for the orbiting scroll. Driving power from motor is transmitted to one of the crankshafts.

To reduce leakage through the wrap tip clearance of the neighboring compression pockets, tip seal is applied to the wrap top surface. Sliding bush used for reducing flank leakage in scroll compressors is not considered here for simplicity.

2.2 Scroll wrap configuration factors

There are 7 scroll wrap configuration factors as in Tables 1 and 4 relations among them can be obtained.

The wrap height is limited compared to the wrap thickness. Because gas force exerted on the wrap side could cause some degree of deflection and some difficulty could be encountered in machining scroll wrap with large aspect ratio. For fuel cell application, relatively low-pressure air is required, so that the effect of the gas force exerted on the wrap side may be negligible. So the wrap height limitation could come from the manufacturing consideration. In the present design, aspect ratio of the wrap of $h/t=5$ will be chosen. Also a wrap thickness of $t=3.7$mm will be used. This is nearly the minimum thickness for tip seal installation.

With this determination of the wrap thickness and the aspect ratio of the wrap, it can be regarded that the number of unknown parameters was reduced from 7 to 6, and that one more relation among the parameters was added to the existing 4 relations in Table 1. Therefore, since there are 6 unknowns with 5 relations among them, only one parameter can be selected as an independent parameter. In this study, the orbiting radius will be chosen as an independent one, since it has a direct influence on the compressor performance.

Table 1 Scroll configuration factors

Configuration factors		Relations
symbols	Description	
a	Base circle radius	
t	Wrap thickness	
h	Wrap height	$r_s = a\pi - t$
r_s	Orbiting radius	$t = 2a\alpha$
ϕ_e	Wrap end angle	$V_s = 2\alpha a r_s h(2\phi_e - 3\pi)$
ϕ_a	Cutter angle	$V.R = \frac{2\phi_e - 3\pi}{2\phi_a + 3\pi}$
α	Starting angle	
7 parameters		4 equations

Since built-in volume ratio $V.R$ is related to the design pressure ratio as in equation (1), and displacement volume V_S is related to the design flow rate Q_S as in equation (2), these two, $V.R$ and V_S, can be determined by operating conditions at the design point.

$$V.R = V_s / V_d = (p_d / p_s)^{1/n} \tag{1}$$

$$Q_s = \eta_v V_S N / 60 \tag{2}$$

2.3 Design conditions

To design a scroll compressor that supplies air to the fuel cell of 2 kW power output, required air-flow rate can be estimated by equation (3) (Larminie, 2003).

$$\dot{m}_s = 3.57\times10^{-7}\times\lambda\times\frac{P_e}{V_c}\,[\mathrm{kg/s}] \tag{3}$$

For stoichiometry of $\lambda=2$, and stack voltage of $V_c=0.6V$, required air-flow rate $\dot{m}_s=0.00238\,kg/s$ was calculated. This corresponds to the volume flow rate of $Q_S=120\,lpm$ for the suction condition of 1 bar and 25°C. Operating conditions with required air-flow rate are summarized in Table 2.

Assuming volumetric efficiency of $\eta_v=80\%$ for shaft speed $N=3500\,rpm$, displacement volume is determined to be $V_S=42.9cc$ from equation (2). From design pressure ratio of 2, built-in volume ratio is obtained to be $V.R=1.6407$ by equation (1).

Table 2 Design conditions

Notation	Description	Values
Q_s	Flow rate	120 lpm
P_s	Suction pressure	1 bar
t_s	Suction temperature	25 °C
P_d	Discharge	2 bar
N	Shaft speed	3500 rpm

Table 3 Combination of scroll configuration factors for displacement volume of 42.9cc

r_s	a	α	ϕ_e	ϕ_a
2.5	1.814 mm	53.7°	1340°	562°
3	1.973 mm	49.7°	1095°	412°
3.5	2.132 mm	46.3°	928°	311°
4	2.291 mm	43.3°	808°	237°

2.4 Effects of orbiting radius on scroll configuration

Figure 2 shows variation of $a\phi_e$, corresponding to the distance from scroll center to the wrap end, and $a\phi_a$, an indication of discharge port size, and orbiting scroll mass, m_{OS}, with the variation of the orbiting radius, r_s. With increasing r_s, the distance from scroll center to the wrap end and the discharge port size decrease. In the present design, an orbiting scroll base plate diameter not larger than 120mm and discharge port not smaller than 10mm are required, yielding to a range of the orbiting radius of $2.5\text{mm} < r_s < 4.0\text{mm}$. In Fig. 3, scroll profiles at the two extreme cases are shown.

3 Performance Analysis and Discussions

3.1 Volume diagram

Volume diagrams for various orbiting radius are shown in

Fig. 4. As the orbiting radius increases, the decreasing rate of the compression chamber volume increases with an earlier start of discharge.

3.2 Pressure and gas force

Calculated P-V diagram is shown in Fig. 5. The pressure calculation was carried out by assuming polytropic compression, taking into account leakages among neighboring compression pockets (Kim, 1998). Leakage clearance was assumed to be 20 μm for both wrap tip and flank leakages. With increasing the orbiting radius, leakage loss decreases, but over-compression loss also increases. This is because the leakage length for the wrap tip increases and discharge port diameter decreases with increasing the orbiting radius.

Particularly at the orbiting radius of $r_s = 4.0\text{mm}$, over-compression loss becomes larger in compression pocket B than in pocket A, since it is more difficult to secure enough passage for discharge for compression pocket B at this scroll configuration. As a whole, the gas compression loss appeared to be a minimum at $r_s = 3.5\text{mm}$.

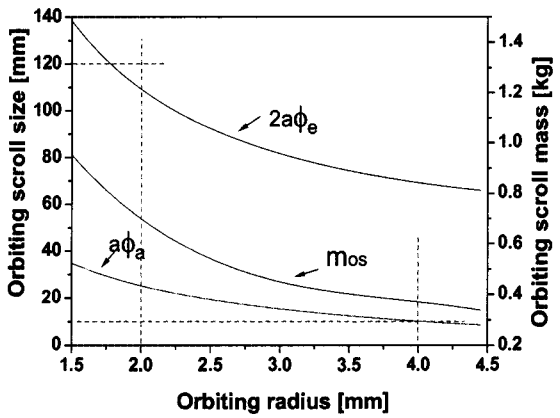

Fig. 2 Scroll size vs. orbiting radius

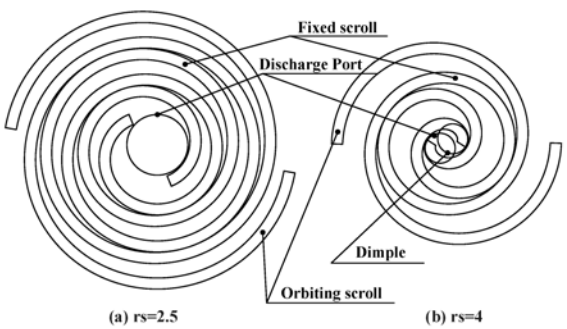

Fig. 3 Scroll wrap profiles

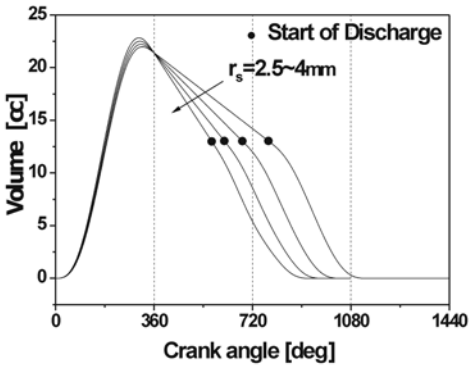

Fig. 4 Volume diagram

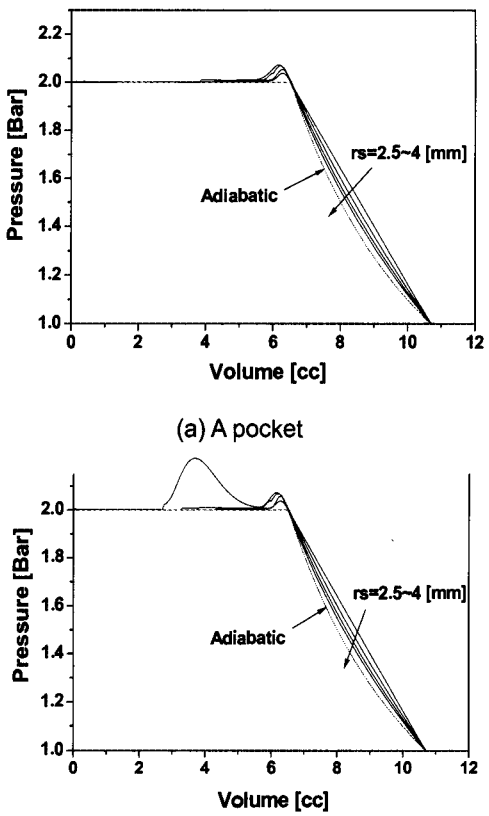

Fig. 5 P-V diagram

Figure 6 shows gas forces acting on the orbiting scroll together with its centrifugal force. Tangential gas force F_{rg} deceases with increasing r_s. This is due to a smaller scroll size with a larger orbiting radius while the wrap height is held constant, as shown in Fig. 2. Radial gas force F_{rg} is smaller compared to F_{rg}, its magnitude being insensitive to the change of r_s. While the mass of the orbiting scroll becomes smaller with larger r_s as shown in Fig. 2, the centrifugal force F_{osc} increases

slightly as a result of the product of the mass and the orbiting radius.

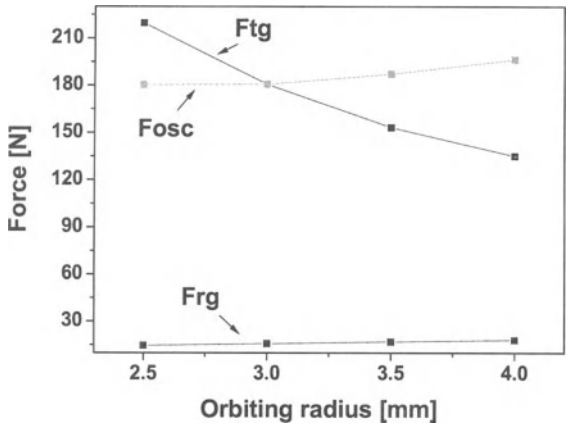

Fig. 6 Gas forces

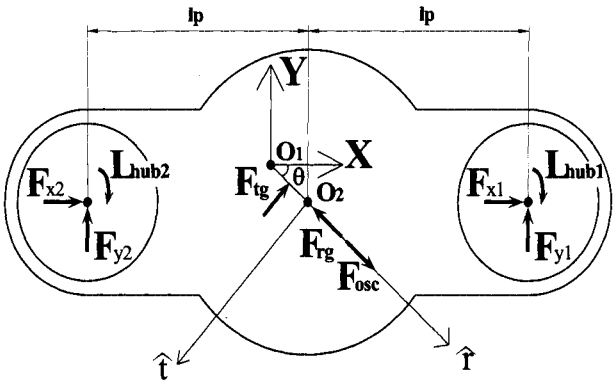

Fig. 7 Force diagram on orbiting scroll

3.3 Dynamics of Moving Elements

Figure 7 and Fig. 8 show forces acting on the orbiting scroll and the crankshaft, respectively. From these force diagrams, equations of force and moment balances can be obtained as in equations (4)~(10).

$$F_{x1}+F_{x2}+2F_{tg}\sin\theta+(F_{osc}-2F_{rg})\cos\theta=0 \quad (4)$$

$$F_{y1}+F_{y2}+2F_{tg}\cos\theta-(F_{osc}-2F_{rg})\sin\theta=0 \quad (5)$$

$$F_{y1}l_p-F_{y2}l_p+r_sF_{tg}+r_{cp}\mu_{cp}F_{cp1}+r_{cp2}\mu_{cp}F_{cp2}=0 \quad (6)$$

$$-F_{ur}+\mu_{ub}F_{ut})-F_{dr}+\mu_{db}F_{dt}-F_{uwc}-F_{dwc}+F_{cpc}+F_{cpr}=0 \quad (7)$$

$$-(F_{ut}-\mu_{ub}F_{ur})-(F_{dt}-\mu_{db}F_{dr})+F_{cpt}=0 \quad (8)$$

$$(F_{ur}-\mu_{ub}F_{ut})l_{ub}+F_{uwc}l_{uw}-F_{dwc}l_{dw}-(F_{dr}-\mu_{db}F_{dt})l_{db}=0 \quad (9)$$

$$-(F_{ut}-\mu_{ub}F_{ur})l_{ub}+(F_{dt}-\mu_{db}F_{dr})l_{db}=0 \quad (10)$$

Resultants of force components at the two crankshaft eccentrics engaged with the corresponding orbiting scroll hubs, (F_{x1},F_{y1}) and (F_{x2},F_{y2}) can be written as $F_{cp1}=\sqrt{F_{x1}^2+F_{y1}^2}$ and $F_{cp2}=\sqrt{F_{x2}^2+F_{y2}^2}$, respectively. Also, shaft bearing loads at upper and lower supports are $F_{ub}=\sqrt{F_{ut}^2+F_{ur}^2}$ and $F_{db}=\sqrt{F_{dt}^2+F_{dr}^2}$, respectively.

Mechanical losses at all sliding surfaces are given by equation (11).

$$L_{mech}=2\omega(r_{cp}\mu_{cp}F_{cp}+r_{ub}\mu_{ub}F_{ub}+r_{db}\mu_{db}F_{db}) \quad (11)$$

Ball bearings were used for the crankshaft eccentrics and shaft supports. Friction coefficient of the ball bearing was 0.0015.

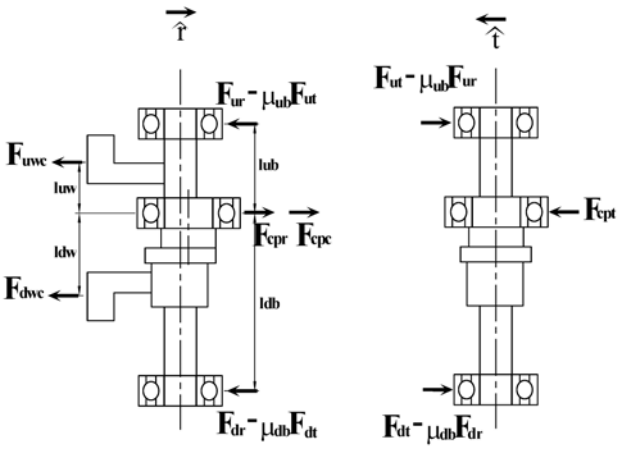

Fig. 8 Force diagram on crankshaft

3.4 Calculation Results

Calculated bearing forces at the crankshaft eccentrics and shaft supports are shown in Fig. 9. As the orbiting radius r_s increases, bearing forces decrease due to decreasing F_{tg} with increasing r_s.

For various values of the orbiting radius, compressor input power together with various compressor losses were summarized in Table 4. Adiabatic compression power to compress the ambient air to 2 bar at the flow rate of 120 lpm is 191.4 W.

Gas compression loss was calculated to be around 5~9W, depending on r_s. Minimum gas compression loss was obtained at r_s = 3.5mm.

Mechanical loss increased slightly with increasing r_s, in the range of 2~3W. As a consequence, minimum compressor input power was obtained at r_s = 3.5mm.

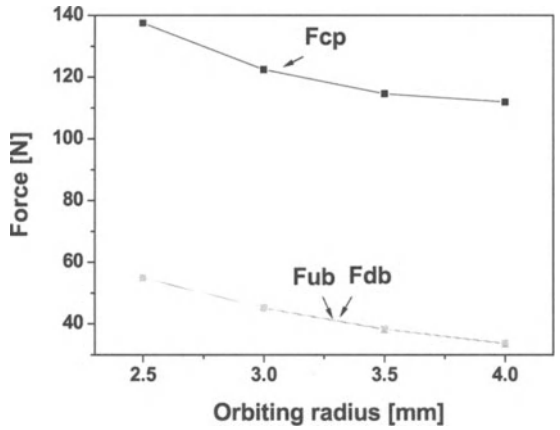

Fig. 9 Bearing loads

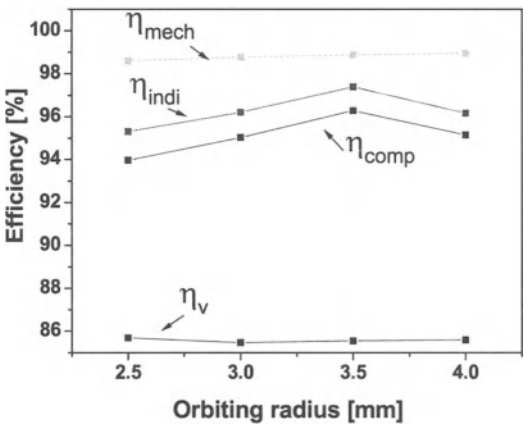

Fig. 10 Compressor efficiencies

Table 4 Calculation results of compressor input power and loss breakdown

r_s (mm) / Loss	2.5	3.0	3.5	4.0
L_{gas} (W)	9.44	7.54	5.15	7.7
L_{mech} (W)	2.86	2.47	2.24	2.11
W_c (W)	203.8	201.5	198.8	201.1

Figure 10 shows various efficiencies of the compressor. As r_s increased, mechanical efficiency increased slightly from 98.59% to 98.94%. Indicated efficiency showed a maximum value of $\eta_{indi} = 97.38\%$ at $r_s = 3.5$mm, resulting in a maximum of the total compressor efficiency as the product of the mechanical and indicated efficiencies at the same r_s. The maximum compressor efficiency was $\eta_{comp} = 93.28\%$. Volumetric efficiency of around 85.5% did not change much with r_s.

4 Conclusions

In an analytical study on the applicability of scroll type compressor to oil-less air compressor used for the fuel cell systems:

(1) Conceptual design has been carried out to supply air of 2 bars to 2 kW fuel cell system: Designed scroll compressor is characterized by a double-sided orbiting scroll driven by two crankshafts, which also function as anti-rotation devices.

(2) Orbiting radius was selected as an independent variable among 7 scroll wrap configuration factors. As the orbiting radius increased, the diameters of the scroll base plate and discharge port decreased: In order to design the base plate smaller than 120mm and the discharge port larger than 10mm, the orbiting radius needs to be in the range of $2.5\text{mm} < r_s < 4.0\text{mm}$.

(3) As the orbiting radius increased from 2.5mm to 4.0mm, the mechanical efficiency increased slightly from 98.59% to 98.94%, and the indicated efficiency showed a maximum of 97.38% at $r_s = 3.5$mm, resulting in a maximum compressor efficiency of 96.28% at the same orbiting radius. Volumetric efficiency was about constant at 85.5%, regardless of r_s.

References

Drive, R.W., Davidson, D.P., 1999, "Applications for the hinge-vane positive displacement compressor-expander", *International Conference on Compressors and Their Systems, Institution of Mechanical Engineers*, London, September, pp. 339 – 348

Kim, H.J., Kim, J.H., Lee, J.K., 1998, "Dynamic behavior of a scroll compressor with radial compliant device", Korean Journal of Air-Conditioning and Refrigeration Engineering, Vol. 10, No.1, pp.33 – 43

Kim, H.Y., Lee, Y.H., Kim, H.J., Joo, B.S., 2007, "A study on the friction loss reduction in a rotary vane air compressor", *Proceedings of SAREK 2007 Summer Annual Conference*, Paper No. 07-S-002

Larminie, J., Dicks, A., 2003, "Fuel Cell Systems Explained", *Wiley*, Hoboken

The 4th International Symposium on Fluid Machinery and Fluid Engineering
November 24-27, 2008, Beijing, China
NO. 4ISFMFE-Ch05

Studies on Moving Coil Linear Compressor Used for Refrigerator

Zhihai Li, Shuiying Zheng* and Rongren Wu

* Dept. of Chemical Engineering, Zhejiang University,
38#, Zhe Da Road, Hangzhou 310027, China
Tel: +86-571-8795-3065 / Fax: +86-571-8795-1216
E-mail: zhengshuiying@zju.edu.cn

Abstract Linear compressor is composed of the linear oscillating motor directly coupled with the piston and springs for resonance operation. One clear advantage of moving coil linear compressor is absence of radial forces. And this makes it possible to achieve high performance. Design and optimization of linear motor for moving coil type linear compressor used for refrigerator and the characteristics of that are studied in this paper. The model of linear oscillating motor is analyzed and simulated by using finite element analysis software. From the analysis the motor constant representing force of motor per unit current can be obtained. The coil wire diameter was changed to find out its affect to motor constant and loss of resistance, from which the best coil wire diameter can be found to get the best energy efficiency. Distribution of static magnetic field can also be got, which is used to optimize the magnetic circuit. Through these analyses the parameters of the linear motor are optimized. The iron loss analysis of linear motor is studied by using the analytical and numerical method. For the validation of the iron loss result, the experiment measuring the iron loss of linear motor is performed. The optimization between area of piston and design stroke for a given exhaust volume are also studied. The piston of linear compressor can move freely, a controller is needed to control the stroke of piston and decrease the gap volume. The operating frequency is a significant parameter of linear compressor. Experiments showed that without pumping the minimum input power and current are obtained near the mechanical resonant frequency. And charging pressure had significant effect to resonant frequency. Moreover compare with Technical Specifications for Energy Conservation Product Certification for air compressors vocabulary-General, our linear compressor met it very well. From the above analyses a prototype of linear compressor was designed. From the experiments the performance of linear compressor was better than conventional compressor.

Keywords linear compressor, linear motor, moving coil, refrigerator

Nomenclature

B	magnetic flux density in the air gap
c	damping coefficients
k	spring stiffness
l	effective coil length
L	inductance of coil
m	mass of moving assembly
P	pressure of compression chamfer
P_0	pressure of back end of piston
R	resistor including copper loss and iron loss
W_1	width of core of part I
W_2	width of core of part II
W_3	width of core of part III
W_4	width of core of part IV
H	length of coil

1 Introduction

Small refrigerator compressor driven by linear compressor has been studied for many years due to their potential for low cost and high performance (Unger, 1996; Unger, 1998; Unger, 1999). LGE successfully used moving magnet type linear compressor in his DIOS refrigerator (Babyak, 2001). Koh et al (Koh and Hong, 2002) studied the characteristics of moving coil type liner compressor for

Stirling cryocooler. Yee-Pien Yang (Yang and Huang, 1998) discussed a new dual fuzzy controller for the linear compressor of a split-Stirling cryocooler. But their amplitude of stroke and power is small. He et al(He and Li, 2003) had reported the linear motor compressor for refrigerator, but due to friction and leakage their experience results are not very well.

Sunpower Inc., who has been developed linear compressor for over twenty years, abandons moving coil type linear compressor for the expensive magnet (Redlich, 1995; Redlich and Unger, 1996). But with the development of magnet the price of it drop sharply today. And moving coil type has the advantage of absence of radial forces. All the driving forces act along the line of motion. And it is hard to achieve in other type of linear compressor.

This study analyzed the characteristics of moving coil type linear compressor used for refrigerator. Through the experiments we got well performance and verified the advantage of moving coil type for the low wear.

2 System Models

The mechanical structure of the linear compressor in this study is shown in Fig. 1. Forces which are loaded on the moving parts contain the following parts: (1) inertia forces, (2) damping forces, (3) restoring forces, (4) forces induced by pressure difference between compression and back end of piston, (5) electric forces. Following equation can be obtained from Newton's second law.

$$m\ddot{x} + c\dot{x} + kx + (P - P_0)A = \alpha i \tag{1}$$

where, α is a function of coil position.

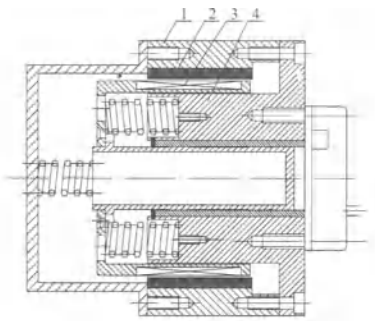

1- outer core; 2-magnet; 3-coil; 4- inner core;

Fig. 1 Structure of moving coil linear compressor

The electromagnetic part can be modeled as an electric circuit. The governing equation can be written as follows:

$$Ri + L\dot{i} + \alpha\dot{x} = V \tag{2}$$

As the gas force is nonlinear, we can get the only analytical solution without load. With load the numerical solution can be obtained in Newmark Method or Runge-Kutta Method.

In order to analyze thrust and improve the performance of linear motor, the characteristic analysis of linear compressor is achieved by Finite Element Method (FEM). Flux distribution and the motor constant are obtained. Due to the symmetric magnetic circuit, a 2D FEA model is used. And the static analysis is performed by using ANSYS.

Figure 2 shows the analysis model of the linear motor. As shown in Fig. 2, the linear motor is composed to the core, magnet and coil. The core design is to obtain the dimension of core, magnet and coil for the best thrust. Flux density and thrust is decided by the width of core. Also the thrust is affected by the position of coil due to the limited length of magnet.

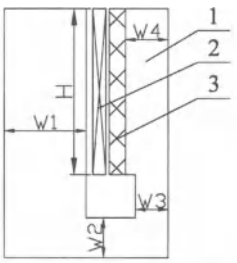

1- outer core; 2- coil; 3- magnet;

Fig. 2 Analysis model of the linear motor

Figure 3 shows flux density of linear motor performed by static analysis under magnet and coil excitation.

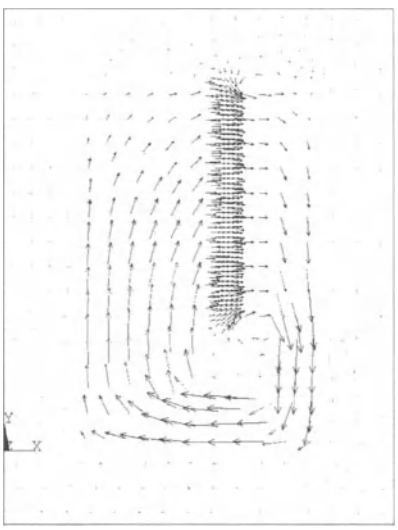

Fig. 3 Flux density of linear motor

Curves are modeled by changing one parameter, and the other dimensions remain the same. Fig.4 shows the thrust changes with the width of core. Figure 5 shows thrust

changes with different coil position. The original position is the magnet center, where the maximum thrust is obtained.

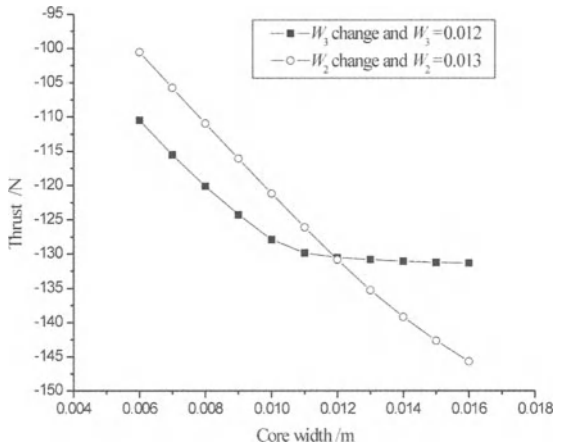

Fig. 4 Thrust with different core width

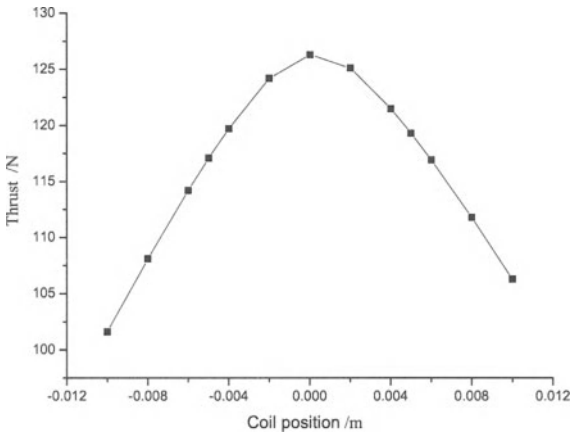

Fig. 5 Thrust with different coil position

3 Experiment RIG

Figure 6 is experimental rig to study the linear compressor characteristics. Linear compressor used in this study is a moving coil type linear compressor designed for refrigerator. The linear compressor consists of (1) a piston, (2) linear motor which drives the piston, (3) valve assemble controlling suction and discharging.

An AC power source is used to provide and control the operating frequency and input voltage of linear compressor. It also has the functions of showing currents, power, and power factor. A vacuum meter and manometer are used to measure the suction and discharge pressure respectively. The displacement of the piston is measured by displacement sensor.

Experiments are done as follows:

I) Experiments to study the frequency features without loads.

II) Experiments to research the effect of spring stiffness.

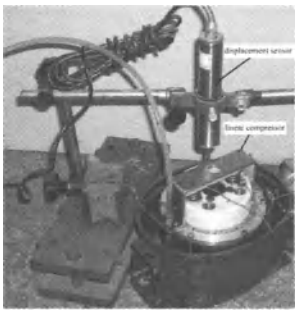

Fig. 6 experimental rig

4 Results and Discussion

4.1 Frequency features of linear compressor without load

Without pumping Eq. (1) can be changed to a linear equation. The analytical solution can be obtained as follows. The theory calculation and experiment data of input power and current of the linear compressor are shown in Fig. 4 and Fig. 5 respectively.

$$U_m = I_m R \frac{\sqrt{((1-s^2)^2+(2\xi s)^2+2\alpha\xi s^2)^2+(\eta s((1-s^2)^2+(2\xi s)^2)+\alpha s(1-s^2))^2}}{(1-s^2)^2+(2\xi s)^2+2\alpha\xi s^2} \tag{3}$$

$$P = \frac{1}{2}U_m I_m \cos(\varphi) = \frac{1}{2}I_m{}^2 R \frac{(1-s^2)^2+(2\xi s)^2+2\alpha\xi s^2}{(1-s^2)^2+(2\xi s)^2} \tag{4}$$

where

$$\omega_0 = \sqrt{\frac{k}{m}}, \xi = \frac{c}{2\sqrt{mk}}, s = \frac{\omega}{\omega_0}, \eta = \frac{L\omega_0}{R}, \alpha = \frac{B_e{}^2 L_e{}^2}{mR\omega_0}$$

Figure 7 and Fig. 8 shows that the minimum input power and current are obtained near the mechanical resonant frequency (frequency ratio is equal to 1). And the frequency of minimum input power is a little lower than that of current.

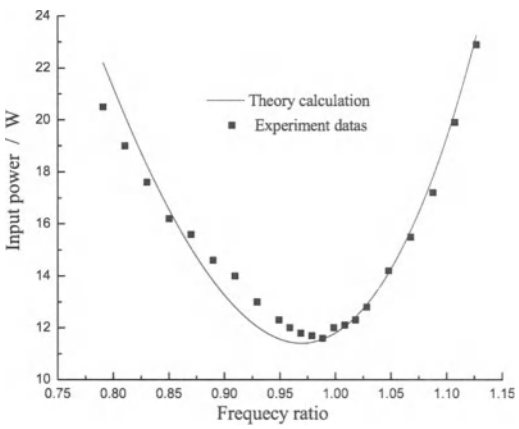

Fig. 7 Input power with different applied AC frequency of the same stroke

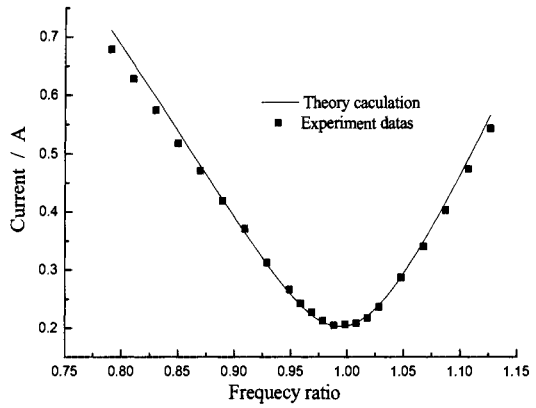

Fig. 8 Current with different applied AC frequency of the same stroke

4.2 The effect of spring stiffness

Following Fig. 9 shows how resonant frequency changes according to the change of charging pressure. As figure showing, the resonant frequency increases as charging pressure increases. This phenomenon can be explained due to the increase of gas spring stiffness. When the charging pressure increases the working fluid becomes hard to be compressed and the stiffness increases.

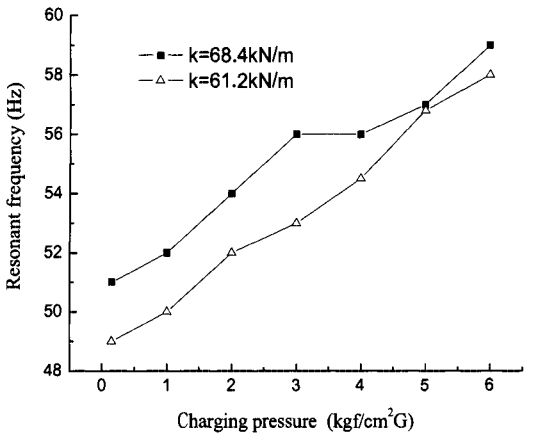

Fig. 9 Resonant frequency with charging pressure

Figure 10 and Fig. 11 are the specific power with charging pressure at different suction pressure. Jiaxipera compressor, which has a coefficient of performance (COP) of 1.75 and power of 102W, is a control rotating reciprocating compressor. Due to experimental setup limitation we use air as working fluid. As the figures showing, when the charging pressure is lower than 3 kgf/cm2G at suction pressure of 0.103MPa and 2.5 kgf/cm2G at suction pressure of 0.063MPa, the specific power of linear compressor is lower than the Jiaxipera compressor. This phenomenon illustrates the advantages of linear compressor. The rotating compressor has crank mechanism which enforces sideways thrust on the piston. However, all the driving forces in a linear compressor act along the line of motion, without any sideways thrust on the piston, substantially reducing wear losses. So the specific power of linear compressor is smaller. When the charging pressure gets higher, specific power of the linear compressor is larger than the Jiaxipera compressor. This phenomenon can be explained due to leakage of working fluid as the charging pressure increases. Moreover, the effect of the clearance gets more important and it is hard to control.

Compared with two figures we can see that specific power is smaller as the suction pressure is lower.

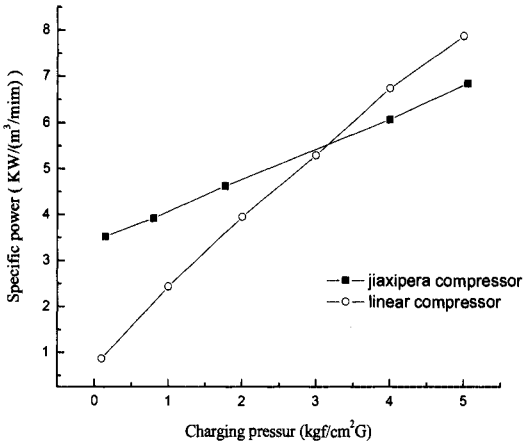

Fig. 10 Specific power with charging pressure at the suction pressure of 0.103MPa

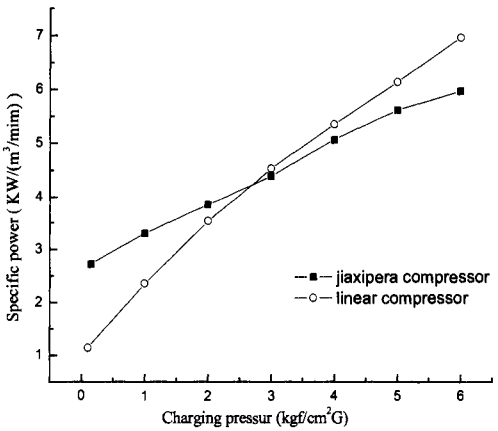

Fig. 11 Specific power with charging pressure at the suction pressure of 0.063MPa

Performance of linear compressor

According to the ASHRAE (The American Society of Heating Refrigerant and Air-conditioning Engineers Inc.) operating condition (−23.3℃ evaporator, 54.4℃ condenser), the suction pressure is −0.37 kgf/cm^{2}G and discharging pressure is 6.7 kgf/cm^{2}G. For the adiabatic index of air is

bigger than that of R600a (isobutene), So with the same power we can obtain higher pressure when the working fluid is R600a. So our charging pressure is 5kgf/cm^2.

Table 1 is Technical Specifications for Energy Conservation Product Certification for air compressors vocabulary-General (CCEC/T08—2001). From the table 2 we can see the specific power of linear compressor is 6.26kW/(m^3/min) and it is far better than the CCEC/T08—2001 standard, which is 14.6-17.1kW/(m^3/min). That of the control compressor which is an approved product is 5.9kW/(m^3/min). We are very close.

Table 1 Technical Specifications for Energy Conservation Product Certification for air compressors vocabulary-General (China)

Compressor series	Driving power/W	Pressure ratio	
		8	11
		Specific power kW/(m^3/min)≤	
single	180	14.6	17.1

Table 2 Performance of linear compressor Compared with Rotating Compressor

	Linear Compressor	Rotating Compressor
Frequency / Hz	46.1	50
Suction Pressure / bar	−0.37	−0.37
Discharge Pressure / (kgf/cm^2)	5	5
Pressure ratio	9.5	9.5
Voltage / V	134.5	212
Current / A	1.001	0.565
Power / W	125.2	118
Power factor	0.923	0.982
Flow / (m^3/h)	0.72	0.76
Specific power / [kW/(m^3/min)]	6.26	5.9

5 Conclusion

From the analysis above the characteristics of linear compressor used for refrigerator can be obtained as follows:

The minimum input power and current are obtained near the mechanical resonant frequency.

The frequency of minimum input power is a little lower than current.

The resonant frequency increases as charging pressure increases because of increase of gas spring stiffness

The specific power of linear compressor is lower than the control compressor at low charging pressure due to the low wear.

Compared with Technical Specifications for Energy Conservation Product Certification for air compressors vocabulary-General, our linear compressor met it very well.

Acknowledgment

I would like to appreciate Bureau of Science and technology of Jiaxing for the research grand.

Reference

Koh, D.-Y., Hong, Y.-J., Park, S.-J., Kim, H.-B. and Lee, K.-S., 2002, "A study on the linear compressor characteristics of the Stirling cryocooler", *Cryogenics*, Vol.42, pp. 427 – 432

Redlich, R., 1995, "A Summary of Twenty Years Experience with Linear Motor and Alternators", *Linear Drives for Industry Applications*, Nagasaki, Japan

Unger, R., 1999, "Development and testing of a linear compreesors sized for the european market", *Proceedings International Appliance Technical Conference*, Purdue University, West Lafayette, Indiana, USA

Yang, Y. P. and Huang, B. J., 1998, "Fuzzy control on the phase and stroke of a linear compressor of a split-Stirling cryocooler", *Cryogenics*, Vol.38, pp. 231 – 238

Unger, R., 1998, "Linear compressors for clean and specialty gases", Proceedings International Compressor Engineering Conference, Purdue University, West Lafayette, Indiana, USA

Unger, R., 1996, "Linear compressor for non-CFC refrigeration", *Proceedings International Appliance Technical Conference*, Purdue University, West Lafaayette, Indiana, USA

Redlich, R., Unger, R. and Walt, N. v. d., 1996, "Linear Compressors: Motor Configuration, Modulation And Systems", *International Compressor Engineering Conference*, Purdue University, West Lafayette

Babyak, R. J., 2001, "Linear launch", *Appliance Manufacturer*

He, Z., Li, L. and Shu, P., 2003, "Study on linear compressor for household refrigerator", Hsi-An Chiao Tung Ta Hsueh/*Journal of Xi'an Jiaotong University*, Vol.37, pp. 1119 – 1123

The 4th International Symposium on Fluid Machinery and Fluid Engineering
November 24-27, 2008, Beijing, China
NO. 4ISFMFE-Ch22

Two-Zone Modeling Prediction Method of Centrifugal Compressor Performance

Shuqi Li*, Junyue Zhang and Weidong Xing

* National Key Laboratory of Diesel Engine Turbocharging Technology,
P.O.B 22, Datong 037036, China
Tel: +86-352-536-2083 / Fax: +86-352-536-2085
E-mail: lishuqi_0202101@163.com

Abstract In an effort to produce an effective performance prediction method of centrifugal compressor, based on the test data completed with current test facilities in turbocharger, theory of two-zone modeling performance prediction and its simulation method have been studied. The results demonstrate: 1) For two-zone modeling method, although the details of diffusion and loss processes have been actually considered, as well as the basic viscous flow processes under the influence of adverse pressure gradients, its simulation method is rather simply and practical, easier to apply in engineering design. 2) This method can effectively predict the performance of centrifugal compressor in turbocharger, including its surge boundary and choke boundary, and can effectively present its overall performance characteristics. 3) Cases provided in this article also indicate: comparing prediction value with test data, the difference of the total to total pressure ratio is less than 3%, the difference of adiabatic efficiency based on total to total pressure ratio is less than one point, and the mass flow difference on surge line or choke line is less than 0.06 at transonic operation conditions.

Keywords two-zone model, compressor, performance prediction, turbocharger

Nomenclature

※ List of Symbols

A	Flow area
C	Absolute velocity
DR	Diffusion velocity ratio
h	Specific enthaply
h_T	Rotational total enthaply
I	Incidence angle
k	Ratio of the specific heats
M	Mach number
m	Mass flow rate
p	Static pressure
R	Radius
Re	Reynolds number
T	Static temperature
U	Blade speed
W	Relative velocity

※ Greek Symbols

β	Relative angle (meridional reference)
δ	Deviation angle
ε	Area ratio of secondary to impeller exit
η	Efficiency
ν	Kinematic viscosity
ρ	Density
χ	Secondary flow mass fraction

※ Subscripts

0	Stagnation condition
1	Impeller inlet
2	Impeller outlet
a	Inlet region (two-zone model)
b	Blade property; outlet region(two-zone model)
m	Meridional direction; Mixed-out property
p	Primary zone
rel	Relative to rotating coordinates

s	Secondary zone
t	Tip
θ	Tangential component

1 Introduction

In the preliminary design stage, by making use of the performance prediction method of centrifugal compressor, not only the variation of design and off-design performance can be obtained, including the surge line and choke line, but the key variable of compressor design can also be approximately estimated and optimized. And so, to find an effective performance prediction method of compressor is rather important. In an effort to this intention, based on the experimental data completed with current test facilities, the theory of two-zone modeling performance prediction and its simulation method have been investigated. As a result, the validity of this method and comparison analysis of two case between prediction value and test data have been gained. Along with this, an effective prediction method of compressor performance in turbocharger has been established and demonstrated.

2 Outline of Two-Zone Modeling Method

Many studies of performance prediction method of centrifugal compressor have been conducted (Connor, 1984; Galvas, 1972; Herbert, 1978). Studies on axial compressor are even earlier than that of centrifugal compressor, the typical cases of these are Howell (1945) and Ainley and Mathieson (1951). These prediction method were all based on determined correlations obtained from prior test experience of cascades and vanes, and had classified the loss possibly existing in turbomachinery, such as: skin friction loss, disk friction loss, recirculation loss, etc. These methods were widely applied in 60's and 70's of last century.

For two-zone modeling performance prediction method, the model does not depend on overall empirical correlations, but instead relies on basic flow model. These are built on the most basic understanding of the fundamental flow physics. The impeller exit is solved using the two-zone model. The flow at the impeller outlet is divided into isentropic primary and secondary zones, and all the loss inside the impeller passage is assumed to be concentrated inside the secondary zone. The level of total pressure loss associated with the formation of the secondary flow and the discharge mixing process would be estimated. For this method, the details of diffusion and loss processes have been actually considered, as well as the basic viscous flow processes under the influence of adverse pressure gradients. The designer is, therefore, attempting to established a more accurate and easy applied performance prediction method.

※ *Description of Two-zone Model*

Two-zone model is employed to simulate interactive influence between impeller and other components, and solve the flow and state parameters at impeller exit. In this model there are a hypothesis that two zones of primary and secondary exists in the impeller exit (Fig.1 illustrates this), and other basic assumptions as the following:

a. The flow in the primary zone is assumed to have reached the impeller exit plane through an isentropic process. All the loss inside the impeller passage is assumed to be concentrated inside the secondary zone.

b. At the impeller exit, static pressure in secondary zone p_{2s} is equal to static pressure in primary zone p_{2p}.

The following key modeling parameters are presented in two-zone calculation:

c. Diffusion ratio DR_2 : ratio of the inlet tip relative velocity W_{1t} to primary zone relative velocity at the impeller exit W_{2p}.

d. Secondary mass fraction χ : ratio of the secondary mass rate m_s to total mass flow rate passing the impeller m.

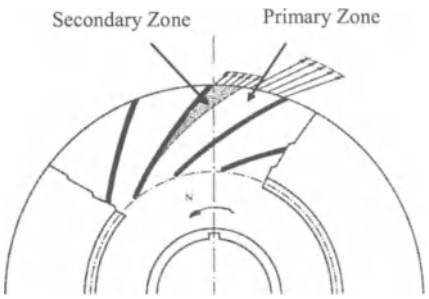

Fig. 1 Schematic two-zone model

※ *Solving the Primary Zone*

According to rothalpy conservation equation, isentropic process equation, and physical state equations, linking to deviation modeling (Fig. 2 shows that deviation angle δ_p is related to impeller exit blade angle β_{2b}), the major equations solving the primary zone from the impeller inlet to exit are:

$$T_{2p} = T_{1t}\left(p_{2p} / p_{1t}\right)^{(k-1)/k} \tag{1}$$

$$h_{2p} + W_{2p}^2 / 2 - U_2^2 / 2 = h_T \tag{2}$$

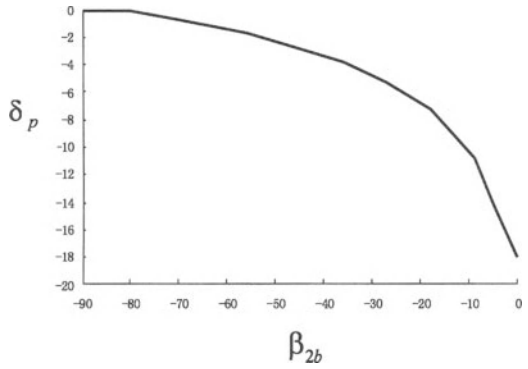

Fig. 2 Deviation model

※ Solving the Secondary Zone

According to rothalpy and mass conservation equation, and state equations, the key equations solving the secondary zone are the following:

$$\varepsilon A_2 \cdot C_{m2s} \cdot \rho_{2s} = \chi m \tag{3}$$

$$h_{2s} + W_{2s}^2/2 - U_2^2/2 = h_T + W_{front\ cover} \tag{4}$$

where

$$\varepsilon = 1 - \frac{(1-\chi)m}{\rho_{2p} A_2 C_{m2p}}$$

Front cover friction of the impeller $W_{front\ cover}$ (Fig. 3) has not been dealt with realistically in the literature. It is extremely difficult to measure, and there is virtually no solid design information available for guidance. However, according to Navier-Stokes calculation results of centrifugal compressor (Moore and Moore 1981), the shear stresses, and hence energy dissipation, in the shroud region was approximately equal to the same level as experienced with (rear) disk friction as computed according to Daily and Nece (1960). And so, the Daily and Nece (1960) skin friction correlation could be used for the front cover friction as well while solving the secondary zone. The detail of this correlation will be introduced within the following text.

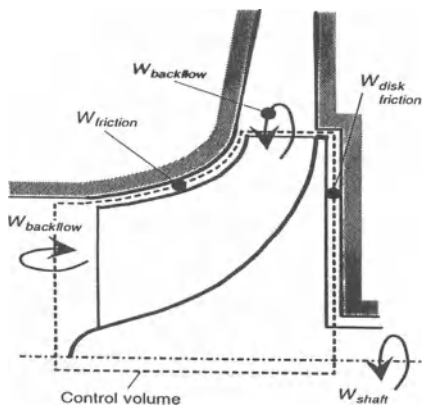

Fig. 3 Schematic losses of impeller

※ Mixing of the Primary Zone and Secondary Zone

According to the reduced conservation equations of mass, momentum and energy, plus isentropic process equations and state equations, the key description equations solving the mixing of the primary zone and secondary zone (David 1996) have been established, namely:

radial momentum equation:

$$m_p C_{m2p} + m_s C_{m2s} = m C_{m2m} + (p_{2m} - p_{2p}) A_2 \tag{5}$$

tangential momentum equation:

$$m_p C_{\theta 2p} + m_s C_{\theta 2s} = m C_{\theta 2m} \tag{6}$$

energy equation:

$$m_p h_{02p} + m_s h_{02s} + W_{disk\ friction} + W_{backflow} = m h_{02m} \tag{7}$$

where the rear disk loss $W_{disk\ friction}$ is to use the equations from Daily and Nece (1960) which are as follows:

$$W_{disk\ friction} = K \rho U_2^3 R_2^2/2 \tag{8}$$

where $K = 0.0402/\mathrm{Re}^{1/5}$, $\mathrm{Re}=U_2 R_2/\nu$

The recirculation loss is not analytically modeled by any fundamental concept. Instead, only the most primitive methods have been used, namely the simple correlations from past experience. The approach used in the two-zone modeling technique is to fit a piecewise parabola through the data given by the designer. Around the region of best efficiency, its value has been assumed to be zero.

※ Diffusion Ratio Modeling

One of the key parameters in the two-zone model is the diffusion ratio, the author selected the primitive Two-Elements-In-Series modeling (Fig. 4) to estimate the value of the diffusion ratio. The first element (subscript "a") is from the inlet to impeller throat, which could be a diffuser or a nozzle. The second element (subscript "b") is the passage portion from the impeller throat to impeller exit, which is usually a diffuser. And then, the diffuser ratio could be calculated as follows:

$$\mathrm{DR}_2 = \left(\frac{1}{1-\eta_a C_{pa,i}} \times \frac{1}{1-\eta_b C_{pb,i}} \right)^{1/2}$$

$$C_{p,i} = 1 - \frac{1}{AR^2},\ AR_a = \frac{\cos\beta_{1b}}{\cos\beta_{1t}}, \tag{9}$$

$$AR_b = \frac{A_2 \cos\beta_{2b}}{A_{throat}}$$

where A_{throat} is the throat area in blade passage, exclude blade thickness.

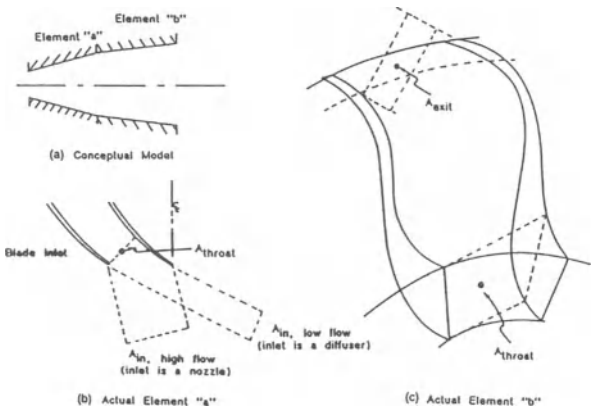

Fig. 4 Schematic two-elements-in-series model

With this model, the three parameters of η_a, η_b and DR_{stall} which limits the maximum value of diffuser ratio DR_2, is to form the simulation dominative parameters of two-zone modeling performance prediction of compressor.

※ Boundary of surge and choke

When the impeller inlet incidence is larger than the critical incidence, it has been thought that the impeller stall would happen. During the preliminary design stage, when the impeller is stalled, it is deemed that the impeller is surged. With this model, the critical incidence is a function of inlet relative Mach number.

$$I_{1t\text{-}stall} = A_1 + A_2 \cdot M_{rel} + A_3 \cdot M_{rel}^2 \tag{10}$$

where A_1=44.553, A_2=-49.5, A_3=14.1667

Choking is calculated when the impeller throat reaches sonic condition. The throat area is the geometry area minus the area blocked by the area dynamic blockage.

3 Validation Study of Two-Zone Modeling

Based on the actual test data of compressor performance in turbocharger applied in great power and high power diesel engine, the validation study of two-zone modeling performance prediction had been conducted. The two typical cases would be demonstrated within this text. Table 1 show the key parameters and test conditions.

※ Analysis of Performance Property

Figures 5 and 6 present comparison between prediction value and test data of compressor performance of the two cases. The results indicate: compared with the test, it seems that the prediction value near choke and surge has a great difference, but as a whole, the prediction value has a good consistency with the test, and the performance prediction could effectively present the overall flow property of compressor operating at all conditions.

Table 1 Description of two typical cases

Description	CASE150	CASE93
Impeller exit diameter	150 mm	93 mm
Pressure measurement	Transducers	"U" tube
Pressure type	Total pressure	Static pressure
Flow measurement	Thermal flow	Flow nozzle
Manufacture	Milling	Casting
Blade surface shape	Straight	Unrestricted
Simulation parameters	η_a : 0.7	η_a : 0.9
	η_b : 0.2	η_b : 0.5
	DR_{stall} : 1.18	DR_{stall} : 1.3

Excluding noise point, choke point, and surge point in performance map of compressor, the value of the difference between prediction and test has been shown on Fig. 7.

According to Fig. 7, for CASE150, comparing to the test value, the difference of efficiency is from -2% to 7%, the absolute value is from -0.01 to 0.05. The maximum difference exists at the high rotating speed when the relative Mach number of the impeller inlet tip diameter exceeds 1.18. The total pressure ratio difference is from -3% to 1%, the absolute value is -0.07 to 0.02.

For CASE93, the efficiency difference is from -3% to 3%, the absolute value is from-0.03 to 0.02. The pressure ratio distinctness is from -2% to 1%, and the absolute value is from -0.04 to 0.01.

Based on the above analysis results, the following conclusions could be made: in the preliminary design stage, the performance obtained through two-zone modeling prediction method would completely present the flow property which compressor could reach. It has been thought that the pressure ratio of prediction is the same to actual test value which would be obtained. The efficiency is the same during low rotating speed and small inlet tip relative Mach number of impeller, the maximum difference at the same rotational speed is less than one point. For high rotating speed and transonic conditions, the difference become greater, the maximum difference is less than 3 point, which exists in the straight surface and milling impeller product.

※ Analysis of Choke and Surge Boundary

Figure 8 presents comparison the choking prediction of the case mass flow rate with test. Excluding these noise point (superscript "*"), the maximum difference is 0.06.

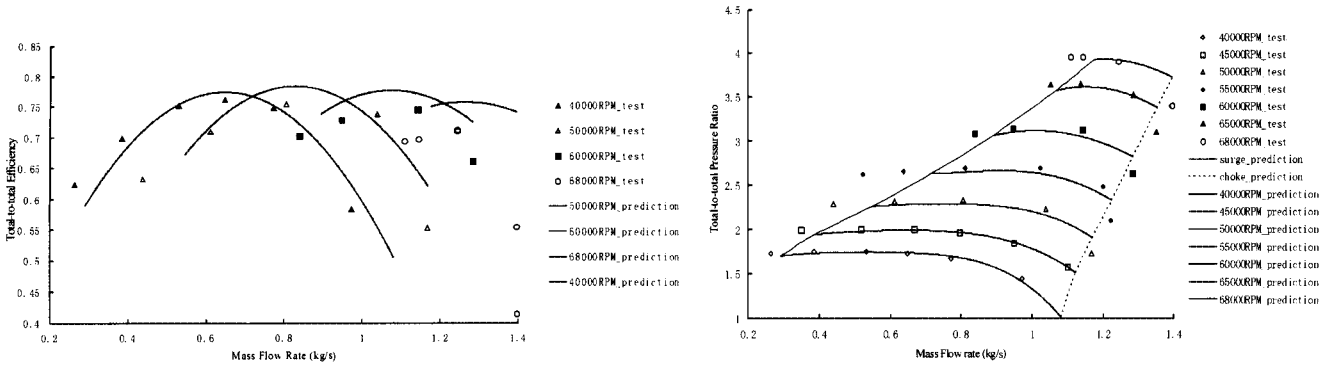

Fig. 5 CASE150 compressor performance

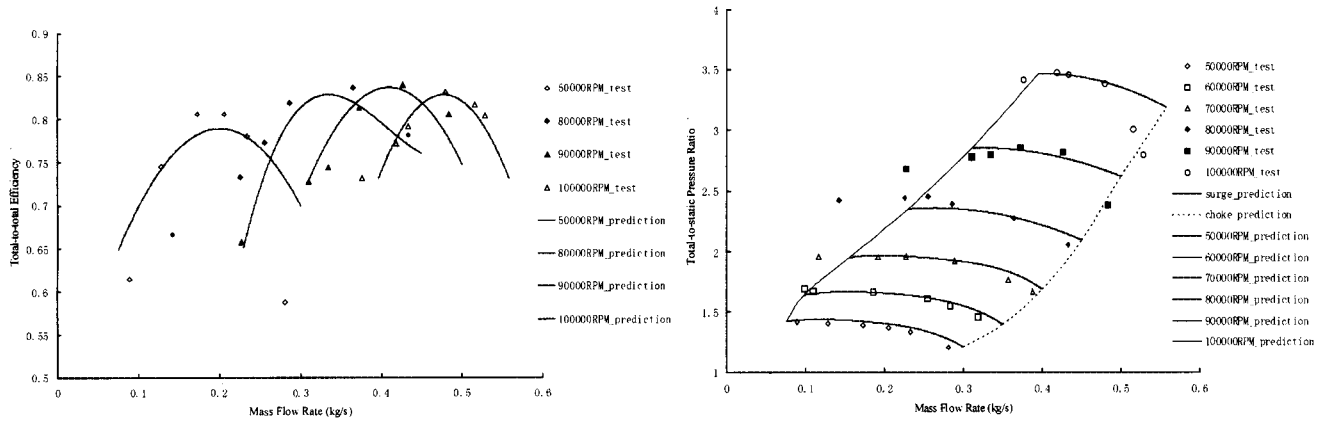

Fig. 6 CASE93 compressor performance

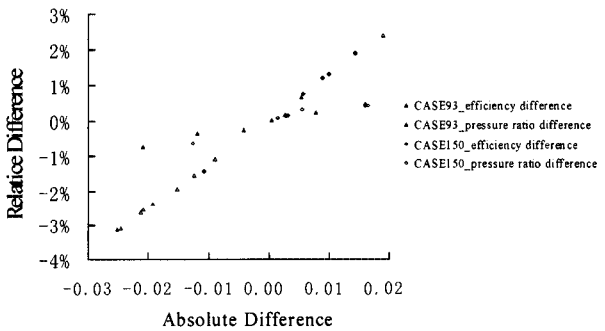

Fig. 7 Difference between prediction and test

CASE150				CASE93			
Rotational speed	Predicting flow rate	Test flow rate	Absolute difference	Rotational speed	Predicting flow rate	Test flow rate	Absolute difference
RPM	kg/s	kg/s	kg/s	RPM	kg/s	kg/s	kg/s
40000*	1.081	0.973	0.108	50000	0.298	0.281	0.060
45000	1.122	1.1	0.020	60000*	0.346	0.318	0.088
50000	1.169	1.168	0.001	70000	0.397	0.388	0.023
55000	1.223	1.222	0.001	80000	0.448	0.433	0.035
60000	1.284	1.285	-0.001	90000	0.503	0.483	0.041
65000	1.352	1.351	0.001	100000	0.555	0.528	0.051
68000	1.397	1.396	0.001				

Fig. 8 Choke boundary of prediction and test

Figure 9 shows the difference of surge mass flow rate, during transonic operating conditions at high rotating speed, the maximum difference compared with test is 0.066. Operating at subsonic conditions of low rotating speed, the maximum difference is 0.244. This great difference may be caused by the equivalent concept between stall and surge.

CASE150				CASE80			
Rotational speed	Predicting flow rate	Test flow rate	Absolute difference	Rotational speed	Predicting flow rate	Test flow rate	Absolute difference
RPM	kg/s	kg/s	kg/s	RPM	kg/s	kg/s	kg/s
40000	0.291	0.263	0.028	50000	0.075	0.089	-0.157
45000	0.386	0.348	0.109	60000	0.098	0.096	0.021
50000	0.546	0.439	0.244	70000	0.155	0.136	0.140
55000	0.715	0.636	0.124	80000	0.229	0.225	0.018
60000	0.894	0.839	0.066	90000	0.311	0.31	0.003
65000	1.071	1.055	0.015	100000	0.396	0.376	0.053
68000	1.175	1.145	0.026				

Fig. 9 Surge boundary of prediction and test

According to above analysis about boundary of choke and surge, the boundary obtained by two-zone modeling prediction method would be conservatively estimated. Comparing with the test, the boundary of the surge and choke on compressor performance map is approximate to peak island of maximum efficiency. Assuming the boundary of surge or choke is fitted to linear boundary, the difference between prediction and test had been less than 0.1. For high rotational speed, the difference had been less than 0.06. The accuracy is enough to meet the preliminary design stage.

4 Conclusions

Two-zone modeling method can effectively predict the performance of the centrifugal compressor in turbochargers, including its surge boundary and choke boundary. And it can effectively present overall performance property of the compressor.

To select appropriate simulation parameters, excluding near the boundary of surge and choke, comparing prediction value with test data, the difference of the total to total pressure ratio is less than 3%.

According to the level of design and manufacture, the difference of adiabatic efficiency based on total to total pressure ratio is less than one point, comparing with the test data completed by current experimental facilities.

Comparing with test data, the predicting mass flow on surge boundary or choke boundary could been rather perfectly fitted, the difference between them is less than 0.1, for transonic operating condition at high rotational speed, the difference is set to become smaller than 0.06.

Acknowledgements

The author would like to thank the National Key Laboratory of Diesel Engine Turbocharging Technology and the China North Engine Research Institute for financial support. The author would appreciate the assistance from Junyue Zhang and Weidong Xing.

References

Ainley D. G., Mathieson G. C. R., 1951, "An Examination of the Flow and Pressure Losses in Blade Rows of Axial Flow Turbine", *ARC, R&M 2891*

Connor W A, 1984, "Design and off-design Performance Prediction of High Pressure Ratio Centrifugal Compressors", *VKI lecture series*, 1984-07

Daily J W, Nece R E, 1960, "Chamber Dimension Effects on Induced Flow and Frictional Resistance of Enclosed Rotating Disks", ASME Paper NO.59-HYD-9, *Trans ASME Journ Basic Eng*, pp. 217 – 232

David Japikse, 1996, "Centrifugal Compressor Design and Performance", *Vermont USA: Concepts ETI, Inc.*

Galvas M R, 1972, "Analytical Correlation of Centrifugal Compressor Design Geometry for Maximum Efficiency with Specific Speed", *NASA TN D-6729*

Herbert M V, 1978, "Method for Performance Prediction of Centrifugal Compressor", *NGTE memorandum*, 78029

Howell A R, 1945, "the Design of Axial Flow Compressor", *Proc. ImechE*, 153

Moore J, Moore J G, 1981, "Viscous Flow Calculations in Turbomachinery", *Advanced concepts in turbomachinery*, Fluid Dynamics Institute, Hanover, NH

The 4th International Symposium on Fluid Machinery and Fluid Engineering
November 24-27, 2008, Beijing, China
NO. 4ISFMFE-Ch29

Effect of Swept Blade on Performance of a Small Size Axial Fan

Ailing Yang*, Tao Tang, Hui Zhang and Kangmin Chen

* College of Power Engineering, University of Shanghai for Science and Technology,
JunGong Road 516#, PO419, Shanghai 200093, China
Tel: +86-021-5527-0508 / Fax: +86-021-5527-2376
E-mail: alyang@usst.edu.cn

Abstract Skewed-swept blade shows excellent performance in improving the efficiency and decreasing the air noise of compressors and gas turbines. A great of research indicates that the flow mechanism of skewed-swept blade is controlling the aggregation of low energy flow in the end wall regions and radial second flow. In this paper numerical research is carried out to study the effects of swept blade on the aerodynamic and aeroacoustic performance of a 77.6-mm-diameter cooling fan. The cooling fans are normally small size and axial, which are widely used to cool the electronic elements. The 3D steady numerical simulations of three fans, which have forward-swept 10° blade, 0° blade and backward-swept 10° respectively, are finished based on the CFD commercial software Fluent. The efficiency and pressure curves of fans are gained and compared with experiment data. Results show that both the forward-swept blade and backward-swept blade worsens the efficiency of the cooling fan. The sweep of blade changes the radial distribution of the axial velocity at the inlet of the fan. The unsteady flows of above three fans are simulated with LES model at a same flow rate 0.99m^3/min. The aerodynamic noise sources are gained. Then the levels of noise emitted by the fans are calculated with FW-H equation. Compared with the 0° fan, the forward-swept 10° blade increased the noise about 1.2dB,but the backward-swept 10° blade decrease the noise 1.1dB.

Keywords swept blade, small axial fan, aerodynamic performance, aeroacoustic performance

Nomenclature

$C1z$	Axial velocity at the inlet of the fan in m/s
D	Diameter of the fan in m
Pt	Pressure of the fan in Pa
p	Pressure in Pa
Q	Air flow rate of the fan in m^3/min
t	Time in second
λ	Relative blade height

1 Introduction

The heat generated by the electronic elements continuously rises with the increase of the running speed. To ensure the electronic elements work safely the small size axial fans are widely applied to cool them. For example, there are 3 or 5 fans in one PC computer, more in a highly parallel computer. The cooling fans impel the air flow, take out the heat generated by the instruments and generate aerodynamic noise at same time. Moreover, larger the flow rate of the cooling fan is, better the cooling effect is. On the other hand, the level of noise is increasing with the increase of flow rate of the cooling fans. There fore how to improve the aerodynamic performance and decrease the aerodynamic noise of cooling fans are the important problems which the designers have to overcome.

Murray (2006) studied the noise emission of computer cooling fans by experiments. The method how to obtain the acoustic performance of the fans was discussed and a way to evaluate the fan' acoustic performance provided. H.Z.Lu (2007) analyzed the noise source of the small size axial fan with CFD. The noise induced by the interaction between the wake and underprops was also researched.

Skewed-swept blade shows excellent performance in improving the efficiency and decreasing the air noise of

compressors and gas turbines Beiler (1999) & Myung (1999). The researches indicate that the flow mechanism of skewed-swept blade is controlling the aggregation of low energy flow in the end wall regions and radial second flow. However, the researches about the effect of swept blades on the aerodynamic and aeroacoutic performance of the fans are few. Ailing Yang (2002) simulated the three dimensional flow in the fans and calculated the noise with Fukano's model. The research indicates that the forward swept improves the performance of the fan. But, Huang Xiaolong (2007) measured the variation of a computer cooling fan's pressure with flow rate, and their noise levels in a hemi-anechoic chamber. His researches show that the forward-swept had no improvement on the fan's aerodynamic and aeroacoutic performance.

Based on commercial CFD software Fluent, numerical research is carried out to investigate the effects of swept blade on the aerodynamic and aeroacoustic performance of a small size axial fan in this research. The numerical simulations of 3D steady flow in these fans with different swept blades are finished firstly. The efficiency and pressure curves of fans are gained and compared with experiment data. Results show that the forward and backward sweep of the blade worsens the flow around the blade so as to decrease the efficiency of the fan. The unsteady flows in three fans with forward-swept, radial and backward-swept blade respectively are simulated with LES model. Moreover, the noise radiated by the fans is calculated and analyzed with FW-H equation.

2 Swept Fans and Grid Generation

The fan calculated in the paper is a 77.6-mm-diameter computer cooling fan with 1mm tip-clearance and 7 blades. The rotational speed is 4500rpm. The geometries of the blade at different radius are measured and introduced into Pro-E. Fig. 1(a) gives the model of this fan rebuilt in Pro-E, which is named 0^0 fan. Then the leading edge of the blade is upstream inclined 10^0 when keeping others blade parameters unchanged. The new fan, so-called forward-swept 10^0 fan shown as Fig.1(b), is named 10^0 fan. Fig.1(c) presents the model of backward-swept fan named -10^0 fan, the leading edge of which is downstream inclined 10^0. These three fans have same blade width, geometric intake angle and other cascade parameters because the blades of the swept fans are only translated along axis.

Figure 2 gives the computational domain, which is divided into three zones. The upstream and downstream extended zones are static zone and connect with the rotational zone. In the rotational zone only one flow passage is calculated to decrease the grid number. The unstructured meshes on the blade surface shown in Fig.2 are generated with great care. The figure shows that the boundary layer meshes are set around the blade to catch the detail of the turbulent flow. The total grid number is about one million and grid quality check shows that the minimum skewness is mainly ranged from 0.1 to 0.5. According to the criteria of Fluent, the grid has high quality.

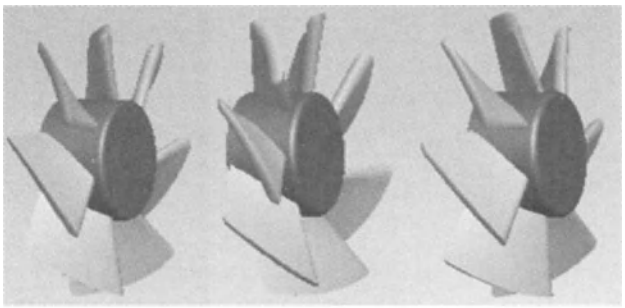

(a) 0^0 fan (b) 10^0 fan (c) -10^0 fan

Fig. 1 Three models of the computer fan with different swept angle

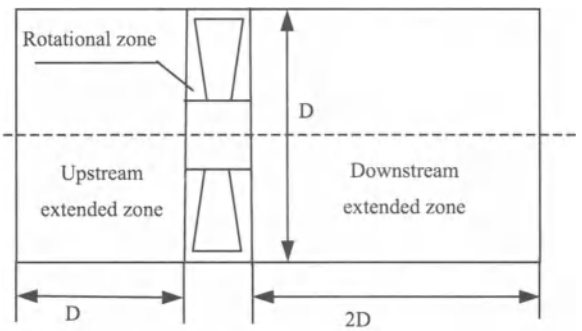

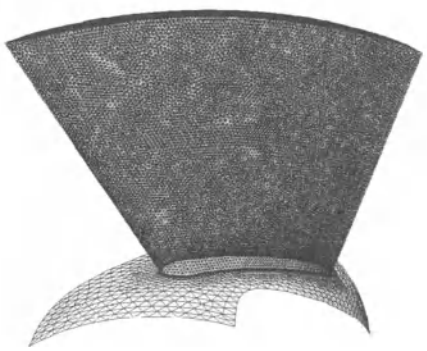

Fig. 2 Computational domain and meshes on the blade surface

3 Numerical Method

The incompressible Navier-Stokes equations are resolved to simulate the three dimensional flow of the above fans shown as in Fig.1.The second order upwind scheme is used to discrete the convection terms of the N-S equations

and Realizable k-ε model is applied to simulate the turbulent flow for the steady calculation.

In order to investigate the effect of swept-blade on the aeroacoustic performance of the fans, FW-H method is used to predict the noise emitted by the fan. The aeroacoustic sources are computed by resolving the unsteady incompressible Navier-Stokes equations. The turbulent flows are simulated with large eddy simulation (LES) to improve the precision of the source solution. The exchange for information at the interface between the static zone and rotational zone is carried with Moving Mesh model provided by Fluent.

4 Results

4.1 Pressure and efficiency of the fans

The pressure distributions of three fans are shown in Fig. 3. E0 and E10 stand for the experiments of 0^0 fan and 10^0 fan. When the flow rate is ranged from $0.8m^3$/min to $1.10.8m^3$/min the difference between simulations and experiments is less than 5% and the numerical solution is credible. The error is added rapidly as the flow rate is less than $0.8m^3$/min. Therefore, the results in this range of flow rate are not discussed in the paper. Fortunately, the fan always operates at larger flow-rate range. Fig. 3 shows that the pressure of 0° fan is larger than 10° fan (forward-swept fan) and -10° fan (backward-swept fan). It suggests the swept blades decrease the pressure of the fan in this research. Moreover, the efficiency of 10° fan and -10° fan is also smaller than that of 0° fan (shown as Fig. 4). The efficiency of 0° fan come to a head 0.364 at air flow rate $0.99m^3$/min. The highest efficiency of 10° fan has dropped to 35% and the corresponding flow rate also drops to 0.86 m^3/min. Fig. 3 and Fig. 4 indicate that -10° fan has modest aerodynamic performance comparing with other two fans.

According the researches which had been published, forward-swept blade can improve the performance of the fan and decrease the aerodynamic noise. On the other hand, backward-swept blade may deteriorate the performance of the fan. Why the results in this paper have not suggested the same rules? As we known, the mechanism of skewed-swept blade is controlling the radial second flow and the aggregation of low energy flow in the end wall regions. However, the radial pressure gradient and circumferential pressure gradient in the flow passage are not great because the pressure of the fan investigated in the paper is very small according to the numerical solutions. It implies that the loss generated by the radial second flow may not be significant. In addition, the swept blades change the radial distribution of axial velocity at the inlet of the fan (shown as Fig. 5). Figure 5 is obtained at flow rate 0.99 m^3/min.The axial velocity of -10° fan becomes more uniform relative to that of 0° fan, but the forward-swept blade (10° fan) increase the flow rate of 60% flow passage near the hub (λ <0.6) and decrease the flow rate near the blade tip. So the velocity vector diagram of 10° fan and -10° fan at the inlet must be changed. The impingement angles of flow also offset from the design value and the flow loss may be increased.

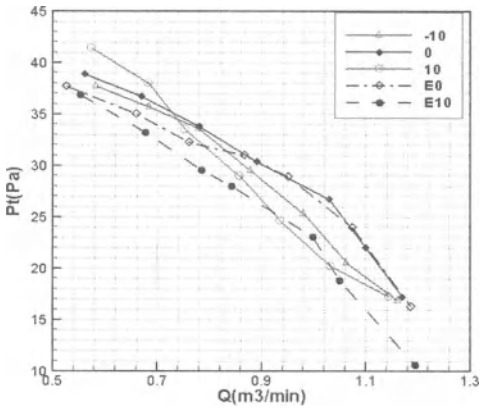

Fig. 3 Variation of pressure with flow rate of the fans

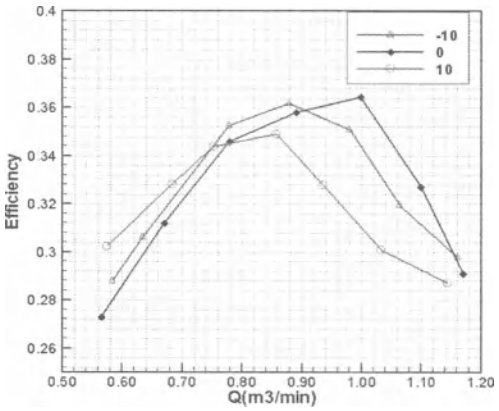

Fig. 4 Variation of efficiency with flow rate of the fans

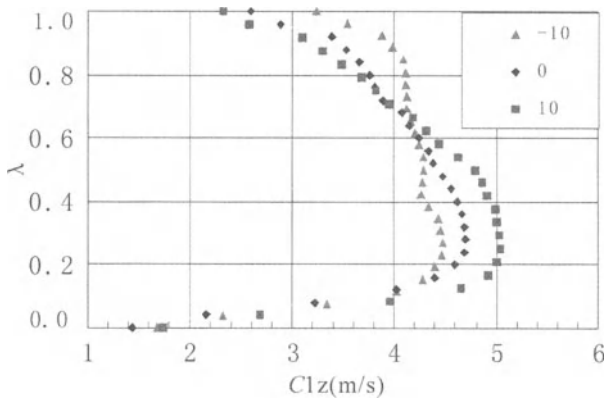

Fig. 5 Axial velocity at the inlet of the fan

4.2 Aeroacoustic performance

The unsteady flows of above three fans are simulated with LES model and moving mesh technology at the flow rate 0.99m^3/min. Then the noise level emitted by the fans is calculated with FW-H equation. The rotational walls including the blades are chosen as the integrating surfaces and the quadrupole term of FW-H equation is not included to simplify the calculation.

Table 1 gives A-weighted levels of the aero-dynamic noise incepted by the observer located at 45° direction(see Fig. 6). Compared with 0° fan, the noise level of -10° fan decreases about 1.1dB, but the forward-swept 10° fan adds the noise level about 1.2dB. Fig. 7 shows the noise levels in dB picked by the observers which are located at different orientations. Here, the circular axis is the orientation of noise emission. This figure illuminates the radiation of the fans is not circumferential uniformly. The noise level in 180° direction (far-field inlet, see Fig. 6) and 0° direction(far-field exit) is much larger than other directions. Moreover, -10° fan radiates smaller noise than 0° fan and 10° fan in every direction, but the noise levels of 10° fan are bigger than that of 0° fan.

Table 1 A-weighted noise levels

	Simulation (dB)
-10°	41.27 (4500rpm)
0°	42.37 (4500rpm)
10°	43.45 (4500rpm)

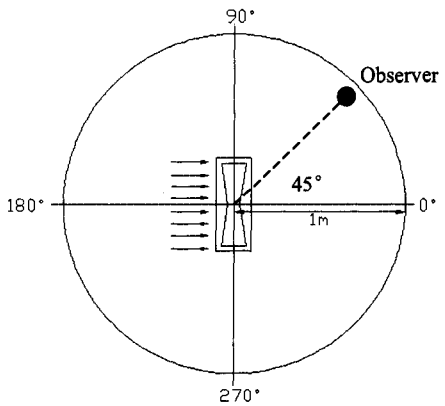

Fig. 6 Sketch of sound field

Figure 8 shows the third-octave-band spectrum of the fans. As seen in Fig. 8, the three fans have similar spectrum. The noise from 500Hz to 600Hz dominates the spectrum, with levels around 39, 41 and 43dB, respectively corresponding to -10°, 0° and 10° fan. The blade passing frequency of the fans is 525Hz, lying in the band from 500Hz to 600Hz. This means the noise of the fans is mainly generated by the periodically beating the air. Figure 9

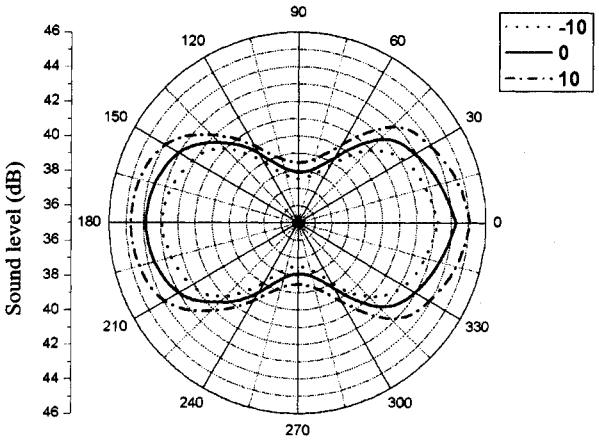

Fig. 7 Noise directivities of the fans

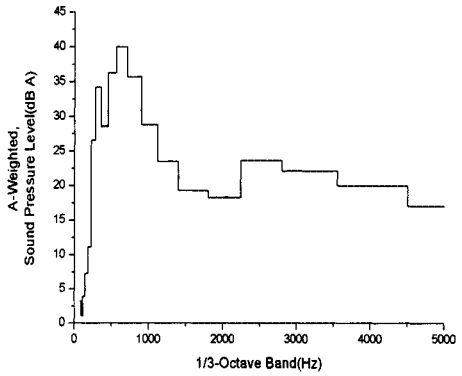

(a) -10° fan

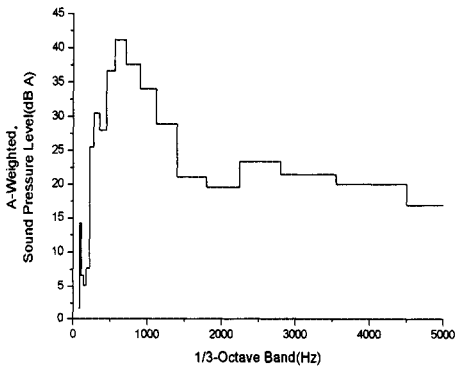

(b) 0° fan

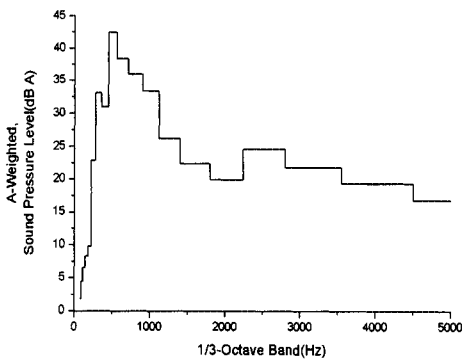

(c) 10° fan

Fig. 8 1/3 octave-band spectrum of the fans

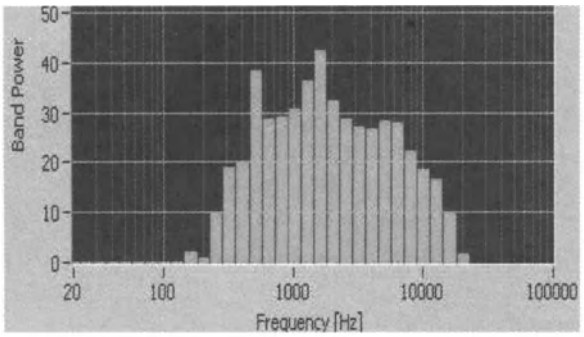

(a) 0° fan

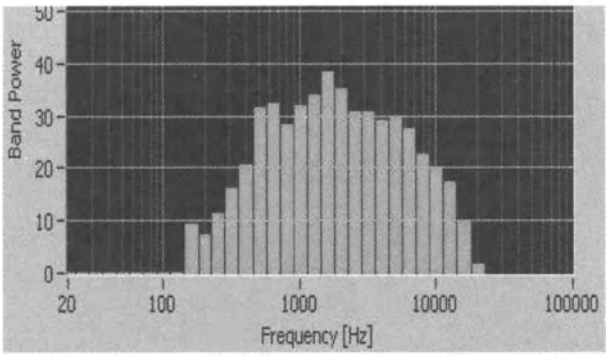

(b) 10° fan

Fig. 9 1/3 octave-band spectrum of the fans given by experiments (Huang Xiaolong, 2007)

gives the third-octave-band spectrum tested in hemi-anechoic chamber[Huang Xiaolong, 2007]. The simulations accord with experiments well as the frequency less than 1000Hz. There is noise generated by the motor during testing. The difference between Fig. 8 and Fig. 9 as frequency larger than 1000Hz does not denote the failure of the simulation.

Figure 10 and Fig. 11 present the distribution of root mean square of the pressure derivative $\partial p / \partial t$ on the blade, which represents the intensity of the dipole source. The RMS of pressure fluctuating on the pressure surfaces is stronger than that on the suction surfaces. It implies that the dipole sources distributed on the pressure surfaces are the primary noise sources of the fans. On the other hand, the pressure fluctuating near the tip of the blade is larger than that near the root. According to the method of calculating the noise level, it is favorable to damp the pressure fluctuating near the tip on the pressure surface for the controlling of the aerodynamic noise of the fans. The figures also show that backward-swept 10° blade enhances the pressure fluctuating near the root, but weakens fluctuation near the tip on the pressure surface. In contrast, the forward-swept 10° blade greatly increase the pressure fluctuating on the pressure surface. Consequently, the noise level of -10° fan is smaller than 0° fan and that of 10° fan is bigger than 0° fan (see Table 1 and Fig. 7). Obviously, the backward-swept 10° blade is beneficial to the aeroacoutic performance of the fan, and the forward-swept 10° blade is unfavorable.

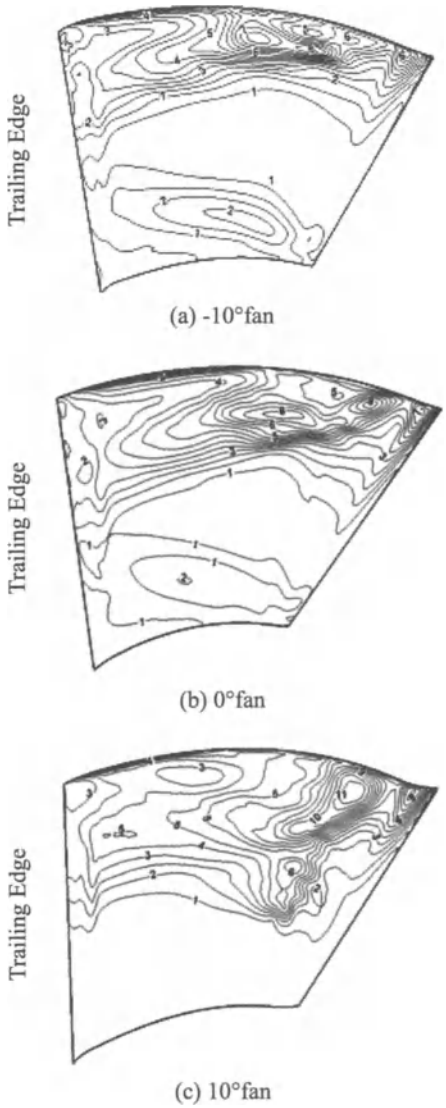

(a) -10°fan

(b) 0°fan

(c) 10°fan

Fig. 10 The root mean square of the pressure derivative $\partial p / \partial t$ on the pressure side

5 Conclusions

The effect of swept-blade on the aerodynamic and aeroacoutic performance of the small size axial fan is researched with CFD software Fluent. The results illustrate that swept blades make the impingement angles offset the design values and worsen fan's efficiency. The backward-swept 10° blade reduces the pressure fluctuating of the pressure surface and decreases the aerodynamic noise of the fan. The influence of forward-swept blade on acoustic performance of the fan is just opposite to backward-swept blade.

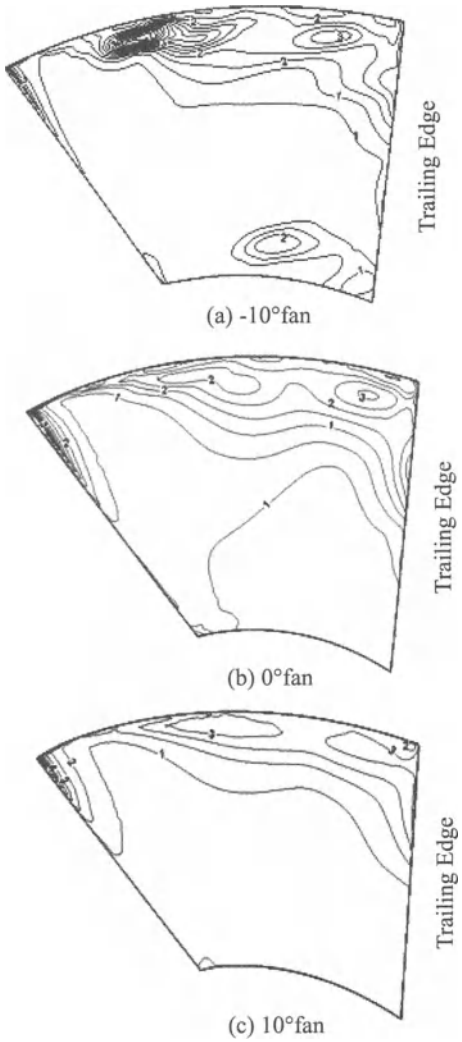

Fig. 11 The root mean square of the pressure derivative $\partial p / \partial t$ on the suction side

Acknowledgements

This work was supported by Shanghai Leading Academic Discipline Project (Project Number: J50501), the Shanghai Municipal Education Commission (Project Number: 05zz27).

References

Murray Hodgson, Isabella Li, 2006, "Experimental Stu-dy of the Noise Emission of Personal Computer Cooling Fans", *Applied Acoustics*, Vol.67, pp. 849 – 863

H.Z.Lu, Lixi Huang, R.M.C.So and J.Wang, 2007, "A computational study of the interaction noise from a small axial-flow fan", *Acoustical Society of America*, Vol.122, No.3, pp. 1404 – 1415

Beiler, M.G.; Carolus, T.H, 1999, "Computation and Measurement of the Flow in Axial Flow Fans with Skewed Blades", *Journal of Turbomachinery*, Vol.121, No.1, pp. 59 – 66

Myung H J, Back J H, 1999, "Mean Velocity Characteristics behind a Forward-Swept Axial-Flow Fan.", *JSME International Journal*, Series B, Vol.42, No.3, pp. 476 – 488

Ailing Yang, Kangmin Chen, 2002, "The Influence of Swept Blades on the Aerodynamic-aeroacoustic Perform-ance of the Rotors of small Axial flow Fans", *Fluid mec-hanics*, Vol.30, No.1, pp. 18 – 20

Huang Xiaolong, 2007, "Study on the Acoustics and Dynamics characters of Cooling Fan Using in Computer", Ma.D. Thesis, *University of Shanghai for Science and Technology*

The 4th International Symposium on Fluid Machinery and Fluid Engineering
November 24-27, 2008, Beijing, China
NO. 4ISFMFE-IL0

Multi-Objective Optimization of Blood-Pump with Conical Spiral Groove Bearings

Masahiro Kaneko[1], Yoichi Nakamura[1], Koji Miyazaki[2] and Hiroshi Tsukamoto[*3]

[1] Graduate School of Life Science and Systems Engineering, Kyushu Institute of Technology,
[2] Faculty of Engineering, Kyushu Institute of Technology
[*3] Graduate School of Life Science and Systems Engineering, Kyushu Institute of Technology,
2-3 Hibikino, Wakamatsu-ku, Kitakyushu, Fukuoka 808-0196, Japan
Tel: +81-93-695-6027 / Fax: +81-93-695-6027
E-mail: tsukamoto@life.kyutech.ac.jp

Abstract Multi-Objective Genetic Algorithm (MOGA) optimization was developed to realize a smaller and higher efficiency blood pump without hemolysis. The hydrodynamic efficiency, impeller outer diameter, and shear velocity were chosen as GA objective functions. The measured pump performance of the GA optimized pump was acceptable as a blood pump. And unsteady RANS calculations showed that the hemolysis can be suppressed in the GA optimized pump by eliminating higher shear velocity region in flow. As the result of the present study the GA optimization is found to be effective for the design of blood pumps.

Keywords blood pump, centrifugal pump, optimal design, genetic algorithm, CFD, medical device

Nomenclature

K	Number of generations
M	Probability of mutation
N	Number of individuals
n	Rotational speed of impeller [min^{-1}]
Q	Flow rate [L/min]
w_D	Weighting factor of outer diameter of impeller
w_h	Weighting factor of Hydraulic efficiency
Z	Number of blades
β_1	Inlet blade angle [deg]
β_2	Outlet blade angle [deg]
γ	Shear velocity [s^{-1}]
η_h	Hydraulic efficiency
μ	Viscosity coefficient [Pa · s]
ρ	Density [kg/m^3]
τ	Shear stress [Pa]

1 Introduction

Recently blood pumps have come to the front as the therapeutic instrument for serious heart failure. The centrifugal pump may be superior among many types of blood pumps because of its compact structure. In centrifugal blood pumps, however, the suppression of the hemolysis as well as the thrombus is the important problem to be solved. Thrombus has been avoided by use of the magnetically-levitated bearing or the conical spiral groove bearing (Yoshino et al. 1994, Nakamura et al. 2007), while trial-and-error approaches have been taken to prevent hemolysis. Therefore further development will be necessary for centrifugal blood pump.

Numerical optimization methods constitute an efficient tool for using effectively the information provided by CFD calculations, for analyzing the correlations between geometrical parameters and pump performance, and for finding their optimum combination. The Genetic Algorithm (GA) is one of the most employed global optimization methods to get the optimized solution for the problems such as blood pump that includes many factors to be solved.

In this study, the Multi-Objective Genetic Algorithm (MOGA) optimization was performed for the design of a small and high efficiency blood pump without hemolysis. And experimental and numerical study was done on the blood pump with the optimized impeller.

2 Optimization of Blood-Pump Geometry

2.1 Design methodology

Figure 1 illustrates the shematic diagram of the test blood pump. The test pump consists of a pump casing and a pump rotor. As shown in this figure, the casing contains the suction and discharge ports. The pump rotor consists of an impeller, bearings and a cupling magnet. The pump is driven through the cupling magnet by a motor. The bearing, Conical Spiral Groove Bearings (CSGB), are set at both ends of the impeller (Nakamura et al. 2007).

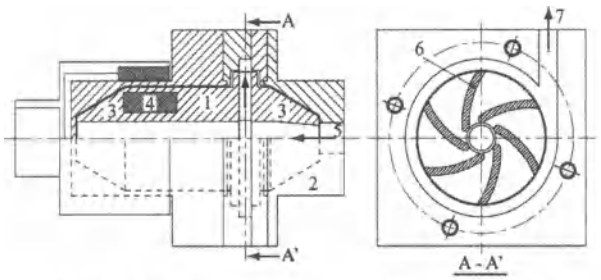

1.Rotor, 2.Pump casing, 3.Conical spiral groove bearing,
4.Cupling magnets, 5.Suction port, 6.Impeller, 7.Discharge port

Fig. 1 Schematic diagram of test blood pump

Figure 2 shows the flowchart of GA process in this study. In this design process, at first, the inner diameter D_1, outer diameter D_2, inlet passage width b_1, outer passage width b_2, and rotational speed n of impeller were assigned at random. Next, inlet blade angle β_1 and outlet blade angle β_2 were determined based on the concept of slip. The number of blades was determined based on the empirical equation by Pfleiderer. Circular arc was chosen as the impeller blade profile. And hydrodynamic loss analysis was done by considering the friction and shock losses. Flow rate Q = 8 L/min and total pump head H = 4.0 m were assigned as the rated condition. Although the occurrence of hemolysis has relations to the gap width between impeller blade tip and pump casing wall, the gap width was set to be 5 mm based on Niino et al. (2005), in the present study where the optimization was done only for impeller.

2.2 Evaluation function

Design parameters of an impeller were treated as genotype, and the multi objective optimization was performed with evaluation functions; the hydraulic efficiency η_h, the impeller outer diameter D_2 and the shear velocity γ. The evaluation functions are defined so that fitness values may become high for high hydraulic efficiency η_h and small impeller outer diameter D_2:

$$f(D_2) = (D_{max} - D_2) \tag{1}$$

$$f(\eta_h) = \eta_h \tag{2}$$

$$f(I) = w_D f(D_2) + w_\eta f(\eta_h) \tag{3}$$

Here w_D and w_η are the weighting factor of impeller outer diameter and hydraulic efficiency, and set to be 0.5. Shear velocity is the evaluation parameter for hemolysis, and it becomes the biggest value on the pump casing surface and the tip of impeller. In this study, the rotational speed of impeller was constrained so that $\gamma < 1500$ s^{-1} according to Handa et al. (1998), under the assumption that the flow between the impeller tip and the pump casing wall is the Couette-Flow:

$$n \leqslant 5000 \text{ min}^{-1} \tag{4}$$

The fitness values of each individual were evaluated with the above evaluation functions, and the optimized solution was achieved when the fitness value becomes maximum ones.

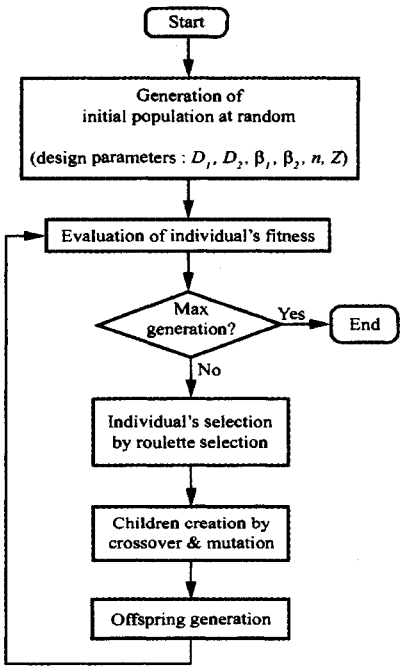

Fig. 2 Flowchart in GA process

2.3 Crossover and mutation

The one-point crossover was adopted in the crossover process. The crossover point was chosen at random, whenever the crossover process was performed. The number of generations and the number of individuals were empirically given for the optimization parameters as K = 50 and N = 60, respectively. And the probabilities of crossover and mutation were given to avoid converging in a local solution as C = 0.3 and M = 0.05.

3 Numerical Analysis

3.1 Methodology

The numerical simulation was carried out using the universal thermo-fluid analysis code ANSYS CFX (ANSYS 2007) to examine the flow in the blood pump. The RNG (Re-Normalization Group) k-ε model was adopted as the turbulence model. The law of wall was selected to reasonably solve the near wall flow conditions. The unsteady analysis was carried out, in which the step-angle was set to be 6 degrees.

Unstructured computational grids were generated for the simulation model of the blood pump as shown in Fig. 3. The simulation model was consisted of the rotor, the inlet and casing, and the outlet. The rotor is the rotationally component, and the inlet, casing, and outlet are the stationary ones. The rotor and the stators were coupled by the interface between them, and the sliding mesh was used to solve the interactions between the rotational and stationary domains. The full computational pump model consists of 796,165 elements as shown in Table 1.

The boundary conditions are the rotational speed n for impeller, the flow rate Q at inlet, and the static pressure (0 Pa) at outlet. And the no-slip condition was set on the wall surface. The blood was assumed to be incompressible and Newtonian fluid. The physical properties of the blood were assumed to have viscosity μ of 0.0028 Pa • s and density ρ of 1048 kg/m^3 (Oka 1974).

3.2 Evaluation of blood damage

In the present study, the blood damage in blood pump was evaluated by the Bludszuweit's mathematical model for the hemolysis (Bludszuweit 1995). The shear stress in blood, which is comprised of the viscous shear stress and the Reynolds stress, can be expressed by the following simple scalar stress:

$$\tau = \left[\frac{1}{6}\sum\left(\tau_{ii}-\tau_{jj}\right)^2 + \sum\tau_{ij}^2\right]^{\frac{1}{2}} \tag{5}$$

The time histories of the shear stress on the blood cells are calculated with the assumption that the blood cells flow along streamlines. The streamlines were calculated from the inlet to outlet of the pump based on CFD results. Giersiepen et al. (1990) indicated that the blood damage under the uniform shear stress field depends on both the shear stress and the exposure time. The blood damages are expressed as the one D_i during the very short time interval Δt from the pump inlet to outlet as follow:

$$D_i = \sum_{i=inlet}^{outlet} 3.62\times10^{-7}\tau^{2.416}\Delta t^{0.785} \tag{6}$$

The blood damage index D_i is calculated on each streamline, and the average value of D_i is adopted as the measure of the hemolysis.

Table 1 Number of elements

Inlet	Rotor	Casing/Outlet	Total
12,894	636,999	146,272	796,165

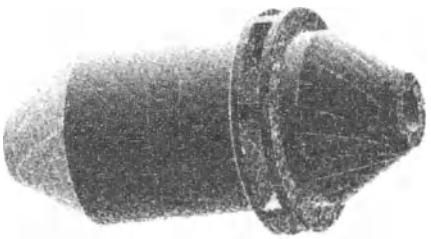

(a) Pump rotor

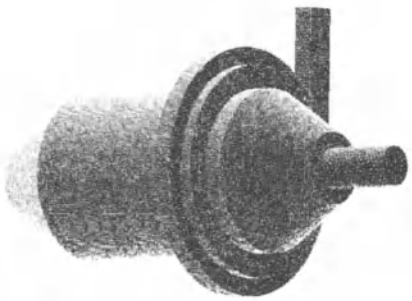

(b) Pump casing

Fig. 3 Computational domain and grids

4 Results and Discussions

4.1 Optimized impeller

The optimized solution was obtained in the present optimization process. Table 2 presents the parameters of the impeller optimized by GA.

The design parameters of optimized impeller were the impeller outer diameter D_2 = 52 mm, the outlet blade angle β_2 = 55 deg, the rotational speed n = 2700 min^{-1}, and the number of blades Z = 6, respectively. And the calculated hydraulic efficiency was 77.3%.

Table 2 Parameters of optimized blood pump

Impeller outer diameter D_2	52 mm
Impeller inner diameter D_1	10 mm
Outlet blade angle β_2	55 deg
Inlet blade angle β_1	12 deg
Rotational speed n	2700 min^{-1}
Number of blades Z	6
Hydraulic efficiency η_h	77.3 %

4.2 Pump characteristics

Figure 4 shows the measured performance curve of the optimized blood pump. The optimized blood pump satisfies the required specifications at the design point (Q = 8 L/min, and n = 2,700 min^{-1}). And the total pump efficiency is 13% at the rated condition. The calculated curve of the optimized blood pump is also shown for the rotational speed of 2,700min^{-1} in this figure. There can be seen small difference between calculated and measured performances for low flow rate range, while the calculated pump performance agrees well with the measured one at the design point. It shows the validity of the present numerical analysis, and hence the calculated flow field in the blood pump will be helpful for further discussions.

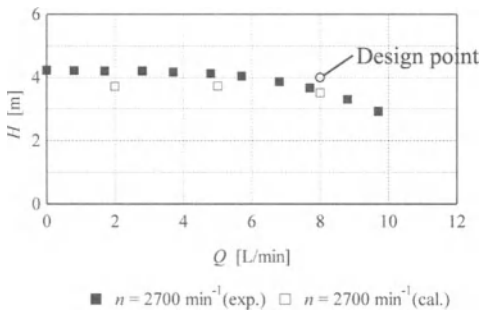

Fig. 4 Measured and calculated performance curves of an optimized blood pump; n = 2,700 min^{-1}

4.3 Thrombus

Figure 5 shows the velocity and velocity vector distributions in A-A' plane of the optimized blood pump (see Fig. 1). The generation of vortex is observed in the blade-to-blade passage. The thrombus may generate when the vortex occurs in the blood pump, because the shear velocity becomes small and thus flow will be stagnant near the vortex. Therefore, the probability of the thrombus was evaluated by checking the shear velocity distribution in the optimized blood pump.

Figures 6 and 7 indicate the shear velocity distributions in A-A' and X-Y plane of the impeller, respectively. The shear velocity is γ>500 s^{-1} in the most region of impeller. And the shear velocity is γ > 300 s^{-1} in other passages including the gap between the pump casing and the rotor. According to the Clotting Ratio by Hashimoto et al. (1993), the above values seem to be large enough for the shear velocity to prevent the thrombus formations. However, the region of γ < 300 s^{-1} appears in the passage between the suction and impeller as well as the downstream of the impeller. There the thrombus may be formed, and thus further improvement will be necessary for the geometry.

4.4 Hemolysis

Figure 8 shows the shear velocity distribution on A-A' plane. For the most part of the impeller the shear velocity is γ < 1500 s^{-1}, which is lower than the threshold level of the hemolysis by Handa et al. (1998). There exists the region of γ > 1500 s^{-1} between the pump casing wall and the impeller tip in the impeller. This is the result of too big velocity based on the assumption of Couette-Flow for the flow between the pump casing wall and impeller tip in the optimization process.

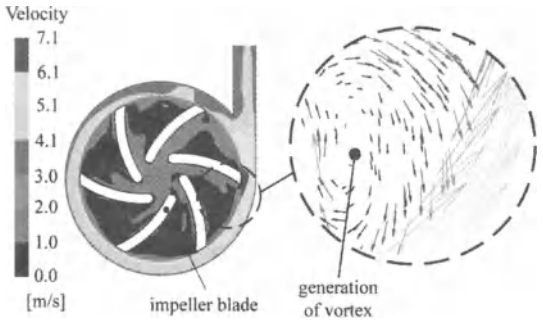

Fig. 5 Velocity and velocity vector distributions in A-A' plane; Q = 8 L/min, n = 2700 min^{-1}

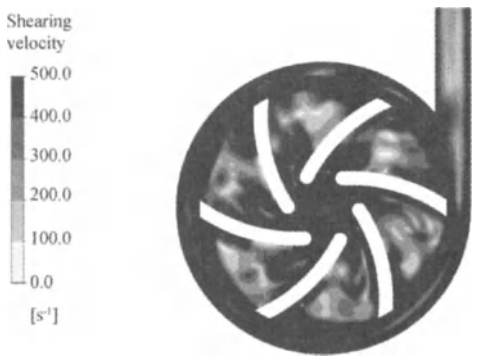

Fig. 6 Shearing velocity distribution in A-A' plane; Q = 8 L/min, n = 2700 min^{-1}

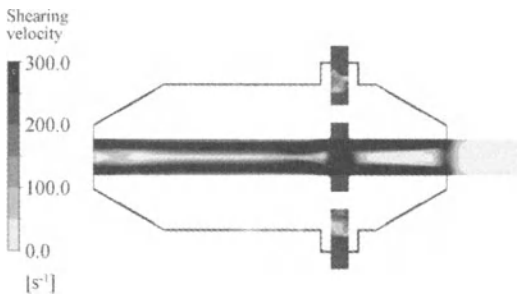

Fig. 7 Shearing velocity distribution in X-Y plane; Q = 8 L/min, n = 2700 min^{-1}

Figures 9 and 10 show the shear stress distribution on the rotor wall surface and pump casing, respectively.

Leverett et al. (1972) showed that the threshold level is 150 Pa for the hemolysis caused by shear stress τ. The region of $\tau > 150$ Pa was not found on the bearing as well as the cylinder part of the rotor. Although the shear stress is relatively high on the impeller surface, however, the maximum value is about 140 Pa which is less than the threshold of the hemolysis.

On the pump casing, the region of $\tau > 150$ Pa is found near the cut water, in which the largest value of τ is 187 Pa. The hemolysis may occur in the region of $\tau > 150$ Pa, however, it is not as large for the present optimized blood pump as the commercial blood pump of the same pump size (the Nikkiso HPM15, Nikkiso, Inc., Tokyo, Japan), as shown in Fig. 11 (Niino et al. 2005).

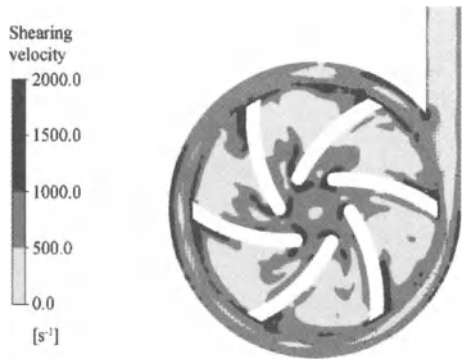

Fig. 8 Shearing velocity distribution in A-A' plane; Q = 8 L/min, n = 2700 min^{-1}

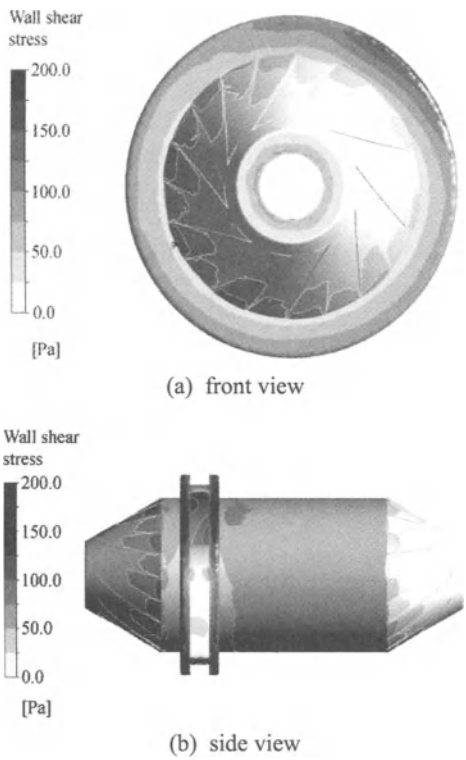

Fig. 9 Wall shear stress on pump rotor; Q=8L/min, n=2700min^{-1}

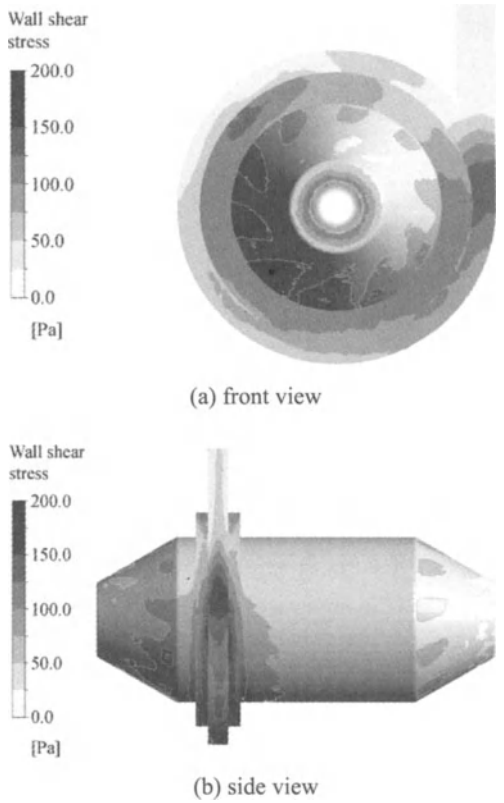

Fig. 10 Wall shear stress on pump casing; Q = 8 L/min, n = 2700 min^{-1}

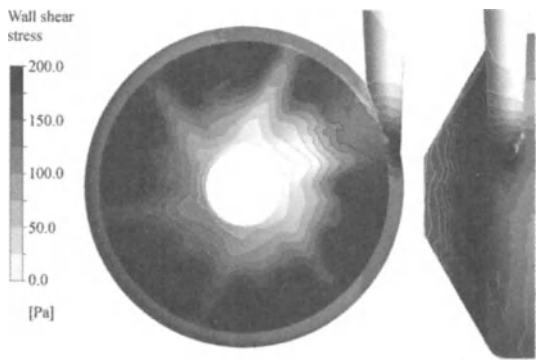

Fig. 11 Wall shear stress on pump casing of HPM-15; Q = 5 L/min, n = 3000 min^{-1}

4.5 Blood damage

The blood damage index D_i was calculated for the optimized blood pump as well as the commercial blood pump HPM-15. The optimized pump has $D_i = 1.08\times10^{-4}$, whereas $D_i = 1.05\times10^{-5}$ for HPM-15. The blood damage index in the optimized blood pump is greater than the one in the HPM-15. The main cause is the longer time staying in the present pump, because of longer passage from the inlet through the impeller to the outlet and the longer passage of the gap between the pump casing and rotor. The blood damage index D_i was confirmed to be reasonable

and valid as a measure of the blood damage (Yano et al. 2005). De Wacher, et al. (2002) suggested that the calculated D_i is greater than the experimental one. On the contrary, the D_i calculated by the CFD is lower than the measured one in the clinical practice and the experiment for HPM-15 (e.g., Araki et al. 1994, Masuzawa et al. 1998 & 1999). Therefore further discussion will be needed on the blood damage indexes.

5 Conclusions

In this study, Multi-Objective Genetic Algorithm (MOGA) optimization was developed for a small and high efficiency blood pump without hemolysis. The hydrodynamic efficiency, impeller outer diameter, and shear velocity were chosen as GA objective functions. The performance of the optimized blood pump was evaluated with the experiment and the numerical analysis.

The measured pump performance of the GA optimized pump showed good agreement with the required one. And unsteady RANS calculations presented that the GA optimized pump can suppress higher shear velocity in blood pump.

As the result of the present study the GA optimization was found to be effective for the design of blood pumps.

Acknowledgements

We gratefully acknowledge financial support by Japan Science and Technology Agency (A Research for Promoting Technological Seeds No.15-1122) and Grant-in-Aid for Scientific Research (Scientific Research (B) No.20360086). We are also grateful to Mr. Masashi Nishida for his contribution to this work.

References

ANSYS, Inc., 2007, ANSYS CFX Release 11.0

Araki, K., et al., 1994, In-vitro performances in centrifugal blood pumps, *Jpn. J. of Artif. Organs*, vol.23, No.3, pp. 898 – 903

Bludszuweit, C., 1995, Model for general mechanical blood damage prediction, *Artif. Organs*, Vol.19, No.7, pp. 583 – 589

De Wacher, D., et al., 2002, Numerical calculation of hemolysis cannulas, *Artif. Organs*, Vol.26, No.7, pp. 576 – 582

Giersiepen, M., et al., 1990, Estimation of shear stress-related blood damage in heart valve prostheses—in vitro comparison of 25 aortic valves, *Int. J. Artif. Organs*, Vol.13, No.5, pp. 300 – 306.

Handa, N., et al., 1998, The relation between physical factors and hemolysis, *Japanese Journal of Artificial Organs*, Vol.27, No.1, pp. 118 – 123

Hashimoto, S., and Sasada, T., 1993, Clot Formation under Uniform Shear Fields (Evaluation of Clot Growth by Concave—Convex Cone System), *Trans. JSME, Ser. B*, Vol.59, No.568, pp. 39 – 42

Leverett, L. B., et al., 1972, Red blood cell damage by shear stress , *Biophysical Journal*, Vol.12 , pp. 257 – 273

Masuzawa, T., et al., 1998, Effect of gaps between impeller tip and casing wall upon hemolysis property of a centrifugal blood pump, *Journal of the Society of Life Support Technology*, Vol.10, No.3, pp. 102 – 105

Masuzawa, T., et al., 1999, Development of design methods for a centrifugal blood pump with a fluid dynamic approach: results in hemolysis tests, *Artif. Organs*, Vol.23, No.8, pp. 757 – 761

Nakamura, Y., et al., 2007, Experimental study of Dynamic Characteristics of a Centrifugal Blood Pump with a Conical Spiral Groove Bearing for a Ventricular Assist Device, *5th Joint ASME / JSME Fluids Engineering Conference*, FEDSM2007-37235

Niino, S., et al., 2005, Improvements of blood pump configurations for less thrombosis and hemolysis, *Turbomachinery*, Vol.33, No.4, pp. 199 – 205

Oka, S., Rheology, 1974, Shokabo Publishing Co., Ltd., (in Japanese)

Pfleiderer, C., 1961, *Die Kreiselpumpen*, Springrr-Verlag

Yano, T., et al., 2005, Design Improvement of the Rotary Blood Pump by Computational Fluid Dynamics Analysis, *Trans. JSMBE*, vol.43, No.1, pp. 85 – 92

Yoshino, Y., and Akamatsu, T., 1994, Performances and Characteristics of Magnetically Suspended Centrifugal Blood Pump, *Trans. JSME, Ser. B*, vol.60, No.579, pp. 3687 – 3692

The 4th International Symposium on Fluid Machinery and Fluid Engineering
November 24-27, 2008, Beijing, China
NO. 4ISFMFE-Ab08

Analysis of Unsteady Flow in a Radial Diffuser Pump

Jianjun Feng*, Friedrich-Karl Benra, Hans Josef Dohmen

* Chair of Turbomachinery, Department of Mechanical Engineering,
University of Duisburg-Essen, Duisburg, 47048, Germany
Tel: +49 (203)-3793414, Fax: +49 (203)-3793038
E-mail: jianjun.feng@uni-due.de

Abstract Three-dimensional, unsteady Reynolds-averaged Navier-Stokes equations are solved by the CFD code CFX-10 in a radial diffuser pump. The turbulence is simulated by the k-ε based shear stress transport turbulence model. To validate the CFD results, two-dimensional Laser Doppler Velocimetry (LDV) measurements have also been conducted. Both the phase-averaged velocity field and the turbulence field have been analyzed in detail. A comparison of the phase averaged velocity fields at the radial gap for both methods shows a very good agreement for the global periodic flow field. The analysis shows that a jet-wake structure is observed near the impeller outlet, and the diffuser flow strongly depends on the relative impeller positions which provide different inflow conditions for the downstream diffuser. The effects from the impeller rotation to the diffuser flow become very small at the diffuser outlet.

Keywords unsteady flow, radial pump, turbulence, CFD, LDV

Nomenclature

C_r	m/s	absolute radial velocity
C_u	m/s	absolute circumferential velocity
PS	-	pressure side
Q	m^3/s	volume flow rate
R	mm	radius
SS	-	suction side
Tu	-	turbulence intensity
u	m/s	absolute component in x-direction
U	m/s	circumferential velocity
v	m/s	absolute component in y-direction
W	m/s	relative velocity
α	deg	absolute flow angle
β	deg	relative flow angle
φ	deg	rotating angle
θ	deg	circumferential position

Subscripts

1	impeller inlet
2	impeller outlet
3	diffuser inlet
4	diffuser outlet
des	design operating point

Superscripts

–	phase averaged
'	turbulent

1 Introduction

The internal flow developing in a radial diffuser pump is extremely complicated and highly turbulent, caused by streamline curvatures, system rotation, flow separations, rotor-stator interaction and turbulence effects. The rotor-stator interaction is assumed to have an important influence on the time-variant flow behavior in the case of a small radial gap between the impeller trailing edge and the diffuser leading edge (Arndt et al., 1990).

With the development of computational algorithms and computer technology, the application of CFD (Computational Fluid Dynamics) is becoming more and more popular and acceptable for the investigation of the unsteady flow in radial pumps, such as the work by Bert et al. (1996), Ardizzon and Pavesi (2004), He and Sato (2001), Benra and Dohmen (2005). Some measurements on velocity fields by Particle Image Velocimetry (PIV) were also reported by Akin and Rockwell (1994), Sinha et al. (2000)

and Wuibaut et al. (2002) in radial diffuser pumps.

The Laser Doppler Velocimetry (LDV) measurement technique is a non-contact way of measuring the velocity in the flow. Compared to PIV, LDV is more time-consuming but predicts more accurate results due to the measurement directly on the points of interest. Because PIV uses the correlation based on the interrogation size and the moving average method, the vectors are made to be consistent with adjacent ones compulsorily. Thus, some accuracy will be smoothed out in the case of a big velocity gradient existing between two adjacent measuring points.

In order to enhance the comparison of the unsteady phenomena from the impeller-diffuser interaction, in the present work the internal flow field in a low specific speed radial diffuser pump has been analyzed numerically by CFD simulation with the help of CFX-10. Two-dimensional LDV measurements are also conducted to validate the numerical results.

2 Numerical and Experiemtal Setups

2.1 Pump geometry

The pump stage under investigation is a low specific speed (n_q=22.6) radial diffuser pump, consisting of an impeller, a vaned diffuser and a vaned return channel. The impeller is shrouded with six strongly backswept blades. Both the diffuser and the return channel have nine vanes. All the blades are designed in two dimensions with constant thickness of 4 mm. The whole pump is manufactured completely with plexi-glass to provide optical access for LDV measurements. Figure 1 shows the 3D model of the pump, with the shroud removed for better view. The geometric data and the design operating point of the pump stage are summarized in Table 1.

Table 1 Geometric data and operating point

Impeller		
number of blades	Z_i	6
inlet radius	R_1	40 mm
outlet radius	R_2	75.25 mm
inlet blade angle	β_1	17.9 deg
outlet blade angle	β_2	22.5 deg
Diffuser		
number of blades	Z_d	9
inlet radius	R_3	77.5 mm
outlet radius	R_4	95 mm
inlet blade angle	α_3	9 deg
outlet blade angle	α_4	17.9 deg
Design operating point		
volume flow rate	Q_{des}	0.0045 m^3/s
rotating speed	n_{des}	1450 rpm
delivery head	H_{des}	7 m

Fig. 1 3D model of the pump

2.2 Numerical simulation setup

Three-dimensional, unsteady Reynolds-averaged Navier-Stokes equations are solved by the CFD code CFX-10. The structured grid for the computational domains is generated by using the commercial software ICEM-CFD 10. The impeller side chambers are also included in the grid to take leakage flow effects into account. The turbulence is simulated by the $k-\omega$ based shear stress transport turbulence model (Menter, 1994). The interface between the impeller and the diffuser is set to "transient rotor-stator", in which the relative position between the rotor and the stator is updated each time step. More details about the computational grid and boundary conditions can be taken from our previous work (Feng et al., 2007).

2.3 LDV Measurements

2.3.1 LDV test stand

Figure 2 presents the test stand for the LDV measurements. The pump is driven by a motor with a maximum power of 45 kW. A water tank is used to feed the water into the pump and also to recollect the water out of the pump. An electromagnetic flow meter is installed on the pipe behind the pump to measure the volume flow rate. In the LDV measurement, the light source is an Argon-Ion laser with a maximum power of 5W operating in multiline mode. The multicolor beam separator is utilized to obtain the green (514.5 nm) and blue (488 nm) beams. An optical probe with a 500 mm focusing lens is used to derive a two-pair beam configuration. The optical probe with the lens is mounted on a two-axis traversing system in order to place the probe volume at the location of interest. The measuring region shown in Fig. 3 covers a part of the impeller, starting from $r/R2=0.757$ due to the design

limitations of the pump test stand, and a full diffuser channel. All the measurements are conducted at midspan. There are 168 points measured in the impeller region, distributed on seven radii and 21 circumferential positions which cover a whole diffuser pitch (40 deg). In the diffuser region, 217 points are measured, which can give a good resolution of the flow field in one diffuser channel. To relate the velocity measurement to the angular position of the impeller, an optical encoder fixed on the pump shaft is utilized to synchronize the measurement with the impeller position. For each measuring point in the impeller, 100,000 sets of data are acquired, and 50000 sets of data are collected for each measuring point in the diffuser.

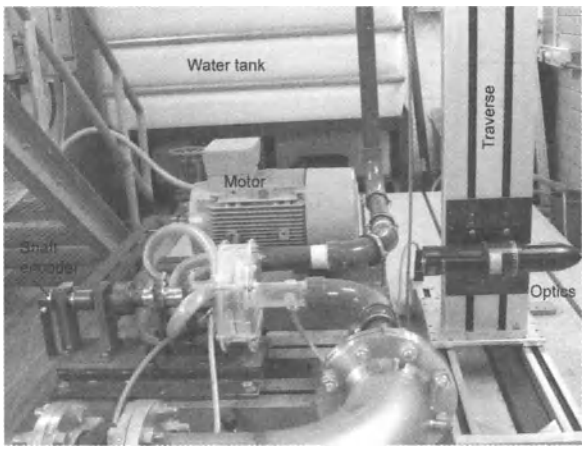

Fig. 2 LDV test stand

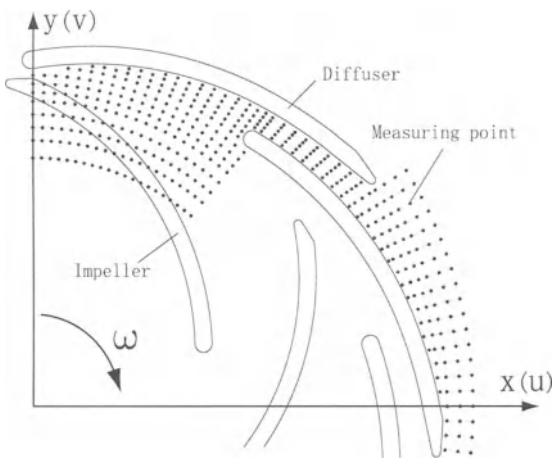

Fig. 3 Measuring region for LDV

2.3.2 Data postprocessing

In the LDV measurements, each of the measured velocity components (u and v) in two orthogonal directions (x and y) can be decomposed into two parts: a phase-averaged component ($\overline{u}$ and $\overline{v}$) depending on the measuring point position and the impeller circumferential position, and a fluctuating component (u' and v') representing the turbulence effects, as denoted in Eqs. (1) and (2). A good estimation of the phase averaged absolute velocity at a certain impeller position can therefore be obtained by Eqs. (3) and (4). The turbulence intensity Tu is calculated in Eq. (5) based on the turbulent components and normalized by the impeller tip speed U_2 ,

$$u_i(x,y,\varphi)=\overline{u}(x,y,\varphi)+u_i'(x,y,\varphi) \qquad i=1,\cdots,N \tag{1}$$

$$v_i(x,y,\varphi)=\overline{v}(x,y,\varphi)+v_i'(x,y,\varphi) \qquad i=1,\cdots,N \tag{2}$$

$$\overline{u}(x,y,\varphi)=\frac{1}{N}\sum_{i=1}^{N}u_i(x,y,\varphi) \tag{3}$$

$$\overline{v}(x,y,\varphi)=\frac{1}{N}\sum_{i=1}^{N}v_i(x,y,\varphi) \tag{4}$$

$$Tu(x,y,\varphi)=\frac{\sqrt{\frac{3}{2}\frac{1}{N}\sum_{i=1}^{N}\left[\frac{1}{2}u_i'^2(x,y,\varphi)+\frac{1}{2}v_i'^2(x,y,\varphi)\right]}}{U_2} \tag{5}$$

where N is the number of measurement signals during a certain bin width; φ is the impeller circumferential position to which a certain bin is corresponding. The factor 3/2 in Eq. (5) is compensating for the fact that only two components are available in the LDV data.

3 Results

All results presented in this paper are limited to the half blade height and the design operating point of the pump stage.

Figure 4 shows relative velocity contours obtained by CFD at one impeller position. The impeller rotation sense is clockwise. The shown impeller position is defined to the zero position ($\varphi=0$ deg) to the pre-defined diffuser vane, and all other impeller positions are based on it. A positive incidence is found at the impeller leading edge, producing a local region near to the suction side with relatively high relative velocity. The adverse pressure gradients decelerate the flow from the leading edge to the trailing edge on the suction side. It is also observed that the relative velocity near the suction side is bigger than near the pressure side in the front impeller part. However, this phenomenon is reversed in the impeller rear part due to the fact that the Coriolis force accumulates strength in large radiuses and drives the fluid from the suction side to the pressure side. Near the impeller outlet, a wake region characterized by low relative velocity is found on the impeller suction side near the trailing edge, and a local region with relatively high velocity on the corresponding pressure side. This kind of flow non-uniformity near the

impeller outlet is the so-called jet-wake structure, which has been reported by Wuibaut et al. (2002). Concerning the flow in the diffuser region, the stagnation point is found at the diffuser leading edge deviating slightly from the expected one to the suction side, causing a negative incidence, which suggests that the flow out of the impeller to the diffuser is in the over flow range for this impeller position. In addition, a small wake region with low velocity is also found behind the diffuser vane trailing edge.

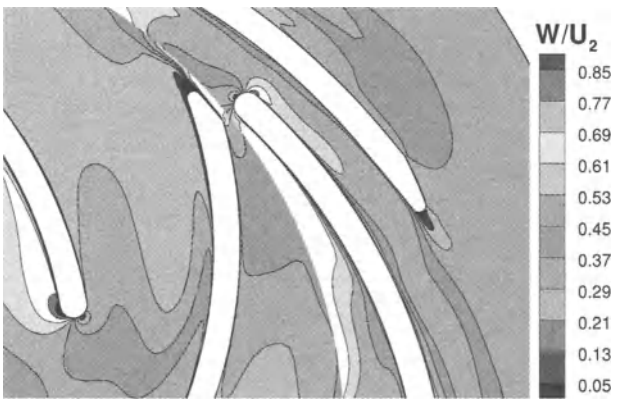

Fig. 4 Relative velocity contours at the impeller position $\varphi = 0$ deg, obtained by CFD

The flow in the radial gap region between the impeller and the diffuser is the most interesting since the unsteady phenomena occurring there are the strongest both for the pressure and velocity fields caused by the impeller-diffuser interactions. In order to investigate the strong unsteady flow in the gap region, 21 measuring points at the radius r/R_2=1.01 covering a whole diffuser pitch with a circumferential position difference of 2 deg between two adjacent points have been placed in the LDV measurements.

Figure 5 presents the distributions of the relative flow angle, defined in Eq. (6), obtained by both LDV and CFD calculation.

$$\beta = \arctan\left(\frac{C_r}{U - C_u}\right) \tag{6}$$

For clarity, the circumferential positions of the impeller blades and diffuser vanes are marked at the top and bottom of the figure, respectively. It is obvious that the relative flow angle β experiences a very strong variation depending on both the circumferential positions of the impeller trailing edges and diffuser vane leading edges, and the peak-to-peak difference is around 40 deg for the CFD result and even 50 deg for the LDV result. Similar distributions of β between CFD and LDV results are observed at the shown impeller positions. The flow angle β attains a local minimum in the vicinity of each diffuser leading edge where negative radial velocity C_r is registered. A big change in the relative flow angle can be found in the area faced by the impeller trailing edge from the pressure side to the suction side where β decreases firstly from pressure side to a valley then increases to a peak near the suction side. It can also be observed that the relative flow angle β tends to increase in the impeller wake region, it decreases when the wake impinges the diffuser leading edge and it increases again after the impingement. This phenomenon has also been observed by Yu and Lakshminarayana (1995) in an axial turbine through a two-dimensional unsteady simulation.

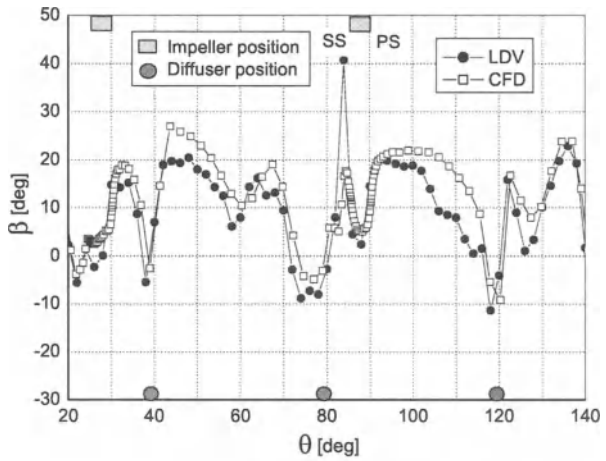

(a) $\varphi = -10$ deg

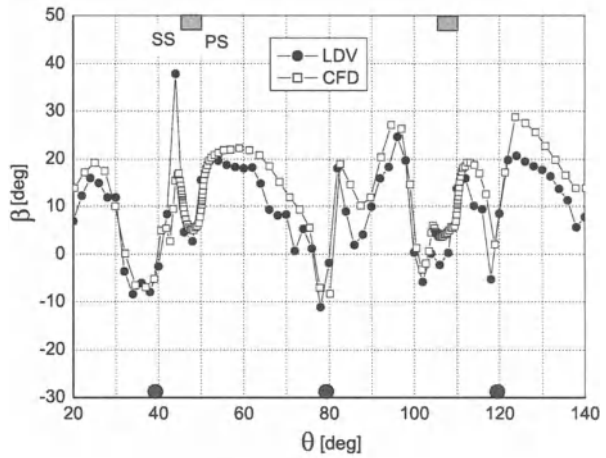

(b) $\varphi = 10$ deg

Fig. 5 Relative flow angle distributions near the impeller outlet, r/R_2 = 1.01

The absolute flow angle ($\alpha = \arctan(C_r/C_u)$) distributions are compared near the impeller outlet in Fig. 6 between CFD and LDV. Obviously, the comparisons for all shown impeller phases show very satisfying agreements between the two types of results. For both results, a local

maximum can be observed near the impeller pressure side, and the highest value is as high as around 30 deg, which is much higher than the blade angle of the diffuser vane ($\alpha_3 = 9$ deg). Near each diffuser leading edge, α holds a local minimum with negative value of around -5 deg, which is caused by the local backflow there. Since the flow out of the impeller acts as flow sources to the diffuser downstream, it is very clear that the impeller rotation provides different inlet flow conditions in the circumferential direction for the downstream diffuser. This non-uniformity of the flow creates or increases the unsteadiness of the flow in the diffuser region.

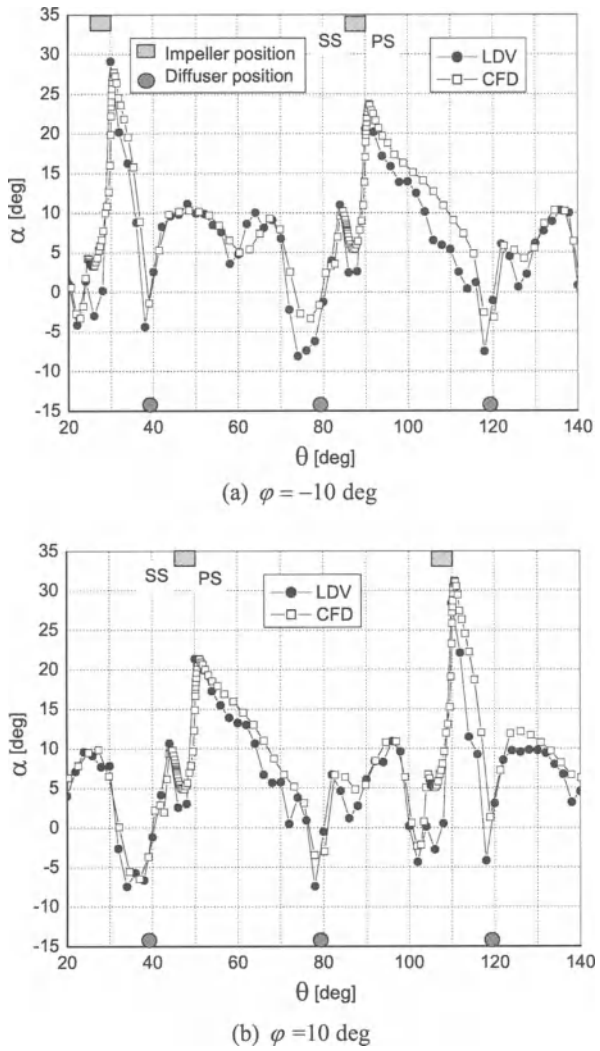

Fig. 6 Absolute flow angle distributions near the impeller outlet, r/R_2=1.01

The comparison of the turbulence intensity is illustrated in Fig.7 for the above mentioned two impeller positions. One can observe that the turbulence level predicted by LDV measurements is higher than that by CFD calculations in the whole range for all shown impeller positions. The highest turbulence intensity *Tu* in CFD results is about 6% (based on the impeller tip speed) occurring in the impeller wake region, which is about 2% smaller than that by LDV. Both LDV and CFD give comparable turbulence trends although some discrepancies exist: *Tu* decreases generally from the suction side to the pressure side.

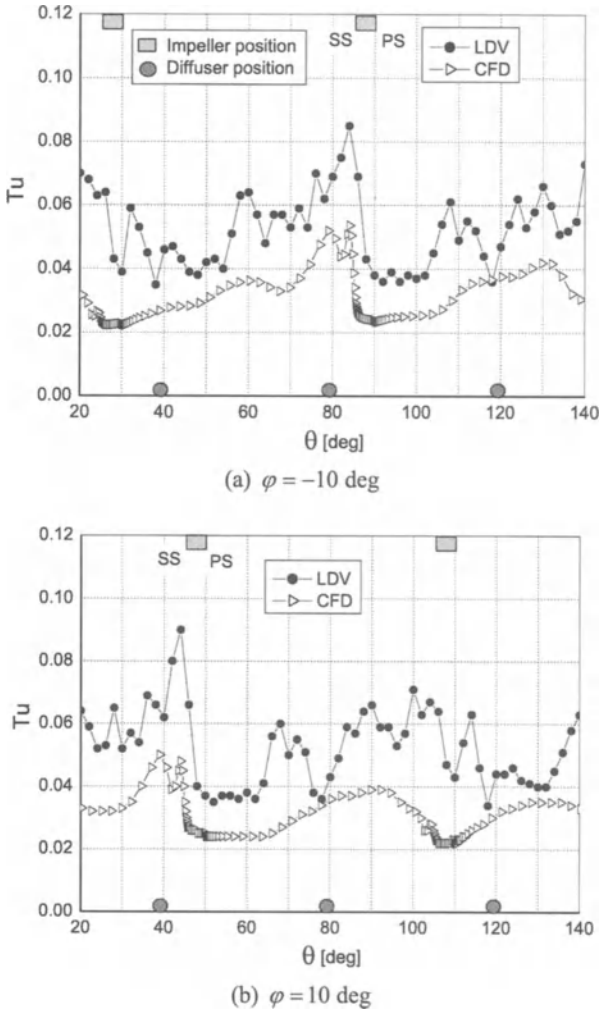

Fig. 7 Turbulence intensity distributions near the impeller outlet, r/R_2 = 1.01

Figure 8(a) shows the absolute flow angle distributions near the diffuser vane outlet for three impeller positions. It can be observed that the impeller position has only a limited effect on the flow angle distribution since α seems to be only dependent on the circumferential position of the diffuser vane. This is due to the fact that the stator unsteadiness is very small after the diffuser outlet. In addition, α reaches a local minimum in the region where the trailing edge is faced, located circumferentially in the middle of the trailing edge. Furthermore, the turbulence intensity near the diffuser outlet is also plotted in Fig. 8(b).

Tu is also hardly influenced by the impeller rotation. The highest *Tu*, around 7% based on the impeller tip speed U_2, is located near the suction side of the diffuser vane, caused by the high turbulence in the wake of the diffuser vane, and the lowest value is still higher than 3%.

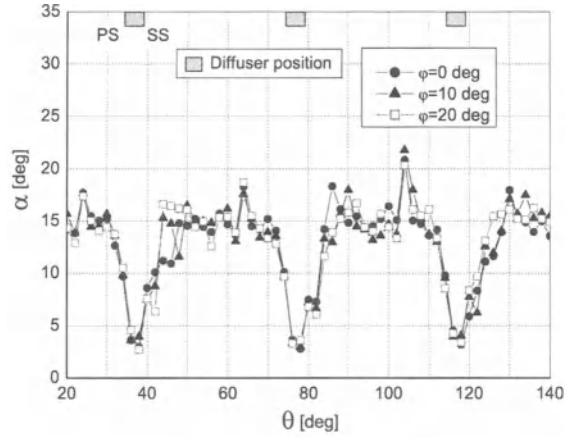

(a) Absolute flow angle

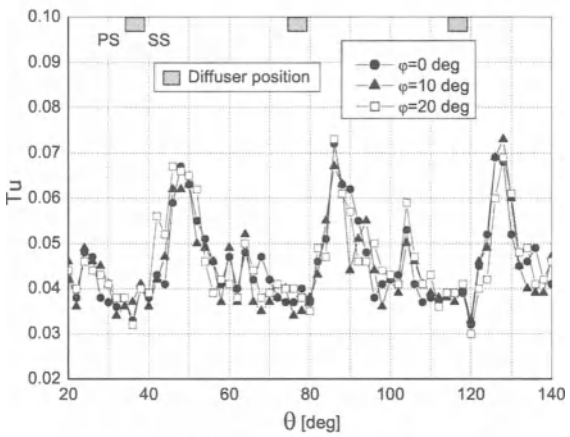

(b) Turbulence intensity

Fig. 8 Flow angle and turbulence distributions near the diffuser outlet, $r/R_4 = 1.01$, obtained from LDV

4 Conclusions

In this paper, the unsteady flow field in a low specific speed radial diffuser pump has been investigated in detail both numerically by CFD calculation with the CFD code CFX-10 and experimentally by LDV measurements. The following conclusions could be drawn:

(1) CFD predicts the same phase-averaged velocity fields with LDV even for each velocity component. However, the turbulence predicted by LDV is evidently higher than predicted by CFD, but show the same trends.

(2) The impeller rotation provides different inlet velocity profiles for the downstream diffuser, which is the source of the unsteady interactions.

(3) A jet-wake flow structure is observed near the impeller outlet, which is characterized by high relative velocity on the pressure side and low relative velocity on the suction side.

(4) The relative flow angle tends to increase in the impeller wake region, it decreases when the wake impinges the diffuser leading edge and it increases again after the impingement.

(5) The effects from the impeller rotation to the diffuser flow field become very small after the diffuser outlet.

References

Akin, O. and Rockwell, D., 1994, "Flow Structure in a Radial Flow Pumping System Using High-Image-Density Particle Image Velocimetry", *Journal of Fluids Engineering*, Vol.116, pp. 538 – 554

Ardizzon, G. and Pavesi, G., 2004, "Analysis of Unsteady Flow in a Vaned Diffuser Radial Flow Pump", *10th International Symposium on Transport Phenomena and Dynamics of Rotating Machinery*, Honolulu, Hawaii, March 07-11

Arndt, N., Acosta, A.J., Brennen, C.E., and Caughey, T.K., 1990, "Experimental Investigation of Rotor-Stator Interaction in a Centrifugal Pump with Several Vaned Diffusers", *Journal of Turbomachinery*, Vol. 112, pp. 98 – 108

Benra F.-K. and Dohmen. H. J., "Numerical Investigation of the Transient Flow in a Centrifugal Pump Stage", *2005 ASME Fluids Engineering Division Summer Meeting and Exhibition*, Houston, TX, USA, June 19 – 23

Bert, P.F., Combes, J.F. and Kueny. J.L., 1996, "Unsteady Flow Calculation in a Centrifugal Pump Using a Finite Element Method", *XVIII IAHR Symposium on Hydraulic Machinery and Cavitation*, Valencia, Spain, September 16-19

Feng, J., Benra F.-K. and Dohmen. H. J., 2007, "Numerical Investigation on Pressure Fluctuations for Different Configurations of Vaned Diffuser Pumps", *International Journal of Rotating Machinery*, Vol.2007, pp. 1 – 10

He, L. and Sato, K., 2001, "Numerical Solution of Incompressible Unsteady Flows in Turbomachinery", *Journal of Fluids Engineering*, Vol. 123, pp. 680 – 685

Menter, F. R.. 1994, "Two-equation Eddy-viscosity Turbulence Models for Engineering Applications", *AIAA-Journal*, Vol. 32, pp. 269 – 289

Sinha, M. and Katz, J., 2000, "Quantitative Visualization of the Flow in a Centrifugal Pump with Diffuser Vanes. Part I: On flow structures and turbulence", *Journal of Fluids Engineering*, Vol. 122, pp. 97 – 107

Wuibaut, G., Bois, G., Dupont, P., and Caignaert, G., 2002, "Rotor Stator Interactions in a Vaned Diffuser of a Radial Flow Pump for Different Flow Rates Using PIV Measurement Technique", *9th International Symposium on Transport Phenomena and Dynamics of Rotating Machinery*, Hawaii, USA, September 9 – 12

W.S. Yu and B. Lakshminarayana. 1995, Numerical simulaiton of the effects of rotor-stator spacing and wake/blade count ratio on turbomachinery unsteady flows. *Journal of Fluids Engineering*, Vol.117, pp. 639 – 646

The 4th International Symposium on Fluid Machinery and Fluid Engineering
November 24-27, 2008, Beijing, China
NO. 4ISFMFE-Ch07

Design and Research of Vertical Multistage Barrel Condensate Pump

Jiegang Mu*, Shuihua Zheng, Hongying Deng and Shengchang Zhang

* Institute of Process Equipment and Control Engineering, The MOE Key Laboratory of Mechanical Manufacture and Automation, Zhejiang University of Technology, Hangzhou 310032, China
Tel: +86-571-88871053 / Fax: +86-571-88871053
E-mail: mjg1964@zjut.edu.cn

Abstract Vertical multistage barrel condensate pump is important equipment applied in the wide range of industry. However, the pump performances such as efficiency, net positive suction (NPSH) and reliability are not so good and could not meet the use requirements. In this paper, based on investigations of the traditional vertical multistage barrel condensate pump, some innovative design methods were proposed, which had the following main aspects: first stage wheel with an inducer praevia, the new design of hydraulic element, the innovative design of sets for seal and equilibrium of axial forces, the numerical analysis and optimum design. The experiment results show that the new designs could improve performances of the pump and meet the use requirements. The research achievement won the second prize for Science and Technology Award of Zhejiang Province.

Keywords condensate pump, vertical multistage, NPSH, reliability

1 Introduction

Vertical multistage barrel condensate pump is an important type of pumps applied in the wide range of industry, such as petroleum, petrochemical, electric power, metallurgy, cryogenic engineering, off-shore platform and so on. The products are used mainly in transfer liquid in process system and closed vessel with higher-vacuum.

Considering the liquid in lower-vacuum or critical saturation state, vertical multistage barrel condensate pump must be provided with high net positive suction to meet the use requirements [1]. Up till now, in view of its high NPSH, poor efficiency, bad reliability, short service life and high expenses of manufacture installation and maintenance, the vertical multistage barrel condensate pump made in China could not satisfy the application demands. Neither could the import products for the lower NPSH [2].

With the national policy of energy-saving and environment-protecting established, in order to meet the demands for the performance improvement of pump and the process, it's a feasible proposal to heighten the $NPSH_a$ (net positive suction head available for pump). However, in this way, the height of vertical multistage barrel condensate pump and its installation cost would increase, and the reliability and service life would be declined. The manufacture would become more complicated, also.

Presently, the import vertical multistage barrel condensate pumps are adopted widely in domestic key items. However, the price of import pumps is almost ten times more than domestic products with the same performance parameters. Therefore, it is worth for the research and design of vertical multistage barrel condensate pump.

2 Technical Analysis

The researches and investigations are carried out by many institutes and manufacturing companies at home and abroad. Also, the finished products are adopted. The most typical manufacturer abroad is Company profile Sulzer, with the representative products TTMC vertical multistage barrel condensate pump. In China, Shenyang pump

manufacturing company limited is the most typical manufacturer. LDTN series of vertical multistage barrel condensate pump are popular in domestic pump market. Whereas, vertical multistage barrel condensate pumps made at home and abroad could not meet the use requirements and there are a few defects as following.

2.1 Unsatisfactory NPSH

NPSH is one of the key technical indexes of condensate pump. Traditionally, an inducer praevia first stage blade and first stage double-suction wheel are adopted to decrease the value of NPSH [3]. The NPSH of condensate pump ranges form 1m to 2m commonly. As the technical requirements enhanced, NPSH should be lower than 1m in certain condition such as supercritical generating set in power plant and large fertilizer production set.

Recently years, there haven't been new products schemed out in China, and the present vertical multistage barrel condensate pumps could not meet the use requirements due to bad NPSH. Neither could the import products in despite of better NPSH [4,5]. There is no alternative but to lengthen the barrel of condensate pump. As a result, the expenses used in manufacturing would go up, and the running condition would become unreliable.

2.2 Low efficiency

Nowadays, in China, the similarity transition algorithm is still adopted in the design of hydraulic element. Experiences and tests play an important role in the process of design [6]. The advance computer technique hasn't been integrated with the design method. As a result, the inaccurate design results in the low efficiency, which could not live up to the application needs [7,8]. The efficiency index of domestic condensate pumps is 5%~8% lower than that of import products averagely.

2.3 Poor reliability and short service life

As for the running reliability and service life, the import condensate pumps are superior to the domestic obviously. Based on the quality failure analysis of domestic products, the factors leading to poor reliability and short service life are showed as following:

(1) The cavitation comes into being, which results in performance declining, vibration and noise.
(2) Half balance of axial force of condensate pump makes the bearing to run under high load.
(3) Owing to the poor sealing effect, seal must be often replaced.
(4) Quality failure often takes place in the guide bearing, so regular maintenance should be carried out.
(5) There is no quality guarantee in the process of parts manufacturing and unit assembly.

3 Prototype Design

Based on the running technical analysis of the vertical multistage barrel condensate pump, considered the use requirements, the prototype was researched and designed. The performance parameters for the prototype were as follows: $Q = 125m^3/h$, $H = 125m$, $N = 1480r/min$, $\eta = 75\%$, NPSHr=0.85m.The innovative design focused mainly on the improvement of NPSH, efficiency and reliability. The design contains the following aspects.

3.1 Structure design of prototype

In order to meet the requirements of cavitation and hydraulic performances, further researches and tests on the overall structure were developed and a few available methods were summarized.

Firstly, we enlarge the inlet area. The value of NPSH is directly proportional with the inlet velocity of wheel. Single-inlet wheel is taken as the first stage wheel to reduce the inlet velocity. That is to say, with the same flux, the inlet area would be enlarged by two times. The inlet velocity would be decreased half. And the velocity squared value would be reduced to a quarter.

Secondly, to adopt optimal design of inlet parts, including to enlarger the inlet area, to extend and thin the inlet edge of impeller blade reasonably, to adopt the contorted blade and the positive attack angle.

What's more, to install an inducer praevia in the front of the inlet wheel could enhance the cavitation performance. The cavitation induced by centrifugal force and liquid separation would be removed by the inducer. The primary vapor cell would be taken along with the liquid and would not bring on the channel jam.

There are two structure types of inducer: one is space inducer, and the other is radial inducer. The former is adopted in domestic condensate pumps, and both are used in import products. In the same operation condition, the two structure types were compared with each other. The test result showed that the hydraulic performance of radial inducer was superior to that of space inducer. Therefore, radial inducer was adopted in the structure design of prototype to shorten the radial length and to improve the hydraulic performance.

The structure of prototype was vertical multistage. The center lines of inlet flange and outlet flange should be in

the same surface, which could make installation easy. And the inlet and outlet flanges were put up the unit flange. The angle between the two surfaces would be 90°, 180°, and 270°. The combination of a pair of thrust ball bearing and two pairs of slide bearing was applied as the bearing parts. Axial force was balanced by the balancing drum and thrust ball bearing. Mechanical seal was adopted, and elastically pin coupling was taken as transmission gear.

3.2 Optimal design of hydraulic elements

Traditional methods to design the hydraulic elements are similarity transition algorithm and velocity coefficient algorithm, combined with field test, which has low technical level, high expenses, long production cycle and poor efficiency. In this paper, advanced CFX-BladecGen was adopted to analyze the hydraulic element of prototype. Numerical simulation to the inside flow state on the operation condition was carried out. Pressure distribution profile, velocity distribution profile and vapor phase distribution profile of the hydraulic element at different flux were got. According to the analysis, the principle of inside flow state of hydraulic element could be educed.

Based on the analysis of numerical simulation results, by means of changing the value of geometric parameters, internal connecting link between the hydraulic performance and geometric parameters could be concluded and hydraulic and cavitation performance of pump would be doped out. In allusion to different proposals, the optimal design of hydraulic elements could be waged integrated with the traditional design method. Finally, the optimum scheme would be found out.

3.3 Design of axial force balancing device

To prevent rotator from axial jumping, axial force was balanced by the balancing drum and thrust ball bearing. The balancing drum played an important role, and the rudimental axial force was balanced by the thrust ball bearing. However, because the internal flow state of hydraulic element hasn't been mastered yet, so the design method of balancing drum is not perfect. Therefore, large deviation exists in the process of design. The thrust ball bearing must endure more load, which often brings on faults. In this design, a valve was set in the backwater line, which was used to control the pressure difference between forward and backward of the drum cavity. The balancing force would be adjustable, and the load of the ball bearing would be reduced effectively, which would extend service life of the ball bearing.

3.4 Design of sealing device

Mechanical sealing device was used as shaft seal. The sealing efficiency is related to the pressure in the sealing cavity. The higher pressure is, the more difficult it is to seal. In this project, a sealing backwater pipeline with a control valve was added between the inlet of pump and seal cavity. The functions of this structure are shown as follows: firstly, to reduce the pressure in cavity; secondly, to keep the pressure in the seal cavity higher than the atmosphere and to avoid cavitation; thirdly, to wash the inclusions out of the seal cavity and to take the heat away. The innovation structure could improve the reliability of mechanical sealing, and lengthen its service life.

4 Contrastive Analysis on the Running Results

The prototype of 200LDNT125×5 vertical multistage barrel condensate pump was examined by China National Center for Quality Supervision and Test of Pump, and also was tested in site. The results were satisfied. The performance indexes reached to the standards (shown in Table 1) and could meet the use requirements. Also the research results had got the Award for Science and Technology of Zhejiang Province.

Table 1 The performance index contrast among homogeneous condensate pumps

Pump type	Flux (m^3/h)	Pump lift (m)	Rotational speed (r/min)	Efficiency (%)	NPSH (m)
200LDTN 125×5, Prototype	125	125	1480	75	0.75
TTMC-125, Advanced Import products	125	125	1475	69	1.8
5LDTN-7, Advanced domestic products	120	122	1480	74	2.5

5 Conclusions

According to the research and design of vertical multistage barrel condensate pump, the following conclusions could be obtained.

(1) The structure of first stage single-inlet wheel and an inducer praevia could improve cavitation performance and meet the requirements of condensate pumps.

(2) Numerical simulation, analysis computation and optimal design by virtue of CFX-BladecGen technique could enhance the hydraulic performance and the NPSH index.

(3) In the balancing device, the valve in the backwater pipeline could control the pressure difference between the forward and backward cavity of the balancing drum, and adjust the balance force.

(4) In the sealing device, the backwater pipeline with a controlling valve between the inlet and the sealing cavity could improve the sealing efficiency and lengthen service life of mechanical seal.

References

Pump Institute in Shenyang, 2004, "Vane pump design handbook", *Mechanical industry publisher*, Beijing

Daochun Wu, Jianhua Zheng, 2006, "Modification design and experimental investigation of condensate pump"[J], *Pump technology*, 1: 46 – 48

Yanrui Wang, 2007, "Design and manufacturing of condensate pump in 600MW supercritical unit"[J], *Pump technology*, 5: 6 – 8

Mengqiang Xie, 2006, "Cavitation performance of condensate pump"[J], *Pump technology,* 5: 32 – 34

Hongyu Sun, Dehui Li, Mingchun Li, and so on, 2003, "The application of vertical barrel condensate pump in ethylene unloading mechanism at low temperature" [J], *Equipment & Apparatus*, 2: 52 – 55

Shouqi Yuan, 2001, "Design theory of vane pump with low specific speed" [J], *Mechanical industry publisher*, Beijing

Chunlin Hao, Jielian Zhou, Ying Zhou, 2006, "Optimal design of condensate pump in 600MW unit" [J], *Pump technology*, 5: 44 – 47

Jianhua Zheng, 1996, "Test and research on improvement of efficiency and cavitation performance" [J], *Pump technology*, 3: 15 – 18

The 4th International Symposium on Fluid Machinery and Fluid Engineering
November 24-27, 2008, Beijing, China
NO. 4ISFMFE-Ch12

Influence of Support Shapes on the Efficiency of Bulb Tubular Pumps

Yan Jin*[1], Chao Liu[2], Fangping Tang[1]

*[1] College of Hydraulic Engineering, Yangzhou University,
131, Jiangyang Middle Road, Weiyang District, Yangzhou, Jiangsu 225009, China
Tel: +86-514-8797-9520 / Fax: +86-514-8797-9520
E-mail: sunshine20080208@163.com

[2] Yangzhou University, 88 South University Ave. Yangzhou, Jiangsu 225009, China

Abstract With the characteristics of high efficiency, small hydraulic loss, compact unit structure, simple construction arrangement and low cost both for construction and operation, bulb tubular pumps are especially suitable for large discharge and low lift head pumping stations of the east route of South to North Water Diversion Project in China. It is important to analyze the flow characteristics and performance of bulb tubular pumps.

The flow inside the flow-passage components is three-dimensional incompressible turbulence flow. Bulb support unit which including manhole and bottom support is an important flow-passage component of bulb tubular pumps. In this paper CFD method is used to simulate a bulb tubular pump with different support shapes. Based on the RNG k-ε turbulent model with Wall-Function Law, the SIMPLEC algorithm is applied for the solution of the discretizaton governing equations. The results of the calculation indicate that the shape of support has affected total hydraulic losses of the pump and it also obvious influence on flow pattern. Reasonable support shapes not only improve the turbulent flow, but also reduce circumference velocity.

Keywords bulb tubular pump, supporting shapes, hydraulic loss, numerical simulation

Nomenclature

g	gravity
H	lift head
p	pressure
Q	discharge
H_f	hydraulic loss
T_p	torque
η	efficiency
ρ	density of the fluid (water in this paper)
ω	rotating speed

1 Introduction

Bulb tubular pumps have small hydraulic loss and high pumping system efficiency, which especially suit to the low lift head, large discharge and long running time situation.

Since the 1970s, the Western countries began to study, design and manufacture tubular pumps which came into operation successively in some pumping stations. In China, the research on tubular pumps started since after mid-80s, several scientific research units such as Beijing Institute of Water Resources and Hydropower Research, Wuhan University, Yangzhou University and so on, which analyzed the tubular pumps by theory and experiments. However, the study on the internal characteristics of the whole pump installation is comparatively less and the accumulation experiences of bulb tubular pumps are limited.

In the east route of South to North Water Diversion Project, many pump stations choose bulb tubular pumps because of their characteristics. For searching the effects of flow passage on system performance, in this paper, a bulb tubular pump which includes inlet passage, outlet passage, guide vane and bulb unit is computed by CFD,

especially the influence of supporting shape. Thus provide reference for the pump structure design and pumping station renovation.

2 Model Pump System

The physical dimension of the model bulb tubular pump system which includes inlet passage, impeller, guide vane, bulb unit and outlet passage is shown in Fig. 1, and the bulb unit includes bulb and the support unit (one manhole and two bottom supports).

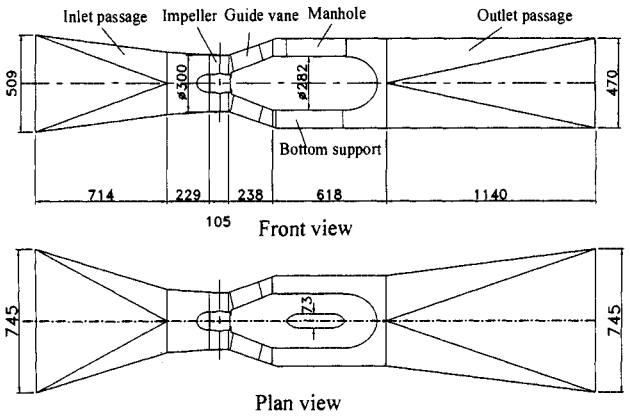

Fig. 1 Physical dimension of the model bulb tubular pump system

The main parameters of the model pump are presented in Table 1.

Table 1 Parameters of the model pump

Impeller diameter (m)	0.3
Rotate speed	1375
Discharge range (l/s)	280~360
Number of blades	3
Number of guide vane blades	5

3 Computational Method

Flow in tubular pumps produces a complex three-dimensional phenomenon involving turbulence, secondary flows, unsteadiness, etc. In this paper, calculations have been performed with a commercial software package, FLUENT. This code uses the finite volume method and the 3D Navier-Stokes equations are solved on an unstructured grid.

Figure 2 shows the three dimensional view of the computational model, the components inside the pump system can be seen clearly.

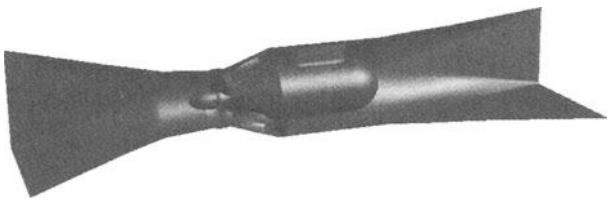

Fig. 2 Three dimensional view of the computational model

3.1 Mathematical model

Turbulence is simulated with the RNG $k-\varepsilon$ model. Reynolds time-averaged control equations are applied. The SIMPLEC algorithm is applied for the solution of the discretizaton governing equations.

3.2 Boundary conditions

Inlet condition

A pump sump is added in front of the inlet conduit which can guarantee the flow pattern of the conduit inlet. The inlet boundary condition is specified by mass-flow-inlet.

Outlet condition

An outlet sump is added after the outlet conduit, and the outlet is that the outlet of the outlet sump. The outlet one is set to outflow condition.

Wall condition

No slip boundary conditions and wall functions are used for the solid walls.

In order to calculating the flow of whole bulb tubular pump, the rotor-stator must be ideally simulated. In common, the method of multiple reference frames (MRF) is applied for numerical simulation. The flow in blade is considered steady relative to moving reference system that rotates at the speed 1375 rpm. Fluid in other domains are computed in a fixed reference system.

Grid generation

In this paper, unstructured cells are used to define the inlet zone, impeller, guide vane, and outlet zone (97609 cells, 194312 cells, 382520 cells and 217220 cells, respectively) because of the geometric structure of the entire system more complicated, a view of the generated grid can be seen in Fig. 3.

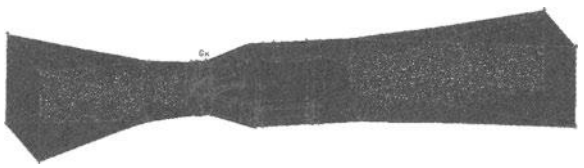

Fig. 3 Sketch of the pump unstructured mesh

4 Comparision of Different Schemes

Bulb support unit including manhole and bottom support is an important flow-passage component of bulb tubular pumps. There are three schemes (shown in Fig. 4) adopted in this paper. The support unit in first scheme includes one manhole and two bottom support. The second scheme merged two bottom supports into one and widened the size to the width of the manhole. In the third scheme, the supports from top to bottom changed into streamline pattern and symmetry (Note: Figure in size unit mm).

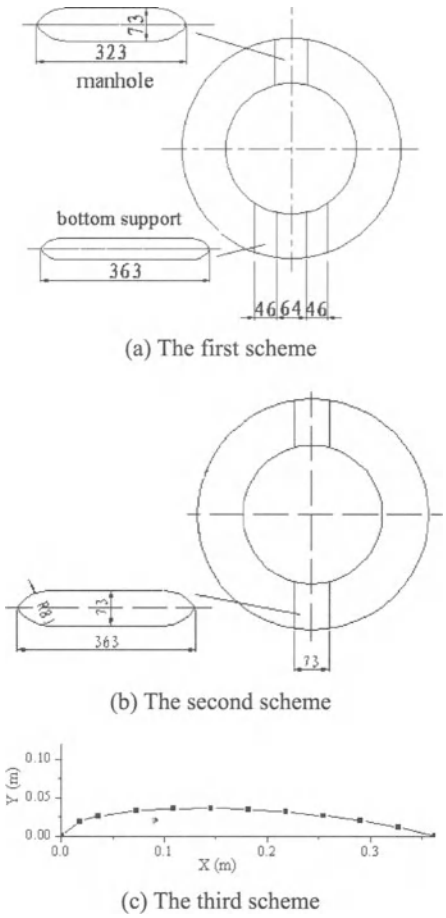

Fig. 4 Support shapes of each scheme

5 Results and Discussion

Three different axial velocity contour maps of each scheme are compared in Fig. 5. The supports in scheme includes one manhole and two bottom supports (shown in Fig. 4(a)), and the distance between the two bottom supports is 64 mm, When the water flow through this region, the flow rate will increase rapidly, axial velocity contour changes disorder because of the components of bulb and supports, at the tail of the support, there exists a low-speed zone (shown in Fig. 5(a)). Merging the two bottom supports into one in the second scheme eliminates the high-speed zone, although the flow pattern does not improve much, the hydraulic loss of the bulb part decreases and the efficiency of the pump system increases about 0.5% (shown in Fig.6 and Fig.8). The third scheme changes the

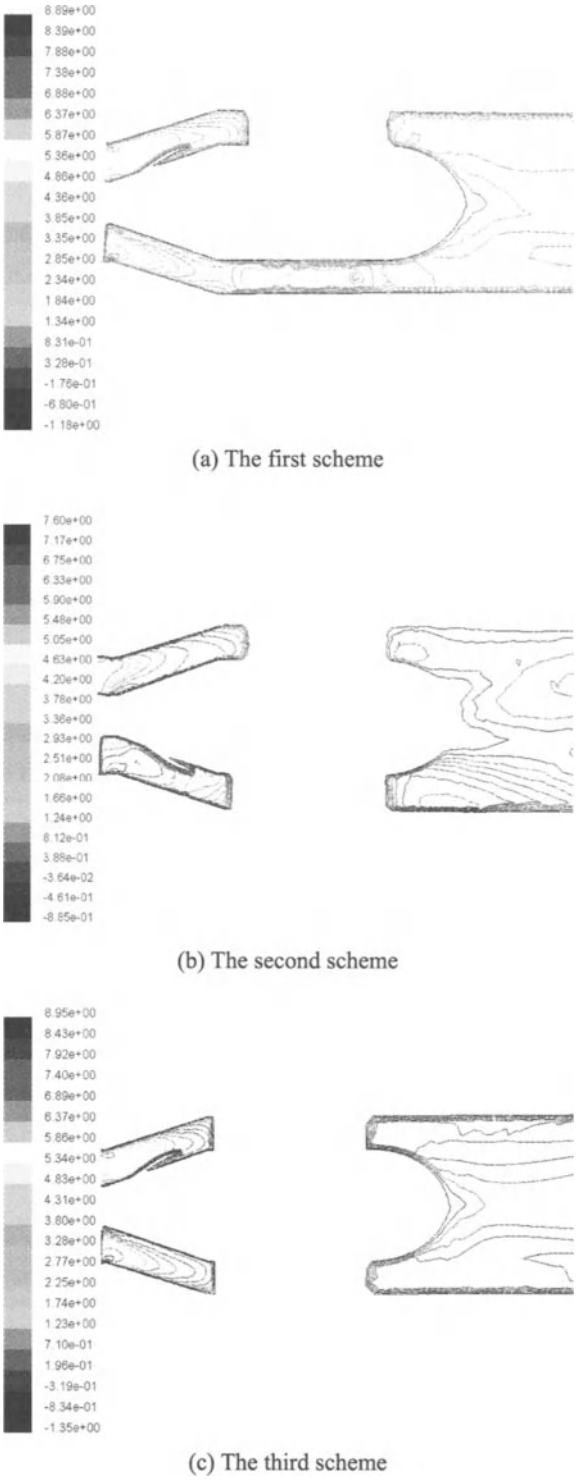

Fig. 5 Axial velocity contour map of bulb zone

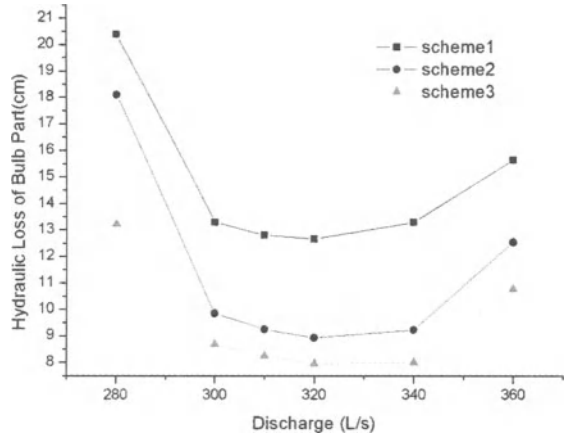

Fig. 6 Flow-hydraulic loss of bulb unit

shape of support into streamline pattern, which not only make the flow smoother than those of the first and the second scheme, but also improve the efficiency of the pump system (shown in Fig. 5(c) and Fig. 8).

The performance curves of bulb tubular pump are shown in Fig. 7 and Fig. 8. Compare with the Flow-Lift Curve, there is no great difference between the different schemes, concerning the efficiency is calculated with the torque values, discharge and lift head, thus written as:

$$\eta = \frac{\rho g Q H}{N_a} \tag{1}$$

Where

$$N_a = T_p \omega \tag{2}$$

$$H = \left(\frac{\int_{s2} p_2 u_t ds}{\rho Q g} + H_2 \right) - \left(\frac{\int_{s1} p_1 u_t ds}{\rho Q g} + H_1 + \frac{\int_{s1} u_1^2 u_t ds}{2Qg} \right) \tag{3}$$

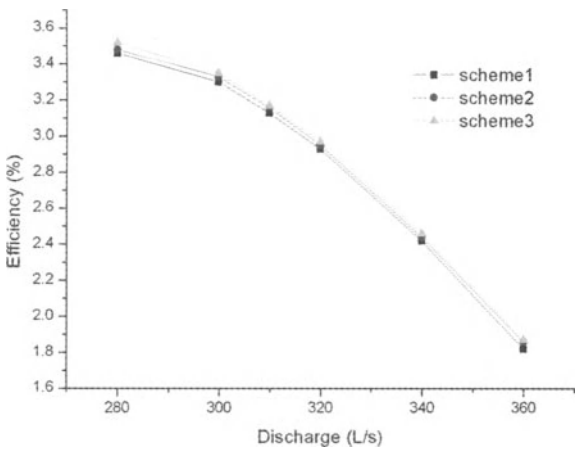

Fig. 7 Flow-lift head curve of pump system

Right side of the equation (3): the first item is the total energy of the outlet section, and the second item is the total energy of the inlet section.

Figure 8 shows the Q - η curve of the model pump system, the efficiency of second scheme and the third one are superior to the first one, which indicates that the support number is a factors affecting the hydraulic loss of the bulb unit. Resistance coefficient of the streamline supports in the third scheme is relatively small which can reduce the hydraulic loss separation flow. So the shape of the support also affects the efficiency of the pump system.

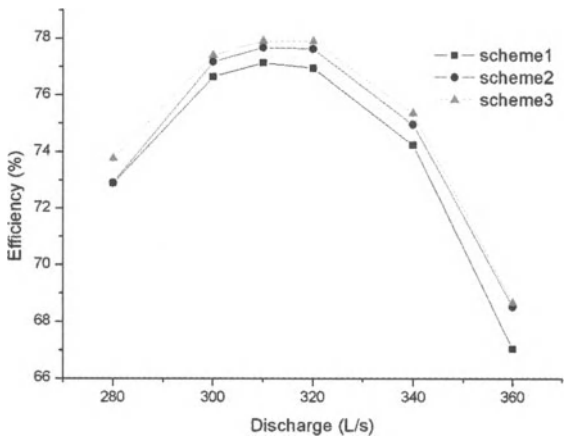

Fig. 8 Flow-efficiency curve of pump system

6 Conclusions

The performances of bulb tubular pump are obtained by numerical simulation, the calculation results show the following conclusions though comparing the different shapes of the bulb support unit which includes the manhole and the bottom supports.

(1) Bulb support Shapes have an impact on the flow pattern and hydraulic loss, reasonable support shapes not only improve the turbulent flow, but also reduce the circumference velocity.

(2) The number of the support is also an important parameter which affect on the flow, minimize the number of support when meet with the requirements of structural strength.

(3) Prediction of the bulb tubular pump system by numerical simulation is effective and feasible, which can meet with the needs of engineering.

Acknowledgements

This work was supported by the Science and Technology Department 11th Five-year Plan State science and

technology support projects (No. 2006BAB04A03－04), and the National Natural Science Foundation of China (No.50779060 and No.50379047).

References

B.E. Launder, D.B. Spalding. 1974, "the Numerical Computation of Turbulent Flows[M]. *Computer Methods in Applied Mechanics and Engineering*, Vol. 3, pp. 269 – 289

Liu Chao. 2003, "Hydraulic Performance Assess Target Research of Low-head Pump Equipment in South-North Water Transfer Project". *Drainage and Irrigation Machinery*, Vol. 21, pp. 2 – 5

Liu Chao, Tang Fangping, Zhou Jiren etc. 2003. "Analysis of Performance and Stability of Large Vertical, Axial-flow Pump Device". *China Water & Wastewater.* Vol. 19, pp. 69 – 71

Liu Jun, Huang Haitian, Liu Lijun.2004, "Select Use of Tubular Pumps in Jiangsu's First-stage of South-to North Water Project". *South-to-North Water Transfers and Water Science & Technology*, Vol. 2, pp.15 – 16

Luo Ting. 2006, "Analysis on the Flow Characteristics of Postpositional Bulb Tubular Pumps". M.D. Disseration, Yangzhou: Yangzhou University

Mo Weize, Yang Rongdi, Zhang Haiping. 2005, "Brief Introduction of the hydraulic model of postposition bulb tubular pump device". *Pump technology*, Vol. 5, pp. 10 – 11

Wang Zhengwei, Zhou Lingjiu, Cheng Yanguang etc.,2004. "Hydraulic Loss in Bulb Turbine". *Large Motor Technology*, Vol. 5, pp. 40 – 43

Wang Fujun. 2005. "Computational Fluid Dynamics Analysis", *Tsinghua University Pres, Beijing.s*

Tao Wenquan. 2002. "Numerical Heat Transfer(Second Edition)", *Xi'an Jiaotong University Press,* Xi'an.

Tang Fangping, Liu Chao, Zhou Jiren etc. 2004. "Tests on the device Model of Low Lift Bulb Tubular Pump". *Pump Technology*, Vol. 4, pp. 28 – 31

Zheng Yuan, Zhang Dehu, Liu Yimin etc.,2003. "Experimental Study on Equipment Energy Characteristic of Tubular Pump". *Fluid Machinery*, Vol. 31, pp. 1 – 4

Zhang Yongxue, Li Zhenlin. 2006., "Summarization on Numerical Simulation of Internal Flow in Fluid Machinery". *Fluid Machinery*. Vol. 34, pp. 34 – 38

The 4th International Symposium on Fluid Machinery and Fluid Engineering
November 24-27, 2008, Beijing, China
NO. 4ISFMFE-Ch27

Computing Critical Speeds for Multiple-stage Centrifugal Pumps with Dependent Support Properties

Chunxin Chen, Dazhuan Wu, Shanguang Tan and Leqin Wang*

* Chemical and Mechanical Research Institute, Zhejiang University,
Yuquan Campus, Hangzhou, Zhejiang 310027, China
Tel: +86-0571-8795-2406 / Fax: +86-0571-8795-2406
E-mail: hj_wlq2@zju.edu.cn

Abstract In a multiple-stage centrifugal pump rotor with 3000kW power, the influence of journal bearing stiffness under the critical speeds is studied, which shows great impact of bearing stiffness on critical speeds at certain extent. In the light of above, physical models of the bearings are founded up, taking into consideration the stiffness of oil film and the impact of rotor speed on the stiffness coefficient of bearings at the meanwhile. Since the thickness of oil film changes with rotor speed according to relevant laws, the stiffness of oil film is calculated in different conditions based on short bearings theory. In addition, a range of natural frequencies are calculated with the help of Ansys software, and the relevant campbell diagram are made as well, thus the critical speed of the rotor is obtained. It shows that when the rotor speed is not high, the stiffness of bearings has great impact on critical speeds of lower steps, while the influence on critical speeds of higher steps is not obvious.

Keywords journal bearing, critical speeds, stiffness coefficient, high pressure pumps

Nomenclature

c	damping coefficient
C	zero dimension damping coefficient
D	radius of the shaft
k	stiffness coefficient
kb	stiffness of the bearing system
k_p	stiffness coefficient of oil film
K	zero dimension stiffness coefficient
L	width of the bearing
Mb	equivalent mass of the bearing system
ε	factor of eccentricity
μ	dynamic damping coefficient of oil,
ω	the speed of the rotor
ϕ	clearance ratio ($\phi=c/r$).

1 Introduction

Centrifugal pumps are developed with larger capacity and higher head from now and then, and the one discussed in this paper has the head up to 3000m, and power up to 3000KW, which takes important task in transportation of high pressure liquid in large-scale power and coking plant. In the design of large rotating machinery, one of the most fundamental considerations is the set of values of the critical speeds relative to the intended operating speed range of the machine. However, with the machine developing into larger and higher speed groups, the factors which work on critical speeds of the rotor become more important than ever before, such as bearing stiffness.

Computationally, finding critical speeds is not straightforward, particularly for machines having journal bearings because the dynamic properties of these bearings are strongly dependent on rotor speed. Therefore, more precise models are required to analysis the rotor to ensure the stable movement of the machine for a long time. In order to make certain the impact of journal bearings on critical speeds of a rotor, this paper takes multiple-stage centrifugal pumps as analysis object, in which that bearing stiffness changes with rotor speed is discussed with the help of reduced anisotropic bearing model. Finally the critical

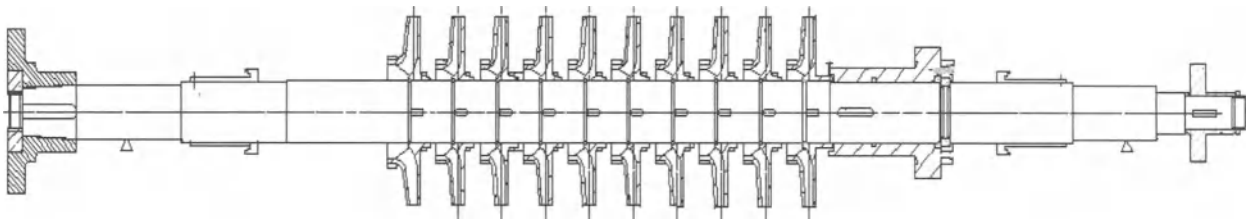

Fig. 1 Model of multi-stage centrifugal pump

speeds of the rotor are acquired from the Campbell diagram.

2 The In Fluence of Bearing Stiffness on Critical Speeds of Multiple—Stage Centrifugal Pump Rotor

The critical speeds of a rotor change with the bearing stiffness during operation, which is shown in Fig. 2. The first step of critical speed is almost unaffected from bearing stiffness, when the bearing stiffness is lower than 10^5 Hz. But when the bearing stiffness is greater than 10^5 Hz, the influence is remarkable, and moreover, we will arrive at the conclusion that the dividing point of which influences the second critical speed and not is around 2×10^6 Hz.

From what has been mentioned above, we can come to the conclusion that lower steps of critical speeds are more easily influenced by the bearing stiffness, while the higher steps not. However, once the higher steps are impacted, it will be more sensitive.

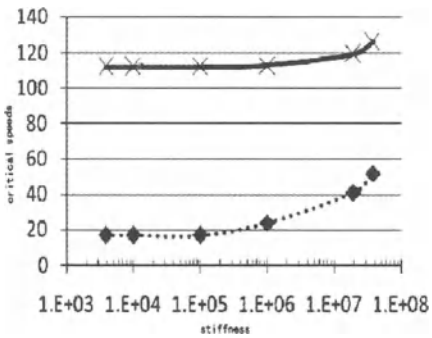

Fig. 2 The relationship between critical speeds and bearing stiffness (the first and second step)

3 Bearing Model

In the light of anisotropic bearing model, the oil-film force of hydrodynamic bearing is often characterized by a set of linear or nonlinear stiffness and damping coefficients.

$$[C]=\begin{bmatrix} c_{xx} & c_{xy} \\ c_{yx} & c_{yy} \end{bmatrix}, \quad [K]=\begin{bmatrix} k_{xx} & k_{xy} \\ k_{yx} & k_{yy} \end{bmatrix}$$

When the base of the bearing has good rigidity, the bearing system can be simplified as spring-damper-mass system, and the relevant hydrodynamic characteristic coefficients matrix can be described as following.

$$[C_b]=\begin{bmatrix} c_{bxx} & c_{bxy} \\ c_{byx} & c_{byy} \end{bmatrix}, [K_b]=\begin{bmatrix} k_{bxx} & k_{bxy} \\ k_{byx} & k_{byy} \end{bmatrix}$$

The total stiffness coefficients which are speed dependent are calculated by the following formula.

$$K=\frac{k_p(k_b-M_b\omega^2)}{k_p+k_b-M_b\omega^2}$$

This is just some compendium, and more details refer to literature.

When the stiffness coefficient and equivalent mass of the support in X and Y direction are close to each other, the coupled interaction between the two directions are negligible. In addition, bearings are fixed on the base, so the influence of the base stiffness and mass of vibration is also little, which also can be neglect during analysis. So only the stiffness of master vibration direction is considered, and others are simplified as the same.

On the basis of narrow bearing theory, the zero dimension coefficients of the journal bearing on the vertical direction can be calculated according to the following formula.

$$K_{yy}=(L/D)^2\frac{4\varepsilon[\pi^2+(\pi^2+32)\varepsilon^2+2(16-\pi^2)\varepsilon^4]}{(1-\varepsilon^2)^3[\pi^2(1-\varepsilon^2)+16\varepsilon^2]} \quad (1)$$

The stiffness of the bearing can be obtained by the formula bellow.

$$k_{yy}=K_{yy}\mu\omega L/\psi^3 \quad (2)$$

The stiffness of the bearing system can be calculated through the formula (1) and (2),

4 Calculation of the Critical Speeds

The parameters used during the analysis of rotor dynamics are list in Table 1.

Table 1 Dynamic parameters of the model

Diameter	0.1 m	density	915 kg/m^3
Width	0.095 m	Viscosity	46 mm^2/s
Clearance	0.145 mm		

Because experimental data can't be obtained in practical way, we can't use the real vibration data. According to literature, when the rotor speed from 0 to 200Hz, and the thickness of oil film is assumed to increase from 30 μm to 50 μm in the light of logarithm, therefore, we can get the following datasheet, which including nature frequency of the rotor calculated by the way of ansys.

Table 2 Nature frequency of the rotor

ω	0	40	80	120	160	200
δ	30	38.94	42.64	45.48	47.9	50
K_{yy}	8.96	5.10	4.11	3.48	3.03	2.7
k_{yy}(e7)	(2)	2.67	4.30	5.47	6.34	7.0
ω_1	41	46.50	54.65	58.81	61.3	62.9
ω_2	119	122.4	129.1	134.0	137.6	140.3
ω_3	215	215.6	215.6	215.6	215.6	215.6
ω_4	309	310.5	311.8	312.7	313.4	314.0

The Campbell diagram can be worked out as following (Fig. 3).

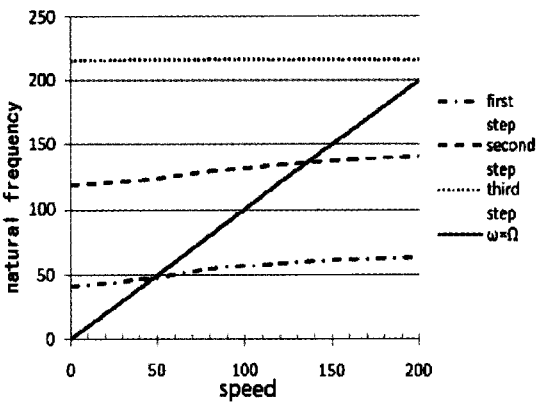

Fig. 3 Campbell diagram of the rotor

From Fig. 3, the first three steps of critical speed can be acquired, which are 48Hz, 133Hz and 215Hz. Due to the influence of dynamic characteristic of bearing oil film, it comes to the conclusion that the change of nature frequency is nonlinear related to speed. Since the curve is stick out, it illustrate that the bearing can decrease the critical speed.

5 Summary

The oil film characteristic of the journal bearing has great influence on the critical speed of rotor, what's more, the characteristic changes along with the speed. So this influence is a non-negligible factor in the situation needing accurate analysis.

Although the dramatic increases in available computation power have been such that the computation of critical speeds of a single machine design is now a comparatively trivial exercise, the computation requirements become significant again when the calculation procedure is embedded in design optimization studies, when it is used in model based diagnostics of rotating machines or when it is used repeatedly in certain classes of parameter identification methods.

Acknowledgements

This paper is a part of the project (project number: 2007C11030) that the Industrialization development for super high pressure centrifugal pump assembly with 3000kW power, which is included in the important equipment of Zhejiang province. This project is funded by the science and technology office. It is appreciated that Mr Wang and Mr Wu help me a lot on the researching and writing process as my instructor. Thanks for the support of my fellows and teachers and the opportunities given by Keer pump limited company.

References

M.I. FRISWELL, 1998, "COMPUTING CRITICAL SPEEDS FOR ROTATING MACHINES WITH SPEED DEPENDENT BEARING PROPERTIES", *Journal of Sound and Vibration* vol213 (1), 139 – 158

Madhumita Kalitaa, S.K. Kakotyb,2004, "Analysis of whirl speeds for rotor-bearing systems supported on fluid film bearings", *Mechanical Systems and Signal Processing*, pp. 1371 – 1380

Hua Zhou, Sanxing Zhao, Hua Xu, Jun Zhu, 2004, An experimental study on oil-film dynamic coefficients, *Tribology International*, pp. 245 – 253

G. D. Jiang, H. Hu, W. Xu, 1997, "Identification of oil film coefficients of large journal bearings on a full scale journal bearing test rig", *Tribology International* Vol. 30, No. 11, pp. 789 – 793

Zhao Rongzhe, Song Xi, "Calculation of effect of dynamic property of oil film on critical rotation speed of rotor in journal bearings", *Journal of Gansu University of Technology*, vol 25(1), pp. 40 – 44

Project Support

Zhejiang Provinces importance special equipment project (project code: 2007C1 1030)

Zhejiang Provinces Technology project (project code: 2007C2 1059)

The 4th International Symposium on Fluid Machinery and Fluid Engineering
November 24-27, 2008, Beijing, China
NO. 4ISFMFE-Ch35

Numerical Investigation on Impeller-Volute Interaction In a Low Specific Speed Centrifugal Pump with Tongue Profile Variation

Pengcheng Guo*, Xingqi Luo, Jinglin Lu and Xiaobo Zheng

* Dept. of Hydropower Engineering, Xi'an University of Technology,
Pillar Box 207, No.5 South Jinhua Road, Xi'an 710054, China
Tel: +86-29-8231-2720 / Fax: +86-29-8231-2857
E-mail: guoyicheng@hotmail.com

Abstract Numerical simulations on impeller-volute interactions in a low specific speed centrifugal pump equipped with variable tongue profiles were carried out using the commercial code CFX-10. The numerical results indicated that the influence of the different tongue profiles on the performance and operation stability of the centrifugal pump is very remarkable. The high-efficiency range of the centrifugal pump can be widened to some extent while the profile of the tongue is replaced from sharp tongue to middle tongue, and the maximum efficiency point is shifted along the higher flow rate direction. The operation stability of the centrifugal pump may be influenced while the fluid flows in the diffuser of the centrifugal pump with short tongue. The amplitude of pressure fluctuation in the tongue zone drops notably while the pump equipping with the middle tongue or the short one is in running.

Keywords low specific speed centrifugal pump, tongue profile variation, numerical investigation

Nomenclature (bold, arial, 10pt)

b_2	impeller width at outlet [m]
b_3	volute width at inlet [m]
D_1	impeller diameter at inlet [m]
D_2	impeller diameter at outlet [m]
D_3	volute diameter at inlet [m]
z	number of blades
R_T	radius at tongue edge [mm]
a	angle of tongue [deg]
F_t	throat section area [mm^2]
F_2	area of impeller outlet [mm^2]
Y	F_2/F_t: area ratio
N_d	rotational speed [rpm]
N_s	$3.65\ N_dQ_d^{1/2}/H_d^{3/4}$: specific speed
H, H_d	head, head at nominal flow-rate [m]
Q, Q_d	flow-rate, nominal flow-rate [m^3/h]
$P, \Delta P$	pressure, pressure amplitude [Pa]
t	time [s]

1 Introduction

From the beginning of 1990s, numerical studies of flow field in the centrifugal pumps impeller have already stridden into a three-dimensional viscous flow simulation period and many studies concerning this flow in centrifugal impellers have been reported. Goto [1] computed exit-flow fields of a mixed flow impeller with various tip gaps and confirmed the applicability of the incompressible three-dimensional Navier-Stokes code. Gopalakrishnan [2] carried out the performance prediction of a high specific speed mixed flow impeller using the commercial software CFX-TASCflow, Goto [3] presented a comparison between calculation and measurement for the H-Q and efficiency of a mixed flow impeller stage. Gülich and Favre [4] studied a thorough analysis of the validity of CFD technique. Thirty impellers ranging in specific speed from 12 to 160 metric were analyzed and tested for head and efficiency using a commercially available CFD code and

the theoretical head could be predicted with a standard deviation of 2.5%.

Recently, with the further development of computer technology and computational fluid dynamics (CFD), the impeller-volute interaction has aroused great concern, and several studies have been carried out numerically or experimentally in order to understand the interaction. Eduardo [5] used a commercial software package FLUENT 5 to simulate unsteady flow pattern through a water pump taking into account the impeller-volute interaction and the pressure fluctuations induced by the blade passage and the influence of the blade position relative to the tongue over these fluctuations. Shi and Tsukamoto [6] calculated an unsteady flow caused by impeller-diffuser interaction in a diffuser pump using the commercial software STAR-CD and indicated that the impeller-diffuser interaction is caused chiefly by potential interaction and wake impingement with the diffuser vanes. González [7] studied the relative tongue effect on the pressure fluctuations inside the volute of a centrifugal pump and confirmed that pressure fluctuations at any volute location are mainly caused by the effect of the tongue on the flow structure exiting the impeller and gives rise to radial non-symmetric forces on the impeller shaft. Chung [8] obtained the interaction between impeller and volute casing of an industrial double suction centrifugal pump at the rated and off-design points.

In this paper, numerical simulations on impeller-volute interactions in a low specific speed centrifugal pump were carried out to investigate the effects of varying the tongue profile on the flow field, respectively. A CFX-10 commercial code, based on shear stress transport (SST) turbulent model with automatic near wall treatments, was employed for turbulent flow calculation.

2 Model Description and Numerical Method

The investigated centrifugal pump is a specific speed of $N_s = 66\ \text{min}^{-1}$, which consists of an impeller with 6 strongly backward curved blades and a volute casing. The main geometric data and operating conditions of the pump are shown in Table 1. Figure 1 shows the cross-sectional view of the investigated pump and three different tongue profiles. The main data of three different tongues are indicated in Table 2.

One of the most important and time-consuming tasks in the CFD simulation process is the generation of the computational grid. Because of the complexity of the combined geometry, the grid generation tool ICEM-CFD is utilized to generate the tetrahedral unstructured grid which includes 423,039 nodes for the impeller. The total number of nodes for the complete problem is 866,186. The numerical code CFX-10 is used to solve the fully three dimensional incompressible Reynolds Averaged Navier-Stokes (RANS) equations. The turbulence is simulated with a k-ω turbulence model using the SST near wall treatment from Menter [9], which can give a highly accurate prediction of the onset and the amount of flow separation under adverse pressure gradients by inclusion of transport effects into the formulation of the eddy viscosity.

Table 1 Main geometric data and operating conditions

Main geometric data	
Number of blades	$z=6$
Inlet diameter of impeller	$D_1=0.05$ m
Outlet diameter of impeller	$D_2=0.13$ m
Outlet width of impeller	$b_2=0.006$ m
Inlet diameter of volute	$D_3=0.14$ m
Inlet width of volute	$b_3=0.016$ m
Design operating conditions	
Volume flow rate	$Q_d=12.5\text{m}^3/\text{h}$
Rotating speed	$N_d=2900$ rpm
Delivery head	$H_d=20$ m

Table 2 Main data of three different tongues

Type of tongue	A-Tongue	B-Tongue	C-Tongue
Radius at tongue edge R_T(mm)	1.5	3.0	6.0
Angle of tongue a (°)	70	80	90
Throat section area F_t (mm^2)	444.78	488.76	538.67
Area of impeller outlet F_2 (mm^2)	1335.24	1335.24	1335.24
Area ratio Y ($Y=F_2/F_t$)	3.00	2.73	2.48

The discretization in space used is of second order accuracy. Boundary conditions have to be specified to the surfaces exposed to the fluid to solve the RANS equations. At the inlet of the pump, the total pressure and the direction of the velocity vector are imposed. At the outlet of the flow regime, the mass flow rate is given. A no slip condition is given for the flow at the wall boundaries.

The numerical calculations are carried out with a multiple frame of reference, whereby the impeller flow field is solved in a rotating frame and the casing in a fixed one. For steady state calculations the grids of the impeller and the casing are connected by means of a frozen rotor interface and for unsteady calculations by means of a rotor/stator interface. For the unsteady calculations the

time step has been set to 5.747×10^{-5} seconds. This time step is related to the rotational speed of the impeller and is chosen in such a way that one complete impeller revolution is performed after each 360 time steps. The chosen time step is small enough to get the necessary time resolution. The number of iteration in each time step has been set to 8. This number of iterations is in most cases sufficient to reduce the residuals below 10^{-4}.

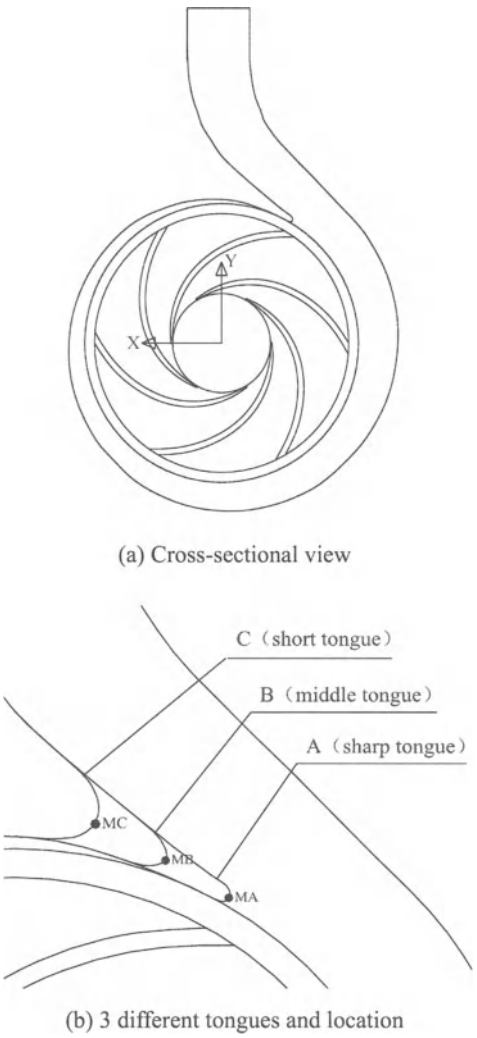

(a) Cross-sectional view

(b) 3 different tongues and location

Fig. 1 Cross-sectional view of the investigated centrifugal pump

3 Effect of Tongue Profile VARIATION on Pump Performance

Based on the design theory of centrifugal pump's volute casing, three different tongue profiles were designed to investigate the effect of varying the tongue profile on the pump flow field, which are the sharp tongue (A-Tongue), the middle one (B-Tongue) and the short one (C-Tongue), with 3 aforementioned flow rates. Figure 1 shows the cross-sectional view of three different tongue profiles and the locations of three investigated monitor points, MA, MB and MC. The main data of three different tongues is shown in Table 2.

In the investigated pump, when the volute tongue is set from A-Tongue to B-Tongue, the area ratio change from $Y=3.0$ to 2.73. The variation is 9%; When the volute tongue is further set from B-Tongue to C-Tongue, the area ratio vary from $Y=2.73$ to 2.48. The variation is 9.2%. The variation of area ratio has not exceeded 20% from A-Tongue to C-Tongue in the whole.

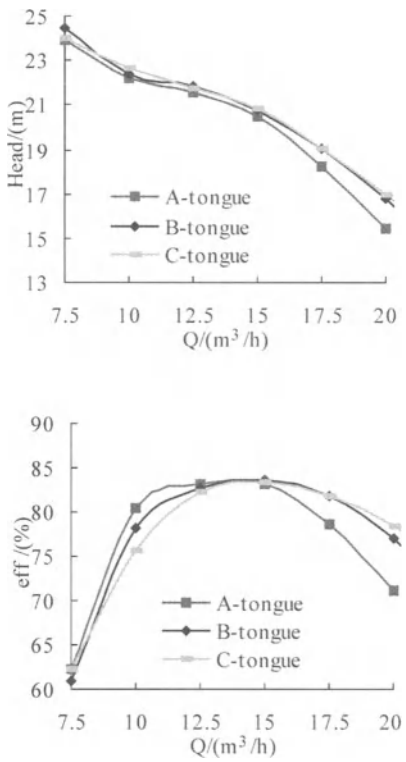

Fig. 2 Centrifugal pump performance curves with different tongues. The abscissa refers to flow rate, and the ordinate denotes head and hydraulic efficiency

The varying of the head and efficiency curves of the investigated pump with the tongue profiles and the flow rates was shown in Figure 2. It can be seen, to change the tongue profiles from A-Tongue to C-Tongue, the head can been increased at the same flow rate. Among that, when A-Tongue is replaced with B-Tongue, the head increase obviously. At the higher flow rate condition, with the flow rate increasing, the increment of the head is more evident and lead to the head curve more flat. But when B-Tongue is replaced by C-Tongue, the head increment is not obvious. When A-Tongue is displaced by C-Tongue, the

hydraulic efficiency can be improved slightly, the range of high efficiency can be broadened and the best efficiency point shifts along the higher flow rate direction. And the efficiency change extent which the tongue is changed from A-Tongue to B-Tongue is much bigger than the extent which the tongue is replaced from B-Tongue to C-Tongue.

4 Effect of Tongue Profile Variation on pump flow field

In Fig. 3 it can be seen the pressure distribution in the volute middle surface for three different tongue profiles and different time steps $t = 0$ and $t = T/2$ with nominal flow rate. The distinction of three pressure distribution plots is not obvious. But due to the tongue profiles different, the flow fields in the downstream of the diffuser appear difference. For the volute casing equipped with C-Tongue, because the radius of base circle is relative large, the inflow of diffuser induce flow turbulence in downstream diffuser. The pressure distribution in middle surface of diffuser outlet is very non-uniform, and it can be seen in Fig. 3(c).

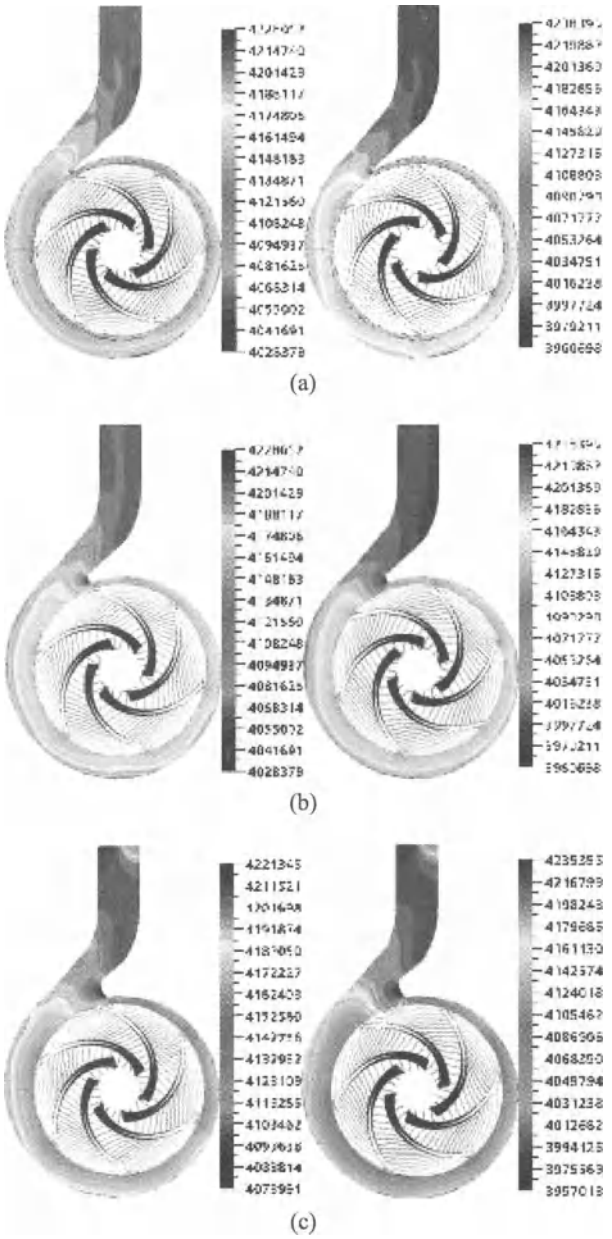

Fig. 3 Pressure distribution in the midspan for 3 tongues at t=0 and $T/2$ at rated flow. (a)A-Tongue; (b) B-Tongue; (c) C-Tongue

The velocity distribution in the volute middle surface near the tongue zone for three different tongue profiles and different flow rates at $t = 0$ time step is plotted in Fig. 4. It can be seen that the inflow direction of diffuser is consistent with the tongue angle at nominal flow rate, the stagnation point located at the tongue leading near the diffuser side at lower flow rate, and the stagnation point is at the tongue leading near volute casing side at higher flow rate. This result is accordant with the one with different radial gaps and shows that the stagnation point shifting around the tongue tip is only correlated with the varying of flow rate condition, but is independent of the tongue profile variation.

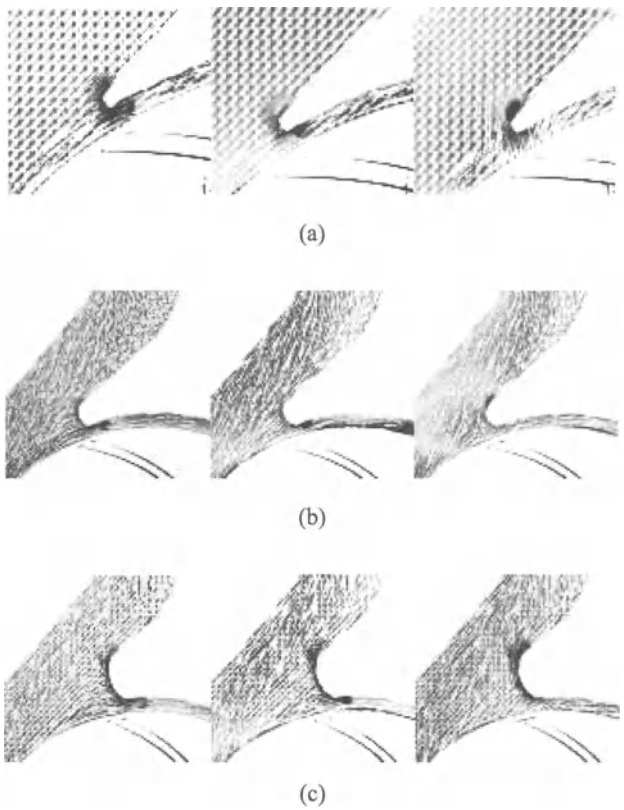

Fig. 4 Velocity distribution in the tongue zone for 3 tongues at 3 different flow-rates,Q=0.4Q_d,1.0Q_d, and 1.6Q_d from left to right, at t=0 timestep. (a)A-Tongue; (b) B-Tongue; (c) C-Tongue

In order to study unsteady pressure fluctuation characteristics in centrifugal pump with different tongue

profiles, three monitor points were arranged at tongue tip and Fig. 1 plots the locations of three points. The instantaneous pressure fluctuation along time at every monitor point for nominal flow rate and higher flow rate is shown in Figure 5. It can be seen, at the nominal flow rate, when the tongue is replaced from A-Tongue to B-Tongue, the maximum amplitude of pressure fluctuation decreases from 23.1kPa to 15.5kPa. The decrement is 32.9%. When the tongue is changed from B- Tongue to C-Tongue, both of them have the same amplitude of pressure fluctuation. At the higher flow rate, when A-Tongue is replaced with B-Tongue, the maximum amplitude of pressure fluctuation decreases from 95.1kPa to 38.3kPa. The decrement is 59.7%. When C-Tongue is used to replace B-Tongue, the maximum amplitude of pressure fluctuation decreases from 38.3kPa to 23.8kPa, the decrement is 37.9%. It can show, at nominal flow rate, when the tongue is changed from A-Tongue to B-Tongue, the amplitude of pressure fluctuation is decreased obviously. But when the tongue is replaced from B-Tongue to C-Tongue, both of them have the same amplitude of pressure fluctuation. At higher flow rate, when the tongue is replaced from A-Tongue to B-Tongue, then to C-Tongue, the amplitudes of pressure fluctuation all drop gradually. Among them the tongue is replaced from A-Tongue to B-Tongue, the amplitude decrement of pressure fluctuation is much notable.

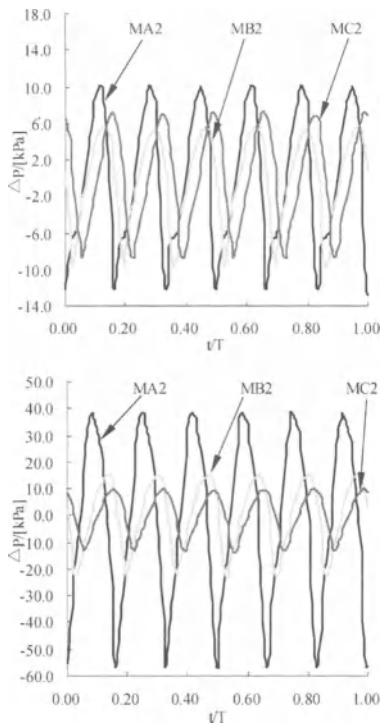

Fig. 5 The time histories of pressure fluctuation at investigated point at rated flow and over flow

5 Conclusions

The numerical results obtained show that the flow in the impeller and volute of centrifugal pump is periodically unsteady. The flow interaction between the impeller and the volute is characterized by pressure fluctuations, and which are more violent at impeller outlet and at the vicinity of the tongue.

The numerical simulation results of the influences of three different tongue profiles on the flow field indicated that the influence of the different tongue profiles and its relative positions on the performance and operation stability of the centrifugal pump is very remarkable.

The head of the centrifugal pump can be improved and the high-efficiency range of can be widened to some extent while the profile of the tongue is replaced from sharp tongue to middle tongue, and the maximum efficiency point is moved along the higher flow rate direction. The operation stability of the centrifugal pump may be influenced while the fluid flows in the diffuser of the centrifugal pump with short tongue.

The amplitude of pressure fluctuation in the tongue zone drops notably while the pump equipping with the middle tongue or the short one is in running.

Acknowledgements

This work is part of a project supported by the National Natural Science Foundation of China (90410019), Specialized Research Fund for the Doctoral Program of Higher Education of China (20040700009) and Specialized Research Plan in The Education Department of Shaanxi Province of China (05JK264). The supports are gratefully acknowledged.

References

[1] Goto, A. Study of internal flows in a mixed-flow pump impeller at various tip gaps using three-dimensional viscous flow computations[J]. *J. of Turbomachinery*, 1992, 114(2): 373 – 382

[2] Gopalakrishnan, S., Cugal, M., and Ferman, R. Experi-mental and Theoretical Flow Field Analysis of Mixed Flow Pumps[C]. *2nd International Conference on Pumps and Fans*, 1995, Tsinghua University, Beijing, China

[3] Goto, A. Prediction of Diffuser Pump Performance Using 3-D Viscous Stage Calculation[C]. *3rd ASME Pumping Machinery Symposium*, 1997, Vancouver, Canada

[4] Gülich, J.E., and Favre J.N. An Assessment of Pump Impeller Performance Predictions by 3D Navier-Stokes Calculations[C]. *3rd ASME Pumping Machinery Symposium, 1997*, Vancouver, Canada

[5] B. M. Eduardo, F. F. Joaquin, G. P. José. Numerical Flow Simulation a Centrifugal Pump with Impeller-Volute Interaction[C]. *Proceedings of ASME FEDSM200-11297*, June, 11 – 15, 2000, Boston, Massachusetts

[6] F. Shi, H. Tsukamoto. Numerical Study of Pressure Fluctuations Caused by Impeller-Diffuser Interaction in Centrifugal Pump Stage[J]. *ASME Journal of Fluids Engineering, 2001*, 123(3): 466 – 474

[7] José González, Carlos SANTOLARIA, Eduardo BLANCO. The Effect of The Volute Tongue on The Pressure Oscillations inside Centrifugal Pump[C]. *Proceedings of the 21st IAHR Symposium on Hydraulic Machinery and Systems,* Sept., 9 – 12, 2002, Lausanne

[8] Kyung-Nam Chung, Pyun-Gu Park, Jin-Young Kim. A Study on the Impeller-Volute Interactions of a Double-Suction Centrifugal Pump[C]. *Proceedings of 4th ASME/JSME Joint FEDSM2003-45405*, July, 6 – 10, 2003, Honolulu, Hawaii

[9] Menter, F. R. Two-Equation Eddy-Viscosity Turbulence Models for Engieering Applications. *AIAA Journal*, 32(8), 1994

The 4th International Symposium on Fluid Machinery and Fluid Engineering
November 24-27, 2008, Beijing, China
NO. 4ISFMFE-IL05

Experimental Study on a Direct Drive Turbine for Wave Power Converter System

Young-Ho Lee[*1], Young-Do Choi[2], Chang-Goo Kim[3], Young-Jin Cho[3], Sang-Hyun Nam[3] and You-Taek Kim[4]

[*1] Division of Mechanical Engineering and Information Engineering, Korea Maritime University
1 Dongsam-dong, Youngdo-ku, Busan 606-791, Korea
Tel: +82-51-410-4293 / Fax: +82-51-403-0381
E-mail: lyh@hhu.ac.kr (Corresponding Author)
[2] Industry-Academic Cooperation Foundation, Korea Maritime University
[3] Department of Mechanical Engineering, Graduate School, Korea Maritime University
[4] Department of Marine System Engineering, Korea Maritime University

Abstract Performance and internal flow of a direct drive turbine (DDT) model for wave power converter system is investigated experimentally. Three kinds of test turbine model are adopted for the examination. Test results show that rotational speed of test runner, differential pressure between front and rear nozzle passages and passage flow rate increase by the increase of wave height and wave period. Maximum output power and best efficiency of the test turbine model locate at the different rotational speed by wave height. Installation of front guide wall and rear water reservoir of the test turbine improves the turbine performance. Large passage vortex occurs both at the front and rear nozzle passages in turn by reciprocating flow in the internal flow passage of the turbine model.

Keywords direct drive turbine, wave power converter system, performance, internal flow, PIV

Nomenclature

A	nozzle inlet cross-sectional area
b	width of nozzle and runner
D_1	outer diameter of runner
D_2	inner diameter of runner
g	acceleration of gravity
ΔH	effective head
L	turbine length from the front to rear edges
N	rotational speed
p	static pressure
p_f	maximum pressure difference at front nozzle by wave height
Δp	differential pressure between front and rear nozzle passages
P	output power
Q	volumetric flow rate
T	torque
T_p	wave period
Z	number of runner blade
β_1	blade inlet angle at runner outer blade edge
β_1	blade outlet angle at runner inner inner edge
η	turbine efficiency ($=P/\rho gQ\Delta H$)
ρ	density of working fluid

1 Introduction

Wave energy converters are usually classified as fixed or floating type. The converters are further grouped as hydraulic, pneumatic or rotating. The oscillating water column is a pneumatic wave energy converter (i.e., Setoguchi et al, 1990). It uses the rise and fall of waves to create an oscillating flow of air, which in turn drives a bi-directional flow turbine. However, the turbines using the oscillating flow of air have some problems of rotational

speed variation and air noise occurring from runner passage.

Fukutomi et al. (1990) and Choi et al. (2007) have proposed a cross-flow type hydro turbine, which uses water as working fluid. The turbine maintains runner rotational direction into one direction from the oscillating flow.

This study introduces a newly developed Direct Drive Turbine (DDT) and is focused on the examination of the turbine performance for a basic turbine configuration. Output power and efficiency of the turbine are investigated experimentally. PIV measurement technique is adopted for the visualization of the turbine internal flow.

2 Experimental Apparatus and Test Turbine

Figure 1 shows schematic view of DDT model. Design concept of this turbine is to apply the operating mechanism of a cross-flow type hydro turbine by Fukutomi et al. (1990) to a wave energy converter.

The dimensions of the turbine are summarized as shown in Table 1. Turbine 1 is used for the examination of normal performance of the turbine model. Turbine 2 is adopted to investigate the effect of front guide wall and rear water reservoir on the turbine performance. Moreover, Turbine 3 is used for the internal flow visualization of the turbine model passage.

All the experiments for the test turbine models are carried out in a 2-D wave channel. The wave channel has the length of 30m, width of 1m and depth of 1m. Test turbine model is installed into the position of 14m downstream from a wave maker of the wave channel. For the examination of the effect of nozzle shape on the turbine performance, the front guide wall and rear water reservoir are designed to be separated from the main frame of the turbine model and to be attached into opposite positions.

Torque meter is installed outside of the turbine and the output torque occurring at the runner shaft is transferred to torque meter by timing belt and pulley. Rotational speed of the test runner is measured using a revolution counter which is attached to the torque meter. Two pressure transducers are installed both on the sidewalls of front and rear nozzles to measure differential pressure between the front and rear nozzles. Two wave height meters are located in the water channel of 2m upstream of the test turbine model and in the rear water reservoir of the turbine model.

Figure 2 shows test runner. Dimensions of the test runner are as shown in Table 2. The sizes of the test runners are suited for each test turbine model. Runner blade and sidewall of the test runner are made of acrylic resin.

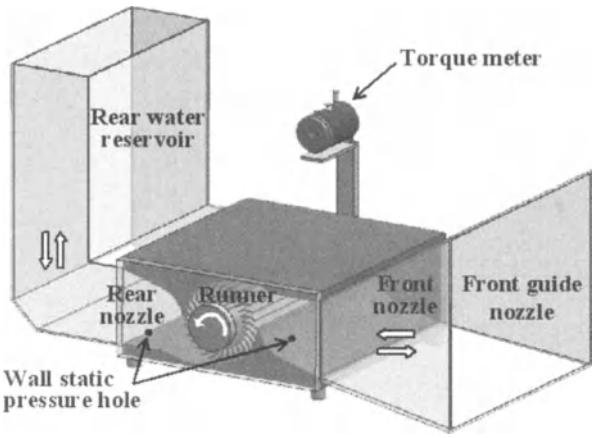

Fig. 1 Schematic view of Direct Drive Turbine tested

Table 1 Dimensions of test turbine model

Turbine	1	2	3
Nozzle inlet cross-sectional area A [mm x mm]	250 × 700	190 × 700	125 × 700
Length L [mm]	700	540	350
Width b [mm]		700	

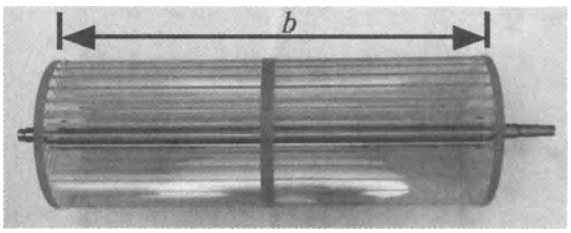

Fig. 2 Test runner of the turbine model

Table 2 Dimensions of test runner

Runner		1	2	3
Outer Diameter	D_1 [mm]	260	200	130
Diameter ratio	D_2/D_1		0.644	
Inner blade angle	β_1 [deg.]		30	
Outer blade angle	β_2 [deg.]		90	
Blade number	Z		30	

For the visualization of the internal flow in the nozzle passage of test turbine model, PIV (Particle Image Velocimetry) system is adopted. Figure 3 shows the schematic view of the two-dimensional PIV measurement system. A high speed camera (Resolution of 1K × 1K pixel) takes the consecutive images on the center plane of

the nozzle passage from the direction perpendicular to a plane of light sheet. A continuous laser sheet (542nm, Green, 500mW) are used as a source of illumination for PIV measurement.

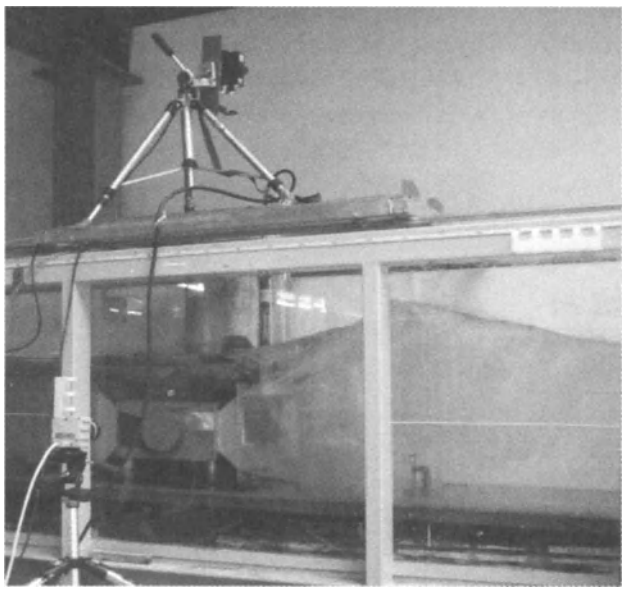

Fig. 3 Experimental apparatus for the visualization of internal flow passage in the test turbine by PIV

The light sheet is aligned from the upper side of the test turbine model. The light sheet is illuminated through the windows installed on the upper side of the front and rear nozzles. The thickness of the light sheet is fixed to 0.5mm at each plane measured. The time interval of the consecutive two images is set to 2ms in consideration of a maximum fluid velocity at the nozzle passages. A vinylchloride polymer (diameter about 100μm, specific gravity 1.1) is used as a tracer particle. A cross-correlation PIV algorithm (Raffel et al., 1998) is used as a particle tracking method.

3 Time Serial Output Data

Figure 4 shows time serial output data measured from Turbine 1 under the no load and loaded conditions. When there is no load on the runner axis, the rotational speed, torque and effective head vary periodically. Wave height in front of front nozzle inlet decreases after passing the runner passage at the rear water reservoir. It is clear that variation of output power and torque is periodical and the two components have close relationship with the variation of effective head, which is calculated from the differential pressure between the front and rear nozzles.

When axial load is applied on the runner axis, output power and torque increase simultaneously. Effective head under loaded condition becomes larger in comparison with that under the condition of no load on the runner axis. As the load is applied to runner axis, pressure at the front nozzle is consumed at the runner passage and thus, torque becomes larger.

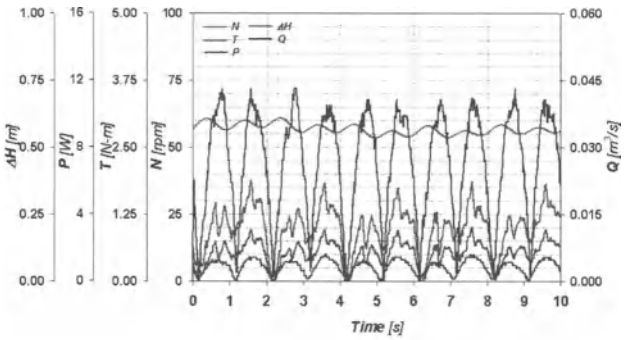

(a) No load condition

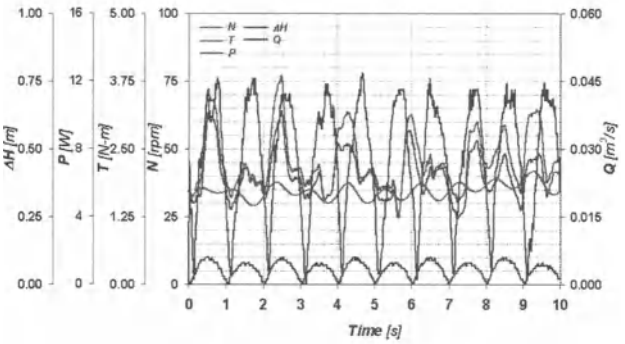

(b) Loaded condition (N=34 rpm)

Fig. 4 Time serial output data by Turbine 1 (T_p = 2sec., H = 20cm)

4 Performance by the Variation of Wave Height

Figure 5 reveals performance curves by the variation of wave height under the condition of no load. As wave height increases, flow rate passing through the turbine passage, static pressure at front nozzle and rotational speed increase considerably.

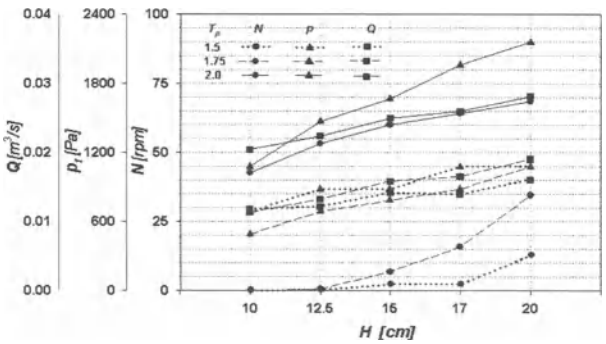

Fig. 5 Performance by the variation of wave height under no load condition (Turbine 1)

Moreover, detailed performance by the wave height under the loaded condition is shown in Fig. 6. Torque decreases almost linearly by the increase of rotational speed. As wave height increases, best efficiency of the turbine model also increases. Rotational speed at the best efficiency increases by the increase of wave height.

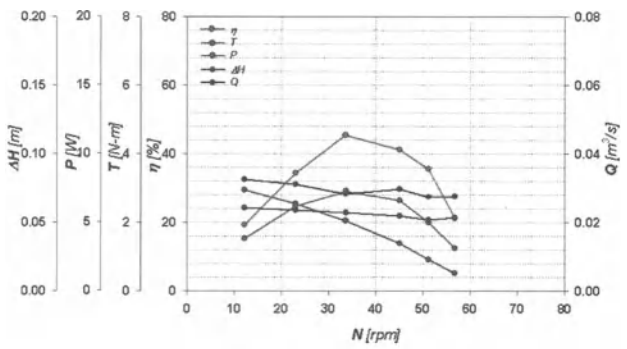

(a) Wave height H = 20cm

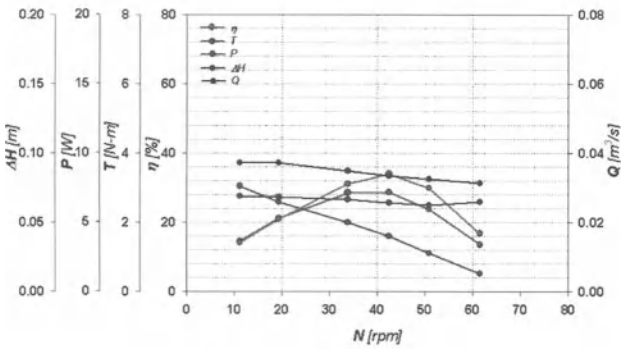

(b) Wave height H = 23cm

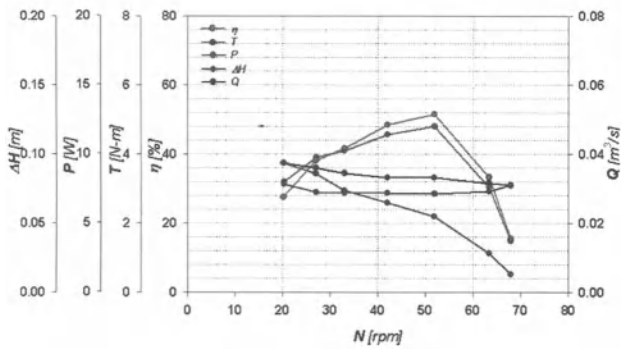

(c) Wave height H = 26cm

Fig. 6 Performance of test turbine model by wave height (Turbine 1)

5 Performance by the Variation of Wave Period

Figure 7 shows the performance of the turbine model by wave period under no load condition. When the wave height is relatively low, flow rate, static pressure at front nozzle and rotational speed almost does not change below period of T_p = 1.9sec. However, in the case of rotational speed, as the wave height increases, the rotational speed increases proportionally.

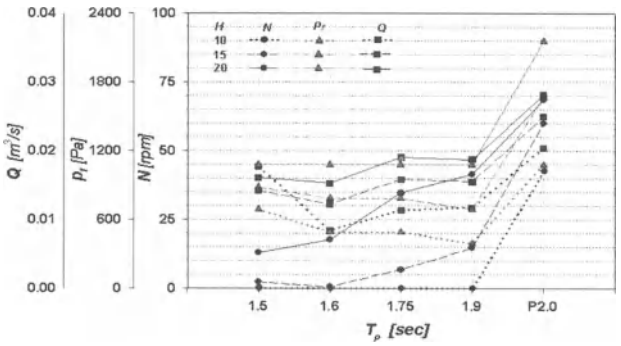

Fig. 7 Performance of test turbine model by wave period under no load condition (Turbine 1)

When the period is T_p = 2.0sec., all the output components increase remarkably. This result implies that there is an optimum wave period for the improvement of turbine performance.

6 Performance by the Configuration of Attached Devices at the Turbine Front and Rear Entrance

Tables 3 and 4 show the test cases by attached devices at the turbine front and rear entrances, and the cases by the relative turbine direction to the attached devices at the turbine front and rear entrances, respectively.

Figure 8 shows the effect of attached devices at the front and rear nozzle passages. When front guide wall and rear water reservoir are installed (Case 1), the output components reveals maximum among the cases. The front guide wall gives relatively large effect on the performance of the turbine. As the attached devices are taken away from the front and rear passage area, the performance decreases accordingly.

Moreover, the effect of nozzle direction on the turbine performance is examined as shown in Fig. 9. When the front guide wall and rear water reservoir are installed to the turbine as same direction as shown in Fig. 1 (Case I), the output power and efficiency shows almost same as the case of reverse nozzle direction (Case II). However, when there is no attached device to the test turbine, normal direction of the turbine nozzles to the attached devices shows better turbine performance than the case of reverse installation.

Table 3 Test cases by attached devices at the turbine front and rear entrances

Division	Front guide wall	Rear water reservoir
Case 1	Attached	Attached
Case 2	Attached	None
Case 3	None	Attached
Case 4	None	None

Table 4 Test cases by the relative turbine direction to the attached devices at the turbine front and rear entrances

Division	Turbine direction	Front guide wall	Rear water reservoir
Case I	Normal	Attached	Attached
Case II	Reverse	Attached	Attached
Case III	Normal	None	None
Case IV	Reverse	None	None

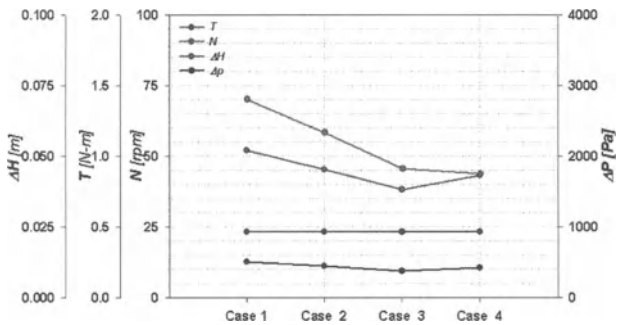

Fig. 8 Effect of attached devices by front guide wall and rear water reservoir (Turbine 2)

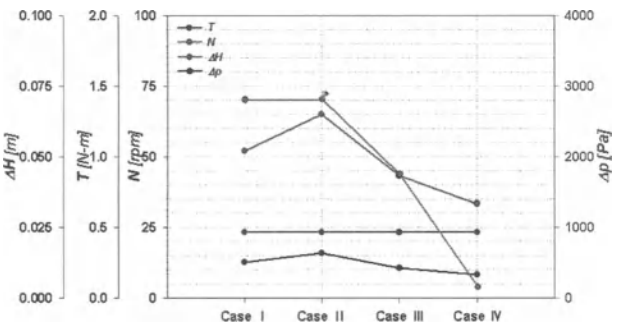

Fig. 9 Effect of nozzle direction to the attached devices (Turbine 2)

7 Visualization of Internal Flow in the Nozzle Passages

Figure 10 shows an instantaneous raw image on the center plane of the front nozzle passage by PIV measurement. Moreover, velocity vectors calculated from the raw images in the nozzle passages are revealed as shown in Fig. 11.

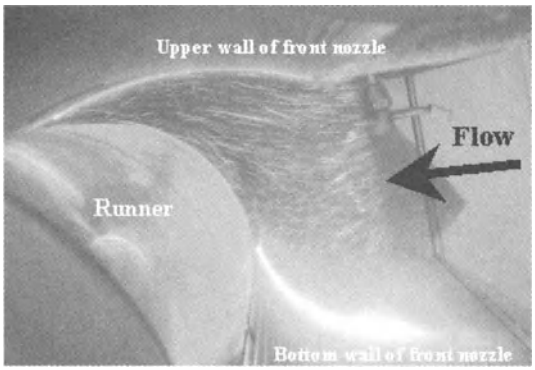

Fig. 10 Instantaneous raw image on the center plane of the front nozzle passage taken by PIV (Turbine 3)

When flow enters from the front nozzle (nozzle located at the right side of test runner) as shown in Fig. 11(a), flow velocity at the front nozzle passage increases at the relatively narrow nozzle region just before the runner inlet. After passing through the runner passage, the flow velocity becomes maximum at the bottom region of the rear nozzle. Moreover, There exists large vortex in the rear nozzle passage as shown in Fig. 11(a). When the flow direction changes to reversal as shown in Fig. 11(b), the flow pattern also changes to reverse direction.

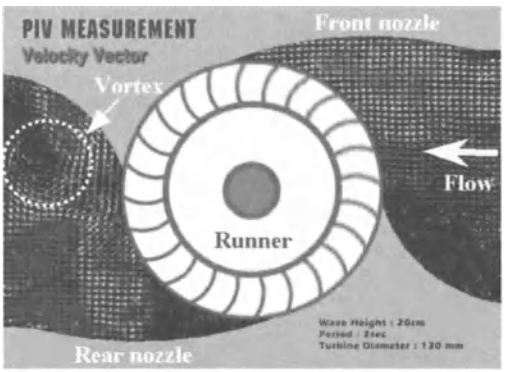

(a) Normal flow direction from front nozzle passage

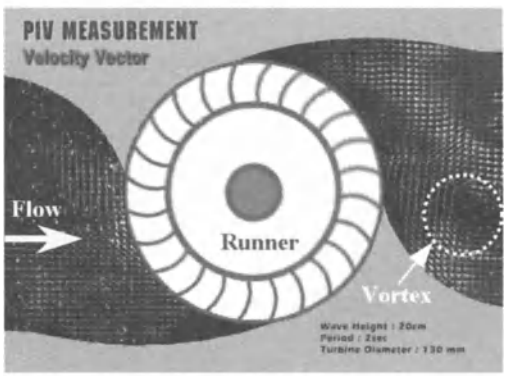

(b) Reverse flow direction from rear nozzle passage

Fig. 11 Velocity vectors in the nozzle passages by reciprocating flow (Turbine 3)

The result suggests that reciprocating flow passing through the symmetric nozzle passage is influenced remarkably by the nozzle shape. The velocity distribution in the nozzle passage and vortex formation has the close relationship with the nozzle shape.

Figure 12 shows streak lines in the nozzle passages by reciprocating flow. It is clear that there exists large vortex in the nozzle passage.

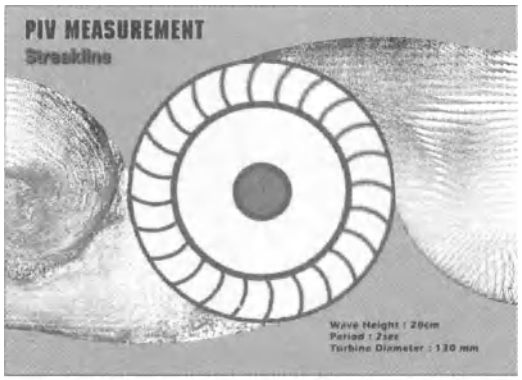

(a) Normal flow direction from front nozzle passage

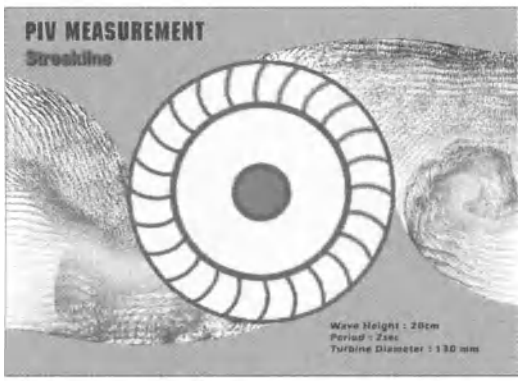

(b) Reverse flow direction from rear nozzle passage

Fig. 12 Streak lines in the nozzle passages by reciprocating flow (Turbine 3)

8 Conclusions

(1) Cross flow type hydro turbine for wave energy converter shows good performance for the input wave energy. Relatively high efficiency of the turbine shows its good possibility of applying to the development of wave energy converter.

(2) Effect of wave height on the performance of cross flow type hydro turbine for wave energy converter is considerable and almost proportional to the turbine performance. Rotational speed at the best efficiency increases by the increase of wave height.

(3) Wave period gives relatively small effect on the turbine performance in comparison with wave height but there exist an optimum wave period for the improvement of turbine performance.

(4) The shape of front guide wall, which is attached to the inlet of front nozzle, gives considerable effect on the turbine performance. The guide wall has function of gathering the wave energy efficiently and the device changes the rise and fall of waves to reciprocating flow in the turbine passage.

(5) PIV measurement reveals that there exists large vortex in the nozzle passage downstream of the test runner passage. The flow pattern changes by the flow direction of reciprocating flow in the turbine passage.

References

Choi, Y-D., Kim, C-G., Cho, Y-J., Kim, Y-T. and Lee, Y-H. (2007). "Internal Flow Characteristics of Cross-Flow Hydraulic Turbine for Wave Power System", Proceedings of 9th Asian International Conference on Fluid Machinery, Jeju, Korea, Paper No. AICFM9-296

Fukutomi, J, and Nakase, Y (1990). "A Study of turbine for wave power generation", *Proc. of the 1st Pacific Asia Offshore Mechanics Symposium*, pp. 193 – 198

Raffel, M., Willert, C., and Kompenhans, J.(1998). "*Particle Image Velocimetry—A Practical Guide*", Springer-Verlag, New York, pp.105 – 146

Setoguchi, T, Kaneko, K, Maeda, H, Kim, W, and Inoue, M (1990). "Impulse Turbine with Self-Pitch-Controlled Tandem Guide Vanes for Wave Power Conversion", *Proc. of the 4th AICFM*, Vol. 1, pp. 171 – 176

The 4th International Symposium on Fluid Machinery and Fluid Engineering
November 24-27, 2008, Beijing, China
NO. 4ISFMFE-Ab06

Determination of Optimum Nozzle Shape of a Direct Drive Turbine by CFD Analysis

Young-Do Choi[*1], Chang-Goo Kim[2], You-Taek Kim[3] and Young-Ho Lee[4]

[*1] Industry-Academic Cooperation Foundation, Korea Maritime University
1 Dongsam-dong, Youngdo-ku, Busan 606-791, Korea
Tel: +82-51-410-4940 / Fax: +82-51-403-0381
E-mail: ydchoi@pivlab.net
[2] Department of Mechanical Engineering, Graduate School, Korea Maritime University
[3] Department of Marine System Engineering, Korea Maritime University
[4] Division of Mechanical Engineering and Information Engineering, Korea Maritime University

Abstract The purpose of this study is to examine the influence of nozzle shape on the performance of a direct drive turbine for wave energy converter. The performance of the turbine is calculated by the variation of nozzle shape using a commercial CFD code. The results show that nozzle shape should be designed considering wave height and flow rate entering to the turbine. Best efficiencies of the turbine by 4 types of the nozzle shape do not change largely but overall performances vary mainly by the cross-sectional area of nozzle inlet. The output power of the direct drive turbine changes considerably by the nozzle shape, and a partial region of Stage 2 in the runner blade passage obtain maximum regional output power in comparison with the other region of the runner blade passage.

Keywords direct drive turbine, wave energy converter, nozzle shape, performance, internal flow

Nomenclature

b	width of nozzle, runner and runner chamber
C_p	pressure coefficient ($= (p - p_{ref})/\rho g H$)
d_1	outer diameter of runner
d_2	inner diameter of runner
H	effective head
N	rotational speed
N_{bep}	unit rotational speed at the B.E.P.
p	static pressure
p_{ref}	reference static pressure at rear nozzle passage
P	output power
Q	volume flow rate
u	absolute velocity of runner inlet at Stage 1
z	number of runner blade
v	fluid velocity
η	efficiency
θ_1^*	normalized peripheral blade position at Stage 1
θ_2^*	normalized peripheral blade position at Stage 2
ρ	density of working fluid

Subscripts

11	inlet of runner Stage 1
21	inlet of runner Stage 2
r	radial component of velocity
θ	tangential component of velocity

1 Introduction

Among the ocean energy resources, wave power takes a growing interest because of its enormous amount of potential energy in the world. Therefore, various types of wave power system to capture the energy of ocean waves have been developed so far (i.e., Carcas (2004), Fukutomi et al. (1990) and Setoguchi et al. (1990)).

However, suitable turbine type is not normalized yet because of relatively low efficiency of the turbine systems. The purpose of this study is to investigate the optimum nozzle configuration for a direct drive turbine for wave energy converter, which will be built in a caisson for wave power plant.

Numerical simulation using a commercial CFD code is conducted to clarify the effects of the nozzle shape on the turbine characteristics.

2 Direct Drive Turbine for Wave Energy Converter

Figure 1 shows operation mechanism of a direct drive turbine, which is built in a caisson of wave power plant. When the wave enters the caisson guide wall, the wave motions of rising and dropping change to the reciprocating flow of inflow and outflow by the internal flow passage in the caisson, as shown in Fig. 1.

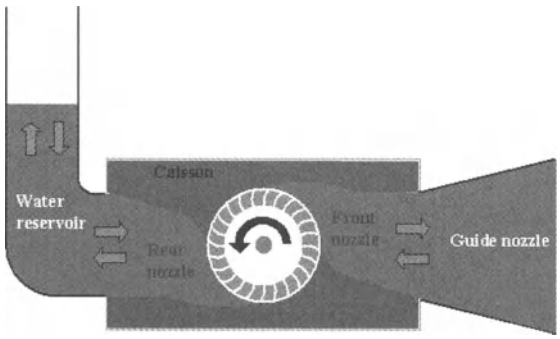

Fig. 1 Operation mechanism of a direct drive turbine which is built in a caisson of breakwater

The turbine uses reciprocating water flow in the flow passage of the caisson to obtain output power by runner rotation. The runner of the turbine is designed to maintain its rotation in one direction even in the case of reciprocating flow in the flow passage.

This turbine is designed to apply to the wave energy converters of both fixed and floating types. Present study is mainly focused on the application of the turbine to the fixed type wave energy converter using breakwater in the nearshore waters. Figure 2 shows a schematic image view of caisson built-in type wave energy converter with the direct drive turbine.

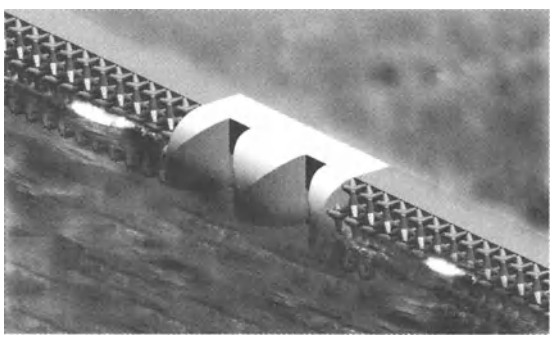

Fig. 2 Schematic image view of caisson built-in type wave power generation plant with direct drive turbine

3 Configuration of Nozzle and Runner

Figure 3 reveals 4 kinds of nozzle shape adopted in the direct drive turbine. The turbine performance and internal flow are compared by the variations of the nozzle shape. As the runner of the cross flow type hydro turbine for the wave energy converter should be rotated in one direction, the nozzle shape is determined to be symmetric to the axis of the runner in order to obtain the required condition of one directional rotation even for the reciprocating flow in the internal flow passage of the turbine.

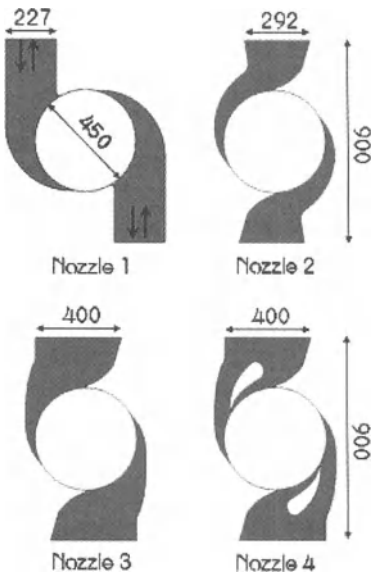

Fig. 3 Variation of symmetric nozzle shape

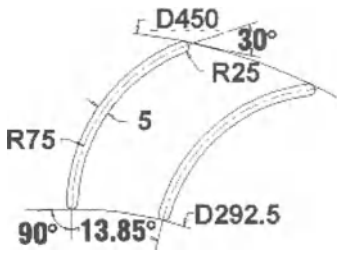

Fig. 4 Shape of runner blade and its dimensions

The size of the turbine is designed to be suited for the wave height ranges of 0.5 – 2.0m. The runner shape and dimensions are equal to all nozzle shapes. Nozzle 1 has basic nozzle shape. Nozzles 2 and 3 have different cross-sectional area at inlet. Nozzle 4 has guide vanes in the nozzle passage and the nozzle shape is same as that of Nozzle 3.

Moreover, shape of runner blade and its dimensions are shown in Fig. 4. The runner outer diameter $d_1 = 450$mm and the diameter ratio $d_2/d_1 = 0.65$ are set. The number of runner blade is z=26. The inlet and outlet angles of the

blade are 30 and 90 degree, respectively. The widths of nozzle, runner and runner chamber are determined to be equal value of b = 225mm.

4 Numerical Analysis Method

For the numerical analysis of the performance and internal flow characteristics of the turbine model, a commercial CFD code ANSYS-CFX (2007) is adopted. Determination of grid number and turbulence model is referred to simulation results by Choi et al.(2007). The grid number of about 1.5×10^6 is adopted to the four nozzle shapes with same runner. Fine hexahedral grids are employed at the whole flow field to ensure high accuracy of calculated result for the turbine model. Runner and nozzle regions are divided into two different grid blocks. Dimensionless grid distance from the wall, y^+, is kept below 15 and below 50 in the regions of runner and nozzle passages, respectively.

As a turbulence model, *SST* model is used. Constant pressure at inlet and averaged outflow at outlet are the used boundary conditions. All the calculations for the test cases are conducted under the conditions of one-way flow and steady state. Water is used as a working fluid.

5 Performance Characteristic Curves

Figure 5 presents performance characteristic curves of turbine model for the cases of different nozzle shape with the variation of rotational speed N.

Effective head H between inlet and outlet of the turbine increases considerably by the increase of rotational speed. Output power P increases by the increase of rotational speed at the relatively low rotational speed range but there is a peak point of the output power by a nozzle shape at the range of relatively high rotational speed. However, efficiency curve shows best efficiency at the range of relatively low rotational speed and best efficiency does not differ so much each other except for the case of Nozzle 4.

From the comparison with the nozzle shapes between Nozzles 2 and 3, it is clear that the turbine with relatively wide nozzle inlet area have relatively low available head and output power in the range of almost whole rotational speed. However, relatively high available head and output power occurs in the case of relatively narrow nozzle inlet area.

This result implies that in order to obtain the same output power from different wave height (effective head) conditions, nozzle inlet area should be wider in the case of relatively low wave height but in the case of relatively high wave height, nozzle inlet shape should be narrower. As the output power of the turbine is proportional to the flow rate and effective head, considering the actual ocean wave conditions, the nozzle inlet area should be designed as possible as wider to receive enough flow rate because the turbine can not receive enough head from the wave in the ocean.

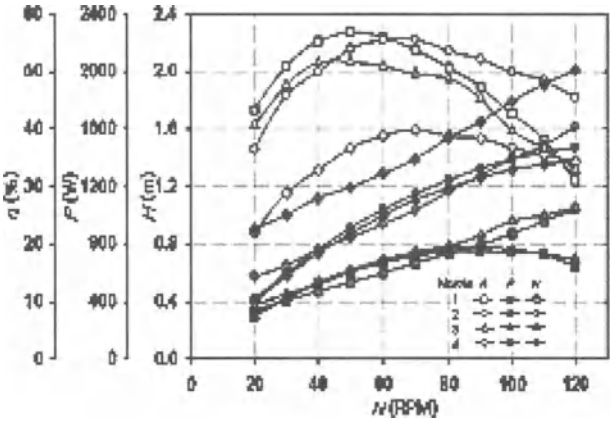

Fig. 5 Performance characteristic curves of direct drive turbine models by the variation of nozzle shape

6 Output Power Analysis

In order to investigate the output power obtained at the runner, the detailed output power is calculated at each separated region of the runner passage. Figure 6 shows the divided runner passages for the comparison of the each output power at the divided passage regions when the nozzle shape of Nozzle 3 is installed.

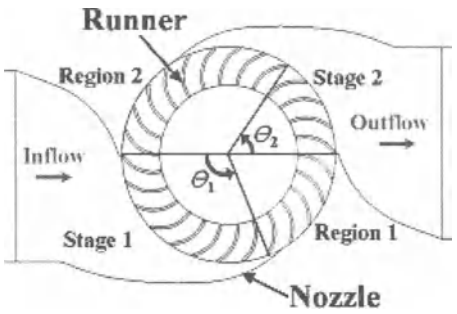

Fig. 6 Division of runner passage in the direct drive turbine by Nozzle 3

Figure 7 shows the output power by the variation of nozzle shape at the best efficiency point. In the case of Nozzle 3, for the total output power (100%) at the best efficiency point, Stage 1, Stage 2, Region 1 and Region 2 indicate the proportions of output power by 16.8%,

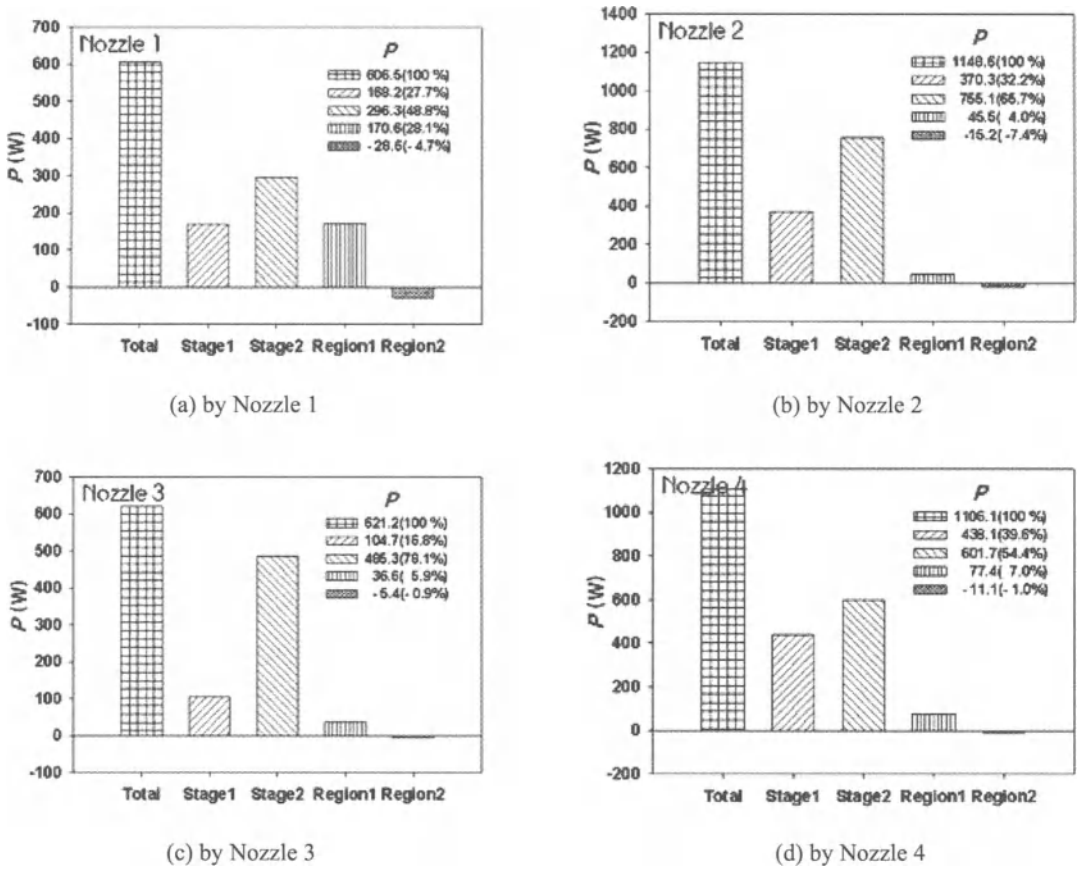

Fig. 7 Output power by the variation of nozzle shape at the best efficiency point

78.1%, 5.9% and – 0.9%, respectively. By the way, in the case of cross-flow hydro turbine for hydropower plant on the ground (i.e., Mockmore (1949)), Stage 1 produces about 70% of total output power and 30% of output power is obtained at Stage 2.

However, present study reveals that most of output power is obtained at Stage 2. The reason of the unusual output power ratio obtained among the areas is conjectured that the inlet and outlet nozzle shape of the present turbine is designed by symmetric configuration to the runner axis and the flow passage strongly influences to the ratio of output power at each runner passage region.

Moreover, by the variation of the nozzle shape, the ratio of output power at each runner passage changes largely as shown in Fig. 7. In the case of the Nozzle 1, there exists relatively considerable output power loss.

7 Velocity Vectors and Distributions

Figure 8 shows velocity vectors in the internal flow passage of turbine models. The velocity vectors in the nozzle passage and runner blade passage are expressed using absolute velocity vectors. It is clear as a whole from

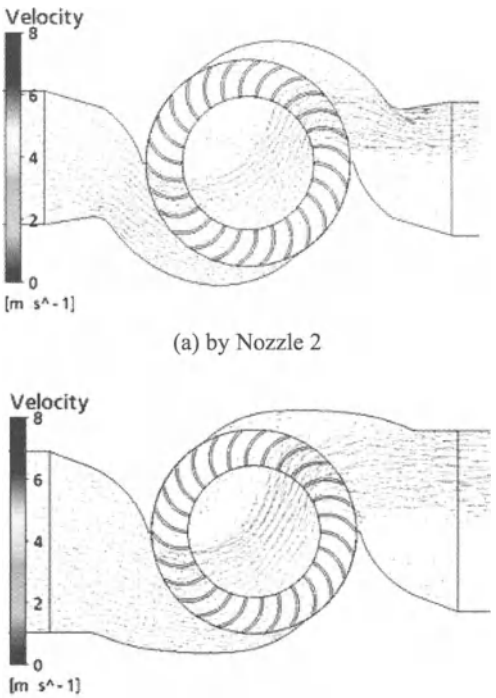

Fig. 8 Velocity vectors in the turbine flow passage

the figure that fluid velocity becomes accelerated within the runner center region after passing through Stage 1 and then, the velocity of mainstream becomes higher when the fluid passes Stage 2.

While, large vortex exists at the upper-left region in the runner center area and the vortex forms large recirculating flow area within the runner passage. The vortex region gives considerable influence to the output power of this turbine because the runner blades at Region 2 consumes the output power which is obtained at the other runner passage as shown in Fig. 7.

When the flow patters of the velocity vectors are compared with the different nozzle shapes as shown in Fig. 8, velocity at the nozzle passage differs remarkably by the nozzle shape.

As angular momentum composed of the tangential velocity component v_θ and flow rate changes to output power in the runner passage, the change of the velocity components by the nozzle shape should be examined in detail.

Figure 9 reveals the velocity distributions at the inlet of Stages 1 and 2 by nozzle shape. Velocity ratio of the tangential component v_θ at the inlet of Stage 1 is relatively higher compared with that of velocity ratio by the component of v_r in the radial direction. The velocity ratio by the $v_\theta$at each runner passage changes slightly, and relatively higher velocity ratio by the $v_\theta$is located at the region near the nozzle end edge (θ_1^*=1.0) at the inlet of Stage 1. Velocity ratio by the v_r varies largely in the passages near the nozzle start edge(θ_1^*=0).

However, the values of velocity ratio by the v_θ and v_r at the inlet of Stage 2 are different from those at the Stage 1. Contrary to the velocity distribution at the inlet of Stage 1, velocity ratio by the v_r maintains relatively higher velocity distribution than that of the v_θ in the almost inlet flow passage region of Stage 2. Moreover, velocity distributions of v_θ and v_r vary largely at Stage 2.

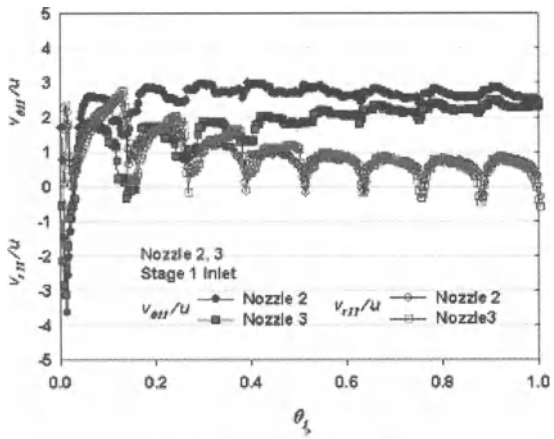

(a) at the inlet of Stage 1

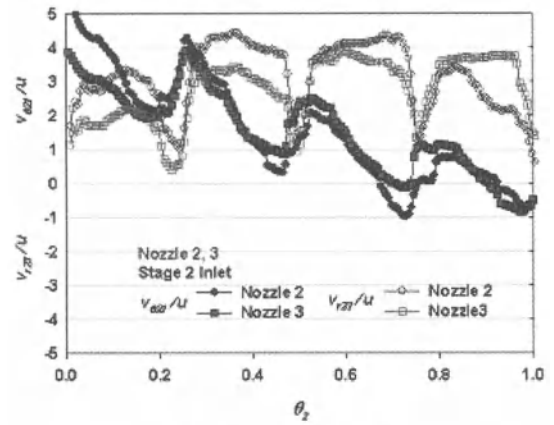

(b) at the inlet of Stage 2

Fig. 9 Velocity distributions in the flow passage

8 Pressure Contours in the Flow Passage and Pressure Distributons on the Runner Blade

Figure 10 shows static pressure contours in the flow passage by the variation of nozzle shape. As a whole in the both cases of Nozzles 2 and 3, inlet pressure decreases considerably along the runner passage at Stage 1 and internal center passage of the runner, but the pressures at Stage 2 and downstream of the turbine runner are relatively very low. From this result, it is assumed that the fluid pressure passing through the runner passage at Stage 1 is taken by the runner blades and changes to output power.

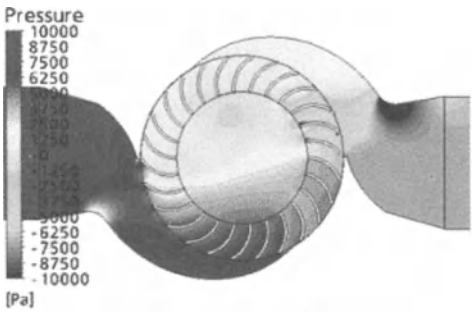

(a) by Nozzle 2

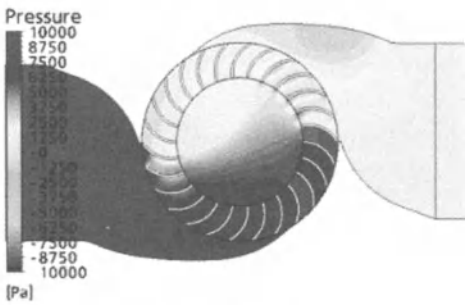

(b) by Nozzle 3

Fig. 10 Pressure contours in the flow passage by the variation of nozzle shape

Moreover, Fig. 11 shows the averaged pressure distributions around the surfaces of all runner blades at Stages 1 and 2 in the both cases of Nozzles 2 and 3. The area filled with the pressure curve means the pressure difference between pressure and suction sides of the runner blade. Therefore, larger pressure difference becomes higher output power in the runner passage.

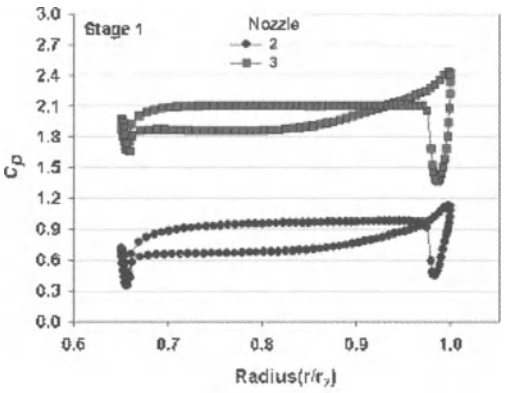

(a) at Stage 1

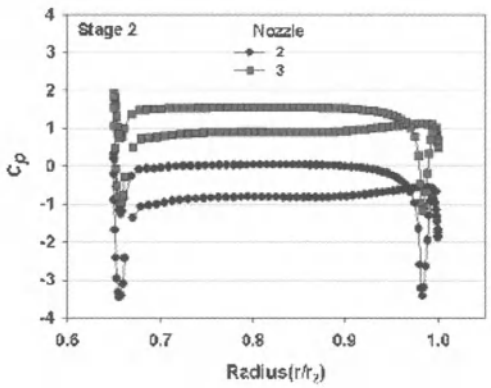

(b) at Stage 2

Fig. 11 Averaged pressure distributions on the surface of the runner blade by nozzle shape at the best efficiency point

The values of pressure distribution and area filled with the pressure curve at Stage 1 vary largely by nozzle shape but the areas at Stage 2 does not change so much compared with those at Stage 1.

The closed area filled with the pressure curve by Nozzle 2 is wider than that by Nozzle 3.

9 Conclusions

(1) Performance of the direct drive turbine with symmetric nozzle configuration for wave energy converter is influenced considerably by nozzle shape. By the nozzle shape, wave height and input flow rate at the design point changes largely.

(2) Total output power of the direct drive turbine with symmetric nozzle shape is obtained mainly at the Stage 2. If the cross-sectional area at nozzle inlet becomes relatively wider by use of Nozzle 3, 78% of total output power can be obtained at Stage 2.

(3) Large vortex exists in the center area of runner internal passage. The vortex forms large recirculating flow area within the runner passage and the reciruculating flow decreases output power.

References

ANSYS Inc. (2007). "ANSYS CFX Documentation", Ver. 11, http://www.ansys.com

Carcas, M (2004). "The Palamis Wave Power Program", *Proc. Energy Ocean*

Choi, Y. D., Lim, J. I., Kim, Y. T. and Lee, Y. H. (2007). "Internal Flow Characteristics of Cross-Flow Hydraulic Turbine with the Variation of Nozzle Shape", Proceedings of FEDSM2007, 5th Joint ASME/JSME Fluids Engineering Conference, San Diego, USA, Paper No. FEDSM2007-3754

Fukutomi, J, and Nakase, Y (1990). "A Study of turbine for wave power generation", *Proc. of the 1st Pacific Asia Offshore Mechanics Symposium*, pp. 193 – 198

Mockmore, C.A. and Merryfield, F (1949). "The Banki Water Turbine", Engineering Experiment Station of Oregon State College, Bulletin Series No. 25

Setoguchi, T, Kaneko, K, Maeda, H, Kim, W, and Inoue, M (1990). "Impulse Turbine with Self-Pitch-Controlled Tandem Guide Vanes for Wave Power Conversion", *Proc. of the 4th AICFM*, Vol. 1, pp. 171 – 176

The 4th International Symposium on Fluid Machinery and Fluid Engineering
November 24-27, 2008, Beijing, China
NO. 4ISFMFE-Ch10

Comparison of Several Subgrid-Scale Models for Large-Eddy Simulation of Turbulent Flows in Water Turbine

Jiamei Ma*, Fujun Wang and Xuelin Tang

* Dept. of Fluid Machinery, College of Water Conservancy & Civil Eng, China Agricultural University,
17#, Qinghua East Road, Haidian District, Beijing 100083, China
Tel: +86-10-8238-0734
E-mail: jiameima@gmail.com

Abstract Subgrid-scale (SGS) models for large-eddy simulation (LES) define the formalism of an effective eddy-viscosity model. The aim of this work is to quantify and compare different SGS models with experimental data. The first model investigated here is Smagorinsky model (SM), which is the earliest SGS model employed in LES, and given the Smagorinsky coefficient. The second model is dynamic model (DM), which has represented a great improvement in LES, and the coefficient is obtained dynamically. The third model is wall-adapting local eddy viscosity model (WALE), which based on the square of the velocity gradient tensor and has a proper near wall behavior. The last model investigated here is scale-dependent dynamic model (SDDM), which does not rely on the assumption that the model coefficient is scale invariant. The model is based on a second test-filtering operation which allows us to determine from the simulation how the coefficient varies with scale, but it was only validated in atmospheric boundary layer. The finite volume method is used to discretize the turbulence equations on a staggered grid system. The SMPLEC algorithm is used to solve the discrete turbulence equations. Body-fitted coordinates are used to simulate flows over complex geometry fields. The case here investigated are four SGS model of a three-dimension turbulence flows in 90°curved duct at Re = 40000. Finally, we find that the WALE model's results agreed well with experimental results, indicating that the model and the calculated results are reliable. Meanwhile, the dynamic model also has an acceptable behavior to simulate turbulent flow, but its behavior is not as good as the WALE model, and better than Smagorinsky model. However, the SDDM has a bad performance to simulate turbulent flows of complex geometries. Therefore, the WALE model and dynamic model are applied in water turbine simulations.

Keywords subgrid-scale model, large-eddy simulation, turbulent flow

Nomenclature (Bold, Arial, 10pt)

C_s	Smagorinsky coefficient
C_K	Kolmogorov constant
D	length of cross-section side
$\overline{G}(x_i, x')$	filter function
L_{ij}	Leonard stresses
r_i, r_o	inner and external radius of curving duct
$\overline{S}_{ij}$	resolved strain-rate tensor
$\lvert\overline{S}\rvert$	magnitude of the resolved strain-rate tensor
τ_{ij}, T_{ij}	subgrid-scale stress, test subgrid-scale stress
$u, \overline{u}$	velocity, filtered velocity
x_i	axis of the Cartesian coordinate system
ν_t	eddy viscosity
$\overline{\Delta}, \tilde{\Delta}$	grid filter scale, test grid filter scale
$\hat{\Delta}$	secondary test filter scale
θ	angle of bend cross-section
i, j	coordinate index

1 Introduction

One of the important problems in turbulent flow simulation is the construction of turbulent model. Recently, large eddy simulation (LES) has a rapid development, which is one of the most successful techniques in the numerical

simulation of turbulent flow and be used in many fields (Walter, 2006). But there is only a primary using for numerical simulation in fluid machinery, such as pump, water turbine, compressor, etc., because of the complicated structure of them.

In LES the large-scale field is computed directly from the solution of the filtered Navier-Stokes equations, and the small-scale stresses are modeled. The SGS model then represents the effect of the small scales on the large-scale motions. The severe Reynolds number restriction in direct numerical simulation (DNS) is largely alleviated in LES. However, since the small scales are presumably more isotropic and more universal in character for different flows than the large scales, it should be possible to parameterize the small scales using simpler and more universal models. Thus, a good LES model should be able to compute an accurate approximation of the filtered variables.

In fact, the most popular LES models is eddy-viscosity type, based on (variants of) the Smagorinsky model (1963). The main feature of the eddy-viscosity models is that they properly transfer kinetic energy from large scales to smaller and smaller scales, until this energy is dissipated through viscous effects. The Smagorinsky model remains as the most widely used model in LES, but it still has some limitations (Moin et al, 1991), such as: (1) the optimal model constant must be changed in different flows; (2) the model does not have the correct limiting behavior near the wall; (3) the model does not vanish in laminar flow and too dissipative in the laminar/turbulent transition region; (4) the model does not account for backscatter of energy from small scales to large scales; (5) compressibility effects are not included in the model.

So, several modifications to the Smagorinsky model have been proposed by many scholars. Germano (1991) introduced the dynamic model. This model has represented a great improvement in LES, but it has some defects (Vreman, 2004). It only modifies the model coefficient in the Smagorinsky model and, consequently, the dynamic model is momentum conserving. It is guaranteed to dissipate kinetic energy, but only if the dynamic coefficient is positive. This is usually achieved with by a somewhat ad hoc clipping procedure, which simply puts the eddy-viscosity to zero at locations where the dynamic procedure a negative value.

Another eddy-viscosity model is wall-adapting local eddy viscosity model (WALE), which is proposed by Nicoud and Ducros (1999). This model based on the square of the velocity gradient tensor with the following advantages compared to the classical Smagorinsky model: (1) the spatial operator consists of a mixing of both the local strain and rotation rates; (2) the eddy-viscosity goes naturally to zero in the vicinity of a wall; (3) the model produces zero eddy viscosity in case of a pure shear. Moreover, the WALE model is invariant to any coordinate translation or rotation and only local information are needed so that it is well suited for LES in complex geometry.

We can also note the scale-dependent dynamic model (SDDM) of Fernando (2000), which does not rely on the assumption that the model coefficient is scale invariant. The model is based on a second test-filtering operation which allows us to determine from the simulation how the coefficient varies with scale. One of the main advantages of this model is that it does not require any special parameter tuning, since the model coefficient is calculated dynamically at every position in the flow as a function of the resolved flow as the simulation progresses. This model has shown a good performance in simulations of a neutral atmospheric boundary layer, but it does not be validated in simulations of complex flows.

Purpose of this paper is to compare the performances of the four SGS stresses models including Smagorinsky model (SM), dynamic model (DM), WALE model, and SDDM. Eventually, we can obtain a result which SGS model is more adaptive the complex flows. Two cases have been considered: the turbulent flow in a curving duct, and the flow in a water turbine.

In the following, the mathematical formulation of LES combining SGS model is given. Then, four mathematical models of SGS stresses for LES are presented. Finally, numerical results generated by the four models are discussed, and some conclusions are drawn.

2 Mathematics of Large-Eddy Simulation

In the LES method the filtration operation proposed by Leonard (1974) is applied to the initial equations. Each physical parameter is expanded into large-scale and small-scale components. The effects on large scales are calculated directly and those on small scales are modeled. The filtered part $\bar{f}(x_i)$ is defined as follows:

$$\bar{f}(x_i) = \int f(x_i')\bar{G}(x_i, x')\mathrm{d}x_i' \tag{1}$$

where the integral is extended to the entire computational domain, $\bar{G}(x_i, x')$ is the filter function satisfying the normalization property, $x_i = (x, y, z)$ are axes of the Cartesian coordinate system.

Different filter functions have been considered in LES. In this paper, we employ the box filter which is widely used in the calculation of LES. It can be defined as

$$\overline{G}(x_i - x_i') = \begin{cases} \prod_{i=1}^{3} 2/\Delta_i, & |x_i - x_i'| < \Delta_i/2, \\ 0 & otherwise. \end{cases} \quad (2)$$

By applying the grid filter to the dimensionless continuity and Navier-Stokes equations, one obtains the filtered equations of motions for incompressible flow

$$\frac{\partial \overline{u}_i}{\partial x_i} = 0 \quad (3)$$

$$\frac{\partial \overline{u}_i}{\partial t} + \frac{\partial \overline{u}_j \overline{u}_i}{\partial x_j} = -\frac{\partial \overline{p}}{\partial x_i} + \frac{\partial}{\partial x_j}\left[\nu\left(\frac{\partial \overline{u}_i}{\partial x_j} + \frac{\partial \overline{u}_j}{\partial x_i}\right)\right] - \frac{\partial \tau_{ij}}{\partial x_j} \quad (4)$$

where overbar denotes the resolved quantities, x_1, x_2, x_3 is the streamwise, normal to the walls and spanwise direction, respectively. These are the equations of conservation of mass and of momentum for the large, energy-containing scales of motion. The effects of the small scales appear in the subgrid scale (SGS) stress term

$$\tau_{ij} = \overline{u_i u_j} - \overline{u}_i \overline{u}_j = L_{ij} + C_{ij} + R_{ij} \quad (5)$$

which must be modeled. The Leonard stresses $L_{ij} = \overline{\overline{u}_i \overline{u}_j} - \overline{u}_i \overline{u}_j$ represent interactions between resolved scales that result in SGS contributions. The cross terms $C_{ij} = \overline{\overline{u}_i u_j'} - \overline{u_i' \overline{u}_j}$ represent the interactions between resolved and unresolved scales, while the SGS Reynolds stresses $R_{ij} = \overline{u_i' u_j'}$ represent the interactions between unresolved scales. We shall define in the next section the models which be used in the present paper.

3 Subgrid Scale Models

In this study, four SGS models in LES are discussed and employed in the LES analysis, including the Smagorinsky model (SM), Dynamic model (DM), Wall-adapting local viscosity model (WALE), and Scale-dependent dynamic model (SDDM). All of them use the eddy-viscosity assumption, which try to simulate the diffusive transport and dissipation of kinetic and magnetic energy. The eddy-viscosity model is defined as

$$\tau_{ij} - \frac{1}{3}\delta_{ij}\tau_{kk} = -2\nu_t \overline{S}_{ij} \quad (6)$$

where $\delta_{ij} = 1$ if $i = j$ and zero otherwise, ν_t is the eddy viscosity and $\overline{S}_{ij} = 1/2\left(\partial \overline{u}_i/\partial x_j + \partial \overline{u}_j/\partial x_i\right)$ is the deformation tensor of the resolved field.

3.1 Smagorinsky Model

The earliest SGS model employed in LES, is the Smagorinsky eddy-viscosity model (Smagorinsky 1963). In Smagorinsky's model, the eddy viscosity is assumed to be proportional to the subgrid characteristic length scale $\overline{\Delta}$ and $|\overline{S}|$:

$$\nu_t = \left(C_s \overline{\Delta}\right)^2 |\overline{S}| \quad (7)$$

Here C_s is the Smagorinsky coefficient, $|\overline{S}| = \sqrt{2\overline{S}_{ij}\overline{S}_{ij}}$ is magnitude of the resolved strain rate tensor, and $\overline{\Delta}$ is the grid filter scale, typically equal to the grid spacing.

Following Lilly (1992), the constant C_s may be obtained by assuming that the cut-off wave number $k_c = \pi/\overline{\Delta}$ lies within a $k^{-5/3}$ Kolmogorov cascade for the energy spectrum $E(k) = C_k \varepsilon^{2/3} k^{-5/3}$ and requiring that the ensemble-averaged subgrid dissipation is identical to ε. An approximate value for the constant is then:

$$C_S = \frac{1}{\pi}\left(\frac{3}{2}C_K\right)^{-3/4} \quad (8)$$

For a Kolmogorov constant of $C_K \simeq 1.4$, this yields $C_S \simeq 0.18$. However, C_s should have a less value in order to weaken the effect of diffusion in SGS. Deardorff (1970) used $C_s = 0.1$ (also with filter width equal to grid size) which got a better result. Piomelli (1988) found the optimum value of C_s to be around 0.1 (again assuming the filter width to be equal to the grid size).

In our investigation, we use $C_s = 0.1$ to study the turbulent flows in curving duct and water turbine.

3.2 Dynamic Model

The dynamic procedure to model the τ_{ij} tensor was first introduced by Germano (1991). It is based on the assumption of similarity between different scales in the inertial range of the energy spectrum. A second filter (the test filter) with width $\tilde{\Delta}$ larger than $\overline{\Delta}$ is introduced. Applying the test filter to the equations of motion, we can obtain the SGS stress

$$T_{ij} = \widetilde{u_i u_j} - \tilde{\overline{u}}_i \tilde{\overline{u}}_j \quad (9)$$

T_{ij} and τ_{ij} are related by the Germano identity.

$$L_{ij} = T_{ij} - \tilde{\tau}_{ij} = \widetilde{\overline{u}_i \overline{u}_j} - \tilde{\overline{u}}_i \tilde{\overline{u}}_j \quad (10)$$

which relates the resolved turbulent stress L_{ij}, which can be calculated explicitly, to the SGS stresses at the test and grid levels, T_{ij} and τ_{ij}.

Assuming that the same functional form can be used to parametrize both T_{ij} and τ_{ij} (the Smagorinsky model, for example).

$$\tau_{ij} = -2C_S\bar{\Delta}^2\left|\bar{S}\right|\bar{S}_{ij},\ T_{ij} = -2C_S\tilde{\bar{\Delta}}^2\left|\tilde{\bar{S}}\right|\tilde{\bar{S}}_{ij} \tag{11}$$

where $\left|\bar{S}\right|$ and $\bar{\Delta}$ have the same definition in the SM, $\tilde{\bar{S}}_{ij} = 1/2\left(\partial\tilde{\bar{u}}_i/\partial x_j + \partial\tilde{\bar{u}}_j/\partial x_i\right)$, $\left|\tilde{\bar{S}}\right| = \sqrt{2\tilde{\bar{S}}_{ij}\tilde{\bar{S}}_{ij}}$. We obtain five equations in the unknown coefficient C_S. Applying a least square technique to the equations (Lilly, 1991), a value for the Smagorinsky model coefficient is obtained

$$C_S = -\frac{1}{2}\frac{L_{ij}M_{ij}}{M_{ij}^2} \tag{12}$$

where $M_{ij} = \bar{\Delta}^2\left(\widetilde{\left|\bar{S}\right|\bar{S}_{ij}}\right) - \tilde{\bar{\Delta}}^2\left|\tilde{\bar{S}}\right|\tilde{\bar{S}}_{ij}$.

3.3 Wall-Adapting Local Eddy Viscosity Model

In this model, the SGS viscosity is evaluated using the square of the velocity gradient tensor; it is also negligible in laminar flow regions and in the viscous sublayer and it has proper near wall behavior (Nicoud and Ducros, 1999).

The SGS viscosity of the WALE model is taken as

$$\nu_t = L_s^2\frac{\left(S_{ij}^d S_{ij}^d\right)^{3/2}}{\left(\bar{S}_{ij}\bar{S}_{ij}\right)^{5/2} + \left(S_{ij}^d S_{ij}^d\right)^{5/4}} \tag{13}$$

where $\bar{S}_{ij}$ is same as mention in the front. $L_s = \min\left(\kappa d, C_w V^{1/3}\right)$, and $S_{ij}^d = \left(\bar{g}_{ij}^2 + \bar{g}_{ji}^2\right)/2 - \delta_{ij}\bar{g}_{kk}^2/3$, $\bar{g}_{ij} = \partial\bar{u}_i/\partial x_j$.

It is verified to have the proper y^3 near wall behavior. We can assign to $C_w = 0.325$ in this paper.

3.4 Scale-Dependent Dynamic Model

Recently, Porté-Agel et al. (2000) proposed a scale-dependent dynamic model, a modification of the dynamic procedure that allows the model coefficient to change with scale (i.e. not assuming that $C_S^2(\bar{\Delta}) = C_S^2(2\bar{\Delta})$). We can still write down the Germano identity for the Smagorinsky model. However, now M_{ij} is not fully determined but also depends on the ratio of the coefficients according to (Menevean and Lund, 1997)

$$M_{ij} = 2\bar{\Delta}^2\left(\widetilde{\left|\bar{S}\right|\bar{S}_{ij}} - 4\frac{C_S^2(2\bar{\Delta})}{C_S^2(\bar{\Delta})}\left|\tilde{\bar{S}}\right|\tilde{\bar{S}}_{ij}\right) \tag{14}$$

Note that we introduce a new variable $\beta = C_S^2(2\bar{\Delta})/C_S^2(\bar{\Delta})$. For scale invariant situations, $\beta = 1$. In order to obtain a dynamic value for β, we employ a second test filter at scale $\hat{\Delta} > \bar{\Delta}$, e. g. $\hat{\Delta} = 4\bar{\Delta}$. Writing the Germano identity between scale $\bar{\Delta}$ and $4\bar{\Delta}$ yields

$$Q_{ij} - \frac{1}{3}\delta_{ij}Q_{kk} = C_S^2 N_{ij} \tag{15}$$

where $Q_{ij} = \widehat{\bar{u}_i\bar{u}_j} - \hat{\bar{u}}_i\hat{\bar{u}}_j$,

and $N_{ij} = 2\Delta^2\left(\widehat{\left|\tilde{\bar{S}}\right|\tilde{\bar{S}}_{ij}} - 4^2\frac{C_S^2(4\Delta)}{C_S^2(\Delta)}\left|\hat{\tilde{\bar{S}}}\right|\hat{\tilde{\bar{S}}}_{ij}\right)$

We can obtain another equation for $C_S^2(\bar{\Delta})$:

$$C_S^2(\bar{\Delta}) = \frac{\left\langle Q_{ij}N_{ij}\right\rangle}{\left\langle N_{ij}N_{ij}\right\rangle} \tag{16}$$

Setting equation (16) equal to (12) yields an equation of the form

$$\left\langle L_{ij}M_{ij}\right\rangle\left\langle N_{ij}N_{ij}\right\rangle - \left\langle Q_{ij}N_{ij}\right\rangle\left\langle M_{ij}M_{ij}\right\rangle = 0 \tag{17}$$

More detailed descriptions can be found in Porté-Agel et al. (2000). In this paper, we study the performance of the scale-dependent dynamic model in simulations of curving duct flows.

4 Results and Discussion

As a typical example, the flow through a closed curved duct is provided to investigate the performance of different SGS models. This flow field presents large recirculation zones, secondary vortices and in general, three-dimensional phenomena. The curved duct flow is widely existed in the engineering, such as in centrifugal pump inner, draft tube of water turbine, inlet of some flying device and so on. All those object have a remarkable characteristic which have a visible secondary flow in elbow bend.

In the present paper, we use a curved duct which has a same size with Taylor et al. (1982). The average radius is 92mm, the length of side in square cross-section is 40mm, the straight tube before bend is 150mm, and the straight tube after bend is 300mm, as shown in Fig. 1. In this figure, $X_h = X/D$, $Y^*(Y) = 2Y/D$, $r^* = (r - r_o)/(r_i - r_o)$, where D is the length of side in square cross-section, r_i and r_o are inner and external radius of curved duct, respectively.

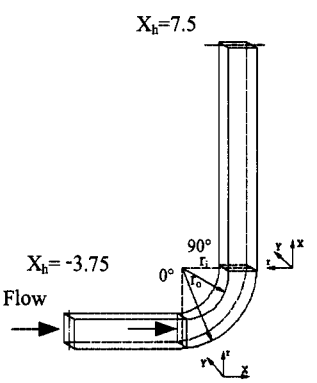

Fig. 1 Geometry and coordinate system of curved duct

Ten cross-sections are obtained along the width direction from $Y = 2$mm to $Y = 20$mm. We choose $Y = 20$mm cross-section which is a symmetrical plane of curved duct. Then, a comparison of the numerical and experimental velocity vector is made. Figure 2 shows the experimental velocities, and Fig. 3 shows the numerical results by using the SGS stresses model including the SM, DM, WALE and SDDM.

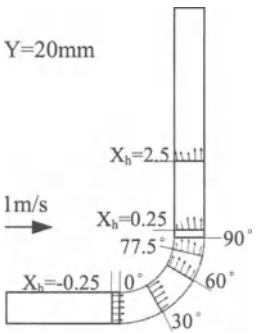

Fig. 2 Experimental velocity vector in Y=20mm

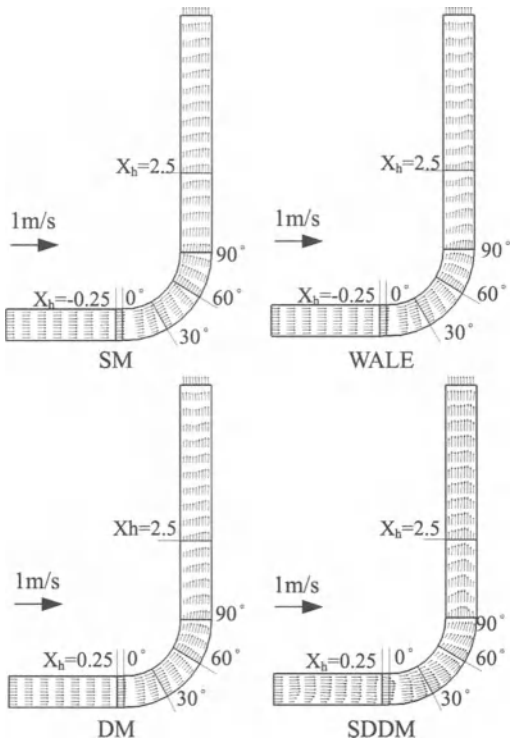

Fig. 3 Numerical velocity vector in Y=20mm

From Fig. 3 we can know that the velocity is decrease gradually from the concave to convex wall before 30° cross-section in SM, WALE and SM, and this law is unobvious in SDDM. The centrifugal force has a visible strengthen, which make the difference of velocity reduce between the convex and concave wall after 60° cross-section. Comparison with the results of experimental velocity vector in $Y = 20$mm, we can observed that the WALE, SM and DM are able to predict the local acceleration of the axial velocity close to the convex wall, and the WALE has the best behavior. Contrarily, the SDDM has a poor behavior.

In order to observe the flow in cross-section of length direction and compare the computational results of the four SGS models, we choice seven cross-sections at $X_h = -0.25$, $\theta = 30°$, $\theta = 60°$, $\theta = 77.5°$, $\theta = 90°$, $X_h = 0.25$ and $X_h = 2.5$ and compare the numerical magnitude contours of velocity with the experimental. We only compare $X_h = -0.25$ cross-section in the present paper. In these plots, the left boundary is the convex wall, the right boundary is the concave wall and the upper and lower boundaries correspond to the top at bottom walls of the curved duct.

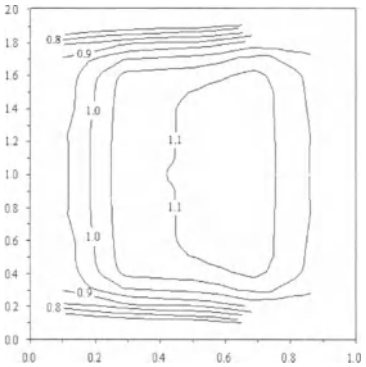

Fig. 4 Experimental contour of velocity in $X_h = -0.25$

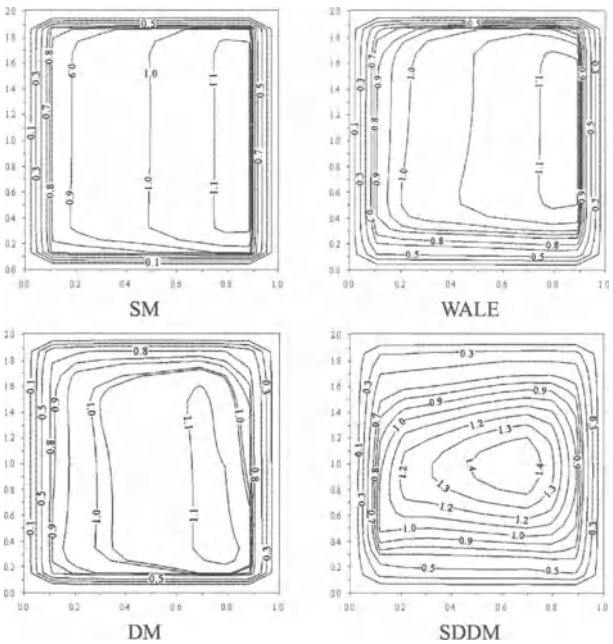

Fig. 5 Numerical contour of velocity in $X_h = -0.25$

The comparative plots of the computed and measured magnitude contours of velocity, as shown in Fig. 4 and Fig. 5, we can obtain that the WALE, SM and DM are better to predict the turbulent flow than the SDDM. Meanwhile, the results also show that the WALE and the DM are agreed well with experimental results, indicating that the two models have a better behavior to simulate turbulent flow than the SM and the SDDM. As a special application, we choose a Francis turbine runner to investigate the turbulent flow by using the four SGS models.

As we all know, the flow in the Francis turbine is a periodic flow, so a single flow region is chose and it has an extension in the inlet and outlet zones, which is shown in Fig. 6. Structured hexahedral cells are generated to define zones (the nodes are 73185, 94605, and 117810 in inlet zone, runner zone and outlet zone, respectively). A localized refinement of mesh is employed at regions close to wall boundary. The grid generated for the geometry is shown in Fig. 7.

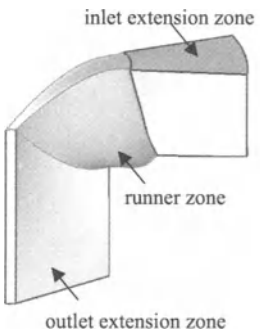

Fig. 6 Single flow region of turbine

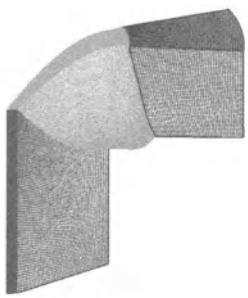

Fig. 7 Grid assembly of the turbine

The modeled boundary conditions are the ones considered with more physical meaning for turbomachinery flow simulations, that is, velocity at the inlet is given. The second boundary condition, $\left.\frac{\partial \phi}{\partial n_{outlet}}\right|_{outlet} = 0$ ($\phi = u, v, w$), is employed at the outlet cross-section. Also, the no-slip condition with a logarithmic law for the boundary layers have been imposed over the runner blades and walls. Meanwhile, periodic condition is given at the runner inlet and outlet extension zones.

Four SGS models are employed in the Francis turbine which is mentioned in front of paragraph, and the results of the WALE and the DM are discussed.

Fig. 8 shows the computed pressure distribution with WALE and dynamic model. It indicates that the pressure gradient is gradually decreased from inlet to outlet on blade. The maximum value of pressure appears at the inlet region near band side, and the minimum value of pressure can be observed at the outlet region near crown. This result is coincident with actual pressure distribution.

Fig. 9 shows the computed streamline with WALE and dynamic model. It is clearly seen that vortex flow appears at inlet/band corner on the runner. Moreover, a secondary flow can been found at the crown region near outlet on the runner.

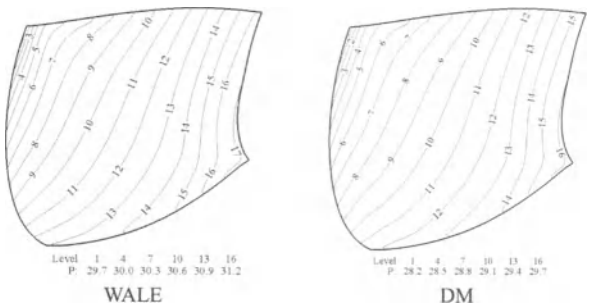

Fig. 8 Pressure distribution on the intermediate cross-section of runner in water turbine

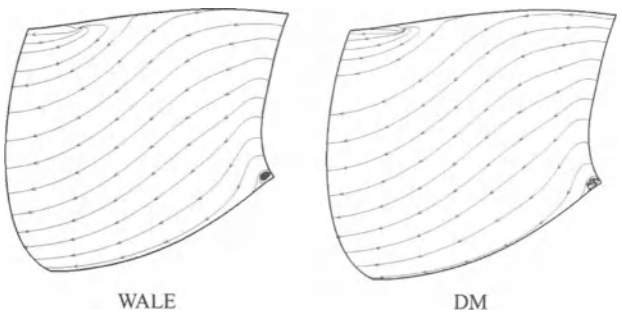

Fig. 9 Streamline on the intermediate cross-section of runner in water turbine

5 Conclusions

Four SGS models of LES, including the Smagorinsky model, the dynamic model, the wall-adapting local eddy viscosity model and the scale-dependent dynamic model, were implemented for predicting the turbulent flow in water turbine, and comparison the numerical results with the experimental results with four SGS models at the curved duct. On the basis of these results presented and discussed in front of paragraph, we draw the main conclusions below:

The WALE model can be a better choice to turbulent flow simulations. This model is also able to give acceptable predictions for turbulent flows in water turbine which are validated in the curved duct with experimental

results. Meanwhile, the dynamic model also has an acceptable behavior to simulate turbulent flow, but its behavior is not as good as the WALE model, and better than the Smagorinsky model. However, the SDDM has a bad performance to simulate turbulent flows of complex geometry. Maybe, this model is only applies to neutral atmospheric boundary layer.

The result of pressure distribution with the WALE model and the dynamic model in water turbine is coincident with actual pressure distribution. Furthermore, it can clearly compute the vortex flow at inlet/band corner on the runner with the two models.

In future investigations, we will study other SGS stresses model and look for a good model which can able to give accurate predictions for turbulent flows of complex geometry.

Acknowledgements

The authors would like to acknowledge the financial supports given by the National Nature Science Foundation of China (90510007, 50779070) and by the Program for New Century Excellent Talents in University of China (NCET-04-0133).

References

Deardorff, J.W., 1970, "A numerical study of three-dimensional turbulent channel flow at large Reynolds numbers", *Journal of Fluid Mechanics*, Vol. 41, pp. 453 – 480

Fernando Porté-Agel, 2000, "A scale-dependent dynamic model for large-eddy simulation: application to a neutral atmospheric boundary layer", *Journal of Fluid Mechanics*, Vol. 415, pp. 261 – 284

Germano, M., Piomelli, U., Moin, P., et al,. 1991, "A dynamic subgrid-scale eddy viscosity model", *Physics of Fluids*, Vol. A 3(7), pp. 1760 – 1765

Gyllenram, W., Nilsson, H., Davidson L.. 2006, "Large eddy simulation of turbulent swirling flow through a sudden expansion". *23rd IAHR Symposium*, Yokohama. pp. 1 – 10

Leonard, A., 1974, "Energy cascade in large eddy simulations of turbulent fluid flows", *Adv. Geophys*, Vol. 18, pp. 237 – 248

Lilly, D. K., 1992, "A proposed modification of the Germano subgrid-scale closure method", *Physics of Fluids*, Vol, A 4(3), pp. 633 – 635

Menevean, C., Lund, T. S., 1997, "The dynamic Smagorinsky model and scale-dependent coefficients in the viscos range of turbulence", *Physics of Fluids*, Vol. 9, pp. 3932 – 3934

Nicoud, F., Ducros, F., 1999, "Subgrid-scale stress modelling based on the square of the velocity gradient tensor", *Flow, Turbulence and Combustion*, Vol. 62, pp. 183 – 200

Piomelli, U, Moin, P., Ferziger. J. H., 1988, "Model consistency in large eddy simulation of turbulent channel flows", *Physics of Fluids*, Vol. 31(7), pp. 1884 – 1891

Smagorinsky, J., 1963, "General circulation experiments with the primitive equations, Part 1: the basic experiment. Mon", *Weath. Rev*, Vol. 91, pp. 99 – 164

Vreman, A. W., 2004, "The adjoint filter operator in large-eddy simulation of turbulent flow", *Physics of Fluids*, Vol. 16(6), pp. 2012 – 2022

The 4th International Symposium on Fluid Machinery and Fluid Engineering
November 24-27, 2008, Beijing, China
NO. 4ISFMFE-Ch31

Flow Simulation and Performance Prediction of a Kaplan Turbine

Shuhong Liu[*1], Shangfeng Wu[2], Michihiro Nishi[3] and Yulin Wu[1]

[*1] Dept. of Thermal Engineering, Tsinghua University, Tsinghua Garden, Haidian District, Beijing 100084, China
Tel: +86-10-6279-4735 / Fax: +86-10-6279-4735, E-mail: liushuhonhg@tsinghua.edu.com

[2] Shanghai Electric Power Generation Equipment Co., Ltd. (SEPG) Turbine Works, 333 Jiangchuan Road, Minhang District, Shanghai, China, Zip: 200240, Tel:86-21-64358331-2895, wushf2@shanghai-electric.com

[3] Senior Academy, Kyushu Institute of Technology, 1-1 Sensui-cho, Tobata-ku, Kitakyushu-shi, 804-8550, Japan

Abstract As it is almost impossible to carry out a prototype hydro-turbine experiment before the power plant is built up, rational prediction of its performance is really expected to design the turbine and to operate the turbine properly. In this paper, as the series of R&D of a numerical test stand for a prototype turbine, we treat hydraulic performances of a prototype Kaplan turbine having a runner diameter of 8 m, which are predicted by using the steady turbulent flow analysis with standard k-ε turbulence model for the entire flow passage.

Characteristics curves for on-cam operation are derived from the calculated results, and the performance hill chart is prepared for comparison with the model test results. Reasonable agreement between them encourages us to use the present simulation technique for the performance test of a prototype Kaplan turbine.

Keywords Kaplan turbine, performance prediction, steady flow simulation

Nomenclature

A	area
a_0	guide vane opening
D_1	runner diameter
g	gravitational acceleration
H	working head
H_e	Euler head
H_s	suction head
N	output
n	rotational speed
n_1'	design unit speed
Q	flow rate
Q_1'	design unit flow rate
U	rotational speed of runner
V	velocity
v_u	circumferential component of absolute velocity
Z	elevation
Z_0	number of guide vanes
Z_1	number of runner blades
η	efficiency
σ_{cr}	critical cavitation number
φ	runner blade angle

Subscripts

Cr	critical
h	hydraulic
in	inlet of domain
out	outlet of domain
p	installation
ri	runner inlet
ro	runner outlet

1 Introduction

Thinking of the efficient usage of hydro-power, Kaplan turbines have been widely installed at those sites of low head hydro-power, as they provide the efficiency higher than 90% in the wide range of operation. And we now see such a large machine having the runner diameter more than 8m. Though the model test is generally made to examine its performance, it is quite convenient if we will be able to use CFD techniques at the design stage and at

the test stage of the turbine. From this aspect, Gehrer and Schmidl (2006) and Shingai et al. (2006) applied numerical flow simulation for designing of Kaplan runners.

Regarding typical numerical studies to treat hydro-turbines, the following are mentioned here. Ruprecht et al. (2000, 2002) reported the unsteady simulation of an entire Francis turbine. Skotak (2000) modeled the unsteady flow of helical vortex in the turbine draft tube by LES. And Rudolf and Skotak (2001), Sick et al (2002) and Paik and Sotiropoulos (2004) conducted the flow simulation in the elbow draft tube and compared their results with test data. Muntean et al. (2004) completed the flow analysis in the spiral case and distributor of a Kaplan turbine.

In this paper, as the series of R&D of a numerical test stand for a prototype turbine, we study the hydraulic performances of a prototype Kaplan turbine having a runner diameter of 8 m, which are predicted by using the steady turbulent flow analysis with standard k-ε turbulence model for the entire flow passage from the inlet of spiral casing to the exit of draft tube. Characteristics curves for on-cam operation are derived from the calculated results, and the performance hill chart is prepared for comparison with the model test results in order to clarify the usability of the present numerical technique. Further, features of the flow are investigated as typical examples of Kaplan turbine.

2 Numerical Simulation of Turbulent Flow Through a Kaplan TurbinE

The conventional turbulent flow analysis based on the continuity equation and Reynolds Averaged N-S equation with the standard k-ε turbulence model is adopted to simulate the steady flow through a prototype Kaplan turbine, computational domain of which is shown in Fig. 1. The finite volume method is adopted to make the governing equations under the unstructured mesh for space discretization. The second-order central difference is used to the source term and the diffusion term of the equations, and the second-order upwind difference is for the convective term.

Following the actual situation of Kaplan turbine operation, the working head H is selected as one of input data in the simulation. Thus, the flow rate through the turbine is predicted by the iterative way for each operating condition given by the guide vane opening and the setting angle of runner blade. To get its solution, the following procedure is used: The total pressure is set initially at the outflow plane of the computational domain or the exit of the draft tube assuming the flow rate, since the static pressure is prescribed from the level of tail water surface. As the working head is given, it is possible to specify the velocity and the static pressure at the inlet of spiral casing as the initial boundary conditions of inflow plane, where the uniform flow is assumed. The non-slip flow condition on the solid walls of the domain and the wall function near the solid walls are also used. From the assumed inflow and outflow conditions, the steady flow in the domain is calculated. If the difference between assumed and calculated flow-rates is not tolerable, the calculation is repeated using a corrected flow rate until the solution is regarded as converged.

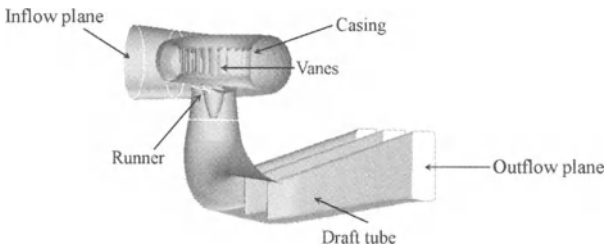

Fig. 1 Computational domain for Kaplan turbine

3 Test Kaplan Turbine and Parameters

A prototype Kaplan turbine, primary specifications of which are listed in Table 1, is numerically tested by using the above 3D steady turbulent flow calculation method. Fig. 2 shows the hill chart of the turbine, which is obtained from the test results of model turbine considering the scale effect.

Table 1 Primary specifications of prototype Kaplan turbine and parameters

Runner blade angle	φ (°)	5 ~ 25
Guide vane Opening	a_0 (%)	0 ~ 95
Design unit speed	n_1' (r/min)	118.6
Design unit flow rate	Q_1' (l/s)	805
Rotational speed	n (r/min)	107
Working head	H (m)	52.2
Suction head	H_s (m)	3.5
Runner diameter	D_1 (m)	8
Number of runner blades	Z_1	6
Number of guide vanes	Z_0	24

As all components, spiral casing, stay vanes, guide vanes, runner and draft tube are included in the computational domain, the unstructured tetrahedron mesh generation is

used (Hassan et al. 2000). Table 2 shows the mesh scheme for each component of the turbine passage, so that 2,578,000 mesh and 543,000 crunodes of the mesh are used to represent the whole flow passage.

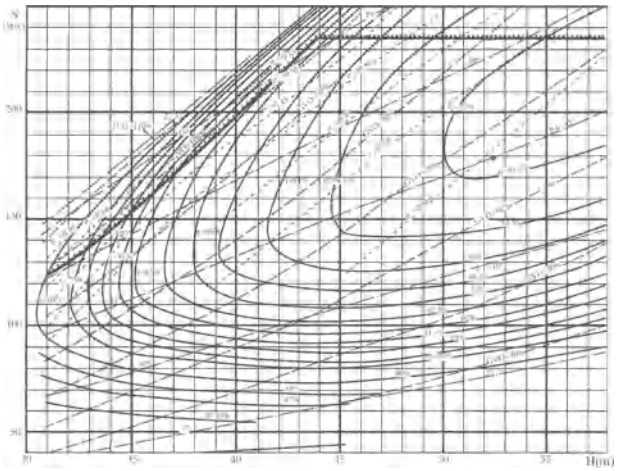

Fig. 2 Characteristic chart of the prototype turbine (GVO: Guide vane opening, BA: Blade angle, η: Efficiency, σ_{cr} -Cavitation number)

Table 2 Mesh for each component of the turbine passage

	Casing and vanes	Runner	Draft tube
Crunodes	171,000	254,000	118,000
Mesh	813,000	1,204,000	561,000

The hydraulic efficiency of Kaplan turbine is expressed as

$$\eta_h = H_e / H \tag{1}$$

In the above equation, H_e is the Euler head calculated from the velocity data at the runner inlet (*ri*) and outlet (*ro*) by using the following equation:

$$H_e = \frac{1}{gQ}\left[\left(\iint_{A_{ri}} u v_u v_n dA\right)_{ri} - \left(\iint_{A_{ro}} u v_u v_n dA\right)_{ro}\right] \tag{2}$$

where Q denotes the flow rate, which is given by

$$Q = \iint_{A_{in}} v_n dA = \iint_{A_{out}} v_n dA$$

It is noted that v_n is the velocity component normal to the surface, v_u is the circumferential component of absolute velocity and u is the rotational speed of runner. And g is gravitational acceleration. A_{in} and A_{out} are areas of inflow and outflow planes.

The working head of turbine H is:

$$H = H_{in} - H_{out} = H_{in} - \left[\left(\frac{p}{\rho g} + z\right)_{out} + \frac{(Q/A)^2_{out}}{2g}\right] \tag{3}$$

where p is static pressure, z is elevation ($z = 0$: guide vane center), and ρ is water density.

After the flow rate through the turbine Q is predicted, the output of the Kaplan turbine is also determined from:

$$N = \rho g H Q \eta_h \tag{4}$$

The pressure level for its minimum point is evaluated from the following cavitation number:

$$\sigma = \frac{h_{VA}}{H} = \left(\frac{p_s - p_K}{\rho g} + \frac{V_s^2}{2g} + z_s - z_K\right) \Big/ H \tag{5}$$

where h_{VA} is the dynamic vacuum head, p_s is the pressure at draft tube outlet, p_K and z_K are the pressure and elevation respectively at the lowest pressure point K on the suction surface of runner blade, V_s is velocity at draft tube outlet, and z_s is the outlet elevation.

If σ_p is the installation cavitation number calculated from the turbine setting, we obtain:

$$\frac{p_K - p_v}{\rho g H} = \sigma_p - \sigma \tag{6}$$

When $\sigma_p = \sigma = \sigma_{cr}$, then $p_K = p_v$. This indicates that the lowest pressure on the suction surface of runner blade equals to the vapor pressure at a working temperature. At this condition, the cavitation must occur at K on the runner surface. Thus, a turbine unit is to be installed at the location where $\sigma_p > \sigma$.

4 Prediction of Performances for Kaplan Turbine

Features of double-regulated Kaplan turbines are high efficiency, minimal swirl at runner outlet and low risk of draft tube surge, as the on-cam control both of guide vane opening and of runner blade setting is used at the operation. Thus, it is essential to predict the on-cam position of guide vane opening at each setting angle of runner blade under a certain working head. Fig. 3 shows the general way to determine the on-cam control condition. Once the blade angle is set, the curve of efficiency $\eta = f_\varphi$ $(a_0, \varphi = const.)$ is obtained with respect to the guide vane opening. After preparing such curves corresponding to prescribed blade angles, the peak efficiency curve $\eta = f(Q_1', n_1')$ can be drawn as the envelope around those

curves. Then, the optimal guide vane opening is pinpointed for every blade angle. Finally, the on-cam condition expressed as $\varphi = g\,(a_0\,,\,n_1')$ is determined for the working head, as shown in Fig. 3.

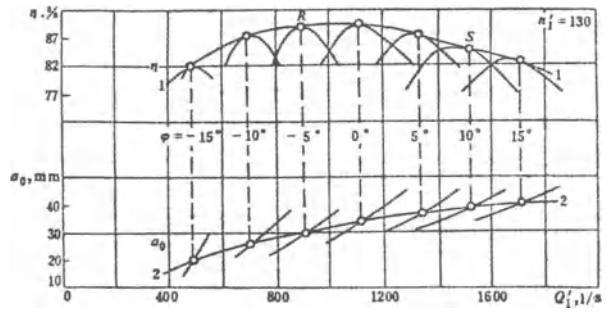

Fig. 3 Determination of on-cam operating condition

Following the above procedure, the on-cam characteristics of the prototype Kaplan turbine were predicted by using the turbulent flow simulation, where the following conditions were selected:

Working head: 32m, 37m, 42m, 47m, 52.2m, 55m and 57m Blade setting angle: 5°～25°with an increment of 2.5° Guide vane opening: 5 cases near the peak efficiency

As typical numerical results, those for the working head H=52.2m are summarized in Table 3, where efficiency η, critical cavitation number σ_{cr}, flow rate Q, and output N are shown against the operating condition specified by blade setting angle φ and guide vane opening a_0. And those results are plotted in Fig. 4, where the overall efficiency curve and critical cavitation number curve are plotted against the output to demonstrate the on-cam performance graphically. Table 4 shows the numerical values of the on-cam performance for three cases, which are compared with the experimental results from the model test considering the scale effect. From the figure, we can see the present numerical method is basically acceptable to predict the on-cam performance of a Kaplan turbine, though slight differences between them are observed and further improvement of the method is still expected.

After post-processing the results of numerical simulation for six other cases of working head, which is similar to that of H = 52.2m case, the characteristic chart of the prototype turbine is drawn in Fig. 5. The abscissa is the working head, H (unit: m), and the ordinate is output power, N (unit: MW) for direct comparison with Fig. 2. The limits of turbine operation in the power station are shown by red lines. Black dash-dotted lines show the runner blade angle, (which is expressed as BA in Fig. 2), orange dashed lines the guide vanes opening (GVO in Fig. 2), pink dashed lines the cavitation number σ_{cr}, and blue solid lines the efficiency η. We can see that fair reproduction of the performance is achieved, though further improvement of the technique is still expected.

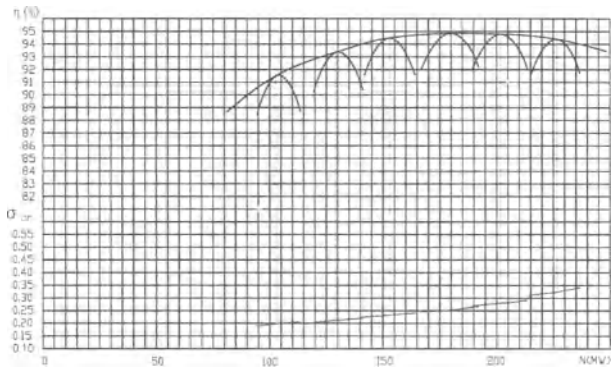

Fig. 4 On-cam performance for H = 52.2m

Table 3 Numerical results for the working head H = 52.2m

φ (°)	a_0 (%)	43	45	47	49	51
7.5	η (%)	88.4	90.3	91.7	90.2	88.5
	σ_{cr}	0.19	0.193	0.196	0.199	0.203
	Q (m³/s)	189.9	197.7	208	222.5	228.9
	N (MW)	94.2	97.8	103	110	113.1
10	a_0 (%)	50	52	54	56	58
	η (%)	90.3	92.1	93.5	92.3	90.7
	σ_{cr}	0.205	0.208	0.212	0.215	0.219
	Q (m³/s)	241.6	249.7	264.2	279.4	287.3
	N (MW)	119.2	123.1	130	137.3	141.1
12.5	a_0 (%)	57	59	61	63	65
	η (%)	91.6	93.2	94.5	93.3	91.8
	σ_{cr}	0.225	0.229	0.233	0.237	0.242
	Q (m³/s)	288	296.8	312.1	326.3	335.8
	N (MW)	141.4	145.6	152.9	159.6	164.1
15	a_0 (%)	63	65	67	69	71
	η (%)	92.1	93.7	94.9	93.8	92.3
	σ_{cr}	0.246	0.25	0.254	0.258	0.263
	Q (m³/s)	343	353.1	369.6	385.8	395.9
	N (MW)	167.5	172.2	180	187.6	192.3
17.5	a_0 (%)	68	70	72	74	76
	η (%)	91.9	93.5	94.8	93.8	92.2
	σ_{cr}	0.269	0.274	0.279	0.284	0.29
	Q (m³/s)	389.9	400.2	416.1	432.5	443.5
	N (MW)	189.5	194.3	201.7	209.1	214.2
20	a_0 (%)	74	76	78	80	82
	η (%)	91.6	93.2	94.6	93.5	92.1
	σ_{cr}	0.311	0.318	0.325	0.332	0.34
	Q (m³/s)	446.1	451.8	465.1	482.5	492.2
	N (MW)	215.4	219.1	226.2	232.2	236.8

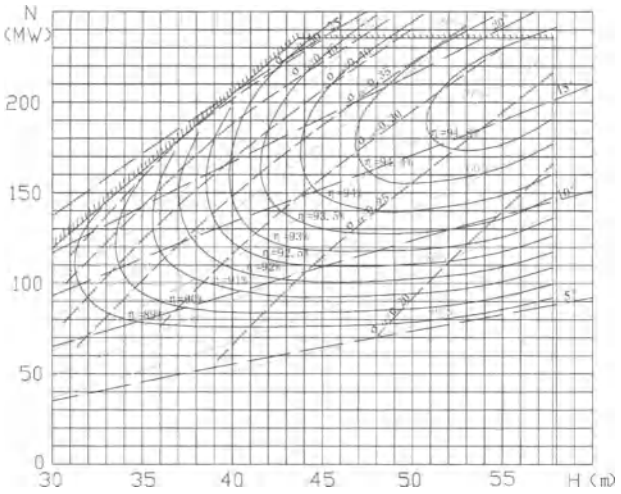

Fig. 5 Characteristic chart from numerical simulation

5 Simulation of the Flow in Kaplan Turbine

As the turbine performance is reasonably predicted, features of the flow are studied using the numerical results. Figs. 6 – 11 show the velocity and pressure distributions on several sections of the prototype Kaplan turbine at the on-cam operating condition, which is specified by guide vane opening of 46.6%, blade angle of 7.5°, working head of 52.2m, the suction head of 9m and output of 102MW. Thus, the operating condition nearly corresponds to the half load.

From pressure and velocity distributions in Fig. 6, the non-uniform flow is observed at the exit of spiral casing. Velocity is higher near the inlet side and it decreases in the circumferential direction to some extent. This is understandable because the casing geometry is decided based on the rated load. This non-uniformity is reduced in the stay vanes and guide vanes, and the flow discharging from the guide vanes is almost regarded as axisymmetric at this low capacity operation, as shown in Fig. 7.

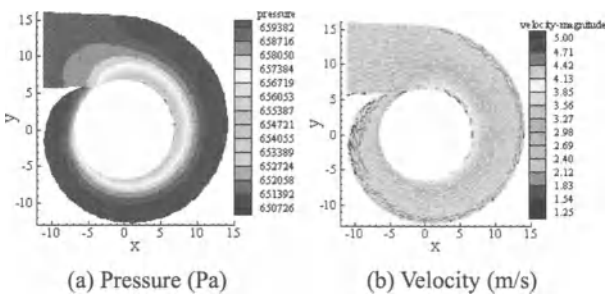

Fig. 6 Pressure and velocity on spiral casing central section

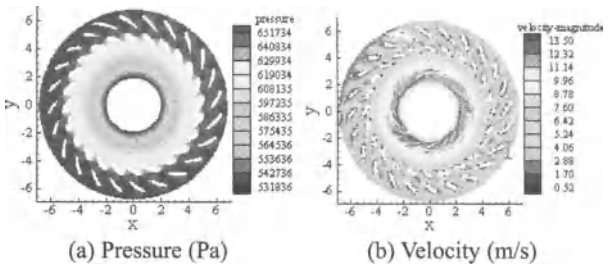

Fig. 7 Pressure and velocity on central section of stay vanes and guide vanes

Figure 8 (a) shows the general trend that pressure decreases from leading edge to trailing edge along the pressure surface of runner blade. It also shows that the pressure varies in the radial direction due to the centrifugal force. Distribution of pressure on the suction surface is observed in Fig. 8 (b). The effect of tip clearance on the flow near the surface of discharge ring is observed in the pressure pattern shown in Fig. 8 (c).

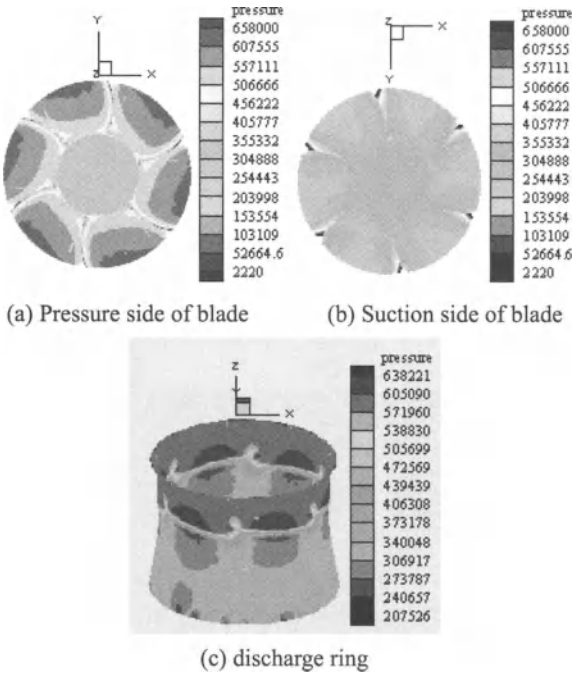

Fig. 8 Pressure (Pa) in runner and discharge ring

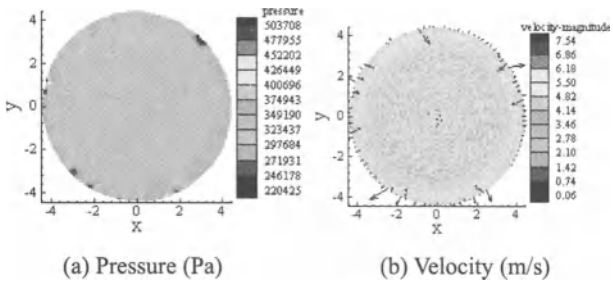

Fig. 9 Pressure and velocity distributions at draft tube inlet

As shown in Fig. 9 (a), the pressure distribution in the radial direction is not clearly observed at the draft tube inlet, and there are small areas with high or low pressure at the outskirt of the section. Figure 9 (b) shows that incoming flow to the draft tube has some amount of swirl, which looks like a clockwise vortex. Due to this swirling flow, low velocity region appears just downstream of the draft tube inlet, as shown in Fig. 10 (b). Fig. 11 shows the pressure distribution at the draft tube outlet, where similar pattern is observed in every channel.

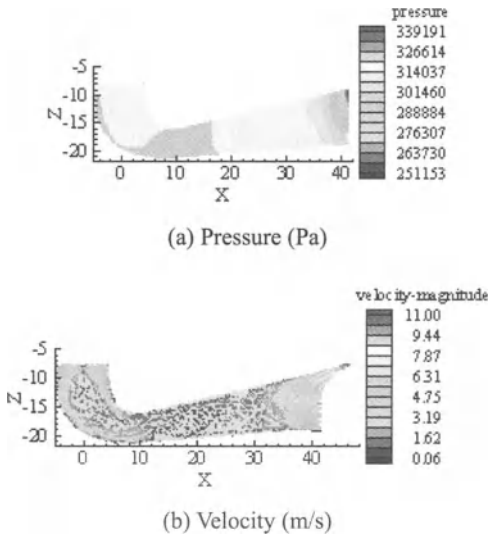

(a) Pressure (Pa)

(b) Velocity (m/s)

Fig. 10 Pressure and velocity on draft tube central section

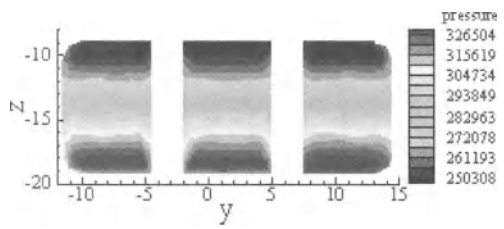

Fig. 11 Pressure (Pa) on outlet section of draft tube

6 Concluding Remarks

In this paper, as the series of R&D of a numerical test stand for a prototype turbine, we treat hydraulic performances of a Kaplan turbine having a runner diameter of 8m, which are predicted by using the steady turbulent flow analysis with standard k-ε turbulence model for the entire flow passage, and the following remarks are obtained:

(1) Prediction of the performances is robustly conducted by the computational method, where the working head is used as the given condition.

(2) The satisfactory agreements are observed between the numerical on-cam performances and the results estimated from the model tests.

(3) Characteristic chart of the Kaplan turbine is reasonably reproduced by the present simulation.

(4) Features of the flow in each component are clarified from the numerical results.

Acknowledgements

The research is support by Chinese National Foundation of Natural Science (No. 90410019)

References

Gehrer, A., Schmidl, R., Sadnik, D., 2006, Kaplan turbine runner optimization by numerical flow simulation (CFD) and an evolutionary algorithm, *Proceedings of 23rdIAHR Symposium on Hydraulic Machinery and Systems*, October 17-21, Yokohama, F125

Shingai, K., et al., 2006, Optimization of axial turbine runner blade using a simulated annealing algorithm, *Proceedings of 23rdIAHR Symposium on Hydraulic Machinery and Systems*, October 17-21, Yokohama, F141

Ruprecht, A., et al., 2000, Numerical simulation of a complete Francis turbine including unsteady rotor/stator interactions, *Proceedings of the 20th IAHR Symposium on Hydraulic Machinery and Systems*, August 6-9, Charlotte, USA, CFD-S03

Ruprecht, A., et al., 2002, Simulation of vortex rope in a turbine draft tube, *Proceedings of the XXIst IAHR Symposium on Hydraulic Machinery and Systems*, September 9-12, Lausanne, A640

Skotak, A., 2000, Of the helical vortex in the turbine draft tube modeling. *Proceedings of the 20th IAHR Symposium on Hydraulic Machinery and Systems,* August 6-9, Charlotte, USA, CFD-G02

Rudolf, P., Skotak, A., 2001, Unsteady flow in the draft tube with elbow. Part B-Numerical investigation, *10th International IAHR Work Group Meeting*, Trondheim, Norway

Sick, M., Doerfler, P., Casey, M., 2002, CFD simulation of the draft tube vortex. *Proceedings of the XXIst IAHR Symposium on Hydraulic Machinery and Systems*, September 9-12, Lausanne, A31

Paik, J., Sotiropoulos, F., 2004, Numerical simulation of flow in a hydroturbine draft tube using unsteady statistical turbulence models, *Proceedings of 22nd IAHR Symposium on Hydraulic Machinery and Systems*, June 29 – July 2, Stockholm, A10(1)

Muntean, S, et al. 2004, 3D Flow analysis in the spiral case ad distributor of a Kaplan turbine, *Proceedings of 22nd IAHR Symposium on Hydraulic Machinery and Systems*, June 29 - July 2, Stockholm, A10 (2)

Hassan O, et al. 2000, Unsteady flow simulation using unstructured meshes, *Computer Methods in Applied Mechanics and Engineering*, 189(4): 1247 – 127

The 4th International Symposium on Fluid Machinery and Fluid Engineering
November 24-27, 2008, Beijing, China
NO. 4ISFMFE-Ch36

Analysis of Pressure Fluctuation in Draft Tube of Kaplan Turbine

Xiaobo Zheng, Xingqi Luo and Pengcheng Guo

Dept. of Hydropower Engineering, Xi'an University of Technology,
Pillar Box 207, No.5 South Jinhua Road, Shaanxi, Xi'an 710048, China
Tel: +86-29-8231-2720/Fax: +86-29-8323-0217
E-mail:zhengxbb@163.com

Abstract Based on a 3-D unsteady turbulent numerical simulation of the whole passage in Kaplan turbine, the unsteady flow field in draft tube was analyzed in this paper. The shape of vortex rope in draft tube was studied. The pressure fluctuation in draft tube was analyzed by the characteristics of amplitude and frequency.

Keywords Kaplan turbine, unsteady flow, pressure fluctuation, vortex rope

1 Introduction

Operation stability of the hydraulic turbine is one of the difficult problems to perplex the power generation of hydro-power station (Ref. 1,2,3). There are very complex factors to lead to unstable operation of the hydro-power units. The hydraulic reasons include four aspects, which are vortex rope in draft tube, pressure fluctuation in sealing device, Karman vortex and flow separation about outlet of the blade. The vortex rope in draft tube is the main reason to lead to unit vibration. As a result, it is important for operation stability of the hydraulic turbine to analyze the action mode and mechanism of the pressure fluctuation caused by vortex rope in draft tube.

At present, the study on vortex rope in draft tube of hydraulic turbine is done from three directions, which are theory research, test analysis and numerical simulation (CFD). Although the theory research and test analysis are still important, CFD is used more and more widely in hydraulic machinery field with the rapid development of computer technology. Powerful function and special superiority of CFD are shown gradually in research on flow in draft tube. The steady flow in draft tube of hydraulic turbine was studied by Shyy and Braaten with k-ε model (Ref. 4 and Ref. 5). A simple model for predicting the draft tube surge was developed by XM Wang with theory of eddy moving (Ref. 6 and Ref. 7). In this paper, 3-D unsteady flow in draft tube of Kaplan turbine was studied based on the unsteady turbulent numerical simulation of the whole passage in Kaplan turbine.

2 Mathematical Model and Numerical Approach

Reynolds time-averaged N-S equations and the standard k-ε model were used to simulate the flow in whole passage in Kaplan turbine with unstructured mesh and FVM. The whole passage includes scroll case, guide vanes, runner and draft tube (Fig. 1).

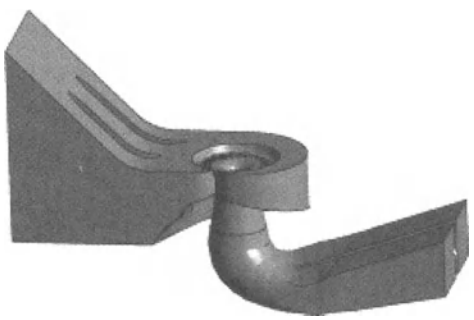

Fig. 1 Geometric model

Sliding grid method was used to deal with the rotor-stator interaction between guide vanes and runner, and also between runner and draft tube.

3 Coputational Condition

The work was conducted with the Kaplan turbine of a certain power station. Four operation conditions shown in

Table 1 were decided to be solved. The time step is 0.00467s, which equal to 1/180 runner cycle. The runner rotates 2° in one time step. Total time step equal to five runner cycles.

Table 1 Operation condition for calculation

Number	Guide vane opening of the model turbine	turning angles of the runner blade
1	10mm	5°
2	25mm	15°
3	35mm	25°
4	40mm	35°

4 Results and Analysis

4.1 Shape of vortex rope in draft tube

Taking result of condition 4 for example, pressure distribution of six time points in one runner cycle at inlet of draft tube was shown in Fig. 2. Shape of vortex rope in draft tube on different time point in one runner cycle for condition 4 was shown in Fig. 3.

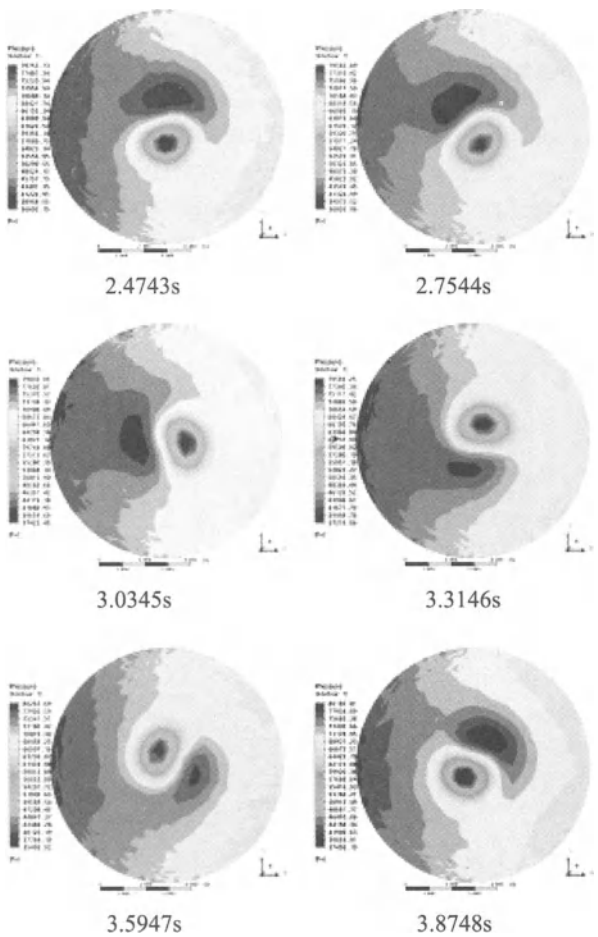

Fig. 2 Pressure distribution at inlet of draft tube for condition 4

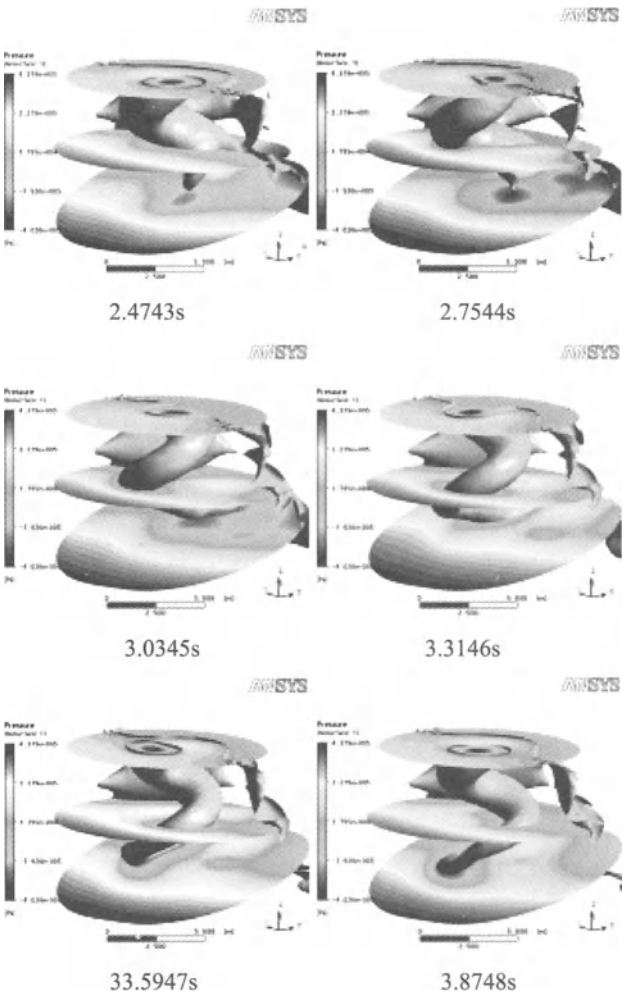

Fig. 3 Shape of vortex rope in draft tube for condition 4

According the results, there is a low frequency and low pressure vortex rope with a direction opposite to rotation direction of runner under condition 4, whose frequency is about 0.53Hz, about 0.44 times of the units running frequency (Fig. 3). The low pressure vortex rope changes to small vortex rope gradually on the effect of wall of elbow section, and flows to downstream. The intensity of the low pressure vortex core becomes weaker with the screw pitch increasing.

According to the pressure distribution at inlet of draft tube, there is a high pressure vortex core in cone section under condition with big flow (Fig.4). The position of the high pressure vortex core is symmetrical to the low frequency vortex rope. The intensity of the high pressure vortex core changes greatly with the time.

4.2 Amplitude and frequency of pressure fluctuation at inlet of draft tube

There are three points selected at inlet of draft tube to be studied (Fig. 5).

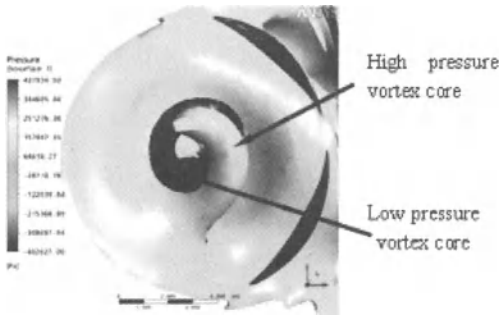

Fig. 4 High pressure vortex core in draft tube

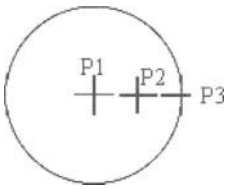

Fig. 5 Position of the points to be studied at inlet of draft tube for pressure analysis

The results indicate that the Amplitude of pressure fluctuation on the three points is less on condition 1. And the amplitude of pressure fluctuation on the three points is bigger on condition 4 (Fig. 6 and Table 2).

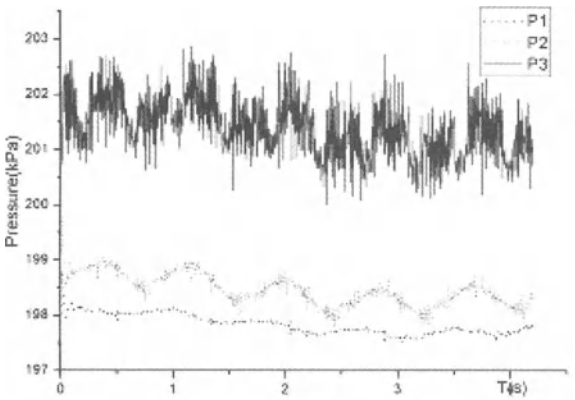

Condition 1

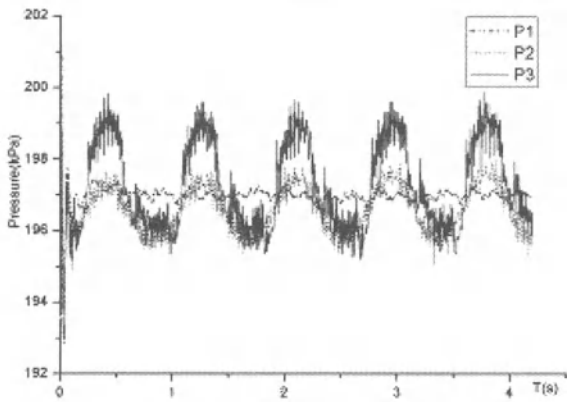

Condition 2

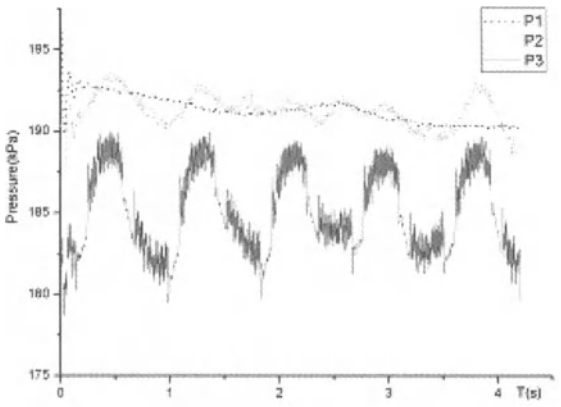

Condition 3

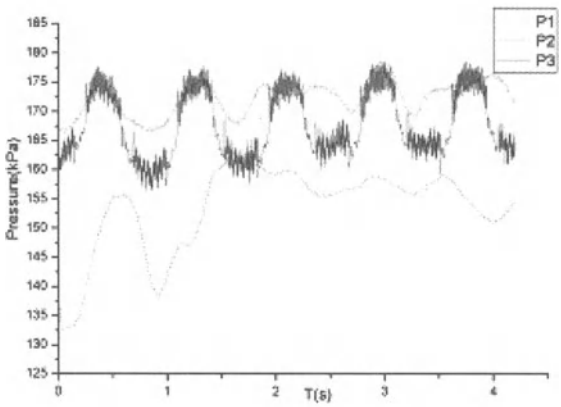

Condition 4

Fig. 6 Pressure fluctuation at inlet of draft tube

Table 2 the relative amplitude of pressure fluctuation of different point at inlet of draft tube

Number	P1	P2	P3
1	0.72%	1.10%	1.29%
2	5.58%	3.13%	3.72%
3	4.60%	4.17%	7.61%
4	10.31%	7.37%	8.75%

According to the results, the pressure at three computational points change greatly with the time. The pressure change law at P2 and P3 is more obvious. P3 locates at edge of inlet, and the pressure at P3 changes with a same period as runner rotation.

According the results, the main frequency components of the pressure fluctuation at three points of inlet include low frequency of 0.2091Hz, 0.4183Hz, 0.83646Hz, etc, which equal to 0.175-0.7 times of the units running frequency. This kind of pressure fluctuation with low frequency will transmit through the whole passage of the turbine after formed, and lead to low frequency pressure

fluctuation on the point it arrived. According the analysis results, this kind of pressure fluctuation with low frequency is one of the main vibration sources in hydraulic turbine. Also, the high frequency pressure fluctuation of 86.78Hz and 83.22Hz were found at draft tube wall, which are caused by the rotor-stator interaction between runner and draft tube.

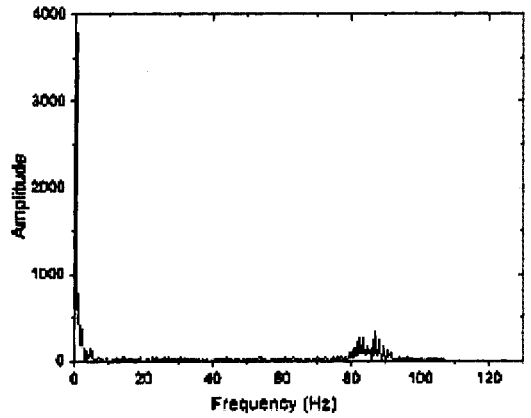

Fig. 7 Pressure fluctuation frequency domains of P12 for condition 4

5 Conclusion

The unsteady flow in whole passage of Kaplan turbine has been calculated under four given conditions. The results indicate that there is low frequency and low pressure vortex rope with a direction opposite to rotation direction of runner under condition with big flow, and also a high pressure vortex core in cone section. The main frequency components of the pressure fluctuation at inlet of draft tube are low frequency components, which equal to 0.175-0.7 times of the units running frequency. This kind of pressure fluctuation with low frequency is one of the main vibration sources in hydraulic turbine.

Acknowledgements

This work is part of a project supported by the National Natural Science Foundation of China (90410019), Specialized Research Fund for the Doctoral Program of Higher Education of China (20040700009) and Specialized Research Plan in The Education Department of Shaanxi Province of China (05JK264). The supports are gratefully acknowledged.

References

TAO Xing_ming, LIU Guang_ning. Hydraulic Stability Problem of Francis Turbine. Large Electric Machine and Hydraulic Turbine, 2002,(2): 40 – 49.(Chinese)

PAN Luoping, et al. Analysis of hydraulic stability of turbine. Journal of Changchun Institute of Technology, 2002, Vol.3(4): 41 – 43. (Chinese)

The China Institute of Water Resources and Hydropower Research. Translation Corpus of Hydraulic Vibration for Hydraulic Turbine. Beijing: China Waterpower Press, 1979, 21 – 25. (Chinese)

W Shyy, E Braaten. Three Dimensional Analysis of the Flow in Curved Hydraulic Turbine Draft Tube. Int J Num Meth in Fluid, 1986 (6): 861 – 882

T C Vu, W Shyy. Viscous Flow Analysis for Hydraulic Turbine Draft Tubes. IAHR Symposium Trondheim, Norway, 1988

XM Wang, M Nishi, H Tsukamoto. A Simple Model for Predicting the Draft Tube Surge. In: Duan Chan-guo, R Schilling, Mei Zu-yan, X VII IAHR Symposium Beijing: International Research Center on Hydraulic machinery, 1994: 95 – 106

X. M. Wang, M Nishi. Swirling Flow with Helical Vortex Core in Draft Tube predicted by a Vortex Method. In: E Cabrera, V Espert and F Martinez, X XII IAHR Symposium Dordrecht: Kluwer Academic Publishers Incorporates, 1996: 965 – 974

The 4th International Symposium on Fluid Machinery and Fluid Engineering
November 24-27, 2008, Beijing, China
NO. 4ISFMFE-Ch39

Numerical Simulation of Hydraulic Turbine Based on Fluid-Structure Coupling

Demin Liu[1], Shuhong Liu[1], Yulin Wu[1] and Xiao-bing Liu[2]

[1] State Key Laboratory of Hydro science & Engineering, Dept. of Thermal Engineering, Tsinghua University, Tsinghua Garden, Haidian District, Beijing 100084, China
Tel: +86-10-6279-4735 / Fax: +86-10-6279-4735
E-mail: liudemin999@126.com
[2] School of Energy and Environment, Xihua University, Chengdu 610039, China

Abstract By adopting the arbitrary Lagrange-Euler (ALE) method of software ADINA, fluid-structure coupling (FSC) calculation of a Francis turbine is conducted. The vibration frequency and mode of the runner in the air and water are obtained. The calculation results show that runner frequency of the turbine is reduced in certain degree under the effect of water pressure and viscous force, and the mode is changed, too. By using dynamic fracture mechanics, the possible cracking damage of the runner is predicated.

Keywords fluid-structure coupling, hydraulic turbine, vibration, numerical simulation

Nomenclature

EX	elastic modulus 2.1×10^{11}Pa
$d(\xi,T)$	the displacement
d_s^k	the structural displacement
$F(t)$	the normal traction force
$\vec{f}_B$	the applied load
h^v	the velocity value at the boundary
T	the time in the new coordinate system
t	time
$\vec{w}$	the velocity in the moving coordinate system
X_f^k	fluid pressure
$\vec{\tau}$	stress tensor
∇	Hamilton operator
ξ	the position
λ_d	the displacement relaxation factor
λ_τ	the stress relaxation factor
τ_{nn}	the time-varying normal stress
ρ	fluid density 7850kg/m^3
μ	Poisson ratio 0.3

1 Introduction

With the development of turbine unit towards large dimension and large capacity, its natural frequency is decreasing, and is very close to the frequency of excitation force. On the one hand, during the operation of turbine, the Kerman vortex, periodic separation vortex, vibration of tailrace vortex band, pressure fluctuation at the runner inlet, and other factors can produce periodic excitation force which may evoke the vibration of runner blades, especially resonance happened when the excitation force's frequency is the same or close to the runner's natural frequency. On the other hand, severe vibration of units not only can lead to structural damage and shorten of service life of units, but also can greatly reduce the efficiency and output of units. In the meanwhile, the vibration of hydraulic structures can be aroused. So the unit's natural frequency should be calculated and tested, and the characteristics of structural components during the design and manufacture stages should be evaluated.

Recently some researchers have always been perfecting the calculation method of static and dynamic stresses of

Francis turbine runner under the effect of hydraulic excitation. For example, reference calculates the influence to dynamic stress characteristics of the runner by water pressure with the method of artificial added water pressure on the blade. References calculate the static stresses of Francis turbine runner under several working conditions with the sequences coupling method. But references only conduct 3D calculation to the flow field in the runner without considering the influences of draft tube, guide vane and spiral case to the flow in the runner. So the pressure load on the surface of blade obtained by this kind of flow field calculation is not quite accurate.

By using CFD software, simulates the whole passage of Francis turbine, and obtains water pressure distribution on the surface of runner blade. Then by using the sequences coupling method, the runner is coupling calculated.

Through the using of software ADINA, close coupling computing pattern is realized in this paper. Its frequency and mode changes and state of stress and strain are obtained.

2 Mathematical Model

2.1 Basic Equations

The Navier-Stokes equations of incompressible viscous fluid can be expressed as

$$\nabla \cdot \vec{u} = 0 \tag{1}$$

$$\frac{\partial \vec{u}}{\partial t} + (\vec{u} \cdot \nabla)\vec{u} - \frac{1}{\rho}\nabla \cdot \vec{\tau} = \vec{f}_B \tag{2}$$

2.2 Control Equations Under ALE Coordinate

Arbitrary Lagrange-Euler method is good at tracing the motion states of solid boundary and fluid boundary. The continuity equations and momentum equations in rectangular coordinate system are changed into corresponding equations in Arbitrary Lagrange-Euler coordinate system by coordinate transformation. After transformation, these equations can reflect the mesh variation of the coupling interface.

The Arbitrary Lagrange-Euler coordinate system can be obtained by adding the coordinate transformation if displacements to the original coordinate system. So the equation can be expressed as

$$x = \xi + d(\xi, T) = x(\xi, T) \tag{3}$$

$$f(x,t) = f(\xi + d(\xi,T), T) \tag{4}$$

Where, the variable (x, t) in the moving coordinate system is changed to (ξ, T) in Arbitrary Lagrange-Euler coordinate system.

The partial derivative of f to T is given as

$$\frac{\partial f}{\partial T} = \frac{\partial f}{\partial t} + \frac{\partial f}{\partial x}\frac{\partial x}{\partial T} \tag{5}$$

If using $\vec{w}$ ($w = \partial x / \partial T$), the fluid governing equations in ALE coordinate system can be expressed as

$$\nabla \cdot \vec{u} = 0 \tag{6}$$

$$\frac{\partial \vec{u}}{\partial t} + ((\vec{u} - \vec{w}).\nabla)\vec{u} - \frac{1}{\rho}\nabla \cdot \vec{\tau} = \vec{f}_B \tag{7}$$

3 Geometry Physical Model of Turbine Flowing Parts

By using the powerful geometric modeling function of software Unigraphic, the physical model of runner blades of turbine (HLA551—LJ—84) in a power station is established, as is shown in Fig. 1. Figure 2 is the geometric model of whole flowing passage. Basic parameters of the turbine are:

Design water head: H = 20 m,
Design discharge: Q = 3.4 m^3/s,
Rotational speed: n = 428.5 r/min,
Number of stationary guide vanes: Z_2 = 8,
Number of guide vanes: Z_1 = 16,
Height of guide vanes: b_0 = 255mm,
Diameter of guide vane distribution circle: D_0 = 986 mm,
Type of guide vanes: positive curvature guide vanes,
Nominal diameter of runner: D_1 = 840 mm,
Number of runner blades: Z = 14

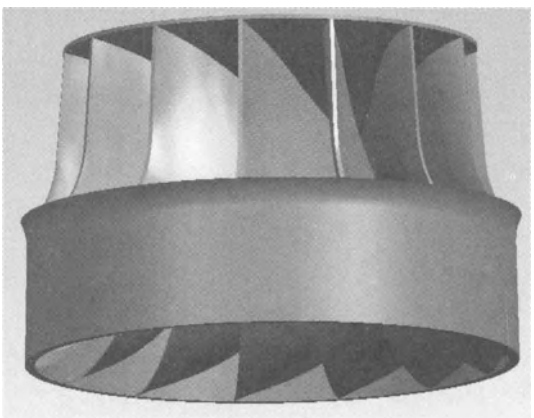

Fig. 1 3D diagram of the runner

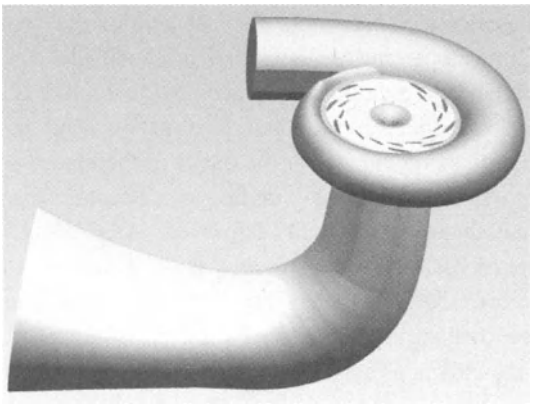

Fig.2 3D model of all flowing parts of the turbine

4 Numerical Computation

4.1 Solving Method

In the many coupling problems, the pressure of fluid affects the deformation of solid which in turn affects the shape of fluid. This type of analysis is named as close cou-pling. However, in some situations, the solid deformation is very small and its influence to the fluid can be neglected. Only the applying of boundary pressure of fluid on the solid is required. Iteration between the fluid and solid models is not required. This type analysis is named as loose coupling. The fluid-structure close coupling method is adopted in this paper. The iterative computation method is used to solve the coupling equations. This method is suitable for solving large scale problems and has relatively lower requirements for compute resources.

Main solving steps of iterative computation method are as follows:

1) Solving X_f^k with the method for independently solving fluid equations.

$$F_f[X_f^k, \lambda_d \underline{d}_s^{k-1} + (1-\lambda_d)\underline{d}_s^{k-2}] = 0 \tag{8}$$

Where $\lambda_d (0 < \lambda_d < 1)$, The fluid vectors is solved by pre-obtained solid displacement variables d_s^{k-1} and d_s^{k-2}.

2) Solving the structural displacement X_s^k with the method for independently solving solid equations.

$$F_s[X_s^k, \lambda_\tau \underline{\tau}_f^k + (1-\lambda_\tau)\underline{\tau}_f^{k-1}] = 0 \tag{9}$$

Where $\lambda_\tau (0 < \lambda_\tau < 1)$,The structural displacement is solved by pre-obtained fluid pressure variable $\underline{\tau}_f^k$ and $\underline{\tau}_f^{k-1}$.

3) Displacement d_f^k of fluid nodes

$$d_f^k = \lambda_d d_s^k + (1-\lambda_d) d_s^{k-1} \tag{10}$$

During the iterative computation process, each step will be judged by the convergence criteria to see if the convergence condition is satisfied. If so, the iteration will be stopped and the results will be outputted.

4.2 Setting Method of Interface

In the process of computation, the coupling interfaces between fluid and blades are set with the following method: for blade with structural model, specify six faces of the blade as coupling faces, and specify six corresponding faces in the fluid as coupling faces. Fig. 3 is the schematic diagram of the coupling interface.

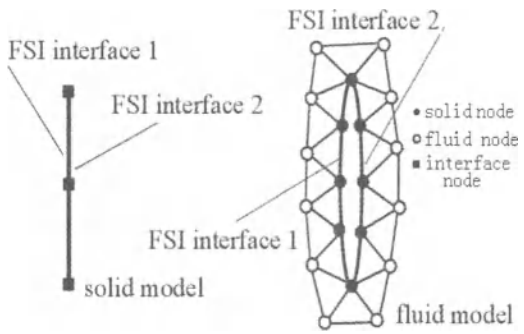

Fig. 3 Schematic diagram of the fluid-structure coupling interface

4.3 Mesh Partition

3D-Fluid unit in software ADINA is used for solution in this paper. This unit is three dimensional tetrahedron units (4 nodes). Structural partition is done to the spiral case, guide vane, runner parts, and local refinement is done to the blade and guide vane.

4.4 Boundary Conditions

Given the normal traction force at the inlet of spiral case related to the time, employ it on the right of momentum conservation equation as intensive force. The normal traction force can be written as

$$F(t) = \int h^v \tau_{nn} dS \tag{11}$$

On open boundary conditions, normal shear force can be ignored comparing with pressure. So the normal traction force is usually employed on the open boundary with known pressure. Side wall of the spiral case is set as rigid wall, and boundary conditions of the rigid wall is set as slip boundary conditions.

Translational constraints are employed on the runner crown and bottom ring. Fixed constraints are applied on the connection parts between the blades and the crown, bottom ring and runner hub.

The FSI boundary conditions are applied on the interface of fluid-structure coupling. The coupling sequence numbers of all blades are appointed. The FSI interfaces are not only interfaces, but also moving wall boundary conditions, which require the solution of structural displacement.

3D-Solid unit in ADINA is adopted for mesh partitioning. To simulate the welding parts of runner crown and bottom ring, fixed constraints are employed, as shown in Fig. 4. The FSI boundary conditions of all blades are specified as corresponding to the fluid model Time step for solution is specified in the fluid model.

The selected structural material is ZG0Cr13NiMo.

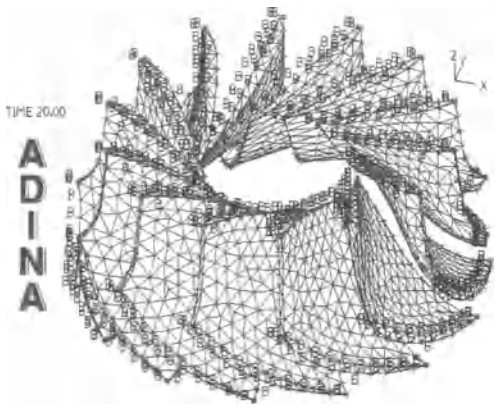

Fig. 4 Fixed constraints applied on the blade

4.5 Numerical Calculation Results

Three working conditions: design flow (H = 20m, Q = 3.40 m^3/s), small flow (H = 20m, Q = 2.38m^3/s), and large flow (H = 20m, Q = 3.74m^3/s) are calculated in this paper.

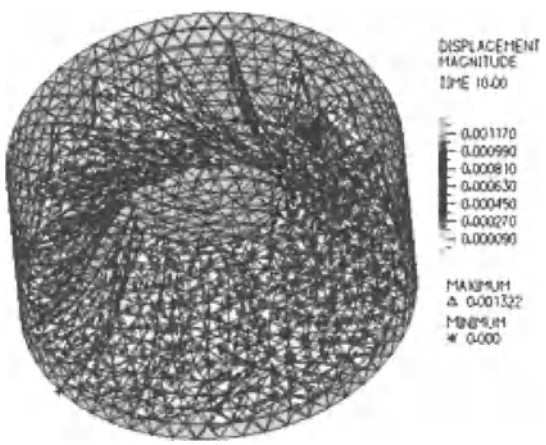

Fig. 5 the strain numerical simulation on the blade

The calculated maximum displacement on the runner is 1.322mm appearing at the outlet of the blade near the crown, and the minimum displacement is 0mm as shown in Fig. 5. From cross sectional diagram Fig. 6 we can see that, large strain appears at the outlet of the blade. So the outlet of the blade is similar to a beam which is continually distorted and deformed. After long time influence of this kind of fatigue load, the outlet of the blade can be damaged. The maximum stress on the thirteenth blade is 10^4MPa appearing at the outlet of blade near the crown, as shown in Fig. 7.

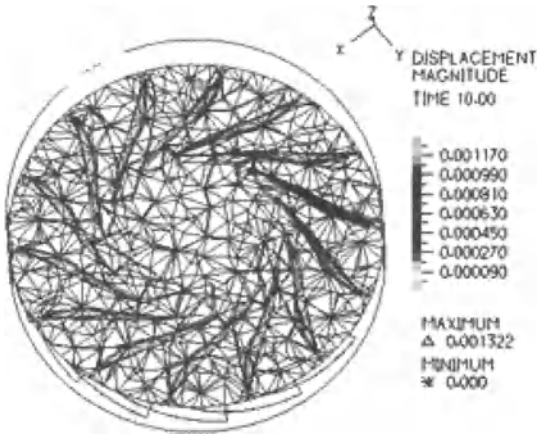

Fig. 6 the strain numerical simulation on the blade's cross section

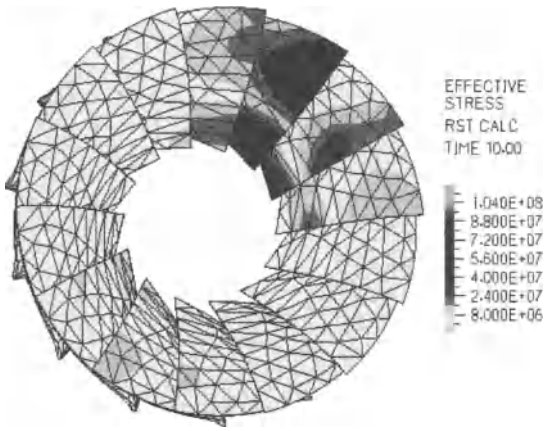

Fig. 7 Numerical simulation of the blade stress

From structural mechanics we know that, this part is the welding area and the focus point of stress, as well as the concentrated point for fatigue damage. Damage of the blade at this part is serious.

Furthermore, this part is the main area of cavitations damage. With the combined action of stress and cavitations, this area of the runner is damaged in many power stations.

Table 1 Runner frequency and influence coefficient under design flow

Order	Operating state in the water (Hz)	Static state in the air (Hz)	Influence coefficient
1	1756	2195	0.800
2	1758	2197	0.801
3	1759	2204	0.798
4	1759	2204	0.798
5	1761	2210	0.796
6	1762	2221	0.793
7	1763	2269	0.776
8	1764	2280	0.773
9	1765	2287	0.771
10	1765	2288	0.771

Table 2 Runner frequency and influence coefficient under small flow

Order	Operating state in the water (Hz)	Static state in the air (Hz)	Influence coefficient
1	1441	2195	0.656
2	1442	2197	0.656
3	1443	2204	0.654
4	1444	2204	0.655
5	1445	2210	0.653
6	1446	2221	0.651
7	1447	2269	0.638
8	1448	2280	0.635
9	1449	2287	0.634
10	1449	2288	0.633

Table 3 Runner frequency and influence coefficient under large flow

Order	Operating state in the water (Hz)	Static state in the air (Hz)	Influence coefficient
1	1590	2195	0.724
2	1592	2197	0.724
3	1593	2204	0.722
4	1593	2204	0.723
5	1595	2210	0.721
6	1596	2221	0.719
7	1597	2269	0.704
8	1598	2280	0.701
9	1599	2287	0.699
10	1599	2288	0.698

Through calculation, 10 order frequency of runner in the air under three working conditions and 10 order frequency of the runner through coupling calculation are obtained. Frequency variations under design flow, small flow and large flow are shown in Tables 1, 2 and 3, separately.

At the same time, mode variations of all orders of the runner under these three working conditions are calculated. Figure 8 describes the variation of first order mode of runner under design flow. The variation situation of the mode is shown by broken lines and their areas.

5 Results Analysis and Conclusions

The calculated results in this paper are compared with calculated data at home and abroad and with similar type tests. Calculated results and tested data of frequency influence coefficient of the runner in some studies are shown in Figs. 9 and Fig. 10.

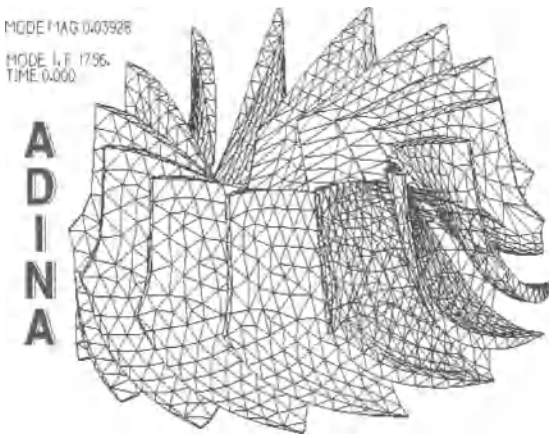

Fig. 8 Numerical simulation of the first order mode under the design flow

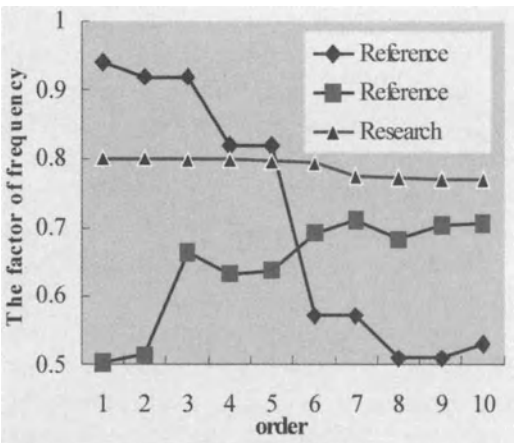

Fig. 9 Comparison of influence coefficient of frequency calculation of the runner

From Fig. 9 we can see that, the fourth and fifth order frequency influence coefficients are 0.798 and 0.796 which are close to 0.82 and 0.821 in reference 13; the sixth order to the tenth order frequency influence coefficients vary from 0.793 to 0.771, and the increasing first and reducing later rule is similar to values in reference 14 from 0.792 to 0.605 except that the above values are larger. Furthermore, the frequency influence coefficient calculated in this paper which varies between 0.77 and 0.8 is relatively close to the ten orders vibration mode. Many units are running well under the design flow, therefore, operating under the design flow is the best measure to avoid vibration damage of the units.

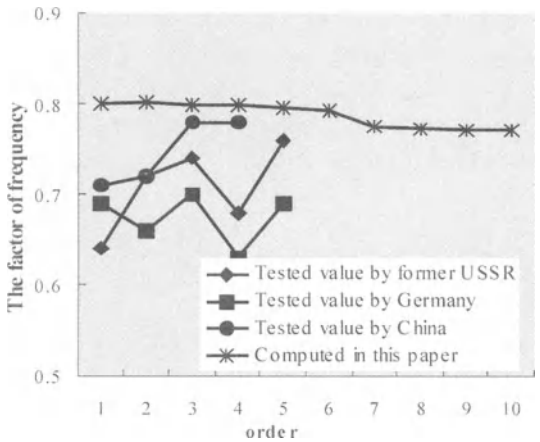

Fig. 10 Comparison of influence coefficient of tested frequency of the runner

From Fig. 10 we can see that, the calculated data of fluid-structure coupling in this paper are larger than the tested data, and the influence to self-excitation frequency of the blade by water pressure is weak. Because the tested data are obtained by laying the blade in still water and the water body range is wide in this circumstance. Therefore the water is disturbed more seriously than laying the blade in the flow passage and the influence on the blade will be greater[15]. Close coupling is adopted in this calculation and the interaction between water pressure and structure are taken into account, and the obtained influence coefficient of frequency domain is from 0.77 to 0.80. The influence coefficient is steady and close to the actual situation. It fully demonstrates that the influence coefficient of the turbine is basically constant without large variation under design flow. Large frequency fluctuation only occurs during the transition from bad working condition to the optimum working condition. The runner has to endure large instantaneous load due to this fluctuation and the structure of the runner will be damaged.

The cracking on the hydraulic turbine blades belongs to finite size cracking and blades are affected by the impact load. From stress analysis results we can see that, both normal impact load and impact shear stress are acting on the blade. These two loads determine that the cracks on the runner belong to mixed cracks between the I type crack (edge-opened crack caused by normal impact load) and II type crack (edge-opened crack caused by impact shear stress). This kind of crack can be prevented by reducing the possibility of resonance in design. Fatigue strength probability of the blade caused by limit load should be avoided. The calculation results are compared with previous calculated data and tested data, which proves the reliability of algorithm adopted in this paper.

Acknowledgements

The authors would like to thank the tutor and classmates for supporting this work

References

Chang Jin-shi. *Turbine operations* [M]. Beijing: China Waterpower Press, 1983 (In Chinese)

Liang Quan-Wei. Dynamic characteristic analysis of Francis turbine with considering FSI [D]. Master Thesis, Beijing: Tsinghua University, 2003. (In Chinese)

Luo Yong-yao, Wang Zheng-wei. Stress characteristic of Francis turbine under dynamic load [J]. *Journal of Tsinghua University (Science and Technology)*, 2005, 45 (2):235-237. (In Chinese)

Liu De-min, Liu Xiao-bing. The turbine vibration analysis based on the fluid structural interaction [J].*Mechanical In Engineering*, 2008.4. 120 – 125

Adina theory and model guide [M]. Adina R&D.Inc, 2007

Liu Xiao-bing, Cao Shu-you. Numerical prediction of vortex flow in hydraulic turbine draft tube for LES [J].*Journal of Hydrodynamics, Ser.B*, 2005. 4. 132 – 136

Guo Peng-cheng, Luo Xing-qi.3D turbulence numerical research of the Francis Turbine [J]. *Journal of Hydrodynamics, Ser.A*, 2006. 21(2): 181 – 189. (In Chinese)

Liu Xiao-bing. Studies of solid-liquid two-phase turbulent flow and wear in hydraulic machinery [J]. *Journal of Hydrodynamics, Ser.A*, 1996.2. 45 – 50. (In Chinese)

Liu Xiao-bing.Analysis of basset force of particle motion in turbulent flows by spectral method [J]. *Journal of Hydrodynamics, Ser.B*, 2001.12.125 – 131

Liu Xiao-bing est. Study of Optimal Hydraulic Design and development of the software package of Francis Turbine and Axial Turbine in Sandy Water [J]. *Journal of Hydrodynamics, Ser.A*, 2002.3.580 – 585. (In Chinese)

Liu De-min, Liu Xiao-bing. Numerical simulation of turbulent flow in hydraulic turbine draft tube and discharge weep and its improving design [J]. *Waterpower,* 2007.11.65 – 69. (In Chinese)

GAO jamming est. The reason analysis report of San Men George hydraulic power station[R]. Beijing:Tsinghua University hydraulic department, 1991. (In Chinese)

Chen Xiang-lin.Dynamic Characteristic Studies of Francis Hydro Turbine Blades in Fluid-Structure Interaction [D]. Doctor Thesis, Kunming: Kun Ming Science and Technology University, 2004, 12. 73 – 80. (In Chinese)

Wang Shao-bo. Dynamic Characteristic Analysis and Synthetically Optimization of Francis Turbine's Runner [D]. Doctor Thesis, Zhen Zhou: Mechanical Scientific research institute, 2003(5), 65 – 68. (In Chinese)

K.Dasgupta. Cognition of medium head Francis turbine evokes cracks[C]. Cao Chun-lin translates the IAHR Symposium 1986, foreign large motor, 1989.224 – 230

Li Cheng-jia est. Detection analysis and research of Hydraulic turbine runner cracks [J], *Northwest eclectic power technology,* 2001 (6), 21 – 23. (In Chinese)

The 4th International Symposium on Fluid Machinery and Fluid Engineering
November 24-27, 2008, Beijing, China
NO. 4ISFMFE-Ab11

Numerical Simulation of Drawdown in Pump Sumps

S.N. Shukla[*1] and J.T. Kshirsagar[2]

[*1] Corporate Research and Engineering Division,
Kirloskar Brothers Limited,
Udyog Bhavan, Tilak Road, Pune, 411002, India
Tel: +91-20-24402065 / Fax: +91-20-24440400 E-mail: Shyam.shukla@kbl.co.in

[2] Corporate Research and Engineering Division,
Kirloskar Brothers Limited,
Udyog Bhavan, Tilak Road, Pune, 411002, India
Tel: +91-20-24402064 / Fax: +91-20-24440400 E-mail: jtkshirsagar@kbl.co.in

Abstract Sump is designed to provide adequate water supply to pumps installed in sump. It is also essential to design the sump to provide fairly uniform and swirl free flow to pumps The Hydraulic Institute Standards specify general guidelines for the design of sumps and is based on extensive studies on variety of sumps. In case the sump is designed as per the guidelines of HIS, it is ensured that the flow pattern will be relatively uniform and swirl free to pumps.

However it is not always possible to follow guidelines of HIS and to ensure uniform and swirl free flow to pumps, investigation of sump is required prior to installing the pumps at site. There are two major approaches followed for such investigation. One is the experimental model study and the other is numerical simulation. Both these approaches are well accepted by pump industries and refinements on model studies are still going on.

Large capacity pumps are used in parallel to meet the circulating water requirements in thermal power station. The sump to operate these pumps is generally optimized using experimental approach or computational approach.

Despite the care taken during model testing, a peculiar situation occurred during testing of pumps installed in a particular sump. To carry out performance guarantee test of the pump only one pump was allowed to operate at site and tests were carried out. Draw down of water level in the operating pump showed a noticeable water level difference with other pump chambers in the sump.

Draw down in multiple pump sumps is a common phenomenon with large capacity pumps. The free surface level difference in the pump chamber is observed in the case wherein one pump is running and other neighboring pumps are stopped.

This phenomenon was not anticipated during model testing using experimental or computational approach.
Once the tests were over, in the absence of experimental set up, numerical approach was used to investigate the draw down phenomenon in sumps.

The paper presents results from numerical simulation compared with experimentally observed data from site.

Keywords draw down, pump sumps, free surface, numerical simulation, computational fluid dynamics

1 Introduction

The basic purpose of a pump intake is to supply water with uniform velocity at the entry of an impeller. Electric power generating plants utilize circulating-water cooling systems that typically require a number of large-scale pumps to draw water from river or a reservoir. The fluid flow in pump intakes is rather complex involving expansions and turns together with fluid structure interactions. It is essential to ensure that the pumps operating in such pump intakes get smooth swirl free flow at their inlets. Proper intake design provides uniform swirl free flow to the pumps. Intakes of such pumps and the geometrical layout of the channel surrounding the

pump bells are usually designed in an empirical fashion, relying on laboratory model studies and experiences with previous installations. The Hydraulic Institute Standards specify general guidelines for the design of pump intakes. The site constraints usually call for a deviation from the Standards. It then, becomes essential to investigate the pump intake to ensure smooth flow over the entire flow range of the pumps and in all the combinations of the pumps. In case of multiple pumps sump, investigations are necessary to check the suitability of sump for various combinations of operating pumps. When only one pump operates and other pumps are closed, there will be water level difference between two pump's chambers. This draw down of water in the running pump's pump chamber is quite noticeable with respect to other stationary pump chambers.

Draw down is reduction or depletion of water level. In case of multiple pump sump arrangement, there will be reduction of water level in working pump's chamber with respect to standby pump's chamber. The usual solution is to conduct experimental study on a reduced scale model. The severity of this draw down is mostly not judged in reduced scale experimental study. Although draw down is sumps are known for quite some time, there is no theoretical method for predicting the draw down. From a purely numerical perspective, the complexity of the physics is such that it demands the full power of modern Computational Fluid Dynamics (CFD) to solve the equation of motion and turbulence model in domains. There are additional difficulties associated with modeling free surface, because this free surface varies in case of draw down and physics of which are not fully understood. With the latest version of commercially available software, an effort is made in this direction to predict those complex fluid flow phenomena.

This paper describes the use of commercially available software for predicting the draw down in pump intakes. In one of the sites, it was observed that on starting a single pump, there was large draw down in the pump chamber with respect to other pump chambers. The paper brings out results and observations from numerical approach and compared with data from site.

2 Multi Phase Flow Studies

Multiphase flow refers to the situation where more than one fluid is present. In general, the fluids consist of different species, e.g. air-water. The fluids in a multiphase flow are assumed to be mixed art macroscopic length scales, much larger than molecular. Each fluid may possess its own flow field, or all fluids may share a common flow field. The pump intake flow is a multiphase, free surface flow where the phases are separated by a distinct interface (free surface). In such case the multi phase flows inter-phase transfer rate is very large. This results in all fluids sharing a common flow field, as well as other relevant fields such as turbulence. In free surface flows, the water flows under gravity, the phases are completely stratified and interface is well defined. The volume fractions of the phases are equal to one or zero everywhere except at the phase boundary.

As already depicted that open channel flow phenomena is a complex multi-phase and unsteady flow phenomena. This mainly because of the water surface changes its position with respect to time. The complexity itself is increased multi-fold if the multi-phase flow physics are included. To reduce the complexity of the analysis, we have carried out two-phase flow in steady state condition with a view to detect the draw down in the pump intake.

3 Computational Model Description

3.1 Geometry Generation

The sump geometry chosen to validate the CFD model replicates the actual prototype sump. The approximate total size of the geometry is 75M × 30M × 9.6M (L × B × H). As only one pump is working out of four pumps, only one draft tube and outlet extensions is modeled. However all four pump bays and full sump geometry is prepared. The quantity of water passing through single pump is 30000m^3/hr. The draft tube inlet dimensions are 2.1 M × 4.3 M (B × H) and the diameter at the draft tube outlet is 1.44M. The average velocity at the inlet of draft tube is 0.92 M/s while at the entry of draft tube is 5.27 M/s (Please refer Fig. 1). The Froud Number calculated at the entry of suction bell is 0.16.

The water enters into the sump through an inlet channel of size 7.8 M × 4.1 M (B × H). The velocity of flow is 1.04 M/s when all 4 pumps are operating. The flow takes 90° turn with a slope of 10°. There was high recirculation of water body in the forebay by virtue of sudden 90° turn and sufficiently high velocity. Then there is high slope in the pump chamber itself in two steps. The available submergence in the prototype sump is 4.9 M as against required submergence (as per HIS) 4.6 M.

The model testing of the sump was conducted at a 1:10 scale ratio. It was found that there was heavy mass rotation in the forebay. There was formation of air entrainment in some of the combinations of operating pumps and water levels. The flow was highly unstable at higher Froud scale tests. The sump was modified. Guide walls were introduced and shape of the pier (partition) walls was changed. These changes improved the sump performance. The modifications are implemented at site.

Performance guarantee test at field was offered to client. During performance guarantee test of the pumps, only one pump was allowed to operate and tests were carried out. As soon as single pump started, a noticeable difference of water level in the operating pump chamber to that of standby pump chamber was noticed. This draw down phenomena motivated authors to validate using CFD techniques. Once validation is done, a care can be taken for future analysis. The same modified geometry is considered for analysis and validation.

The generated grid in the sump is an unstructured hybrid tetrahedral grid with mostly tetrahedral elements in the passage. The grid distribution was optimized keeping a good balance between computational time and better computational results. No of generated elements in the passage are 780000.The geometry of the pump bay is shown in Fig. 1 while the computational mesh of the geometry is shown in Fig. 2.

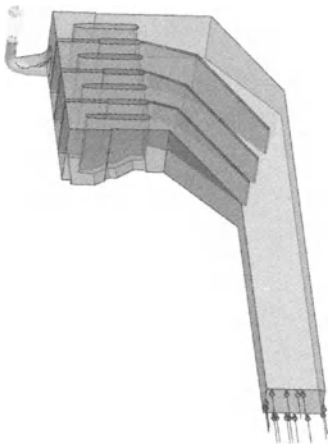

Fig. 1 Geometry of pump sump

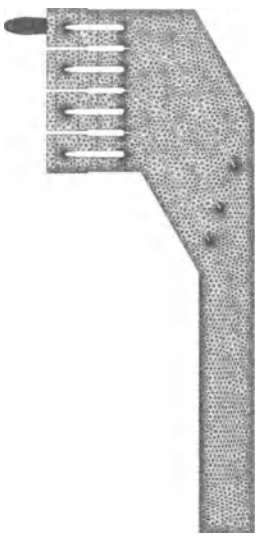

Fig. 2 Grid surface plot of pump sump

3.2 Boundary & Initial Conditions

The numerical solution of any system demands for well defined boundary conditions. Looking at the complications of the physics of multi phase flow, following boundary conditions were considered to be appropriate.

The geometry is a single domain of two phases. The free surface height is given at the inlet. As the draw down phenomena consist of the level difference of free surface, the domain separation and intermixing was sought from the solution and hence the domain was not separated into air phase and water phase. A homogeneous model of multi phase option is selected as fluid model. The materials for two-phases of fluids are taken as water and air. Both the fluids are treated as continuous fluids. The difference in density between phases (water and air) produces a buoyancy force in multiphase flows. Hence buoyant option, with density difference fluid buoyant model, is assigned to all domains. Buoyant reference density of air is assigned in all domains. It is said to choose the density of the lighter fluid since this gives an intuitive interpretation of pressure (i.e., constant in the light fluid and hydrostatic in the heavier fluid). This simplifies pressure initial conditions, pressure boundary conditions and force calculations in post-processing. The turbulence model, which is used in the solution was standard κ-ε turbulence model with scalable wall function. A scalable wall-function take care the problem of inconsistencies due to first grid point location near the wall. The top surface of the sump is assigned as wall with free slip. All other surfaces are defined as smooth walls with no slip condition. The inlet of the sump is assigned the velocity of flow and water level height is assigned at the inlet. The volume fraction is of water phase is given as one and air phase as zero. Average static pressure is assigned at the outlet of the pump. The pressure averaging is done by averaging the pressure over whole outlet.

CFD analysis requires initial flow parameters to initiate the iteration process. This multi-phase flow analysis is very sensitive to the initial guess. If the initial guess is proper then the solver gives good results. Proper velocity components and static pressure values are assigned. The turbulent kinetic energy and turbulence eddy dissipation are assigned as automatic. Volume fraction in till inlet water level height is initialized as 100 percent water while above water height it is assigned as no water. The Discretisation scheme used was high resolution scheme. With this setting, the blend factor values vary throughout the domain based on the local solution field in order to

enforce a boundedness criterion. In flow regions with low variable gradients, the blend factor will be close to 1.0 for accuracy. In areas where the gradients change sharply, the blend factor will be closer to 0.0 to prevent overshoots and undershoots and maintain robustness. Here a value of 0.0 is equivalent to using the first order advection scheme and a value of 1.0 uses second order differencing for the advection terms. The advantage of this scheme is that the solution is accurate to the 2nd order while maintaining the robustness.

4 Results & Discussions

The results are demonstrated in the form of contour plots and iso-surface plots. Fig. 3 shows the contour plot of water volume fraction in the sump.

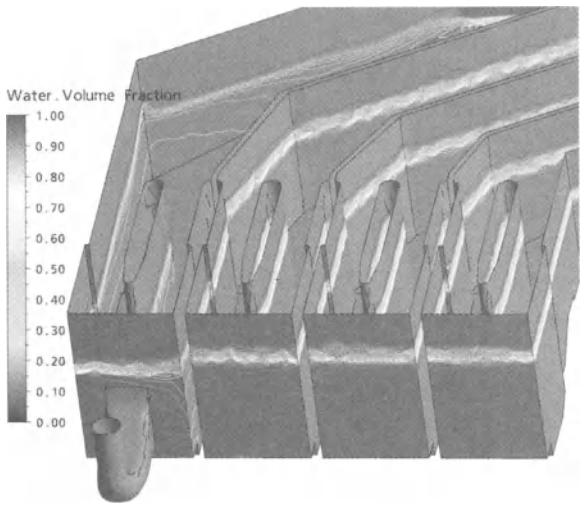

Fig. 3 Contour plot showing level difference

The level variation due to change in the direction and due to change in bottom slope is well captured. As soon as water enters in the operating pump there is sudden drop of water level. The contour plot at the back wall shows the difference in water level between working pump's chamber and stationary water pump chamber. Fig. 4 is shown to get a clear picture at the back wall. The level difference points in the two chambers are shown in Fig. 4. The difference of level is 0.54M. This difference is comparable to the difference found at site.

Figure 5 shows the fringe plot at the back wall. The working pump chamber is showing a shorter band of water than standby pump's chamber. The air portion on the wall is more in the working pump's chamber.

Iso surface plot of Fig. 6 show the changes of water levels in the passage. The sudden drop of water level on two sides of partition wall dividing running pump's chamber and standby pump's chamber is clearly shown. There is raise in water level just after sudden drop. This hydraulic jump is a combined effect of change in direction of flow in the pump chamber as well as change in bottom slope.

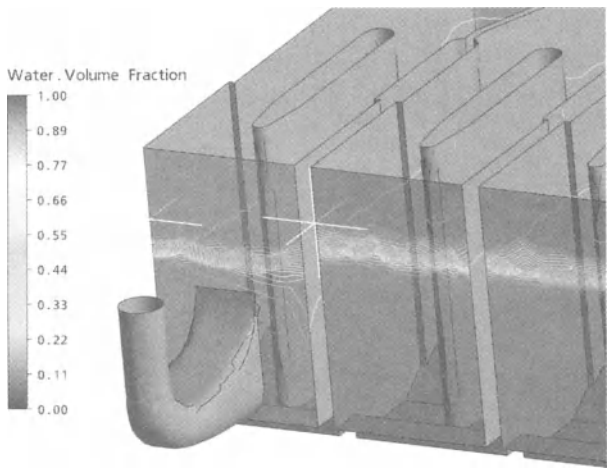

Fig. 4 Contour plot showing level difference (Enlarged view)

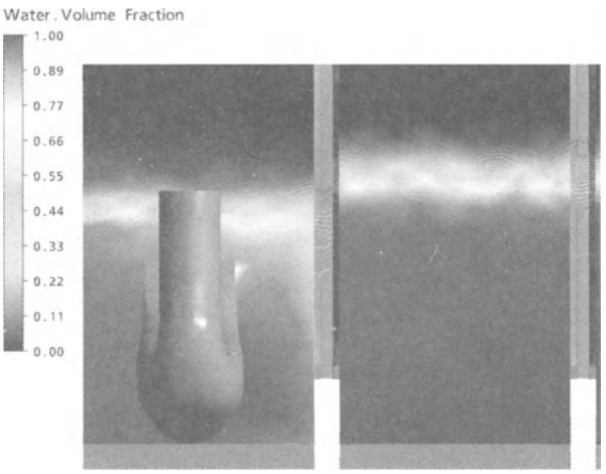

Fig. 5 Contour plot of at the back wall

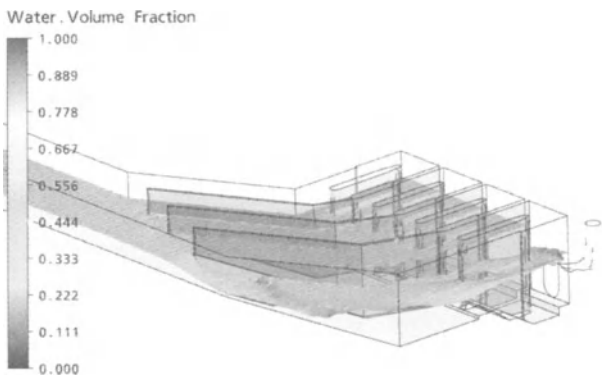

Fig. 6 Iso-surface plot of free surface of water

Acknowledgements

Authors would like to place on record their gratitude to the Management of Kirloskar Brothers Ltd. Pune, India for the encouraging attitude towards Research & Engineering Division, which led to this paper. We are also very thankful to our colleagues in the Research & Engineering Division, Pune for co-operation during this work.

References

ANSYS – CFX users guide, V. 11.0, By M/s ANSYS Inc., USA

Experimental study report on "Sump model studies for 4 Nos. of concrete volute pumps: project – 2X 500 MW Vindhyanchal STPP (Stage – II)"

Constantinescu G.S. and Patel V.C., "Numerical Model for Simulation of Pump-Intake flow and Vortices" Journal of Hydraulic Engineering, February 1998

White, F. M., 2003, "Fluid Mechanics, 5th ed.", *McGraw-Hill*, New York

American National Standard for Pump Intake design (ANSI / HI 9.8–1998) by Hydraulic Institute, 9 Sylvan Way, Parsippany, New Jersey, USA

The 4th International Symposium on Fluid Machinery and Fluid Engineering
November 24-27, 2008, Beijing, China
NO. 4ISFMFE-Ab21

Recent Development of Lagrangian Vortex Method and Its Application into Fluid Machinery and Fluid Engineering

Kyoji Kamemoto[*1] and Akira Ojima[2]

[*1] Professor Emeritus, Yokohama National University
2-23-31 Tatsunodai, Zama, Kanagawa, 228-0023 Japan
Tel: +81-46-256-1207 / Fax: +81-46-255-5137
E-mail: kamemoto@bg.mbn.or.jp
[2] Researcher, College Master Hands Inc.
1st Floor NT Bldg., 2-1-31 Midorigaoka, Zama, Kanagawa, 228-0021 Japan

Abstract This paper is to introduce recent works of practical applications of vortex methods in the field of fluid machinery and fluid engineering, explaining the mathematical basis of the method based on the Biot-Savart law. It is pointed as one of the most attractive features of the vortex method that the numerical simulation using the method is considered to be a new and simple technique of large eddy simulation, because they consist of simple algorithm based on physics of flow of viscous fluid and it provides a completely grid-free Lagrangian calculation. As typical examples of simulation of complex flows, the internal flow of a mixed-flow pump calculated by the vortex method and the vortical flow around a flexible circular cylinder in a uniform stream which was simulated by a coupled structure and fluid analysis based on FEM and the vortex method are digested.

Keywords CFD, vortex method, unsteady flows, mixed flow pump, coupled structure and fluid analysis, flexible cylinder

Nomenclature

A	oscillation aqmplitude
C	matrix element for damping factor
D	diameter of circular cylinder
F	fluid force
f	frequency
G	fundamental solution
H	Bernoulli function or pump head
K	matrix element for stiffness
L	shaft power or length of circular cylinder
M	matrix element for mass of oscillating structure
m	mass od circular cylinder
$\vec{n}$	normal unit vector
p	pressure
Q	flow rate
Re	Reynolds number
$\vec{r}$	position vector
S	boundary surface
T_o	period of one revolution of impeller
t	time
U_o	uniform velocity
$\vec{u}$	velocity vector
Vr	reduced velocity
$\vec{v}_w$	moving velocity of a boundary

Greek symbols

β	integration coefficient
ρ	density of fluid
ν	kinematic viscousity
$\vec{\omega}$	vorticity
η	pump efficiency

Subscripts

d	design point
n	natural frequency
o	integration variable
x	x-direction
y	y-direction
*	non-dimensional value

1 Introduction

The vortex methods have been developed and applied for analysis of complex, unsteady and vortical flows in relation to problems in a wide range of industries, because they consist of simple algorithm based on physics of flow. Nowadays, applicability of the vortex element methods has been developed and improved dramatically, and it has become encouragingly clear that the vortex methods have so much interesting features that they provide easy-to-handle and completely grid-free Lagrangian calculation of unsteady and vortical flows without use of any RANS type turbulence models. Leonard (1980) summarized the basic algorithm and examples of its applications. Sarpkaya (1989) presented a comprehensive review of various vortex methods based on Lagrangian or mixed Lagrangian-Eulerian schemes, the Biot-Savart law or the vortex in cell methods. Kamemoto (1995) summarized the mathematical basis of the Biot-Savart law methods. Recently, Kamemoto (2007) reported several attractive applications involving simulation of various kinds of unsteady flows with an advanced vortex method.

As well as many finite difference methods, it is a crucial point in vortex methods that the number of vortex elements should be increased when higher resolution of turbulence structures is required, and then the computational time increases rapidly. In order to reduce the operation count of evaluating the velocity at each vortex element or particle through a Biot-Savart law, fast N-body solvers, by which the operation count is reduced from $O(N^2)$ to O(N log N), have been proposed by Greengard and Rohklin (1987) On the other hand, in order to reduce the computational load in calculation of turbulence structures, Fukuda and Kamemoto (2005) proposed an effective redistribution model of vortex elements with consideration of convective motion and viscous diffusion in a three-dimensional core-spreading model.

Recently, in order to expand the applicability of the advanced vortex method, the group of the present author has made attempts to apply it into further complicated and vortical flows in several fields. Kamemoto and Ojima (2007) applied the method into the fluid dynamics in sports science, and they simulated three-dimensional, complex and unsteady flows around an isolated 100 m runner, and also Kamemoto and Ojima (2008) reported interesting results of a study on numerical simulation of unsteady flows around a swimming fish by using their vortex method. Iso and Kamemoto (2005) developed a coupled vortex method and particle method analysis tool for numerical simulation of internal unsteady two-phase flows, and they numerically simulated internal liquid-solid two-phase flows in a vertical channel and a mixing tee.

In this paper, in order to overview the recent attempts, the mathematical background and numerical procedure of the advanced vortex method applied to the recent studies are briefly explained, and a couple of studies on simulation of such hard-to-solve and vortical flows as the internal flow of a mixed-flow pump calculated by Kamemoto and Ojima (2004) and the vortical flow around a flexible circular cylinder in a uniform stream by Kamemoto, Ojima and Nakamura (2008), which was simulated by a coupled structure and fluid analysis based on FEM and the vortex method, are digested.

2 Algorithm of Lagrangian Vortex Method

The governing equations of viscous and incompressible flow are described by the vorticity transport equation and the pressure Poisson equation which can be derived by taking the rotation and the divergence of Navier-Stokes equations, respectively.

$$\frac{\partial \vec{\omega}}{\partial t} + (\vec{u} \cdot grad)\vec{\omega} = (\vec{\omega} \cdot grad)\vec{u} + \nu \nabla^2 \vec{\omega} \tag{1}$$

$$\nabla^2 p = -\rho \, div(\vec{u} \cdot grad \, \vec{u}) \tag{2}$$

Where $\vec{u}$ is a velocity vector and a vorticity $\vec{\omega}$ is defined as follows

$$\vec{\omega} = rot \, \vec{u} \tag{3}$$

As explained by Wu and Thompson (1973), the Biot-Savart law can be derived from the definition equation of vorticity as follows:

$$\vec{u} = \int_V (\vec{\omega}_0 \times \nabla_0 G) dv + \int_S \{(\vec{n}_0 \cdot \vec{u}_0) \cdot \nabla_0 G - (\vec{n}_0 \times \vec{u}_0) \times \nabla_0 G\} ds \tag{4}$$

Here, subscript "0" denotes variable, differentiation, and integration at a location $\vec{r}_0$, and $\vec{n}_0$ denotes the normal unit vector at a point on a boundary surface S. And G is the fundamental solution of the scalar Laplace equation with the delta function $\delta(\vec{r} - \vec{r}_0)$ in the right hand side, which is written for a three-dimensional field as $G = 1/4\pi |\vec{r} - \vec{r}_0|$.

In equation (4), the inner product $\vec{n}_0 \cdot \vec{u}_0$ and the outer product $\vec{n}_0 \times \vec{u}_0$ stand for normal velocity component and tangential velocity vector on the boundary surface. They correspond to the source distribution on the surface and the vortex distribution that has the rotating axis in parallel to the surface. In this study, a boundary surface is represented by the panel method. The source and vortex corresponding to the second and third terms of right hand

side of equation (4) are distributed on the boundary surface. The strengths of source and vortex are obtained by using the following two conditions; zero normal component of relative velocity to the boundary surface $(\vec{u}-\vec{v}_w)\cdot\vec{n}=0$ and the relation of the conservation of the vortex strength, respectively. $\vec{v}_w$ is a moving velocity of a boundary.

The pressure in the field is obtained from the integration equation formulated by Uhlman (1992), instead of the finite difference calculation of equation (2) as follows:

$$\beta H+\int_S H\frac{\partial G}{\partial \vec{n}}ds=-\int_V \nabla G(\vec{u}\times\vec{\omega})dv-\int_S G\vec{n}\frac{\partial \vec{u}}{\partial t}ds -\nu\int_S \vec{n}(\nabla G\times\vec{\omega})ds \quad (5)$$

Here, β=1 in the flow field and β=1/2 on the boundary S. G is the fundamental solution. H is the Bernoulli function defined as $H=p/\rho+|\vec{u}|^2/2$. The value of H on the boundary surface is calculated from equation (5) by using the panel method. After the pressure distribution around the boundary surface is calculated from equation (5), integration of the pressure acting on the body surface yields the force acting on the body. One of the most important schemes in the vortex methods is how to represent the distribution of vorticity in the proximity of the body surface, taking account of viscous diffusion and convection of vorticity under the non-slip condition on the surface. In the present method, a thin vorticity layer is considered along the solid surface, and discrete vortex elements are introduced into the surrounding flow field considering the diffusion and convection of vorticity from discrete elements of the thin vorticity layer. The details of treatments have been explained in the paper by Ojima and Kamemoto (2000). In this paper, they validated the basic technique of the present method by comparisons with experimental results of the flows past a sphere.

The discrete vortex element is modeled by a vortex blob which has a spherical structure with a radially symmetric vorticity distribution proposed by Winkelmans & Leonard (1988). The motion of the discrete vortex elements is represented by Lagrangian form of a simple differential equation $d\vec{r}/dt=\vec{u}$. Then, trajectory of a discrete vortex element over a time step is approximately computed from the Adams-Bashforth method. On the other hand, the evolution of vorticity is calculated from equation (1) with the three-dimensional core spreading method proposed by Nakanishi & Kamemoto (1992). It should be noted here that in order to keep higher accuracy in expression of a local vorticity distribution, a couple of additional schemes of re-distribution of vortex blobs are introduced in the present advanced vortex method. When the vortex core of a blob becomes larger than a representative scale of the local flow passage, the vortex blob is divided into a couple of smaller blobs. On the other hand, if the rate of three-dimensional elongation becomes large to some extent, the vortex blob is divided into plural blobs to approximate the elongated vorticity distribution much more properly.

3 Application Example for Simulation of a Mixed Flow Pump Operation

In order to predict the fluctuation of radial force acting on a rotating impeller, the internal flows of a mixed-flow pump were simulated by Kamemoto and Ojima (2004) under three operating conditions; the design point (Q/Q_d= 1.0), an off-design point (Q/Q_d= 0.65) and a shut-off point (Q/Q_d= 0.0). This pump was manufactured and tested by DMW Corporation in Japan, and it was composed of a 4 bladed mixed-flow impeller, 5 bladed guide vanes and an inlet whirl stop. Here, the outlet diameter of this impeller is 360 mm and the tip clearance is 0.4mm. Specifications of the pump are as follows: designed flow rate (Q_d) = 18.1 m^3/min, head (H) = 16.0m, rotational speed = 1480rpm.

Figure 1 shows instantaneous flow patterns for the three operation conditions which are represented by a number of discrete vortex elements in the flow fields. It is observed that for both cases of flow rate Q/Q_d= 1.0 and 0.65, any remarkable flow separations are not detected around every impeller vane. In the case of Q/Q_d= 0.65 shown in Fig. 1 (b), however, strong tip-leakage vortices are formed from the tips of impeller vanes, and the tip-leakage vortices develop to the pressure side surface of the adjacent impeller vane or flow downstream in the passage of diffuser vanes. And then, a strong vortex bubble is formed in a vane-to-vane flow-passage in the diffuser. On the other hand, as shown in Fig. 1 (c) in the case of the shut-off operation (Q/Q_d= 0.0), the reverse flow appears and longitudinal vortices tend to develop in the inlet region of the pump.

Figure 2 shows the computed radial fluid-forces acting on the impeller under the three operation conditions. In this figure, F_x and F_y denote the radial forces exerting on the impeller in the horizontal direction x and the vertical direction y. It was confirmed that radial force components were periodically fluctuating with the interaction between rotating impeller-vanes and stationary guide-vanes, and the magnitude of fluctuations becomes larger as the flow rate decreases.

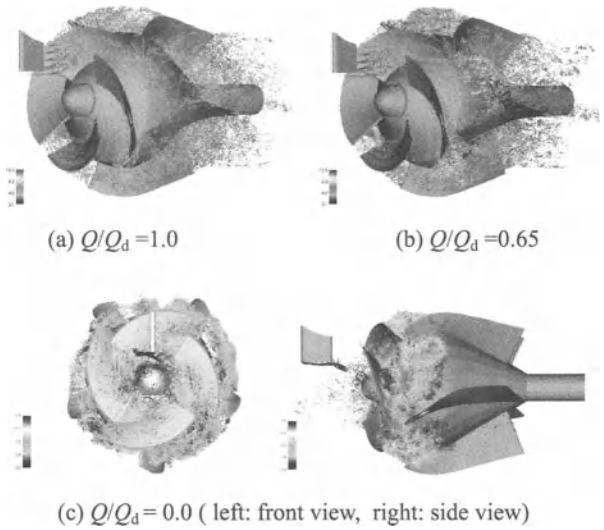

Fig. 1 Instantaneous flow patterns

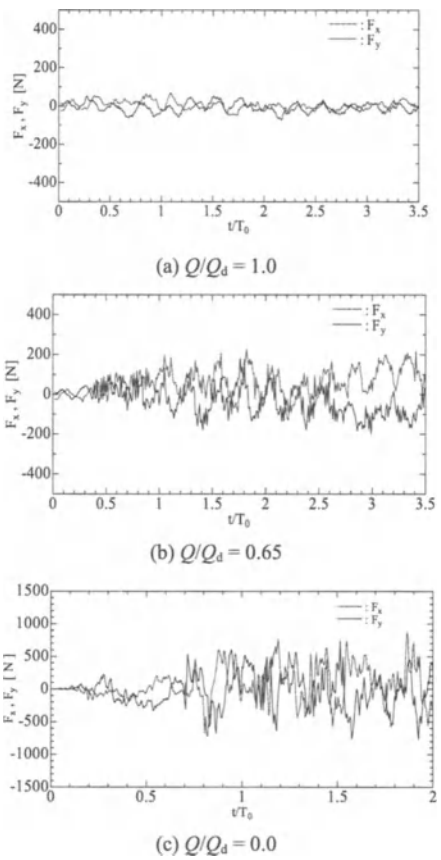

Fig. 2 Fluid forces acting on the impeller

In Fig. 3, the computed total head, shaft power, and pump efficiency are plotted together with the measured ones. Although only three cases of operation condition were simulated in the present study, the predicted characteristics of the pump reasonably agree with the experimental ones.

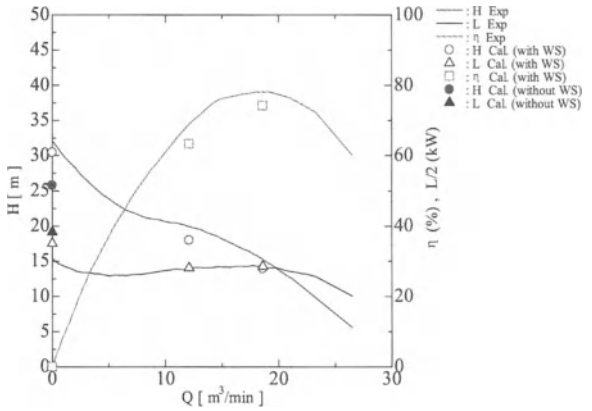

Fig. 3 Performance of the calculated mixed-flow pump

4 Application Example for a Coupled Structure and Fluid Analysis

The procedure to analyze dynamic behavior of structures is based on a beam element representation using a consistent mass-matrix formulation (i.e., no mass lumping). The resulting equations of motion for each structure are a set of second-order ordinary differential equations (ODEs) of the following form

$$[M]\ddot{\boldsymbol{q}}+[C]\dot{\boldsymbol{q}}+[C]\boldsymbol{q}=\boldsymbol{F} \tag{6}$$

Where $[M]$ is the mass matrix, $[C]$ is the damping matrix, $[K]$ is the stiffness matrix, q is the vector displacements, and F is the fluid forcing vector which is calculated by the vortex method. In the three-dimensional and coupled structure and fluid analysis, the open source finite-element solver CalculiX developed by Dhondt (1998-2004) was used to obtain the structural solutions for the isolated cylinder. The cylinder was assumed to be solid in this study.

Within a physical time step, the structural motion and the flow field are unknown and are solved iteratively between the fluid and structural systems in a fully couple manner. The details of the procedure has been reported in the paper by Kamemoto and Ojima (2008).

In order to confirm the applicability of the code, simulation of water flow around a flexible cantilever circular cylinder was performed, and the calculation results were compared with experimental ones.

As the calculation model, the circular cylinder model used to the experimental investigation by Jauvtis and Williamson (2004) was employed in this study. Figure 4 shows a diagram of the test equipment. The circular cylinder has an aspect ratio (length/diameter) of L/D=10.0. Reynolds number and time interval are set as $\mathrm{Re} = U_0 D/\nu = 2.89\times10^3$ and $\Delta t^* = \Delta t U_0/D = 0.1$, respectively. Where U_0

is the free-stream flow speed, and ν is the kinematic viscosity. Here, it should be noted that the upper surface was assumed to be the slip wall and the mirror condition was imposed in this calculation.

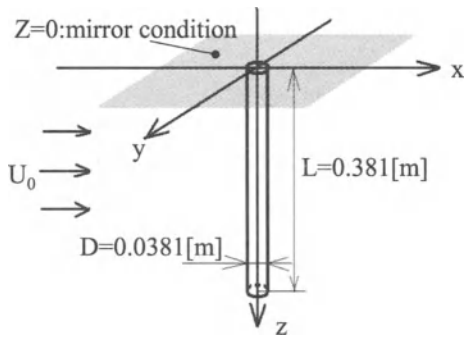

Fig. 4 Coordinate system for calculation model.

The cylinder mass ratio $m^*= 4m/\rho_f \pi D^2 L=2.6$, where m is the mass per unit length of the cylinder length, and ρ_f is the density of fluid. Here, it should be noted that the damping ratio and gravity were not considered in this calculation. Reynolds numbers and dimensionless dynamic parameters in the present calculations were chosen to match those in the experimental set-up by Jauvtis and Williamson (2004) as shown in Table 1. A reference Reynolds number is $\mathrm{Re} = U_0 D/\nu = 2.93\times10^3$ at a reduced velocity $V_r=U_0/f_n D=5.0$, where U_0 is the average free-stream flow speed and f_n is the free-vibration natural frequency in fluid.

Table 1 Calculation conditions

Structure	
Density of structure: ρ_s	2.595×10^3 [kg/m^3]
Young's modulus: E	4.265×10^5 [N/m^2]
Pisson's ratio: σ	0.34
Natural frequency: f_n	0.406 [Hz]
Fluid (Water)	
Density of fluid: ρ_f	9.982×10^2 [kg/m^3]
Kinematic viscousity: ν	1.004×10^{-6} [m^2/s]

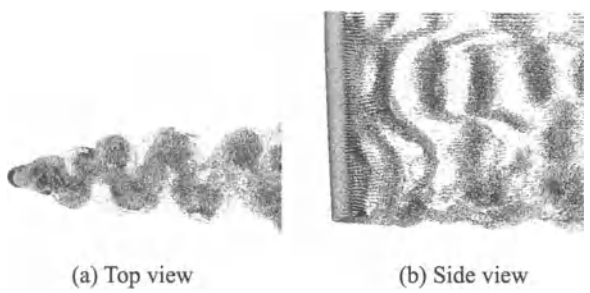

Fig. 5 Instantaneous flow pattern around the circular cylinder at reduced velocity $V_r = 5.91$

The three-dimensional simulations were carried out for reduced velocities chosen to place near the highest expected amplitude on the upper and lower response branches ($V_r = 3.94, 4.93, 5.91, 7.18, 8.53$).

It is interesting to investigate the topology of the vortical wake structure formed behind the flexible cylinder. Figure 5 shows the instantaneous flow pattern around the cylinder oscillating at the case of $V_r = 5.91$ by expressing with relative velocity vectors at the instantaneous positions of vortex elements. As shown in Fig. 5, it can be seen vortex dislocations at the case of $V_r = 5.91$ are associated with the difference of modes between the bottom and the tip of the cylinder. The present result is very similar to the phenomenon of vortex formation mode which comprises co-rotating vortex pairs for the pivoted circular cylinder by Flemming and Williamson (2005).

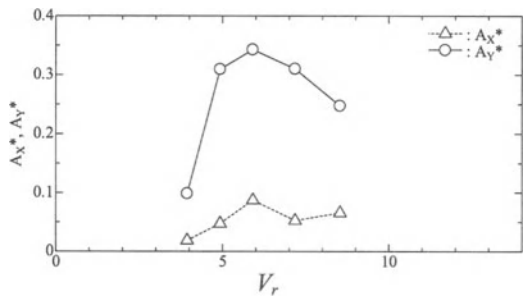

Fig. 6 Amplitude response of the cylinder tip for the reduced velocity

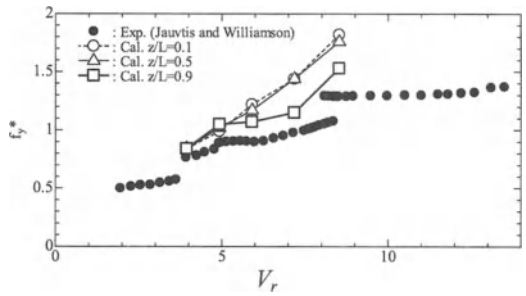

Fig. 7 Frequency Response of lift force for the reduced velocity

The amplitude response of the cylinder tip is shown in Fig. 6 and the frequency response of lift force is shown in Fig. 7. Here, the normalized amplitude and frequency are defined as $A_{(x,y)}^* = (x,y)/D$, $f_{(x,y)}^* = f_{(x,y)}/f_n$, respectively. The response amplitudes obtained by present calculations were similar to the experimental results for the case of vibration in two degree freedom of uniform amplitude to the spanwise direction (Jauvtis and Williamson (2004)). However, these amplitudes obtained by present calculations are somewhat smaller than their experimental results. It is thought likely to be a consequence of the differences in type of the spanwise amplitude distribution.

Transverse frequencies f_y*, which were obtained from sectional lift force acting on the section near the tip ($z/L = 0.9$) and mid-span ($z/L = 0.5$) of the cylinder, are presented in Fig. 7, and we have omitted the streamwise frequency f_x*, since it is precisely twice of f_y*. It seems that the lock-in phenomena are caused near the tip of the cylinder ($z/L = 0.9$), since the frequency of vortex shedding is almost equal to that of cylinder oscillation as shown in Fig. 7. However, similar phenomena are not seen in the mid-span of the cylinder ($z/L = 0.5$). It is thought that the onset of the lock-in phenomena depends upon the magnitude of local oscillation amplitude.

5 Conclusion

In this paper, the mathematical background and numerical treatment of a vortex method developed by the group of the present authors were briefly explained. And it became clear that the vortex methods have so much interesting features that they consist of simple algorithm based on physics of flow and provide easy-to-handle and completely grid-free Lagrangian calculation of unsteady and vortical flows without use of any RANS type turbulence models. From the results of recent works of application, it has been confirmed that the vortex method is available and useful for research and development of fluid machinery and flow-induced vibration problems. Finally, the present authors would like to state that the advanced vortex method is one of the most capable methods to contribute to the new generation of computational fluid dynamics (CFD) and it provides virtual reality of complex flow phenomena in fluid machinery and fluid engineering.

Acknowledgements

The authors would like to thank Dr. Takeda, Dr.Ido, and Dr. Yonayama of DMW Corporation in Japan for providing us with experimental data of the mixed-flow pump calculated in this study.

References

Dhondt, G., 1998-2004, CalculiX USER'S MANUAL version 1.5.

Flemming, F. and Williamson, C. H. K., 2005, "Vortex-induced vibrations of a pivoted cylinder", J. Fluid Mech., Vol.552, pp. 215 – 252

Fukuda K., and Kamemoto, K., 2005, "Application of a redistribution model incorporated in a vortex method to turbulent flow analysis", Proc. the Third International Conference on Vortex Flows and Vortex Models—ICVFM2005, Yokohama, Japan, November 2005, pp. 131 – 136

Greengard, L. and Rohklin, V., 1987, "A fast algorithm for particle simulations", J. Comp. Phys. 73, pp. 325 – 348

Iso Y. and Kamemoto K., 2005, "Vortex method and particle trajectory tracking method for Lagrangian-Lagrangian simulation applied to internal liquid-solid two-phase flows", Proc. the Third International Conference on Vortex Flows and Vortex Models—ICVFM2005, Yokohama, Japan, November 2005, pp. 287 – 292

Jauvtis, N. and Williamson, C. H. K., 2004, "The effect of two degrees of freedom on vortex-induced vibration at low mass and damping", J. Fluid Mech., Vol.509, pp. 23 – 62

Kamemoto, K., 1995, "On attractive features of the vortex methods", Computational Fluid Dynamics Review, ed. M.Hafez and K.Oshima, JOHN WILEY & SONS, pp. 334 – 353

Kamemoto, K., 2007, "Recent contribution of an advanced vortex element method to simulation of unsteady vortex flows", Computational Fluid Dynamics Journal, 15(4):55, pp. 422 – 437

Kamemoto, K. and Ojima, A., 2004, "Capability of the vortex method for virtual reality by computational hydraulics," Proc. 22nd IAHR Symp. on Hydraulic Machinery and Systems, Stockholm, June 29-July 2, Vol. B, B14-3.doc-1(11)-11(11)

Kamemoto K. and Ojima A., 2007, "Application of a vortex method to fluid dynamics in sports science", Proc. FEDSM2007 5th Joint ASME/JSME Fluids Engineering Conference July30-August 2, San Diego, FEDSM2007-37066

Kamemoto K. and Ojima A., 2008, "Vortex method for the analysis of complex, unsteady and vertical flows around a swimming fish", Advances in Science and Technology, Trans Tech Publications, Switzerland, Vol.58 pp. 183 – 192

Kamemoto, K., Ojima,A. and Nakamura, A., 2008, "A Virtual Wind Tunnel for Numerical Simulation of Flow-Induced Vibrations", Proc. the 9th International Conference on Flow-Induced Vibrations, Prague, June 30 - July 3, Paper No. 155

Leonard, A., 1980, "Vortex methods for flow simulations", J. Comp. Phys. 37, pp.289 – 335

Nakanishi, Y. and Kamemoto, K., 1992, "Numerical simulation of flow around a sphere with vortex blobs", Journal Wind Eng. and Ind. Aero, Vol. 46 & 47, pp. 363 – 369

Ojima A. and Kamemoto, K., 2000, "Numerical simulation of unsteady flows around three dimensional bluff bodies by an advanced vortex method", JSME Int. Journal, 43-2 B, pp. 127 – 135

Sarpkaya, T., 1989, "Computational methods with vortices—the 1988 Freeman scholar lecture", J. Fluids Engng., 111, pp.5 – 52

Uhlman, J. S,. 1992, "An integral equation formulation of the equation of motion of an incompressible fluid", Naval Undersea Warfare Center T.R., 10 086

Winkelmans, G. and Leonard, A., 1988, "Improved vortex methods for three-dimensional flows", Proc. Workshop on Mathematical Aspects of Vortex Dynamics, Leeburg, Virginia, pp. 25 – 35

Wu, J. C. and Thompson, J .F., 1973, "Numerical solutions of time-dependent incompressible Navier-Stokes equations using an integro-differential formulation", Computers & Fluids, Vol. 1, pp.197 – 215

The 4th International Symposium on Fluid Machinery and Fluid Engineering
November 24-27, 2008, Beijing, China
NO. 4ISFMFE-Ch01

Computer Stimulation of Air-Flowed Smashing Process

Yan Cui*, Xiaoling Ge

* Machinery and Power Engineering Institute, ECUST
MeiLong Road 130#, Xuhui District, Shanghai 200237, China
Tel: +86-13917337356 / Fax: +86-21-6425-2043
E-mail: cuiyan0320@sohu.com

Abstract Some technologies of computer simulation are introduced into the smashing-mechanic field in the article. The specific method in the course of air-flowed colliding smash, including model building, calculates and the image display of the actual working-situation is emphasized. In the end the article points out that competitive, intelligentize and visualize are the development and application direction of the computer simulation technique in the air-fluent smash field in the future.

Keywords air- smashing, visualize, simulation

Nomenclature

B	Young's modulus
E	kinetic energy
M	quality
Q	gravity
U	velocity
δ	velocity revert coefficient
ρ	grain density
σ	strength limit

1 Introduction

The situation of different kinds of materiel and process condition is also different in the air-flowed smashing process. There is still not one single machine which can deal with all kinds of material grain. Using computer technology to research the air-flowed smashing process can settle both of the two questions. Once a computer simulation system is set up, all of the consequence would be achieved only by two or three experiments and a simulation calculation on the computer.

Thus, except shorting the work time, enhancing the working efficiency and the material of the experiment research is also saved. But there is still not a precedent that uses the computer simulation to research the air-flowed smashing process in China. So, it is necessary to introduce the computer simulation technology to the air-flowed smashing process.

2 Theory Base of the Simulation System

There are two main grain break distinguish theory in the air-flowed smashing process: stress distinguish theory and energy distinguish theory. The latter is adopted in the article, comparing the kinetic energy and the broken work of the grain to judge that the grain is broken or not.

In the air-smashing process, there are approximate 80% grains is broken by collide with each other. The collision energy mainly depends on the grain's velocity, destiny and the concentration of the air fluent. If the quality of the grain is m, the velocity of the grain is U, and then the kinetic energy of the grain is:

$$E=\frac{1}{2}mU^2 \tag{1}$$

In fact, there is only part of the energy worked in the smash process, so if this part energy is defined as ΔE, Then:

$$\Delta E=\frac{1}{2}mU^2(1-\delta^2) \tag{2}$$

The assumption that the grain is absolute elastomer, then the broken work is:

$$W=\frac{\sigma^2 Q}{2B\rho} \tag{3}$$

The necessary condition is: $\Delta E > W$.

In the air-smashing process, the necessary kinetic energy of the grain is related with the Young's modulus and the strength limit. Furthermore, the surface morphology and the structure morphology also have a great effect to the necessary velocity of the grain. There are some gaps, cracks and tiny holes on the grain surface. These defects make the stress highly concentrate and urge the grains' break. As the velocity of the grain is so fast, mainly kinds of the grain can be conferred as absolute elastomer. But there are still some organic can not be deal with as elastomer in the common temperature, and some modification should be done on them.

3 Building of the Simulation System

The whole simulation system consists of two departments. The analysis and calculation system and simulation display system.

The calculate department use Access database to store the formula of the grain diameter, the material parameter, and the processing parameters.

The output department use Matlab software to show the numerical value and 3ds max software to display the whole smash process.

In the air-smashing process, different kinds of grains have different kinds of characters, and the effect by environment factor such as temperature, humidity ect. is also different. When the grain diameter is smaller than a certain value, the necessary parameter of the energy distinguish theory is almost impossible to obtain. So, there are some difficulties to use the energy distinguish theory directly o calculate the smash result. However, the common analysis software such as Ansys, Fluent is good at the analysis of the fluent field, but is not so accurate in the calculate of the smash result. In order to get a accurate smash result and a precise fluent field analyses, the paper fitting a formula between the material parameter, processing parameters and the smashing result according to the experiment research in advance. The formulas are stored in the database established before. The system is coupled with the Ansys software when it worked, and the smashing result is calculated by the formula stored in the database and the Ansys software analyze the fluent field. Thus, a better simulation result is achieved. The simulation calculation program is showed as the Fig. 1.

Once the calculate result is obtained, the data achieved by the calculate department is transmitted to the display system through a inner interface. And the final result can be displayed through a window to the researcher in a numerical form. The numerical display department output the numerical value of the smashing result, and image display department displays the whole smashing process in 3d fluent field forms according to the analysis of the fluent field . Include the force conditions, the movement tracks, and the smashing diameter of the grains. The velocity, diameter and the other parameter could be adjusted to get best simulation efficiency when the display system worked.

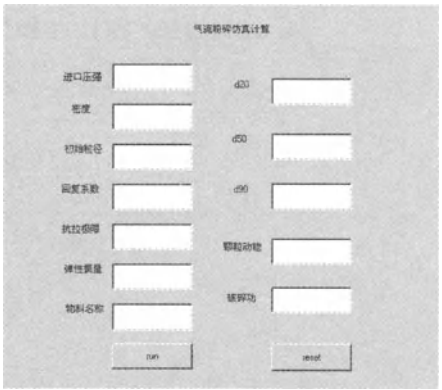

Fig. 1 Simulation calculate program figure

The 3ds max software is chose to work as the image display department. The reactor dynamics simulation system of the software can simulate the real-time collide of either rigid body or elastomer. So, it can display the whole smashing process comparatively true.

In order to building a visualize and integrated system finally, a linkage is insert to connect the two part of the simulation system. The linkage is designed by Visual C++ language, and the real frame of the whole system is showed as the Fig. 2.

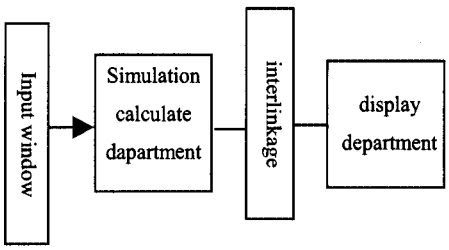

Fig. 2 Simulation system frame figure

4 Run of the Simulation System and the Analysis of the Calculate Result

In order to test the accuracy of the system, the paper chose to kinds of superfine grains and compare the calculate result to the experiment. The circumstance of the simulation system as the following:

Hardware: Core 2 Duo
2G DDR2 Kingston
200G 7200 r/min
128M 3D independent card
Gigabyte GA-P35-DS3L mainboard

Software: windows XP system
Visual C++ program
Matlab software
3ds max software
Ansys software
Experiment equipment: H100 flat form airflow mill
Operate: Handiwork
Comparison of the simulation and the experiment of the Pearl powder
Sample source: Shanghai Huali superfine technology LTD.
Sample fineness: 80 head
Feed rate: 3.95kg/h
Feeder pressure: 4kg/h
Smash pressure: 8kg/h
The result and comparison as follow.

Table 1 Experimental granularity distributing table of pearl powder

Diameter/ μ m	Accumulate vol./%
1.00	13.3
2.00	53.2
4.00	95.1
6.00	99.7
8.00	100

Table 2 Simulation calculation granularity distributing table of pearl powder

Diameter/ μ m	Accumulate vol./%
1.00	15.2
2.00	56.8
4.00	98.5
6.00	100
8.00	100

Table 3 Comparison table of simulation and experiment of pearl powder

	Simulation	experiment	Error/%
D20 μ m	1.36	1.61	18.38
D50 μ m	1.72	1.91	11.76
D90 μ m	3.23	3.44	6.5

Comparison of the simulation and the experiment of the doxycycline
Sample source: Shanghai Huali superfine technology LTD.
Sample fineness: 80 head
Feed rate: 3.95kg/h
Feeder pressure: 4kg/h
Smash pressure: 8kg/h
The result and comparison as follow.

Table 4 Experimental granularity distributing table of doxycycline

Diameter/ μ m	Accumulate vol./%
1.00	15.8
2.00	38.0
3.00	54.5
4.00	67.4
6.00	84.7
8.00	94.0
10.00	98.5
15.00	100

Table 5 Simulation calculation granularity distributing table of doxycycline

Diameter/ μ m	Accumulate vol./%
1.00	17.2
2.00	41.1
3.00	58.3
4.00	71.5
6.00	87.8
8.00	98.3
10.00	100
15.00	100

Table 6 Comparison table of simulation and experiment of doxycycline

	Simulation	experiment	Error/%
D20 μ m	1.2	1.5	25
D50 μ m	2.5	2.9	16
D90 μ m	6.6	7.1	7.8

5 Summary

Comparing the simulation and the experiment result it can be concluded that: the error between the simulation and the experiment range between 10~25%. The result calculated by simulation is smaller than experiment. The reason is that the effect of the environment is not considered in simulation calculation. From the phenomenon that the error of D90 is bigger than D50, and the error D50 is bigger than D20, it can be concluded that the error is related to the diameter, the bigger of the volume percent, the smaller of the error.

How to calculate the percent of the grain which can not be smashed due to the lost of the energy is the difficulty of the establishing of the system. The method that instead the velocity decrease of the part grain by the whole energy lost is adopted in the paper, and the effect is approved by the experiment.

References

Su mingde, Huang suyi.1997, "CFD Basis". TshingHua University publishing house.pp. 21 – 25

Wernet, M. P., 2000, "Development of Digital Particle Imaging Velocimetry for Use in Turbomachinery", *Experiments in Fluids*, Vol. 28, pp. 97 – 115

White, F. M., 2003, "Fluid Mechanics, 5th ed.", *McGraw-Hill*, New York

Wu ziniu, 2001.CFD "Prime Theory". Science publishing company. pp. 45 – 47

Zhang hang, Li bo, 2004. "3d cartoon master 3ds max6 quick directory", China Aerospace Publishing house. pp.175

The 4th International Symposium on Fluid Machinery and Fluid Engineering
November 24-27, 2008, Beijing, China
NO. 4ISFMFE-Ch28

Analysis on Modeling Rotor System with Sidling Bearing and Ring Seal by Using FEM

Shiliang Ping, Shanguang Tan, Dazhuan Wu and Leqin Wang*

* Chemical and Mechanical Research Institute, Zhejiang University,
Yuquan Campus, Hangzhou, Zhejiang, 310027, China
Tel: +86-0571-8795-2406 / Fax: +86-0571-8795-2406
E-mail: hj_wlq2@zju.edu.cn

Abstract An Ultrahigh-pressure multi-stage centrifugal pump works in high speed, with a long shaft and featured in complex structure. To improve the safety and reliability of operations demanded in a high level, the Ultrahigh-pressure multi-stage centrifugal pump develops in the direction of large equipment and integration of pump and electromotor. Except that the hydraulics, structure and control of electric must fulfill the design requirements, the research on vibration characteristic and stability of the shafting areatter is also important. Those characteristics are of great impacts on quality, life and reliability of Ultrahigh-pressure multi-stage centrifugal pumps. Therefore, it is very important to do dynamic analysis for the rotor shafts of ultrahigh-pressure centrifugal pumps. In this paper, the problems of modeling steady rotor system with sliding bearings and ring seal by using Finite Element Method are discussed. Discussion is conducted on the film force of sliding bearings and the method of its application in modeling, as well as the method of simulating film stiffness. Radial stiffness and damping of the film are the important factors of dynamic characteristics of the rotor systems, however the circumferential stiffness and damping are both small and generally not considered. In this dynamics model, the assumption of a rotor system in static equilibrium position plus small disturbance of the film is used to calculate the incremental film force, and the dynamic characteristic of film. Aiming for Rotor- Bearing System for 3800kW EHV, multi-stage centrifugal pumps are built. In the simulation analysis, modal shapes and critical speeds of the rotor are calculated, and the stability of the rotor system is analyzed. The results show that the method is reliable and useful for the design of the structures and parameters of EHV multi-stage centrifugal pumps.

Keywords multi-stage centrifugal pump, sliding bearing, oil film force, ring seal, dynamic characteristics, oil stiffness, FEM modeling

Nomenclature

F_x , F_y	component of oil film forces
F_{x0} , F_{y0}	component of oil film forces in equilibri-um position
f_x f_y	dynamic force of the oil film
K	stiffness of oil film
C	damping of oil film
e_0 , ψ_0	equilibrium position of journal
h_0	thickness of oil film
p_0	pressure of oil film
ε_0	eccentricity
F_r	radial force of ring seal
F_τ	circle force. of ring seal
k	stiffness of ring seal
c	damping of ring seal
m	additional quality
B	average radius clearance of bearing.
D	radius of the shaft
μ	dynamic damping coefficient of oil,
ω	the speed of the rotor
Ω	the speed of whirl

1 Introduction

An Ultrahigh-pressure multi-stage centrifugal pump with

a long shaft and complex structure works in high speed. To improving the safety and reliability of operations demanded in a higher level, the Ultrahigh-pressure multi-stage centrifugal pump develops in the direction of large equipment, and integration of pump and electromotor. Except that the hydraulics, structure and control of electric must fulfil the design requirements, vibration characterist-ics and stability of the shafting are matter also needed to be focused on. Those characteristics are of important impacts on quality, life and reliability of Ultrahigh-pressure multi-stage centrifugal pumps. Therefore, it is very important to do dynamic analysis for the rotor shafts of ultrahigh-pressure centrifugal pumps.

In the Ultrahigh-pressure multi-stage centrifugal pumps, sliding bearings are currently adopted. Because of the errors of design and manufacturing, improper installation after overhaul or the other reasons, the shaft and bush vibrate sharply in some large-scale rotor system, which result in failure of frequent or not working properly. Therefore, it is needed to study the dynamic nature of the rotor system, or redesign the pump's structure. The Finite Element Method (FME) is an effective method in dynamic design of the structure. In the FME analysis of a rotor system, the simulation of bearing oil film force is a difficult problem. The oil film force is a dynamic force, it directly provide rigidity and damping effect to a rotor system. When a rotor system operates in the steady-state circumstances, the oil film force is similar to regular force. When a rotor system operates in the unsteady-state circumstances, the situation would become much more complex. In the engineering, dynamic characteristics of rotor systems in steady-state circumstances are generally gained through the slowgrow and slowdown speed experiment or measure the steady-state response in steady speed. But in dynamics designing, engineering experiment could not predict the data, so it must use the finite element analysis and theoretical calculations.

Different from the general rotor system, in analysis the rotor system of multi-stage centrifugal pumps, the force of seal clearance is needed considered, besides the dynamic characteristic of the sliding bearings. As the rotor is generally horizontal and the seals are between in the two journal bearings. So the dynamic characteristic of the seals affect the entire rotor vibration. On the dynamic characteristics, the effect of the seal ring resembles the sliding bearing, but those working theories are different. The force of the seal clearance is resulted by the axial flow, which is resulted by high pressure, rather than dynamic pressure effect. Because of comparative large clearance of seal ring, high axial pressure, and low viscosity of water, water flow in circle and axial direction and are turbulent. So it makes and analysis great difficultly. In the study of sealed fluid effect, early it general based on assumptions the film's whole flow model(Bulk—Flow Models),This is a kind of empirical model which derived from Hirs turbulence lubrication theory. Followed Child filed "limited length theory" based on the Hirs turbulence equation. Antunes etc, used the overall flow model and Hirs wall friction coefficient equation on studing of static and dynamic characteristics of the rotor, which worked with large seal clearance. And analytical solution was obtained under certain assumptions. Hsu and Brennen collected equations which were needed in analysis on pumps and turbine with ring seals, and advanced a currency numerical calculation method. But it would be no longer applied when the seal flow of the work beyond the scope of the film when the assumptions. In this paper, CFD—Fluent would be used to the model the liquid ring seal with a quasi-steady-wide three-dimensional model, and analyze its flow field to obtain its static and dynamic characteristics.

2 The Model of Oil Film Bearing

The main factor effected the rotor dynamic characteristics are the radial stiffness and damping of oil film. the stiffness and damping in circle direction are week ,which generally not be considered.

To this end, the establishment of the mechanical as shown by increases approach to calculating the dynamic properties of oil film. Fig. 1 show the dynamic model, the method, giving small disturbances in static equilibrium position and calculating the increment of oil film force, is used to calculate the dynamic characteristics of the oil film. Use small disturbances $\Delta x, \Delta y$ and slow speed $\Delta\dot{x}, \Delta\dot{y}$, and suppose that force of oil Film and disturbance changed with linear relationship.

$$\begin{cases} F_x = F_{xo} + \dfrac{\partial F_x}{\partial x}\Big|_0 \Delta x + \dfrac{\partial F_x}{\partial y}\Big|_0 \Delta y + \dfrac{\partial F_x}{\partial x}\Big|_0 \Delta\dot{x} + \dfrac{\partial F_x}{\partial y}\Big|_0 \Delta\dot{y} \\ F_y = F_{yo} + \dfrac{\partial F_y}{\partial x}\Big|_0 \Delta x + \dfrac{\partial F_y}{\partial y}\Big|_0 \Delta y + \dfrac{\partial F_y}{\partial x}\Big|_0 \Delta\dot{x} + \dfrac{\partial F_y}{\partial y}\Big|_0 \Delta\dot{y} \end{cases} \quad (1)$$

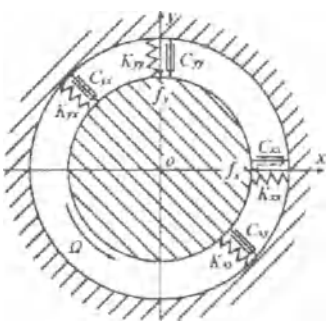

Fig. 1 The dynamic model of sliding be aring

In Eq. (1) F_x, F_y are component of oil film forces in x, y direction; F_{x0}, F_{y0} are component of oil film forces in x, y direction, when the journal is in static equilibrium position.

Film stiffness would be defined as increment of oil film force caused by displacement from static equilibrium position.

$$\left.\begin{aligned} K_{xx} &= \frac{\partial F_x}{\partial x}\Big|_0, \quad K_{xy} = \frac{\partial F_x}{\partial y}\Big|_0 \\ K_{yx} &= \frac{\partial F_y}{\partial x}\Big|_0, \quad K_{yy} = \frac{\partial F_y}{\partial y}\Big|_0 \end{aligned}\right\} \tag{2}$$

Film damping would be defined as increment of oil film force caused by disturbances speed.

$$\left.\begin{aligned} C_{xx} &= \frac{\partial F_x}{\partial \dot{x}}\Big|_0, \quad C_{xy} = \frac{\partial F_x}{\partial \dot{y}}\Big|_0 \\ C_{yx} &= \frac{\partial F_y}{\partial \dot{x}}\Big|_0, \quad C_{yy} = \frac{\partial F_y}{\partial \dot{y}}\Big|_0 \end{aligned}\right\} \tag{3}$$

So Eq.(1) could be transfered.

$$\begin{Bmatrix} \Delta F_x \\ \Delta F_y \end{Bmatrix} = [K]\begin{Bmatrix} \Delta x \\ \Delta y \end{Bmatrix} + [C]\begin{Bmatrix} \Delta \dot{x} \\ \Delta \dot{y} \end{Bmatrix} \tag{4}$$

In the Eq.(4)

$$\begin{Bmatrix} \Delta F_x \\ \Delta F_y \end{Bmatrix} = \begin{Bmatrix} F_x - F_{x0} \\ F_y - F_{y0} \end{Bmatrix}$$

$$[K] = \begin{bmatrix} K_{xx} & K_{xy} \\ K_{yx} & K_{yy} \end{bmatrix}$$

$$[C] = \begin{bmatrix} C_{xx} & C_{xy} \\ C_{yx} & C_{yy} \end{bmatrix} \tag{5}$$

K_{xy}, K_{yx} and C_{xy}, C_{yx} are cross-stiffness and Cross-damping coefficient, show oil film force in two perpendicular directions to each other the role of coupling.

Suppose the origin of the coordinates xoy is equilibrium position of journal, x, y are displacement of journal, f_x f_y are dynamic force of the film.

$$\begin{Bmatrix} f_x \\ f_y \end{Bmatrix} = [K]\begin{Bmatrix} x \\ y \end{Bmatrix} + [C]\begin{Bmatrix} \dot{x} \\ \dot{y} \end{Bmatrix} \tag{6}$$

Equilibrium position of journal e_0, ψ_0 as show in Fig.2. The film thickness is h_0, the film pressure p_0. So the Reynolds equation is described as Eq. (7).

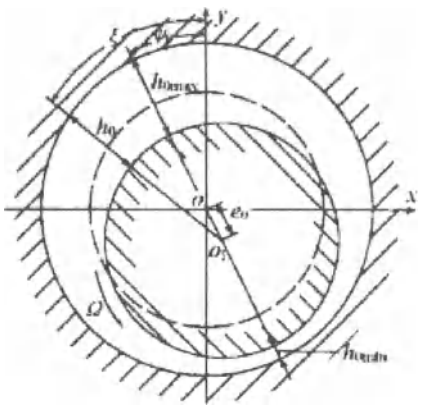

Fig. 2 Equilibrium position of journal

$$\frac{1}{R_2}\frac{\partial}{\partial \xi}\left(\frac{h_0^3}{12\eta}\frac{\partial p_0}{\partial \xi}\right) + \frac{\partial}{\partial z}\left(\frac{h_0^3}{12\eta}\frac{\partial p_0}{\partial z}\right) = \frac{1}{2}\Omega\frac{\partial h_0^3}{\partial \xi} \tag{7}$$

In Eq. (7). $h_0 = B\left[1+\varepsilon_0\cos(\xi-\psi_0)\right]$, $\varepsilon_0 = \frac{e_0}{B}$ is eccentricity, B is average Radius clearance of bearing.

Give journal a small disturbances $\Delta x, \Delta y$ and slow speed $\Delta\dot{x}, \Delta\dot{y}$ (Fig. 3).

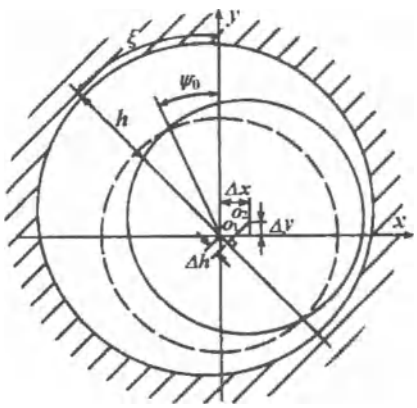

Fig. 3 The position of journal after disturbed

$$h = h_0 + \Delta x\sin\xi - \Delta y\cos\xi \tag{8}$$

$$\begin{aligned} p &= p_0 + \Delta p \\ &= p_0 + \frac{\partial p}{\partial x}\Big|_0\Delta x + \frac{\partial p}{\partial y}\Big|_0\Delta x \\ &\quad + \frac{\partial p}{\partial \dot{x}}\Big|_0\Delta\dot{x} + \frac{\partial p}{\partial \dot{y}}\Big|_0\Delta\dot{y} \end{aligned} \tag{9}$$

The Reynolds equation of oil film is described as Eq. (10) when the shaft neck's position is random.

$$\frac{1}{R_2}\frac{\partial}{\partial \xi}\left(\frac{h_0^3}{12\eta}\frac{\partial p_0}{\partial \xi}\right) + \frac{\partial}{\partial z}\left(\frac{h_0^3}{12\eta}\frac{\partial p_0}{\partial z}\right) = \frac{1}{2}\Omega\frac{\partial h}{\partial \xi} + \frac{\partial h}{\partial t} \tag{10}$$

From Eq. (7)~(10), Eq. (11) could be elicit.

$$\frac{1}{R^2}\frac{\partial}{\partial\xi}\left(\frac{h_0^3}{12\eta}\frac{\partial p'}{\partial\xi}\right)+\frac{\partial}{\partial z}\left(\frac{h_0^3}{12\eta}\frac{\partial p'}{\partial z}\right)$$
$$=\begin{cases}\frac{1}{2}\Omega\left(\cos\xi-3\frac{\sin\xi}{h_0}\frac{\partial h_0}{\partial\xi}\right)-\frac{h_0^3}{4\eta}\frac{1}{R}\frac{\partial p_0}{\partial\xi}\frac{\partial}{\partial\xi}\left(\frac{\sin\xi}{h_0}\right) & \left(p'=\frac{\partial p}{\partial x}\right)\\ \frac{1}{2}\Omega\left(\sin\xi-3\frac{\cos\xi}{h_0}\frac{\partial h_0}{\partial\xi}\right)-\frac{h_0^3}{4\eta}\frac{1}{R}\frac{\partial p_0}{\partial\xi}\frac{\partial}{\partial\xi}\left(\frac{\cos\xi}{h_0}\right) & \left(p'=\frac{\partial p}{\partial y}\right)\\ \sin\xi & \left(p'=\frac{\partial p}{\partial\dot{x}}\right)\\ -\cos\xi & \left(p'=\frac{\partial p}{\partial\dot{y}}\right)\end{cases} \tag{11}$$

Translate Eq. (11)into the form of differential equations and integrate in the region of entire Film and shaft neck length within the numerical, p' could be obtained . Then integrate again, we could elicit dynamic coefficients of the oil film.

$$\begin{Bmatrix}K_{xx}\\K_{yx}\end{Bmatrix}=-\int_{-L/2}^{L/2}\int_A\frac{\partial p}{\partial x}\begin{Bmatrix}\sin\xi\\-\cos\xi\end{Bmatrix}R\mathrm{d}\xi\mathrm{d}z$$
$$\begin{Bmatrix}K_{xy}\\Ky\end{Bmatrix}=-\int_{-L/2}^{L/2}\int_A\frac{\partial p}{\partial y}\begin{Bmatrix}\sin\xi\\-\cos\xi\end{Bmatrix}R\mathrm{d}\xi\mathrm{d}z \tag{12}$$

3 Dynamic Model of Ring Seal

The equation of Seal fluid exciting force, stiffness, damping and the following additional quality is described as Eq. (13).

$$-\begin{Bmatrix}F_r\\F_\tau\end{Bmatrix}=\begin{bmatrix}k_{xx}&k_{xy}\\k_{yx}&k_{yy}\end{bmatrix}\begin{bmatrix}X(t)\\Y(t)\end{bmatrix}+\begin{bmatrix}c_{xx}&c_{xy}\\c_{yx}&c_{yy}\end{bmatrix}\begin{bmatrix}\dot{X}(t)\\\dot{Y}(t)\end{bmatrix}+\begin{bmatrix}m_{xx}&m_{xy}\\m_{yx}&m_{yy}\end{bmatrix}\begin{bmatrix}\ddot{X}(t)\\\ddot{Y}(t)\end{bmatrix} \tag{13}$$

In Eq. (13), $k_{xx}=k_{yy}=\mathrm{K}$, $k_{xy}=-k_{yx}=\mathrm{k}$, $c_{xx}=c_{yy}=\mathrm{C}$, $c_{xy}=-c_{yx}=\mathrm{c}$, $m_{xx}=m_{yy}=\mathrm{M}$, $m_{xy}=-m_{yx}=0$

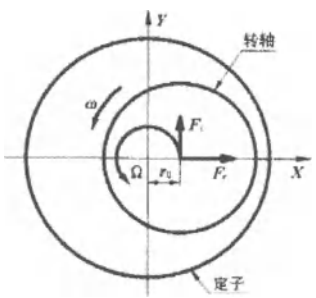

Fig. 4 Dynamic model of ring seal

F_r is radial force, F_τ is circle force.

In the rotation coordinates the flow is steady, for ease of analysis, choose $t = 0$ to study. In this time

$$X(0)=r_0, Y(0)=0, \dot{X}(0)=0, \dot{X}(0)=r_0\Omega,$$
$$\ddot{X}(0)=-r_0\Omega, \ddot{Y}(0)=0$$

So Eq. (13) could translate into Eq. (14).

$$\begin{cases}\frac{F_r}{r_0}=K-c\Omega+M\Omega^2\\ \frac{F_\tau}{r_0}=k-D\Omega\end{cases} \tag{14}$$

r_0 is amplitude of whirl. When F_r is more than 0, amplitude of whirl would increase. Because F_r is the factor leading the whirl, when it more than 0 and its direction is same as the direction of the whirl, it would accelerate whirl and to instability. By Eq. (14) it needs to use 3 different whirl frequency to calculate dynamic coefficient of ring seal, which could obtain 3 groups of equations.

4 Calculation of the Centrifugal Pump Rptor Dynamic Characteristics

In analysis of centrifugal pumps, the concept of "dry" and "wet" critical speed are introduced. the "dry" is critical speed which don't consider the effect of the dynamic characteristics of seal; "wet" is critical speed when the pump is in the working station, in this station dynamic characteristics of seal need to be considered.

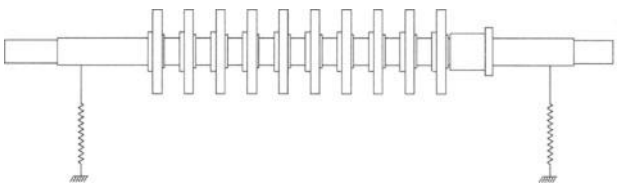

Fig. 5 the model of Shaft operation in the air

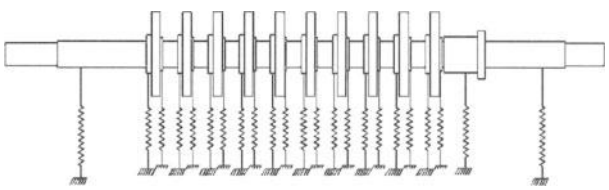

Fig. 6 the model of Shaft operation in the water

Table 1 The result of the calculation

Type of critical speed	First Order bending (rpm)	Second Order bending (rpm)
"dry" critical speed	3158	9731
"wet" critical speed	6342	12956

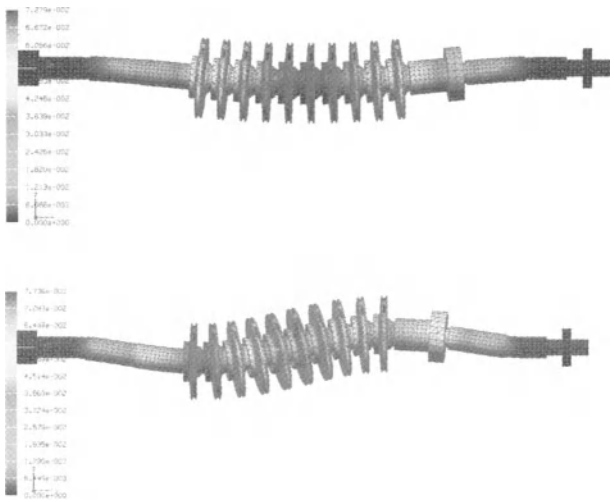

Fig. 7 The first and second mode diagram

5 Summmary and Conclusions

The "wet" critical speed is significantly higher than the "dry" critical speed, which explains that dynamic characteristics of seal have great effect on the rotor critical speeds in centrifugal pump, so in the design the characteristics of seal should be considered.

The results of calculation should have some error with practical date, mainly because in this paper motor parts were not considered. And in practice testing centrifugal pump is driven by the motor, its shaft and whirl coupling between two bearings have a certain influence on rotor system dynamic characteristics.

References

Santos I F, Watanabe F Y, 2004, "Compensation of Cross-Coupling Stiffness and Increase of Direct Damping in Multirecess Journal Bearings Using Active Hybrid Lubrication: part I2Theory " *Journal of Tribology*, Vol.126, pp. 146 – 155

Santos I F, Watanabe F Y, 2006, "Lateral Dynamics and Stability Analysis of a Gas Compressor Supported by Hybrid and Active Lubricated Multirecess Journal Bearing", *Journal of the Brazilian Society of Mechanical Sciences and Engineering*, Vol. 28, pp. 485 – 495

Rho B H, Kim KW, 2002, "A study of the dynamo-iccharacteristics of synchronously controlled hydrody-namic journal bearings", *Tribology International*, Vol.35, pp. 339 – 345

Cai Z, Queiroz M S De, Khonsari M M, 2004, "On the active stabilization of tilting2pad journal bearings", *Journal of Sound and Vibration*, Vol.273, pp. 421 – 428

Hirs G, 1973, "A Bulk Flow Theory for Turbulent in Lubricant Films", *ASME Journal of Lubrication Technology*, Vol.95, pp. 137 – 1461

Childs D W, 1983, "Finite—length solution for retordv-namic cocients of turbulent annular seals", *ASME Journal of LubricatiOn Technology*, Vol.105, pp. 437 – 444

Childs D W., 1983, "Dynamic Analysis of Turbulent Annular Seals Based on Hirs' Lubrication Equation", *ASME Journal of Lubrication Technology*, Vol.105, pp.429 – 436

Antunes J, Axisa F, Granenwald T, 1996, "Dynamics of rotors immersed in eccentric annular flow. Part I: Theory", *Journal of Fluid and Structures*, Vol.10, pp. 893 – 918

Hsu Y, Brennen C E, 2002, "Fluid flow equations for rotordynamic flows in seals and leakage paths", *ASME Journal of Fluids Engineering*", Vol.124

Project Support

Zhejiang Provinces importance special equipment project（project code: 2007C1 1030）

Zhejiang Provinces Technology project（project code: 2007C2 1059）

The 4th International Symposium on Fluid Machinery and Fluid Engineering
November 24-27, 2008, Beijing, China
NO. 4ISFMFE-Ch30

Cavitating Flow Analysis in a Closed Pump Sump

Yu Xu[*1], Shuhong Liu[2], Yong Li[3] and Yulin Wu[2]

[*1] Institute of Engineering Thermophysics, Chinese Academy of Sciences, Beijing 100080, China
E-mail: xuyu@mail.etp.ac.cn
[2] Dept. of Thermal Engineering, Tsinghua University, Tsinghua Garden, Haidian District, Beijing 100084, China
[3] Beijing Institute of Control Engineering, Beijing, P.R. China

Abstract Pump sumps are widely used in various installations like cooling water systems. The flow conditions in pump suction sump are very complicated, especially, in the surrounding of the pump bell In the present work, the two-fluid model of the two-phase flow has been applied to simulate the three-dimensional cavitating flow. The RNG k-epsilon-kca turbulence model, that is the RNG k-epsilon turbulence model in the liquid phase and kca model in the cavity phase, is used to close the governing Navier-Stokes turbulent equations of two-phase flow. And the computation of the cavitating flow through a model pump sump of closed type has been carried out. The calculated results have been compared with a PIV experiment. Good agreement exhibits the reliability of the numerical simulation model.

Keywords cavitating flow, two-fluid model, RNG k-epsilon-kca turbulence model, closed pump sump

Nomenclature

d	cavity diameter
E, k	constants
g	gravity acceleration
k	turbulent kinetic energy
n	cavity number in unit volume, normal
p	pressure
S	mass transfer term
Re	Reynolds number
t	time
u_j	velocity component
u, v, w	velocity components along X, Y, Z in sump
X, Y, Z	ordinates in sump
x_j	Cartesian ordinate
α	volume fraction (VF)
ε	turbulent kinetic energy dispassion rate
μ	viscosity
ν	kinetic viscosity
ρ	density
τ	stress

Subscripts

ca	cavity phase
f	fluid phase
p	point near wall

1 Introduction

A cavitating flow is a special two-phase flow, a turbulent, highly dynamic and highly unstable two-phase (cavity/ liquid) flow in which there is not only momentum transfer between the liquid phase and cavity phase, but also mass transfer, that is, the vaporizing process and the liquidizing process.

Beginning in the 1960s and 1970s, many cavitating flow models have been established based on the ideal fluid assumption and the singularity method. Yamaguchi and Kato (1983) proposed a cavitating flow model, which was used widely in calculation. Brewer and Kinnas (1995) used this model to calculate the flow around 2-D hydrofoils and 3-D hydrofoils, and Pellone and Peallat (1995) used it to predict the local bubbles near the hydrofoil surface. De Lange and De Bruin (1998) numerically simulated the periodic variation of bubbles.

As turbulent flow simulation has developed, it has been used for cavitating flow analysis. Up to now, the most widely used method for this analysis is the single-phase flow model, although a cavitating flow is a two-phase flow consisting of a cavity phase and a liquid phase. This is called the single-phase cavitating flow model, which numerically models the flow through direct computation

of the single-phase Navier-Stokes equations. A possible simplification of this type of complex flow is to assume the gas-liquid flow is a virtual single-phase, with a sharp density change as soon as the pressure drops below some critical pressure (Kubota et al 1992; Song et al 1997).

Because the single-phase simulation for cavitating flow is simple and easy, the single turbulent simulation model and numerical method have been developed.

In contrast with the single-phase flow, in a cavitating flow there is a continuing phase (liquid phase) as well as a dispersed phase (cavity phase). The cavities are distributed in the liquid flow in the form of dispersion. The cavitating flow is actually two-phase (cavity-liquid) flow, in which there exists a mass and momentum transfer between the liquid phase and cavity phase.

For the two-phase simulation, two models can be chosen: the two-fluid model and the mixture model.

In the mixture model, it is assumed that there is a dynamic balance in both the liquid phase and cavity phase in the cavitating flow. Using the mixture model researchers simulated turbulent cavitating flow using N-S equations and an additional equation of the cavity (or liquid) volume (or mass) fraction.

In the two-fluid model, the dispersed phase is treated as a pseudo-fluid. In the Eulerian approach, the flow of the dispersed phase is described by conservation equations of the mass, momentum and energy in continuity mechanics. This model includes not only the slip of parameters between the carrier fluid and the dispersed phase, but also reflects the differences in the diffusion for the carrier fluid and the dispersed phase. For example, the diffusion of the cavity phase is different from liquid diffusion. So the two fluid model can reflect more turbulent flow transport in two-phase cavitating flow. Reiger (1992) first introduced the two-fluid model for cavitating flow simulation. Grogger and Alajbegovic (1998) introduced the calculation for a cavitating flow in a Venturi tube.

In the two-fluid model, the "single-pressure" description for the continuous phase is widely used in computation, which fails to account the cavity rebounding effect by walls and cavity collision with each other. In order to involve these effects in the frame of the two-fluid model, the dispersed phase pressure and the internal transport should be considered to the dispersed phase with the dense volumetric fraction based on the kinetic theory of heterogeneous media.

In the cavitating flow, the volumetric fraction of the cavity phase is changed greatly. In most of the flow field, the fraction is very low, but at the cavitation area, it will be high. So it is necessary to use the two-fluid model to analyze the cavitating flow in the present study.

2 Governing Equations of Cavitating Two-Phase Flow in Two-Fluid Model

So far, most researchers have obtained the governing equations of the cavitating flow in terms of the macroscopic continuum mechanics theory. As the fluid vaporizes if the local pressure in the flow undergoes the vapor pressure of the fluid, and the gas quickly condensates if the pressure is higher than vapor pressure, the diameters of the cavity vary with the local pressure, which results in the mass and momentum transportations.

Let that α_k ($k = f, ca$) is the volume fraction of liquid phase and cavity phase. And $\alpha_{ca} + \alpha_f = 1$. The governing equations for the liquid-phase are

$$\frac{\partial \alpha_f \rho_f}{\partial t} + \frac{\partial}{\partial x_j}(\alpha_f \rho_f u_{fj}) = S_f \tag{1}$$

$$\frac{\partial(\alpha_f \rho_f u_{fi})}{\partial t} + \frac{\partial}{\partial x_j}(\alpha_f \rho_f u_{fi} u_{fj}) = \alpha_f \rho_f g_{fi} - \frac{\partial(\alpha_f p)}{\partial x_i} + \alpha_f \frac{\partial \tau_{fij}}{\partial x_j} + \frac{\alpha_f \rho_f}{\tau_{rca}}\left(u_{cai} - u_{fi}\right) + u_{fi} S_f \tag{2}$$

where $\boldsymbol{u}$ is the mean velocity in the liquid phase or cavity phase. And

$$S_{ca} = -S_f = (n4\pi)^{1/3}(3\alpha_{ca})^{2/3}\frac{\rho_{ca}\rho_l}{\rho}\left[\frac{2}{3}\left(\frac{p_v - p}{\rho_l}\right)\right]^{1/2} \tag{3}$$

$$\rho = \alpha_{ca}\rho_{ca} + \alpha_l \rho_l$$

$$\tau_{rca} = \frac{d_{ca}^2 \rho_{ca}}{18\mu_f}\left(1 + \frac{Re_{ca}^{2/3}}{6}\right)^{-1} \quad Re_{ca} = \left|\boldsymbol{u}_{ca} - \boldsymbol{u}_f\right|\frac{d_{ca}}{\nu_f} \tag{4}$$

The governing equations for the cavity-phase are

$$\frac{\partial \alpha_{ca}\rho_{ca}}{\partial t} + \frac{\partial}{\partial x_j}(\alpha_{ca}\rho_{ca}u_{caj}) = S_{ca} \tag{5}$$

$$\frac{\partial(\alpha_{ca}\rho_{ca}u_{cai})}{\partial t} + \frac{\partial}{\partial x_j}(\alpha_{ca}\rho_{ca}u_{cai}u_{caj}) = \alpha_{ca}\rho_{ca}g_{cai} - \frac{\partial(\alpha_{ca}p)}{\partial x_i} + \alpha_{ca}\frac{\partial \tau_{caij}}{\partial x_j} + \frac{\alpha_{ca}\rho_{ca}}{\tau_{rca}}\left(u_{fi} - u_{cai}\right) + u_{cai}S_{ca} \tag{6}$$

In the computation, the RNG $k-\varepsilon-k_{ca}$ turbulence model, that is RNG $k-\varepsilon$ model in the liquid phase and k_{ca} model in the cavity phase, is used to close the governing equations. In the numerical procedure, one of the SIMPLE algorithms, the SIMPLEC, is used to solve the equations both liquid and cavity phases.

3 Simulation of Two-Phase Cavitating Flow in a Closed Model Pump Sump .

Pump sumps are widely used in various installations like cooling water systems. Present day industrial requirements demand pump sumps of very large capacities with good performances. The flow conditions in pump suction sump are very complicated, especially, in the surrounding of the pump bell (Fig. 1), where there are various vortexes and even there occurs vortex cavitation, which result in vibration and cavitation, and decrease of the efficiency all of those will harm the performance of pump station, and even lead it out of order.

The 3D cavitating two-phase turbulent flow calculations are based on a closed pump sump, for which the experimental data is available. The configuration of the test pump sump is shown in Fig. 1. The main section is divided into two same channels (A and B) vertically by clapboard. The pipe bell with special structure is manufactured using Plexiglas material. The experimental data is obtained based on PIV technology.

3.1 Parameters of the Model Pump Sump

The flow rates in two channels are 0.965m^3/min (A) and 0.64m^3/min (B) respectively. In the calculation, the whole flow area is modeled in computation, and some representative planes are chosen here to show the results. The sketch map of measurement planes is shown in Fig.2 and Table 1.

Here, Planes X_2, Y_1, and Y_3 are tangent with the bell edge; Plane X_1 is near the back wall; Planes X_3 and Y_2 are on the center of pipe bell; Planes Z_1, Z_2 and Z_3 are below, tangent with and above the bell inlet.

According to the equations and methods above, the computation of three-dimensional two-phase cavitating flow through a model pump sump has been carried out. Results are showed below, compared with a PIV experiment.

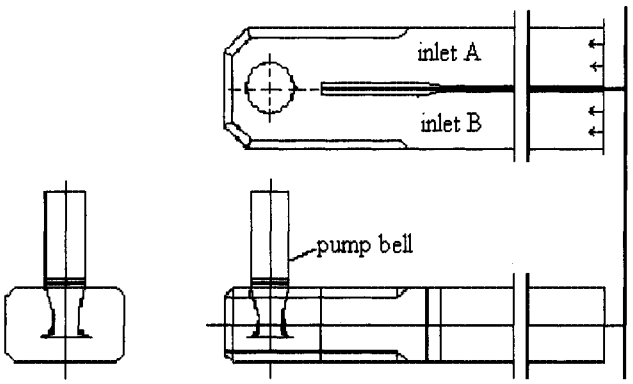

Fig. 1 pump sump model configuration

Table 1 Detailed position of measuring planes

Planes	Positions	Coordinates
X_1	Near back wall	x = 40mm
X_2	Tangent to bell edge	x = 120mm
X_3	Center of pipe	x = 200mm
Y_1	Tangent to bell edge	y =40 mm
Y_2	Center of pipe	y = 120mm
Y_3	Tangent to bell edge	y = 200mm
Z_1	Below the bell inlet	z = 50mm
Z_2	Tangent to bell edge	z = 80mm
Z_3	Above the bell inlet	z = 120mm

3.2 Boundary Conditions

Inlet condition: The first type of boundary conditions is given at the inlet.

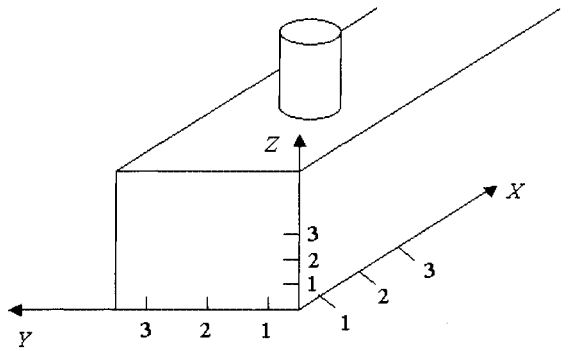

Fig. 2 Positions of measuring planes

Outlet condition: The derivatives of velocity components u_j and k,ε are zero along the normal of the boundaries, that is,

$$\frac{\partial u_j}{\partial n}=0,\quad j=1,2,3,\ \frac{\partial k}{\partial n}=0,\quad \frac{\partial \varepsilon}{\partial n}=0 \tag{7}$$

Wall conditions: Near solid walls, the logarithmic velocity profile was used to calculate the velocity and k,ε. Supposing that the distance from the nearest station P to the wall is y_p, then the values of u_p,k_p,ε_p can be defined as:

$$\frac{u_p}{u_\tau}=\frac{1}{\kappa}\ln(Ey_p^+),\quad k_p=\frac{u_\tau^2}{\sqrt{C_\mu}},\quad \varepsilon_p=\frac{u_\tau^3}{\kappa y_p} \tag{8}$$

where:

$$y_p^+=\frac{\rho u_\tau y_p}{\mu}=\frac{\rho c_\mu^{1/4}k_p^{1/2}y_p}{\mu},\quad \mu_\tau=\sqrt{\tau_w/\rho_f} \tag{9}$$

Pressure conditions: The normal derivatives of pressure on all boundaries is zero. And the inlet pressure which was obtained through experiment is given as the reference pressure.

The inlet conditions of velocity and volumetric fraction are given according to the liquid phase. Outlet condition and the wall condition is the second type, and the derivatives along the normal to boundaries are zero.

$$\left.\frac{\partial u_i}{\partial n}\right|_{y=0} = 0\,,\quad i = 1,2,3 \tag{10}$$

4 Simulation Results

In this paper, simulation results on some planes are compared with the experimental results. From the numerical simulation and the PIV experiment, flow characters can be obtained respectively. And the comparison of the results is as follows.

4.1 Velocity Magnitude Distribution

Fig. 3-1 to Fig. 3-9 show the comparison od the two dimensional velocity distributions on planes of Y_1, Y_2 and Y_3 (parallel to the back walls), X_1, X_2 and X_3 (parallel to the side wall of the sump), and Z_1, Z_2 and Z_3 (parallel to the bottom) respectively, in which figures on the left side, named as (a) are experiment results, and others (b) are simulation ones. Fig. 4-1 to Fig. 4-9 show the streamlines on these planes.

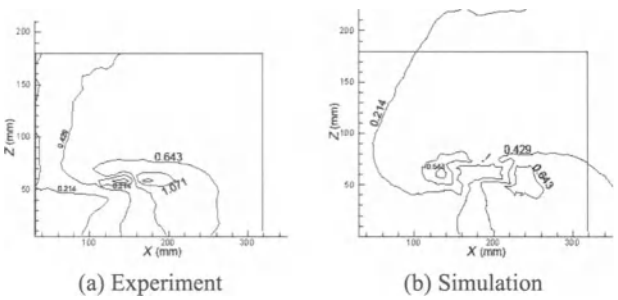

Fig. 3-1 Velocity on Y_1 plane (velocity unit: m/s)

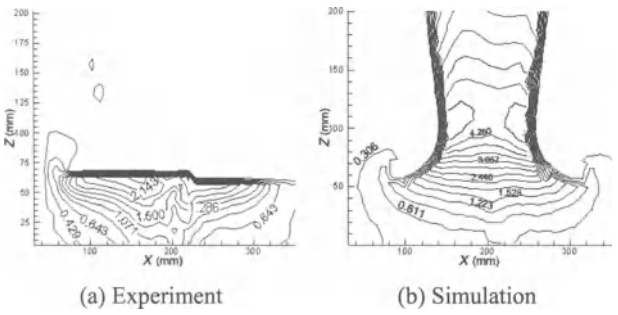

Fig 3-2 Velocity on Y_2 plane (velocity unit: m/s)

Figure 5-1 to Fig. 5-4 indicate the volume fraction of cavity phase on X_2, Y_2, Z_1 and Z_2 planes from computational results. The volume fraction of cavity is caused by the vortex cavitation on the central area of the suction pipe in sump. On the other area in the sump there is not any cavitation to be observed in the experiment.

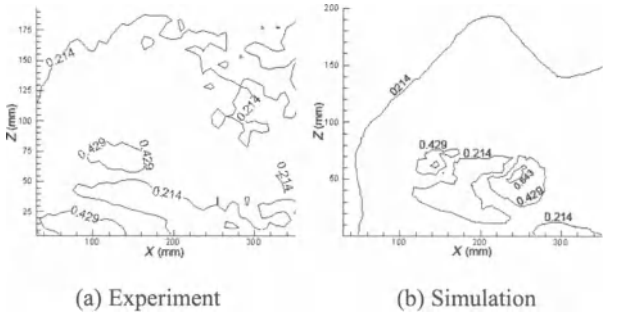

Fig. 3-3 Velocity on Y_3 plane (velocity unit: m/s)

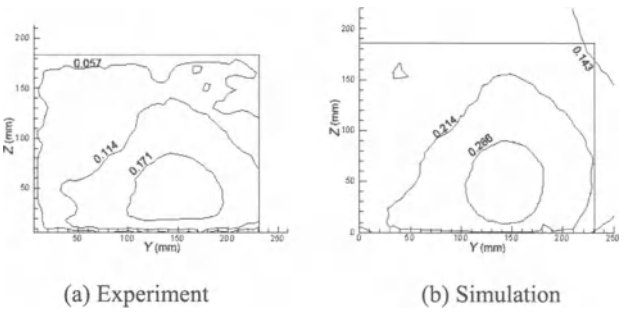

Fig. 3-4 Velocity on X_1 plane (velocity unit: m/s)

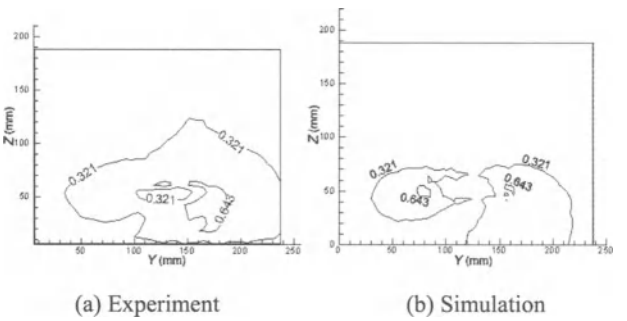

Fig. 3-5 Velocity on X_2 plane (velocity unit: m/s)

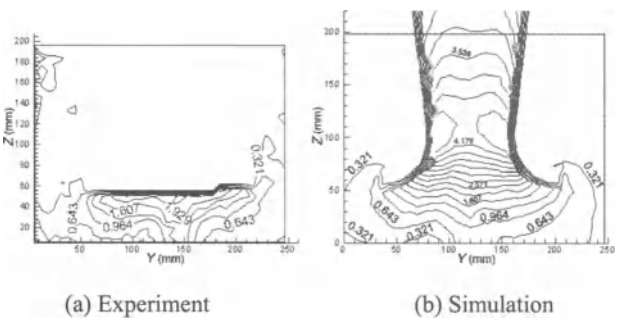

Fig. 3-6 Velocity on X_3 plane (velocity unit: m/s)

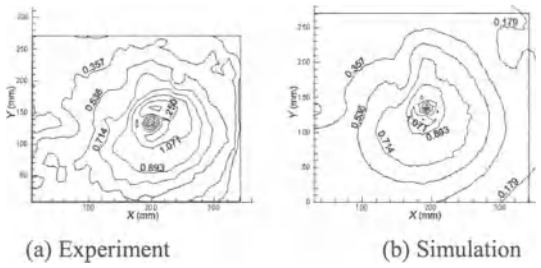

Fig. 3-7 Velocity on Z_1 plane (velocity unit: m/s)

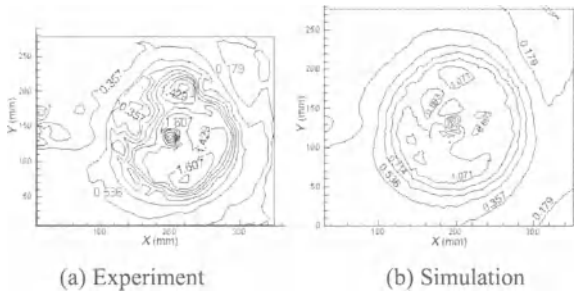

Fig. 3-8 Velocity on Z_2 plane (velocity unit: m/s)

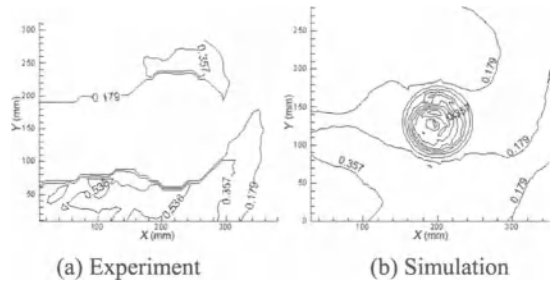

Fig. 3-9 Velocity on Z_3 plane (velocity unit: m/s)

4.2 Streamline and Velocity Vector

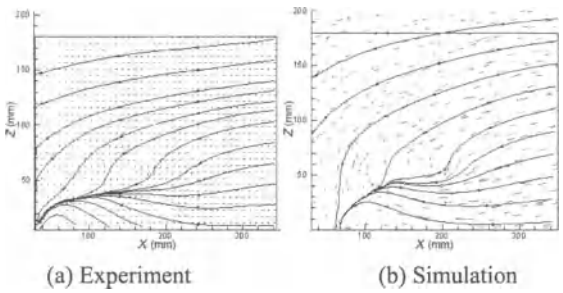

Fig. 4-1 Streamlines and velocity vectors on Y_1 plane

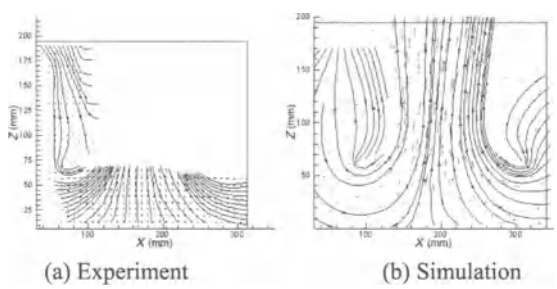

Fig. 4-2 Streamlines and velocity vectors on Y_2 plane

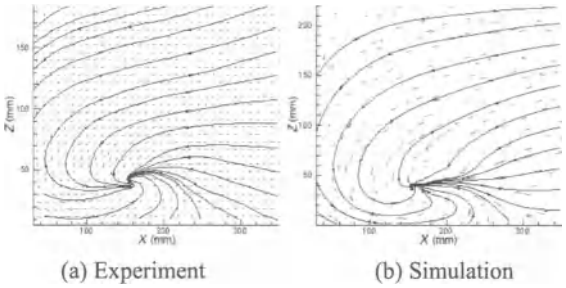

Fig. 4-3 Streamlines and velocity vectors on Y_3 plane

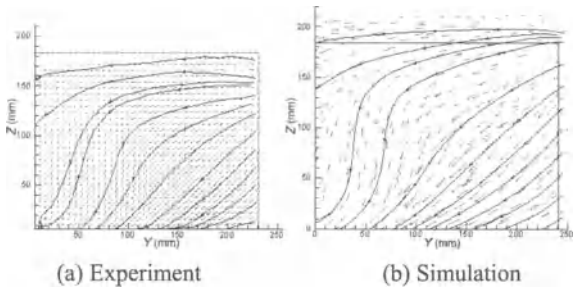

Fig. 4-4 Streamlines and velocity vectors on X_1 plane

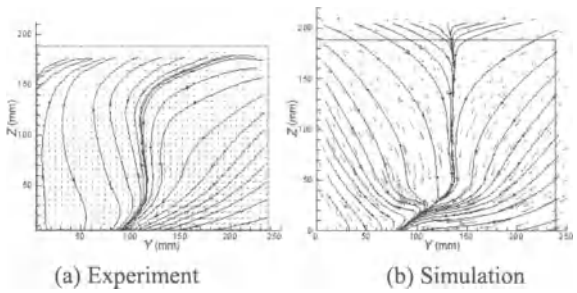

Fig. 4-5 Streamlines and velocity vectors on X_2 plane

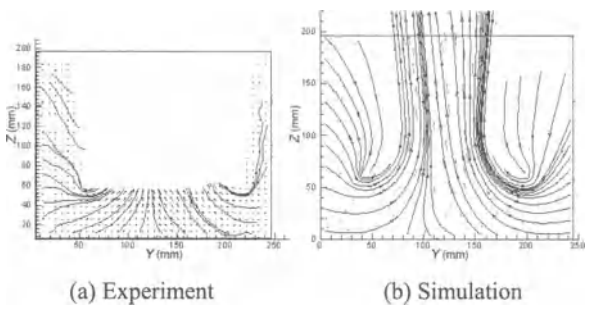

Fig. 4-6 Streamlines and velocity vectors on X_3 plane

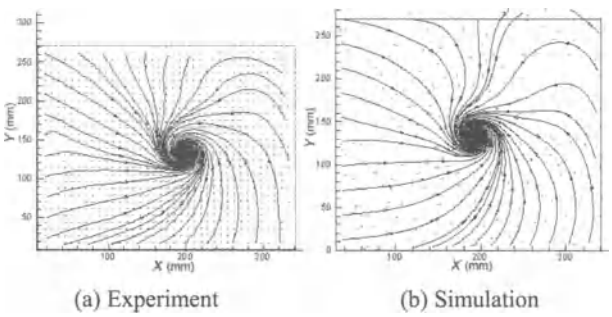

Fig. 4-7 Streamlines and velocity vectors on Z_1 plane

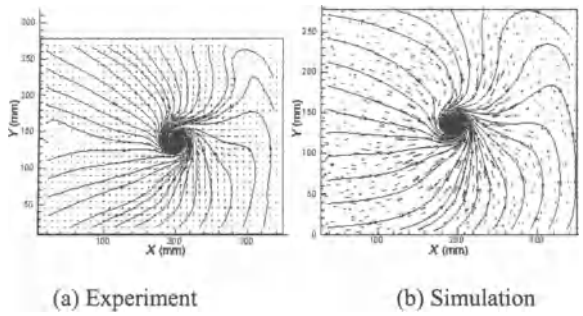

Fig. 4-8 Streamlines and velocity vectors on Z_2 plane

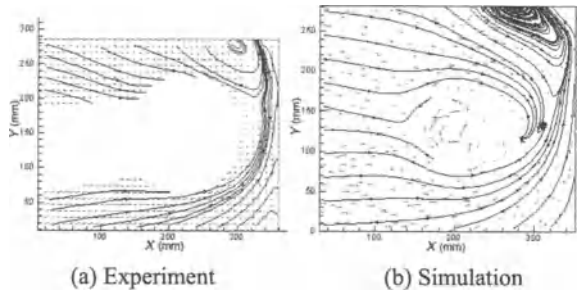

Fig. 4-9 Streamlines and velocity vectors on Z_3 plane

4.3 Volume Fraction of the Cavity Phase

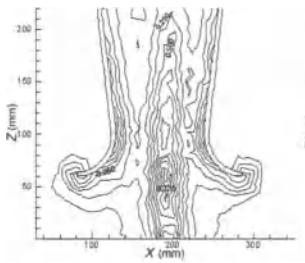

Fig. 5-1 VF of cavity on Y_2

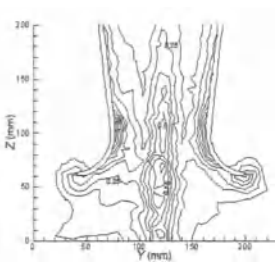

Fig. 5-2 VF of cavity on X_3

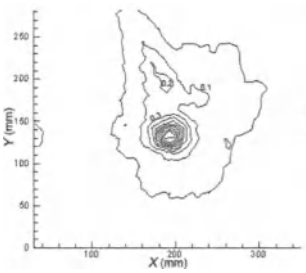

Fig. 5-3 VF of cavity on Z_1

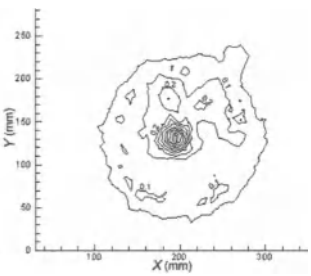

Fig. 5-4 VF of cavity on Z_2

5 Conclusions

In the two-phase cavitating flow, the volume fraction of the cavity changes greatly. So it is necessary to use the two-fluid model to analyze the cavitating flow.

The RNG $k-\varepsilon-k_{ca}$ turbulence model, that is RNG $k-\varepsilon$ model for the liquid phase and k_{ca} model for the cavity phase, is used to close the Reynolds time-averaged equations.

In the present paper, the two-fluid model was used to simulate the cavitating flow in a 3D closed pump sump.

After comparing with the PIV experimental data for the 3D case, it is verified that the two-fluid model is able to reproduce all states of cavitations.

Acknowledgements

This research work was funded by the Chinese National Foundation of Natural Science (No. 90410019).

References

Arndt R E A. Kjeldsen M. Song C C S. Keller A. 2002. Analysis of Cavitation Wake Flows, *Proceedings of the 21st IAHR Symposium on Hydraulic Machinery and Systems*, September 9 – 12

Brennen C E. 1995. Cavitation and Bubble Dynamics. *Oxford University Press,* New York, 1995

De Lange D F. De Bruin G J. 1998. Sheet Cavitation and Cloud Cavitation Re-entrant Jet and Three-dimensionality. *Applied Scic Research*, 58: 91 – 114

Grogger H A and Alajbegovic A. 1998. Calculation of the cavitation flow in Venturi geometries using two fluid model. *Proceedings of ASME Fluids Engineering Division Summer Meeting.* Washington D C

Kubota A. Kato H. and Yamaguch H. 1992. A New Modeling of Cavitating Flows: A Numerical Study of Unsteady Cavitation on a Hydrofoil Section. *J. Fluid Mech.* 240: 59 – 96

MANSA Kante et al. 2003. PIV Experimental Investigation on the Flow in a Model of Closed Pump Sump.*TSINGHUA SCIENCE AND TECHNOLOGY,* Volume 8,Number 6: 681 – 686

Pellone C. Peallat J M. 1995. Non-linear Analysis of Three-dimensional Partially Cavitating Hydrofoil. *Proc. of the International Symposium on Cavitation*, Deauville, France, 63 – 67

Rieger R. 1992. Mehrdimensionale Berechnung zweiphasiger Stroemungen, *PhD-Thesis*, Graz: Technical University Graz

Sauer J and Schnerr G H. 2000. Unsteady cavitating flow – a new cavitation model based on modified front capturing method and bubble dynamics. In *Proc. of FEDSM'00 4th Fluids Engineering Summer Conference*, No.FEDSM2000-11095

Singhal A K, Li H Y, Athavale M M and Jiang Y. 2001. Mathematical basis and validation of the full cavitation model. In *ASME FEDSM'01* (New Orleans, Louisiana, USA)

Song C C S. He J. Zhou F. and Wang G. 1997. Numerical simulation of cavitating and non-cavitating flows over a hydrofoil, *SAFL project report no. 402*, University of Minnesota

The 4th International Symposium on Fluid Machinery and Fluid Engineering
November 24-27, 2008, Beijing, China
NO. 4ISFMFE-IL23

Aerodynamic Performance of Double-Sided Labyrinth Seals

Tong Seop Kim[*1], Yungmo Kang[2] and Hee Koo Moon[3]

[*1] Dept. of Mechanical Engineering, Inha University
253 Yonghyun-Dong, Nam-Gu, Incheon 402-751, Korea
Tel: +82-32-860-7307 / Fax: +82-32868-1716 E-mail: kts@ihnha.ac.kr (Corresponding Author)
[2] Solar Turbines Inc.
9330 Sky Park Court, San Diego, CA 92123
Tel: +1- 858-715-1042 E-mail: Kang_Yungmo@solarturbines.com
[3] Solar Turbines Inc.
2200 Pacific Highway, San Diego, CA 92101
Tel: +1- 619-544-5226/ Fax: + 1-619-544-2682 E-mail: Moon_Hee_Koo_X @solarturbines.com

Abstract A test rig for double-sided labyrinth seals, which simulated the rim seal of a gas turbine rotor disk, was set up and aerodynamic performances of two different configurations (straight and stepped) were tested. Influences of pressure ratio and various combinations of tip clearances of the two sides on the seal performance were investigated. In addition to the overall seal performance, leakage behaviors of the individual seals (upstream and downstream) were separately analyzed and compared. The leakage reduction effect of step decreases with decreasing clearance. If the difference in the clearances of the two sides is sufficiently large, the smaller clearance side fully dominates the overall seal leakage behavior. Predictions by an analytic model and CFD were also carried out, and CFD gives better agreements with the test n general.

Keywords labyrinth seals, test, straight, stepped, clearance, pressure ratio

Nomenclature

A_c	clearance area
B	teeth width
C_d	discharge coefficient
D	distance to contact
H	step height
K	teeth height parameter
k	specific heat ratio
$\dot{m}$	mass flow rate
P	pressure, pitch
R	gas constant
S	clearance
T	temperature
β	taper angle
θ	teeth front angle

subscripts

1	rig inlet
2	middle chamber
3	rig exit
d	downstream side
in	inlet
out	outlet
u	upstream side

1 Introduction

Labyrinth seals are widely used in rotating machinery either to minimize undesirable leakage flow between rotating and stationary parts or to control flow rates. Despite many other advanced sealing techniques, it is still the most important and widely used technique because of its structural simplicity, reliability, high temperature resistance, wide operating range in terms of pressure difference, and so on. The secondary airflow system of gas turbines is the most important area of application of labyrinth seals. They are used to reduce leakage loss at blade shrouds, prevent hot gas ingress or minimize cooling air leakage at rotating disk space.

Vermes (1961) conducted one of the early systematic investigations on the seal performance and suggested analytic prediction models. There have been published several test results and performance prediction tools. Stocker's works (1977, 1978) are typical examples of test results for various configurations. Tipton et al. (1986) summarized previous efforts to predict seal performance and proposed another prediction method. Zimmerman and Wolff (1998) provided an insight into the seal performance behavior, and discussed main design parameters and their effect of performance. Even with those efforts, no simple analytic models to satisfactorily predict performances of wide variants of seal configuration are available. Therefore, in order to accurately predict the seal leakage flow, rig test is recommended.

As the requirements for performance upgrade of gas turbines becomes tight, optimization of the secondary air flow system becomes more important. In particular, since the first turbine rotor blade is the most thermally highly loaded component, a good sealing in coolant supply region of the rotor disk is quite important. Improper sealing would significantly reduce the coolant supply to the rotor blades, which may increase blade temperature and thus reduce blade life. In this work, a static test rig for double-sided labyrinth seals, which simulates the rim seal of a gas turbine rotor disk, was set up and aerodynamic performances of two different configurations (straight and stepped) were tested. Influences of pressure ratio and various combinations of tip clearances of the two sides on the seal performance were investigated. Results of an analytic seal performance prediction model as well as CFD analysis have also been compared with the test results.

2 Test

It has been reported (Waschka et al., 1990) that the effect of rotation is important only at a very high speed (more exactly, the ratio between the circumferential speed of the seal arm and the flow speed). Without the effect of the rotation, a 2-D rig is expected to provide nearly the same results as an axisymmetric 3-D rig does (Stocker, 1978). Accordingly, a 2-D rig is used in this study. Fig. 1 shows the geometries of the seals tested. Dimensions are listed in Table 1. The seal is double sided. In a real axisymmetric engine situation, the y direction is the radial direction. The upstream seal is a two-teeth converging seal and the downstream seal is a three-teeth diverging seal. Two different seal configurations are tested: straight and stepped. The rig is scaled up version of a real engine seal. Since other dimensions are fixed, the clearance is the only variable dimension depending on operating condition. Four different clearances were tested. (approximately 1.0, 1.5, 2.0, 4.0mm, see Table 1 for exact values).

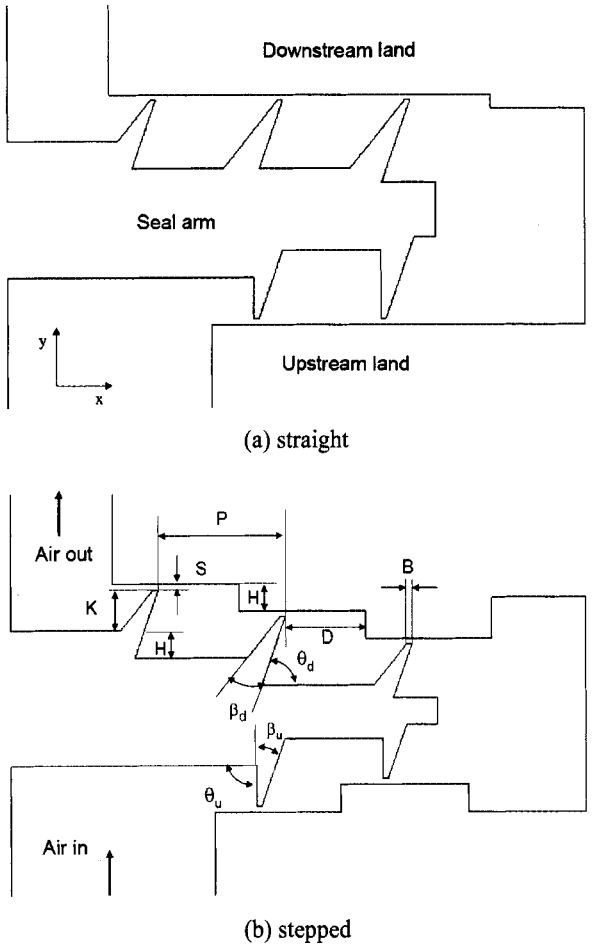

Fig. 1 Seal geometry

Table 1 Seal dimensions

P	K	B	H	θ	β	D	S
49.78	15.24	2.18	10.16	90 (u)	20	31.50	1.016
				70 (d)			1.524
							2.032
							4.064

All lengths are in mm and angles are in degree.

An open loop test rig was used. Air flow rate was measured at the air supply pipe using a turbine flow meter. At the test section inlet and the middle chamber, pressures were measured with pressure transducers along three depth-wise locations and averaged. Temperature was also measured with T-type thermocouples at the rig inlet. Two flow straighteners were inserted at the rig inlet. The exit pressure was maintained at the ambient pressure and the inlet pressure was changed to obtain various pressure ratios.

Performance of a seal can be described by relations between pressure ratio and a flow parameter. The most common flow parameter is the following flow function.

$$\frac{\dot{m}\sqrt{T_{in}}}{A_c P_{in}} \tag{1}$$

Seal performance can also be described by the discharge coefficient defined as follows.

$$C_d = \frac{\dot{m}}{\dot{m}_{ideal}} \tag{2}$$

where

$$\dot{m}_{ideal} = \frac{A_c P_{in}}{\sqrt{T_{in}}} \sqrt{\frac{2k}{R(k-1)} \left[\left(\frac{P_{out}}{P_{in}} \right)^{2/k} - \left(\frac{P_{out}}{P_{in}} \right)^{(k+1)/k} \right]}$$

Not only the overall double-sided seal performance, but also the performances of the individual seals (upstream and downstream) can be analyzed because the pressure at the middle chamber is measured. The pressure ratio in Eq. (2) is P_1/P_3, P_1/P_2, P_2/P_3 for the overall seal, the upstream seal, and the downstream seal, respectively.

3 Test results

Almost all combinations between the clearances of the upstream seal and the downstream seal are tested. Fig. 2 exemplifies the leakage behavior of the stepped seal with clearances of 2.0/2.0. The first and second numbers denote clearances, in mm, of the upstream side and the downstream side respectively. The downstream seal outperforms much (lower flow function) for all pressure ratios. This trend seems very reasonable because the down stream seal has more teeth (3 vs 2). It is also noticeable that even though the clearance sizes are equivalent, the downstream seal dominates the overall performance. In other words, a much larger pressure drop (or larger pressure ratio) occurs at the downstream seal than at the upstream seal for a given overall pressure ratio because the downstream seal provides more flow resistance. Fig. 3 shows the results of the stepped seal with clearances of 0.4/0.1. This is an extreme case where the upstream seal hardly impose flow resistance. The discharge coefficient of the overall seal is calculated using the smaller clearance area. The downstream seal dominates so much that the overall seal leakage behavior is almost same as that of the downstream seal alone. The straight seal exhibits the same trend as in the stepped seal. However, the flow functions are larger than those of the stepped seal for all of the cases tested as will be explained in the next paragraph.

Now, the leakage performance of individual seals (up and downstream seals of both the straight and stepped

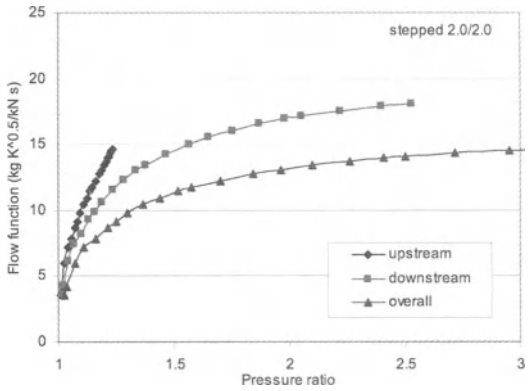

Fig. 2 Flow function for stepped seal with clearances 2.0/2.0

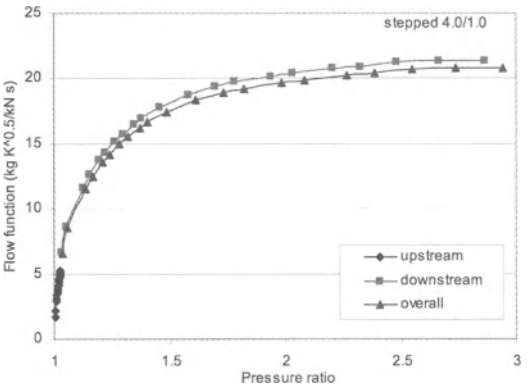

Fig. 3 Flow function for stepped seal with clearances 4.0/1.0

configurations) will be discussed comparatively. Since we performed tests for various clearance combinations, there exist several performance curves for a fixed clearance of each side, depending on the clearance size of the opposite side. However, in most of the cases, the different data usually merge into a single curve. This confirms that any of the flow function curves can represent the performance characteristics of the specific seal with a sufficient reliability. Among many choices, the performance curve of each side combined with the largest clearance (4.0mm) for the opposite side was selected because this condition provides the largest pressure ratio range of the specific seal of interest. Figs. 4 and 5 present the leakage performance of the straight seals in terms of discharge coefficient. For all test conditions, the downstream seal shows a better performance, i.e., a smaller flow function or discharge coefficient. The main reason is because the downstream seal has more teeth, providing more resistance. Figs. 6 and 7 show the discharge coefficient of the stepped seals. As in the straight cases, the downstream seal outperforms the upstream seal. Comparison of the results reveals that both the upstream and downstream stepped seals have lower discharge coefficients, i.e. lower leakage at the same operating condition, than the corresponding straight seals. It is generally accepted that a step provides additional resistance to the flow and thus

the stepped seal allows less leakage. Thus, the present test confirms the favorable effect of the step in terms of leakage reduction.

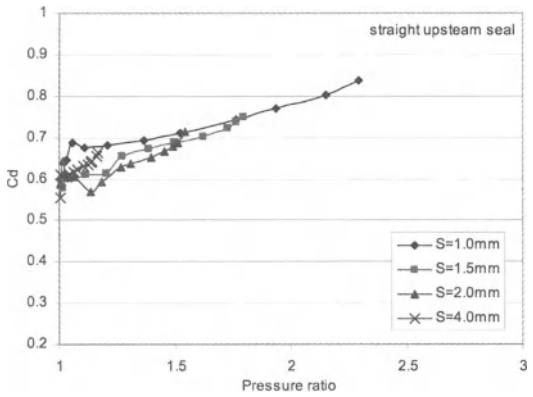

Fig. 4 Discharge coefficient of straight upstream seal

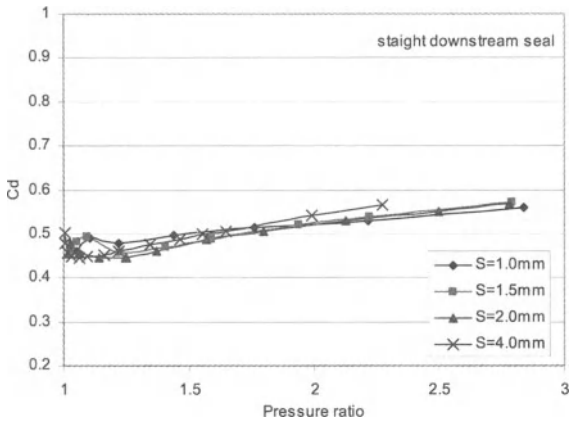

Fig. 5 Discharge coefficient of straight downstream seal

The straight and stepped seals show different trends regarding the dependence of the discharge coefficient on the clearance. As shown in Figs. 4 and 5, it is not easy to see a distinctive dependence of the discharge coefficient on the clearance in the straight seals. However, in the stepped seals (Figs. 6 and 7), the discharge coefficient generally gets higher as the clearance becomes smaller. In a previous research (Wittig et al, 1987), a rather reversed result was reported. They observed a strong clearance dependence in the straight seal (discharge coefficient decreases with decreasing clearance) and a relatively weak clearance dependence in the stepped seal. Their test rig had more teeth than the present test, and they mentioned that as the number of teeth reduces the tendency of the clearance dependence might change.

In order to summarize the performance difference between the stepped seal and the straight seal, the flow function ratio between the stepped and straight seals is calculated. For every clearance, the ratio ($C_{d,stepped}$/ $C_{d,straight}$) is calculated at various pressure ratios and then the average ratio is plotted in Fig. 8. As explained in

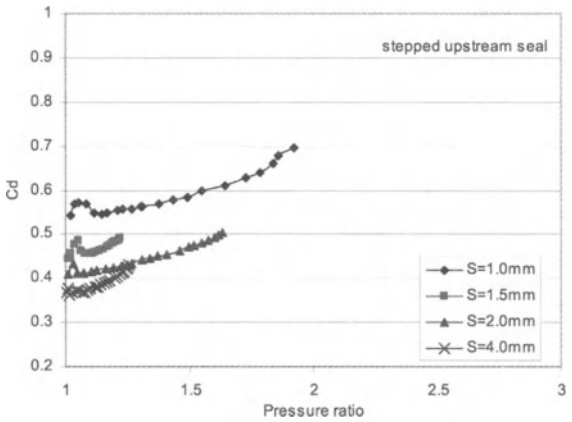

Fig. 6 Discharge coefficient of stepped upstream seal

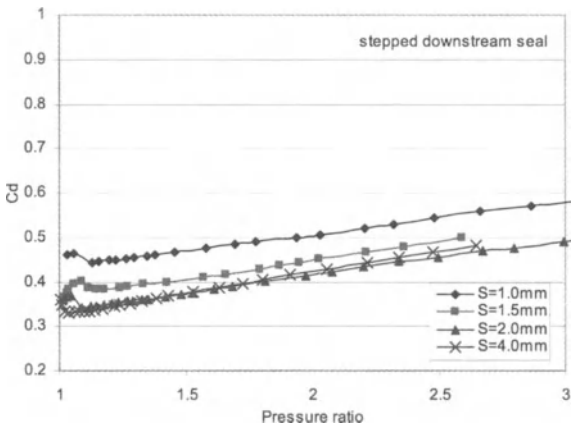

Fig. 7 Discharge coefficient of stepped downstream seal

previous paragraphs, the stepped seal always reduces leakage for all clearance tested in this work. Thus, the ratio is less than 1.0. The positive effect of a stepped seal increases as clearance increases. Calculation of this ratio from the measured data of the previous study (Wittig et al., 1987) also shows a same trend. Therefore, a tentative conclusion is that even though the dependence of the discharge coefficient itself on the clearance may vary depending on seal geometry, the leakage reduction effect of step increases as the clearance becomes larger. The test also shows that the leakage reduction effect of step is more effective in the upstream seal. This result seems reasonable because the upstream side is a converging seal and thus the flow hits the vertical step wall before entering the next teeth section, which may dissipate the dynamic energy more effectively.

Figs. 9 and 10 present performances of overall seals. Several typical clearance combinations are exemplified. Four of them are with equal clearances at both upstream and downstream sides. The other two cases are combinations between the smallest (1.0mm) and the largest (4.0mm) clearances. In a real engine, thermal expansion rate of the stationary part (lands) and the rotating part (seal arm) are different. Thus, the clearances of both aides at the hot

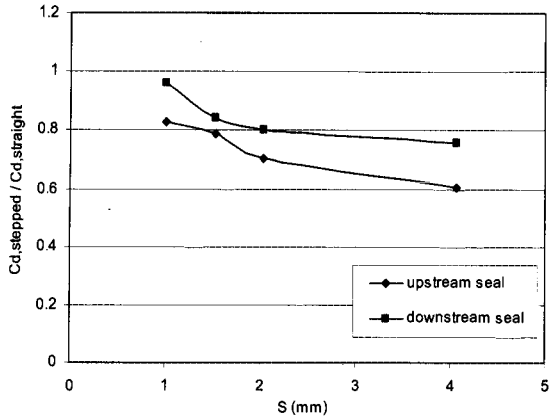

Fig. 8 Relative performance comparison of stepped and straight seals

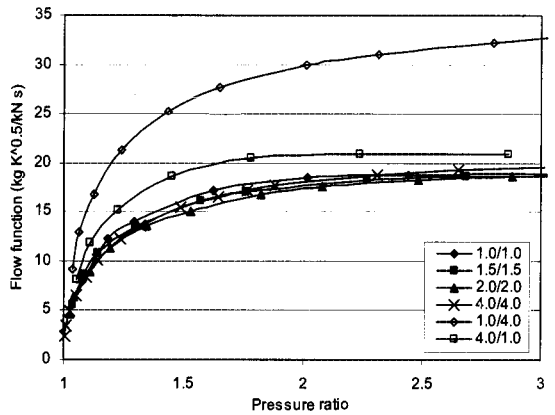

Fig. 9 Overall double-sided straight seal performance

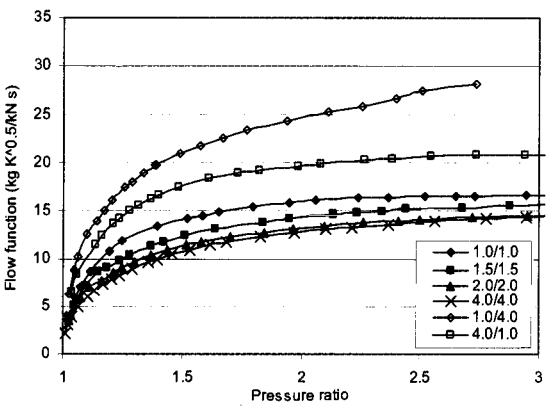

Fig. 10 Overall double-sided stepped seal performance

running condition are different from those at cold conditions. Here, 1.0/4.0 and 4.0/1.0 are assumed to simulate cold and hot running conditions, respectively. First, equal-clearance cases (1.0/1.0, 1.5/15., 2.0/2.0 and 4.0/4.0) are discussed. The stepped seal naturally exhibits lower leakage for all of the clearances tested, which conforms to the individual seal result. The dependence of the flow function on the clearance is also consistent with the individual seal result. The clearance dependence is not distinct in the straight seal. In the stepped seal, the flow function increases as the clearance gets smaller and becomes less sensitive to the clearance when the clearance exceeds a certain value. In the cases where two clearances are different, the flow functions are calculated using the smaller clearance area, that is, the area corresponding to the clearance of 1.0mm. As explained in Fig. 3, if the clearance difference is larger enough, the larger clearance side does not provide sensible flow resistance, thus the overall seal performance is almost represented by the performance of the smaller clearance side (the downstream side in case of 4.0/1.0 and the upstream side in case of 1.0/4.0). Between the two combinations, 4.0/1.0 case allows much less leakage than 1.0/4.0 case because the downstream side has a better performance (a lower leakage). Thus, a higher leakage flow is expected in the starting phase of the engine than in the hot running condition. As in any other conditions, the stepped seal outperforms the straight seal in general.

4 Prediction

4.1 Analytic Model

There exist several analytical performance prediction tools. Various modeled can be classified into two categories: global and knife-to-knife (teeth-to-teeth) models. A knife-to-knife model suggested by Tipton et al. (1986) is used in this study because it is based on vast experimental data and a computerized program (Chupp et al., 1986) exists. The model dealt with three loss mechanisms inside a seal separately: contraction, venturi and friction, and partial or full expansion. Thus, performance of each tooth is stacked to produce overall seal performance. Detailed information can be referred to the literatures.

4.2 Numerical Analysis

Recently, efforts have been increased to apply computational fluid dynamics (CFD) to labyrinth seal flows. Depending on each researcher's interest, the degree of complexity of CFD analysis (2-D vs 3-D, refinement of grids, etc.) varies. Since the rig is two dimensionality was confirmed in the test, a 2-D calculation is adopted. A commercial finite volume code, STAR-CCM+ V.2.07 (CD-adapco, 2007), has been used. The medium is ideal gas air and the flow is assumed to be steady and adiabatic. Polyhedral meshes were used. A Two-layer k-ε turbulent model and a two-layer all y+ wall treatment were adopted. Grid dependence was checked to produce sufficiently converged solutions according to mesh size. Number of meshes are 13,000~15,000.

4.3 Result

The analytic model and CFD were applied to most of the tested cases. However, we limit our interest only to the overall seal performance and present example results. Compared with the test data, the analytic model generally underestimates the flow function in both the straight stepped seals. In general, CFD predictions are closer to the test data than the analytic model predictions in both the straight and stepped seals. Figs. 11 and 12 exemplify comparisons of the prediction results with test data for a fixed inlet to exit pressure ratio (1.4). Results of five different clearance combinations are presented. The flow functions of the cases 4.0/1.0 and 1.0/4.0 are calculated using the smaller area, as explained in Fig. 9 and 10. The analytic model generally under-predicts. CFD gives better agreements with the test data in general. In particular, agreements between CFD and test are good in the stepped seal except the highest leakage case (4.0/4.0).

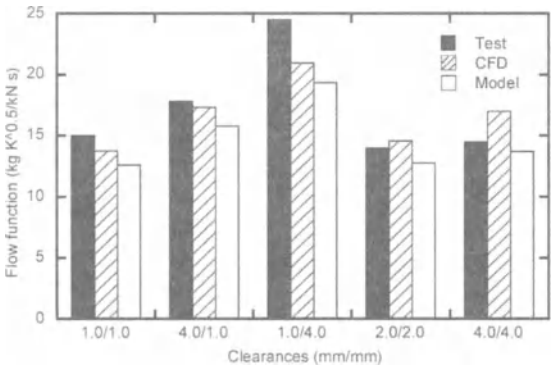

Fig. 11 Comparison of predictions with test for the straight seal

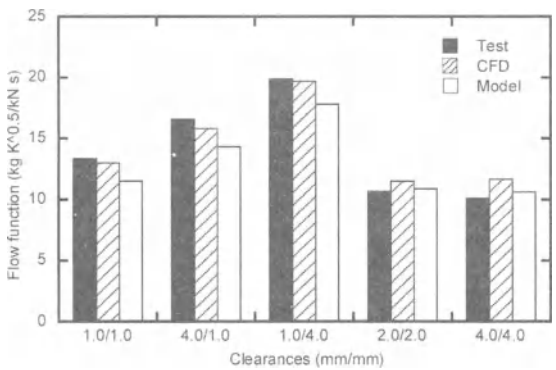

Fig. 12 Comparison of predictions with test for the stepped seal

5 Conclusion

Aerodynamic performances of double-sided labyrinth seals were investigated and the following are found. The downstream seal, which has more teeth, outperforms the upstream seal in both straight and stepped configurations. The straight seal does not show a sensible dependence of the discharge coefficient (or flow function) on the clearance. In the stepped seal, the flow function decreases as the clearance get smaller. As a result, the leakage reduction effect of step decreases as the clearance becomes smaller. If the difference in the clearances of the two sides is sufficiently large, the smaller clearance side fully dominates the overall seal leakage behavior, providing almost all the flow resistance. Consequently, among two extreme clearance combinations, the one with a smaller clearance at the downstream side gives a less leakage. Agreements between test and predictions are acceptable, but CFD gives better results than the analytic model in general.

Acknowledgements

T.S. Kim thanks Inha University and Solar Turbines Inc. for supporting this research.

References

CD-adapco, 2007, STAR-CCM+, ver. 2.07

Chupp, R. E., Holle, G. and Scott, T. E., 1986, Labyrinth Seal Analysis—Vol. IV : User's Manual for the Labyrinth Seal Design Model, AFWAL-TR-85-2103, Vol. IV

Stocker, H. L., et al., 1977, "Aerodynamic Performance of Conventional and Advanced Design Labyrinth Seals with Solid-Smooth, Abradable, and Honeycomb Lands", NASA CR-135307

Stoker, H. L., 1978, "Determining and Improving Labyrinth Seal Performance in Current and Advanced High Performance Gas Turbines", *AGARD Conference Proceedings 237*, Paper 13

Tipton, D. L., Scott, T. E. and Vogel, R. E., 1986, Labyrinth Seal Analysis—Vol. III : Analytical and Experimental Development of a Design Model for Labyrinth Seals, AFWAL-TR-85-2103, Vol. III

Vermes, G., 1961, "A Fluid Mechanics Approach to the Labyrinth Seal Leakage Problem," *ASME J. of Engineering for Power*, April, pp. 161 – 169

Zimmermann and Wolff, K. H., 1998, "Air System Correlations, Part 1: Labyrinth Seals," ASME paper 98-GT-206

Waschka, W., et al., 1992, "Influence of High Rotational Speeds on the Heat Transfer and Discharge Coefficients in Labyrinth Seals", *Journal of Turbomachinery*, Vol. 114, pp. 462 – 468

Wittig, S., Schelling U., Jacobsen, K. and Kim, S., 1987, "Numerical Predictions and Measurements of Discharge Coefficients in Labyrinth Seals," ASME paper 87-GT-188

The 4th International Symposium on Fluid Machinery and Fluid Engineering
November 24-27, 2008, Beijing, China
NO. 4ISFMFE-Ch09

Study on the Leakage Flow Field in the Shaft Brush Seal of Steam Turbines

Jun Li[*1,2], Xin Yan[1], Zhenping Feng[1], Shinnosuke Obi[2]

[*1] Institute of Turbomachinery, Xi'an Jiaotong University, Xi'an 710049, China
Tel: +86-29-8266-5062 / Fax: +86-29-8266-5062
E-mail: junli@mail.xjtu.edu.cn
[2] Department of Mechanical Engineering, Keio University, Yokohama 223-8522, Japan

Abstract The leakage flow behavior through a three stages shaft brush seal in steam turbines was numerically investigated using the Reynolds-Averaged Navier-Stokes (RANS) solution and the porous medium model based on the commercial CFD software FLUENT. At first, the permeability coefficients of the bristle pack were determined according to the published experimental data. Then, the leakage flow rate and flow characteristics of a typical shaft three stages brush seal used in steam turbines were studied at seven pressure ratios and five sizes of the sealing clearances using the calibrated permeability coefficients. In addition, the leakage flow field of the stepped labyrinth seal with the same axial distance at the same flow condition was also conducted. The numerical results show that the leakage flow rate of the three stages shaft brush seal with five sizes of sealing clearance is smaller than that of the labyrinth seal at the same pressure ratio. Moreover, the pressure ratio can affect the leakage flow rate while its influence on the leakage flow pattern can be neglected. The leakage flow rate increases linearly with the increase of the pressure ratio at the fixed sealing clearance for the three stages shaft brush seal. The leakage flow rate of the three stages shaft brush seal decreases with the decrease of sealing clearance at the fixed pressure ratio.

Keywords brush seal, leakage flow, porous medium model, numerical simulation

1 Introduction

Brush seal is considered to be most promising among the advanced type seals are presently in use in turbomachinery industry due to their superior leakage performance. Brush seals are generally a circular contacting seals used to restrict parasitic leakage flow between rotating and stationary components in turbomachinery (Dinc, et al. 2002, Chupp et al. 2006, Andres, et al. 2008). A brush seal is made of bristle pack, front plate and backing plate (Fig. 1) three main components. The bristle pack containing flexing-fine wires is clamped at a lay angle between front plate and backing plates and circumferentially welded at the outer periphery. The seal is mounted to the rotor over the rotor surface between two cavities to prevent leakage flow from the high to low pressure zone. The front plate is located at the upstream side of the bristle pack and tightly holds the bristles pack in place while protecting them from turbulent flow. The backing plate is positioned downstream of the bristle pack and it must be strong enough to provide mechanical support to bristle pack for axial pressure loads. As illustrated in Fig. 1, fence height is the unsupported portion of the bristles and it is exposed to the full differential pressure. Materials selection for the front and backing plate depends on bristle pack material, operating condition, and the housing material where the brush seal will be installed (Neef et al. 2006).

Brush seal can significantly reduce leakage flows in turbomachinery between the stationary and rotating components. Ferguson (1988) firstly presented the better sealing performance of brush seals compared labyrinth seals. He concluded four advantages of brush seals as 1) reduced leakage compared to labyrinth seals; 2) accommodation of shaft excursions; 3) significantly less axial space than labyrinth seals required; and 4) more stable leakage characteristics over long operating periods.

The leakage flow rate is one of the key techniques for design considerations of brush seals. At present, bulk flow model and porous medium model are two main numerical approaches to analysis the leakage flow rate and flow fields of brush seals. Bulk flow model (Chupp and Holle, 1996) described semi-empirical relations based

on flow-driven dimensionless parameters and geometrical configurations. The definitions of flow-driven parameters are based on analysis results of cross flow through bristles. Kudriavstev and Braun (1996) investigated the leakage flow characteristics using their introduced numerical approach involve the segmentation of the brush in repetitive core segments, bound by an inlet and an exit segment. Their development numerical method belongs to bulk flow model.

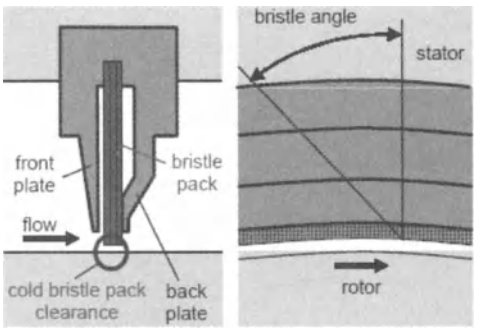

Fig. 1 Schematic drawing of the brush seal (adapted from Neef et al. 2006)

Porous medium model is to treat the entire bristle pack as a single porous medium with defined resistance to flow (Chew et al., 1995). The porous medium approach is basically solving the RANS equation with the additional flow resistance due to friction between flow and bristles. Bayley and Long (1993) were firstly introduced the porous medium model to analysis the leakage flow of brush seals. In their numerical approach, the boundary layer equations in the bristle pack were simplified by neglecting the inertial terms that yielded a balance equation between pressure and viscous forces. Chew and Hogg (1997) developed one-dimensional and two-dimensional porous medium method for bristle pack leakage flow analysis. They determined the bristle packed as an axisymmetric and anisotropic porous region with non-linear flow resistance coefficients. The RANS equations were solved coupled with added resistance forces for the bristle pack. Both viscous and inertial forces were considered in the resistance term. Chen et al (2000) carried out an experimental and numerical study on a five-time large-scale brush seal with geometrical and physical similarities. The large scale model enabled measurement of the pressure distribution within the bristle pack using hollow bristles. They measured the pressure on the backing plate and at bristle tips using pressure tapings. Their CFD model is based on Chew (1997) approach. They divided the bristle pack into several regions to match the linear axial pressure distribution on rotor surface over bristle pack thickness for their large scale brush seal model. Dogu (2005) applied an axis-symmetric CFD model and calibrated anisotropic permeability coefficients for the bristle pack based on available experimental data: leakage, axial pressure on the rotor surface, and radial pressure on the backing plates. In his approach, a simplified form of the force balance equation was introduced for the flow in the porous bristle pack. Different sets of permeability coefficients were defined for the fence height region below the seal backing plate and upper region of the seal to correlate the different physical structures and behavior of these regions during operation. Dogu and Aksit (2006a, 2006b) employed a CFD model and a bulk porous medium approach for effects of front and backing plate configurations on brush seal pressure and flow fields. In their studies, a long front plate or damper shim considerably changed the flow fields while at the same time having limited effect on the pressure field. In addition, the single backing plate groove formed a constant pressure behind the bristle pack. In contrast, multiple grooves formed multiple constant pressure regions.

There are several locations in steam turbines where applying brush seals can significantly improve performance. In this work, a three-dimensional RANS and porous medium model with periodic boundary condition analysis has been carried out to determine an outline for calibrating the anisotropic permeability coefficients for the porous bristle pack using available experimental data. Then, the flow characteristics of a typical shaft brush seal with three stages bristle packs is investigated under seven pressure ratios and five sizes of sealing clearance flow conditions using the presented RANS solution and porous medium model based on the calibrated permeability coefficients. The flow fields of the shaft brush seal and labyrinth seal are also illustrated and discussed.

2 Porous Medium Model

The leakage flow across the brush seal divided into two parts (shown in Fig. 2). One part is the flow across the sealing clearance between the brush pack tips and rotational axis surface. The other part is the flow infiltrate across bristle packs. The flow in the upstream high pressure and downstream low pressure zone and sealing clearance regions is modeled as turbulent and compressible flow. Thus, the RANS is solved to analysis the flow characteristics in these regions.

$$\partial \rho u_i / \partial x_i = 0 \tag{1}$$

$$u_j \cdot (\partial \rho u_i / \partial x_j) = -\partial P / \partial x_i + \mu \partial^2 u_i / (\partial x_j \partial x_j) \tag{2}$$

In this work, the porous medium model coupled RANS solution is utilized to analysis the leakage flow characteristics of brush seals. The bristle pack in a brush seal forms a porous medium. The leakage infiltration flow across the brush pack is considered as the flow across the

porous medium. The flow in a porous medium is subject to additional resistance forces compared to flow in a nonporous medium. This additional resistance forces is the fluid friction with solid bristle pack surfaces. The permeability of a porous medium is the ability to conduct the fluid. The bulk resistance to a Newtonian fluid flow through a porous solid matrix. Equation (3) defines one updated Darcian porosity model with added inertial resistance term according to Dogu (2005).

$$-\mathrm{d}P/\mathrm{d}x_i = \left(Ci_i|u_i| + Cv_i\right)u_i \tag{3}$$

where x_i represents the orthotropic flow direction, u_i is the superficial velocity in the direction of x_i. Ci_i and Cv_i are inertial and viscous resistance. The permeability coefficients, Cv_i and Ci_i, are to be determined through a calibration procedure using experimental data.

To obtain the permeability coefficients of equation (3), the experimental brush seal (Bayley and Long, 1993) is utilized to obtain the leakage flow rate using commercial CFD software FLUENT based on the RANS and porous medium model solution. Bayley and Long's paper (1993) is one of a few papers with all the experimental information of the brush seal. The seal is assembled with a 0.25mm radial interface. The rotor radius is 60.88mm. The bristle diameter is 0.0762mm with a pack thickness of 0.6mm. The bristle lay angle is 45°. The fence height and bristle height are 1.4mm and 10.32mm, respectively. Fig. 2 shows the geometrical parameters of the experimental brush seal from Bayley and Long (1993).

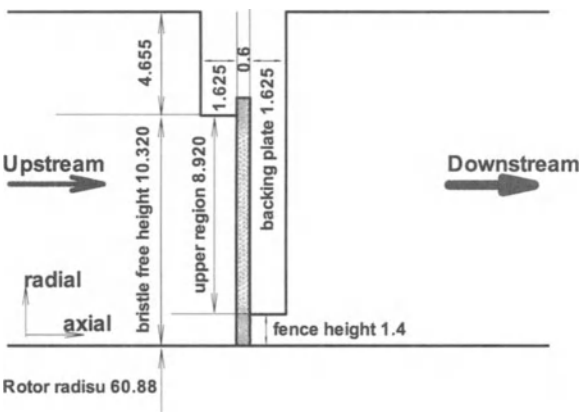

Fig. 2 Geometrical parameters of the experimental brush seal (Bayley and Long, 1993)

To obtain the permeability coefficient of the bristle pack, the commercial CFD software FLUENT coupled with the porous medium model is applied to obtain the leakage flow rate of the experimental brush seal. The calibrated permeability coefficients for the fence height region are inertial resistances and viscous resistances obtained from Dogu (2005).

Figure 3 shows the comparison of the numerical leakage flow rate with the experimental data. The leakage flow rate increases almost linearly for the pressure ratios considered, $\pi = 1.01 - 4.0$. The present numerical results are well agreement with the experimental data using the calibrated permeability coefficients of Dogu (2005). Thus, the same permeability coefficients are also used in a typical shaft brush seal with three stages bristle packs in this work.

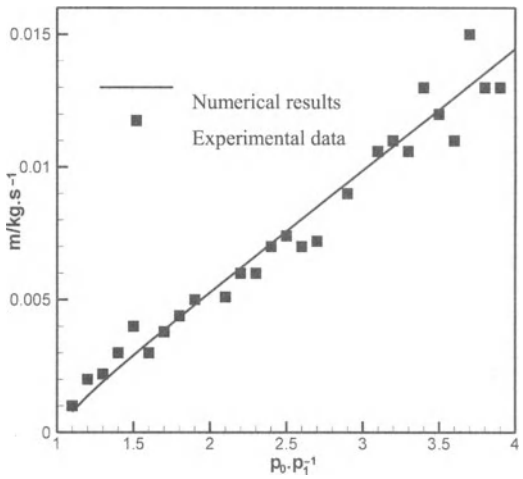

Fig. 3 Comparison of experimental leakage with numerical results

3 Computational Model

Fig. 4 shows a cross-section view of the stepped labyrinth seal. There exist two short fins between two neighbor long fins. In this work, the long fins of the stepped labyrinth seal can be redesigned the bristle pack at the same axial distance. Fig. 5 gives the three-dimensional structural profile of the brush seal with three stages bristle packs. The radial distance between the front plate and rotor surface is set to be 2.5mm. The radial distance between the backing plate and rotor surface is 1.1mm. The thickness of the each stage bristle pack is 1.0mm. The boundary condition definition of the numerical simulation is also illustrated in Fig. 5.

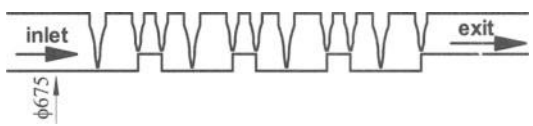

Fig. 4 Two-dimensional structural configure of the labyrinth seal

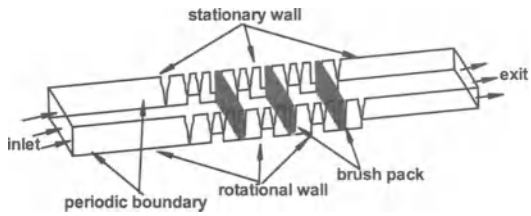

Fig. 5 Three-dimensional structural configure of the brush seal and boundary conditions

In addition, the flow characteristics of the brush seal with three stages bristle packs under five sizes of sealing clearance and seven different pressure ratio is also investigated using the RANS and porous medium model with calibrated permeability coefficients. The inlet total pressure of the stepped labyrinth seal and brush seal is set to 146.413bar for steam turbine industry. Seven pressure ratios from 1.02 to 1.14 are calculated for the stepped labyrinth seal and brush seal. In addition, radial clearance with 0mm, 0.10mm, 0.15mm, 0.18mm and 0.20mm between the bristle pack tip and rotor surface for the brush seal is also simulated. The comparison of the sealing performance between the labyrinth seal and brush seal at the same flow condition is conducted. The fluid is steam and treated as the ideal gas in this work.

For the numerical simulation of the flow field in the stepped labyrinth seals, the commercial finite volume code, FLUENT is used. This commercial CFD software solves the RANS equations on a body-fitted, unstructured and structural grid. Wang et al.(2004) and Denecke et al. (2005) utilized this commercial software to investigate the flow pattern in labyrinth seals. They obtained numerical results that compared well to experimental data. The validation of the numerical model of FLUENT was illustrated in their works. Thus, FLUENT is applied to investigate the leakage flow characteristics in the stepped labyrinth seal. As to the brush seal, the CFD software FLUENT and porous medium model is applied to analysis its flow fields.

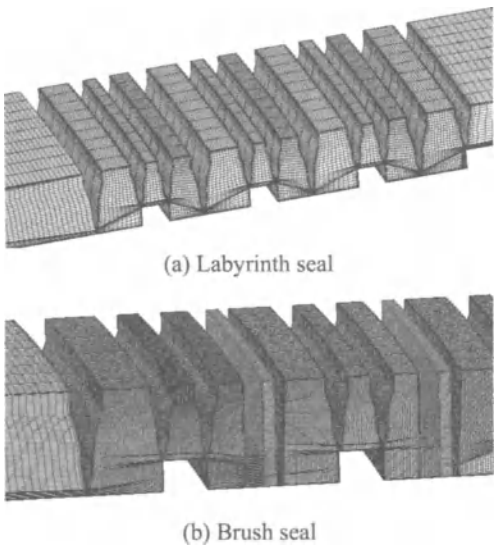

Fig. 6 Computational grid of the seal model

The computational time is to be saved and the eccentricity is not taken into account, the arc with 5 degrees radian of the stepped labyrinth seal and brush seal is to be worked as the computational field. A generated computational multiple structural grid for the stepped labyrinth seal and brush seal (part) is shown in Fig. 6. To ensure grid independence, additional testing with grids containing about 200,000, 400,000 and 800,000 cells was considered for the brush seal. The results show that the three kinds of grid numbers give the similar leakage flow rate at the same flow condition. Therefore about 400,000 cells are used in this work for the shaft brush seal.

In this simulation, a periodic boundary condition is assumed in the circumferential direction. In the flow direction, specifications at the flow inlet and exit boundaries are needed. The inlet boundary is placed at the seal entrance and total pressure, total temperature and turbulence quantities are defined, while the averaged static pressure is specified at the outlet of the seal. The stationary walls are defined to be adiabatic. The rotational adiabatic wall is fixed at 3000*rpm* of the rotating speed. As to the shaft brush seal, porous medium model is utilized for bristle packs.

4 Results and Discussions

To obtain the flow field of the brush seal with three stage bristle pack under five sizes of sealing clearances and seven pressure ratios, the RANS and porous medium model with calibrated permeability coefficients are utilized. In addition, the leakage flow rate of the stepped labyrinth seal at the same flow condition is also calculated using RANS solutions.

4.1 Flow Fields in the Labyrinth Seal

Fig. 7 and 8 shows the static pressure contours and stream line distribution of the stepped labyrinth seal at $\pi = 1.04$ and $\pi = 1.10$, respectively.

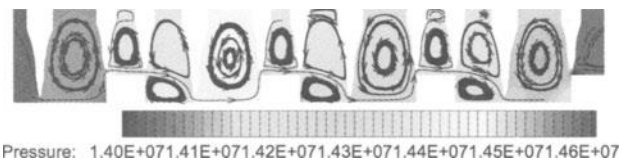

Fig. 7 Static pressure contours and stream line distribution of the stepped labyrinth seal ($\pi = 1.04$)

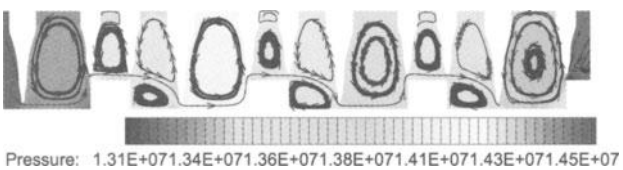

Fig. 8 Static p ressure contours and stream line distribution of the stepped labyrinth seal ($\pi = 1.10$)

The static pressure in Fig. 7 and 8 is the relative value comparison with the ambient pressure. The pressure value decreases step by step from the inlet and to the outlet of

the stepped labyrinth seal. The kinetic energy of the leakage flow transfers into heat energy in the cavity between the sealing fin and rotational axis. The steam passes the labyrinth gap and impinges on the wall of the sequence cavity and sealing knife. The jet is then deflected and directed towards the step wall and bottom of the labyrinth chamber. Inside the cavity the jet formed some smaller recirculation zones. Due to this flow patterns, the leakage flow kinetic energy is dissipated into heat energy. The influence of the pressure ratio on the flow pattern was observed to be very small according to Fig. 7 and 8. At the same sealing clearance, the same flow pattern of the leakage flow fields is obtained at different pressure ratio according to comparison of Fig. 7 and 8. This point demonstrates the pressure ratio can only influence the leakage flow rate of the labyrinth seal. The linear rise of the leakage flow rate with increasing the pressure ratio is observed as shown in Fig. 12.

4.2 Flow Field in the Brush Seal

The leakage flow characteristics of the shaft brush seal with three stages bristle packs at seven pressure ratios and five sizes of sealing clearance is investigated using the RANS and porous medium model with the calibrated permeability coefficients.

Streamline distribution of the shaft brush seal at two sizes of sealing clearance with 0.00mm and 0.20mm is shown in Fig. 9. As shown in Fig. 9(a), the jet of the leakage flow between the step and short fins direct impinges on the bristle pack, three recirculation zooms is generated in the cavity among the step, short fin and bristle pack due to zero sealing clearance. The large anti-clock recirculation region is generated at the downstream cavity of the bristle pack. The leakage flow rate across the porous bristle pack is much smaller than that of the clearance between labyrinth fins and rotor surfaces. The similar leakage flow pattern is observed for the sealing clearance with 0.20mm case according to Fig. 9(b).

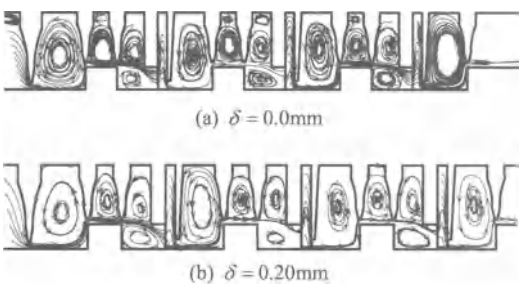

Fig. 9 Streamline distribution of the brush seal ($\pi = 1.04$)

Figure 10 and 11 plots the static pressure contours distribution of the brush seal at pressure ratio of 1.04 and sealing clearance of 0.00mm and 0.20mm, respectively. According to these figures, the pressure is almost constant at the upstream and downstream region of each bristle pack, especially in the case of zero sealing clearance. It gradually drops from the upstream to downstream at each bristle pack thickness. The densely plotted contour lines closer to downstream face indicate the sudden pressure drop.

The pressure gradient is observed at the bottom of the labyrinth chamber beneath the step in the downstream region of the bristle pack at the sealing clearance 0.20*mm* case. The reason is that the jet from the sealing clearance directed towards the bottom of the labyrinth chamber beneath the step. Inside the cavity the jet generate a large anti-clock recirculation zones. This results in leakage flow rate increases of the non-zero sealing clearance than that of the zero case.

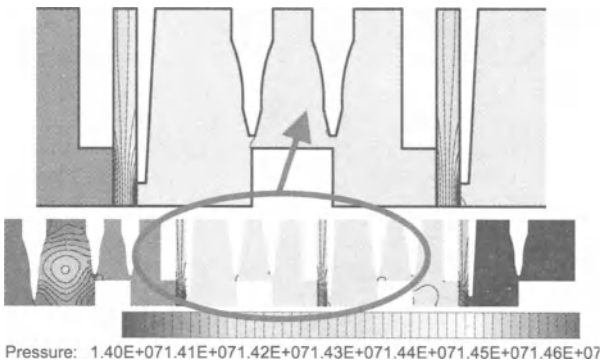

Fig. 10 Static pressure contours of the brush seal ($\delta = 0.0$mm and $\pi = 1.04$)

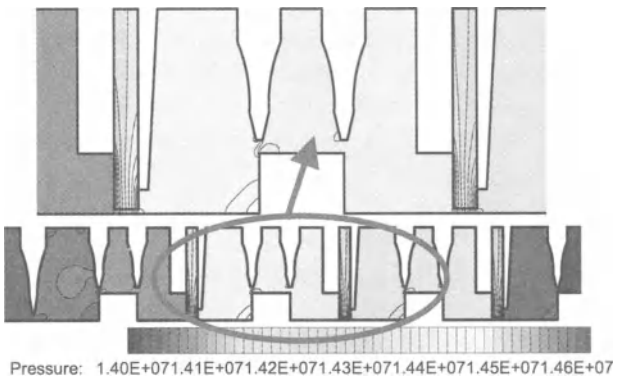

Fig. 11 Static pre ssure contours of the brush seal ($\delta = 0.20$mm and $\pi = 1.04$)

Comparison of the dimensionless leakage flow rate between the stepped labyrinth seal and brush seal at seven pressure ratios is shown in Fig. 12. In addition, the dimensionless leakage flow rate of the brush seal at five sizes of sealing clearance is also plotted. At the same pressure ratio, the leakage flow rate of the brush seal is much smaller than that of the stepped labyrinth seal at five sizes of sealing clearance, especially at the zero sealing clearance case, according to Fig. 12. As to the sealing clearance 0.10mm to 0.20mm, the leakage flow not only from the porous bristle pack, but also across the

sealing clearance between the bristle pack and rotor surfaces. Therefore, the leakage flow rate increases. Due to the sealing clearance between the bristle pack and rotor surfaces is small; the jet from the sealing clearance does not influence the leakage flow pattern. The leakage flow rate is almost linearly increases with the increasing pressure ratio for the stepped labyrinth seal and brush seal. The effect of the pressure ratio on the leakage flow pattern is omitted from Figs. 9 and 12.

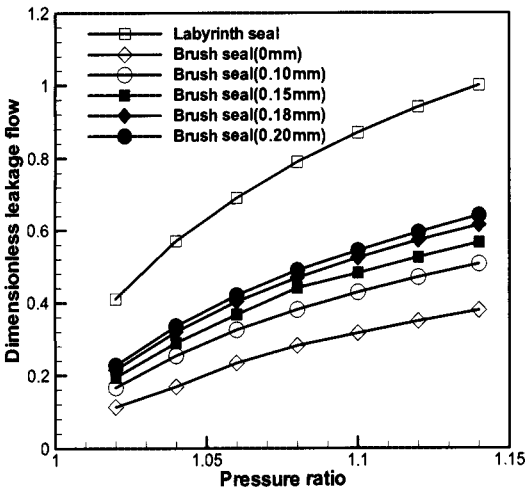

Fig. 12 Dimensionless leakage flow rate of the stepped labyrinth seal and brush seal

5 Conclusions

The influence of pressure ratio and sealing clearance on the leakage flow characteristics in the brush seal with three stages bristle packs is numerically determined using the RANS and porous medium model with calibrated permeability coefficients.

Numerical simulations covered seven pressure ratios and five sizes of sealing clearance for the brush seal. The influence of the sealing clearance on the leakage flow rate is observed. The influence of the pressure ratio and sealing clearance on the leakage flow pattern is omitted. The leakage flow rate increases linearly with the increasing pressure ratio at the fixed sealing clearance for the brush seal. At the same pressure ratio, the leakage flow rate of the brush seal at five sizes of sealing clearance is much smaller than that of the stepped labyrinth seal, especially at the zero sealing clearance case.

Acknowledgements

The authors are grateful for the project 2007CB707705 supported by National Basic Research Program (973 Program) and Program for New Century Excellent Talents in University (NCET-07-0669) of China.

References

Andres, L. S., Baker, J., Delgado, A., 2008, "Measurements of Leakage and Power Loss in a Hybrid Brush Seal", ASME Paper GT2008-50532, *ASME Turbo Expo 2008: Power for Land, Sea and Air*

Bayley, F. J., Long, C. A., 1993, "A Combined Experimental and Theoretical Study of Flow and Pressure Distribution in a Brush Seal", *ASME J. Eng. Gas Turbine Power*, Vol.115(2), pp. 404 – 410

Chen, L. H., Wood, P. E., Jones, T. V., Chew, J. W., 2000, "Detailed Experimental Studies of Flow in Large Scale Brush Seal Model and a Comparison with CFD Predictions", *ASME Journal of Engineering for Gas Turbines and Power*, Vol.122(3), pp. 672 – 679

Chew, J. W., Hogg, S., 1997, "Porosity Modeling of Brush Seals", *ASME J. Tribology*, Vol. 119, pp.769 – 775

Chew, J. W., Lapworth, B. L., Millener, P. J., 1995, "Mathematical Modeling of Brush Seals", *Int. J. Heat Transfer Fluid Flow*, Vol.16(6), pp. 494 – 500

Chupp, R. E., Hendricks, R. C., Lattime, S. B., Steinetz, B. M., 2006, "Sealing in Turbomachinery", *JOURNAL OF PROPULSION AND POWER*, Vol. 22(2). pp. 313 – 349

Chupp, R. E., Holle, G. F., 1996, "Generalizing Circular Brush Seal Leakage Through a Randomly Distributed Bristle Bed". *ASME J. Turbomachinery*, Vol. 118, pp. 153 – 161

Denecke, J., Dullenkopf, K., Wittig, S., et al. 2005, "Experimental Investigation of the Total Temperature Increase and Swirl Development in Rotating Labyrinth Seals", GT2005-68677, *ASME Turbo Expo 2005: Power for Land, Sea and Air*

Dinc, S., Demiroglu, M., Turnquist, N., et al., 2002, "Fundamental Design Issues of Brush Seals for Industrial Applications", *Journal of Turbomachinery*, Vol.124(2), pp. 293 – 300

Dogu, Y., 2005, "Investigation of Brush Seal Flow Characteristics Using Bulk Porous Medium Approach", *ASME Journal of Engineering for Gas Turbines and Power*, Vol.127(1), pp. 136 – 144

Dogu, Y., Aksit, M. F., 2006a, "Effects of Geometry on Brush Seal Pressure and Flow Fields – Part I: Front Plate Configurations". *ASME Journal of Turbomachinery*, Vol.128(1), pp. 367 – 378

Dogu, Y., Aksit, M. F., 2006b, "Effects of Geometry on Brush Seal Pressure and Flow Fields—Part II: Backing Plate and Configurations", *ASME Journal of Turbomachinery*, Vol.128(1), pp. 379 – 389

Ferguson, J. G., 1988, "Brushes as High Performance gas Turbine Seals". *ASME paper 88-GT-182*

Kudriavtsev, V. V. and Braun, M. J., 1996, "Model Developments for the Brush Seal Numerical Simulation", *JOURNAL OF PROPULSION AND POWER*, Vol. 12(1), pp. 193 – 201

Neef, M., Sulda, E., Suerken, N., Walkenhorst, J., 2006, "Design Features and Performance Details of Brush Seals for Turbine applications", ASME Paper, GT2006-90404. *ASME Turbo Expo 2006: Power for Land, Sea and Air*

Wang, Y., Young, C., Snowsill, G., Scaclon, T., 2004, "Study of Airflow Features through Step Seals in the Presence of Dis-engagement due to Axial Movement", ASME Paper GT2004-53056, *ASME Turbo Expo 2004: Power for Land, Sea and Air*

The 4th International Symposium on Fluid Machinery and Fluid Engineering
November 24-27, 2008, Beijing, China
NO. 4ISFMFE-Ab19

Transverse Jets Analysis on High Speed Rotating Body of Revolution

Khaled Alhussan

Associate Research Professor, Deputy Director of Space Research Institute
King Abdulaziz City for Science and Technology, Riyadh, Kingdom of Saudi Arabia
Tel: +966-1-4814508/ Fax: +966-1-4813845
Email: alhussan@kacst.edu.sa

Abstract This research discusses the transverse jet characteristics issuing from a three dimensional body of revolution into a high speed external flow. This phenomenon creates a complex flow field whose influence on the flow structure is not always easy to predict. In order to investigate the fundamental theory of the transverse jet interaction process, extensive numerical calculations have been conducted in this paper, which has led to the creation of a comprehensive understanding of the structure of the complex flow field. The analysis will show the contour plots of Mach number and the pressure distribution that are function of angle of attack, Reynolds number and the velocity of jet exit. This research demonstrates the creation of bow shock, shock waves interactions, and boundary layer separation and recirculation zone. The results will show that adding a transverse jet will change the flow structure around and behind the body especially with regard to viscous drag and pressure drag, shock waves interactions, boundary layer separations, recirculation and wake.

Keywords supersonic flow, viscous flow, boundary layer separation, deceleration devices, numerical analysis, total drag

1 Introduction

Flow over external bodies has been studied extensively because of their many practical applications, in some applications of aerodynamics, a surface control of a moving body is required therefore the prediction and controlling of the forces is essential. This research discusses the transverse jet characteristics issuing from a three dimensional body of revolution into a high speed external flow. This phenomenon creates a complex flow field whose influence upon the flow structure is not always easy to predict and to simulate.

In order to investigate the fundamental theory of the transverse jet interaction process, extensive numerical calculations have been conducted in this paper, which has led to the creation of a comprehensive theoretical understanding of the structure of the complex flow field. The use of the transverse jets has a great potential to replace the conventional control surface methods especially for the maneuverability of the body, due to the less response times and effective for low dynamic pressure, Alhussan (2005), Bobin (1993), Brandeis et al. (1998). and Champigny et al. (1994).

The study of the complex flow interaction of the external supersonic flow with the transverse jets was conducted in this research. The analysis will show the contour plots of Mach number and the pressure distribution that are function of angle of attack, Reynolds number and velocity of the jet exit. This research shows the creation of bow shock, boundary layer separation and recirculation region. The main objective of the present work consists of conduct numerical simulations of the interaction of the transverse jet with the external flow of the body of revolution configuration and to study the shock waves interactions between the free stream and the jets. This research shows that the numerical analysis can predict the shock waves interactions between the jets and the free stream flows. The results will show that adding a transverse jet will change the flow structure around and behind the body especially with regard to viscous drag and pressure drag, shock waves interactions, boundary layer separations, recirculation and wake.

This research showed the numerical solution for flow over rotating slender body moving with Mach number of 2.0 and rotating with angular speed of 10,000RPM. The

jet exit velocity injected normal to the surface body with a range of Mach number ratio from 1 to a maximum of 1.5. The Mach number ratio is defined as the free stream velocity to jet exit velocity. The governing equations are a set of coupled nonlinear, partial differential equations. In order to formulate or approximate a valid solution for these equations they must be solved using computational fluid dynamics techniques. To solve the equations numerically they must be discretized. That is, the continuous control volume equations must be applied to each discrete control volume that is formed by the computational grid. The integral equations are replaced with a set of linear algebraic equations solved at a discrete set of points.

The numerical investigations around the complete body allow a detailed exploration of the flow, which is difficult to realize experimentally. A numerical approach using different density meshes and a robust numerical scheme should be used as an initial case in order to fully understand the rotating three-dimensional flow interaction of the external supersonic flow and transverse jets. The strong influence of the computational mesh size around the body and transverse jet exit is evident in this research. To accurately capture the separation in the boundary layer a high dense mesh is required due to the adverse pressure gradient.

2 Numerical Analysis

The study of the complex flow interaction of the external supersonic flow with the transverse jets was conducted in this research. The analysis shows the contour plots of Mach number and the pressure distribution that are function of angle of attack, Reynolds number and velocity of the jet exit. This research shows the creation of oblique shock waves expansion fans jet interaction waves, boundary layer separation and recirculation zone. The main problem here is to determine velocity field and the states of the fluid: its pressure, density, and temperature at all time and all space. There are six unknowns *u, v, w, p,* ρ and *T.* with four independent variables *x, y, z,* and *t.* Hence six independent equations for these six unknowns are needed. The continuity equation in index notation is therefore:

$$\frac{\partial \rho}{\partial t}+\frac{\partial}{\partial x_j}\left(\rho \overline{V_j}\right)=0 \tag{1}$$

The momentum equation in tensor form is:

$$\frac{\partial}{\partial t}\left(\rho \bar{u}_i\right)+\frac{\partial}{\partial x_j}\left(\rho \bar{u}_i \bar{u}_j\right)=-\frac{\partial p}{\partial x_i}-\frac{\partial \tau_{ij}}{\partial x_j}+\rho \bar{f}_i \tag{2}$$

The three terms on the right-hand side of Eq. 2 represent the x-components of all forces due to the pressure, p, the viscous stress tensor, τ_{ij}, and the body force, f_i . Energy equation; the differential form of the energy equation is given by using Green's theorem, hence, in tensor form the energy equation therefore is:

$$\frac{\partial}{\partial t}\left(\rho h^{o}\right)+\frac{\partial}{\partial x_j}\left(\rho u_i h^{o}\right)=\frac{\partial p}{\partial t}-\frac{\partial}{\partial x_j}\left(u_i \tau_{ij}+Q_j\right)+\rho u_i f_i \tag{3}$$

Considering an infinitesimal control volume, the two terms on the left-hand side of Eq. 3 describe the rate of increase of h^{o} and the rate at which h^{o} is transported into and out of the control volume by convection. The first term on the right-hand side describes the influence of the pressure on the total enthalpy. The second term describes the rate at which work is done against viscous stresses by distortion of the fluid. The gradient of Q is the rate of energy transfer into the control volume by conduction, and the last term describes the rate of work done by body forces.

If the Navier-Stokes equations do not hold an equation of the stress tensor must be found and solved simultaneously with the four basic equations. Even when the Navier-Stokes relations hold, the relation of the coefficient of viscosity must be given with respect to the state variables of the fluid such as temperature and density. There are many other cases where the basic equations of fluid dynamics are not sufficient or should be modified such as in the cases of the two-phase flow, multi-fluid flow theory, relativistic fluid mechanics and biomechanics.

Now, after stating all the flow equations, mass, momentum, and energy it is time to formulate a solution. But, since, these equations are coupled nonlinear, partial differential equations, it is impossible to have a closed form of solution. In order to formulate or approximate a valid solution for these equations they must be solved using computational fluid dynamics technique. In order to solve these equations numerically with a computer, they must be discretized. That is, the continuous control volume equations must be applied to each discrete control volume that is formed by the computational grid. The integral equations are substituted with a set of linear algebraic equations solved at a discrete set of points.

In a finite element discretization the grid breaks up the domain into elements over which the changes of the fluid variables are evaluated. Adding all the variations for each element then gives an overall visualization of how the variables vary over the entire domain. The primary advantage of the finite element method is the geometric

flexibility allowed by a finite element grid. In a finite volume discretization the grid breaks up the domain into nodes, each associated with a discrete control volume. The fluxes of mass, momentum, and energy for each control volume are then calculated at each node. An advantage of the finite volume method is that the principles of mass, momentum, and energy conservation are applied directly to each control volume, so that the integral conservation of quantities is exactly satisfied for any set of control volumes in the domain. Thus, even for a coarse grid, there is an exact integral flux balance, Alhussan (2005), Bobin (1993), Brandeis et al. (1998), Champigny et al. (1994), Naumann et al.(1985), and Gnemmi et al. (2005).

A numerical analysis must start with breaking the computational domain into discrete sub-domains, which is the grid generation process. A grid must be provided in terms of the spatial coordinates (x, y and z location) of grid nodes distributed throughout the computational domain. At each node in the domain, the numerical analysis will determine values for all dependent variables including pressure, velocity components and temperature. The nodes must be distributed throughout the volume enclosed by the exterior boundary surface of the domain such that they form a complete three-dimensional matrix of nodes. Each node in the matrix will be referred to by the index triplet (i, j, k).

To complete the description of the distribution of nodes in the computational domain, it is useful to introduce the concept of a flux element. A flux element is a linear hexahedral element defined by eight nodes. Conforming to the finite element approach, linear shape functions representing the variation of variables within the flux element are applied. Each flux element has four octants for two-dimensional domain and eight octants for three-dimension region. The six sides of each octant are divided into two groups; those that are coincident with the flux element sides and those that are in the interior of the flux element. Because the latter group will form the surfaces of the control volume over which surface integrals will be evaluated.

In finite volume method a control volume exists for each node, with the boundary of each interior control volume defined by eight line-segments in two dimensions and 24 quadrilateral surfaces in three dimensions. To solve the governing or the natural equations that were derived in theoretical section they must be converted to their discrete or algebraic form.

Discretization is the process whereby the governing equations are converted by their discrete form. Discretization identifies the node locations and flux elements to model the flow problem. The differential equations are transformed to algebraic equations, which should correctly approximate the transport properties of the physical processes. Next, the fluxes are evaluated at integration points, which are shared by adjacent control volumes. The same flux that leaves one control volume enters the next one. Thus, even with a low accuracy advection scheme numerical conservation is guaranteed. This is the fundamental advantage of a finite volume method. The discretization is evaluated in an elemental basis.

3 Theoritical Disscusion

This research showed the numerical solution for flow over rotating slender body moving with Mach number of 2.0 and rotating with angular speed of 10,000RPM. Air is working fluid. The jet exit velocity injected normal to the surface body with a range of Mach number ratio from 1 to a maximum of 1.5. The Mach number ratio is defined as the free stream velocity to jet exit velocity.

The numerical investigations around the complete body allow a detailed exploration of the flow, which is difficult to realize experimentally. A numerical approach using different density meshes and a robust numerical scheme should be used as an initial case in order to fully understand the rotating three-dimensional flow interaction of the external supersonic flow and transverse jets. The strong influence of the computational mesh size around the body and transverse jet exit is evident in this research.

To accurately capture the shock waves interaction region and the separation in the boundary layer a high dense mesh is required due to the adverse pressure gradient. The study of the complex flow interaction of the external supersonic flow with the transverse jets was conducted in this research. The analysis shows the contour plots of Mach number and the pressure distribution that are function of angle of attack, Reynolds number and velocity of the jet exit. This research shows the creation of oblique shock waves expansion fans jet interaction waves, boundary layer separation and recirculation zone. The main objective of the present work consists of conduct numerical simulations of the interaction of the transverse jet with the external flow of the body of revolution configuration. Figure 1 shows a contour plots of Mach number for flow over rotating body of revolution.

Figure 1 shows the formation of the deflected jet streams and separation zone that develops upstream from the jets. The surface pressure in the separation region is higher than the static mean flow pressure hence it expands in the

recirculation region formed downstream of the transverse jets. From Fig. 1 also, one can notice the creation of oblique shock waves in the front of the deflected streams.

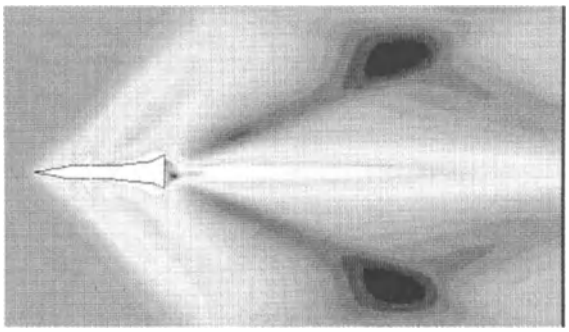

Fig. 1 Contour plots of Mach number showing oblique shock waves and jet interactions of complete body

Figure 2 shows contour plots of static pressure for flow over rotating body of revolution. Figure 3 shows contour plots of Mach number showing oblique shock waves and Jet interaction of complete body, close-up view. One can see the creation of the oblique shock waves, the expansion waves and the waves interactions with the transverse jets. Figure 4 contour plots of static pressure showing oblique shock waves and jet interactions of complete body close up view. One can notice the creation of the oblique shock waves, the expansion waves and the waves interaction with the transverse jets. Figure 5 contour plots of static pressure showing oblique shock waves and jet interactions of complete body close up view. One can observe the creation of the oblique shock waves, the expansion waves and the waves interactions with the transverse jets.

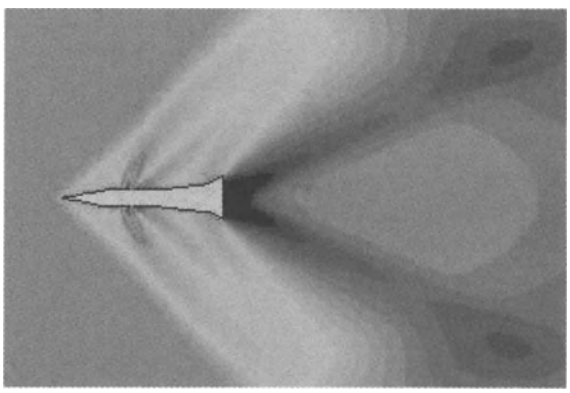

Fig. 2 Contour plots of static pressure showing oblique shock waves and jet interaction of complete body

The numerical investigations around the complete body allow a detailed exploration of the flow, which is difficult to realize experimentally. A numerical approach using different density meshes and a robust numerical scheme should be used as an initial case in order to fully understand the rotating three-dimensional flow interaction of the external supersonic flow and transverse jets. This research shows the strong influence of the computational mesh size around the body and transverse jet exit. To accurately capture the separation in the boundary layer a high dense mesh is required due to the adverse pressure gradient.

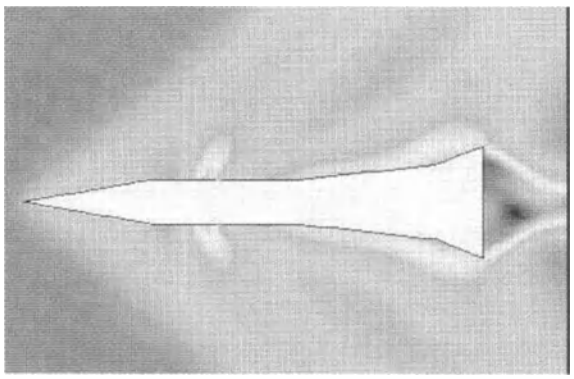

Fig. 3 Contour plots of Mach number showing oblique shock waves and jet interaction of complete body, close-up

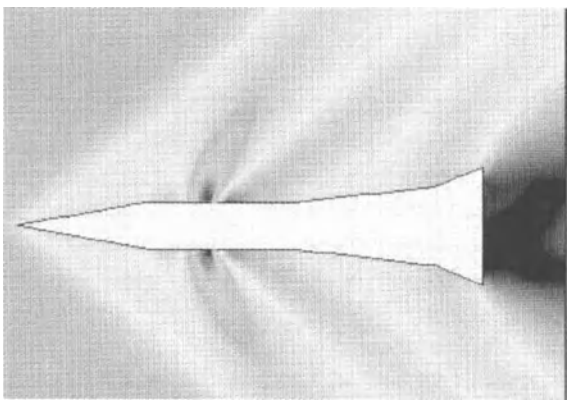

Fig. 4 Contour plots of static pressure showing oblique shock waves and jet interaction of complete body, close up

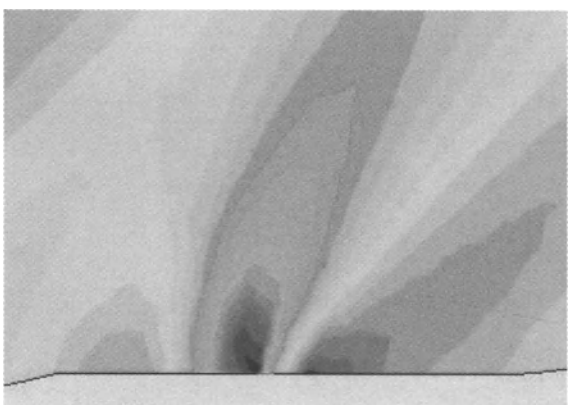

Fig. 5 Contour plots of static pressure showing oblique shock waves and jet interaction of complete body

4 Conclusion

This research showed the numerical solution for flow over rotating slender body moving with Mach number of 2.0 and rotating with angular speed of 10,000RPM. Air is working fluid. The jet exit velocity injected normal to the surface body with a range of Mach number ratio from 1 to a maximum of 1.5. The Mach number ratio is defined as the free stream velocity to jet exit velocity.

The governing equations are a set of coupled nonlinear, partial differential equations. In order to formulate or approximate a valid solution for these equations they must be solved using computational fluid dynamics techniques. To solve the equations numerically they must be discretized. That is, the continuous control volume equations must be applied to each discrete control volume that is formed by the computational grid. The integral equations are replaced with a set of linear algebraic equations solved at a discrete set of points.

The numerical investigations around the complete body allow a detailed exploration of the flow, which is difficult to realize experimentally. A numerical approach using different density meshes and a robust numerical scheme should be used as an initial case in order to fully understand the rotating three-dimensional flow interaction of the external supersonic flow and transverse jets. The strong influence of the computational mesh size around the body and transverse jet exit is evident in this research. To accurately capture the separation in the boundary layer a high dense mesh is required due to the adverse pressure gradient. The study of the complex flow interaction of the external supersonic flow with the transverse jets was conducted in this research. The analysis shows the contour plots of Mach number and the pressure distribution that are function of angle of attack, Reynolds number and velocity of the jet exit. This research shows the creation of oblique shock waves expansion fans jet interaction waves, boundary layer separation and recirculation zone.

Acknowledgements

The author gratefully acknowledges sponsorship of this research from the Space Research Institute of the King Abdulaziz City for Science and Technology.

References

Alhussan, K. "Supersonic Flow over Blunt Body with a Decelerator" IASME Transaction Issue 3 Volumes 1, 98 – 104, August 2005

Alhussan, K. "Oblique Shock Waves Interaction in a Non-Steady Three Dimensional Rotating Flow" Proceedings of FEDSM2005 ASME Fluids Engineering Division Summer Meeting and Exhibition FEDSM2005-77442 June 19 – 23, 2005, Houston, TX, USA

Bobin, L., "Experimental Investigation of a Jet in a Cross-Flow by Spontaneous Raman Scattering," International Congress on Instrumentation in Aerospace Simulation Facilities (ICIASF'93 Record), IEEE Publ. 93CH3199-7, 1993, pp. 14.1 – 14.4

Brandeis, J, and Gill, J., "Experimental Investigation of Super- and Hypersonic Jet Interaction on Missiles Configuration," AIAA Journal of Spacecraft and Rockets, Vol. 35, No. 3, 1998, pp. 296 – 302

Champigny, P., and Lacau, R. G., "Lateral Jet Control for Tactical Missiles," Special Course on Missile Aerodynamics, AGARD-FDP Von Karman Institute, Brussels, Belgium, 6 – 10 June 1994, pp. 3.1 – 3.57

Naumann, K. W., and Srulijes, J., "Die Steuerung mittels seitlich austretender Strahlen. Literaturübersicht," ISL Report R 117/85, 1985

Gnemmi, P and Schafer H. J. "Experimental and Numerical Investigations of a Transverse Jet Interaction on a Missile Body" AIAA Aerospace Sciences Meeting and Exhibit, paper number AIAA2005-52, 10-13 January 2005, Reno, Nevada

The 4th International Symposium on Fluid Machinery and Fluid Engineering
November 24-27, 2008, Beijing, China
NO. 4ISFMFE-Ch14

Numerical Investigation of High-Power Synthetic Jet Actuator Flowfield and Its Influence on Vectoring Control

Yanming Liu*[1], Baoguo Wang[1], Shuyan Liu[1], Naiming Wu[2]

*[1] School of Aerospace Science and Engineering, Beijing Institute of Technology
5 South Zhongguancun Street, Haidian District, Beijing 100081, China
Tel: +86-10-6891-4865
E-mail: liuym@bit.edu.cn

[2] School of Energy and Dynamic Engineering, Beijing University of Aeronautics and Astronautics,
XueYuan Road No.37, HaiDian District, Beijing 100083, China

Abstract Detailed two-dimensional unsteady numerical simulation is carried out to investigate a high-power synthetic jet actuator flow field and its design characteristic. Simultaneously, vectoring control of a primary jet and the dynamic mechanism are also studied. Firstly, the results show the actuator become more desirable as the rotating speed increases or the piston displacement enlarges with the invariable model and concerned parameters. Secondly, acting forces resulting from the synthetic jets have the "push" or "pull" effect on the primary jet and spanwise static pressure difference appears, which is the important reason for the variation of primary jet. Thirdly, with the given motor rotating speed, there is the maximal variation angle at certain velocity value of primary jet. Strictly speaking, the variation angle is the average value of variation angles at different center points of primary jet.

Keywords high-power synthetic jet actuator, vectoring control, exit velocity, variation

1 Introduction

In the recent years, the development of active flow control and their potential for shear flow control has received a great deal of attention. Synthetic jets have the unique property that they are zero-mass-flux in nature; i.e., they are synthesized from the working fluid of the system in which they are deployed. Thus, in contrast to conventional continuous or pulsed jets, synthetic jet transfers linear momentum to the flow without net mass injection across the flow boundary and can be used for flow control: drag reduction, noise abatement, separation control, jet thrust vectoring and mixing enhancement, etc. From the early fifties to the sixties in the 20th century, flow control was applied in rocket to achieve thrust vectoring. At present, jet vectoring has also become an area of flow control that can receive benefits from the application of synthetic jet actuators. And the area is of extreme importance in the development of jet engine exhaust systems to reduce the system's complexity and cost.

For the thrust vectoring model in this paper, a motor-driven high-power synthetic jet actuator is employed to overcome the disadvantages of piezoelectric actuator: the amplitude of oscillation can be on the order of millimeters; and the driving frequency is variable. For these actuators, the motor can supply enough power to achieve flow control. Now, synthetic jet actuator is developing towards the high-power, predominant-performance and compact actuator, which also determines its applied potential for flow control area.

The current research focuses on the motor-driven synthetic jet actuator flowfield and vectoring control of primary jet. Not only the influence of concerned actuator parameters (rotating speed and piston displacement) on the controlling ability is studied, but the mechanism of thrust vectoring is also analyzed from the dynamic point of view.

2 Numerical Method

Flow Configuration And Grid

In the paper, two-dimensional unsteady Renolds-averaged N-S equations are solved. And realizable k- ε turbulence model and second order unwind scheme are employed in the solution. The computational model comes from related experimental model and the mesh is structural (Fig. 1).

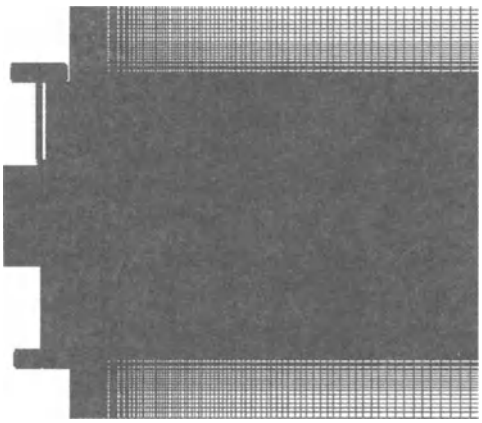

Fig. 1 Computational Grid

Figure 1 shows the computational domain and grid employed in the simulations. There are ((150 × 300) + (30 × 200)) grid points in the external flow region, (105 × 40) grid points in each cavity; the orifices of the two actuators have (69 × 5) and (50 × 5) grid points respectively. The size of the external flow domain is (206mm × 250mm). The diameter of primary jet D = 25mm. The width of the actuator orifice is h_0 = 0.5mm. The piston diameter d =13.7. These parameters are fixed in all the simulations.

Table 1 Case design

	for actuator				for vectoring control		
Case	I	II	III	IV	V	VI	VII
Velocity for primary jet (m/s)					20	40	60
Piston displacement (mm)	1	3	5	3	3	3	3
Motor rotating speed (r/min)		10000		14000		14000	

As shown in Table 1, there are different velocity values in different cases for primary jets. The far-field boundary condition is employed on the external flow field condition. All the other boundary conditions are adiabatic, no-slip boundary condition. The piston movement would be described in the next section.

3 Synthetic Jet Actuator Modeling

For the motor-driven actuator, the dynamic mesh method and in-cylinder model are used. For example, the setting parameters for case IV are: piston stroke A =3mm, motor rotating speed n =14000r/min and the time step specified to use for advancing the solution in terms of crank angle step size t^*. In the computation, $t^* = 0.6°$ and the period $T = 360 \times 60/(n \times 360) = 6 \times 10^{-3}$. Driving frequency f = 1/T. There is the expression for the piston movement as follows:

$$p_s = L + \frac{A}{2}(1-\cos(\theta_c)) - \sqrt{L^2 - \frac{A^2}{4}\sin^2(\theta_c)}$$

Where p_s is piston location (0 at top-dead-center (TDC) and A at bottom-dead-center (BDC)), L is the connecting rod length, θ_c is the current crank angle calculated from: $\theta_c = \theta_s + t\Omega_{shaft}$, where θ_s is the starting crank angle and Ω_{shaft} is the crank shaft speed.

In addition, the corresponding cases of actuator itself are also listed in table 1. Using the actuator arrangement described above, the primary jet can be vectored either toward or away from each of the synthetic jet actuators. These two actuators are denoted "SJA_{pull}" (for actuator fixed above primary jet and the synthetic jet is nominally collinear with the primary jet in Fig. 1(a)) and "SJA_{push}" (for actuator fixed under the primary jet and synthetic jet impinges normal to and along the span of the primary jet). The distances between these two kinds of actuators and the primary jet are expressed by d_1 and d_2 respectively.

4 The Results and Analysis

The Effect of Different Parameters on The Exit Flowfield of Actuator

When t/T =0.25, the exit velocity and centerline velocity distribution for case II and case IV are shown in Fig. 2, which indicate the effect of rotating speed on the controlling ability of actuator obviously.

As shown in Fig. 2 (a), the exit velocity increases evidently as the motor rotating speed increases. The comparison of mass-averaged exit velocity $\bar{V}$ between the case II and case IV: 44.41314 (case II) < 63.647 (case IV) indicates the higher exit velocity in case IV because of the increased rotating speed and frequency of piston movement. Fig. 2 (b) shows the higher centerline velocity near the actuator exit with higher rotating speed

and the less velocity difference while $\bar{x}$ =0.25～1 to the exit, which results from the mixing between synthetic jet and ambient fluid. The employment of actuators with different rotating speed can achieve nearly same mixing effect at last, but there is higher mixing velocity with higher rotating speed. In conclusion, the controlling effect of actuator is more significant as its rotating speed increases with the specified actuator model.

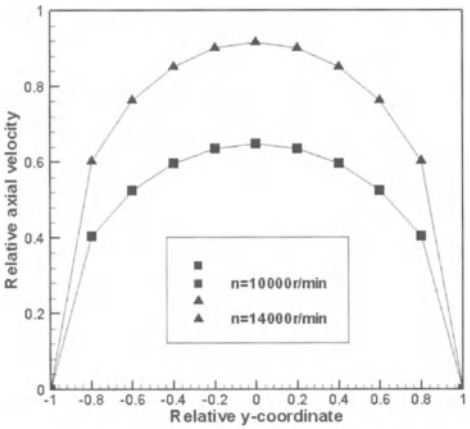

(a) Comparison of exit velocity

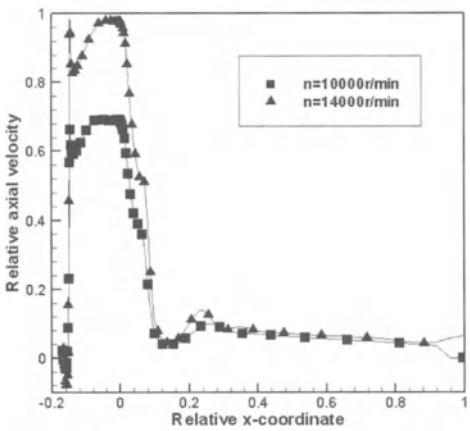

(b) Comparison of centerline velocity

Fig. 2 Distribution of velocity at different rotating speed

At the constant rotating speed n =10000r/min, the numerical simulation of motor-driven actuator flow field is carried out for Case Ⅰ, Case Ⅱ and Case Ⅲ respectively. The comparison of exit velocity is plotted in Fig. 3. The x-coordinate denotes the name of case. Figure 3 show the exit velocity of actuator is in direct proportion to A, it is to say, the average velocity and the maximal velocity increase at the exit section as the piston displacement increases. It is obvious that piston has acceleration at larger displacement and the stronger force occurs near the exit airflow as the piston stroke increases, which results in the increased airflow velocity and stronger controlling ability.

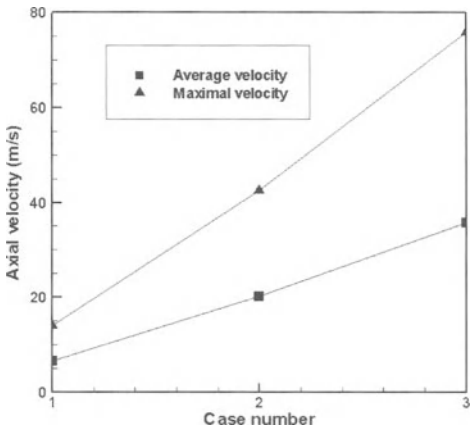

Fig. 3 The influence of "A"

In addition, the requirement of motor performance is rigorous and normally too difficult to satisfy while keeping the high acceleration of piston for a longer time though there are stronger controlling ability and higher efficiency with the increased piston stroke, but which should be considered in the optimal design.

5 Comparative Analysis

The variation of different cases is shown in Fig. 4. The figure indicates that primary jet velocity has some relation with the variation angle. The spanwise uneven pressure distribution, i.e., the spanwise pressure difference due to the synthetic jet is the important reason for the primary jet vectoring.

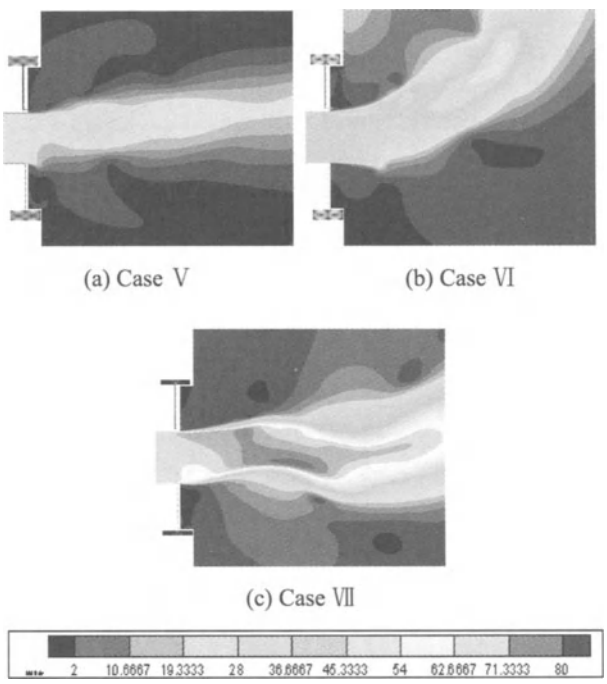

(a) Case Ⅴ (b) Case Ⅵ

(c) Case Ⅶ

Fig. 4 The variation of primary jet for different cases

The Fig. 4 shows smaller variation angle in case Ⅴ and case Ⅶ but larger variation angle in case Ⅵ. As mentioned above, there is clearer influence on the primary jet vectoring for the stronger controlling ability of actuator. On the contrary, at the given actuator parameters, variation angle increases as primary jet velocity decreases in a certain extent, i.e., variation angle is in simple inverse proportion to the primary jet velocity. In sum, given motor rotating speed, there is optimal variation angle at a certain primary velocity value, which should be considered in the optimization design.

Mechanism of Thrustt Vectoring From The Dynamic Point Of View

In the last section of the paper, the mechanism of primary jet vectoring is described aerodynamically. But on the other hand, primary jet variation must have close relation with its forced state. Because the effect of synthetic jet on the external flow field is represented by disturbing force, we suppose controlling forces of the two synthetic jets: F_{*1} and F_{*2} respectively, so its resultant force can be expressed as F that accounts for the primary jet variation. As shown in Fig. 6, variation angles are expressed by α and γ, so the effect of d_1 and d_2 on the variation angle can be explained as follows.

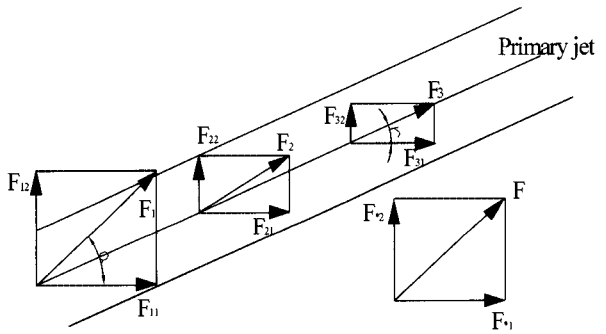

Fig. 5 Mechanical explanation of vectoring

SJA_{push} is operated in the push mode. As shown in Fig. 5, spanwise force F_{*2} is the main reason for the primary jet variation: variation angle increases with the increased F_{*2} and specified F_{*1}. For the actuator with constant parameters, the closer to the exit of the primary jet actuator is, i.e., the less d_2 is, the more obvious "push" effect is. When primary airflow moves away from the exit and develops towards downstream, the "push" force will have less effect on it. F_{*2} reduces more rapidly than that of F_{*1}, which results in the reduced angle γ (Fig. 5). By reason of the continuous variation process and effect of ambient fluid shear stress, strictly speaking, primary jet variation angle should be the average value of variation angles at different centerline locations.

SJA_{pull} is operated in the pull mode. As described in the conclusion of literature: variation angle in the "pull/push" mode is larger than that in the push mode, in the external flow field, the existence of F_{*1} keeps stability of primary jet variation from far-field ambient fluid. As shown in figure 6, F_{*1} decreases far downstream due to the vortex pair dissipation in the period of its interaction with ambient fluid. Only F_{*1} can not impel to achieve optimal variation, which show SJA_{pull} to primary jet exit not the closer and better, it is to say, d_1 not the smaller and better. However, "pull" force reduces while d_1 is too large and optimal variation can't be achieved. In general, two points need to be considered during d_1 selection: not only to obtain largest "pull" force, but to achieve optimum variation. Optimum d_1 has close relation with actuator's geometric parameters and aerodynamic parameters, i.e., the parameter variation would lead to the change of optimum d_1, which is in good agreement with related conclusion in literature.

6 Conclusions

(1) During the characteristic research of high-power synthetic jet actuators, excitation frequency (rotating speed n) and piston displacement A have great impact on the controlling ability and controlling efficiency. With the given model and relative parameters of actuator, its controlling effect is more obvious as the rotating speed increases. Exit average velocity and maximum velocity increase with the increased piston displacement, which results in the stronger controlling ability.

(2) The span-wise pressure difference of primary jet resulting from the periodic excitation, i.e., span-wise nonuniform static pressure distribution is the important reason for the primary jet variation.

(3) With the given motor rotating speed, the variation angle doesn't increase with the reduced primary jet velocity normally. There is an optimum variation angle according to a certain velocity value of primary jet.

(4) There is an optimum d_1 value in achieving optimum variation. And the value has close relation with the actuator's geometric parameters and aerodynamic parameters. Primary jet variation angle should be average value of variation angles at different centerline locations.

Acknowledgements

This investigation was supported by Postdoctoral Science Foundation of China. Grant No. 20070420300.

References

Kral, L.D., Donovan, J.F., Cain, A.B., Cary., A.W., 1997, "Numerical Simulation of Synthetic Jet Actuators", *AIAA* 97-1824

Jing Cui, Ramesh K. Agarwal, Dahai Guo, Andrew W. Cary., 2003, "Numerical Simulation of Behavior of Synthetic Jets in Cross-Flow", *AIAA* 2003-1264

Donald P. Rizzetta, Miguel R. Visbal, Michael J. Stanek., 1998, "Numerical Investigation of Synthetic Jet Flowfields", *AIAA* 98-2910

He Gaorang, Wang Liang., 2000, "Numerical Analysis of Micro Jet Actuator Flow Field", *ACTA AERODYNAMICA SINICA*, 18(4): 395 – 400

Luo Zhenbing, Xia Zhixun., 2006, "Advances in Synthetic Jet Technology and Applications in Flow Control", *Advances in Mechanics*, Vol35(2): 221 – 234

Gilarranz, J.L., Rediniotis, O.K., 2001, "Compact, High-Power Synthetic Jet Actuators for Flow Separation Control", *AIAA* 2001-0737

Smith B.L., Glezer A., 1997, "Vectoring and Small-Scale Motions Effected in Free Shear Flows Using Synthetic Jet Actuators", *AIAA* 97-0213

Staci A.Davis, Ari Glezer., 2000, "The manipulation of large- and small- scales in coaxial jets using synthetic jet actuators", *AIAA* 2000-0403

The 4th International Symposium on Fluid Machinery and Fluid Engineering
November 24-27, 2008, Beijing, China
NO. 4ISFMFE-IL07

Use of CFD for Thermal Coupling in Aeroengine Internal Air Systems Applications

Zixiang Sun*, John W. Chew and Nicholas J. Hills

* Thermo-Fluid Systems UTC, School of Engineering, University of Surrey
Guildford, Surrey, GU2 7XH, UK
Tel: +44-1483-682333 / Fax: +44-1483-686611
E-mail: Zixiang.Sun@surrey.ac.uk

Abstract With the rapid progress of computational fluid dynamics (CFD) and computer technology, CFD has been increasingly used for aero-engine component temperature predictions. This paper presents a review of the latest progress in this aspect with emphasis on internal air system applications. The thermal coupling methods discussed include the traditional finite element analysis (FEA), the conjugate heat transfer, FEA/CFD coupling procedure and other thermal coupling techniques. Special attention is made to identify the merits and disadvantages between the various methodologies. Discussion is further extended on the steady and transient thermal coupling applications.

Keywords thermal coupling, computational fluid dynamics, finite element analysis, internal air systems

Nomenclature

r	radius
T	temperature
t	time
Ω	angular speed

1 Introduction

Fast and accurate prediction of component metal temperature is one of the key issues in engine design process. With the rapid progress of CFD capability and computer power, CFD has been increasingly used to assist and to improve the metal temperature prediction in addition to the widely used finite element analysis (FEA). There are broadly three types of techniques in using CFD solutions for solid/fluid heat transfer simulations. One is generally called "conjugate heat transfer analysis", the second "non-coupled FEA/CFD procedure" and the third one "coupled FEA/CFD approach". These are hereafter referred as conjugate analysis, non-coupled procedure and coupled approach, respectively. A good review on the thermal coupling development was made by Dixon et al in 2004. This was followed by a recent brief discussion on the issue by Chew and Hills in 2007. In the present paper, a more comprehensive review was made with emphasis on the latest progress in the internal air system applications in the recent years.

2 Conventional FEA Method

Traditionally in industry, finite element analysis (FEA) is routinely used to predict metal temperatures in engine design. The thermal boundary conditions needed for FEA simulations are provided by thermocouple measurements and/or empirical correlations. The practice is still widely used in industry today. A latest innovative application of the technique was reported by Benito et al. (2008) at the ASME Turbo Expo 2008. Generally speaking, a FEA simulation could be obtained in minutes, which fits well in time scale in the design process. However, the limitation of this practice is obvious. Its effectiveness is subject to availability and applicability of the current database and correlations for a new design. A good example in comparing the traditional FEA prediction with the conjugate analysis was recently demonstrated

by Starke et al (2008), showing FEA was good for global assessment, but struggled in complex geometry applications.

3 Conjugate Analysis

In conjugate analysis, the solid/fluid heat transfer calculation may be realized by expanding the CFD capability to include heat conduction calculation in solid regions neighboring the fluids. Examples of such expanded CFD solvers for the conjugate analysis are NASA Glenn-HT code by Rigby and Lepicovsky (2001), and Aachen's CHTflow solver by Bohn et al. (2001). A number of papers have been published showing application of the conjugate analysis for engine component temperature predictions, such as a real turbine rotor-stator system simulation by Okita and Yamawaki (2002), a blade film cooling prediction by Bohn et al. (2003) and an internally cooled turbine blade application by Kusterer et al. (2004). The latest developments and applications of the conjugate analysis were reported recently by Alizadeh et al (2008) for high pressure (HP) turbine firtrees, Davison et al (2008) for an automated analysis of turbine blade cooling simulation and Okita (2006) for a simple transient simulation of a turbine disc rotor-stator rig.

The applications of the conjugate analysis were found to be limited to steady and simple transient calculations. Generally speaking, a conjugate analysis using an expanded CFD code is computationally expensive. This would be especially true for a time accurate calculation of a flight cycle, as a relatively very small time step has to be used to resolve the flow unsteadiness. A time scale in months was reported for a simple transient simulation of a rotor-stator rig (Okita, 2006). Therefore, the computational cost of performing a transient conjugate flight cycle analysis with an unsteady CFD solution for an engine application is prohibitive.

Another disadvantage of the conjugate analysis is difficult to provide further functionality of stress analysis. A latest attempt in adapting the finite volume method (FVM) for stress analysis was reported by Davison et al (2008). However, the accuracy and stability of such an adaptation for stress analysis are still questionable, compared with the matured FEA method.

4 Non-Coupled Procedures

Non-coupled procedures alleviate the CFD cost, where only a limited number of steady CFD calculations are performed at key engine operating conditions to produce a set of CFD based correlations, which eventually provide the necessary thermal boundary conditions for the traditional FEA calculation. Examples are two turbine disc cavity applications by Lewis and Provins (2004) and Alizadeh et al. (2007). This technique has received much attention these years. However, successful application of the non-coupled procedure is very much dependent on users' experience and expertise, such as boundary segment partitioning for the discrete correlations, and scaling of the correlations between the engine operating conditions.

5 Coupled Approach

Coupled FEA/CFD analysis is an alternative technique, where separate FEA and CFD codes are used for solid and fluid regions, respectively, with a smooth exchange of information between the two codes to ensure continuity of temperature and heat flux. There are a variety of approaches in implementing the coupled FEA/CFD analysis. For instance, Heselhaus et al. (1992) demonstrated a 3D FEA to 3D CFD coupling procedure for cooled turbine blade application. Li and Kassab (1994) described a coupled Finite Volume Method/ Boundary Element Method (FVM/BEM) approach with application to turbine blade calculation. Bohn et al. (1995) reported their coupled procedure for film-cooled turbine blade applications. Recently, Illingworth et al. (2005) reported a well established procedure coupling an in-house FEA code to a commercial CFD code, and successfully applied the procedure to turbine disc cavity calculations for flight cycle simulations. This followed work on steady state coupling by Mirzamoghadam and Xiao (2002), and Verdicchio et al. (2001). The latest extensions to the work of Illingworth et al. (2005) and validations were completed by Sun et al (2008). As a result, in this "FEA/CFD coupling" approach, an in-house FEA solver is coupled to two CFD codes, either commercial CFD software or an in-house CFD code, which provides choice for users. A plugin is designed to exchange information between the FEA and CFD calculations to ensure the continuity of temperature and heat flux across the FEA/CFD boundaries. A thermal coupling simulation is realized through an iterative procedure between the FEA and CFD calculations. Convergence of the coupling is recognized when a pre-set criterion is met in terms of a required tolerance between two successive intermediate thermal coupling solutions. Convergence of the FEA and CFD calculations in the iterative loop is satisfied as in normal individual FEA and

CFD simulations, respectively. The major features of the "FEA/CFD coupling" approach are described in the following sections.

Multiple CFD Domain strategy

Within a FEA model, one or more CFD domains can be set up to fit in local geometry as appropriate. They may cover part or the whole of the FEA model boundary. The FEA/CFD coupling approach provides coupling capability for the CFD/FEA boundaries, while the rest of FEA model is still simulated using conventional thermal boundary conditions provided by thermocouple measurements and/or empirical correlations. This practice ensures great flexibility and choice for users.

Steady CFD Approximation

For a transient flight cycle, the FEA calculations in the thermal coupling must be unsteady to reproduce the relatively slow response of metal heat conduction to a change in operating conditions of engine. Compared to this, the fluid flow time scales are much shorter, as they are determined by the fast convection of the flow. As a result, the flow may be assumed to adjust instantaneously to changes in the flow boundary conditions, and the influence of unsteadiness of fluid flow may be expected to be negligible. Therefore, steady CFD calculations could be employed. This approximation can result in significant saving in computing time for the FEA/CFD thermal coupling, as it avoids expensive unsteady CFD simulation in fluid regions and allows much larger time steps for unsteady FEA simulation of the metal heat conduction in solid regions, which means fewer time steps are needed to resolve a given transient cycle.

Multiple CFD Model Facility

In the FEA/CFD thermal coupling approach, the FEA/CFD coupling approach is designed to allow a set of CFD models to be defined at key time points/conditions in the transient cycle to represent "steady" operating conditions, such as idle, maximum take-off (MTO) and cruise conditions. For each "steady" operating condition, a CFD solution is obtained by solving the corresponding CFD model. For a transient operating condition, such as engine acceleration and deceleration, a CFD solution is obtained, as an approximation, by a linear interpolation of two corresponding CFD solutions obtained at its neighboring "steady" operating conditions. To speed up the CFD calculations, initial CFD solutions are prepared in advance for each CFD model, assuming CFD wall boundaries being temporarily adiabatic. The CFD solution obtained with dynamically updated boundary conditions at a time step is always used as initial flow field for the next. As the difference of CFD solutions between two successive time steps is expected to be small, fewer iterations are needed for each CFD solution. All these contribute to further saving in computational time.

"Energy Equation Only" Option

Normally, a CFD solution is obtained by solving all the governing equations of fluid flow. This type of solution is hereafter referred as "full equations" option. As an alternative to the "full equations" option, the "energy equation only" option is developed, where energy equation only is solved during the thermal coupling, and the corresponding flow field is frozen, i.e., re-solution of flow field is bypassed. This further approximation can produce extra saving in the computational time.

The "energy equation only" option has been proven very useful in many applications. It has long been recognized that there are situations where fluid properties are essentially independent of temperature and the flow energy equation has no influence on the flow field. In this case, the flow energy equation is linear in temperature. Chew et al (1996) made use of this in their coupled CFD/FEA thermal solution for a turbine blade. This option was also demonstrated with good results by Sun et al (2008) for a rotor-stator example and two engine rig test cases.

Parallel Computation

For a mediate and large thermal coupling problem, parallel computation is always a wise option to reduce the wall clock time. In the "FEA/CFD coupling" approach, parallel computation has been implemented on both UNIX and LINUX systems. Satisfactory parallel computation performance was demonstrated on PC cluster platforms.

Coupling Example

The described "FEA/CFD coupling" approach has been successfully applied to a number of test cases with satisfactory results. For the demonstration purpose, only a 4 stage low pressure (LP) turbine disc cavity was given here. The geometry of the FEA and CFD models are shown in Figure 1. The area highlighted by red lines encloses the CFD domain, and FEA/CFD thermal coupling takes place through these boundaries. Both FEA and CFD models are axisymmetric. Three key dimensions are also shown in this figure for reference.

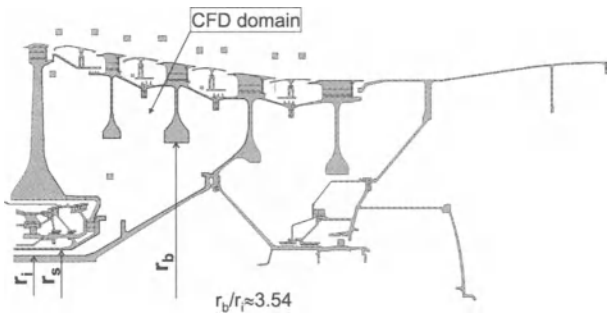

Fig. 1 FEA and CFD models for a LP turbine cavity

The simulated transient cycle in terms of the LP turbine disc angular speed Ω versus time is given in Fig. 2. It can be seen that the transient cycle covers a typical range of operating conditions from idle, engine acceleration to maximum take-off (MTO). All the flows were simulated with the standard k-ε turbulence model, as the both rotational and inflow Reynolds numbers for both the idle and MTO conditions were estimated to be high enough to justify a turbulent flow simulation.

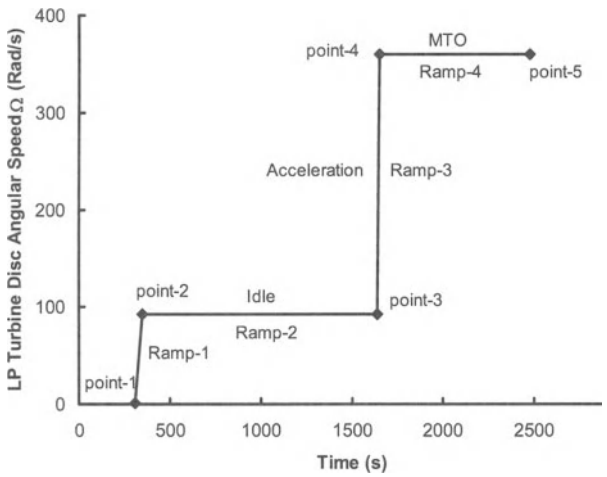

Fig. 2 Transient thermal cycle for the LP turbine cavity

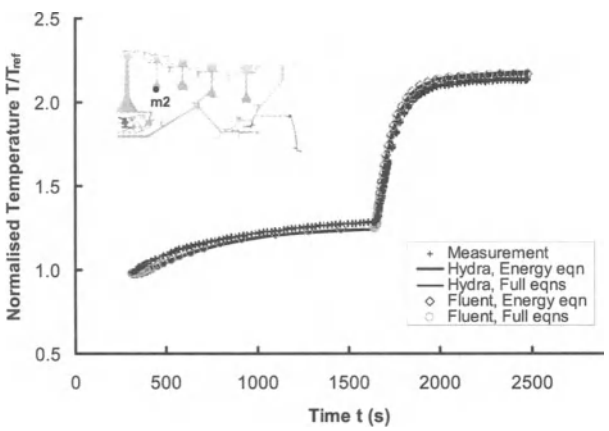

Fig. 3 Comparison of temperature history at point m2

Figure 3 shows a comparison of the temperature histories at a typical monitoring point m2, obtained using both "energy equation only" and "full equations" options. The metal temperature contours obtained at the end of the thermal coupling transient cycle are also given in this figure for an overall picture of temperature distribution at $t = 2477$s. For reference, the thermocouple data provided by Rolls-Royce plc were also plotted, together with coupling results using the FLUENT CFD code. In Figure 3, the red and blue solid lines indicate the results obtained using Hydra CFD solutions with "energy equation only" and "full equations" options, respectively. The black plus signs denote the Rolls-Royce thermocouple measurements. The pink diamonds and green circles designate their corresponding counterparts obtained using FLUENT. It can be seen that agreement between the thermal coupling results using "energy equation only" and "full equations" options with the Hydra and FLUENT codes is very good. The agreement between the thermal coupling predictions and Rolls-Royce measurements is satisfactory, which is generally within the measurement uncertainty.

With regard to the computational cost, it was reported that all coupling simulations conducted so far finished within 25 hours in terms of wall clock time (Sun et al 2008). The timings were obtained on a PC-cluster cluster node with a 2.4GHz Xeon CPU. Use of the "energy equation only" option was proven helpful in reducing the computing time. The speedup obtained so far is up to 3.1. Obviously, the speedup is case dependent. The speedup is defined as a ratio of the wall-clock time consumed between using the "energy equation only" option and its corresponding "full equations" one.

6 Concluding Remarks

A comprehensive review on the solid/fluid thermal coupling techniques was conducted with emphasis on the internal air system applications. It is believed the traditional finite element analysis (FEA) will be still a practical tool in engine design for many years to come, as it can provide useful information in minutes. Huge database and extensive experience accumulated make it very helpful to fit in the design requirements and time scale. The technique is still in evolution and more innovative applications and developments of the technique can be expected.

Conjugate heat transfer analysis is expensive, although significant progress has been achieved in this area. Its application will be mainly limited to steady simulations for foreseeable years. Its disadvantage in the stress

analysis capability is also a major challenge to become a design tool in industry.

The non-coupled procedures are very useful as long as the technique is used wisely with experience and expertise. More application and development in the technique can be expected. However, the usage of technique is believed to be limited for many years to come until a standardized and automated procedure of procedure is developed.

Coupled approaches take advantages of two separate codes, i.e. FEA for solid domain and CFD for fluid regions, respectively. Both metal temperature prediction and stress analysis can be conducted simultaneously through FEA when required. The FEA/CFD coupling approach developed by Illingworth et al (2005) and further extended by Sun et al (2008) demonstrated good results for engine applications with encouraging computational efficiency. The "energy equation only" option has been proven useful with good speedup. More improvements were reported under way to include an enhancement in computational efficiency, automation of the CFD model and mesh generation, and adaptation of displacement and deformation from "cold" to "hot" engine operating conditions. The technique can be integrated with CAD to speed up the investigation of effect of geometry alteration, metal temperature prediction and stress analysis, tip clearance simulation in the design process. The whole process could be achieved in weeks and possibly in days in future. It is very promising to become a part of design tool set to be used in industry.

Acknowledgements

Funding from the Department of Trade and Industry (DTI) and Rolls-Royce plc is gratefully acknowledged.

References

Alizadeh, S., Mabilat C., Jackson D. and Clarkson R., 2008, "Conjugate Heat transfer study of a biaxial rig: application to the lifing of HP turbine disc firtrees", Proc. ASME Turbo Expo 2008, Paper no. GT2008-51297, pp. 1-13. June 9-13, 2008, Berlin Germany

Alizadeh, S., Saunders, K., Lewis, L.V. and Provins, J., 2007, "The Use of CFD to Generate Heat Transfer Boundary Conditions for a Rotor-Stator Cavity in a Compressor Drum Thermal Model", GT2007-28333, ASME Turbo Expo 2007, May 14-17, 2007, Montreal, Canada

Benito, D., Dixon, J and Metherell, P. 2008, "3D Thermo-mechanical modeling method to predict compressor local tip running clearances", Proc. ASME Turbo Expo 2008, Paper no. GT2008-50780, pp. 1 – 10. June 9 – 13, 2008, Berlin, Germany

Bohn, D., Bonhoff, H., Schonenborn, H. and Wihelmi, H., 1995, "Validation of a Numerical Model for the Coupled Simulation of Fluid Flow and Adiabatic Walls with Application to Film-Cooled Turbine Blades", VDI-Berichte 1186, pp. 259 – 272

Bohn, D., Kruger, U. and Kusterer, K., 2001, "Conjugate Heat Transfer: An Advanced Computational Method for the Cooling Design of Modern Gas Turbine Blades and Vanes", Heat Transfer in Gas Turbine, eds. Sunden B. and Faghri M., pp. 58 – 108, WIT Press, Southampton, UK

Bohn, D., Ren, J. and Kusterer, K., 2003, "Conjugate Heat Transfer Analysis for Film Cooling Configurations with Different Hole Geometries", ASME 2003-GT-38369

Chew, J.W. and Hills, N.J., 2007, "CFD for Turbomachinery Internal Air Systems", Philosophical transactions of the Royal Society (Series A), Aerospace CFD Theme Issue

Chew, J. W.; Taylor, I. J.; Bonsell, J. J., 1996, "CFD developments for turbine blade heat transfer", IMECHE CONFERENCE TRANSACTIONS - 1996 ; VOL 1 ; Pages: 51-64

Heselhaus, A., Vogel, D.T. and Krain, H, 1992, "Coupling of 3D-Navier-Stokes External Flow Calculations and Internal 3D-Heat Conduction Calculations for Cooled Turbine Blades", AGARD, p. 40.1 – 40.9

Dixon, J. A., Verdicchio, J. A., Benito, D., Karl, A. and Tham, K. M., 2004, "Recent developments in gas Turbine component temperature prediction methods, using computational fluid dynamics and optimization tools, in conjunction with more conventional finite element analysis techniques", Proc. Instn Mech. Engrs, Vol. 218, Part A; J. Power and Energy, pp. 241 – 255

Davison J.B., Ferguson S. W., Mendonca, F.G., Peck A. F. and Thompson, A., 2008, "Towards an automated simulation process in combined thermal, flow and stress in turbine blade cooling analysis", Proc. ASME Turbo Expo 2008, Paper no. GT2008-51287, pp. 1 – 8. June 9 – 13, 2008, Berlin Germany

Illingworth, J.B., Hills, N. J. and Barnes, C.J., 2005, "3D Fluid-Solid Heat Transfer Coupling of an Aero Engine Pre-Swirl System", GT2005-68939, ASME Turbo Expo 2005, June 6 – 9, 2005, Reno-Tahoe, Navada, USA

Kusterer, K., Bohn, D. Sugimoto, T. and Tanaka, R., 2004, "Conjugate Calculations for a Film-Cooled Blade under Different Operating Conditions", ASME 2004-GT-53719

Lewis, L. V. and Provins, J. I., 2004, "A Non-Coupled CFD-FE Procedure to Evaluate Windage and Heat Transfer in Rotor-Stator Cavities", ASME GT2004-53246, ASME Turbo Expo 2004, June 14 – 17, 2004, Vienna, Austria

Li, H. and Kassab, A. J., 1994, "A Coupled FVM/BEM Approach to Conjugate Heat Transfer in Turbine Blades", AIAA paper 94 – 1981

Mirzamoghadam, A.V., and Xiao, Z., 2002, "Flow and Heat Transfer in an Industrial Rotor-Stator Rim Sealing Cavity",

ASME Journal of Engineering for Gas Turbines and Power, Vol. 124, pp. 125 – 132, 2002

Okita, Y., 2006, "Transient thermal and flow field in a turbine disk rotor-stator system", Proc. ASME Turbo Expo 2006, Paper no. GT2006-90033, pp. 1 – 11. May 8 – 11, 2006, Barcelona, Spain

Okita, Y. and Yamawaki, S. 2002, "Conjugate Heat Transfer Analysis of Turbine Rotor-Stator Systems", ASME 2002-GT-30615

Rigby, D. L. and Lepicovsky, J., 2001, "Conjugate Heat Transfer Analysis of Internally Cooled Configurations", ASME 2001-GT-0405

Starke C. and Janke E., Hofer T. and Lengani D., 2008, "Comparison of a conventional thermal analysis of a turbine cascase to a full conjugate heat transfer computation", Proc. ASME Turbo Expo 2008, Paper no. GT2008-51151, pp. 1 – 11. June 9 – 13, 2008, Berlin Germany

Verdicchio, J.A., Chew, J.W., and Hills, N.J., 2001, "Coupled Fluid/Solid Heat Transfer Computation for Turbine Discs", ASME paper 2001-GT-0123

The 4th International Symposium on Fluid Machinery and Fluid Engineering
November 24-27, 2008, Beijing, China
NO. 4ISFMFE-Ab14

Optimization of Patterned Grooves Micromixer Using the Design of Experiments

Chul-Kyu Kim[1], Joon-Yong Yoon[*2], Hyun-Jong Lee[1], Myung-Seob Shin[1] and Sung-Joon Byun[1]

[1] Department of Mechanical Engineering, Hanyang University, Seoul, Republic of Korea
[*2] Division of Mechanical and Management Engineering, Hanyang University,
1271 Sa-3-Dong, Sangnok-gu, Ansan City, Gyeonggi-do 426-791, Republic of Korea
Tel: +82-310-400-5282 / Fax: +82-310-400-4707
E-mail: joyoon@hanyang.ac.kr

Abstract Mixing independent fluid is of significantly important in microfluidics application, however, is difficult to mix solutions in microchannels. Efficient mixing was also hampered by comparatively slow molecular diffusion process at the micro-scale. In this study, in order to enhance the mixing efficiency, the configuration of patterned grooves micromixer is optimized using an approximate optimization technique. First of all, mixing characteristics analyzed by 3-D Computational Fluid Dynamics. The effective of geometrical parameters on the mixing performance of the staggered herringbone mixer with patterned grooves on the floor are numerical investigated. Groove parameters choose the most effective parameters such as the patterned groove of depth, the patterned groove of length, between grooves distance, and the patterned groove of angle. Design of experiments is applied to the optimization procedure. The optimum micromixer models in parameters region performed to generate using Design of experiments in effective parameters. A mixing index and a pressure drop values calculated at the cross-sections compared each models and proposed optimization of models.

Keywords microfluidic, micromixer, staggered herringbone mixer, optimization, design of experiments

Nomenclature

c	concentration
D	diffusivity coefficient
l	characteristics length
p	pressure
Pe	Peclet number
Re	Reynolds number
u	average velocity
V	vector of velocity
μ	viscosity coefficient
ρ	density
σ	mixing index
ν	dynamics viscosity coefficient

1 Introduction

Recently, MEMS industries have increased requiring microfluidic devices for mixing such as active and passive micromixers on the chemical and biological fields. Passive micromixers are widely utilized in Lab-on-a-Chip systems and micro total analysis systems. Lab-on-a-chip devices are used to perform many functions such as separation, mixing, reaction, and analysis on a single chip. The problem of controlling fluid mixing in these microfluidic devices is significant in a variety of applications in the homogenization of solutions of reagents in the micromixer.

Generally, fluids in the passive micromixer are stretched and folded when passing the channel, which can effectively mix two or more fluids. One of the passive methods to improve the mixing process is patterning of one or more surfaces of the channel. Stroock et al. (2002) showed experimentally that mixing can be improved by using a repeating sequence of bas-relief herringbone shaped asymmetric structures at an oblique angle on the floor of the channel.

The key concept in this design is to create transverse flow patterns that increase the interfacial area between the fluids to be mixed. In a simple microchannel (a channel without grooves or any other shape) with flow at low Reynolds number (Re <100), the mixing of the fluids is only diffusive that is very low or negligible as compared with convective mixing. Stroock et al. (2002) also analyzed the mixing performance of a staggered herringbone mixer. They showed that at high Peclet number mixing efficiency decreases, and hence the longer channel length is needed to achieve the required mixing.

Numerous detailed investigations on mixing for the geometry proposed by Stroock et al. (2002) have been reported, representing that groove shape can be very effective in mixing fluids. Aubin et al. (2003, 2005) numerically investigated the effect of different geometrical parameters of a staggered herringbone groove micromixer on the mixing quality with the purpose of improving the mixer design. Engler et al. (2004) demonstrated that vorticity generated by convection can be used to mix the fluids.

It is obvious that mixing can be effectively increased by optimizing the shape of the grooves. Some previous investigations have been carried out on the effects of geometric parameters on the mixing performance. The staggered herringbone mixer (SHM) with patterned grooves is more effective at micro scale because of the important dominance of the surface effects. Although there have been many studies concerning the staggered herringbone mixer, a systematic investigation into geometric effects on the SHM's performance was found to be rare.

The design of experiments was established to be a controlling tool in the research field of the optimum design. By adopting this approach, the number of experimental parameters is reduced and the sensitivity of each parameter is analyzed. Yang et al. (2005) have been numerically investigated influences leading the SHM's performance of the geometric parameters by orthogonal array method with 9 cases. They have been performed to conduct the effectiveness of geometric parameters. However, the optimal investigation had not sufficient cases to propose a model of effective mixer for optimization of geometry. Therefore, this paper is developed in a more efficient approach by the design of experiments. One of the design of experiments is uses the graeco-latin square method. The grid independence is estimated at the very beginning; the sensitivity of the geometric parameters and the optimum design considering the mixing index are then obtained simultaneously. This investigation also proposes the enhanced optimum design of micromixer models.

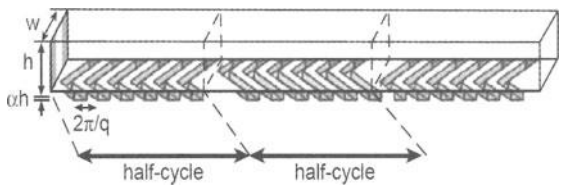

Fig. 1 The geometry of the micromixer with staggered herringbon micromixer

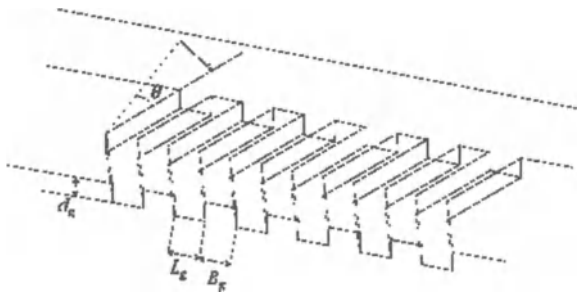

Fig. 2 Geometric parameters of the patterned groove micromixer

2 Numerical Analysis

For the numerical analysis of mixing and flow field of the staggered herringbone micromixer for each case, the commercial CFD-code Fluent 6.2 was used. This is common purpose code that solves Navier-Stokes equations using the finite volume method. The flow in the micromixer is governed by the incompressible Navier-Stokes equations. The mixing of two fluid streams of uniform and equal properties is governed by convection diffusion equation. The solver calculates the steady continuity, momentum, and diffusion equations, represented as follows:

$$\nabla \cdot \vec{V} = 0 \tag{1}$$

$$\frac{D\vec{V}}{Dt} = -\nabla p + \frac{1}{\mathrm{Re}}\nabla^2 \vec{V} \tag{2}$$

$$\frac{Dc}{Dt} = \frac{1}{Pe}\nabla^2 c \tag{3}$$

Where c is concentration, $Pe = Ul/D$ is the Peclet number, and D is the molecular diffusivity. In this study, we set $Re = 1$ and $Pe = 2e5$ and $U = 1\ cm/s$

Figure 1 shows the geometry of the micromixer with herringbone grooves patterned on the floor of mixer, which is similar to the geometry used by Strook et al. (2002) The mixer is composed six mixing cycles with 12

grooves in each cycle. Fig. 2 shows the mixer consists of a rectangular channel (w = 200μm, h = 85μm, L = 1cm) with grooves of depth, d_g, grooves of length, L_g, between grooves length, B_g, and grooves of angle, θ. In this study, case models were used to generate structured grid in the micromixer. A mesh composed of approximately 1 800 000 hexahedral elements was used. The boundary condition at the mixer inlet was a uniform velocity profile. This corresponds to a laminar flow regime with a Reynolds number (Re) = 1. At the outlet, a constant pressure condition (P = 0) was imposed and no-slip boundary conditions were applied at all walls.

Table 1 Parameters and Levels of micromixer geometry

Level	A(d_g)	B(L_g)	C(B_g)	D(θ)
1	11 μm	30 μm	30 μm	30°
2	15 μm	50 μm	50 μm	45°
3	20 μm	70 μm	70 μm	60°

Table 2 Generating cases for optimization by design of experiments

Case No.	A	B	C	D
1	1	1	3	1
2	3	3	1	1
3	3	3	1	3
4	3	3	3	1
5	1	3	1	3
6	3	1	3	3
7	1	2	2	2
8	1	1	1	3
9	2	3	2	2
10	2	1	2	2
11	2	2	2	3
12	3	2	2	2
13	3	3	3	3
14	3	1	1	3
15	1	3	3	1
16	2	2	2	2
17	2	2	3	2
18	2	2	2	2
19	1	1	1	1
20	3	1	3	1
21	1	3	3	3
22	1	3	1	1
23	1	1	3	3
24	3	1	1	1
25	2	2	1	2
26	2	2	2	1

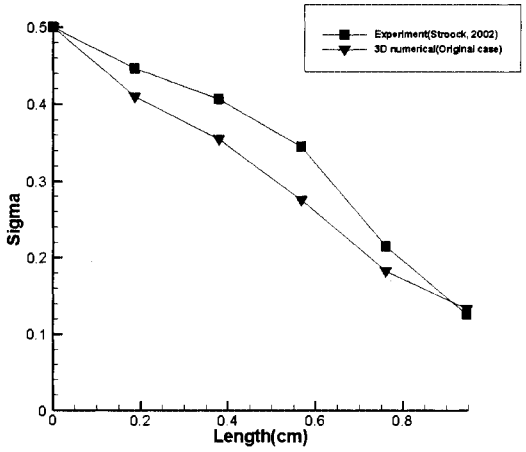

Fig. 3 Comparison and validation of numerical and experimental mixing index (Sigma) results

3 Optimization Technique

This purpose of optimization for micromixer was designed to achieve a most effective mixing and a small pressure gradient by determining appropriate geometry parameters of the mixer. Influence parameters have been also investigated by Aubin et al. (2005) and Yang et al (2003). However, we choose the parameters that affected importantly influence mixing to the groove geometry of mixer on the floor; groove of depth, length, angle, and distance between grooves. Table 1 shows determined 3 levels for each parameter, respectively.

In this study, one of design of experiments is uses the graeco-latin square method that obtained 81(3^4) cases (9 matrixes of 3 by 3.) combining two Latin square on each parameter and level. We also determined only 26 cases of all case by using sampling process algorithm; 1) to select the most extremely combined values among the corner matrixes, and 2) to select the centered values among the inner matrixes. In order to determine an optimal case models of generated every case by using the graeco-latin square method.

Table 2 shows to select the cases of micromixer geometry, using above the process algorithm.

In order to evaluate and compare the performance of the mixer within each case, which calculated the mixing index and the pressure gradient at the cross-section of micromixer. The mixing index was calculated using the standard deviation of the intensity distribution in the cross-section of mixer, as follow;

$$\sigma = \sqrt{\left\langle \left(c - \langle c \rangle\right)^2 \right\rangle} \tag{4}$$

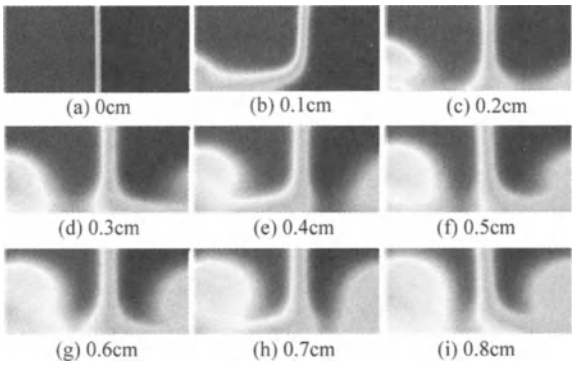

Fig. 4 Concentration distribution trend of calculated numerical model at cross-section each points with proposed by Stroock et al. (2002)

where c is the concentration value(between 0 and 1) of a cross-section, and $\langle\ \rangle$ means an average over all the concentration value at cross-section of mixer. The value of σ is 0.5 for completely segregated streams and 0 for completely mixed streams by using Strook et al. (2002)

Table 3 Comparison of mixing index and pressure drop each case

Case No.	Mixing Index (σ)	Pressure drop (kPa)
1	0.2599	0.641
2	0.1043	0.547
3	0.0047	1.190
4	0.1274	0.625
5	0.0457	0.670
6	0.2255	0.540
7	0.1734	0.524
8	0.2882	0.383
9	0.0309	0.805
10	0.2516	0.493
11	0.1332	0.556
12	0.1231	0.551
13	0.0293	0.871
14	0.2488	0.391
15	0.1515	0.675
16	0.1409	0.686
17	0.1467	0.659
18	0.1409	0.686
19	0.3011	0.436
20	0.2425	0.628
21	0.0855	0.710
22	0.1347	0.529
23	0.2485	0.533
24	0.2143	0.591
25	0.0754	0.648
26	0.1943	0.568

4 Results and Discussion

In this study, firstly, numerical simulation for 3D geometric micromixer was performed to validate to the experimental result by Strook et al. (2002) Fig. 1 shows a comparison of the sigma values of numerical simulation and experimental result that evaluated the mixing efficiency at the cross section through into micromixer. However, sigma value represents the efficiently mixing to a smaller value. Accordingly, above result shows a significantly similar trend of mixing gradient along the micromixer length with numerical simulation and experimental result. Furthermore, the error of numerical simulation be shown within approximation 11%; however, simulation result is properly predicts closing the mixing efficiency with experimental results.

Mixing was compared only until 0.95 cm from the inlet as affected the atmospheric pressure. We assumed to calculate numerical model by determining the main dimensionless values, *Re=1*, and *Pe=2e5* by Strook et al. Fig. 1 also shows to predict a more accurate Mixing Index (sigma value) in the numerical result at the inlet and the outlet. The other side, however, shows to estimate increased the error of numerical result to the sigma value at the middle of micromixer. Significantly, this result shows to predict an excellent the tendency of mixing gradient of numerical simulation result at the cross section in the micromixer with compared to the experimental results. Therefore, we can that use to evaluate the numerical simulation of an optimal model by validated similar conditions.

Fig. 4 shows the concentration distribution at the each cross-section of micromixer along axis length. When this validation result evaluated the results to investigate by Stroock et al. (2002), Aubin et al. (2005), and numerous researcher, this study has a similar trend to the numerical calculation result, however, the numerically concentration distribution based on the validation results verified to appropriate the calculation results by generated the model of the cases in this investigation. Fig. 4 also showed that the mixing pattern of two fluids only was observed the mixing characteristics of staggered herringbone mixer. Mixing in the mixer effectively occur this local mixing pattern by asymmetry patterned grooves on the floor.

Table 3 shows according to sequence the calculation results of each case. Mixing index values at the micromixer outlet and Pressure drop values from inlet to outlet on different pressure passing fluids in the micromixer were respectively obtained numerical analysis. Generally, we observe that if mixing index had more small value, however, pressure drop was obtained

more great value. However, when comparison in these results, we also significantly obtain that above trend certainly not agree several cases.

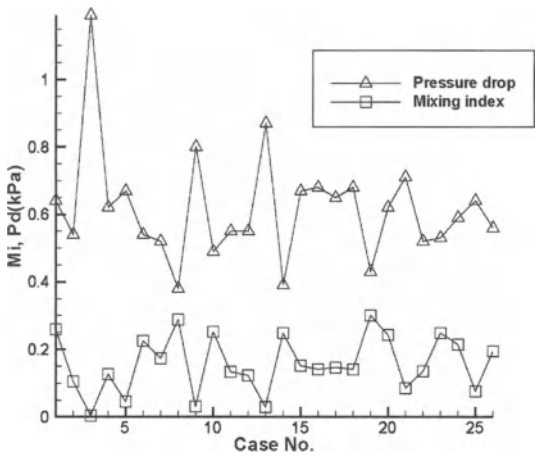

Fig. 5 Characteristics relationship of mixing index and pressure drop of all of the cases

Figures 5 and Fig. 6 show to compare the mixing index and the pressure drop of every case. Figure 5 mainly shows to obtain the high values of pressure drop at the low values of mixing index. Figure 6 shows to compare the descending values of mixing index with pressure drop values. Here, we observe that not increase the pressure drop each case value according to decrease the mixing index values at the several case. We also observe that to control the effective mixing and the pressure drop was achieved through the appropriately combination of micromixer geometry. In this case no. 3 that extremely has the smallest value of mixing index, mixer geometry has the depth of patterned groove; 20μm, the length of patterned groove; 70μm, the distance of between grooves; 30μm, and the angle of patterned groove; 60′ . However, it has most large the value of pressure drop. In opposition case, case No. 19 has the depth of patterned groove; 11μm, the length of patterned groove; 30μm, the distance of between grooves; 30μm, and the angle of patterned groove; 30′ , also has most large the mixing index value and most small the pressure drop in the every case.

When case no. 1 and no. 14 compared the mixing index and the pressure drop, the value of mixing index has 0.2599 and 0.2488. However, the pressure drop has 0.641kPa and 0.391kPa, respectively. Case No. 5 and No. 3 compared each result that obtained mixing effectiveness of 90% the mixing index is 0.0457 and 0.0047. Furthermore, the pressure drop observed to obtain large different values; 0.670kPa and 1.190kPa, respectively. The average mixing index and pressure drop values in the every case obtained 0.1585 and 0.621kPa. We consider for a model of optimization that limited mixing effectiveness of 90% and less than the average pressure drop value, however, also propose by these results that if consideration of the more effective mixing, propose the case no. 5 and if consideration of the more small different pressure, propose case no. 25.

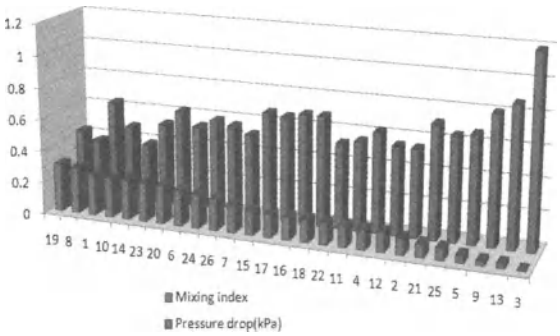

Fig. 6 Relationship of sequence of low mixing index and pressure drop

5 Conclusion

In this paper, the optimization of staggered herringbone mixer has been performed design of experiments for generating an optimal model of cases. However, proposed model by Stroock et al. (2002) also has been validated to compare the experimental results and the numerical results with mixing index at each cross-section in the micromixer. Each mixer case was also performed to calculate the mixing index and pressure values using the numerical analysis by commercial CFD-codes Fluent. We analyzed the results of mixing index and pressure drop values at each case. Therefore, the appropriate combination of geometry parameters can controls the mixing effectiveness and pressure gradient by using design of optimization. However, we propose two models; the significant mixing effectiveness model and the significant pressure drop model that based on these optimization results.

Acknowledgements

This work was supported by the second stage of the Brain Korea 21 Project in 2008.

References

Ansari, M. A., and Kim, K. Y., 2007, "Shape optimization of a micromixer with staggered herringbone groove", *Chemical Engineering Science*, Vol 62, pp.6687 – 6695

Aubin, J., Fletcher, D.F., Bertrand, J., and Xuereb, C., 2003, "Characterization of the mixing quality in micromixers", *Chemical Engineering Technology* Vol. 26(12), pp.1262 – 1670

Aubin, J., Fletcher, D.F., and Xuereb, C., 2005, "Design of micromixer using CFD modeling", *Chemical Engineering Science* Vol. 60, pp.2503 – 2516

Engler, M., Kockmann, N., Kiefer, T., and Woias, P., 2004, "Numerical and experimental investigations on liquid mixing in static micromixers", *Chemical Engineering Journal*, Vol. 101, pp.315 – 322

Nguyen, N. T and Wereley, S. T., 2002, "Fundamental and Applications of Microfluidics", *Artech House*, Boston

Nguyen, N. T and Wu, Z., 2005, "Topical review Micromixers-review", *Journal of Micromechanics and Microengineering*, pp.R1 – R16

Stroock, A.D., Dertinger, S.K., Ajdari, A., Mezic, I., Stone, H.A., and Whitesides, G.M., 2002, "Chaotic mixer for microchannels", *Science* Vol. 295, pp.647 – 651

Wang, H., Ioveitti, P., Harvey, E., Masood, S., 2003, "Numerical investigation of mixing in microchannels with patterned grooves", *Journal of Micromechanics and Microengineering*, Vol. 13, pp.801 – 808

Yang, J. T., Huang, K. J., and Lin, Y. C., 2005, "Geometry effects on fluid mixing in passive grooved micromixers," *The Royal Society of Chemistry(Lap chip)*, Vol. 5, pp.1140 – 1147

The 4th International Symposium on Fluid Machinery and Fluid Engineering
November 24-27, 2008, Beijing, China
NO. 4ISFMFE-Ch02

Numerical Study on Mechanical Characteristics of Aerostatic Bearing

Zhaoqin Yin*, Dongsheng Li

* Dept. of Flow Measurement & Simulation, China Jiliang University,
Hangzhou, 310018, China
Tel: +86-571-8687-5662
E-mail: yinzq@cjlu.edu.cn

Abstract In order to study how the turbulence of the air film flow field, the changing of velocity and the distance of the inlets induce the vibration, k-ε model has been used to simulate the pressure variation of two inlets air film. The air velocity of throttle pore, the distance of the two inlets have been changed to study the effect on the vibration. The results show that the parameters of the air film will change the characteristic of flow field. The periodical vibration velocity of the throttle pores will increase the vibration of the air film than constant velocity. Furthermore the more distance between the two inlets will also strength the vibration. These results can help the researchers and engineers to further understand the basic characteristics of aerostatic lubrication and correct the design for their application.

Keywords aerostatic lubrication, numerical analysis, vibration

1 Introduction

The aerostatic lubrication uses the air as lubrication between the moving block and the bearing to prevent the high friction between the two moving joint. It is because the friction will cause the unstable condition between the moving block and the guide and also increase the control difficulty. The aerostatic lubrication use the air as lubrication, the effect of the friction will be eliminated. The principle of the aerostatic lubrication is shown in Fig. 1.It is the key technology in the field of precision engineering.

There are a lot of works already acknowledged in various researches. Boffey *et al.* and Chen *et al.* have done experimental investigation on steady-state performance characteristics like stiffness because of orifice restrictor size and pocket dimensions. Stout *et al.* have presented design charts to enable the design of rectangular type of aerostatic Gang Lin *et al.* proposed a computer simulation method for the dynamic and stability analysis of journal air bearings.

Fourka and Bonis have developed a simulation program to investigate the influence of feeding system type on the performance of externally pressurized gas bearings. They used different kinds of multiple inlets specifically designed with orifices or porous compensation. Renn and Hsiao did experimental and CFD study on the mass flow-rate Lin W. J. *et al.* obtained the numerical solution of the pressure distribution and the flow speed between the surface of aerostatic bearing and the slide surface.

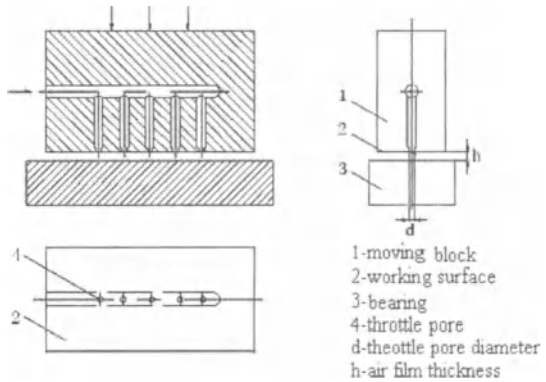

Fig. 1 Principle of aerostatic lubrication

Recently simplified Reynolds equation is widely employed in aerostatic bearing design to study the characteristic through an orifice-type restrictor, but leads large static error.

The mechanical characteristics of air film, such as pressure distributing; bearing capacity and stiffness is the main factor that determines the stability of air-bearing position. Because of the complexities, the detailed reason of the vibration of air film is not clear. The vibration induced by the turbulence of the air film flow field has not been studied.

In order to study how the turbulence of the air film flow field, the changing of velocity and the distance of the inlets induce the vibration, the standard k-ε turbulence model has been used to simulate the pressure variation of two inlets air film. The standard k-ε turbulence model is based on the fully developed turbulence and fit to calculate the high Reynolds number turbulence flow. The air velocity of throttle pore, the distance of the two inlets and thickness of the air film have been changed to study the effect on the vibration.

2 Controlling Equation

The controlling equations for the two-dimensional incompressible flow are as follows:

Continuity equation:

$$\frac{\partial u_i}{\partial x_i} = 0 \tag{1}$$

Momentum equation:

$$\frac{\partial}{\partial t}(\rho u_i) + \frac{\partial}{\partial x_j}(\rho u_i u_j) = \frac{\partial}{\partial x_j}\left(\mu \frac{\partial u_i}{\partial x_j}\right) - \frac{\partial p}{\partial x_i} \tag{2}$$

The turbulence viscosity is calculated by the following equation:

$$\mu_t = \frac{\rho C_\mu k^2}{\varepsilon} \tag{3}$$

where ρ is the density of air , u the velocity of flow, p the pressure, μ the viscosity, μ_t the turbulent viscosity coefficient.

The standard k-ε turbulence model was adopted to carry out numerical simulation.

k equation:

$$\frac{\partial}{\partial x_i}(\rho k u_i) = \frac{\partial}{\partial x_j}\left[\left(\mu + \frac{\mu_t}{\sigma_k}\right)\frac{\partial k}{\partial x_j}\right] + G_k - \rho\varepsilon \tag{4}$$

ε equation:

$$\frac{\partial}{\partial x_i}(\rho \varepsilon u_i) = \frac{\partial}{\partial x_j}\left[\left(\mu + \frac{\mu_t}{\sigma_\varepsilon}\right)\frac{\partial \varepsilon}{\partial x_j}\right] + C_{1\varepsilon}\frac{\varepsilon}{k}(G_k + C_{3\varepsilon}G_b) - C_{2\varepsilon}\rho\frac{\varepsilon^2}{k} \tag{5}$$

where k is the turbulence kinetic energy, ε the dissipation rate of turbulence kinetic energy, G_k the turbulence kinetic energy produced by the gradient of average velocity, G_k turbulence kinetic energy produced by the buoyancy.$C_{1\varepsilon}$, $C_{2\varepsilon}$ and $C_{3\varepsilon}$ are the constant coefficients, σ_ε and σ_k are turbulence Prandtl number for k and ε respectively.

The turbulence kinetic energy G_b and the related coefficient C_3 produced by buoyancy are included for the compressibility flow. When the flow is incompressibility flow, $G_b = 0$. The related constant coefficients are set to be $C_{1\varepsilon} = 1.44$, $C_{2\varepsilon} = 1.92$, $C_{3\varepsilon} = 0$.

3 The Model of Numerical Simulation

The purpose of this paper is study how the turbulence of the air film flow field induce the vibration. So the load capability of the aerostatic bearing is a constant. The simulation model is simplified as two inlets air film flow field. $d = 0.5$mm is the diameter of the air inlet. $h = 0.2d$ is the air film thickness. s is the distance of the two inlets.

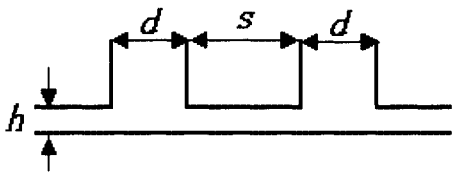

Fig. 2 Simulation model

Knudsen number is used to set the wall boundary, the expression is

$$K_n = \frac{2\lambda_{air}}{h} \tag{6}$$

K_n is the Knudsen number, λ_{air} is the mean-free-path of air.

When $K_n < 0.01$, the flow is in the continuum region; when $0.01 < K_n < 0.1$, the flow is in the slip flow region; when $0.1 < K_n < 10$, the flow is in the transition region; when $K_n > 10$, the flow is in the free molecule or kinetic regime

In the simulation, the wall boundary condition is no slip boundary condition because $K_n < 0.1$.

The simulation used FLUENT software. About 0.3M square cells have been used to discrete the computational domains.

The temperature, density and viscosity of the inlet air are 293K, 1.189kg/m^3,and 1.789×10^{-5}Ns/m^2 respectively. The step time is 0.01s.

4 The Simulation Results and Discussions

Figure 3 shows the pressure fluctuation of the air gap with the time when $s = 2d$,$h = 0.2d$ and $u_0 = 1$m/s. when the inlet velocity is a constant, the pressure of the air gap change. The most fluctuation happens at the moment when the air inpour the air gap because of the flow field structure changes sharply. When the air gap is full of air, the main reason of the pressure fluctuation is the turbulence of the flow field. The fluctuant rang decreases comparing to the moment of the air inlet.

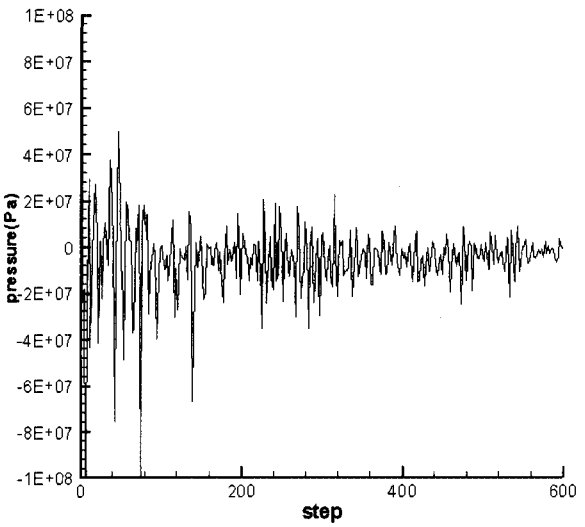

Fig. 3 The pressure fluctuation profile of $s = 2d$, $h = 0.2d$ and $u_0 = 1$m/s

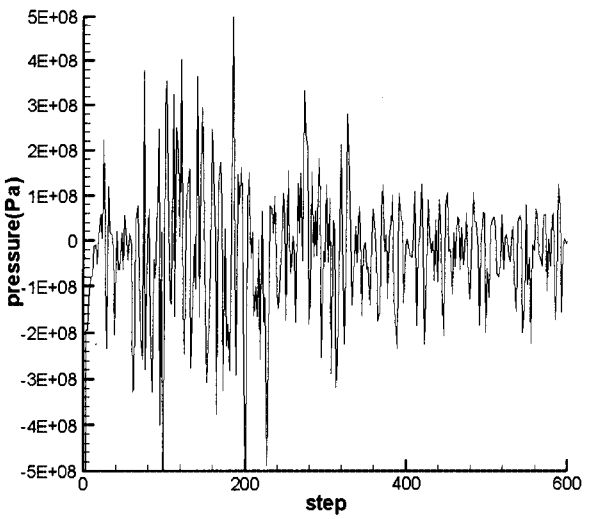

Fig. 4 The pressure fluctuation profile of $s = 2d$, $h = 0.2d$ and $u_0 = 1+0.2\sin(10t)$m/s

When the aerostatic bearing works, the airflow entering into the air gap is unsteady. In order to simple the study, the air velocity is set as the sinusoidal signal $u_0 = 1+0.2\sin(10t)$m/s. Figure 4 shows the pressure fluctuation of the air gap with the time when $s = 2d$, $h = 0.2d$ and $u_0 = 1 + 0.2\sin(10t)$m/s. Comparing figure 3 to figure 4, the pressure fluctuation of figure 4 is about ten times of figure 3, which means the vibration velocity of the throttle pores is the main factor causing the pressure fluctuation.

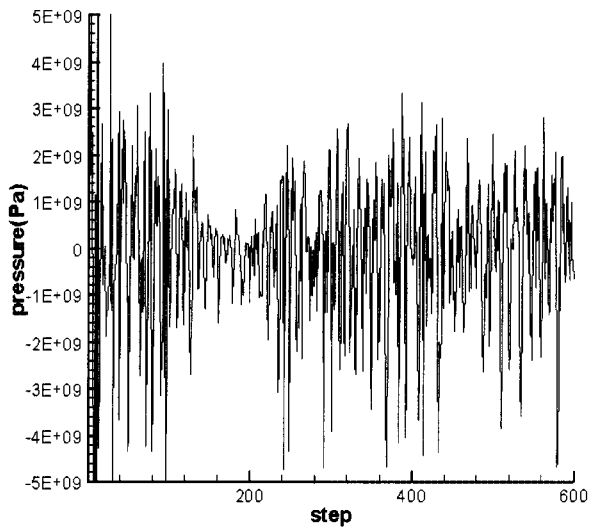

Fig. 5 The pressure fluctuation profile of $s = 4d$, $h = 0.2d$ and $u_0 = 1+0.2\sin(10t)$m/s

Figure 5 shows the pressure fluctuation profile of $s = 4d$, $h = 0.2d$ and $u_0 = 1+0.2\sin(10t)$m/s. The distance of the two inlet infect on the pressure fluctuation has been studied. Comparing Fig. 5 to Fig. 4, the distance of the inlets changes the flow field of the air gap, even changes the pressure fluctuation. The larger distance produces more pressure fluctuation. So when the aerostatic lubrication is used for precision machine, the less distance of the inlets should been considered.

5 Conclusion

k-ε turbulence model has been used to simulate the air gap flow field of aerostatic lubrication. The turbulence of the air film flow field, the changing of velocity and the distance of the inlet induce the vibration have been studied.

The results show that the parameters of the air film will change the characteristic of flow field. The periodical vibration velocity of the throttle pores will increase the vibration of the air film than constant velocity. Furthermore the more distance between the two inlets and the air film thickness will also strengthen the vibration.

These results can help the researchers and engineers to further understand the basic characteristics of aerostatic lubrication and correct the design for their application.

Acknowledgements

The authors give acknowledgement to the Natural Science Foundation of Zhejiang province (No. Z106280).

References

Xi,L., Yu,X.F., Fan,W., 2006, "Research on the Two-coordinate Platform of Novel Nano-CMM", *Journal of Hefei University of Technology*,Vol29, pp .1605 – 1608

Zhang,J.H., Zhang,S.G., Zhao, H.X., *et al.*2007, "Structure Design and Test for Guide Unloading System of Large Ultra-precision Machine",*Optics and Precision Engineering*, Vol15, pp. 1382 – 1390

Boffey,D.A., Barrow,A.A., and Dearden,J.K., 1985, "Experimental Investigation into the Performance of an Aerostatic Industrial Thrust Bearing", *Tribology International*,Vol. 8, pp. 165 – 168

Boffey,D.A., Waddell,M., and Dearden,J.K., 1985, "Theoretical and Experimental Study into the Steady-state Performance Characteristics of Industrial air Lubricated Thrust Bearings", *Tribology International*,Vol. 18, pp. 229 – 233

Chen,M.F., and Lin,Y.T.,2002, "Static behavior and dynamic stability analysis of grooved rectangular aerostatic thrust bearings by modified resistance network method", *Tribology International*, Vol. 35, pp. 329 – 338

Stout,K.J.,1985, "Design of Aerostatic Flat Pad Bearings using Annular Orifice Restrictors", *Tribology International*,Vol. 18, pp. 209 – 214

Lin,G., Aoyala,T., and Inasaki,I.,1988, "A Computer Simulation Method for Dynamic and Stability Analyses of Air Bearings", *Wear*, Vol. 126, pp. 307 – 319

Fourka,M., and Bonis,M.,1997, "Comparison Between Externally Pressurized Gas Thrust Bearings with Different Orifice and Porous Feeding Systems", *Wear*, Vol.210, pp. 311 – 317

Renn,J.C., and Hsiao, C.H., 2004, "Experimental and CFD Study on the Mass Flow-rate Characteristic of Gas Through Orifice-type Restrictor in Aerostatic Bearings", *Tribology International*, Vol. 37, pp. 309 – 315

Zhou,S. 1995, "The Introduction of Fluid Solid Coupling Model on Blade Machine",*Gas Turbine Experiment and Research*, Vol. 3, pp. 1 – 7

Wang, F.J., 2004, "The Analysis of Computation Fluid Dynamics", *Tsinghua University Press*, Beijing

The 4th International Symposium on Fluid Machinery and Fluid Engineering
November 24-27, 2008, Beijing, China
NO. 4ISFMFE-Ch06

Valve Dynamic Characteristic and Stress Analysis of Reciprocating Compressor Under Stepless Capacity Regulation

Jiangming Jin[1], Weirong Hong[*2], Rongren Wu[1]

[1] Institute of Chemical Machinery, Zhejiang University, 310027 Hangzhou, China
[*2] Institute of Chemical Machinery, Zhejiang University, 310027 Hangzhou, China
Tel: +86-571-8795-1241/ Fax: +86-571-8795-1241
E-mail: hongwr@zju.edu.cn (Corresponding Author)

Abstract The method that depresses the suction valves in the partial compression stroke to realize the stepless capacity regulation for reciprocating compressor makes the compressor power consumption reduce along with the decreasing of capacity. However, the operation condition of suction valves is greatly changed by this method and it is necessary to analyze the stress distribution of suction valve to guarantee the safety operation. In this paper, a FEA model of the suction valve used in reciprocating compressor with the unloader is given. It is found that there is more than one impact between valve plate and unloader prong in the process of depressing the suction valves. The impact stress and speed of the suction valve plate varying with the different assemble error or the hydraulic pressure is obtained. Compared with the normal condition, it can be seen that the maximum stresses arisen from the over-high hydraulic oil pressure or the assemble error are in an order of the plastic deformation and crack initiation.

Keywords reciprocating compressor, stepless capacity regulation, FEA, suction valve, impact and stress

1 Introduction

Reciprocating compressor has been widely used in petrochemical and other process industries. It has played an irreplaceable role in the gas compression fields of high compression ratio, light gas and extra-high pressure, compared with other compressors. In many applications, the compressor always works at partial load, not the maximum volume condition under which the compressor was initially selected, and it is extremely wasteful to compress the redundant gas. The capacity regulation method by depressing the suction valve makes the inhalational intake gas back to suction chamber during partial compression stroke, only the gas required is compressed. By using this method, compressor capacity can be regulated steplessly in a range between 0~100% and the power consumption is saved. Fig.1 shows the principle of the regulation method. The P-V cycle of normal situation is 1-2-3-4-1, whereas in the case of capacity regulation, it changes to 1-2-3-5-6-1.

The key problem for realizing the stepless capacity regulation is to control the suction valve open or close actively. It's accomplished by an unloader acted by a hydraulic pressure pulse that is produced from the special designed distributors.

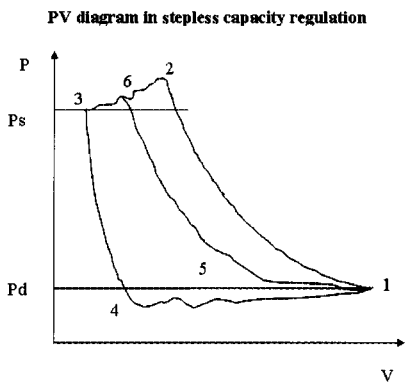

Fig. 1 P-V diagram in stepless capacity regulation

The hydraulic pressure keeps the suction valve open when the piston begins the compression stroke. The suction

valve is passively closed under the gas force action when the hydraulic force withdraws. In this situation, the suction valve works abnormal and should be analyzed carefully; especially the process of the depressing the suction valve for which the hydraulic force is bigger than the return gas force. Fig.2 provides a typical ring type suction valve failure case that the pits are caused by the unloader prongs.

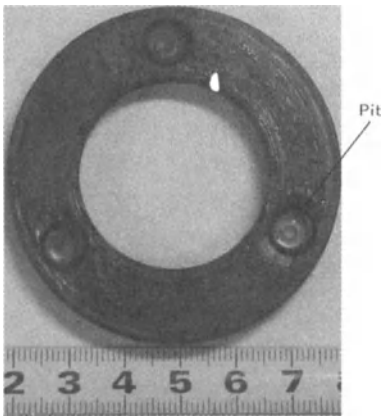

Fig. 2 Ring type valve failure caused by unloader

In this paper, take the type 3L-10/8 reciprocating compressor for example, the FEA models are built in the nonlinear dynamical analysis software Dytran to analyze the depressing process of the net type suction valve. Since it is the end of the suction process and the hydraulic depressing force is much greater than gas force, this paper just focus on the valve open and without considering gas force affect.

The suction valve live-time affected by the capacity regulating mechanism is estimated by analyzing dynamic characteristics and stress distributions of the suction valves under different situations. The simulation results will provide the theory basis for design of stepless capacity regulation system.

2 Structure and Material

The typical unloader assembling is made of unloader hydraulic piston, suction valve cap, unloader connecting rod, and suction valve. The diagram of the single unloader with the suction valve is shown in Fig.3. Figure 4 is the suction valve assembling diagram with the unloader which describes the relative position between unloader, valve plate, and valve seat. The valve plate limiter shown in Fig.4 has little influence the valve impact during the process of depressing the valve and hasn't been taken into consideration.

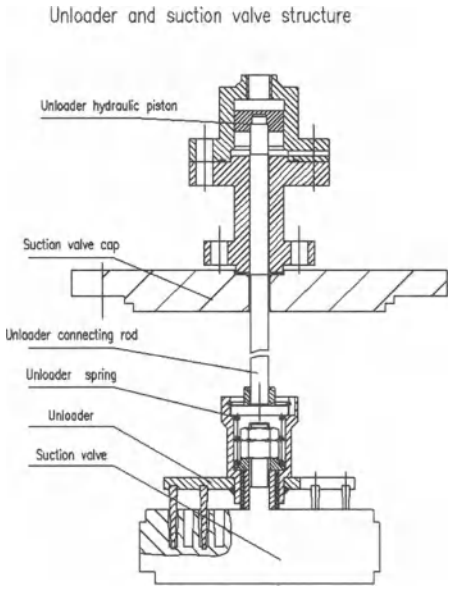

Fig. 3 Valve depressed machine structure

The unloader hydraulic piston controlled by the high pressure oil in unloader hydraulic pushes the unloader through the unloader connecting rod to depress the suction valve. Table 1 and Table 2 present the material data used in the unloader which is taken from. The geometry dimension is listed in Table 3.

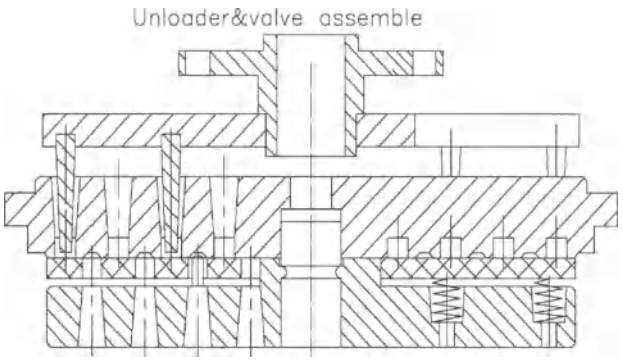

Fig. 4 Unloader and suction valve structure diagram

Table 1 Part material

Part	*Material*
Unloader connecting rod	45# Steel
Unloader	45# Steel
Unloader prong	PEEK-CF 30
Unloader spring	50CrV
Valve plate	PEEK-CF 30
Valve seat	45# steel
Valve limiter	45#steel
Valve spring	17-7PH

Table 2 Material data for calculation

Material	*Item*	*Data*
45 Steel	Density	7800 kg/m^3
	Young Modulus	205 GPa
	Yield strength	220 MPa
PEEK-CF 30	Density	1440 kg/m^3
	Tensile modulus	11.5 GPa
	Tensile strength	212 MPa
	Carbon fiber	30%

Table 3 Key dimension date

Part	*Size*	*Number*
Unloader prong longer	26mm	8
Valve plate thickness	5mm	
Valve lift	2mm	
Unloader prong away form valve plate	1.5mm	
Hydraulic piston diameter	20mm	
Valve plate diameter	140mm	
Valve spring	971N/m	12
Unloader spring	9800N/m	

3 Fea Model

Under the assumption of the symmetry of the structure, only 1/2 section model with the symmetry boundary conditions need to be calculated, even in the situations of the inclination of valve plate and unloader. For the steel, the isotropic elastic is used because the stress does not exceed the yield point in the unloader. The bilinear isotropic material model is adopted for the short reinforce thermoplastic of the random distribution fiber with the lack of the material data for orthotropic model. Though some researchers suggest that the orthotropic model will give more accurate results, the isotropic model is sufficient to analyze the structure in this situation.

All volumes are meshed by solid element, and the linear elastic element is used to simulate the spring. In order to avoid the virtual stress concentration introduced applying the single element to simulate the unloader spring, up to 13 elements are used.

The surface-to-surface contact is used to define the contact model, the friction coefficient between PEEK and metal is set to 0.2. It is assumed the hydraulic force acting on the unloader is invariable. The constant force is applied on the unloader top surface. The valve seat is fixed in space, and the unloader is modeled to move along its central axis. The hydraulic pressure rang in hydraulic cylinder is from 1.1MPa to 10MPa. Lagrange algorithm is used to solve the model. There are 51683 solid elements and 21 combine elements in final FEA model. The graphical representation of the FEA model is shown in Fig. 5.

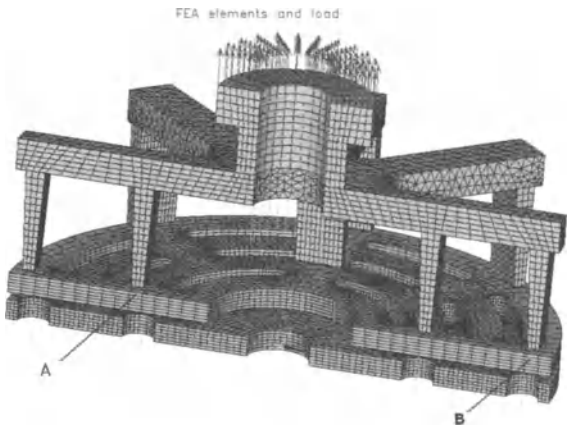

Fig. 5 FEA Model

4 Impact in Normal Position

Figure 6 shows the displacement curves in the moving direction of the nodes that are nearly point A shown in Fig. 5, and dedicate the impact history of unloader and valve plate.

The unloader prong pushes first the valve plate (point 1 in Fig. 6), gives some momentum to the valve plate and makes it move a little faster than the unloader. Therefore the valve plate impacts the valve seat (point 2 in Fig. 6), then the unloader prong with the rebounded valve plate impacts together the valve seat (point 3 in Fig. 6). At this point, unloader has the maximum energy and the maximum stress occurs in the valve plate. After three or four impact cycles, the mechanical system comes into stabilization.

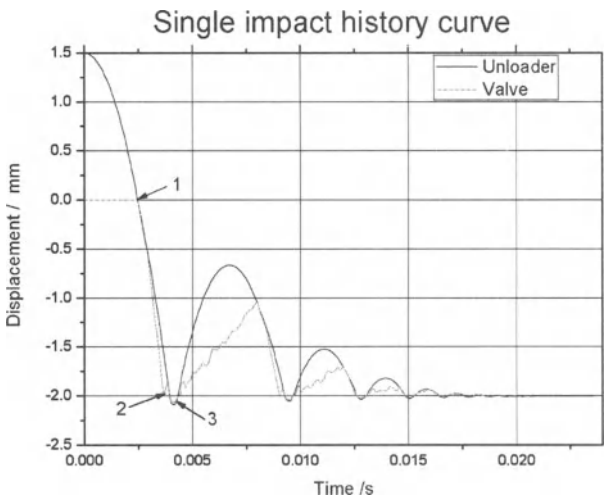

Fig. 6 Impact history curve on point A, hydraulic pressure 1.1MPa

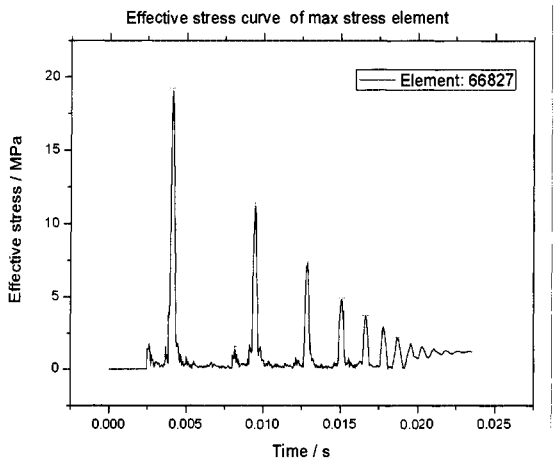

Fig. 7 Stress history curve in maximum stress element (nearly point A), the hydraulic pressure: 1.1MPa

Figure 7 shows Von Miser stress of the maximum stress element just located in point A (Fig. 5) of valve plate in the pressure of 1.1MPa. The maximum stress point occurs in the valve plate corresponds to the point 3 in Fig. 5 with the value of 19.22MPa. The first litter peak is consistent with point 1 in Fig. 5 representing the firs impact between unloader and valve plate. The maximum impact stress in each impact cycle decreases in exponential with the impact time. Because of no consideration of the solid and spring dump, the maximum stress will decrease much faster in practical.

In order to keep open the suction valve, the hydraulic force must be larger than the maximum reverse gas force. In the other similar system, the used hydraulic pressure must not be lower than 9MPa. Therefore, it is very important to analyze the valve max stress varying with hydraulic pressure. Figs. 8 and Fig. 9 show the results of this simulation, which the hydraulic pressure vary from 1.1MPa to 10MPa, the max stress grows from 19.2MPa to 69.8MPa and the max impact speed of the valve plate is up to the 6.5m/s in the 10MPa hydraulic pressure.

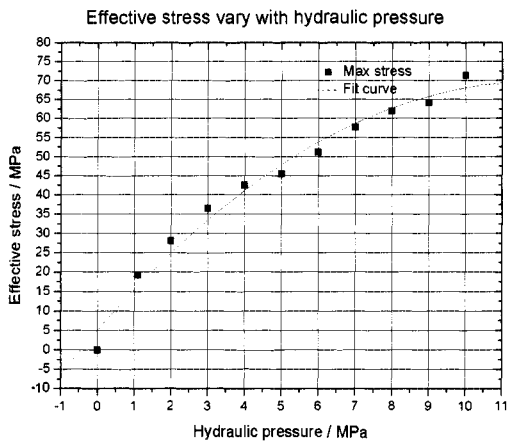

Fig. 8 Effective stress vary with the hydraulic pressure

Use the second-order polynomial curve to fit the effective stress, which is:

$$P_s = 5.04\times10^6 + 1.08\times10^7 P_{oil} - 4.54\times10^5 P_{oil}^{\ 2} \quad (1)$$

And use the second-order exponential curve to fit the impact speed, which is:

$$V_s = 5.557 - 4.769\times e^{\frac{-P_{oil}}{14.53}} - 0.788\times e^{\frac{-P_{oil}}{0.657}} \quad (2)$$

As shown in Fig. 9, over hydraulic pressure will bring about the over high stress in valve plate. It is necessary that reducing the hydraulic pressure as low as possible to improve the valve plate status greatly. The advised maximum hydraulic pressure should be no more than 6MPa.

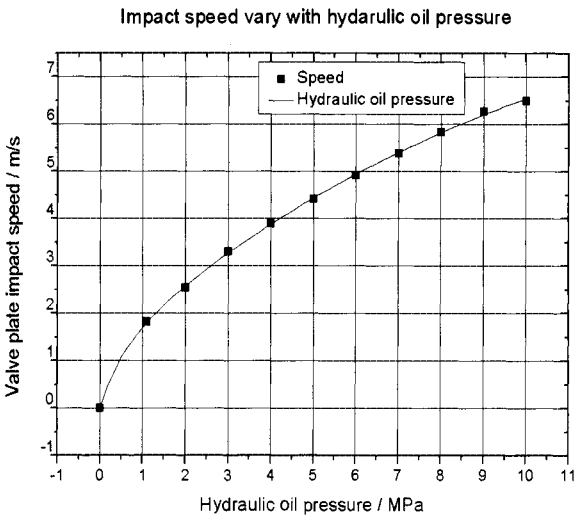

Fig. 9 Valve plate impact speed vary with hydraulic pressure

Since the impact energy varies with the impact weight in constant force boundary, the influence of the weight of the unloader must be considered. Figure 10 describes the

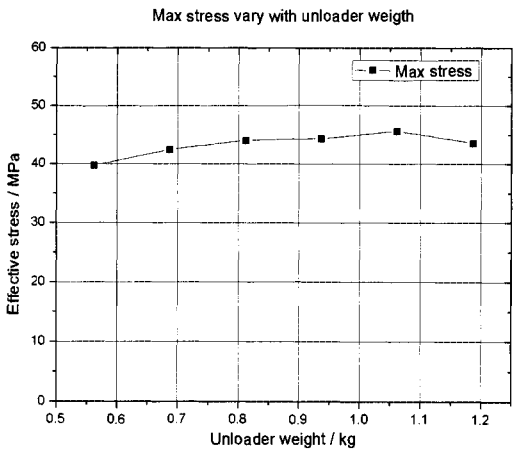

Fig. 10 Effective stress vary with the unloader weight hydraulic pressure: 4MPa

relationship between unloader weight and the maximum stress in valve. It can be seen that the weight of unloader has little affection on the maximum valve stress

5 Stress Affected by Assemble Error

Three abnormal assembling cases are considered in the calculation of stress affected by assembling error, namely valve plate oblique, unloader oblique and both of them, Fig. 11 show the three states.

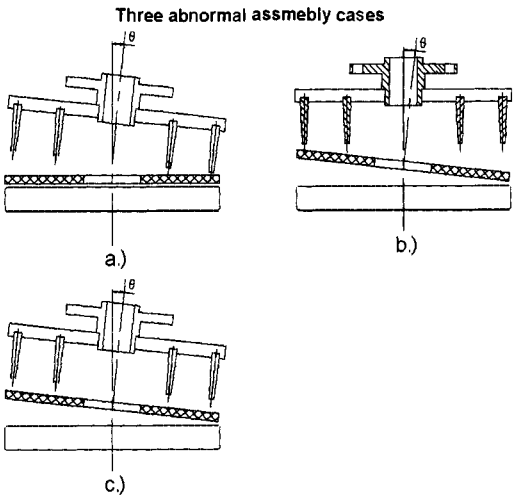

Fig. 11 abnormal assemble situation

5.1 Case a: Inclined Unloader

In this case, inclined unloader makes the stress concentrations more serious (Point B in Fig. 5), as only one side prongs are impact with the valve plate. Fig. 11 shows the maximum stress varying with the unloader incline degree.

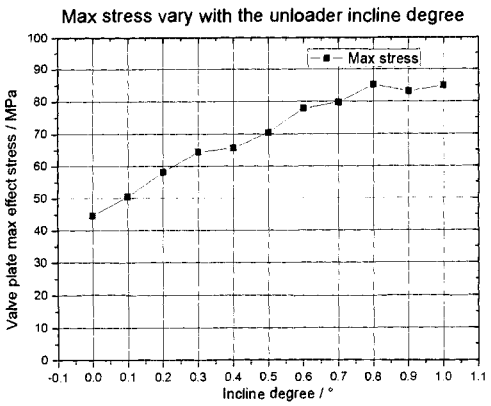

Fig. 12 Max stress vary with the unloader incline degree

5.2 Case b: Inclined Valve Plate

Figure 13 describes the maximum effective stress increasing with the valve plate inclination angle, as the prong show, the maximum stress does not increase obviously with the increasing of the inclination degree. This phenomena can be explained as the first impact between the valve plate and the unloader at the valve plate initial position makes the valve incline release and do not greatly affect the impact stress for unloader, valve plate and valve seat.

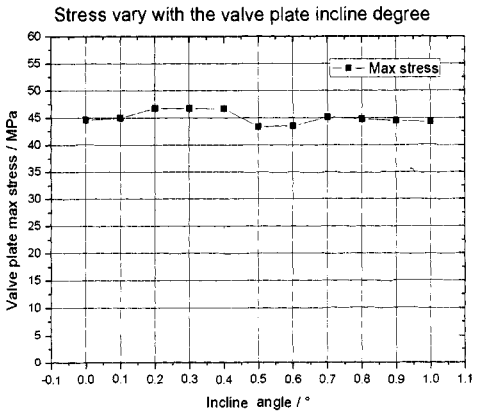

Fig. 13 Max stress vary with the valve plate incline degree

5.3 Case c: Inclined Unloader& Valve Plate

Figure 14 shows the maximum stress varying with the unloader and the valve plate inclination degree which is the different from the other cases. It may be because that the unloader inclined makes the stress increased but the parallel of the valve and unloader weakens this situation.

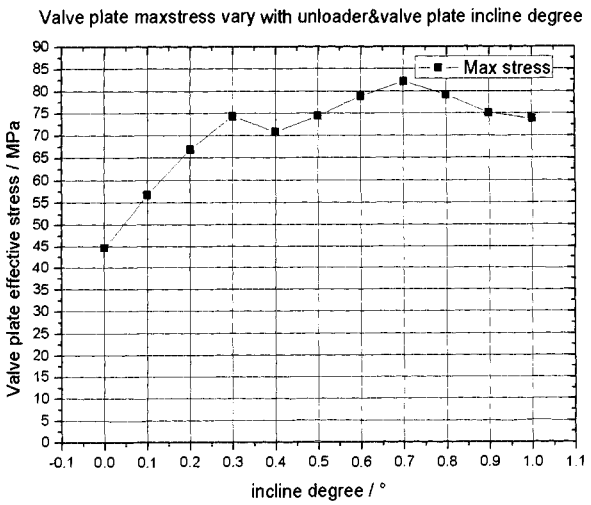

Fig. 14 Max stress vary with the valve plate incline degree

6 Unloader Material

In the original design, all the unloader parts are made of PEEK-CF 30. It seems to us that the more flexible unloader will have a lower impact stress, but the FEA calculation results indicate the opposite conclusion, as

shown in Fig. 15. Based on the fact that unloader weight do not largely affect the stress, the main body of improved unloader is made of 45# steel and the prongs are still made of PEEK-CF 30. The re-calculation results indicate that the max stress reduces obviously.

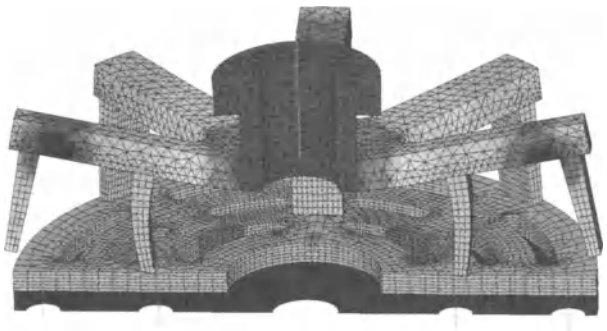

Fig. 15 The deformation of the PEEK CF 30 unloader

7 Conclusion

Analyzing the stress distribution of the suction valve affected by the unloader is the design basis of the capacity regulation system for reciprocating compressor. A FEA model of suction valve together with the unloader is built to simulate this situation. The stress distribution affected by the hydraulic pressure, the unloader weight and material, the part assembling error is achieved. The analysis results of the simulation are as followings:

(1) Impact between the unloader and valve is more than one time, grows stably after three or four impact in one impact history in one cycle.

(2) The increasing of the hydraulic oil pressure makes the max stress in valve plate grown fast, the max oil pressure shown no more than 6MPa in order to keep a lower stress level and impact speed.

(3) Unloader weight do not have greatly affect on the result when it vary from the 0.56kg to 1.18kg.

(4) The unloader assembly error makes the stress in valve plate increase greatly, and the error should keep below the 0.2°.

(5) The unloader that is totally made of PEEK CF does not possess the enough stiffness. Only the inner prongs contacted with the valve plate need to be made of PEEK CF.

Acknowledgements

The authors would like to acknowledge the China National Key Technology R&D Program (No. 2008BAF34B13) financial support.

References

Hong, W.R., Jin, J.M., 2006: "A time based pressing off suction valves device for reciprocating compressor", *China Invention Patent*, Patent Number: 200610155395.8

Zhao, Q.S., 2003, "Handbook of Advanced Composite Materials", *China Machine Press*, Beijing

Qiu, X.H. et, 1988, "Machine Design Handbook : Vol. 1", *China Machine Press*, Beijing

Spiegl, B. J, Mlekusch, B. A, 1999, "Thermoplastic in Reciprocating Compressor Valves. Part II-Stress Calculations in Short-fibre reinforced thermoplastic Compressor Valve Plates", *Proc. Of IMechE C542/038*, London, pp. 387 – 398

John O. Hallquist, 2006.3, "LS-DYNA Theory manul", Livermore Software Technology Corporation. USA

Yan, H.X., 2002.7, "Study on Property of PEEK Composites", *China Plastics Industry*, Vol. 30 No.4, pp. 44 – 45

Steinruck, P., Ottitsch, F, 1997, "Better Reciprocating Compressor Capacity Control", *Hydrocarbon Processing*, Feb, 79 – 8

The 4th International Symposium on Fluid Machinery and Fluid Engineering
November 24-27, 2008, Beijing, China
NO. 4ISFMFE-Ch17

Influence of the Floating-Ring Bearing Parameters on Stability of Turbocharge Rotor-Bearing System

Xinjun Zhao*, Hong He and Siyou Xu

* National Key Lab. of Diesel Engine Turbo-charging Tech.
P.O.B 22, Datong Shanxi, 037036, China
Tel: +86-352-5362096 / Fax: +86-352-5362085
E-mail: kunpeng_zhao@163.com

Abstract In the paper, the finite element computational model of rotor-bearing system is presented using the software DyRoBeS. Based on the numerical simulating method, dynamical characteristics in the different working conditions of bearing are analyzed such as span, width, gap and so on. By the theoretical analysis of critical speed and spectrum cascades, the changing rule of stability of the rotor system and the reason of oil whirl and oil whip are discovered. The influence of parameters on the system stability is different, and the significant effect is attained by one or two parameters. The investigation is helpful to design the bearing and optimize the rotor-bearing system in a turbocharger.

Keywords floating-ring bearing, turbocharger, stability

Nomenclature

C_x	The first critical speed in station X (r/min)
L	The width of bearing (mm)
L_y	The width of bearing in state Y (mm)
S	The span of two bearings (mm)
S_y	The span of two bearings in state Y (mm)
δ_1	The inner gap of bearing (mm)
δ_{1y}	The inner gap of bearing in state Y (mm)
δ_2	The outer gap of bearing (mm)
δ_{2y}	The outer gap of bearing in state Y (mm) material

1 Introduction

At present, the stability of rotor system has been the emphases of study in the domain of rotor dynamics. However, the most investigation was focused on the study of large-scale low-speed rotor system (such as turbo-generator rotor system), not the instability study of high-speed turbocharger rotor system. The rotational speed of the turbocharger rotor in this paper reaches 100,000rpm, and there is strong connection between the stability of rotor-bearing system and the stability of turbocharger. Therefore, the stability of a turbocharger rotor system is investigated by using the method of adjusting floating-ring parameters in this paper.

2 Computational Results of Rotor-Bearing System

In the paper, the finite element computational model of rotor-bearing system is presented using the software DyRoBeS. Based on the numerical simulating method, dynamical characteristics of different working condition of bearing is computed such as span, width, gap and so on. By the analysis of critical speed and spectrum cascades, it is the changing rule of stability of rotor system and the reason of oil whirl and oil whip that are found. The computational model of the rotor-bearing system is shown in Fig. 1, and it mainly consists of a nut (station 1), compressor impeller (left), shaft, floating-ring bearings and turbine impeller (right).

Based on changing one parameter of bearing in the computation, it is obtained that the relation between parameter and stability. Because of station 1 far from the bearing, the amplitude at this station is bigger than that at other stations. In the test the vibration characteristic at this station also represents the characteristic of the whole rotor-bearing system, so the vibration spectrum cascade in

station 1 represents the rotor-bearing system's characteristic in the paper.

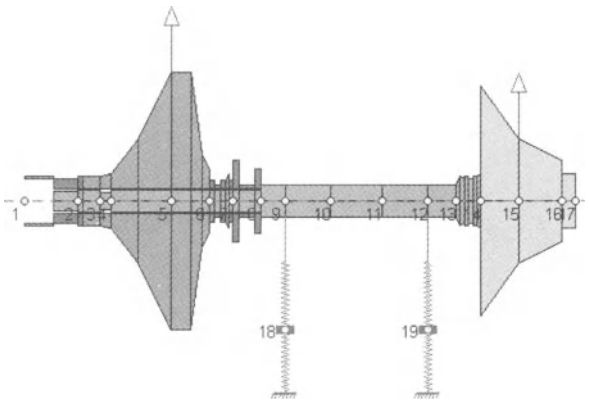

Fig. 1 Finite element model

2.1 Influence of Span on Stability

In this computational model only the span is changed. A typical data set consisting of the span and the first critical speed at the different stations is shown in Fig. 2. It is shown that C_1, C_5 and C_9 linearly increase with augment of span, but the increment are slight. The difference between C_1 and C_5 is small, but either of them is bigger than C_9.

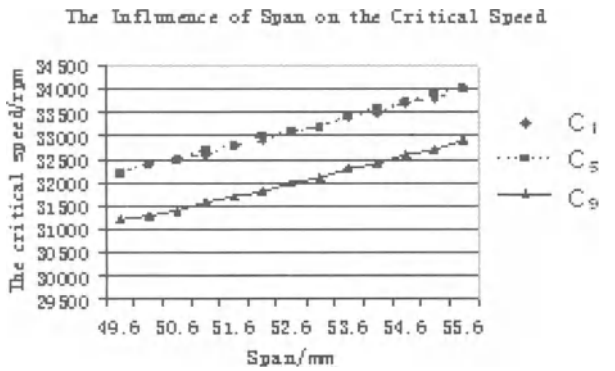

Fig. 2 The influence of span on the critical speed

For 3 computational cases the vibration spectrum cascades are shown in Fig. 3. It is obvious that the change set is almost uniform in 3 plots, and the amplitudes of fundamental frequency vibration persist in the range of all the velocity. The amplitudes of low frequency vibration do not appear until in the range of high velocity, which increase rapidly and exceed the amplitude of the fundamental frequency vibration in the identical velocity. When rotational speed sequentially increases, the amplitudes of low frequency vibration decrease suddenly. From the phenomenon it can be sure that the vibration characteristic is basically same in these conditions, and the amplitude of the fundamental frequency vibration keep stable. So the amplitude of vibration is mainly affected by the unbalance of rotor. Although the vibration rule is approximately uniform, the rotational speed of low frequency vibration threshold, namely rotational speed of oil whirl, increases gradually with augment of S(from 44000 rpm in Fig. 3(1) to 60000 rpm in Fig. 3(3)). It is helpful for the stability of rotor-bearing system to increase span, but the impact is not evident.

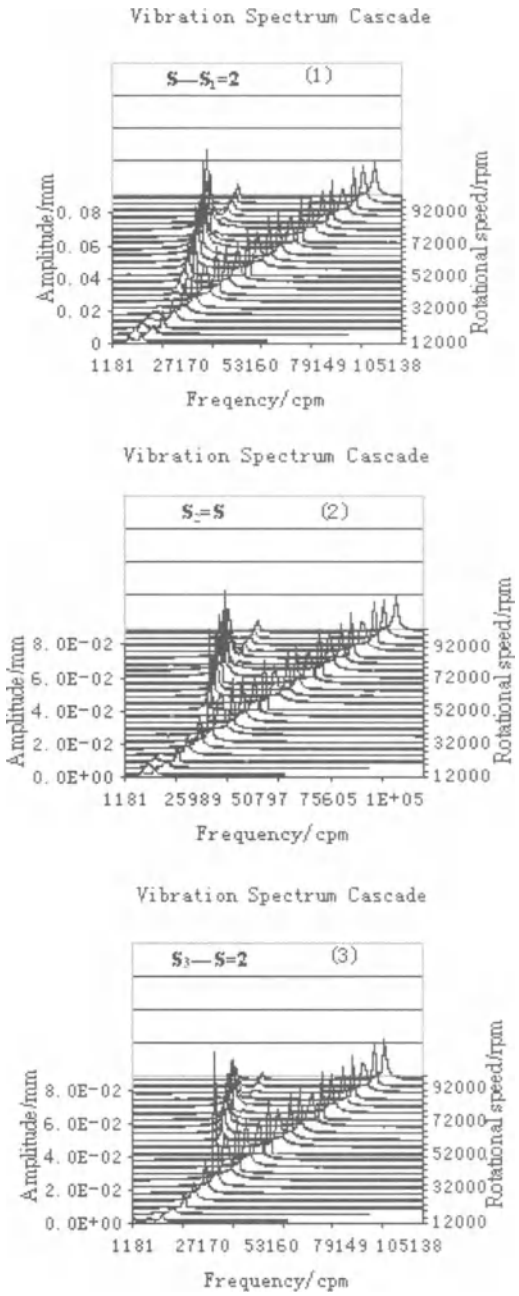

Fig. 3 The influence of span on the spectrum cascade

2.2 Influence of Width on Stability

In this computational model only the width of bearing is changed. The typical relative curses consisting of the width and the first critical speed at different stations are shown in Fig. 4. C_1 and C_5 decrease with augment of width, but C_9 increases in some sort.

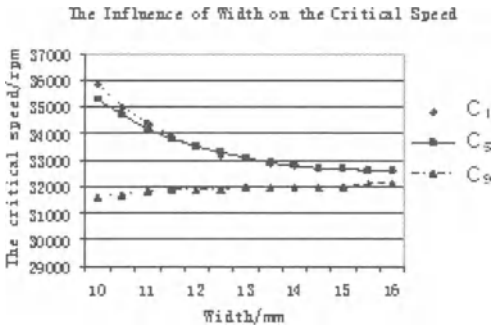

Fig. 4 The influence of width on the critical speed

The vibration spectrum cascades for the variation with width are shown in Fig. 5. There is the phenomenon of oil whirl in the range of all the velocity Except for the Fig. 5 (3) and Fig. 5 (5), and the amplitude is rather large. The amplitude of low frequency vibration increases firstly and decreases afterward with the augment of L, and the rotational speed of amplitude changing decreases gradually. From the Fig. 5 (3) it can be seen that the stability of rotor-bearing system is good. So, there is the optimal L correspond to the optimal instability of the rotor-bearing system.

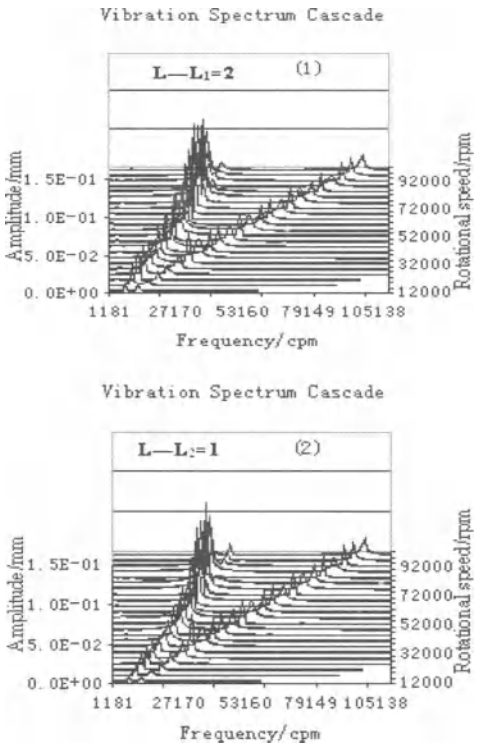

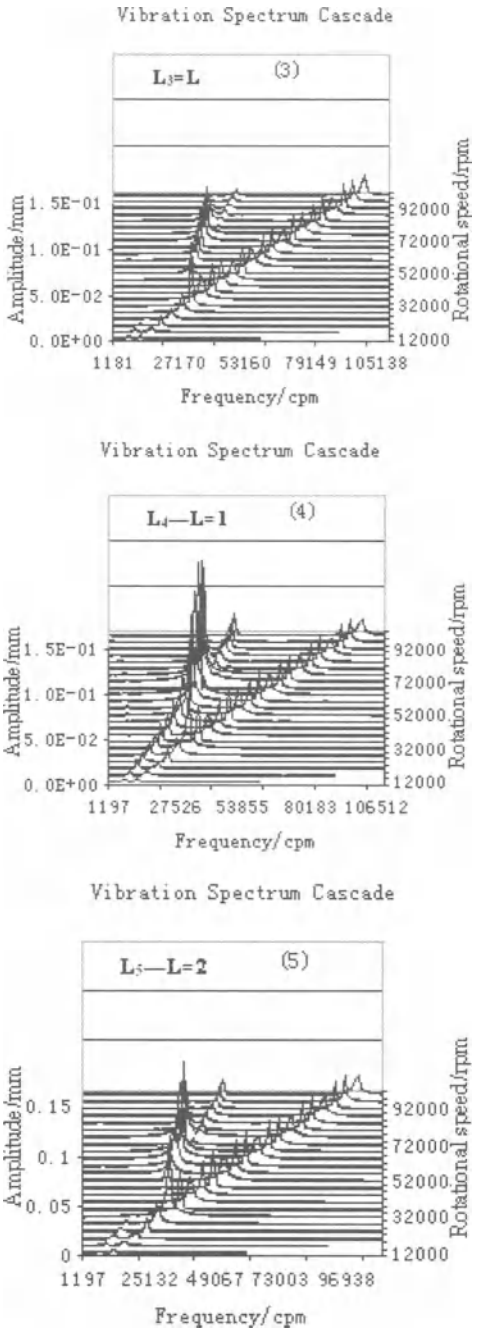

Fig. 5 The influence of width on thespectrum cascade

2.3 Influences of Gaps on Stability

In this computational model the inner and outer gaps of the bearing are changed. Fig. 6 shows the vibration spectrum cascades for the variation with gaps. The amplitudes of low frequency vibration do not appear until arriving at some speed and increase rapidly in Fig. 6(1) and Fig. 6(2). The frequency of this amplitude are changeless, which approach not the first critical speed but

the half of the speed. So the phenomenon of the oil whips is not the total effect of the inner and outer oil-films but is the single effect of the outer oil-film. The reason of this phenomenon may be that outer oil-film of which pressure is low is affected by the high-speed vortex coming from the inner oil-film of which pressure is high. It is so tiny that the amplitude of inner oil whirl is difficult to be observed. From the Fig. 6 (3) and Fig. 6 (4) the phenomenon of the inner oil whirl appear in the range of low speed, the reason is that the vortex loss is small comparatively caused by the tiny pressure difference between the inner oil-film and outer oil-film. The influence of outer oil-film is evident when the rotational speed is high, so inner oil whirl disappears and the outer oil whirl emerges. The effect of vibration is mainly affected by the fundamental frequency vibration in Fig. 6 (3), so the stability of rotor-bearing system is better in this condition. It can be found that the difference of δ_1 and δ_2 should not be large when the bearing is designed, or else the rotor-bearing system could be unstable easily.

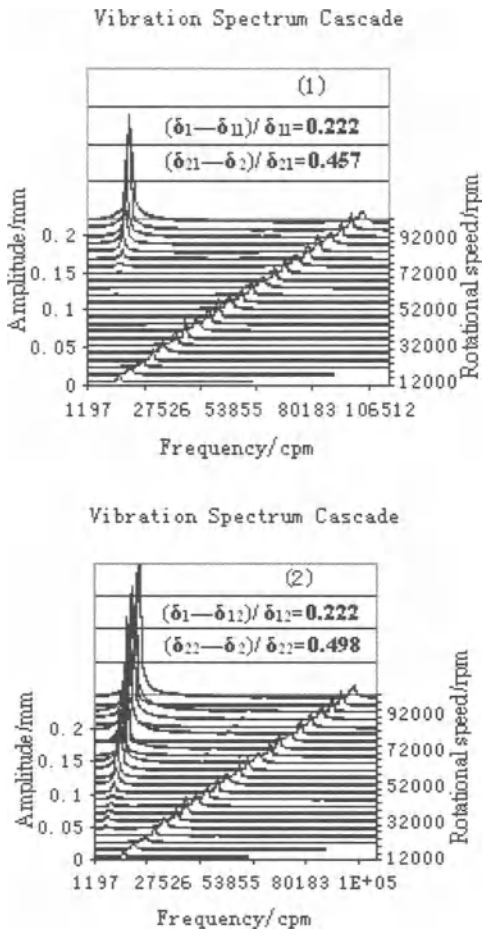

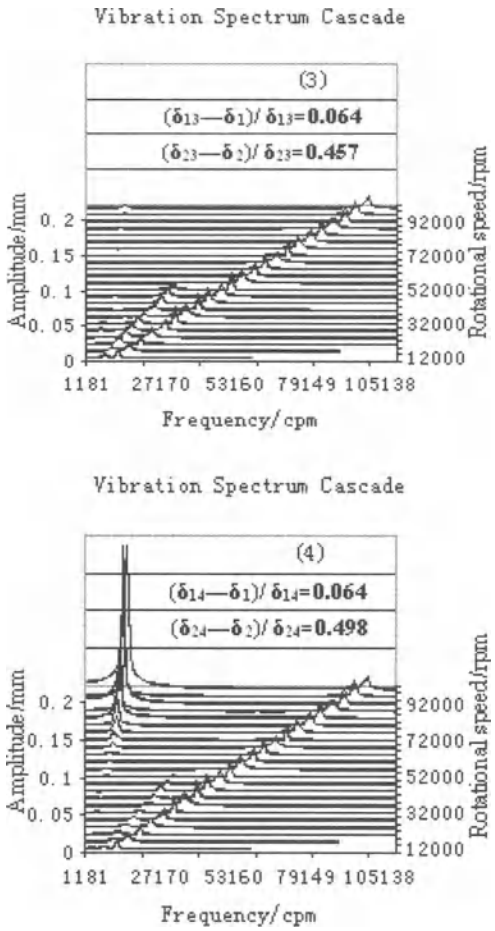

Fig. 6 The Influence of gap on the Spectrum cascade

3 Conclusions

The relation between the bearing parameters and the stability of the rotor is found according the computational results of the rotor-bearing system.

(1) The first critical speed at the nut station increases with the augment of span. Increasing the span will improve the performance of the stability of rotor-bearing system, but the impact is not evident.

(2) As the width of bearing increases, the first critical speed at the nut station is strongly influenced, and the total vibration trend of rotor-bearing system is that the amplitude decrease firstly and then increase. It is concluded that there is the optimal width correspond to the optimal instability of the rotor-bearing system.

(3) The influence of gaps on the stability is evident. The outer gap should be not too large compared with inner gap, or else the oil whip emerges easily.

Therefore, it is evident that the influence of inner and outer gaps on stability of rotor is the most important, and it should be considered firstly at the beginning of designing the rotor-bearing system.

Acknowledgements

The author is indebted to Ph.D.Candidate GAO Wei, Beijing University of Aeronautics and Astronautics, and Dr. LIU Yanming, Beijing Institute of Technology, for supplying the information.

References

Cui Ying, Liu Zhansheng et al, 2005, "Study on nonlinear stability for a 200 MW turbo-generator rotor-bearing system", *Chinese Journal of Mechanical Engineering*, Vol.41, pp.170 – 175

Shan Yingchun, Liu Xiandong, Zhang Hongting, 2006, "Vibration analysis and fault diagnosis of the supercharger rotor", Noise and Vibration Control

Guo Jianye, Lian Bin, 2005, "A study on design of the outer gap of floating bearing of automotive supercharger", Automobile Technology

Tanaka M, Hori Y. 1972, "Stability characteristics of floating bush bearing", Journal of Lubrication Technology, 93(3):248 – 259.

Li C.H., 1982, "Dynamics of rotor bearing systems supported by floating ring bearings", J of Lub Tech Trans ASME, 104(4): 469 – 477

The 4th International Symposium on Fluid Machinery and Fluid Engineering
November 24-27, 2008, Beijing, China
NO. 4ISFMFE-CH032

Investigation of the Meter Factor of Turbine Meter with Unsteady Numerical Simulation

Gang Chen[*1,2] Yulin Wu[1], Suhong Fu[2], Mingjie Li[3], Guangjun Cao[2]

[*1] Dept. of Thermal Engineering, Tsinghua University,
Tsinghua Garden, Haidian District, Beijing 100084, China
Tel: +86-10-6279-4735 / Fax: +86-10-6279-4735
E-mail: gang-chen05@tsinghua.edu.com
[2] Beijing Petroleum, Oil & Lubrication Institute, Beijing 102300,
[3] Tianjin Xinke Whole Set Instrument Meter Co.,Ltd
XiQing Development Zone, Tianjin, 300385,China

Abstract The torque balancing equations and the bearing drag torque were deduced in the paper, unsteady numerical simulation is carried out with RNG turbulence model and UDFs (User Defined Functions) in Fluent Code. The meter factors of the turbine meter at different flow rate are calculated by the unsteady numerical simulation. The influence of bearing drag torque is considered. Compared with the calibration experiment, the prediction results based on the numerical simulation showed good agreement. It makes clear that the possibilities to improve the accuracy of the meter and to predicate the meter factor by CFD.

Keywords turbine flow meter, meter factor, unsteady numerical simulation, bearing torque drag

Nomenclature

T_{dr}	driving torque on the impeller, [N·m]
T_i	hydraulic drag torque on the impeller, [N·m]
T_{dr}	blade tip clearance drag torque, [N·m]
T_b	bearing drag torque, [N·m]
T_h	hub fluid drag torque, [N·m]
T_{disk}	hub fluid drag torque, [N·m]
K_e	volumetric meter factor of turbine meter from calibration experiment, [rpm/L]
Err	error between numerical simulation and calibration experiment, [%]
f	pulse frequency from the turbine meter, [-]
Z	number of impeller blades, [-]
n	rotational speed of the impeller, [rpm]
M	hydraulic moment vector on the impeller, [N·m]
J	rotational inertia of the rotational system, [kg·m^2]
ω	angular velocity vector, [rad/s]
Q	volumetric flow rate, [m^3/h]
ρ	density of water, [kg/m^3]
ν_e	effective kinetic viscosity of water, [m^2·s^{-1}]
f	body force vector, [N]
r	radius vector from the rotational axis to the mass particle, [m]
R	vector from the origin to the mass particle
k	turbulent kinetic energy, [m^2·s^{-2}]
ε	turbulent dissipation rate, [m^2·s^{-3}]
μ	turbulent viscosity coefficient, [kg m^{-1}·s^{-1}]
μ_{eff}	effective viscosity coefficient, [kg m^{-1}·s^{-1}]
μ_t	eddy viscosity coefficient, [kg m^{-1}·s^{-1}]

1 Introduction

In a recent Product Research article on flowmeters, *Control Engineering* found that two technologies tied for first place among end users: turbine and magnetic flow meters. Turbine flow meter represents an old style technology, but it is still very popular in many applications and is available from a variety of manufacturers. In the right situations, they offer a useful combination of

simplicity, accuracy, and economy (*Control Engineering* 2007).

The technical structure of a turbine flowmeter is very simple: a turbine that is on a shaft coaxial with the pipe is placed in the liquid stream where passing process fluid flow through it. Since higher flow means higher velocity, the shaft rotates faster when there is more liquid. A sensor is mounted in the pipe wall where it can detect passing turbine blades. This creates electrical pulses that translate into liquid velocity which translate into flow. In order to get the uniform flow when fluid passes the turbine, the conditioners are installed before and after the turbine, the structure is showed in Fig. 1.

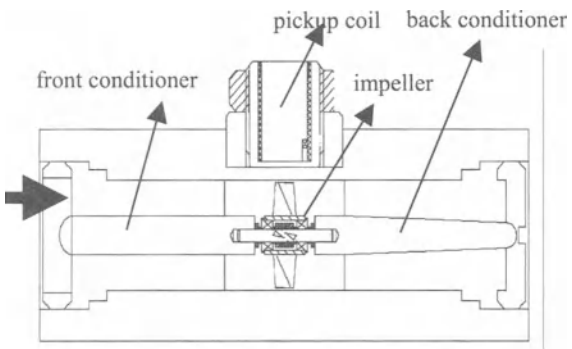

Fig. 1 Structure of turbine meter

Most the investigations on turbine flowmeter were done by analytically and experimental in the past years (R.C. Backer, 1993;).The most famous theory is done by Thompson (1970) and Tsukamoto(1984,1985), who bring forward the theory of torque balance, and analyzed the torque on the impeller from the foil theory. Y.Xu(1992) developed a prediction model to study the meter factor, and it showed the good agreement with the experiment. Also, Y. Xu (1993) simulated the separated leading edge flow and the trailing edge wake by shed vortices. A.F. Skea and A.W.R. Hall, (1999)investigated the effects of water in oil and oil in water on turbine flow meter by experiment, and also the viscosity and the inlet flow condition will influence its precision (Schmidts M, Marliani G, Vasanta Ram VI, 1998 and Backer, 1993).

Due to the development of fast digital computers, nowadays, the CFD studies are becoming the part of the design methodologies. Qin Hongxin etc. (1990, 1991) calculated the meter factor by Finite Element Analysis method, the results has good agreement with experiment. (Th. Huwener and E. von Lavante, etc, 2001 and Zheng Dandan and Zhang Tao, 2005).

In this paper, the analysis method of predicting the meter factor of the turbine meter is proposed based on the balance equation. The expression of bearing drag torque is deduced from the bearing theory. With the analysis method, the turbine flow meter is investigated by numerical simulation with CFD subsequently and the meter factor is deduced. Finally, calibration experiment has been carried out on the volume tube systems which can get the meter factor by experiment. The results confirm that the computational method in predicting the meter factor of turbine meter is feasible and effective and the influence of bearing drag torque on the predicting the meter factor is studied.

2 Analysis on Theory

The turbine meter consists of a helix type impeller which turns around the axis due to the flow in the pipe. In order to hold the impeller in the stream, there are two supports in the upstream flow and downstream flow, which is also called conditioner (Fig. 1). The impeller rotates along its axis when fluid flow through the conditioner and impeller. The rotational speed has close relation with the flow rate of the pipeline, which can be obtained by the magnetic pickup.

The meter factor of turbine is described by volumetric meter factor K as follow:

$$K = \frac{f}{Q} \tag{1}$$

where f is the pulse frequency, which can be described as the follows:

$$f = zn \tag{2}$$

where Z is the number of rotor blades and n is the rotational speed of the impeller.

From the equation, the meter factor K is the function of rotational speed, which should be obtained by calibration experiment. Meter factor K is only affected by meter structural parameter; While it is not affected by volumetric flow rate Q, density ρ, ect. So K can be regard as a constant value. But when considering the friction drag and other factors, K shows different value at different flow rate (Fig. 2).

When a turbine flow meter is applied in stable conditions (without any unsteady disturbances), all the torques acting on the impeller must balance each other all the time, so the rotor speed remains constant. The balance equation is as follows (Backer 1993):

$$T_{dr} = T_i + T_t + T_b + T_h + T_{disk} \tag{3}$$

where T_{dr} is the driving torque on impeller;

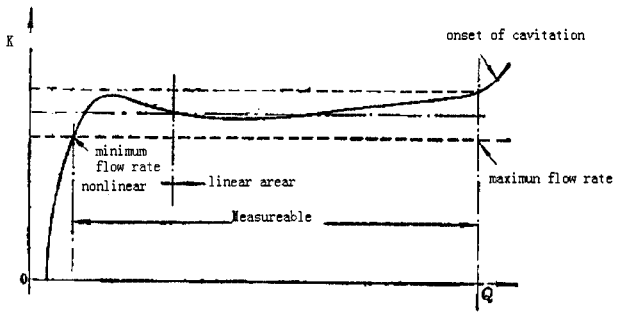

Fig. 2 Relation between meter factor K and flow rate Q

T_i is the hydraulic drag torque on impeller,

T_t is the blade tip clearance drag torque,

T_b is the bearing drag torque,

T_h is the hub fluid drag torque,

T_{disk} is the hub disc friction drag.

The hydraulic driving torque, the hydraulic drag torque and blade tip clearance drag torque can be calculated by numerical simulation. Compared with other torque, the three torque. T_b, T_h and T_{disk} are very small, so in the most study they are neglected in the balance equation. But in the numerical simulation, the drag torques T_h and T_{disk} are calculated and the influences of them are considering.

The bearing drag torque T_b could not solved by the numerical simulation, so we induced the expression of it, and the influence of it is considering in the predicting the meter factor. So in the paper two ways are investigated, one considering the bearing drag and the other one neglecting the bearing drag.

$$T_{dr} = T_i + T_t + T_h + T_{disk} \tag{4}$$

3 Bearing Drag Torque

The bearing drag torque is composed of two parts for rolling bearing (Xu Yuejin, 2007): Bearing drag torque from outer load and viscous bearing drag torque.

3.1 Bearing Drag Torque From Outer Load

The bearing drag torque from outer load is calculated by the expression:

$$M_1 = f_1 F_\beta d_m \tag{5}$$

where $d_m$is the diameter of the rolling bear,

f_1 is the friction coefficient for the rolling ball bearing, it is calculated by the function,

$$f_1 = x\left(\frac{F_s}{C_s}\right)^y \tag{6}$$

where F_s is the static load of the rolling bear; C_s is the rated static load of the rolling bear, they are offered by the bearing manufacture factory.

The coefficient of x and y is selected based on the bearing type, $x = 0.0003$ and $y = 0.4$.

In equation (5), the value of F_β is determined by magnitude and direction of the outer load, or rolling ball bear, it equals the radial load, and can be calculated by the CFD

$$F_\beta = F_r \tag{7}$$

where Fr is the radial load of the rolling ball bearing.

3.2 Viscous Bearing Drag Torque

The viscous bearing drag torque is calculated by the expression as follows,

$$M_v = 10^{-7} f_o (v_o n)^{2/3} d_m^{\ 3} \tag{8}$$

where v_o is the kinematics viscosity of lubricate oil for the bearing; n is the rotating speed of the bearing; f_o is a coefficient considering the type of bearing drag and lubrication model, in the paper $f_o = 5.5$。

4 Governing Equation and Simulation Methods

4.1 Governing Equation

From the analysis, we have known that in order to predict the turbine factor, we should known the rotational speed at given flow rate, at this time the torque on the impeller should be balanced. At the beginning, we give a relatively small rotational speed than the balance state. At the given speed and given flow rate we calculate the steady flow field, and the torque on the impeller can't balanced, then in the UDFs we increase the rotational speed gradually, until the torques on the impeller get balanced. This means that the torque on the impeller showed small than 10^{-4}. During this process, momentum equation of the rotational system is depicted as follows:

$$\boldsymbol{M} = J\frac{\mathrm{D}\boldsymbol{\omega}}{\mathrm{d}t} \tag{9}$$

where $\boldsymbol{M}$ is the hydraulic moment vector on the impeller, J is the rotational inertia of the rotational system, $\boldsymbol{\omega}$ is angular velocity vector.

As for water in the impeller, the governing equations are still Reynolds-averaged continuity and Navier-Stokes equations in the rotational relative coordinate. While there is still something different, the coordinate is being at an accelerated status. Through deduction, the governing

equations are as follows:

$$\nabla \cdot \boldsymbol{W} = 0 \tag{10}$$

$$\frac{\mathrm{D}\boldsymbol{W}}{\mathrm{d}t} = \boldsymbol{f} + \omega^2 \boldsymbol{r} - 2(\boldsymbol{\omega} \times \boldsymbol{W}) - \nabla p / \rho + \nabla \cdot \nu_e (\nabla \boldsymbol{W}) - \frac{\mathrm{D}\boldsymbol{\omega}}{\mathrm{d}t} \times \boldsymbol{R} \tag{11}$$

where $\boldsymbol{W}$ is the relative velocity vector in the Cartesian coordinates with the accelerated rotational speed; $\boldsymbol{f}$ is body force vector; ν_{eff} is kinetic viscosity coefficient of water; $\boldsymbol{r}$ is radius vector from the rotational axis to the mass particle; and $\boldsymbol{R}$ is vector from the origin to the mass particle.

From equation (11), it is seen that there is an additional source force $-\frac{\mathrm{D}\boldsymbol{\omega}}{\mathrm{d}t} \times \boldsymbol{R}$, which is decomposed into three components in directions of x, y, z in the Cartesian coordinate, which are $y\frac{\mathrm{D}\boldsymbol{\omega}}{\mathrm{d}t}$, $-x\frac{\mathrm{D}\boldsymbol{\omega}}{\mathrm{d}t}$ and 0 respectively.

4.2 RNG $k-\varepsilon$ Turbulence Model

Two-equation turbulence models are very widely used, as they offer a good compromise between numerical effort and computational accuracy. The most common two-equation turbulence models are standard $k-\varepsilon$, Realizable $k-\varepsilon$ and renormalization group (RNG) $k-\varepsilon$. In the paper we used the RNG $k-\varepsilon$ turbulence model in order to predicting the turbine meter, which is the most suitable turbulence model for simulation the turbine's vortex and separation (Chen Qingguang, Xu Zhong and Zhang Yongjian, 2003).

The RNG $k-\varepsilon$ turbulence model is similar with the standard $k-\varepsilon$ turbulence model, the k equation and ε transport equation are described as follows (Lam S H. 1992):

$$\rho\frac{\mathrm{D}k}{\mathrm{D}t} = \frac{\partial}{\partial x_j}\left(\alpha_k \mu_{eff}\frac{\partial k}{\partial x_j}\right) + G_k + G_b - \rho\varepsilon - Y_M \tag{12}$$

$$\rho\frac{\mathrm{D}\varepsilon}{\mathrm{D}t} = \frac{\partial}{\partial x_j}\left(\alpha_\varepsilon \mu_{eff}\frac{\partial \varepsilon}{\partial x_j}\right) + C_{1\varepsilon}\frac{\varepsilon}{k}(G_k + C_{3\varepsilon}G_b) - C_{2\varepsilon}\rho\frac{\varepsilon^2}{k} - R \tag{13}$$

The coefficient in the function is deduced from the RNG theory and as follows:

$$C_\mu = 0.085, C_{1\varepsilon} = 1.42, C_{2\varepsilon} = 1.68$$

$$\alpha_k = 1.393, \alpha_\varepsilon = 1.393$$

4.3 Simulation Method

Based on the governing equations in the accelerated rotational relative coordinate, we can calculate the flow field in the turbine meter. The numerical simulation is a unsteady turbulent, as it is in the accelerated rotational relative coordinate. That means that in the CFD process, we should consider the following two aspects to realize simulation of the unsteady transient: 1. Rotational speed of the impeller increases along with time based on equation (11). 2. Additional source forces should be added during the simulation process. According to the above consideration, UDFs (User Defined Functions) is made in Fluent 6.3, and the simulation process is depicted as Fig. 3. Steady result at rotational speed n=100 rpm is the initial simulation condition.

The governing equations are discredited with Finite-Volume-Method (FVM). In the unsteady simulation, "Segregated solver", "implicit formulation" and "unsteady time" method are adopted; Second-order implicit format for time item; second-order central difference format for source and diffusion item, second-order upwind format for convection item, and SIMPLEC method is used for velocity-pressure coupling solution. Standard wall function is adopted at the wall contacted with fluid.

4.4 Meshed model and Boundary Condition

In the simulation process, when the impeller is in rotating, its upstream and downstream flow conditioners are stationary. So the computational domain is composed of moving zone and stationary zone. And the entire turbine meter is divided into three parts, which consist of the upstream conditioners, impeller and downstream conditioners, between the three parts are the boundary "Interface", which can separate the two neighbor flow regions and transfer the vector between the two parts. The data of flow field can be transferred from one region to the other at the interface boundary efficiently.

In the study, the turbine meter is a helix type impeller (Fig. 4), whose outer diameter is 25mm. The length of the turbine meter, including the upstream conditioner and downstream conditioner (Fig. 5), is 138mm, and the pipe's inner diameter is 26mm. The function of the conditioner is to make the fluid flow into the impeller smoothly, in order to avoid the vortex and other phenomena which could decrease the precision of measuring the flow rate. Meshed turbine flow meter model is shown in Fig. 6. For

its high complexity of the computation region, it is plot with unstructured tetrahedron mesh of high applicability. Total number of computational meshes is about 0.96 million. In order to get the uniform velocity, 10 D upstream pipe and 10 D downstream pipe are added at the inlet and the outlet of meter respectively. The fluid medium of numerical computation is water at 20℃, which density and viscosity are 998.2kg/m^3 and 0.001003kg/ms respectively.

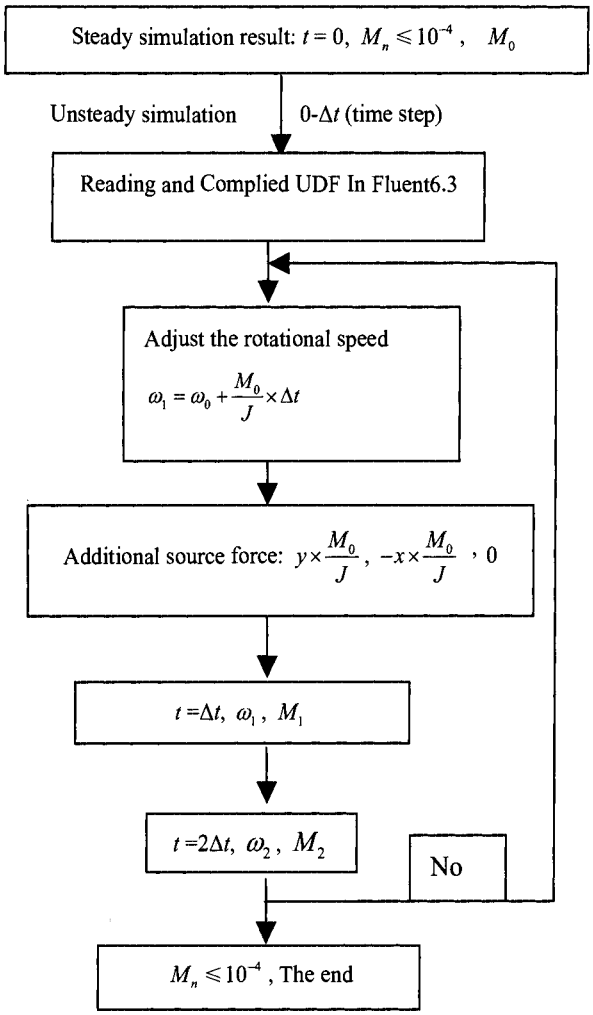

Fig. 3 Unsteady simulation process

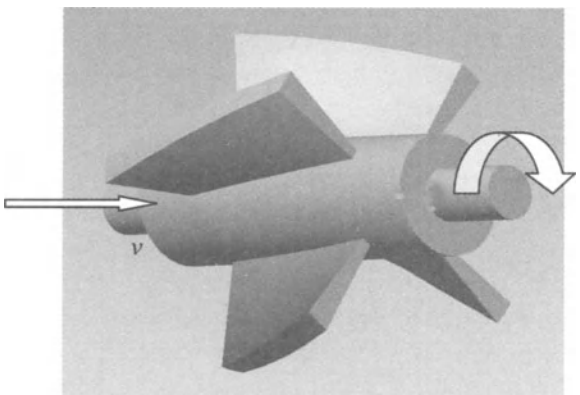

Fig. 4 Helix type impeller

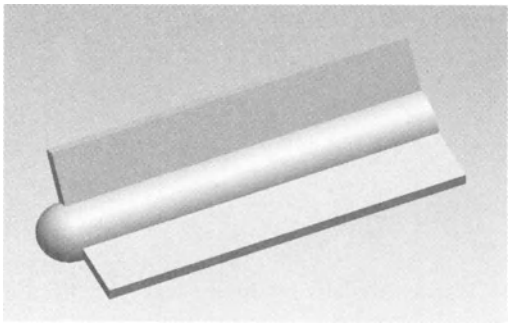

Fig. 5 Conditioner of the turbine flow meter

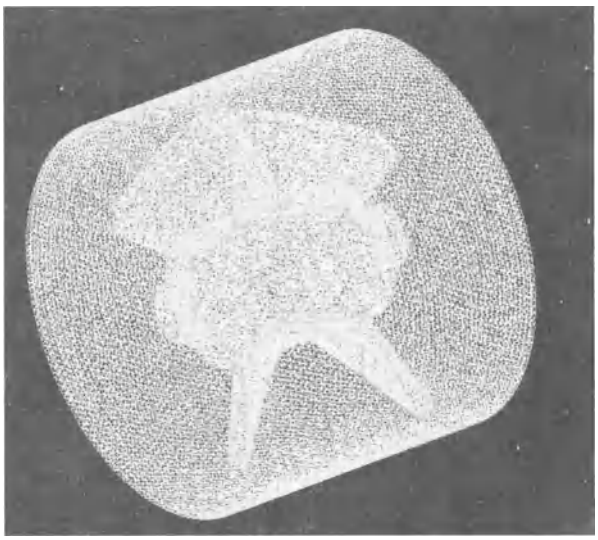

Fig. 6 Meshed the impeller

Inlet condition: mass flow rate, turbulent kinetic energy and turbulent dissipation rate;

Outlet condition: outflow;

Boundary condition: no-slip condition for the wall, and standard wall function for region near the wall; Steady simulation result under rated working condition as initial flow field of the unsteady simulation.

5 Comparsion Results Between Numerical Simulation and Calibration Experiments

5.1 Numerical Simulation Results

From the analysis of above, we know that in order to get the meter factor Kc from the numerical simulation, we should know the rotational speed of impeller at the given flow rate, that is the rotational speed at the impeller's torque balance. Through the CFD, we got the meter factor K_c at different flow rate and listed them in table 1. From the data, we get the idea that the turbine meter's meter factor keeps constant at different flow rate, That is the same with the meter factor Ke from the traditional experiment

methods. And the errors between CFD and experiment will be discussed in the latter section.

The total pressure distribution at surface of z = 0mm is showed in Fig. 7. The flow rate is $Q = 8m^3/h$, The unit of pressure contours is Pa, The last figure gives the pressure distribution at balance rotational speed. We can see the change of pressure with the rotating speed increase. As the rotating speed increase, the pressure near the pressure side is increasing, the lower pressure area decrease as the rotational speed increase. From the pressure around the impeller, the torque acted on impeller can be calculated.

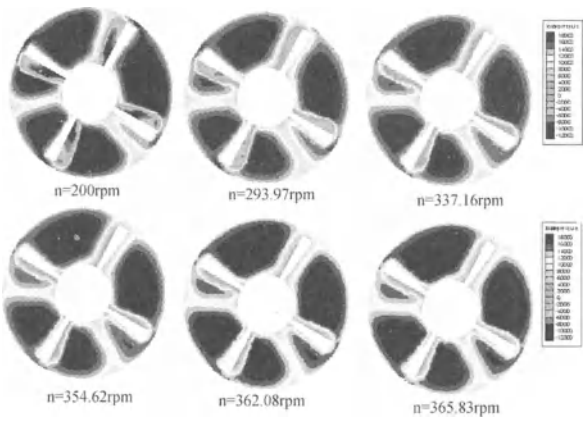

Fig. 7 Total pressure distribution at the surface of z=0mm at different rotating speed

5.2 Calibration Experiment Research

The calibration experiment has been implemented on the standard flow calibration facilities shown in Fig. 8.

Piston type Pipe prover (GB/T 13282—1991) is a standard system used to calibrate the turbine flow meter. Through the equipment the turbine's meter factor can be calculated because the fluid volume flow through the pipe prover is constant. In the calibration process, the computer records the constant volume from the piston type pipe prover and the number of pulse from the turbine meter at the same time at a given flow rate. The turbine's meter factor can calculate by the experiment. The calibration system in the experiment is a system authenticated by National Institute of metrology. P.R. China. Its precision is 0.0292% in calibration a turbine type flow meter. In order to improve the accuracy of the test, three times of measurement were carried out consequently at one test point. According to the standard of JB/T 9246-1999, the meter factor *K*e of every test point is calculated, and the values are listed in Table 1.

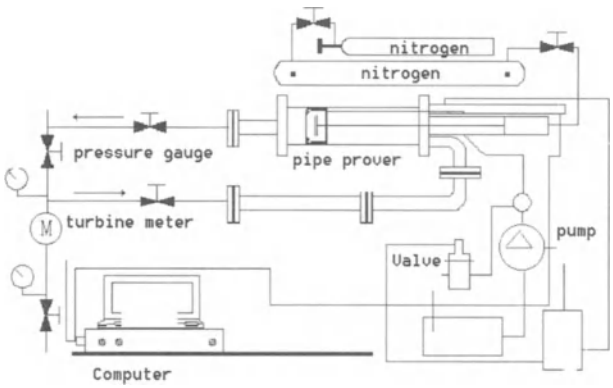

Fig. 8 Pipe prover system in calibrate the turbine flow meter

5.3 Comparison Between CFD and Experiment Research

Comparing simulation meter factor K_c with calibration experiment meter factor K_e, the error between them is also listed in Tab.1, which is calculated by the following formula:

$$Err = \frac{K_c - K_e}{K_e} \times 100\% \tag{14}$$

According to Table 1, the maximum relative error between simulative meter factor K_c and experimental meter factor K_e is about 8.91% if neglecting the influence of bearing

Table 1 Comparison between numerical result *K*c and experimental results *K*e

Volume flow rate Q (m^3/h)	K_e from Experimental (rpm/L)	K_c From CFD Considering bearing drag torque (rpm/L)	K_c From CFD No considering bearing drag torque (rpm/L)	Relative errors Considering bearing drag torque (%)	Relative errors No considering bearing drag torque (%)
11	102.57	103.80	110.25	1.20	7.48
8	102.87	104.23	110.32	1.32	7.24
5	103.26	104.58	110.45	1.28	6.97
3	103.69	105.19	111.00	1.45	7.05
2	105.46	106.73	114.85	1.21	8.90
1	107.90	109.91	114.79	1.86	6.39
0.4	124.20	127.43	131.89	2.60	6.19

drag torque, the error could be decreased if considering the bearing drag torque, which shows bearing drag torque has some influence on the predicting the meter factor, on other hand, we find the expression of the bearing drag torque deduced in the paper is correct. The method finding the meter factor through numerical simulation model is feasible, but it need more accurate in prediction the meter factor considering the bearing friction drag.

Figure 9 showed the meter factor comparison between the calibration experiment and CFD simulation. They showed the same trends, which it is constant when the flow is in fully developed turbulent flow, but at the low flow rate, such as $Q = 0.4m^3/h$, the meter factor showed lager than at other flow rate. It showed non-linear character of the the meter factor, which indicates that the bearing friction drag play a different role at different flow rate, and also at the lowest flow rate, the flow in the pipeline is in the turning point between laminar flow and turbulent flow. It is the same with the traditional analysis (Backer 1993).

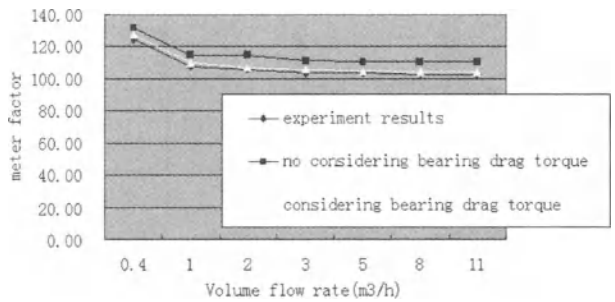

Fig. 9 Meter factor comparison betweenexperiment and CFD

6 Conclusions

In the paper, we introduced a method which can be used to predict the meter factor. The methods, which based on the theory of torque balance on impeller, are quite different from the traditional method in validation the meter factor by experiment. From the paper, three major conclusions are as follows:

(1) The methods on the basis of turbulence models and Fluent Code are feasible, and the precision should be improved in the future by considering the bearing friction drag. Comparing simulation meter factor K_c with experimental meter factor K_e, we found the simulation results are consistent with the experimental measurements. The maximum error is about 8.91%, and the trends are the same with the experiments.

(2) The influence on predicting the meter factor of bearing drag torque has been studied by the numerical simulation, which plays a important part on the turbine meter, the results showed the errors between numerical simulation and calibration haves decreased by considering the bearing drag torque, which also showed that the expression of bearing drag torque is correct in predicting the meter factor.

(3) The flow field of turbine meter is investigated by the rotational acceleration relative coordinate system. As the rotating speed increase, the pressure near the pressure side is increasing, the lower pressure area decrease as the rotational speed increase. From the pressure around the impeller, the torque acted on impeller can be calculated. In order to improve the accuracy of measuring the flow filed and exploit the application in multi-phase measurement, it is necessary to study the flow field more clearly.

Turbine meter is quite different from the pump and power turbine, the meter aims to cut through the fluid without disturbing the flow. But the unsteady flow conditions can affect its precision, such as the swirl flow in the pipeline. The method used in the paper can used as a useful tool to study the turbine meter in other area, such as the flow rate measuring in multiphase flow. Cavitations can occur in the turbine meter which needs study more deeply.

Acknowledgements

The program was supported by a grant from The National Natural Science Foundation of China (No. 10532010). The author would like to thank Senior Engineer Zhang JinLin from Tianjin Xinke Whole Set Instrument Meter Co., Ltd, who gives the opportunity to test the turbine meter on the pipe prover system.

References

A.F. Skea, A.W.R. Hall, Effects of water in oil and oil in water on single-phase flowmeters, Flow Measurement and Instrumentation, 10(1999) 151 – 157

Chen Qingguang, Xu Zhong and Zhang Yongjian, Application of RNG $k-\varepsilon$ models in numerical simulations of Engineering Turbulent flows, Chinese Quarterly Mechanics, Vol. 24, No.1, 2003 (in Chinese)

Lam S H. On the RNG Theory of Turbulence. Physics of Fluids, 1992, 4: 1007-1017

Qin Hongxin, Chen Kangmin, Zhao Xueduan, Analysis the flow field of impeller of turbine flow meter by FEA method: part1 and part2,Journal of Astronautic Metrology and Measurement, 1990, No.6 and 1991, No.2. (in Chinese)

R.C. Baker, Turbine Flowmeters: Theoretical and Experimental published Information, Flow measurement and Instrumentation. 4(1993) 123 – 144

Schmidts M, Marliani G, Vasanta Ram VI (1998) A study of the metering error of turbine flow meters caused by swirl in the flow. FLOMEKO 98, Proceedings:399 – 403

Thompson, R.E. and Grey, J. Turbine flowmeter performance model. J Basic Eng., Trans. ASME December (1970) 712-723

Tomas Humener, E. Von lavante, E.Ernst, Schieber W M, Numerical investigation and design optimization of a 2-Stage turbine flow meter, In: 31st AIAA Fluid Dynamics Conference & Exhibit, 11-14 June 2001, Anaheim, CA, AIAA2001-2928

Tsukamoto, H. Theoretical prediction of meter factor for a helical meter, University of Southampton Report No ME/84/1(1984)

Tuskamoto. H. and Hutton, S.P. Theoretical prediction of meter factor for a helical turbine flowmeter, Conference on Fluid Control and Measurement, Tokyo, Japan, September 1985

Xu Yuejin, Calculation of Moment of Friction of High speed Grease lubricated Rolling Bearing, JOURNAL OF ZHUZHOU TEACHERS COLL EGE, Vol . 12 No. 5, Oct . 2007, p18 – 21, (in Chinese)

Y. Xu, A model for the prediction of turbine flowmeter performance, Flow. Meas. Instrum. Vol.3 No.1, 1992, p37 – 43

Y. Xu, Calculation of the flow around turbine flowmeter blades, Flow. Meas. Instrum. Vol.3 No.1, 1992, p25 – 35

Zheng Dandan, Zhang Tao, Simulation research on turbine meters. Automation and instrumentation, 2005, vol.7, p29 – 33, (in Chinese)

Flow measurement calibration facility-Pipe prover, GB/T 13282-1991 (In Chinese)

Turbine flow meter, JB/T 9246-1999, Publishing Company of Mechanical Industrial Press (In Chinese)

Flow tutorial: Turbine flow meters, Control Engineering, 6/21/2007, http://www.controleng.com/article/CA6452632.html?q =Turbine+flowmeters

Author Index

Ahn SW	122-129
Alhussan K	201-205, 389-393
Ary BKP	122-129
Bakir F	20-26
Barr L	115-121
Benra FK	291-296
Böhle M	107-114
Bohn D	57-65
Bois G	153-160
Botas RM	1-7
Byun SJ	191-194, 195-200, 405-410
Caignaert G	153-160
Cao GJ	426-433
Cervonel A	80-88
Cheah KW	66-71
Chen CK	44-56
Chen CX	306-309
Chen G	426-433
Chen KM	173-178, 215-220, 279-284
Chen L	215-220
Chen Z	173-178
Chew JW	399-404
Cho HH	8-13
Cho YJ	316-321
Choi JW	122-129
Choi YD	316-321, 322-327
Cui Y	363-365
d'Agostino L	80-88
Dai R	173-178, 215-220
Dažin A	153-160
Deng HY	297-300
Dohmen HJ	291-296
Dupont P	153-160
Eynon P	115-121
Feng JJ	291-296
Feng ZP	383-388
Fu SH	426-433
Furukawa A	161-166
Gajic A	97-106
Galindo J	72-79
Ge XL	363-365
Guo PC	310-315, 341-344
Guo Y	206-214
He H	234-237, 238-241, 421-425
Hills NJ	399-404
Hong WR	415-420
Huang ZH	173-178
Hurault J	20-26
Husain A	185-190
Jeon SY	191-194
Ji JB	234-237
Jin JM	415-420
Jin Y	301-305
Kamemoto K	357-362
Kaneko M	285-290
Kang HK	122-129
Kang YM	377-382
Kato C	206-214
Kim BS	8-13
Kim CG	316-321, 322-327
Kim CK	405-410
Kim HJ	167-172, 262-267
Kim KM	8-13
Kim KY	185-190
Kim TS	377-382
Kim YJ	255-261
Kim YT	316-321, 322-327
Kouidri S	20-26
Kshirsagar JT	352-356
Kwon TH	262-267
Lee DH	8-13
Lee HJ	405-410
Lee JH	191-194
Lee TS	66-71
Lee YH	262-267, 316-321, 322-327
Li J	383-388
Li L	238-241
Li MJ	426-433
Li QS	33-43
Li SQ	273-278
Li SS	411-414
Li XB	179-184
Li Y	221-226, 371-376
Li ZH	268-272
Liu C	301-305
Liu DM	345-351
Liu SH	221-226, 335-340, 345-351, 371-376
Liu SY	394-398

Liu XB 345-351
Liu XN 130-136
Liu YM 394-398
Lu JL 145-152, 310-315
Luo XQ 145-152, 310-315, 341-344
Luo XW 221-226
Ma JM 328-334
Mao F 33-43, 137-144
Miyazaki K 285-290
Mohamad AA 27-32
Moon HK 377-382
Mu JG 297-300
Muntean S 89-96
Nakamura Y 285-290
Nakayama H 249-254
Nam SH 316-321
Nishi M 249-254, 335-340
Obi S 383-388
Ojima A 357-362
Okamoto M 249-254
Okuma K 161-166
Park IW 195-200
Pasini A 80-88
Pei W 238-241, 242-245
Ping SL 366-370
Rey R 20-26
Romagnoli A 1-7
Serrano JR 72-79
Shin MS 191-194, 195-200, 405-410
Shin S 8-13
Shukla SN 352-356
Spence S 115-121
Stark U 107-114
Su WD 33-43
Sun ZX 399-404
Sung NW 167-172
Susan-Regiga R 89-96
Tan ACC 14-19
Tan SG 306-309, 366-370
Tang FP 301-305
Tang T 279-284
Tang XL 328-334
Tiseira A 72-79
Torre L 80-88
Torregrosa A 72-79
Tsujimoto Y 44-56
Tsukamoto H 285-290
Tsunenari Y 161-166
Usami S 161-166
Wang BG 394-398
Wang FJ 328-334
Wang GY 179-184
Wang H 206-214
Wang LQ 306-309, 366-370
Wang XJ 246-248
Watanabe S 161-166
Winoto SH 66-71
Wu DZ 306-309, 366-370
Wu H 33-43
Wu JZ 33-43, 137-144
Wu NM 394-398
Wu RR 268-272, 415-420
Wu SF 335-340
Wu YL 335-340, 345-351, 371-376, 426-433
Xi G 145-152
Xing WD 273-278
Xu HY 221-226
Xu JZ 227-233
Xu SY 234-237
Xu SY 421-425
Xu Y 371-376
Xuan LJ 137-144
Yamade Y 206-214
Yan RQ 234-237
Yan X 383-388
Yang AL 215-220, 279-284
Yin ZQ 411-414
Yonezawa K 44-56
Yoon JY 167-172, 191-194, 195-200, 405-410
Yoshida K 249-254
Zhang DM 242-245
Zhang H 279-284
Zhang JH 242-245
Zhang JY 273-278
Zhang MD 179-184
Zhang MK 221-226
Zhang SC 297-300
Zhang SY 227-233
Zhang WB 130-136
Zhang YJ 227-233
Zhang Y 221-226
Zhao XJ 421-425
Zhao ZM 66-71
Zheng SH 297-300
Zheng SY 268-272
Zheng XB 310-315, 341-344
Zhuge WL 227-233